AD-A955 183

DTIC ACCESSION NUMBER

PHOTOGRAPH THIS SHEET

LEVEL

INVENTORY

①

THE AIR FORCE MANUAL FOR DESIGN AND ANALYSIS OF HARDENED STRUCTURES

DOCUMENT IDENTIFICATION

DISTRIBUTION STATEMENT A
Approved for public release;
Distribution Unlimited

DISTRIBUTION STATEMENT

ACCESSION FOR		
NTIS	GRA&I	☑
DTIC	TAB	☐
UNANNOUNCED		☐
JUSTIFICATION	Per letter 23 Aug 82	
BY	AFWL	
DISTRIBUTION /		
AVAILABILITY CODES		
DIST	AVAIL AND/OR SPECIAL	
A-1	25	

DISTRIBUTION STAMP

UNANNOUNCED

DTIC
ELECTE
DEC 1 0 1986
S D
D

DATE ACCESSIONED

DATE RETURNED

86 12 09 051

DATE RECEIVED IN DTIC

REGISTERED OR CERTIFIED NO.

PHOTOGRAPH THIS SHEET AND RETURN TO DTIC-FDAC

DTIC FORM 70A
MAR 86

DOCUMENT PROCESSING SHEET

PREVIOUS EDITION MAY BE USED UNT
STOCK IS EXHAUSTED.

AFWL-TR-74-102

AFWL-TR-
74-102
REV.
C.1

AD-A955 183

THE AIR FORCE MANUAL FOR DESIGN AND ANALYSIS OF HARDENED STRUCTURES

Robert E. Crawford
Cornelius J. Higgins
Edward H. Bultmann

Civil Nuclear Systems Corporation
Albuquerque, New Mexico 87102

October 1974 (Thirteenth printing, August 1981)

Final Report for Period June 1971 through May 1974

This and subsequent printings have unlimited distribution.

This research was sponsored by the Defense Nuclear Agency under Subtask Y99QAXSC157, Work Unit 04, Work Unit Title, "Strategic Structures Vulnerability/Hardening."

AIR FORCE WEAPONS LABORATORY
Air Force Systems Command
Kirtland Air Force Base, NM 87117

This final report was prepared by the Civil Nuclear Systems Corporation, Albuquerque, New Mexico, under Contract F29601-74-C-0018, Job Order WDNS3408 with the Air Force Weapons Laboratory, Kirtland Air Force Base, New Mexico. Dr. Maynard A. Plamondon (DEV) was the Laboratory Project Officer-in-Charge.

This technical report has been reviewed and is approved for publication.

Maynard A. Plamondon

MAYNARD A. PLAMONDON
Project Officer

FOR THE COMMANDER

John J. Osborn

JOHN J. OSBORN
Lt Colonel, USAF
Chief, Facility Survivability
Branch

William B. Liddicoet

WILLIAM B. LIDDICOET
Colonel, USAF
Chief, Civil Engineering Research
Division

DISCLAIMER NOTICE

UNCLASSIFIED
SECURITY CLASSIFICATION OF THIS PAGE (When Data Entered)

REPORT DOCUMENTATION PAGE

READ INSTRUCTIONS BEFORE COMPLETING FORM

1. REPORT NUMBER AFWL-TR-74-102	2. GOVT ACCESSION NO. / 3. RECIPIENT'S CATALOG NUMBER
4. TITLE (and Subtitle) THE AIR FORCE MANUAL FOR DESIGN AND ANALYSIS OF HARDENED STRUCTURES	5. TYPE OF REPORT & PERIOD COVERED Final Report June 1971 - May 1974 6. PERFORMING ORG. REPORT NUMBER
7. AUTHOR(s) Robert E. Crawford Cornelius J. Higgins Edward H. Bultmann	8. CONTRACT OR GRANT NUMBER(s) F29601-74-C-0018
9. PERFORMING ORGANIZATION NAME AND ADDRESS Civil Nuclear Systems Corporation Albuquerque, New Mexico 87102	10. PROGRAM ELEMENT, PROJECT, TASK AREA & WORK UNIT NUMBERS Program Element 62704H Project: 5710, WDNS
11. CONTROLLING OFFICE NAME AND ADDRESS Air Force Weapons Laboratory Kirtland AFB, NM 87117	12. REPORT DATE October 1974 13. NUMBER OF PAGES 1216
14. MONITORING AGENCY NAME & ADDRESS (if different from Controlling Office) Air Force Weapons Laboratory Kirtland AFB, NM 87117	15. SECURITY CLASS. (of this report) Unclassified 15a. DECLASSIFICATION/DOWNGRADING SCHEDULE

16. DISTRIBUTION STATEMENT (of this Report)

Same as block 16.

18. SUPPLEMENTARY NOTES

Much of the preliminary investigation pertaining to this manual was conducted by Mechanics Research Inc., Los Angeles, California under Contract F29601-71-C-0136.

19. KEY WORDS (Continue on reverse side if necessary and identify by block number)

Nuclear Weapon Effects	Structural Response
Airblast	Structure Media Interaction
Ground Shock	Shock Isolation
Cratering	

20. ABSTRACT (Continue on reverse side if necessary and identify by block number)

Methods and procedures are presented for estimating nuclear weapon effects pertinent to hardened structures and for designing and analyzing such structures subjected to these effects. Weapon yields considered range from kiloton through multi-megaton size. Overpressure levels which may be treated range from thousands of psi to less than 5 psi. The free-field environments covered include airblast, cratering and ejecta, ground shock and radiation. The treatment of radiation is restricted to methods for preliminary estimates of

DD FORM 1 JAN 73 1473 EDITION OF 1 NOV 65 IS OBSOLETE

UNCLASSIFIED
SECURITY CLASSIFICATION OF THIS PAGE (When Data Entered)

UNCLASSIFIED
SECURITY CLASSIFICATION OF THIS PAGE (When Data Entered)

ABSTRACT (Cont'd)

mechanical effects and shielding requirements. Methods are presented for translating the free-field environments into loads on, and motions of, aboveground, shallow buried and deep underground structures. The behavior and dynamic response of typical structures and structural elements are discussed. The protection of structure contents, including shock isolation, hardmounting, radiation and EMP shielding, is included. Emphasis throughout the manual is on basic understanding of phenomena and methods which are suitable for hand calculations. The methods are believed suitable for feasibility studies, preliminary designs and analyses and for establishing bounds on areas where more refined investigation may be necessary. A large number of examples illustrate the use of these methods. An extensive list of references for more detailed and/or sophisticated information and methods is also provided.

UNCLASSIFIED
SECURITY CLASSIFICATION OF THIS PAGE (When Data Entered)

CONTENTS

CONTENTS (Continued)

CONTENTS (Continued)

CONTENTS (Continued)

CONTENTS (Continued)

CONTENTS (Continued)

CONTENTS (Continued)

CONTENTS (Continued)

CONTENTS (Continued)

CONTENTS (Continued)

CONTENTS (Continued)

CONTENTS (Continued)

CONTENTS (Continued)

CONTENTS (Continued)

CONTENTS (Continued)

CONTENTS (Continued)

ILLUSTRATIONS

ILLUSTRATIONS (Continued)

ILLUSTRATIONS (Continued)

ILLUSTRATIONS (Continued)

ILLUSTRATIONS (Continued)

ILLUSTRATIONS (Continued)

ILLUSTRATIONS (Continued)

ILLUSTRATIONS (Continued)

ILLUSTRATIONS (Continued)

ILLUSTRATIONS (Continued)

ILLUSTRATIONS (Continued)

ILLUSTRATIONS (Continued)

ILLUSTRATIONS (Continued)

ILLUSTRATIONS (Continued)

ILLUSTRATIONS (Continued)

ILLUSTRATIONS (Continued)

ILLUSTRATIONS (Continued)

ILLUSTRATIONS (Continued)

ILLUSTRATIONS (Continued)

ILLUSTRATIONS (Continued)

ILLUSTRATIONS (Continued)

ILLUSTRATIONS (Continued)

ILLUSTRATIONS (Continued)

TABLES

TABLES (Continued)

TABLES (Continued)

SYMBOLS AND NOTATION

Section II

x_m	Maximum deflection
x_y	Yield deflection
μ	Ductility ratio

Section III

C	Constant for precursor dynamic pressure calculation (Fig. 3-41)
I	Overpressure positive phase impulse
I_q	Dynamic pressure positive phase impulse
K	Constant for precursor dynamic pressure calculation (Fig. 3-41)
P_o	Ambient pressure ahead of shock front
P_{so}	Peak overpressure
R	Range; engineering gas constant
T	Absolute temperature
U	Shock velocity
W	Weapon yield
a, b, c	Coefficients (Eq. 3-4)
c_o	Ambient speed of sound ahead of shock front
d, f	Coefficients (Eq. 3-11)
e	Natural logarithm base

SYMBOLS AND NOTATION (Continued)

g	Acceleration of gravity
k_p	Constant for precursor overpressure calculation (Fig. 3-31)
k_q	Constant for precursor dynamic pressure calculation (Fig. 3-39)
p(t)	Overpressure as a function of time
P_1, P_3, P_{3a}, P_4	Precursor peak overpressures (Fig. 3-31)
q(t)	Dynamic pressure as a function of time
q_1', q_2', q_3', q_4'	Precursor peak dynamic pressures (Fig. 3-39)
q_o	Peak dynamic pressure
t	Time
t_1, t_3, t_{3a}, t_4	Durations for precursor overpressure curves (Fig. 3-31)
t_1', t_2', t_3', t_4'	Durations for precursor dynamic pressure curves (Fig. 3-39)
t^*	Time after detonation
t_a	Time of arrival
t_o	Duration of overpressure positive phase
t_i	Duration of pulse that has same total impulse as actual overpressure-time curve
t_{oo}	Duration of pulse that has same slope as initial decay of actual overpressure-time curve
t_{50}	Duration of pulse that has same time ordinate as 50% of the peak value of the actual overpressure-time curve
t_i', t_{oo}', t_{50}'	Same relationships for dynamic pressure curves as t_i, t_{oo}, t_{50} have for overpressure curves

t_u	Duration of dynamic pressure positive phase
u	Air particle velocity
α, β	Coefficients (Eq. 3-4)
γ	Coefficient (Eq. 3-4); ratio of specific heats
δ, ϕ	Coefficients (Eq. 3-11)
ρ	Air Density
ρ_o	Ambient air density
τ	Parameter, $\frac{t^* - t_a}{t_o}$
ω	Parameter, $\frac{t^* - t_a}{t_u}$

Section IV

C_d	Drag coefficient (nominally about 0.6 for angular fragments)
C_N	A crater dimension (depth, radius or volume) after N detonatins
C_1	A crater dimension (depth, radius or volume) after one detonation
D	Ejecta depth
$\bar{D}$	Average ejecta depth at a given range
D_a	Apparent crater depth
D_{max}	Maximum ejecta depth (greater than 95% of the ejecta measurements at a given range)
D_{med}	Median ejecta depth (greater than 50% of the ejecta measurements at a given range)

D_{min}	Minimum ejecta depth (smaller than 95% of the ejecta measurements at a given range)
D_{Nmax}	Maximum crater apparent depth after N repeated detonations
D_{Nmin}	Minimum crater apparent depth after N repeated detonations
D_1	Apparent crater depth after 1 detonation
E_o	TNT surface burst cratering efficiency
F	Crater shape factor
HE	High explosive
HOB	Height of burst to center of charge mass
H_s	Scaled Height of Burst = $HOB/V_o^{1/3}$
I	Expected number of impacts per square foot of missiles with equivalent diameters between a_1 and a_2, where a_2 is the larger missile size
K	A geology dependent factor used in estimating a_m
M	Cummulative ejecta mass at all ranges with equivalent diameters less than or equal to the value a
M_a	Apparent crater mass
M_t	Total ejecta mass
N	Number of repeated detonations
NE	Nuclear explosive
P	Probability of one or more missiles with equivalent diameters between a_1 and a_2 impacting on an area with length ℓ_1 and width ℓ_2

SYMBOLS AND NOTATION (Continued)

R	Ground range
R_a	Apparent crater radius
R_{Nmax}	Maximum apparent crater radius after N repeated detonations
R_{Nmin}	Minimum apparent crater radius after N repeated detonations
R_o	A scaling range in missile impact velocity prediction
R_S	Scaled ground range = $R/V_a^{1/3}$
R_1	Apparent crater radius after 1 detonation
S	An exponent associated with repeated cratering relationships
SGZ	Surface ground zero
V	Apparent crater volume in layered geology
V_a	Apparent crater volume
V_i	Missile impact velocity
V_H	High yield nuclear surface burst apparent crater volume in layered geology
V_L	Apparent crater volume in base material of layered geology
V_o	Apparent crater volume due to TNT surface (half buried) burst
V_u	Apparent crater volume in surface material of layered geology
V_1	Apparent crater volume in top layer of two layer geology; apparent crater volume after 1 detonation

SYMBOLS AND NOTATION (Continued)

V_2	Apparent crater volume in second layer of two layer geology
V_3	Apparent crater volume in base material of two layer geology
V_{Nmax}	Maximum apparent crater volume after N repeated detonations
V_{Nmin}	Minimum apparent crater volume after N repeated detonations
W	Explosive yield (in equivalent TNT units)
a	Equivalent missile diameter
a_m	Maximum missile diameter found at a given range
a_{max}	Absolute maximum missile diameter from a cratering event
d	Layer depth in one layer geology
d_1	Depth of top layer in two layer geology
d_2	Depth of middle layer in two layer geology
f	A geology dependent factor relating total ejecta mass to apparent crater mass
k	Azimuthal distribution variable - percentage probability that a preselected ejecta depth will be greater than a randomly chosen ejecta depth at some range where D_{max} and D_{min} are known
m	Missile mass
m_m	Maximum missile mass at a given range
m_{max}	Absolute maximum missile mass from a cratering event

SYMBOLS AND NOTATION (Continued)

δ	Ejecta areal density
γ	Bulk unit weight of ejecta
γ_p	Preshot unit weight in cratered region
θ	Missile ejection angle
	Section V
C	Seismic or compression wave velocity
C_e	Effective wave velocity
C_i	Velocity of wave front, seismic velocity; compression wave velocity in i^{th} layer
C_L	Loading wave velocity; peak stress velocity
C_p	Compression wave (dilatation wave, P-wave) velocity
C_s	Shear wave (distortional wave, S-wave) velocity
E	Modulus of elasticity
G	Shear modulus of elasticity
H	Layer depth; a horizontal ground shock component
H_i	Thickness of i^{th} layer
$I(t)$	Impulse-time history
I_m	Total airblast impulse
K	Bulk modulus of elasticity; earth pressure coefficient
K_a	Coefficient of active earth pressure
K_o	Coefficient of earth pressure at rest, ratio of principal stresses in uniaxial strain

SYMBOLS AND NOTATION (Continued)

K_p	Coefficient of passive earth pressure
M	Constrained modulus
M_i	Initial tangent modulus
M_L	Loading modulus, constrained modulus
M_u	Unloading modulus
P_{so}	Peak overpressure
ΔR	Difference between ground range of interest and range at which outrunning begins
R	Range; slant range
T_2	Characteristic time of outrunning wave form
U	Airblast shock front velocity
V	A vertical ground shock component
V_a	Apparent crater volume
W	Yield
W_e	Equivalent yield
Z	Depth
ΔZ	Increment in depth
a	Acceleration
a_{max}	Maximum acceleration
d	Displacement
d_h	Peak horizontal crater-induced displacement
d_{hp}	Permanent horizontal crater-induced displacement
d_{max}	Maximum vertical displacement

SYMBOLS AND NOTATION (Continued)

d_r	Residual vertical displacement
Δd_r	Residual vertical compression in depth increment ΔZ
d_z	Vertical displacement
f_1, f_2, f_3	Generalized scaling relations for direct-induced ground shock
$i(\tau)$	Normalized impulse-time history
$p(t)$	Overpressure-time history
$\bar{p}(\tau)$	Normalized overpressure-time history
r	Strain recovery ratio
t	Time
t_a	Arrival time
t_d	Total duration of outward phase of radial direct-induced particle velocity pulse
t_i	Time of arrival of wave front
t_o	Total positive phase duration of overpressure
t_p	Rise time to peak crater-induced displacement
t_r	Rise time
v	Peak particle velocity
v_h	Peak crater-induced horizontal particle velocity
v_m	Peak outrunning particle velocity
v_{max}	Maximum particle velocity
w	Vertical displacement
x	Distance along ground surface from point of excitation to detector in seismic survey

SYMBOLS AND NOTATION (Continued)

β_i	Angle between airblast-induced incident ground shock front and ground surface
β_L	Angle between airblast-induced peak ground shock front and ground surface
γ	Unit weight
ϵ	Compressive strain
ϵ_{max}	Maximum compressive strain
ϵ_z	Vertical strain
ϵ_r	Residual strain
ν	Poisson's ratio
ρ	Mass density
σ	Normal stress
σ_h	Horizontal stress
σ_i	Incident stress
σ_{max}	Maximum stress
$\overline{\sigma_{max}}$	Average maximum vertical stress reached in depth increment ΔZ
σ_r^L	Reflected stress due to layer interface reflection
σ_r^S	Reflected stress due to ground surface reflection
σ_t	Refracted or transmitted stress
σ_v	Vertical stress
σ_z	Vertical stress
τ	Normalized time
ψ	Ratio of acoustic impedances

SYMBOLS AND NOTATION (Continued)

Section VI

A	Coefficient in Eq. 6-6
B	Coefficient in Eq. 6-6
D_n	Neutron dose
D_γ	Gamma dose
E_i	Incident electric field
E_o	Coefficient in Eq. 6-6
E_1	Induced voltage without EMP shielding
E_2	Induced voltage with EMP shielding
F	Integrated X ray flux on a surface
Q	Integrated thermal flux
R	Range, slant range
SE	Effectiveness of EMP shield in terms of field attenuation in decibels
T	Transmission factor for thermal radiation
W	Yield
Y_r	Radiant yield
a	Coefficient in Eq. 6-6
$dB(\omega)$	Energy content, expressed in decibels, of that portion of the incident electric field having frequency ω
f	Fission yield fraction
t	Time
y	Coefficient in Eq. 6-6

SYMBOLS AND NOTATION (Continued)

α	Effective amplification of yield
δ	Coefficient in Eq. 6-6
γ	Mean free path of gamma radiation
μ	Mass absorption coefficient for X radiation
ρ	Mass density of air
ω	Frequency (in radians) of electric field

Section VII

A	Projected area of an object perpendicular to the air flow for drag or parallel to the airflow for lift; area of a structure roof or foundation
A_B	Area of structure foundation
A_E	Embedded area of front and back face of aboveground structure
A_s	Projected area of a surface perpendicular to air flow for drag or parallel to air flow for lift
A_T	Area of structure roof
B_s	Bulk modulus of elasticity at constant entropy
B_t	Bulk modulus of elasticity at constant temperature
C	Outside perimeter of a structure in a plane parallel to the ground surface
C_{db}	Drag coefficient for back surface of an object
C_{df}	Drag coefficient for front surface of an object

SYMBOLS AND NOTATION (Continued)

C_{dr}	Drag coefficient for roof of an object
C_i	Seismic velocity
C_L	Loading wave velocity of medium
C_o	Ambient speed of sound in air; drag or lift coefficient for an object
C_p	Heat capacity
C_r	Airblast rarefaction front velocity after reflection
C_s	Shear wave velocity of medium; drag or lift coefficient for a surface
C_s^i	Propagation velocity of shear stresses of low intensity
C_1	Loading wave velocity of impacting ejecta missile material
C_2	Loading wave velocity of structure element material
D	Cylinder diameter; base dimension of a dome or arch; depth of foundation embedment for aboveground structure
F_A	Total vertical load on region A of horizontal cylinder approximation (Fig. 7-47)
F_B	Total vertical load on region B of horizontal cylinder approximation (Fig. 7-47); total horizontal load on exposed back face of an aboveground structure
F_B'	Total horizontal load on embedded back face of an aboveground structure
F_F	Total horizontal load on exposed front face of an aboveground structure

---

SYMBOLS AND NOTATION (Continued)

F_F'	Total horizontal load on embedded front face of an aboveground structure
F_H	Total horizontal load on front face of a surface flush structure
F_H'	Total horizontal load on back face of a surface flush structure
F_O	Total drag or lift on an object
F_P	Limiting value of F_B' for horizontal strains $\geq 5\%$
F_R	Total load on the roof of an aboveground structure
F_S	Total drag or lift on a surface; total interface shear force acting on a structure
F_{SM}	Maximum allowable value of the interface shear force on a structure
H	Structure height; height of rectangular underground opening
H_o	Height of rectangular underground opening
I	Total impulse
K	Strain concentration factor
K_o	Coefficient of lateral earth pressure
L	Structure length; dimension of structure in direction of airblast propagation; approximate radiation deposition depth
M	Structure mass; mass of impacting ejecta missile; a parameter defining the stress field at large distances from underground openings
M_L	Loading modulus in uniaxial strain

SYMBOLS AND NOTATION (Continued)

M_u	Unloading modulus in uniaxial strain
N	Total normal force acting on foundation or sides of a structure
p_c	Uniform radial stress component of simplified aboveground dome or arch loading
p_{dm}	Maximum stress of drag component of simplified aboveground dome or arch loading
p_{in}	Maximum stress of initial component of simplified flexural loading for an aboveground arch or dome
p_m	Maximum pressure of vertical pressure time history on the roof of an aboveground or surface flush structure
p_{max}	Peak shock pressure due to thermal energy deposition
p_o	Ambient air pressure
p_{ro}	Total reflected pressure due to airblast
Δp_{ro}	Peak reflected pressure above the peak overpressure
p_{so}	Peak overpressure
$p_{so}(t)$	Overpressure-time history
p_1, p_2	Characteristic pressures associated with airblast loadings on arches and domes
Q	Amount of radiation deposited
$Q(X)$	Radiation deposition profile as a function of distance into material
Q_{max}	Maximum value of Q(X)
R	Cylinder radius

SYMBOLS AND NOTATION (Continued)

S	Stagnation distance; least distance from stagnation point on the face of a structure to the edge of the structure
S_v	Vertical stress in free-field at a large distance from an underground opening
T_{eq}	Equilibrium temperature
T_o	Ambient temperature
U	Airblast shock front velocity
U_r	Reflected shock velocity with respect to a point fixed in space
$\overline{U_r}$	Reflected shock relative velocity with respect to air
W	Least dimension of a buried structure roof; width of an underground opening in rock
W_o	Width of an underground opening in rock
z_e	Effective free-field depth corresponding to the late-time vertical velocity decay of an aboveground structure
z_s	Depth to buried structure roof
a	Unit adhesion between foundation and soil
c	Unit cohesion of soil
c_ℓ	Longitudinal sound speed in material
c_t	Transverse sound speed in material
d	Distance in front of a reflecting surface to which a reflection persists
e	Base of the natural logarithm

k	Constant in Eq. 7-1; multiplying factor in Eq. 7-12; thermal conductivity
$p(t)$	Overpressure-time history; vertical pressure-time history on an aboveground or surface flush structure roof
$p_f(t)$	Flexural component of simplified loading on an aboveground arch or dome, consisting of initial component, $p_{f1}(t)$, and a drag component, $p_{f2}(t)$; airblast pressure acting on the exposed front face of an aboveground rectangular structure
$p_{f1}(t)$	Initial flexural component of simplified loading on an aboveground arch or dome
$p_{f2}(t)$	Flexural component of simplified loading on an aboveground arch or dome due to drag
$q(t)$	Dynamic pressure-time history; vertical pressure due to airblast acting on the soil behind an aboveground structure
r	Strain recovery ratio
s	Constant in Eq. 7-1
$\|sgn(\ )\|$	Notation indicating that the sign of the quantity in parentheses is to be used
t_d	Duration of reflection on a structure
t_i	Time at which rarefactions begin to erode a reflected shock
t_o	Arrival time at a point of interest; total duration of an applied pressure or stress; total duration of stress wave in a structural member due to an impacting ejecta missile
t_r	Rise time
t_s	Stagnation time

t_1, t_2	Characteristic times associated with loadings on surface flush structural elements (Fig. 7-17)
t_1, t_2, t_3	Characteristic times associated with loadings on aboveground arches (Figs. 7-18 and 7-19) and domes (Fig. 7-22)
u	Air particle velocity associated with incident overpressure
v	Peak direct-induced radial particle velocity; structure rigid body velocity
Δv	Difference between free-field and structure velocity
v_{ff}	Free-field particle velocity at depth of a point of interest
v_H	Horizontal rigid body structure velocity
v_m	Maximum structure rigid body velocity
v_o	Velocity of impacting ejecta missile
w	Structure displacement in radial direction
$\dot{w}$	Structure velocity in radial direction
w_o	Free-field displacement in radial direction
$\dot{w}_o$	Free-field particle velocity in radial direction
x	Horizontal distance from aboveground structure center of gravity to rear foundation edge; distance into material
α	Angular coordinate defining location on an arch (Fig. 7-18 and 7-19); a phase of iron (Fig. 7-56)
α_v	Volumetric coefficient of thermal expansion

β	A phase of iron (Fig. 7-56)
γ	A phase of iron (Fig. 7-56)
δ	Normalized mass ratio (Eq. 7-23)
ϵ	Peak direct-induced radial strain
ϵ_u	Rock strain at ultimate strength in unconfined compression
θ	Spherical coordinate defining location on an aboveground dome (Fig. 7-23)
μ	Mass absorption coefficient
ρ	Mass density
ρ_1	Mass density of impacting ejecta missile
ρ_2	Mass density of structural element material
σ_{ff}	Free-field stress at the depth of a point of interest
σ_m	Peak stress of ground shock stress wave incident on a buried structure
σ_{max}	Peak stress of the stress wave induced in a structural element due to an impacting ejecta missile
σ_o	Free-field radial stress
σ_r	Total radial stress on a buried cylinder; reactive stress on a structure foundation
σ_t	Total stress on the roof of a buried rectangular structure
τ	Transit time of airblast shock across an arch or dome; thermal shock coefficient; normalized time (Eq. 7-23)
τ_m	Normalized time at which maximum structure rigid body velocity occurs

τ_{max}	Limiting value of shear stress that may be developed on a structure surface which bears against soil
ϕ	Half the central angle of an arch or dome; angle of internal friction of soil
$\bar{\phi}$	Angle of foundation friction

Section VIII

A	Cross sectional area of individual reinforcing bar, steel member or circular ring; gross cross sectional area
A_c	Cross sectional area of concrete section in compression
A'_c	Area of core of spirally reinforced concrete member measured to the outside diameter of the spiral
A_g	Gross cross sectional area of a section
A_L	Loaded area of slab producing shear
A_s	Cross sectional area of tension steel; area of steel in the column on the compression edge of a shear wall
A''_s	Cross sectional area of transverse spiral reinforcement
A'_s	Cross sectional area of compression steel
A_{sH}	Area resisting shear (Fig. 8-22)
A''_{sH}	Cross sectional area of transverse rectangular hoop reinforcement
A_{st}	Cross sectional area of longitudinal reinforcing steel in concrete member under axial load

SYMBOLS AND NOTATION (Continued)

A_v	Total cross sectional area of web reinforcing over distance s
$A_{v\|\|}$	Total cross sectional area of longitudinal web reinforcing over distance $s_{\|\|}$
C	Column influence factor for a shear wall
C_c	Maximum value of slenderness ratio in plane of bending to insure development of a plastic hinge at ultimate loading
C_m	Factor defined by Eq. 8-31
C_v	Empirical constant in Eq. 8-61
D	Outside diameter of a spirally reinforced circular member; diameter of an individual reinforcing bar
D"	Diameter of concrete confined by spiral or circular hoops
E	Modulus of elasticity
E_c	Modulus of elasticity of concrete corresponding to the slope of the initial portion of the stress-strain curve
E_p	Modulus of elasticity of backpacking
E_s	Modulus of elasticity of steel
F	Moment modification factor defined by Eq. 8-28
H	Shear wall height to center of top beam
I	Moment of inertia; moment of inertia about centroid of horizontal section through a shear wall including the frame but ignoring all reinforcement
I_c	Moment of inertia of concrete section
K	Winkler-Bach curvature correction factor for curved members

SYMBOLS AND NOTATION (Continued)

K_f	Factor defined by Eq. 8-124
K_o	Coefficient of lateral earth pressure
K_s	Effective length factor for computing slenderness ratio
L	Unsupported length of a member; length of slab or beam; clear span of a slab or beam; shear wall length center-to center of columns
L_d	Required bond development length for deformed bars in tension
M	Bending moment
M'	Moment at critical shear section of reinforced concrete member
M"	Moment at critical shear section of reinforced concrete member modified to account for axial thrust
M_B	Moment at Point B of a circular ring (Fig. 8-25)
M_{Be}	Moment at Point B of a circular ring at first yield (Fig. 8-25)
M_{Bp}	Fully plastic moment capacity at point B of circular ring (Fig. 8-25)
M_b	Moment at the balance point of the interaction diagram for a reinforced concrete member
M_e	Moment capacity of a circular ring at first yield
M_{Lc}	Ultimate moment capacity per unit width of two-way slab at the center of and in the direction of the long span
M_{Le}	Ultimate moment capacity per unit width of a two-way slab at the supports and in the direction of the long span

M_m	Modified moment which accounts for reduced member strength due to large slenderness ratio
M_{max}	Maximum probable moment in a circular ring
M_n	Maximum moment resistance of steel member in the absence of axial load
M_p	Ultimate moment capacity of a member
M_p^c, M_p^e	Fully plastic moment capacities at the center and ends, respectively, of a beam; ultimate moment capacities per unit width of slab at the center and edge, respectively, of a circular slab
M_{sc}	Ultimate moment capacity per unit width of a two-way slab at the center and in the direction of the short span
M_{se}	Ultimate moment capacity per unit width of a two-way slab at the supports and in the direction of the short span
M_1, M_2	Smaller and larger values, respectively, of end moments acting on a member
M_θ	Internal moment in a circular ring at position θ
N	Axial thrust
N_c	Total normal load resistance at first cracking of a shear wall with no shear load
N_c'	Total normal load resistance at first cracking of a shear wall under combined loading
N_u	Normal load resistance at yield of reinforcement of a shear wall with no shear load
N_u'	Normal load at yielding of reinforcement of a shear wall under combined loading
P	Axial load or thrust; panel influence factor for shear wall

P_b	Axial load at the balance point of the interaction diagram for a reinforced concrete member
P_c	Critical buckling load (Eq. 8-29)
P_e	Thrust capacity of a circular ring
P_f	Concentrated load resistance of member based on flexural capacity
P_{max}	Maximum thrust in a circular ring
P_o	Limiting strength of a reinforced concrete member under pure axial load
$\overline{P_o}$	Maximum total pressure on circular ring $(q + \bar{p})$
$\overline{P_{oE}}$	$\bar{p}_o$ at first yield of circular ring
$\overline{P_{oc}}$	$\bar{p}_o$ at collapse of circular ring
P_s	Concentrated load resistance of member based on shear capacity
P_u	Axial load capacity under combined axial load and bending
P_y	Maximum axial load resistance of steel member in the absence of bending
P_θ	Internal thrust in a circular ring at position θ
Q	Parameter defined in Eq. 8-126
R	Radius of a circular slab; radius to mid-thickness of a circular ring; clear span radius of a composite closure
R_c	Horizontal static load resistance of a shear wall at first cracking
R_c'	Horizontal static load resistance of a shear wall at first cracking under combined loading

R_i	Inside radius of a circular ring; inside radius of a backpacked cavity liner
R_o	Outside radius of a circular ring; radius of undeformed cylindrical rock cavity in rock
R_s	Slenderness ratio
R_u	Ultimate horizontal resistance of a shear wall with no normal load
R_u'	Ultimate horizontal resistance of a shear wall under combined loading
S, S_1, S_2	Elastic stress factors
T_α	Compressive membrane force per unit width of an arch or dome in the direction of coordinate α
$T_{\alpha\theta}$	Shearing force per unit width in a dome shell at the foundation
T_θ	Compressive membrane force per unit width of a dome in the direction of coordinate θ
V'	Shear force at critical section of a reinforced concrete member
V_u	Total shear capacity ($V_{uc} + V_{us}$)
V_{uc}	Ultimate shear capacity of concrete
V_{us}	Shear capacity contributed by shear (web) reinforcing
V_θ	Internal shear in a circular ring at position θ
Y, Y_1, Y_2	Inelastic stress factors
Z	Plastic section modulus
Z_t	Plastic section modulus of trial section

a	Pitch of transverse spiral reinforcement; spacing of rectangular hoop reinforcing; width over which applied uniform load acts on a beam or one-way slab; center-to-center distance between adjacent slabs; inward displacement of rock cavity (Fig. 8-31)
b	Width of member; width of flange of a concrete I or T section; inward displacement of rock cavity (Fig. 8-31)
b'	Width of web of concrete I or T section
c	Half-thickness of wall of circular ring
d	Effective depth of a member; distance from extreme compression fiber to center of tensile steel; diameter of the circle through the centers of longitudinal reinforcing in a circular member
d'	Depth from extreme compression fiber to center of compression steel
d_w	Depth of web of steel member ($h - t_f$)
e	Eccentricity of axial load from the centroid of the tensile reinforcement of a symmetrically reinforced rectangular concrete member
e'	Eccentricity of axial load from the plastic centroid of a symmetrically reinforced rectangular concrete member
e_b	Eccentricity measured from the plastic centroid of a reinforced concrete member for the balanced case
f_a	Allowable axial stress in steel member in absence of bending
f_{ax}	Allowable axial stress in steel member when member is restrained from bending in the weak direction

f_{ay}	Allowable axial stress in steel member when member is not restrained from bending in the weak direction
f'_c	Unconfined compressive strength of concrete
f_{cu}	Average compressive stress in concrete at ultimate strength
f_p	Parameter defined in Eq. 8-44
f_r	Residual stress due to casting of a section
f''_s	Stress in transverse spiral reinforcement
f''_{sh}	Stress in transverse rectangular hoop reinforcement
f_y	Yield strength of steel in uniaxial tension
f''_{yh}	Yield strength of hoop reinforcement
h	Total depth of a member
h''	Larger dimension of rectangular concrete area confined by rectangular hoops
h_b	Thickness of bottom steel plate of a composite closure
h_s	Thickness of steel liner portion of a rock cavity composite liner
h_t	Depth of concrete within the steel shell of a composite closure
h_p	Nominal backpacking thickness
i_1, i_2	Ratios of ultimate moment capacities at supports 1 and 2 to that at the center of the longer span of a two-way slab (Fig. 8-21)

i_3, i_4	Ratios of ultimate moment capacities at supports 3 and 4 to that at the center of the short span of a two-way slab (Fig. 8-21)
k	Parameter defined in Eq. 8-7
k_s	Factor defined in Eq. 8-7
k_u	Parameter defined in Eq. 8-7
n	Ratio of modulus of elasticity of steel to modulus of elasticity of concrete (E_s/E_c)
p	Tension steel ratio
p'	Compression steel ratio
$\bar{p}$	Maximum amplitude of the nonuniform component of external pressure on a circular ring (Fig. 8-25)
p_b	Tensile steel ratio required to balance the compression force in the rectangular portion of an I or T section
p_c	Tensile steel ratio at the center of a beam or one-way slab; average tensile steel ratio at the center of a two-way slab; uniform load component for arch or dome
$(p_c)_{cr}$	Critical uniform pressure on a ring, arch or dome required to cause buckling
p_e	Tensile steel ratio at the ends of a beam or one-way slab; average tensile steel ratio at the edge of a two-way slab
p_F	Tensile steel ratio required to balance the compressive force in the overhanging portions of the flanges of T or I sections

SYMBOLS AND NOTATION (Continued)

p_f	Uniformly distributed load on beam or one-way slab; uniform load resistance based on flexural capacity; nonuniform load component for an arch or dome
p_h	Horizontal soil stress
p_{lc}	Average tensile steel ratio at the centerline spanning the long direction of a two-way slab
p_{le}	Average tensile steel ratio at the edge spanning the long direction of a two-way slab
p_o	Free-field stress
p_s	Uniform load resistance of a member based on shear capacity; ratio of spiral reinforcing
p_{sc}	Average tensile steel ratio at the centerline spanning the short direction of a two-way slab
p_{se}	Average tensile steel ratio at the edge spanning the short direction of a two-way slab
p_t	Total steel ratio of reinforced concrete member under axial load based upon the gross cross section area of the member
p_v	Vertical soil stress
p_w	Total tensile steel ratio in I or T section
q	Magnitude of uniform component of external pressure on a circular ring (Fig. 8-25)
q^*	Factor defined in Eq. 8-15
q_{cr}	Critical buckling pressure
r	Radius of gyration of member cross section

SYMBOLS AND NOTATION (Continued)

r_a	Radius from center of circular rock cavity to inside of concrete lining
r_e	Boundary between elastic and inelastic regions in a medium measured from the center of a cylindrical cavity
r_y	Minimum value of radius of gyration
s	Spacing of vertical shear (web) reinforcement
s_H	Vertical spacing of longitudinal web reinforcement
t	Flange thickness of an I or T reinforced concrete section; thickness of a member in the direction of bending; thickness of a shear panel; circular ring thickness; thickness of confining steel ring of composite closure; thickness of backpacked rock cavity liner
t_f	Flange thickness
t_w	Web thickness
v	Average web shear stress
v_c	Volume of core measured out-to-out of spiral
v_s	Volume of spiral reinforcement
w	Unit weight of concrete; uniform load applied to a slab
x, x_y	Deflection of backpacked liner (Fig. 8-31)
$\bar{x}$	Distance from extreme compressive fiber to neutral axis
Γ, Γ'	Dimensionless parameters defined in Fig. 8-20
α	Ratio of short span to long span for a two-way slab or plate; angular coordinate defining location on a dome or arch

β	Pressure ratio for a circular ring $(q/\bar{p})$
γ	π/ϕ
γ_c	Ratio of ultimate moment in the long span direction to that in the short span direction at the center of a two-way slab
γ_{12}, γ_{34}	Parameters defined in Eq. 8-56
δ_A	Deflection of Point A (Fig. 8-25)
δ_{AE}	Deflection of Point A at elastic limit (Fig. 8-25)
δ_c	Deflection of shear wall at first cracking
δ_{max}	Peak probable elastic deflection of circular ring
δ_o	Initial ellipticity of circular ring
$\delta_{\bar{p}}$	Elastic deflection due to nonuniform load component, $\bar{p}$, on a perfectly round circular ring
δ_q	Deflection due to uniform pressure on circular ring with initial ellipticity
δ_u	Deflection of shear wall at ultimate resistance
ϵ_{cu}	Strain in concrete at ultimate strength
ϵ_o	Limiting strain in backpacking before strain hardening occurs
ϵ_p	Strain in backpacking
ϵ_r	Peak direct-induced radial strain
ϵ'_s	Strain in compression steel
ϵ_y	Yield strain
ϵ_θ	Circumferential strain at a point
θ	Angular coordinate defining location on a dome or circular ring
θ_e	Angle θ on circular ring which defines the threshold of plasticity

κ	Curvature
κ_u	Beam curvature at ultimate moment
κ_y	Beam curvature at yield moment
μ	Ductility ratio
ν	Poisson's ratio
σ_a	Axial compressive strength in triaxial compression
σ_{max}	Maximum value of triaxial stress; maximum fiber stress in circular steel ring
σ_{min}	Minimum value of triaxial stress
σ_o	Yield stress of backpacking
σ_p	Stress in backpacking
σ_r	Unconfined compressive strength of concrete; radial stress at a point
σ_{ra}	Radial pressure exerted by an inner steel liner on the concrete portion of a composite rock cavity liner
σ_u	Unconfined compressive strength of a medium
σ_y	Yield stress
$\sigma_1, \sigma_2, \sigma_3$	Principal triaxial stresses at failure of a concrete specimen where σ_1, is the major principal stress, σ_2 the intermediate principal stress and σ_3 the minor principal stress
σ_2	Uniform lateral confining pressure in triaxial compression; confining pressure provided by spiral, circular or rectangular hoops
σ_θ	Circumferential strength of the concrete portion of a rock cavity liner
ϕ	One-half the central angle of a circular arch or dome

Section IX

A	Response spectrum acceleration; amplitude coefficient; coefficient (Table 9-12c); area
A^*	Arbitrary constant
B_{ir}	Constant coefficients
C	Response spectrum reduction factor; arbitrary constant
C_r	Arbitrary constant
C_1, C_2	Dynamic reaction coefficients
C_H	Coefficient (Eq. 9-182)
D	Response spectrum displacement; maximum relative displacement between mass and support
E	Modulus of elasticity
E_c	Concrete modulus of elasticity
E_r	Arbitrary constant
$F(t)$	Forcing function
F_f	Frictional force
F_o	Peak value of load
F_o', F_o''	Parameters (Eqs. 9-18)
F_r	Arbitrary constant
F_s	Maximum spring force
F_t	Total force
F_{eq}	Equivalent force

H	Wall height
I	Moment of Inertia
I_c	Moment of inertia of reinforced concrete section
I_o	Initial Impulse
I_p	Polar moment of inertia
I_x	Moment of inertia with respect to radial line
K	Column lateral stiffness
K_L	Load transformation factor
K_M	Mass transformation factor
K_R	Resistance transformation factor
K_{LM}	Load-mass transformation factor
K_{rr}	Parameter (Eq. 9-117)
L	Length
M	Mass
M_i	Lumped mass coefficients
M_p	Ultimate or plastic moment
M_t	Total mass
M_{eq}	Equivalent mass
M_{pc}	Ultimate positive moment capacity per unit width at center of circular slab
M_{ps}	Ultimate negative moment capacity per unit width at edge of circular slab
M_{rr}	Arbitrary constant

M_{uc}	Column ultimate moment capacity
M_{pfa}	Total ultimate positive moment capacity along midspan section parallel to short edge of two-way slab
M_{pfb}	Total ultimate positive moment capacity along midspan section parallel to long edge of two-way slab
M_{psa}	Total ultimate negative moment capacity along short edge of two-way slab
M_{psb}	Total ultimate negative moment capacity along long edge of two-way slab
M^o_{psa}	Ultimate negative moment capacity per unit width at center of short edge in direction of long span of two-way slab
M^o_{psb}	Ultimate negative moment capacity per unit width at center of long edge in direction of short span of two-way slab
N	Mode number; integer
R	Resistance; radius of ring, arch or dome
R_c	Shear wall resistance at cracking
R_m	Resistance required or provided
R_u	Ultimate shear wall resistance
R_{me}, R_{meq}	Equivalent resistance
S	Length of arch axis
T_N	Natural period
U	Energy
V	Dynamic reaction; response spectrum pseudo-velocity
V_A	Total dynamic reaction along short edge of two-way slab

V_B	Total dynamic reaction along long edge of two-way slab
W	Relative displacement between mass and support; weight
$\ddot{W}$	Relative acceleration between mass and support
a	Diameter of circular slab (Table 9-8); Arbitrary constant; peak spectral absolute acceleration
b	Arbitrary constant
c	Damping coefficient
c_{cr}	Critical damping coefficient
e	Natural logarithm base
f	Frequency (Hz)
f'_c	Ultimate compressive strength of concrete
g	Acceleration of gravity
h	Frame story height; thickness of plate
k	Spring constant; stiffness coefficient
k_c	Shear wall stiffness prior to cracking
k_u	Shear wall stiffness at ultimate load
k_{ef}	Effective spring constant
k_{eq}	Equivalent spring constant
m	Unit mass
$\bar{m}$	Parameter (Eq. 9-183)
n	Integer
p	Pressure

SYMBOLS AND NOTATION (Continued)

q_i	Set of coordinates
r	Rebound resistance; radius of cross section; radius of gyration of arch section
t	Time; thickness
t_m	Time of maximum response
t_o	Duration of overpressure or dynamic load
t_r	Rise time
u	Relative displacement between mass and support
$\dot{u}$	Relative velocity between mass and support
$\ddot{u}$	Relative displacement between mass and support
u_m	Maximum relative displacement between mass and support
u_y	Relative displacement between mass and support at yielding of spring
u_{me}	Equivalent relative displacement between mass and support
v	Velocity
w	Unit weight of reinforced concrete
x	Displacement
$\dot{x}$	Velocity
$\ddot{x}$	Acceleration
x_e	Elastic displacement
x_i	Set of coordinates

SYMBOLS AND NOTATION (Continued)

x_m	Maximum displacement
$\ddot{x}_m$	Maximum acceleration
x_o	Displacement at time zero
$\dot{x}_o$	Velocity at time zero
x_p	Permanent set
x_{ef}	Effective displacement
x_{eq}	Equivalent displacement
$\ddot{x}_{me}$	Maximum equivalent acceleration
x_{st}	Static displacement
y	Displacement of support; displacement coordinate
$\dot{y}$	Velocity of support
$\ddot{y}$	Acceleration of support
y_o	Peak support displacement
$\dot{y}_o$	Peak support velocity
$\ddot{y}_o$	Peak support acceleration
Λ	Distortion coefficient
α	Arbitrary constant; parameter (Eq. 9-19)
$\alpha_{\bar{m}}$	Parameter (Eq. 9-184)
β	Parameter (Eq. 9-15); damping ratio or fraction of critical damping; arbitrary constant
γ	Weight density
γ_r	Parameter (Eq. 9-150)

SYMBOLS AND NOTATION (Continued)

θ_o	Arch central angle
$\lambda_{\bar{n}}$	Parameter (Eq. 9-184)
μ	Ductility factor; mass per unit length of beam; Poisson's ratio
ν	Poisson's ratio
ρ	Mass density
τ	Dummy integration variable
ϕ	Function; phase angle
ϕ_i'	Assumed mode shape
ϕ_i''	Computed mode shape
ψ	Dynamic load factor
ω	Frequency (rad/sec)
ω_d	Damped natural frequency (rad/sec)
ω_n	Natural frequency (rad/sec)
ω_p	Pseudo frequency (rad/sec)
ω_{nP}	Natural frequency with axial load (rad/sec)

Section X

A	Area; shock spectrum acceleration
A_c	Cylinder area
A_e	Effective area
A_p	Piston area
A_{ed}	Air bellows effective area at height h_d

SYMBOLS AND NOTATION (Continued)

$A_{e0.8d}$	Air bellows effective area at 80% height h_d
A_{es}	Air bellows effective area at static deflection
B	Fluid bulk modulus
B_t	Parameter (Eq. 10-53)
C	Spring index; compressibility
C_d	Liquid spring fluid compressibility at maximum dynamic deflection
C_f	Factor of safety against bottoming
C_h	Constant (Eq. 10-12)
C_s	Parameter (Eq. 10-52); liquid spring fluid compressibility at static deflection
D	Coil diameter; air bellows diameter; shock spectrum displacement
D_c	Liquid spring cylinder diameter
D_p	Liquid spring piston diameter
D_r	Liquid spring piston rod diameter
E	Modulus of elasticity
F	Force
F_h	Lateral force
F_v	Vertical force
G	Shear modulus
H	Free height of coil spring
H_s	Compressed height of coil spring
I	Moment of inertia
J	Torsion constant

SYMBOLS AND NOTATION (Continued)

L	Length
L_c	Cylinder length
L_d	Length of uniform diameter portion of torsion bar
L_e	Effective length of torsion bar
L_o	Pneumatic spring cylinder chamber length
L_t	Length of torsion bar taper
M	Mass
N	Number of active coils; number of bellows; number of straining cycles to failure
P	Axial load
P^*	Load corresponding to full compression of coil spring
P_s	Static load on air bellows
R	Effective length of torsion lever
T	Torque
T^*	Maximum torque at total deflection of torsion bar
V	Volume; shock spectrum pseudo-velocity
V_c	Chamber volume
V_d	Liquid spring volume at maximum dynamic deflection
V_o	Liquid spring volume under no load
V_R	Reservoir volume
V_s	Surge tank volume; rolling bellows cylinder volume; liquid spring volume at static deflection
W	Axial load; weight

SYMBOLS AND NOTATION (Continued)

a	Dimension of length; acceleration
b	Dimension of length
c	Rolling bellows sleeve dimension
d	Bar diameter; displacement
d_o	Diameter of torsion bar splined end
f	Frequency (Hz)
f_d	Dynamic natural frequency (Hz)
f_o	Frequency (Hz) at neutral position
f_s	Static natural frequency (Hz)
$f(y)$	Frequency (Hz) at extended position
g	Acceleration of gravity
h	Effective solid height of coil spring; rolling bellows sleeve dimension
h_d	Air bellows height at peak dynamic displacement
$h_{0.8d}$	Air bellows height at 80% design displacement
h_{st}	Air bellows height at static displacement
k	Spring constant
k_d	Dynamic spring constant
k_h	Lateral spring constant
k_m	Maximum spring constant
k_o	Spring constant at neutral position
k_s	Static spring constant
$k(y)$	Spring constant at extended position

n	Number of turns; number of inactive coils; gas constant for air
p	Pressure
p'	Pneumatic spring cylinder pressure at displaced position
p_c	Chamber pressure
p_o	Pneumatic spring air pressure at neutral position
p_s	Rolling bellows piston pressure; surge tank pressure; pressure in liquid spring at static deflection
p_{dg}	Air bellows gage pressure at height h_d
p_{gs}	Air bellows static gage pressure
p_{pl}	Preload pressure
p_{1a}, p_{2a}	Air bellows absolute pressure at volume V_1, V_2
p_{1g}, p_{2g}	Air bellows gage pressure at volume V_1, V_2
r	Torsion bar fillet radius; rolling bellows radius
t	Time
u	Rolling bellows chamber height
v	Velocity
x	Displacement; coordinate
y	Displacement of support; deflection; coordinate
y_a	Available displacement
y_d	Dynamic displacement

---

y_s	Static displacement
z	Coordinate
Δ_h	Lateral deflection
Δ_t	Total deflection
Δ_{cr}	Critical buckling deflection
Δ_{st}	Static deflection
Δ_{dyn}	Dynamic deflection
β	Damping ratio
δ	Allowable deflection per unit length of solid height of coil spring
η	Displacement ratio
θ	Angle
θ_t	Total angular deflection of torsion bar
κ	Wahl correction factor
σ_w	Allowable working stress
τ	Shear Stress
ω	Frequency (rad/sec)
ω_N	Natural frequency (rad/sec)

Section XI

A	Area; burst coefficient
A_v	Area of shear reinforcement
A_{st}	Total area of steel reinforcement
B	Arch span

SYMBOLS AND NOTATION (continued)

C	Seismic velocity; mean number of protuberances per unit length of duct or tunnel
C_L	Wave peak velocity
C_N	Arch natural frequency coefficient (Eq. 9-182)
C_p	Experimental coefficient (Eq. 11-7)
C_{df}	Front face drag coefficient
C_{dr}	Roof drag coefficient
D	Duct or tunnel diameter
D_n	Neutron dose
D_γ	Gamma dose
E	Modulus of elasticity
F	X ray flux
F_o	Peak value of applied load
H	Arch height
H_{avg}	Average depth of cover
I	Moment of inertia
J	EMP shielding characteristic dimension
K	Curvature correction factor
K_o	Coefficient of lateral earth pressure
K_{LM}	Load-mass factor
L	Length
M	Moment; coefficient (Fig. 7-49)
[illegible]	Moment at critical section for shear in reinforced concrete members

---

SYMBOLS AND NOTATION (Continued)

M_p	Plastic moment; ultimate moment
M_t	Total mass of element
M_t'	Total mass of additional material which responds with an element
M_u	Ultimate moment
M_{pm}	Ultimate moment capacity at midspan of beam or one-way slab
M_{ps}	Ultimate moment capacity at support of beam or one-way slab
M_{sc}	Ultimate moment capacity per unit width at the center of and in the direction of the short span of a two-way slab
M_{pfa}	Total ultimate positive moment capacity along midspan section parallel to short edge of two-way slab
M_{pfb}	Total ultimate positive moment capacity along midspan section parallel to long edge of two-way slab
M_{psa}	Total ultimate positive moment capacity along short edge of two-way slab
M_{psb}	Total ultimate moment capacity along long edge of two-way slab
M_{psb}^o	Ultimate negative moment capacity per unit width at center of long edge in direction of short span of two-way slab
M_θ	Moment at angle θ (polar coordinate)
N	Designator for arch mode of vibration being considered
P_c	Pressure in chamber
P_n	Peak pressure in duct or tunnel after n 90° bends
$\bar{P}_o$	$q + \bar{p}$ (Fig. 8-25)

SYMBOLS AND NOTATION (Continued)

P_u	Ultimate axial load
P_{dm}	Peak value of drag load component on arch or dome
P_{im}	Peak value of nonuniform load component on arch or dome
P_{ro}	Peak dome reflected pressure
P_{so}	Peak overpressure
P_{21}	Ratio of shock pressure to ambient pressure
P_θ	Peak pressure on cylinder or ring at angle θ (polar coordinates)
Q	Integrated thermal flux
R	Radius; range; duct or tunnel roughness factor
R_i	Internal radius
R_m	Resistance required or provided
S	Length of arch perimeter; parameter (Eq. 9-182); elastic stress factor (Eq. 8-118); perimeter of duct or tunnel section
T_c	Compression mode natural period
T_f	Flexural mode natural period
T_N	Natural period
T_α, T_θ	Compressive force per unit width in α and θ directions in dome shell
$T_{\alpha\theta}$	Shear force per unit width in dome shell at the foundation
U	Shock front velocity
V	Volume

SYMBOLS AND NOTATION (Continued)

V'	Shear force at critical section
V_{uc}	Ultimate shear capacity of concrete in a reinforced concrete member
V_{us}	Ultimate shear capacity of shear reinforcement in a reinforced concrete member
W	Weight; weapon yield
Y	Inelastic stress factor (Eq. 8-119)
Y_r	Weapon radiant yield
a, b	Dimensions of length
c	Distance from extreme fiber to neutral axis
c_o	Ambient sound velocity
c_1	Sound velocity behind shock front
d	Effective depth of reinforced concrete member
e	Natural logarithm base
e'	Eccentricity
f	Frequency (Hz)
f'_c	Ultimate concrete compressive strength
f_y	Steel yield strength
f'_{dc}	Dynamic concrete compressive strength
f'_{dy}	Dynamic steel yield strength
g	Acceleration of gravity
h	Thickness of dome shell
i	Impulse
k	Spring Constant

SYMBOLS AND NOTATION (Continued)

k_{ef}	Effective spring constant
k_{sc}, k_{sr}	Factors relating maximum and minimum principal stresses for concrete and rock, respectively
m	Unit mass; parameter $f_y/0.85f'_c$
m'	Distributed unit soil mass
$\bar{m}$	Mode shape parameter (Eq. 9-183)
n	Number of 90° bends in duct or tunnel; parameter (Table 9-12a)
$\bar{p}$	Nonuniform component of pressure
p_c	Tension steel ratio at center of element; unit resistance in compression mode
p_e	Tension steel ratio at edge (or end) of element
p_f	Unit resistance in flexural mode
p_h	Horizontal pressure
p_t	Total steel ratio
p_v	Vertical pressure
p_{cr}	Critical buckling pressure
q	Uniform component of pressure
q_o	Peak dynamic pressure
r	Radius
r_e	Distance to boundary between elastic and inelastic regions (Eq. 8-122)
t	Thickness; time
t_a	Time of arrival

SYMBOLS AND NOTATION (Continued)

t_i	Duration of pulse that has same total impulse as actual overpressure-time curve
t_m	Time of maximum response
t_o	Duration of overpressure or dynamic load
t_r	Rise time
t_s	Stagnation time
$\bar{t}_i$	Average time intercept
t_{io}	Time intercept
t_{oo}	Duration of pulse that has same slope as initial decay of actual overpressure-time curve
t_{50}	Duration of pulse that intersects the actual overpressure-time curve at 50% of the peak overpressure
u_o	Air particle velocity behind shock front
v	Soil particle velocity
w	Uniformly distributed load per unit area
w_c	Unit weight of reinforced concrete
x	Deflection
Γ, Γ'	Parameters (Fig. 8-20)
θ_o	Arch central angle
α	Effective amplification of yield (Eq. 6-1); slab aspect ratio (Eq. 8-56); angle (Fig. 7-4)
β	Parameter, $q/\bar{p}$

SYMBOLS AND NOTATION (Continued)

γ	Unit weight
γ_c	Ratio of ultimate moment capacity in long span direction to that in short span direction at center of two-way slab
γ_{12}, γ_{34}	Parameters (Eq. 8-56)
δ	Deflection
ϵ	Strain; mean height of protuberances per unit length of duct or tunnel
λ	Mean free path of gamma radiation (Eq. 6-1)
μ	Ductility factor
ν	Poisson's ratio
ρ	Unit mass
σ	Stress
τ	Parameter, B/U
ϕ	One-half central angle of arch or dome
ω_c	Natural frequency in compression mode (rad/sec)
ω_f	Natural frequency in flexural mode (rad/sec)
ω_n	Natural frequency (rad/sec)

This page intentionally left blank.

THE AIR FORCE MANUAL FOR DESIGN AND ANALYSIS OF HARDENED STRUCTURES

SECTION I

INTRODUCTION

1.1 OBJECTIVES

The objectives of this manual are to present methods and procedures for the estimation of nuclear weapon effects pertinent to protective structures and techniques for design and analysis of such structures subjected to these effects.

The intent is to present in a condensed and concise format much of the data and procedures currently available in unclassified form. These data and procedures can be used to obtain results of acceptable accuracy in most cases requiring determination of structural response in the environment of a nuclear detonation.

1.2 BACKGROUND

Since publication of the initial version of the Air Force Design Manual in December 1962, important advances have been made in understanding nuclear weapon effects on civil engineering type structures. In particular, significant effort has been expended in advancing an understanding of nuclear ground shock and cratering phenomena. In addition, the areas of interest have been expanded to very high overpressure levels for defensive systems. Increased interest in the high overpressure regions has in turn generated a concern regarding the effects of certain types of nuclear radiation on the survivability of hardened structures. There was also a need to provide some guidance for the analyst concerned with an evaluation of the vulnerability of a facility to nuclear weapon effects. In many such cases, the type of conservatism inherent in design procedures is inappropriate. Accordingly, it was considered

necessary to revise the initial version of the manual to reflect the latest technology and treat those areas of interest not covered in the previous edition.

Defining any one of the various nuclear phenomena with any degree of precision is a vast and formidable task. The complexity of the task is compounded by the multiplicity of weapon designs, burst conditions, material properties of the media between the detonation and the target, and threat levels which can be of interest in considering particular weapon system protection requirements. Similarly, design or analysis of structural systems or subsystems located in these environments poses problems of equal magnitude. Although it is obviously impossible to specifically treat every situation which can arise in the design and analysis of hardened structures, it is possible to provide methods of prediction and analysis which are generally applicable to a wide range of situations. This manual is oriented toward the latter approach.

The methods presented herein are primarily hand calculation procedures. A detailed treatment of almost any aspect of the overall problem, either environment or response, typically involves complex analytical techniques which require the utilization of large, high speed computers. Although such computers are widely available, it is felt that there will always be a requirement for simplified, quick hand calculation methods for establishing bounds on areas where more refined investigation may be necessary. In addition, many of these methods are equally useful in determining inputs to a more detailed analysis utilizing computer resources.

The information presented in the various sections of this manual has been drawn from a large number of sources. The prediction techniques and methods of analysis have been substantiated in varying degrees by analytical and experimental investigations. Much of the information related to structural design or analysis is based upon well established principles of design and analysis of conventional structures. While the procedures presented are considered adequate for purposes of simplified preliminary design and analysis, final design or analysis of important facilities should utilize those computational techniques and input data which represent the best available and most pertinent approach to the problem under consideration.

An effort has been made to include a reasonable amount of basic information herein in an attempt to make this manual as self-contained as possible. Since it is not feasible to completely cover all the disciplines and phenomena involved, numerous references have been cited for those desiring more detailed information on a particular subject or requiring a more detailed analysis of some aspect of a problem than is possible with the methods presented herein.

1.3 PRESENTATION

1.3.1 Organization

Section II includes a discussion of the factors affecting nuclear weapon effects in general. It also summarizes the advantages and disadvantages of aboveground, shallow buried and deep underground structures, and the nuclear weapon effects of primary importance to each class of facility. Criteria and procedural differences between the design and analysis processes are also reviewed.

Section III treats the subject of airblast phenomena. Appropriate curves and equations are provided for the prediction of free-field overpressures and dynamic pressures for combinations of burst and ground surface conditions. Section IV summarizes the most current techniques for prediction of nuclear crater dimensions, ejecta and missiles. Both homogeneous and layered media are treated.

A compilation of nuclear ground shock prediction techniques is presented in Section V. Three general classes of

ground shock, airblast-induced, direct-induced and crater-induced, are considered. Both homogeneous and layered media are treated. Field exploration programs and laboratory investigations related to the site selection or evaluation process are reviewed and typical properties of soil and rock media are included.

Section VI provides curves and equations for the prediction of gamma, neutron, X ray, and thermal radiation intensities. Some general guidance is provided regarding permissible radiation levels for personnel and equipment and radiation shielding requirements. Because of its classified nature, only upper limit estimates of the EMP are included. However, classified sources of more detailed information are provided. EMP shielding techniques are discussed and suggestions made for reducing the vulnerability of equipment to this phenomenon.

Section VII presents methods of using the information provided in Sections III, IV, V and VI to obtain loads on aboveground, shallow buried and deep underground structures. Also included are suggested approaches for prediction of structure motions. Section VIII provides basic information for determining the strength of structures or structural elements. Equations or curves are given for assessing the strength of the principal types of structural elements. Both reinforced concrete and structural steel are treated.

Section IX presents several methods for the analysis of structures subjected to dynamic loading or base motions. Modeling of structures is introduced and factors are provided for transforming distributed mass systems into equivalent single degree of freedom systems. Expressions are also given for calculation of periods of vibration of various types of structural elements.

Section X presents guidance for preliminary design of shock isolation systems. Some data are also included on the shock tolerance of personnel and equipment. Advantages and disadvantages of the more common isolators and isolator arrangements are reviewed briefly, and equations and curves for preliminary sizing of the more common isolators are provided. Section XI summarizes the general considerations in design or analysis and provides general criteria guidance for the two processes. A review of the steps in the design or analysis process with references to other parts of the manual for appropriate data and equations is included.

Illustrative examples have been included at the end of various sections to demonstrate use of the material provided in that section.

1.3.2 Units

There are presently three major systems of measuring units in use in the world today. These are the English, the metric, and the Systeme International de Unites, or SI. The SI is a modernized version of the metric system.

The primary system of units used in this manual is the English system. The SI has been included as a secondary system to the maximum extent feasible. Many of the equations herein are homogeneous, i.e., any consistent system of units can be used. In the case of nonhomogeneous equations, two versions are typically given, the first in the English system and the second in the SI. When units are specified for the variables in an equation, these are the only units compatible with the equation constants.

Frequently used conversion factors between the English system and the SI are summarized in Table 1-1.

Table 1-1

CONVERSION FACTORS

English	SI	SI	English
1 in	2.540 cm	1 cm	0.3937 in
1 ft	0.3048 m	1 m	3.281 ft
1 yd	0.9144 m	1 m	1.094 yd
1 mi	1.609 km	1 km	0.6214 mi
1 in^2	6.452 cm^2	1 cm^2	0.1550 in^2
1 ft^2	929.0 cm^2	1 m^2	10.764 ft^2
1 in^3	16.387 cm^3	1 cm^3	0.0610 in^3
1 ft^3	28,317 cm^3	1 m^3	35.315 ft^3
1 yd^3	0.7646 m^3	1 m^3	1.308 yd^3
1 lb (mass)	0.4536 kg	1 kg	2.205 lb (mass)
1 lb (force)	4.448 N	1 N	0.2248 lb (force)
1 dyne (force)	10^{-5} N	1 N	10^5 dyne (force)
1 lb/in	1.751 N/cm	1 N/cm	0.5711 lb/in
1 lb/in^2	0.6895 N/cm^2	1 N/cm^2	1.450 lb/in^2
1 lb/ft^2	0.00479 N/cm^2	1 N/cm^2	208.8 lb/ft^2
1 lb/ft^3	0.000157 N/cm^3	1 N/cm^3	6369 lb/ft^3
1 lb-in	11.299 N-cm	1 N-cm	0.00885 lb-in
1°F	0.5556°C	1°C	1.800°F
°F (temp)	0.5556 (°F-32)°C	°C (temp)	(1.8°C + 32)°F
1 erg	10^{-7} j	1 j	10^7 ergs
1 cal	4.184 j	1 j	0.239 cal
1 kT	4.184×10^{12} j	1 j	2.39×10^{-13} kT

SECTION II

GENERAL CONSIDERATIONS

2.1 INTRODUCTION

Design and/or analysis of structures subjected to the effects of nuclear weapons is influenced by a multitude of interrelated factors and considerations. Among these are

- Types of nuclear weapon effects
- Types of burst
- Types of protective facilities

Types of nuclear weapon effects can vary with the design of the weapon, the height (or depth) of burst, and the medium in which it is detonated. Types of protective facilities will vary with the intended function of the facility, and different types of facilities may respond in different fashions to the same effect.

The same general considerations inherent in the design and analysis of conventional facilities are also present in protective construction. *One significant difference between design* and analysis of conventional facilities and protective facilities, however, is the absence of a code in protective construction. This factor, plus the lack of a great deal of realistic experimental data, places much more emphasis on engineering judgment in the case of protective structures.

2.2 TYPES OF EFFECTS

A nuclear explosion results in the very rapid release of a tremendous amount of energy within a very limited space. This sudden release of energy causes a very large increase in the pressure and temperature *and converts the close-in materials* to extremely hot gases. These gases expand rapidly and initiate a shock wave in the surrounding medium.

The destructive power of nuclear weapons, like conventional weapons, is generally due to blast and shock. Beyond this similarity, however, there are several basic differences. A nuclear explosion can be *several thousand times more* powerful than the largest conventional detonation. In addition, nuclear explosions release large amounts of energy in the form of initial nuclear radiation, thermal radiation and residual nuclear radiation. Initial nuclear radiation consists of highly penetrating and harmful invisible rays which are released essentially simultaneously with the detonation. Thermal radiation is emitted in the form of heat and light. Residual nuclear radiation, or residual radioactivity, results from the radioactive substances *remaining* after a nuclear detonation emitting radiations over an extended period of time.

The *energy* in a conventional explosion is produced by chemical reactions. The energy produced by a nuclear explosion results from the formation of different atomic nuclei. Two types of nuclear interactions which produce large amounts of energy in a short period of time are known as fission and fusion. In the fission process, a free (or unattached) neutron enters the nucleus of a fissionable atom, causing the nucleus to split into smaller parts. The resulting smaller (or lighter) nuclei *are* called the fission products. The complete fission of one pound (0.45 kg) of uranium or plutonium releases as much energy as the explosion of 8000 tons (7×10^6 kg) of TNT (8×10^{12} cal; 3.4×10^{13} j).

In the fusion process, a pair of light nuclei unite (or fuse) together to form the nucleus of a heavier atom; e.g., two deuterium (heavy hydrogen) nuclei may combine to form the nucleus of the heavier element, helium. Nuclear fusion reactions can only be initiated by means of very high temperatures and are thus referred to as thermonuclear processes. The fusion of all the nuclei in one pound (*0.45 kg*) of deuterium would release approximately the same amount of energy as the explosion of 26,000 tons (2.2×10^7 kg) of TNT (2.6×10^{13} cal; 1.1×10^{14} j).

Temperatures on the order of several million degrees are necessary to produce nuclear fusion reactions. Such temperatures can be obtained by means of a fission explosion. Accordingly, by combining a quantity of hydrogen isotopes (deuterium or tritium) with a fissionable material, a thermonuclear explosion may be realized. In general, the energy released by a thermonuclear weapon is generated in roughly equal amounts by the fission and fusion processes.

The power of a nuclear weapon is generally expressed in terms of the energy release (or yield) when it explodes compared with the energy released by the explosion of TNT. Thus, a 1-kiloton (kT) nuclear weapon is one which produces the same amount of energy as 1000 tons (8.8×10^5kg) of TNT, and a 1-megaton (MT) nuclear detonation is the equivalent of 1,000,000 tons (8.8×10^8kg) of TNT (approximately 10^{15} calories or 4.2×10^{15} joules). The distribution of energy and the damaging effects resulting from a nuclear explosion depend upon many factors. Two of the most important of these factors are (1) the composition of the nuclear device, i.e., fission or various combinations of fission-fusion, and (2) the physical properties of the medium in which the explosion takes place, i.e., underwater, underground, the atmosphere, etc. A typical distribution of energy at a distance from a fission device detonated in the atmosphere is shown in Fig. 2-1. The types of effects resulting from these forms of energy which are pertinent to the design and analysis of protective structures will be briefly introduced in following paragraphs.

2.2.1 Airblast

A shock wave in air, or airblast, resulting from an explosion resembles and is accompanied by a very stong wind. The airblast from a nuclear detonation is similar to that from a conventional detonation, except the damaging effects extend for much greater distances and are present for much longer periods of time.

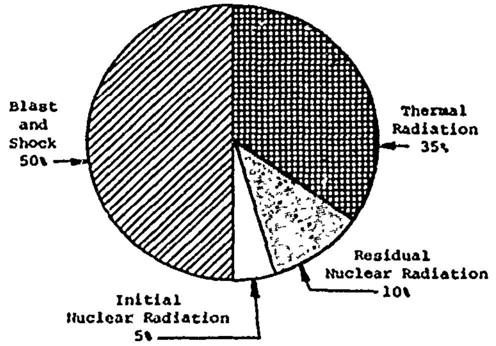

Figure 2-1 Distribution of Energy at a Distance from a Typical Air Burst of a Fission Weapon in Air at an Altitude Below 100,000 Feet (Ref. 2-1)

Airblast phenomena will be treated in two broad categories herein: (1) the overpressure, or sudden rise in atmospheric pressure due to the detonation, and (2) the dynamic pressure, or high velocity wind resulting from the rapidly moving airblast shock front. Airblast effects are of importance in protective construction whenever the structure of interest is located in, or exposed to, the atmosphere. In addition, the airblast from a nuclear detonation can cause severe ground shock.

2.2.2 Cratering and Ejecta

An explosion which occurs in contact with, or near, the surface of the earth will cause a crater to be formed. The material thrown out of the crater is herein termed ejecta. Ejecta may include both discrete missiles of significant size and smaller particles which are deposited from the edge of the crater out to appreciable distances.

A manmade structure which would survive within or immediately adjacent to the crater from a nuclear detonation is not practical. Cratering effects are important, however, when considering the digging out of a buried structure and because the crater is the source of ejecta and of certain types of ground shock. Ejecta can damage protective structures by impact from large discrete missiles or by deposition of large quantities of smaller particles on or over the structure.

2.2.3 Ground Shock

Detonation of a nuclear weapon in contact with, or near, the surface of the earth creates a very severe shock wave and attendant motions and stresses in the earth. These shock waves can be the result of the mechanical coupling of energy from the crater region or from the very high pressures present in a nuclear airblast wave propagating over the earth's surface. In most cases of practical interest, the ground shock resulting from a nuclear explosion will be a combination of the effects of the energy coupled to the earth both from the region of the crater and from the airblast.

Ground shock effects are very important in the design and analysis of protective structures. Buried structures may fail due to inability to withstand the pressures or motions associated with ground shock, and surface structures may fail due to inability to withstand the forces resulting from foundation motions, similar to earthquake effects. Even though a structure may have sufficient strength to survive severe ground shock, the resulting in-structure shock may be severe enough to damage the structure contents unless appropriate measures are taken to protect the contents.

2.2.4 Initial Nuclear Radiation

The term initial nuclear radiation as used in this manual includes gamma rays, neutrons and X rays which are

released essentially instantaneously by a nuclear detonation. Initial nuclear radiation is rarely the governing effect in considering possible damage to protective structures (as opposed, e.g., to airblast or ground shock), although there are certain conditions under which structural damage can result due to neutron and X ray effects.

Even though initial nuclear radiation effects may not be the primary structural damage mechanism, they can cause very serious damage to structure contents such as personnel, electronic gear, etc. For these reasons, initial radiation effects will require investigation in almost every protective construction application.

2.2.5 Electromagnetic Pulse

A nuclear explosion can cause the creation of electric and magnetic fields of very high intensity which may extend over long distances. This phenomenon, called the electromagnetic pulse (EMP), does not have any effect on protective structures, per se, but can create havoc with electrical and electronic circuits and equipment. Such disturbance may range from temporary disruption of the functioning of the equipment through damage severe enough to require replacement of the affected components. The designer of protective facilities must be aware of these effects and take appropriate steps for their mitigation.

2.2.6 Thermal Radiation

A far greater portion of the energy from a nuclear explosion is emitted as thermal radiation than is the case for a conventional explosion due to the vastly higher temperatures resulting from a nuclear detonation. Thermal radiation, if of sufficient intensity, can cause ablation of structural materials such as steel and concrete and thereby reduce the capability of such materials to accomplish their intended function. Nuclear thermal radiation can also start fires, char combustible materials and cause skin burns in the same manner as thermal radiation of equal intensity from conventional explosions. Thermal radiation effects are important in protective construction whenever thermal radiation is likely to cause a reduction in structural strength.

2.2.7 Residual Nuclear Radiation

Residual nuclear radiation is due almost entirely to the radioactivity of the fission products present in the weapon residues after the explosion and is emitted over a considerable period of time. The greater the proportion of fissionable material present in the weapon, the greater will be the amount of residual nuclear radiation. Residual nuclear effects are important in protective construction only from the standpoint of protection of the structure contents, primarily personnel.

2.3 TYPES OF BURST

The nuclear weapon effects of primary interest in protective construction are strongly dependent upon the location of the weapon with respect to the surface of the earth at the time of detonation. The types of burst of interest in this manual can be broadly categorized as

- Air burst
- Surface burst
- Underground burst

These types of burst will be defined and the types of effects associated with each assessed qualitatively in following paragraphs. Underwater bursts, although quite important in many applications, will not be covered.

2.3.1 Air Burst

An air burst will be defined as one in which the fireball does not come in contact with the ground. Such a burst will produce negligible, if any, cratering effects. Airblast, initial nuclear radiation, EMP, thermal and residual nuclear radiation effects will be present to greater or lesser extent depending largely upon the altitude of the burst. Ground shock effects will be due solely to the energy coupled to the earth by the airblast wave.

High altitude bursts, e.g., above 100,000 feet (30,480 m), are normally of little interest in protective construction. At such altitudes, the air density is so low that more of the explosion energy appears as thermal radiation and less as blast and shock. High altitude bursts, then, are almost totally ineffective in causing structural damage to hardened structures located on or beneath the earth's surface. EMP effects can still be important, however.

2.3.2 Surface Burst

A surface burst is one in which the fireball comes in contact with the earth. A true surface burst will be defined as a burst where the center of gravity of the weapon is coplanar with the earth's surface at the time of detonation. A contact burst is one in which the tip or edge of the device just touches the surface. A true surface burst can be expected to be more efficient than a contact burst in the generation of crater and direct-induced ground shock effects.

All of the nuclear weapon effects of concern in protective construction will be present in the case of a surface burst. After determining that a proposed facility is not in or too near the crater, the effects of overriding importance in most cases of practical interest will generally be airblast and ground shock. Radiation effects will always be of concern to assure that a protective system is equally hardened against all effects consistent with a given threat spectrum.

Crater ejecta effects fall in a category similar to radiation. That is, these effects are always important but rarely control the survivability of a structure, except possibly systems which are intended to survive very near the crater. The amount and extent of residual radiation, or fallout, will be considerably greater from a surface burst than from an air burst due to the large quantities of dust and earth particles generated and carried into the atmosphere. A large portion of this added material becomes radioactive and can spread over very large areas and remain active for long periods of time.

2.3.3 Underground Burst

An underground burst is one in which the center of gravity of the weapon is located beneath the surface of the earth at the time of detonation. Two limiting cases for an underground burst are the near-surface, or slightly buried, and the fully contained burst. A fully contained burst is defined as one in which the fireball does not vent to the surface.

With increasing depth of burial, more and more of the weapon energy is utilized in cratering and ground shock with a corresponding decrease in airblast and radiation effects. Radiation effects will be present, but the range to which they will extend will decrease somewhat in proportion to the amount of earth through which they must travel to reach the surface or a buried target of interest.

2.3.4 Summary

The burst types described above are specialized cases and obviously do not cover all situations that may be encountered in practice. In an actual problem of interest, the weapon may be detonated anywhere from high altitude, where the only effects of interest in protective construction would probably be some of the radiation and EMP phenomena, to fully contained, where the only noticeable effect would likely be

the directly induced ground shock. Both of these extremes are highly unlikely. The great preponderance of practical cases will fall within the spectrum ranging from air bursts to slightly buried bursts. The important points in considering types of burst are (1) to recognize the effect of different bursts on the nuclear phenomena and (2) to be able to estimate these effects on at least a semiquantitative basis for a particular problem of interest.

2.4 TYPES OF FACILITIES

Protective structures can be grouped into three broad categories. These are

- Aboveground
- Shallow buried
- Deep underground

Each of these facility types has advantages and disadvantages, is more susceptible to certain effects than others, and has inherent differences in survival potential.

2.4.1 Aboveground Structures

Aboveground structures as a class are simpler to construct and present fewer problems in day-to-day operation and maintenance than the buried types. Consequently, they can be the most economical type in the long run, provided the threat to be survived is not too severe.

Being located above the earth's surface, aboveground structures are directly exposed to the full free-field intensity of the nuclear weapon effects. They experience the full range of airblast phenomena, overpressure and dynamic pressure. The structure itself must provide any required radiation shielding. Ground shock and crater ejecta of significant magnitude may be experienced. Airblast and initial nuclear radiation are usually found to be the critical effects controlling the proportioning of aboveground structures. It will rarely be found economically feasible to provide adequate protection with an aboveground facility at the more severe environments.

2.4.2 Shallow Buried Structures

Shallow buried structures can be made capable of surviving nuclear weapon environments associated with maximum overpressures of thousands of psi. A dramatic increase in achievable hardness is obtained merely by placing the structure flush with, or beneath, the ground surface and eliminating the reflected airblast and dynamic pressure loads. Burial is also beneficial in protecting against initial nuclear and thermal radiation effects, since earth material is reasonably effective in attenuating these phenomena. In addition, the earth itself can provide a significant amount of structural strength to the protective system under certain conditions.

Ground shock is frequently found to be the most critical effect in proportioning shallow buried structures. At less severe environments, which are relatively far removed from the burst point, the ground shock produced by the airblast will generally predominate over any directly coupled ground shock that may be present. Crater ejecta and direct-induced ground shock become increasingly important as the point of interest becomes closer to the burst point.

Shallow buried protective structures are subject to the same drawbacks as any buried structure, i.e., increased construction costs, ground water problems, and generally decreased operating efficiency. For the more severe threat environments, however, buried facilities are usually found to be the only feasible means of providing the required protection.

2.4.3 Deep Underground Structures

In those cases where it is necessary to provide protection from a direct hit or near miss by a nuclear weapon

of any appreciable yield, it will be found necessary to consider deeply buried structures. Cratering is a very important effect, along with the directly coupled ground shock when considering such facilities. The facility must be deep enough, not only to be out of the expected crater, but also to be at a range where the ground shock has attenuated to a tolerable level. Airblast, airblast-induced ground shock, thermal radiation, initial and residual radiation effects will almost always be found to be of little or no importance for deep underground structures. EMP effects may be significant, however, particularly if electronic equipment must be protected.

While deep underground structures can be made the most nearly invulnerable of the facility types, they are also the most costly and present the most operational problems. Deep underground facilities can be typically several hundreds or thousands of feet below the surface. The operational problems and cost implications of a facility so far beneath the surface are readily apparent. On the other hand, there are no alternatives available at this time which could be expected to survive extremely severe threats.

2.4.4 Summary

Types of protective facilities are shown qualitatively in Figs. 2-2, 2-3 and 2-4, along with types of burst and the associated weapon effects which are generally found to be most important. As was the case with types of burst, there is rarely any clear demarcation by facility type in problems of practical interest. Deep underground facilities, for example, must have survivable entrances, exits, communications links, and so on, which will be shallow buried or aboveground facilities. The designer or analyst of protective systems, then, must be constantly alert to assure that all probable effects have been considered for a particular problem of interest.

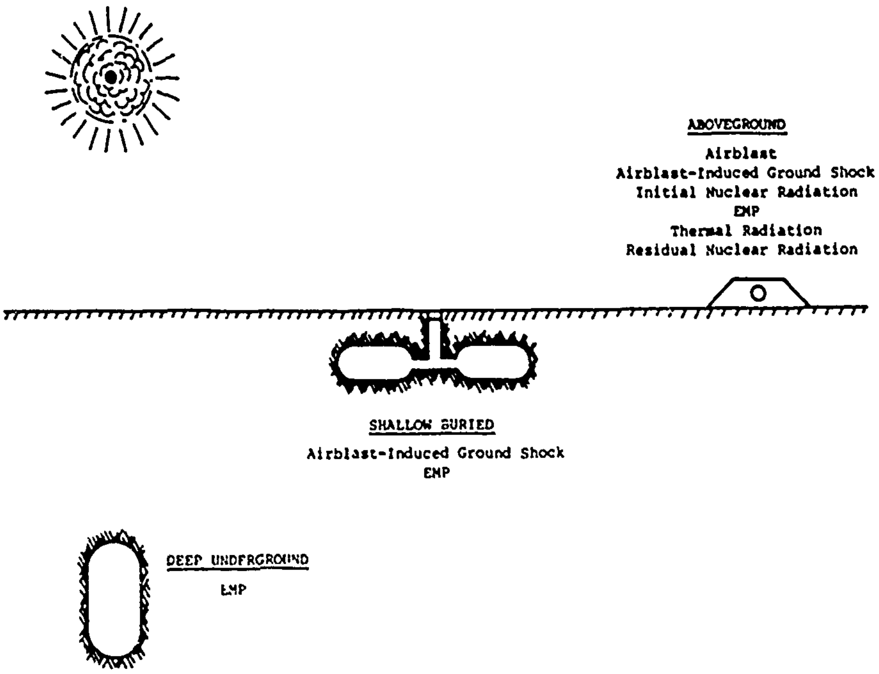

Figure 2-2 Air Burst-Primary Effects on Different Facility Types

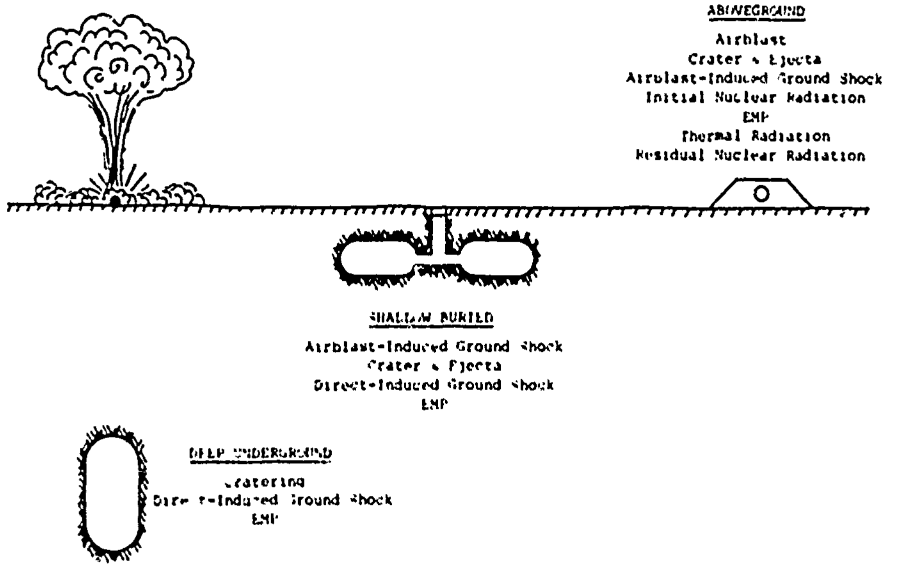

Figure 2-3 Surface Burst-Primary Effects on Different Facility Types

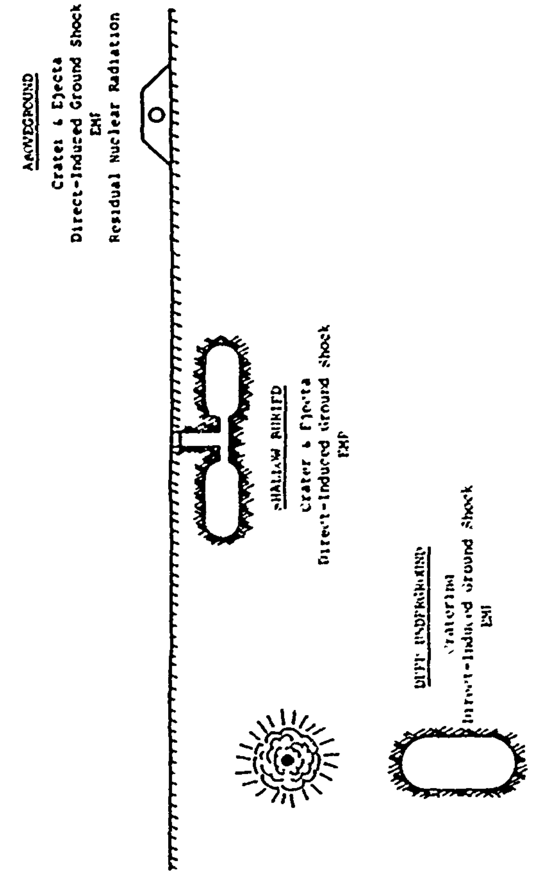

Figure 2-4 Underground Burst-Primary Effects on Different Facility Types

2.5 FACTORS IN DESIGN AND ANALYSIS

Even though analysis is an integral part of the design process, there are inherent differences in the philosophy and basic approach to the two procedures, design and analysis. These differences will be discussed in following paragraphs.

2.5.1 Design

Design, in the context of this manual, is the creation of a protective facility, or system, to accomplish a given function. This function will ordinarily consist of one or more pieces of equipment and/or personnel with a mission to accomplish either during or after an attack by nuclear weapons. In many cases, this mission may be only to survive the attack. One of the first steps in the design process is the provision of a suitable operational environment, i.e., required power, space, heat, ventilation, etc. These requirements are the same for the design of any facility. Next, a protective envelope (for purposes of this manual, a structure) must be provided for the function which will survive the specified attack. Finally, it must be assured that the contents within the protective envelope also survive the attack. That is to say, the protective structure may easily survive the attack environment while the contents have been damaged or destroyed by radiation or violent motions. In such cases, the protective structure has failed just as surely as if it had collapsed.

After the functional requirements to be protected have been established, design of the protective envelope involves many assumptions. The loads from a nuclear attack will never be known precisely beforehand. While the protective structure configuration and materials may be the designer's option, the behavior of the structural entity under the design loads must be known or assumed with sufficient confidence to assure the design will accomplish its intended purpose. During the design process, all assumptions are usually taken on the conservative side as pertains to survival. For example, maximum probable loads from the design threat are generally assumed; minimum specified concrete strengths and metal yield points are used; additional strength due to strain hardening of metal is typically neglected, and so on. Appropriate consideration of these kinds of phenomena increase the designer's margin for error in assuring that his design will accomplish its intended purpose.

2.5.2 Analysis

Analysis is the inverse of design in that the facility to be analyzed is given; it is not to be created. Whereas the designer has various options in selecting structural materials, proportions, etc., the analyst has none.

The approach and assumptions commonly used in design which are conservative insofar as survival is concerned will be misleading or unconservative in a failure or target analysis. Whereas a designer should assume a weapon will detonate at the precise point which will result in the maximum credible damaging effects, a target analyst should assume a reasonable miss-distance and a corresponding degradation of effects. Similarly, minimum allowable structural strength parameters are used in the design process while the analyst should use the maximum values which could be realistically expected.

Stated another way, it should be assumed in the design process that the detonation is such that the airblast, ground shock, or other effect of interest. loads the structure in the most severe manner that can be realistically expected. This is not meant to imply that unreasonable combinations of worst cases should be utilized. For example, a surface burst will typically generate more severe airblast and lesser crater and ejecta effects than a buried burst. It would be unreasonable, then, to combine the surface burst airblast and buried burst crater and ejecta effects into the same load matrix (unless the specified threat included two weapons detonated simultaneously). Rather, one would consider the burst types separately and use the more severe load matrix which resulted. In addition to choosing a reasonable set of the worst loads to be expected, it is generally assumed in design that the concrete and steel, for example, placed by the construction contractor just equals the specifications for compressive strength and yield point. Further, if inelastic action of the structure is to be allowed under the design loads, the amount of such inelasticity is usually something short of collapse.

A target analyst, on the other hand, looks at the above factors from a different viewpoint. He knows that the probability of a weapon being precisely on target and exploding with a full, high-order detonation is something less than one. If he is interested in airblast, for example, he knows that the surface of the earth is not the ideal level half-space inherently assumed to some degree in airblast prediction. Accordingly, he can be sure that rolling terrain, vegetation or dusty surface, etc., will alter the ideal airblast wave in some fashion, may or may not cause a precursor wave to form, and so on. He also knows that specified material strengths are minimum values to be equaled or exceeded in well-inspected construction, that concrete increases in compressive strength with age (up to a point), and that properly designed and constructed structures can stand a great deal more distress before collapse than the amount of inelastic action typically assumed in design. The nature of the assumptions made in target analysis, then, will typically be in the opposite direction of those in design. The extent of conservatism or confidence required will influence the assumptions in the same fashion for either analysis or design.

2.5.3 Factor of Safety

A factor of safety in conventional design is commonly reckoned against yield, or the beginning of inelastic action, which would be designated failure in such cases. For example, with an allowable design stress of 20,000 psi (13,800 N/cm^2) for a member made of steel with a yield stress of 33,000 psi (22,800 N/cm^2), the factor of safety is ordinarily said to be 33/20 = 1.65. That is to say, the member could experience a stress 1.65 times the allowable before yielding.

It is well known that first yielding in a ductile structure does not necessarily mean collapse of the structure. Indeed, there is a great deal of reserve strength in the inelastic, or plastic, region prior to collapse, provided the member or structure exhibits ductile behavior. Limit, or ultimate strength, design procedures endeavor to take advantage of this reserve strength. The design allowable in limit design is commonly expressed in terms of the load necessary to cause collapse of the member or structure. Rather than a safety factor, limit design employs a load factor; a load factor of 1.65 would indicate that the structure is designed such that a load 1.65 times the design load would be required to cause failure.

Protective structures are almost universally designed on an ultimate strength basis. The load factor in the conventional sense can generally be said to be one, i.e., the design load is normally the maximum load expected. Accordingly, it is difficult to specify or recommend a factor of safety in the sense in which the term is generally used. Rather than a factor of safety, it may be better to think in terms of margin for error in protective structure design.

Some margin for error is inherent in the usual protective construction design practice, which is strongly oriented toward assuring ductile behavior. If there were one

key word in protective construction design, it would probably be ductility. Minimum specified yield strengths are used; strain hardening effects are generally neglected; and the structure is never designed to the point of collapse. Even though the design usually assumes inelastic behavior, allowable limits are estimated and placed on the amount of such behavior. These limits are usually incorporated in terms of the ratio of maximum allowable deflection to the yield deflection, i.e., $\mu = x_m/x_y$. Since it has been shown that μ can be as much as 20-50 for ductile members in flexure, margin for error can be incorporated into the design by selection of conservative values of μ for flexural behavior. Where brittle behavior is anticipated, such as concrete in shear or diagonal tension, columns, etc., μ is rarely taken greater than 1.3, and usually as 1.0. Margin for error can also be incorporated in the design through the values selected for the design loads, by the behavior parameters chosen for the soil or rock in the case of buried structures, and so on.

The term factor of safety as used in design has no real meaning in analysis. If one is analyzing the response of a structure to a given load, he is generally interested in the actual response within some specified tolerance. In such cases, it is usually necessary to estimate the accuracy of the analysis as within so many percent based on consideration of the factors involved in the problem of interest. If one is considering target analysis, or kill probability, the design assumptions are essentially all reversed as previously discussed. Aside from attacking weapon system reliability, CEP, etc., the target analyst is forced to consider the best probable structural behavior and the least probable loads if he is to incorporate any margin for error into his analysis for sure kill, heavy damage, etc.

In conclusion, incorporation of an appropriate factor of safety or margin for error is sound practice for either designer or analyst in his effort to achieve meaningful results. Both should be constantly on guard, however, to avoid piling on so many conservatisms that the final results are unrealistic.

2.5.4 Accuracy and Precision

Accuracy and precision should be commensurate with the input data. Obviously, time-consuming sophisticated techniques should not be utilized in situations where the loads, soil properties, structural details, etc. are not known closer than ± 25 to 50 percent. This is not meant to imply, however, that gross assumption should be piled upon gross assumption until the results are nothing more than a crude guess.

In analysis, the structure is generally well defined and more sophisticated procedures are often justifiable than would be the case in design. Further, the loads must in general be known in more detail, particularly for a dynamic analysis. This is because the response of a given structure is as strongly dependent upon the shape of the load-time history as it is on the peak value thereof. Much of the philosophy and reasoning discussed in preceding paragraphs also bears on the justifiable precision and expected accuracy of protective construction calculations.

2.6 REFERENCES

2-1 Glasstone, S., et al., The Effects of Nuclear Weapons, Government Printing Office, Washington, D.C., 1964. (U)

SECTION III

AIRBLAST PHENOMENA

3.1 BLAST WAVE IN AIR

3.1.1 General

An explosion is characterized by the sudden release of energy. The source of this energy is relatively immaterial. The release, however, must be a sudden one. A nuclear explosion releases a tremendous amount of energy in a very small space in an exceedingly short time. This sudden release of energy converts the surrounding material into extremely hot gases which expand rapidly and generate a shock wave in the material. In air, this shock wave is termed a blast wave and causes a sudden increase in pressure which immediately begins to decrease as shown in Fig. 3-1. Approximately 50 percent of the energy yield of a typical air burst (at altitudes below 100,000 feet or 30,480 m) results in blast and shock (Fig. 2-1).

As the expansion of the hot gases continues, the front of the blast wave travels rapidly away from the explosion in the manner of a moving wall of highly compressed air. The velocity of the blast front and the peak pressure decrease while the spatial extent increases as shown in Fig. 3-2.

3.1.2 Overpressure and Dynamic Pressure

The transient pressure in excess of the ambient, or surrounding atmospheric pressure, is defined as the overpressure. The peak overpressure is the maximum value of the overpressure at a given location. As the blast wave arrives at a given point, the overpressure rapidly increases from zero to the peak overpressure. In the absence of perturbations, the rise time to peak overpressure will be less than a microsecond. The value of the peak overpressure and the variation of the

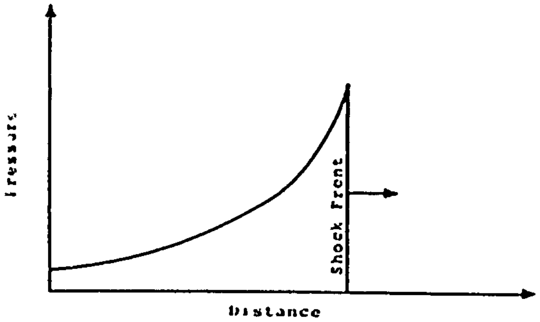

Figure 3-1 Variation of Pressure in a Blast Wave

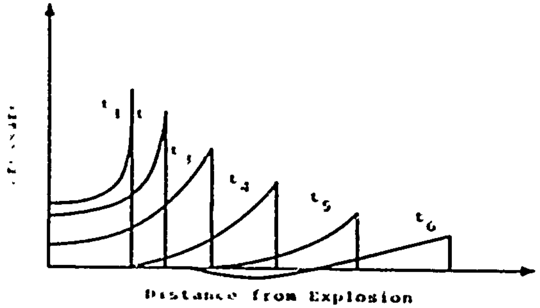

Figure 3-2 Variation of Pressure with Distance at Successive Times

overpressure with time are functions primarily of the weapon yield, the height of burst, and the distance from the burst.

As the blast wave moves outward from the explosion, the flow of the mass of air behind the blast front produces a wind. The resulting pressure is termed the dynamic pressure and is a function of the density of the air through which the blast wave passes and the wind velocity behind the shock front. Under some conditions, the density of the air may be increased by dust and other material picked up by the blast wave as it moves across the earth's surface. As will be seen later, it is usually convenient, but not always correct, to relate the peak dynamic pressure to the peak overpressure with which it is associated.

3.1.3 Time of Arrival, Duration and Impulse

A finite time elapses between the detonation and the arrival of the blast front at a given location. This time of arrival is primarily dependent upon the weapon yield and the distance from the point of burst.

The duration of the blast wave is characterized by two distinct phases. During the first, or positive, phase, the overpressure rises very rapidly (essentially instantaneously) from ambient to its peak value and then decreases more slowly to ambient. In general, the duration of this positive phase increases and the peak overpressure decreases with distance from the explosion. The positive phase for the dynamic pressure is somewhat longer than for the overpressure.

In the second, or negative, phase, a partial vacuum is created and the air is sucked in rather than being pushed away, as when the overpressure is positive. Consequently, the wind blows toward the point of detonation during the negative phase. Peak values of the underpressure during the negative phase rarely exceed four or five psi (2.8 or 3.4 N/cm^2) below ambient. Underpressure peak values decrease with distance from the explosion similar to peak overpressures, although at a slower rate. Peak values of both dynamic pressure and overpressure during the negative phase are typically so much smaller than during the positive phase that the negative phase is never critical in determination of structural response in most practical situations. Variation of dynamic pressure and overpressure at a point is shown qualitatively in Fig. 3-3.

Often an important parameter in connection with determining airblast effects on protective structures is the impulse. Impulse is defined as the area under the pressure-time curve and may be associated with either overpressure or dynamic pressure and positive or negative phase duration - or all of these.

3.1.4 Scaling

Pertinent airblast parameters are ordinarily presented in terms of a reference weapon yield, usually 1kT or 1MT. In the international system of units, 1KT = 4.184 x 10^{12} joules and 1MT = 4.184 x 10^{15} joules. These parameters can then be determined for other yields of interest by scaling from the reference yield values.

If certain assumptions are made regarding the properties of air- and shock-wave propagation, it can be concluded that a given pressure will occur at a distance from an explosion that is proportional to the cube root of the energy yield. High-explosive and nuclear tests have shown this relation to hold approximately true for yields up into the megaton range. Accordingly, the range (distance), R, at which a particular overpressure or dynamic pressure will occur due to detonation of a weapon of yield, W, may be found from

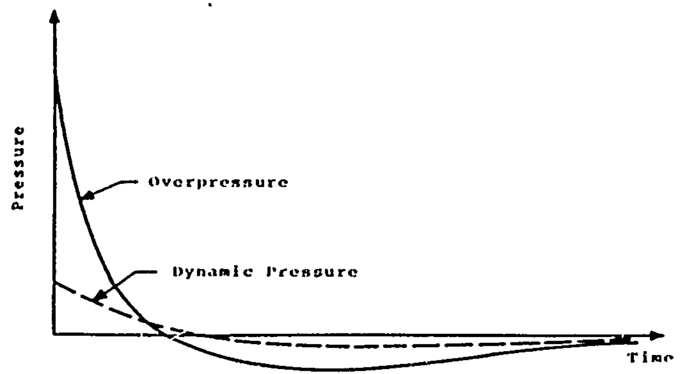

Peak Overpressure = 10 psi (6.89 N/cm^2)

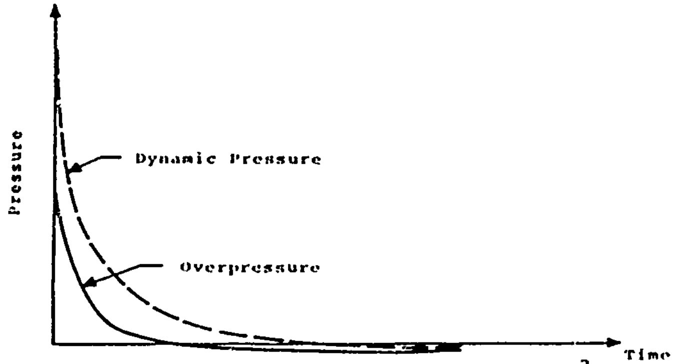

Peak Overpressure = 500 psi (344.7 N/cm^2)

Figure 3-3 Qualitative Variation of Overpressure and Dynamic Pressure with Time at a Point for Two Peak Over-Pressure Values

$$\frac{R}{R_1} = \left[\frac{W}{W_1}\right]^{1/3} \qquad (3\text{-}1)$$

where R_1 is the range at which the pressure of interest occurs due to the reference yield, W_1.

Cube root scaling such as the above can also be applied to the airblast time of arrival, positive phase duration and impulse, i.e.,

$$\frac{t}{t_1} = \left[\frac{W}{W_1}\right]^{1/3} \quad \text{and} \quad \frac{I}{I_1} = \left[\frac{W}{W_1}\right]^{1/3} \qquad (3\text{-}2)$$

where t denotes time of arrival or positive phase duration, and I is the impulse of interest; the subscripted terms are the reference yield values.

When using surface burst data as the basis of scaling effects for a free air burst, it is usually assumed that the surface burst is twice as effective in blast effects as the air burst. For subsurface bursts where the depth of burial is only a few feet, the airblast scaling will be similar to that for a surface burst. As the depth of burial increases, more and more of the available energy goes into cratering and ground shock and correspondingly less into airblast. For a crude approximation of the airblast effects in such cases, one could assume a fraction of the actual yield inversely proportional to the depth of burial compared to the burial depth for full containment, and treat this reduced yield as a surface burst (e.g., the yield for airblast effects would be zero for a depth of burial equal to or greater than the depth required for full containment).

In using the foregoing expressions, it must be understood that both distance and time are being scaled. For example, if a peak overpressure of 10 psi (6.89 N/cm^2) occurs at 9500 feet (2896 m) from a 1MT (4.184 x 10^{15} j) surface burst, 10 psi from an 8MT (33.5 x 10^{15} j) surface burst will occur at

9500 x $(8)^{1/3}$ = 19,000 feet (5785 m). Similarly, if the airblast time of arrival at the 10 psi range (9500 feet) for a 1MT surface burst is 3.9 seconds, the time of arrival for an 8MT surface burst at the 10 psi range (19,000 feet) would be 7.8 seconds.

3.1.5 Summary

The airblast parameters which are generally most important in protective construction are

- Peak overpressure
- Peak dynamic pressure
- Pressure-time history

The peak pressures and the pressure-time history determine the impulse present in an airblast wave.

Other free-field airblast parameters which are frequently important in specific applications include the shock front velocity and the particle (or wind) velocity behind the shock front. These airblast effects and characteristics are treated further in following paragraphs.

3.2 OVERPRESSURE

3.2.1 Peak Overpressure

One of the most important airblast effects is overpressure, i.e., the excess of pressure in the blast wave over the ambient (atmospheric) pressure. The maximum value of the overpressure directly behind the shock front is called the peak side-on overpressure or, more generally, the peak overpressure. Side-on overpressure is the overpressure recorded by a gage mounted flush with the surface of the ground as the airblast wave passes over that point (Fig. 3-3). The peak overpressure at a given location depends upon the energy yield of the explosion, the ground range from the point of burst, the height of burst (or depth of burst), and the medium in which the weapon is detonated. The peak overpressure which will occur at a given range from a given yield can be predicted with confidence within a factor of two. The predicted range at which a given overpressure will occur can be considered accurate within 20 percent.

The peak overpressure as a function of weapon yield and distance from the burst point has been measured in nuclear field tests and calculated theoretically. The following expressions represent good approximations for the variation of peak overpressure, P_{so}, with distance and yield for a surface burst.

$$P_{so} = 3300 \left[\frac{W}{1MT}\right]\left[\frac{1000ft}{R}\right]^3 + 192 \left[\frac{W}{1MT}\right]^{1/2} \left[\frac{1000ft}{R}\right]^{3/2} \quad psi \tag{3-3}$$

$$= 15\left[\frac{W}{10^{15}J}\right]\left[\frac{1000m}{R}\right]^3 + 11 \left[\frac{W}{10^{15}J}\right]^{1/2} \left[\frac{1000m}{R}\right]^{3/2} \quad N/cm^2$$

Equations 3-3 are based on the assumption that one-half the energy of the detonation goes into producing airblast. Figure 3-4 shows the relationship between peak overpressure, weapon yield and horizontal range for a surface burst and agrees very well with the expressions presented above.

As mentioned previously, surface bursts are assumed to be twice as effective as free air bursts for blast effects. Accordingly, if one wished to use Eqs. 3-3 to estimate peak overpressure from a free air burst, he would use one-half the actual air burst yield, W, in the equations. It should be borne in mind that the overpressures thus calculated will be free air overpressures. Overpressures on the ground surface from an air burst involve reflections from the ground and will be treated in a later paragraph.

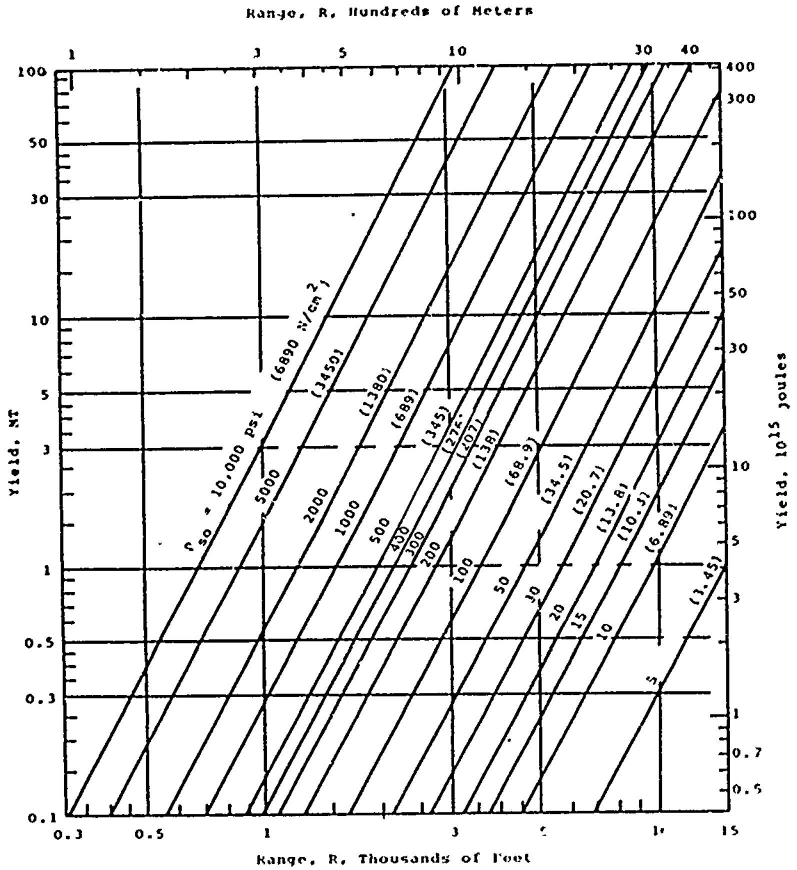

Figure 3-4 Peak Overpressure at Ground Surface Versus Range for Various Yields--Surface Burst at Sea Level (Note: Assumes 50% of energy effective in producing airblast.)

3.2.2 Time of Arrival, Duration and Impulse

Since time of arrival, t_a; positive phase duration, t_o; impulse, I; and distance for a given peak overpressure all scale according to the cube root scaling law, it is convenient to relate these three parameters to peak overpressure. Figure 3-5 shows these relationships for a surface burst of 1MT (4.184×10^{15}J). For other surface bursts, values of t_a, t_o and I given in Fig. 3-5 are multiplied by the cube root of the ratio of weapon yield of interest to 1MT to obtain corresponding values of these parameters for the yield of interest. For free air burst parameters, the cube root of the ratio of one-half the air burst yield would be used to utilize surface burst data.

3.2.3 Variation of Overpressure with Time

The rate of decay of overpressure behind the shock front is a function of peak overpressure with the initial rate of decay extremely rapid at higher overpressures. From the initial peak value, the overpressure variation with time for surface bursts can be described as the sum of exponentially decreasing components given in the following equation from Ref. 3-1.

$$p(t) = P_{so}\ (1-\tau)\ (ae^{-\alpha\tau} + be^{-\beta\tau} + ce^{-\gamma\tau}) \quad (3\text{-}4)$$

where

$$\tau = \frac{t^* - t_a}{t_o}\ (\geq 0)$$

and t^* is time after detonation with $t = t^* - t_a$. The coefficients a, b, c, α, β and γ are given in Fig. 3-6. Figure 3-7 shows the normalized overpressure, i.e., the overpressure relative to the peak overpressure ($p(t)/P_{so}$) as a function of the normalized time, i.e., the elapsed time after arrival of the blast wave at the point of interest divided by the positive phase duration, t/t_o, for various peak overpressures. The semilog plots of Fig. 3-7 distort the typical shape of the

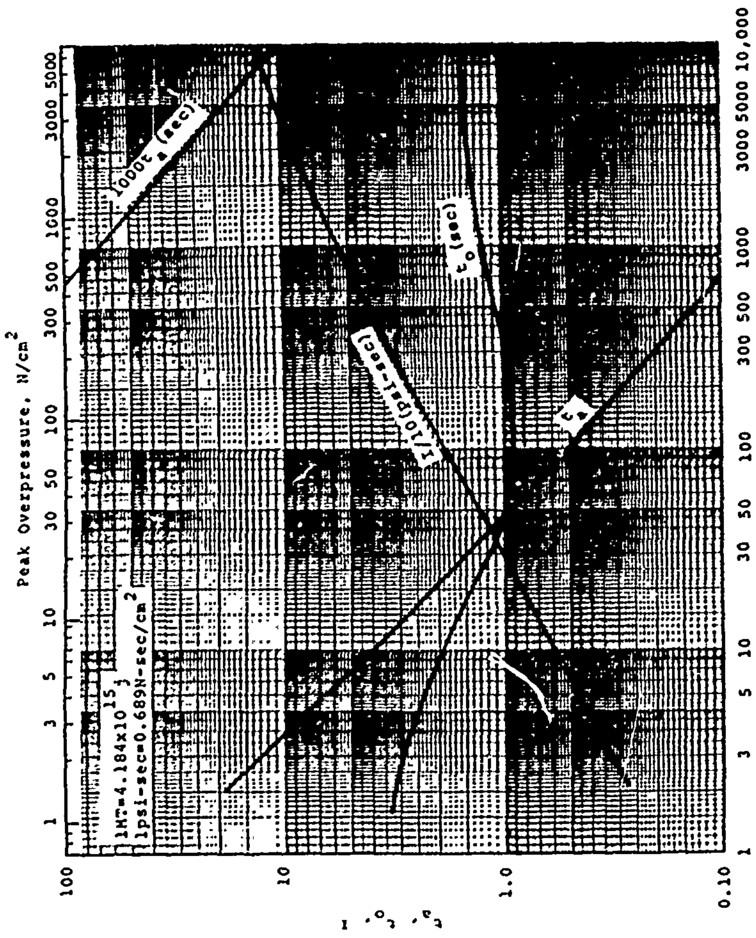

Figure 3-5 Overpressure Time of Arrival, Duration and Impulse as a Function of Peak Overpressure for a 1MT Surface Burst (Ref. 3-1)

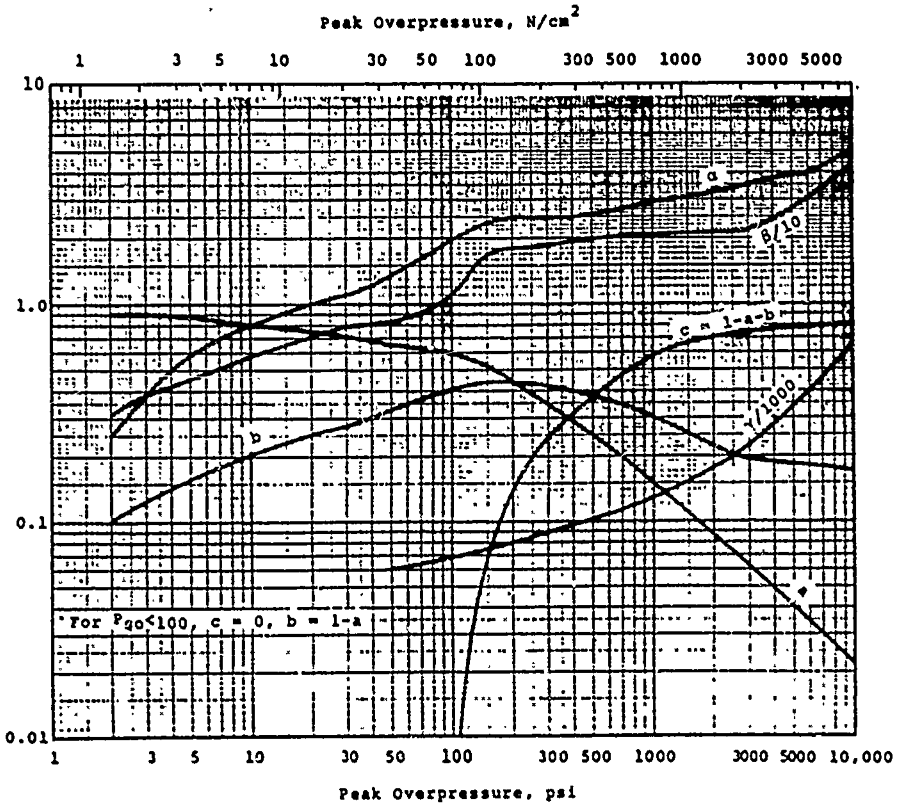

Figure 3-6 Values of Quantities for Computing Overpressure Wave Forms for Surface Bursts (Ref. 3-1)

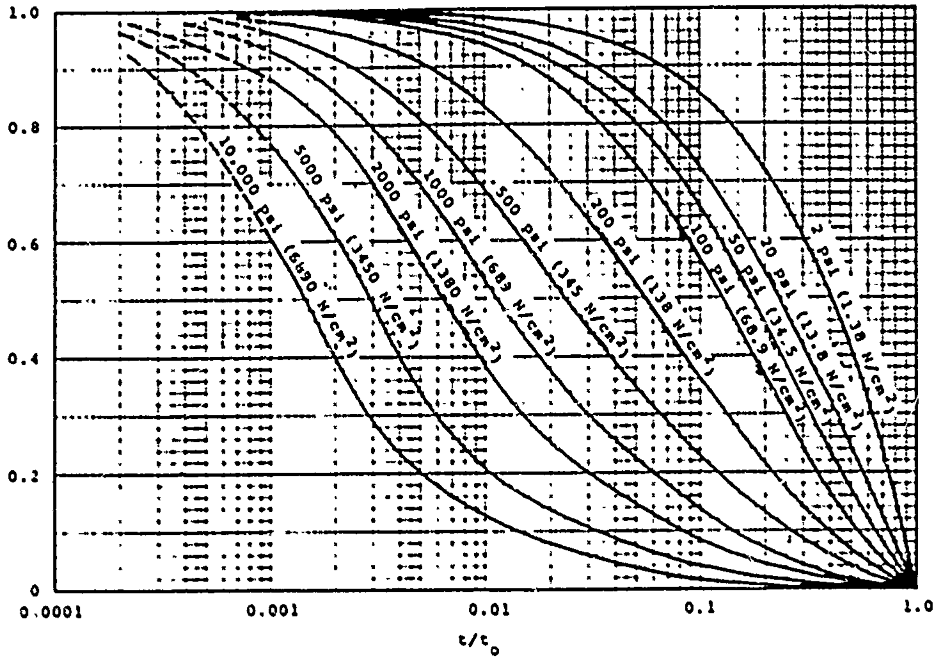

See note on pp 55/56

Figure 3-7 Normalized Overpressure-Time Curves pressure-time curve from that shown in Fig. 3-3 but provide greater detail of the early portions of the waves at the very high overpressures.

Normalized impulse-time curves for a 1MT (4.184 x 10^{15}J) surface burst are shown in Fig. 3-8. These curves are useful for determining the impulse at various times during the overpressure positive phase duration and can be used for other yields by scaling the I_{max} values as described previously.

3.2.4 Overpressure-Time Approximations

Since the overpressure-time curves of Fig. 3-7 are not readily usable for rapid structural response computations, they are usually represented by triangular equivalents as shown in Fig. 3-9. These equivalent triangles all have the same initial peak overpressure, P_{so}, but have different durations depending on the expected time of maximum structural response. The durations are determined as follows:

a. If maximum structural response occurs after the overpressure has decayed to zero, a duration, t_i, is selected so that the total impulse of the equivalent triangular curve is equal to that of the actual overpressure-time curve.

b. If maximum response occurs early in the pressure-time history, the slope of the equivalent triangular pulse is assumed tangent to the actual curve resulting in the duration t_{oo}.

c. For response situations intermediate to those above, the duration t_{50} is found by assuming the equivalent triangular pulse passes through the actual curve at $P_{so}/2$.

Figure 3-10 gives values of t_i, t_{oo} and t_{50} as a function of peak overpressure for a 1MT surface burst. The times may be scaled to other yields by multiplying by the ratio $[W/W_1]^{1/3}$, where W_1

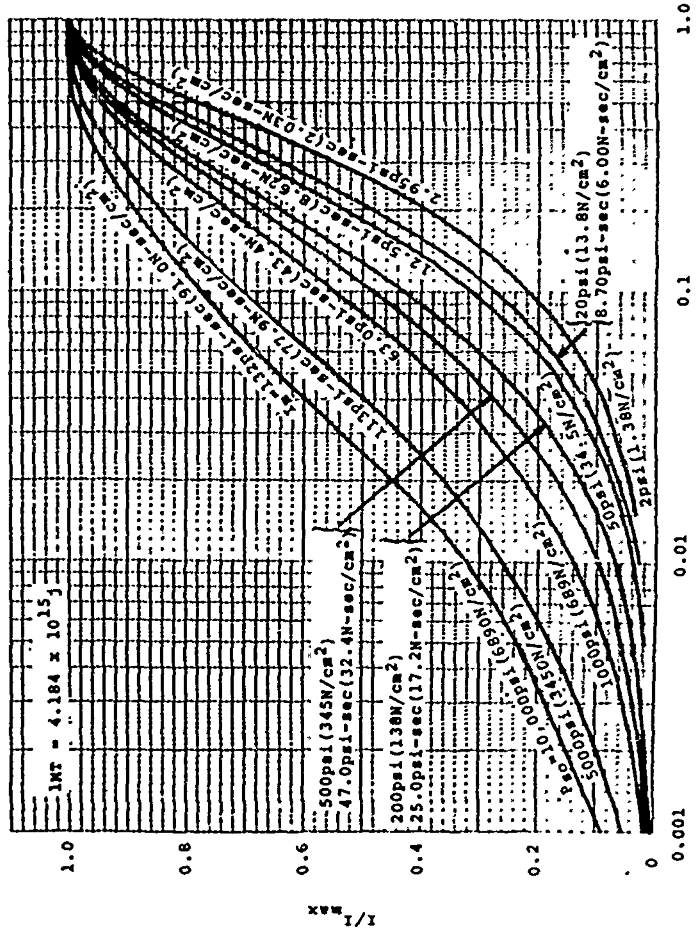

Figure 3-8 Normalized Impulse-Time Curves for a 1MT Surface Burst

See note on pp 55/56

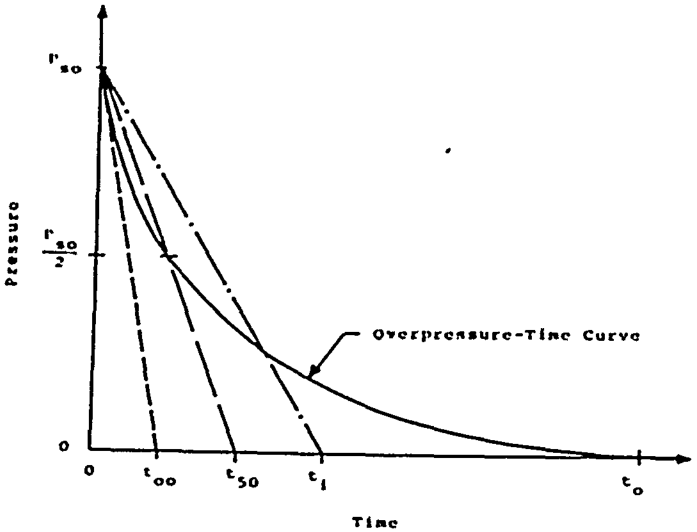

Figure 3-9 Triangular Representations of Overpressure-Time Curves

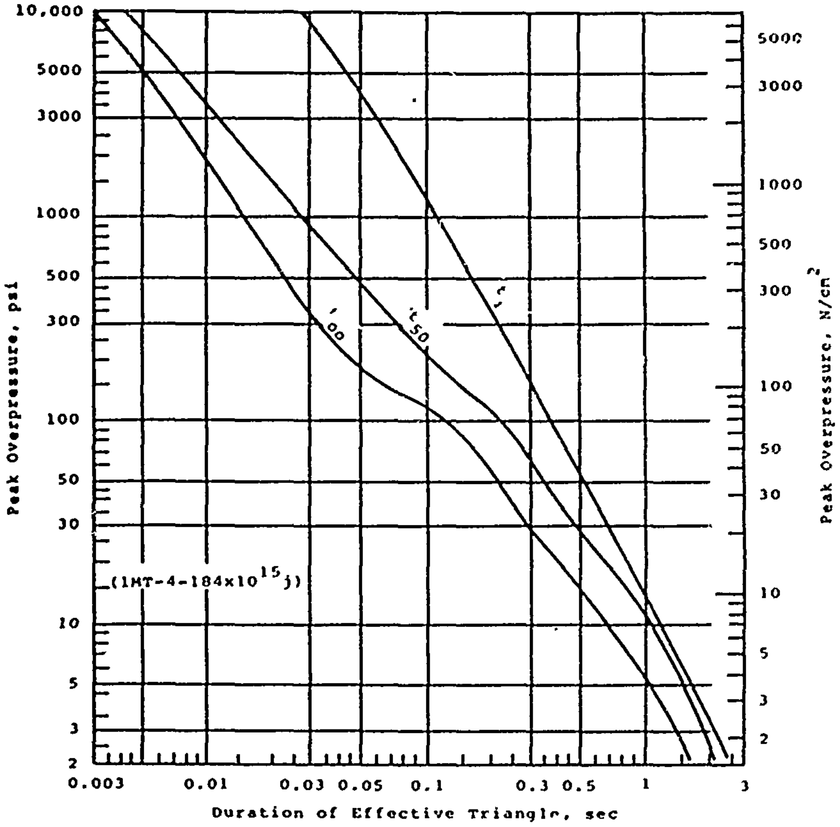

Figure 3-10 Duration of Effective Triangles for Representation of Overpressure-Time Curves--1MT Surface Burst (Ref. 3-2)

is the reference yield, as described previously.

If a computer is available for the structural response calculations, the actual pressure-time curve can be easily used for the forcing function rather than the simplified approximations discussed above.

3.2.5 Shock Front Velocity

The shock front velocity is important in determining the airblast loading of aboveground structures and the time inter-relationship of airblast-induced and direct ground shock.

The shock front propagates outward from the burst point with a velocity which is a funciton of the peak overpressure just behind the shock front and the ambient conditions [illegible] ir ahead of the shock front. The shock velocity, U, is expressed by (for $P_{so} < 300$ psi or 207 N/cm^2)

$$U = c_o \left[1 + \frac{6P_{so}}{7P_o} \right]^{1/2} \qquad (3-5)$$

where

c_o = ambient speed of sound ahead of shock front

P_{so} = peak overpressure

P_o = ambient pressure ahead of shock front

The ambient speed of sound can be found by

$$c_o = (\gamma g R T)^{1/2} \qquad (3-6)$$

where

γ = ratio of specific heats

g = acceleration of gravity

R = engineering gas constant

T = absolute temperature

The shock front velocity as a function of peak overpressure for sea level conditions is presented in Fig. 3-11. Shock front velocities at other altitudes will depend upon the ambient conditions at the altitude of interest; see, for example, Ref. 3-3.

3.2.6 Reflected Overpressure

Whenever the blast wave strikes a surface which is not parallel to its direction of propagation, a reflection process takes place which causes an increase in the peak overpressure. This reflection process is caused by the momentum change when the moving air changes direction as a result of striking the surface. The ratio of reflected overpressure to incident pressure is called the reflection factor. The reflection factor varies with both the peak overpressure in the incident wave and the angle at which the blast wave strikes the surface.

If a nuclear weapon is detonated at some distance above the ground surface, the reflection process depicted in Fig. 3-12 occurs. In the regular reflection region, the incident and reflected waves merge at the ground surface. The magnitude of the peak reflected overpressure will depend on the incident peak overpressure and the angle of incidence of the blast wave with the ground surface. At some distance from ground zero (GZ), the reflected wave, travelling through air that has been heated and compressed, overtakes the incident wave and the two waves fuse into a single front as shown in Fig. 3-12. The region where this fusion takes place is called the Mach reflection region, and the fused wave front is called the Mach stem. The point at which the two waves merge is called the triple point and its height above the ground surface increases with distance from GZ. Any object above the path of the triple point will experience two distinct shocks, one from the incident wave and one from the reflected wave. An object below the path of the triple point will experience only a single shock. Since the

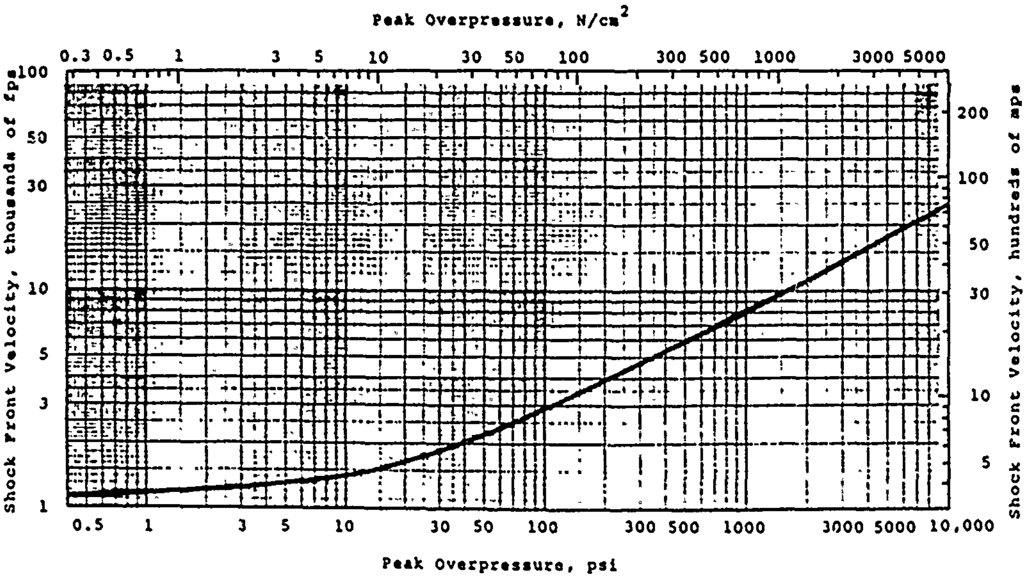

Figure 3-11 Shock Front Velocity as a Function of Peak Overpressure at Sea Level

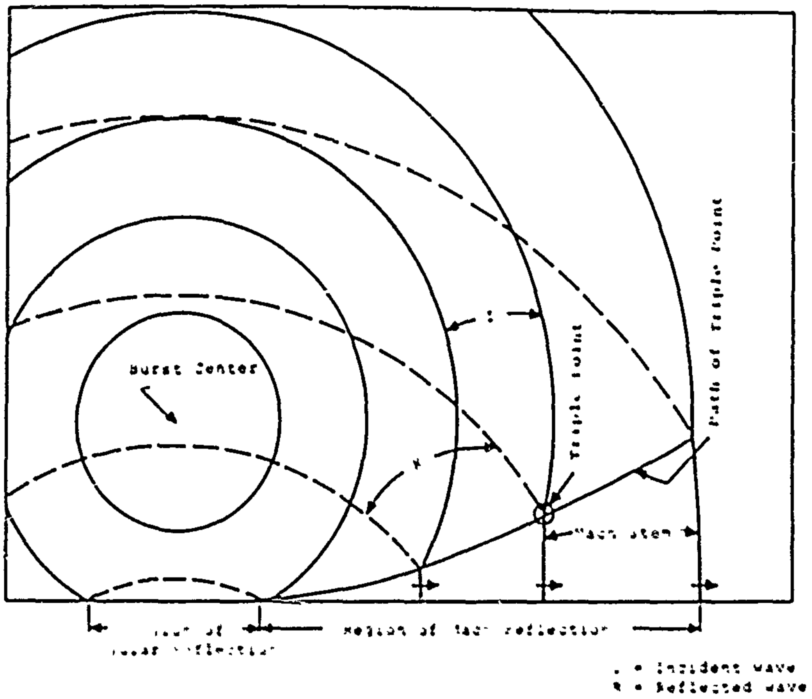

Figure 3-12 Ground Reflection of Airblast Wave

Mach stem is nearly vertical, blast forces in the Mach reflection region will be directed parallel to the ground surface, i.e., the shock front is perpendicular to the ground surface.

If the angle of incidence is defined as the angle between the shock front and the reflecting surface, a 90-degree angle of incidence would correspond to a surface parallel to the direction of propagation of the blast wave. Highest reflection factors occur at a zero angle of incidence, i.e., a surface normal to direction of propagation of the blast wave.

3.2.7 Effect of Height of Burst

Although it will generally be found that a surface burst is the most effective type in attacking hard targets, there are some situations in which an air burst can be more advantageous. At peak overpressures of less than about 20-30 psi (14-21 N/cm^2), the range to a particular peak overpressure can be significantly increased by detonating the weapon at some optimum height above the ground surface. At the 30 psi (21 N/cm^2) contour, the increase in range is about 15 percent, which results in an increase in the area covered by 30 psi or greater of about 30 percent. At the 10 psi (6.9 N/cm^2) contour, the corresponding increases in range and area covered are about 45 and 100 percent, respectively. Almost all conventional structures would be destroyed or severely damaged by the total effects at a range corresponding to a 10 psi overpressure environment from a moderate yield nuclear burst. Accordingly, an air burst could be the most efficient means of attacking such targets.

In addition to the aboveground soft targets mentioned above, there is reason to believe that air bursts can be effective in attacking hard targets under some conditions. It is concluded in Ref. 3-5 that relatively low air bursts, up to a height of about 200 $(W/1kT)^{1/3}$ feet (0.19 $(W/10^{12}j)^{1/3}m$) should be about as effective as surface bursts in producing airblast effects. Crater and ejecta effects will, of course, be forfeited since burst heights above about 100 $(W/1kT)^{1/3}$ feet (0.095 $(W/10^{12}j)^{1/3}m$) will not produce a crater. A reduction in the

dust and ejecta associated with crater formation can be desirable in the case of multiple attacks, since dust raised by previous bursts can present a hazard to subsequent reentry vehicles.

Figures 3-13, 3-14 and 3-15 show the effect of height of burst (HOB) on peak overpressures on the ground surface. The optimum HOB for a given peak overpressure is that HOB which corresponds to the maximum ground range. The HOB also affects the pressure-time history of the overpressure on the ground surface. Analytical approximations which are consistent with such empirical data as are available are developed in Ref. 3-5 with which overpressure-time histories on the ground due to air bursts can be calculated. These expressions are summarized in Table 3-1.

While the expressions in Table 3-1 are readily adaptable to computer solution, they are quite formidable for hand calculations. Figures 3-16 and 3-17 which show overpressure, positive phase duration and overpressure positive phase impulse, respectively, as functions of HOB can be utilized for crude estimates of overpressure-time histories. With the peak overpressure from Fig. 3-13, 3-14 or 3-15 and the duration from Fig. 3-16, a time history can be approximated with the aid of Fig. 3-7. Alternatively, equivalent triangular representations of the overpressure-time history can be constructed as described in paragraph 3.2.4. When other than preliminary estimates are required, and particularly at higher overpressures, the procedures developed in Ref. 3-5 should be utilized.

It is estimated that overpressures from air bursts can be predicted with roughly the same precision as from surface bursts, i.e., within a factor of two for peak overpressure at a given range and roughly 20 percent for range to a given peak overpressure. It is important to remember in scaling HOB effects that both the HOB and distance from ground zero must be scaled. That is, both the given HOB and ground range must be scaled to 1kT (4.184×10^{12}j) to obtain the corresponding burst conditions in Figs. 3-13 through 3-17. Alternatively, the HOB and ground range from Figs. 3-13 through 3-17 corresponding to the phenomena of interest are scaled to the given yield.

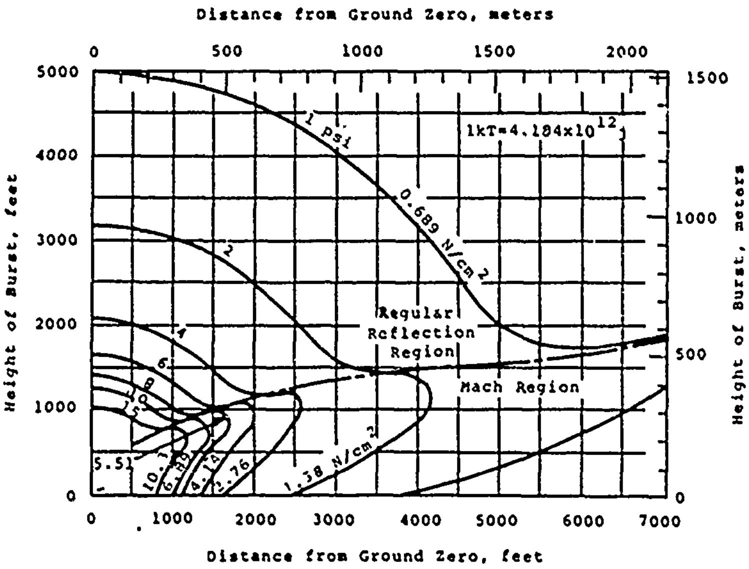

Figure 3-13 Peak Overpressures on the Ground for a 1kT Burst (Low-Pressure Range) (Ref. 3-4)

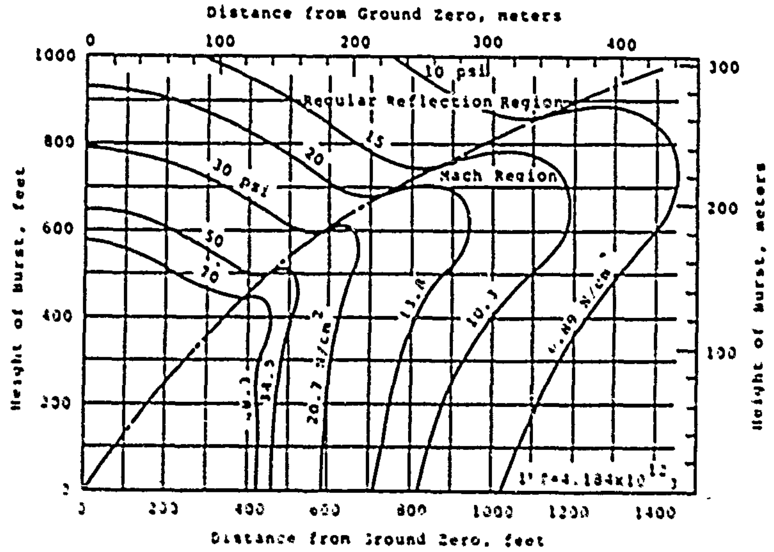

Figure 3-14 Peak Overpressures on the Ground for a 1kT Burst (Intermediate-Pressure Range) (Ref. 3-4)

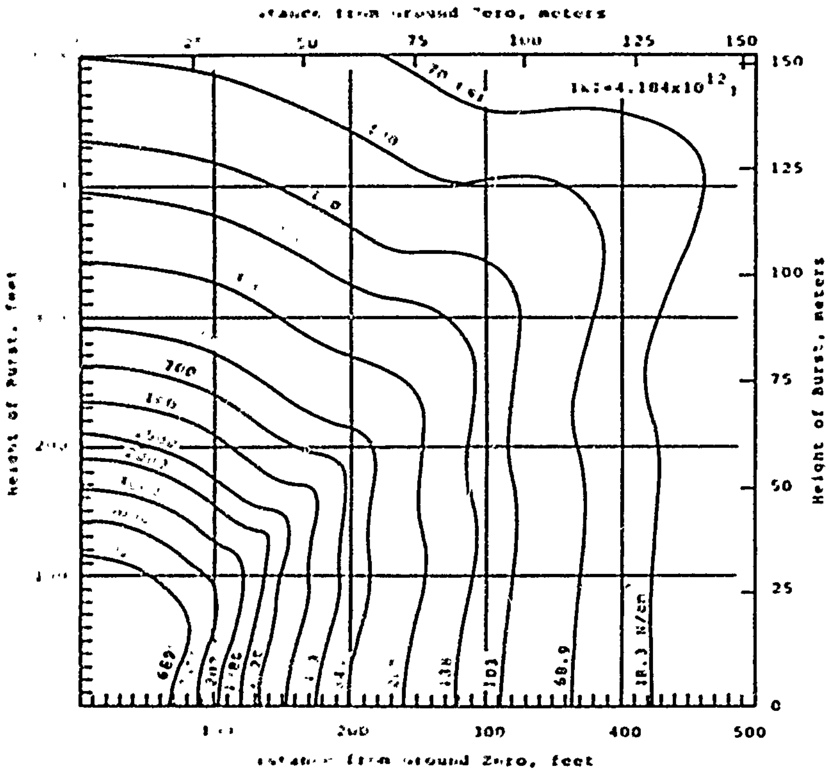

Figure 3-15 Peak Overpressure on the Ground for a 1kT Burst (High-Pressure Range) (Ref. 3-5)

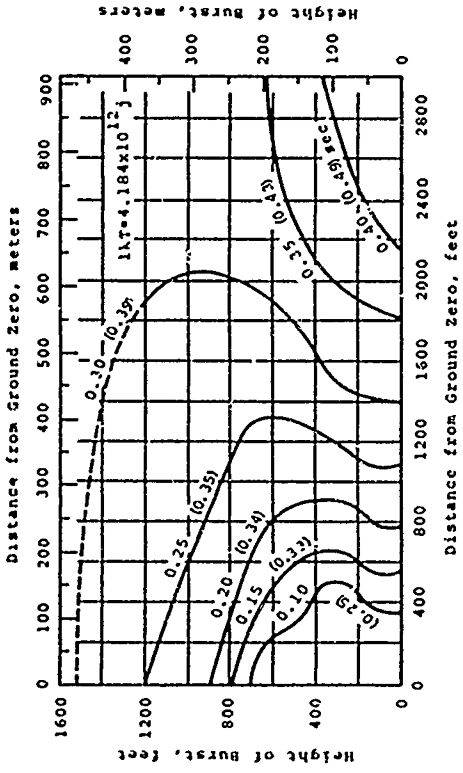

Figure 3-16 Positive Phase Duration on the Ground of Overpressure and Dynamic Pressure (in Parentheses) for a 1kT Burst (Ref. 3-4)

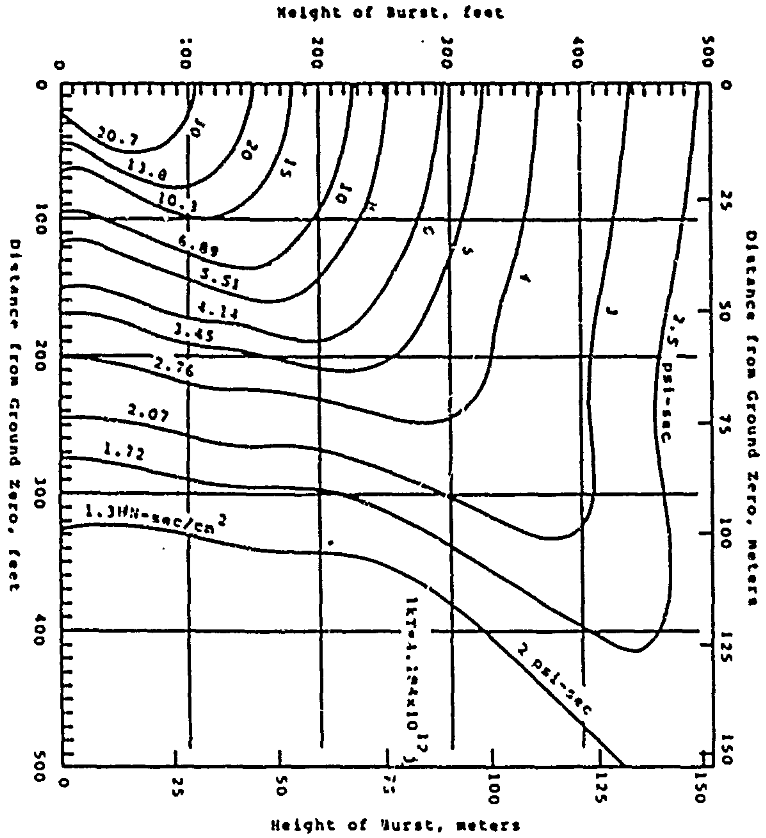

Figure 3-17 Overpressure Impulse on the Ground for a 1kT Burst (Ref. 3-5)

NOTE

* See Attachment to RDA letter dated 12 DEC 78 from H.L. Brode Subject: Improvements & Corrections to DASA 2506 "Height of Burst Effects at High Overpressures" Available from HQ DNA or AFWL for minor corrections at early times of p(t) *

Table 3-1

OVERPRESSURE-TIME HISTORY ON THE GROUND FROM AIR BURSTS (Ref. 3-5)

Overpressure-time analytical approximation:

$$p(t) = H(P,z)\left[1 + \frac{E(p)}{1+0.4/z^4}\right]\left[ap(t,t_a,W) + (1-a)p(t,t_a,2W)\right] \text{ psi} \qquad (1)$$

in which

$z = y/x$

y = height of burst

x = horizontal range to shock front

$$a = \frac{z^2(1+2z^4)}{1+2z^6} \qquad (2)$$

Function $p(t,t_a,W)$:

$$p(t,t_a,W) = \frac{13{,}493W^{1/3}}{(t+0.135W^{1/3})}\left[0.4587 + 0.6413\left(\frac{t_a}{t}\right)^6\right]\left(1 - \frac{t-t_a}{D}\right) V \text{ psi} \qquad (3)$$

in which

$$t_a(R,W) = \frac{0.5429W - 21.185RW^{2/3} + 361.8R^2W^{1/3} + \overset{2383}{\text{[illegible]}}R^3}{W^{2/3} + 2.048RW^{1/3} + 2.687R^2} \text{ msec} \qquad (4)$$

Table 3-1 OVERPRESSURE-TIME HISTORY ON THE GROUND FROM AIR BURSTS (Ref. 3-5) (cont.)

with

W = yield in kT

$R = \sqrt{x^2 + y^2}$ in kilofeet

Solve Eq. 4 with $W = W$ for t_a (W) and with $W = 2W$ for t_a (2W). Then find

$$t_a = t_a(W) \qquad \text{for } x \leq y$$

$$t_a = t_a(W)y/x + t_a(2W)(1-y/x) \qquad \text{for } x > y \tag{5}$$

$$D = \frac{820{,}350W + 15{,}515W^{2/3}t_a + 330.3W^{1/3}t_a^2}{6854W^{2/3} + 491.9W^{1/3}t_a + t_a^2} \text{ msec} \tag{6}$$

$$V = \frac{W^{2/3} + 0.6715W^{1/3}t + 0.004813t^2}{W^{2/3} + 1.8836W^{1/3}t + 0.02161t^2} \tag{7}$$

t = time of interest, msec

For the initial step, $t = t_a$ as determined from Eq. 5. In succeeding steps, increment the horizontal range, x; find the new slant range, R; recompute $t_a' = t$ with Eq. 5. All expressions involving R, t and z are recomputed with each increment of x.

Function $p(t, t_a 2W)$:

Same as the preceding, i.e., Eq. 3, with $W = 2W$.

Function $H(P,z)$:

$$H(P,z) = 1 + A + \frac{BP^{1.5}}{C+p^3} + \frac{FP}{I+p^2} \tag{8}$$

Table 3-1 OVERPRESSURE-TIME HISTORY ON THE GROUND FROM AIR BURSTS (Ref. 3-5) (cont.)

in which

$$A = \frac{0.743(1.136-z)z^2}{1.544+z^6} - \frac{0.0257z^6}{0.004435+z^{12}} \tag{9}$$

$$B = \frac{z(20.42+35.5z)}{3.57+z^2} + \frac{2500z^4}{29.3+z^{14}} \tag{10}$$

$$C = \left[1 + \frac{z(2.23z-0.225)}{0.148+z^2} + \frac{28.4z^7}{0.905+z^7}\right]^3 \tag{11}$$

$$P = \frac{1.58W}{R^3} + \frac{5.40\sqrt{W/R}}{R} + 0.0215 \text{ psi} \tag{12}$$

$$F = \frac{2.07z^2}{0.00125+0.0146z^2+z^8} + \frac{221.25z^8}{1+z^{20}} \tag{13}$$

$$I = 40{,}000 - \frac{17{,}650z^2}{0.235+z^6} \tag{14}$$

Function $E(P)$:

$$E(P) = 1 + \frac{0.002655P}{1+0.0001728P+P^2(1.921)^{-9}} + \frac{0.004218+0.04834P+P^2(6.856)^{-6}}{1+0.008P+P^2(3.844)^{-6}} \tag{15}$$

3.3 DYNAMIC PRESSURE

3.3.1 Peak Dynamic Pressure

The most destructive effects of a blast wave are generally due to the overpressure; however, in some cases, the drag forces associated with the strong transient winds behind the shock front can be of greater significance. In particular, some structure geometries are described as drag sensitive because they are quickly enveloped by the blast wave and translatory forces are primarily a result of drag forces acting on the structure. These drag forces are a function of the size and shape of the structure and the peak value of the dynamic pressure.

Dynamic pressure, q, is pressure which results from the mass air flow (wind), behind the shock front. It is proportional to the square of the wind velocity and to the density of the air behind the shock front. Under ideal conditions, both the wind velocity, u, and the air density, ρ, are related to the overpressure as follows (assuming an ideal gas)

$$u = \frac{5P_{so}}{7P_o}\left[\frac{c_o}{\left(1 + 6P_{so}/7P_o\right)^{1/2}}\right] \qquad (3\text{-}7)$$

and

$$\rho = \rho_o\left[\frac{7 + 6P_{so}/P_o}{7 + P_{so}/P_o}\right] \qquad (3\text{-}8)$$

where ρ_o is the ambient air density. The dynamic pressure, q, is given by

$$q = \frac{1}{2}\rho u^2 \qquad (3\text{-}9)$$

Introducing appropriate Rankine-Hugoniot conditions based on mass, energy, and momentum conservation, the peak dynamic pressure, q_o, is

$$q_o = \frac{5}{2}\,\frac{P_{so}^2}{7P_o + P_{so}} \qquad (3\text{-}10)$$

Figure 3-18 shows the variation of peak dynamic pressure with peak overpressure at sea level. Equation 3-10, which is based on ideal gas conditions, agrees reasonably well with Fig. 3-18 up to overpressures of about 1000 psi (689 N/cm^2). The curve in Fig. 3-18 represents more realistic behavior of the air at higher pressures and temperatures. Neither Eq. 3-10 nor Fig. 3-18 considers the effect of nonideal conditions such as the mass of dust and debris picked up by the blast wave on dynamic pressures. The latter effect can be significant over dusty surfaces and can result in higher dynamic pressures due to the increased air density.

Since dynamic pressure is directly relatable to overpressure as indicated by the above equations, it would be expected that peak dynamic pressures could be predicted with the same order of precision as overpressure even though the possibility of dust being picked up by the blast wave could have more effect on the dynamic pressure. In general, it is estimated that peak dynamic pressure at a given range will be reliable within a factor of two and the predicted range at which a given dynamic pressure will occur reliable within 25 percent.

3.3.2 Time of Arrival, Duration and Impulse

The dynamic pressure time of arrival is considered to be the same as that of the peak overpressure discussed earlier. The dynamic pressure positive phase duration, t_u, and positive phase impulse, I_u, are shown as functions of peak overpressure from a 1MT (4.184 x 10^{15}j) surface burst in Fig. 3-19. Values of these parameters for other yields can be obtained by cube-root scaling.

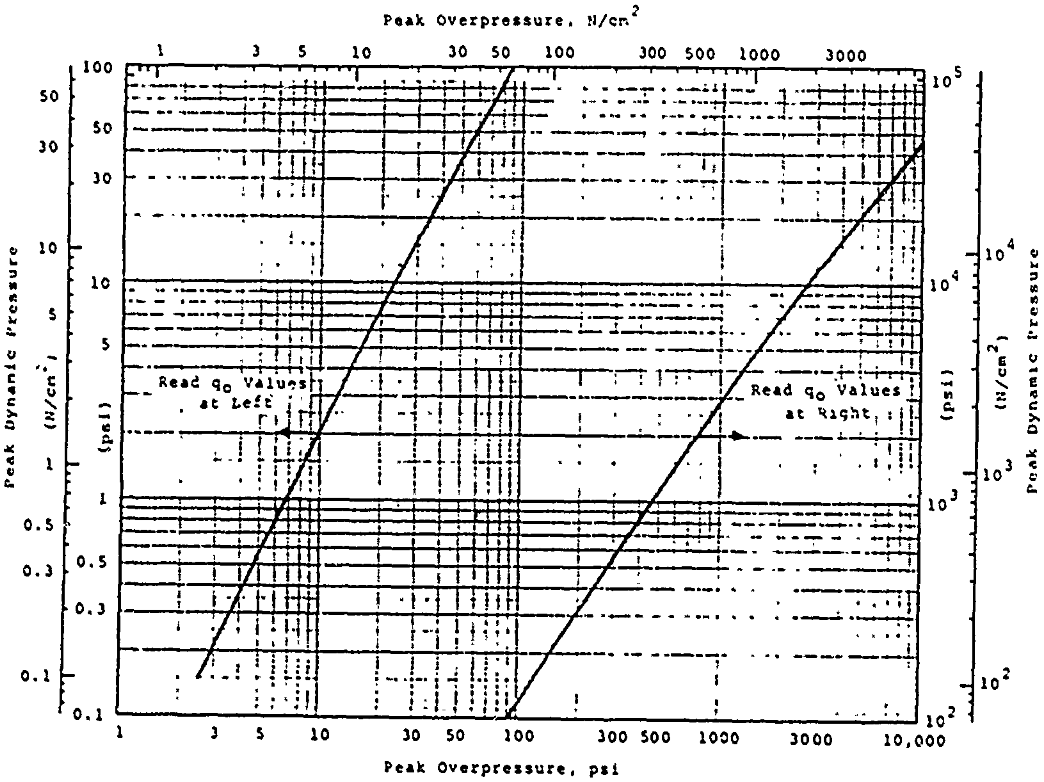

Figure 3-18 Peak Dynamic Pressure as a Function of Peak Overpressure at Sea Level

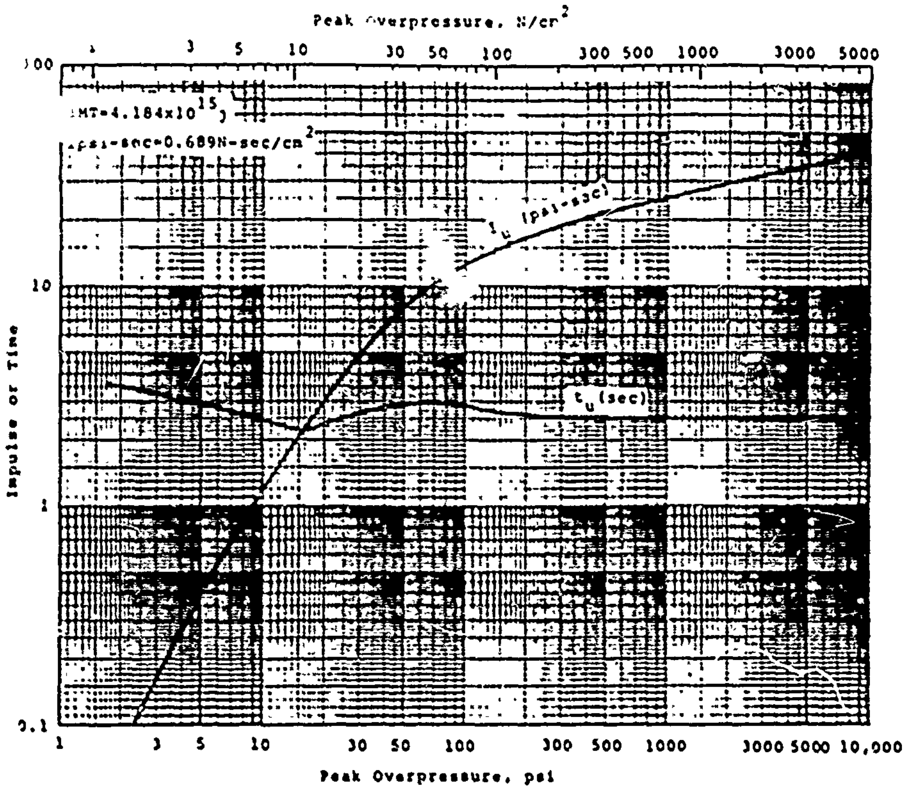

Figure 3-19 Dynamic Pressure Duration and Impulse as a Function of Peak Overpressure for a 1MT Surface Burst (Ref. 3-1)

3.3.3 Variation of Dynamic Pressure with Time

As with overpressure, the decay of the dynamic pressure with time can be expressed in an exponential form as follows (Ref. 3-1)

$$q(t) = q_o(1-\omega)^2 \left(de^{-\delta\omega} + fe^{-\phi\omega}\right) \qquad (3\text{-}11)$$

where

$$\omega = \frac{t' - t_a}{t_u} \quad (\geq 0)$$

and d, f, δ and ϕ are given in Fig. 3-20. Figure 3-20 also shows the flow Mach number immediately behind the shock front. The Mach number is the ratio of the wind velocity to the local speed of sound. Figure 3-21 presents a series of curves of normalized dynamic presure as a function of the normalized time, the time being normalized with respect to the duration of the positive phase of the dynamic pressure.

3.3.4 Dynamic Pressure-Time Approximations

As in the case of peak overpressure, it is more convenient for rapid response calculations to use an equivalent triangular pulse to represent the actual dynamic pressure-time curve. Three equivalent durations, t'_i, t'_{oo}, and t'_{50}, having the same significance as those described in paragraph 3.2.4, are used. Figure 3-22 shows the variation of each of these factors with peak overpressure for a 1MT (4.184×10^{15} j) surface burst. Although the effective durations are shown as a function of peak overpressure in Fig. 3-22, the peak dynamic pressure is used as the initial value of the equivalent triangular pulse. Values for other yields of interest can be obtained by scaling data from Fig. 3-22.

3.3.5 Effect of Height of Burst

The height of burst affects the variation of peak

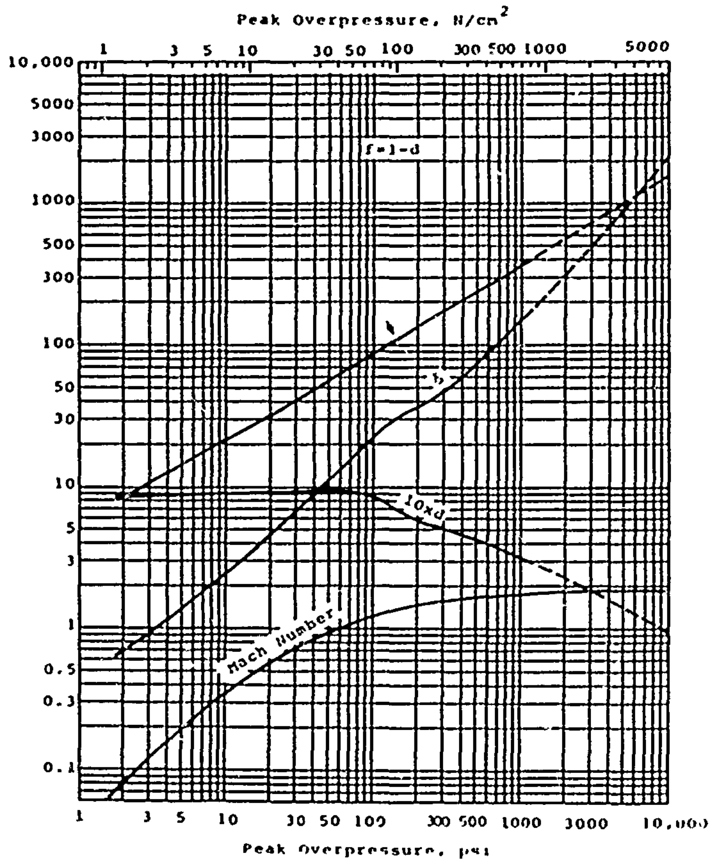

Figure 3-20 Values of Quantities for Computing Dynamic Pressure Wave Forms for Surface Bursts (Ref. 3-1)

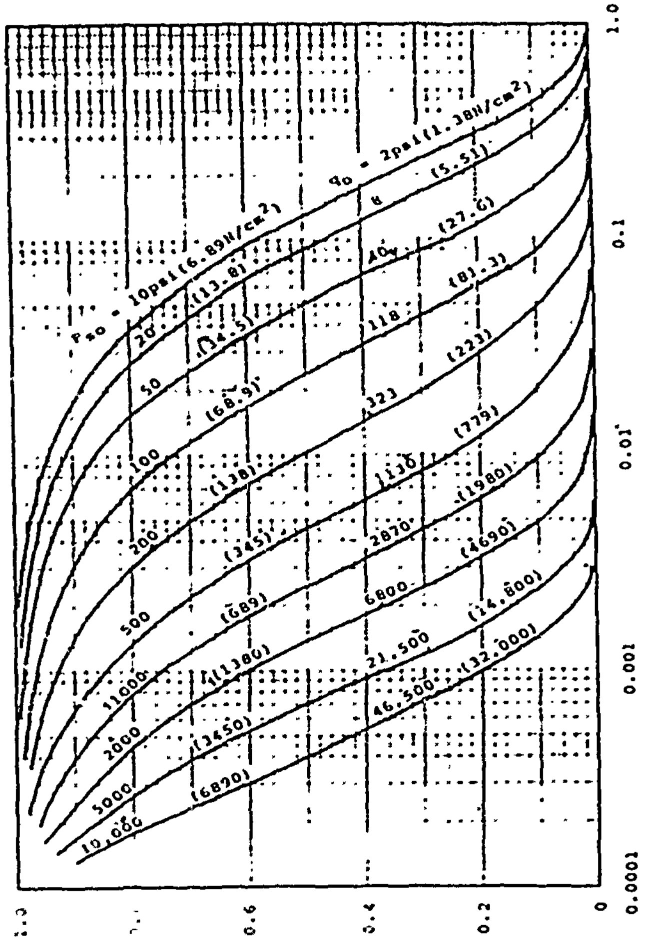

Figure 3-21 Normalized Dynamic Pressure-Time Curves

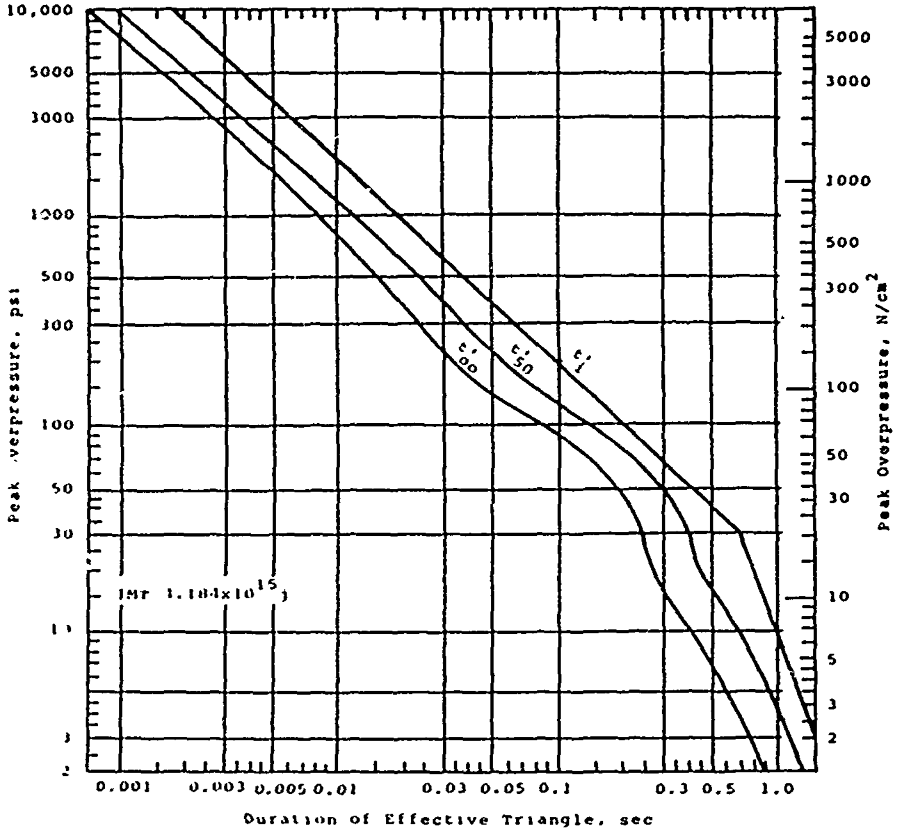

Figure 3-22 Duration of Effective Triangles for Representation of Dynamic Pressure-Time Curves--1MT Surface Burst (Ref. 3-2)

dynamic pressure with ground range as was found to be the case with peak overpressure. Figures 3-23 and 3-24 show the horizontal component of peak dynamic pressure on the ground surface as a function of burst height and ground range for 1kT (4.184×10^{12}J). In order to use these figures for other weapon yields, the actual height of burst and ground range must be scaled to 1kT using the cube root scaling relationship of Eq. 3-1. The dashed portions of the curves in Fig. 3-24 show slight differences between ideal and real reflecting surfaces. Even larger differences occur under precursor conditions. Precursor waves are discussed in paragraph 3.4.

The effect of height of burst on dynamic pressure durations is shown in Fig. 3-16. Estimation of dynamic pressure-time histories on the surface due to air bursts can be accomplished along the lines outlined earlier for overpressure. Dynamic pressure-time histories from air bursts can be even more uncertain than overpressure-time histories since less data are available on dynamic pressures.

3.4 PRECURSOR EFFECTS

3.4.1 General

The discussion of airblast phenomena in preceding paragraphs has been based primarily on the assumption that the only effect the earth surface has on the blast wave is to act as an idealized reflecting surface. The ranges of uncertainty in predicted values mentioned previously represent an effort to take account of the effects the semi-infinite possible combinations of atmospheric conditions, actual ground surfaces, uneven terrain, etc., might have on the airblast phenomena predicted for a particular problem of interest. In addition to these uncertainties, there is another phenomenon, the precursor, which can further affect the prediction of airblast parameters.

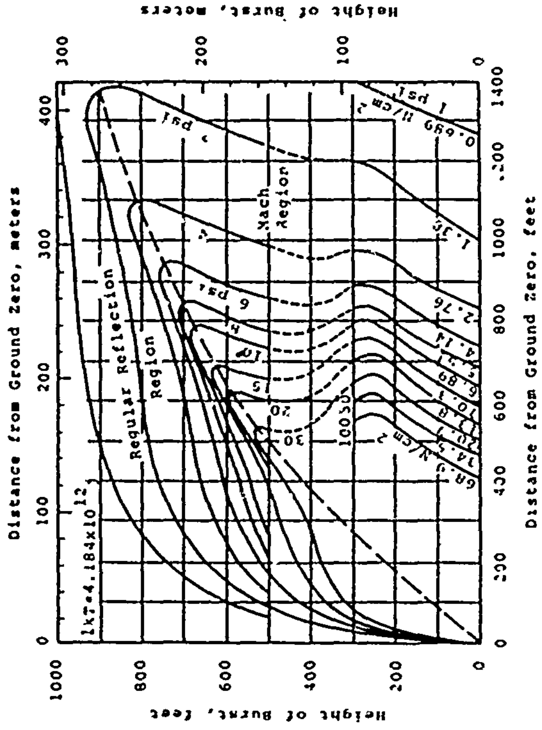

Figure 3-23 Peak Dynamic Pressures on the Ground for a 1kT Burst, Near-Ideal Surface Conditions (Low-Pressure Range) (Ref. 3-6)

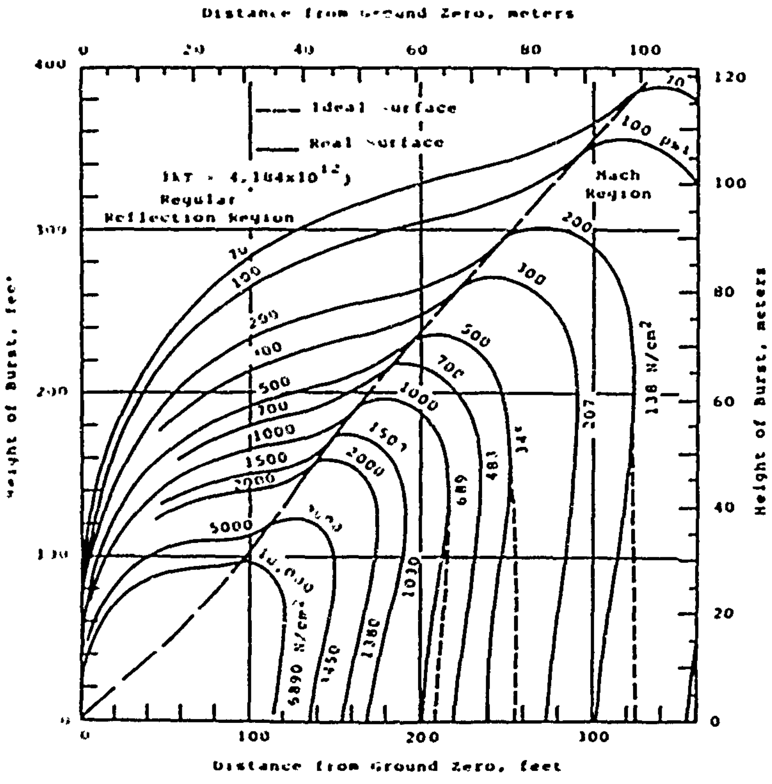

Figure 3-24 Peak Dynamic Pressures on the Ground for a 1kT Burst (High-Pressure Range) (Ref. 3-6)

If the intense thermal radiation from a nuclear detonation impinges on a heat absorbing surface, a hot thermal layer is formed near the surface. Since the thermal radiation propagates faster than the airblast, this hot layer is formed ahead of the blast wave. The shock propagation velocity in this hot layer is higher than that in the unheated air, and under the right combination of weapon yield, height of burst and surface conditions, an auxiliary blast wave called a precursor may propagate ahead of the main shock. The development of a precursor usually results in lower peak overpressures, increased rise times to peak overpressure, and increased dynamic pressures. The increased dynamic pressures can be attributed to higher particle velocities and/or greater air densities due to dust and other debris picked up by the blast wave as it passes over the ground surface.

3.4.2 Precursor Formation

Formation of a precursor is not to be expected with a high air burst or over nondusty and heat-reflecting surfaces such as snow, ice, or water. Precursors are likely to occur over dry soil, sand or other similar surfaces. They are less likely to occur as the height of burst increases or at overpressure levels less than about 10 psi (6.89 N/cm^2).

There are several characteristic wave shapes which have been used to describe precursor effects, and various procedures have been developed for predicting the occurrence of these wave shapes. Figure 3-25 shows one method for prediction of the formation of precursors for various combinations of height of burst and ground range. Also shown are typical waveforms for the overpressure pulse in the various regions. The Type I and V waveforms are the normal single peak variety as shown in Fig. 3-3. The Types II, III and IV are characterized by double peaks; the initial peak is of smaller magnitude than the second. As noted in Fig. 3-25, Type II, III and IV waveforms

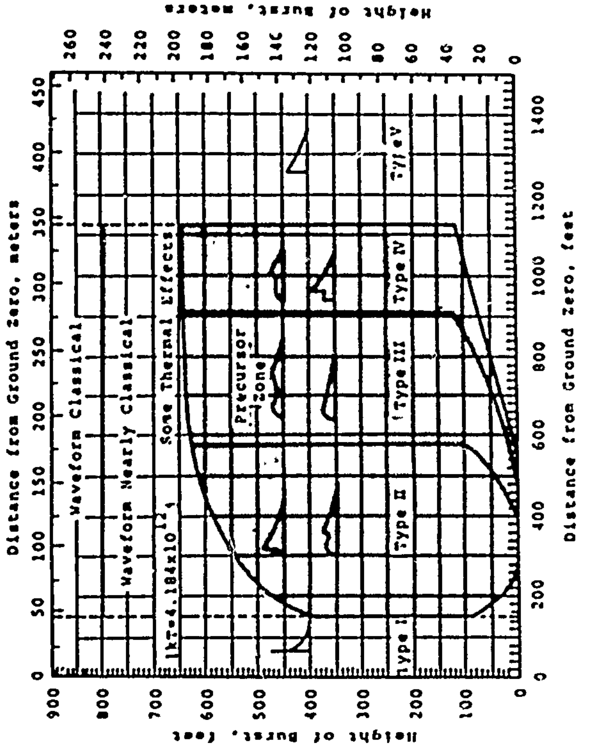

Figure 3-25 Precursor Formation Over Nonideal Surfaces for a 1kT Burst (Ref. 3-6)

are considered typical of the precursor zone. For those combinations of height of burst and ground range falling outside of the shaded area of Fig. 3-25, precursors are not expected to occur. The ground ranges and heights of burst in Fig. 3-25 can be scaled to other weapon yields by cube root scaling. Figure 3-26 shows the effect of weapon yield and height of burst on precursor formation. In the absence of better guidance, it can be assumed that the curves shown in Fig. 3-26 can be extended to include larger yield weapons with considerable uncertainty.

3.4.3 Overpressure and Dynamic Pressure Prediction

When the ground surface conditions, height of burst and ground range are such that precursor formation is predicted by Fig. 3-25 or 3-26, Figs. 3-27 through 3-30 can be used for prediction of peak values of the free-field airblast phenomena. All distances and times must be scaled to or from 1kT (4.184×10^{12}J) to use these figures. The solid portions of the curves in Figs. 3-27 through 3-30 are based on large scale test data; the dotted and dashed portions are from theory and small scale tests. The shaded areas of Figs. 3-27 and 3-28 represent regions of even greater uncertainty. Peak pressures, along with time histories, can also be estimated as outlined in following paragraphs.

As noted earlier, there can be significant changes in the character of the airblast wave in precursor regions. It is extremely difficult to predict, with any degree of confidence, the time variation of either overpressure or dynamic pressure. Reference 3-6 describes two prediction techniques but notes significant difference between predicted and measured values. One technique is more generally applicable than the other and is included here for those cases where a more detailed description of the precursor airblast phenomena is necessary.

The procedure assumes three different overpressure waveforms depending upon the ground range and height of burst.

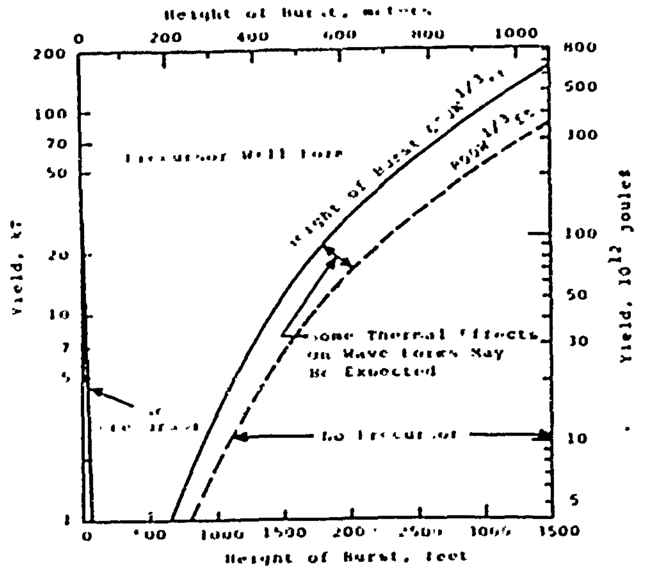

Figure 3-26 Criteria for Precursor Formation (Nonideal Surface Conditions) (Ref. 3-6)

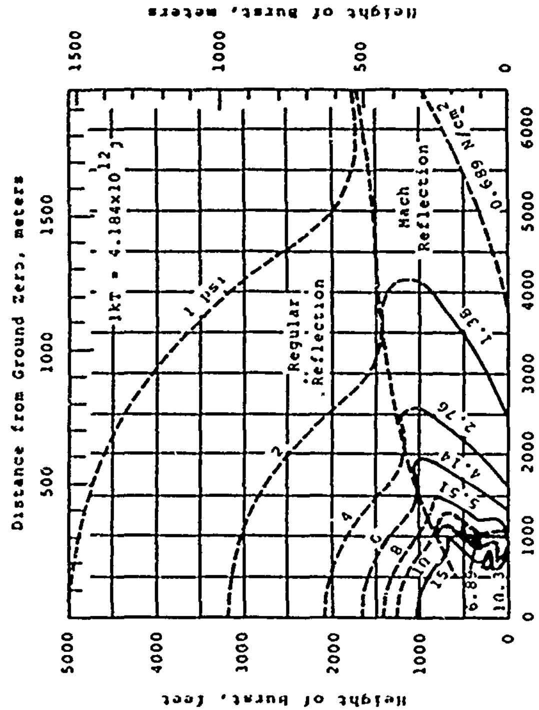

Figure 3-27 Peak Overpressures on the Ground for a 1kT Burst, Nonideal Surface Conditions (Low-Pressure Range) (Ref. 3-6)

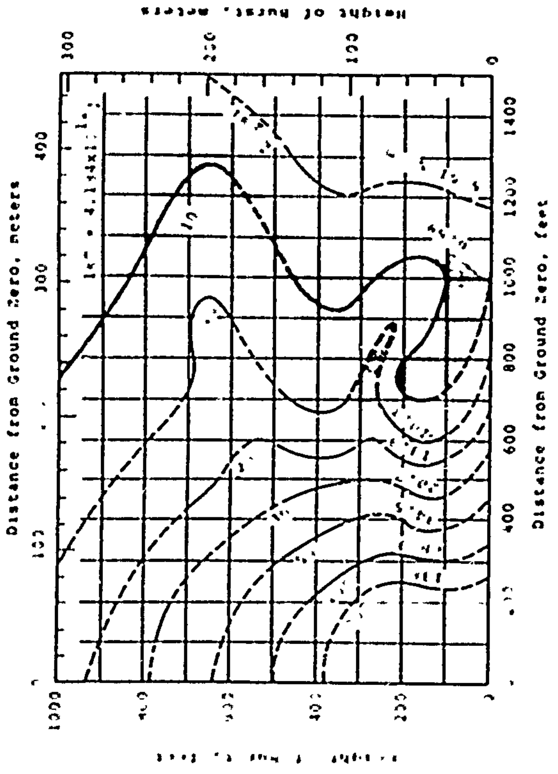

Figure 3-28 Peak Overpressures on the Ground for a 1kT Burst, Nonideal Surface Conditions (Intermediate-Pressure Range) (Ref. 3-6)

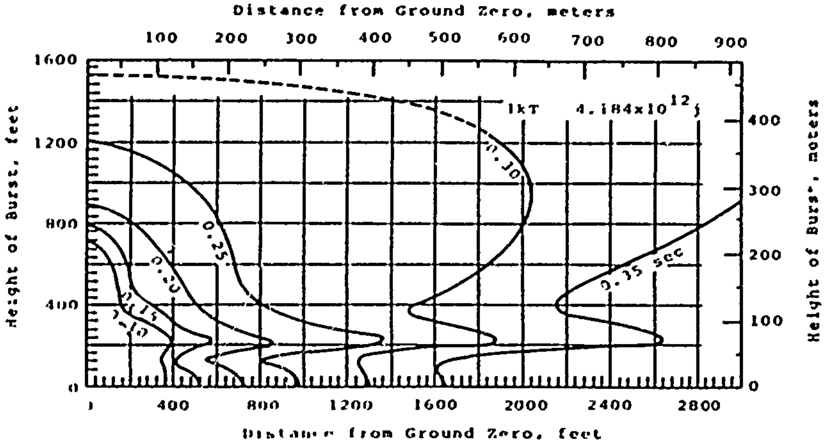

Figure 3-29 Overpressure Positive Phase Duration on the Ground for a 1kT Burst, Nonideal Surface Conditions (Ref. 3-6)

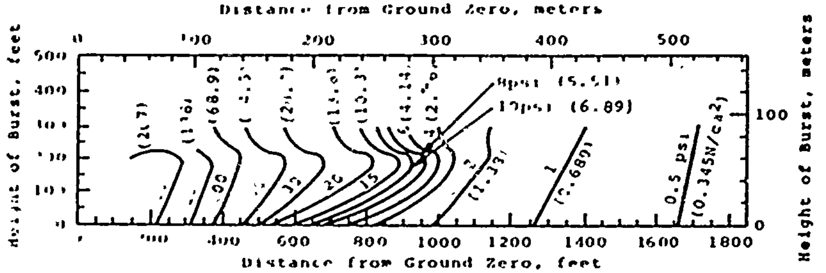

Figure 3-30 Peak Dynamic Pressures on the Ground for a 1kT Burst, Nonideal Surface Conditions (Ref. 3-6)

The three waveforms are shown in Fig. 3-31 along with a table summarizing the source of information required to define the critical points. The waveform range corresponding to a particular combination of scaled height of burst and ground range is determined from Fig. 3-32. The range of the waveform will determine which of the parameters shown in Fig. 3-31 are necessary to describe the overpressure wave. In the case of the low range, for example, it would not be necessary to determine p_1, p_3, p_{3a}, t_1, t_3 or t_{3a}. Note that p_4 is always the maximum overpressure regardless of the waveform and that it is obtained from Fig. 3-35. All times in the figures are times after detonation. For example, the rise time to peak overpressure for the low range form is given by $t_4 - t_a$. The coefficient k_p from Fig. 3-38 is used as shown in Fig. 3-31 to describe the decay of overpressure after reaching the peak value, p_4. In the high range only, p_{3a} and p_3 are taken equal to 1 psi (0.689 N/cm^2).

The dynamic pressure-time curve for the precursor region is obtained using a procedure similar to that used for overpressure. The dynamic pressure waveform will be similar to that obtained for the overpressure. The general waveform for the precursor dynamic pressure pulse is shown in Fig. 3-39 along with a table showing the source of information for determining the critical points. Note the correspondence between certain times in the overpressure and dynamic pressure waves. As in the case of the overpressure, only those values necessary to define the waveform of interest are used. The dynamic pressures q_1,, q_2,, q_3, and q_4, are obtained as indicated in the table of Fig. 3-39. The quantity $\rho u^2/2$ is obtained from the Rankine-Hugoniot relationship between dynamic pressure and overpressure shown in Fig. 3-40. The subscripts indicate which overpressure value is used in determining $\rho u^2/2$. For example, in calculating q_3,, $\rho_4 u_4^2/2$ is taken equal to the Rankine-Hugoniot dynamic pressure for an overpressure p_4. The multipliers K and C are obtained from Fig. 3-41. The dynamic pressure decay factor, k_q, is obtained from Fig. 3-38.

COMPUTATIONAL PROCEDURE	
GIVEN: Height of Burst Ground Range, Yield	
TO FIND	SEE
t_3	Fig. 3-32
t_4	$t_4 = t_3 + 6msec(W)^{1/3}$. Fig. 3-32 for Low Range.
t_a	Fig. 3-36
t_1	Fig. 3-37
t_{3a}	Fig. 3-32
p_1	Fig. 3-33
p_3	Fig. 3-34
p_{3a}	Fig. 3-34
p_4	Fig. 3-35
k_p	Fig. 3-38

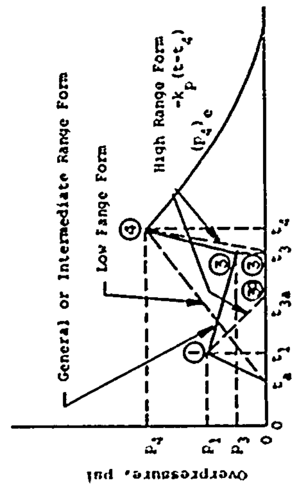

Figure 3-31 Precursor Overpressure: Time and Overpressure Notation (Ref. 3-6)

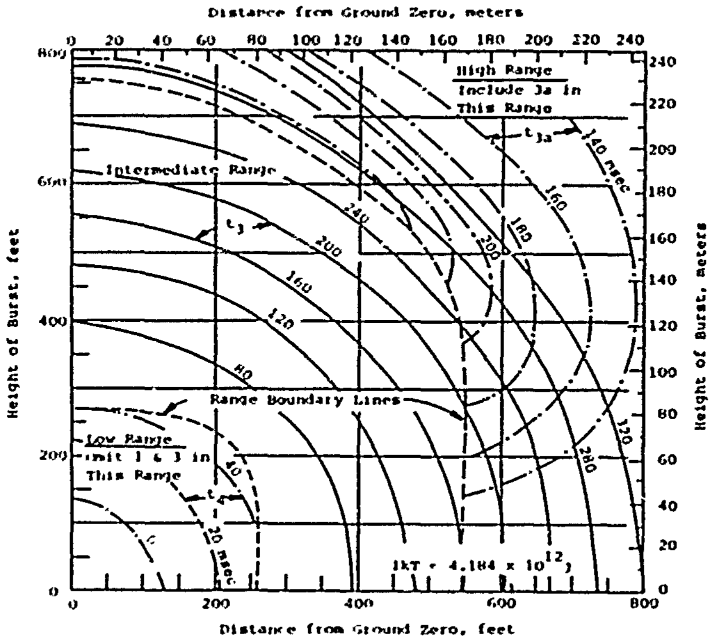

Figure 3-32 Precursor Overpressure: Times t_3, t_{3a} and t_4 for a 1kT Burst (Ref. 3-6)

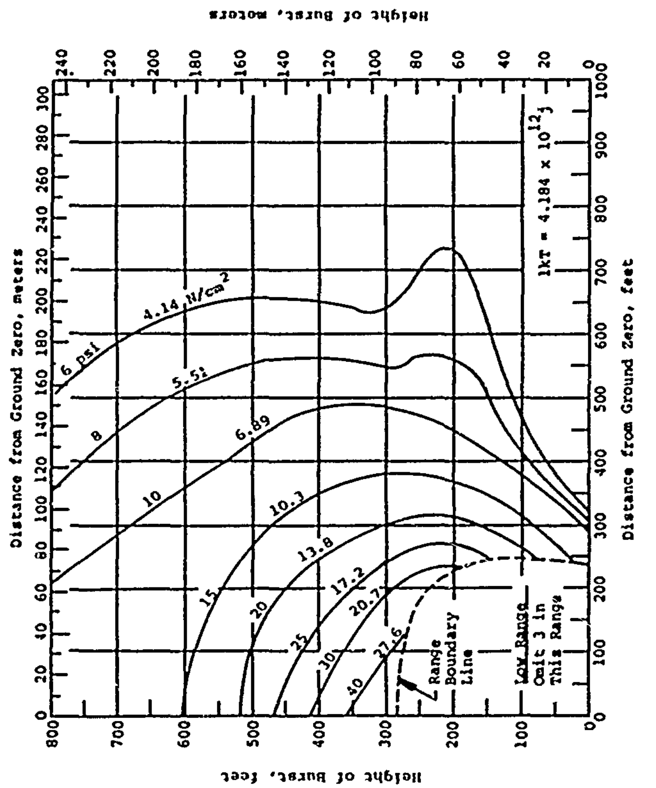

Figure 3-33 Precursor Overpressure: Pressure p_1 for a 1kT Burst (Ref. 3-6)

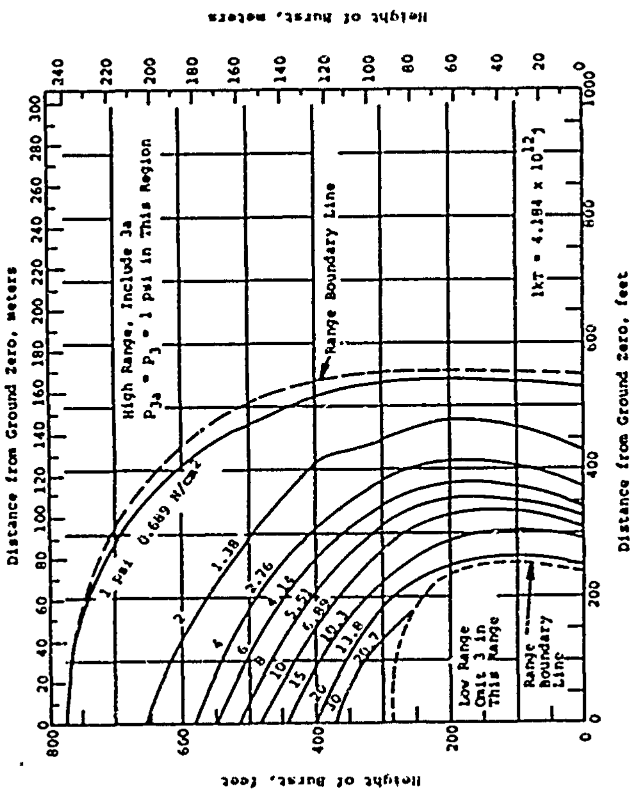

Figure 3-34 Precursor Overpressure: Pressures P_3 and P_{3a} for a 1kT Burst (Ref. 3-6)

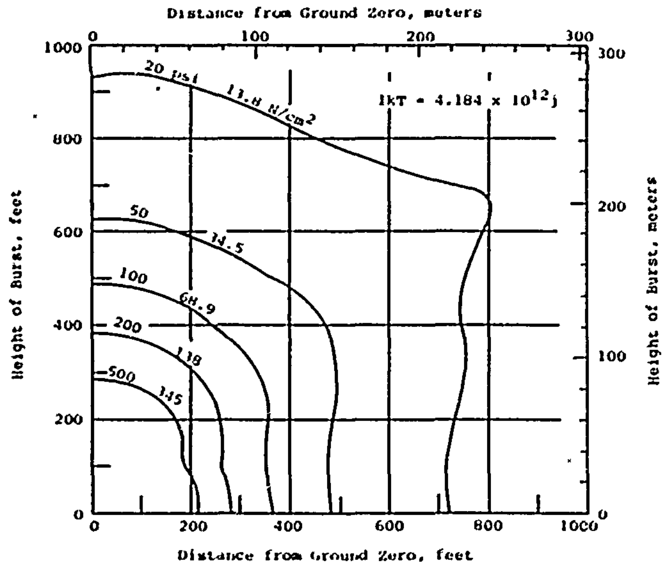

Figure 3-35 Precursor Overpressure: Pressure P_4 for a 1kT Burst (Ref. 3-6)

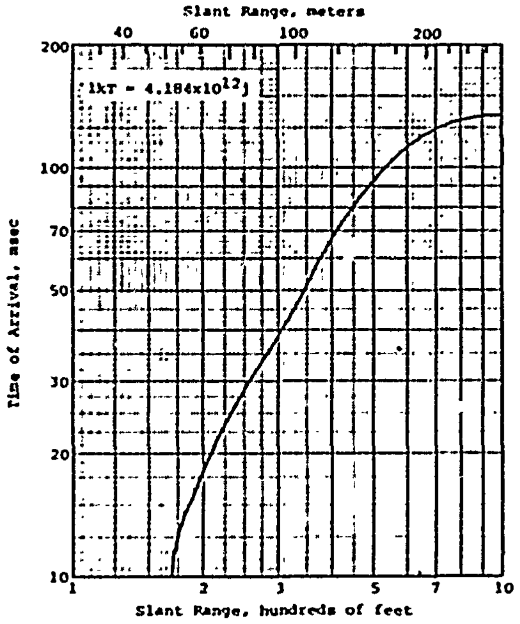

Figure 3-36 Precursor Overpressure: Time of Arrival, t_a, vs. Slant Range for a 1kT Burst (Ref. 3-6)

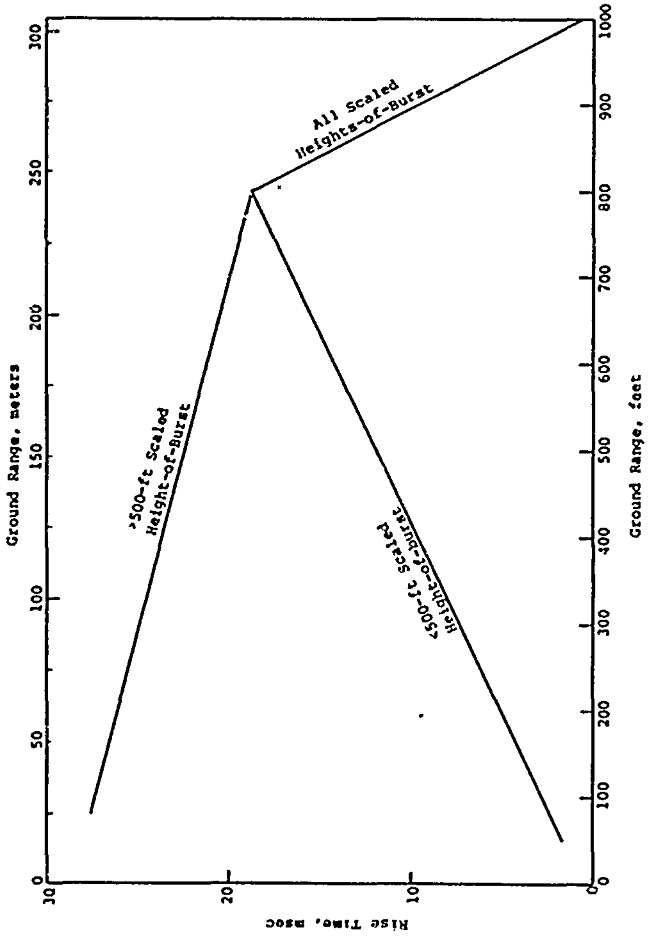

Figure 3-37 Precursor Overpressure: Rise Time, t_1-t_a, vs. Ground Range for a 1kT Burst (Ref. 3-6)

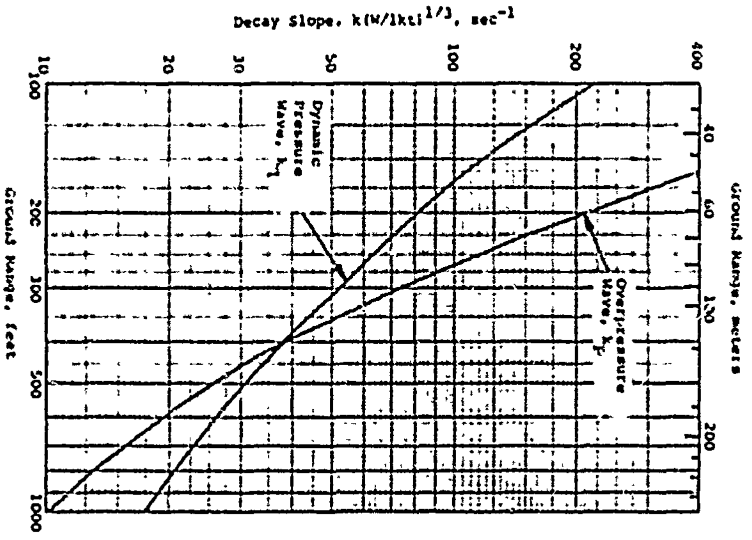

Figure 3-38 Precursor Overpressure and Dynamic Pressure: Constants k_p and k_q vs. Ground Range for a 1kT Burst (Ref. 3-6)

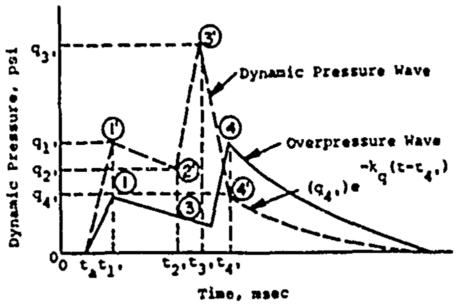

COMPUTATIONAL PROCEDURE	
GIVEN Overpressure Wave	
TO FIND	SEE
t_1'	$t_1' = t_1$
t_2'	$t_2' = (t_1' + t_4')/2$ for scaled HOB<400 ft. Fig. 3-42 for scaled HOB≥400 ft.
t_3'	$t_3' = (t_2' + t_4')/2$
t_4'	$t_4' = t_4$
q_1'	$q_1' = K[\rho_1(u_1^2/2)]$
q_2'	$q_2' = K[\rho_2(u_2^2/2)]$
q_3'	$q_3' = C[\rho_4(u_4^2/2)] = Cq_4'$
q_4'	$q_4' = [\rho_4(u_4^2/2)]$
K	Fig. 3-41
C	Fig. 3-41
k_q	Fig. 3-38
$\rho(u^2/2)$	Fig. 3-40

Figure 3-39 Precursor Dynamic Pressure: Time and Dynamic Pressure Notation (Ref. 3-6)

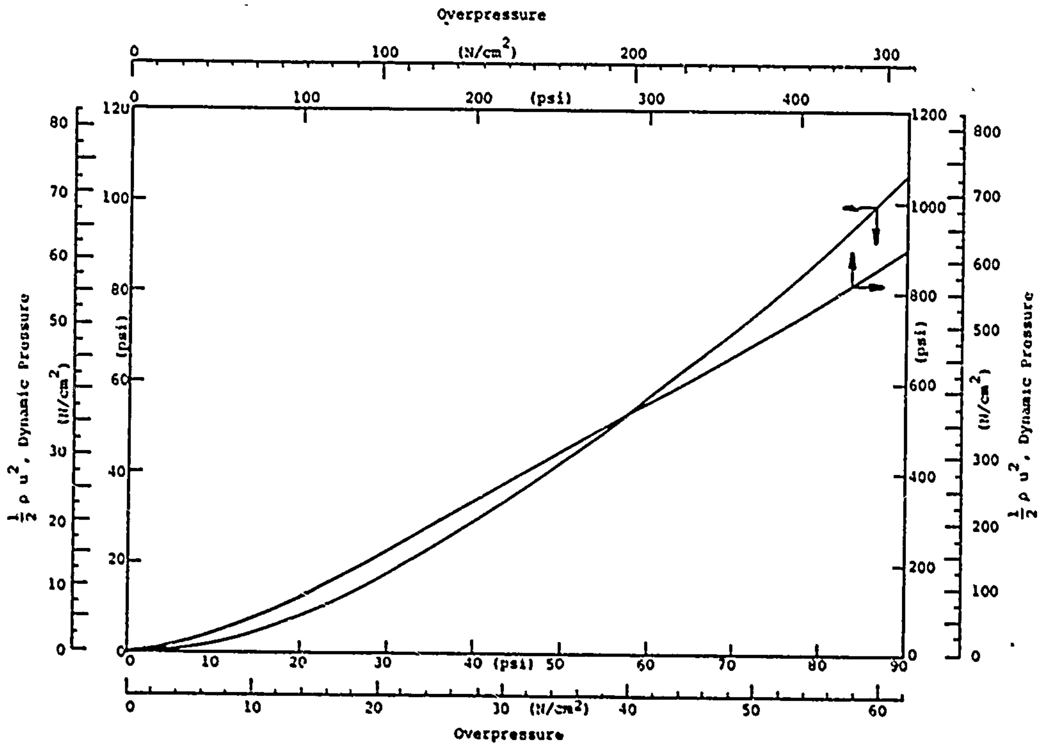

Figure 3-40 Precursor Dynamic Pressure: Rankine-Hugoniot Approximation of Dynamic Pressure vs. Overpressure (Ref. 3-6)

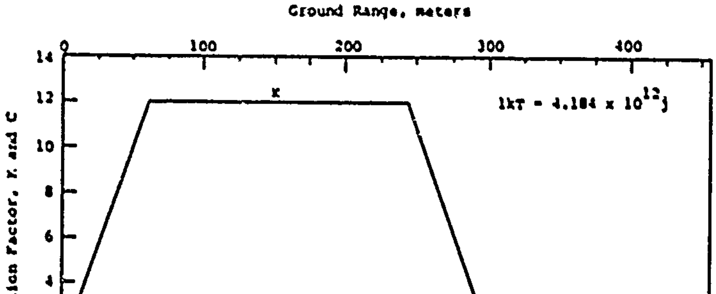

Figure 3-41 Precursor Dynamic Pressure: Constants K and C vs. Ground Range for a 1kT Burst (Ref. 3-6)

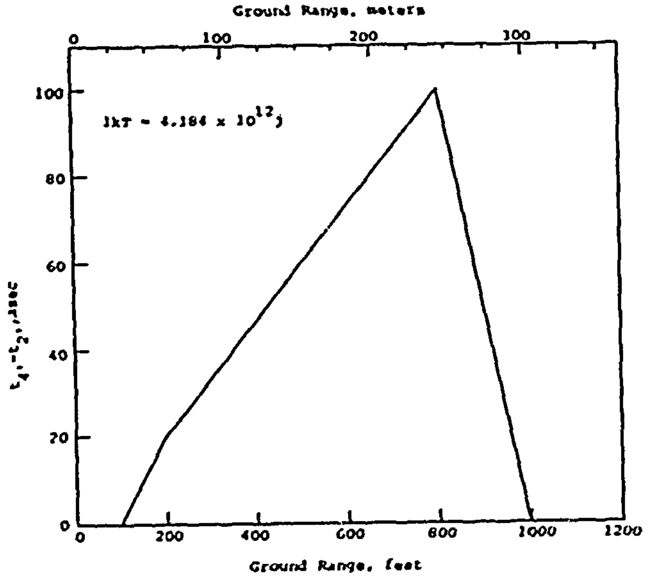

Figure 3-42 Precursor Dynamic Pressure: Times $t_{4'}-t_{2'}$, vs. Ground Range for a 1kT Burst (Ref. 3-6)

In view of the large number of variables involved and the limited data available, prediction of precursor effects is even more uncertain than that of the more classical airblast waveforms. It is estimated that predicted precursor peak pressures can vary by a factor of three or four and ranges by 50 percent.

3.5 *ILLUSTRATIVE EXAMPLES*

3.5.1 Prediction of Ground Range and Time of Arrival for a Specified Overpressure Level

a. GIVEN: A 1MT (4.184×10^{15}j) surface burst over an ideal surface.

b. FIND: The ground range at which a peak overpressure of 1000 psi (689 N/cm^2) will occur and the time of arrival of the blast wave at this location.

c. SOLUTION:

(1) From Fig. 3-4 for a 1MT surface burst, 1000 psi peak overpressure occurs at a ground range of 1500 feet (689 N/cm^2 at 457 m).

(2) From Fig. 3-5, the time of arrival of the shock front is roughly 0.07 second.

3.5.2 Definition of Airblast Phenomena at a Specified Ground Range

a. GIVEN: 1MT (4.184×10^{15}j) surface burst over an ideal surface.

b. FIND: Pertinent positive phase free-field overpressure and dynamic pressure parameters at a ground range of 1500 feet (457 m).

c. SOLUTION:

(1) From example 3.5.1, P_{so} = 1000 psi (689 N/cm^2) and t_a = 0.07 second.

(2) For an ideal surface, the peak dynamic pressure from Fig. 3-18 corresponding to 1000 psi (689 N/cm^2) overpressure is 2800 psi (1930 N/cm^2).

(3) From Fig. 3-11, the shock front velocity at a peak overpressure of 1000 psi (689 N/cm^2) is 8400 ft/sec (2560 m/sec).

(4) From Fig. 3-5, the overpressure positive phase duration, t_o, is 1.2 seconds and the overpressure impulse, I, is 56 psi-sec (38.6 N-sec/cm^2).

(5) From Fig. 3-19, the dynamic pressure positive phase duration, t_u, is 2.4 sec and the dynamic pressure impulse is 25 psi-sec (17.2 N-sec/cm^2).

(6) The variation of overpressure with time is given by Eq. 3-4 with constants taken from Fig. 3-6 for P_{so} equal to 1000 psi (689 N/cm^2).

$$p(t) = P_{so}\ (1-\tau)(ae^{-\alpha\tau} + be^{-\beta\tau} + ce^{-\gamma\tau})$$

$$p(t) = P_{so}\ (1-\tau)(0.15e^{-2.9\tau} + 0.30\ e^{-21\tau} + 0.55e^{-130\tau})$$

$$\tau = \frac{t^* - t_a}{t_o}$$

$$\tau = \frac{t^* - 0.07}{1.2}$$ where t^* is measured from the time of detonation

(7) The variation of dynamic pressure with time is described by Eq. 3-11 with constants from Fig. 3-20 for q_o = 2800 psi (1930 N/cm^2).

$$q(t) = q_o\ (1-\omega)^2\ (de^{-\delta\omega} + fe^{-\phi\omega})$$

$$q(t) = q_o\ (1-\omega)^2\ (0.32e^{-150\omega} + 0.68e^{-360\omega})$$

$$\omega = \frac{t^* - t_a}{t_u}$$

$$\omega = \frac{t^* - 0.07}{2.4}$$ where t^* is measured from the time of detonation

(8) The overpressure and dynamic pressure positive phase time histories described analytically in Steps (6) and (7) above can be utilized for machine calculations. The time histories can also be constructed graphically with the aid of Figs. 3-7 and 3-21. Table 3-1 illustrates the manner in which the normalized pressure-time curves are utilized to construct the overpressure and dynamic pressure time histories shown in Figs. 3-43 and 3-44. Equivalent triangular representations of the time histories are also shown on Figs. 3-43 and 3-44.

3.5.3 Prediction of Peak Overpressure on the Ground for a Specified Air Burst

a. GIVEN: A 1MT (4.184 x 10^{15}j) detonation at a height of 1000 feet (305 m) above an ideal surface.

b. FIND: Peak overpressure on the surface at a ground range of 4000 feet (1219 m).

c. SOLUTION:

(1) Since the air burst curves are based on a weapon yield of 1kT (4.184 x 10^{12}j), the height of burst and ground range must be scaled down to 1kT. The equivalent HOB for 1kT is

$$HOB = HOB_1\left[\frac{W}{W_1}\right]^{1/3}$$

$$HOB = 1{,}000\left[\frac{1}{1000}\right]^{1/3}$$

$$HOB = 100\ ft = 30.5\ m$$

(2) The equivalent range for 1kT is

$$R = R_1\left[\frac{W}{W_1}\right]^{1/3}$$

Table 3-2

VALUES FOR PRESSURE-TIME HISTORIES OF FIGURES 3-43 AND 3-44

Overpressure, t_o = 1.2 sec					Dynamic Pressure, t_u = 2.4 sec				
t/t_o	p/P_{so}	t sec	p psi	p N/cm^2	t/t_u	q/q_o	t sec	q psi	q N/cm^2
0	1.0	0	1000	689	0	1.0	0	2800	1930
0.001	0.93	0.0012	930	641	0.001	0.75	0.0024	2100	1448
0.005	0.70	0.006	700	483	0.003	0.44	0.0072	1232	849
0.01	0.54	0.012	540	372	0.005	0.265	0.012	742	512
0.02	0.375	0.024	375	259	0.007	0.165	0.0168	462	318
0.04	0.258	0.048	258	178	0.01	0.09	0.024	252	174
0.05	0.225	0.06	225	155	0.015	0.035	0.036	98	68
0.10	0.138	0.12	138	95	0.02	0.015	0.048	42	29

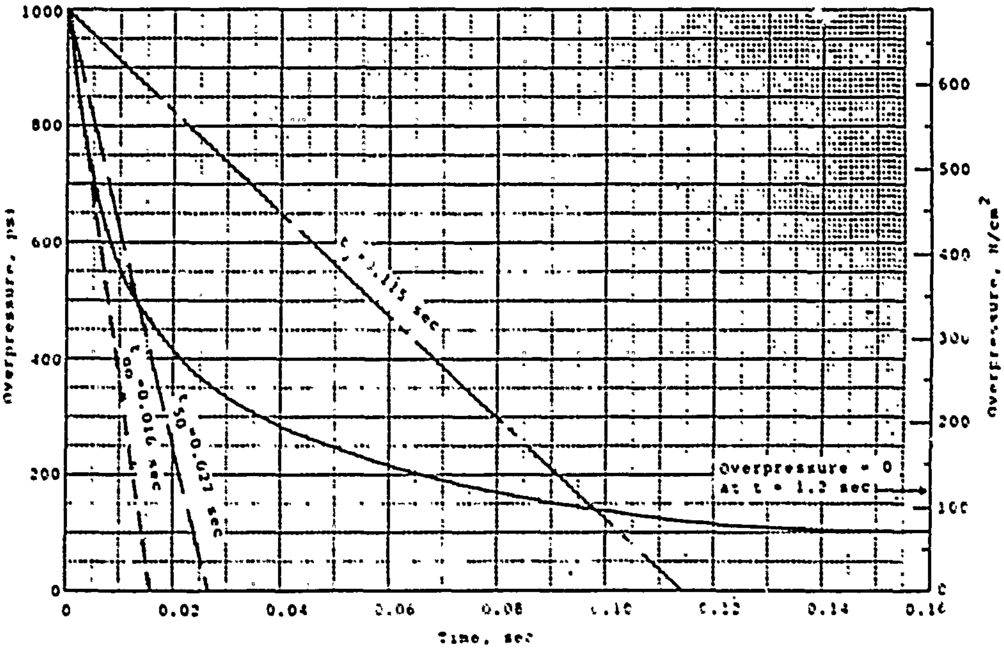

Figure 3-43 Overpressure-Time History for Example 3.5.2

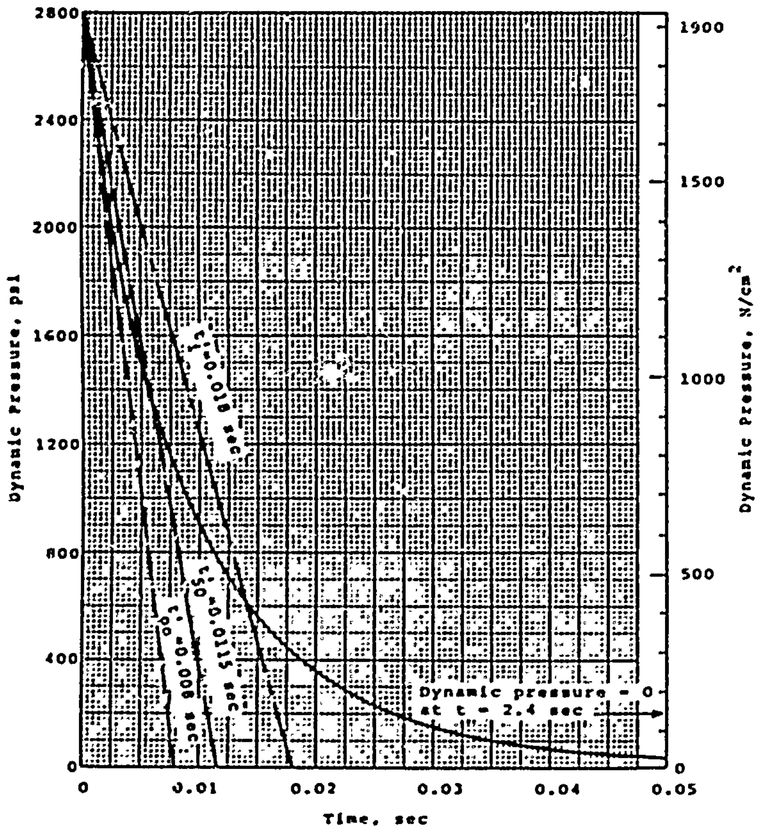

Figure 3-44 Dynamic Pressure-Time History for Example 3.5.2

$$R = 4,000 \left[\frac{1}{1000}\right]^{1/3}$$

$$R = 400 \text{ ft} = 122 \text{ m}$$

(3) From Fig. 3-15 for W = 1kT, HOB = 100 ft and R = 400 ft, the peak overpressure is about 83 psi (57 N/cm^2).

3.5.4 Definition of Airblast Phenomena in the Precursor Region

a. GIVEN: An 8MT (33.5 x 10^{15}j) detonation at a height of 10,000 feet (3050 m) above a dusty surface.

b. FIND: Pertinent positive phase free-field overpressure and dynamic pressure parameters at a ground range of 8000 feet (2438 m).

c. SOLUTION:

(1) Scale the given conditions to 1kT (4.184 x 10^{12}j).

$$HOB = HOB_1 \left[\frac{W}{W_1}\right]^{1/3}$$

$$HOB = 10,000 \left[\frac{1}{8000}\right]^{1/3}$$

$$HOB = 500 \text{ ft} = 152 \text{ m}$$

$$R = R_1 \left[\frac{W}{W_1}\right]^{1/3}$$

$$R = 8000 \left[\frac{1}{8000}\right]^{1/3}$$

$$R = 400 \text{ ft} = 122 \text{ m}$$

Entering either Fig. 3-25 or 3-26 with these values of ground range and height of burst indicates that a precursor can be expected to form.

(2) The slant range for a 1kT (4.184×10^{12}j) and the given conditions is

$$\text{Slant Range} = \left[(500)^2 + (400)^2\right]^{1/2}$$

$$\text{Slant Range} = 640 \text{ ft} = 195 \text{ m}$$

From Fig. 3-36, the time of arrival, t_a, for a 1kT burst is 115 msec. For the given burst (8MT = 33.5×10^{15}j),

$$t_a = 115 \left[\frac{8000}{1}\right]^{1/3}$$

$$t_a = 2.30 \text{ sec}$$

(3) Enter Fig. 3-32 with an HOB of 500 ft (152 m) and a ground range of 400 ft (122 m) and find t_3 = 220 msec in the intermediate waveform range. For the given burst,

$$t_3 = 220 \left[\frac{8000}{1}\right]^{1/3}$$

$$t_3 = 4.40 \text{ sec}$$

From Fig. 3-31, it is seen that the following parameters are needed to define the overpressure intermediate range waveform:

- Overpressures p_1, p_3 and p_4
- Times t_a, t_1, t_3 and t_4
- Constant k_p

(4) From Fig. 3-33, p_1 = 11 psi (7.58 N/cm^2) for the given conditions scaled to 1kT (4.184×10^{12}j). Similarly, p_3 = 1.5 psi (1.03 N/cm^2) and p_4 = 49 psi (33.8 N/cm^2) from Figs. 3-34 and 3-35, respectively.

(5) Times t_a and t_3 have been determined in Steps (2) and (3) above. From Fig. 3-37, the rise time, $t_1 - t_a$, scaled to 1kT is about 17 msec. For the given conditions,

$$t_1 - t_a = 17 \left[\frac{8000}{1}\right]^{1/3}$$

$$t_1 - t_a = 0.34 \text{ sec}$$

$$t_1 = 2.64 \text{ sec}$$

From the table in Fig. 3-31 for the intermediate range waveform and a 1kT burst,

$$t_4 = t_3 + 6W^{1/3}$$

$$t_4 = 4.40 + 0.006(8000)^{1/3}$$

$$t_4 = 4.52 \text{ sec}$$

From Fig. 3-38, $k_p(W)^{1/3}$ = 38 sec^{-1} at a scaled ground range of 400 ft (122 m).

$$k_p = \frac{38}{(8000)^{1/3}} = 1.90 \text{ sec}^{-1}$$

The resulting overpressure-time history is shown in Fig. 3-45.

(6) The arrival time for the dynamic pressure pulse is the same as for the overpressure, i.e., 2.30 seconds. The remaining parameters needed to define the dynamic pressure-time history are

- Dynamic pressures $q_{1'}$, $q_{2'}$, q_3, and q_4.
- Times $t_{1'}$, $t_{2'}$, t_3, and t_4.
- Constants k_q, K and C

Certain pressures from the corresponding overpressure-time history will also be needed to determine the dynamic pressures.

(7) From the table in Fig. 3-39,

$$t_{1'} = t_1 = 2.64 \text{ sec}$$

$$p \text{ at } t_{1'} = 11 \text{ psi } (7.58 \text{ N/cm}^2)$$

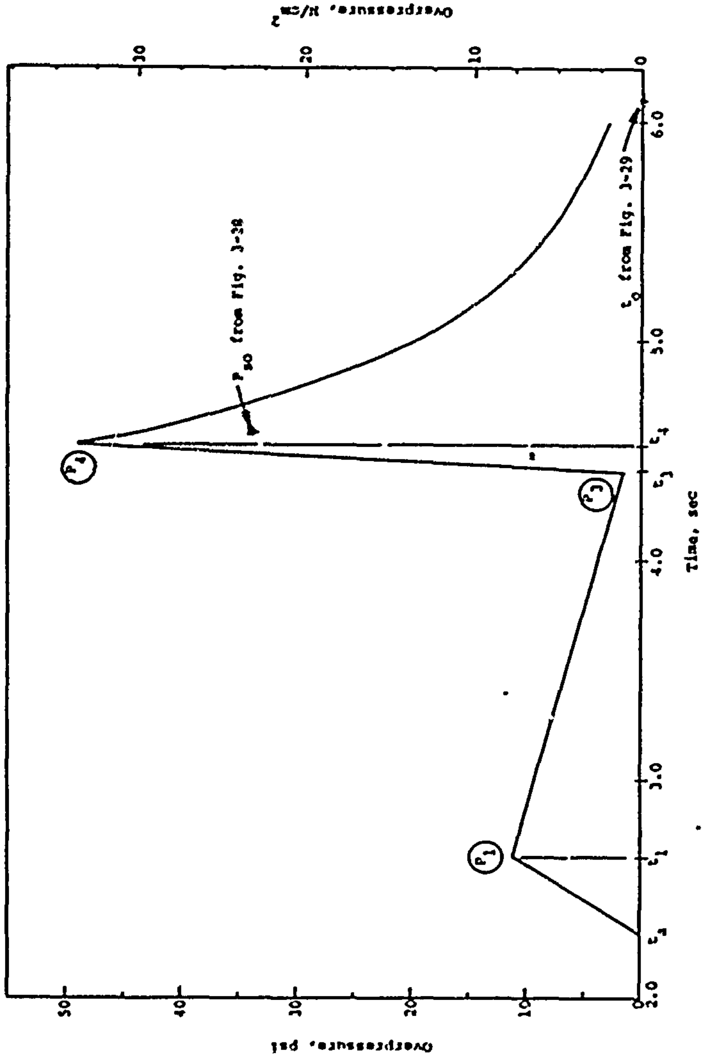

Figure 3-45 Overpressure-Time History for Example 3.5.4

$t_{4'} = t_4 = 4.52$ sec

p at $t_{4'} = 49$ psi (33.8 N/cm^2)

The quantity $(t_{4'} - t_{2'})$ is found to be 46.5 msec from Fig. 3-42, since the HOB scaled to 1kT (4.184×10^{12}j) is greater than 400 ft (122 m). For the given conditions,

$t_{4'} - t_{2'} = 46.5\left[\frac{8000}{1}\right]^{1/3}$

$t_{4'} - t_{2'} = 0.93$ sec

$t_{2'} = 3.59$ sec

p at $t_{2'} \approx 5.8$ psi (4.0 N/cm^2) from Fig. 3-45

$t_{3'} = (t_{2'} + t_{4'})/2$

$t_{3'} = (3.59 + 4.52)/2$

$t_{3'} = 4.05$ sec

(8) The constants K and C are needed to determine the dynamic pressures as indicated in the table of Fig. 3-39. From Fig. 3-41, K = 12 and C = 2.5 for the scaled ground range of 400 ft (122 m). The quantities $\rho u^2/2$ are found from Fig. 3-40 for corresponding values of the overpressure, e.g.,

$\rho_1 u_1{}^2/2 \approx 2$ psi (1.38 N/cm^2) for p = 11 psi

$\rho_2 u_2{}^2/2 \approx 0.5$ psi (0.345 N/cm^2) for p ≈ 5.8 psi

$\rho_4 u_4{}^2/2 \approx 40.5$ psi (27.9 N/cm^2) for p = 49 psi

$q_{1'} = K(\rho_1 u_1{}^2/2)$

$q_{1'} = 12(2) = 24$ psi $= 16.5$ N/cm^2

$q_{2'} = K(\rho_2 u_2^2/2)$

$q_{2'} = 12(0.5) = 6.0$ psi $= 4.13$ N/cm^2

$q_{4'} = \rho_4 u_4^2/2$

$q_{4'} = 40.5$ psi $= 27.9$ N/cm^2

$q_{3'} = Cq_{4'}$

$q_{3'} = (2.5)(40.5) = 101$ psi $= 69.6$ N/cm^2

The value of $k_q(W)^{1/3}$ for a scaled ground range of 400 ft (122 m) from Fig. 3-38 is about 38 sec^{-1}.

$$k_q = \frac{38}{(8000)^{1/3}} = 1.90 \text{ sec}^{-1}$$

The dynamic pressure-time history as determined above is shown in Fig. 3-46.

(9) It is of interest to compare precursor values obtained from Figs. 3-27 through 3-30 with those obtained in the preceding steps. The peak overpressure from Fig. 3-28 for the given conditions is about 34 psi (23.4 N/cm^2). The peak dynamic pressure from Fig. 3-30 is estimated at about 75 psi (51.7 N/cm^2). The scaled overpressure positive phase duration from Fig. 3-29 is about 0.19 second. For the given conditions,

$$t_o = 0.19\left[\frac{8000}{1}\right]^{1/3}$$

$$t_o = 3.80 \text{ sec}$$

These values are shown on Figs. 3-45 and 3-46 for comparative purposes and to illustrate the uncertainties which will be encountered in attempting to predict airblast phenomena in the precursor region. When considering a particular problem of

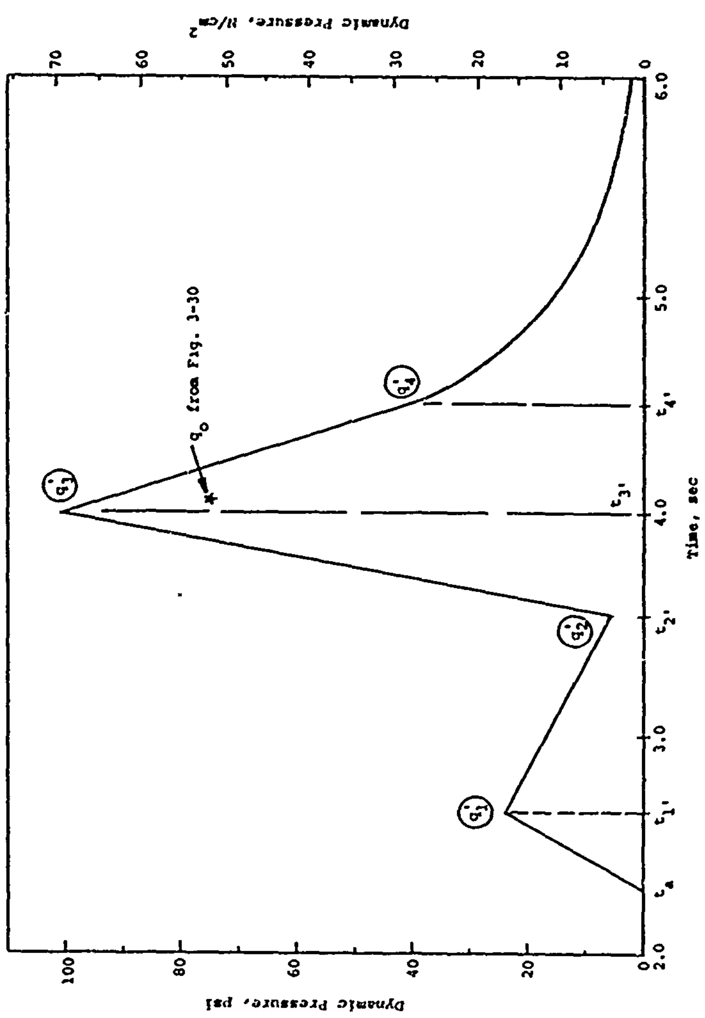

Figure 3-46 Dynamic Pressure-Time History for Example 3.5.4

interest, it is suggested that the predictions be made with the different methods and information available and the values most conservative for the purpose at hand be selected.

3.6 REFERENCES

3-1 Brode, H.L., "Review of Nuclear Weapons Effects," Annual Review of Nuclear Science, Vol. 18, 1968. (U)

3-2

3-3 Kinney, G.F., Explosive Shocks in Air, The Macmillan Co., New York, N.Y., 1962. (U)

3-4 Glasstone, S., et al., The Effects of Nuclear Weapons, Government Printing Office, Washington, D.C., 1964. (U)

3-5 Brode, H.L., Height of Burst Effects at High Overpressures, RM 6301, The Rand Corp., Santa Monica, Calif., July 1970. (U)

3-6 Air Blast Loading in the High Shock Strength Region, Part II, Prediction Methods and Examples, DASA 1460, Defense Atomic Support Agency, Washington, D.C., February 1965. (U)

SECTION IV

CRATERING PHENOMENA

4.1 INTRODUCTION

4.1.1 General

The detonation of a nuclear weapon at or near the earth's surface will produce a crater and cause the ejection of a large quantity of debris. Cratering must be considered in the design and analysis of protective structures since no system can survive in the cratered region, and ejected debris deposited on the ground surface outside the crater may interfere with the operation of exposed systems and components. In addition, discrete ejecta missiles (either rocks or earth clods) can damage surface structures and components at considerable distances from the detonation. Cratering is also an important consideration in estimating ground shock since crater volume correlates with near-surface late-time ground motions.

This section includes some comments on cratering mechanisms. Prediction techniques are given for obtaining nuclear and high explosive crater dimensions as a function of yield, height (or depth) of burst and geology (including layered geologies). Prediction techniques are also given for ejecta thickness distributions, ejecta size distributions, ejecta missile impact probabilities, and velocity of impacting missiles. Illustrative examples at the end of the section demonstrate the use of the prediction techniques.

4.1.2 Crater Terminology

Table 4-1 explains the symbols and terms used in the part of this section dealing with cratering phenomena. Figure 4-1 depicts an idealized crater cross section from a near-surface explosive burst and further clarifies some of the terms in Table 4-1. References 4-1 to 4-4 provide background material for the reader.

4.1.3 Cratering Mechanisms

The factors exerting the most influence on crater formation are as follows:

- Height (or depth) of burst
- Explosive source characteristics (yield, mass, shape and method of energy release)
- Geological structure (e.g., depth to bedrock, depth to water table, etc.)
- Material properties

Figure 4-2 shows some idealized crater cross sections from nuclear bursts illustrating the effect of HOB and DOB on crater volumes and cratering mechanisms. If a nuclear or HE burst is sufficiently high above the ground surface, only a shallow compressional crater is formed and no ejecta is produced. As the height of burst decreases, the crater volume increases and an increasing fraction of the crater is due to excavation and ejection of material from the crater region. For optimum DOB, nearly all the excavated material lies above the burst point, and excavation is accomplished primarily by the expanding explosive gases accelerating the cratered material over a relatively long period of time. For deeply buried bursts, an underground cavity is produced and there may be little or no resulting surface expression.

Table 4-1

CRATERING TERMS AND SYMBOLS

Apparent Crater - The visible crater, with radius, depth and volume measured with respect to the original ground surface. The crater depth is the deepest part of the crater and need not be co-axial with surface ground zero. A structural uplift, or mound, is frequently found in the central part of the crater.

Surface Ground Zero - The intersection of the vertical axis containing the burst point with the original ground surface.

Lip - The upthrusted ground plus overlying ejecta blanket extending from the apparent crater edge out to a distance of about 2 or 3 apparent crater radii from ground zero.

Fallback, Rupture Zone, Plastic Zone, Elastic Zone - Four intergrading regions in and around the cratered region characterized by progressively less distortion of the ground. The fallback consists of material that was disassociated and ejected into the air during cratering and has fallen back into the crater. In the rupture zone, the material, while severely fractured, sheared and displaced, has not been completely disassociated. The material in the rupture zone will, therefore, preserve some of the gross structural and compositional features that may have existed before the cratering took place. In the plastic zone, the material is permanently displaced, but in a more or less homogeneous fashion. The plastic zone grades into an "elastic zone," where no measurable permanent displacements occur.

True Crater - The crater defined by the approximate boundary between the fallback and the rupture zone.

Ejecta - The crater debris that falls outside the apparent crater, the thickness nominally decreasing with increasing range and varying by an order of magnitude or more with azimuth at a fixed range.

Ejecta Missiles - Individual soil clods or rocks thrown from the crater region, sometimes out to distances exceeding 20 or 30 crater radii.

Surface Burst - Center of explosive mass at the ground surface.

Table 4-1 (cont.)

CRATERING TERMS AND SYMBOLS

Tangent Above - Explosive resting on ground surface, touching only at one point (used primarily for spherical HE sources).

Contact Burst - Explosive devise resting on ground surface (used primarily for nuclear bursts).

Tangent Below - Top of buried explosive flush with ground surface (used primarily for spherical HE sources).

Optimum DOB - The DOB where the apparent crater volume is a maximum.

HE - High Explosive.

NE - Nuclear Explosive.

HOB - Height of burst to center of charge mass.

DOB - Depth of burst to center of charge mass.

SGZ - Surface ground zero.

W - Explosive yield.

V_a, R_a, D_a - Volume, radius and depth, respectively of the apparent crater.

Cratering Efficiency - V_a/W, a measure of the craterability of a material.

Energy Density - Ratio of explosive yield (in equivalent TNT units) to explosive weight. Thus, TNT has an energy density of one, by definition, in English units where both yield and weight are expressed in tons.

Aspect Ratio - R_a/D_a

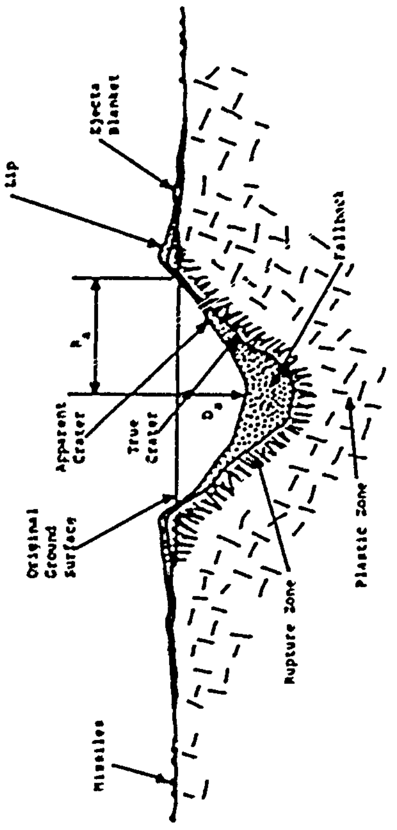

R_a = Radius of Apparent Crater
D_a = Depth of Apparent Crater

Figure 4-1 Idealized Crater Profile from a Near-Surface Burst (Modified from Ref. 4-1)

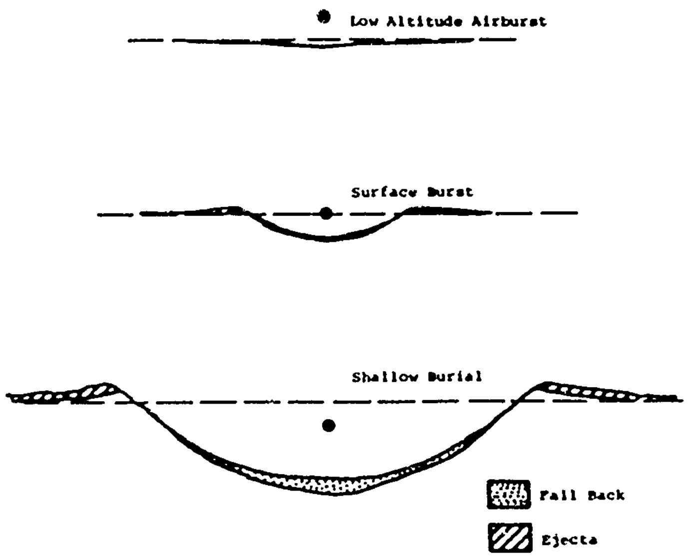

Figure 4-2 Effect of Depth of Burst on Crater Size and Shape for Nuclear Bursts

The large difference in energy density (ratio of explosive yield to explosive mass) between HE and NE devices can cause substantial differences in cratering efficiency (V_a/W) and in the relative importance of various cratering mechanisms between the two types of sources. Airblast compression of the ground is generally a more important cratering mechanism with near-surface nuclear bursts than with near-surface HE bursts although sufficient burial of the nuclear source causes the cratering phenomenology to be similar to that from an HE source at the same DOB. A tangent-above 1 kiloton (4.184×10^{12}j) TNT detonation (17 ft (5.2 m) HOB) will produce a largely excavational crater, with ejecta throwout. A 1 kiloton (4.184×10^{12}j) nuclear detonation at the same HOB will produce a purely compressional crater, with no ejecta formation. The crater volumes of the two craters are expected to differ by at least a factor of 30. On the other hand, a tangent below 1 kiloton (4.184×10^{12}j) TNT detonation (17 ft (5.2 m) DOB) should have a crater volume within about a factor of two of a 1 kiloton (4.184×10^{12}j) 17 ft (5.2 m) DOB nuclear detonation, and the cratering mechanisms for the two craters will be essentially the same. In the latter case, the ground surrounding the nuclear detonation increases the effective mass of the explosion and causes it to transmit nearly as much energy to the ground from the standpoint of cratering as the TNT explosion.

The material properties in the crater region influence the crater volume primarily through their compressibility and shear strength under dynamic loading conditions. Water content plays a large role in determining shear strength, especially in soils. The largest crater volumes are found in wet soils, and the smallest crater volumes are found in rock. Jointing is an important factor in determining the crater size in rock geologies. Geologic layering is a rough indicator of the variation of material properties with depth and must be evaluated when predicting crater volumes.

4.2 CRATER PREDICTION

4.2.1 HE and Nuclear Test Data

The crater (and ejecta) prediction methods described in this manual are empirical, being primarily derived from HE and nuclear test data. Theoretical attempts to study cratering, while yielding valuable qualitative information, are not yet sufficiently reliable to be used as the basis of a prediction technique.

The available nuclear cratering data are summarized in Table 4-2. The high yield above-surface nuclear cratering bursts are restricted to the Pacific atoll geologies at Eniwetok and Bikini. Low yield nuclear cratering bursts are restricted to desert alluvium and rock at the Nevada Test Site. With the exception of JANGLE S, the NTS bursts are buried. Because of the severe limitations in the nuclear cratering data, many HE shots have been conducted over the last 25 years to help supplement the nuclear data. HE yields range from less than a gram (9.8×10^{-3}N) to 500 tons (4.45×10^{6}N). Burst locations vary from below optimum depth of burial to several charge radii above the ground surface. HE bursts have occured in a large range of soil and rock geologies (sometimes layered) with varying water contents.

Figure 4-3 shows an idealized cross section at Eniwetok Atoll. A key feature is the horizontal variation in the depths to various geologic layers. Since bursts occurred along the entire cross section from the reef plate to barges in the lagoon, the geologies exercised during cratering varied significantly between different shots. Many of the craters breeched into the lagoon, resulting in possible water washing of the newly formed craters.

4.2.2 Crater Volume Prediction Technique: Homogeneous Geologies

Because of the substantial limitations and

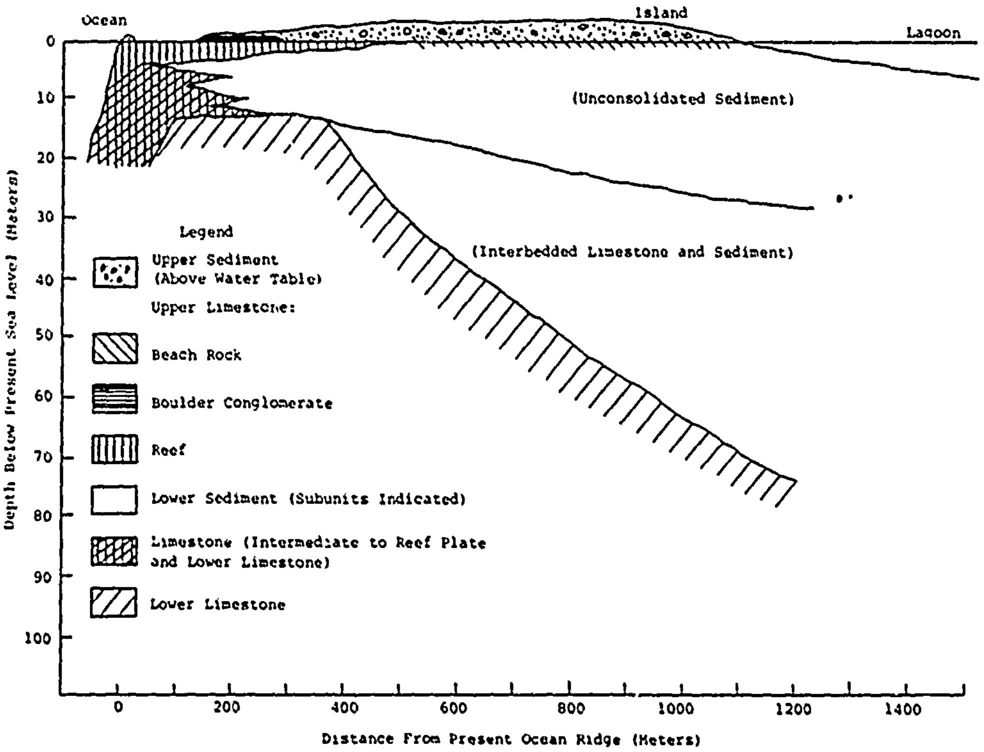

Figure 4-3 Near-Surface Geology at Eniwetok Atoll (Ref. 4-5)

Table 4-2

NUCLEAR CRATERING EVENTS

Event	Yield	Height of burst (ft)	Medium	Radius (ft)	Depth (ft)	Volume (ft^3)	Source of Data
JANGLE S	1.2 kT	+ 3.5	Alluvium	45	17	4.45×10^4	Ref. 4-6
JANGLE U	1.2 kT	- 17	Alluvium	129	53	1.32×10^6	Ref. 4-6
TEAPOT ESS	1.2 kT	- 67	Alluvium	146	90	2.60×10^6	Ref. 4-6
JOHNIE BOY	.5 kT	- 1.75	Alluvium	61	30	1.4×10^5	Ref. 4-6
SEDAN	100 kT	- 635	Alluvium	608	323	1.8×10^8	Ref. 4-6
IVY MIKE	10.4 MT	+ 10.0	Pacific Atoll Geology	3275	187	1.44×10^9	Ref. 4-6
CASTLE BRAVO	15 MT	+ 7	Pacific Atoll Geology	3180	225	2.01×10^9	Ref. 4-6
CASTLE KOON	150 kT	+ 9.3	Pacific Atoll Geology	538	75	1.50×10^7	Ref. 4-6
CACTUS	18 kT	+ 3.0	Pacific Atoll Geology	173	37.2	1.99×10^6	Ref. 4-6
OAK	9 MT	+ 6.5	Pacific Atoll Geology	3200	203	1.83×10^9	Ref. 4-6
KOA	1.30 MT	+ 3.0	Pacific Atoll Geology	2310	171	8.11×10^8	Ref. 4-6
ZUNI	3.38 MT	+ 9.6	Pacific Atoll Geology	1145	113	2.04×10^8	Ref. 4-6
TEWA	4.6 MT	+ 12.3	Pacific Atoll Geology	2160	129	7.63×10^8	Ref. 4-6
LACROSSE	39.5 kT	+ 8.0	Pacific Atoll Geology	200	46.5	3.06×10^5	Ref. 4-6
SEMINOLE	13.7 kT	+ 7.0	Pacific Atoll Geology	324	32.2	6.99×10^6	Ref. 4-6
DANNY BOY	.42 kT	- 110	Basalt	107	62.3	1.13×10^6	Ref. 4-7
SCHOONER	31 kT	- 355	Welded & Nonwelded Tuff	426	208	6.16×10^7	Ref. 4-7
CABRIOLET	2.3 kT	- 171	Rhyolite	179.4	116.4	4.86×10^6	Ref. 4-7
PALANQUIN	4.3 kT	- 280	Rhyolite	119.1	78.8	1.26×10^6	Ref. 4-7

Conversion factors for SI units:

$1\text{kT} = 4.184 \times 10^{12}\text{J}$

$1\text{ft} = 0.3048\text{m}$

uncertainties in the nuclear and HE cratering data, considerable engineering judgement and intuition is required in formulating a credible crater prediction technique. In this manual, the crater volume is calculated first and then used to calculate crater radius and depth. The scaling techniqu shown in Fig. 4-4 (from Ref. 4-8) is the one used in this manual to predict nuclear crater volumes for a given geology, HOB and yield W. This crater prediction technique is quite similar to one given in Ref. 4-9. The crater volume, V_a, and HOB are scaled by V_o, which is the TNT surface burst crater volume in the geology of interest. The scaling parameter, V_o, is defined as the product of the yield, W, and the cratering efficiency, E_o, of a TNT surface burst in the geology of interest. Figure 4-5 gives the cratering efficiencies for TNT surface bursts (E_o) in a number of different geologies. Table 4-3 gives some suggested nominal values for TNT and nuclear surface bursts in 5 idealized geologies and can be used if insufficient information is available to make use of the TNT test data summarized in Fig. 4-5. Thus, Fig. 4-4 in combination with Fig. 4-5 or Table 4-3 allows the prediction of a crater volume from a near-surface nuclear burst.

The following assumptions were made in establishing the above prediction technique:

a. The ratio of the crater volumes from an explosive burst in two different geologies is <u>independent</u> of the explosive source, which can be HE or nuclear. This assumption holds for both surface and nonsurface bursts. Other cratering investigators (e.g., Ref. 4-10) have made a similar assumption.

b. While surface nuclear cratering efficiencies are expected to decrease with increasing energy density and increasing radiation output, it is more practical to express these relationships in terms of

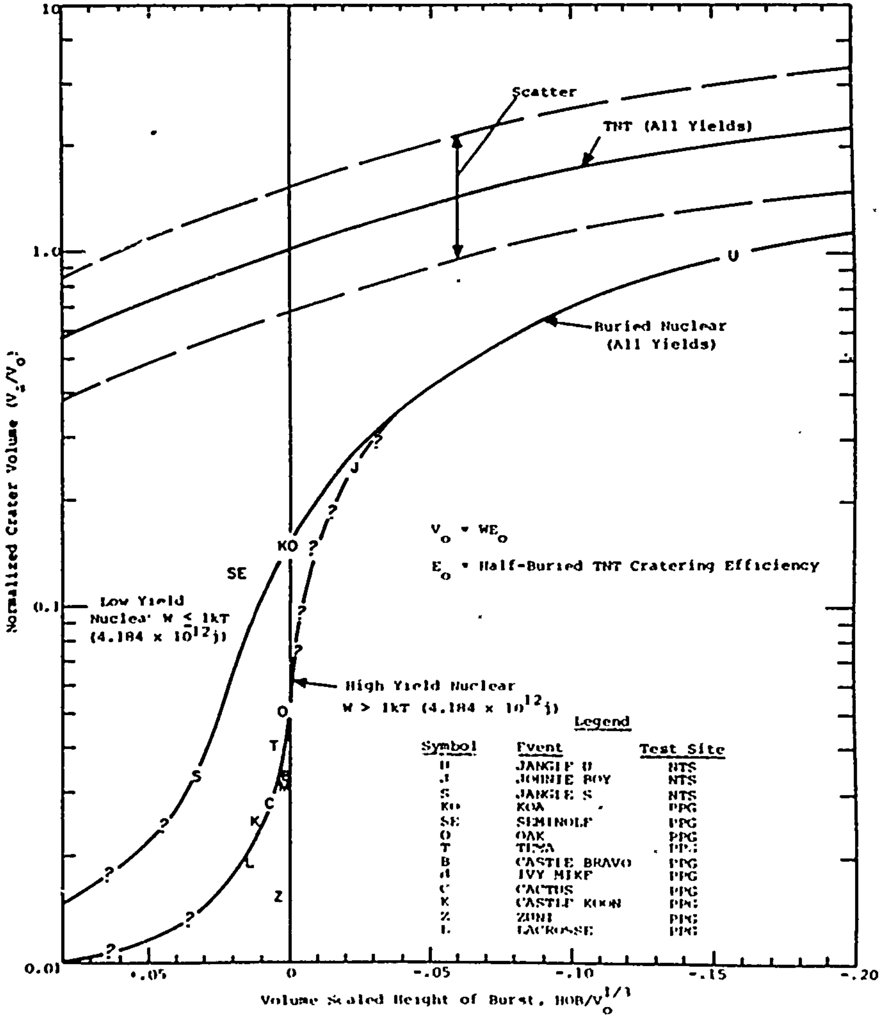

Figure 4-4 Height of Burst Effects in the Near-Surface Region

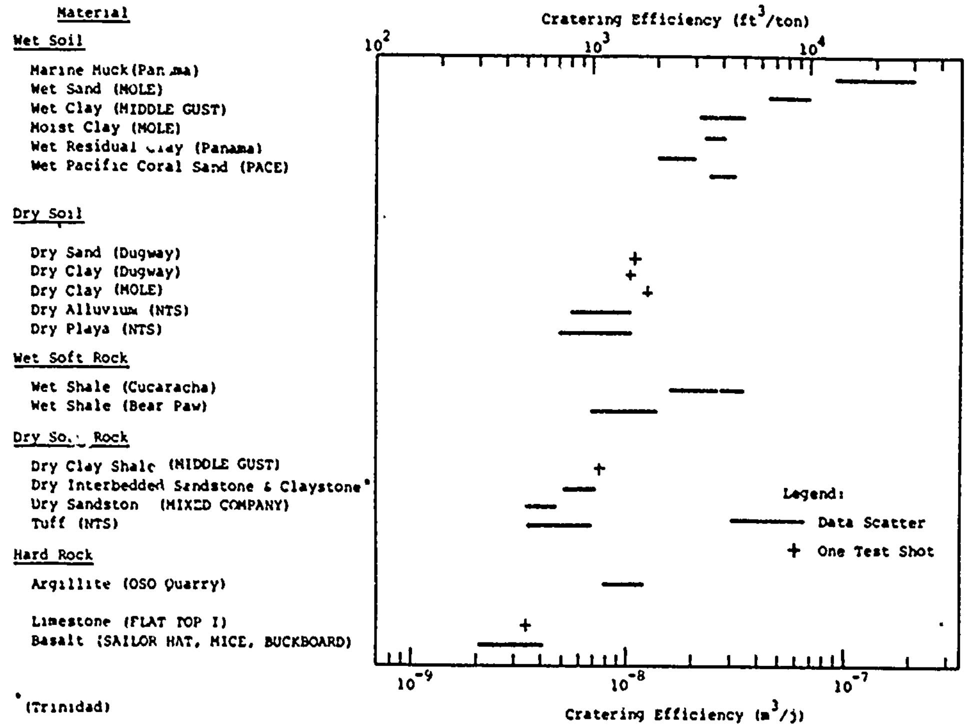

Figure 4-5 Cratering Efficiencies for TNT Surface Bursts

Table 4-3

SURFACE BURST CRATERING EFFICIENCIES IN IDEALIZED GEOLOGIES

Geology	Cratering Efficiency		
	TNT	High Yield Nuclear $W \geq 1kT$ ($4.184 \times 10^{+12}$ j)	Low Yield Nuclear $W < 1kT$ ($4.184 \times 10^{+12}$ j)
Dry Soil (e.g., alluvium, clay, sand)	1400 ft³/ton ($9.5 \times 10^{-9} m^3/j$)	70 ft³/ton ($4.7 \times 10^{-10} m^3/j$)	210 ft³/ton ($1.4 \times 10^{-9} m^3/j$)
Wet Soil (e.g., surface water table)	4000 ft³/ton ($2.7 \times 10^{-8} m^3/j$)	200 ft³/ton ($1.4 \times 10^{-9} m^3/j$)	600 ft³/ton ($4.1 \times 10^{-9} m^3/j$)
Dry Soft Rock (e.g., shale, sandstone)	1000 ft³/ton ($6.8 \times 10^{-9} m^3/j$)	50 ft³/ton ($3.4 \times 10^{-10} m^3/j$)	150 ft³/ton ($1.0 \times 10^{-9} m^3/j$)
Wet Soft Rock (e.g., surface water table)	2000 ft³/ton ($1.4 \times 10^{-8} m^3/j$)	100 ft³/ton ($6.8 \times 10^{-10} m^3/j$)	300 ft³/ton ($2.0 \times 10^{-9} m^3/j$)
Hard Rock (e.g., basalt, granite)	600 ft³/ton ($4.1 \times 10^{-9} m^3/j$)	30 ft³/ton ($2.0 \times 10^{-10} m^3/j$)	90 ft³/ton ($6.1 \times 10^{-10} m^3/j$)

The expected uncertainty in the table values is plus or minus a factor of 1.6 (e.g., for wet soil, TNT cratering efficiencies are considered to range between 2500 ft³/ton (1.7×10^{-8} m³/j) and 6400 ft³/ton (4.3×10^{-8} m³/j)). The TNT cratering efficiency is 20 times the high yield nuclear cratering efficiency and 20/3 times the low yield nuclear cratering efficiency.

yield. Most of the events in the Pacific had energy densities and radiation outputs sufficiently high that they can be grouped with modern "high yield" strategic weapons. On the other hand, JANGLE S, KOA and SEMINOLE had energy densities and radiation outputs sufficiently low that they can be grouped with modern "low yield" tactical weapons, even though all three events had yields exceeding one kiloton. KOA and SEMINOLE were detonated in large tanks of water, which greatly increased the effective mass of the devices and greatly decreased the radiation output. Previous investigators (e.g. Ref. 4-9) have expressed the above two categories in terms of "hot and "cold" sources, where the terms "hot" and "cold" refer to the relative radiation output of the sources. This last categorization implies that the amount of radiation coupling to the ground is a dominant consideration in initial coupling of energy to the ground. Attempts at quantitatively relating crater size with the temperature and mass of the device are in progress but not complete. This manual therefore, uses the high yield and low yield categories in evaluating the effects of nuclear source characteristics on cratering. From Fig. 4-4, the TNT surface burst cratering efficiency is 20 times the high yield nuclear surface burst cratering efficiency, and 20/3 times the low yield nuclear surface burst cratering efficiency.

c. In Fig. 4-4, V_o for NTS alluvium was taken as 1140 ft^3/ton ($7.715 \times 10^{-9}\ m^3/j$), from JANGLE HE and MOLE test series data. V_o for Pacific Coral was taken as 4000 ft^3/ton ($2.707 \times 10^{-8}\ m^3/j$), from the PACE HE series at Eniwetok. The first value was used to scale JANGLE S, JOHNIE BOY and JANGLE U. The second value was used to scale all of the nuclear events at Eniwetok and Bikini atolls.

d. The crater volume technique used in Fig. 4-4 assumes that crater volume is proportional to yield, where V_a/W vs $DOB/W^{1/3}$ scaling holds in a given geology. While this is a good assumption for surface events (Ref. 4-11) it is not valid for events near optimum DOB, where $V_a/W^{3/3.4}$ vs $DOB/W^{1/3.4}$ scaling gives good results for HE and nuclear events in NTS alluvium (Ref. 4-12). For events with scaled DOB values near that of JANGLE U, a scaling law intermediate between the above two types may hold. The simplification in Fig. 4-4 should be sufficiently accurate, however, considering all the other uncertainties involved in the scaling technique.

e. "High yield" and "low yield" nuclear cratering efficiencies are assumed to be the same at a depth where the mass of the ground surrounding the high yield device causes its effective mass to be similar to that of a low yield device at the same DOB.

f. Although a single line is drawn through the "high yield" and "low yield" nuclear data, the scatter is assumed to be similar to that shown in Fig. 4-4 for the TNT data.

4.2.3 Crater Volume Prediction Technique: Layered Geologies

Most sites of interest are layered and may have a near-surface water table and/or a soil-rock interface. There are 4 HE test series with sufficient data to analyze the effect of layering on crater dimensions, two series having soil geologies with a shallow water table, and two series having a sand layer over a concrete or cemented sand base.

The MONO LAKE dry volcanic sand over wet volcanic sand series (Ref. 4-13) consisted of 4 half-buried rectangular 250 lb (1112 N) ammonium nitrate slurry charges detonated on a lake shore at varying distances from the water edge (thus varying the depth to water table). The CERF dry clay-sand over wet clay-sand series (Ref. 4-14) consisted of 2-radii-above to half-buried 1 lb (4.45 N) C-4 charges detonated in a prepared test bed, with variable water table depth. A sand over concrete study (Ref. 4-15) consisted of 3 different explosives (27 lbs (120 N) C-4, 57 lbs (253.5 N) dynamite and 256 lbs (1139 N) TNT) detonated at varying DOB's with varying depths to the concrete pad. THE UDRI Ottawa Sand over cemented Ottawa Sand Series (Ref. 4-16) consisted of 1.7 gram (0.017 N) lead azide spheres in tangent-above to tangent-below charge configurations with varying depth to the cemented sand base.

Figures 4-6 and 4-7 show the normalization technique that is used (Ref. 4-18, 4-8) for plotting crater data in the one-layer test geologies just described (layer over base material) where

d = depth to base material (water table or cemented layer)

V = apparent crater volume in the layered geology

V_u = apparent crater volume in the surface material when $d = \infty$

V_L = apparent crater volume in the base material when $d = 0$

The curve fitted to the water table crater data in Fig. 4-6 is given by the expression

$$(V - V_L)/(V_u - V_L) = 1 - \exp(-5.4d/V^{1/3}) \qquad (4\text{-}1)$$

The data from the soil-over-cemented layer studies (Fig. 4-7) exhibit considerable scatter. Some of the data indicate that a sharp interface involving a large impedance mismatch can produce larger craters than would be expected in either material considered separately. The effect is illustrated in Fig. 4-8. For certain depths of overburden, it appears that a hard layer may limit the crater depth while causing the crater shape to be more nearly trapezoidal than parabolic or conic. The alteration of shape may cause no change

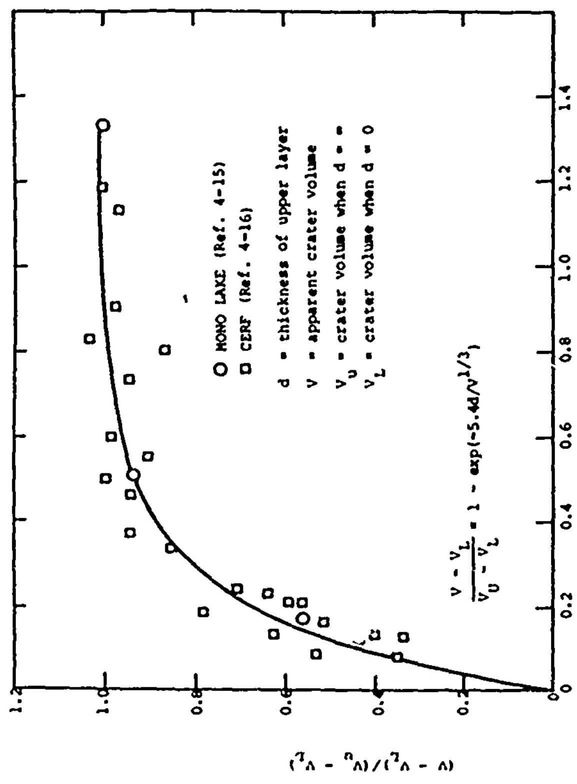

Figure 4-6 Dry Soil Over Wet Soil Cratering Data

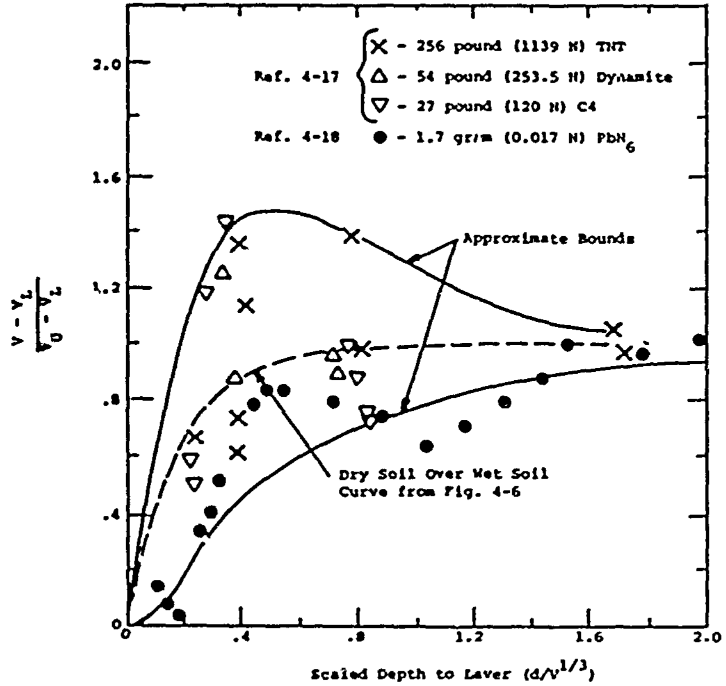

Figure 4-7 Cratering Data: Sand Over a Cemented Layer

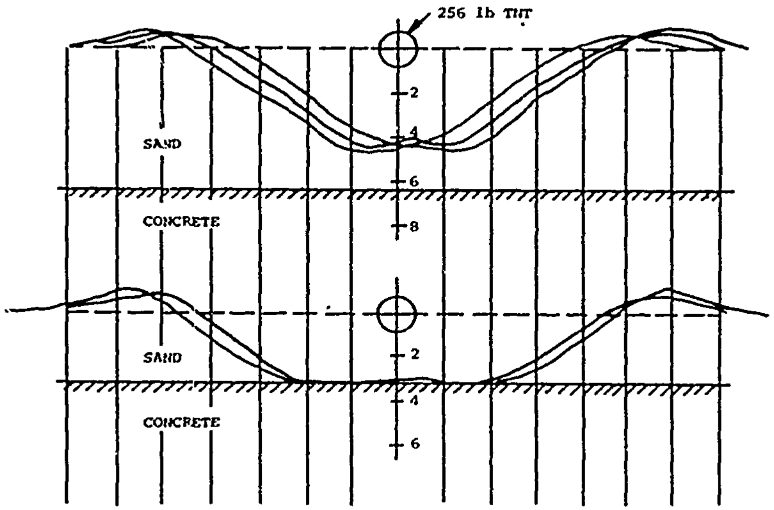

Figure 4-8 Effects of a Hard Near-Surface Layer Upon Cratering (Ref. 4-15)

or an increase in volume for certain depths of overburden. The effect probably results from a strong compressive reflection from the hard underlying which intensifies cratering action in the softer surface layer.

For sites having a single layer caused by a water table, it is recommended that the water table curve of Fig. 4-6 be used to predict crater volume. In cases involving a soil-rock interface, consideration should be given to the sharpness of the transition from soil to rock. Figure 4-7 shows two curves which bound the data and a third curve which, rather arbitrarily, is the curve derived from the water table study. Although the effect of a water table and the effect of a hard layer are recognized as different, the water table curve is within the data scatter and provides a gradual transition which is expected in many layered geologies involving a gradual transition to rock, such as would occur if an intervening weathered rock layer were present. In the case of gradual transitions, the curve through the data is recommended. For cases involving a sharp transition to rock, crater volumes may approach the upper bounding curve.

The one-layer problem can be generalized to two layers. Let V_1, V_2 and V_3 be the crater volumes associated with the top, middle and bottom materials considered separately. V_{23} is the crater volume associated with the middle layer and base material, and V is the crater volume in the total layered medium. The thickness of the middle layer is d_2, and the thickness of the top layer is d_1. With these definitions,

$$(V_{23} - V_3)/(V_2 - V_3) = 1 - \exp(-\ 5.4d_2/V_{23}{}^{1/3}) \qquad (4\text{-}2)$$

$$(V - V_{23})/(V_1 - V_{23}) = 1 - \exp(-\ 5.4d_1/V^{1/3}) \qquad (4\text{-}3)$$

The value of V_{23} is calculated from Eq. 4-2 and then used in Eq. 4-3 to calculate V.

Equations 4-1, 4-2 and 4-3 place no restriction on the height-of-burst or depth-of-burst of the explosion. Burst location enters the problem only through the effect of burst location on V_1, V_2, V_3 and V. To find the crater volume in a layered medium, one first calculates V_1, V_2 and V_3 assuming homogeneous conditions. Given the volumes V_1, V_2 and V_3, one calculates V by iteration with Eqs. 4-2 and 4-3.

A common type of two layer geology consists of a layer of soil over soft bedrock (generally shale or sandstone) with a water table either above or below the soil-rock interface. Using the nominal cratering efficiencies of Table 4-3 for dry soil, wet soil, dry soft rock and wet soft rock due to high yield nuclear surface bursts, and Eqs. 4-2 and 4-3, contours of equal cratering efficiency can be drawn on a plot of yield-scaled depth to bedrock versus yield-scaled depth to the water table (Fig. 4-9). Figure 4-9 is expected to provide a reasonable estimate of surface nuclear burst cratering efficiencies for many geologies likely to be encountered. The cratering efficiencies of Fig. 4-9 can be modified to incorporate the effect of height or depth of burst and different sources with the use of Fig. 4-4. Iteration is required. The scaled depths to the water table and bedrock are successively multiplied by the ratio $(V_H/V)^{1/3}$ where V_H is the high yield nuclear surface burst crater volume in the layered geology from the previous iteration (using Fig. 4-9) and V is the current estimate of crater volume in the layered geology as determined from V_H and Fig. 4-4. The technique converges very rapidly to a unique value of V, which is close to the value that would be obtained from a more "rigorous" analysis using Eqs. 4-2 and 4-3.

4.2.4 Crater Radius and Depth in Homogeneous and Layered Geologies

In Fig. 4-10, the radii (R_a) and depths (D_a) of HE craters are scaled by $V_a^{1/3}$ and plotted against yield

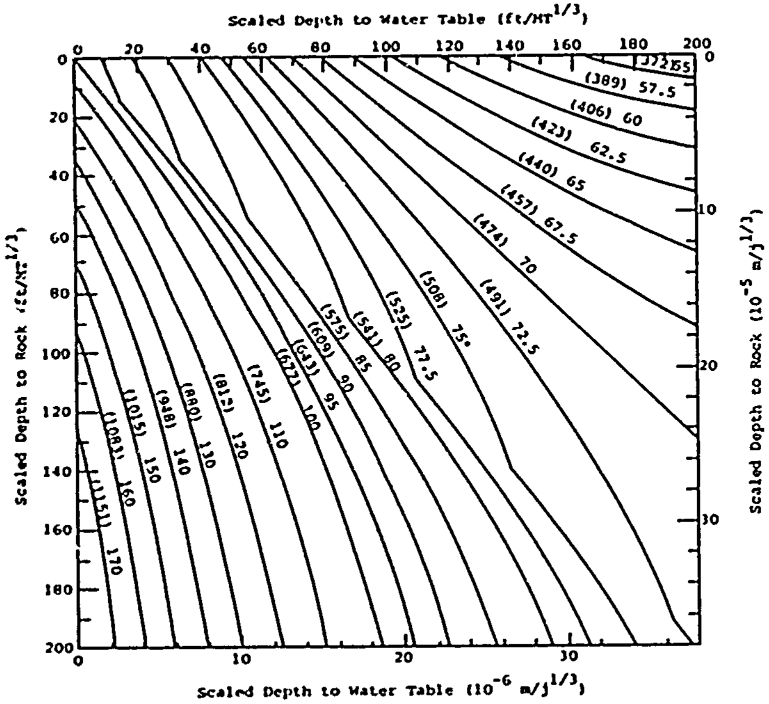

*Numbers adjacent to contours indicate cratering efficiency in ft^3/ton (10^{-12} m^3/j). Generic high yield nuclear cratering efficiencies of Table 4-3 are assumed for individual materials under homogeneous conditions.

Figure 4-9 High Yield Nuclear Surface Burst Cratering Efficiencies in a Two Layer Geology as a Function of Layer Depths

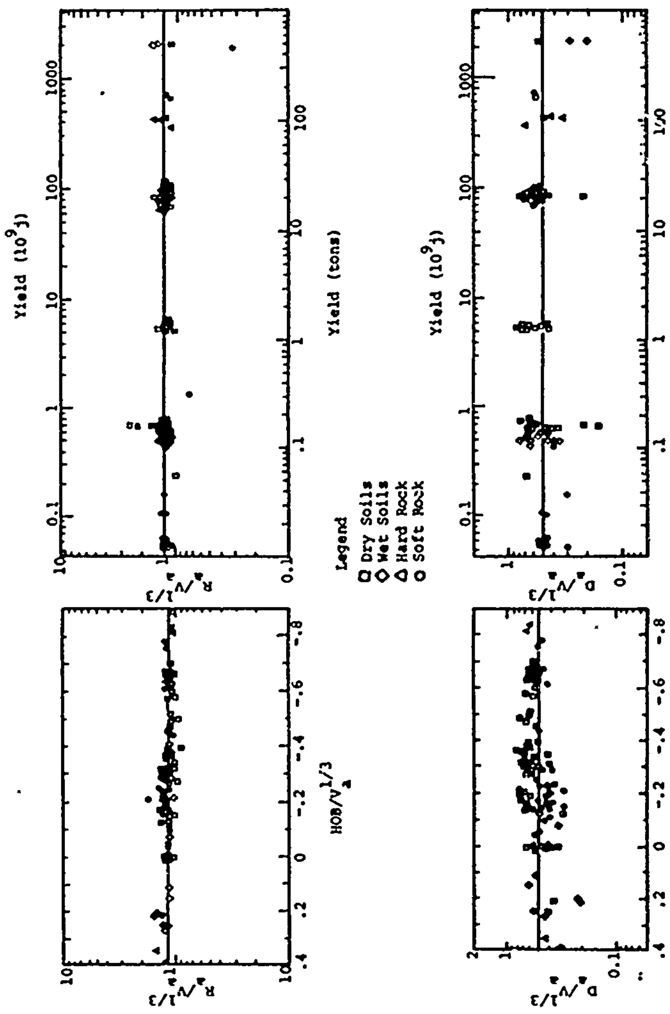

Figure 4-10 Crater Shape Characteristics for HE Sources (Ref. 4-9)

and $HOB/V_a^{1/3}$. The aspect ratio (R_a/D_a) of HE craters is not strongly dependent on yield, HOB or geology, within the data scatter. From Fig. 4-10,

$$R_a/V_a^{1/3} = 1.20 \tag{4-4}$$

$$D_a/V_a^{1/3} = 0.50 \tag{4-5}$$

Figure 4-11 shows volume scaled radii and depths for nuclear bursts plotted against yield. The bursts are separated into two categories: near-surface bursts and buried bursts. All of the buried bursts are at or near optimum depth of burst. Equations 4-4 and 4-5 were considered to provide an acceptable fit to the buried nuclear data, considering the rather deep depths of burial. The nuclear near surface data at $W \leq 1$ kT (4.184×10^{12}j) (JOHNIE BOY and JANGLE S) were fitted by equations 4-4 and 4-5. The following equations are applicable to the nuclear near-surface data for $W \geq 1$ kT (4.184×10^{12}j):

$$\begin{aligned} R_a/V_a^{1/3} &= 1.2\ (W/1\ \text{kT})^{0.08} \\ R_a/V_a^{1/3} &= 1.07(W/10^{12}\text{j})^{0.08} \end{aligned} \tag{4-6}$$

$$D_a/V_a^{1/3} = 0.5(W/1\ \text{kT})^{-0.12}$$

$$D_a/V_a^{1/3} = 0.59(W/10^{12}\text{j})^{-0.12} \tag{4-7}$$

Equations 4-6 and 4-7 are based completely on the Pacific data. The reason for the apparent increase in crater aspect ratios with yield in the Pacific is unclear and may be due to the layered Pacific atoll geology. All the Pacific craters that have been investigated appear to "bottom out" against a relatively competent layer. The crater depths from the largest events are about equal to the depths to the lower limestone layer in Fig. 4-3. CACTUS and LACROSSE crater depths are controlled by the depth to a hard layer intermediate to the reef

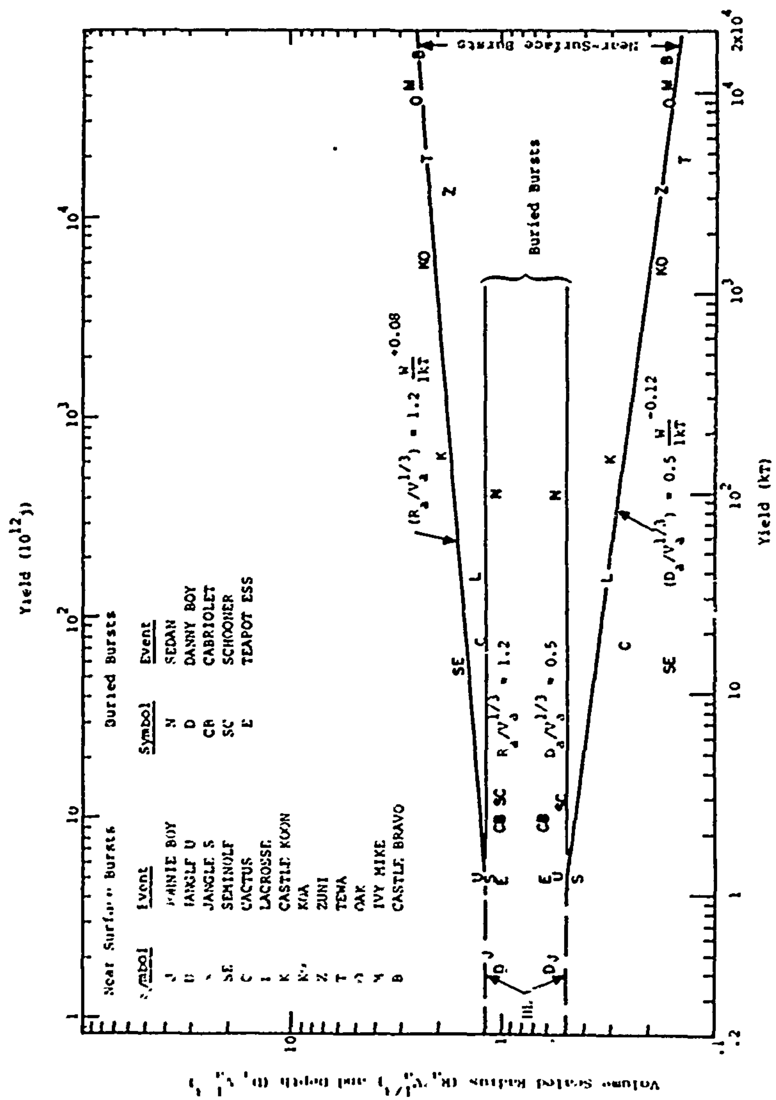

Figure 4-11 Crater Volume Scaled Radius and Depth as a Function of Yield for Buried and Near-Surface Nuclear Bursts

plate and the lower limestone. SEMINOLE bottomed out against the interface between the unconsolidated sediment and the interbedded limestone and sediment as shown in Fig. 4-3. This observed "bottoming out" could also increase aspect ratios by helping to increase the crater radius. Post-shot water washing and slumping of the Pacific craters will also help to increase the aspect ratio. And, of course, there could be some purely yield-related effect that has not yet been identified.

Because of the relative lack of knowledge of the reasons for the Pacific crater radius and depth relations given by Eqs. 4-6 and 4-7, it seems advisable to use these relations for both layered and homogeneous geologies for surface bursts, especially as most geologies of practical interest are layered. Assuming the validity of Eqs. 4-6 and 4-7 at the surface, it is not very clear what the HOB and DOB effect on the scaling will be, especially since geologic layering influences the crater aspect ratio to some extent.

It is possible, however, to put reasonable bounds on the possible variations of crater radius and depth with HOB and DOB. Several assumptions are made to accomplish this:

- Crater radius and depth must monotonically increase with decreasing HOB (increasing depth).
- At a scaled DOB of 0.2, the HE scaling of Eqs. 4-4 and 4-5 is assumed to hold for all layered geologies.
- Above a scaled HOB of 0.02 and higher, the crater radius is assumed to be about constant, which is reasonably consistent with crater volumes observed from Pacific low-altitude air bursts.

The upper bound for crater radius for buried bursts is assumed to be either the crater radius calculated from Eq. 4-6 or the crater radius at $DOB/V_o^{1/3} = 0.2$ as calculated from Eq. 4-4, whichever of the two values is smaller. The lower bound for crater radius for buried bursts is assumed to be either the crater radius of the surface bursts or the crater radius as calculated from Eq. 4-4, whichever of the two values is the larger. The bounds on the crater depth are determined from the bounds on the crater radius by the relation

$$D_a = V_a/\pi f R_a^2 \qquad (4\text{-}8)$$

where f is 0.5 for craters with parabolic cross sections and 0.33 for craters with conical sections. From Eqs. 4-4 to 4-7, $f = 0.44(W/1\ kT)^{-0.04}$ $(f = 0.47(W/10^{12}j)^{-0.04})$ for surface bursts, and f = 0.04 for bursts at 0.2 scaled DOB. A nominal value for crater radius and depth can be obtained by an arithmetical average of the bounding values.

Crater radii for above surface bursts can be obtained from Eq. 4-6 up to a scaled HOB of 0.02. Above that HOB, use a constant crater radius obtained at the scaled HOB of 0.02 (from Eq. 4-6) and obtain a crater depth using Eq. 4-8 where $f = 0.44(W/1\ kT)^{-0.04}$ $(f = 0.47\ (W/10^{12}j)^{-0.04})$.

Thus, is can be seen that there is considerably more uncertainty in estimating nuclear crater radii than in estimating nuclear crater volumes. While the available HE data indicate that high crater aspect ratios can result from geologic layering, insufficient HE and nuclear data exist to permit inclusion of layered geology effects into a quantitative prediction technique for nuclear crater radii and depths at this time.

4.2.5 Repeated Cratering

Repeated cratering is defined as the creation of an increasingly large crater through the repeated detonation of charges at or near the bottom of the crater created by preceding detonations. The first detonation is a contact burst, and each succeeding detonation is at or near the crater bottom below surface ground zero. In some cases, it may be more advantageous to successively detonate N charges of yield W in the manner described above, rather than detonate a single charge of yield $N \cdot W$.

References 4-18 and 4-19 review the existing HE repeated cratering data. In this manual, a synthesis of the data from the above two reports is made (Ref. 4-20). Most existing data have resulted from gram-sized charges in soil and cemented grout. In addition, a few data are available for yields ranging from 1 lb (4.45 N) to 4000 lbs (17,790 N) in soil and basalt.

The effects of repeated cratering upon crater radius, depth and volume are shown in Figs. 4-12 through 4-14, which represent the average behavior of soil and rock for yields greater than 1 lb. (4.45 N). The effect of repeated cratering upon crater dimensions can be approximated by

$$\frac{C_N}{C_1} = N^S \qquad (4\text{-}9)$$

where

C_N = a crater dimension (radius, depth or volume) after N detonations

C_1 = the corresponding crater dimension after 1 detonation

N = the number of detonations

S = an exponent dependent upon the geology and crater dimension under consideration

Average values of S for soil and rock are indicated in Figs. 4-12 through 4-14. On the average, a deeper crater can be obtained by repeated cratering than from a single burst with the total yield of the repeated cratering events. The reverse is true with respect to the crater radius.

The extrapolation of HE results to the nuclear case is uncertain. Since a single high yield nuclear surface

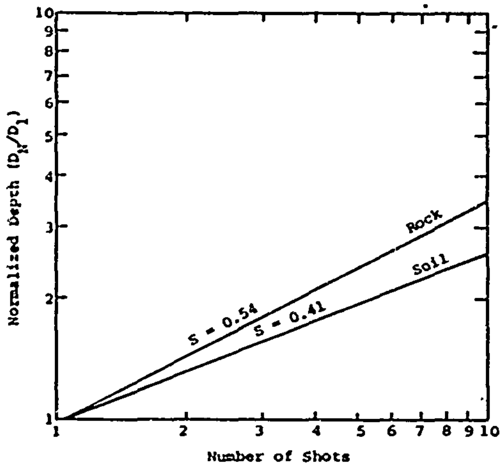

Figure 4-12 Repeated Cratering: Crater Depth vs Number of Shots for HE Surface Bursts

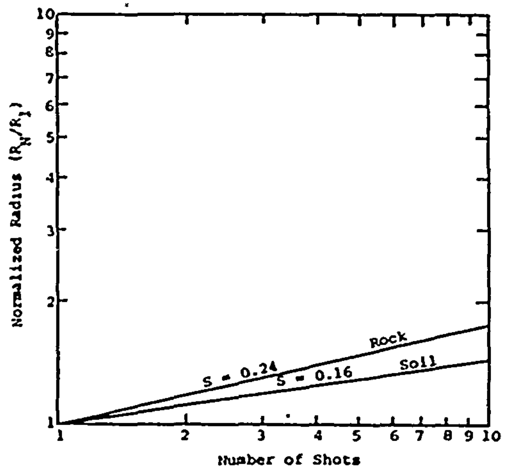

Figure 4-13 Repeated Cratering: Crater Radius vs Number of Shots for HE Surface Bursts

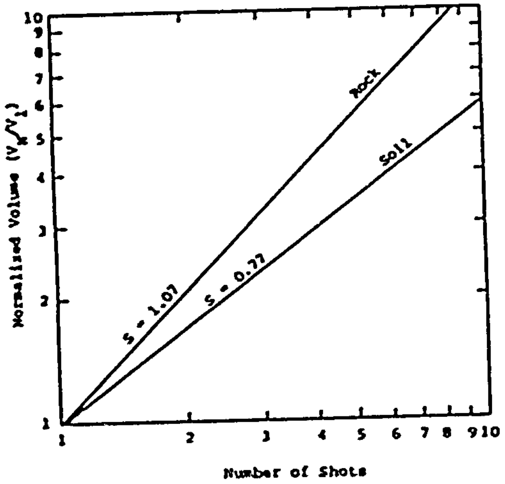

Figure 4-14 Repeated Cratering: Crater Volume vs Number of Shots for HE Surface Bursts

burst can result in a crater with a relatively small depth and large radius, Figs. 4-12 to 4-14 should give a minimum estimate of nuclear crater depth from repeated cratering, and a maximum estimate of crater radius. If the initial nuclear crater aspect ratio is assumed to be similar to that of an HE surface burst, the reverse will occur. Using these concepts, the following bounding equations can be formulated for nuclear surface bursts. The high yield nuclear surface burst radius and depth relations are taken from Eqs. 4-6 and 4-7 and the high explosive relations from Eqs. 4-4 and 4-5.

Crater Volume:

Rock: $V_N = V_1 N^{1.07}$ (4-10)

Soil: $V_N = V_1 N^{0.77}$ (4-11)

Crater Radius-Maximum Value:

Rock:
$$R_{N\max} = 1.2\left(\frac{W}{1kT}\right)^{0.08} V_1^{1/3} N^{0.24}$$
$$R_{N\max} = 1.07\left(\frac{W}{10^{12}J}\right)^{0.08} V_1^{1/3} N^{0.24} \qquad (4\text{-}12)$$

Soil:
$$R_{N\max} = 1.2\left(\frac{W}{1kT}\right)^{0.08} V_1^{1/3} N^{0.16}$$
$$R_{N\max} = 1.07\left(\frac{W}{10^{12}J}\right)^{0.08} V_1^{1/3} N^{0.16} \qquad (4\text{-}13)$$

Crater Radius-Minimum Value:

Rock: $R_{N\min} = 1.2 V_1^{1/3} N^{0.24}$ (4-14)

Soil: $R_{N\min} = 1.2 V_1^{1/3} N^{0.16}$ (4-15)

Crater Depth-Maximum Value:

Rock: $$D_{Hmax} = 0.5V_1^{1/3}N^{0.54} \qquad (4\text{-}16)$$

Soil: $$D_{Hmax} = 0.5V_1^{1/3}N^{0.41} \qquad (4\text{-}17)$$

Crater Depth-Minimum Value:

Rock: $$D_{Hmin} = 0.5\left(\frac{W}{1kT}\right)^{-0.12} V_1^{1/3}N^{0.54}$$

$$D_{Hmin} = 0.59\left(\frac{W}{10^{12}J}\right)^{-0.12} V_1^{1/3}N^{0.54} \qquad (4\text{-}18)$$

Soil: $$D_{Hmin} = 0.5\left(\frac{W}{1kT}\right)^{-0.12} V_1^{1/3}N^{0.41}$$

$$D_{Hmin} = 0.59\left(\frac{W}{10^{12}J}\right)^{-0.12} V_1^{1/3}N^{0.41} \qquad (4\text{-}19)$$

If each successive cratering burst is buried, then the crater depth may approach the maximum value, and the crater radius may approach the minimum value. For nuclear yields less than 1 kiloton (4.184 x 10^{12}J), only Eqs. 4-14 and 4-15 should be used for calculating crater radius, and only Eqs. 4-16 and 4-17 should be used for calculating crater depth.

4.3 EJECTA

4.3.1 General

Near-surface explosions eject large quantities of debris which can be deposited at considerable distances from the burst point. The type of material deposited ranges from fine dust to large discrete rock and soil clod missiles. The ejecta environment may be divided into three general regions defined as follows:

- Crater lip - where ejecta often takes the form of an overturned flap from the crater.

- Continuous ejecta region -- consisting of an ejecta blanket the thickness of which varies with range and azimuth (nominally, at a range less than 3.5 to 7 R_a).
- Discontinuous ejecta region - consisting of discrete missiles with the pre-shot ground surface visible.

The characteristics of the ejecta environment which are important for the design of protective systems are:

- Average ejecta thickness or areal density (ejecta weight per unit area) as a function of explosive yield and type, height of burst, ground range and geology.
- Azimuthal variation in ejecta thickness or areal density at a given range. Significant variation occurs due to raying phenomena which results in radially oriented mounds of debris.
- Ejecta size distribution, both after impact and just prior to impact.
- Number of missile impacts per unit area.
- Impact velocity and impact angle of missiles.

Since the total volume of ejecta is related to the total volume of the crater, uncertainties in crater volume are directly reflected in uncertainties in the ejecta distribution. In addition, there are uncertainties with regard to the mechanisms causing the crater. Compaction, for example, produces a crater but no ejecta.

4.3.2 Ejecta Thickness and Azimuthal Variation

Since ejecta results from cratering, it is reasonable to expect that the total ejecta mass is closely related to the crater volume. Test data substantiates this relation, except for nuclear bursts occurring far enough above the surface to produce a depression crater with no ejecta. The prediction method for ejecta depth, areal density and azimuthal variation presented herein is based upon Ref. 4-8 wherein apparent crater volume is used to scale range and ejecta depth.

The following equations (Ref. 4-8) may be used to calculate maximum, median, minimum and average ejecta depths (D_{max}, D_{med}, D_{min} and $\bar{D}$) at any range, R, outside the crater in soil and soft rock geologies.

$$D_{max} = V_a^{1/3}\ [0.767\ \exp(-2.121R_S) + 0.0443\ \exp(-0.3793R_S)] \quad (4\text{-}20)$$

$$D_{med} = V_a^{1/3}\ [0.8914\exp(-2.569R_S) + 0.01668\exp(-0.5359R_S)] \quad (4\text{-}21)$$

$$D_{min} = V_a^{1/3}\ [1.036\exp(-2.978R_S) + 0.00628\exp(-0.6925R_S)] \quad (4\text{-}22)$$

$$\bar{D} = V_a^{1/3}\ [0.749\exp(-2.30R_s) + 0.0168\exp(-0.423R_S)] \quad (4\text{-}23)$$

where $R_S = R/V_a^{1/3}$. The distribution of ejecta depth at a given range may be approximated by

$$D(k) = D_{min}^{\frac{95-k}{90}}\ D_{max}^{\frac{k-5}{90}} \quad (4\text{-}24)$$

where k is the probability of obtaining an ejecta depth less than D(k) at a given range and D(95) = D_{max}; D(50) = D_{med}; D(5) = D_{min}. For hard rock geologies (e.g., basalt) calculated ejecta depths should be multiplied by a factor of 2. The maximum ejecta thickness relation (Eq. 4-20) results in a value that is larger than about 95% of the ejecta measurements at a given range from a cratering burst. The median thickness (Eq. 4-21) is larger than 50% of the measurements, and the minimum ejecta thickness (Eq. 4-22) is smaller than 95% of the measurements. The variation of maximum, median and minimum ejecta depth with range is shown in Fig. 4-15.

The parameters of yield, height-of-burst, explosive source characteristics, and geology are assumed to influence the ejecta distribution through their influence on the crater volume. The variation in ejecta depth at a given

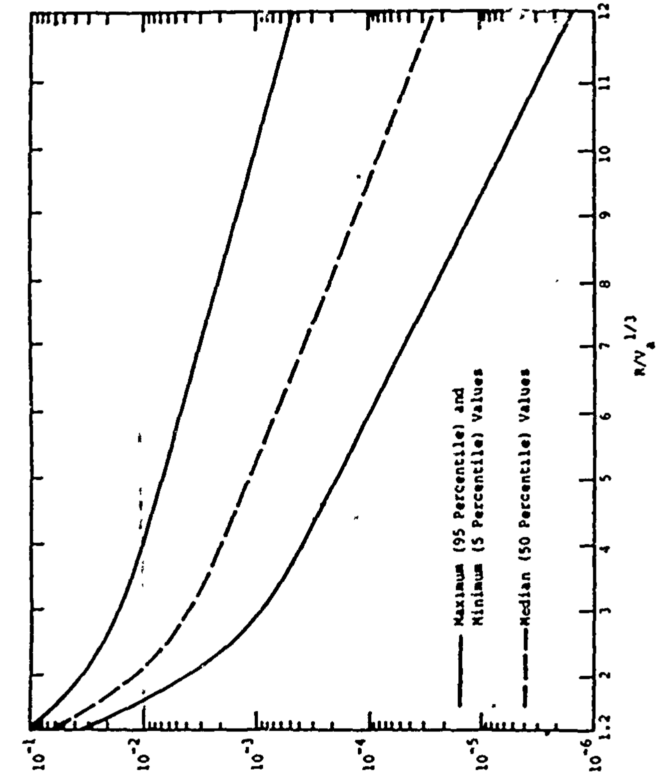

Figure 4-15 Ejecta Depth as a Function of Range: Nuclear Bursts

range (ejecta raying is an example) is intrinsic in the ejecta problem and cannot be decreased significantly by more exact knowledge of ejecta phenomenology. The equations presented are primarily intended for nuclear cratering bursts, but they can be used with reasonable validity for HE bursts as well.

Equations 4-20 through 4-24 are valid for any range beyond the crater lip, for above-surface bursts and for below-surface bursts down to scaled depths of burst $(HOB/V_o^{1/3})$ of 0.2. The validity of Eqs. 4-20 through 4-24 for more deeply buried bursts is uncertain, and use for scaled depths of burst greater than 0.2 is not recommended.

Areal weight density may be estimated from ejecta depth by the relation

$$\delta = \gamma D \tag{4-25}$$

where

δ = areal density

γ = bulk unit weight of ejecta

D = ejecta depth

A bulk ejecta unit weight of 100 lb/ft^3 (157 N/m^3) may be assumed.

It should be noted that the measurements upon which Eqs. 4-20 through 4-24 are based were taken over physical areas which vary with scaled range. On the crater lip, the measurement may average over a negligible area to several square feet. In the discontinuous region, the averaging may be over several thousand square feet. The measurements in the continuous ejecta region, when scaled up to a high-yield nuclear burst, might correspond to an area of about 10 ft. (3.05 m) by 10 ft. (3.05 m). In the discontinuous region, the measurements would correspond to an area of the order of 1000 ft. (305 m) by 1000 ft. (305 m).

Crater volumes for use in Eqs. 4-20 through 4-24 may be estimated with the relations given below.

High yield bursts $(W \geq 1 \text{ kT } (4.184 \times 10^{12} \text{j}))$

$$V_a = 0.04V_o \exp(-55.1 HOB/V_o^{1/3}) \quad [HOB/V_o^{1/3} > 0.002] \tag{4-26}$$

$$V_a = 0.05V_o \exp(-166. HOB/V_o^{1/3}) \quad [0 \leq HOB/V_o^{1/3} < 0.002] \tag{4.27}$$

$$V_a = 4.07V_o \exp(0.0033 + DOB/V_o^{1/3}) \quad [0 < DOB/V_o^{1/3} \leq 0.2] \tag{4-28}$$

Below-surface low yield bursts $(W < 1\text{kT } (4.184 \times 10^{12} \text{j}))$

$$V_a = 4.39V_o (DOB/V_o^{1/3} + 0.0216)^{0.88} \quad [0 \leq DOB/V_o^{1/3} < 0.055] \tag{4-29}$$

$$V_a = 4.07V_o (0.0033 + DOB/V_o^{1/3})^{0.77} \quad [0.055 \leq DOB/V_o^{1/3} < 0.2] \tag{4-30}$$

where V_o is the crater volume due to a half-buried sphere of TNT $(V_o = WE_o)$.

Above-surface apparent crater volumes from Fig. 4-4 should not be used, since most of the crater volume for $HOB/V_o^{1/3} > .02$ is thought to result from compaction. Equations 4-26 through 4-30 estimate the crater volume resulting primarily from excavational processes. Equations 4-28 to 4-30 are fits to the buried nuclear curves of Fig. 4-4.

The ratio of total ejecta mass* to apparent crater mass can be determined to an excellent approximation as (Ref. 4-8)

$$\left.\begin{aligned} M_t/M_a &= 0.54F(W/1\text{kT})^{-0.0477} \quad (W > 1\text{kT } (4.184 \times 10^{12}\text{j})) \\ M_t/M_a &= 0.58F(W/10^{12}\text{j})^{-0.0477} \end{aligned}\right\} \tag{4-31}$$

---

*The normal convention of ejecta literature in which the word "mass" is loosely defined to mean "weight" is used herein.

$$M_t/M_a = 0.54F \qquad (W < 1\text{kT } (4.184 \times 10^{12}\text{J})) \qquad (4\text{-}32)$$

where

M_t = total ejecta mass

M_a = apparent crater mass

F = 2 for hard rock and unity for all other geologies

Figures 4-16, 4-17 and 4-18 present ejecta distributions under a variety of conditions. Figure 4-16 shows ejecta depth as a function of overpressure level for 1 MT (4.184×10^{15}J), 5 MT (2.092×10^{16}J) and 25 MT (1.046×10^{17}J) yields and an assumed cratering efficiency of 100 ft^3/ton (6.77×10^{-10}m^3/J). Figure 4-17 gives scaled ejecta depth as a function of cratering efficiency at the 1000 (689 N/cm^2) and 600 psi (414 N/cm^2) levels. The D(90), D(50) and D(10) values are shown. Figure 4-18 plots ejecta thicknesses at the 1000 psi (689 N/cm^2) level for nuclear surface bursts on layered sites as a function of scaled depth to water table and bedrock.

4.3.3 Ejecta Missile Size Distribution

Knowledge of the missile size distribution is important both from the standpoint of proper design of debris removal systems and as a necessary input in determining the expected number of missile impacts on a given area.

The general form for the ejecta missile size distribution for cratering events in rock (Refs. 4-21 and 4-22) is

$$M/M_t = (a/a_{max})^n \qquad (4\text{-}33)$$

where

M/M_t = the cumulative mass fraction of ejecta

M = the cumulative ejecta mass at all ranges with equivalent diameters less than or equal to the value a

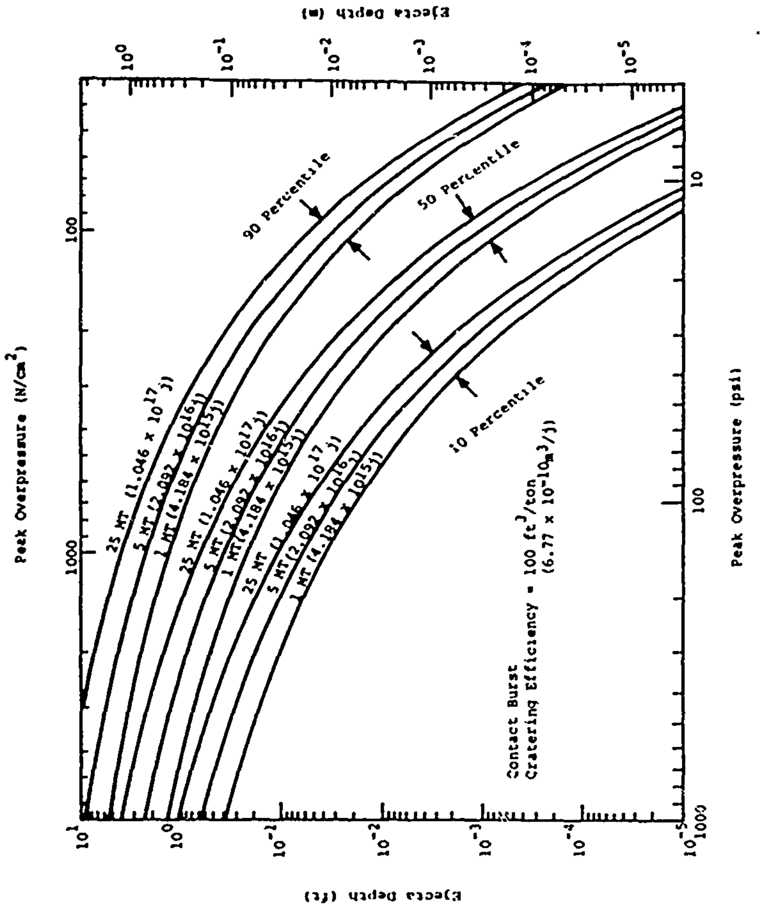

Figure 4-16 Ejecta Depth as a Function of Overpressure

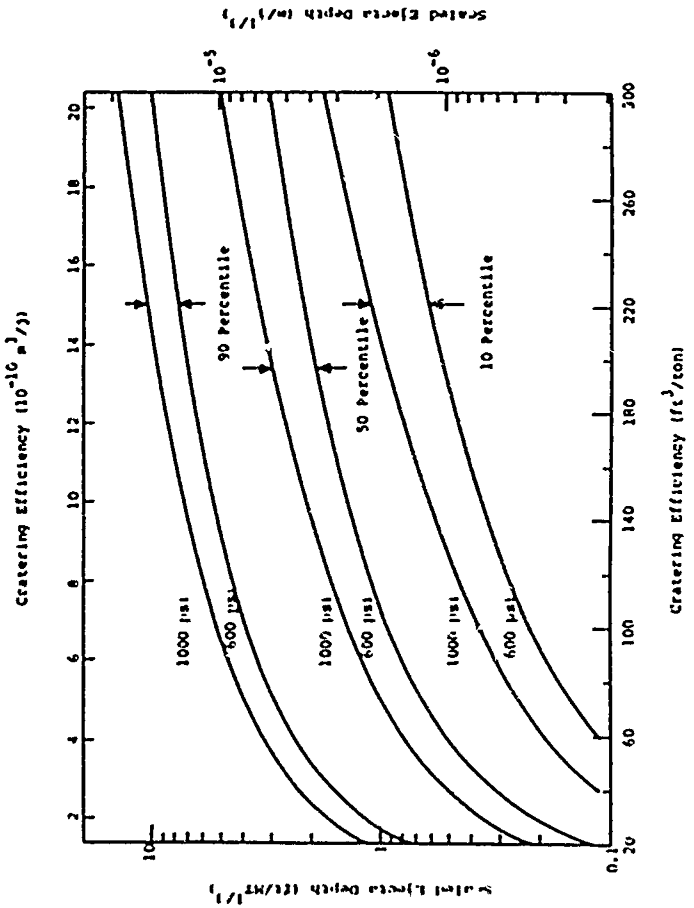

Figure 4-17 Scaled Ejecta Depth at 1000 psi (689 N/cm^2) and 600 psi (414 N/cm^2) Levels as a Function of Cratering Efficiency

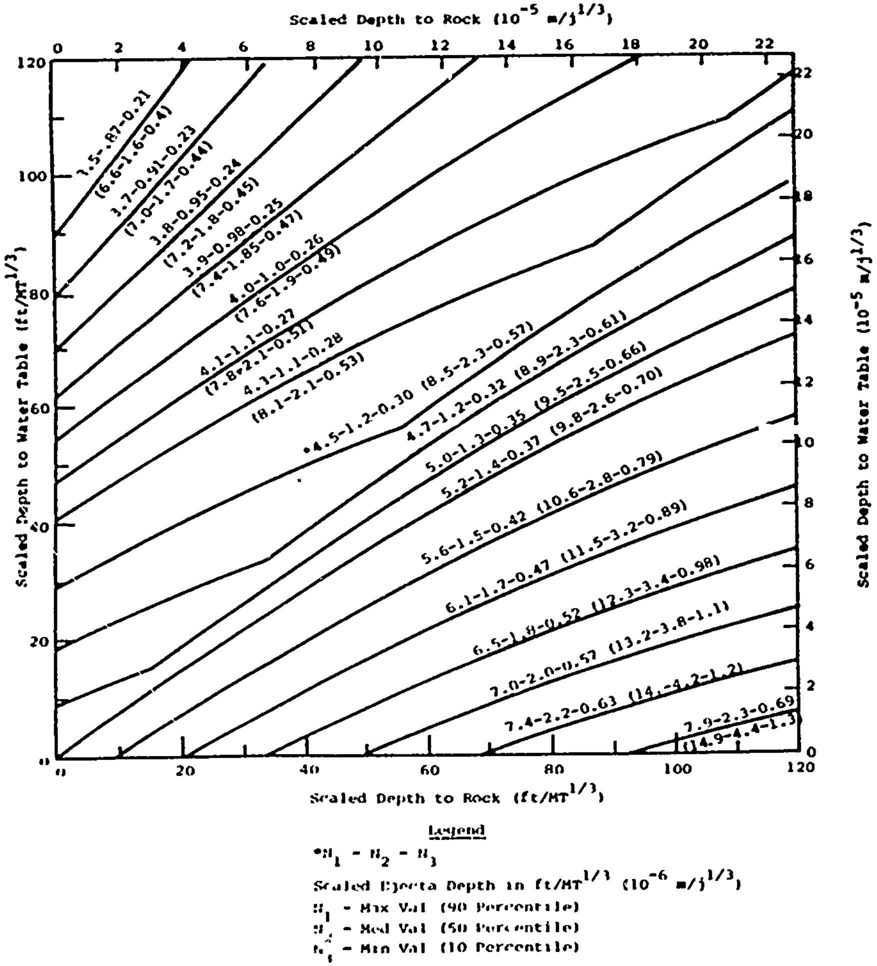

Figure 4-18 Ejecta Thickness at 1000 psi (690 N/cm^2) Level From High Yield Surface Burst in Layered Geology

M_t = the total ejecta mass

a_{max} = the absolute maximum equivalent missile diameter

n = an exponent that is about equal to 0.5

The equivalent missile diameter and the missile mass are related by the expression

$$m = \pi\gamma_p a^3/6 \tag{4-34}$$

where

m = missile mass

a = missile diameter

γ_p = preshot unit weight of material

From Eqs. 4-31 and 4-32, M_t is

$$M_t = 0.54F\gamma_p \left(\frac{W}{1kT}\right)^{-0.0477} V_a \quad (W > 1kT(4.184 \times 10^{12}j))$$

$$M_t = 0.54F\gamma_p \left(\frac{W}{10^{12}j}\right)^{-0.0477} V_a \tag{4-35}$$

$$M_t = 0.54F\gamma_p V_a \quad (W \leq 1kT(4.184 \times 10^{12}j)) \tag{4-36}$$

The absolute maximum missile mass of a single missile from a cratering event is related to the total missile mass by (Ref. 4-22)

$$m_{max} = 0.05884\left(\frac{M_t}{1\ lb}\right)^{0.8} \text{lbs}$$

$$m_{max} = 0.0793\left(\frac{M_t}{1N}\right)^{0.8} N \tag{4-37}$$

where

- m_{max} = absolute maximum mass of a single missile

M_t = total ejecta mass

However, the maximum missile size at a given range and azimuth will be less than the absolute maximum missile size for the following reasons:

- The maximum missile size at a given range decreases as the range increases. The absolute maximum missile size will be found at or near the crater lip.
- The limited area of measurement at a given range and aximuth means that in general the maximum missile size at that range will not be found in the measurement area.

Similar considerations apply to the median missile size (50 percent cumulative ejecta mass fraction) as well.

The maximum missile mass, m_m, found at a given range is given by the expression

$$m_m = 0.1094 \left(\frac{M_t}{1\ lb}\right)^{0.8} R_S^{-1.644} \text{lbs}$$

$$m_m = 0.1474\left(\frac{M_t}{1N}\right)^{0.8} R_S^{-1.644}\ N \tag{4-38}$$

where $R_S = R/V_a^{1/3}$.

Equation 4-38 was derived from limited test data from the five large MIDDLE GUST events, the FLAT TOP I event, and the MIXED COMPANY III event (Ref. 4-23). The actual maximum missile mass found in a given measurement area at some scaled range depends on the measurement area and the aximuthal coverage. For areas of several hundred to several thousand square feet on a large HE event (crater volume of several tens of thousand cubic feet), a median value for observed missile mass may only be 5% or 10% of that predicted by Eq. 4-38.

An important observation (Ref. 4-23) is that when the effect of range is taken into account, the particle size distributions in rock and many cohesive stiff soils may not be significantly different, especially when it is noted that the maximum missile size for large cratering events in rock will probably be controlled by the joint spacing in the rock. However, the dynamic missile size distribution for unconsolidated, weak, non-cohesive soils differs significantly from that in rock, and the static missile size distribution differs even more. The dynamic missile size distribution refers to the size distribution of the missiles in flight. Static distribution refers to sizes after all missiles have fallen to the ground. In the case of hard rock missiles, the dynamic and static particle size distributions may be very similar. For non-cohesive soils, the difference may be substantial, as shock-agglutinated soil clods will break on impact.

Reference 4-22 presents data which illustrates the difference in static particle size distributions between unconsolidated soil (alluvium) and hard rock cratering events. The static particle size distributions in soil do not differ significantly from the pre-shot particle size distributions. Analysis of secondary impact craters from the 100 kt (4.184 x 10^{14}j) SEDAN event (Ref. 4-23) indicates that the dynamic missile size distribution (shock agglutinated soil clods) at missile sizes about 1 meter diameter may follow the form of Eq. 4-33 with n = .00147, and an m_{max} consistent with Eq. 4-37.

For unconsolidated weak soils (e.g., NTS alluvium), the following dynamic particle and missile size distribution is recommended (Ref. 4-23)

$$M/M_t = (a/a_{max})^{0.00147} \tag{4-39}$$

for a ≥ 0.33 ft (0.1 m)

$$M/M_t = 1.1434 - 0.0038 \log\left(\frac{a_{max}}{1ft}\right) + \left[0.2995 - 0.0011 \log\left(\frac{a_{max}}{1ft}\right)\right] \log\left(\frac{a}{1ft}\right)$$

for a < 0.33 ft

(4-40)

$$M/M_t = 1.2956 - 0.0044 \log\left(\frac{a_{max}}{1m}\right) + \left[0.2989 - 0.0011 \log\left(\frac{a_{max}}{1m}\right)\right] \log\left(\frac{a}{1m}\right)$$

for a < 0.1 m

where a_{max} is given by Eq. 4-34 using m_{max} from Eq. 4-37. For the static particle size distribution, use Eq. 4-40 for all particle sizes. To determine the particle size distributions in soil (a ≥ 0.33 ft (0.1 m)) and rock at a <u>given range</u>, use the relation

$$F(a) = (a/a_m)^n \tag{4-41}$$

where F(a) is the cumulative mass fraction over a given measurement area and a_m is the equivalent diameter of m_m as defined in Eqs. 4-34, 4-39 and 4-40. The exponent n may be taken as 0.5 for hard rock geologies and 0.00147 for unconsolidated alluvial soil. For cohesive soil or layered geologies, n = 0.5 is recommended as a conservative estimate.

From Eqs. 4-34, 4-35 and 4-38

$$a_m = 0.504K\left(\frac{\gamma_p}{1pcf}\right)^{-0.0667} \left(\frac{V_a}{1ft^3}\right)^{0.267} \left(\frac{W}{1kT}\right)^{-0.0127} R_S^{-0.548}\ ft$$

(4-42)

$$a_m = 0.568K\left(\frac{\gamma_p}{1N/m^3}\right)^{-0.0667} \cdot \left(\frac{V_a}{1m^3}\right)^{0.267} \left(\frac{W}{10^{12}j}\right)^{-0.0127} R_S^{-0.548} m$$

(W > 1kT (4.184 x 10^{12}j))

$$a_M = 0.504K \left(\frac{\gamma_p}{1\text{pcf}}\right)^{-0.0667} \left(\frac{V_a}{1\text{ft}^3}\right)^{0.267} R_S^{-0.548}\,\text{ft}$$

$$a_m = 0.557K \left(\frac{\gamma_p}{1\text{N/m}^3}\right)^{-0.0667} \left(\frac{V_a}{1\text{m}^3}\right)^{0.267} R_S^{-0.548}\,\text{m} \qquad (4\text{-}43)$$

$$(W \leq 1\text{kT } (4.184 \times 10^{12}\text{j}))$$

where K is 1.2 for hard rock geologies, and 1 for layered and cohesive soil geologies.

4.3.4 Expected Number of Impacts and Missile Impact Probabilities

The expected number of impacts per unit area of missiles with equivalent diameters between a_1 and a_2 is given by the expression (Ref. 4-23)

$$I(a_1,a_2) = 6\delta n(a_2^{n-3} - a_1^{n-3})/\pi\gamma_p a_m^n(n-3) \qquad (4\text{-}44)$$

where δ is the ejecta areal density and n is the exponent in the particle size distribution equation (Eq. 4-41).

To calculate I at a given range, R, taking into account the azimuthal distribution of Eq. 4-24, let $\delta = \gamma\bar{D}$, where the average ejecta depth is calculated from Eq. 4-23. To find the expected number of missile impacts per square foot of missiles equal to or larger in equivalent diameter than a, let $a_1 = a$, and $a_2 = a_m$ in Eq. 4-44, where a_m is calculated from Eq. 4-42 or 4-43.

The probability of impact on a given area of missiles with equivalent diameters between a_1 and a_2 can be estimated by (Ref. 4-23)

$$P = 1 - \exp\left[-I(\ell_1 + a_1)(\ell_2 + a_1)\right] \qquad (4\text{-}45)$$

where ℓ_1 and ℓ_2 are the length and width respectively of the given area.

4.3.5 Ejecta Impact Velocities and Angles

Code calculations of the trajectories of 1, 10 and 100 cm diameter spheres through 0.1 MT (4.184 x 10^{14}j) and 10 MT (4.184 x 10^{16}j) nuclear surface burst environments are presented in Ref. 4-24. The calculations are analyzed and fitted by equations in Ref. 4-25. The results are given by the following equations:

$$V_i = 5.673 \left(\frac{R/\sin 2\theta}{1\text{ft}}\right)^{0.5} \exp\left(-\frac{R}{R_o}\right) \text{ft/sec}$$

$$[R \leq R_o/2] \qquad (4\text{-}46)$$

$$V_i = 3.132 \left(\frac{R/\sin 2\theta}{1\text{m}}\right)^{0.5} \exp\left(-\frac{R}{R_o}\right) \text{m/sec}$$

$$V_i = 23.08\left[\left(\frac{a}{1\text{ft}}\right)\left(\frac{\gamma_p}{1\text{pcf}}\right)\left(\frac{1}{C_d}\right)\right]^{0.5} \text{ft/sec}$$

$$[R > R_o/2] \qquad (4\text{-}47)$$

$$V_i = 1.017\left[\left(\frac{a}{1\text{m}}\right)\left(\frac{\gamma_p}{1\text{N/m}^3}\right)\left(\frac{1}{C_d}\right)\right]^{0.5} \text{m/sec}$$

where

V_i = impact velocity

$$R_o = 90\left(\frac{\gamma_p}{1\text{pcf}}\right)\left(\frac{a}{1\text{ft}}\right)\sin(2\theta/C_d)\ \text{ft}$$

$$= 0.573\left(\frac{\gamma_p}{1\text{N/m}^3}\right)\left(\frac{a}{1\text{m}}\right)\sin\,(2\theta/C_d)\ \text{m}$$

R = ejecta impact range

a = effective missile diameter

γ_p = unit weight of material in cratered region

θ = initial ejection angle measured from the horizontal

C_d = drag coefficient

A nominal value of $C_d = 0.6$ is recommended, with a possible range in drag coefficients of 0.3 to 1.2. A value of $\theta = 45^o$ can be taken as a nominal ejection angle, with $\theta = 15^o$ and $\theta = 75^o$ as reasonable bounding values.

Although explosive yield affects the range at which a given missile will impact, all missiles with the same value of θ, a, γ_p and C_d that impact at a given range will do so with about the same velocity, regardless of the yield and initial ejection velocity. Impact angles tend to have about the same magnitude as ejection angles at the higher overpressure levels. At the lower overpressure levels (several psi and less) the angles are more nearly vertical. For low yield nuclear bursts, the impact and ejection angles should be nearly the same at nearly all ranges.

4.3.6 Ejecta Prediction Summary

Table 4-4 presents a summary of the symbols, terms and units used in ejecta prediction. The ejecta prediction equations and procedures are summarized in Table 4-5.

Table 4-4

SYMBOLS, TERMS AND UNITS USED IN EJECTA PREDICTION EQUATIONS

V_o	surface burst crater volume of TNT
V_a	crater volume (adjusted for non-zero height of burst, if necessary)
W	explosive yield (in equivalent TNT units)
HOB	height of burst
H_S	$HOB/V_o^{1/3}$
R	ground range
R_S	$R/V_a^{1/3}$
D	ejecta depth
D_{max}	maximum ejecta depth (greater than 95% of the ejecta measurements at a given range)
D_{med}	median ejecta depth (greater than 50% of the ejecta measurements at a given range)
D_{min}	minimum ejecta depth (smaller than 95% of the ejecta measurements at a given range)
$\bar{D}$	average ejecta depth at a given range
k	azimuthal distribution variable - percentage probability that a preselected ejecta depth will be greater than a randomly chosen ejecta depth at some range where D_{max} and D_{min} are known
δ	ejecta areal density
γ	bulk unit weight of ejecta
γ_p	preshot unit weight in cratered region
a	equivalent missile diameter
a_m	maximum missile diameter found at a given range
I	expected number of impacts per square foot of missiles with equivalent diameters between a_1 and a_2, where a_2 is the larger missile size
P	probability of one or more missiles with equivalent diameters between a_1 and a_2 impacting on an area with length ℓ_1 and width ℓ_2
v_i	missile impact velocity
C_d	drag coefficient (nominally about 0.6 for angular fragments)
θ	missile ejection angle

Table 4-5

SUMMARY OF EJECTA PREDICTION EQUATIONS

Ejecta Depths and Areal Densities

1. Determine V_o from paragraph 4.2.2.

2. High Yield Bursts ($W \geq$ 1kT (4.184×10^{12} j))

$$V_a = 0.04V_o\exp(-55.1\ H_S) \qquad (H_S > 0.002) \qquad \text{(S-1)}$$

$$V_a = 0.05V_o\exp(0.0033 - H_S) \qquad (0 \leq H_S \leq 0.002) \qquad \text{(S-2)}$$

$$V_a = 4.07\ V_o(0.0033 - H_S)^{0.77} \qquad (0 \geq H_S \geq -0.2) \qquad \text{(S-3)}$$

Below-Surface Low Yield Bursts ($W <$ 1kT)

$$V_a = 4.39V_o(0.0216 - H_S)^{0.88} \qquad (0 \geq H_S > -0.055) \qquad \text{(S-4)}$$

$$V_a = 4.07V_o(0.0033 - H_S)^{0.77} \qquad (-0.055 \geq H_S \geq -0.2) \qquad \text{(S-5)}$$

3. Use the following equations (at any range) to determine maximum, median, minimum and average ejecta depths.

$$D_{max} = V_a^{1/3}\left[0.767\exp(-2.121R_S) + 0.044\exp(-0.3793R_S)\right] \qquad \text{(S-6)}$$

$$D_{med} = V_a^{1/3}\left[0.8914\exp(-2.549R_S) + 0.01668\exp(-.5359R_S)\right] \qquad \text{(S-7)}$$

$$D_{min} = V_a^{1/3}\left[1.036\exp(-2.978R_S) + 0.00628\exp(-.6925R_S)\right] \qquad \text{(S-8)}$$

$$\overline{D} = V_a^{1/3}\left[.749\exp(-2.30R_S) + .0168\exp(-.423R_S)\right] \qquad \text{(S-9)}$$

To calculate an areal density from an ejecta depth, D, use

$$\delta = \gamma D \qquad \text{(S-10)}$$

4. Geology Correction:

No geology correction is needed except for hard rock geologies in which case D (or δ) is multiplied by 2.

Azimuthal Distribution

$$D(k) = D_{min}^{\frac{96-k}{90}}\ D_{max}^{\frac{k-5}{90}} \qquad \text{(S-11)}$$

where $D(5) = D_{min}$; $D(50) = D_{med}$; $D(95) = D_{max}$

Impact Probabilities and expected Number of Impacts Per Unit Area from Ejecta Missiles

1. (a) To calculate expected number of impacts per unit area from missiles with equivalent diameters between a_1 and a_2, use

$$I = 6 n (a_2^{n-3} - a_1^{n-3})/\pi\gamma_p a_m^n\ (n-3) \qquad \text{(S-12)}$$

Table 4-5 (cont.)

SUMMARY OF EJECTA PREDICTION EQUATIONS

n = 0.5 for hard rock, and 0.00147 for unconsolidated alluvial soil. For cohesive soils and layered geologies, n = 0.5 is recommended as a conservative estimate.

$$a_m = 0.504K\left(\frac{\gamma_p}{1\text{pcf}}\right)^{-0.0667}\left(\frac{V_a}{1\text{ft}^3}\right)^{0.267}\left(\frac{W}{1\text{kT}}\right)^{-0.0127} R_S^{-0.548}\ \text{ft} \qquad \text{(S-13)}$$

$$a_m = 0.568K\left(\frac{\gamma_p}{1\text{N/m}^3}\right)^{-0.0667}\left(\frac{V_a}{1\text{m}^3}\right)^{0.267}\left(\frac{W}{10^{12}\text{j}}\right)^{-0.0127} R_S^{-0.548}\ \text{m}$$

$$a_m = 0.504K\left(\frac{\gamma_p}{1\text{pcf}}\right)^{-0.0667}\left(\frac{V_a}{1\text{ft}^3}\right)^{0.267} R_S^{-0.548}\ \text{ft}$$

$$a_m = 0.557K\left(\frac{\gamma_p}{1\text{N/m}^3}\right)^{-0.0667}\left(\frac{V_a}{1\text{m}^3}\right)^{0.267} R_S^{-0.548}\ \text{m} \qquad \text{(S-14)}$$

(K = 1 except for hard rock geologies, where K = 1.2).

(b) To calulate a nominal value of I at a given range let $\delta = \gamma\overline{D}$. To find I for all missiles equal to or larger in diameter than some value a, use a_1 = a and $a_2 = a_m$ in Eq. S-12.

Note: n = 0.00147 is valid for soils only for a $\geq$ 0.33 ft (0.1 m). For a < 0.33 ft (0.1 m) refer to text.

2. $$P = 1\exp\left[-I(\ell_1 + a_1)(\ell_2 + a_1)\right] \qquad \text{(S-15)}$$

where I is calculated from Eq. S-12.

Terminal Velocities

$$V_i = 5.673\left(\frac{R/\sin 2\theta}{1\text{ft}}\right)^{0.5}\exp\left(-\frac{R}{R_o}\right)\ \text{ft/sec}$$

$$V_i = 3.132\left(\frac{R/\sin 2\theta}{1\text{m}}\right)^{0.5}\exp\left(-\frac{R}{R_o}\right)\ \text{m/sec} \qquad \left[R \leq R_o/2\right] \qquad \text{(S-16)}$$

$$V_i = 23.08\left[\left(\frac{a}{1\text{ft}}\right)\left(\frac{\gamma_p}{1\text{pcf}}\right)\left(\frac{1}{C_d}\right)\right]^{0.5}\ \text{ft/sec}$$

$$V_i = 1.017\left[\left(\frac{a}{1\text{m}}\right)\left(\frac{\gamma_p}{1\text{N/m}^3}\right)\left(\frac{1}{C_d}\right)\right]^{0.5}\ \text{m/sec} \qquad \left[R > R_o/2\right] \qquad \text{(S-17)}$$

Table 4-5 (cont.)

SUMMARY OF EJECTA PREDICTION EQUATIONS

where

$$R_\omega = 90\left(\frac{Y_p}{1 psf}\right)\left(\frac{a}{1 ft}\right)\sin(2\theta/C_d)\,ft = 0.57)\left(\frac{Y_p}{1 N/m^2}\right)\left(\frac{a}{1 m}\right)\sin(2\theta/C_d)\,m$$

a nominal value of C_d = 0.6 is recommended. A value of $\theta = 45°$ can be taken as a nominal ejection angle value, with $\theta = 15°$ and $\theta = 75°$ as reasonable bounding values.

4.4 ILLUSTRATIVE EXAMPLES

4.4.1 Crater Prediction for a Surface Burst

a. GIVEN: A 10 MT (4.184×10^{16}j) surface burst at a site composed of wet clay extending to very large depth.

b. FIND: Apparent crater volume, radius and depth.

c. SOLUTION:

1. The cratering efficiency of a high yield nuclear surface burst in a wet clay site is given by Table 4-3 as 200 ft^3/ton.

2. The crater volume due to the nuclear surface burst is then

$$V_a = E_o^H W$$

$$V_a = (10 MT)\left(\frac{10^6 tons}{1 MT}\right)(200\ ft^3/ton)$$

$$V_a = 2 \times 10^9\ ft^3\ (5.7 \times 10^7 m^3)$$

3. Crater radius and depth are estimated from Fig. 4-[illegible] (Eqs. 4-6 and 4-7). For a 10 MT yield,

$$\frac{R_a}{V_a^{1/3}} = 2.51$$

$$R_a = (2.51)(2 \times 10^9)^{1/3}$$

$$R_a = 3160\ ft\ (963\ m)$$

$$\frac{D_a}{V_a^{1/3}} = 0.17$$

$$D_a = (0.17)(2 \times 10^9)^{1/3}$$

$$D_a = 214\ ft\ (65\ m)$$

4.4.2 Crater Prediction for a Shallow Buried Burst

a. GIVEN: A 1 MT (4.184×10^{15} j) burst at a depth of 10 feet at a site composed of wet clay extending to very large depth.

b. FIND: Apparent crater volume, radius and depth.

c. SOLUTION:

1. Assume the clay to have a half-buried TNT cratering efficiency (E_o) of 4000 ft^3/ton as given in Table 4-3.

2. The apparent crater volume for a half-buried TNT burst of 1 MT yield is

$$V_o = E_oW$$

$$V_o = (4000)(10^6)$$

$$V_o = 4 \times 10^9 \; ft^3$$

3. A 1 MT TNT burst at 10-foot depth has a scaled depth of burst of

$$\frac{DOB}{V_o^{1/3}} = \frac{10}{(4 \times 10^9)^{1/3}}$$

$$\frac{DOB}{V_o^{1/3}} = 0.0063$$

4. The ratio of the crater volume of a high yield shallow buried burst to the crater volume of a half-buried TNT burst (V_a/V_o) is given as a function of scaled depth of burst in Fig. 4-4. For a scaled depth of burst of 0.0063

$$\frac{V_a}{V_o} = 0.12$$

Therefore,

$$V_a = (0.12)(4 \times 10^9)$$

$$V_a = 4.8 \times 10^8 \; ft^3 \; (1.36 \times 10^7 \; m^3)$$

5. Crater radius and depth for near-surface nuclear bursts are estimated from Fig. 4-10 (Eqs. 4-6 and 4-7). For a 1 MT yield

$$R_a = (2.09)(4.8 \times 10^8)^{1/3}$$

$$R_a = 1635 \; ft \; (499 \; m)$$

$$D_a = (0.218)(4.8 \times 10^8)^{1/3}$$

$$D_a = 171 \; ft \; (52 \; m)$$

4.4.3 Crater Prediction for a More Deeply Buried Burst

a. GIVEN: A 20 kT (8.368×10^{13} j) burst at a depth of 50 feet (15.2 m) in wet clay.

b. FIND: Apparent crater volume, radius and depth.

c. SOLUTION:

1. Assume a half-buried TNT cratering efficiency of 4000 ft^3/ton (Ex. 4.4.2). The crater volume due to a 20 kT half-buried TNT burst is then

$$V_o = (4000)(20 \times 10^3)$$

$$V_o = 8 \times 10^7 \; ft^3$$

2. The depth of burst scaled by the half-buried TNT crater volume is

$$\frac{DOB}{V_o^{1/3}} = \frac{50}{(8 \times 10^7)^{1/3}}$$

$$\frac{DOB}{V_o^{1/3}} = 0.116$$

3. From Fig. 4-4, $V/V_o = 0.78$ Thus, $V_a = (0.78)(8 \times 10^7) = 6.24 \times 10^7 \text{ ft}^3 \ (1.76 \times 10^6 \text{ m}^3)$

4. The bounds for the apparent crater radii and depths are obtained from the procedure described in paragraph 4.2.4. The radius calculated from Eq. 4-6 is

$$R_a = (1.2)(6.24 \times 10^7 \text{ ft}^3)^{1/3} \ (20)^{0.08} = 605 \text{ ft } (184 \text{ m})$$

At $DOB/V_o^{1/3} = 0.2$, the crater radius from Eq. 4-4 is

$$R_a = (1.2)(1.15 \times 8 \times 10^7)^{1/3} = 542 \text{ ft } (165 \text{ m})$$

The upper bound for crater radius is therefore 542 ft (165 m) The crater radius of a surface burst from Eq. 4-6 is

$$(1.2)(8 \times 10^7/20)^{1/3} \ (20)^{0.08} = 242 \text{ ft } (73.8 \text{ m})$$

The crater radius using Eq. 4-4 is

$$(1.2)(6.24 \times 10^7)^{1/3} = 476 \text{ ft } (145 \text{ m})$$

The lower bound for crater radius is, therefore, 476 ft (145 m). The nominal value for crater radius is $R = (542 + 476)/2 = 509$ ft (155 m). The values for crater depth are calculated from Eq. 4-8, where $f = (0.44 + 0.44(20)^{-0.04})/2 = .415$ (where f was assumed to be an arithmetic average of the value for $DOB/V_o^{1/3} = 0.2$ and the value for $DOB/V_o^{1/3} = 0$). From Eq. 4-8, the lower bound for crater depth (using the upper bound for crater radius) is

$$D_a = 6.24 \times 10^7/(\pi)(0.415)(542)^2 = 163 \text{ ft } (49.7 \text{ m})$$

The upper bound for crater depth is

$$D_a = 6.24 \times 10^7/(\pi)(0.415)(476)^2 = 211 \text{ ft } (64.3 \text{ m})$$

The nominal crater depth is

$$D_a = 6.24 \times 10^7/(\pi)(0.415)(509)^2 = 185 \text{ ft } (56.4 \text{ m})$$

(An average of the upper and lower bounds gives 187 ft.)

4.4.4 Crater Prediction for a Low Altitude Airburst

a. GIVEN: A 1 MT (4.184×10^{15} J) burst at a height of 25 feet (7.6 m) above a wet clay site.

b. FIND: Apparent crater volume, radius and depth.

c. SOLUTION:

1. Assume the wet clay has cratering properties similar to the wet clay treated in Examples 4.4.1 through 4.4.3. The crater volume due to a half-buried TNT burst of 1 MT is then $4 \times 10^9 \text{ ft}^3$.

2. The scaled height of burst is

$$\frac{HOB}{V_o^{1/3}} = \frac{25}{(4 \times 10^9)^{1/3}}$$

$$\frac{HOB}{V_o^{1/3}} = 0.016$$

3. From Fig. 4-4 the normalized crater volume (V_a/V_o) for a scaled height of burst of 0.016 is read as

$$\frac{V_a}{V_o} = 0.02$$

Therefore, the apparent crater volume is

$$V_a = 0.02(4 \times 10^9)$$

$$V_a = 8 \times 10^7 \text{ ft}^3 \ (2.3 \times 10^6 \text{m}^3)$$

4. The apparent crater radius and depth are estimated from Eqs. 4-6 and 4-7. For a 1 MT yield,

$R_a = (2.09)(8 \times 10^7)^{1/3}$

$R_a = 901$ ft (275 m)

$D_a = (0.218)(8 \times 10^7)^{1/3}$

$D_a = 94$ ft (29 m)

4.4.5 Crater Prediction in a Single Layer Geology

a. GIVEN: A 1 MT (4.184×10^{15}J) surface burst at a site composed of 100 feet (30.5 m) of wet clay overlying shale which extends to great depth.

b. FIND: Apparent crater volume, radius and depth.

c. SOLUTION:

1. Assume nominal wet soil and wet soft rock high yield surface burst cratering efficiencies (Table 4-3) of 200 ft^3/ton and 100 ft^3/ton in the wet clay and wet shale, respectively. The crater volume in a wet clay halfspace is, therefore,

$$V_u \approx (200\ \text{ft}^3/\text{ton})\left(\frac{10^6\text{tons}}{1\text{MT}}\right)(1\text{MT})$$

$$V_u = 2 \times 10^8 \text{ft}^3$$

The crater volume in a wet shale halfspace is

$$V_L = (100\ \text{ft}^3/\text{ton})\left(\frac{10^6\text{tons}}{1\text{MT}}\right)(1\text{MT})$$

$$V_L = 10^8 \text{ft}^3$$

2. Equation 4-1 may be used to estimate the effect of layering.

$$\frac{V - V_L}{V_U - V_L} = 1. - \exp(-5.4d/V^{1/3})$$

$$\frac{V - 10^8}{(2 \times 10^8) - (10^8)} = 1. - \exp - 5.4\left(\frac{100}{V^{1/3}}\right)$$

or

$$V = \left(2 - \exp\ - \left(\frac{540}{V^{1/3}}\right)\right) \times 10^8$$

which must be solved by iteration.

3. As a first trial, assume the crater is not influenced by the layer. An estimate for V is then

$$V = V_u = 2 \times 10^8 \text{ft}^3$$

$$V^{1/3} = 585 \text{ ft}$$

A new estimate for V is

$$V = \left(2 - \exp\left(- \frac{540}{585}\right)\right) \times 10^8$$

$$V = 1.60 \times 10^8$$

Two additional iterations result in an estimate of the crater volume in the layered geology of

$$V_a = 1.63 \times 10^8 \text{ft}^3 \ (4.61 \times 10^6 \text{m}^3)$$

Note that this volume may be obtained directly from Fig. 4-9 since Fig. 4-9 is based upon the nominal cratering efficiencies of Table 4-3.

4. The predicted crater radius and depth from Eqs. 4-6 and 4-7 are

$R_a = (2.09)(1.63 \times 10^8)^{1/3}$

$R_a = 1142$ ft (348 m)

$D_a = (.218)(1.63 \times 10^8)^{1/3}$

$D_a = 119$ ft (36 m)

4.4.6 Crater Prediction in a Two Layer Geology

a. GIVEN: A 1 MT (4.184×10^{15}j) surface burst at a site composed of 100 feet (30.5m) of clay overlying shale with a water table at a depth of 50 feet (15.2 m).

b. FIND: Apparent crater volume, radius and depth.

c. SOLUTION:

1. The site consists of three materials: dry clay, wet clay and wet shale. The crater volumes in wet clay and wet shale half spaces are assumed the same as in Ex. 4.4.5. The high yield surface burst cratering efficiency in dry clay is assumed to be the nominal dry soil cratering efficiency of Table 4-3 (70 ft^3/ton). Using the notation of paragraph 4.2.3,

Dry clay: $V_1 = (70)(10^6) = 7 \times 10^7 ft^3$

Wet clay: $V_2 = 2 \times 10^8 ft^3$

Wet shale: $V_3 = 10^8 ft^3$

2. The crater volume associated with the middle layer, 50 feet of wet clay, and underlying half-space, wet shale, is determined using Eq. 4-2 and the method illustrated in Ex. 4.4.5 to be

$V_{23} = 1.4 \times 10^8 ft^3$

Equation 4-3 is then

$$\frac{V - (1.4 \times 10^8)}{(7 \times 10^7) - (1.4 \times 10^8)} = 1 - \exp\left(- 5.4 \ \frac{50}{V^{1/3}}\right)$$

or

$$V = \left[7.0 + 7.0\exp\left(- \frac{270}{V^{1/3}}\right)\right] \times 10^7$$

3. Taking V_{23} as an initial estimate of V yields a new estimate of V as

$$V = \left[7.0 + 7.0\exp\left(- \frac{270}{519}\right)\right] \times 10^7$$

$$V = 1.12 \times 10^8$$

Four additional iterations result in a final estimate of the apparent crater volume in the layered geology of

$$V_a = 1.10 \times 10^8 ft^3 \quad (3.11 \times 10^6 m^3)$$

Radius and depth are estimated as illustrated in Ex. 4.4.5. Note that since nominal cratering efficiencies are assumed, the crater volume result may be read directly from Fig. 4-9.

4.4.7 Ejecta Environment Prediction

a. GIVEN: A 1 MT (4.184×10^{15}j) surface burst at a site with a geology as described in Ex. 4.4.5.

b. FIND: Maximum, median, minimum and average ejecta depths, missile size distribution, impact probabilities and terminal characteristics at the 100 psi (48.9 N/cm^2) level.

c. SOLUTION:

1. The equations referred to in this solution are found in Table 4-5.

2. From Ex. 4.4.5, the apparent crater volume is $1.63 \times 10^8 ft^3$. From Fig. 3-4, the 100 psi level from a 1 MT surface burst corresponds to the 3400 ft range.

3. The scaled range of interest is

$$R_S = \frac{R}{V_a^{1/3}} = \frac{3400}{(1.63 \times 10^8)^{1/3}}$$

$$R_S = 6.22$$

The maximum ejecta depth (Eq. S-6) is

$$D_{max} = (1.63 \times 10^8)^{1/3} \left[0.767\exp(-2.121 \times 6.22) + 0.0443\exp(-0.3793 \times 6.22)\right]$$

$$D_{max} = 2.27 \text{ ft } (0.69 \text{ m})$$

The corresponding areal density (Eq. S-10), assuming a bulk ejecta unit weight of 100 lbs/ft^3, is

$$\delta_{max} = (100 \text{ lbs/ft}^3)(2.27 \text{ ft})$$
$$\delta_{max} = 227 \text{ lbs/ft}^2 (4.74 \text{ N/m}^2)$$

Median and minimum ejecta depths (Eqs. S-7 and S-8) and areal densities are calculated similarly as

$$D_{med} = 0.32 \text{ ft } (0.10 \text{ m})$$
$$\delta_{med} = 32 \text{ lbs/ft}^2 \ (0.67 \text{ N/m}^2)$$
$$D_{min} = 0.046 \text{ ft } (0.014 \text{ m})$$
$$\delta_{min} = 4.6 \text{ lb/ft}^2 \ (0.096 \text{ N/m}^2)$$

4. The average ejecta depth (Eq. S-9) is

$$\bar{D} = (1.63\text{x}10^8)^{1/3} \left[0.749\exp(-2.30\text{x}6.22) + 0.0168\exp(-0.423\text{x}6.22)\right]$$

$$\bar{D} = .66 \text{ ft } (0.20 \text{ m})$$
$$\bar{\delta} = 66 \text{ lbs/ft}^2 \ (1.38 \text{ N/m}^2)$$

5. The maximum missile diameter at the 100 psi level is given by Eq. S-13. Taking K = 1 and assuming the insitu total unit weight in the cratered region (γ_p) to be 125 lb/ft^3,

$$a_m = 0.504(1)(125)^{-0.0667}(1.63\text{x}10^8)^{0.267}(10^3)^{-0.0141}(6.239)^{-0.548}$$

$$a_m = 18.93 \text{ ft } (5.8 \text{ m})$$

6. The expected number of impacts per square foot at a given range from missiles with equivalent diameters between a_1 and a_2 is given by Eq. S-12. Taking n = 0.5 since the geology of interest is cohesive and layered, and $D = \bar{D}$ and assuming γ = 100 lb/ft^3, Eq. S-12 becomes

$$I = \frac{600(0.66)(0.5)\left(a_2^{-2.5} - a_1^{-2.5}\right)}{\pi(125)(18.93)^{0.5}(-2.5)}$$

$$I = 0.0464\left(a_1^{-2.5} - a_2^{-2.5}\right)$$

Results for missiles with equivalent diameters between 0.01 ft and 18.93 ft are given in Table 4-6, where $a_2 = a_m$ and $a_1 = a$.

7. The probability of the impact of at least one missile with equivalent diameter between a_1 and a_2 is given by Eq. S-15.

$$P = 1 - \exp\left[-I\left(\ell_1 + a_1\right)\left(\ell_2 + a_1\right)\right]$$

Probabilities for missile impacts on target areas of 10 ft x 10 ft, 50 ft by 50 ft and 100 ft by 100 ft for various diameter missiles are also given in Table 4-6. The probabilities are plotted as funciton of equivalent missile diameter in Fig. 4-19. The impact probabilities in Table 4-6 and Fig. 4-19 are the probability

Table 4-6

PROBABILITY OF IMPACT AS A FUNCTION OF
MISSILE DIAMETER FOR EXAMPLE 4.4.7

Missile Diameter (ft)	1 Impacts/ft^2	Impact Probability		
		$\ell_1 = \ell_2 = 10$ ft	$\ell_1 = \ell_2 = 50$ ft	$\ell_1 = \ell_2 = 100$ ft
0.01	4640	1.0	1.0	1.0
0.025	470	1.0	1.0	1.0
0.05	83	1.0	1.0	1.0
0.075	30	1.0	1.0	1.0
0.1	1.5	1.0	1.0	1.0
0.15	5.3	1.0	1.0	1.0
0.25	1.5	1.0	1.0	1.0
0.50	0.26	1.0	1.0	1.0
1.0	0.046	1.0	1.0	1.0
1.5	0.017	0.89	1.0	1.0
2.0	8.2E-3	0.69	1.0	1.0
3.0	3.0E-3	0.39	1.0	1.0
5.0	8.0E-4	0.17	0.91	1.0
8.0	2.3E-4	0.071	0.53	0.93
12.0	6.3E-5	0.030	0.22	0.55
15.0	2.4E-5	0.015	0.095	0.27
17.0	9.2E-6	0.0067	0.40	0.12
18.0	4.0E-6	0.0031	0.018	0.054

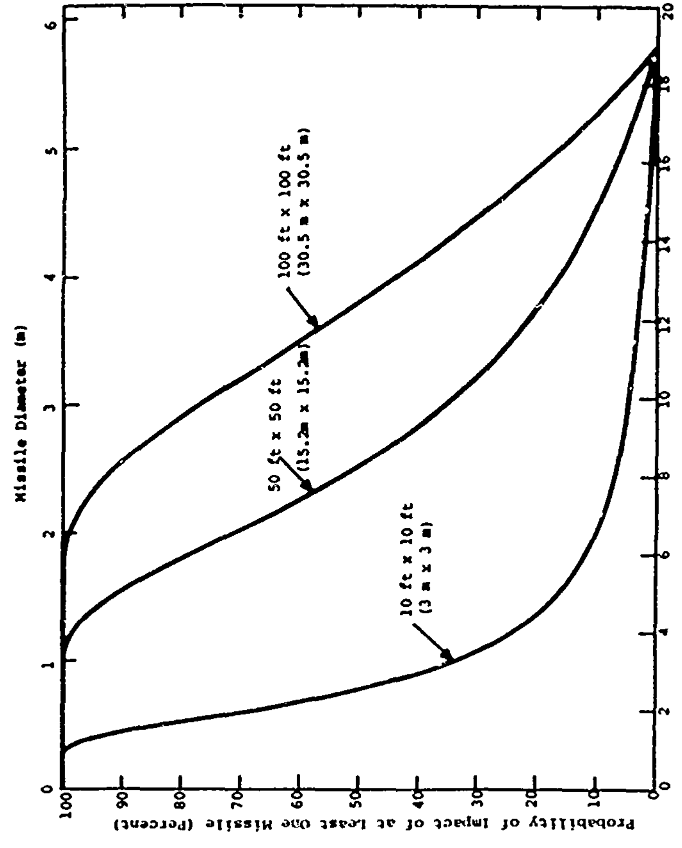

Figure 4-19 Probability of Impact of at Least One Missile Equal to or Greater in Diameter than the Missile Diameter on the Horizontal Axis (Example 4.4.7)

of at least one missile impact with diameter equal to or greater than a.

8. Terminal impact velocity is estimated by Eq. S-16 or S-17. Taking $\theta = 45°$ as a nominal impact angle, C_d as 1, γ_p as 125 lbs/ft^3 and a conservatively as 17 feet,

$$R_o = (90)(125)(17)(\sin 90°)$$

$$R_o = 191250 \text{ ft}$$

Equation S-16 is used to estimate impact velocity since the 100 psi range is 3400 ft which is less than $R_o/2$. The impact velocity is

$$V_i = (5.673)\left(\frac{3400}{\sin 90°}\right)^{0.5} \exp\left(-\frac{3400}{191250}\right)$$

$$V_i = 325 \text{ ft/sec } (100 \text{ m/sec})$$

4.5 REFERENCES

4-1

4-2 Cooper, H.F., Jr., Brode, H.L., and Leigh, G.G. Some Fundamental Aspects of Nuclear Weapons, paper presented at NATO Defense Seminar Bodo, Norway, 15 September 1974. (U)

4-3 Nordyke, M.D., On Cratering: A Brief History, Analysis and Theory of Cratering, UCRL-6578, Lawrence Radiation Laboratory, Livermore, Calif., August 1961. (U)

4-4 Johnson, Stanley, M., Explosive Excavation Technology, NCG Technical Report No. 21, U.S. Army Engineer Nuclear Cratering Group, Livermore, Calif., June 1971. (U)

4-5 Henny, R.W., Mercer, J.W., and Zbur, R.T., Near Surface Geologic Investigations at Eniwetok Atoll, Proc. of the 2nd International Symposium on Coral Reefs, Brisbane Aust., June 1973 (Draft) (U)

4-6 Unpublished AFWL Work by K.L. Mills.

4-7 Dillon, L.A., The Influence of Soil and Rock Properties on the Dimensions of Explosion Produced Craters, AFWL-TR-71-144, Air Force Weapons Laboratory, Kirtland AFB, N.Mex., February 1972. (U)

4-8 Post, R.L., Jr., Ejecta Distributions from Near Surface Nuclear and HE Bursts, AFWL-TR-74-51 (in preparation) Air Force Weapons Laboratory, Kirtland AFB, N.Mex. (U)

4-9

4-10

4-11

4-12 Nordyke, M.D., "Nuclear Craters and Preliminary Theory of Explosive Crater Formation," Journal of Geophysical Research, Vol. 66, No. 10, October 1961 (U)

4-13 Davis, L.K., Effects of a Near-Surface Water Table on Crater Dimensions, Miscellaneous Paper No. 1-939, U.S. Army Engineer Waterways Experiment Station, Vicksburg, Miss., October 1967. (U)

4-14 Pinker, R.W., Hooks, L.E., and Stephenson, D.E., Explosive Cratering in Simulated Layered Geology, Vol. I, Relationship of Crater Dimensions and the Depth to Layering Formed by a Water Table, Forthcoming Technical Report, Air Force Weapons Laboratory, Kirtland AFB, N.Mex. (U)

4-15 Strange, J.N., Effects of a Soil-Rock Interface on Cratering, Technical Report No. 2-478, U.S. Army Engineer Waterways Experiment Station, Vicksburg, Miss., May 1958. (U)

4-16 Laboratory Scale Explosive Cratering and Ejecta Phenomenology Studies, Forthcoming Technical Report, Air Force Weapons Laboratory, Kirtland AFB, N.Mex. (U)

4-17

4-18 Mills, K.L., Maximum Crater Depths From Repeated Nuclear Attacks, Forthcoming Technical Report, Air Force Weapons Laboratory, Kirtland AFB, N.Mex. (U)

4-19 Stephenson, D.E., and Hooks, L.E., Repeated Cratering Experiment: Data and Analysis, AFWL-TR-73-102, Air Force Weapons Laboratory, Kirtland AFB, N.Mex., February 1974. (U)

4-20 Unpublished AFWL Work by R.L. Post.

4-21 Anthony, M.V., Day, T.P., and Wauchose, C.R., Ejecta Distribution from FLAT TOP I Event, Ferris Wheel Series, Project 1.5b, POR-3007, Defense Atomic Support Agency, Washington, D.C., October 1965. (U)

4-22

4-23 Post, R.L., Jr., Ejecta Missile Size Distributions from Cratering Events in Soil and Rock, Forthcoming Technical Report, Air Proce Weapons Laboratory, Kirtland AFB, N.Mex. (U)

4-24 Ganong, G.P. and Roberts, W.A., The Effect of the Nuclear Environment on Crater Ejecta Trajectories for Surface Bursts, AFWL-TR-68-125, Air Force Weapons Laboratory, Kirtland AFB, N.Mex., October 1968. (U)

4-25 Post, R.L., Jr., Ejecta Impact Velocities and Angles from Nuclear Cratering Bursts, Forthcoming Technical Report, Air Proce Weapons Laboratroy, Kirtland AFB, N.Mex. (U)

SECTION V

GROUND SHOCK PHENOMENA

5.1 INTRODUCTION

5.1.1 Forms of Ground Shock

The ground shock area of weapon effects includes all the motions and stresses induced in the earth as a result of a nuclear explosion. This section deals with free-field ground shock, defined as the ground shock experienced in the absence of structures in the vicinity of the point of interest. The free-field phenomenology does not include the complicated interaction of stress waves with structures which will alter the ground shock in the region of a structure. The problem of structure-medium interaction, which deals with the translation of free-field ground shock quantities into loads on and motions of structures, is treated in Section VII.

The ground shock induced at a point in the free-field by a nuclear explosion is a function of several variables, including

- Weapon type and yield
- Height or depth of burst
- Range and depth of the point of interest
- Geology between burst point and the point of interest

The strength of the ground shock is proportional to the amount of energy coupled directly into the ground at the point of detonation and/or the forces induced on the ground surface by the propagating airblast. One extreme is produced by a fully-contained burst in which all the ground shock results from the directly coupled energy. The other extreme is produced by a high altitude burst in which all ground shock is caused by the

airblast wave pushing on the ground surface. For a burst at or near the ground surface, ground shock from both sources will occur in complex combination as illustrated in Fig. 5-1.

Although the ground shock environment at a point in the free-field results from a complicated interaction of many different phenomena and is not theoretically separable, ground shock is often categorized according to source. The following definitions are used herein:

Airblast-Induced Ground Shock - the ground stresses and motions caused by the propagating airblast.

Direct-Induced Ground Shock - the ground stresses and motions caused by the initial stress wave due to energy coupled at the burst point in near-surface or underground bursts.

Crater-Induced Ground Shock - the late-time ground stresses and motions caused by crater formation in cratering bursts.

5.1.2 Bases for Prediction Methods

The prediction methods herein combine nuclear and high explosive test data with relationships and concepts derived from theoretical and calculational studies. Some introductory comments on available data and present theoretical capability are provided in this paragraph. Specific data and assumptions are cited in the presentation of the methods.

The threat of major interest in the design and analysis of protective systems is the nuclear surface or near-surface burst. Available near-surface burst data consist of the few tests conducted at Nevada Test Site (NTS) and the Pacific Proving Grounds (PPG). The bulk of unclassified data are summarized in Ref. 5-1. The available data have limited

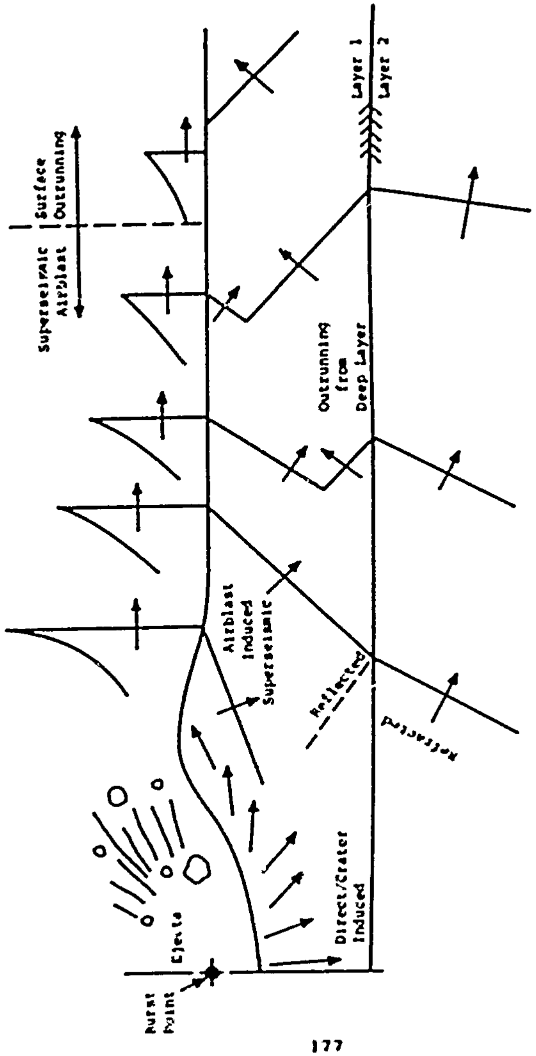

Figure 5-1 Schematic Representation of Ground Shock Effects

direct application for most problems because of the unique geologies of the test sites. In general, the nuclear test geologies are not representative of the majority of sites of practical interest. Tests at NTS were conducted at relatively homogeneous sites of alluvium or playa silt. Reflection/refraction phenomena associated with major layer interfaces, such as water tables or hard bedrock, are not represented in the data. In addition, severe yielding phenomena associated with wet soils, which generally have low shear strength under dynamic load, are not exhibited.

The available large yield tests were conducted on Eniwetok and Bikini Atolls in the Pacific. The geologic constituents of the atolls include coral sand, shells, coral fragments and limestone layers. As with NTS soils, the Pacific geologic materials are not representative of most sites of practical interest. The fact that the water table is very close to the surface in most of the Pacific tests introduces a significant complication in the interpretation of Pacific data. In addition, the small land area of the Pacific atolls limited the acquisition of ground shock data and raises the question of how much channeling of ground shock was accomplished by the ring configuration of the atolls. Pacific data are generally in low overpressure regions and stations are widely separated.

Non-nuclear test data are available from simulation tests and large high explosive detonations. The High Explosive Simulation ~~Test~~ Technique (HEST) has provided ground motion data in various geologies under conditions simulating traveling overpressure effects. The Direct-Induced High Explosive Simulation Technique (DIHEST) has provided ground motion data in rock under simulated direct-induced conditions. Large spheres of high explosive have provided various combinations of airblast, direct-induced and cratering effects depending on height of burst. Although the degree of nuclear simulation achieved by the non-nuclear test is subject to dispute, the non-nuclear data provide information on the insitu behavior of real geologic materials and a check case to evaluate the capability of various analytical methods.

Theoretical capability in ground shock prediction and phenomenological understanding has made large advances through the application of large-scale, two-dimensional axisymmetric continuum computer codes. Such codes (e.g., Refs. 5-2, 5-3 and 5-4) solve finite difference or finite element approximations to the equations of motion for a continuum. They are capable of treating layered materials with constitutive relations that simulate the behavior of real geologic materials.

Large-scale codes still have major shortcomings, however. The codes have been unable to predict late-time phenomena in all materials, particularly phenomena associated with cratering, near-surface effects and effects at large distances from the explosion. In addition, large uncertainties remain with respect to energy coupling for the surface burst configuration. Although the codes are not yet completely perfected, they do provide qualitative insight into the areas of uncertainty and to some extent quantitative relationships between parameters.

5.1.3 Organization of the Section

The remainder of this section is organized into six major paragraphs as follows:

- Properties of Geologic Materials (Para. 5.2)
- Airblast-Induced Ground Shock (Para. 5.3)
- Direct-Induced Ground Shock (Para. 5.4)
- Crater-Induced Ground Shock (Para. 5.5)
- Composite Ground Shock (Para. 5.6)
- Illustrative Examples (Para. 5.7)

Paragraph 5.2 describes the subsurface information and material properties which are necessary for ground shock prediction. Emphasis is given to the properties required to use the methods of this manual. Approximate material property values are presented for use in preliminary calculations.

Ground shock prediction methods are presented in paragraphs 5.3, 5.4 and 5.5 wherein it is assumed that airblast-induced, direct-induced and crater-induced effects are independent and may be predicted separately. A method for combining the ground shock effects from the various sources is presented in paragraph 5.6. It is assumed that simple superposition according to relative time phasing may be used to estimate the composite ground shock environment at a point of interest. Paragraph 5.7 presents examples which illustrate the application of the methods.

The material presented in this section assumes that the reader has some basic understanding of wave propagation phenomena. References 5-5 and 5-6 are suggested as introductions to wave propagation.

5.2 PROPERTIES OF GEOLOGIC MATERIALS

5.2.1 Introduction

The prediction of ground shock is strongly dependent on the properties of the material through which the ground shock propagates. The behavior of the material governs both the magnitude of the motions at a particular point and the attenuation of effects with depth and range. Field and laboratory investigations must provide information which will allow the selection of suitable sites for protective structures and estimates of insitu static and dynamic material properties.

Since protective structures must withstand all normal operating conditions (static loads, earthquakes, etc.), field and laboratory investigations will always include standard procedures applicable to conventional structures. This manual concentrates on the material property information which is required to estimate behavior under nuclear loads.

As in conventional soil and rock mechanics, the major material parameters affecting response are stress-deformation behavior and strength. The major complications in ground shock prediction arise from the need for dynamic properties of geologic materials over large areal regions and to great depths under complex three-dimensional states of stress in loading, unloading, and reloading.

The major tools used for obtaining geologic parameters are

- Field exploration
- Laboratory investigation
- Insitu test

The extent of exploration and investigation required for a given site is governed largely by the degree of confidence required in the ground shock prediction. Preliminary estimates of low confidence may be made using only a seismic profile while higher confidence estimates will require extensive subsoil exploration and sampling, laboratory testing and insitu tests. The use of two dimensional codes required detailed information on material behavior under complex states of stress.

It is important to note that to this point in time, two dimensional claculations based upon the best laboratory test data now obtainable have not been totally successful in predicting ground shock. The difficulty appears to be associated with an inability to adequately measure all aspects of insitu behavior in the laboratory. Soil samples are always disturbed to some extent due to sampling procedures, removal from the ground, and processing in the laboratory. The laboratory response of small, intact rock samples does not reflect

the effects of widespread insitu joints and fissures. As a result, considerable engineering judgement is required in ground shock prediction regardless of the prediction method employed. The greater the amount of subsoil information available, especially insitu data, the more intelligently judgement can be applied in the prediction process.

The prediction methods presented in this manual require a knowledge of the site stratigraphy, the seismic profile and the stress-strain behavior of the geologic units under a one-dimensional state of strain. The following paragraphs outline methods for obtaining the required information and present typical material properties which may be used for preliminary calculations. Laboratory tests and insitu techniques for obtaining material property data necessary for two dimensional calculations are briefly mentioned. References for more detailed information on all topics are provided.

5.2.2 Field Exploration

The objectives of field exploration are to

- Establish the type, condition, and arrangement of geologic materials in the region of interest
- Establish the seismic profile of the region
- Obtain ground water information
- Obtain samples for laboratory testing

The major sources of the necessary information are

- Visual reconnaissance
- Literature survey
- Subsurface drilling and sampling
- Geophysical exploration

Reference 5-7 is a useful guide to field exploration. Reference 5-8 describes a subsurface exploration performed in support of a major HE field test series.

The first steps undertaken in site selection or specific site investigation should be visual reconnaissance of the area and study of information available in the literature. Site visits should record the general topography of the area, the condition and types of structures in the area, and exposed soil profiles in neighboring cuts, quarries, bluffs, etc. Discussion with local engineers or residents will usually yield some information on local soil conditions, ground water level and bedrock depth.

A large amount of information on geology and topography is available in published sources such as those of the U.S. Geological Survey, the U.S. Department of Agriculture, state geological surveys, and state highway departments.

The information gathered through site visits and literature studies will allow definition of the extent of actual exploration necessary. In general, at sites where soil types vary rapidly or where subsoil information is lacking, more extensive subsurface explorations will be necessary.

The major difference between explorations for protective and conventional structures is the extent of the subsurface region of interest. For conventional structures, the geologic materials in the immediate vicinity of the structure are of interest. For protective structures, the materials at large depth and range from the structure may influence response. For example, the time phasing and relative strength of effects arriving from the point of detonation and from the expanding airblast are governed by the complete geology between the burst point and the point of interest.

An effective field exploration will involve coordinated geophysical and boring programs. The seismic refraction survey is an important geophysical method which provides information on the general characteristics of a region. Seismic refraction results should form a major input to the planning of subsurface boring programs. The refraction method involves exploding small charges in shallow holes and measuring the travel times of induced waves to points on the surface at varying distances from the explosion. Refraction survey results provide information on the lateral homogeneity of materials, major layering, such as water table depth and depth to bedrock, the location of fault zones and other discontinuities, and the propagation velocities (seismic velocities) of low-intensity stress waves. Seismic velocities are particularly important since they are used directly in some of the prediction methods presented herein.

Other important geophysical methods which should be employed in field exploration are

- Uphole velocity logs
- Gamma and Neutron logs
- Electric logs

These methods generally are employed in conjunction with subsurface borings since they all require exploratory holes and provide information useful in correlating boring samples. Uphole velocity logs, as with refraction surveys, provide seismic velocity data. Since the primary direction of travel is upward, comparison with refraction results gives an indication of the isotropy of the materials. In addition, uphole velocity logs will reveal seismic reversals (a lower velocity material underlying a higher velocity material) which cannot be detected with refraction surveys. Gamma and neutron logs are correlatable with insitu material density and moisture content, respectively. Electric logs provide data for estimating the water content and permeability of the various strata. Reference 5-9 provides information on the various geophysical methods.

There are no hard and fast rules for defining the depth, number and type of borings. In general, the borings must be of sufficient number and extend to sufficient depth to allow identification and sampling of all materials which may influence site response. The results of the reconnaissance, literature and seismic refraction surveys should form major inputs into subsurface exploration planning. The exploration program should be established by personnel thoroughly familiar with ground shock phenomenology and the sensitivity of site response to geologic parameters. As a general rule for near-surface structures, borings should allow identification of all interfaces and stratigraphic units which provide means by which incident ground shock can be directed back to the surface (either by reflection or head wave transmission). Typically, this means that borings should extend to hard bedrock (as distinguished from soft rocks, such as shales and sandstones). For deep underground structures, borings should extend sufficiently beyond the structure location to allow identification of reflecting surfaces which may significantly affect response. Special emphasis should be placed on identifying major faults.

Ground water conditions, water table depths, the existence of a perched water table, artesian water, etc. should be observed during exploration. If a large water source is required at the site, samples for physical and chemical tests, test wells, and pumping and injection tests should also be included in the exploration. Borrow pit investigations and other miscellaneous studies may also be performed during site exploration.

Sampling procedures should be the best available for the particular material. Techniques causing a minimum of sample disturbance should be employed. Five-inch diameter samples are required because of the design of commonly used uniaxial strain devices. Samples of smaller diameter can be cored from the 5-inch diameter smaples in the laboratory for other tests. Piston type or Shelby tube samplers are recommended for undisturbed sampling of soft cohesive soils. The modified

Denison sampler (Ref. 5-8) is recommended for hard and/or gravelly soils. If it is not possible to obtain undisturbed samples of granular soils, a split-spoon sampler should be used in conjunction with the standard penetration test. Drilling mud should be avoided in drilling and sampling granular soils if at all possible.

The drilling equipment should be capable of drilling a 6-inch diameter (0.15 m) or larger hole several hundred feet deep. It must have a hydraulic feed travel of at least 5 feet (1.52 m) for pushing samplers. Special equipment may be required for investigation of sites for deeply buried structures.

Continuous sampling should be performed in the upper 100 to 200 feet (30.5 to 61 m) in at least one hole. In other holes, soil samples should be taken at a minimum of 5-foot (1.52 m) intervals. In rock, core recovery of 100 percent is desired. A minimum recovery of 70 percent for any single run is acceptable provided the average recovery is not less than 85 percent. The method of coring in hardrock may be any approved standard and accepted method of rock core drilling by which continuous and complete cores of at least the minimum specified diameter are obtained. The modified Denison sampler mentioned above is recommended for soft rock. Cutting samples should be taken in each exploratory core hole at intervals of approximately 5 feet.

Continuous bore hole photography is desirable in all core holes through rock. The type bore hole camera used by the U.S. Army Corps of Engineers consists of a 16 mm moving picture camera mounted in a stainless steel tube approximately 2-3/4 inches in diameter and 33-inches long. A circular image of the hole is photographed as it appears on a conical mirror; orientation is obtained by a compass visible through the truncated top of the conical mirror. A visual record of the core hole is a great aid in evaluating the data. In addition, the extent of joints and fissures in the rock may be evaluated.

All soils and rocks should be identified, classified, and logged on the boring log as they are taken from the ground. The Unified Soil Classification System is recommended for field and laboratory identification of soil. Field procedures for its use are given in Ref. 5-10. The genetic system in use by geologists should be used for identifying rocks. A system for describing insitu rock discontinuities, joint spacings, and bedding thicknesses, and relating insitu rock properties to the properties of intact specimens through the "Rock Quality Designation" (RQD) is given in Ref. 5-11. The rock classification system of Ref. 5-12 is recommended for laboratory classification.

5.2.3 Laboratory Investigation of Soil

Laboratory investigations for soil start with the standard tests required for conventional structures, i.e.,

- Grain-size distribution
- Atterberg limits
- Unit weights
- Specific gravity of solids
- Triaxial tests
- Consolidation tests

Procedures for such standard tests are described in several references, for example, Refs. 5-13 and 5-14. The types and extent of testing for estimating ground shock depend mostly upon the sophistication of the geologic constitutive model used in prediction.

The major constitutive model used herein requires only the dynamic uniaxial strain (also called one-dimensional compression or oedometer) test. The test measures the dynamic stress-strain response of a soil under conditions of zero lateral strain (K_o condition). Such a strain condition is thought to be representative of the strain condition under

certain nuclear airblast loading conditions (described more fully in paragraph 5.3).

An example of a dynamic uniaxial strain device is shown in Fig. 5-2. A typical stress-strain curve is shown in Fig. 5-3. The constitutive model herein utilizes a linear approximation to the one-dimensional stress-strain curve, also shown in Fig. 5-3. The constrained (or loading) modulus is defined by a secant line from the origin to the maximum stress of interest in the problem under consideration and is given by

$$M_L = \frac{\sigma}{\epsilon} \qquad (5\text{-}1)$$

where

M_L = constrained modulus
σ = maximum stress of interest
ϵ = corresponding strain

The unloading modulus, M_u, is defined by the slope of an eyeball fit to the unloading-reloading portion of the stress-strain curve. The strain recovery ratio of the bilinear approximation is defined by

$$r = \frac{M_L}{M_u} = \frac{\epsilon - \epsilon_r}{\epsilon} \qquad (5\text{-}2)$$

where

r = strain recovery ratio of bilinear approximation
M_u = unloading modulus
ϵ = strain corresponding to maximum stress
ϵ_r = residual strain

For maximum stresses of interest less than the maximum stress achieved in the test, it is assumed that material unloading and reloading are governed by the same unloading-reloading modulus, M_u, as for the maximum stress in the test. References 5-15,

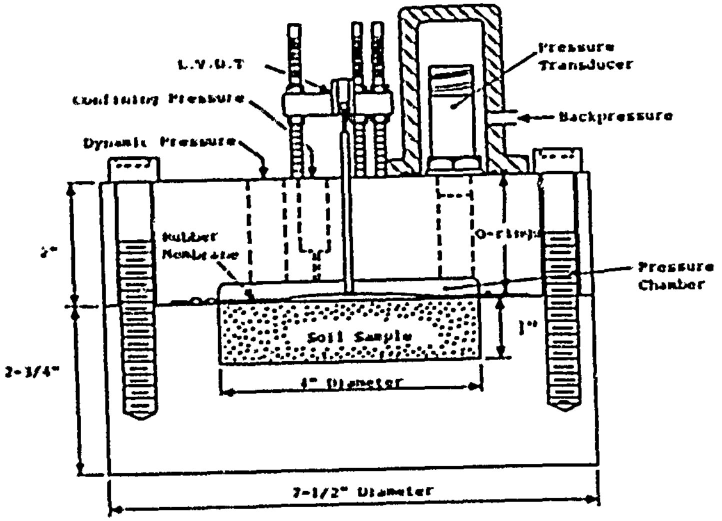

Figure 5-2 MIT Uniaxial Strain Device (Ref. 5-15)

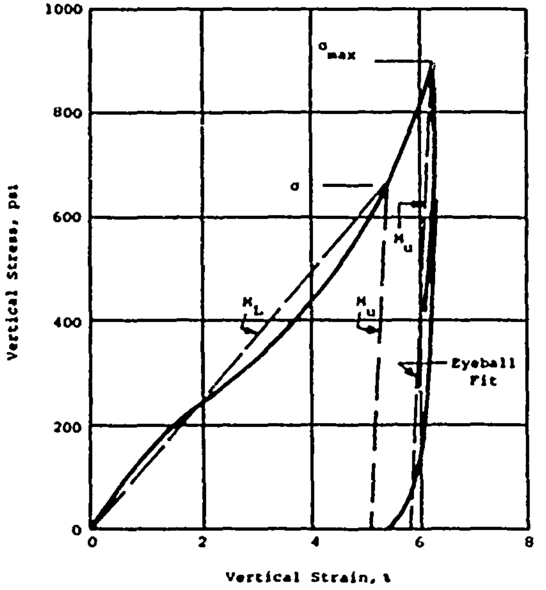

Dashed lines indicate linear approximations of this manual.

Figure 5-3 Dynamic Stress-Strain Curve for Glacial Till in Uniaxial Strain (Ref. 5-16)

5-17. and 5-18 present detailed information on the performance of the uniaxial strain test. Some general comments on test performance and interpretation of results are provided in the following.

The stress pulses due to the dynamic loading in the uniaxial strain test repeatedly reflect through the sample. Consequently, the loading function should provide a rise time long enough to allow the stress to equalize within the sample. Since the sample for such a test is generally very thin, special care should be taken in preparing it and placing it in the confining ring. Good seating should be ensured. Small disturbances of the ends of the sample will reduce the measured stiffness, particularly for the stiffer materials. Before testing, a static pressure equal to the calculated effective overburden stress should be applied and the sample allowed to consolidate. The stress increment used in testing should be greater than the increase in stress due to the design loading at the depth from which the sample was taken. Behavior through a dynamic unloading and reloading cycle should be measured.

Caution should be used in the interpretation of test data from samples taken from below the water table because the behavior of soil below the water table is governed largely by the degree of saturation. Minute variations in air content in near-saturated soils lead to large variations in constrained modulus. The constrained modulus of water is equal to its bulk modulus, or approximately 300,000 psi (206,808 N/cm^2). The constrained modulus of fully saturated soils, therefore, should be at least 300,000 psi (206,808 N/cm^2) since the bulk modulus of individual soil grains exceeds that of water. Small amounts of air, however, greatly reduce the constrained modulus of water. The bulk modulus of air is very low (about 21 psi at atmospheric pressure) and as little as 0.1% air (99.9% saturation) decreases the constrained modulus of the air-water phase to about 20,000 psi (13,787 N/cm^2). Small amounts of air in soil below the water table, therefore, will cause the constrained modulus of the wet soil to approach the constrained modulus of the soil skeleton at stress levels which do not cause strains large enough to drive the air into solution.

Laboratory tests of samples from below the water table often show degrees of saturation less than 100% and constrained modulii consistent with that expected of an air entrained soil (e.g., Ref. 5-19). Seismic velocities in soils below the water table, on the other hand, typically are about 5000 ft/sec (1520 m/sec), indicating essentially no air in the air-water phase. Seismic velocities in an air-water mixture containing 0.1 and 0.01 percent air would be about 1200 and 3000 ft/sec (366 and 914 m/sec), respectively. It is believed that the conflict between laboratory data and field measurements indicating near 5000 ft/sec (1520 m/sec) seismic velocities results from the introduction of small amount of gas into the sample due to sample processing in the field and laboratory and the relief of geostatic and hydrostatic stresses in sampling.

It is recommended that measured seismic velocity be used as a guide to the selection of appropriate soil constrained moduli below the water table. Where measured seismic velocity is near 5000 ft/sec (1520 m/sec) it is recommended that a modulus of 150,000 psi (103,404 N/cm^2) be used unless laboratory data give a higher value. The recommendation of 150,000 psi (103,404 N/cm^2) allows for a minute fraction of gas, expected to be present under natural conditions in the insitu material. Where measured seismic velocities are 3000 ft/sec (914 m/sec) or less, it is suggested that laboratory test data be relied upon. It is strongly recommended that some insitu measure of constrained modulus be obtained if at all possible. Special investigation methods, mentioned in paragraph 5.2.5, may be used.

In the absence of dynamic uniaxial strain test data, other more conventional tests may be used to infer a constrained modulus. A great deal of judgment and a thorough knowledge of the behavior of soils are necessary to interpret the tests. Some of the soil phenomena that must be taken into account are discussed below (Ref. 5-20).

Sample disturbance, mentioned previously, often produces irreversible changes in the properties of a soil removed from the ground. Direct laboratory determination of soil properties is seldom possible; however, good sampling techniques and corrections based on judgment and experience can lead to reasonably reliable test interpretations. Removal of a sample from the ground involves stress changes and corresponding deformations and distortions. This is illustrated in Figs. 5-4(a) and (b), which present typical void ratio, e, versus log of the effective vertical pressure, p, curves for a normally loaded and a preloaded soil. The solid lines represent the curves obtained in ordinary consolidation tests from the best available undisturbed samples. The coordinates e_o and p_o represent the void ratio and overburden pressure insitu, respectively. The dashed lines through these points represent the probable field behavior of the samples. Another set of dashed lines represent the test results on disturbed samples. Disturbance masks the probable true insitu behavior of the soil. It is especially important to note that even the best sampling distorts stress-strain behavior in the range of existing insitu stress. As a result, laboratory data at the insitu stress and for some stress range above insitu is not wholly reliable.

In Fig. 5-4(b), the coordinate p_c' represents the probable pressure to which the sample was previously loaded. The preload indicated in Fig. 5-4(b) does not necessarily mean that the sample was subjected to a higher pressure earlier than now exists insitu. Chemical alteration, cementation, and other effects may cause the sample to be cemented and thus stiffer than if these alterations had not occurred. Regardless of the cause of the indicated preload, the change in load-deformation characteristics due to disturbance is the same and is the phenomenon of importance. For pressures lower than p_c', the soil has a higher loading modulus than at pressures above p_c'.

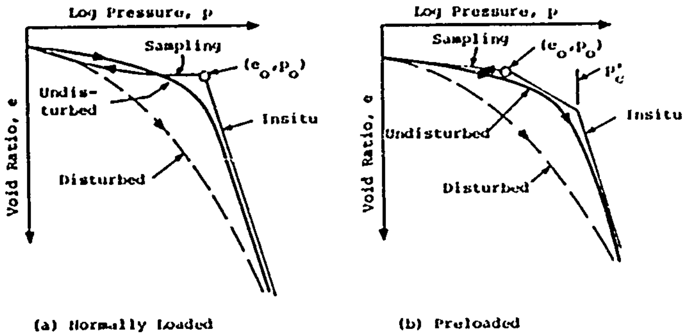

(a) Normally Loaded (b) Preloaded

Figure 5-4 Typical Soil Consolidation Curves (Fig. 5-20)

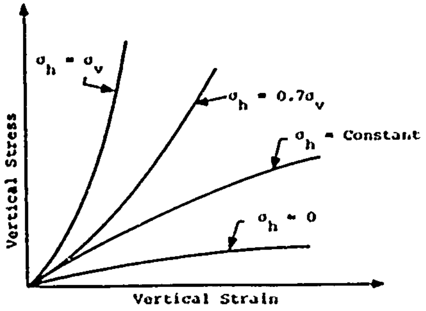

Figure 5-5 Triaxial Test Results (Modified from Ref. 5-20)

The modulus of a soil is known to increase with lateral confinement, at least in the upper few hundred feet of the earth's crust. The effect of confinement can be demonstrated by running several triaxial tests with different ratios of lateral to vertical stress. Typical results of such tests are shown in Fig. 5-5. The slope of the stress-strain curve increases markedly with increasing ratio of horizontal-to-vertical stress. If the ratio of horizontal-to-vertical stress throughout the test were such that no lateral strain resulted, the stress-strain curve would be that exhibited in uniaxial strain. Strain application rate also influences stress-strain behavior. In general, stiffness increases with increasing strain rate.

The effects of sampling, lateral stress and strain rate mentioned above can be used to infer an approximate constrained modulus from the following sources of data

- Seismic refraction and uphole surveys
- Vibration tests
- Unconfined compression tests
- Triaxial tests
- Static uniaxial strain tests

Seismic investigations yield the transmission velocities of low-intensity stress waves. The velocity, C_p, of a compression wave in an isotropic, linearly elastic medium is related to the elastic constants of the medium as shown below.

$$C_p^2 = \frac{M}{\rho} = \frac{E(1-\nu)}{\rho(1+\nu)(1-2\nu)} \qquad (5\text{-}3)$$

where

C_p = compression wave (dilatation wave, P-wave) velocity

M = constrained modulus

ρ = mass density = $\frac{\gamma}{g}$

γ = insitu total unit weight of material

g = acceleration due to gravity

E = Young's modulus

ν = Poisson's ratio

Other elastic relationships often useful in the interpretation of stress-strain and wave propagation data at low stress levels or in unloading-reloading are the following

$$M = \frac{(1-\nu)}{(1+\nu)(1-2\nu)} E = \frac{3(1-\nu)}{(1+\nu)} K \qquad (5\text{-}4)$$

$$K = \frac{2(1+\nu)}{3(1-2\nu)} G \qquad (5\text{-}5)$$

$$E = 3(1-2\nu) K = 2(1+\nu) G \qquad (5\text{-}6)$$

$$K_o = \frac{\nu}{1-\nu} \qquad (5\text{-}7)$$

$$C_S^2 = \frac{G}{\rho} \qquad (5\text{-}8)$$

where

K = bulk modulus

G = shear modulus

K_o = ratio of principal stresses (coefficient of earth pressure at rest)

C_s = shear wave (distortional, S-wave) velocity

Seismic pulses are propagated at a very low stress level and, therefore, generally yield a modulus greater than obtained at stress levels of interest in ground shock problems. Measured ground shock data indicate that the constrained modulus ranges from 3/4 to 1/2 the modulus determined from the seismic velocity.

The vibration test is performed on a cylinder of soil subjected to a confining pressure. Compression and shear waves are propagated at various frequencies until resonance is found. Young's modulus and the shear modulus are derived from the data and are used to calculate Poisson's ratio (Ref. 5-21). Equation 5-3 may then be used to calculate the constrained modulus. Elastic behavior is assumed throughout. The vibration test applies more energy to the soil than does a seismic refraction survey, but the stress levels are very much below the stresses of interest in nuclear ground shock problems. The effects of sample disturbance tend to reduce the modulus while the low stress level causes observed moduli higher than constrained moduli associated with ground shock stress levels. The two factors tend to compensate each other. However, the modulus determined by the test is close to the seismic modulus because of the low stress levels applied. A constrained modulus of about 1/2 the calculated value should be used for high stress levels.

When a sample can be treated in no other way, the initial tangent modulus from the stress-strain curve of a static unconfined compression test will yield some information. Because of the effect of disturbance and lack of confining pressure, the results will be quite low compared to the insitu value. Equation 5-3 indicates that a Poisson's ratio of 0.3 and 0.4 would cause the constrained modulus to be 34 percent and 114 percent, respectively, greater than the initial tangent modulus. Considering sample disturbance and the lack of confining pressure, a reasonable interpretation of the test would be to consider the constrained modulus to be three times the initial tangent modulus from an unconfined compression test.

The initial tangent modulus from a triaxial test is more reliable than that from an unconfined test because of the confining pressure effects. It is recommended that the constrained modulus be taken as twice the initial tangent modulus determined from a triaxial test.

Static uniaxial strain tests may be performed in consolidation equipment, in the sampling tube itself, or by various other means. The magnitude of the strain rate effect varies from material to material. Static and dynamic tests on playa silt (Ref. 5-18) indicate that the modulus for rise times on the order of 1 to 10 milliseconds is approximately twice the static modulus. It is recommended that dynamic modulus be taken as two times the static modulus. If possible, sensitivity to strain rate should be checked within the strain rate ranges attainable with available equipment.

As mentioned earlier, the geologic constitutive relations employed in large scale continuum codes require material properties under a wide range of stress and strain conditions. Tests to provide the needed data include dynamic triaxial and direct-shear tests, dynamic isotropic compression tests and static null tests. Reference 5-8 describes a comprehensive laboratory investigation in support of a major HE test series. Reference 5-22 describes several complex geologic material models used with large scale computer codes.

5.2.4 Laboratory Investigation of Rock

Laboratory test programs for rock have as their objectives the same material properties required for soil. The methods of this manual employ dynamic uniaxial strain behavior and insitu unit weight. Classification and composition tests plus density, specific gravity and moisture determinations are minimum requirements. The dynamic uniaxial strain behavior of soft rock is usually determined in the same uniaxial strain devices used for soil.

Intact samples of hard rock (basalt, granite, gneiss, etc.) have lower strain rate sensitivity and behave elastically over a larger stress range than soil and soft rock. As a result, static unconfined compression and triaxial tests may often be used directly in establishing dynamic constitutive properties. The constrained modulus of intact samples may be computed directly from Eq. 5-3 using measured values of Young's modulus and Poisson's ratio.

Material models employed in continuum codes require information on complex stress state behavior plus yielding and tensile behavior. The required data are derivable from triaxial tests, modulus of rupture tests, direct tension tests, torsion tests and dynamic Young's modulus tests. References 5-23 and 5-24 are recommended as introductions to laboratory test procedures for rock and to rock properties in general.

It is extremely important to recognize that the gross insitu properties of a rock mass will govern response. Faults, joints and joint filler material, the effects of which are not generally reflected in laboratory investigations, cause behavior significantly different from that inferred from laboratory tests on intact samples. Insitu moduli are lower and insitu stress-strain behavior is considerably more inelastic than implied by laboratory tests (Ref. 5-25). In addition, joints and faults control late time displacements and can result in much larger displacements than expected from continuum models. Reference 5-26 describes near-surface relative block displacements in rock which measured greater than two feet and severed a reinforced concrete model silo. The method of Ref. 5-11 is recommended for estimating the relation between insitu and laboratory behavior. Insitu tests are recommended if at all possible.

5.2.5 Insitu Investigations

Significant differences between measured field test and laboratory behavior of geologic materials dictate an increasing need for more reliable data on insitu properties. Major field tests such as HEST (Ref. 5-27), DIHEST (Ref. 5-25) and large HE surface and near-surface detonations are, in fact, insitu tests. However, the cost and time required to field large tests make them impractical for use at every site for which ground shock predictions are required. Practical field methods on a smaller scale are currently being developed and evaluated. One such method is the CIST (Cylindrical Insitu Test) which measures the dynamic response of significant near-surface layers to a cylindrically symmetric high explosive shock input (Ref. 5-28).

Other potential insitu test methods include spherically symmetric tests and small scale HEST tests. In hard rock, insitu investigations which should be considered, in addition to high explosive tests, are jacking and plate bearing tests to evaluate the effect of joints. Joint mapping should also be performed.

5.2.6 Typical Material Properties

Typical material properties to provide a frame of reference for the reader and to aid in preliminary calculations are provided in the tables of this section. The reader is cautioned that the use of typical properties involves considerable uncertainty. Typical properties should only be used for preliminary analyses or conceptual studies.

Table 5-1 presents typical seismic velocities for soils and rocks. The range in velocity for a given material and the overlap in velocity for different materials should especially be noted. In cases where only seismic velocity is available, it is recommended that 1/2 the seismic velocity be used to estimate the constrained modulus of soils and soft rocks and that 3/4 the seismic velocity be used to estimate the constrained modulus of heavily jointed hard rocks. The ratio of loading to unloading modulus may be taken as 1/3, 2/3, and 3/4 for loose soils, dense soils and soils below the water table, respectively. Ratios of 3/4 and 9/10 may be used for soft rocks and jointed hard rocks, respectively.

TABLE 5-1

TYPICAL SEISMIC VELOCITIES FOR SOILS AND ROCKS (REF. 5-7)

Material	Seismic Velocity ft/sec	Seismic Velocity m/sec
Loose and Dry Soils	600 - 3,300	180 - 1,000
Clay and Wet Soils	2,500 - 6,300	760 - 1,900
Coarse and Compact Soils	3,000 - 8,500	910 - 2,600
Sandstone and Cemented Soils	3,000 - 14,000	910 - 4,300
Shale and Marl	6,000 - 17,500	1,800 - 5,300
Limestone - Chalk	7,000 - 21,000	2,100 - 6,400
Metamorphic Rocks	10,000 - 21,000	3,000 - 6,400
Volcanic Rocks	10,000 - 22,000	3,000 - 6,700
Sound Plutonic Rocks	13,000 - 25,000	4,000 - 7,600
Jointed Granite	8,000 - 15,000	2,400 - 4,600
Weathered Rocks	2,000 - 10,000	600 - 3,100

Table 5-2 presents unit weights, mass densities and specific gravities for typical soils and rocks. Table 5-3 presents some typical dynamic properties of intact rock. As stated previously, intact rock behavior may not be representative of insitu behavior.

5.3 AIRBLAST-INDUCED GROUND SHOCK

5.3.1 *General*

The propagating airblast wave is a major source of ground shock. The characteristics of the ground shock are governed by the properties of the airblast wave and the properties and structure of the geologic medium. The properties of the airblast wave are described in Section III. Briefly, under ideal conditions, the airblast arrives at a point on the ground surface as a sharply defined shock front traveling at a velocity which is a function of the peak overpressure. After passage of the shock front, the overpressure decreases and eventually becomes negative. With increasing range, the peak overpressure and shock front velocity decrease while the total duration of the airblast wave increases.

The effect of the expanding airblast upon a point in the earth results not only from the airblast loading immediately above the point but also from the airblast loading at higher overpressures. The effect of a single instantaneously applied load is illustrated in Fig. 5-6. A point located immediately beneath the load experiences two distinct wave arrivals: (1) the compressive wave (P-wave) and (2) the shear wave (S-wave). At locations nearer the surface, a von Schmidt wave (SP-wave) and a Rayleigh wave (R-wave) are also experienced.

Typical normalized vertical displacement-time histories in an elastic medium due to an instantaneously applied point load are illustrated in Figs. 5-7 and 5-8. In the region beneath the load, the motion is mostly downward and outward.

TABLE 5-2

UNIT WEIGHT, MASS DENSITY AND SPECIFIC GRAVITY FOR TYPICAL SOILS AND ROCKS (Ref. 5-29)

Material	γ Unit Weight (lbs/ft^3)	ρ Mass Density ($slugs/ft^3$)	Specific Gravity
Loose Dry Sand	95	2.95	1.52
Loose Saturated Sand	120	3.73	1.92
Dense Dry Sand	110	3.42	1.76
Dense Saturated Sand	135	4.19	2.16
Dry Clay	75	2.33	1.21
Saturated Clay	110	3.42	1.76
Dry Sandy Silt	105	3.26	1.68
Saturated Sandy Silt	130	4.04	2.08
Basalt	171	5.31	2.74
Granite	165	5.12	2.64
Limestone	150	4.66	2.40
Sandstone	140	4.35	2.24
Shale	145	4.50	2.32
Concrete	150	4.66	2.40

TABLE 5-3

TYPICAL ELASTIC PROPERTIES OF ROCK (Ref. 5-29)

Rock Type	E (10^6 psi)	E (10^6 N/cm^2)	ν	K_o
Basalt				
Glassy (high strength)	5	3.5	0.11	0.12
Vesicular (high strength)	7	4.8	0.25	0.33
Vesicular (low strength)	4	2.8	0.20	0.25
Gneiss				
Augite, hornblend	15	10.3	0.28	0.38
Biotite, hornblend	10	6.9	0.24	0.31
Granite				
Coarse grained, biotite	9	6.2	0.14	0.16
Low Strength	8	5.5	0.25	0.33
Limestone				
Porous	4	2.8	0.20	0.25
Medium grained	8	5.5	0.31	0.45
Shale				
Silicified	10	6.9	0.12	0.14
Sandstone				
Soft	2	1.4	0.04	0.05
Hard	5	3.5	0.30	0.43

where

E = Young's modulus

ν = Poisson's ratio

$K_o = \frac{\nu}{1-\nu}$ = ratio of horizontal stress to vertical stress in one-dimensional compression

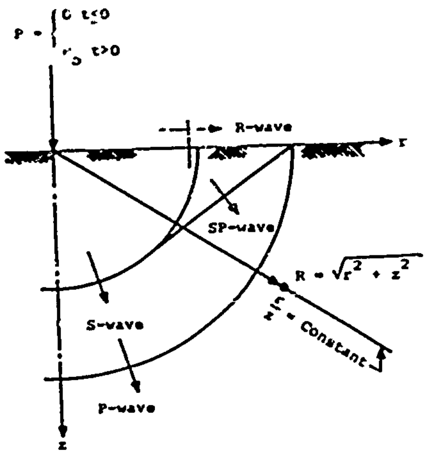

Figure 5-6 Waves Resulting from Instantaneously Applied Point Load (Ref. 5-15)

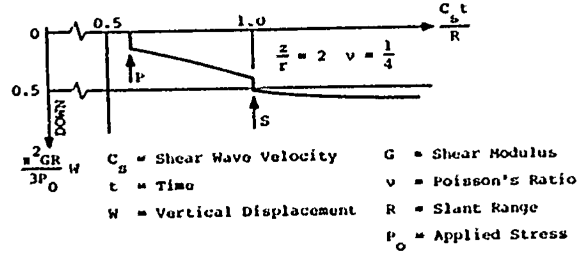

Figure 5-7 Time History of Vertical Displacement Along Ray Beneath Concentrated Load (Ref. 5-15)

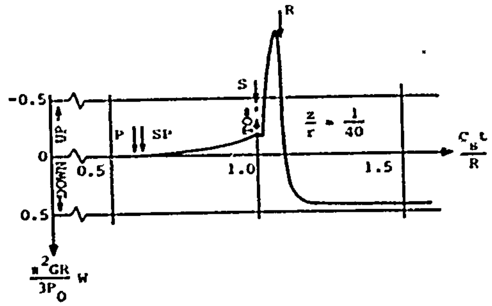

Figure 5-8 Time History of Vertical Displacement at Shallow Depth Near Concentrated Load (Ref. 5-15)

The motion is much more complex at points near the surface where the initial motion may be upward and outward followed by a later downward and inward motion.

An expanding airblast wave, in effect, applies instantaneous loads in succession at an infinite number of points spaced outward from ground zero, as illustrated in Fig. 5-9 (Ref. 5-15). The loading experienced at a point in the earth can be envisioned to result from some complex superposition in time of the effects of the successively applied loads.

In a homogeneous half-space, the character of the early-time effects is governed largely by the relative magnitudes of the airblast shock velocity and the wave velocities of the underlying medium. Three seismic regions, superseismic, transseismic and subseismic, can be defined, as illustrated in Fig. 5-10.

The superseismic region is defined to be the region in which the shock velocity of the airblast exceeds both the dilatational and shear wave velocities in the underlying medium, i.e.,

$$U > C_p > C_s \qquad (5\text{-}9)$$

where

U = airblast shock front velocity

C_p = dilatational wave velocity in the medium

C_s = shear wave velocity in the medium

Since the airblast velocity in the superseismic region is larger than either of the wave speeds of the medium, no disturbance can be propagated ahead of the airblast. The shock in the ground can only trail behind and below the airblast. Although the earth response at later times can be influenced by the airblast previously applied at points nearer ground zero, the dominant

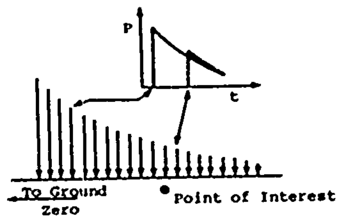

Figure 5-9 Sequence by Loadings Applied by Airblast (Ref. 5-15)

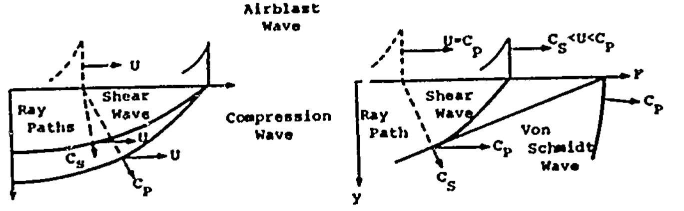

(a) Superseismic Airblast Wave System (b) Transseismic Airblast Wave System

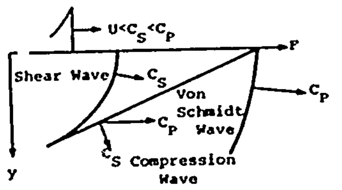

(c) Subseismic Airblast Wave System

Figure 5-10 Underground Wave Systems Due To Airblast-Induced Ground Motion (Ref. 5-1) response will be due primarily to the airblast loading above the point.

When the airblast shock front velocity becomes less than the dilatational wave velocity, shear wave velocity or both, disturbances propagate through the ground ahead of the airblast. Two cases are possible. The transseismic case (Fig. 5-10b) occurs when the airblast shock velocity is less than the dilatational wave velocity but greater than the shear wave velocity, i.e.,

$$C_p > U > C_s \qquad (5\text{-}10)$$

In the transseismic case a dilatational wave propagates ahead of the airblast while shear propagation continues to be controlled by the airblast front.

The subseismic case (Fig. 5-10c) occurs when the airblast shock velocity becomes less than both the dilatational and shear wave velocities in the medium, i.e.,

$$U < C_s < C_p \qquad (5\text{-}11)$$

In the subseismic case both dilatational and shear waves propagate in front of the airblast.

In both the transseismic and subseismic regions, the ground disturbance arrives at the point of interest prior to the arrival of the airblast wave. These regions are often referred to as outrunning regions because the ground motions outrun the airblast.

Motions in the outrunning region are quite complex. Time phasing of signals from all overpressure levels can cause reinforcements and oscillations at both early and late times. The sequence of motion prior to airblast arrival is a generalization of the simple effects illustrated in Fig. 5-7 for an instantaneously applied point load.

The presence of geologic layering introduces additional complications at both early and late times. As shown in Fig. 5-11, a complex pattern of wave fronts develops due to reflections and refractions at the layer interface. Refracted energy in underlying layers reentering the top layer can cause outrunning to occur in the top layer prior to the point where the airblast wave becomes transseismic or subseismic with respect to the surface layer (see Fig. 5-12). Multiple reflections within the top layer can have significant influence upon the late time motion.

Comprehensive ground shock analyses in real geologic media have not progressed to the point where simplified techniques are available for use in design and analysis. Most of the existing prediction techniques are in the development stage and large uncertainties are associated with material properties and the required complexity of the problem. The prediction methods which follow are based upon concepts and data derived from both theoretical studies and field test observations.

5.3.2 One Dimensional Analysis of Vertical Ground Shock in Homogeneous Geologies

In regions where the airblast wave is highly superseismic, the angle between the airblast-induced ground shock wavefront and the ground surface is small and the vertical deformation conditions at early times are approximately one dimensional. Under such conditions, early time vertical stresses, and motions may be reasonably estimated with one-dimensional wave propagation prediction procedures.

Before proceeding to prediction procedures it is important to discuss some characteristics of airblast induced ground shock. The effect of the nonlinear hysteretic

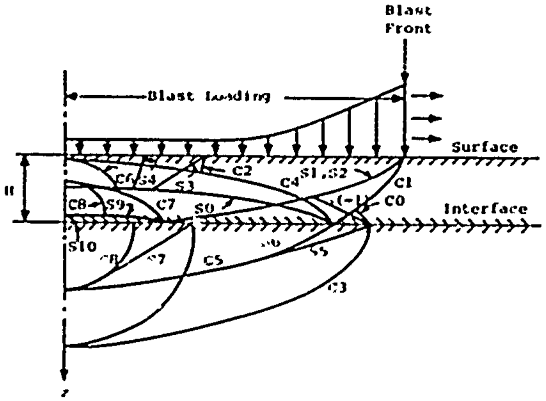

Figure 5-11 Wave Fronts at a Time When Initial Disturbance Front is Superseismic on Z=0 and Transseismic on Z=H (Ref. 5-30)

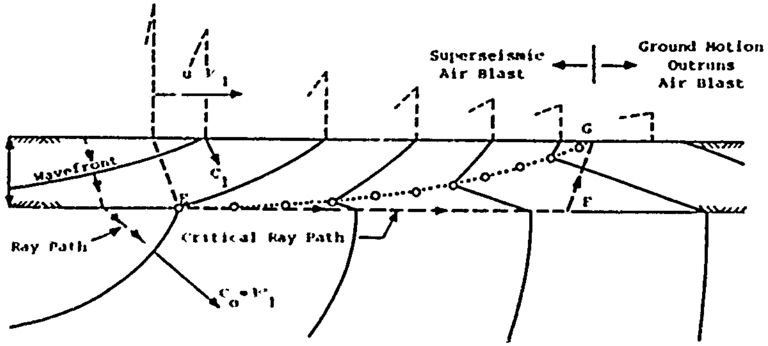

Figure 5-12 Ray Path Diagram for Determination of Critical Ray Path for Two-Layer Medium (Ref. 5-1)

nature of geologic materials upon the airblast-induced stress wave is illustrated in Fig. 5-13. Peak stress attenuates, rise time to peak stress increases and the decay rate behind the peak stress decreases as the stress wave propagates into the ground. The total impulse of the stress wave at some depth is essentially the same as the impulse delivered by the airblast wave at the surface.

The changes in stress pulse shape result primarily from the stress-strain characteristics of geologic materials. A typical uniaxial stress-strain curve for soil and its influence upon wave propagation in soil are shown in Fig. 5-14 (Ref. 5-31). The stress-strain curve is concave to the strain axis at lower stress levels, reverses curvature, and finally becomes increasingly stiff at higher stress levels. Upon unloading, considerable permanent strain remains.

The increase in rise time with depth is related to the decrease in loading slope at the beginning of the stress-strain curve. Stress levels below point A in Fig. 5-14(a) propagate at a velocity proportional to the slope of the stress-strain curve at the stress level of interest. Therefore, the rise time increases with depth as the pulse propagates into the ground because the lower stresses propagate at higher velocities than the higher stresses.

For pulses with peak pressures above point A, such as p_m in Fig. 5-14(a), the peak stress will propagate at a velocity corresponding to the modulus of the secant line drawn from point B tangent to the stress-strain curve at C. Theoretically, all stress levels between p_c and p_m travel at the same velocity in a shock which trails the faster stress levels below p_c. For a stress wave with a peak stress p_m, a stress wave similar to that shown in Fig. 5-14(b) would theoretically result. True shocks have been observed in laboratory wave propagation experiments. However, a true shock has never been observed

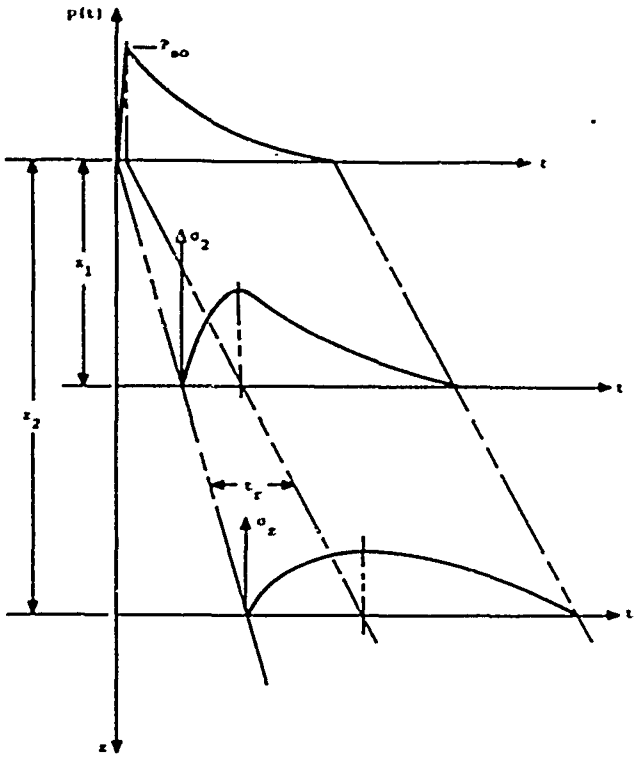

Figure 5-13 Changes in Stress Wave with Depth

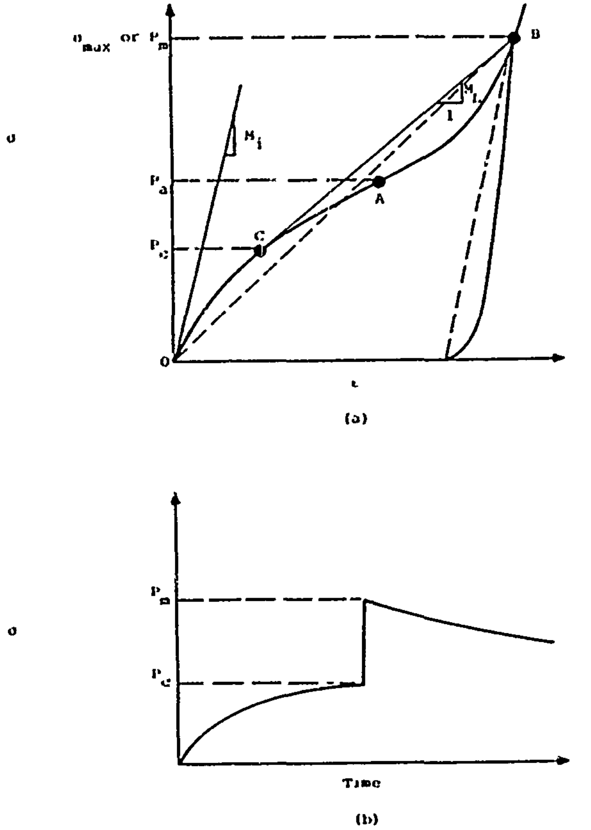

(a)

(b)

Figure 5-14 Influence of Stress-Strain Curve on Wave Propagation in Soils (Ref. 5-31) in the field at stress levels at which a shock would be predicted by laboratory stress-strain curves. Differences between field and laboratory behavior, strain rate effects and/or deviations from one-dimensional behavior may prevent the formation of a shock.

In one dimension, the attenuation of peak stress with increasing depth is due to the absorption of energy due to the hysteretic behavior (development of permanent strains) illustrated in Fig. 5-14(a). In the nuclear case, attenuation of stress also occurs along ray paths due to spatial attenuation. However, an axisymmetric elastic study (Ref. 5-32), has demonstrated that the maximum stress at a particular depth may be equal to or exceed the peak overpressure immediately above the point. This results from the fact that the stress experienced at a particular point at depth actually originates at an overpressure level higher than that immediately above the point. Accordingly, the effect of spatial attenuation should not be considered when the superseismic problem is treated one dimensionally.

An estimate of one dimensional wave propagation in real geologic materials is possible by considering bounding cases to the bilinear uniaxial stress-strain curve approximation introduced in paragraph 5.2.3. The bilinear approximation is defined by a loading modulus, M_L, which is the slope of a secant from the origin to the stress level of interest (taken as the peak overpressure, P_{so}) and an unloading modulus, M_u, which is the slope of an eyeball fit to the unloading-reloading portion of the laboratory measured stress-strain curve. The strain recovery ratio (r) of the bilinear approximation is given by

$$r = \frac{M_L}{M_u} = \frac{\epsilon_{max} - \epsilon_r}{\epsilon_{max}} \qquad (5\text{-}12)$$

where

r = strain recovery ratio

M_L = loading modulus

M_u = unloading modulus

ϵ_{max} = strain corresponding to maximum stress

ϵ_r = residual strain upon unloading to zero stress

The possible range of r is zero to one, zero corresponding to no strain recovery and one corresponding to elastic behavior.

Wave propagation in bilinear materials may be treated analytically (e.g. Ref. 5-33), but closed form solutions are derivable only for very simple input pressure functions. However, the bounding cases of $r = 0$ and $r = 1$ may be treated rather simply. Consider the bilinear approximation and bounding cases illustrated in Fig. 5-15. For $r = 1$, loading, unloading and reloading are all governed by the same modulus, M_L (Fig. 5-15b). For $r = 0$, virgin loading is governed by M_L while unloading and reloading up to the previous maximum stress occur with no change in strain.

Figure 5-16 presents the translation of a superseismic airblast problem into a one dimensional wave propagation problem. It is assumed that a half space of material is instantaneously loaded over its entire boundry by the overpressure-time function. The rise time to peak overpressure at the surface is assumed to be zero, i.e., the airblast front is assumed to be a shock.

Regardless of the assumed strain recovery ratio, a shock front propagates into the half space with a velocity C_L which is related to the loading modulus by

$$C_L = \sqrt{\frac{M_L}{\rho}} \qquad (5\text{-}13)$$

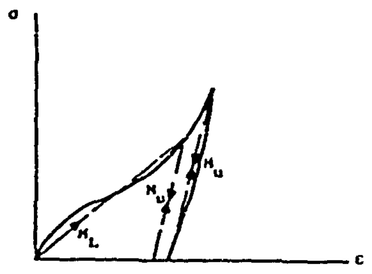

(a) Bilinear Approximation

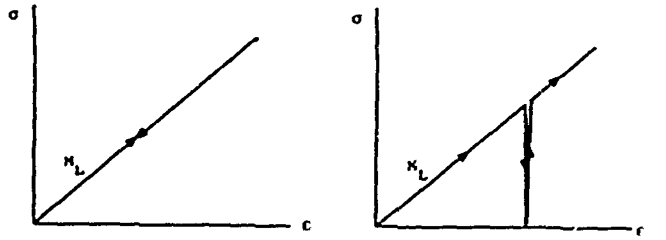

(b) Linearly Elastic (r=1)

(c) Linear Loading-No Recovery (r=0)

Figure 5-15 Uniaxial Stress-Strain Approximations

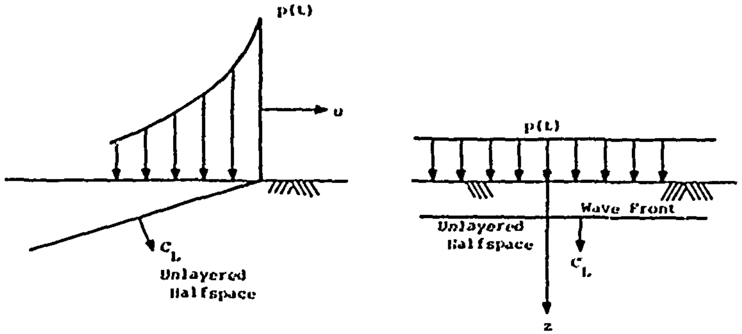

(a) Superseismic Airblast

(b) One-Dimensional Approximation

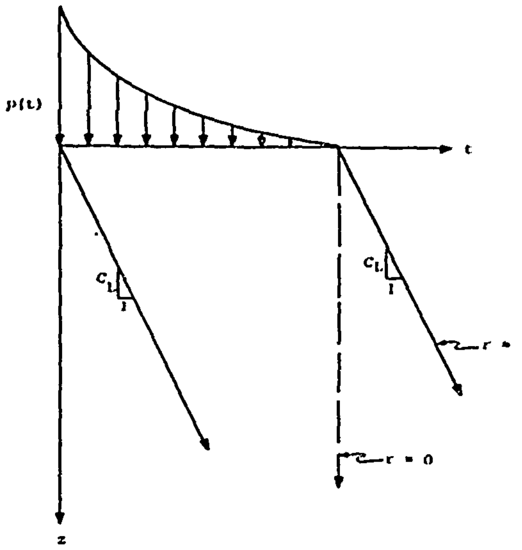

(c) Wavefront Diagram

Figure 5-16 One Dimensional Wave Propagation Formulation

where

C_L = loading wave propagation velocity

ρ = mass density of the soil

The tail of the pressure time function (or rarefaction) propagates into the ground at a velocity governed by the unloading modulus. For r = 1, the unloading velocity is equal to the loading velocity. For r = 0, the rarefaction travels at an infinite velocity. The locations of the wave front and wave tail as functions of time are illustrated on the wave front diagram of Fig. 5-16(c).

The stress, particle velocity and displacement as functions of time and depth for the elastic case (r = 1) are well known (e.g., Ref. 5-5) and are given by

$$\sigma_z(z,t) = p(t - z/C_L) \tag{5-14}$$

$$v_z(z,t) = \frac{\sigma_z(z,t)}{\rho C_L} = \frac{p(t - z/C_L)}{\rho C_L} \tag{5-15}$$

$$d_z(z,t) = \int_{z/C_L}^{t} v_z(z,t)dt \tag{5-16}$$

for

$$t > \frac{z}{C_L}$$

where

z = depth
t = time
σ_z = vertical stress
$p(t)$ = overpressure-time history
C_L = loading wave propagation velocity
v_z = vertical particle velocity
ρ = mass density
d_z = displacement

The stress and motions as functions of time and depth for the case of no strain recovery (r = 0) are derived in Ref. 5-34. Taking compression as positive and assuming small strains, conservation of momentum may be written

$$\frac{\partial \sigma_z}{\partial z} = -\rho \frac{\partial v_z}{\partial t} \tag{5-17}$$

Since there is no strain recovery after passage of the initial shock

$$\frac{\partial \epsilon_z}{\partial t} = 0 \tag{5-18}$$

at all depths. Eq. 5-18 may be written

$$\frac{\partial}{\partial t}\left(\frac{\partial d_z}{\partial z}\right) = \frac{\partial}{\partial z}\left(\frac{\partial d_z}{\partial t}\right) = \frac{\partial v_z}{\partial z} = 0 \tag{5-19}$$

which implies that the particle velocity is a function only of time and not depth. Eq. 5-19 has a solution

$$v_z = \phi(t) \tag{5-20}$$

Differentiating Eq. 5-20 with respect to time and substituting into Eq. 5-17 yields

$$\frac{\partial \sigma_z}{\partial z} = -\rho\dot{\phi}(t) \tag{5-21}$$

which has the solution

$$\sigma_z(z,t) = -z\rho\dot{\phi}(t) + \psi(t) \tag{5-22}$$

where $\psi(t)$ is determined by the boundary conditions. Since the vertical stress is equal to the overpressure-time history at z = 0, Eq. 5-22 becomes

$$\sigma_z(z,t) = -z\rho\dot{\phi}(t) + p(t) \tag{5-23}$$

which must be solved simultaneously with Eq. 5-20 to obtain a complete solution.

On the wave front, the stress and particle velocity are related by

$$\sigma_z(z,z/C_L) = \rho C_L v_z(z,z/C_L) \qquad (5\text{-}24)$$

i.e., virgin loading is governed by the loading modulus, M_L. Equation 5-24 allows the determination of the following general solution for stress and particle velocity in homogeneous materials which load linearly but do not recover strain upon unloading

$$\sigma_z(z,t) = \frac{z}{C_L t}\left[\frac{I(t)}{t} - p(t)\right] + p(t) \qquad (5\text{-}25)$$

$$v_z(z,t) = \frac{1}{\rho C_L}\,\frac{I(t)}{t} \qquad (5\text{-}26)$$

for

$$\frac{z}{C_L} < t < t_o$$

where

$I(t) = \int_0^t p(t)dt$

P_{so} = peak overpressure

t_o = total duration of the overpressure time history

As for the elastic case, displacements are determined by Eq. 5-16. The solutions for σ_z and v_z at times greater than t_o differ from Eqs. 5-25 and 5-26; however, two dimensional effects predominate at late times and one dimensional solutions are not valid.

Equations 5-25 and 5-26 are readily solved by graphical means for nuclear overpressure functions using the overpressure and impulse information provided in Section III. The solutions take a particularly simple form for input functions defined by

$$p(t) = \begin{cases} P_{so}(1-t/t_o)^n & 0 < t < t_o \\ 0 & t > t_o \end{cases} \qquad (5\text{-}27)$$

in which case

$$\sigma_z(z,t) = P_{so}\left\{\left(1 - \frac{t}{t_o}\right)^n + \frac{zt_o}{C_L(n+1)t^2}\left[1-\left(1 - \frac{t}{t_o}\right)^{n+1} - (n+1)\left(1 - \frac{t}{t_o}\right)^n\left(\frac{t}{t_o}\right)\right]\right\} \qquad (5\text{-}28)$$

$$v_z(z,t) = \frac{P_{so}t_o}{\rho C_L t(n+1)}\left[1-\left(1 - \frac{t}{t_o}\right)^{n+1}\right] \qquad (5\text{-}29)$$

for

$$\frac{z}{C_L} < t < t_o$$

Normalized solutions for the cases n=1,5 and 10 are given in Figs. 5-17, 5-18 and 5-19. The normalized solutions may be used in preliminary calculations where the early overpressure time history (100 to 300 msec.) can be approximated by Eq. 5-27 using n=1, 5 or 10. The parameters t_o and n should be selected so that the approximation contains the same impulse as the actual overpressure up to the maximum time of interest.

The full recovery (r=1) and no recovery (r=0) one-dimensional wave propagation solutions bound the solutions for intermediate values of r. Given the bounding solutions, an approximation for intermediate values of r may be made by simple linear interpolation on r. Interpolations for stress and velocity time histories due to a triangular input are shown in Figs. 5-20 and 5-21.

The solutions for stress and particle velocity in bilinear material with arbitrary recovery ratio due to a triangular decaying shock are derivable from Ref. 5-33 as

$$\sigma_z(z,t) = P_{so}\left\{1 - \frac{t}{t_o} + \frac{(1+r)z}{2C_L t_o}\right\} \qquad (5\text{-}30)$$

$$v_z(z,t) = \frac{P_{so}}{\rho C_L}\left\{1 - \frac{(1+r)t}{2t_o} + \frac{rz}{C_L t_o}\right\} \qquad (5\text{-}31)$$

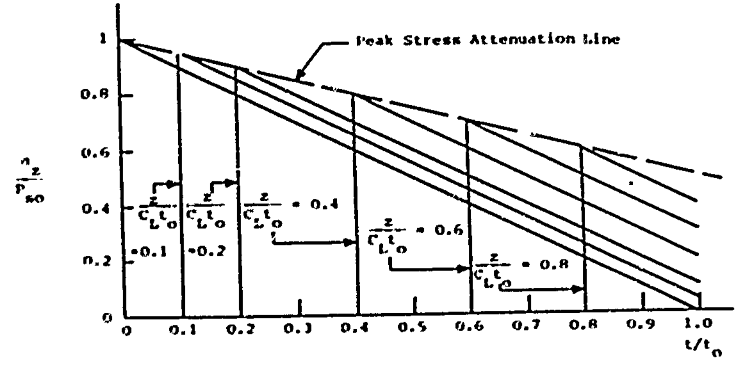

(a) Normalized Vertical Stress

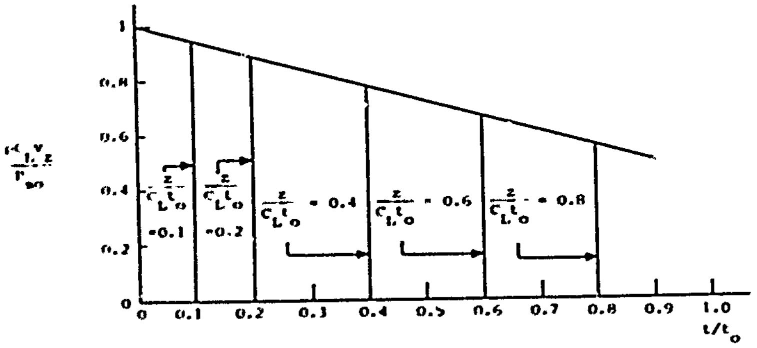

(b) Normalized Particle Velocity

Surface Overpressure $p(t) = P_{so}(1-t/t_o)$

Figure 5-17 Normalized Solutions to Equations 5-28 and 5-29 for $n = 1$

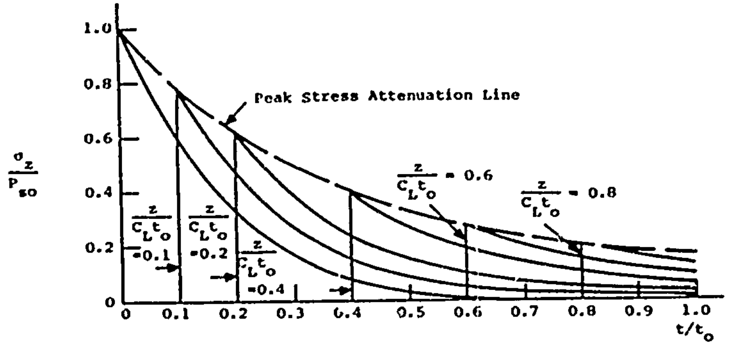

(a) Normalized Vertical Stress

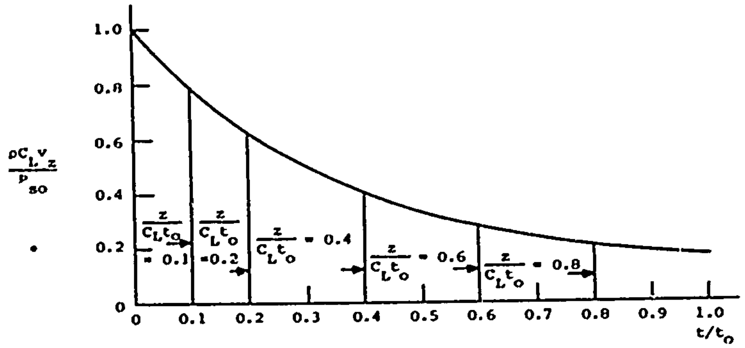

(b) Normalized Particle Velocity

Surface Overpressure $p(t) = P^{*}_{so}(1 - t/t_o)^5$

Figure 5-17 Normalized Solution to Equations 5-28 and 5-29 for $n = 5$

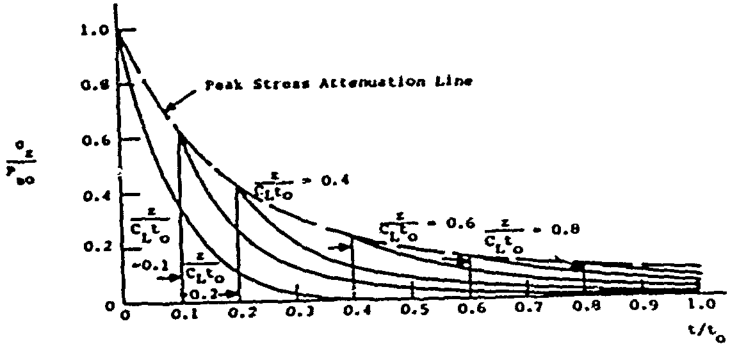

(a) Normalized Vertical Stress

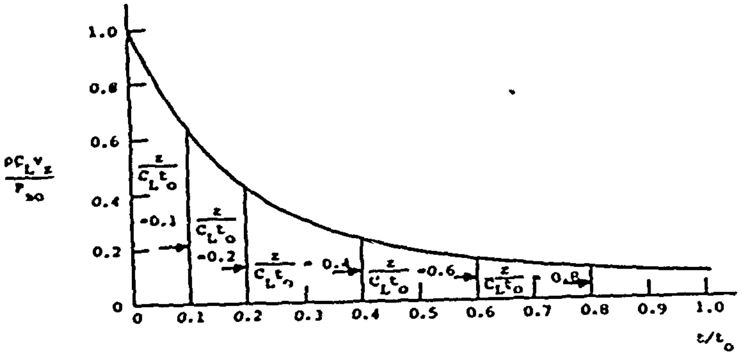

(b) Normalized Particle Velocity

Surface Overpressure $p = P_{so}(1 - t/t_o)^{10}$

Figure 5-19 Normalized Solution to Equations 5-28 and 5-29 for $n = 10$

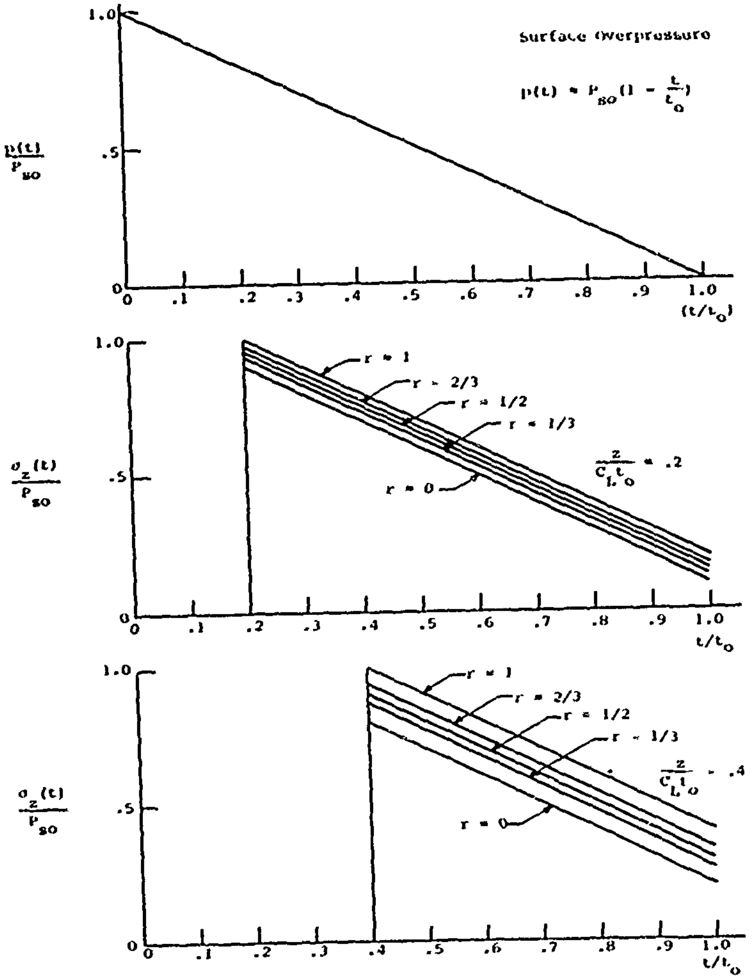

Figure 5-20 Illustration of Linear Interpolation to Estimate Stress Time Histories for Strain Recovery Ratios Between Zero and One

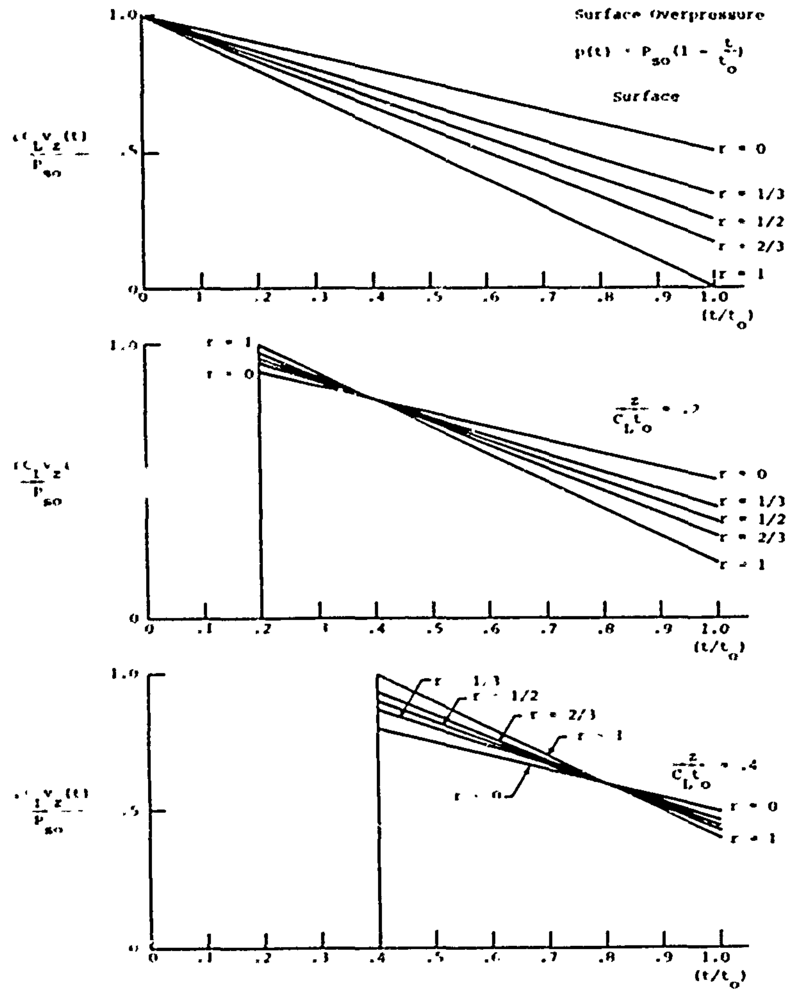

Figure 5-21 Illustration of Linear Interpolation to Estimate Particle Velocity Time Histories for Strain Recovery Ratios Between Zero and One

Equations 5-30 and 5-31 are linear in r and, therefore, linear interpolation between r=0 and r=1 is exact for triangular input. Linear interpolation for input forms other than triangular results in an underestimate of peak stress and velocity attenuation. The error is dependent upon the form of the overpressure decay, the depth of the point of interest and the loading wave velocity of the material. Within the top 100 feet (30 m) of typical geologic materials, errors due to linear interpolation will be no greater than 20 to 30% which is considered acceptable in view of overall uncertainties associated with the bilinear approximation and the exact form of the overpressure-time history.

The prediction procedure outlined in the foregoing assumes that the stress wave propagates into the ground as a shock. It has already been noted that measured field data indicate an increase in rise time as the stress wave propagates into the ground. The bilinear approximation does not account for the high propagation velocities associated with the lower stress levels. High initial velocities are indicated by seismic surveys and the initial loading slopes of many laboratory stress strain curves. Accordingly, it is recommended that predictions derived from interpolation between the elastic and no strain recovery cases be modified to incorporate a linear rise to peak stress and velocity as shown in Fig. 5-22. The peak stress and velocity arrival and the decay behind the peaks remain unchanged. However, the initial arrival is assumed to occur at a time given by

$$t_i = \frac{z}{C_i} \tag{5-32}$$

where

t_i = wave front arrival
z = depth
C_i = velocity of the wave front

The wave front velocity, C_i, should be taken as the insitu

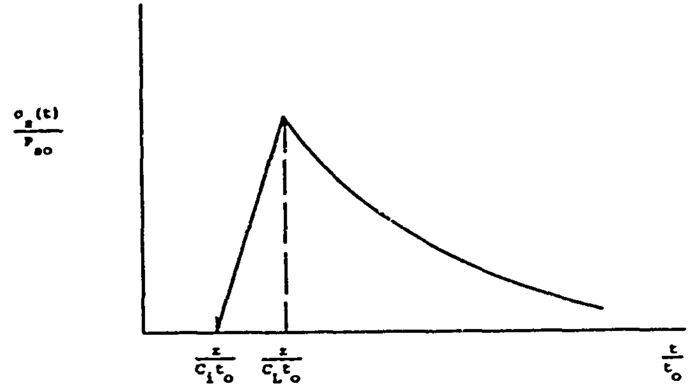

(a) Normalized Stress Time History

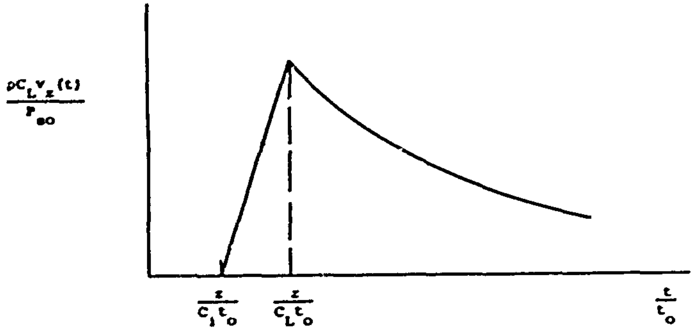

(b) Normalized Velocity Time History

Figure 5-22 Rise Time Modification of Stress and Velocity Time History Predictions

seismic velocity since laboratory test data at low stress levels are not sufficiently accurate to provide a reasonable measure of the initial loading slope.

The consequences of assuming one dimensional wave propagation in a homogeneous half-space are in some disagreement with measurements at sites which are considered relatively homogeneous (e.g., NTS). In the elastic case, the velocity returns to zero upon unloading but since upward velocities never occur a permanent displacement equal to the peak displacement remains. In the linear loading-no strain recovery case, the particle velocity never returns to zero, which leads to continually increasing displacement. Actual field measurements, even at so-called homogeneous sites, almost always show an upward velocity phase and some recovery of displacement. The disagreement is related to layering and two dimensional effects. Real sites are always layered to some extent. At a minimum, homogeneous soils will become increasingly stiff with depth which will result in a continuous reflection process with depth and the ultimate reversal of particle velocity. In addition, two dimensional effects will degrade one dimensional assumptions at later times. However, the prediction procedures recommended are considered reliable for estimates of the response of relatively homogeneous sites and for estimates of the incident wave propagating into the uppermost layer of layered sites at early times after airblast arrival.

5.3.3 Effect of Layering

Layering has an effect upon stress and motion time histories because of reflections and refractions which occur at interfaces. Strongest reflections will occur at well defined water tables and soil-rock interfaces. Minor layering within soil or rock, gradual transitions between layers, such as might occur in fine-grained soils where capillary action draws water above the water table and the gradual stiffening of a soil with increasing depth, will cause reflections of lesser magnitude but still of significance. General one-dimensional wave propagation in inelastic materials, including the effects of layering, may be treated with the methods given in Refs. 5-35 and 5-36. This manual employs some simplifying assumptions to provide insight into the effect of layering and allow estimates for one or, at most, two layer interfaces. Interfaces considered in predictions should be well defined water tables and/or soil-rock interfaces where they occur. At sites where interfaces do not occur at depths which will cause reflections influential during the first few hundred milliseconds, homogeneous estimates can be refined by introducing artificial layers which partially account for the effect of stiffening with depth.

Figure 5-23 presents a partial wave front diagram for a single-layer, one-dimensional problem. The positions of the incident stress wave front and wave peak are indicated by the circled ①. The incident wave front is assumed to travel at velocity C_I^1, which may be taken as the seismic velocity. The incident wave peak is assumed to travel at a velocity, C_L^1, determined from the loading modulus of a bilinear stress-strain model. Interaction of the incident stress wave with the layer interface results in a reflected loading wave, ②, travelling upward into the layer and a refracted loading wave, ③, which continues downward into the half-space.

In general, the reflected wave moving upward into the layer will load the layer material to a higher stress level than caused by the incident wave to some distance above the layer interface. As a result, two wave fronts will be generated by the reflection, one with velocity governed by

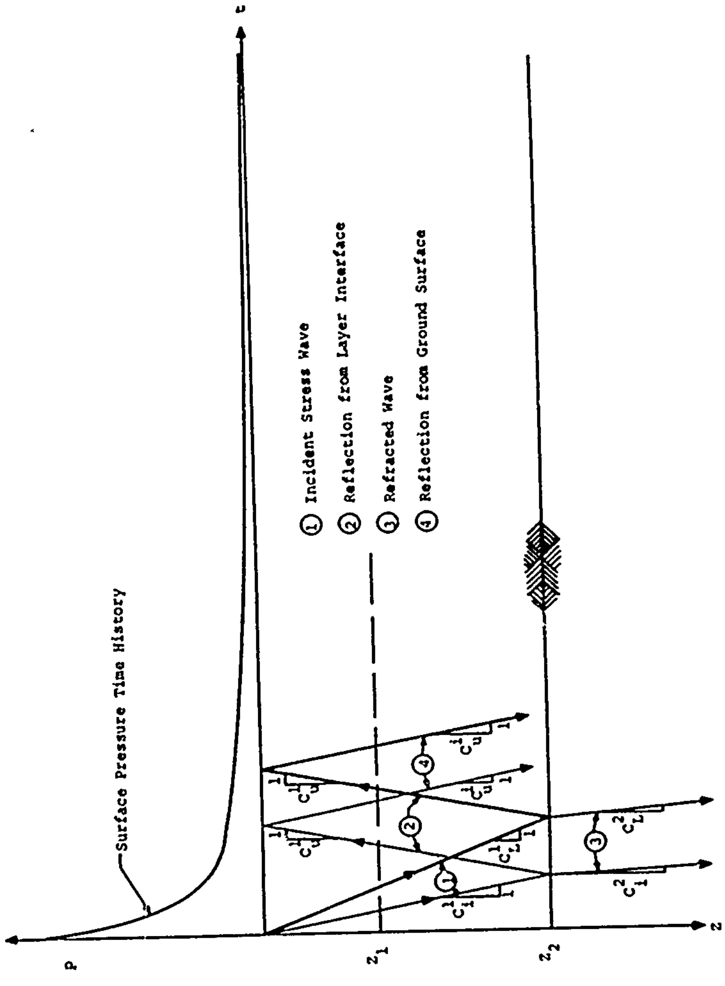

Figure 5-23 Wave Front Diagram for Estimating Layering Effects

the unloading and reloading slope of the bilinear material model, C_u^1, and one with velocity governed by the virgin loading slope, C_L^1. For most practical problems, the incident stress decays rapidly behind the peak and the magnitude of the reflected peak is less than one-half the incident peak. As a result, reloading above the incident peak occurs only for a relatively short distance above the interface. For simplification purposes, it is assumed herein that reloading above the peak can be ignored and that the reflected wave front and peak will travel with velocity, C_u^1, determined by the unloading-reloading modulus of the bilinear model of the layer material.

Interaction of the reflected wave with the ground surface results in a reflected unloading wave, ④ which travels downward. The wave velocity associated with the ground surface reflection is assumed equal to that determined by the unloading-reloading modulus of the bilinear model.

Figure 5-24 illustrates the various waves experienced at a depth Z_1 located within the layer. Figure 5-24(a) shows the incident wave in the absence of a layer. The incident stress wave at depth Z_1 is taken as equal to the stress wave predicted at Z_1 in a homogeneous half space composed of the layer material.

Figure 5-24(b) illustrates the wave reflected from the layer interface. The ratio of the peak stress of the reflected wave at the interface to the peak stress of the incident wave may be estimated from the relation

$$\frac{\sigma_r^L}{\sigma_I} = \frac{1-\psi}{1+\psi} \qquad (5\text{-}33)$$

where

$\psi = \dfrac{\rho_1 C_L^1}{\rho_2 C_L^2}$ = ratio of acoustic impedances of the two media

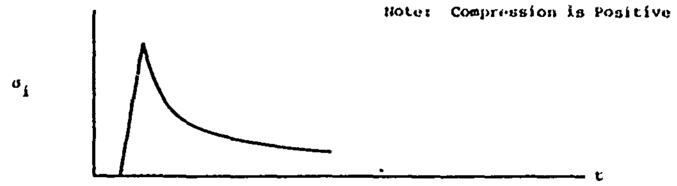

(a) Incident Wave at Depth, Z_1

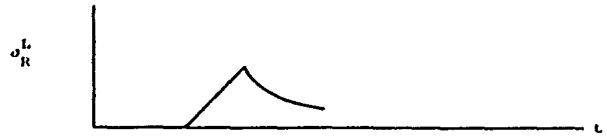

(b) Reflection from Layer Interface

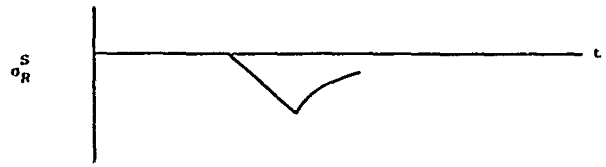

(c) Reflection from Ground Surface

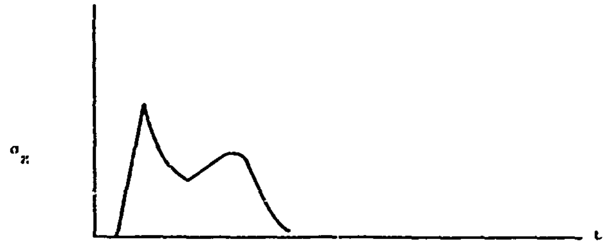

(d) Total Stress History at Depth Z_1

Figure 5-24 Effect of Layering Upon Vertical Stress-Time History in Surface Layer

ρ_1, ρ_2 = mass densities of the overlying layer and underlying half-space, respectively

C_L^1, C_L^2 = loading wave velocities in the overlying layer and underlying half-space, respectively

σ_i = peak stress of the incident wave at the interface

σ_r^L = peak stress of the reflected wave at the interface

The incident wave at the interface is taken as the stress wave predicted at the depth of the interface in a homogeneous half-space composed of the layer material. An elastic reflection process is assumed and, therefore, the time history of the reflected wave at the interface is simply the incident wave times the reflection factor computed according to Eq. 5-33. The reflection factor for peak stress (Eq. 5-33) is theoretically correct for bilinear materials. However, the assumption of a complete elastic reflection process is not theoretically correct. However, the assumption is considered consistent with the overall uncertainties of the problem. An exact solution for reflections in bilinear material is given in Ref. 5-37.

It is assumed that the layer material behaves elastically, i.e., remains on the unload-reload portion of the stress-strain curve, after passage of the incident wave peak. Therefore, the reflected wave propagates upward into the layer without change.

Figure 5-24(c) illustrates the wave which is reflected from the ground surface. In order to maintain the pressure boundry condition at the surface, an unloading (tensile) wave, equivalent in magnitude to the incident reflected wave from the layer interface, must be created, i.e.,

$$\sigma_r^S(t) = -\sigma_r^L(t) \tag{5-34}$$

where

$\sigma_r^S(t)$ = stress time history of reflected wave from ground surface

$\sigma_r^L(t)$ = stress time history of the reflected wave from the interface

The estimated stress history experienced at depth Z_1 determined from simple superposition of the various waves is shown in Fig. 5-24(d). Since one dimensional estimates are restricted to early-time effects, only the first layer and surface interactions are considered. Later time effects will be governed by two-dimensional phenomena, including spatial dispersion and arrivals from higher overpressure levels.

The refracted wave transmitted into the underlying material may be treated as an incident wave entering a homogeneous half-space. The ratio of the peak stress of the refracted wave to the peak stress of the incident wave may be estimated by

$$\frac{\sigma_t}{\sigma_i} = \frac{2}{1 + \psi} \tag{5-35}$$

where

σ_t = peak stress of the refracted or transmitted wave

σ_i = peak stress of the incident wave at the interface

The stress time history at the interface is assumed the same as the incident wave multiplied by the factor computed by Eq. 5-35. The interface stress time history may be treated as the boundary condition for a homogeneous half-space problem to determine the response of the material underlying the layer.

Early-time velocity time histories in layered media may be estimated by superposition, in a manner similar to that for stresses. In performing superposition, it must be recognized that loading (compressive) stress waves cause particle velocities in the direction in which the wave is propagating while unloading (tensile) waves cause particle velocities opposite to the direction of propagation.

Consider the same two layer problem for which stress time histories have been estimated (Fig. 5-23). The incident stress wave and associated particle velocity time history are predicted using the methods for homogeneous unlayered media given in paragraph 5.3.2. In the case of stress, it has been assumed that the reflection process at the interface is elastic and governed by the loading moduli of the two media but that the reflected stress wave propagating upward into the layer and subsequently reflected from the ground surface is governed by the unload-reload modulus of the layer material. The particle velocity-time histories associated with reflected stress waves in the layer are, therefore, given by

$$v_r(t) = \frac{\sigma_r(t)}{\rho\, C_u} \qquad (5\text{-}36)$$

where

v_r = particle velocity associated with the reflected stress

σ_r = reflected stress

ρ = mass density of material

C_u = wave velocity associated with unload-reload modulus of bilinear model

The particle velocities at depth Z_1, of the single-layer site of Fig. 5-23 are shown in Fig. 5-25. Figure 5-25(a) illustrates the particle velocity time history associated with the incident stress wave. Since the incident wave is compressive and moving downward, the associated particle velocities are downward. The velocity time histories associated with the waves reflected from the layer interface and the ground surface are shown in Figs. 5-25(b) and (c), respectively. The interface reflection is an upward moving loading wave (compressive) and, therefore, the associated particle velocities are upward. The ground surface reflection is a downward moving unloading wave (tensile) and the associated particle velocities are also upward. The composite velocity time history at depth Z_1, which results from superposition, is shown in Fig. 5-25(d).

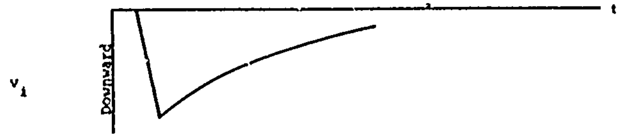

(a) Particle Velocity Time History Due to Incident Wave

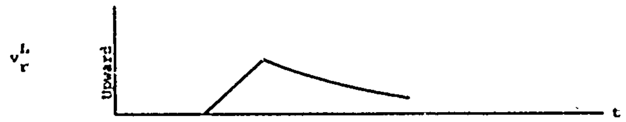

(b) Particle Velocity-Time History Due to Reflection from Layer Interface

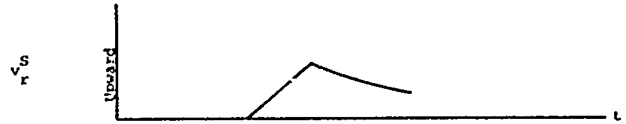

(c) Particle Velocity-Time History Due to Reflection from Ground Surface

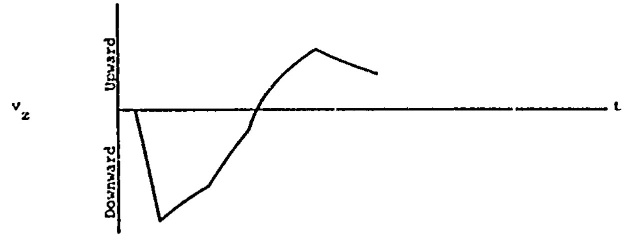

(d) Composite Time History

Figure 5-25 Effect of Layering Upon Vertical Particle Velocity Time History in Surface Layer

The early time vertical displacement time history at a point in the free field, whether the geology is homogeneous or layered, is simply the integration of the predicted vertical particle velocity time history using Eq. 5-16. Residual displacement is influenced by late time behavior including effects arriving from higher overpressure levels and the crater region and, in general, cannot be predicted by one dimensional methods. In cases where the vertical components of motion are judged to be influenced exclusively by superseismic airblast, e.g. in the region beneath an airburst, vertical residual displacements can be estimated by considering vertical residual strains.

The residual strain which remains at a particular point after all load has been removed is simply

$$\epsilon_r = (1 - r) \frac{\sigma_{max}}{M_L} \qquad (5\text{-}37)$$

where

σ_r = residual vertical strain
r = strain recovery ratio
σ_{max} = maximum vertical stress experienced at the point
M_L = uniaxial loading modulus at the point

Integration of Eq. 5-37 from infinity to the depth of interest gives the total residual displacement

$$d_r = \int_{\infty}^{z} \epsilon_r \, dz \qquad (5\text{-}38)$$

where

d_r = total residual displacement

Total residual displacement may be estimated by solving Eq. 5-38 graphically or by treating depth increments.

The residual compression in a particular increment is

$$\Delta d_r = (1 - r) \frac{\overline{\sigma_{max}} \Delta z}{M_L} \qquad (5\text{-}39)$$

where

Δd_r = residual vertical compression
$\overline{\sigma_{max}}$ = average maximum vertical stress reached in the increment ΔZ
ΔZ = height of increment of interest

The total residual displacement at a particular point is computed by summing the residual compressions in all underlying increments.

An approximate expression may be used for estimating peak vertical displacements if soil properties are ill defined and histories are not of importance. If the medium below a particular point can be considered reasonably uniform to a depth equal to the length of the stress wave in the earth, the maximum transient absolute displacement of the point can be computed from the airblast impulse as

$$d_{max} = \frac{I_m}{\rho C_L} \qquad (5\text{-}40)$$

where

I_m = total airblast impulse

5.3.4 Vertical Accelerations

The maximum vertical downward acceleration is related to the shape of the rise to the maximum velocity. The rise cannot be estimated accurately by analytical methods, therefore, semi-empirical procedures are presented for maximum vertical acceleration prediction.

For a linear rise of particle velocity, the maximum acceleration is simply

$$a_{max} = v_{max}/t_r \qquad (5\text{-}41)$$

where

a_{max} = maximum acceleration

v_{max} = maximum particle velocity

t_r = rise time to maximum velocity

At the surface, the rise time is equal to the rise time of the airblast. Field test observations show little dependence of the airblast rise time on yield or peak side-on overpressure level. It is more nearly a function of the ground surface conditions (Ref. 5-20). The value of rise time which results in accelerations comparable to measured field values is on the order of 0.001 second. Application of a rise time of 0.001 second to Eq. 5-41 and increasing the results by 20 percent to account for nonlinearity of the rise yields the following expression for maximum vertical acceleration at the surface (Ref. 5-20)

$$a_{max} = 150g\left[\frac{P_{so}}{100psi}\right]\left[\frac{1000fps}{C_L}\right]\left[\frac{115pcf}{\gamma}\right]$$

$$a_{max} = 66g\left[\frac{P_{so}}{100N/cm^2}\right]\left[\frac{1000m/sec}{C_L}\right]\left[\frac{1842kg/m^3}{\rho}\right] \qquad (5\text{-}42)$$

The value for C_L in Eq. 5-42 should correspond to the soil conditions at the surface.

Maximum acceleration attenuates rapidly with depth. The sharp attenuation is due more to the increase of rise time with depth than to attenuation of the maximum vertical velocity. The stretching out of the wave front is due to the nonlinearity of the stress-strain curve for soil. Since the stress rise at depth is more nonlinear than at the surface, it is recommended that the peak acceleration at depth be taken as twice that appropriate to a linear rise time (Ref. 5-20), i.e.,

$$a_{max} = 2\,\frac{v_{max}}{t_r} \qquad (5\text{-}43)$$

Assuming an airblast rise time of 0.001 second, the rise time at depth z would be

$$t_r = 0.001 + \frac{z}{C_L} - \frac{z}{C_i} \qquad (5\text{-}44)$$

When the values for C_L and C_i are not well defined, the rise time in soil or soft rock may be taken as one half the time required for the peak stress to reach the depth of interest (Ref. 5-38), i.e.,

$$t_r = \frac{1}{2}\,\frac{z}{C_L} \qquad (5\text{-}45)$$

5.3.5 Horizontal Stresses and Motions

The one-dimensional methods for vertical ground shock parameters yield little information on horizontal stresses and no information on horizontal motions. Peak horizontal stresses may be estimated on the basis of one-dimensional assumptions. No consistent method, empirical or otherwise, is presently available for the prediction of horizontal wave forms. Procedures for estimating peak horizontal motions have developed from empirical studies and two dimensional code calculations.

Horizontal stress is generally taken as some constant times the vertical stress, i.e.,

$$\sigma_h = K\,\sigma_v \qquad (5\text{-}46)$$

where

σ_h = horizontal stress

K = earth pressure coefficient

σ_v = vertical stress

The earth pressure coefficient, K, depends upon the properties of the soil, the degree of saturation, the stress level, the condition of lateral restraint, and the previous stress history.

A soil element under an increment of vertical stress, σ_v, is shown in Fig. 5-26. The vertical stress increment produces a vertical strain increment, ϵ_v. The lateral strain, ϵ_h, and resulting lateral stress depend upon the restraint of the confining medium. Under conditions of uniaxial strain, as is assumed under superseismic conditions, the lateral strain is zero. The earth pressure coefficient corresponding to the condition of zero lateral strain is called the earth pressure coefficient at rest, usually designated K_o.

In fluids, K_o is unity, i.e., the horizontal stress is equal to the vertical stress. In perfectly elastic materials, K_o is given by

$$K_o = \frac{\nu}{1 - \nu} \tag{5-47}$$

where ν is Poisson's ratio. In soils, the insitu value K_o may be greater or less than unity depending upon the degree of homogeneity, isotropy and prior geologic history. For example, K_o may exceed one in cases where the soil has been heavily preloaded in the past by large depths of overburden which have since been eroded. The high horizontal stresses may be envisioned as "locked in."

In general, K_o for soils is not constant but varies with stress level, stress application rate, and whether the soil is being loaded or unloaded. K_o during unloading generally exceeds the loading K_o because of the hysteretic nature of soils. A load-unload cycle is similar to the preloading of soil insitu.

For the prediction of peak horizontal stresses due to superseismic airblast, K_o due to an increment of stress, rather than the existing insitu K_o is necessary. Under dynamic

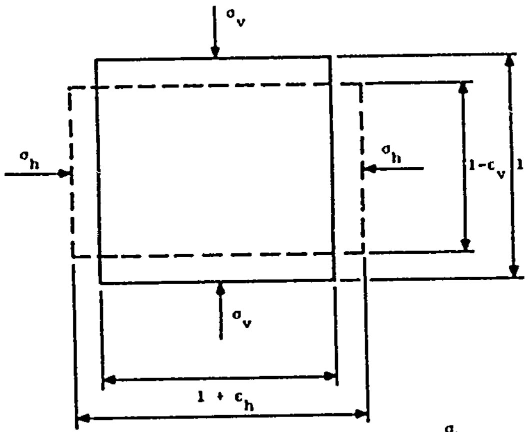

$$K = \frac{\sigma_h}{\sigma_v}$$

(1) If $\epsilon_h = 0$, $K = K_o = \frac{\sigma_h}{\sigma_v}$

(2) If ϵ_h is positive, K approaches the lower limit, K_a, the active case

(3) If ϵ_h is negative, K approaches the upper limit, K_p, the passive case

Figure 5-26 Definition of Earth Pressure Coefficient, K (Ref. 5-20) conditions, the value of K_o depends to a large extent on whether or not the soil is saturated. A stress suddenly applied to an element of a saturated soil is transmitted almost entirely through the water phase because the loading rates are much higher than the rates at which drainage can occur. Therefore, K_o assumes a value of near unity in most saturared soils.

An exception occurs in very stiff cohesive soils, e.g., shale of relatively high dry density and low permeability. In stiff cohesive soils, the soil skeleton may be stiffer than the water phase; hence, a considerable part of the applied dynamic stress may be transmitted through the soil skeleton. Therefore, the K_o value will be less than unity even for complete saturation and may be as low as one-third, a value corresponding to the soil skeleton without water present.

For all materials under static loads and drained conditions, K_o assumes a value corresponding to that of the soil skeleton. Table 5-4 presents suggested dynamic K_o values for several soil categories. Cohesive soils are categorized according to consistency which is defined beneath the table.

K_o values for rock may be determined from the elastic properties of rock cores. Measurement of vertical and circumferential strains on a rock core tested in unconfined compression at the stress levels of interest will furnish the data necessary to compute Poisson's ratio, ν. K_o may then be computed according to Eq. 5-47.

Horizontal stress-time histories for Shot PRISCILLA, conducted in Nevada Test Site Alluvium, are compared with corresponding vertical-time histories in Fig. 5-27. In spite of missing data and significant variations and differences between the available vertical and horizontal waveforms, the horizontal waveforms appear to generally follow the vertical waveforms.

Table 5-4

RATIO OF HORIZONTAL TO VERTICAL SOIL PRESSURES (Ref. 5-20)

	K_o, for Stresses Up to 1000 psi (690 N/cm^2)		
	Dynamic	Static	
Soil Description	Undrained	Undrained	Drained
Cohesionless Soils, Damp or Dry	1/4	1/3-dense 1/2-loose	1/3-dense 1/2-loose
Unsaturated Cohesive Soils of Very Stiff to Hard Consistency*	1/3	1/2	1/2
Unsaturated Cohesive Soils of Medium to Stiff Consistency*	1/2	1/2	1/2
Unsaturated Cohesive Soils of Soft Consistency*	3/4	1/2 to 3/4	1/2 to 3/4
Saturated Soils of Very Soft to Hard Consistency* and Cohesionless Soils	1	1	1/2-stiff 3/4-soft
Saturated Soils of Hard Consistency*	3/4 to 1	1	1/2
Saturated Soils of Very Hard Consistency*	3/4	1	1/2
Rock	Obtain from tests on rock cores and correlate with seismic data		

*Consistency Definitions:

Consistency	Unconfined Compression Strength - q_u - tsf	(N/cm^2)	Standard Penetration Test - N - Blows Per ft.	(m)
Very Soft	< 0.25	(< 2.4)	< 2	(< 0.6)
Soft	0.25-0.50	(2.4-4.8)	2-4	(0.6-1.2)
Medium	0.50-1.00	(4.8-9.6)	4-8	(1.2-2.4)
Stiff	1.00-2.00	(9.6-19.1)	8-15	(2.4-4.6)
Very Stiff	2.00-4.00	(19.1-38.3)	15-30	(4.6-9.1)
Hard	4.00-20.00	(38.3-191)	> 30	(> 9.1)
Very Hard	> 20	(> 191)		

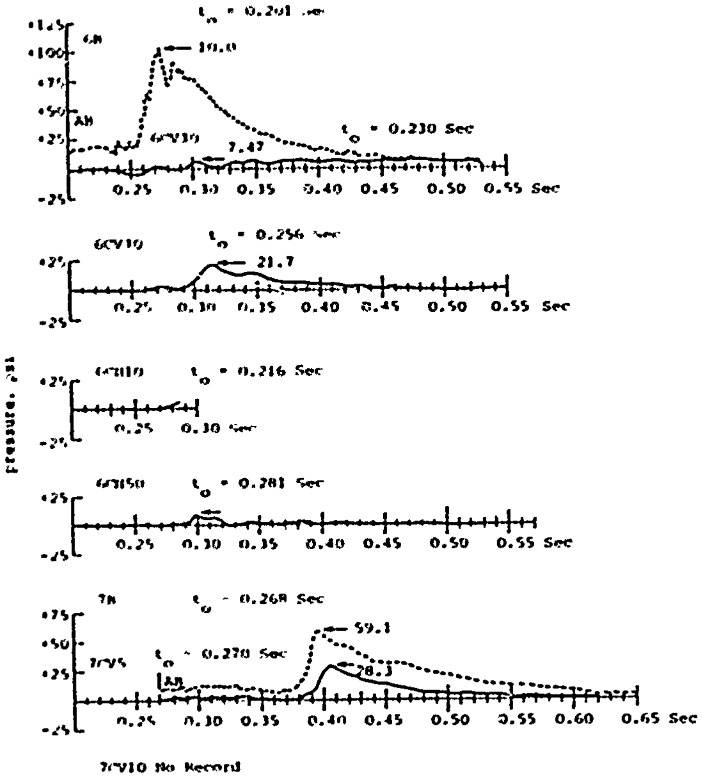

Figure 5-27 Vertical and Horizontal Stress Vs. Time, Station 6 (GR: 1050 ft), Shot PRISCILLA (Ref. 5-39)

The conclusion of similarity between the vertical and horizontal stress waveforms may be related to the relative homogeneity of the test site. However, it is tentatively recommended that the horizontal waveform be taken similar to the predicted vertical waveform regardless of site conditions.

Estimates of horizontal components of acceleration, velocity and displacement must rely upon empirical data and two-dimensional theoretical and code calculation results. At relatively homogeneous sites, the ratios of peak horizontal motion components to peak vertical components appear related to the angle of inclination between the incident wave front and the ground surface.

Two dimensional studies of superseismic airblast induced ground shock in elastic unlayered media (Ref. 5-32) indicate the motions at the wave front occur perpendicular to the wave front. Therefore, the ratio of the horizontal components of motion to the vertical components of motion at the wave front in an elastic medium is equal to the tangent of the angle of inclination of the wave front with respect to the ground surface. (See Fig. 5-28(a)), or

$$\frac{H}{V} = \tan\beta = \tan(\arcsin\frac{C}{U}) \qquad (5\text{-}48)$$

where

H = horizontal motion component at wave front
V = vertical motion component at wave front
β = angle of inclination of wave front
C = dilatational wave velocity
U = airblast shock front velocity

Wave propagation in real geologic materials differs from elastic wave propagation in that lower stress levels propagate at the seismic velocity, C_I, while stress peaks propagate at the velocity associated with the loading modulus, C_L. The wave fronts and inclination angles associated with the two velocities in a homogeneous halfspace are shown in Fig. 5-28(b).

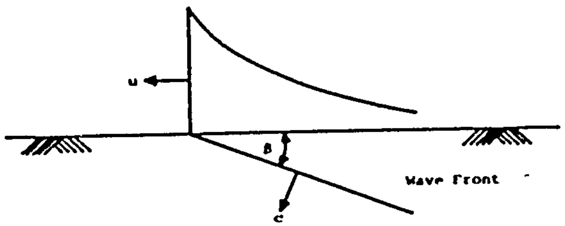

$\beta = \arcsin\left(\frac{C}{U}\right)$

(a) Elastic Case

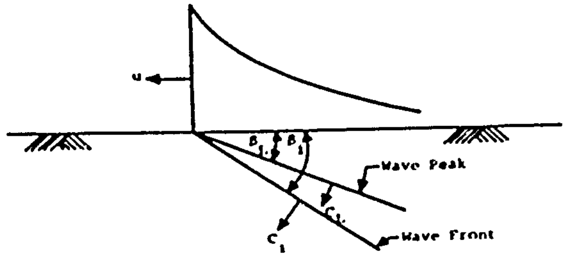

$\beta_L = \arcsin\left(\frac{C_L}{U}\right)$

$\beta_i = \arcsin\left(\frac{C_i}{U}\right)$

(b) Nonlinear Case

Figure 5-28 Wave Fronts Due to Superseismic Airblast

Peak downward vertical accelerations due to the incident wave usually occur with the arrival of the wave front and, therefore, it is recommended that the ratio of peak horizontal acceleration to peak vertical acceleration due to the incident stress wave be estimated by Eq. 5-48 using $C = C_i$.

Peak downward particle velocities due to the incident stress wave occur simultaneously with the peak stress and, therefore, it is recommended that at homogeneous sites the ratio of peak horizontal particle velocity to peak vertical particle velocity due to the incident stress wave be estimated by Eq. 5-48 using $C = C_L$. Assuming similar vertical and horizontal particle velocity waveforms at homogeneous sites leads to the use of the same ratio for peak displacements as used for velocities.

Available data on the ratios of horizontal to vertical motion components tend to scatter. There is a definite trend, however, toward increasing ratios as the airblast shock velocity decays. The recommendations herein are consistent with the increasing ratio trend and lie within the scatter of the data.

Horizontal components of velocity and displacement at layered sites may be significantly higher than at homogeneous sites because of reflections. Although there are no existing data for layered sites subjected to airblast only, the existence of large horizontal components of velocity and displacement is suggested by two-dimensional axisymmetric code studies (Refs. 5-40 and 5-41) which should be at least qualitatively correct.

Reflections tend to enhance the outward and reduce the downward motions of the incident wave. Typical vertical and horizontal particle velocities from calculations for a single-layer site are illustrated in Fig. 5-29. The effect of reflection is evident in both the vertical and horizontal pulses. A major observation is that peak horizontal velocity does not occur at the wave front, as does the peak vertical velocity.

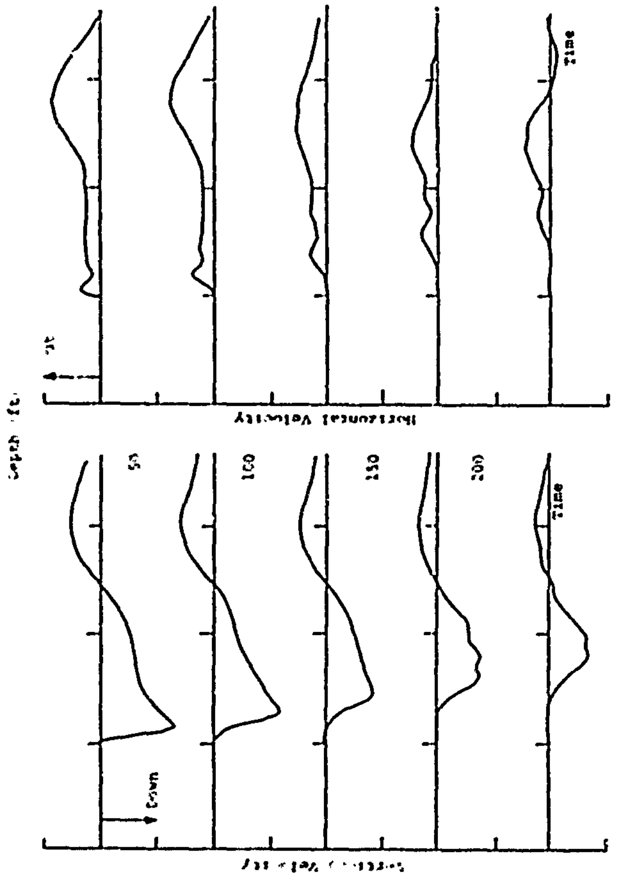

Figure 5-29 Typical Particle Velocities for 300 Foot Layer of Soil Overlying Rock (Ref. 5-41)

In the presence of strong geologic layering, the calculations suggest that peak horizontal velocities may be approximately 2/3 of the peak vertical velocity and that peak horizontal displacements may range from 2/3 to 1 times the peak vertical (Ref. 5-41). The recommended horizontal to vertical ratios for layered sites and homogeneous sites are summarized in Table 5-5.

Aside from two-dimensional code calculations, there is no reliable method available for the prediction of horizontal airblast-induced pulse shapes. In homogeneous media, where peak velocities are expected to occur at the wave front, the horizontal velocity pulse at early times may be assumed similar to the vertical pulse. Late-time history, however, is uncertain. It will be influenced by arrivals from higher overpressure levels as well as by reflections which inevitably exist because of real inhomogeneities and layers at sites which are assumed homogeneous.

In strongly layered media, the peak horizontal velocity does not occur at the incident front but occurs later in time. The calculated time histories given in Fig. 5-29 provide a clue to credible shapes. However, there is no reliable method available to establish the characteristic times needed to fully estimate the time history. However, the arrival of the strong outward movement should be consistent with the travel time from the surface to the layer interface and back to the point of interest. The development of a plausible horizontal velocity waveform is illustrated by a numerical example in Para. 5.7.

5.3.6 Outrunning Ground Shock

Depending upon yield and geology, ground disturbances may arrive at a point of interest prior to the arrival of the airblast. These early disturbances may result from

Table 5-5

RECOMMENDED RATIOS OF PEAK HORIZONTAL TO PEAK VERTICAL GROUND SHOCK COMPONENTS IN THE SUPERSEISMIC REGION

	Homogeneous Sites	Layered Sites	
		Wave Front	Late Time
Stress	K_o	K_o	—
Acceleration	$\tan\left(\arcsin \frac{C_i}{U}\right)^*$	$\tan\left(\arcsin \frac{C_i}{U}\right)$	—
Velocity	$\tan\left(\arcsin \frac{C_L}{U}\right)^*$	$\tan\left(\arcsin \frac{C_L}{U}\right)$	2/3
Displacement	$\tan\left(\arcsin \frac{C_L}{U}\right)^*$	—	1

*If $\tan(\arcsin \frac{C}{U}) > 1$, let peak horizontal component equal the peak vertical component.

air-induced energy propagating ahead of the airblast wave in the surface layer or from energy which has been refracted into a deeper, faster layer. Energy in the latter case may be direct induced or originate in the upstream airblast. Such early disturbances, regardless of energy source, are called outrunning ground motions because they outrun the airblast. The characteristics of motions arriving prior to the airblast are such that their source is not distinguishable.

The range or overpressure at which outrunning first occurs is a function of weapon yield, height of burst, and site geology. For low-yield devices and deep surface layers, outrunning generally begins when the velocity of the airblast wave falls below the dilatational wave velocity in the surface layer. As weapon yield increases and, therefore, high overpressures extend to larger ranges, underlying layers become more important and outrunning may occur at relatively high overpressures. Basically, energy has a longer time in which to travel through a faster underlying layer and still arrive at the surface ahead of the airblast.

Approximate overpressures at which outrunning might be expected to occur at unlayered sites are given in Table 5-6 for various materials. Prediction of the actual overpressure at which outrunning begins is treated in paragraph 5.6 which deals with estimating the combined effect of ground shock from all sources.

The actual motion which occurs at a point in the free-field is the result of some complex superposition of signals arriving from various sources. Typical vertical particle velocities in the outrunning region are shown in Fig. 5-30. The effect of the airblast arriving at the gage stations is evident in the records. The peak accelerations and velocities at airblast passage may be larger or smaller

Table 5-6

APPROXIMATE OVERPRESSURES AT WHICH OUTRUNNING OF GROUND WAVE OCCURS IN UNLAYERED GEOLOGIES (Ref. 5-39)

Formation	Overpressure* (psi)	Overpressure* (N/cm^2)
Alluvium	less than 40	less than 28
Gravel (dry)	10 - 100	7 - 69
Gravel (wet)	40 - 500	28 - 345
Sandy Clay	100 - 500	69 - 345
Sandstone	500 - 2000	345 - 1380
Shale	650 - 2500	450 - 1720
Limestone	1500 up	1030 up
Metamorphic	1000 up	690 up
Granite	3000 up	2070 up

*Outrunning conditions may be anticipated at overpressures less than those tabulated

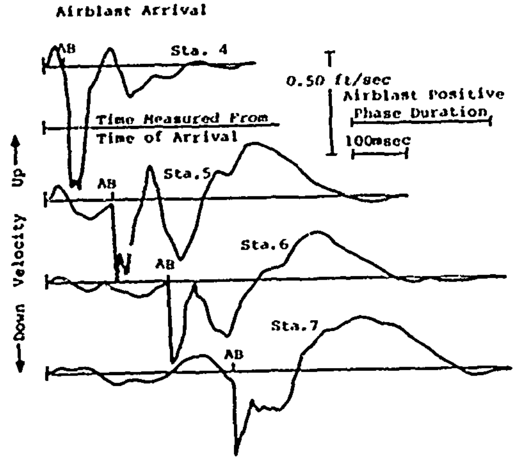

Figure 5-30 Typical Records of Actual Vertical Motions at Several Distances from Ground Zero in Subseismic Region, TUMBLER SHOT 1 (Ref. 5-1)

than those which would result from the airblast alone because of motions already in progress from outrunning sources. Reference 5-1 presents an approach to outrunning velocity and displacement prediction which suggests the superposition of a general outrunning waveform with an airblast-induced waveform predicted assuming superseismic conditions. The average of about a dozen outrunning observations suggests the general outrunning vertical particle velocity waveform (Ref. 5-1) shown in Fig. 5-31. High frequency components of the motion were filtered out in the averaging process and the residual displacement was taken as zero due to conflicting data.

Reference 5-1 suggests a characteristic time, T_2, of the general waveform which appears to be related to the difference between the range of interest and the range at which outrunning first occurs, as given by the relation

$$T_2 = 100 + 0.25\left(\frac{\Delta R}{1\text{ft}}\right)$$

$$T_2 = 100 + 0.82\left(\frac{\Delta R}{1\text{m}}\right) \qquad (5\text{-}49)$$

where

T_2 = characteristic time in milliseconds

ΔR = difference between the ground range of interest and range at which outrunning first occurs

Reference 5-42 presents the following correlations, irrespective of sign, for maximum vertical velocity at the Nevada Test Site and Eniwetok Proving Grounds under fully-developed, outrunning ground motion conditions.

NTS:

$$v_m = 2 \times 10^8\text{ft/sec}\left[\frac{W}{1\text{MT}}\right]^{2/3}\left[\frac{1\text{ft}}{R}\right]^2$$

$$v_m = 2.2 \times 10^6\text{m/sec}\left[\frac{W}{10^{15}\text{J}}\right]^{2/3}\left[\frac{1\text{m}}{R}\right]^2 \qquad (5\text{-}50)$$

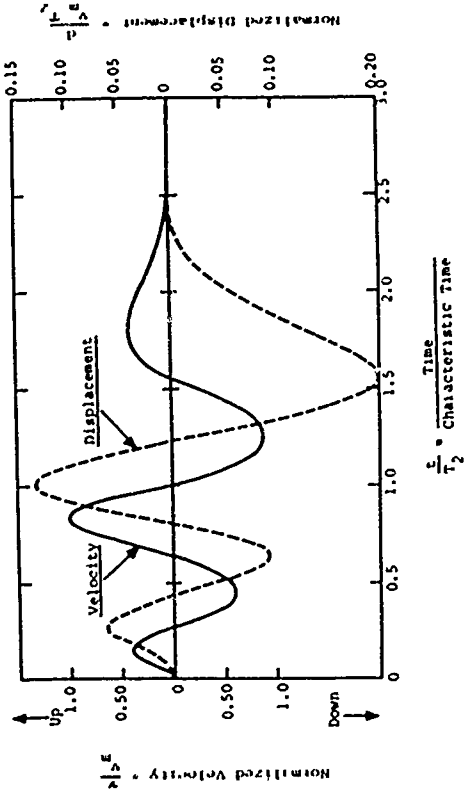

Figure 5-31 Outrunning Ground Motion Vertical Particle Velocity Waveform and Its Displacement (Ref. 5-1)

EPG:

$$v_m = 5 \times 10^7 \text{ft/sec}\left[\frac{W}{1\text{MT}}\right]^{2/3}\left[\frac{1\text{ft}}{R}\right]^2$$

$$v_m = 5.5 \times 10^5 \text{m/sec}\left[\frac{W}{10^{15}\text{J}}\right]^{2/3}\left[\frac{1\text{m}}{R}\right]^2 \quad (5\text{-}51)$$

where

v_m = peak vertical particle velocity

W = nominal yield

R = range

Reference 5-1 notes that the 4:1 ratio of coefficients is roughly consistent with the 5:1 ratio of near-surface seismic velocities between EPG and NTS.

Assuming that particle velocity is inversely proportional to the product of mass density and seismic velocity, taking insitu unit weights of 120 pcf (1.9×10^3 kg/m^3) for both EPG and NTS, and near-surface seismic velocities of 5500 fps (168 m/sec) and 1200 fps (36.6 m/sec) for EPG and NTS, respectively, results in the following average relation for the peak vertical particle velocity, v_m, of the general outrunning waveform

$$v_m = 3.1 \times 10^8 \text{ft/sec}\left[\frac{W}{1\text{MT}}\right]^{2/3}\left[\frac{1\text{ft}}{R}\right]^2\left[\frac{100\text{pcf}}{\gamma}\right]\left[\frac{1000\text{fps}}{C}\right]$$

$$v_m = 1.6 \times 10^6 \text{m/sec}\left[\frac{W}{10^{15}\text{J}}\right]^{2/3}\left[\frac{1\text{m}}{R}\right]^2\left[\frac{10^3\text{kg/m}^3}{\rho}\right]\left[\frac{1000\text{m/s}}{C}\right] \quad (5\text{-}52)$$

where

ρ = mass density

C = seismic velocity

Peak outrunning horizontal particle velocities are in the range of 1/2 to 1/4 the maximum vertical (Ref. 5-1). For lack of conclusive data, it is recommended that the general horizontal outrunning waveform be taken similar to the vertical waveform.

The complete airblast-induced ground motion at the point of interest may be estimated by superposing the general outrunning waveform of Fig. 5-31 with a waveform predicted on the basis of superseismic assumptions. Superposition must be in accord with the relative phasing of the two effects which may be calculated using the procedures of paragraph 5.6. Simple superposition results in reasonable approximations to certain outrunning ground motion data as illustrated in Fig. 5-32. An example illustrating the suggested method is presented in paragraph 5.7.

The variation of outrunning effects with depth is uncertain. Since outrunning motions in many cases originate in a layer at depth, it is possible that outrunning may be stronger at depth than near the surface. In the absence of sufficient data, it is tentatively recommended that the outrunning waveform (Fig. 5-32) be taken constant with depth. The effects of the airblast passing the point of interest may be allowed to attenuate as predicted by the methods of paragraph 5.3.3.

5.4 DIRECT-INDUCED GROUND SHOCK

5.4.1 Introduction

Direct-induced ground shock is defined in this manual as the ground shock which results from the initial stress wave due to the direct coupling of energy into the ground at the point of detonation. For fully-contained bursts, it is the only form of ground shock which exists. For high altitude air bursts, it is nonexistent. For bursts at or near the surface of the ground, direct-induced ground shock is the dominant form of ground shock beneath the burst point beyond the crater region.

Theoretical computer codes for treating direct-induced ground shock are not yet developed to a stage where high confidence quantitative predictions can be obtained. Available prediction methods are largely semi-empirical in nature. The bulk of empirical data is from fully contained nuclear bursts, several of which are listed in Table 5-7. Data from most tests conducted prior to 1964 are consolidated in a single volume in Ref. 5-1.

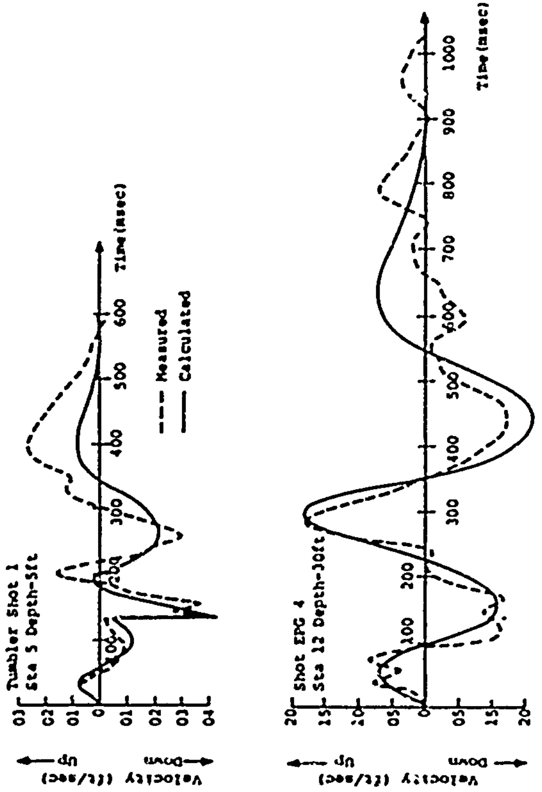

Figure 5-32 Comparison of Calculated and Observed Outrunning Ground Motion (Ref. 5-1)

Table 5-7

SOME CONTAINED NUCLEAR TESTS PROVIDING DIRECT INDUCED GROUND SHOCK DATA

Medium	Shot Name	Yield	
Alluvium*	FISHER	13.3kT	(5.65 x 10^{13}j)
	HAYMAKER	48kT	(2.01 x 10^{14}j)
	HOGNOSE	**	
	RINGTAIL	4.9kT	(2.05 x 10^{13}j)
Tuff (Seismic Velocity - 7000 fps)	RAINIER	1.7kT	(7.11 x 10^{12}j)
	EVANS	55 tons	(2.30 x 10^{11}j)
	TAMALPAIS	72kT	(3.01 x 10^{14}j)
	MADISON	**	
Granite (Seismic Velocity - 18 to 19000 fps)	HARDHAT	5.9kT	(2.47 x 10^{13}j)
	SHOAL	12kT	(5.02 x 10^{13}j)
	PILEDRIVER	61kT	(2.55 x 10^{14}j)
Dolomite (Seismic Velocity - 14,100 fps)	HANDCAR	10kT	(4.18 x 10^{13}j)
Andesite (Seismic Velocity - 14,100 fps)	LONGSHOT	81kT	(3.39 x 10^{14}j)
	MILROW	1MT	(4.18 x 10^{15}j)
	CANNIKIN	5MT	(2.09 x 10^{16}j)
Salt (Seismic Velocity - 13,400 fps)	GNOME	3kT	(1.26 x 10^{13}j)

*Seismic velocity varies with depth ranging from 3000 fps (914 m/sec) from 175 feet (53 m) to 650 feet (198 m) to 10,000 fps (3050 m/sec) below 650 feet (198 m).

**Classified Yield

The extrapolation of contained nuclear results to the near-surface burst configuration requires information or assumptions regarding initial energy coupling, scaling relations, material property dependence and free surface effects. Initial energy coupling considerations are described in some detail in paragraph 5.4.2. Scaling, material dependence and free surface effects are introduced in the following.

Scaling and material property dependence relations are required regardless of whether the burst is contained or near-surface. Yield scaling relations of the form given below have been reasonably successful in correlating peak motion data from contained nuclear bursts in a common material.

$$aW^{1/3} = f_1 \ (R/W^{1/3}) \qquad (5\text{-}53)$$

$$v = f_2 \ (R/W^{1/3}) \qquad (5\text{-}54)$$

$$d/W^{1/3} = f_3 \ (R/W^{1/3}) \qquad (5\text{-}55)$$

where

a = peak acceleration
v = peak particle velocity
d = peak displacement
R = range
W = yield

The introduction of simple material properties into contained scaling relationships does not provide correlation over the range of materials for which data is available. Dimensional analysis, incorporating seismic velocity and mass density (Ref. 5-3), collapses hard rock data (granite, andesite and salt) but does not account for data in tuff. The direct introduction of seismic velocity into scaling relationships based upon elastic plane wave propagation theory (Ref. 5-20) correlates granite, andesite, and tuff data but does not account for salt data. Both methods fail to explain alluvium data. The use of a single material parameter, such as seismic velocity, simply cannot account for the wide range of behavior of different geologic materials.

In spite of difficulties in developing satisfactory correlations applicable to all materials, the existing data base is sufficiently large to allow division of the data into three categories: hard rock (granite, andesite and salt), soft rock (tuff) and dry soil (alluvium). Reference 5-46 has made such a division for hard and porous rock.

A major consideration in relating contained bursts to surface bursts is the effect of the free surface. For a surface burst, the free surface perturbs the motion field to the extent that the assumption that peak direct-induced motions are constant along a spherical contour becomes progressively worse as the location of the free-field point of interest approaches the ground surface. Although the direct-induced shock front is approximately spherical, the combination of free surface and material strength effects lead to lower peak stresses and velocities near the free surface than at an equal radial distance on the axis beneath the burst point (Ref. 5-44).

Reference 5-45, based on experiments in soil, suggests that the field beneath a surface burst may be thought of as consisting of three regions as depicted in Fig. 5-33. Region I consists of a spherical field within a conical surface with an apex angle of about 30 degrees. In region II, between 30 degrees and 65 degrees, the motion is directed spherically but the attenuation rate is higher than in region I. Above 65 degrees, the direct-induced motion is dominated by the attenuation effects of the free surface and occurs in complex combination with airblast-induced effects.

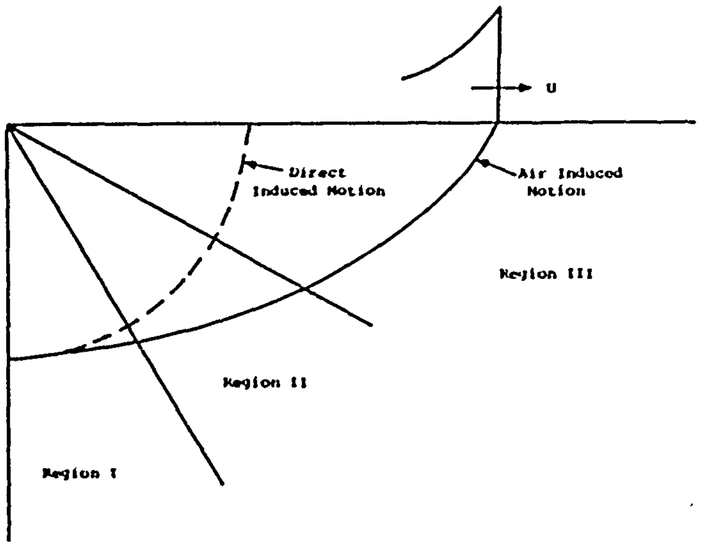

Figure 5-33 Phenomenological Regions for the Surface Burst Geometry (Ref. 5-45)

5.4.2 Initial Energy Coupling

Energy coupling differences between high explosive and nuclear sources were introduced in Section IV in connection with cratering efficiency. Basically, the fact that nuclear explosives partition energy between radiation and moving bomb debris causes a significant reduction in energy coupling as the burst point moves from shallow burial to surface contact (weapon C.G. slightly above the surface). The reduction is caused by the absorption of large amounts of radiation by the air in the contact burst configuration. The absorbed radiation is reemitted over a relatively long period of time and does not contribute to initial energy coupling (Ref. 5-44).

The major factor in energy coupling for the near-surface (contact) burst configuration is the partition between the energy contained in radiation penetrating the weapon case and the kinetic energy in the moving bomb debris. Energy density or ratio of yield to charge mass is often used to account for differences in the coupling of different sources near the ground surface. Since energy density reflects in a general way the amount of mass available to contain radiation and subsequently couple as moving debris, energy density is a qualitative indicator of the amount of energy which will couple in a near-surface burst. However, current understanding is not sufficient to allow high confidence quantitative estimates of near-surface burst coupling. As a result, extrapolation from contained nuclear bursts to near-surface bursts is accomplished using empirically inferred relationships.

An equivalent yield, W_e, is defined as the yield of a contained nuclear explosion that would provide the same peak ground shock quantity as that observed at an equal range beneath ground zero from a nuclear near-surface burst of yield W. The equivalent yield concept is illustrated in Fig. 5-34 for peak stress and particle velocity. The equivalent yield for peak stress and velocity generally is greater than the equivalent yield for peak displacement due to the fact that free surface rarefactions tend to reduce displacements immediately but require some

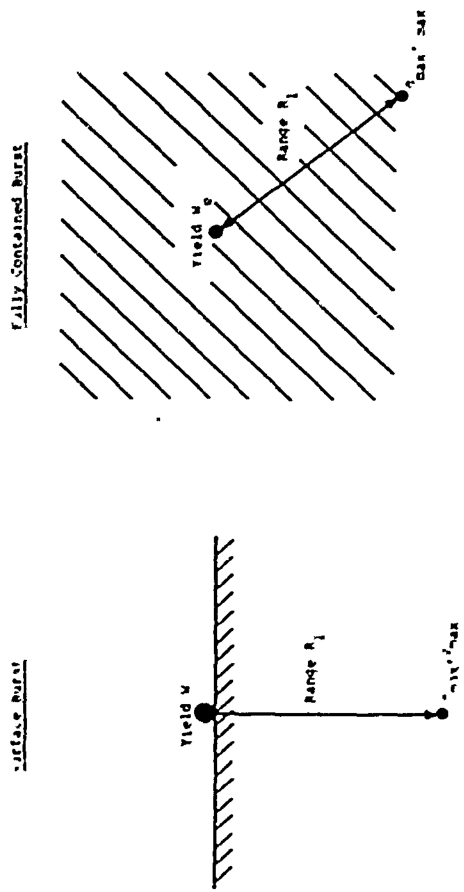

Note: Weapon Sizes Depicted are to Illustrate Differences in Yield Not Necessarily Differences in Physical Size.

Figure 5-34 Equivalent Yield Concept for Peak Stress and Particle Velocity

time before they influence peak stresses and velocities which occur at the wave front (Ref. 5-46). In addition, the equivalent yield for displacement appears to be material dependent, i.e., a function of how fast the rarefaction moves through the material.

Reference 5-46 compares the ground shock data from a low yield half buried nuclear event in granite and a low yield surface tangent nuclear event in tuff, both detonated on the planar surface of hemispherical cavities, with contained data from similar geologies. Considering the differences in energy density between the cavity shot devices and modern weapons, Ref. 5-46 recommends the equivalent yield coupling factors (W_e/W) given in Table 5-8 and 5-9 for hard rock and tuff. Since peak accelerations occur at the wavefront, it is expected that equivalent yield coupling factors for peak stress and particle velocity are equally applicable to peak acceleration.

5.4.3 Contained Nuclear Bursts

Figure 5-35 presents peak particle velocities from contained nuclear bursts in various hard rock geologies. In spite of differences in material types and seismic velocities, all of the data are confined within the bounds of the granite data to a scaled range of about 1000 ft/kT$^{1/3}$ (1.89 x 10^{-2} m/j$^{1/3}$), beyond which the salt data is slightly higher than the upper granite bound. Figures 5-36 and 5-37 present peak displacements and accelerations, respectively, in hard rock geologies. As with particle velocities, the bounds of the granite displacement and acceleration data encompass most other hard rock data over a considerable range. French contained data in Sahara Hogger granite also fall within the bounds of U.S. granite data (Ref. 5-46).

The comparisons of Figs. 5-35, 36 and 37 indicate that the effect of material differences between common hard rocks is within the scatter for a single rock type. The fact that salt data is not within the scatter bounds at all ranges is not disturbing since salt is not a common geologic material and is somewhat unique in that joints and faults in salt tend to heal themselves.

Table 5-8

EQUIVALENT YIELD COUPLING FACTORS FOR SURFACE BURSTS ON HARD ROCK (Ref. 5-46)

Burst Configuration	Stress and Particle Velocity	Displacement
Shallow Buried	0.16	0.04
Contact	0.04	0.01

Table 5-9

EQUIVALENT YIELD COUPLING FACTORS FOR SURFACE BURSTS ON TUFF (Ref. 5-46)

Burst Configuration	Stress and Particle Velocity	Displacement
Shallow Buried	0.16	0.01
Contact	0.04	0.0025

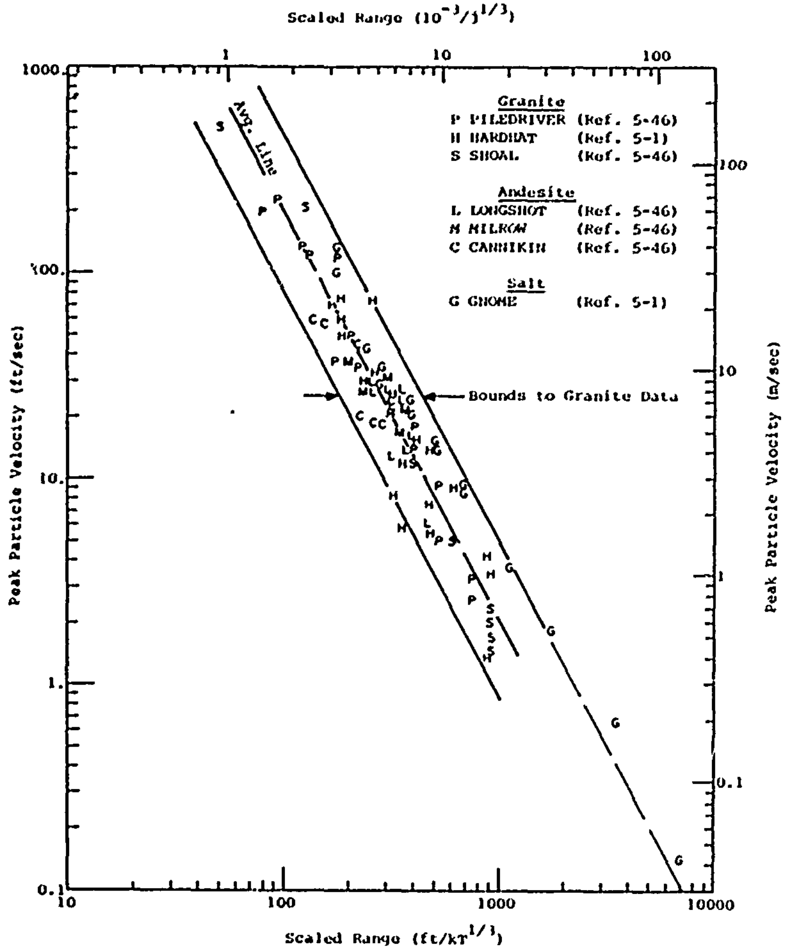

Figure 5-35 Peak Particle Velocities in Hard Rock

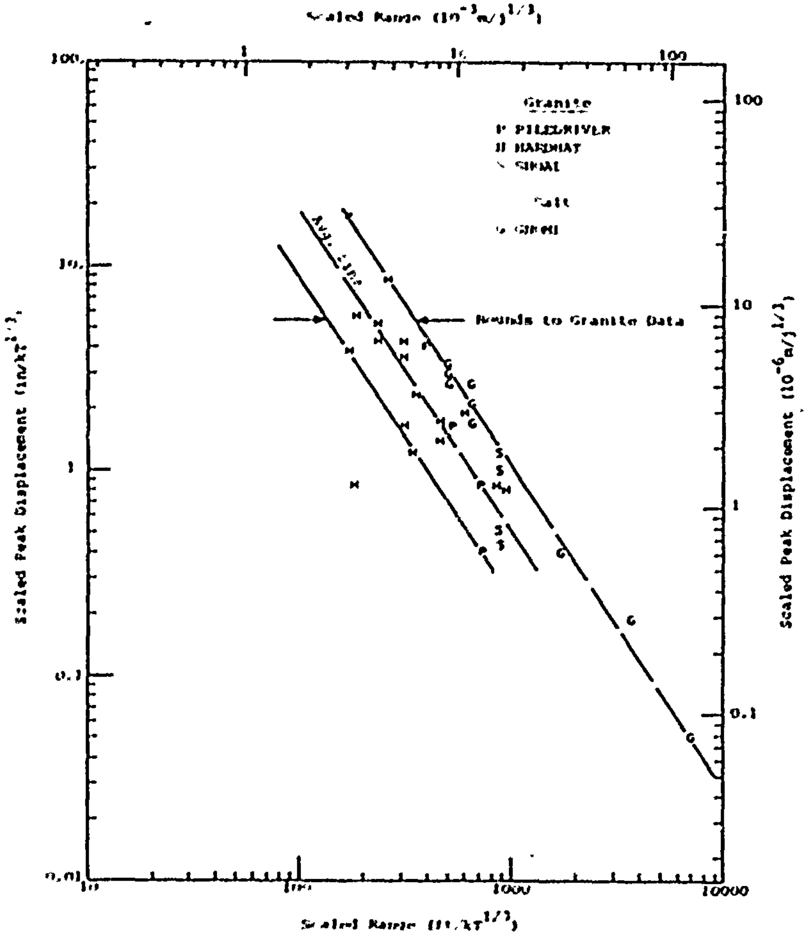

Figure 5-36 Scaled Displacements in Hard Rock

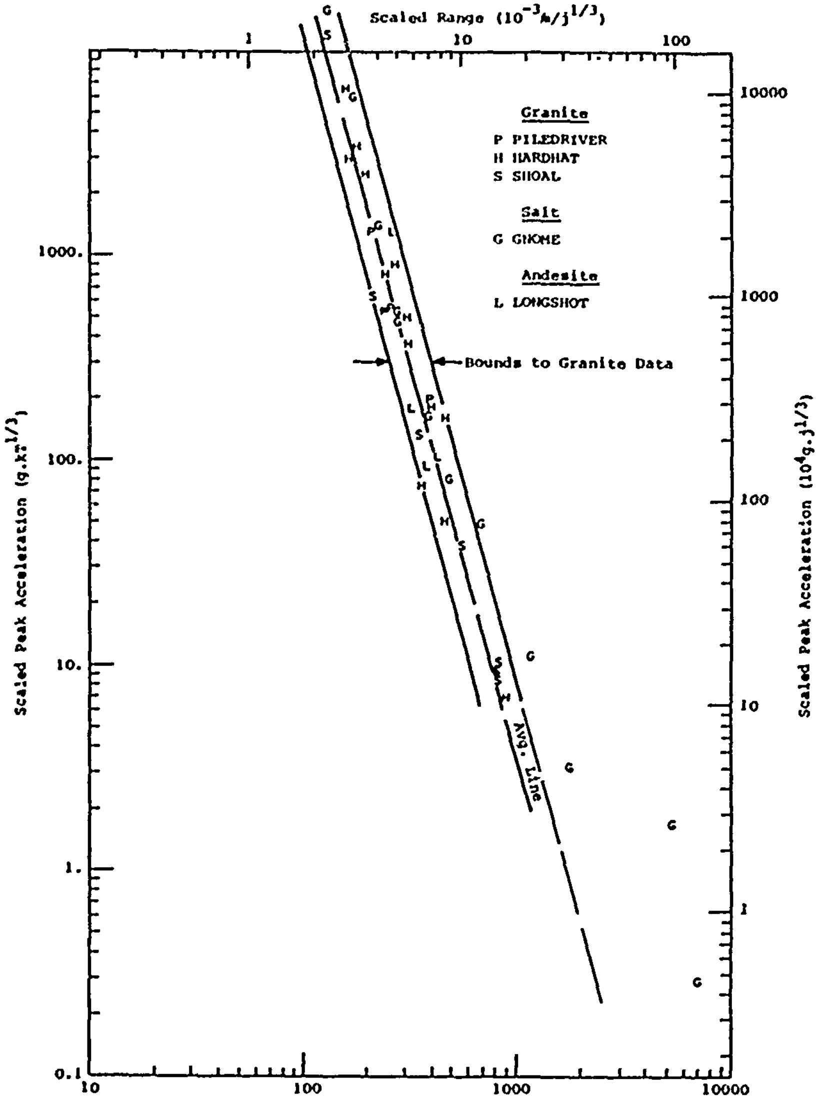

Figure 5-37 Scaled Accelerations in Hard Rock

Average hard rock data suggest that it is reasonable to establish a single category of material called "hard rock" which encompasses granite, andesite and other relatively competent although jointed rocks such as basalt, gneiss, quartzite and dolomite. Seismic velocities of "hard rock" will generally be 12000 ft/sec and greater.

The peak ground motions at intermediate ranges due to contained bursts in hard rock may be estimated by the following relations which define the approximate bounds of the granite data.

$$v = 200\ \text{ft/sec}\left|\frac{W}{1KT}\right|^{2/3}\left|\frac{R}{1kft}\right|^{-2} \qquad \pm \text{ a factor of } 2.5$$

$$v = 2.2\ \text{m/sec}\left|\frac{W}{10^{15}J}\right|^{2/3}\left|\frac{R}{1km}\right|^{-2} \qquad (5\text{-}56)$$

$$d = 200\ \text{in}\left|\frac{W}{1KT}\right|^{5/6}\left|\frac{R}{1kft}\right|^{-3/2} \qquad \pm \text{ a factor of } 2$$

$$d = 0.26\ \text{m}\left|\frac{W}{10^{15}J}\right|^{5/6}\left|\frac{R}{1km}\right|^{-3/2} \qquad (5\text{-}57)$$

$$a = 3500\ g\left|\frac{W}{1KT}\right|\left|\frac{R}{1kft}\right|^{-4} \qquad \pm \text{ a factor of } 2.5$$

$$a = 7.2\ g\left|\frac{W}{10^{15}J}\right|\left|\frac{R}{1km}\right|^{-4} \qquad (5\text{-}58)$$

where

d = peak displacement
v = peak particle velocity
a = peak acceleration
W = yield
R = range

Figures 5-38, 5-39 and 5-40 present velocity, displacement and acceleration data measured in tuff. Tuff is a porous, soft rock compared to granite, andesite and salt. There are insufficient data to positively conclude that other porous and/or soft rocks will behave within the bounds of the tuff data.

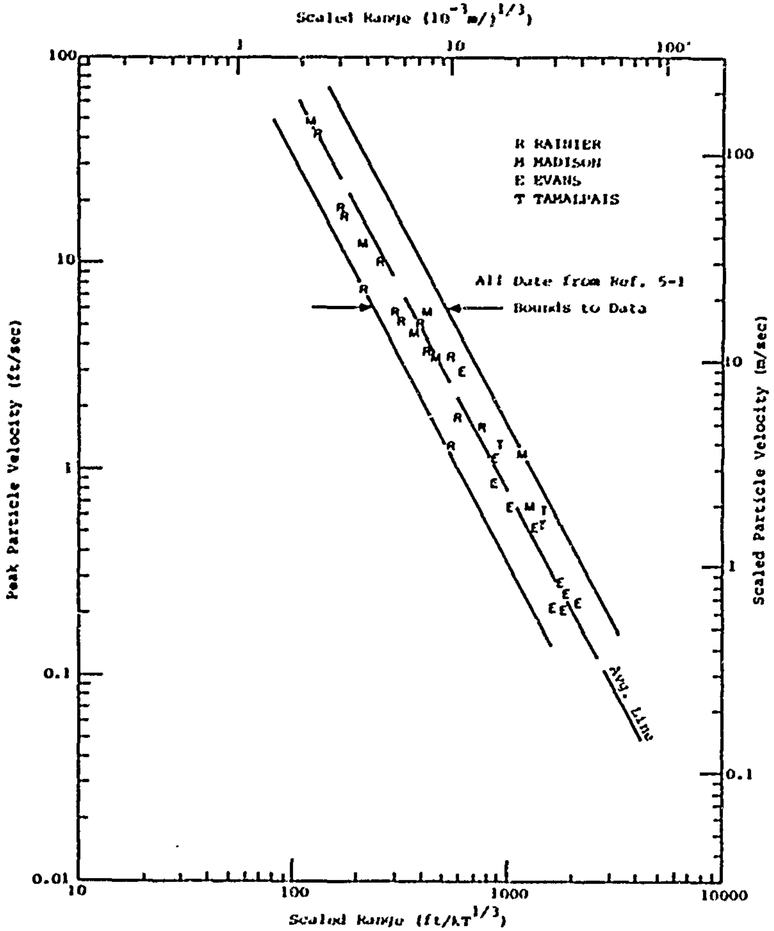

Figure 5-38 Peak Particle Velocities in Tuff

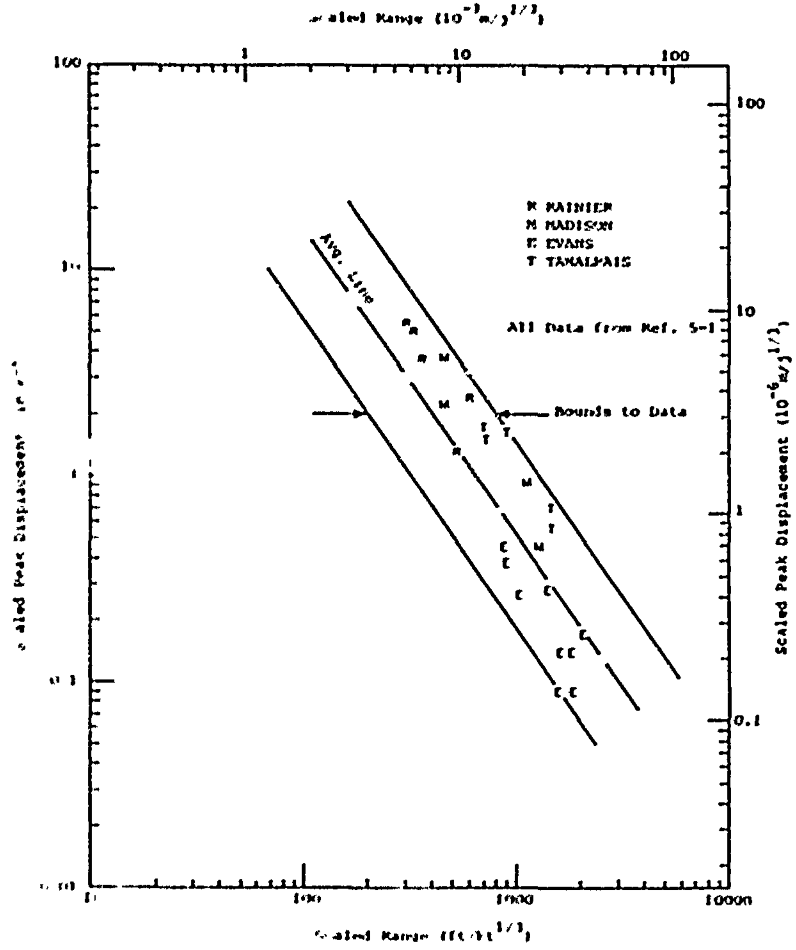

Figure 5-39 Scaled Peak Displacements in Tuff

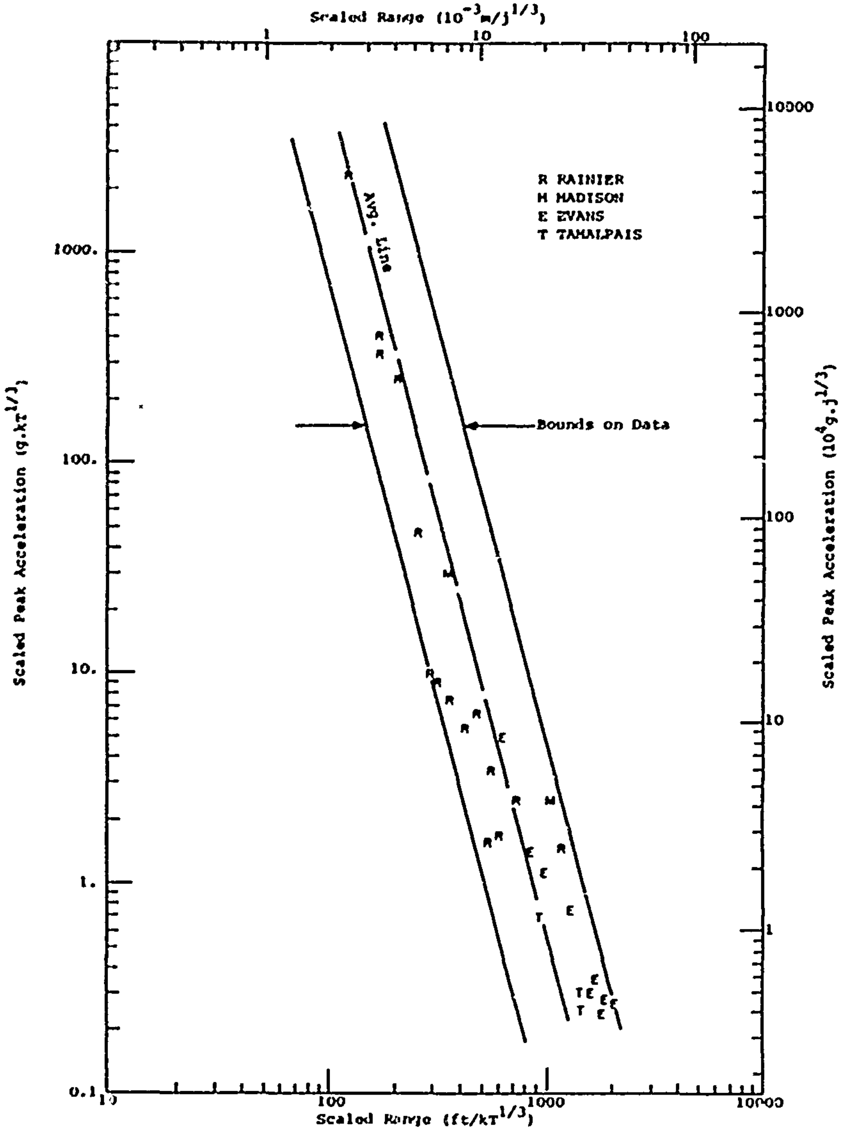

Figure 5-40 Scaled Peak Accelerations in Tuff

However, porous and/or soft rocks are believed more like tuff than hard rock. Therefore, it is recommended that tuff behavior be used as an approximation to the behavior of such soft rocks as shales, sandstones, some limestones and heavily weathered rocks of all types. Seismic velocities of soft rocks generally lie in range 6000 to 10,000 ft/sec.

The peak ground motions at intermediate ranges due to contained bursts in soft rock may be estimated by the following relations which define the approximate bounds of the tuff data.

$$v = 80\ \text{ft/sec}\left|\frac{W}{1\text{MT}}\right|^{2/3}\left|\frac{R}{1\text{kft}}\right|^{-2} \qquad \pm \text{ a factor of } 2$$

$$v = 0.87\ \text{m/sec}\left|\frac{W}{10^{15}\text{J}}\right|^{2/3}\left|\frac{R}{1\text{km}}\right|^{-2} \qquad (5\text{-}59)$$

$$d = 160\ \text{in}\left|\frac{W}{1\text{MT}}\right|^{5/6}\left|\frac{R}{1\text{kft}}\right|^{-3/2} \qquad \pm \text{ a factor of } 3$$

$$d = 0.21\ \text{m}\left|\frac{W}{10^{15}\text{J}}\right|^{5/6}\left|\frac{R}{1\text{km}}\right|^{-3/2} \qquad (5\text{-}60)$$

$$a = 600\ g\left|\frac{W}{1\text{MT}}\right|\left|\frac{R}{1\text{kft}}\right|^{-4} \qquad \pm \text{ a factor of } 5$$

$$a = 1.24\ g\left|\frac{W}{10^{15}\text{J}}\right|\left|\frac{R}{1\text{km}}\right|^{-4} \qquad (5\text{-}61)$$

Figures 5-41, 42 and 43 present peak particle velocity, displacement and acceleration data measured in alluvium. The relatively small data base for alluvium as compared to hard rock and tuff has been extended somewhat by including velocity and acceleration data measured at the ground surface above seventeen underground explosions which were not heavily instrumented for ground shock. One-half the ground surface peak acceleration and velocity data are plotted based upon the assumption of elastic reflection phenomena at the ground surface leading to velocities and accelerations twice those of the incident wave (Ref. 5-1). It is believed that alluvium response is

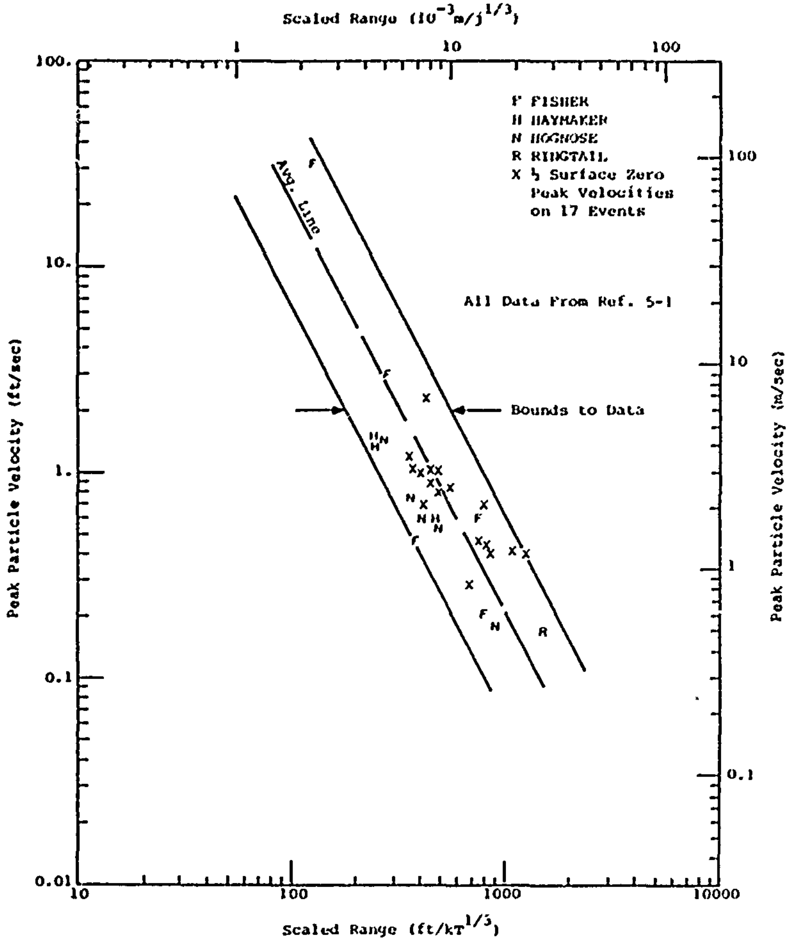

Figure 5-41 Peak Particle Velocities in Alluvium

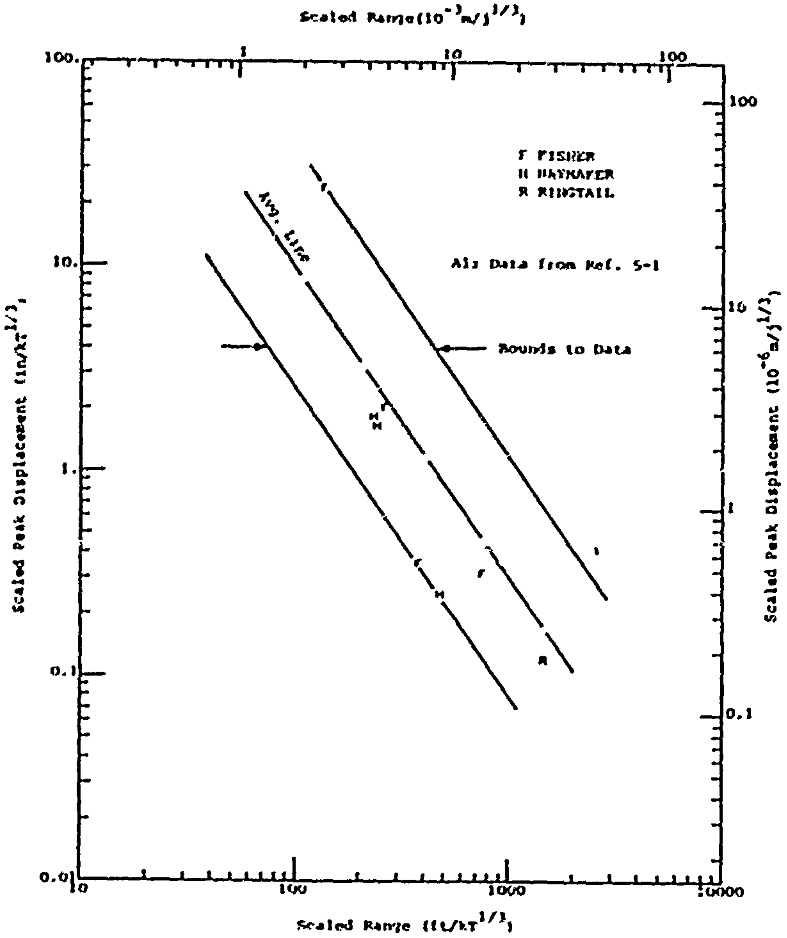

Figure 5-42 Scaled Peak Displacements in Alluvium

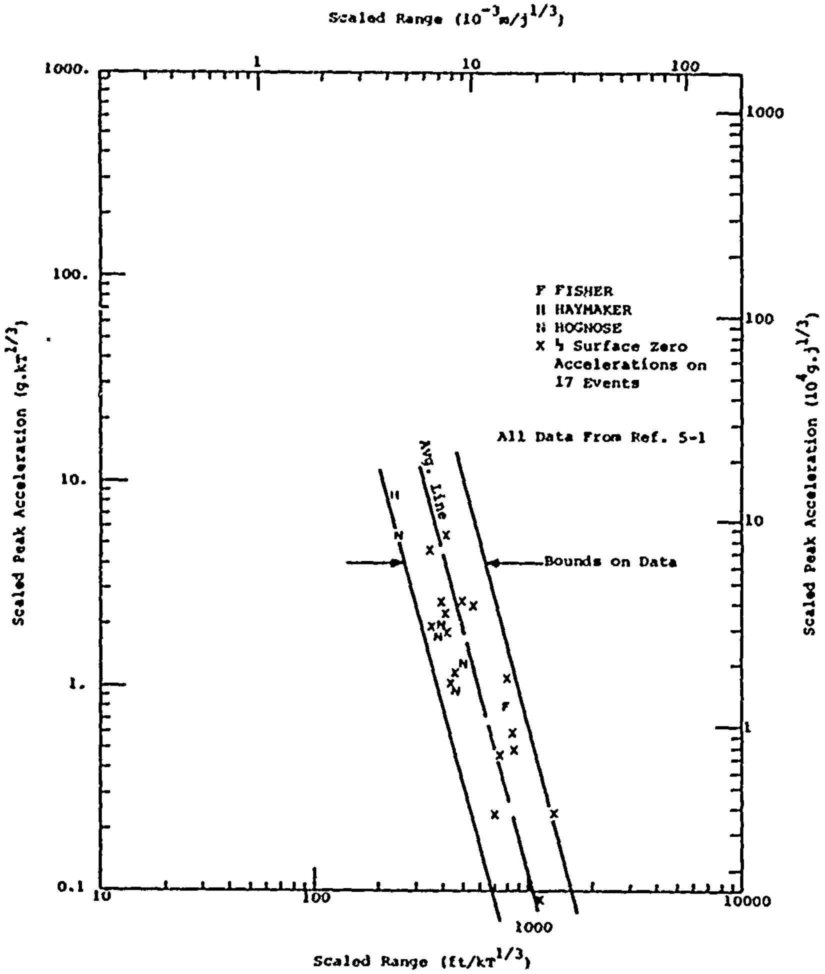

Figure 5-43 Scaled Peak Accelerations in Alluvium

representative of the response of a wide range of dry soils and, therefore, the bounds of the alluvium data, given below, are recommended for estimates of peak motion quantities at intermediate ranges due to contained bursts in dry soils.

$$v = 20\ \text{ft/sec}\left[\frac{W}{1\text{MT}}\right]^{3/2}\left[\frac{R}{1\text{kft}}\right]^{-2}$$

$$v = 0.22\ \text{m/sec}\left[\frac{W}{10^{15}\text{J}}\right]^{2/3}\left[\frac{R}{1\text{km}}\right]^{-2} \quad \pm \text{ a factor of 3} \qquad (5\text{-}62)$$

$$d = 100\ \text{in}\left[\frac{W}{1\text{MT}}\right]^{5/6}\left[\frac{R}{1\text{kft}}\right]^{-3/2}$$

$$d = 0.13\ \text{m}\left[\frac{W}{10^{15}\text{J}}\right]^{5/6}\left[\frac{R}{1\text{km}}\right]^{-3/2} \quad \pm \text{ a factor of 4} \qquad (5\text{-}63)$$

$$a = 120\ g\left[\frac{W}{1\text{MT}}\right]\left[\frac{R}{1\text{kft}}\right]^{-4}$$

$$a = 0.25\ g\left[\frac{W}{10^{15}\text{J}}\right]\left[\frac{R}{1\text{km}}\right]^{-4} \quad \pm \text{ a factor of 5} \qquad (5\text{-}64)$$

The peak motion bounds recommended for hard rock, soft rock and dry soil are compared in Figs. 5-44, 5-45 and 5-46. Particle velocities (Fig. 5-44) at a given range are, on the average, highest for hard rock, intermediate for soft rock and lowest for dry soil. The particle velocity trend is in agreement with the concept that the more hysteretic a material the greater the close-in peak stress and velocity attenuation. A similar trend exists in the acceleration data (Fig. 5-46) and is also in agreement with existing knowledge of material behavior. Increases in rise time and attenuations of peak particle velocity and, therefore, attenuation of acceleration are directly related to material nonlinearity and hysteresis.

Peak displacements (Fig. 5-45) are not readily interpretable. Peak displacements in tuff are, on the average, higher than in hard rock while displacements in dry soil are less than in hard rock. In a homogeneous elastic medium, peak displacement is directly proportional to impulse and inversely

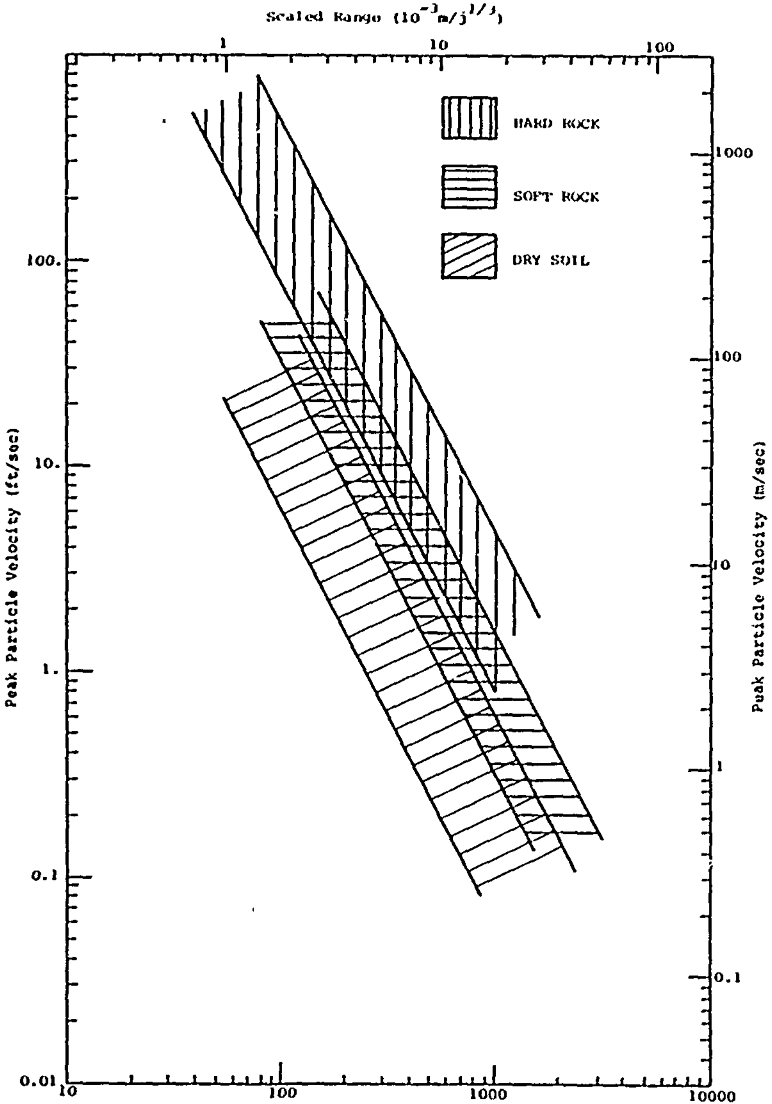

Figure 5-44 Peak Particle Velocity Bounds for Hard Rock, Soft Rock and Dry Soil

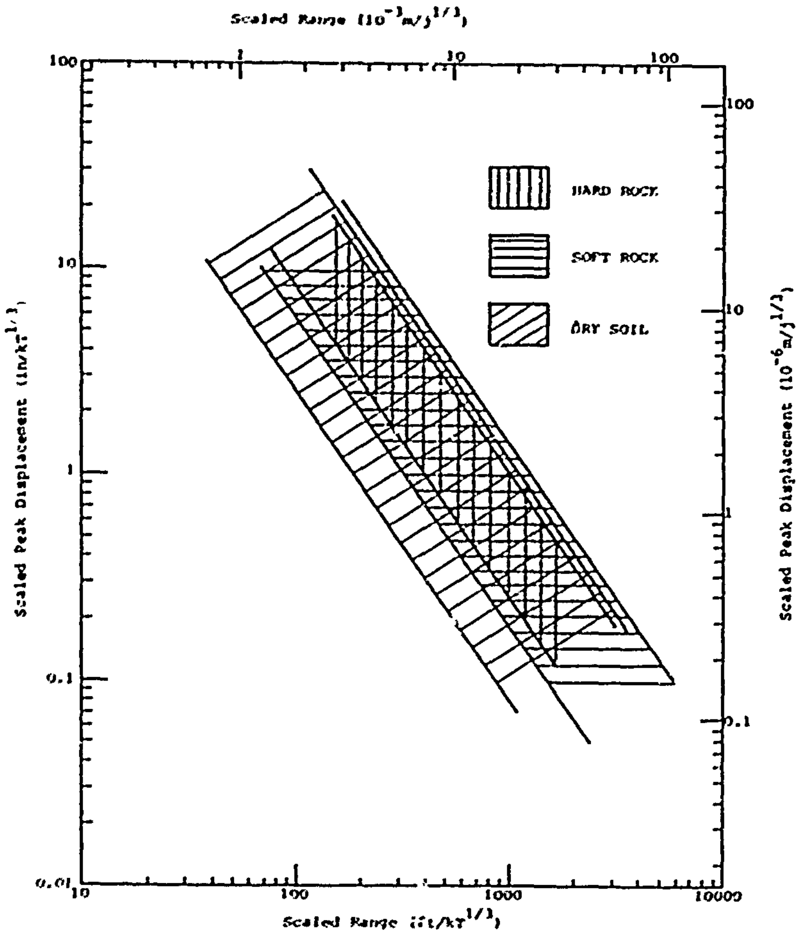

Figure 5-45 Scaled Peak Displacement Bounds for Hard Rock, Soft Rock, and Dry Soil

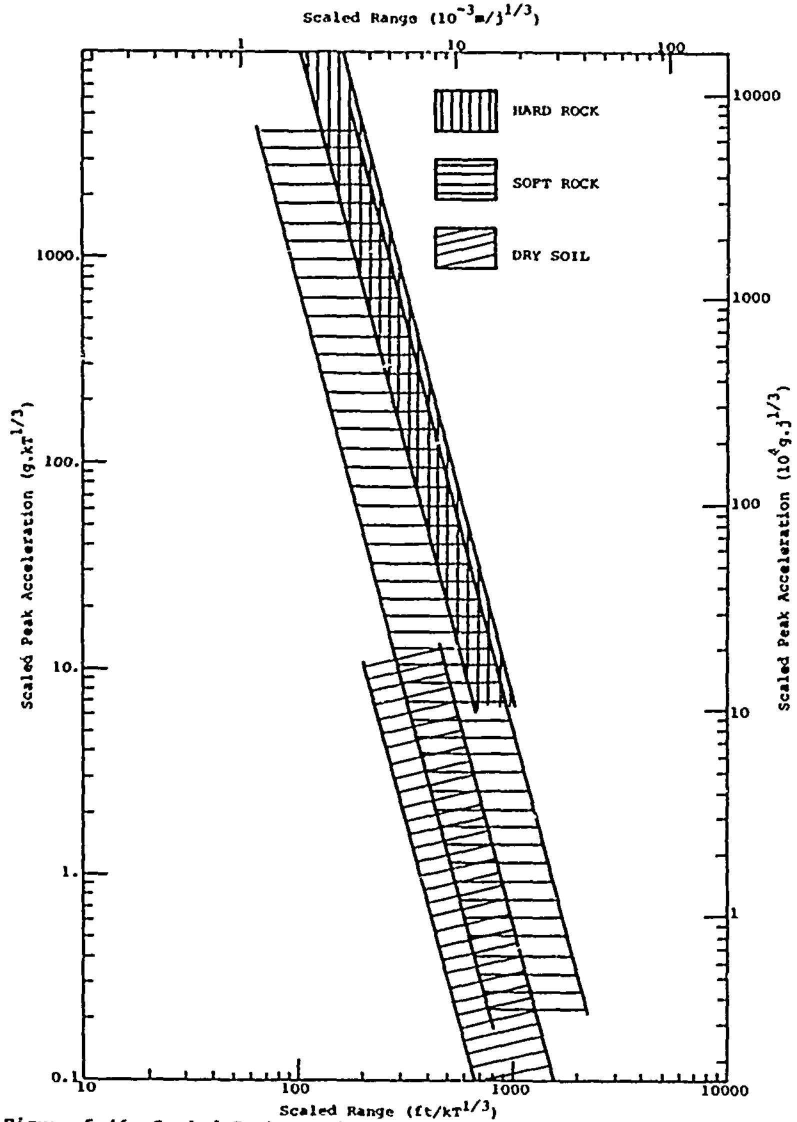

Figure 5-46 Scaled Peak Acceleration Bounds for Hard Rock, Soft Rock and Dry Soil

proportional to characteristic impedance (See Eq. 5-40). Assuming the impulse delivered at a given range is the same in both hard rock and soft rock, displacement will be greater in soft rock because soft rock has a lower characteristic impedance, in agreement with hard rock and tuff data. The impulse argument does not explain the alluvium data, however. Since peak displacement is a late time phenomenon, displacement is easily affected by free surface effects (which ultimately occur in all contained events) and reflections. Free surface and/or reflection effects may be playing a stronger role in alluvium events than in events in rock. In any case, it is believed that the observed displacement differences between the materials are real and should be expected in future events in similar geologies.

5.4.4 Near-Surface Nuclear Bursts

The empirical relations of paragraph 5.4.3 for contained nuclear events in hard rock, soft rock and dry soil may be combined with the equivalent yield concept to provide estimates of direct induced motions due to near-surface bursts.

The contact burst equivalent yield factors given in Table 5-8 for hard rock may be applied to Eqs. 5-56, 5-57 and 5-58 directly to yield the following estimates of peak ground motions on the axis directly beneath near-surface bursts on hard rock:

$$v = 25 \text{ ft/sec}\left[\frac{W}{1MT}\right]^{2/3}\left[\frac{R}{1kft}\right]^{-2}$$

$$v = 0.27 \text{ m/sec}\left[\frac{W}{10^{15}j}\right]^{2/3}\left[\frac{R}{1km}\right]^{-2} \qquad \pm \text{ a factor of } 2.5 \quad (5\text{-}65)$$

$$d = 4.5 \text{ in}\left[\frac{W}{1MT}\right]^{5/6}\left[\frac{R}{1kft}\right]^{-3/2}$$

$$d = 5.8 \times 10^{-3} \text{m}\left[\frac{W}{10^{15}j}\right]^{5/6}\left[\frac{R}{1km}\right]^{-3/2} \qquad \pm \text{ a factor of } 2 \quad (5\text{-}66)$$

$$a = 140 \text{ g}\left[\frac{W}{1MT}\right]\left[\frac{R}{1kft}\right]^{-4}$$

$$a = 0.29 \text{ g}\left[\frac{W}{10^{15}j}\right]\left[\frac{R}{1km}\right]^{-4} \qquad \pm \text{ a factor of } 2.5 \quad (5\text{-}67)$$

It is assumed that the contact burst equivalent yield factors given in Table 5-9 for tuff are reasonable approximations to contact burst equivalent yield factors for soft rock and dry soil as well. Applying the tuff factors to Eqs. 5-59, 5-60 and 5-61 results in the following estimates of peak ground motions on the axis directly beneath near-surface bursts on soft rock.

$$v = 10 \text{ ft/sec}\left[\frac{W}{1MT}\right]^{2/3}\left[\frac{R}{1kft}\right]^{-2}$$

$$v = 0.11 \text{ m/sec}\left[\frac{W}{10^{15}j}\right]^{2/3}\left[\frac{R}{1km}\right]^{-2} \qquad \pm \text{ a factor of } 2 \quad (5\text{-}68)$$

$$d = 1 \text{ in}\left[\frac{W}{1MT}\right]^{5/6}\left[\frac{R}{1kft}\right]^{-3/2}$$

$$d = 1.3 \times 10^{-3} \text{ m}\left[\frac{W}{1MT}\right]^{5/6}\left[\frac{R}{1km}\right]^{-3/2} \qquad \pm \text{ a factor of } 3 \quad (5\text{-}69)$$

$$a = 25 \text{ g}\left[\frac{W}{1MT}\right]\left[\frac{R}{1kft}\right]^{-4}$$

$$a = 0.05 \text{ g}\left[\frac{W}{10^{15}j}\right]\left[\frac{R}{1km}\right]^{-4} \qquad \pm \text{ a factor of } 5 \quad (5\text{-}70)$$

Application of the tuff factors to Eqs. 5-62, 5-63 and 5-64 leads to the following peak motion estimates on the axis directly beneath near-surface bursts on dry soil:

$$v = 2.5 \text{ ft/sec}\left[\frac{W}{1MT}\right]^{2/3}\left[\frac{R}{1kft}\right]^{-2}$$

$$v = 0.027 \text{ m/sec}\left[\frac{W}{10^{15}j}\right]^{2/3}\left[\frac{R}{1km}\right]^{-2} \qquad \pm \text{ a factor of } 3 \quad (5\text{-}71)$$

$$d = .5\ \text{in}\left[\frac{W}{1\text{MT}}\right]^{5/6}\left[\frac{R}{1\text{kft}}\right]^{-3/2}$$

$$\pm \text{ a factor of } 4 \qquad (5\text{-}72)$$

$$d = 6.5 \times 10^{-4}\ \text{m}\left[\frac{W}{10^{15}\text{J}}\right]^{5/6}\left[\frac{R}{1\text{km}}\right]^{-3/2}$$

$$a = 5\ g\left[\frac{W}{1\text{MT}}\right]\left[\frac{R}{1\text{kft}}\right]^{-4}$$

$$\pm \text{ a factor of } 5 \qquad (5\text{-}73)$$

$$a = 0.01\ g\left[\frac{W}{10^{15}\text{J}}\right]\left[\frac{R}{1\text{km}}\right]^{-4}$$

Wet soil behavior may be assumed to be intermediate between dry soil and soft rock. The effect of layering, incompletely understood at present, is introduced in Ref. 5-46.

The peak stress associated with direct-induced ground shock can be estimated by

$$\sigma = \rho\, C_L v \qquad (5\text{-}74)$$

where

σ = peak stress
ρ = mass density
C_L = loading wave velocity
v = peak particle velocity

The loading wave velocity, C_L, may be estimated from laboratory and insitu stress-strain data or taken approximately as one-half the seismic velocity in soil and soft rock and three-quarters the seismic velocity in hard rock. Peak strains result directly from peak stresses, i.e.,

$$\epsilon = \frac{\sigma}{\rho\, C_L^2} = \frac{v}{C_L} \qquad (5\text{-}75)$$

where ϵ is peak strain.

Typical direct-induced motion waveforms from contained bursts are shown in Fig. 5-47. The typical waveforms may be used to estimate waveforms associated with predicted peak radial motion. The rise time to peak velocity (or stress) can be taken as (Ref. 5-47)

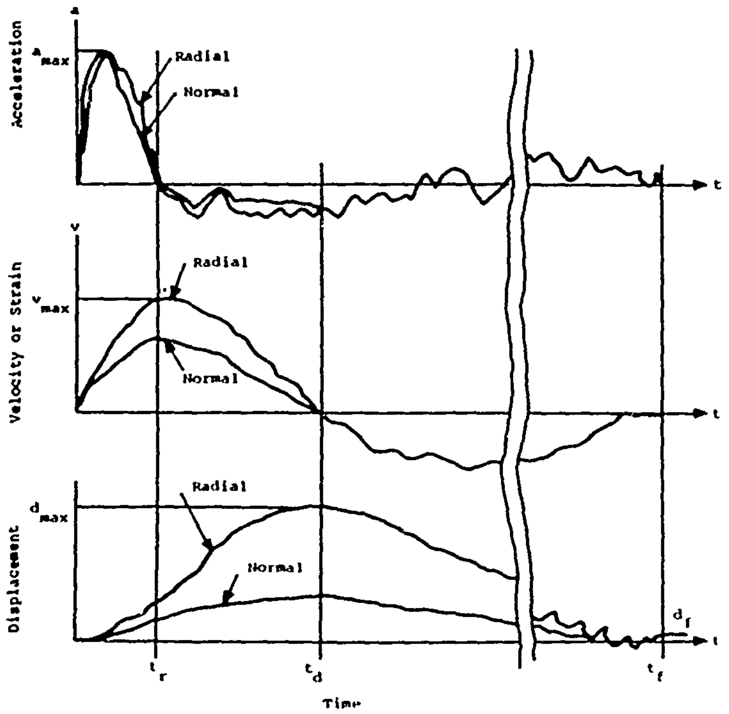

Figure 5-47 Typical Waveform for Direct-Transmitted Ground Shock (Ref. 5-38)

$$t_r = \frac{1}{12}\frac{R}{C_i} \text{ to } \frac{1}{6}\frac{R}{C_i} \qquad (5\text{-}76)$$

where

t_r = rise time

R = range

C_i = seismic velocity

The outward phase duration of the velocity pulse may be taken as one-half to one times the transit time to the point of interest (Ref. 5-47)

$$t_d = \frac{1}{2}\frac{R}{C_i} \text{ to } \frac{R}{C_i} \qquad (5\text{-}77)$$

where t_d = velocity outward phase duration. The compressive phase duration of the stress pulse may also be estimated roughly by Eq. 5-77.

The direct-induced estimates provided to this point are applicable only on the axis directly beneath the burst. Motions at off-axis locations will be affected by the free surface. As noted in paragraph 5.4.1, free surface effects become significant in the region between conical surfaces with apex angles of 30 and 65 degrees and dominant in the region between 65 degrees and the surface. It is recommended that free surface effects not be considered. The recommendation may be somewhat conservative, but free surface effect refinements are believed inconsistent with the inherent scatter in available contained burst data.

5.5 CRATER-INDUCED GROUND SHOCK

5.5.1 General

A recent study (Ref. 5-48) of ground motion data from high explosive and nuclear cratering bursts has

identified correlations between late-time crater formation and late-time near-surface ground motion parameters. The character of crater-induced ground motion is illustrated in Figs. 5-48 and 5-49 which show vertical and horizontal motions at the crater's edge on KOA. The initial motion results from the airblast. Both acceleration and velocity are sharply downward and outward. At approximately 0.3 second, a relatively low frequency, long-duration velocity pulse occurs which reverses the downward airblast-induced displacement and increases the outward horizontal displacement. Because of the long duration of the pulse, the final result is large upward and outward motions much greater than would have resulted from the airblast alone. The arrival time of the low frequency motion is consistent with the P-wave transit time through the ground from the burst point to the gage location. Similar motions related to the crater lip formation have been observed on high explosive detonations.

Although the KOA ground motions are for a location very near the crater, the correlations of Ref. 5-48 indicate that crater-induced near-surface ground motions may also be significant at large distances from the crater. The following paragraphs summarize Ref. 5-48 results.

5.5.2 Scaling Relation

The basic assumption for crater-induced ground motion correlation is that some characteristic length associated with the crater is a common scaling factor in all cratering bursts. Reference 5-48 found that the cube root of apparent crater volume provides correlations with a wide range of high explosive and nuclear sources in several geologic media. Although true crater volume would appear to be a more appropriate parameter and may provide better correlation, apparent volume is the

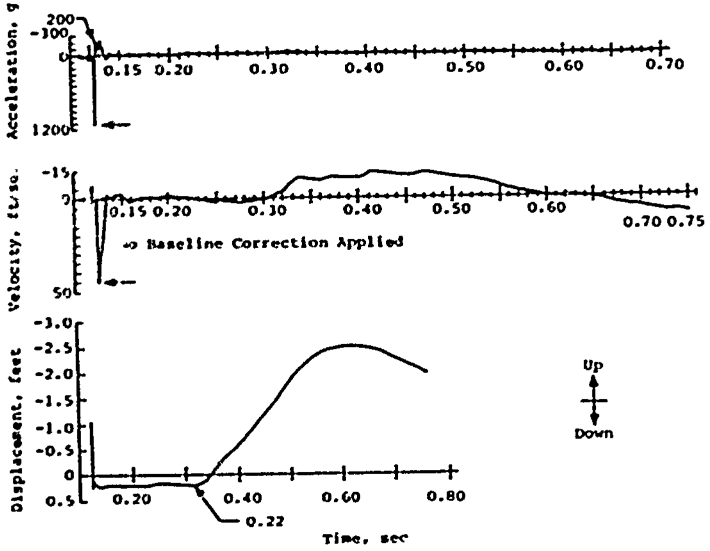

Figure 5-48 Vertical Motion vs. Time, Station 11, KOA (2000-Ft. (610 m) Ground Range, 998 psi (688 N/cm²) Overpressure) (Ref. 5-49)

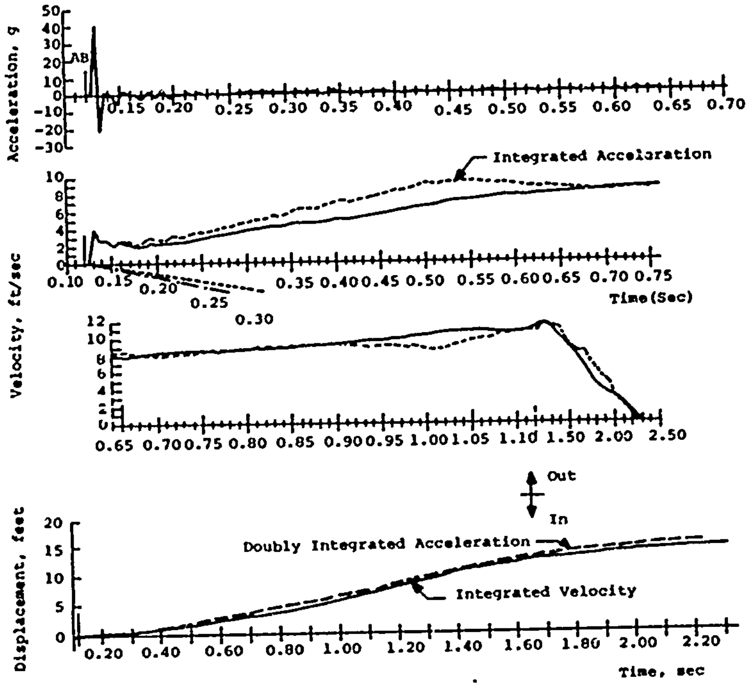

Figure 5-49 Horizontal Motion vs. Time, Station 11, KOA (2000-Ft. (610 m) Ground Range, 998 psi (688 N/cm²) Overpressure) (Ref. 5-49)

only volume which has been measured accurately in past tests. If one accepts the premise that crater volume is a gross measure of the energy that is effectively coupled into the ground then crater volume scaling may inherently compensate for differences in geology and energy source including source type, yield and height of burst.

5.5.3 Horizontal Displacement

Figure 5-50 presents available crater volume scaled data for peak horizontal displacement versus range. Above-surface burst and below-surface burst data do not coincide, and Ref. 5-48 suggests the following equations as representative of the two burst classes.

$$d_h = \frac{0.45\ V_a^{4/3}}{R^3} \quad \text{(above-surface data)} \qquad (5\text{-}78)$$

$$d_h = \frac{0.1\ V_a^{4/3}}{R^3} \quad \text{(half-buried and below-surface data)} \qquad (5\text{-}79)$$

where

d_h = peak horizontal displacement

V_a = apparent crater volume

R = range

Reference 5-48 hypothesizes that the large difference between above-surface and half-buried and below-surface burst data is that the work done in ejecting material is much less effective in producing displacements beyond the crater edge than the work done compressing material. Thus, the scaled displacements for buried bursts are smaller than those for above-surface bursts because a buried burst ejects a much larger percentage of the apparent crater volume than an above-surface burst. There is a factor of almost 5 difference in

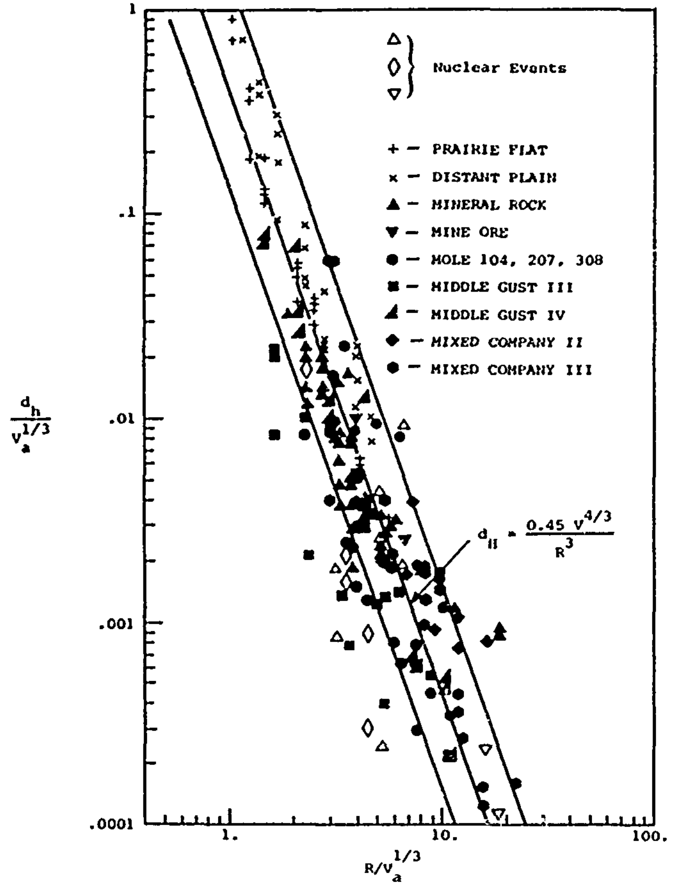

(a) Above Surface Data

Figure 5-50 Peak Crater-Induced Horizontal Displacements (Ref. 5-50)

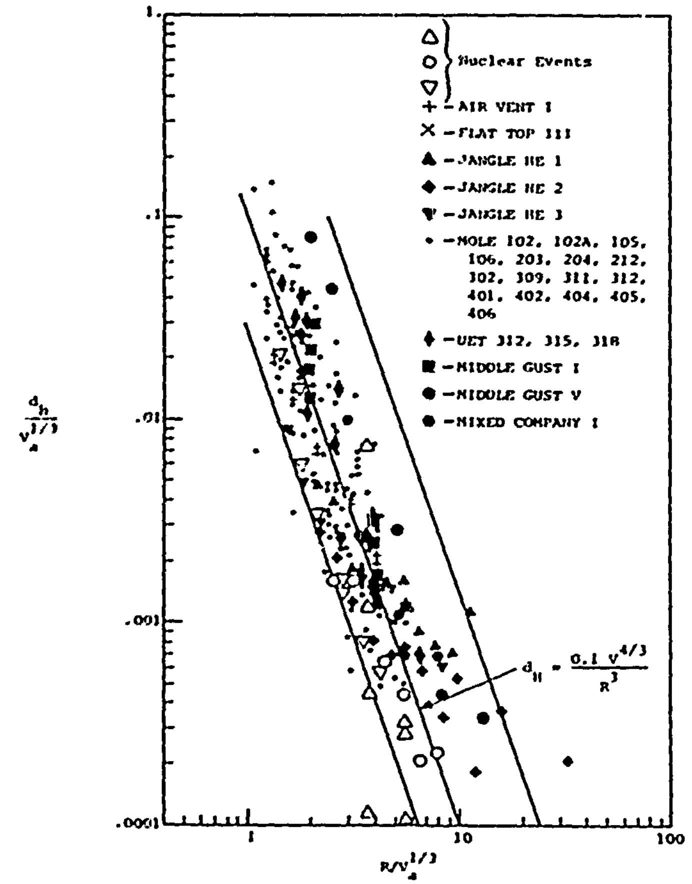

(b) Half Buried and Below Surface Data

Figure 5-50 (Continued)

scaled displacements for buried and above-surface bursts.

Figure 5-51 shows a correlation between permanent horizontal displacement and range derived from experiments with surface tangent HE spheres. The surface tangent configuration is thought to better simulate the cratering and ground motions of near-surface nuclear bursts. The best fit equation for permanent horizontal displacements is

$$d_{hp} = \frac{0.2\ V_a^{4/3}}{R^3} \tag{5-80}$$

where

d_{hp} = permanent horizontal displacement

Although permanent displacements are expected to be material dependent, the data scatter reveals no obvious trend. It appears that on the average only about 50 percent of the peak displacement is recovered for near-surface bursts.

Displacement data scatter by a factor of about ± 6 at a given range. There are several possible reasons for the scatter. Most data are derived from singly and doubly integrated records which generally include subjective baseline shift corrections. Slight baseline shifts can dramatically affect integration results. Also, all data are considered regardless of depth below the ground surface. Reference 5-48 suggests that data scatter may be reduced significantly if only near-surface data (depths less than 0.1 $V_a^{1/3}$) are considered. The fact that apparent crater volume rather than true crater volume is used may also contribute to the scatter in the data.

The major variable in crater-induced ground motion correlations is the apparent crater volume which may be estimated according to the procedures of Section IV. In the absence of detailed site information, Fig. 5-52 may be used to roughly estimate peak horizontal displacements in homogeneous dry soils, wet soils and dry, hard rock due to near-surface nuclear bursts.

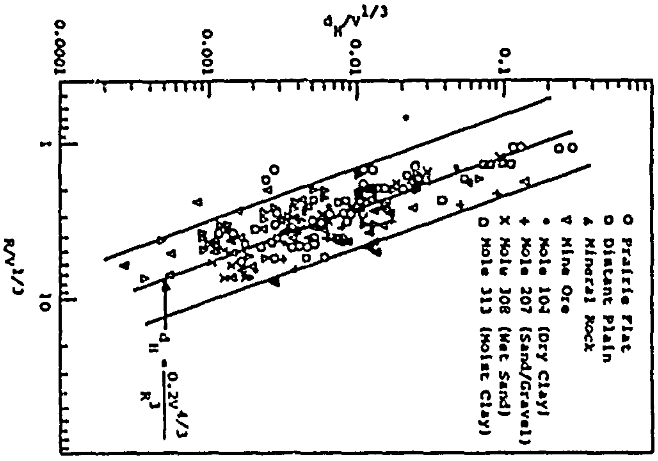

Figure 5-51 Permanent Horizontal Displacements for Surface Tangent HE Spheres (Ref. 5-48)

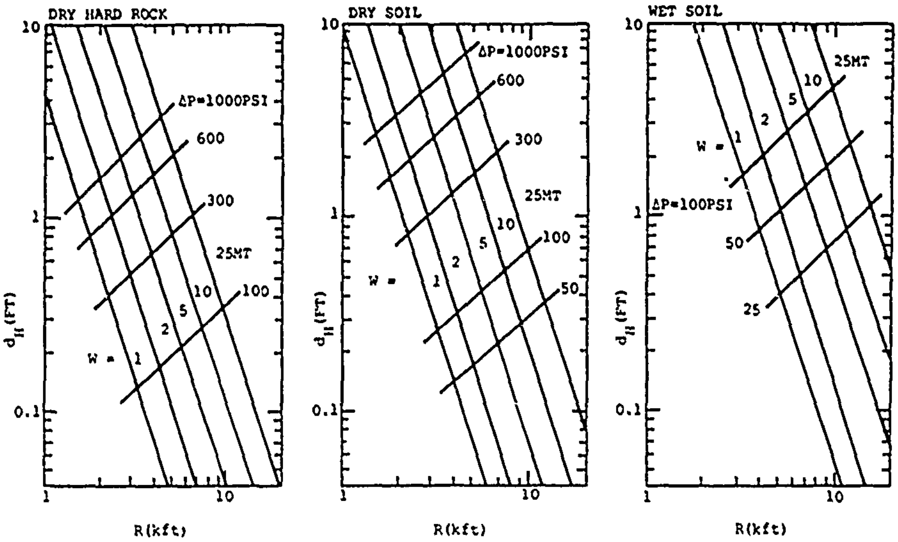

Conversion Factors for SI Units:
1ft = 0.3048 m
1kft = 304.8 m
1MT = 4.184 x 10^{15}J
1psi = 0.68936 N/cm^2

Figure 5-52 Estimates of Horizontal Displacements for Various Geologic Media (5-48)

5.5.4 Other Horizontal Ground Motion Parameters

Figure 5-53 presents peak crater induced horizontal particle velocity data as a function of crater volume scaled range (Ref. 5-50). The data may be represented within a factor of about ± 4 by

$$\frac{v_h}{C_e} = 0.01\left|\frac{R}{V_a^{1/3}}\right|^{-2} \qquad (5\text{-}81)$$

where

v_h = peak horizontal particle velocity

C_e = effective wave velocity = $\frac{R}{t_f}$

R = range

t_f = arrival time of first signal from the burst point

V_a = apparent crater volume

The effective wave velocity, C_e, is approximately equal to the seismic velocity at unlayered sites. At layered sites, C_e accounts for the variation in seismic velocity with depth. A method for calculating C_e is presented in paragraph 5.6.

Figure 5-54 presents a correlation between the rise time to peak horizontal displacement and crater volume scaled range (Ref. 5-50). The rise time may be approximated within a factor of about ± 5 by

$$t_p = \frac{50}{C_c}\left(\frac{V_a^{2/3}}{R}\right) \qquad (5\text{-}82)$$

where t_p is the rise time to peak horizontal displacement.

General waveforms for crater-induced ground shock have not yet been developed. However, the peak velocity and peak displacement rise time correlations of Eqs. 5-81 and 5-82 provide approximate information from which plausible waveforms may be synthesized. An illustrative example is provided in paragraph 5.7.

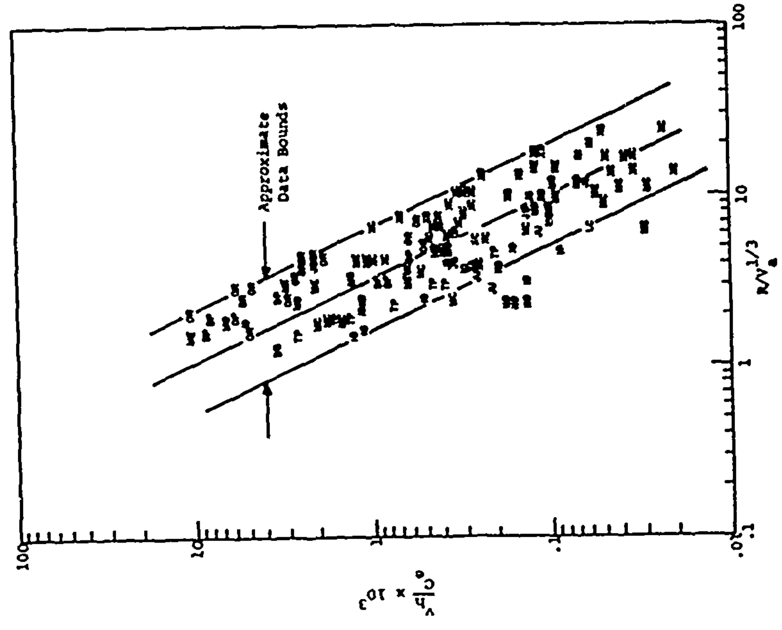

Legend

Event	Symbol
MIDDLE GUST 3	MC
MIDDLE GUST 4	MD
PACE 1D	1D
PACE 1O	1O
LACROSSE	LC
MIKE	1M
SMALL BOY	SB
PRAIRIE FLAT	PF
PRISCILLA	PS
DISTANT PLAIN 6	DP
JOHNNY BOY	JB
TEAPOT-7	TP
JANGLE U	JU
JANGLE S	JS
DANNY BOY	DB
MIXED CO 1	XA
MIXED CO 2	XB
MIXED CO 3	XC
KOA	KO
MIDDLE GUST 5	ME
MINE ORE	OR

Figure 5-53 Peak Horizontal Crater-Induced Particle Velocity as a Function of Range (Ref. 5-50)

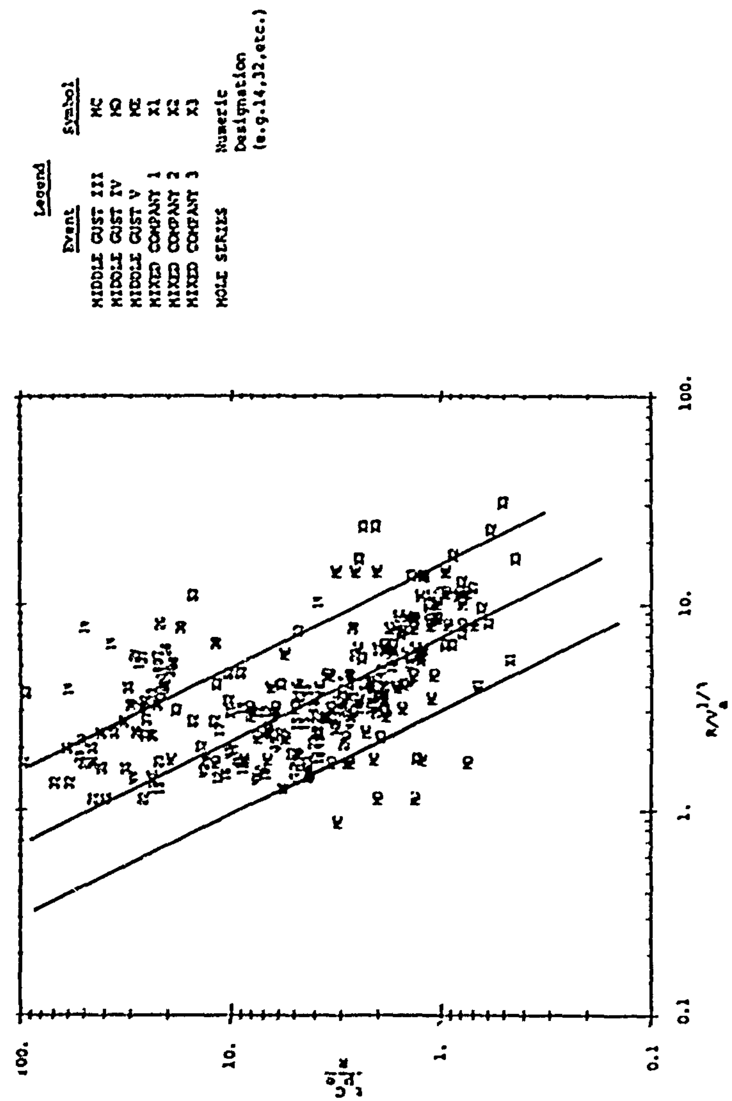

Figure 5-54 Rise Time to Peak Horizontal Crater-Induced Displacement as a Function of Range (Ref. 5-50)

Vertical crater-induced ground motion analyses (Ref. 5-49 and 5-50) indicate vertical displacements, peak velocities and rise time to peak displacement are approximately equal to the corresponding horizontal quantities at the same range.

5.6 COMPOSITE GROUND SHOCK

While it is convenient to categorize ground shock according to source for purposes of discussion and computation, practical problems require an estimate of the complete ground shock environment at a point of interest. The complete environment will result from disturbances arriving from all sources, except in the case of a true air burst or fully-contained burst. Although not theoretically correct, a reasonable approximation to the complete ground shock environment may be obtained by superimposing credible airblast-induced, crater-induced and outrunning waveforms according to their relative time phasing.

The airblast arrival time at a given range may be estimated from Fig. 3-5. The arrival times of disturbances propagated through the ground may be estimated by standard geophysical methods (see, for example, Ref. 5-9). Figure 5-55(a) illustrates the paths by which disturbances may travel in a two-layer system. The discussion is restricted to compression waves since they travel with the fastest velocity and will be the first to arrive along any given path. The incident dilatational wavefront created by an excitation at point S will be hemispherical. The wave paths are represented by rays which are perpendicular to the wavefront and parallel to the direction of wave propagation.

One path from the point of excitation to a point a distance x away is a direct path through the top layer. The arrival time for the direct path is simply

$$t_a = \frac{x}{C_1} \qquad (5\text{-}83)$$

where

t_a = arrival time

x = distance from excitation to point of interest

C_1 = compression wave velocity in layer

The existence of a layer interface creates two additional paths. The interaction of the incident wave with the layer interface causes reflected waves which travel back toward the surface and refracted waves which continue into the lower medium. The arrival time of the reflected wave at a surface point is

$$t_a = \frac{\sqrt{x^2 + 4H^2}}{C_1} \tag{5-84}$$

where H is the layer depth. In general, the refracted wave does not return to the surface unless a deeper interface is encountered. However, there is a critical angle of incidence, i_c, for which the refracted wave travels parallel to the interface in the lower medium. The critically refracted wave causes a disturbance along the interface which, in turn, generates a wave which travels upward into the layer. This new wave is called a head wave and its arrival time at the surface is given by

$$\begin{aligned} t_a &= \frac{x}{C_2} + \frac{2H \cos i_c}{C_1} \\ &= \frac{x}{C_2} + 2H\sqrt{\frac{1}{C_1^2} - \frac{1}{C_2^2}} \end{aligned} \tag{5-85}$$

where

C_1 = compression wave velocity in the top layer

C_2 = compression wave velocity in underlying half space

i_c = critical angle = $\arcsin \frac{C_1}{C_2}$

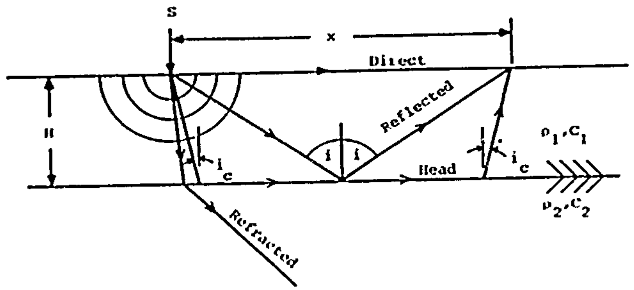

(a) Travel Paths

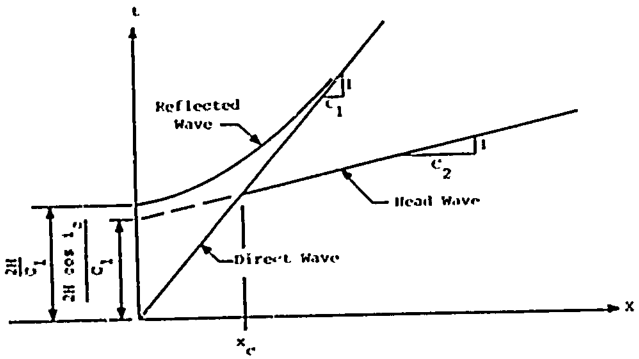

(b) Arrival Time-Distance Curves

Figure 5-55 Wave Transmission Through a Two-Layer System

The arrival times of the direct, reflected and head waves are shown as a function of distance in Fig. 5-55(b). For distances less than x_c, called the crossover distance, the first arrival will be due to the direct wave. At distances greater than x_c, the head wave will arrive first. The reflected wave will lag both the direct and head waves at all distances and, therefore, is not of importance in considering first arrivals.

In multilayered systems, the time of arrival of the head wave from the n^{th} interface (see Fig. 5-56) is given by

$$t_a^{(n)} = \left(\sum_{i=1}^{n} 2H_i \sqrt{\frac{1}{C_i^2} - \frac{1}{C_{n+1}^2}} \right) + \frac{x}{C_{n+1}} \qquad (5\text{-}86)$$

where

$t_a^{(n)}$ = arrival time of head wave from n^{th} interface

H_i = thickness of the i^{th} layer

C_i = compression wave velocity in i^{th} layer

C_{n+1} = compression wave velocity in $(n+1)^{th}$ layer

The use of Eq. 5-86 for two-layer and three-layer systems is illustrated in Fig. 5-57. The summation in the parentheses of Eq. 5-86 is the time axis intercept of the arrival time-distance line for the n^{th} interface head wave. The summation term is designated by T_n (i.e., T_1, T_2, etc.) in Fig. 5-57.

For the two-layer system of Fig. 5-57(a), it can be seen that the direct wave governs the first arrival at distances less than $x_c^{(1)}$. Between $x_c^{(1)}$ and $x_c^{(2)}$, the head wave from the first interface is the first to arrive. Beyond $x_c^{(2)}$, the head wave from the second interface governs.

The general method for determining arrival time-distance curves for ground disturbances may be used with the arrival time-distance curve for the airblast to estimate the time phasing of effects at a point of interest and the ground range

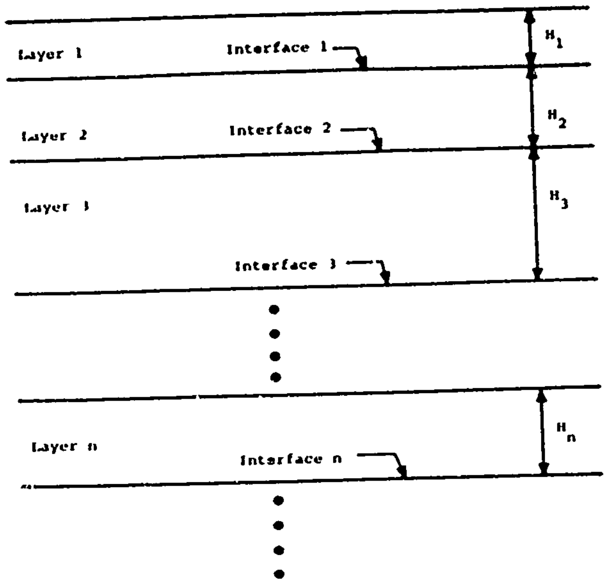

Figure 5-56 Nomenclature for Multilayered Systems

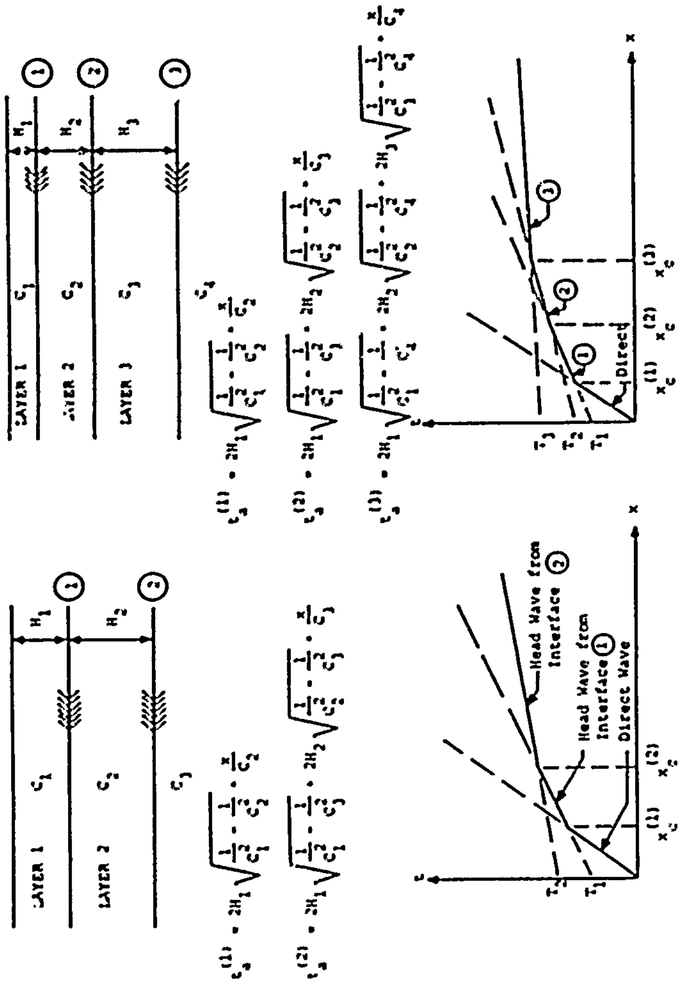

$$t_a^{(1)} = 2H_1\sqrt{\frac{1}{C_1^2} - \frac{1}{C_2^2}} + \frac{x}{C_2}$$

$$t_a^{(2)} = 2H_1\sqrt{\frac{1}{C_1^2} - \frac{1}{C_3^2}} + 2H_2\sqrt{\frac{1}{C_2^2} - \frac{1}{C_3^2}} + \frac{x}{C_3}$$

(a) Two-Layer System

$$t_a^{(1)} = 2H_1\sqrt{\frac{1}{C_1^2} - \frac{1}{C_2^2}} + \frac{x}{C_2}$$

$$t_a^{(2)} = 2H_1\sqrt{\frac{1}{C_1^2} - \frac{1}{C_3^2}} + 2H_2\sqrt{\frac{1}{C_2^2} - \frac{1}{C_3^2}} + \frac{x}{C_3}$$

$$t_a^{(3)} = 2H_1\sqrt{\frac{1}{C_1^2} - \frac{1}{C_4^2}} + 2H_2\sqrt{\frac{1}{C_2^2} - \frac{1}{C_4^2}} + 2H_3\sqrt{\frac{1}{C_3^2} - \frac{1}{C_4^2}} + \frac{x}{C_4}$$

(b) Three-Layer System

Figure 5-57 Construction of Arrival Time-Distance Curves in Two-Layer and Three-Layer Systems

at which outrunning first occurs (Ref. 5-1)(needed for the outrunning prediction method of paragraph 5.3.6). In addition, the arrival-time-distance curves may be used to estimate the effective seismic velocity, C_e, used to estimate crater-induced particle velocities and rise times to peak crater-induced horizontal displacement. The effective seismic velocity is simply the inverse slope of the secant line drawn from the origin to the range of interest.

The time of arrival of the airblast wave can be read directly from the airblast time of arrival curve. Also, the arrival time of effects from the source region can be read directly from the ground disturbance curve intersecting the burst point. The ground range at which earliest ground signals and the airblast wave arrive at exactly the same time is the ground range at which outrunning first occurs. The earliest outrunning arrivals can be found by trial and error shifting of the ground disturbance arrival time curve to various origins on the airblast arrival curve, i.e., times and ranges at which energy is imparted to the ground by the expanding airblast. The time at which earliest ground signals arrive at the point of interest prior to the airblast is the time of outrunning arrival.

Given the ground range at which outrunning first occurs, outrunning motions can be predicted according to paragraph 5.3.6. With the arrival times of the various signals, predicted ground shock from all sources can be superimposed to obtain an estimate of the complete ground shock environment. The procedure is illustrated by an example in paragraph 5.7.

5.7 ILLUSTRATIVE EXAMPLES

5.7.1 Selection of Material Properties

a. GIVEN: A 1 MT (4.184 x 10^{15}J) surface burst at a site composed of 100 feet (30.5 m) of wet clay overlying shale which extends to large depth. The water table is at the ground surface because of spring runoff. Seismic velocities have been measured to be 5100 ft/sec (1550 m/sec) in the clay below the water table and 8000 ft/sec (2440 m/sec) in the shale.

b. FIND: Material property estimates for use in preliminary ground shock calculations.

c. SOLUTION: Properties necessary for calculations are insitu density, seismic velocity, loading wave velocity and strain recovery ratio. Assume the only data available are seismic velocities. Other properties, therefore, must be estimated from past experience with similar materials. Table 5-2 gives typical insitu unit weights of 110 lb/ft^3 (1.76 x 10^3 kg/m^3) for saturated clays and 145 lb/ft^3 (2.32 x 10^3 kg/m^3) for shales. Since the seismic velocity in the clay below the water table is greater than 5000 ft/sec (1520 m/sec), the clay can be assumed nearly completely saturated with a modulus of 150,000 psi (103,404 N/cm^2) (paragraph 5.2.3). The corresponding loading wave velocity for the clay is approximately 2500 ft/sec (760 m/sec). The loading wave velocity in the shale, a soft rock, may be taken as 1/2 the seismic velocity (paragraph 5.2.6). Strain recovery ratios in both the clay and the shale may be taken as 3/4 (paragraph 5.2.6a). Estimated material properties are summarized in Table 5-10.

5.7.2 Time Phasing of Ground Shock Effects

a. GIVEN: The burst, geologic conditions and material properties of Example 5.7.1.

Table 5-10

ESTIMATED MATERIAL PROPERTIES FOR EXAMPLE 5.7.1

Depth	Material Description	Insitu Unit Weight (γ) lb/ft^3	Insitu Mass Density (ρ) $\frac{lb\text{-}sec^2}{ft^4}$	Seismic Velocity (C_1) ft/sec	Loading Wave Velocity (C_L) ft/sec	Strain Recovery Ratio (r)
0-100 ft	Saturated Clay	110	3.42	5100	2500	0.75
100 ft-∞	Shale	145	4.50	8000	4000	0.75

b. FIND: The arrival times of the airblast, outrunning ground shock, and crater-induced ground shock at the 100 psi (69 N/cm^2) overpressure level and the range at which first outrunning occurs.

c. *SOLUTION:* The arrival time of effects from the various ground shock sources are determined from the 1 MT airblast time of arrival curve (Fig. 3-5) and the travel time-distance curve for the one-layer geologic system of interest (Fig. 5-57). Figure 5-58 presents the arrival time-distance curve for the airblast from a 1 MT surface burst and arrival time-distance curves for ground disturbances originating at various ranges. The time of arrival of the airblast wave can be read directly from the airblast time of arrival curve as 0.54 sec. Similarly, the arrival time of direct-induced effects can be read directly from the ground disturbance curve intersecting the burst point (x = 0) as 0.44 sec.

The ground *range* at which outrunning first occurs and the arrival time of outrunning at the 100 psi level are found by shifting the ground disturbance-arrival time curve to various origins on the airblast arrival curve, i.e., times and ranges at which energy is imparted to the ground by the expanding airblast. By trial and error, the origin which delivers the earliest ground signals at times prior to airblast arrival is determined. The intersection of the earliest ground disturbance curve with the airblast time of arrival curve determines the range at which outrunning first occurs. The time of arrival of outrunning at greater ranges is determined by the same ground disturbance time of arrival curve.

Three trials are illustrated in Fig. 5-58 (origins 1, 2 and 3). It can be seen that first outrunning occurs at 2150 feet (655 *m*) (approximately 400 psi

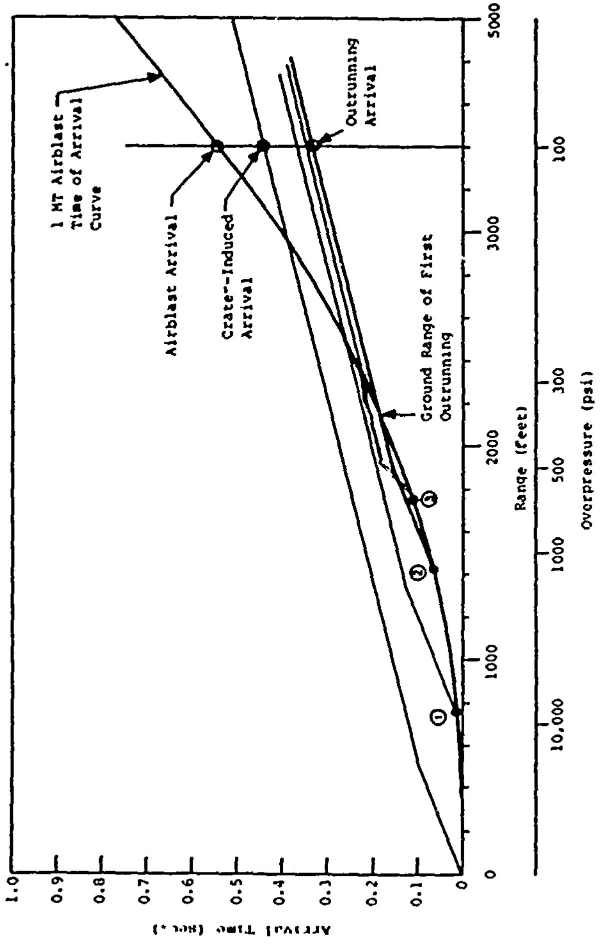

Figure 5-58 Ground Shock Arrival Time Estimates for Example 5.7.2

(276 N/cm^2) level) and originates at overpressures greater than 1000 psi (689 N/cm^2) (origin 2). Outrunning signals first arrive at the 100 psi level at 0.31 sec.

5.7.3 Airblast-Induced Ground Shock

a. GIVEN: The burst, geologic conditions and material properties of Example 5.7.1.

b. FIND: The contribution of the airblast passing over the point of interest to the ground shock at a depth of 25 feet (7.6 m) at the 100 psi (69 N/cm^2) overpressure level.

c. SOLUTION: The contribution of the airblast as it passes over the point of interest is estimated assuming one-dimensional conditions. As described in paragraph 5.3.3, the effect of layering upon early time vertical stress and motion histories may be estimated by superimposing the incident stress wave created by the airblast with subsequent reflected waves created at the layer interface and ground surface.

Figure 5-59 presents a wave front diagram for the problem of interest. The incident wave front is assumed to travel at the seismic vdocity (C_i) of the material through which the wave is traveling, 5100 ft/sec in the clay and 8000 ft/sec in the shale. The incident wave peak is assumed to travel with the loading wave velocity (C_L) of the material through which the wave is traveling, 2500 ft/sec in the clay and 4000 ft/sec in the shale. Reflections in the layer are assumed to travel at a velocity governed by the unloading modulus of the layer material. Solving Eq. 5-2 for C_u, assuming constant density, results in

$$C_u = \sqrt{\frac{1}{r}}\,C_L = \sqrt{\frac{1}{0.75}}\ (2500\ \text{ft/sec})$$

$$= 2890\ \text{ft/sec, say } 2900\ \text{ft/sec } (884\ \text{m/sec})$$

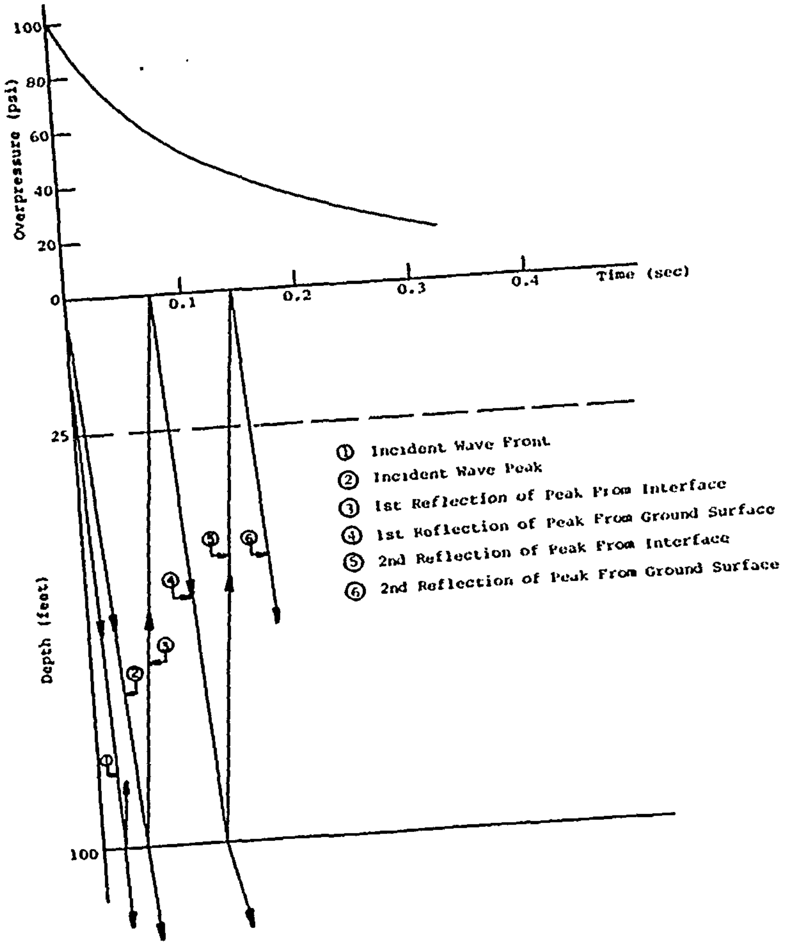

Figure 5-59 Wave Front Diagram for Example 5.7.3

in the clay.

The characteristics of the incident wave are estimated by the method of paragraph 5.3.2 in which the incident wave is determined by interpolation between elastic (r = 1) and bilinear-no recovery (r = 0) solutions. The airblast overpressure and impulse characteristics necessary for calculation, determined from Section III, are shown in Fig. 5-60.

The incident stress and velocity-time histories for the bilinear-no-recovery case are determined from Eqs. 5-25 and 5-26. The equations may be rearranged and written in normalized form as shown below for convenience in computations.

$$\frac{\sigma_z}{P_{so}} = \frac{z}{C_L t_o} \frac{1}{\tau}\left[\frac{I_m}{P_{so} t_o} \frac{i(\tau)}{\tau} - \bar{p}(\tau)\right] + \bar{p}(\tau) \qquad (5\text{-}87)$$

$$\frac{\rho C_L v_z}{P_{so}} = \frac{I_m}{P_{so} t_o} \frac{i(\tau)}{\tau} \qquad (5\text{-}88)$$

where

I_m = total impulse in the overpressure-time history

$i(\tau)$ = normalized impulse-time history (Fig. 5-59(b))

$\bar{p}(\tau)$ = normalized overpressure-time history (Fig. 5-60(a))

$\tau = \frac{t}{t_o}$ = normalized time

and other terms are defined in paragraph 5.3.2. The most convenient calculation sequence is to first calculate the normalized velocity-time history according to Eq. 5-88 and then use the result in calculating the stress time

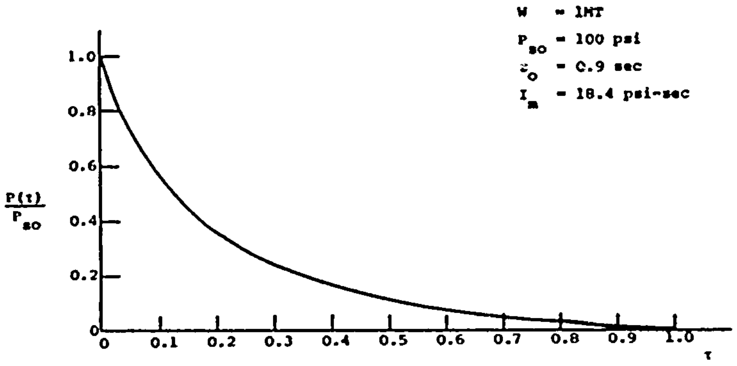

(a) Normalized Overpressure-Time History

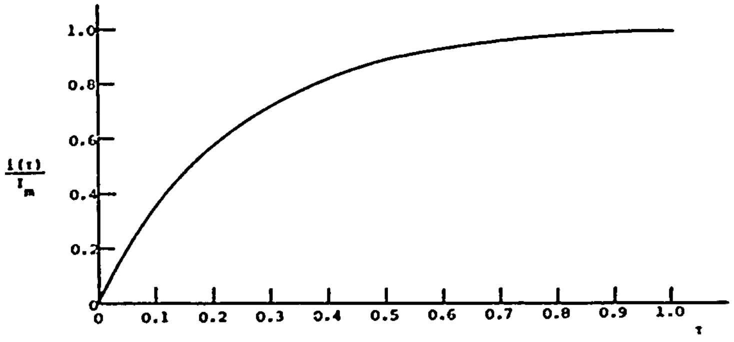

(b) Normalized Impulse-Time History

Figure 5-60 Airblast Characteristics for Example 5.7.3 Calculations history using Eq. 5-87 in the form

$$\frac{\sigma_z}{P_{so}} = \frac{z}{C_L t_o} \frac{1}{\tau}\left[\frac{\rho C_L v_z}{P_{so}} - \bar{p}(\tau)\right] + \bar{p}(\tau) \qquad (5\text{-}89)$$

The procedure leading to the normalized velocity-time history is shown in Fig. 5-61. Figure 5-61(a) plots $i(\tau)/\tau$ versus τ and is readily arrived at from Fig. 5-60(b). Figure 5-61(b) is simply the product of Fig. 5-61(a) and the term

$$\frac{I_m}{P_{so} t_o} = \frac{(18.4)}{(100)(0.9)} = 0.204$$

Values of $i(\tau)/\tau$ are inaccurate for τ less than about 0.05. However, the inaccuracy has no effect upon the velocity since at $\tau = 0$

$$\frac{\rho C_L v_z}{P_{so}} = 1$$

and the velocity-time history between $\tau = 0$ and $\tau = 0.05$ can be reasonably determined by interpolation.

The normalized velocity-time histories at the 25 and 100-foot depths are indicated in Fig. 5-61(b). At the 25-foot depth, the incident wave arrives at a normalized time

$$\frac{z}{C_L t_o} = \frac{(25)}{(2500)(.9)} = 0.111$$

Similarly, the incident wave arrives at the 100-foot depth at a normalized time 0.444. The incident wave at both the 25 and 100-foot depths has an identical decay in time as does the incident wave at all depths in the layer. This feature is characteristic of the bilinear-no recovery material model.

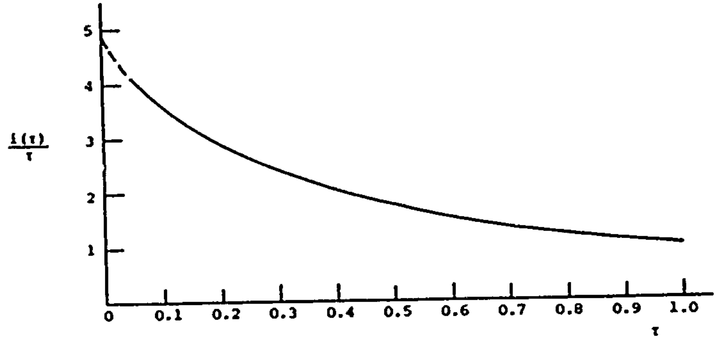

(a) $i(\tau)/\tau$ Versus Normalized Time

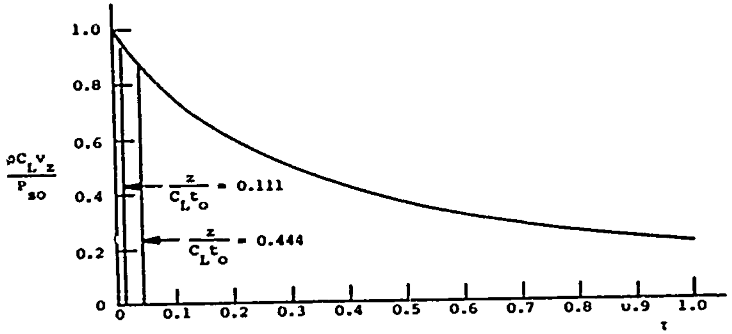

(b) Normalized Velocity-Time History

Figure 5-61 Calculation of Normalized Velocity-Time History in Bilinear-No Recovery Material for Example 5.7.3

Vertical stress time histories at the 25 and 100-foot depths in bilinear-no recovery materials are estimated using Eq. 5-89. Intermediate steps are shown in Fig. 5-62 where F(t) is defined as

$$F(\tau) = \frac{\rho C_L v_z}{P_{so}} - \bar{p}(\tau) \qquad (5\text{-}90)$$

The modification terms in Fig. 5-62(b) and (c) are the first term in Eq. 5-89 for the 25-foot and 100-foot depths. The sum of the modification terms and $\bar{p}(\tau)$ (Fig. 5-60(a)) yield vertical incident stress time histories in a bilinear-no recovery material. The results for this example are shown in Fig. 5-63 where both bilinear-no recovery and elastic time histories are plotted. The elastic results are readily calculated using Eq. 5-14.

The stress time history for the material of interest ($r = 3/4$) is estimated by linear interpolation between the $r = 0$ and $r = 1$ solutions. At the 25-foot depth the effect of the difference between $r = 1$ and $r = 3/4$ is small and the $r = 1$ solution is taken as the estimated vertical stress-time history at 25 feet. The interpolation for the 100-foot depth is shown in Fig. 5-63(b).

The incident wave, estimated as described above, and the first four reflected waves due to interaction of the incident wave with the layer interface and subsequent reflections between the interface and the ground surface are shown in Fig. 5-64. The stress histories are in terms of actual stress and time. The times of arrival of the waves at the 25-foot depth are taken from Fig. 5-59. A rise time has been given to the incident wave using the procedure of Fig. 5-22. The rise time at the 100-foot depth is carried without change in subsequent reflections.

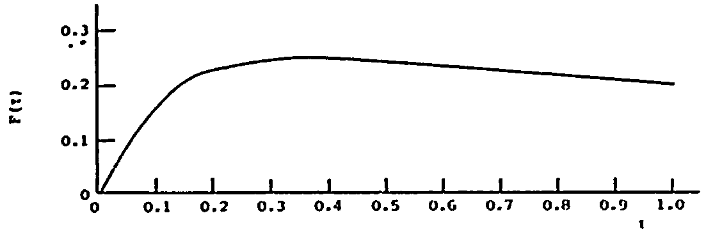

(a) F(τ) Versus τ

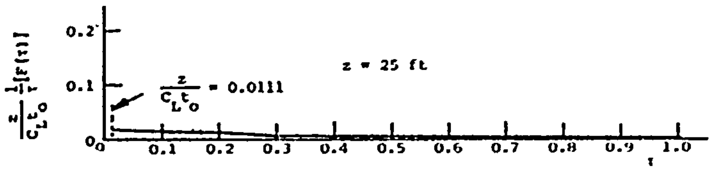

(b) Modification Term for z = 25 Feet

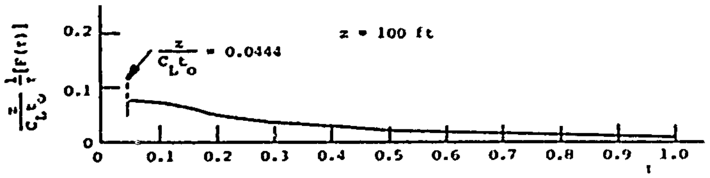

(c) Modification Term for z = 100 Feet

Figure 5-62 Intermediate Calculations for Determining Incident Vertical Stress Time Histories in Bilinear-No Recovery Material for Example 5.7.3

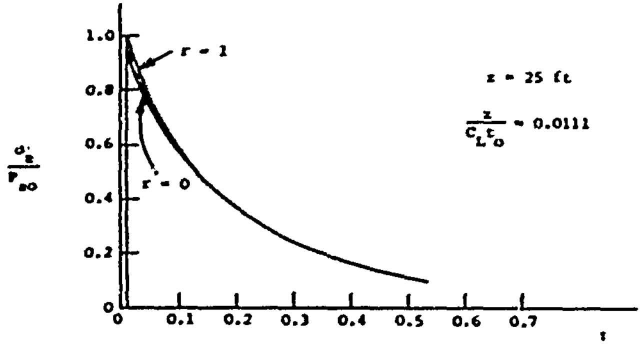

(a) Vertical Stress-Time Histories at 25 feet

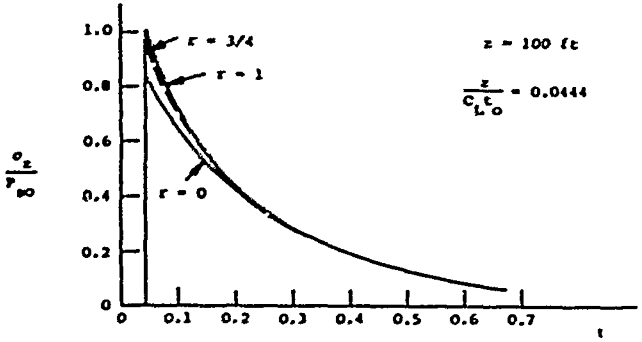

(b) Vertical Stress-Time Histories at 100 feet

Figure 5-63 Normalized Vertical Incident Stress-Time Histories for Example 5.7.3

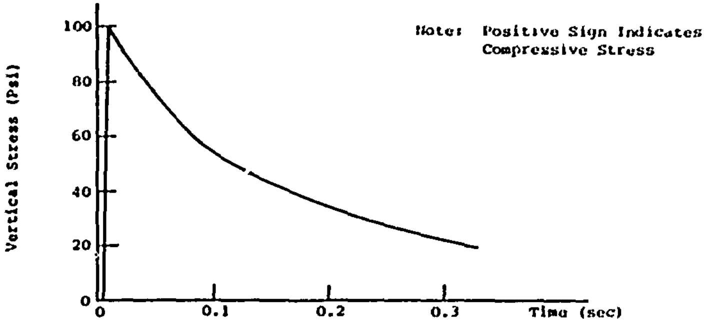

(a) Incident Stress Wave

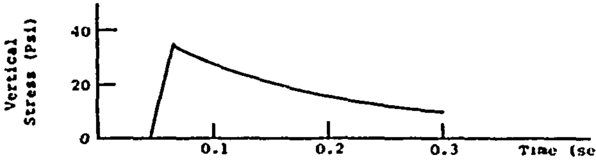

(b) First Interface Reflection

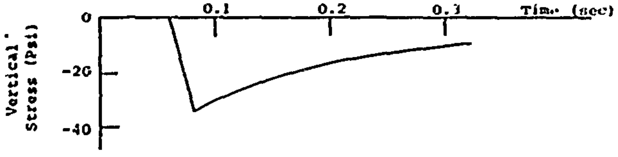

(c) First Ground Surface Reflection

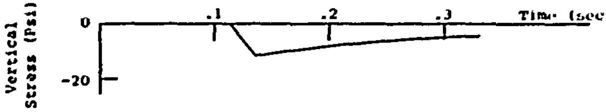

(d) Second Interface Reflection

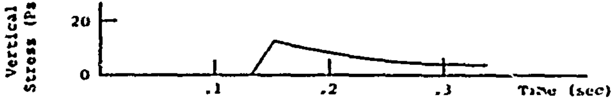

(e) Second Ground Surface Reflection

Figure 5-64 Wave System for Estimated Vertical Stress History of Example 5.7.3

The incident wave (Fig. 5-64(a)) is the $r = 1$ solution of Fig. 5-63(a) converted to actual stress and time. The first reflection from the interface (Fig. 5-64(b)) is determined from the incident wave at the 100-foot depth. The ratio of acoustic impedances across the interface is

$$\psi = \frac{\rho_1 C_L^1}{\rho_2 C_L^2} = \frac{(3.42)(2500)}{(4.50)(4000)} = 0.475$$

Using Eq. 5-33, the peak stress of the first layer reflection is

$$\sigma_r^L = \frac{1 - \psi}{1 + \psi}\,\sigma_i = \frac{1 - 0.475}{1 + 0.475}\,\sigma_i$$

$$\sigma_r^L = 0.36\sigma_i$$

Taking σ_i from Fig. 5-63(b) for $r = 3/4$

$$\sigma_r^L = 0.36\ (96\ \text{psi}) = 34\ \text{psi}\ (23\ \text{N/cm}^2)$$

The decay time history of the reflected stress wave is assumed similar to the decay of the incident wave and the wave is assumed to propagate in elastic material without attenuation or change. The first reflection from the interface subsequently reflects from the ground surface (Fig. 5-64(c)), which simply reverses the sign of the first interface reflection (Eq. 5-34).

Although subsequent reflections are uncertain due to material inelasticity and two dimensional effects, a rough estimate may be made by considering the material to behave elastically on the unload-reload portion of the stress strain curve. The ratio of impedances at the layer for subsequent reflections is

$$\psi = \frac{\rho_1 C_u^1}{\rho_2 C_u^2}$$

Since both the clay layer and underlying shale have $r = 3/4$, ψ remains 0.475. The peak stress associated with the second reflection (Fig. 5-64(d)) at the interface is, therefore,

$$\sigma_r = 0.36\ (-34\ \text{psi}) = -12\ \text{psi}\ (-8.3\ \text{N/cm}^2)$$

As before, the time history of the reflected wave is assumed similar to that of the incident wave. The second ground surface reflection (Ref. 5-64(e)) simply reverses the sign of the second layer reflection. Note that negative stresses associated with reflected waves do not necessarily indicate tension in the material since they are superimposed on an incident stress system which is compressive.

Superposition of the wave system of Fig. 5-64 results in the estimated vertical stress time history for the 25-foot depth shown in Fig. 5-65. The horizontal stress time history can be taken equal to the vertical history since the clay is saturated, i.e., $K_o = 1.0$ (Table 5-4).

Velocity-time histories can be estimated in a manner similar to that used for stresses, recognizing that compressive waves cause particle velocities in the direction of wave propagation while tensile (relief) waves cause particle velocities opposite to the direction of wave propagation. The normalized particle velocity-time histories at the 25-foot depth due to the incident wave are shown in Fig. 5-66. The elastic solution ($r = 1$) is obtained directly from Eq. 5-15. The bilinear-no recovery solution is from Fig. 5-61(b). The solution for the material of interest ($r = 3/4$) is obtained by linear interpolation between the bounding solutions.

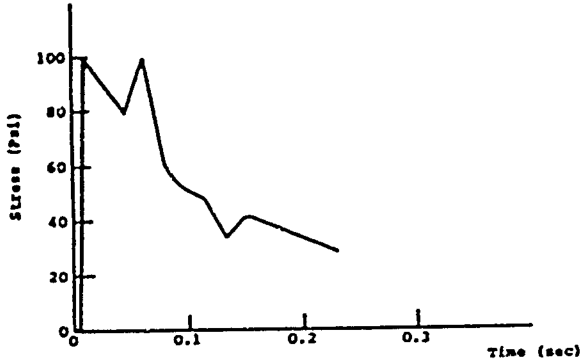

Figure 5-65 Estimated Vertical and Horizontal Stress History at 25-foot Depth for Example 5.7.3

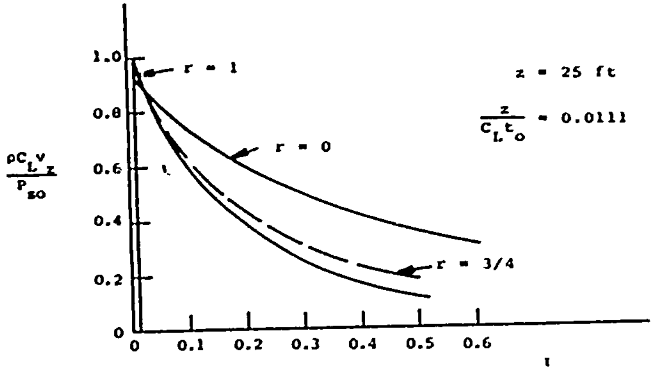

Figure 5-66 Normalized Velocity-Time Histories at 25-Foot Depth Due to Incident Wave for Example 5.7.3

The velocity-time history due to the incident wave and subsequent reflected waves is shown in Fig. 5-67. The velocity-time histories for the reflected waves are derived from the stress time histories of Fig. 5-64 assuming layer behavior is elastic and governed by the unload-reload modulus of the stress-strain curve (Eq. 5-36) after initial passage of the incident wave. Superposition of the individual time histories results in the estimated vertical velocity time history at the 25-foot depth shown in Fig. 5-68(a). Integration of the velocity-time history gives the displacement time history shown in Fig. 5-68(b).

The peak vertical acceleration due to the airblast is estimated using Eq. 5-43.

$$a = 2\frac{v_{max}}{t_r} = 2\,\frac{(1.68\ \text{ft/sec})}{0.006\ \text{sec}} = 560\ \text{ft/sec}^2$$

$$= 17\ g$$

where the rise time t_r has been computed according to Eq. 5-43.

$$t_r = 0.001 + \frac{z}{C_L} - \frac{z}{C_I} = 0.001 + 24\left[\frac{1}{2500} - \frac{1}{5100}\right]$$

$$= 0.006\ \text{sec.}$$

Peak horizontal motions are estimated using Table 5-5. It has already been stated that the horizontal stress may be taken as equal to the vertical stress since K_o is approximately 1. In order to estimate the ratio of peak horizontal acceleration and velocity to peak vertical component, it is necessary to estimate arcsin C_I/U and arcsin C_L/U. From Section III, the airblast shock front velocity, U, can be found to be 2900 ft/sec. Since the seismic velocity, C_I, exceeds U signals are propagating in the surface layer ahead of

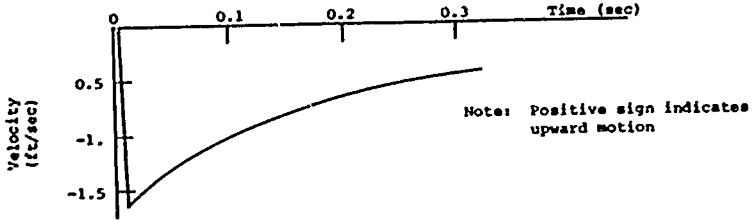

(a) Incident Wave

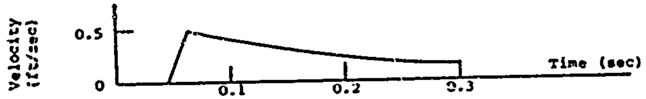

(b) First Interface Reflection

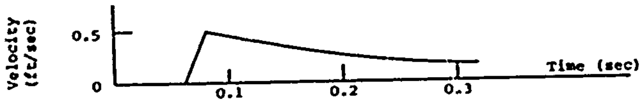

(c) First Ground Surface Reflection

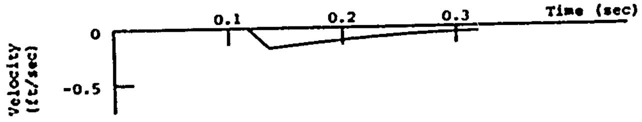

(d) Second Interface Reflection

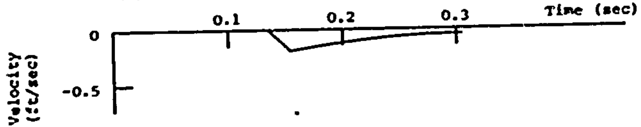

(e) Second Ground Surface Reflection

Figure 5-67 Vertical Velocity-Time Histories Due to Incident and Reflected Waves, Example 5.7.3

Note: Positive sign indicates upward motion

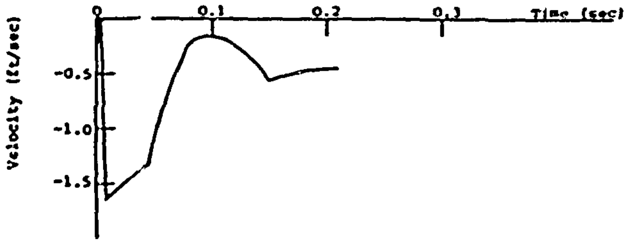

(a) Vertical Particle Velocity-Time History

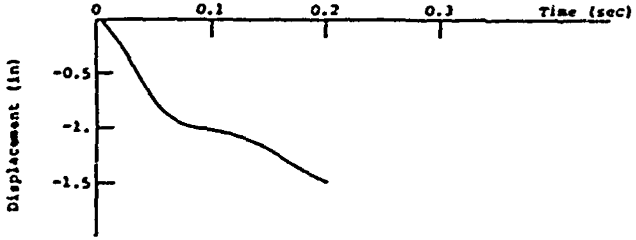

(b) Vertical Displacement Time History

Figure 5-68 Vertical Velocity and Displacement-Time Histories at 25-Foot Depth Due to Local Airblast, Example 5.7.3

the airblast as well as arriving from deeper layers. Under such conditions, the peak horizontal acceleration can be taken equal to the peak vertical.

The ratio of peak horizontal particle velocity to the peak vertical particle velocity is given by

$$\tan\left(\arcsin \frac{C_L}{U}\right) = \tan\left(\arcsin \frac{2500}{2900}\right) = 1.7$$

which exceeds 1. Accordingly, the peak horizontal particle velocity may be taken equal to the peak vertical. The peak horizontal displacement due to local airblast may also be taken equal to the peak vertical.

A very crude estimate of horizontal velocity and displacement time history is given in Fig. 5-69. It has been assumed that the peak horizontal particle velocity associated with each individual wave is equal to the peak vertical. The direction of propagation of the horizontal waves is always outward. Therefore, compressive waves cause outward particle velocities while tensile (relief) waves tend to reduce the outward velocity.

5.7.4 Outrunning Ground Shock

a. GIVEN: The burst, geologic conditions, material properties, arrival times and ranges of Examples 5.7.1 and 5.7.2.

b. FIND: Particle velocities and displacements due to outrunning ground shock.

c. SOLUTION: Peak outrunning vertical particle velocity is estimated from Eq. 5-52 as

$$v_m = 3.1 \times 10^8 \text{ft/sec}\left[\frac{1\text{MT}}{1\text{MT}}\right]^{2/3}\left[\frac{1\text{ft}}{3400\text{ft}}\right]^2\left[\frac{100\text{ pcf}}{110\text{ pcf}}\right]\left[\frac{1000\text{fps}}{5100\text{fps}}\right]$$

$$v_m = 4.8 \text{ ft/sec } (1.8 \text{ m/sec})$$

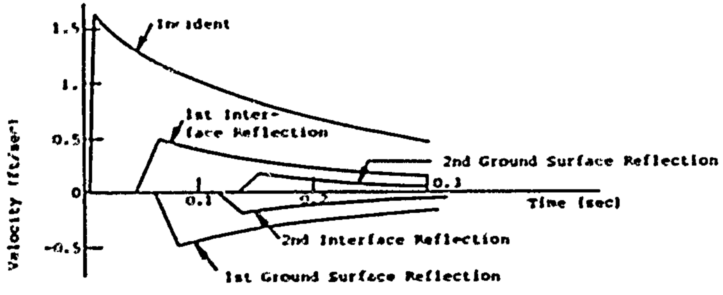

(a) Individual Velocity-Time Histories

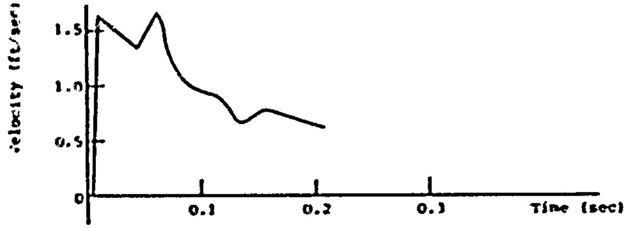

(b) Velocity-Time History

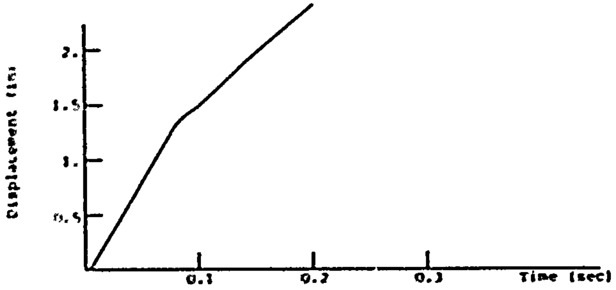

(c) Displacement-Time History

Figure 5-69 Crude Estimate of Horizontal Motion Due to Local Airblast, Ex. 5.7.3

Vertical particle velocity and displacement time histories are established from Fig. 5-31. The characteristic time, T_2, is estimated as

$$T_2 = 100 + \frac{\Delta R}{4} = 100 + \frac{(3400 - 2150)}{4}$$

$$= 413 \text{ msec.}$$

since the range at which first outrunning occurs is 2150 ft as determined in Example 5.7.2.

Outrunning vertical velocity and displacement time histories are given in Fig. 5-70. Horizontal time histories can be assumed equal to the vertical.

5.7.5 Crater-Induced Ground Shock

a. GIVEN: The burst, geologic conditions and material properties of Example 5.7.1.

b. FIND: Crater-induced particle velocities and displacements.

c. SOLUTION: The apparent crater volume for a 1 MT surface burst on 100 ft of wet clay overlying shale was estimated in Example 4.5.5 to be 1.63 x 10^8 cu. ft. Equation 5-78 relates peak horizontal displacement to crater volume, i.e.,

$$d_h = \frac{0.45V_a^{4/3}}{R^3} = \frac{0.45(1.63 \times 10^8)^{4/3}}{(3400)^3} = 1.02 \text{ ft } (0.31 \text{ m})$$

Permanent displacement is approximately one-half the peak transient or 0.51 ft (0.16 m).

The peak horizontal particle velocity is estimated from Eq. 5-81.

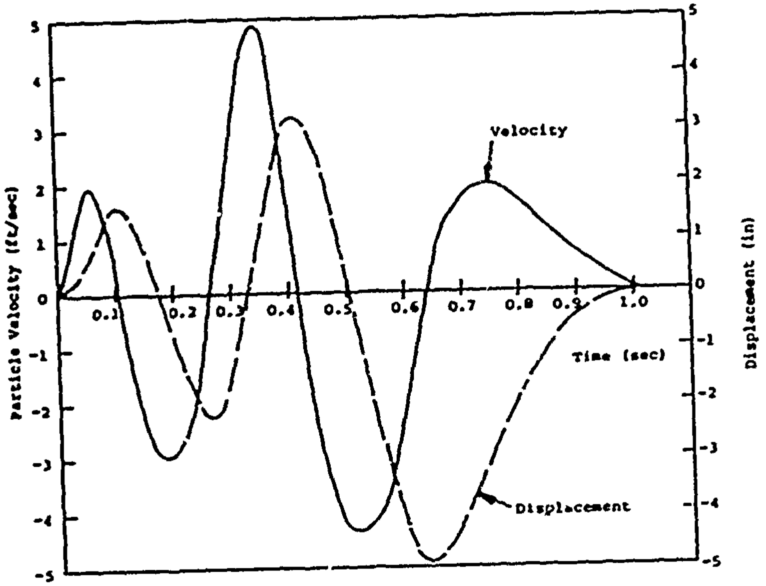

Figure 5-70 Outrunning Ground Motion Estimate for Example 5.7.4

$$v_h = 0.01C_e\left[\frac{R}{V_a^{1/3}}\right]^{-2} = 0.01(7730)\left[\frac{3400}{(1.63 \times 10^8)^{1/3}}\right]^{-2}$$

$$= 2.00 \text{ ft/sec } (0.61 \text{ m/sec})$$

where C_e is determined from Fig. 5-58 as the distance to the 100 psi level (3400 ft) divided by the time of arrival of the crater-induced wave (0.44 sec).

The rise time to peak displacement is computed using Eq. 5-82.

$$t_p = \frac{50}{C_e}\left(\frac{V_a^{2/3}}{R}\right) = \frac{50}{(7730)}\left[\frac{(1.63\times10^8)^{2/3}}{3400}\right] = 0.57 \text{ sec}$$

Wave forms for crater-induced motions are very uncertain. The peak displacement, permanent displacement, displacement rise time and peak velocity are roughly consistent with the trapezoidal horizontal velocity pulse shown in Fig. 5-71(a) (Ref. 5-50). The corresponding horizontal displacement pulse is shown in Fig. 5-71(b). Although the pulse shapes are relatively arbitrary, they agree with the computed parameters and are expected to roughly represent the gross motion. Vertical histories may be taken equal to the horizontal.

5.7.6 Composite Ground Shock

a. GIVEN: The ground shock estimates of Examples 5.7.3, 5.7.4 and 5.7.5 and the arrival times estimated in Example 5.7.2.

b. FIND: Complete vertical and horizontal

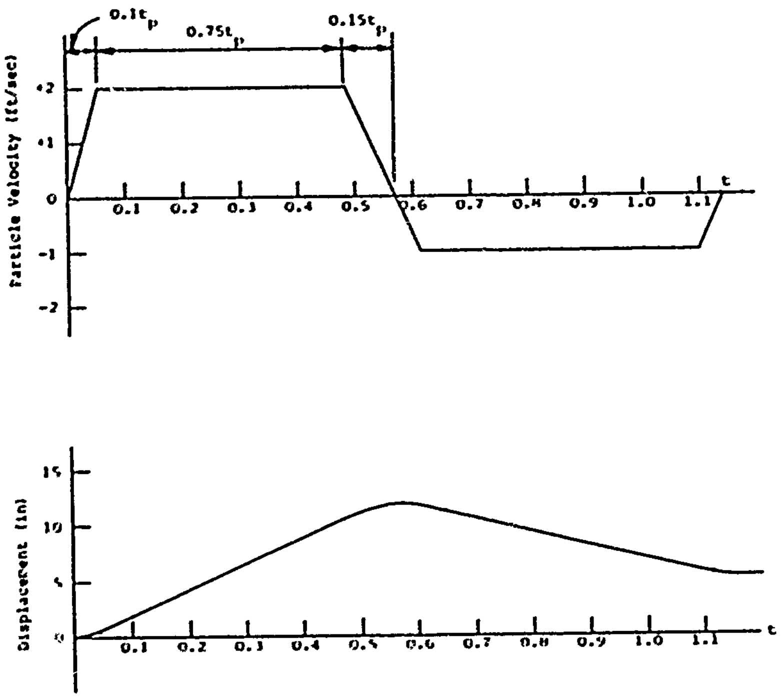

Figure 5-71 Crater-Induced Motion Estimates for Example 5.7.5

ground motion estimates at a depth of 25 feet at the 100 psi overpressure level.

c. SOLUTION: The time of arrival estimates from Example 5.7.2 are summarized below.

• Outrunning Ground Shcok	0.34 sec
• Crater-Induced Ground Shock	0.44 sec
• Airblast	0.54 sec

An estimate of the complete motion environment is obtained by simple superposition of the motions from the outrunning, airblast and crater sources in accordance with the arrival times given above. The results of superposition are shown in Figs. 5-72 through 5-75.

5.7.7 Direct-Induced Ground Shock

a. GIVEN: A 10 MT surface burst at a site composed of granite with a seismic velocity of 17,500 ft/sec.

b. FIND: Peak radial acceleration, velocity and displacement at a point 2000 feet beneath the explosion.

c. SOLUTION: Peak velocity is computed from Eq. 5-65.

$$v = 25 \text{ ft/sec}\left[\frac{W}{1MT}\right]^{2/3}\left[\frac{R}{1Kft}\right]^{-2}$$

$$v = 25 \text{ ft/sec}\left[\frac{10}{1}\right]^{2/3}\left[\frac{2}{1}\right]^{-2}$$

$$v = 29.0 \text{ ft/sec } (8.8 \text{ m/sec})$$

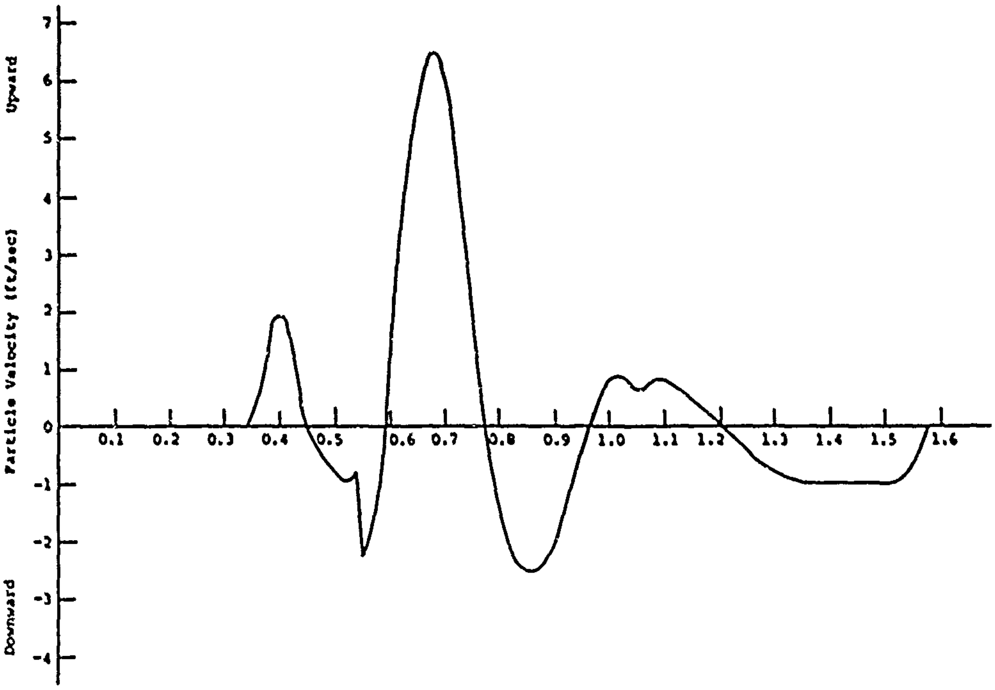

Figure 5-72 Composite Vertical Velocity-Time History for Example 5.7.6

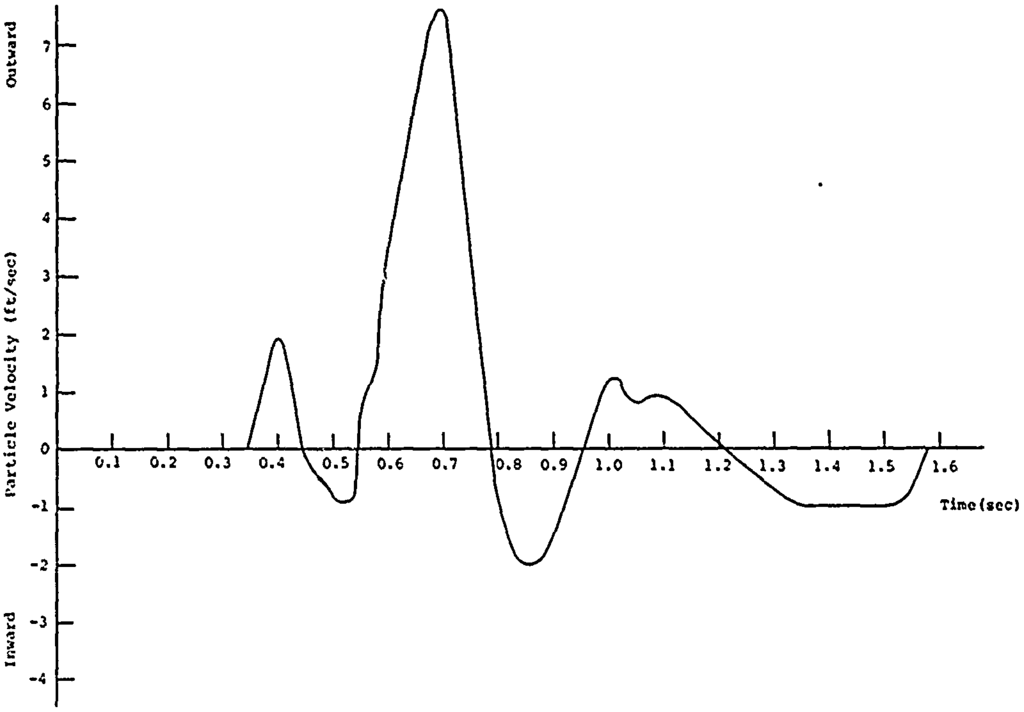

Figure 5-73 Composite Horizontal Velocity-Time History for Example 5.7.6

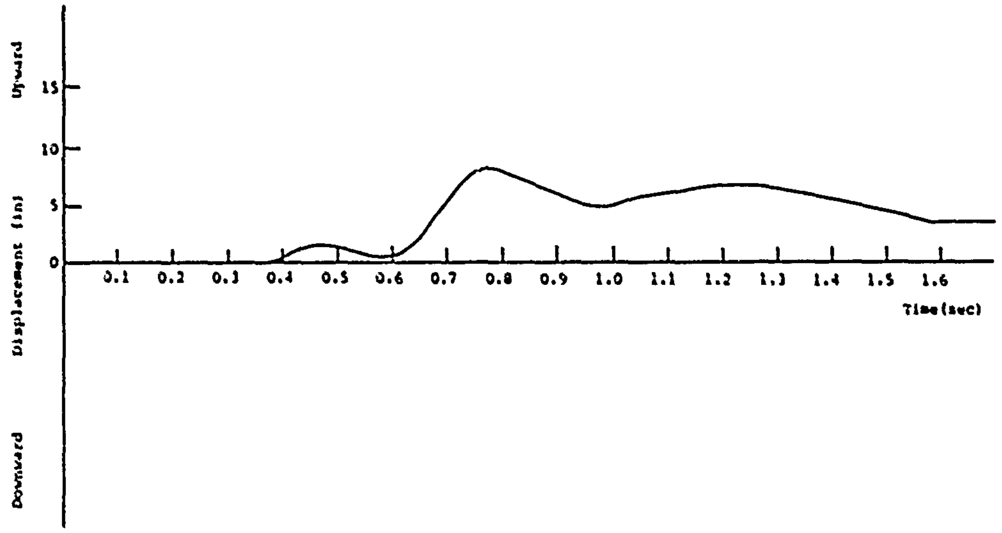

Figure 5-74 Composite Vertical Displacement-Time History for Example 5.7.6

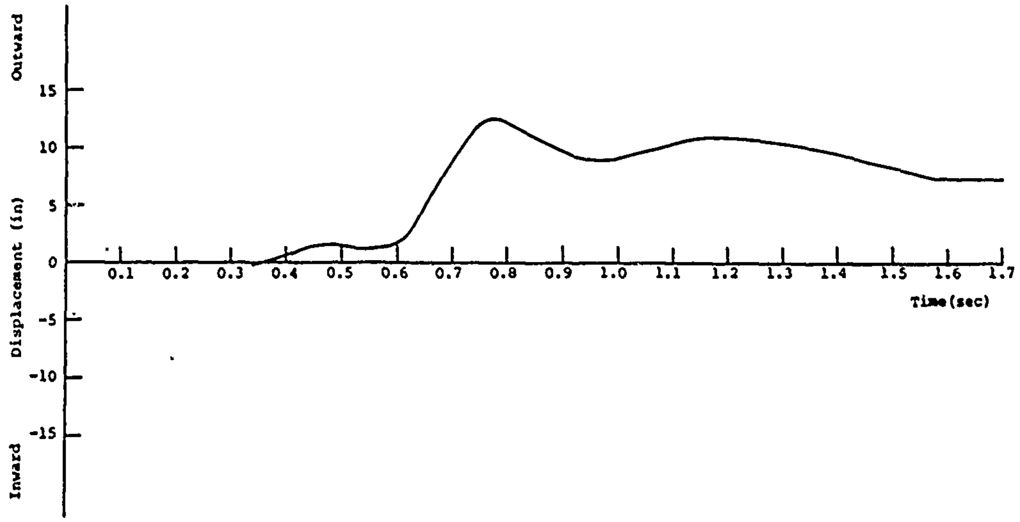

Figure 5-75 Composite Horizontal Displacement-Time History for Example 5.7.6

Peak displacement is computed from Eq. 5-66.

$$d = 4.5 \text{ in}\left[\frac{W}{1\text{KT}}\right]^{5/6}\left[\frac{R}{1\text{kft}}\right]^{-3/2}$$

$$d = 4.5 \text{ in}\left[\frac{10}{1}\right]^{5/6}\left[\frac{2}{1}\right]^{-3/2}$$

$$d = 10.8 \text{ in } (0.27 \text{ m})$$

Peak acceleration is computed from Eq. 5-67.

$$a = 140 \text{ g}\left[\frac{W}{1\text{KT}}\right]\left[\frac{R}{1\text{kft}}\right]^{-4}$$

$$a = 140 \text{ g}\left[\frac{10}{1}\right]\left[\frac{2}{1}\right]^{-4}$$

$$a = 87.5 \text{ g}$$

5.8 REFERENCES

5-1 Sauer, F.M., Clark, G.B. and Anderson, D.C., "Part Four-Empirical Analysis of Ground Motion and Cratering," *Nuclear Geoplosics*, DASA-1285 (IV), Defense Atomic Support Agency, Washington, D.C., May 1964. (U)

5-2 Bertholf, L.D. and Benzley, S.E., *TOODY II, A Computer Program for Two-Dimensional Wave Propagation*, SC-RR-68-41, Sandia Laboratories, Albuquerque, N.M., 1968. (U)

5-3 Trulio, J.G., *Theory and Structure of the AFTON Codes*, AFWL-TR-66-19, Air Force Weapons Laboratory, Kirtland AFB, N.M., June 1966. (U)

5-4 Belytochko, L., Chiapetta, R.L. and Rouse, J.D., *A Computer Code for Dynamic Stress Analysis of Structure-Media Problems with Nonlinearities (SAMSON)*, 4 Vols., AFWL-TR-72-104, Air Force Weapons Laboratory, Kirtland AFB, N.M., Feb. 1973. (U)

5-5 Kolsky, H., *Stress Waves in Solids*, Dover Publications, Inc., New York, N.Y., 1963. (U)

5-6 Richart, F.E., Jr., Hall, J.R., Jr. and Woods, R.D., *Vibrations of Soils and Foundations*, Prentice-Hall, Inc., Englewood Cliffs, N.J., 1970. (U)

5-7 Hvorslev, J., *Subsurface Exploration and Sampling of Soils for Civil Engineering Purposes*, U. S. Army Engineer Waterways Experiment Station, Vicksburg, Miss., Nov. 1949. (U)

5-8 Windham, J.E. et al, *Material Property Investigation for Project MIDDLE GUST, Events I, II and III; Subsurface Exploration and Laboratory Test Results*, Technical report S-73-10, Report 1, U. S. Army Engineer Waterways Experiment Station, Vicksburg, Miss., Oct. 1973. (U)

5-9 Grant, F.S. and West, G.F., *Interpretation Theory in Applied Geophysics*, McGraw-Hill Book Co., New York, N.Y., 1965. (U)

5-10 *Earth Manual*, U. S. Bureau of Reclamation, Denver, Colo., 1960. (U)

5-11 Deere, D.U., Merritt, A.H., and Coon, R.F., Engineering Classification of In-Situ Rock, AFWL-TR-67-144, Air Force Weapons Laboratory, Kirtland AFB, N.M., Jan. 1969. (U)

5-12 Deere, D.U. and Miller, R.P., Engineering Classification and Index Properties for Intact Rock, AFWL-TR-65-116, Air Force Weapons Laboratory, Kirtland AFB, N.M., Dec. 1966. (U)

5-13 Soil Testing Procedures, ASTM Special Compilation of Standards, D-18, American Society for Testing and Materials, Philadelphia, Pa., 1964. (U)

5-14 Lambe, T.W., Soil Testing for Engineers, John Wiley and Sons, New York, N.Y., 1951. (U)

5-15 Whitman, R.V., The Response of Soils to Dynamic Loadings, Contract Report No. 3-26, U. S. Army Engineer Waterways Experiment Station, Vicksburg, Miss., May 1970. (U)

5-16 Jackson, J.G., Jr., Factors That Influence the Development of Soil Constitutive Relations, Misc. Paper No. 4-980, U. S. Army Engineer Waterways Experiment Station, Vicksburg, Miss., July 1968. (U)

5-17 Hendron, A.J., Fulton, R.E. and Mohroz, B., The Energy Absorption Capacity of Granular Materials in One-Dimensional Compression, AFSWC-TDR-62-91, Air Force Special Weapons Center, Kirtland AFB, N.M., Jan. 1963. (U)

5-18 Hendron, A.J. and Davisson, M.T., Static and Dynamic Behavior of Playa Silt in One-Dimensional Compression, RTD-TDR-63-3078, Air Force Weapons Laboratory, Kirtland AFB, N.M., Sept. 1963. (U)

5-19 Taylor, H.M., Jr., Effect of Variation in Conventional Soil Properties on Dynamic Constrained Modulus for Several Glacial Tills, Misc. Paper No. S-73-49, U. S. Army Engineer Waterways Experiment Station, Vicksburg, Miss., June 1973. (U)

5-20 Newmark, N.M. and Haltiwanger, J.D., Principles and Practices for Design of Hardened Structures, SWC-TDR-62-138, Air Force Weapons Laboratory, Kirtland AFB, N.M., Dec. 1962. (U)

5-21

5-22 Nelson, I., Baron, M.L., and Sandler, I., "Mathematical Models for Geological Materials in Wave Propagation Studies," in Shock Waves and the Mechanical Properties of Solids, Syracuse University Press, Syracuse, N.Y., 1971. (U)

5-23 Obert, L., Windes, S.L., and Duvall, W.J., Standardized Tests for Determining the Physical Properties of Mine Rock, R.I. 3891, U. S. Bureau of Mines, 1946. (U)

5-24 Obert, L., Duvall, W.I., Rock Mechanics and the Design of Structures in Rock, John Wiley and Sons, Inc., New York, N.Y., 1967. (U)

5-25 Cooper, H.F., Jr., and Blouin, S.E., "Dynamic In-Situ Rock Properties from Buried High Explosive Arrays," Chapter 3, Dynamic Rock Mechanics, Twelfth Symposium on Rock Mechanics, Society of Mining Engineers, The American Institute of Mining, Metallurgical and Petroleum Engineers, Inc., New York, N.Y., 1971. (U)

5-26 Higgins, C.J., Post-Test Investigation of HANDEC Silos, AFWL-TR-70-39, Air Force Weapons Laboratory Kirtland AFB, N.M., Aug. 1970. (U)

5-27 Auld, H. E., D'Arcy, G.P. and Leigh, G.G., Simulation of Airblast-Induced Ground Motions (Phase II), AFWL-TR-65-26, Vol. I, Air Force Weapons Laboratory, Kirtland AFB, N.M., April 1965. (U)

5-28 Davis, S.E., "Experimental Data from the MIDDLE GUST and MIXED COMPANY CIST Events", Proceedings of the MIXED COMPANY/MIDDLE GUST Results Meeting, 13-15 March 1973, Vol. II, DNA 3151P2, DOD Nuclear Information and Analysis Center, Santa Barbara, Calif., May 1973. (U)

5-29 AFSCM 500-8, Effects of Airblast, Ground Shock, and Cratering on Hardened Structures, Air Force Systems Command, Andrews AFB, Washington, D.C., May. 1967. (U)

5-30 Ablow, C.M. and Sauer, F.M., Computation by the Method of Characteristics of Disturbance in an Elastic Half-Space Caused by a Blast-Like Surface Loading, AFWL-TR-66-113, Air Force Weapons Laboratory, Kirtland AFB, N.M., Jan. 1967. (U)

5-31 Hendron, A.J., et al, Design of Cylindrical Reinforced Concrete Tunnel Liners to Resist Air Overpressures, CR 68.010, Naval Civil Engineering Laboratory, Port Hueneme, Calif., June 1968. (U)

5-32 Neidhard, G.L., Analysis of Free-Field Data in a Half-Space Under Dynamic Loads, WL-TR-64-143, Air Force Weapons Laboratory, Kirtland AFB, N.M., April 1965. (U)

5-33 Davis, R.O., Jr., One-Dimensional Wave Propagation in Bilinear Media, AFWL-TR-70-117, Air Force Weapons Laboratory, Kirtland AFB, N.M., Dec. 1970. (U)

5-34 Lakhov, G.M. and Polyakova, N.I., Waves in Solid Media and Loads on Structures (1967), Translation FTD-MT-24-1137-71, Foreign Technology Division, Wright-Patterson AFB, Ohio, March 1972. (U)

5-35 Heierli, W., "Inelastic Wave Propagation in Soil Columns," Journal of the Soil Mechanics and Foundations Division, ASCE, Vol. 88, No. SM6, Dec. 1962. (U)

5-36 Abbott, P.A., Hand Solution of One-Dimensional Inelastic Wave Propagation Problems, AFWL-TR-67-69, Air Force Weapons Laboratory, Kirtland AFB, N.M., Oct. 1967. (U)

5-37 Weidlinger, P. and Matthews, A.T., "Shock and Reflection in a Nonlinear Medium," Journal of the Engineering Mechanics Division, ASCE, Vol. 91, No. EM3, June 1965. (U)

5-38

5-39 Swift, L.M., et al, Ground Acceleration, Stress, and Strain at High Incident Overpressures, Operation PLUMBOB, WT-1404, Stanford Research Institute, Menlo Park, Calif., May 1960. (U)

5-40 Cooper, H.F., Jr., et al, "Airblast-Induced Ground Motions In a Two-Layer Elastic-Plastic Model of the Earth," Proceedings of the Eric H. Wang Symposium on Protective Structures Technology, Vol. I, Air Force Weapons Laboratory, Kirtland AFB, N.M., July 1970. (U)

5-41

5-42

5-43 Hendron, A.J., Jr., Scaling of Ground Motions from Contained Explosions in Rock for Estimating Direct Ground Shock From Surface Bursts on Rock, Technical Report No. 15, Omaha District, U. S. Army Corps of Engineers, Omaha, Nebr., Jan. 1973. (U)

5-44 Cooper, H.F., Jr., Brode, H.L. and Leigh, G.G., Some Fundamental Aspects of Nuclear Weapons, Paper presented at NATO Defense Seminar, Bodo, Norway, 15 September 1971. (U)

5-45 Alekseyenko, V.C., "Experimental Investigation of the Dynamic Stress Field in Soft Earth During a Contact Explosion," Translation of Applied Mechanics and Technical Physics, No. 5, FTD-MT-64-61, 8 February 1965. (U)

5-46 Cooper, H.F., Jr., Empirical Studies of Ground Shock and Strong Motions in Rock, RDA-TR-3601-002, R & D Associates, Santa Monica, Calif., Oct. 1973. (U)

5-47

5-48

5-49

5-50 Bratton, J.L., (Private Communication), Air Force Weapons Laboratory, Kirtland AFB, N.M., Apr. 1974. (U)

SECTION VI

RADIATION PHENOMENA

6.1 INTRODUCTION

6.1.1 General

Although the blast, shock, cratering and ground motion effects discussed in the preceding sections are undoubtedly the severest structural damage-producing effects, there are additional nuclear effects which impose constraints on the design and analysis of protective construction. Effective and efficient design or analysis of a total weapon system or facility requires that the basic structures serve to mitigate or defeat all nuclear weapon effects which might damage the structure, structure contents, and/or personnel. Radiation shielding requirements for the protection of personnel and equipment can control the structural design in some cases.

The initial radiations (i.e., the gamma rays, neutrons and X rays) from the extremely high temperatures of the bomb vapors are largely determined by the bomb materials and the construction of the nuclear weapon itself. The fraction of energy which may be radiated out as X rays before the bomb begins to blow apart depends largely on its yield-to-mass ratio and the type of material which surrounds the weapon. The total fraction of energy which is released in the various forms of radiation may range from a very small percent to more than 80 percent of the total energy generated (Ref. 6-1).

The types of radiation of interest in protective construction include initial gamma rays and neutrons, X rays, electromagnetic pulse (EMP), thermal radiation and residual gamma radiation. Approximately 5 percent of the total energy from a typical air burst of a fission weapon appears at a distance as initial gamma rays and neutrons, 35 percent as thermal radiation and 10 percent as residual radiation. Because of the high

intensities, very long ranges and long life (in the case of the residual nuclear radiation), these radiations are important as a threat to structures, equipment, and/or personnel. Although radiation effects may not be the governing factor in the design of protective structures, special design considerations are often necessary to provide adequate protection for personnel and equipment within the facility. The designer must have a general knowledge of radiation effects in order to predict levels of radiation at a given location, estimate tolerance levels for personnel and equipment, and provide designs adequate for the desired level of protection. For target analysis, such knowledge is necessary to predict effects on equipment and personnel.

Detailed prediction of the free-field radiation phenomena requires the use of sophisticated computer programs which account for the details of weapon design. energy partition, burst medium, intervening atmospheric conditions, topography, etc. However, none of the major radiation effects are critically dependent on complete details and useful estimates can be, and have been, made by the procedures presented in this section.

The radiation phenomena considered in this section are

- Initial radiation (gamma rays, neutrons and X rays)
- Electromagnetic pulse (EMP)
- Thermal radiation
- Residual nuclear radiation (fallout)

This section will emphasize simple approximations and prediction techniques which are adequate for preliminary design and, in some cases, for detailed analysis and final design. Radiation effects are loosely related to overpressure level roughly as summarized below.

a. At overpressures of about 1000 to 10,000 psi (689 to 6890 N/cm^2), the extremely high surface energy deposition may cause significant damage to exposed structural materials, and transmitted levels may damage internal electronic equipment. All radiation environments must be considered in this region.

b. At overpressures of about 50 to 500 psi (34.5 to 345 N/cm^2), surface-flush structural members required for blast protection are generally sufficiently massive to provide protection from the initial radiation, the thermal radiation, and the residual radiation environments. However, EMP protection will have to be considered.

c. At low overpressures of about 2 to 20 psi (1.38 to 13.8 N/cm^2), the structural members required for blast protection are generally not sufficiently massive to provide protection from initial and residual radiation. Radiation effects may govern the design in this region. EMP protection will also have to be considered.

6.1.2 Definition of Terms

Discussion of the various forms of radiation in the following paragraphs will involve use of terms which may be unfamiliar to some. The following glossary of terms is provided to facilitate an understanding of later material.

Absorbed Dose

The energy absorbed from the nuclear radiation per gram of exposed material. This term is expressed in reps or rads.

Alpha Particles

Alpha particles are identical in structure with the nuclei of helium atoms. Because of their relatively large mass, they are very low in penetrating power.

Beta Particles

Beta particles are identical to the electrons that orbit about the nuclei of atoms except for their origin and speed. They originate in the nucleus of an atom, have a very small relative mass, and travel at high speed.

Dose Rate

Dose rate is the rate at which radiation is being received from the field of contamination. It is the amount of ionizing (or nuclear) radiation to which an individual would be exposed or receive per unit time. It is usually given in roentgens, rads or rem per unit time. Units of ergs per gram (joules per kilogram) per unit time are sometimes used to indicate energy which the material would absorb.

Exposure Dose

This is the integrated dose rate with respect to time. It is the total quantity of radiation to which a point or body would be subjected in a given period of time. When describing gamma radiation, it is usually expressed in roentgens.

Fluence

The total number of particles, waves or energy passing through or impinging upon a unit area. It is the same as integrated flux. Fluence is most often used in describing neutron and X ray radiation doses.

Flux

Flux is the number of particles, waves or energy passing through or impinging upon a unit area per unit time. It is used most often in describing neutron and X ray radiation.

Rad

A unit of absorbed dose of radiation. It represents the absorption of 100 ergs (10^{-5}j) of nuclear (or ionizing) radiation per gram of the absorbing material or tissue. For gamma radiation, an exposure dose of 1 roentgen will cause a tissue-absorbed dose of very nearly 1 rad.

Radiant Exposure

This term has a meaning similar to exposure dose, except that it is only used in describing thermal radiation. It is the integrated thermal dose rate with respect to time and is usually expressed in calories or joules per square centimeter.

Rem

The rem (roentgen equivalent mammal) is a unit of biological dose of radiation. The rem is related to the rad by a factor called the RBE (relative biological effectiveness).

Dose in rem $\cong$ RBE x dose in rads

The RBE is approximately unity for gamma, beta and fast neutron radiation. Therefore, for radiation incident on soft tissue, it can be said that

Number rem $\cong$ number rads $\approx$ roentgens

Rep

The rep (roentgen equivalent physical) is a unit of absorbed dose of any ionizing radiation which results in the absorption of about 97 ergs of energy per gram ($\sim 10^{-2}$ j/kg) of soft tissue. For soft tissue, the rep and rad are essentially the same.

Residual Radiation

Residual radiation is defined as that radiation emitted later than one minute after the explosion. Since direct neutron effects are confined to initial radiation, alpha and beta particles and gamma rays constitute the radioactivity that is associated with residual radiation.

Roentgen

The strength of a gamma radiation field is usually expressed in roentgens. It is an international unit of X ray or gamma radiation and is that quantity of radiation resulting in the absorption of about 87 ergs per gram ($\sim 9\text{x}10^{-3}$ j/kg) of air. It is a measure of exposure dose or dose rate for gamma and X ray radiation.

Slant Range

The distance from a given location, usually on the earth's surface, to the point at which the detonation occurred.

6.2 INITIAL NUCLEAR RADIATION

6.2.1 General

Nuclear radiation results from both the fission and fusion reactions and is released both at the instant of the explosion and over an extended period of time. It is convenient for protective construction purposes to consider nuclear radiation as divided into two categories, initial and residual (fallout), with the latter further subdivided into early and late. The lines of demarcation are not well defined, but initial nuclear radiation is generally considered to be that emitted within the first minute of the explosion, with the residual radiation or fallout as that emitted later. For underground detonations, the initial and residual radiation phases tend to merge into each other and the above distinction is not as meaningful. Initial radiation includes gamma rays, neutrons, X rays and alpha and beta particles.

Because of their low penetrating power, the alpha and beta particles formed in the early stages of the nuclear explosion will not normally reach the ground from an air burst. Although the range of an alpha particle depends on its initial energy, in most cases it will travel no more than about 2 inches (5.08 cm) in air before its energy is dissipated. Beta particles are more penetrating than alpha particles, but in many cases their range in air is still only 10-12 feet (3.05 - 3.66 m). Neither of these particles represents a serious hazard unless inhaled or ingested into the body. Both particles also result from the radioactive decay of bomb debris at later times.

Gamma rays consist of streams of photons, small packets of energy, having no mass or electrical charge and traveling with the speed of light. They are quite similar to X rays except they are higher in energy and originate in a nucleus. A portion of the total gamma environment is emitted in the initial fission process, but the majority of the gamma rays arriving at distant locations are produced by secondary processes, e.g. neutron capture or interaction with nuclei of various materials present in the weapon and surrounding atmosphere. Gamma rays are extremely penetrating. They have a range in air of several thousand yards or meters and can cause damage to structural materials, equipment and personnel. Structures used as protective shelters must have sufficient mass so oriented as to reduce the gamma ray penetration to tolerable limits for electronic equipment and sheltered personnel. If they are absorbed by the body in sufficient quantity, either externally or internally, they constitute a very serious biological hazard. The free-field gamma ray flux is usually expressed in photons per square centimeter per second. Gamma fluence is expressed in photons per square centimeter, while biological doses are in roentgens.

Neutrons are fundamental parts of the nucleus of an atom and are released in both the fission and fusion processes. Neutron shielding is a difficult problem, different from that of shielding against gamma rays. Neutrons, if they have high enough energy, may be captured by nuclei of atoms to form new isotopes that are generally unstable and give off beta and gamma radiation. Thus, although neutrons do not directly cause ionization, they may cause the emission of alpha, beta, and gamma radiation with the attendant biological hazard of ionization. Neutron flux is usually expressed in neutrons per square centimeter per second. Neutron fluence is expressed in neutrons per square centimeter, while doses are in rads or rems.

X rays are electromagnetic radiations of high energy having wavelengths shorter than those in the ultraviolet region. They are frequently classified as hard or soft, with the latter having longer wave lengths, lower energies, and being more easily absorbed than the hard X rays. They are, nevertheless, radiations of high energy compared with ultraviolet or visible light.

The absorption of the thermal X rays, which are mainly in the soft X ray region, by the surrounding ambient medium is accompanied by an increase in temperature resulting in the formation of the fireball which then emits the thermal radiation. When the nuclear detonation occurs in air at near sea-level conditions, these thermal X rays also cause atmospheric ionization with a greatly increased density of electrons. These electrons affect electromagnetic transmission (e.g., radio and radar) by attenuating and/or refracting the signals. Hard X rays at close-in ranges interact with exposed structural elements. This incident X ray radiant energy is absorbed by near-target surfaces, converted into thermal energy and may result in damage to structural materials. X ray flux is usually expressed in calories or joules per square centimeter per second.

Table 6-1 summarizes the above radiation types and their characteristics.

6.2.2 Prediction Techniques

a. Gamma Radiation

The intensity of prompt gamma radiation decreases with distance from the point of detonation because of spherical divergence (inverse-square law) and interactions between the gamma photons and the gas molecules comprising the atmosphere. Atmospheric density affects this attenuation in that the greater the density, the greater the attenuation. The path of radiation deviates locally from simple line-of-sight because of these scattering interactions. For this reason, more than a simple shield is required for protection. Figure 6-1 indicates the total amount of initial gamma radiation which would be measured at various distances from air bursts of varying yields. These data were obtained from the

Table 6-1

TYPES OF INITIAL NUCLEAR RADIATION

TYPE	INTEGRATED FLUX UNITS	RANGE IN AIR	HAZARD	PROTECTION TECHNIQUE
Alpha Particles	-	Two Inches (5.08 cm)	Biological, if inhaled or ingested	Filter incoming water and air, decontaminate personnel
Beta Particles	-	Ten - Twelve Feet (3.05 - 3.66 m)	Biological, if inhaled or ingested	Filter incoming water and air, decontaminate personnel
Gamma Rays	Photons/cm^2 (Roentgens)	Several Thousand Yards or Meters	Structural, Biological, and Equipment	Shielding
Neutrons	Neutrons/cm^2 (Rads or Rems)	Several Thousand Yards or Meters	Structural, Biological, and Equipment	Shielding
X rays	Calories/cm^2 or Joules/cm^2	Several Hundred Yards or Meters	Structural, Biological, and Equipment	Shielding

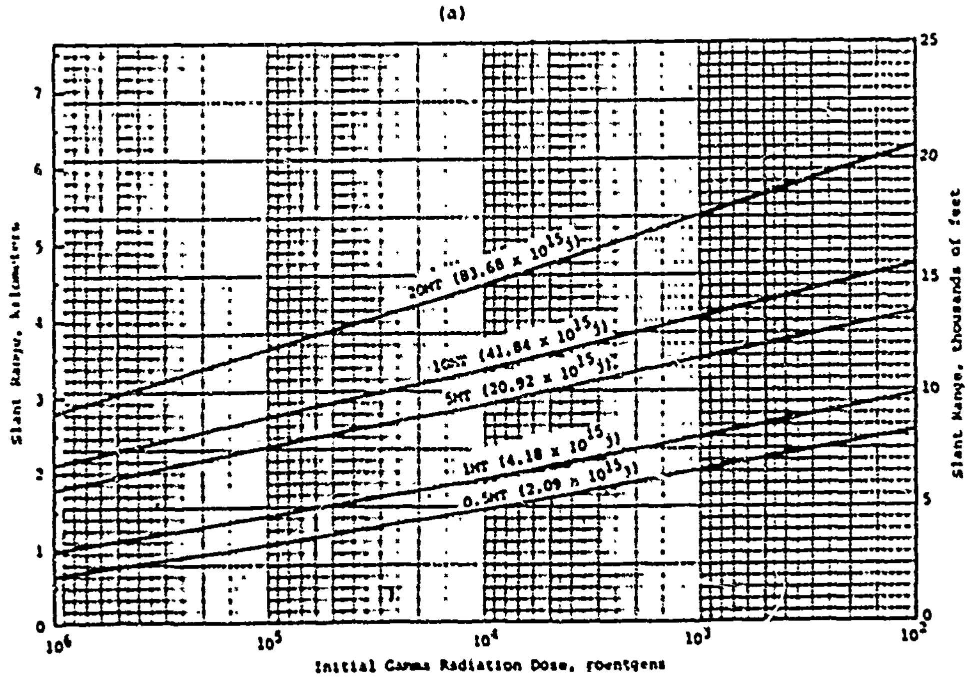

Figure 6-1 Initial Gamma Radiation Dose Vs. Slant Range for Air Density of 1.1gm/liter

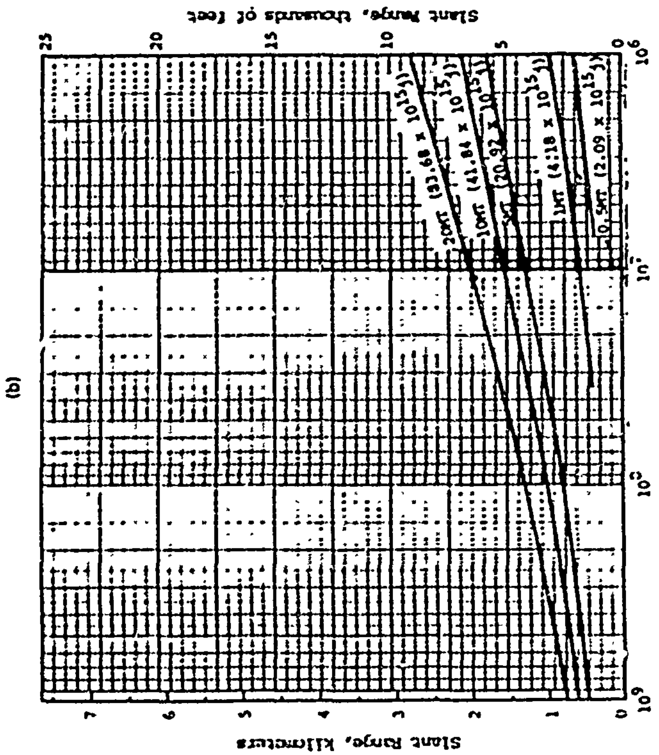

Figure 6-1 (cont.) Initial Radiation Dose Vs. Slant Range for Air Density of 1.1gm/liter

following expressions from Ref. 6-1.

$$D_\gamma = 7 \times 10^{13}\ f\ \alpha \left[\frac{W}{1MT}\right]\left[\frac{1ft}{R}\right]^2 \exp\left[-\left(\frac{\rho}{1gm/liter}\right)\left(\frac{R}{1ft}\right)\left(\frac{1ft}{\lambda}\right)\right] r \qquad (6\text{-}1)$$

$$= 1.55 \times 10^{12}\ f\ \alpha\left[\frac{W}{10^{15}j}\right]\left[\frac{1m}{R}\right]^2 \exp\left[-\left(\frac{\rho}{1kg/m^3}\right)\left(\frac{R}{1m}\right)\left(\frac{1m}{\lambda}\right)\right] r$$

where

D_γ = gamma dose in roentgens

$$\alpha = \left[1 + 6\left(\frac{W}{1MT}\right)^2\right] \Big/ \left[1 + 0.03\left(\frac{W}{1MT}\right)^2 + 0.005\left(\frac{W}{1MT}\right)^3\right]$$

$$= \left[1 + 0.3427\left(\frac{W}{10^{15}j}\right)^2\right] \Big/ \left[1 + 0.0017\left(\frac{W}{10^{15}j}\right)^2 + 0.000068\left(\frac{W}{10^{15}j}\right)^3\right]$$

$$\lambda = 1070 + 1.5\left[\frac{W}{1MT}\right]^2 \text{ ft}$$

$$= 326.14 + 0.0261\left[\frac{W}{10^{15}j}\right]^2 \text{ m}$$

W = yield in MT or joules

R = range

f = fission fraction (typically ≈ 1/2)

ρ = air density in grams per liter or kg per cubic meter

λ = mean free path

α = effective amplification of yield

r = roentgens

For a surface burst, the dust and debris produced by the explosion will cause a reduction in the exposure dose at any given distance from the burst point. Reference 6-2 suggests that the initial gamma dose from a surface burst be taken as two-thirds of that from an air burst at the same slant distance. Reference 6-3 agrees for surface burst-surface target, low yield weapons. However, for large yield weapons, the initial gamma incident on surface targets from surface bursts can be much larger than that from an air burst at corresponding slant ranges. Reference 6-3 presents curves and tables for determining initial gamma dose for various burst and target locations.

b. Neutron Radiation

The production and emission of neutrons and the energy spectrum and total number of neutrons received at a location are a function of weapon design. In general, the thermonuclear fusion processes produce more high-energy neutrons than do the fission processes. Thus, any representation of neutron flux intensities as a function of yield and distance by a single curve must be over-simplified.

The various detection methods using boron counters, fission chambers, and foil activation can provide measurements in absorption units (rad). These must be converted to units of biological dosage (rem) before the effects on humans can be assayed. The RBE conversion factor is different for different energies varying from 1.0 for fast neutrons to 2.5 for thermal neutrons. Reference 6-2 suggests a value of about 1; however, this value is subject to further study and possible future revision.

Despite the preceding deficiencies, it is necessary that a determination be made of neutron dose for design or analysis purposes. Figure 6-2 indicates the amount of initial neutron radiation which would be measured at various slant ranges from a 1MT (4.184 x 10^{15}J) air burst for an average air density of 1.1 grams per liter. These data were obtained from the following expression from Ref. 6-1.

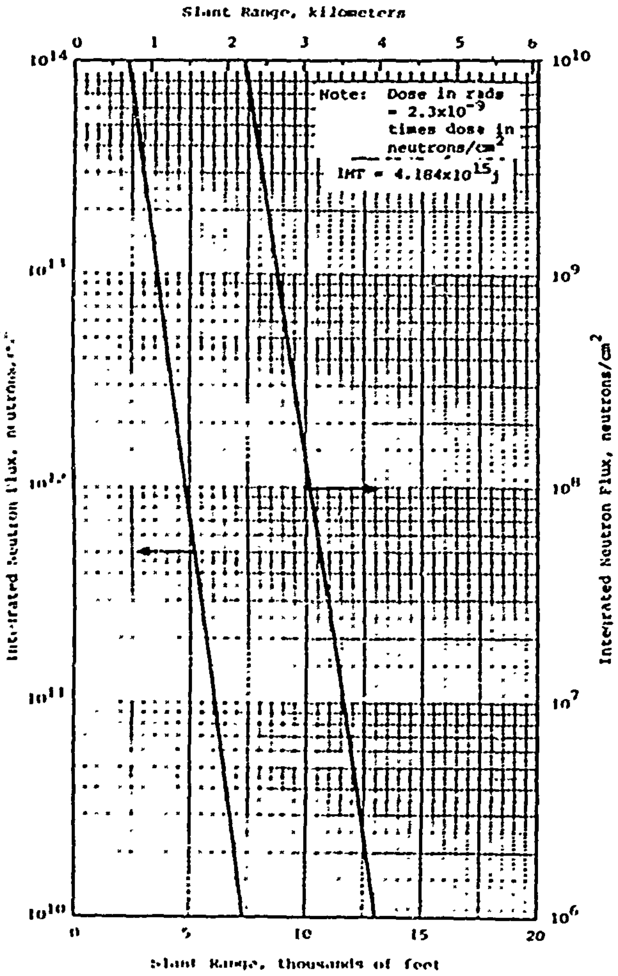

Figure 6-2 Integrated Neutron Flux Vs. Slant Range for 1MT

$$D_n = 2 \times 10^{22}\left[\frac{W}{1KT}\right]\left[\frac{1ft}{R}\right]^2 \exp\left[-\left(\frac{R}{1ft}\right)\left(\frac{\rho}{1gm/liter}\right)\Big/780\right] n/cm^2$$

$$= 4.44 \times 10^{20}\left[\frac{W}{10^{15}j}\right]\left[\frac{1m}{R}\right]^2 \exp\left[-\left(\frac{R}{1m}\right)\left(\frac{\rho}{kg/m^3}\right)\Big/238\right] n/cm^2 \quad (6\text{-}2)$$

$$D_n = 5 \times 10^{13}\left[\frac{W}{1KT}\right]\left[\frac{1ft}{R}\right]^2 \exp\left[-\left(\frac{R}{1ft}\right)\left(\frac{\rho}{1gm/liter}\right)\Big/780\right] rads$$

$$= 1.1 \times 10^{12}\left[\frac{W}{10^{15}j}\right]\left[\frac{1m}{R}\right]^2 \exp\left[-\left(\frac{R}{1m}\right)\left(\frac{\rho}{kg/m^3}\right)\Big/238\right] rads \quad (6\text{-}3)$$

where

D_n = neutron dose.

Although the *neutron dose from a surface burst* is less than that *from* an air burst, a correction factor of unity is recommended in the absence of more definitive information. For other yields, the data shown in Fig. 6-2 are multiplied by the yield in megatons (in SI units, multiply by the ratio $W/4.184 \times 10^{15}j$).

c. X Radiation

As for the other forms of initial nuclear radiation, the characteristics of X rays are dependent upon weapon design. The intensity, or flux, decreases with increasing distance from the point of detonation because of spherical divergence and absorption in the atmosphere. The rate of absorption depends primarily on the density of the atmosphere and the energy level of the radiation. X rays can travel great distances at very high altitudes, but at altitudes of less than approximately 40 miles (64.4 km), they are absorbed within very short distances (a few feet or meters for thermal X rays) and give rise to fireball and blast phenomena.

Reference 6-4 gives the integrated X ray flux on a surface at a distance, R, from a nuclear

detonation in a vacuum as

$$F = 8 \times 10^3\left[\frac{Y_r}{1MT}\right]\left[\frac{1km}{R}\right]^2 cal/cm^2$$

$$= 8\left[\frac{Y_r}{10^{12}j}\right]\left[\frac{1km}{R}\right]^2 joules/cm^2 \quad (6\text{-}4)$$

where

Y_r = radiant yield in megatons or joules

R = range in kilometers

Reference 6-2 suggests that 60 to 70 percent of the total energy from a nuclear detonation *can be initially X rays; therefore, it is suggested* that Y_r be taken equal to 70 percent of the total yield. The integrated X ray flux *(fluence) given by* Eq. 6-4 *represents* an upper limit and actual fluence incident on a structure on the ground surface would be a small fraction of this value.

In order to obtain a more realistic estimate of the flux incident on a structure from a near-surface burst, Eq. 6-4 should be modified to account for X ray absorption by the atmosphere and the ground surface. It is suggested that 30 *percent* of the total X ray radiation be considered an upper limit on the amount of absorption by the earth's surface. Actual absorption may be much less and, under some conditions, most of the incident radiation may be reflected.

Absorption by air molecules can be assumed to be an exponential function of the total mass of air between the source and the target and the energy level of the X radiation. Equation 6-4 then becomes

$$F = 8 \times 10^3 \left[\frac{Y_r}{1KT}\right]\left[\frac{1km}{R}\right]^2 \exp\left[-\left(\frac{\mu}{1cm^2/gm}\right)\left(\frac{R}{1km}\right)\left(\frac{\rho}{1gm/cm^3}\right)\times 10^5\right] cal/cm^2 \tag{6-5}$$

$$\approx 8 \left[\frac{Y_r}{10^{12}J}\right]\left[\frac{1km}{R}\right]^2 \exp\left[-\left(\frac{\mu}{1cm^2/kg}\right)\left(\frac{R}{1km}\right)\left(\frac{\rho}{kg/m^3}\right)\times 10^5\right] joules/cm^2$$

where

μ = mass absorption coefficient for air, cm^2/gm or cm^2/kg

ρ = mass density of air, gm/cm^3 or kg/m^3

Figure 6-3 is a plot of the mass absorption coefficient for air as a function of photon energy level. It is based on data from Ref. 6-5. Also plotted is the mass absorption coefficient for concrete for a density of 2.35 gm/cm^3. In order to use Fig. 6-3, it is necessary to know the X ray photon energy spectrum for the weapon of interest. This spectrum is a plot of the percent of X ray photons at the various energy levels and will have a maximum value at some energy level characteristic of the weapon. The mass absorption coefficients given in Fig. 6-3 assume a monoenergetic source, and it is recommended that the mass absorption coefficient corresponding to this peak value be used in calculating attenuation of the X ray radiation. Equation 6-5, with the proper value of Y_r, μ and R, will give an upper limit on the X ray radiation at a given slant range from the point of detonation. It is suggested that a lower limit be taken as 70 percent of that given by Eq. 6-5.

Since a major portion of the X rays are absorbed so rapidly at lower altitudes, they are not considered a serious threat to most protective structures except at very close slant ranges and for their effect on radio communications.

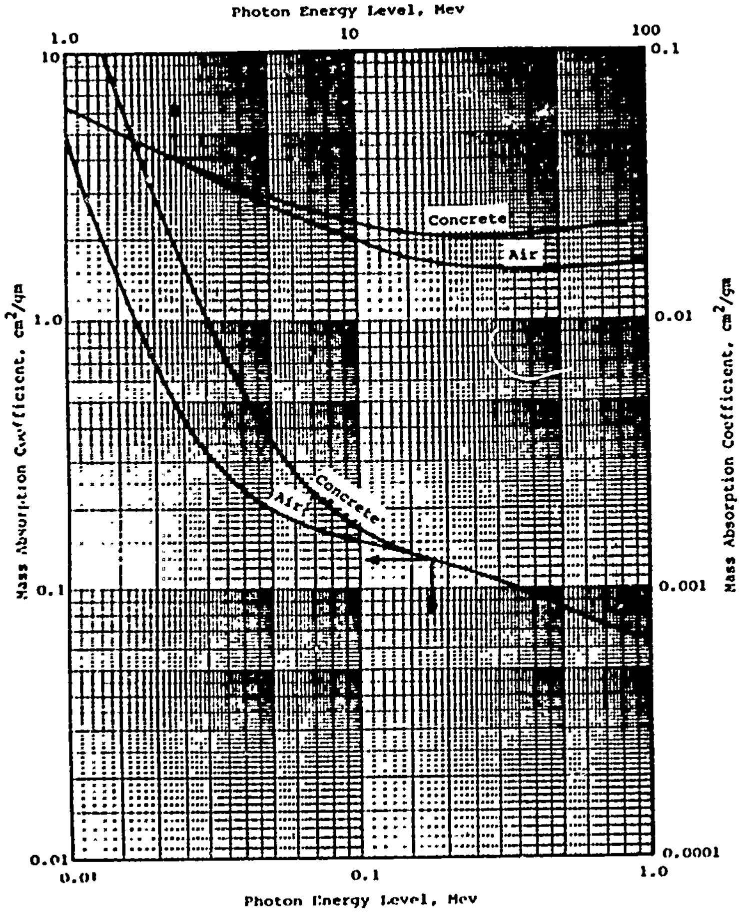

Figure 6-3 Mass Absorption Coefficients (Ref. 6-5)

6.3 ELECTROMAGNETIC PULSE (EMP)

6.3.1 General

A nuclear explosion is accompanied by an electromagnetic pulse which can cause damage to electrical/electronic equipment and systems in hardened protective structures. The EMP is electromagnetic in composition with most of its energy within the radio frequency spectrum, ranging approximately from power-line frequencies to radar-system frequencies. The EMP is crudely similar to the waves generated by nearby lightning or from a radio broadcast station.

There are, in general, two different mechanisms by which a nuclear explosion produces the EMP, i.e., the Compton electron effect and the field displacement effect. In the case of a burst on or near the earth's surface, the Compton-electron effect is the principal mechanism. It is associated with the creation of an asymmetry in the electric charge distributions in the region surrounding the detonation. The field displacement effect is the result of the rapid expansion of weapon residues in the earth's magnetic field. It can be responsible for electromagnetic signals from an underground burst, where the expansion of weapon debris is constrained by the surrounding material in a more or less spherically symmetrical manner, or from those at high altitudes, where the only immediate interaction of the detonation is with the geomagnetic field.

As noted above, the Compton-electron effect is the principal means of EMP generation in near-surface bursts (within 350 feet or 107 meters or so). In this case, the earth's surface confines expansion of weapon debris and radiation to the upward hemisphere and causes asymmetry in the electrical charge distribution around the detonation. The initial gamma radiation emitted from the detonation strikes the molecules in the surrounding atmosphere causing electrons to be violently separated from the air molecules. These Compton recoil electrons move away from the detonation, leaving behind the much heavier and slower moving positive ions, as shown in Fig. 6-4 from Ref. 6-6. From a distance, this outward motion of electrons appears to be a pulse of current in one direction which radiates electromagnetic energy in a manner similar to that of a transmitting antenna. This radiation constitutes the first part of the characteristic signal of the explosion (Ref. 6-2).

The Compton electrons also produce large numbers of electron ion pairs as they move through the air. Under the intense radial electric field produced by the separation of positive and negative charges, the electrons are driven back towards the detonation point producing a *second* current pulse and magnetic field. After these initial motions, the fields decay in a complicated fashion producing intense magnetic and electric fields. The highly ionized gas (or plasma) surrounding the detonation point undergoes oscillations which damp out in a short time, but, while they last, they also produce electromagnetic waves in the radio frequency range.

The sudden separation of two unlike charges also creates force fields, electromagnetic in nature, which can affect the positions of other charges. This disturbance propagates away from the displaced charges at the speed of light and can affect the positions of other charges at great distances. These fields which are not rapidly attenuated are termed the radiated fields. These electromagnetic fields can cause charges to flow in very distant conductors such as metallic structures, antennas, or electrical wiring.

Within the source region, the electric and magnetic field distribution is similar to that in the neighborhood of an AM broadcast antenna. As the fields rise and decay, radiation occurs which is capable of propagating energy over great distances. At distances of about 6 miles (10 km) or more, the higher frequency components are attenuated much more rapidly than the

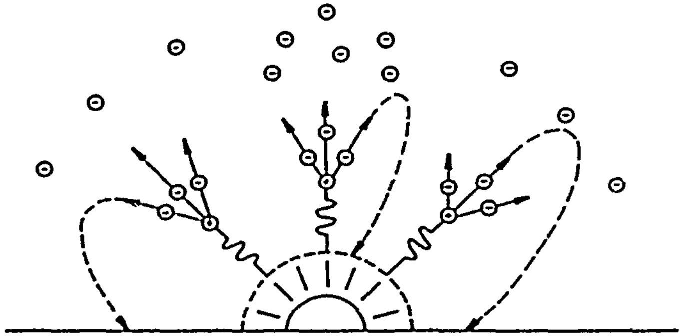

Figure 6-4 Compton Electrons (Ref. 6-6)

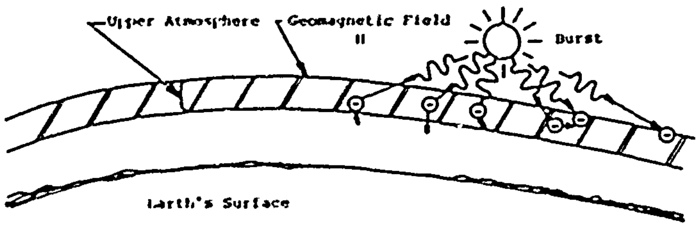

Figure 6-5 High Altitude Phenomena (Ref. 6-6)

lower ones because of radiation and propagation characteristics. Thus, a wide spectrum of waveshapes and amplitudes can be anticipated depending on the location of the detonation, the yield of the weapon, and the location of the installation (Ref. 6-6).

When a detonation occurs outside the earth's atmosphere, i.e., a high-altitude burst, the field-displacement mechanism can create an electromagnetic pulse. Immediately after detonation, the hot weapon debris is essentially a highly ionized vapor which is expanding rapidly creating a source region of high field intensity which is more pancake than hemispherical in shape (Fig. 6-5). The interaction of this vapor with the earth's geomagnetic field causes a violent distortion of the latter, and the disturbance propagates away from the source region as a hydromagnetic wave. This resulting EMP field can appear over a substantial portion of the earth because of the great height of the source region. The actual amplitude and wave shape is highly dependent upon the height and yield of the weapon as well as the geomagnetic field intensity and direction in the upper atmosphere.

It is probable that the field-displacement mechanism may also operate to produce an EMP signal from an underground burst. In this case, the expansion of the debris is limited to a few yards by the containment of the earth overburden, thus producing only small signals detectable at short ranges.

6.3.2 Prediction Techniques

Much of the information pertaining to prediction of EMP field strengths is classified. Reference 6-7 presents procedures and curves for prediction of electric and magnetic field strengths and should be consulted when more than preliminary estimates are required. The following discussion is taken primarily from Ref. 6-6.

The fields produced by a single high-altitude detonation can have considerable variation in amplitude, time dependence and direction, depending upon yield, height of burst, location of the observer and orientation with respect to the geomagnetic field. The prediction of the EMP field strength at a given distance from a given yield is complex and not amenable to simple techniques. Reference 6-6 describes a typical field environment which is defined to be close to a worst case without being too far from the average. Figure 6-6 (from Ref. 6-6) shows the electric field strength near the ground as a function of time for this typical environment. One graph suffices for both the electric and magnetic fields because, as a free-space plane wave, the ratio of electric and magnetic field strength is constant. Direction of the fields is arbitrary, except that the electric field, E, must be perpendicular to the magnetic field. The reason for this is that different orientations of observer and burst can produce any polarization of the fields.

The field shown in Fig. 6-6 is the incident field, i.e., that which propagates towards the earth. The reflection of this field from the ground must, in general, be considered when determining the total (measured) field at a given point. The total field can be either larger or smaller than the incident field depending upon polarization.

The field given in Fig. 6-6 has an analytic representation in terms of exponentials. The incident electric field, E_i, is given by

$$E_i(t) = E_o\,[e^{-\alpha t} - e^{-\beta t} - A\,(e^{-\gamma t} - e^{-\delta t})] \qquad (6\text{-}6)$$

where

t = time in seconds

$\alpha = 1.5 \times 10^6\ \mathrm{sec}^{-1}$

$\beta = 2.6 \times 10^8\ \mathrm{sec}^{-1}$

$\gamma = 2.0 \times 10^5\ \mathrm{sec}^{-1}$

$\delta = 5.0 \times 10^5\ \mathrm{sec}^{-1}$

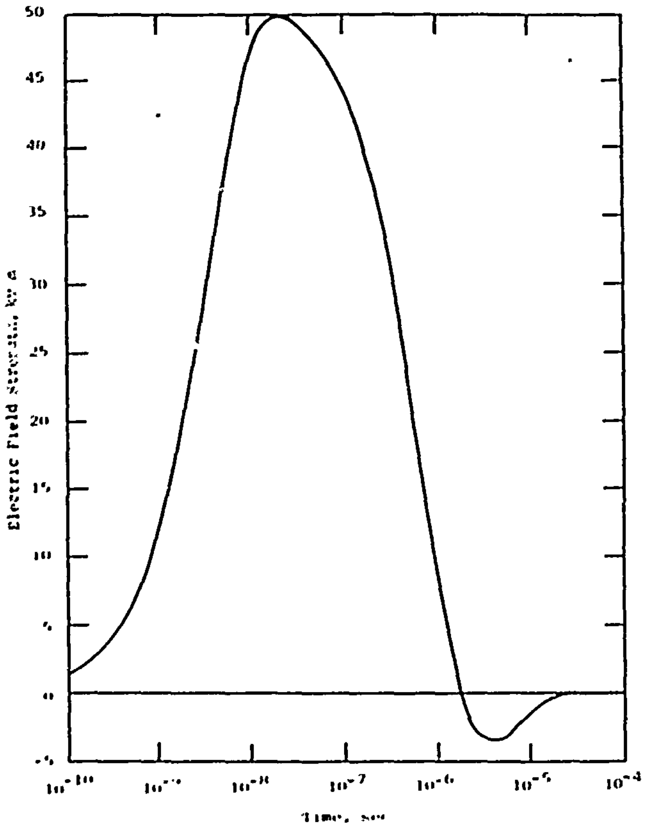

Figure 6-6 Electric Field Strength as a Function of Time for EMP (High-Altitude Detonation) (Ref. 6-6)

$$\Lambda = \frac{\alpha^{-1} - \beta^{-1}}{\gamma^{-1} - \delta^{-1}}$$

$E_o = 5 \times 10^4/0.9646$ volts/meter

The fields comprising the EMP induce currents in conductors in precisely the same fashion as any electromagnetic field, e.g., radio waves. However, because EMP is a pulse, a single frequency cannot be ascribed to it, in contrast to radio waves. The energy content at different frequencies can be studied via the Fourier transform, which for $E_i(t)$ defined by Eq. 6-6 leads to the function $E_i(\omega)$

$$E_i(\omega) = \frac{E_o}{\sqrt{2\pi}}\left[\frac{1}{\alpha + i\omega} - \frac{1}{\beta + i\omega} - \frac{\Lambda}{\gamma + i\omega} - \frac{\Lambda}{\delta + i\omega}\right] \qquad (6\text{-}7)$$

where ω is the frequency of the radiation field.

The energy content is then proportional to the energy spectral density or the square of $E_i(\omega)$. The power spectrum is presented in Fig. 6-7, normalized to the peak value of 0.075 volts/meter-Hertz which occurs at ω_o = 700 kHz. The ordinate is in decibels

$$\text{dB} = 10 \log \left[\frac{(E_i(\omega))^2}{(E_i(\omega_o))^2}\right] \qquad (6\text{-}8)$$

Because the spectrum extends from a few Hertz up to several hundred MHz (depending on how the cutoff point is defined), EMP is difficult to filter and can affect circuits resonant at a wide range of frequencies. It is noted that the energy density peaks in the broadcast band, and even at 1.5 MHz, is down only about 15 dB. This fact indicates that EMP should couple well into broadcast antennas and pass without significant attenuation through transmitter-tuned circuits.

It should be emphasized that Eq. 6-6 is only applicable to high-altitude detonations. It can be significantly

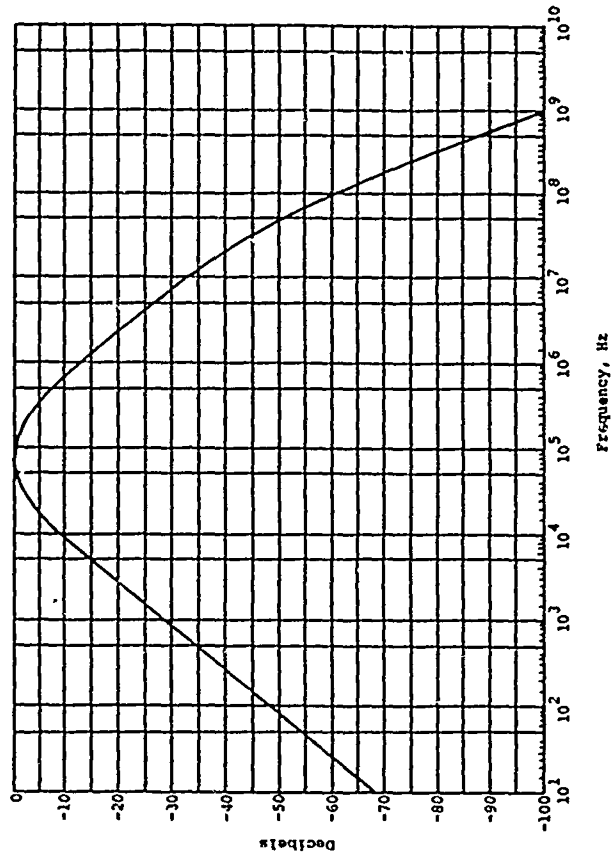

Figure 6-7 Normalized Power Spectrum for EMP (High-Altitude Detonation (Ref. 6-6)

in error for near-surface bursts. Reference 6-7 is recommended for guidance for the near-surface case.

Figure 6-8, from Ref. 6-7, is a series of graphs showing the relationship between the peak current induced in a bare cable versus the distance from the burst point. The cables are assumed to be laid radially with respect to ground zero. Although the data pertain to a soil with a conductivity of 1 x 10^{-3} mho/meter, it agrees fairly well with experimental data obtained in soils varying from 10^{-2} to 1.67 x 10^{-3} mho/meter. The radial distance given in Fig. 6-8 is the distance to the end of the cable away from ground zero. The peak currents given in Fig. 6-8 can also be considered upper bound values for insulated cables. For very short runs of wire, such as in circuitry and connecting cables, the maximum currents will be reduced by at least a factor of 10.

6.4 THERMAL RADIATION

6.4.1 General

The extremely high temperatures in the fireball created by the explosion of a nuclear weapon release a great amount of energy in the form of thermal energy. In a typical air burst, approximately one-third of the total energy yield is emitted from the fireball as thermal energy. This means that approximately 400,000 kilowatt-hours are emitted in the form of thermal energy for each kiloton (4.184 x 10^{12}j) of weapon yield.

In surface and air bursts, the thermal energy is emitted in two pulses. The first pulse, which is quite short and comprises about 1 percent of the total thermal energy, is essentially in the low ultraviolet and visible region. The second pulse, which is more significant and of longer duration, consists primarily of visible and infrared radiations. The duration of the thermal pulse increases with the yield of the explosion.

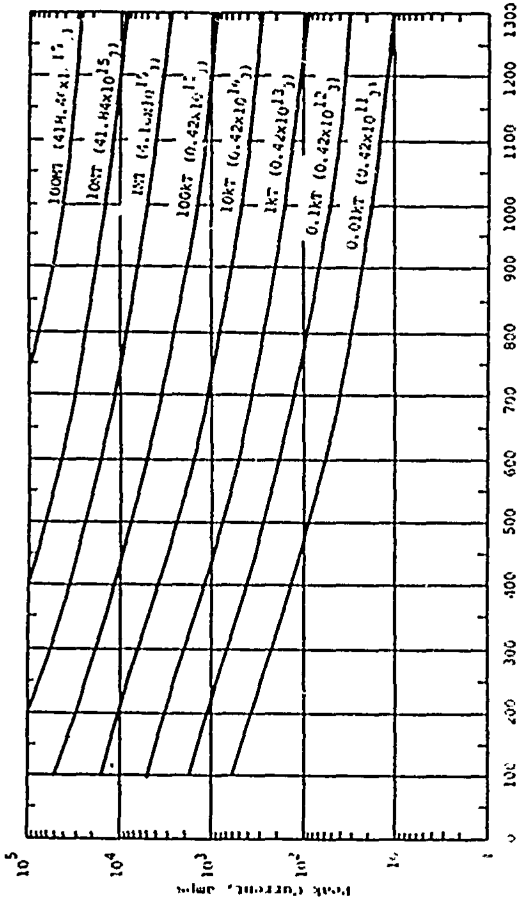

Figure 6-8 Peak Current in Bare Cables for Various Yields (Ref. 6-7)

In a subsurface burst, essentially all of the thermal radiation is absorbed in heating and melting the soil. If there is no penetration of the earth's surface by the fireball, normal thermal radiation effects are absent.

Although the blast and shock effects are the cause of most structural damage, thermal radiation can contribute to the overall damage in several ways. At locations relatively close to the detonation, the intense heat present in thermal radiation from a nuclear burst can result in a degradation of strength. Over considerable distances, combustible materials can be ignited and exposed personnel suffer skin burns and eye damage.

Thermal radiation is attenuated by spherical divergence and by absorption and scattering in the atmosphere. In addition to the type and yield of the burst, the presence of rain, fog, industrial haze, cloud cover, smoke, intervening shields, etc., will also affect the level of thermal radiation received at a site.

6.4.2 Prediction Techniques

The above considerations make the prediction of thermal radiation received at a given distance from an explosion very difficult without many simplifying assumptions. References 6-1, 6-2, and 6-3 present data and procedures for approximating the thermal radiation from air bursts.

From Ref. 6-8 the thermal radiation from an air burst is approximately equal to

$$Q = 2.8 \times 10^4 \, T\left[\frac{W}{1MT}\right]\left[\frac{1000 \text{ ft}}{R}\right]^2 \quad \text{cal/cm}^2 \qquad (6\text{-}9)$$

$$= 2.6 \times 10^3 \, T\left[\frac{W}{10^{15} j}\right]\left[\frac{1000 \text{ m}}{R}\right]^2 \quad \text{joules/cm}^2$$

where

Q = integrated thermal flux

R = slant range

T = transmission factor

W = yield in megatons or joules

Assuming the transmission factor to be equal to unity (infinite visibility), Fig. 6-9 is a plot of the thermal radiation received from a 1MT weapon as a function of distance from the explosion. For other yield weapons, multiply data from Fig. 6-9 by the weapon yield in megatons (in SI units multiply by the ratio $W/4.184 \times 10^{15}$j). Transmission factors for 10- and 50-mile (16 and 80 km) visibility are presented in Fig. 6-10. The data may be considered reliable up to distances of one-half the visibility. Data from Fig. 6-9 would be multiplied by appropriate factors from Fig. 6-10 to correct for atmospheric attenuation.

For surface bursts, the thermal radiation along the earth's surface is less than that at equal distances from an air burst of the same total yield. This difference is due to the decreased transmittance of intervening low air layers. The thermal exposure from a surface burst ranges from about three-quarters at short distances to about one-half at longer distances of that at corresponding distances from an air burst (Ref. 6-2). It also appears that, as the yield of the surface burst increases, the radiant exposure tends toward the larger limit. Since Ref. 6-2 does not define shorter and longer distances or larger yields, it is suggested that an average of the above factors be used for the general case. Equation 6-9 then becomes

$$Q = 1.8 \times 10^4 \, T\left[\frac{W}{1MT}\right]\left[\frac{1000 \text{ ft}}{R}\right]^2 \quad \text{cal/cm}^2 \qquad (6\text{-}10)$$

$$= 1.6 \times 10^3 \, T\left[\frac{W}{10^{15} j}\right]\left[\frac{1000 \text{ m}}{R}\right]^2 \quad \text{joules/cm}^2$$

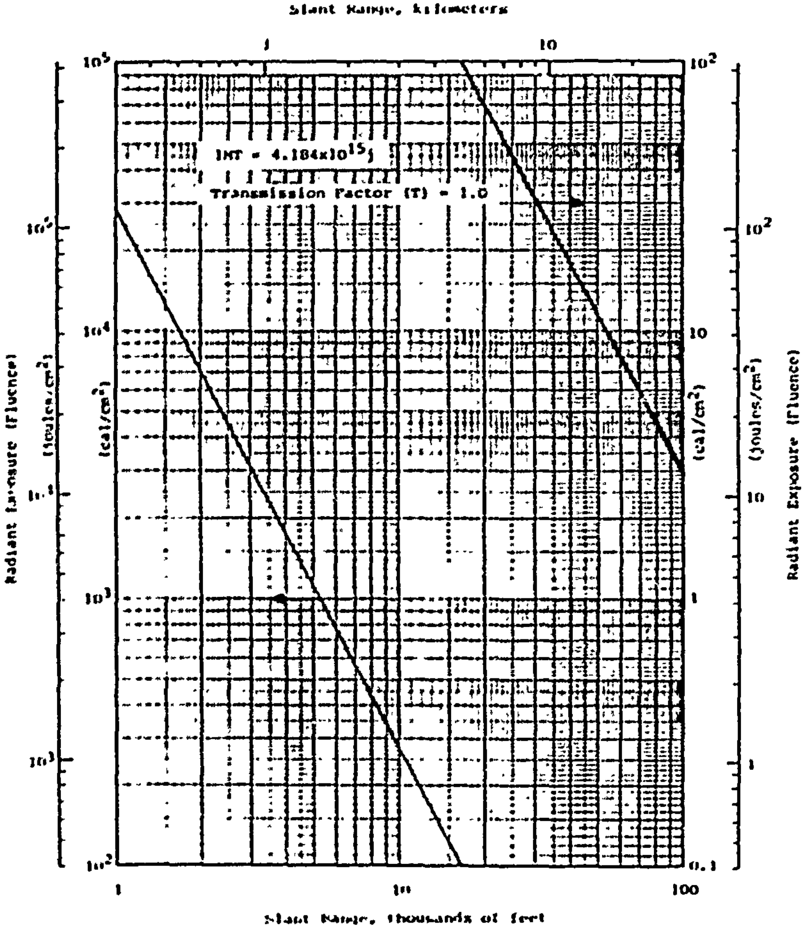

Figure 6-9 Radiant Exposure Vs. Slant Range

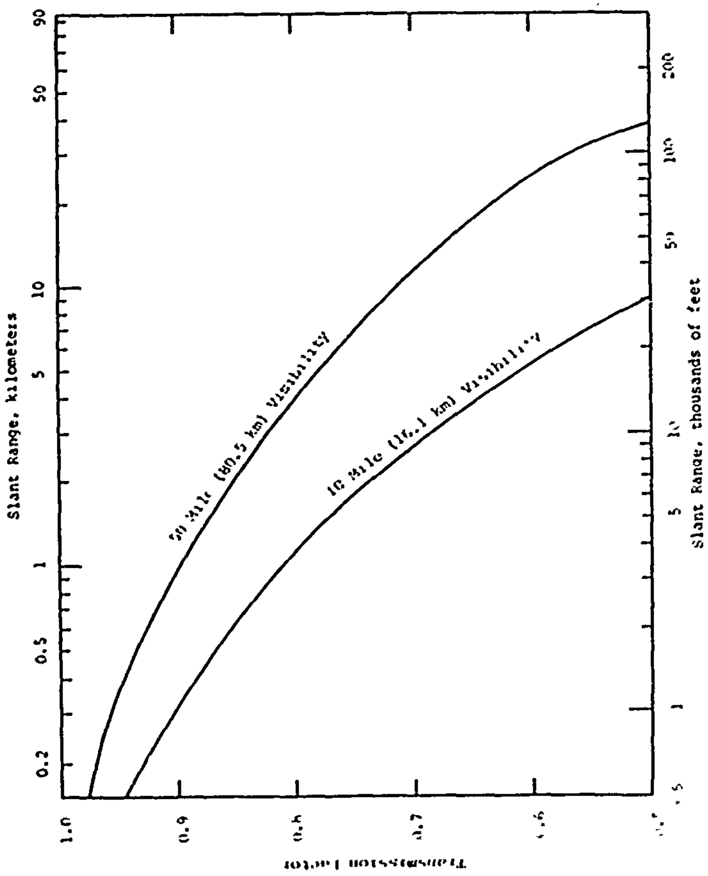

Figure 6-10 Thermal Transmission Factor (T) Vs. Slant Range from Explosion (Ref. 6-2)

6.5 RESIDUAL NUCLEAR RADIATION

6.5.1 General

The residual nuclear radiation is defined as that which is emitted later than 1 minute from the instant of the explosion. The primary hazard from residual radiation is due to the creation of fallout particles which include the radioactive weapon residues and the induced activity in the soil, water and other materials in the vicinity of the explosion. These particles can be dispersed over large areas by the wind. A secondary hazard may result from neutron-induced activity on the earth's surface in the immediate vicinity of the burst point. The relative contributions of the fission products and induced radioactivity depend on weapon design, height of burst, nature of the earth's surface at the burst point and the elapsed time after the explosion.

It is convenient to consider the fallout in two parts, early and delayed. Early fallout is defined as that which returns to earth within a period of 24 hours following the explosion; delayed fallout is that returning to earth after 24 hours. Delayed fallout is so widely dispersed and has decayed to such an extent that, although it may represent a long time health hazard, there is no immediate danger to personnel or equipment. Only early fallout radiation is considered herein.

Particles such as weapon residues from the fission products and unfissioned uranium and plutonium, radioactive isotopes formed by neutron reactions other than fission in the weapon materials, and earth surface materials (soil, rock and/or water) are swept aloft with the fireball into the radioactive cloud. These airborne particles are transported from the explosion site and eventually deposited on the earth as radioactive fallout. The distances from the point of detonation at which fallout is deposited depend upon factors such as wind

velocity, particle size, atmospheric and topographical conditions, etc. The fallout patterns are usually idealized as elliptical contours extending many miles (or kilometers) downwind from ground zero. The intensities upwind or crosswind will be only a fraction of those downwind at corresponding distances from ground zero. The assumption that the structure will be downwind is the most severe and, in many cases, may be too conservative.

The three principal types of radiation of significance in fallout radiation are the residual gamma rays, alpha particles, and beta particles. As mentioned previously, alpha and beta particles do not constitute a serious hazard so long as they are outside the body.

The residual gamma rays are identical in nature to the initial gamma rays previously discussed. However, since the gamma rays are not emitted instantaneously, but rather over a long period of time, intensities are generally measured in terms of a dose rate. The dose rate in roentgens per hour is commonly used to indicate the level or intensity of radioactivity in a contaminated area. The total dose received is the integral of the dose rate over the corresponding exposure time.

6.5.2 Prediction Techniques

In addition to the variables of weapon design, height of burst (or depth of burst), ground surface conditions, wind velocity, atmospheric conditions and particle size, the prediction of residual radiation intensity is complicated by radioactive decay of the fallout particles. This process is a decrease in activity of any radioactive material with the passage of time due to the spontaneous emission from the atomic nuclei of either alpha or beta particles. The decay process is sometimes accompanied by gamma radiation. The net result is a reduction in the level of radioactivity with elapsed time after the detonation. An approximate rule for rate of decay is that for every sevenfold increase in time after the detonation, there is a tenfold decrease in the radiation dose rate.

Winds tend to reduce the level of radioactivity at a given point in two ways, (1) the airborne particles are being deposited continually so that the number of particles deposited decreases with distance, and (2) depending on the wind velocity, a finite time is required for the particles to be deposited and the radioactivity will decay during this time.

It is impossible to devise a curve or graph to show the general concurrent effects of wind and radioactive decay. A reference value of wind velocity and a reference time for radioactive intensity are usually established and fictitious fallout radiation intensities, based on these reference values at various downwind locations from the given surface burst, are given. Figure 6-11, based on data from Ref. 6-2, shows a typical curve of unit time reference dose rate for a wind velocity of 15 MPH (24.1 km/hr) and a 1MT (4.184×10^{15}j) fission-yield surface burst. Figure 6-12 shows idealized unit time reference dose rate patterns for the same conditions. Idealized patterns, such as shown in Fig. 6-12, are unlikely due to variations in direction and velocity of the winds at various altitudes and distances from the point of detonation. These idealized curves can, however, be used to obtain rough estimates of the intensity of fallout radiation at a specified distance from ground zero. In order to obtain radiation intensities for other yields, the values obtained at various distances in Figs. 6-11 and 6-12 should be multiplied by the fission yield in megatons (in SI units multiply by the ratio $W_f/4.184 \times 10^{15}$j, where W_f is the fission yield in joules). Thus, for a 1MT (4.184×10^{15}j) yield which is one-half fission and one-half fusion, the multiplier is one-half. Reference 6-2 suggests a limit of 10,000 roentgens/hour for the unit time reference dose, since higher values are unlikely except for isolated points near ground zero.

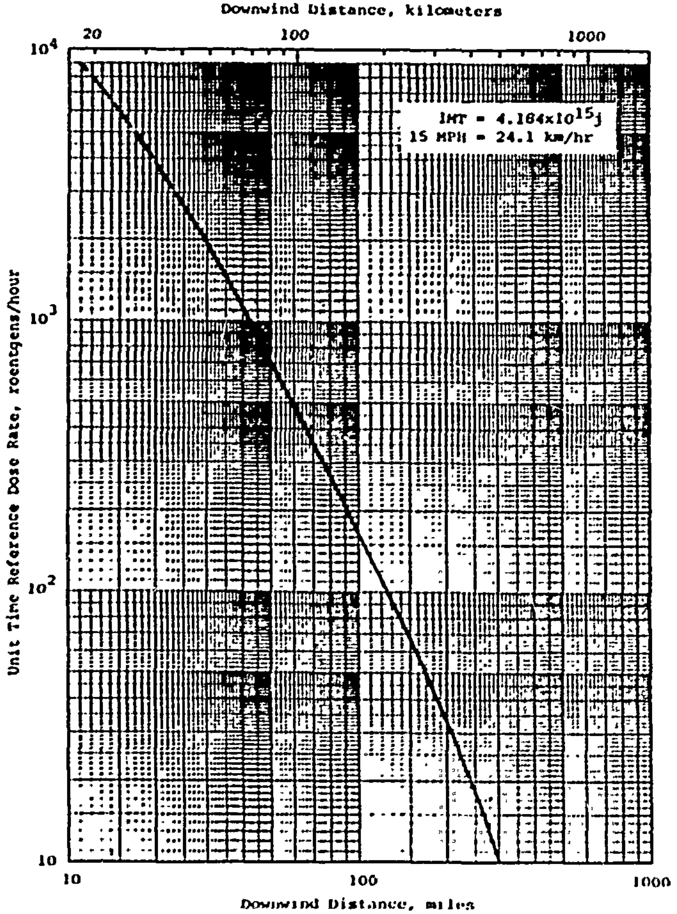

Figure 6-11 Unit Time Reference Dose Rates for Fallout Radiation for 1MT Fission Yield Surface Burst, 15 MPH Wind Velocity

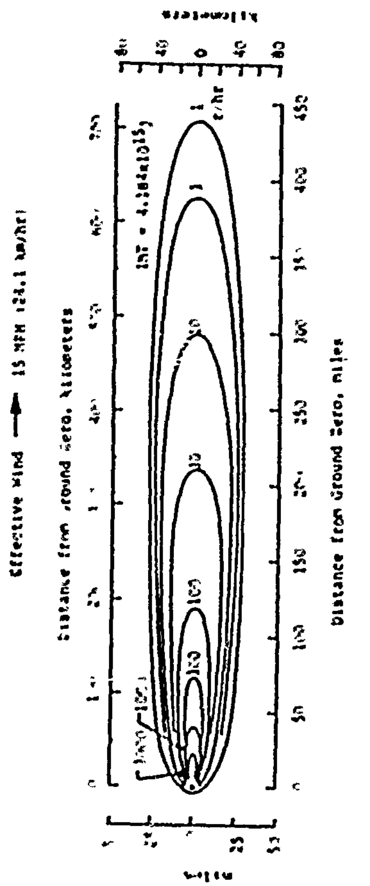

Figure 6-12 Idealized Unit-Time Reference Dose-Rate Pattern for Early Fallout from a 1MT Fission Yield Surface Burst; Effective Wind Velocity 15 MPH (Ref. 6-2)

The unit time reference dose rates must also be scaled for other wind velocities. If there is no wind shear, particles of a given size will reach the ground at a distance downwind which is directly proportional to the wind velocity. If the wind velocity is 30 miles per hour (48.2 km/hr), the radioactive materials will be distributed over roughly twice the area indicated by Fig. 6-12. Thus, the contour values of the unit time reference dose rates given in Figs. 6-11 and 6-12 are multiplied by

$$\frac{15}{v} \text{ or } \frac{24.1}{v}$$

where v is the effective wind velocity in miles per hour (or km/hr), and the downwind distances to each contour are multiplied by

$$\frac{v}{15} \text{ or } \frac{v}{24.1}$$

For an effective wind velocity of 30 miles per hour (48.2 km/hr), the contour values would be halved and the distances doubled. The above scaling procedure gives reasonably good results for surface bursts over the range from 100kT to 10MT (4.184×10^{14}J to 4.184×10^{16}J).

The unit time reference dose rates can be converted to true values at the time of arrival of the fallout by use of Fig. 6-13. In order to use Fig. 6-13, it is necessary to calculate the time required for the fallout to reach the point of interest. This elapsed time is obtained by dividing the distance from ground zero by the effective wind velocity. With this time after the detonation established, the ratio of dose rate at time of arrival to unit time dose rate can be obtained from Fig. 6-13. Alternately, Fig. 6-14 can be used to determine the total accumulated radiation dose received over a period of time after the detonation.

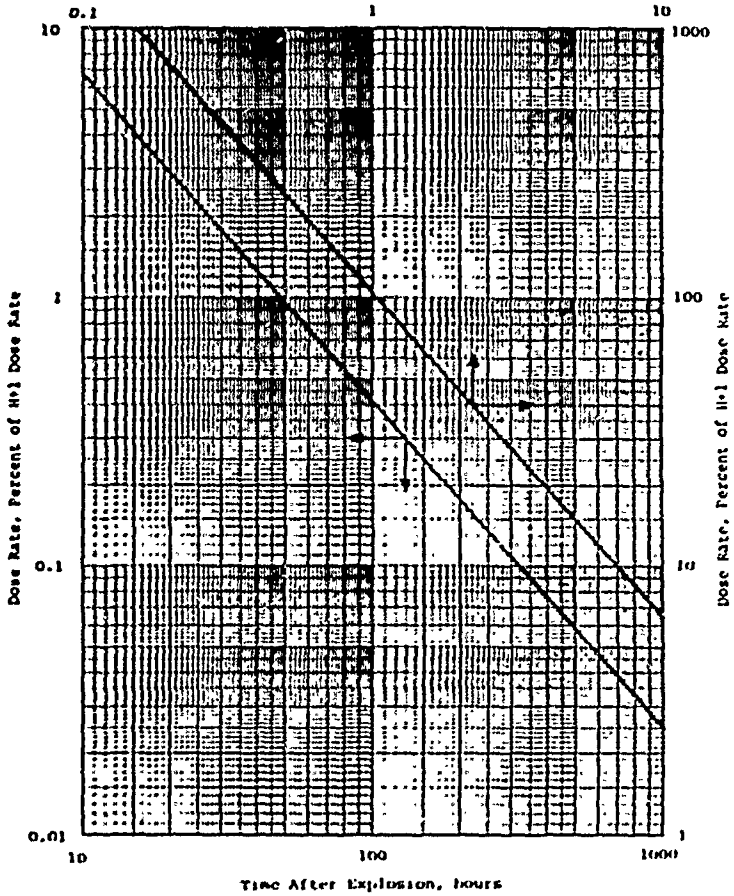

Figure 6-13 Approximate Rate of Decay of Radioactivity from Fallout (Ref. 6-8)

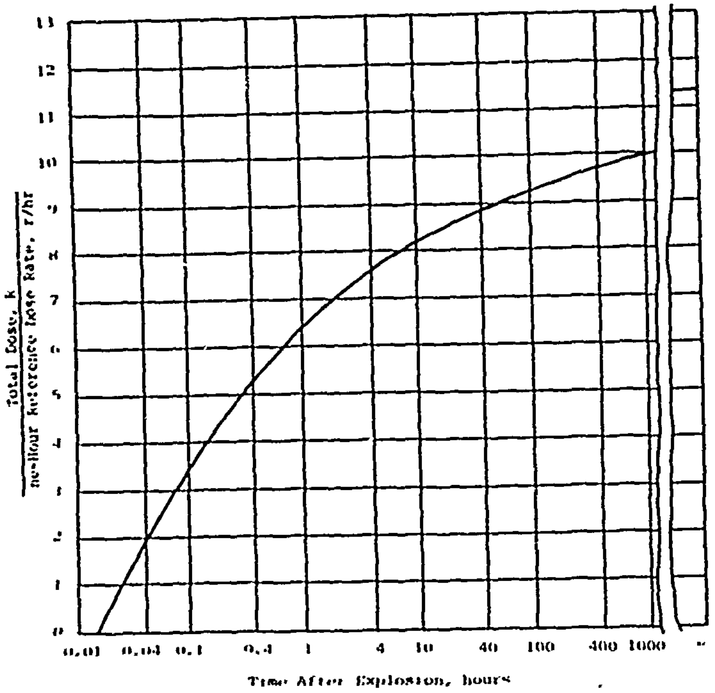

Figure 6-14 Accumulated Total Dose of Residual Radiation from Fission Products from 1 Minute After the Explosion (Ref. 6-2)

Reference 6-2 includes additional guidance regarding the prediction of fallout radiation intensities and should be consulted for other than the simple cases considered herein.

6.6 RADIATION SHIELDING

6.6.1 Introduction

Shielding sensitive components or personnel from the various forms of radiation emanating from a nuclear detonation is a complex process depending on many variables. However, it often happens that when the most critical problem is taken care of, the others are also resolved. For some forms of radiation, the type of material in the shield is most significant and, for others, the total mass of material is of greatest importance. The following paragraphs present a general discussion of the shielding problem with some guidance for making rough estimates of requirements. Final design of radiation shielding requires a detailed analysis of the radiation environment, the system to be protected and the structure surrounding the system.

Gamma, thermal and X radiation, as well as neutrons, will all deposit energy in shielding or other materials in the process of being absorbed or attenuated. The importance of this deposition of energy depends on the energy level of the radiation, its intensity and properties of the material in which the energy is deposited. The higher the energy level, the greater the distance required to absorb or attenuate the radiation. Thus, for a given total flux, the radiations at lower energy levels will generate higher depositions of energy per unit volume of material than those at higher energy levels. This deposition of energy causes heating of the material and can cause melting, spalling or blowoff of material.

X radiation is in general less penetrating than gamma, so it is more likely to be deposited in a thin layer near the surface of the shield. On the other hand, it will also be attenuated more rapidly by the earth's atmosphere. Neutrons cover a fairly wide range in energy levels and corresponding depths of penetration. Thermal radiation energy will normally be deposited in a very thin layer near the surface.

6.6.2 Gamma Shielding

Shielding against initial gamma radiation and fallout will be discussed together, although they differ significantly in energy level. Radiation emitted during the first minute after a nuclear detonation has a higher energy level and presents a more difficult shielding problem.

A fairly accurate estimate can be made of the effectiveness of a shield between a gamma source and the target by proper consideration of the energy distribution of the gamma radiation, its angle of incidence, properties of the shielding materials, the geometry of the shield, and the gamma source. A complicating factor is the fact that, although gamma photons travel in straight lines in a vacuum, they are scattered in passage through the atmosphere or shielding materials and can arrive from random directions. This latter phenomenon has an important bearing on the shielding problem, and it is not sufficient to merely place a barrier between the gamma source and the target. Although an accurate determination of a shield's effectiveness is a complex problem involving many factors which vary with individual situations, it is possible to provide rough indicators of the degree of attenuation of gamma radiation provided by a given amount of shielding.

Gamma rays are attenuated to some extent in the course of their passage through any material. As a rough rule, it may be said that the decrease in gamma radiation intensity is dependent on the total mass of the material placed between the source and the point of observation. This means that a greater thickness of low-density material is required to provide the same attenuation as a specified thickness of high-density material. The approximate effectiveness of a given material in attenuating radiation is sometimes expressed in tenth-value thicknesses. This is defined to be the thickness of the specified material which will attenuate the radiation dose (or dose rate) to one-tenth of that incident on the surface towards the source. Thus, one tenth-value thickness will attenuate the radiation by a factor of ten; two tenth-value thicknesses will attenuate it by a factor of 100, and so on. This approach neglects some of the factors affecting shielding effectiveness mentioned above but does allow rough estimates of required shielding without complex analyses. Table 6-2, from Ref. 6-2, gives approximate tenth-value thicknesses of some common construction materials for gamma rays emitted by the fission products in the first 10 seconds after the detonation and for those accompanying the capture of neutrons by nitrogen in the air. The differences in tenth-value thicknesses are due to energy-level differences of the two gamma rays. A representative value of the product of the tenth-value thickness and density of the material is approximately 150 pounds per square foot (732 kg/m^2) for fission-product gamma and 215 pounds per square foot (1050 kg/m^2) for nitrogen-capture gamma. A fair estimate of the tenth-value thickness for other materials can be obtained by dividing 150 or 215 pounds per square foot (732 or 1050 kg/m^2), as appropriate, by the density of the material.

Figure 6-15, from Ref. 6-9, presents dose-transmission factors for varying thicknesses of common shielding materials subjected to initial gamma radiation. The dose-transmission factor is the fraction of the initial gamma incident on the shield that actually reaches the target. These curves make some allowance for the energy spectrum of the gamma radiation, angle of incidence, and geometry of the shield. They are for a broad

Table 6-2

APPROXIMATE TENTH-VALUE THICKNESSES FOR FISSION PRODUCT AND NITROGEN-CAPTURE GAMMA RAYS

Material	Density (D)		10-sec Fission Product				Nitrogen Capture			
			Tenth-Value Thickness (T)		D x T		Tenth-Value Thickness (T)		D x T	
	lb/ft^3	kg/m^3	in	cm	lb/ft^2	kg/m^2	in	cm	lb/ft^2	kg/m^2
Steel	490	7849	3.7	9.4	150	732	5.3	13.5	215	1050
Concrete	144	2307	12	31	145	708	18	46	215	1050
Earth	100	1602	18	46	150	732	26	66	215	1050
Water	62.4	1000	26	66	135	659	37	94	190	928
Wood	34	545	50	127	140	684	70	178	200	977

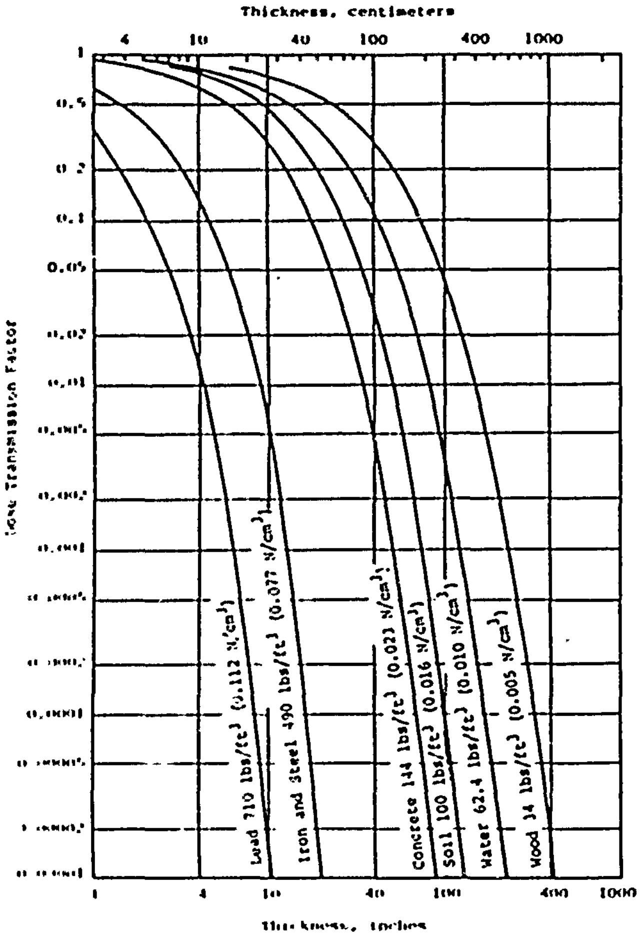

Figure 6-15 Shielding from Initial Gamma Radiation (Ref. 6-9)

beam of radiation impinging on a thick plane shield with very large dimensions in the plane of the shield and with no nearby ceiling, floor or walls from which radiation can scatter. They can be used to obtain rough estimates of the effectiveness of other shielding configurations.

Figure 6-16, also from Ref. 6-9, presents dose-transmission factors for the lower energy residual gamma radiation. These factors are subject to the same conditions as for Fig. 6-15. Note the significant difference in required thickness for the same attenuation of the two types of gamma radiation.

Reference 6-8 provides guidance regarding more accurate procedures for determination of residual radiation shielding requirements.

6.6.3 Neutron Shielding

Neutron shielding is a different, and more difficult, problem than gamma radiation shielding. As in the case of gamma radiation, the effectiveness of the shielding material is dependent on the energy level of the neutrons. Neutrons are also scattered in passage through the atmosphere and shielding materials, so shielding should be provided in all directions. Although heavy metals, such as iron and lead, make good gamma ray shields because of their high density, they should be combined with other more effective materials for neutron attenuation.

The attenuation of neutrons from nuclear detonations involves several phenomena. First, the very fast neutrons must be slowed down to the moderately fast range. This requires an inelastic scattering material such as one containing barium or iron. The moderately fast neutrons are then decelerated into the slow range by means of an element of low atomic number. Water is very satisfactory for this purpose since it consists of hydrogen and oxygen, both having low atomic weights. The slow (thermal) neutrons must then be absorbed. This is not a

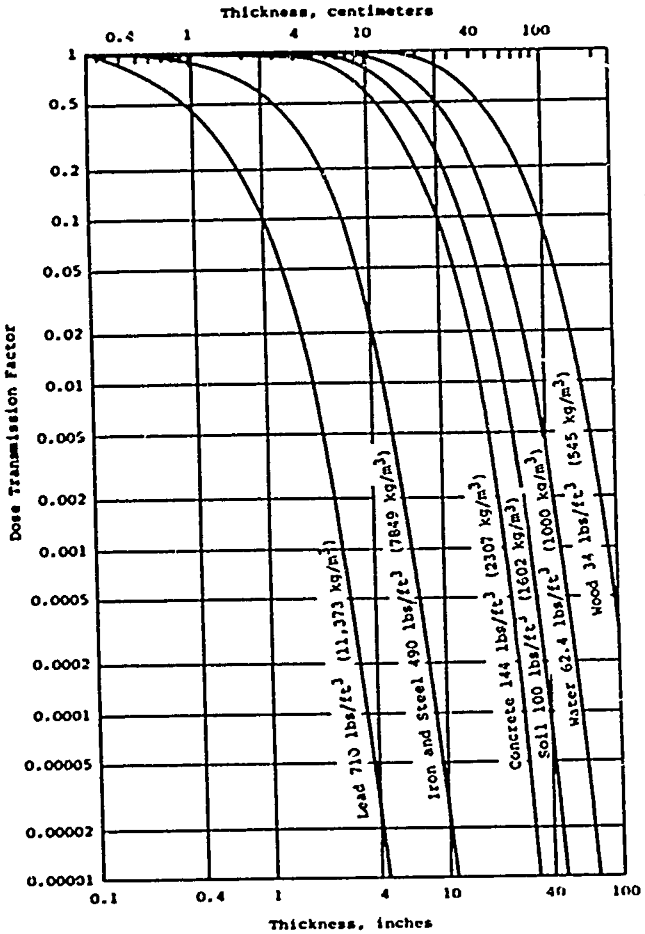

Figure 6-16 Shielding from Residual Gamma Radiation (Ref. 6-9)

difficult problem since the hydrogen in water will serve the purpose. Unfortunately, most neutron-capture reactions are accompanied by the emission of gamma rays, and sufficient gamma attenuating material must also be provided to minimize the escape of capture gamma rays from the shield.

Concrete or damp earth represents a fair compromise for gamma and neutron shielding. Although these two materials do not normally contain high atomic weight elements, they do contain a fairly large percentage of hydrogen and oxygen to slow down and capture neutrons, as well as calcium, silicon and oxygen to absorb the gamma radiations. A thickness of 10 inches (25.4 cm) of concrete will decrease the integrated neutron flux by a factor of about 10. Damp earth acts in a similar manner, although about 15 inches (38.1 cm) would be required to obtain the same decrease in integrated neutron flux.

A decrease in the required thickness of concrete can be obtained by adding a considerable portion of iron ore to the mix and including small pieces of iron or steel. The mineral barytes, a compound of barium, is an alternate additive. The addition of these heavy elements improves the neutron and gamma shielding properties of the concrete and about 7 inches (17.8 cm) of this concrete will provide a reduction in the integrated neutron flux by a factor of 10.

6.6.4 X Ray Shielding

As noted in preceding paragraphs, X ray radiation is very similar to gamma radiation. For this reason, it is suggested that the guidance provided in paragraph 6.6.2 regarding the shielding effectiveness of various materials for gamma radiation also be applied to X ray radiation. Thus, the tenth-value thicknesses in Table 6-2 and dose-transmission factors from Figs. 6-15 and 6-16 can also be applied to X ray radiation shielding.

6.6.5 EMP Shielding

The following discussion of EMP shielding is taken primarily from Ref. 6-6, which contains many practical recommendations for reducing the effects of EMP on electrical systems. Reference 6-7 also includes procedures and criteria for protection of systems from EMP effects. It is currently under revision and much of the data presented in the June 1965 edition is subject to change.

The voltage and current surges induced by EMP fields are attenuated primarily by two techniques: (1) reflection of the incident fields from the shielded envelope protecting the area, and (2) exponential absorption of the residual currents induced in the shielding.

There are two types of fields which may require attenuation before reaching critical components. The first occurs at close-in ranges where the magnetic field predominates, giving rise to a low-impedance field. The second is the radiated field, which emanates from a distant surface burst or a high-altitude burst.

Shielding against a pulsed magnetic field is essentially the same problem as shielding against any magnetic field. It involves both scattering of the magnetic flux away from areas to be protected and dissipation of the magnetic field energy. Maximum protection from low-impedance, high-intensity magnetic fields of low frequency is obtained through absorption of the wave energy in passing through the shield material. For optimum magnetic field absorption, a high-permeability steel gives best results.

Protection from the high-intensity electric fields is obtained primarily by reflection from the shielding surface. For optimum electric field reflection, a highly conductive surface, such as copper, gives the best results.

The effectiveness of the shield if measured in terms of the attenuation of the electric or magnetic field strength. It is defined to be 20 times the logarithm of the ratio of the voltage induced in a conduction loop or circuit without the shielding to that in the same loop or circuit with the shielding. It is measured in decibles (dB). Reference 6-6 defines the shield effectiveness to be

$$SE(dB) = 20 \log \frac{E_1}{E_2} \qquad (6\text{-}11)$$

where

E_1 = induced voltage without shielding

E_2 = induced voltage with shielding

The amount of EMP energy absorbed in passing through a barrier depends on the frequency of the wave, the electrical properties of the barrier, and the thickness of the barrier. Although maximum shielding is obtained from a solid metal shield, some protection is provided by the reinforcing steel or mesh in reinforced concrete. To be most effective, the bars should be welded at all joints and intersections to form many continuous conducting paths around the volume protected. The degree of shielding provided depends on the size and shape of the volume protected, the diameter and spacing of the reinforcing steel, the conductivity and permeability of the steel, and the frequency of the incident wave.

Reference 6-6 presents curves for estimation of the shielding provided by selected reinforcing steel patterns for several structure configurations. These curves are included here as Figs. 6-17 and 6-18. Although obtained for a steel with a conductivity of 6.5 x 10^6 mho/meter and a permeability of 50, the curves are good approximations for conductivities ranging from 4 x 10^6 to 8 x 10^6 mho/meter and relative permeabilities from 10 to 100. The frequency used for the calculations was 10,000 Hz. A bar diameter of 1.692 inches (4.30 cm) and

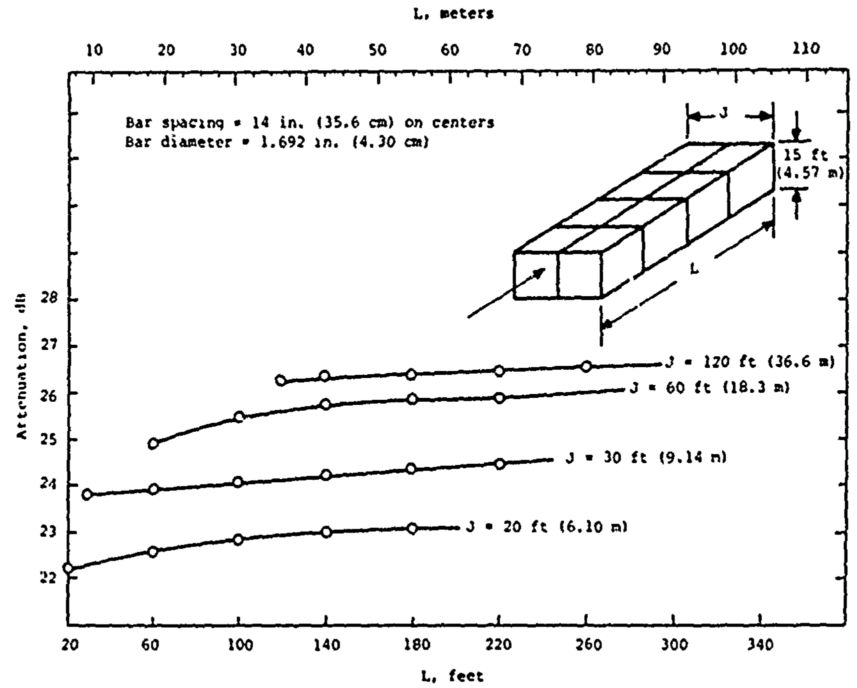

Figure 6-17 Center Area Attenuation of Induced Voltage by 15-foot (4.57 m) High, Single-Course Reinforcing Steel Room (Ref. 6-6)

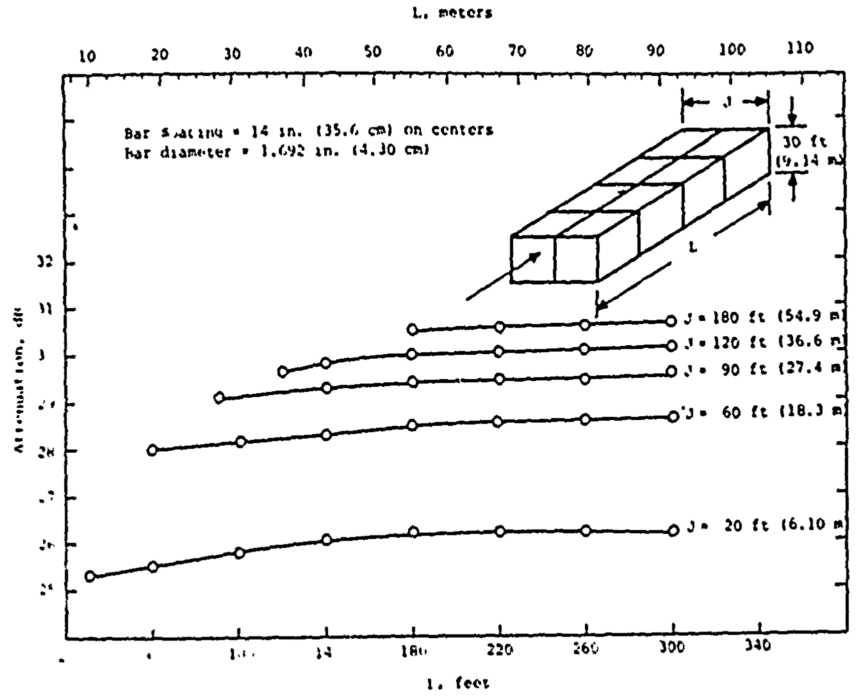

Figure 6-18 Center Area Attenuation of Induced Voltage by 30-foot (9.14 m) High, Single-Course Reinforcing Steel Room (Ref. 6-6)

spacing of 14 inches (35.6 cm) on centers was also assumed.

For other bar diameters and spacing, the curves of Figs. 6-17 and 6-18 should be corrected by the factors given in Fig. 6-19. If the room height is greater than 30 feet (9.14 m), use the curves for a 30-foot (9.14 m) height. If the height is between 15 and 30 feet (4.57 and 9.14 m), use the 15-foot (4.57 m) height curves. If the room width falls between the J-values shown, use the curve just less than the given value. If two layers of steel are provided, use an equivalent single course spacing equal to one-half of the actual.

Figures 6-20 and 6-21, from Ref. 6-7, provide information for other types of shields in a cubic configuration. Although Fig. 6-20 only presents data for a 8-foot by 8-foot by 8-foot (2.44 m by 2.44 m by 2.44 m) cubicle, it can be conservatively applied to larger enclosures. Figure 6-21 presents data for two structure sizes. Figure 6-22 gives data on the shielding provided by soils of various resistivities. Although the above curves apply to magnetic-field shielding, they can be conservatively applied to electric-field attenuation.

The most effective means of shielding is to completely enclose the sensitive components in a continuous metal shield. Such a shield attenuates the EMP by both reflection and absorption of the incident fields. Steel is the most frequently used metal for these shields, because it offers the highest degree of protection per unit cost for low-frequency magnetic fields and can be integrated into the structural design. Figure 6-23 shows the shielding effectiveness of various thicknesses of steel plate. Care must be exercised to avoid degrading the shielding effectiveness indicated in Fig. 6-23 by improper penetrations of the shield with cables, doors, etc.

Reference 6-6 provides the following partial list of construction practices which have proven effective in reducing problems of EMP interference and/or damage of instrumentation during nuclear tests.

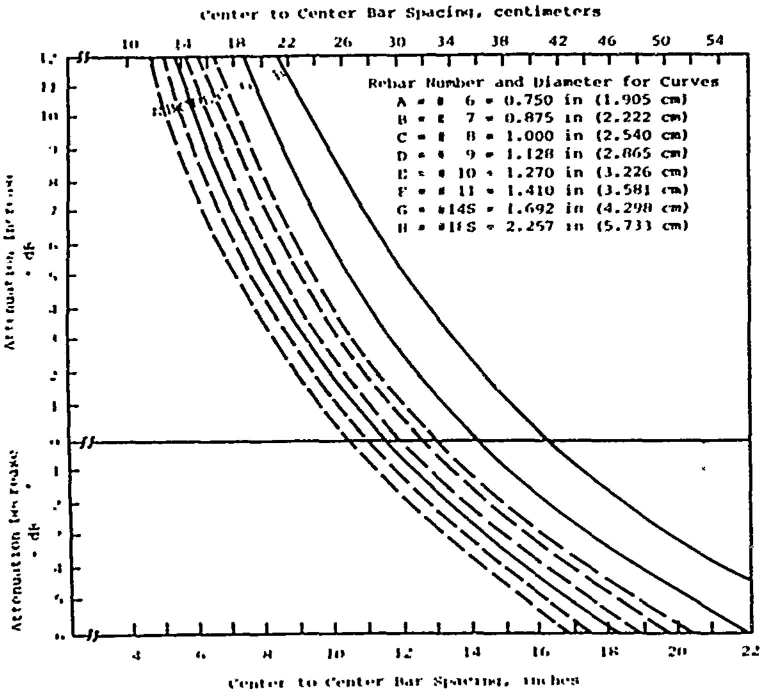

Figure 6-19 Decibel Correction Curves for Various Rebar Diameters and Spacings Using Single-Course Rebar Construction (Ref. 6-6)

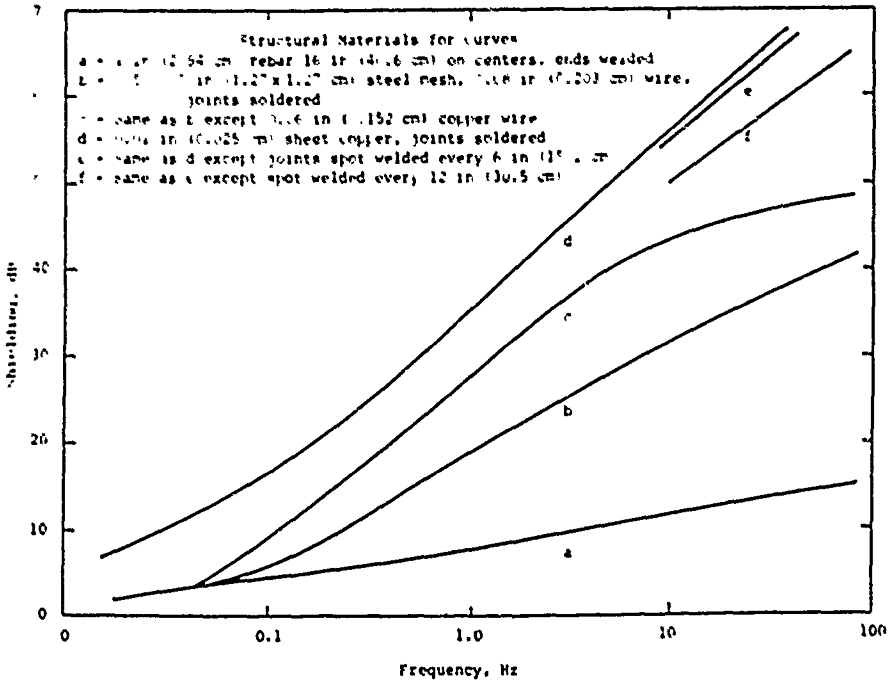

Figure 6-20 Magnetic Shielding Provided by Various Materials in an 8 x 8 x 8 foot (2.44 x 2.44 x 2.44 meter) Enclosure (Ref. 6-7)

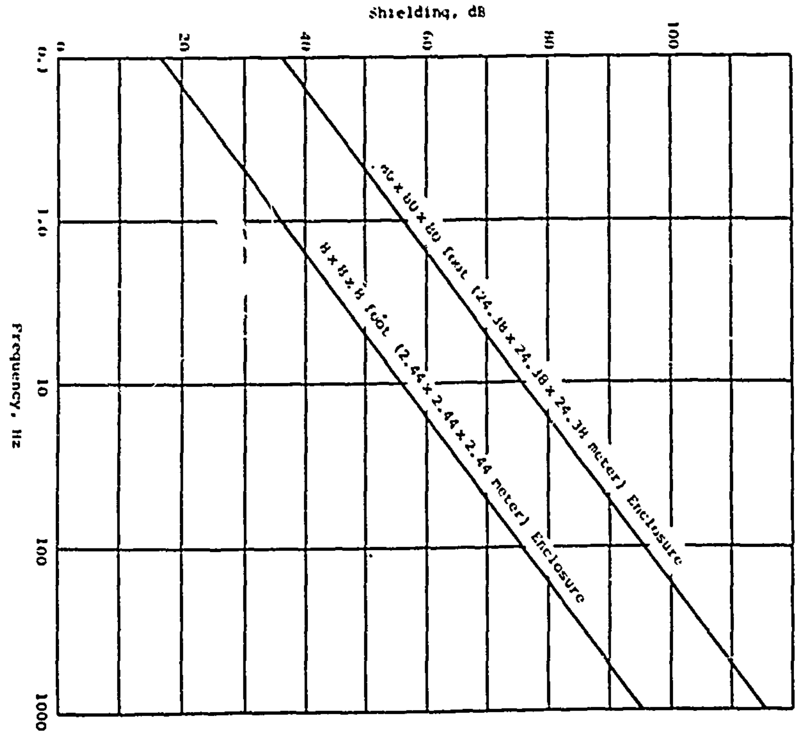

Figure 6-21 Magnetic Shielding Provided by Cubic Enclosures (10-Mil Copper Sheeting) (Ref. 6-7)

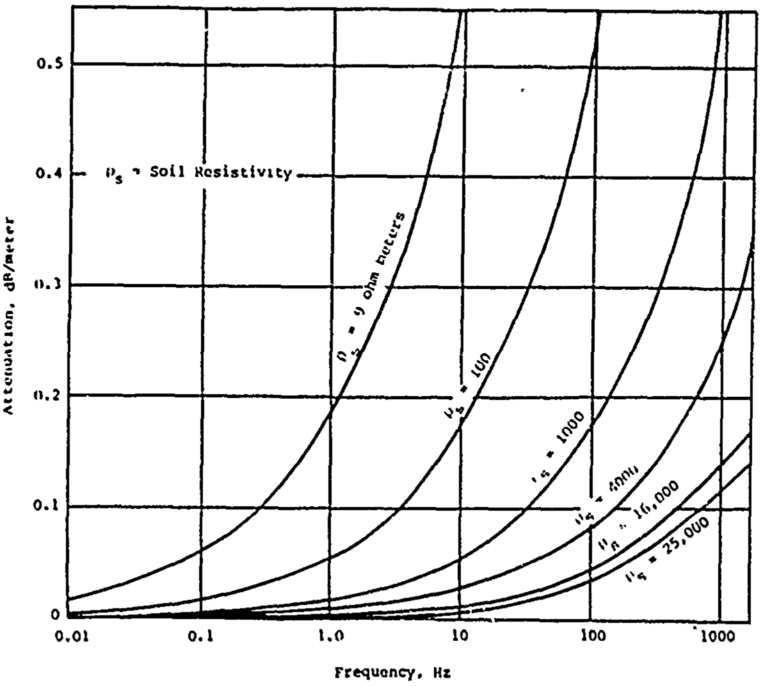

Figure 6-22 Magnetic Shielding Effectiveness Provided by Various Soils (Ref. 6-7)

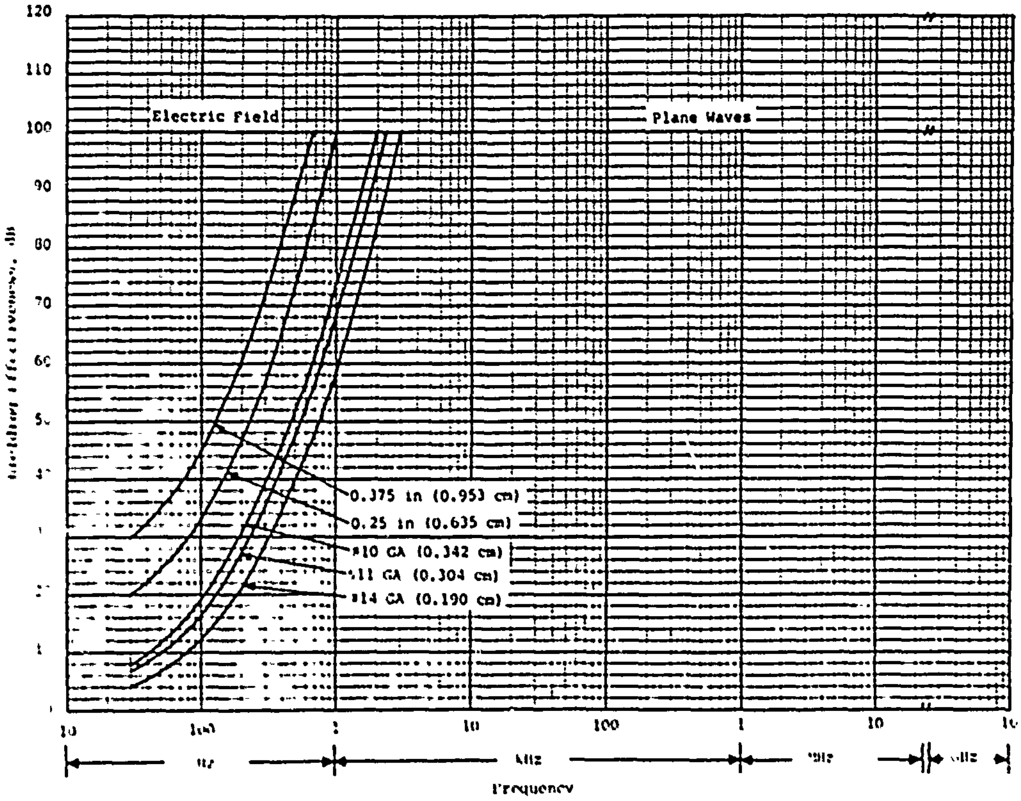

Figure 6-23 Minimum Shielding Effectiveness of Low-Carbon Steel Walls (Ref. 6-6)

1. Isolate power by using internal motor-generator sources and putting lightning arresters on lines.

2. Put wires in boxed, grounded conduits.

3. Use a grounded screen over air-conditioning outlets where they enter shielded areas and ground all ducts.

4. Tie the steel reinforcing bars in concrete into the shielding and grounding system, especially if it is tack-welded.

5. Use the largest rated available lightning *arresters on power station transformers*. Use more sloping devices to lower arrester breakdown voltage.

6. Provide gas gaps on telephone lines with low-impedance grounds.

7. Ground cable outer shields and make them continuous; splicers often do not solder the shielding.

8. Ensure that signal cable shields are well grounded at their point of entry. Large transients inside screened rooms have been traced to poorly grounded coaxial shields.

9. Bury power and signal cables in ferrous conduit as deeply as is economically feasible (greater than 3 feet or 1 m) to reduce current surges and slope-induced wave fronts.

10. Tie water pipes and other entries into the grounding system.

11. Equip both antennas and input leads which cannot be directly grounded with lightning arresters

or protectors. Baluns (a balancing device which provides a balanced transformation between balanced and unbalanced portions of an electronic system, e.g., between an antenna and a transmission line), where installed, need to be self-healing.

12. Educate personnel in protection practices so that, for example, extension cords on outside plugs are not run into shielded areas.

13. Adopt protection measures to fit requirements of particular areas.

14. When a balanced pair lead is tied into a coaxial cable through a matching balun, do not interrupt the *shielding* provided by the outer coaxial conductor. A grounded copper plate mechanically crimped to the coax cable shield has been used effectively.

15. Ground and tie together electrically all seemingly nonessential conductors, such as elevator cables, metal airducts, and equipment cabinets.

16. Because existing grounds are often high impulse impedance, provide a counterpoise at each protector location. Note that counterpoise requirements will vary with geographic location since earth conductivity varies greatly from place to place. Several counterpoise grounds may be required at any one site.

17. Ensure that the entire conduit system is well grounded.

18. Avoid use of nonconducting lubricants when fastening conduit pipes together.

19. Ensure that electrical contact exists between conduit and terminal box. Frequently, the

conduit is pushed against the box but insulated from it by paint.

20. Install a grounding strap from terminal box to door of box for hinged doors.

21. Specify EMP testing of the completed installation with appropriate simulation devices to provide assurance of adequate protection.

22. Either use adequate surge protection on oil-filled transformers and other high-voltage gear to prevent explosions, or use dry transformers (oil-filled transformers can explode and spread burning oil; dry transformers only burn) inside the shielded enclosure.

23. Provide surge protection for emergency power equipment.

24. Use lightning protection techniques on all aboveground lines.

25. If power equipment supplies several sites, install lower value fuses at the equipment end rather than the power end of a system.

26. Use circuit breakers rather than fuses, since breakers can be set more closely and reset more quickly. Check fuses, where provided, periodically for deterioration.

27. Do not use slow-blow or delay fuses or breakers.

28. Design breakers (where feasible) to take no more than the largest expected load.

29. Provide automatic closing doors in preference to mechanical closures and recessed fits for shielded room doors.

30. Store spare parts in a dehumidified area if they are to be used in dehumidified areas.

31. Apply voltages across screened inlet areas to locate poor electrical contact points between the screen and mating surface. This will often burn out the trouble spots.

32. Put single-phase protection on each phase of three-phase power systems.

33. Use passive low-pass L-C radio interference filters on signal, control and telephone lines to provide sloping of pulse wave fronts.

34. The EMP fields in the corners of a shielded structure are usually higher than in other parts of the structure, so corner areas should be avoided or used with caution.

35. Ensure that exposed, nonshielded, intrasystem wiring conforms to a tree or radial wiring scheme. Include all cables, power, signal, and ground in this scheme.

Careful design and adequate quality control during construction is very important in EMP protection. Ensure that operation of the system preserves EMP protection.

6.6.6 Thermal Shielding

Any solid, opaque material between a given point and the fireball will act as a shield and provide protection from thermal radiation. This presumes, of course, that the thermal flux is not high enough to instantly vaporize the material. As in the case of other forms of radiation, thermal radiation undergoes scattering and can arrive from directions other than the point of detonation. In order to be fully effective, the thermal shield must surround the target.

Most structural materials will provide adequate thermal radiation protection to personnel and equipment. However, some materials may ignite or vaporize if too much of the incident thermal radiation is absorbed. Highly reflective materials make better thermal radiation shields, since they do not absorb much of the incident radiation.

Within the fireball, a structure would be exposed to temperatures on the order of tens of thousands of degrees. Thermal protection in this environment is a very difficult problem and generalized solutions are not appropriate. Construction materials have been observed to survive in varying degrees within this region, and reinforced concrete appears to offer very significant resistance to thermal radiation.

6.7 PERMISSIBLE RADIATION LEVELS

6.7.1 General

Exposure to the various types of radiation from nuclear weapons can cause injury to living organisms and the malfunction of electronic equipment. The exact maximum dosage to which personnel may be exposed is a rather arbitrary figure best established by executive decision for the specific mission and circumstance. The designer or analyst, once given this limiting dosage and knowing the design weapon parameters, can then undertake the determination of shielding requirements.

The effects of the various types of radiation on personnel have been fairly well established. Unfortunately, the same is not true for equipment and much of the data that are available are classified. The information presented in the following paragraphs was collected from various sources, but only the unclassified portions are presented here. Wherever possible, the source of additional classified information will be identified. The discussion of permissible radiation levels for equipment is limited to electronic equipment. Except where

noted, it is also assumed that the radiation is received in a relatively short period of time (minutes, except for residual radiation).

6.7.2 Personnel

a. Gamma and Neutron Radiation

Gamma and neutron radiation will cause radiation injury of the same general type, and the relative biological effectiveness (RBE) of both is approximately 1. (RBE of neutrons is higher for eye cataract formation.) Radiation effects on biological systems are related to the dose in rem. For gamma radiation

Dose in rem = absorbed dose in rads
= exposure dose in roentgens

The conversion of neutron fluence to absorbed dose depends upon the energy spectrum of the neutrons. For typical neutron spectra from nuclear explosions, Ref. 6-1 gives

$$4.4 \times 10^8 \ n/cm^2 \sim 1 \text{ rad} \qquad (6\text{-}12)$$

Reference 6-2 suggests for a typical fission weapon

$$5.5 \times 10^8 \ n/cm^2 \sim 1 \text{ rad} \qquad (6\text{-}13)$$

The value given by Eq. 6-12 is used in conversion of Eq. 6-2 to Eq. 6-3. For neutrons,

Dose in rem = absorbed dose in rads
= 2.3×10^{-9} times neutron fluence
in n/cm^2

The effect of ionizing radiation on personnel depends not only on the total absorbed dose but also on the rate of absorption and the extent of the body exposed. For example, if a group of persons received a total body dose of 1000 rem within a period of 1 to 2 days, 95 to 100 percent of those exposed would probably die within 2 weeks. If the same total body dose were received over a period of 30 to 35 years, it would probably not have any noticeable external effect on the majority of the group. The effect of large doses over small portions of the body depends to a large extent on the sensitivity of that portion of the body. Some types of radiation damage are repaired by the body, while others appear to be cumulative.

Acute radiation doses are those received within a relatively short period of time (24 hours). The general effects on personnel of an acute, whole-body radiation dose can be summarized as follows:

25-100 rem

Single doses in the range of from 25 to 100 rem over the whole body will produce nothing other than blood changes. These changes do not usually occur below this range and are not produced consistently at doses below 50 rem. Disabling sickness does not occur and exposed individuals should be able to proceed with their usual duties.

100-200 rem

The illness from radiation doses in this range does not present a serious problem in that most patients will suffer little more than discomfort and fatigue and others may have no symptoms at all. There may be some nausea and vomiting on the first day or so following irradiation, but, subsequently, there is a latent period, up to 2 weeks or more, during which the patient has no disabling illness and can proceed with his regular occupation. The changes in the character of the blood, which accompany radiation

injury, become significant during the latent period and persist for some time. If there are no complications due to other injuries or to infection, there will be recovery in essentially all cases. In general, the more severe the early stages of the radiation sickness, the longer will be the process of recovery. Adequate care and the use of antibiotics, as may be indicated clinically, can greatly expedite complete recovery of the more serious cases.

200-600 rem

Nausea and vomiting occur within 1 to 6 hours, in most cases, and last a few hours to a few days. Fatigue is an early and persisting symptom. Symptoms associated with radiation damage to bone marrow, including hemorrhage and infection, occur within 4 to 5 weeks after exposure. The loss of hair is likely above 300 rem. The recovery probability is good, with the incidence of death varying from 0 to 80 percent.

600-1000 rem

A more rapid onset of nausea and vomiting occurs. There is increased susceptibility to infection from wounds, burns and other lesions, largely due to severe loss of white blood cells, and a marked reduction of the body's immunological processes. There is also an increase of hemorrhaging. Survival is possible, with the incident of death increasing to 80 to 100 percent within 2 months.

Over 1000 rem

There is very little chance of survival, with 90 to 100 percent of those exposed dying within 2 days to 2 weeks.

b. Alpha and Beta Particles

As noted earlier, the most serious hazard from these particles is incurred if they are ingested or inhaled. The RBE for beta particles is close to unity, and for alpha particles, it has been variously reported from 10 to 20. The primary hazard is skin lesions caused by the beta particles. The severity of these lesions depends on the degree of beta contamination and the length of the period of contact with the skin. In most cases, the lesions will eventually heal and all visible signs will disappear.

Even a small quantity of radioactive material present within the body can cause considerable injury. The degree of damage depends on the quantity, how long it remains within the body, and what parts of the body are exposed to the radiation from the materials. No permissible levels can be given.

c. X Radiation

If adequate protection is provided from gamma and neutron radiation, X radiation will be no problem insofar as personnel are concerned.

d. Electromagnetic Pulse

Except for a possible shock hazard due to induced voltages and currents, the EMP is not considered to be a hazard to personnel.

e. Thermal Radiation

Thermal radiation effects on personnel are normally expressed in terms of the degree of burn resulting from the exposure. In first-degree burns, there is only redness of the skin, and healing should occur without special treatment. Second-degree burns are deeper and more severe and are characterized by formation of blisters. In third-degree burns, the full thickness of the skin is destroyed and skin grafting is required to prevent scar formation.

Figure 6-24 shows the radiant exposures required to produce first- and second-degree burns on bare skin as a function of total energy yield. The increase in required radiant energy with yield is due to an extended delivery time for the thermal radiation at higher weapon yields. Differences in skin sensitivity, pigmentation, and other factors will cause some deviation from the values given by Fig. 6-24. The type of clothing worn by an individual will also greatly affect the possibility of thermal radiation injury. Additional information on personnel injuries from thermal radiation is provided in Refs. 6-2 and 6-3.

6.7.3 Equipment

a. Gamma and Neutron Radiation

Nuclear radiation can have both temporary and permanent effects on electronic equipment. The latter usually requires replacement of components while the former may disappear rapidly. There are three general types of effects: (1) ionization, (2) displacement, and (3) thermomechanical. Thermomechanical damage is caused primarily by X rays and is discussed in Ref. 6-10.

Gamma and X ray radiation are the primary causes of ionization effects in electronic components, although they can be caused to a lesser extent by neutrons. Ionization introduces

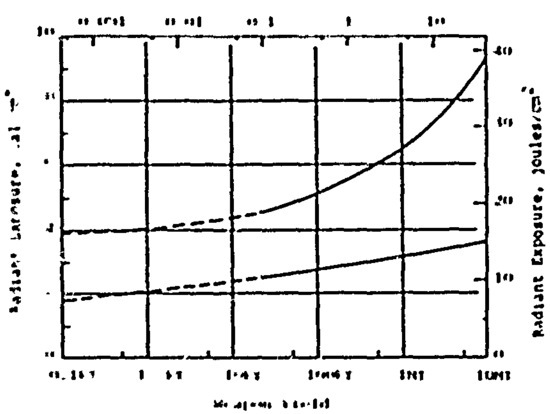

Figure 6-24 Radiant Exposures Required to Produce First- and Second-Degree Burns as a Function of Total Energy Yield (Ref. 6-2)

perturbating voltage and current pulses into the electronic circuitry of a system, and these pulses may cause overload of components, loss of stored information in memory units, saturation of critical components, loss of logic information, second-current overload, and semiconductor surface effects. Most ionization effects are dose-rate dependent.

Displacement effects are caused by the displacement of atoms in the crystal lattice structure of a material and result in changed properties of the component. Neutron radiation is the primary cause of these changes, although high-energy electrons, gamma rays and alpha particles can also be the cause. Neutron displacement effects are total-dose dependent.

The dose at which a semiconductor will fail is strongly dependent on its chemical and physical make-up. Reference 6-11 reports results of tests of many types of semiconductor and vacuum tube components and should be consulted for information on specific items. The maximum possible exposure, without damage to semiconductors, can vary over a range of approximately 10^{11} to 10^{16} n/cm^2. With this wide range in exposure limits, it is obvious that significant decreases in vulnerability can be gained by proper choice of semiconductors.

Reference 6-11 also reports tests of various types of transistors which were subjected to gamma dose rates from 10^7 to 10^{10} ergs/grams/sec ($\sim 10^3$ to 10^6 j/kg/sec) (carbon). One roentgen of gamma radiation is approximately equal to 88 ergs per gram ($\sim 9 \times 10^{-3}$ j/kg) (carbon). Peak transient currents of approximately 1 to 12,000 μA were observed in these tests, and the significance of these radiation-induced transient currents would depend on the characteristics of the transistor and the circuit in which it is used.

Vacuum tubes are affected by nuclear radiation in three ways: (1) formation of a high residual radioactivity in the various materials used in tube manufacture, (2) appreciable changes in electrical characteristics during and after radiation, and (3) increased fragility or, in many cases, complete mechanical failure. The latter effect results from neutron-induced increased brittleness of borosilicate glass commonly used in tube construction. Ceramic tubes have been found to be much more resistant to this type of damage. Cadmium shields have also been found to greatly increase the resistance of glass tubes to neutron radiation.

Reference 6-11 presents results of exposure of many types of vacuum tubes to total radiation exposures up to 10^{19} $(nv_o)t$ and 10^{15} ergs/grams (~10^6 j/kg)(carbon). The unit (nv_o) describes a thermal-neutron flux, preferably called a 2200-meter/sec flux. The associated unit of time-integrated flux is the $(nv_o)t$. The (nv_o) is the neutron density normalized to the velocity, v_o, of 2200 meters/sec. Although vacuum tubes appear to be more resistant to radiation than semiconductors, it is impossible to generalize the results reported in Ref. 6-11. Some glass tubes showed no ill effects at 10^{18} $(nv_o)t$, while others failed at the same neutron flux. The plate current of some tubes was significantly affected during and after irradiation; in others, there were no changes. Reference 6-11 also includes some limited data pertaining to the effects of nuclear radiation on other electronic

components such as resistors and capacitors.

b. X Radiation

X radiation will not normally be a significant problem for electronic equipment since it will be absorbed or attenuated by shields necessary to provide protection from other nuclear weapon effects. This condition is not necessarily valid for very high altitudes, where there is little atmosphere to absorb or attenuate the X rays. Reference 6-10 includes information regarding X ray effects at high altitudes.

c. Thermal Radiation

Thermal radiation effects on electronic equipment are primarily those related to the burning or charring of various materials. Table 6-3 presents selected data from Ref. 6-2 and 6-8 related to thermal effects on materials. The values given in Table 6-3 are approximate and can vary by ±100 percent for different yield weapons and changes in field conditions. In general, light colored reflective materials offer greater resistance to thermal damage than similar dark colored materials. Thickness of the material is also a factor in that smaller thicknesses of a given material are more susceptible to thermal effects. Critical values are generally higher for large yield weapons since the total thermal pulse is spread out over a longer time period.

d. EMP

The way in which EMP energy is collected is quite complex, but, in general, the larger or more extensive the conductor, the greater the amount

Table 6-3

THERMAL RADIATION EFFECTS ON SELECTED MATERIALS

EFFECT	RADIANT EXPOSURE	
	cal/cm^2	j/cm^2
Newspaper ignites	6- 8	25- 33
Unpainted wood chars	10-15	42- 63
Cotton canvas ignites (OD color)	18	75
Heavy cardboard box ignites	25	105
Surface melting or darkening of plastics (e.g., bakelite, cellulose acetate, lucite, plexiglass, polyethylene, and teflon)	60-70	250-290
Thin steel sheets melt (automobile body)	130	540
Automobile body steel vaporized and glass panel melts	400	1670

of energy collected. This energy can be converted into high currents and voltages flowing in any metallic conductor. The importance of these currents and voltages depends on the physical and electrical characteristics of the systems through which they flow. Whereas a power transmission line may easily withstand a 1000-ampere surge of current, a similar current passing through a solid-state communications receiver might reduce it to charred rubble.

Electrical systems subjected to EMP may suffer degradation in two ways: (1) functional damage, and (2) operational upset. Functional damage is that damage which requires replacement of parts or components before full service can be restored. Operational upset is defined to be temporary impairment of the performance of the system, but would not normally require replacement of components. Burnout of fuses, tubes and transistors are examples of functional damage. Erasure of magnetic core memory units or opening of circuit breakers are examples of operational upset.

The maximum permissible exposure to electromagnetic fields is obviously dependent on characteristics of the electrical components making up a system. In a complex system, it would be very difficult to establish overall sensitivity to EMP without physical testing under realistic conditions. Reference 6-6 suggests that electromagnetic radiation shielding for a facility be designed to provide the field attenuation shown in Fig. 6-25. Whether these criteria are adequate or necessary for another facility will depend upon the assumed threat, the sensitivity of the equipment to be housed within

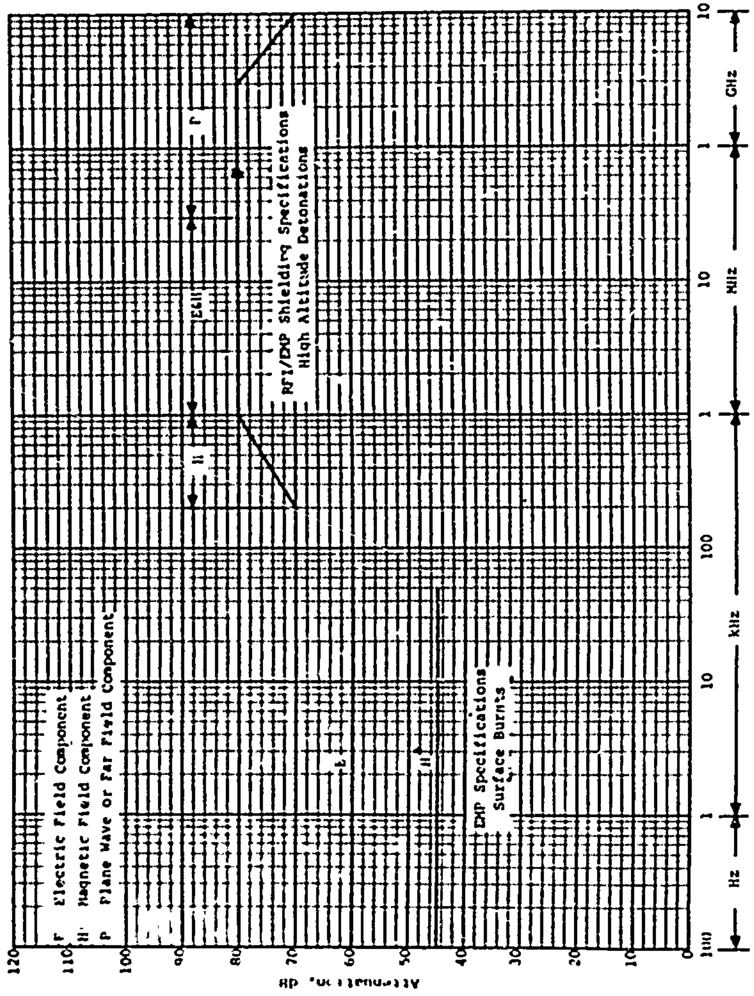

Figure 6-25 EMP and RFI/EMP Shielded Enclosure Specifications for Nuclear Detonation Applications--Attenuation Vs. Frequency (Ref. 6-6)

the facility, and the importance assigned to survivability of the equipment. Because of similarities between EMP and lightning, a good lightning protection system will provide some protection from EMP effects. However, there are significant differences between the two phenomena, and standard lightning protection devices cannot be relied upon for complete EMP protection.

Surge arresters or other limiting devices will normally have to be installed in accordance with the current and voltage limitations specified for equipment and cables. Although numerical values cannot be given for general classes of electronic components, Ref. 6-12 suggests the following listing in the order of decreasing sensitivity to functional damage.

- Microwave semiconductor diodes
- Field-effect transistors
- Radio-frequency transistors
- Audio transistors
- Silicon-controlled rectifiers
- Power rectifier semiconductor diodes
- Vacuum tubes

Thus, in addition to a greater resistance to neutron and gamma radiation, systems employing vacuum tubes are less susceptible to EMP effects than those employing transistors. While most vacuum tube circuits can probably survive 500-volt surges, many transistors and semiconductor diodes will be permanently damaged by 50 volts.

Similarly, Ref. 6-12 groups general classes of electronic or electrical systems according to their susceptibility to malfunction when subjected to EMP effects.

Most Susceptible:

- Low-power, high-speed digital computer (upset) either transistorized or vacuum tube
- Systems employing transistors or semiconductor rectifiers (either silicon or selenium), such as
  - computers
  - computer power supplies
  - transistorized power supplies
  - semiconductor components terminating long cable runs, especially between sites
  - alarm systems
  - intercom systems
  - life-support system controls
  - some telephone equipment which is partially transistorized
  - transistorized receivers
  - transistorized transmitters
  - transistorized 60- to 400-Hz converters
  - transistorized process control systems
  - power system controls; communication links

Less Susceptible:

- All vacuum tube equipment (does not include equipment with semiconductor or selenium rectifiers), such as
  - transmitters
  - receivers
  - alarm systems
  - intercoms
  - teletype-telephone
  - power supplies
- Equipment employing low current switches, relays, and meters, such as

  - alarms
  - power system control panels
  - process controls
  - panel indicators; status boards
- Hazardous equipment containing
  - detonators
  - squibs
  - pyrotechnical devices
  - explosive mixtures
  - rocket fuels
- Other
  - long power cable runs employing dielectric insulation; equipment associated with high energy storage capacitors or inductors

Least Susceptible:

- High-voltage, 60-Hz equipment, such as
  - transformers; motors
  - lamps, filament
  - heaters
  - rotary converters
  - heavy duty relays; circuit breakers
  - air-insulated power cable runs

The vulnerability of any of the above classes of equipment or systems can be drastically altered by long, exposed cable runs or protective devices. References 6-6, 6-12 and 6-13 contain many practical suggestions for decreasing the vulnerability of systems to EMP effects and should be consulted when detailed treatment of the problem is necessary.

6.8 ILLUSTRATIVE EXAMPLES

6.8.1 Description of Initial Radiation Environment at a Specified Ground Range

a. GIVEN: A 1MT (4.184×10^{15}j) surface burst whose fission yield is 50 percent of the total yield.

b. FIND: Complete description of the initial radiation environment on the ground surface at a ground range of 3000 feet (914 m).

c. SOLUTION

(1) Since a surface burst has been specified, the slant range is equal to the ground range. The quantities α and λ for use in Eq. 6-1 are determined first.

$$\alpha = \left[1 + 6\left(\frac{W}{1MT}\right)^2\right] \Big/ \left[1 + 0.03\left(\frac{W}{1MT}\right)^2 + 0.005\left(\frac{W}{1MT}\right)^3\right]$$

$$= \frac{[1+6]}{[1 + 0.03 + 0.005]}$$

$$= 6.7633$$

$$\lambda = 1070 + 1.5\left[\frac{W}{1MT}\right]^2$$

$$= 1070 + 1.5\,[1]$$

$$= 1071.5 \text{ ft } (326.6 \text{ m})$$

Substituting the above into Eq. 6-1 with a fission fraction, f = 0.5 and an average air density of 1.1 gms/liter,

$$D_\gamma = 7 \times 10^{13}\, f\alpha \left[W\right]\left[\frac{1}{R}\right]^2 \exp\left[-\frac{\rho R}{\lambda}\right]$$

$$= 7 \times 10^{13}\,(0.5)(6.7633)(1)\left[\left(\frac{1}{3000}\right)\right]^2 \exp\left[-\left(\frac{1.1 \times 3000}{1071.5}\right)\right]$$

$$= 1.2 \times 10^6 \text{ roentgens}$$

Multiplying by a factor of 2/3 for surface burst conditions, the initial gamma is

$$D_\gamma = 2/3\,(1.2 \times 10^6) = 8 \times 10^5 \text{ roentgens}$$

(2) The neutron dose is given by Eq. 6-2.

$$D_n = 2 \times 10^{22}\left[W\right]\left[\frac{1}{R}\right]^2 \exp\left[-R\rho/780\right]$$

$$= 2 \times 10^{22}\left[1\right]\left[\frac{1}{3000}\right]^2 \exp\left[-3000(1.1)/780\right]$$

$$= 3.23 \times 10^{13} \text{ neutrons/cm}^2$$

No correction is made for surface bursts.

(3) The X ray fluence is given by Eq. 6-5.

$$F = \frac{8 \times 10^3 Y_r}{R^2} \exp\left[-\mu R \rho 10^5\right]$$

Assume $Y_r = 0.7W = 0.7MT$ (2.93×10^{15}j) for these conditions. Assume a photon energy level of 0.1 Mev is representative of the weapon for purposes of selecting a mass absorption coefficient for air. Then, from Fig. 6-3, $\mu = 0.15$ cm^2/gm.

Using the above values in Eq. 6-5 and R = 0.914 km,

$$F = \frac{8 \times 10^3 (0.7)}{(0.914)^2} \exp\left[-0.15(0.914)(1.1)(10^5)\right]$$

$$\approx 0 \text{ cal/cm}^2 = 0 \text{ j/cm}^2 \quad (\text{since } e^{-15000} \approx 0)$$

(4) The integrated thermal flux is given by Eq. 6-10.

$$Q = 1.8 \times 10^4\, T\left[\frac{1000}{R}\right]^2 W$$

Assume 50 mile (80 km) visibility in order to obtain a transmission factor. From Fig. 6-10, T = 0.91 for 50 mile (80 km) visibility and 3000 foot (914 m) slant range. Then

$$Q = 1.8 \times 10^4 \left(0.91\right)\left(\frac{1000}{3000}\right)^2 \quad 1$$

$$- 1800 \text{ cal/cm}^2 = 7530 \text{ j/cm}^2$$

(5) From Fig. 6-6, the maximum electric field strength of the electromagnetic pulse for an airburst is 50 kilovolts/meter. This figure can be used as a rough estimate of the EMP for a surface burst. Reference 6-6 should be consulted for more accurate EMP prediction techniques.

6.8.2 Estimates of Shielding Requirements for Initial Gamma and Neutron Radiation

a. GIVEN: The initial gamma and neutron radiation environment of Example 6.8.1. Assume that a protective shelter is located at the 3000 foot (914 m) ground range.

b. FIND: The thickness of concrete walls required to reduce the initial external radiation to an acceptable level for personnel.

c. SOLUTION:

(1) If it is assumed that it is desired to keep the whole body acute dose to a level where no disabling sickness will occur, the external radiation dose should be attenuated so that personnel receive less than 100 rem total dose from gamma and neutron radiations. For gamma radiation,

Dose in rem ~ exposure dose in roentgens

For neutron radiation,

Dose in rem = 2.3×10^{-9} times the neutron fluence in n/cm^2

(2) The external radiation levels from Example 6.8.1 are

gamma = 8×10^5 roentgens

neutrons = 3.23×10^{13} n/cm^2

Converting to rem, the gamma contribution is 8×10^5 rem and the neutron contribution is

$$(2.3 \times 10^{-9})(3.23 \times 10^{13}) = 7.4 \times 10^4 \text{ rem}$$

(3) The total dose is 8.74×10^5 rem and the required overall attenuation is

$$\frac{100}{8.74 \times 10^5} = .000114$$

(4) Treating the gamma and neutron radiations separately, the thickness of concrete required to provide the overall attenuation can be obtained by selecting successive thicknesses. From Fig. 6-15, 70 inches (178 cm) of concrete would reduce the initial gamma by a factor of 0.0001. The tenth value thickness for neutron shielding is 10 inches (25.4 cm), so 70 inches (178 cm) of concrete would reduce the neutron dose by a factor of 10^7.

(5) The gamma radiation shielding requirement controls and 70 inches (178 cm) of concrete will provide the required degree of protection. The neutron radiation level inside the shelter will be negligible for this thickness of concrete, and a slight reduction in thickness is possible. A more accurate estimate of the shielding requirements could also be obtained from a consideration of the geometry of the structure. The actual required thickness would probably be somewhat less than indicated above.

6.8.3 Estimates of Residual Gamma Dose and Shielding Requirements

a. GIVEN: A protective shelter located 10 miles (16.1 km) downwind from a 1MT (4.184×10^{15}j) surface burst. Assume that the fission yield is 50 percent of the total yield and the average wind velocity between the detonation point and the shelter is 15 MPH (24.1 km/hr).

b. FIND:

(1) The total residual gamma radiation dose accumulated over a 12-hour period after the detonation by a person standing outside the shelter.

(2) The thickness of concrete required to reduce the fallout radiation to an acceptable level.

c. SOLUTION:

(1) From Fig. 6-11, the unit time reference dose rate at a point 10 miles (16.1 km) downwind from a 1MT (4.184×10^{15}j) fission yield surface burst is approximately 10^4 roentgens/hr. Since the fission yield is one-half the total yield, the reference dose rate for this example is

$$0.5 \times 10^4 = 5000 \text{ roentgen/hr}$$

It was assumed that the wind velocity is 15 knots (24.1 km/hr), so no scaling for wind velocity is necessary. The fallout will reach the shelter in

$$\frac{10}{15} = 0.66 \text{ hour}$$

From Fig. 6-14, the accumulated dose rate at 0.66 hour after the detonation is approximately 6 times the unit time reference dose rate, and at 12 hours the accumulated dose is about 8.2 times the reference dose rate. A person outside of the shelter would therefore be exposed to

$$(8.2-6)(5000) = 11{,}000 \text{ roentgens total dose}$$

(2) If an allowable dose of 100 rem = 100 roentgens is assumed, a reduction factor of

$$\frac{100}{11{,}000} = 0.0091$$

is required. From Fig. 6-16, about 18 inches (45.7 cm) of concrete is required to provide this reduction. As in the case of initial gamma, the true thickness would be somewhat less if structure geometry is considered.

6.8.4 Use of Reinforcing Steel for EMP Attenuation

a. GIVEN: A reinforced concrete protective shelter whose nominal dimensions are 15 x 20 x 100 feet (4.57 x 6.10 x 30.5 m).

b. FIND: The reinforcing steel size and spacing which will provide a 25 dB attenuation of the EMP electric field strength.

c. SOLUTION:

(1) From Fig. 6-17, a bar spacing of 14 inches (35.6 cm) on centers, in each direction, in a single course of 1.692-inch (4.30 cm) diameter bars, provides 23 dB attenuation of the signal. Since 25 dB is required, it is necessary to obtain another 2 dB by either changing the bar size, decreasing the spacing, or using double courses.

(2) If the initial bar size is retained but the spacing is decreased to 12 inches (30.5 cm), Fig. 6-19 indicates the attenuation can be increased by 2.5 dB. Therefore, 1.692-inch (4.30 cm) bars on 12-inch (30.5 cm) centers will provide the required attenuation.

6.9 REFERENCES

6-1 Brode, H.L., "Review of Nuclear Weapons Effects," Annual Review of Nuclear Science, Vol. 18, 1968. (U)

6-2 Glasstone, S., et al, The Effects of Nuclear Weapons, Government Printing Office, Washington, D.C., 1964. (U)

6-3

6-4

6-5 X-Ray Attenuation Coefficients From 10 Kev to 100 Mev, NBS Circular 583, National Bureau of Standards, Washington, D.C., April 1957. (U)

6-6 EMP Protection for Emergency Operating Centers, TR-61A, Department of Defense, Office of Civil Defense, Washington, D.C., May 1971. (U)

6-7

6-8 "Protective Construction for Shelters," Shelter Design and Analysis, TR-20 (Vol. 4), Department of Defense, Office of Civil Defense, Washington, D.C., 1970. (U)

6-9 Protective Construction Review Guide (Hardening), Office of the Assistant Secretary of Defense, Installations and Logistics, Washington, D.C., June 1961. (U)

6-10

6-11 Effects of Radiation on Materials and Components, Reinhold Publishing Corp., New York, N.Y., 1964. (U)

6-12 EMP Threat and Protective Measures, TR-61, Department of Defense, Office of Civil Defense, Washington, D.C., August 1970. (U)

6-13 EMP Protective Systems, TR-61B, Department of Defense, Office of Civil Defense, Washington, D. C., November 1971. (U)

SECTION VII

LOADS ON STRUCTURES

7.1 INTRODUCTION

7.1.1 General

Preceding sections have dealt primarily with free-field nuclear weapon phenomena, i.e., phenomena in the absence of facilities in the vicinity of the point of interest. This section presents methods for translating the free-field phenomena into the information required for the design or assessment of hardened facilities.

The design or analysis of a hardened facility involves the consideration of structural integrity and structure motion. Consideration of structural integrity involves evaluation of the stress and deformation conditions in the various elements of a structure and the structure as a whole to establish whether the structure will remain serviceable under the various nuclear environments. The information required for such evaluations consists of the loads (external tractions and inertial loads) which act on the various structural elements.

Motions must be considered so that inertial loads acting on structural elements, internal systems and/or personnel can be evaluated. Structure motion also affects external loads and must be considered in evaluating sliding, overturning and tilting of various structures.

Although this manual is restricted to nuclear environments, designers and analysts must recognize that structures and systems designed to survive nuclear environments must also perform satisfactorily under conventional environments which may include dead and live loads, overburden loads, lateral earth pressures, vibration, wind and earthquake. Earth pressures on deep facilities may be more severe at depth than the loads induced by nuclear ground shock.

The nuclear environments causing structural loads and motions are airblast, ground shock, ejecta and radiation. The relative importance of the various environments is dependent upon the location of the structure with respect to the ground surface and the burst point. Aboveground and surface flush structures are subjected to the complete range of environments while buried structures are subjected primarily to ground shock.

Loads associated with nuclear environments are dynamic and multidimensional. Major factors which determine the loads are:

- Free-field environment
- Medium in which the structure is located
- Properties and configuration of the structure

Ideally, the determination of loads and motions should be based on all the basic principles of mechanics including conservation of mass, momentum and energy. However, the complexity of the environment, geometry, and material behavior requires numerous assumptions, empirical relationships and engineering judgements in every aspect of the loading problem.

In the cases of airblast, debris impact and radiation, imposed external loads are fairly independent of structure motions and reasonable load estimates are obtainable in a relatively straightforward manner. In the case of ground shock, however, external loads and structure motions are interdependent. As a result, loads and motions must be determined by considering structure-medium interaction, i.e., the simultaneous solution of the equations of motion for the structure and the surrounding medium. Special loading problems arise for facilities sites in jointed rock where late-time behavior can potentially lead to relative displacements between adjacent blocks which can literally sever structures of practical size and strength. The magnitude of such relative displacements can only be estimated by empiricism and judgement.

The sequence in which the various nuclear environments are imposed on a structure is important. Radiation will occur first, airblast and ground shock some time later, and lastly, debris impact. Where structures are designed in the inelastic region, the effect of loading history must be considered. This is particularly important when structural degradation due to early loadings may reduce the ability of the structure to withstand later arriving effects.

This section presents relatively simple methods for estimating external structural loads and rigid body motions due to airblast, ground shock, ejecta and radiation. The deformation response of individual structural elements, which must be considered along with rigid body motions in analyzing structural elements and internal equipment is treated in Section IX.

The methods herein are recommended for preliminary estimates. The final design and analysis of major structures will require a more sophisticated treatment of structure-medium interaction, particularly with regard to ground shock. A brief discussion of some methods currently in use is given in the following paragraph.

7.1.2 Interaction Analysis Methods

The major area of uncertainty with regard to structure-medium interaction concern the interaction of ground shock with structures. Such interaction is important for all

types of structures, including aboveground structures which experience ground shock loads on their foundations.

Four approaches to the analysis of ground shock interaction which have been attempted, are under development and/or are currently being employed are

- Closed form solutions
- Lumped parameter models
- Finite difference techniques
- Finite element techniques

Closed form approaches seek analytical solutions to the equations of motion of structures and surrounding media. They are limited to some extent by restrictive assumptions with regard to material behavior, geometry, or loading conditions. However, they yield qualitative insight into phenomena and, in some cases, quantitative information for preliminary estimates. Closed form solutions are employed later in this section to arrive at some preliminary interaction estimates.

Lumped parameter approaches model interaction phenomena by placing discrete springs and dashpots between the structure and the surrounding media. Reference 7-1, for example, proposes that the radial stress on a horizontal or vertical cylinder may be assumed to be made up of three components:

- Free-field stress
- Stress dependent on relative displacement between the free-field and the structure
- Stress dependent on relative velocity between the free-field and the structure

The total radial stress at a particular location on the cylinder surface is given by

$$\sigma_r = \sigma_o + k(w_o - w) + s(\dot{w}_o - \dot{w}) \qquad (7\text{-}1)$$

where

σ_r = total radial stress

σ_o = free-field stress

w_o = free-field displacement in radial direction

w = structure displacement in radial direction

$\dot{w}_o$ = free-field velocity in radial direction

$\dot{w}$ = structure velocity in radial direction

k, s = constants

The constants k and s may be likened to a spring stiffness and viscosity coefficient, respectively, as illustrated in Fig. 7-1.

The general lumped parameter approach is relatively simple in concept and can be extended to include shear at the structure interface (for example Ref. 7-2) and the modeling of various interaction problems. However, the lumped parameter approach is limited by the fact that there is no rational method for selecting the spring stiffnesses and viscosity coefficient or the virtual mass which must be attached to the structure. In the case of small vibrations of foundations, the quantities are selected on the basis of closed form elastic solutions. However, closed form solutions are not generally available for a wide range of structures subjected to nuclear ground shock. Those closed form solutions that are available are more readily used directly. Experimental data may be used to select parameters. However, appropriate data are sparse.

The best available methods for treatment of structure-medium interaction phenomena are the finite difference and finite element methods. Such methods are capable of modeling complicated geometries, layered sites, nonlinear materials and arbitrary loading conditions. The major shortcomings of most present codes are limitation to two-dimensional problems and inability to predict late time displacement behavior. In addition, there are uncertainties associated with treatment of the structure-medium interface and the accurate transmission of high frequency components.

Finite difference codes have not been widespread application in structure-medium interaction studies. However, several codes (for example, Ref. 7-3 and 7-4) have the basic capability for treating such problems. References 7-5, 7-6, 7-7 and 7-8 describe finite element codes which may be used for structure-medium interaction studies. A finite element idealization of an interaction problem (Ref. 7-9) is shown in Fig. 7-2.

7.1.3 Organization of the Section

The remainder of this section is organized into five major paragraphs

Airblast Loads (para. 7.2)
Ground Shock Loads (para. 7.3)
Structures in Hard Rock (para. 7.4)
Loads Due to Ejecta and Radiation (para. 7.5)
Illustrative Examples (para. 7.6)

With the exception of structures in hard rock, the organization is based upon the nature of the free-field environment. Hard rock presents some unique differences which require separate discussion.

Paragraph 7.2 presents methods for estimating the external loads on structure surfaces exposed to the airblast. It is assumed that air is noncompliant and, therefore,

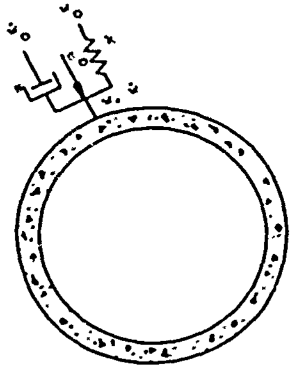

Figure 7-1 Lumped Parameter Model for Interaction Between Underground Cylinder and Medium (Ref. 7-1)

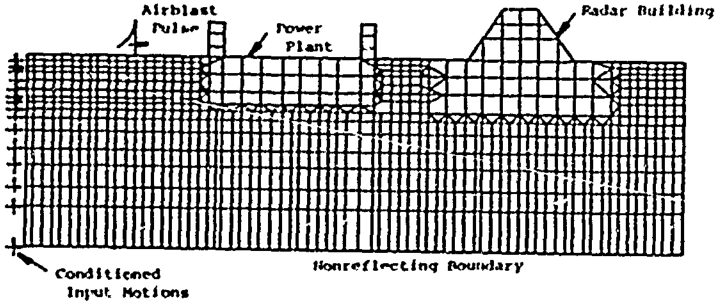

Figure 7-2 Analysis of Soil Structure Interaction Including Effects of Proximity of Buildings (Ref. 7-9)

airblast loads can be estimated directly without consideration of structure motions. Estimation of the motions of structures subjected to airblast loads is deferred to paragraph 7.3 since such motions are dependent upon the loads induced on soil bearing surfaces as well as airblast loads.

Paragraph 7.3 presents methods for estimating loads on structure surfaces which bear against soil as well as the rigid body motions of structures loaded by airblast and/or ground shock. Rigid body motions should be imposed as inertial loads or support motions in the analysis of individual structural elements. Unique differences associated with structures in hard rock are discussed in paragraph 7.4.

Paragraph 7.5 discusses the loads expected from ejecta and radiation. Methods are presented for estimating the intensity of stress waves induced by both phenomena. The methods are illustrated for a shallow buried rectangular structure and a shallow buried horizontal cylinder in paragraph 7.6.

7.2 AIRBLAST LOADS

7.2.1 General

The airblast loading on exposed structure surfaces is a function of the free-field overpressure and dynamic pressure, the size, shape and orientation of the surface, and the location and orientation of other surfaces in the vicinity. A factor of considerable importance is the general character of the airblast front. The simplest loading is that associated with an ideal shock in which the peak overpressure is reached instantaneously after which the overpressure decays in an exponential manner. Ideal shock loadings are of significant interest and are discussed in detail for various structural configurations. In the precursor region, the loading is more complex. The reflected pressure is reduced while the dynamic pressure is increased. Precursor loadings are subject to major uncertainty. Paragraph 7.2.9 provides some discussion of loadings in the precursor region.

Three components of airblast loading are normally considered: overpressure, reflected pressure and dynamic pressure. The overpressure is simply the airblast pressure-time history which occurs in the free-field. Reflected overpressures occur due to momentum change when the propagating airblast strikes a surface in the path of propagation. Dynamic pressures, associated with air flow behind the shock, cause drag and lift on objects which interfere with the flow.

The relative importance of overpressure, reflected pressure and dynamic pressure depends primarily on the size and shape of the structure and the character of the airblast pulse. In many instances, the net loading on a structure or structural element is more important than the load on each surface. In the case of large structures subjected to short duration blast waves, the net loading due to reflected pressures will probably be more important than that due to the dynamic pressures. As the structure becomes smaller, or the blast wave longer, the net loading due to overpressure on front and rear faces is of lesser importance and the dynamic or drag loading is the important component. The period of vibration of the structure basically serves as the factor determining the relative importance of the above components of the airblast loading. Short duration reflected pressure peaks may have a negligible effect on the response of low frequency systems but be an important factor in the response of high frequency systems. No general guidance can be provided regarding the relative importance of the three components of airblast loading. All components should be considered, at least in the preliminary study phases.

The discussions of [illegible]ast loading in the following paragraphs assume that the structure is in the Mach reflection region, where the airblast front is propagating parallel to the ground surface. If a structure is located in the regular reflection region, it will be subjected to higher vertical loads than in the Mach reflection region due to reflection of the incident blast wave on horizontal surfaces. The magnitude of the reflected pressure can be estimated using reflection coefficients which are discussed herein.

Although the airblast environment is probably the best defined of all nuclear environments, much uncertainty remains with regard to airblast loadings. The primary references for the material herein on ideal shock loadings are Refs. 7-10, 7-11 and 7-12 wherein the data base rarely exceeded an incident overpressure of 50 psi (34.5 N/cm^2). The material on precursor effects is derived from Ref. 7-13. Reference 7-13 presents ideal shock loadings which differ in some instances from the loadings herein. However, the differences are within the uncertainty of measured data and there is insufficient evidence to judge which formulation is superior.

7.2.2 Reflection Coefficients

Reflection phenomena were introduced in paragraph 3.2.6 in describing the regular reflection region and the Mach region associated with free-field airblast. Whenever the airblast wave propagating as a shock strikes a surface which is not parallel to its direction of propagation, a reflection process takes place which causes an increase in the peak overpressure. The reflection is caused by momentum change when the moving air changes direction as a result of striking the surface. The ratio of reflected overpressure to incident pressure is called the reflection factor. The reflection factor is a function of the peak overpressure in the incident wave and the angle at which the wave strikes the surface.

Defining the angle of incidence to be the angle between the shock front and the reflecting surface, a 90-degree angle of incidence corresponds to a surface parallel to the direction of propagation. Highest reflection factors occur at zero angle of incidence, i.e., a surface normal to the direction of propagation of the blast wave. Figure 7-3 presents reflection factors as a function of peak overpressure for an angle of incidence of zero. Figure 7-4 shows the effect of angle of incidence on reflection factors for a wide range of overpressure levels.

7.2.3 Drag and Lift Coefficients

The dynamic pressure due to the transient winds behind the airblast shock front exert drag and lift forces on objects which interfere with the airflow. Drag forces are defined as those forces due to dynamic pressure which act in the direction of air flow, while lift forces act perpendicular to the direction of flow. Drag and lift forces are a function of several variables including air flow characteristics and object shape, size, surface texture and location on the object.

The relationships between dynamic pressure and the forces acting on an object are expressed in terms of drag and lift coefficients. The drag or lift acting on an individual surface due to dynamic pressure is given by

$$F_s = C_s q A_s \tag{7-2}$$

where

F_s = total drag or lift on the surface

C_s = drag or lift coefficient for the surface

q = dynamic pressure

A_s = projected area of surface perpendicular to the air-flow for drag or parallel to the air flow for lift

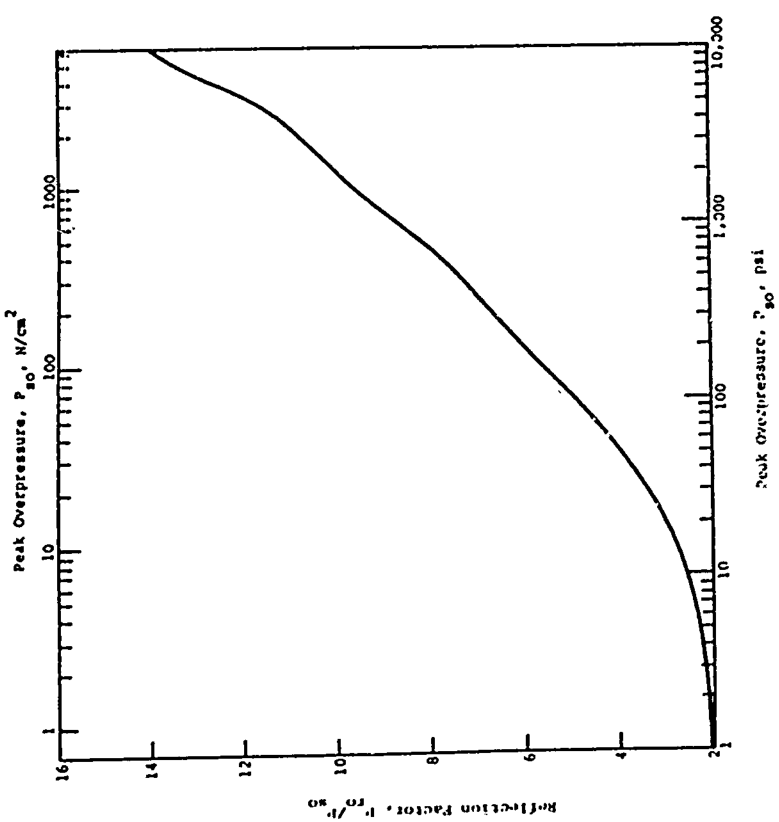

Figure 7-3 Normal Reflection Factor in Sea Level Air Vs. Incident Overpressure (Ref. 7-14)

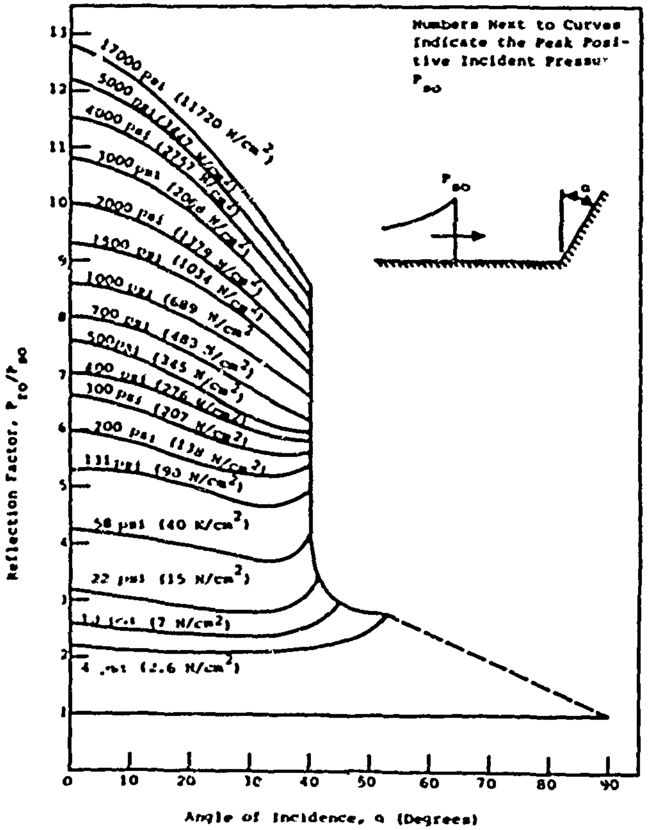

Figure 7-4 Reflected Pressure Coefficient Vs. Angle of Incidence (Ref. 7-15)

The total drag or lift force on an object is given by a similar equation

$$F_o = C_o q A \qquad (7\text{-}3)$$

where

F_o = total drag or lift on the object

C_o = drag or lift coefficient for the object

q = dynamic pressure

A = projected area of the object perpendicular to the air flow for drag or parallel to the air flow for lift.

The total object drag or lift is simply the vector sum of drag or lift acting on individual surfaces and, therefore, the object drag or lift coefficient is the sum of coefficients for individual surfaces.

For structural design or analysis, forces acting on individual surfaces rather than total drag or lift are generally required. Unfortunately, appropriate coefficients for a variety of shapes resting on a flat surface and over the range of pressures of interest in nuclear problems are lacking. With a few exceptions, most data consist of total drag coefficients on objects in the free air flow (i.e., away from the ground surface). Figure 7-5 presents object drag coefficients for four object shapes in the free-air flow. As can be seen, total object drag coefficients vary significantly with peak overpressure. Figure 7-6 presents front surface and rear surface drag coefficients for a circular disc. It should be noted that the rear surface coefficient is negative. The negative drag pressures are the result of vortices formed at the disc edge. The sum of the front and rear surface coefficients is equal to the total drag coefficient for discs given in Fig. 7-5.

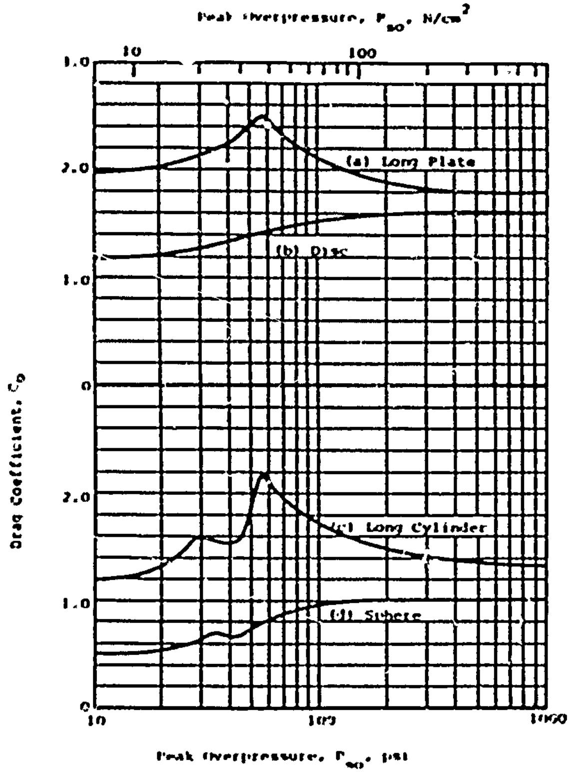

Figure 7-5 Drag Coefficients for Objects in the Free-Air Flow (Ref. 7-16)

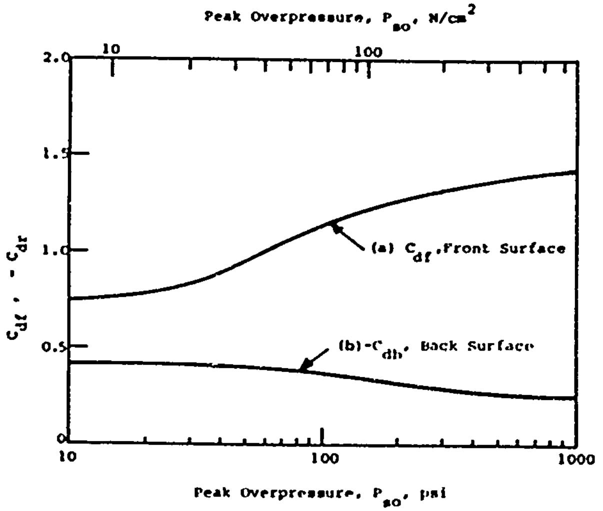

Figure 7-6 Surface Drag Coefficients for a Disc in the Free-air Flow (Ref. 7-16)

The coefficients in Figs. 7-5 and 7-6 may be used for portions of structures which are exposed primarily to the free-air flow. Additional object drag and lift coefficients for various structural shapes are shown in Fig. 7-7. Non-zero lift coefficients occur for unsymmetrical or non-normally oriented shapes. The data are for overpressures less than 20 psi (13.8 N/cm^2). Application at higher overpressures should be guided by the plate results presented in Fig. 7-5.

Protective facilities of most interest consist of enclosed structures resting on the ground surface. Drag and lift coefficients for individual surfaces as a function of overpressure level for such structures are limited. Figure 7-8 presents average surface drag coefficients at overpressures less than about 100 psi (69 N/cm^2) for three different enclosed structures resting on a planar surface. The coefficients assume ideal airblast conditions. Figure 7-9 presents detailed information on the variation with overpressure of the average drag coefficient on the surface of a wedge exposed head-on to dynamic pressure. Recent finite difference calculations (Ref. 7-18) indicate it is reasonable to take the drag coefficient on a wedge or incline facing away from the propagating airblast as about -0.2 as a first approximation for all overpressures and for angles of inclination less than 99 degrees.

Drag coefficients for precursor airblast waves differ somewhat from those under ideal shock conditions. Figure 7-10 presents drag coefficients for several object shapes resting on a planar surface due to precursor affected waves. Also shown in Fig. 7-10 are expressions which relate timewise the loads acting on the front surface to those acting on other surfaces. The time expressions represent a delay between application of average loads on the front face and back face or roof and are used to obtain net loads acting on the structure. In these expressions, U is taken equal to the

Profile and Wind Direction	C_{do}	C_L
→ □ F_L F_d	2.0	0
→ |	2.0	0
→ I	2.0	0
→ ⊢⊣	1.8	0
→ L	2.0	.3
→ ┐	1.8	2 1
→ L	2.0	-.1
→ ┌	1.6	-.5
→ ├	2.0	0
→ T	2.0	-1.2
→ ⊟	2.2	0

(Coefficients of Ref. 7-17 Rounded to the Nearest Tenth)

Figure 7-7 Object Drag and Lift Coefficients for Structural Shapes of Infinite Length at Low Overpressures (Less than 20 psi or 13.3 N/cm^2) (Ref. 7-17)

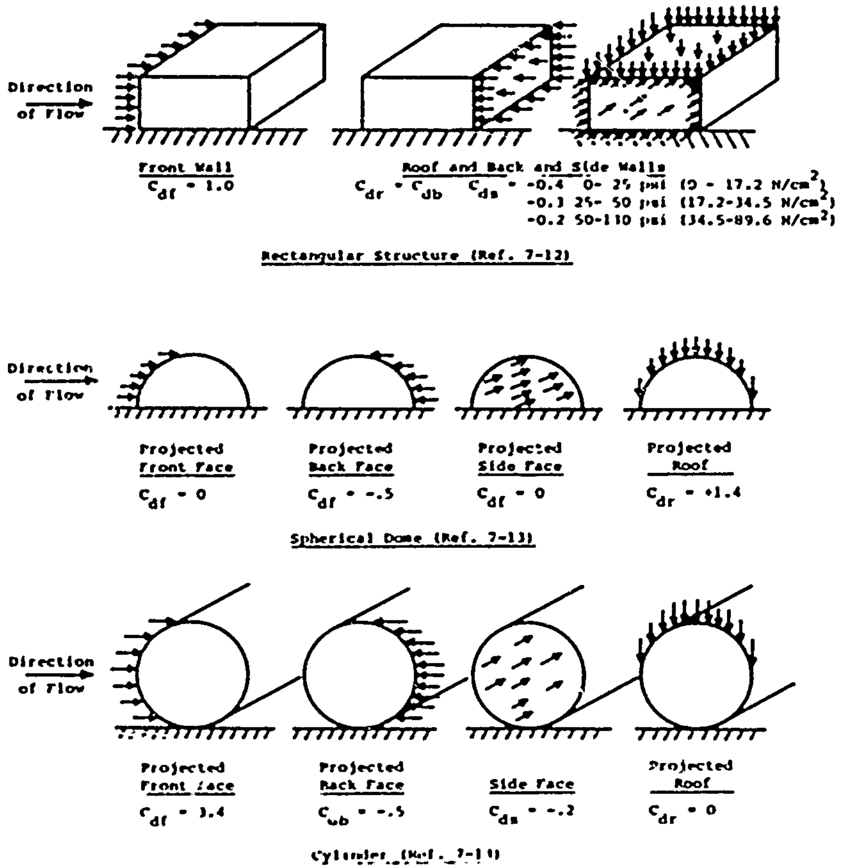

Figure 7-8 Average Surface Drag Coefficients for Objects Resting on the Surface (Ideal Airblast)

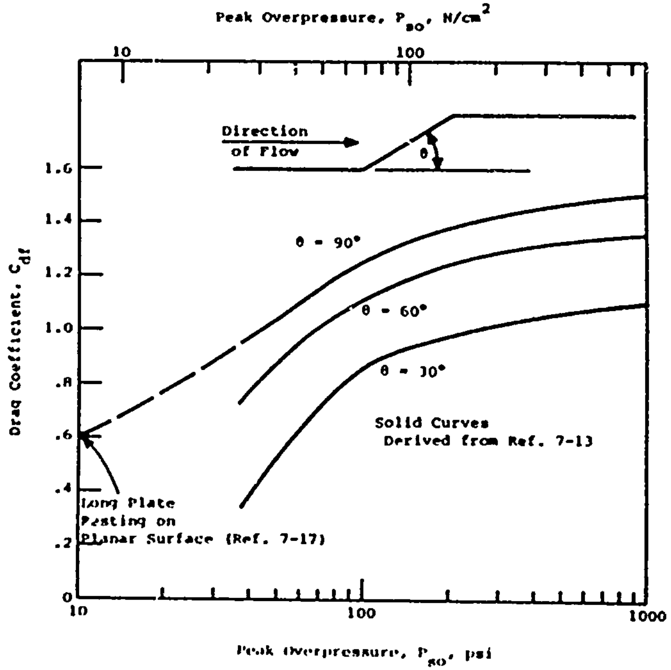

Figure 7-9 Average Drag Coefficient on Front Face of a Long Wedge

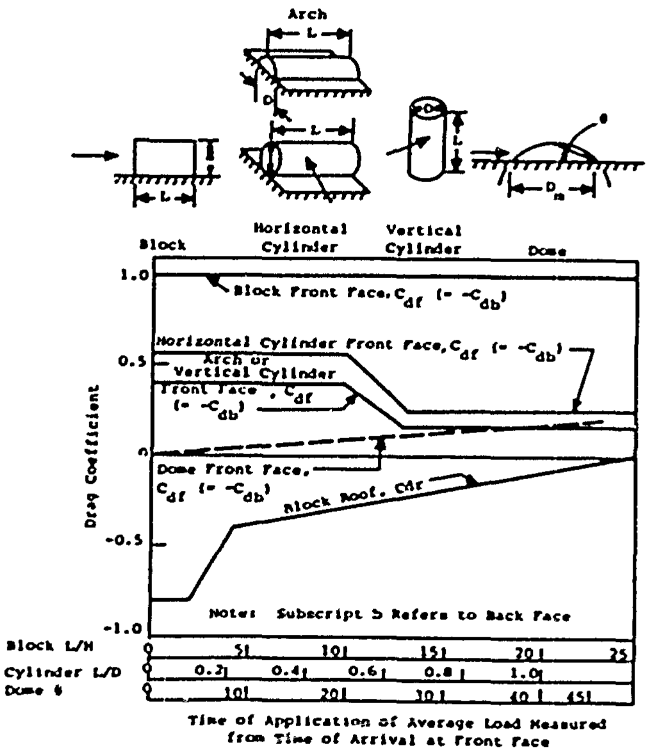

	Block	Arch or Cylinder	Dome
Back Face	L/U	D/2U	$D_n/2U$
Roof	L/2U	——	——

Figure 7-10 Drag Coefficients for Front Faces (C_{df}), Back Faces (C_{db}), and Roofs (C_{dr}) for Precursor-Affected Waves (Ref. 7-13)

precursor wave velocity. Precursor wave velocities for various burst conditions are given in Fig. 7-11. Additional information regarding ideal and non-ideal drag loading on domes and arches is included in a later paragraph.

7.2.4 Aboveground Closed Rectangular Structures

As an ideal blast wave encounters the front face (side facing the point of detonation), it is reflected to some higher value which is a function of the peak incident overpressure and the orientation of the surface with respect to the direction of propagation of the shock front. The blast wave then bends or diffracts around the structure subjecting first the sides and roof and finally the rear face to pressures equal to the incident overpressure. At the same time, these surfaces are also subjected to drag pressures which are a function of the dynamic pressure and drag coefficient for the surface. The total pressure on any face is assumed to be the algebraic sum of the overpressure (or reflected pressure) and drag pressures acting on the face at any instant of time. It is necessary to consider the loadings on the front, rear and roof surfaces of completely closed rectangular structures separately. Since it is usually assumed that the blast wave may approach from any direction, the side and rear walls are normally designed using the same techniques as for the front wall.

a. Front Face

An idealized representation of the load acting on the front face of a rectangular structure (Ref. 7-12) is shown in Figure 7-12(a). The maximum pressure, P_{ro}, is taken equal to the peak reflected pressure on the face. For an overpressure pulse which rises instantaneously from zero to its peak value, the rise time, t_r, to peak reflected pressure on the wall surface can also be taken as zero. For cases where

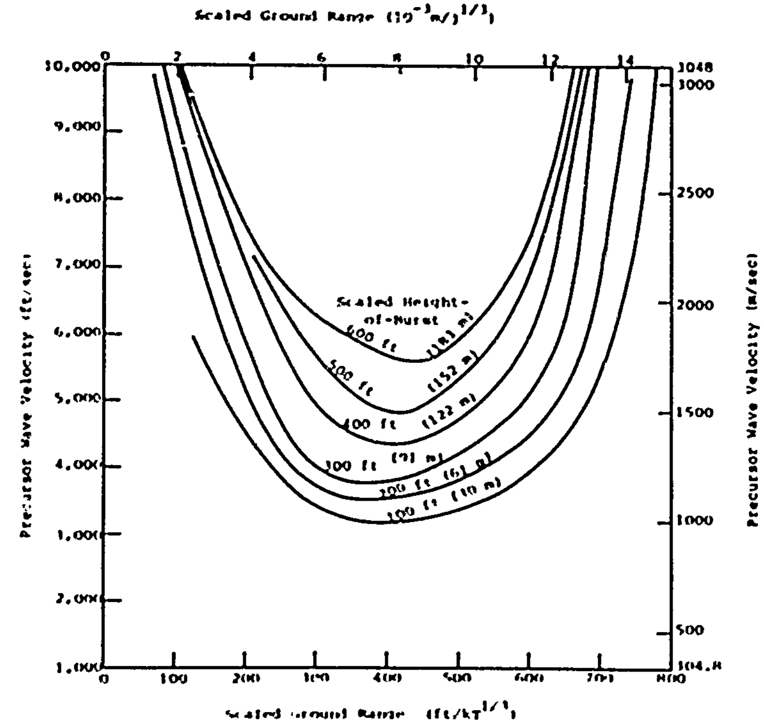

Figure 7-11 Precursor Wave Velocity vs. Ground Range for Various Heights-of-Burst (Ref. 7-13)

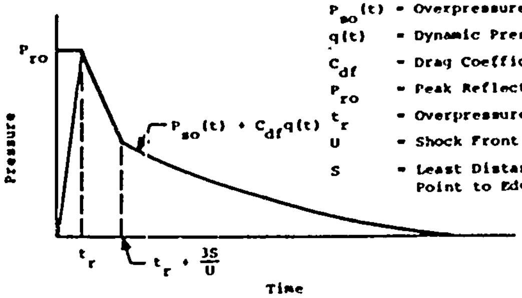

$P_{so}(t)$ = Overpressure-Time Function
$q(t)$ = Dynamic Pressure-Time Function
C_{df} = Drag Coefficient for Front Face
P_{ro} = Peak Reflected Pressure
t_r = Overpressure Rise Time
U = Shock Front Velocity
S = Least Distance from Stagnation Point to Edge of Structure

(a) Front Wall Loading

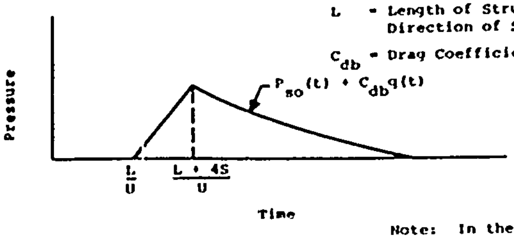

L = Length of Structure Parallel to Direction of Shock Propagation
C_{db} = Drag Coefficient for Rear Face

(b) Rear Wall Loading

Note: In these figures, the t in the expressions $P_{so}(t)$ and q(t) start at the time these expressions first apply, not at the origin of the loading plots.

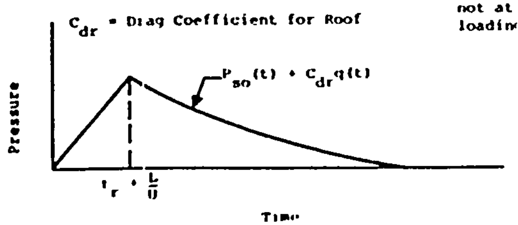

C_{dr} = Drag Coefficient for Roof

(c) Roof Loading

Figure 7-12 Loading on Aboveground, Closed, Rectangular Structure (Ref. 7-12) the rise to peak overpressure is accomplished in a finite time, the maximum intensity of reflected pressure, as well as the time variation of reflected pressure prior to the attainment of its maximum value, is uncertain.

The reflected pressure may be assumed to decay linearly from the peak to a value

$$P_{so}(t) + C_{df}q(t) \tag{7-4}$$

where

$P_{so}(t)$ = overpressure as a function of time

C_{df} = drag coefficient for front surface

$q(t)$ = dynamic pressure as a function of time

in a time, t_s, known as the stagnation time. The stagnation time is the time required for rarefaction fronts to move into the region of reflected stress from the edges of the structure which cannot contain the high reflected pressure (Ref. 7-19).

The stagnation time is related to the rarefaction front speed by (Ref. 7-19)

$$t_s = \frac{2S}{C_r} \tag{7-5}$$

where

t_s = stagnation time

S = least distance from stagnation point on front face to the edge of the structure

C_r = rarefaction front velocity

The stagnation point on the front face is defined to be that point at which no lateral flow occurs. For a rectangular structure with its foundation flush with the ground surface, the quantity S would be equal to the

height of the structure or one-half the structure width, whichever is less.

The rarefaction front velocity may be estimated by (Ref. 7-20)

$$C_r = C_o\left\{\left[\frac{\frac{P_{so}+P_o}{P_o}\left(\frac{P_{so}+P_o}{P_o}+6\right)}{6\,\frac{P_{so}+P_o}{P_o}+1}\right]\left[\frac{\frac{P_{ro}+P_o}{P_{so}+P_o}\left(\frac{P_{ro}+P_o}{P_{so}+P_o}+6\right)}{6\,\frac{P_{ro}+P_o}{P_{so}+P_o}+1}\right]\right\}^{1/2} \tag{7-6}$$

where C_o is the ambient speed of sound in air. The ratio of rarefaction velocity to shock front velocity C_r/U does not vary significantly with overpressure level (e.g., 0.87 at 10 psi (6.9 N/cm^2), 0.70 at 1000 psi (690 N/cm^2)). As a result, Eq. 7-5 can be expressed to a reasonable approximation at all overpressures by

$$t_s = \frac{3S}{U} \tag{7-7}$$

where U is the airblast shock front velocity. Equation 7-7 has been recommended in the past (e.g., Ref. 7-11) based upon shock tube data at low overpressures.

Reference 7-10 states that if the rise time exceeds the stagnation time, t_s, there is no reflection process and the front face pressure is equal to the sum of the overpressure and the dynamic pressure time histories. If the rise time is less than t_s given by Eq. 7-7 but greater than zero, it is conservative for design purposes to take the peak reflected pressure equal to that for a rise time of zero. For analysis of an enemy target, it would be conservative to assume no reflection occurs and the pressure is as given by Eq. 7-4. For a vertical surface, the variation of reflected pressure prior to its maximum value can conservatively be taken to be linear from zero to maximum in a time equal to the rise time of the overpressure pulse.

The idealized reflected pressure loading shown in Fig. 7-12 is not representative of all points on the front face of the structure. After reaching a maximum value, the decay of reflected pressure at any point is dependent on the distance of that point from the free edge of the structure. The idealization shown in Fig. 7-12(a) is recommended as a reasonable approximation to the average load on the front face.

If the front face of the structure is inclined with respect to the ground surface, the blast wave does not impinge on all elements of the wall surface at the same time; rather, the wave front traverses the wall in a finite time equal to the horizontal projection of the wall divided by the shock front velocity. The general nature of the loading on such an inclined surface can still be characterized as indicated in Fig. 7-12(a); however, the variation with time during the build-up to maximum pressure, as well as the decay from this maximum to the quasi-steady-state condition, is subject to an even greater uncertainty than exists in the case of the vertical wall surface. For such a case, it is recommended that the rise time to maximum reflected pressure be taken approximately as the transit time of the shock pulse across the inclined surface plus the rise time of the overpressure pulse. Similarly, it is recommended that a linear decay from peak reflected pressure to the condition of Eq. 7-4 in a time interval equal to 3S/U be used. S is taken equal to the distance from the stagnation point to the edge of the surface measured on the wall surface rather than along its projection on a vertical surface.

It should be noted that on an inclined surface the reflection factor, by which the peak overpressure is multiplied to obtain the peak reflected

pressure, and the drag coefficient, by which the dynamic pressure is multiplied to determine the drag pressure, vary with the slope of the inclined surface. The influence of the angle of incidence on reflection and drag coefficients has been treated in paragraphs 7.2.2 and 7.2.3.

b. Rear Face

As indicated previously, the rear and side walls of a structure are normally designed for the same loading conditions as the front wall, since the blast wave may approach the structure from any direction. However, in order to perform analyses and to determine the net horizontal force and overturning moments acting on a structure, it is necessary to determine the pressures acting on the rear face.

The loading on the rear face of an aboveground closed rectangular structure is shown in Fig. 7-12(b). No pressure is felt on the rear face until the shock front reaches that point. Using the same time reference as for the front face, average pressure begins to build up on the back face at a time equal to the length of the structure parallel to the direction of shock propagation divided by the velocity of shock propagation. At some later time after the rear face has become completely engulfed in the blast, the pressure reaches a maximum value equal to the side-on overpressure reduced by an amount equal to the drag pressure, which acts as a suction on the rear surface. Since the overpressure pulse does not impinge on the rear face, there is no reflected pressure. The pressure on the rear face is assumed to build-up linearly in a time equal to 4S/U or the rise time of the overpressure pulse, whichever is greater. S and U are defined in the same manner as for the front face. The linear variation of pressure with time assumed during this build-up period is only an approximation, as its actual variation is uncertain. As in the case of the reflected pressure decay on the front face, the assumed linear rise with time is not indicative of any particular point on the rear face. Those parts of the rear face adjacent to the free edges of the structure will first receive the influence of the shock pulse and, as the pressure travels around the structure, the entire rear face is loaded. The pressure variation as shown is recommended as a reasonable average condition to be considered for the entire rear face. Appropriate drag coefficients are given in paragraph 7.2.3 for determination of the drag loading on the rear face.

For large yield weapons and structures of normal proportions, it is usually satisfactory to ignore the variation in the free-field conditions between the front and rear faces of the structure. It would be more correct to consider the decrease in free-field overpressure and dynamic pressure consistent with an increase in range equal to the length of the structure in the direction of shock propagation; however, this decrease is usually so small as to be of little consequence. In the case of very large structures and very small weapons, the change in free-field conditions between the front and rear faces may be significant, particularly at very high overpressure levels. In such cases, variations in overpressure and dynamic pressure with range should be taken into account.

c. Roof

As the blast wave passes over the structure, the roof loading at any time is equal to the overpressure reduced by a negative drag pressure, or suction, associated with the flow of air around the structure. Since a finite time is required for the shock wave to traverse the roof of the structure, the average time to maximum pressure will be greater than the rise time of the overpressure pulse. Because of the lateral extent of the roof surface parallel to the direction of shock propagation, the real loading is a complex function of both location on the roof surface and the time-dependent variation of the overpressure pulse. The average roof loading shown in Fig. 7-12(c) is considered reasonable for design or analysis. The total pressure rises linearly from zero to a maximum value in a time equal to the transit time of the shock front across the roof plus the rise time of the overpressure pulse. In most cases, the rise time of the overpressure pulse is small compared to the transit time and can be neglected. Beyond the maximum value, it is equal at all times to the overpressure reduced, as mentioned above, by the negative drag loading. If the roof structure consists of separate panels supported on walls or columns, the lateral dimension used in computing the transit time for individual panels should be taken as the roof panel dimension parallel to the direction of shock propagation.

7.2.5 Surface Flush Structural Elements

The loads on surface flush elements are dependent upon the proximity of the element to aboveground obstructions. Three examples of surface flush elements are shown in Fig. 7-13. In the case of a surface flush roof with no aboveground obstruction in the immediate vicinity, the load acting is simply the free field overpressure. The average load on the roof may be taken as that shown in Fig. 7-12(c) for an aboveground structure, except that drag should be taken as zero, i.e., $C_{dr} = 0$.

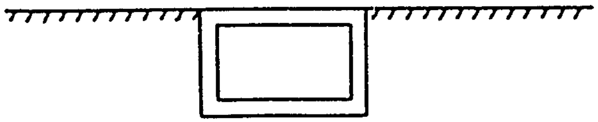

(a) Roof of Surface Flush Structure

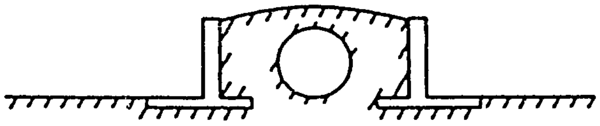

(b) Retaining Wall Foundation

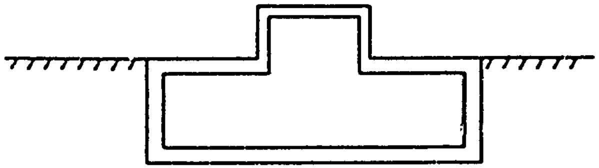

(c) Roof of Surface Flush Structure with Aboveground Protrusion

Figure 7-13 Examples of Surface Flush Structural Elements

The loads on surface flush elements in the vicinity of aboveground obstructions (Fig. 7-13(b) and (c)) are more complicated. Data and analyses concerning loads on such surfaces are not available in the literature. Surface flush elements in front of obstructions will experience reflected and drag pressures as well as overpressure. Elements behind obstructions will experience both overpressure and drag pressure and, possibly, weak reflected pressures.

The regions in which reflections and drag are assumed to act and the character of the loadings expected at points in front of and behind rectangular structures are shown in Fig. 7-14. In the regions both in front and behind the structure, drag is assumed to act over a length equal to the height of the structure. Reflections are assumed to act in front of the structure to a distance kS where k is a constant and S is the stagnation distance defined in Eq. 7-5. Reflections are assumed not to occur behind the structure.

The assumed loading at a point within a distance H ahead of the front face of the structure consists of the free field overpressure up to time t_1, at which time the front wall reflection arrives at the point. The reflection goes to zero at time t_2 after which the pressure is taken as the free field overpressure plus a drag pressure assumed equal to that occurring at the front face.

The loading at a point within the drag region behind the structure is taken equal to the loading on the back face of the structure (Fig. 7-12(b)). The arrival time t_3 is assumed to be the arrival time of the overpressure shock at the rear wall of the structure plus R/U where R is the slant range from the top of the structure to the point.

The character of the reflected shock at the front wall is shown in Fig. 7-15(a). The reflected pressure time history above the overpressure time history is called

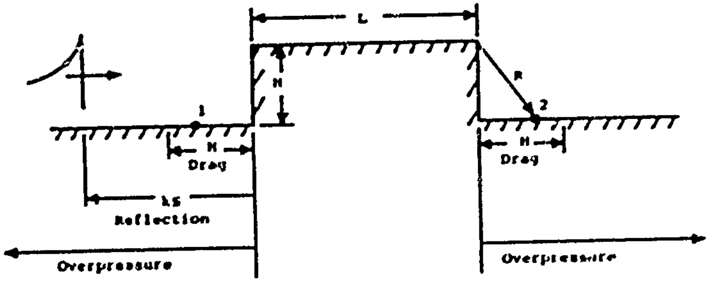

(a) Regions in which Reflection and Drag Act

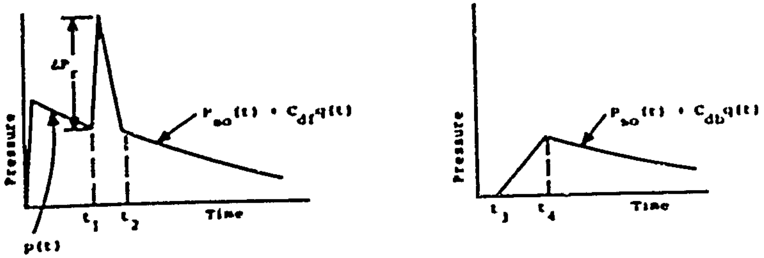

(b) Assumed Loading at Point 1

(c) Assumed Loading at Point 2

Figure 7-14 Loads on Surface Flush Elements Adjacent to Aboveground Rectangular Structures

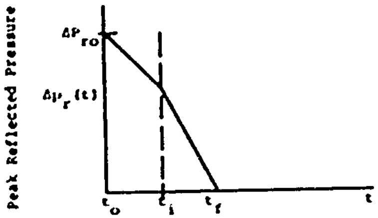

(a) Reflection at Front Wall

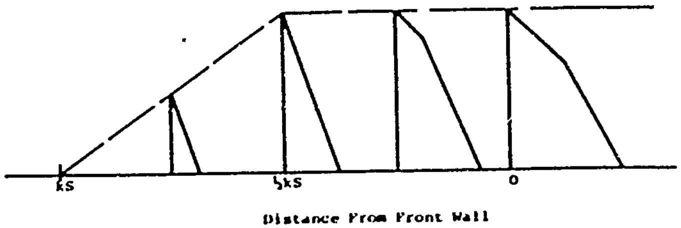

(b) Variation of Reflection Time History with Distance From Front Wall

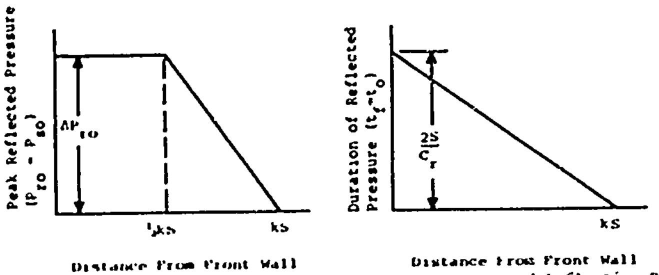

(c) Peak Reflected Pressure Above Peak Overpressure and Reflection Duration as a Function of Distance From Front Wall

Figure 7-15 Reflected Pressure on Surface in Front of Vertical Wall

$\Delta p_r(t)$. The peak reflected pressure above the peak overpressure is defined by

$$\Delta P_{ro} = P_{ro} - P_{so} \tag{7-8}$$

Rarefactions from the front wall edges or roof begin to erode the reflection at time given by

$$t_i = \frac{S}{C_r} \tag{7-9}$$

where

t_i = time at which rarefactions begin to erode the reflected shock

S = stagnation distance

C_r = speed of sound in the air after reflection (Eq. 7-6)

The time at which the reflection is completely eroded is given by Eq. 7-5.

The reflection front moves across the region in front of the structure back toward the burst point at an approximate shock velocity with respect to the structure of

$$U_r = \tilde{U}_r - u \tag{7-10}$$

where

U_r = reflected shock velocity with respect to the structure (assumed fixed in space)

$\tilde{U}_r$ = reflected shock relative velocity with respect to air

u = particle velocity associated with the incident overpressure

The velocity of the rarefaction behind the front, C_r, exceeds U_r and the reflection is continually eroded as it propagates across the surface.

The distance to which the reflection persists is

$$d = kS \tag{7-11}$$

where k may be estimated for overpressures greater than about 1 psi (0.7 N/cm^2) by

$$k = \frac{2}{\left(\frac{C_r}{U_r} - 1\right)} \tag{7-12}$$

The reflected shock velocity and rarefaction velocity may be estimated from Fig. 7-16. At overpressures greater than 100 psi (69 N/cm^2), k is approximately 2.7.

The change in the reflected pulse as it propagates away from the wall is illustrated in Fig. 7-15(b). Figure 7-15(c) shows the approximate variation of ΔP_{ro} (Eq. 7-8) and reflection duration as a function of distance from the front wall.

Recommended average loadings for surface flush elements which extend outward from a vertical wall a distance D which is less than the height of the wall (i.e., surfaces located within the drag region) are shown in Fig. 7-17. The time parameters are defined in the figure. The average peak reflected pressure above the overpressure, $\Delta \bar{P}_{ro}$, is taken as a weighted average of the ΔP_{ro} acting over the length of the surface D using Fig. 7-15(c). The drag coefficients, C_{df} and C_{db}, are the drag coefficients for the front and back wall surfaces, respectively.

7.2.6 Aboveground Closed Arches

The loading on an aboveground arch due to an ideal shock is similar in many respects to that for an aboveground rectangular structure. Major differences in loading result from the curvature of the arch. The angle of incidence between the advancing shock front and the surface being loaded

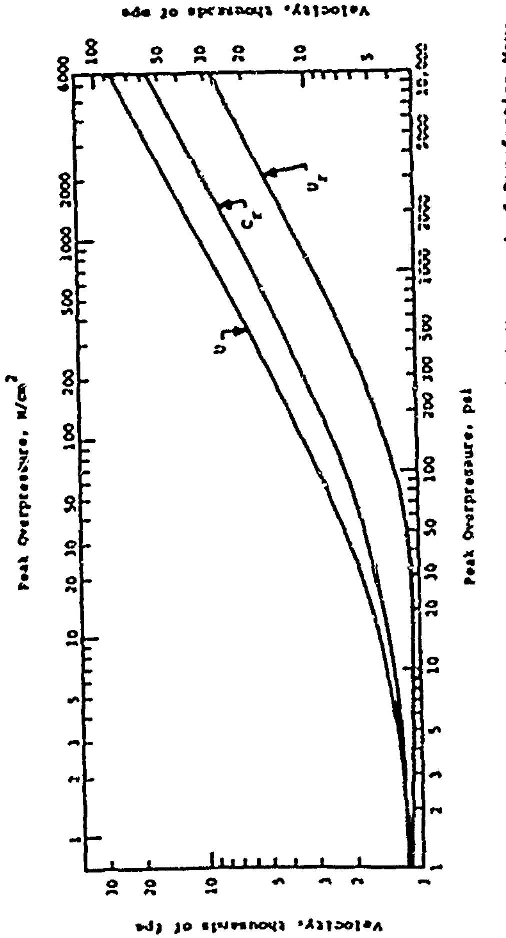

Figure 7-16 Velocities of Incident and Reflected Shock Waves and of Rarefaction Wave Behind Reflected Shock Front Versus Incident Overpressure

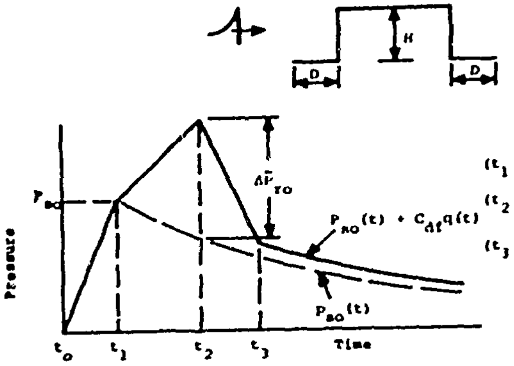

t_o = Arrival time at leading edge of front surface

$(t_1 - t_o) = \frac{D}{U}$

$(t_2 - t_1) = \frac{D}{U_r}$

$(t_3 - t_2) = \frac{1}{2}\left(\frac{4S+D}{C_r} - \frac{D}{U_r}\right)$

$P_{so}(t)$ and $q(t)$ begin to apply at t_1

(a) Average Loading on Surface Flush Element in Front of a Vertical Wall

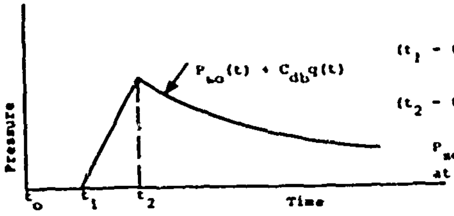

t_o = Arrival time at face of back wall

$(t_1 - t_o) = \frac{H}{U}$

$(t_2 - t_1) = \frac{4S}{U}$

$P_{so}(t)$ and $q(t)$ begin to apply at t_2

(b) Average Loading on Surface Flush Element Behind a Vertical Wall

Figure 7-17 Loadings on Surface Flush Elements Adjacent to Aboveground Obstructions varies continuously around the arch. Thus, the reflection and drag coefficients also change with location on the arch.

It is usually assumed that the shock wave approaches the arch in a direction perpendicular to its longitudinal axis. This direction of loading will produce the largest bending moments in the arch shell and in most cases determine its minimum thickness. The thickness of the shell may also be governed by the bearing load transferred to the shell by the end walls. The design of these end walls and determination of the bearing load applied to the shell should be based upon a loading obtained with the shock wave approaching normal to the end wall. As in the case of a rectangular structure, the load at any point on the surface of an arch may consist of three components: overpressure, reflected pressure, and dynamic pressure.

As the shock front passes across the arch, each point on the arch is subjected to a radially applied pressure equal to the overpressure in the shock wave at that particular point and time. While the shock front is transiting the arch, it is assumed that the arch is subjected to constantly varying nonuniform radial loads. After the arch is completely engulfed in the shock wave, the overpressure is considered to apply a uniform radial load equal to the time-dependent overpressure. If the span of the arch is very large and the duration of the overpressure pulse is very small, it may be desirable to take account of the variation of overpressure intensity around the arch.

As the advancing shock front impinges on successive points along a circumference of the arch, pressures are increased by reflection, with the increase depending on the angle of incidence between the shock front and a tangent to the arch at the point of interest. The reflection coefficient is greatest at the base of the arch, where the tangent

is most nearly vertical, and decreases to one at the crown, where the shock front is traveling parallel to the arch surface.

As the shock wave passes over the arch, each point on the arch is also subjected to a drag force. This drag force is a function of the dynamic pressure and drag coefficients, which vary from point to point around the arch because of the change in angle of incidence. The drag loading is assumed to produce a nonuniform, time-dependent, radial pressure around the arch, not only during transit of the shock front, but also after the arch is completely engulfed in the blast wave.

The preceding paragraphs clearly indicate the complexity of the actual airblast loading on an aboveground arch. Although a substantial amount of effort has been expended on studying the problem, the loading still cannot be rigorously defined. One of the more extensive efforts for low incident overpressure levels is summarized in Ref. 7-21. More idealized loadings of the same general character as those presented in Ref. 7-21 are given in Ref. 7-10 and are reproduced herein as Figs. 7-18 and 7-19. Design procedures for complex loadings of a form similar to those shown in Figs. 7-18 and 7-19 are presented in Ref. 7-21.

Reference 7-22 recommends a simpler loading for the design of aboveground arches which may be used with single degree of freedom models at low incident overpressures. The loading is based upon the assumption that an aboveground arch loaded by a shock wave traversing in a direction normal to its longitudinal axis will respond in two primary modes: (1) a breathing mode consistent with a uniformly applied radial pressure and (2) an antisymmetrical flexural mode corresponding to a load applied radially inward on the windward (front) side and radially outward on the leeward (rear) side of the arch. The first of these modal loadings, referred to as the compression

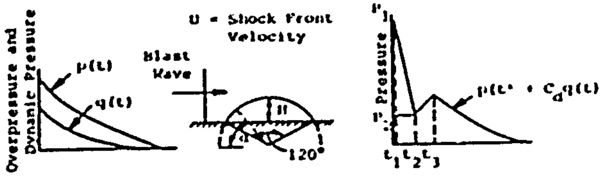

(a) Incident Pressures — Time

(b) Structure Orientation

(c) Loading Scheme at Any Point on Arch — Time

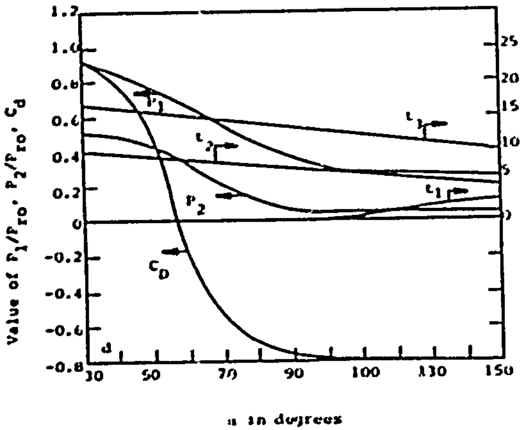

NOTES

1. P_1 and P_2 are related to P_{ro}, the ideal 0° reflection coefficient. These could be related to p, but the relationship to P_{ro} was felt to be more appropriate for front face loading. On the back side, the same relationship was used for consistency.
2. Time units are expressed as a ratio of height of arch, H, to velocity of shock front, U.

Figure 7-18 Ideal Loading Scheme--120° Arch for Peak Incident Overpressures of 25 psi (17.2 N/cm^2) or Less (Ref. 7-10)

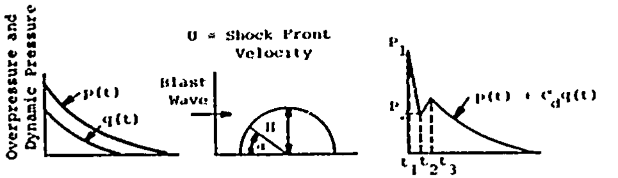

(a) Incident Pressures — Time

(b) Structure Orientation

(c) Loading Scheme at Any Point on Arch — Time

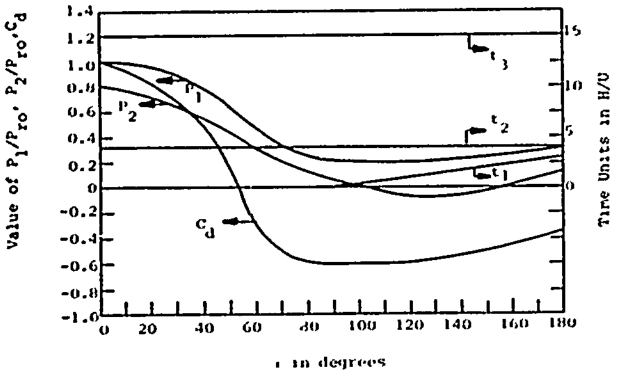

NOTES

1. P_1 and P_2 are related to P_{ro}, the ideal 0° reflection coefficient. These could be related to p, but the relationship to P_{ro} was felt to be more appropriate for front face loading. On the back side, the same relationship was used for consistency.
2. Time units are expressed as a ratio of height of arch, H, to velocity of shock front, U.

Figure 7-19 Ideal Loading Scheme--180° Arch for Peak Incident Overpressure of 25 psi (17.2 N/cm^2) or Less (Ref. 7-10) mode is illustrated in Fig. 7-20(a) and is identified as a uniform radial load of magnitude p_c. The second modal loading, the flexural mode, is an antisymmetrical load of magnitude p_f, as illustrated in Fig. 7-20(b). Both of these modal components are assumed to vary with time as described in the following paragraphs and as shown in Fig. 7-21.

As shown in Fig. 7-21(a), the uniform radial pressure p_c is assumed to increase linearly from zero to a maximum value of P_{so}, the free-field side-on overpressure, in a time t_r given by

$$t_r = (1 - \phi/\pi)\tau \qquad (7\text{-}13)$$

where

τ = transit time of the shock wave across the structure

ϕ = half the central angle of the arch

At times greater than t_r, the uniform radial component of loading is assumed to decay with time in the same manner as the free-field overpressure.

For the flexural mode, the pressure pulse may be considered as two components: (1) an initial component p_{f1} resulting from the unsymmetrical loads imparted to the arch as the shock wave passes over the arch and (2) a drag component p_{f2} resulting from the continuing drag loading after the arch has been engulfed by the shock wave. These components are shown in Fig. 7-21(b) and 7-21(c).

The initial component of the flexural mode, $p_{f1}(t)$, is assumed to increase linearly to a maximum value of

$$p_{im} = [(1/2) + (\phi/\pi)]P_{so} - \left|\frac{C_d q_o}{\frac{2\pi}{\phi} + 6}\right| \qquad (7\text{-}14)$$

at a time $\tau/2$ and to decay linearly to zero at time $(1 + 3\phi/\pi)\tau$, as shown in Fig. 7-21(b).

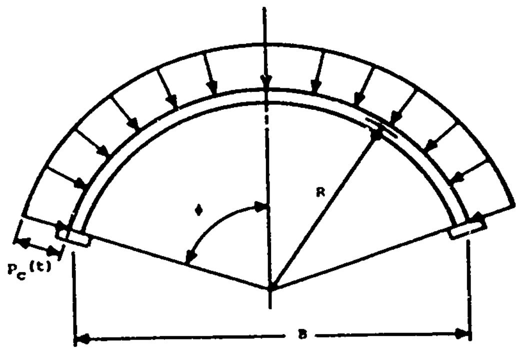

(a) Uniform Compression Loading (see Fig. 7-21 for variation with time)

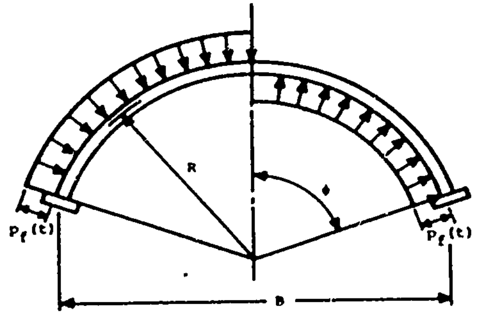

(b) Flexural Loading (See Fig. 7-21 for variation with time)

Figure 7-20 Conventionalized Blast Loading on an Arch (Ref. 7-22)

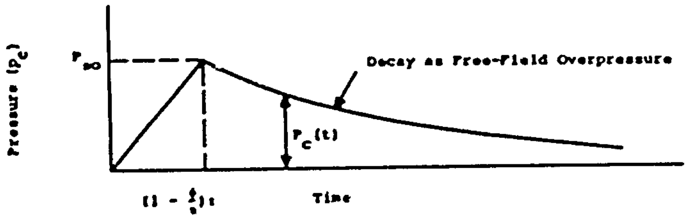

(a) Uniform Compression Loading

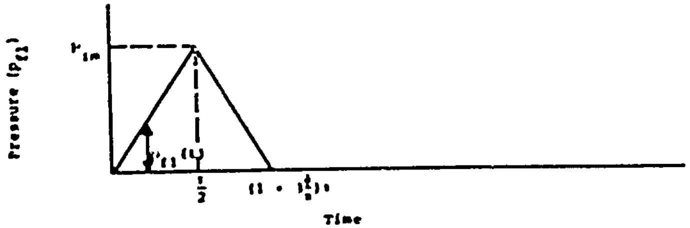

(b) Initial Component of Flexural Loading

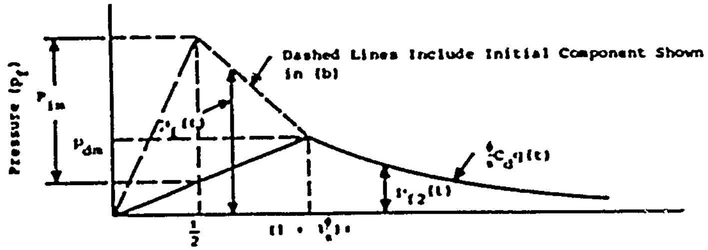

(c) Drag Component of Flexural Loading

Figure 7-21 Time-Dependent Loadings on Aboveground Arches For Single Degree of Freedom Analyses (Ref. 7-22)

The drag component of the flexural loading, $p_{f2}(t)$, increases linearly to a maximum value of

$$p_{dm} = (\phi/\pi)C_d q_o \qquad (7\text{-}15)$$

at a time $(1 + 3\phi/\pi)\tau$ and thereafter remains approximately equal to

$$p_{f2}(t) = (\phi/\pi)C_d q(t) \qquad (7\text{-}16)$$

The initial drag and components of flexural loading are combined as shown in Fig. 7-21(c). For the loadings shown in Figs. 7-20 and 7-21, zero time is taken in all instances to be the time at which the shock front first reaches the windward surface of the arch.

The drag coefficient can be taken as approximately 0.4 for a nearly ideal blast wave when the peak overpressure is less than about 25 psi (17.2 N/cm^2). For higher peak overpressures or nonideal wave forms, such as caused by a precursor, it is recommended that C_d be taken as about 1.0. A later paragraph includes some additional information regarding precursor region loadings.

The combined flexural loading is obtained as a summation at any time of the two loading components p_{f1} and p_{f2}. Thus

$$p_f(t) = p_{f1}(t) + p_{f2}(t) \qquad (7\text{-}17)$$

The simplified loadings of Figs. 7-20 and 7-21 are considered reasonable for many cases of design or analysis at low overpressures employing single degree of freedom models. If circumstances warrant a more rigorous analysis, the methods outlined in Ref. 7-21 may be utilized. Although the loadings used in the procedures of Ref. 7-21 are a more realistic representation of the actual loads on an aboveground arch, there are substantial uncertainties regarding the parameters used to define the loads. The complexity of the loading and analysis presented in Ref. 7-21 may imply a greater accuracy than actually exists.

7.2.7 Aboveground Closed Domes

The loads induced by airblast on aboveground closed domes are similar in characteristics to those on aboveground closed arches. Definition of the load at a specific point on a dome is even more complicated, however, due to the three-dimensional curvature of a dome.

Reference 7-21 presents loading schemes for aboveground domes which are based upon measurements made on the surface of 50-foot (15.2 m) base diameter, 90-degree central angle domes in Operation Plumbbob. Figure 7-22, from Ref. 7-10, shows a more idealized version of the dome loading scheme presented in Ref. 7-21, but it still represents a complex pressure distribution varying with time and location. Nonideal wave forms would alter both peak pressure values and variation with time.

Figure 7-23 presents a simplified load distribution for domes (Ref. 7-22), which is similar to that for arches, except that the simplified loading acknowledges the longitudinal and latitudinal variations associated with the reflected and drag components of the load.

As in the case of arches, it is recommended that for single degree of freedom analyses the loading be taken as composed of two parts, one part corresponding to the compression mode of response and the other the antisymmetrical or flexural mode of response. These loadings are illustrated in Fig. 7-23. The uniform compression component of load has a maximum value equal to the peak side-on overpressure, P_{so}. It has a rise time equal to that given in Eq. 7-13 for an arch, after which the pressure decays in time as the free-field overpressure.

The flexural component of load varies in time with both latitude and longitude. The latitudinal variation can be taken as shown in Fig. 7-23(c). The load is assumed

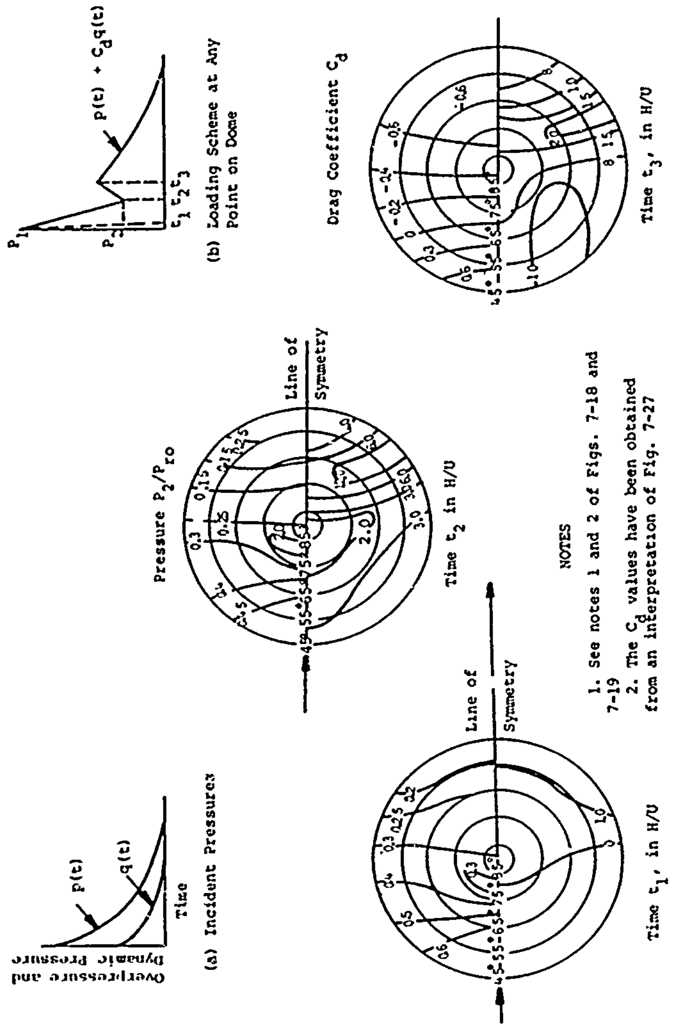

NOTES

1. See notes 1 and 2 of Figs. 7-18 and 7-19
2. The C_d values have been obtained from an interpretation of Fig. 7-27

Figure 7-22 Ideal Loading Scheme for 45° Dome for Peak Incident Overpressures of 25 psi (17.2 N/cm²) or Less (Ref. 7-10)

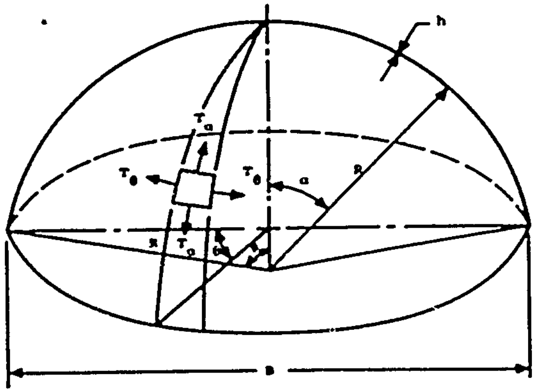

(a) Dome Notation

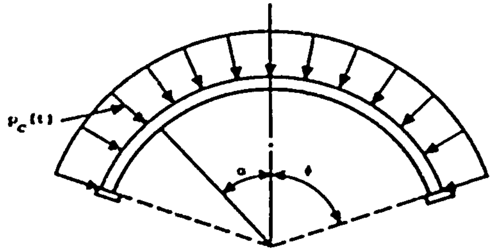

(b) Uniform Radial Component

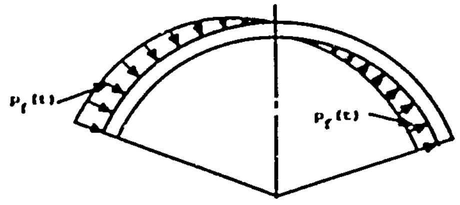

NOTE:
$p_f(t)$ varies sinusoidally with latitude from maximum at α = ϕ to zero at α = 0; it also varies sinusoidally with longitude from maximum at θ = 0° to zero at θ = 90°

(c) Flexural Component

Figure 7-23 Blast Loading on an Aboveground Dome (Ref. 7-22)

to vary sinusoidally from a maximum value at the spring line to zero at the crown. The load is also assumed to vary sinusoidally, with longitude, from a maximum at θ = 0° to zero at θ = ± 90°. The reference line for θ is a horizontal radial line through the center of the dome and ground zero. The time variation of the load is assumed to be the same as that given in Fig. 7-21 for the flexural component of the arch load. As for an arch, it is convenient to separate the flexural loading into two components for subsequent single degree of freedom analyses; one corresponding to the unsymmetrical loading, which occurs during the transit of the shock front across the dome, and the other to be continuing force resulting from drag pressures.

The total unsymmetrical loading, $p_f(t)$, is equal to the sum, at any time, of the initial component, $p_{f1}(t)$, and the drag component, $p_{f2}(t)$. For a dome, P_{im}, the maximum value of p_{f1}, should be equal to the maximum reflected pressure on the windward part of the dome. The drag component is calculated from Eq. 7-16. Both the reflection coefficient and the drag coefficient used to determine the drag loading component, p_{f2}, should be chosen consistent with the slope of the dome surface at its base. Selection of reflection and drag coefficients is discussed in Paragraph 7.2.3.

7.2.8 Open Structures

Reference 7-12 describes the major effects of openings in aboveground structures. If an aboveground structure has openings, the airblast loading is substantially modified. The extent to which the loading is modified is dependent primarily on the percentage of the wall surface area that is open, thereby permitting the blast wave to pass into or through the structure rather than around and over it. The most significant influence of wall openings is that they permit a buildup of pressure inside the structure. This interior buildup of pressure tends to reduce the effects of overpressure on all elements of the structure. If the same overpressure acts on the front and rear surfaces of an element, the net load, insofar as overpressure is concerned, is zero. The interior pressure buildup is a complex process which is a function of several factors, including the pressure differential at the opening and the ratio of the area of the opening to the interior volume. In most cases a detailed analysis of the interior pressures is not justified and gross assumptions are made regarding their influence on structural response.

If the percentage of open wall area is very small, the time required for a build-up of internal pressure will be so long as to have virtually no influence on the loads for which the structure or its elements should be designed. In such a case, the structure should be designed as a completely closed one. At the other extreme, if the structure consists primarily of open framing, the effect of the wall area becomes undetectable and the entire structure is engulfed both internally and externally as the advancing shock passes through it. For such a structure, the only forces which must be considered are those imparted to the relatively small individual structural elements of the frame. Between these two extremes, there exists a broad spectrum of structural types with varying percentages of wall area. It is generally assumed, primarily on the basis of theoretical studies, that a structure can be considered a closed structure if the open wall area is less than about 30 percent of the gross wall area. For these cases, the airblast loading is determined from the procedures discussed in previous paragraphs. For structures in which the wall openings represent more than about thirty percent of the gross wall area, and interior partitions do not influence the passage of the blast wave, structures should be considered open.

The distinction between an open and closed structure is conservative for design purposes, since the loadings for a closed structure are substantially more severe than those for an open structure of the same size and structural configuration. It is not conservative for target analysis or assessment since the assumption of a closed structure estimates a more severe loading condition than actually occurs. If thirty percent wall openings are considered adequate to permit the buildup of internal pressure necessary to counteract the effect of externally applied overpressure, it is obvious that there will be some reduction at smaller percentages of openings. Since there is little basis for recommendations at lower percentages of openings, the assumed interior pressure is dependent upon the degree of conservatism desired in the assessment. It could be assumed, for example, that 15 percent openings would allow an interior pressure buildup to 50 percent of that on the exterior of the structure.

Considering a rectangular structure, the loading on the front wall elements of an open structure can be determined by treating the element as a closed structure, with proper consideration for the effect of the element's dimensions on the time variation of the loading components, for example, the dimension L which determines the time at which pressure begins to build up on the rear face of the structure or element should, for an open structure, be equal to the dimension of the element in a direction parallel to the direction of shock propagation. For a front wall, it would be equal to the thickness of the wall. Similarly, the dimension, S, which defines the time required for the reflected pressure on the front face to decay to the condition of Eq. 7-4, is now the least distance from the stagnation point of the element to the edge of that element. The nearest edge can be either an edge of the structure or an edge of the wall opening. Figure 7-24(a) is an idealized representation of the loading of a front wall element. Note that the drag loading component is neglected on the interior surface of the wall. In an open structure, the effect of the overpressure component of loading and the duration of the reflected pressure component are greatly reduced leaving primarily a drag loading due to the dynamic

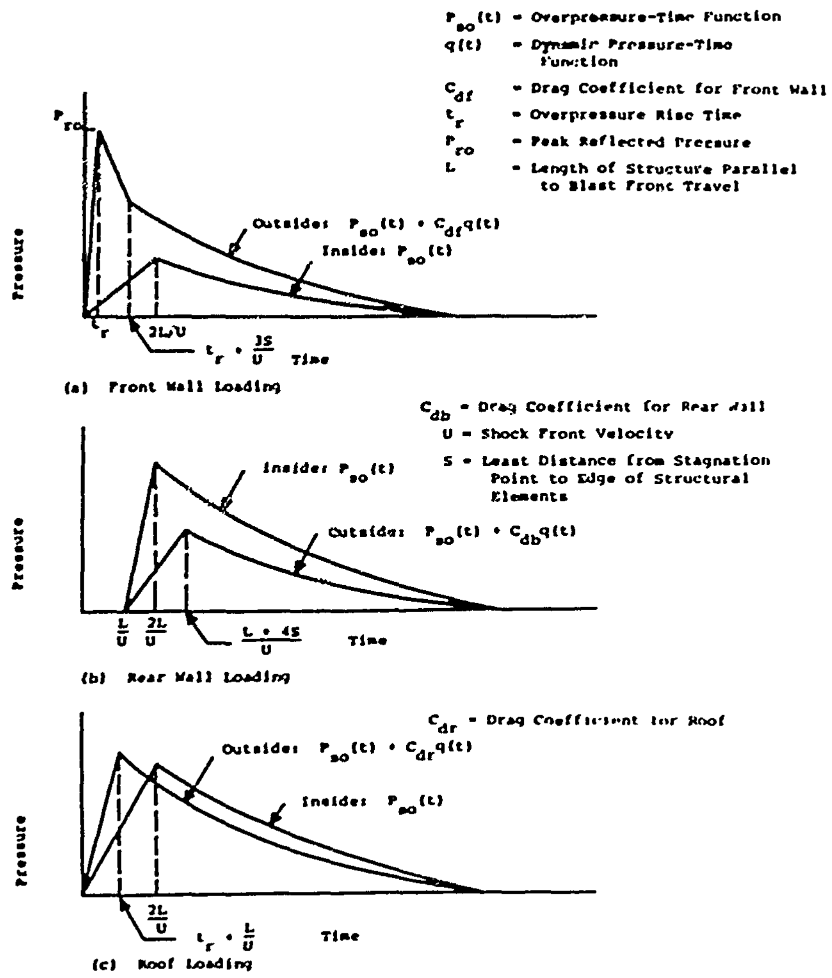

Figure 7-24 Loading on Aboveground, Partially Open, Rectangular Structure (Ref. 7-12)

pressure. For a bare structural frame, it is considered reasonable to neglect the overpressure and reflected pressure components of load.

The rear wall of a rectangular open structure is loaded in a manner similar to that of the front wall. The blast wave passing through the structure loads the inner surface of the wall with overpressure and reflected pressure components. As for the front wall, the drag loading component on the inside surface is assumed to be negligible. An idealized representation of the loads acting on the rear wall of an open structure is shown in Fig. 7-24(b). As seen in Fig. 7-24(b), the loading on the interior surface of the rear wall can exceed that on the outside surface, and all walls of open or partially open structures should be designed to withstand these loads.

The loading on the roof of an aboveground, open, rectangular structure is shown in Fig. 7-24(c). As for other surfaces, the net load acting on the roof is the algebraic sum of the interior and exterior pressures. It should be noted that, at some periods in time, the interior pressures exceed those acting on exterior surfaces, and roof structures must be designed to resist this uplifting force. Reflection and drag loading components on interior roof surfaces are assumed to be negligible.

The shielding of one element by another positioned between it and the source of the blast is neglected in the preceding discussion. If the distances between elements in the direction parallel to shock propagation are greater than 10 times the lateral dimension of the forward element, then shielding effects are negligible. At closer spacings the turbulence caused by the forward element may affect the reflected and drag pressure components of load, but the effect is not sufficiently defined to allow recommendation of procedures for predicting its magnitude.

Although the drag coefficients given in paragraph 7.2.3 assume the elements stand alone, they can also be used for groups of elements. If an estimate must be made of the shielding effect for closely spaced elements, it is suggested that the load on the element be assumed to vary linearly from zero at zero spacing to the full normal load at a spacing of 10 times the lateral dimension of the forward element. In the case of open frame structures, the effects of shielding are usually neglected even though the distance between individual structural elements may be much less than 10 times the lateral dimension.

Although there are few structures which are actually open frame structures, there are many which consist of simple structural frames covered with a lightweight frangible siding such as corrugated metal, cement asbestos or unreinforced masonry. Such walls usually are incapable of resisting even very low pressures and are blown off the frame early in the loading process. While failing, the wall covering imparts an impulse to the structural frame. In most cases, this impulse is so small that it can be neglected. However, if the wall covering is such that an appreciable impulse is required to fracture it, an estimate can be made of this failure impulse, which is then added at time zero to the drag loading determined for the exposed structural frame. In the absence of better information, Ref. 7-11 suggests 0.04 pound-seconds per square inch (0.03 $N\text{-sec/cm}^2$) of siding as an approximate value of the impulse transmitted to the frame by cement-asbestos, corrugated steel or aluminum siding before failure.

7.2.9 Loads in the Precursor Region

Reference 7-13 presents a compilation of data and methods for predicting free-field airblast effects and airblast loadings in the precursor region. Major differences between ideal shock and precursor loadings are: (1) more complicated waveforms, (2) the absence of reflections and (3) increased drag loadings.

When the overpressure rise time is greater than the stagnation time, as is generally the case in the precursor region, reflections do not occur and the pressure acting on a structure surface may be taken as

$$p(t) = P_{so}(t) + C_d q(t) \tag{7-19}$$

where

$p(t)$ = total pressure as a function of time

$P_{so}(t)$ = overpressure as a function of time

C_d = drag coefficient for the surface in the precursor region

$q(t)$ = dynamic pressure as a function of time

Methods for estimating overpressure and dynamic pressure time histories and front velocities in the precursor region are presented in Section III. Drag coefficients are presented in paragraph 7.2.3. The information in Section III can be combined with Eq. 7-18 to develop precursor region loadings by methods analogous to those employed previously for ideal shocks.

The drag coefficients presented earlier for arches and domes are average values and result in average front and rear face loadings for such structures. Precursor loadings which take account of the variation in drag coefficient with location on the structure are shown in Figs. 7-25 and 7-26 for 120° and 180° arches and Fig. 7-27 for 45° domes. Such loadings can be appropriate for use with structural analysis methods which model domes and arches in detail.

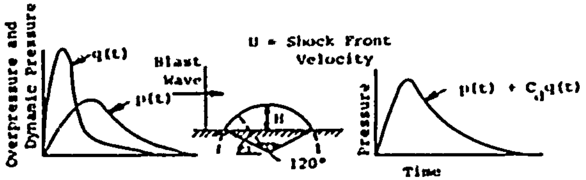

(a) Incident Pressures (b) Structure Orientation (c) Loading Scheme at any Point on Structure

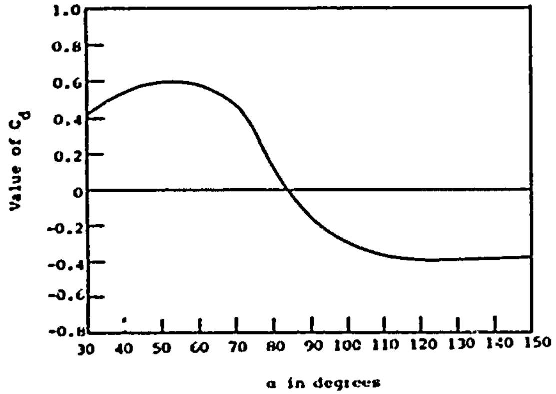

NOTES

1. C_d at 30° is lower than C_d at 50° because of the boundary layer near the ground surface. The q(t) is measured at an elevation that is above the base of the structure and therefore the q(t) is not affected to the same extent by the boundary layer. The test model had a height, H, of 10 ft (3.05 m).

2. In certain cases the value C_d = -0.4 will give unrealistic negative values for the loading scheme. Careful study of test data shows that in no case did the loading go more than 3 or 4 psi (2-3 N/cm^2) below ambient. Therefore, at times where q(t) is large and p(t) small, an adjustment of the loading scheme to these minimum values is necessary.

Figure 7-25 Non-Ideal Loading Scheme - 120° Arch for Peak Incident Overpressure of 100 psi (69 N/cm^2) or Less (Ref. 7-10)

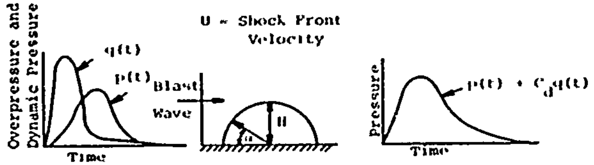

(a) Incident Pressures (b) Structure Orientation (c) Loading Scheme at Any Point on Arch

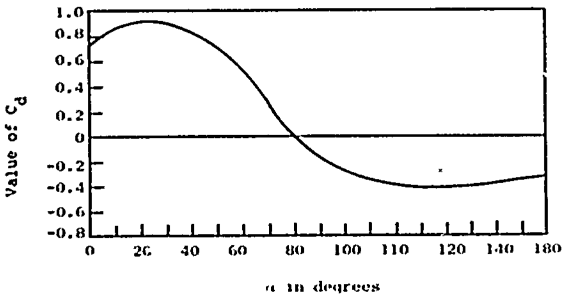

1. This C_d curve has not been derived from full-scale test data as has Fig. 7-25. This curve has been extrapolated from the data used to draw the C_d curves in Figs. 7-25 and 7-19.
2. C_d at 0° is lower than C_d at 25° because of the boundary layer near the ground surface. See Note 1 of Fig. 7-25.
3. See Note 2 of Fig. 7-25.

Figure 7-26 Non-Ideal Loading Scheme - 180° Arch for Peak Incident Overpressures of 100 psi (69 N/cm^2) or Less (Ref. 7-10)

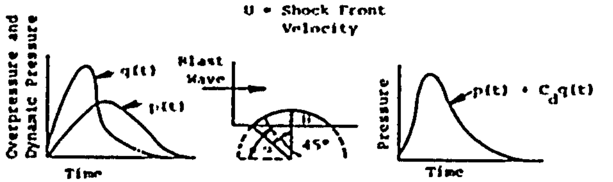

(a) Incident Pressures (b) Structure Orientation (c) Loading Scheme at Any Point on Dome

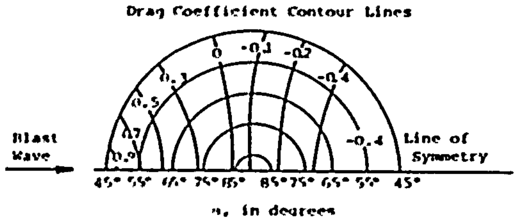

NOTES

1. Boundary layer effect on C_d is not apparent from the plan view plot. This contrasts with the data on arch loading (See Note 1, Fig. 7-25). Possible reasons for this are as follows:
   a. Gage spacing did not make evident the boundary layer effect.
   b. The C_d is decreasing with α so rapidly that even though the boundary layer has actually reduced C_d, such reduction is not enough to be apparent.
2. See Note 2 of Fig. 7-25
3. Test data has been obtained from a model with H = 10 ft (3.05 m).

Figure 7-27 Non-Ideal Loading Scheme - 45° Dome for Peak Incident Overpressures of 100 psi (69 N/cm²) or Less (Ref. 7-10)

The design or analysis of structures subjected to precursor loadings is complicated by irregularity of precursor waveforms. The preliminary methods presented in later Sections rely to a large extent on simplified loading representations (e.g., equivalent triangle representations of ideal shock loadings). Many precursor loadings will not agree with such simplifications. The analyst or designer will have to employ more sophisticated analysis techniques or will have to apply considerable judgment in analyzing or designing structures in the precursor region.

7.3 GROUND SHOCK LOADS AND STRUCTURE MOTIONS

7.3.1 General

In the case of airblast, it is reasonable to determine the loads on the exposed surfaces of structures without taking account of the motion of the structure. Such a procedure is not always satisfactory, however, in the case of ground shock loads. Ground shock loads and structure motions must generally be treated simultaneously through the consideration of structure-medium interaction. The loads induced on the surfaces of below ground structures, as well as the loads induced on the foundations of aboveground structures, are intimately related to the motion of the structure.

For preliminary design, it can be assumed that the stresses acting on soil bearing surfaces are equal to the stresses in the free-field and that the rigid body structure motion is the same as the free-field motion. Depending upon structure mass, size, flexibility and medium properties, the actual stresses and structure rigid body motions will be at variance with the free-field stresses and motions, especially when rise times associated with the incident free field wave are short. Accordingly, system analysis and design verification should be based upon interaction estimates.

The qualitative interaction process for a buried structure in a low impedance medium subjected to an incident plane wave can be described as follows:

a. As the incident stress wave strikes the structure a reflection occurs. Because of the high wave velocities of structural materials compared to most soils, the stress transmitted to the structure propagates through the structure much faster than the incident stress wave propagates in the adjacent medium. As a result, the structure deforms and experiences rigid body motion prior to the incident stress wave reaching the medium behind or below the structure.

b. The effect of structure deformation and motion is to relieve the reflection on the incident face and induce reactive stresses on the back face of the structure. In addition, shear forces are experienced on the structure sides due to relative motion between the structure and the adjacent medium. Initially, the shears will be opposite to the direction in which the incident wave is propagating since the structure is moving while the incident wave has not yet caused motion in the adjacent medium. At some time later, shear usually reverses because particle velocities in the low impedance adjacent medium will exceed the structure velocity.

c. At late times, the structure motion will approach that of the free field. As a result, shears will tend toward zero and the stresses acting on the structure will approach the stresses acting in the free-field.

Solutions to general structure-medium interaction problems incorporating multidimensional effects and inelastic material behavior are obtainable only with finite difference or finite element continuum codes. The methods

of this paragraph employ one-dimensional models to estimate interaction effects for rigid structures. The approach is similar to one used in Ref. 7-23.

7.3.2 Aboveground Structures

Consider a completely enclosed aboveground rectangular structure located in the superseismic airblast region as shown in Fig. 7-28(a). For some period of time after airblast arrival, the loads on the foundation of the structure will be governed by the airblast loads on the exposed structure surfaces and the motion of the structure, i.e., the loads on the foundation will be reactive loads as opposed to incident loads. The period of time during which reactive loads are important is related to the areal extent of the structure. An extreme occurs when the structure is of infinite areal extent in which case the foundation loads at all times are reactive. Although late time loads on finite structures will be affected by free-field ground shock, the reactive loads will generally dominate early time response. In addition, peak structure acceleration and peak structure velocity will occur during the period of time when reactive loads are dominant.

To obtain insight into average vertical foundation loads and vertical rigid body structure motions, consider the model shown in Fig. 7-28(b) where it is assumed that the structure is rigid and that the soil beneath the structure is elastic and loaded in uniaxial strain. The stress on the structure foundation is then given by

$$\sigma_r(t) = \rho C_L v(t) \tag{7-19}$$

where

$\sigma_r(t)$ = stress on the structure foundation

ρ = mass density of the soil

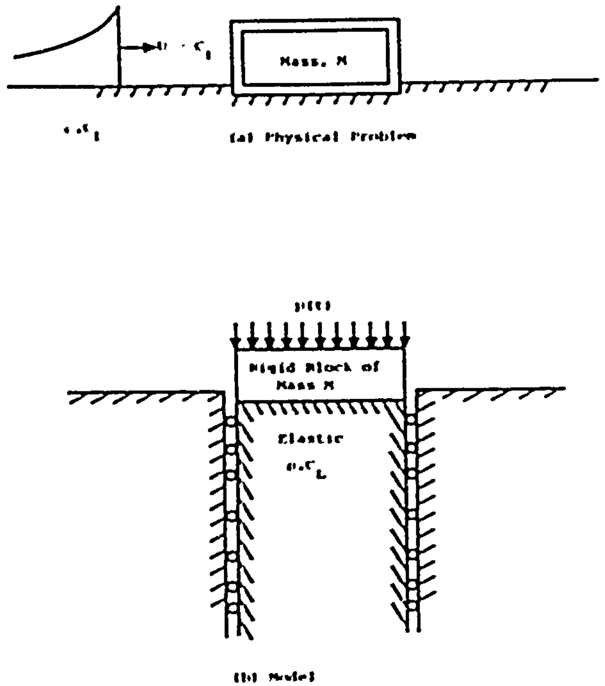

Figure 7-28 Simple Interaction Model for Aboveground Rectangular Structure

C_L = loading wave velocity of the soil

$v(t)$ = velocity of the structure

From conservation of momentum, the equation of motion of the structure is

$$M\dot{v}(t) + \rho C_L A v(t) = A p(t) \qquad (7\text{-}20)$$

where

M = structure mass

A = area of structure roof and foundation

$p(t)$ = vertical pressure-time history acting on the structure roof (Fig. 7-12(c))

Equation 7-20 is a linear first order differential equation which may be solved for an arbitrary p(t) by simple numerical procedures. If the early time history of p(t) is approximated by a triangular decaying shock of the form

$$p(t) = \begin{cases} P_m\left(1 - \frac{t}{t_o}\right) & o < t < t_o \\ 0 & t > t_o \end{cases} \qquad (7\text{-}21)$$

where

P_m = maximum pressure

t_o = total duration

then Eq. 7-20 has the closed form solution

$$v(t) = \frac{P_m}{\rho C_L}\left[\left(1 - e^{-\frac{\rho C_L A}{M} t}\right)\left(1 + \frac{M}{\rho C_L A t_o}\right) - \frac{t}{t_o}\right] \qquad (7\text{-}22)$$

for $t < t_o$. Equation 7-22 may be written in normalized form as

$$\frac{\rho C_L v(t)}{P_m} = \left|\left(1 - e^{-\delta\tau}\right)\left(1 + \frac{1}{\delta}\right) - \tau\right| \qquad (7\text{-}23)$$

where

$$\delta = \frac{\rho C_L A t_o}{M}$$

$$\tau = \frac{t}{t_o}$$

The variable δ is the ratio of the mass of soil contained in a prism of area A and length $C_L t_o$ to the mass of the structure. Equation 7-23 is plotted in Fig. 7-29 for various values of δ. It can be seen that as the mass of the structure increases under a specific set of soil and loading conditions (i.e., δ decreases) the peak structure acceleration and velocity and peak foundation stress decrease while the rise time to peak velocity and foundation stress increases. Rigid structures of finite mass never achieve the peak free field velocity.

The normalized time, τ_m, at which the peak structure velocity is reached is given by

$$\tau_m = \frac{1}{\delta}\ln(\delta + 1) \qquad (7\text{-}24)$$

The peak normalized structure velocity is simply the normalized free-field velocity at the ground surface at normalized time τ_m, i.e.

$$\frac{\rho C_L v_m}{P_m} = (1 - \tau_m) \qquad (7\text{-}25)$$

The decay of normalized structure velocity (and normalized foundation stress) parallels the free field normalized velocity (and stress) at late times. The late time decay is the same as in the free field at a normalized depth given by

$$\frac{z_c}{C_L t_o} = \frac{1}{\delta} = \frac{M}{\rho A C_L t_o} \qquad (7\text{-}26)$$

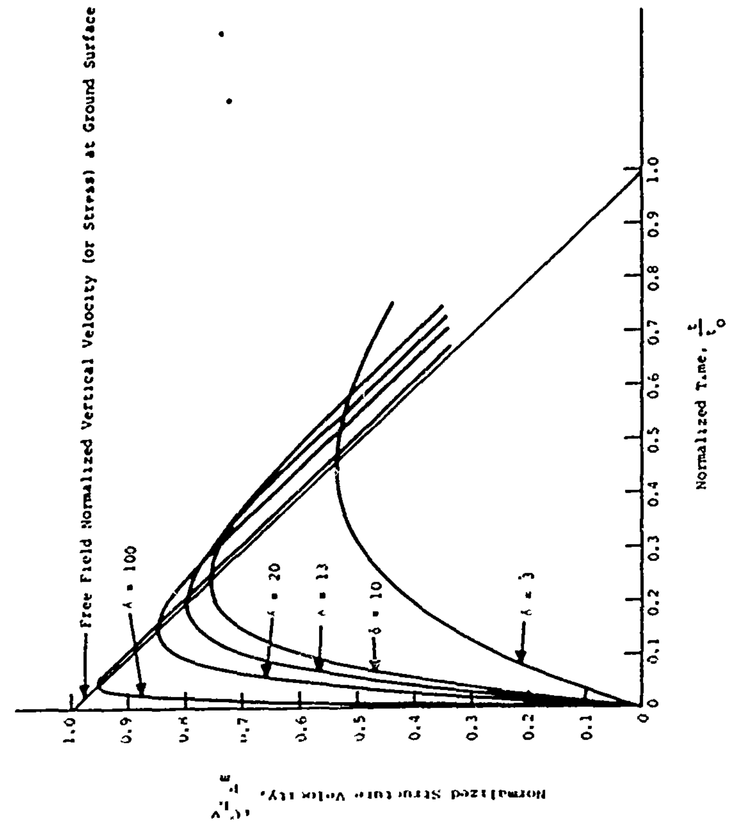

Figure 7-29 Normalized Response of Rigid Mass on Elastic Soil-Triangular Decaying Input Pressure

where Z_e is the effective free-field depth corresponding to late time structure velocity decay. The depth Z_e defines the bottom of a prism of soil having a total mass equal to the mass of the structure.

Although it has been assumed up to this point that the soil behaves elastically, the solution to the time of peak structure velocity is valid for all materials with a linear loading modulus. Therefore, the solution may be used for estimating peak rigid body acceleration, structure velocity and foundation stress and the time to peak structure velocity for soils where uniaxial strain behavior can be approximated by a linear model (see Fig. 5-15).

The response of the rigid mass at times beyond the time of maximum structure velocity is dependent upon the unloading behavior of the soil. Bounding solutions to behavior are the elastic solution decribed above and the solution for material which unloads at constant volume (Fig. 5-15(c)). The differential equations for the response of a rigid mass resting on a material which loads linearly and unloads at constant volume are derived in Ref. 7-24. Numerical results for the case $\delta = 16$ are presented in Fig. 7-30 for foundation stress and in Fig. 7-31 for structure velocity. It can be seen that up to the time of maximum structure velocity (and foundation stress) elastic behavior and bilinear-no recovery unloading behavior are identical.

Beyond the time of maximum structure velocity, elastic results and bilinear-no recovery results differ. As noted earlier, the late time elastic results approach the free field conditions at depth Z_e. As may be seen in Fig. 7-30, the foundation stress in bilinear-no recovery material for the problem investigated also approaches the free field stress at depth Z_e which is equivalent to Z_e for the elastic case. The structure velocity for the bilinear-no recovery case also approaches the free field velocity at late times.

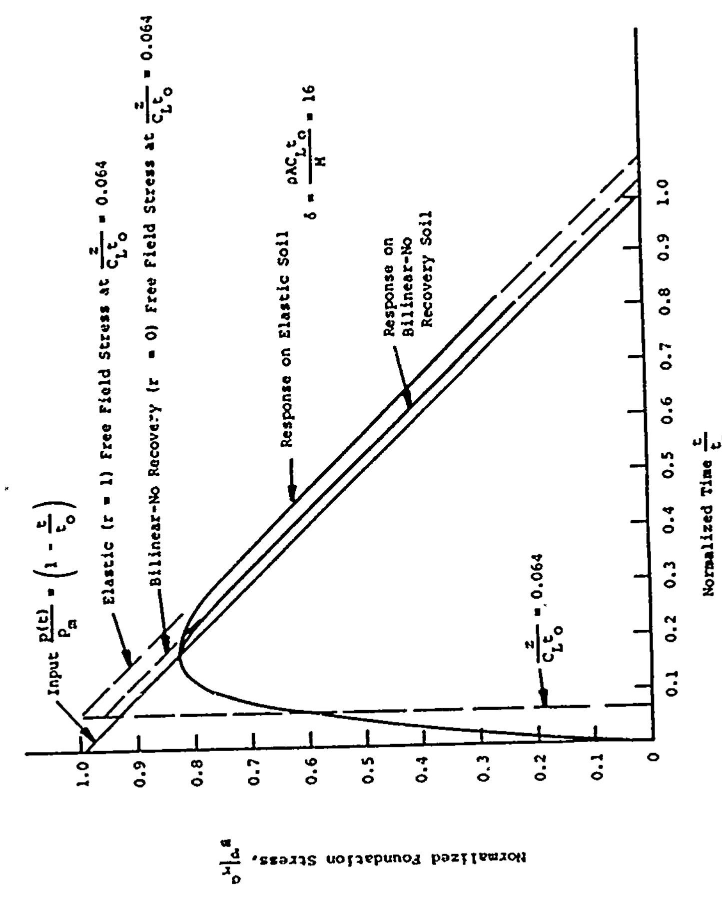

Figure 7-30 Normalized Foundation Stress Acting on the Base of a Rigid Mass Resting on Elastic and Bilinear-No Recovery Material

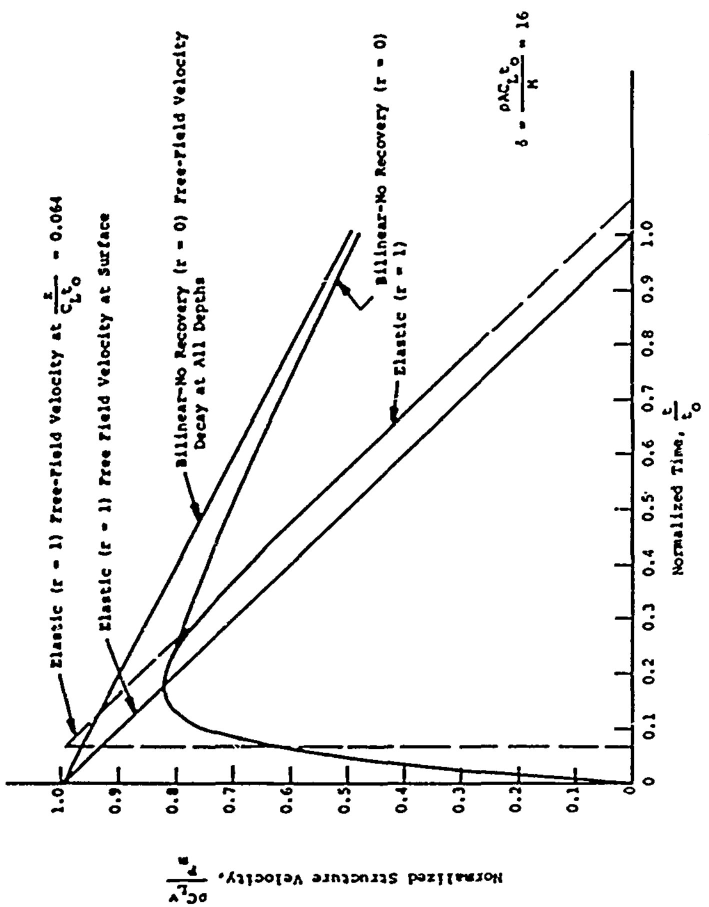

Figure 7-31 Normalized Velocity-Time History of a Rigid Mass Resting on Elastic and Bilinear-No Recovery Materials

It should be noted that the free field velocity decay is independent of depth (paragraph 5.3.2) and, therefore, the free field velocity decay at depth Z_e is equivalent to that at the surface, as well as all other depths within $C_L t_o$ of the surface.

Based upon the foregoing, it is suggested that early time structure velocity and foundation stress time histories be predicted assuming uniaxial behavior of the underlying soil. Equation 7-23 may be used up to the point of peak structure velocity and foundation stress. The input loading function, p(t), should be selected such that the impulse contained in p(t) up to the time of maximum response equals the impulse in the actual loading function. The early time accelerations should utilize a p(t) whose decay is tangent to the decay of the actual loading function at early time. Alternately, Eq. 7-20 may be solved numerically using the actual p(t).

If the input loading contains a significant rise time, the shock assumption of Eq. 7-21 may not yield satisfactory results. As a general rule, numerical calculations using the actual p(t) should be performed if the rise time to incident peak pressure meets the following criteria

$$t_r \geq \frac{10M}{\rho C_L A} \qquad (7\text{-}27)$$

where t_r is the rise time to incident peak pressure.

Late time structure motion will be governed by multidimensional effects as well as reflections from underlying layers. It is expected that late time free-field ground shock will contain rise times of sufficient duration to allow the structure to easily follow the free-field motions. Accordingly, it is suggested that late time motions and stresses be taken equal to those in the free field at an effective depth, Z_e, consistent with the one-dimensional results. The transition between the one-dimensional solution and the free-field motions may be approximated by continuous faired curves.

The approach outlined above may be applied to other shaped structures by using vertical input loading functions consistent with the structural shape of interest.

The differential in load between the front and rear faces of an aboveground structure will tend to cause the structure to translate horizontally. Resistance to translation is provided by shear between the structure foundation and the underlying soil plus resistance due to foundation embedment. The forces required for the analysis of the rigid body horizontal motion of aboveground rectangular structures are shown in Fig. 7-32. The equation of motion for the structure is

$$M\dot{v}_H = (F_F - F_B) + (F'_F - F'_B) - |\text{sgn } v_H| F_S \qquad (7\text{-}28)$$

where

M = mass of the structure
v_H = horizontal velocity of the structure
F_F = total force acting on the exposed front face
F_B = total force acting on the exposed back face
F'_F = total force acting on the embedded front face
F'_B = total force acting on the embedded back face
F_S = total shear force acting on the foundation
$|\text{sgn } v_H|$ = the sign of v_H, positive being to the right in Fig. 7-32

The total forces on the individual surfaces are simply the average pressures or stresses multiplied by the surface area over which they are applied. So long as there is no relative movement between the structure and adjacent soil particles, the shear force on the foundation is related to the shear

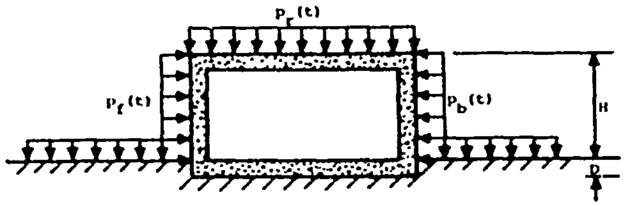

(a) Airblast Pressures Acting on Structure

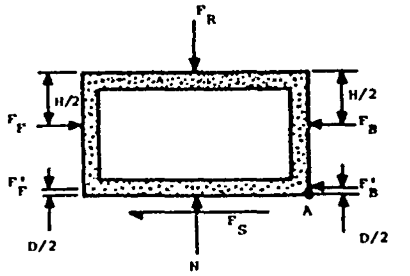

(b) Free Body Diagram and Total Forces Considered in Analysis of Horizontal Motions

Figure 7-32 Loads Applicable to the Analysis of Aboveground Structure Horizontal Motions strain induced in the adjacent soil and can be estimated by

$$F_S(t) = \rho C_S A v_H(t) \quad (7\text{-}29)$$

where

$F_S(t)$ = total shear force

ρ = mass density of soil

C_S = shear wave velocity of the soil

A = area of the foundation

Relative movement between the structure foundation and the soil will occur when the interface shear strength is exceeded. Therefore, the shear force given by Eq. 7-29 is limited to a maximum value which can be approximated by

$$F_{SH}(t) = N(t)\tan\bar{\phi} + aA \quad (7\text{-}30)$$

where

$F_{SH}(t)$ = maximum allowable value of the shear force

$N(t)$ = total vertical force acting on the foundation

$\bar{\phi}$ = angle of foundation friction which may be taken as the angle of internal friction ϕ for rough foundations

a = unit adhesion between the foundation and soil which may be taken as the unit cohesion, c, of the soil for rough foundations

The net translational pressure due to airblast may be determined by taking the difference between the front and rear face loadings at each instant of time. The net translational airblast pressure may be determined graphically as illustrated in Fig. 7-33.

The total force acting on the embedded front face, F_F', may be taken as

$$F_F'(t) = K_o A_E p_f(t) \quad (7\text{-}31)$$

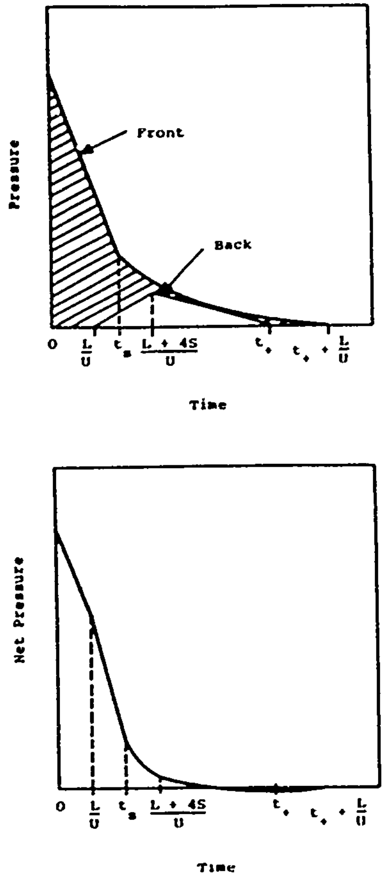

Figure 7-33 Net Horizontal Loading of Closed Rectangular Structure (Ref. 7-11)

where

K_o = coefficient of lateral earth pressure

A_E = embedded area

$p_f(t)$ = airblast pressure acting on the exposed front face (Fig. 7-12(a))

The force on the embedded rear face is largely reactive and may be taken as

$$F'_B(t) = \rho C_L A_E v_H \qquad (7\text{-}32)$$

where C_L is the loading wave velocity in uniaxial strain. The uniaxial strain assumption underestimates resistance initially since the soil surface is free to displace and is unloaded until the airblast arrives at the rear of the structure. However, the underestimate is not expected to be large. If horizontal strains in the soil behind the structure exceed about 5 percent, F'_B will be limited by the passive resistance of the soil which may be estimated by

$$F_p(t) = (\tfrac{1}{2}\gamma D^2 + q(t)D)A_E\tan^2(45° + \tfrac{\phi}{2}) + 2cDA_E\tan(45° + \tfrac{\phi}{2}) \qquad (7\text{-}33)$$

where

F_p = limiting value of F'_B for horizontal strains $\geq 5\%$

γ = total unit weight of the soil

$q(t)$ = vertical pressure due to airblast acting on the soil behind the structure versus time after the time at which 5% strain occurs

The total vertical force acting on the foundation, N, is that which results from the analysis of vertical motions, i.e.

$$N(t) = \rho C_L A v_V(t) \qquad (7\text{-}34)$$

where

A = area of the foundation

v_V = vertical structure velocity

As a first approximation, $N(t)$ may be taken equal to the total vertical force acting on the structure roof, F_R. In addition, the depth of embedment will be small with respect to structure height for many structures and, in such cases, the net force acting on the embedded faces, $(F'_F - F'_B)$, can be neglected.

It should be noted that shear resistance at the structure foundation will go to zero if the structure begins to overturn. Taking moments about point A in Fig. 7-32(b), overturning will begin when

$$\frac{(F_F - F_B)(H + 2D)}{2} + \frac{(F'_F - F'_B)D}{2} > Mgx + \frac{(F_R - N)L}{2}$$

where

H = height of structure above the ground surface

D = depth of embedment

L = structure length in direction of airblast propagation

M = structure mass

x = horizontal distance from structure center of gravity to point A

The approach to the analysis of horizontal motions which has been outlined is expected to yield reasonable results up until the time of maximum horizontal velocity, beyond which time response will approach that of the free field. Analyses of other structure shapes may be performed in a manner similar to that for rectangular structures employing loadings consistent with the structure shape of interest.

7.3.3 Surface Flush Structures

The vertical response of a surface flush structure is similar to that of an aboveground structure, although somewhat different loading conditions must be considered in analysis. Loads induced on the roof surface are those applicable to surface flush elements as discussed in paragraph 7.2.5. In addition, the vertical components of shear forces induced on the structure surfaces which bear against soil may be important.

Typical surface flush structures located away from aboveground obstructions are illustrated in Fig. 7-34(a). The loads acting on surface flush structures which must be considered in vertical response analysis are shown in Fig. 7-34(b).

The vertical equation of motion of surface flush structures on elastic soil can be approximated by

$$M\dot{v}(t) = A_T p(t) - \rho C_L A_B v(t) - F_s(t) \qquad (7\text{-}36)$$

where

A_T = area of the top of the structure

A_B = area of the structure foundation

$F_s(t)$ = load due to shear acting on the vertical surfaces

The distinction between the area of the top of the structure and the structure foundation is necessary to allow treatment of silo headworks. For silos which are isolated from airblast by headworks, all loads result from shear on the vertical walls and the term containing p(t) in Eq. 7-36 is zero.

So long as there is no relative movement between the structure surface and adjacent soil particles, the shear stress at a point on the structure wall is related to the shear strain induced in the adjacent soil and can be estimated by

$$\tau(t) = \rho C_s (v(t) - v_{ff}(t)) \qquad (7\text{-}37)$$

where

τ = shear stress

ρ = mass density of the soil

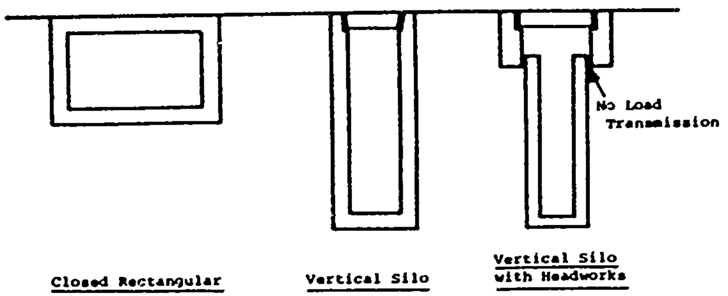

(a) Typical Configurations

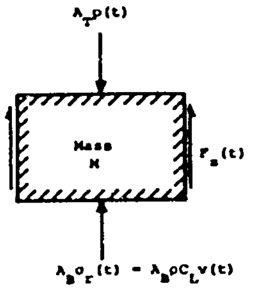

(b) Loads Necessary for Analysis of Vertical Response

Figure 7-34 Surface Flush-Structures

C_s = shear wave velocity of the soil

v_{ff} = free-field vertical particle velocity at the depth of the point of interest

Relative movement between the structure and the soil will occur when the interface shear strength is exceeded. Therefore, the shear stress given by Eq. 7-37 is limited to a maximum value, τ_{max}, which can be approximated by

$$\tau_{max}(t) = \left|\mathrm{sgn}(v - v_{ff})\right| \left[K_o \sigma_{ff}(t) \tan\phi + a\right] \qquad (7\text{-}38)$$

where $\sigma_{ff}(t)$ is the free-field vertical stress at the depth of the point of interest.

$F_s(t)$ at a given instant of time is the integral over the area of all vertical surfaces of the shear stress at individual points. Under one dimensional loading conditions the shear stress is a function only of depth and time and the total shear force can be written

$$F_s(t) = C \int_o^L \tau(z,t)dz \qquad (7\text{-}39)$$

where C is the outside perimeter of the structure in a plane parallel to the ground surface and L is the height of the structure.

Equation 7-36 can be integrated numerically to estimate the early time vertical motion of the structure and the reactive load on the structure foundation. As for aboveground structures, the late time structure motions are expected to approach those of the free field. As a result, shears on the structure sides will diminish and the stress on the structure foundation will approach the vertical stress in the free field.

The importance of the shears acting on the structure vertical surfaces depends upon the area of the vertical surfaces relative to the area of the surface flush elements loaded by the airblast. Shear forces may predominate in long surface flush silos and, as noted previously, will be the only source of load for silos which are isolated from direct airblast loads by headworks.

For preliminary estimates and in cases where shear can reasonably be ignored, Eq. 7-36 with $A_T = A_B$ is precisely Eq. 7-20. Normalized solutions to Eq. 7-20 for a triangular decaying shock have been given in Fig. 7-29. Normalized solutions to Eq. 7-20 for nuclear free-field overpressure-time histories at 100, 500 and 1000 psi (69,345, 690 N/cm^2) are given in Figs. 7-35 through 7-37 (Ref. 7-25).

Response calculations for an infinitely long structure of rectangular cross section using Eq. 7-36 with and without a shear model are compared with two dimensional finite difference calculations (Ref. 7-26) in Fig. 7-38. The shear model employed in the one-dimensional calculations assumed that shear stresses governed by Eq. 7-38 existed whenever the structure velocity differed from that of a point at a corresponding depth in the free field. The effect of shear on the structure investigated was an increase in the peak structure velocity and a somewhat lessened time of peak velocity. At early and late times the effect of shear is not major. The effect of shear upon the structure of Fig. 7-38 sited in bilinear-no recovery soil is shown in Fig. 7-39. As in the elastic case, shear increases the peak velocity and lessens the time of peak velocity somewhat. Velocity decay tends to approach that of the free field.

From the limited calculations performed, it appears that one-dimensional elastic calculations ignoring shear provide a reasonable estimate of the peak structure

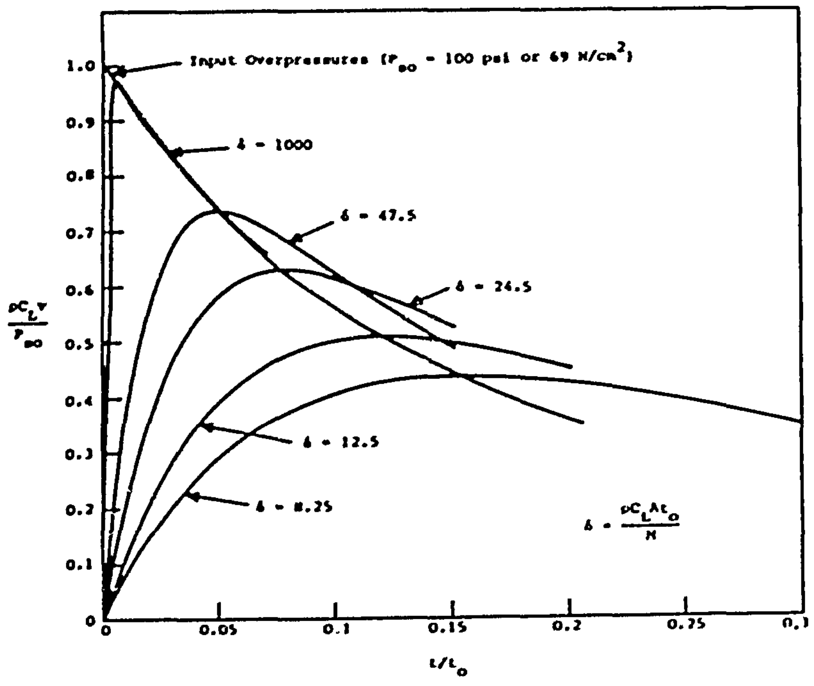

Figure 7-35 Normalized Response of a Surface Flush Rigid Structure to Free Field Overpressure at 100 psi (69 N/cm^2) Level Ignoring Shear (Ref. 7-25)

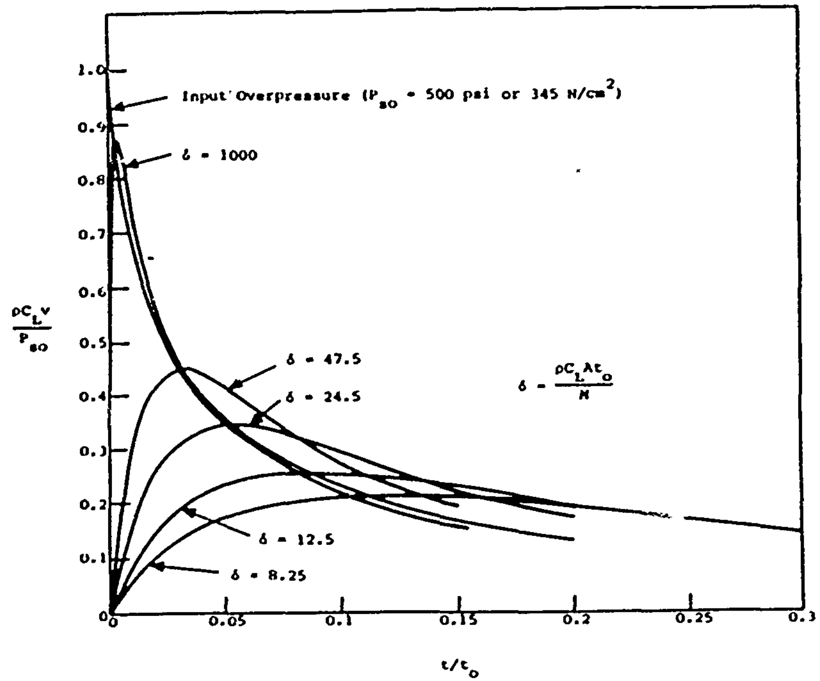

Figure 7-36 Normalized Response of a Surface Flush Rigid Structure to Free Field Overpressure at 500 psi (345 N/cm^2) Level Ignoring Shear (Ref. 7-25)

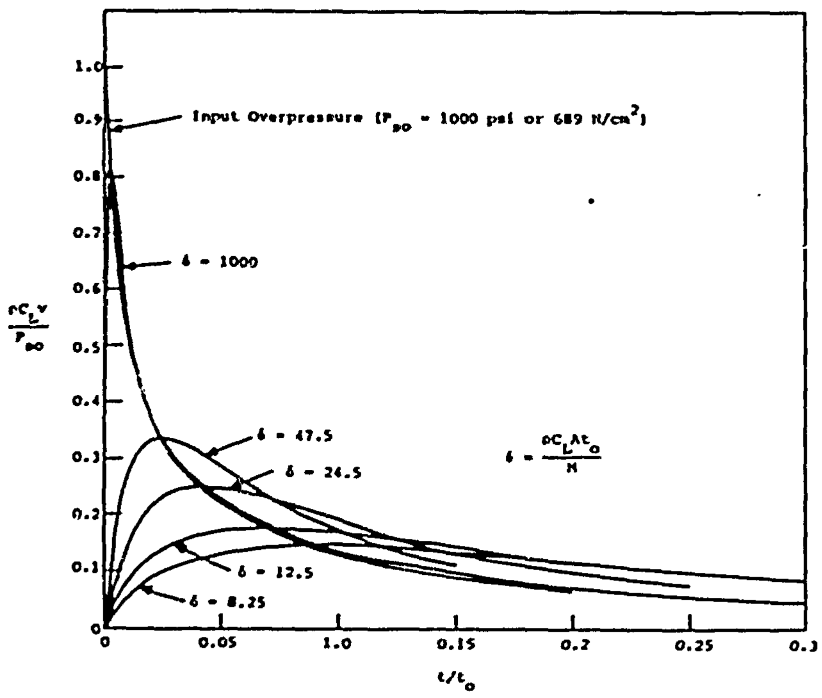

Figure 7-37 Normalized Response of a Surface Flush Rigid Structure to Free-Field Overpressure at 1000 psi (689 N/cm^2) Level Ignoring Shear (Ref. 7-25)

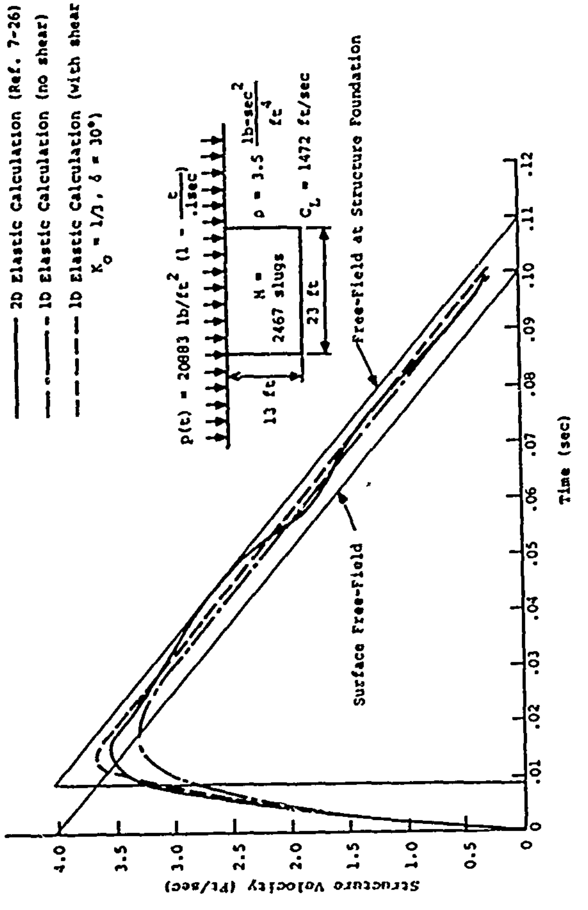

Figure 7-38 Response of a Rigid Surface Flush Structure in an Elastic Half-Space

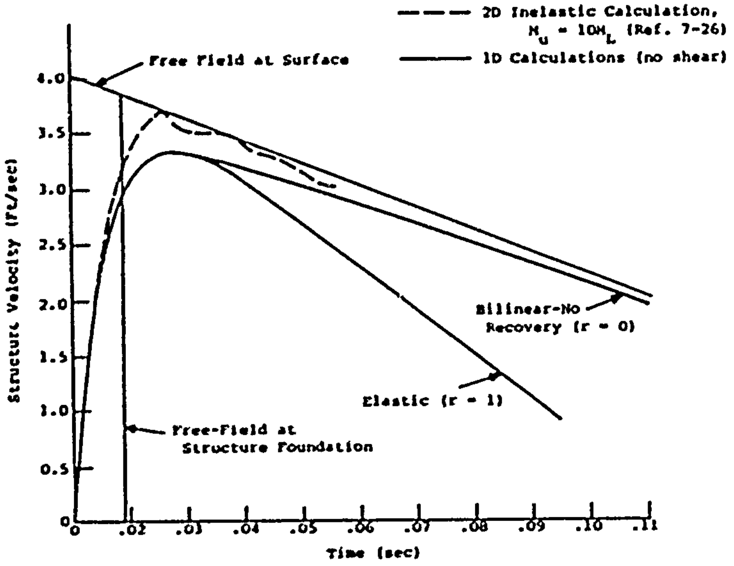

Figure 7-39 Response of a Rigid Surface Flush Structure in an Inelastic Half Space

acceleration and the time of peak structure velocity. The peak structure velocity calculated ignoring shear appears to be a lower bound. An estimate of the upper bound to peak structure velocity may be taken as the free field velocity at a depth Z_e in the free field where Z_e defines the base of a prism of soil enclosing a mass of soil equal to the mass of the structure. Behavior after the peak structure velocity is reached may be allowed to approach that in the free field at depth Z_e.

Whether actual peak structure velocity and foundation stress are nearer to the upper or lower bound depends upon the relative area of the vertical surfaces bearing against soil. Shear will be very important for long vertical silos and numerical calculations should take account of shear for such structures.

The early time horizontal motions of rectangular surface flush structures may be estimated by the same method used for aboveground structures. In the superseismic region, the loads at early times on the vertical surface facing ground zero are due to the airblast ground shock propagating downward while the loads on the rear face are largely reactive, resulting from the structure motion. Since the ground shock is propagating in a near vertical direction (i.e., near parallel to the front vertical face) reflections on the front face can be neglected. The loads assumed for horizontal analysis are shown in Fig. 7-40.

An approximate equation of motion is

$$M\dot{v}_H = F_H(t) - F_H'(t - \frac{L}{U}) - \rho C_L A v_H - F_s(t) \qquad (7\text{-}40)$$

where

$F_H(t)$ = total horizontal force due to ground shock acting on the front face of the structure

$F_H'(t - \frac{L}{U})$ = total horizontal force due to ground shock acting on the rear face of the structure

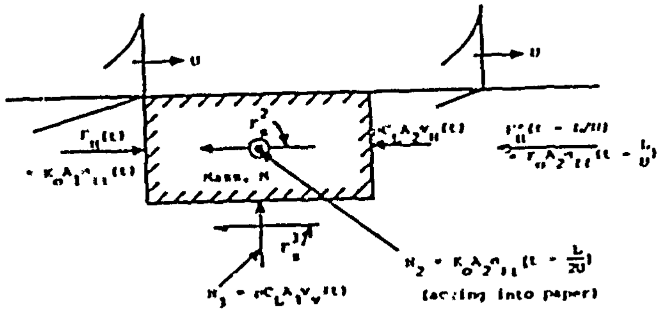

Subscripts or superscripts 1, 2 and 3 are defined as follows:

1 - front and rear faces

2 - side faces

3 - bottom faces

σ_{ff} is defined as the free-field vertical stress at mid-depth of the structure

Figure 7-40 Loads Considered in Horizontal Motion Analysis of Surface Flush Rectangular Structures

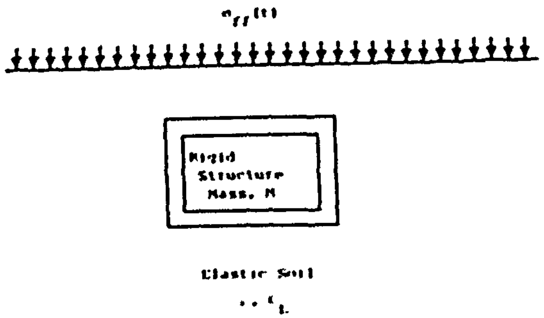

Figure 7-41 Rectangular Structure Buried in Elastic Half-Space

L = length of structure in the direction of airblast propagation

U = airblast shock front velocity

$F_S(t)$ = total shear force acting on the structure

and t is measured from the arrival of ground shock at the mid-height of the structure. It is assumed that passive shear failure does not occur in the soil behind the structure. The assumption can be checked by Eq. 7-30.

The total force acting on the front of the structure may be taken as

$$F_H(t) = K_o A_1 \sigma_{ff}(t) \tag{7-41}$$

where

K_o = coefficient of lateral earth pressure

A_1 = area of the front face

$\sigma_{ff}(t)$ = free-field vertical stress history at the mid-depth of the structure

The term $F_H'(t - \frac{L}{U})$ accounts for the free field stresses expected to be imposed on the rear structure face due to airblast. For high yields and/or relatively short structures, the stress-time history on the rear face may be taken equal to that on the front face except displaced in time by L/U. For low yields and/or long structures, account should be taken of the difference in free field stresses at ranges corresponding to the front and rear of the structure.

The total shear acting on the structure as a function of time should be taken as the sum of the total shears acting on the sides of the structure and the structure base, i.e.,

$$F_S(t) = 2F_S^2(t) + F_S^3(t) \tag{7-42}$$

where

$P_S^2(t)$ = total shear acting on an individual structure side

$P_S^3(t)$ = tota shear acting on structure base

The average shear stress acting on the surfaces can be assumed governed by Eq. 7-37 and 7-38 where the free field stress and velocity are defined at L/2 at the mid depth of the structure for P_S^2 and the bottom of the structure for P_S^3. If the structure is especially long or deep, account should be taken of the variation of the free-field stress and velocity with location on the structure in calculating the shears as well as P_H and P_H'. The variation of shear with location was treated in the analysis of surface flush structure vertical response discussed previously. Late time horizontal motion of surface flush structures will approach the motion in the free field. The general approach to the horizontal motion analysis of rectangular structures is applicable to other structure types although additional complexity is introduced by shape. The approximation of a cylinder by an octagonal shape is discussed in the following paragraph.

7.3.4 Buried Structures

The analysis of buried structures in the superseismic airblast region is complicated by the fact that stress waves propagating downward will reflect at structure surfaces which are in the path of propagation. The stress acting on the roof of a rectangular rigid structure buried in a half-space of elastic soil (Fig. 7-41) at sufficient depth so that free surface reflections do not influence response during the time of interest may be approximated by

$$\sigma_t(t) = 2\sigma_{ff}(t) - \rho C_L v(t) \tag{7-43}$$

where

$\sigma_t(t)$ = total stress acting on the roof

$\sigma_{ff}(t)$ = incident stress wave in the free field at the location of the structure

ρ = mass density of the soil

C_L = compressional wave velocity of the soil

$v(t)$ = velocity of the structure

and it has been assumed that the structure is of relatively large area. The stress acting on the base of the structure, as in the case of a surface flush or aboveground structure is

$$\sigma_r(t) = \rho C_L v(t) \tag{7-44}$$

where $\sigma_r(t)$ is the stress acting on the base of the structure.

Equations 7-43 and 7-44 can be rewritten

$$\sigma_t(t) = \sigma_{ff}(t) \pm \rho C_L \Delta v(t) \tag{7-45}$$

where

$\sigma_t(t)$ = total stress acting on a structure surface perpendicular to the direction of incident wave propagation

$\Delta v(t)$ = $v_{ff}(t) - v(t)$

$v_{ff}(t)$ = free-field particle velocity at the depth of structure

The sign of the second term is taken as positive for incident faces and negative for reactive faces. Equation 7-45 indicates that the stress on a structure consists of the free field stress plus or minus a term which is related to momentum exchange caused by the presence of the structure. A relationship similar to Eq. 7-45 is expected to exist regardless of material stress-strain behavior, structure shape or structure rigidity, i.e., the external tractions on a structure surface will be the free field stress acting on a plane parallel to the surface modified by a term related to the difference in free-field and structure velocities. Of course, the functional dependence on velocity difference will be more complex than in the one dimensional elastic case. Equation 7-45 and its generalization lead to the obvious but important conclusion that whenever the structure velocity differs from the free field velocity, stresses different from those in the free field will act on the structure. Since buried structures of finite mass cannot respond instantaneously to an incident wave, reflections will persist on surfaces facing the propagating incident wave for some time following the arrival of the wave at the structure. The duration and importance of the reflections depend upon the mass and size of the structure, the properties of the medium, the rise time of the incident wave and the flexibility of the structure.

First order estimates of the response of buried rectangular structures may be obtained by methods similar to those applied to aboveground and surface flush structures. The equation of motion in the vertical direction neglecting shear can be taken as

$$M\dot{v}(t) + 2\rho C_L A v(t) = 2A\sigma_{ff}(t) \tag{7-46}$$

Equation 7-43 is of the same form as Eq. 7-20. For a triangular decaying shock input of the form

$$\sigma_{ff}(t) = \begin{cases} \sigma_m\left(1 - \frac{t}{t_o}\right) & o < t < t_o \\ o & t > t_o \end{cases} \tag{7-47}$$

where

σ_m = maximum stress

t_o = total duration

and t is measured from the time the wave strikes the structure,

Eq. 7-43 has a solution

$$\frac{\rho C_L v(t)}{\sigma_m} = \left[\left(1 - e^{-2\delta\tau}\right)\left(1 + \frac{1}{2\delta}\right) - \tau\right] \tag{7-48}$$

where δ and τ are defined as in Eq. 7-23. Normalized solutions to Eq. 7-48 may be obtained from Fig. 7-29 using a normalized mass ratio of 2δ.

The response of a buried structure having $\delta = 16$ is compared with the response of an identical surface flush structure to the same input stress history in Fig. 7-42. The stresses acting on the roof and base of the buried structure are shown in Fig. 7-43. A reflected stress with a peak value twice the incident peak stress persists on the structure roof for some time. The effect of the reflected stress is a higher initial structure acceleration, a higher peak structure velocity and a lesser time to peak structure velocity than occur for the surface flush structure. Late time behavior approaches that of the free field in the vicinity of the structure.

The effect of shear on a buried structure analyzed in one dimension is shown in Fig. 7-44. As for the surface flush results presented in Fig. 7-38, shear causes an increase in peak structure velocity while the time to peak velocity remains essentially unchanged. Late time behavior with and without shear is almost identical. The results of a calculation allowing two dimensional soil behavior are also shown in Fig. 7-44. The two dimensional results are oscillatory and show a peak velocity higher than that of the free-field. The oscillatory behavior is believed associated with the boundary conditions of the two dimensional calculation which provided paths for disturbances reflected from the structure to return to the structure. The accuracy of the computed peak velocity is unknown. Overall agreement between the one dimensional results and the two dimensional calculation is believed reasonable.

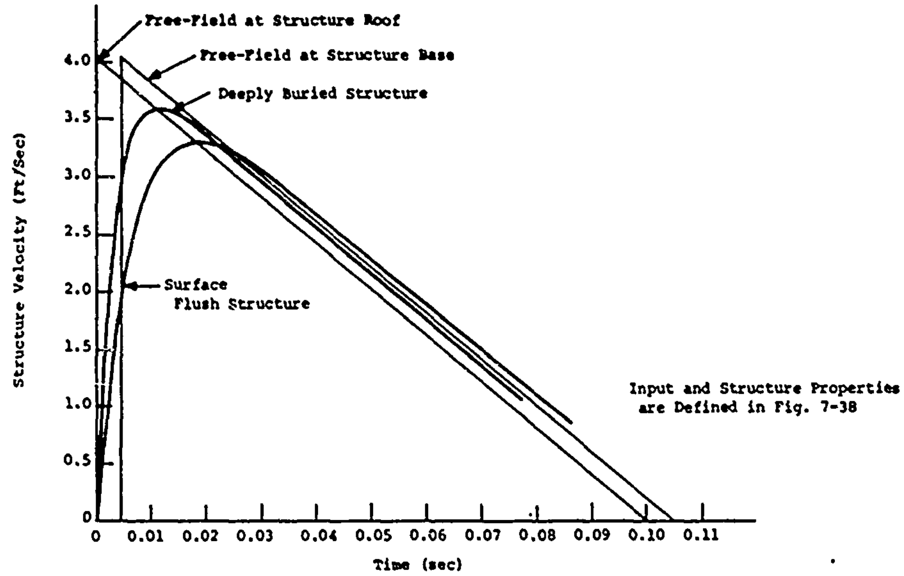

Figure 7-42 Comparison of Structure Velocity-Time Histories for Surface Flush and Buried Structures in an Elastic Half-Space

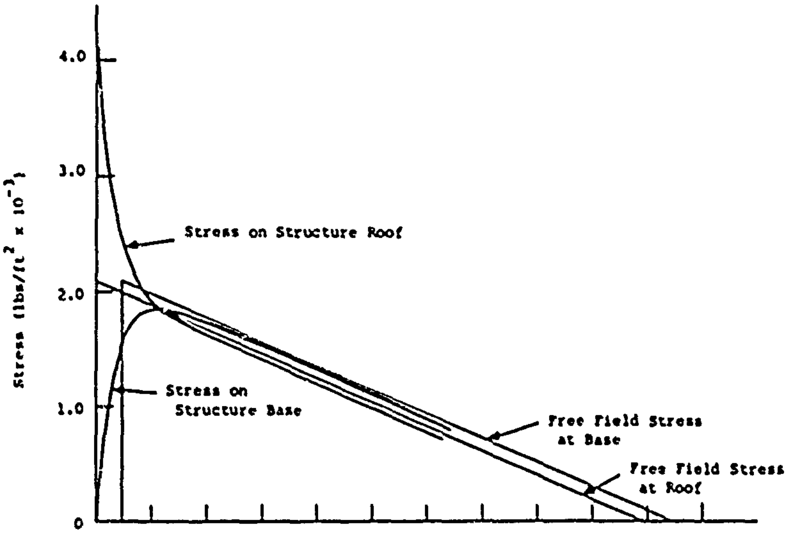

Figure 7-43 Stresses on Roof and Base of a Buried Rectangular Rigid Structure

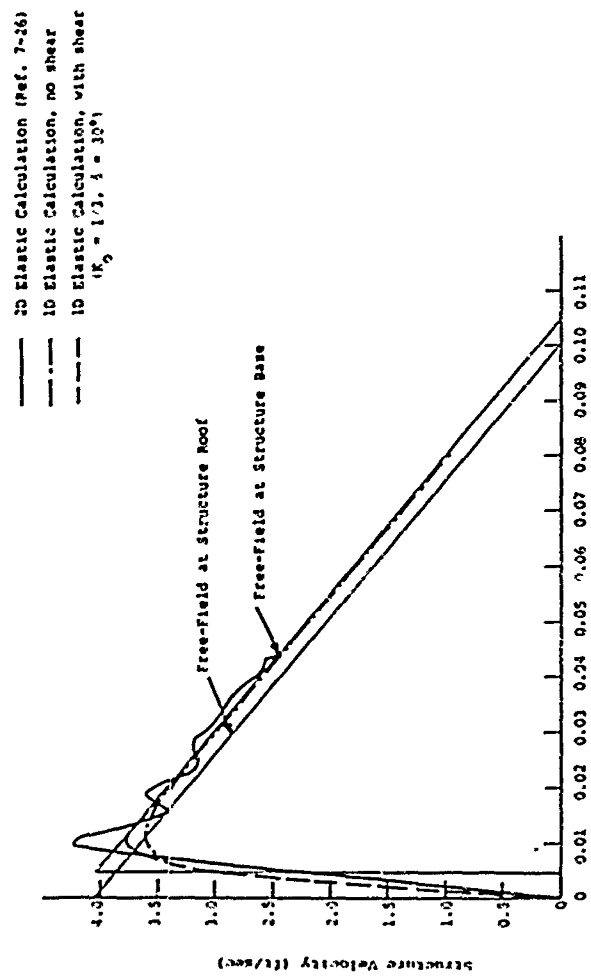

Figure 7-44 Effect of Shear Upon Buried Structure Response

In the cases of aboveground and surface flush structures, it was suggested that one dimensional elastic solutions provide reasonable estimates of behavior up to the time of peak response. Such is not the case for buried structures because the stresses acting on the roof of the structure are dependent upon material behavior immediately upon the incident stress wave striking the structure. In addition, the area of the structure affects the duration of the reflection even for the elastic case. The elastic solution does, however, provide a worst case solution.

Consider first the effect of material inelasticity. Reference 7-24 presents a formulation for the one-dimensional response of a rigid mass within a material which loads linearly but does not recover strain upon unloading. For an incident stress wave which may be approximated as a triangular decaying shock, the maximum duration of the reflection on the structure roof is

$$t_d = \frac{z_s}{C_L} \qquad (7\text{-}49)$$

where

t_d = duration of reflection

z_s = depth to the structure roof

C_L = loading wave velocity in the soil

and t is taken as zero at the time the incident wave strikes the roof. After time t_d the stress acting on the roof is the same as the stress acting on the free surface above the roof, i.e.,

$$\sigma(t) = p\left(t + \frac{z_s}{C_L}\right) \qquad (t \geq t_d) \qquad (7\text{-}50)$$

where

$\sigma_r(t)$ = vertical stress acting on the roof after time t_d

$p\left(t + \frac{z_s}{C_L}\right)$ = vertical stress acting on the ground surface above the structure

The loaded area of a structure will affect the duration of a reflection on a buried structure just as the area affects airblast reflections on aboveground structures. Rarefactions propagating from the edges of the structure will cause complete erosion of a reflection in a time which may be estimated by

$$t_d = \frac{W}{C_u} \tag{7-51}$$

where

t_d = duration of reflection

W = least dimension of structure roof

C_u = unloading wave velocity in the soil

Considering the effects of inelasticity and finite areal extent, a reasonable lower bound to the stresses acting on a structure roof may be taken as shown in Fig. 7-45. The peak reflected stress is twice the peak stress of the incident wave at the roof of the structure. The reflection goes to zero at time t_d which is the lesser value given by Eqs. 7-49 or 7-51. The vertical stress at times greater than t_d is given by Eq. 7-50 and is taken as triangular where the impulse of the triangular surface pressure approximates that of the actual overpressure to the time of maximum structure response.

The lower bound response of the structure may be determined from Eq. 7-36 using the loading of Fig. 7-45 as input. Beyond the time of maximum response of the structure, velocity may be assumed to approach the free field velocity in the vicinity of the structure. The upper bound response

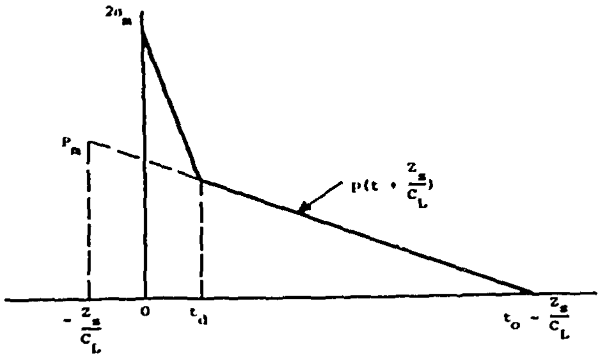

Figure 7-45 Approximate Lower Bound to Stresses on the Roof of a Buried Rectangular Structure

may be determined from Eq. 7-46 modified to include a shear model of the type described in paragraph 7.3.3. The incident stress wave should be taken as the free-field stress wave in the vicinity of the structure. A significant rise time in the incident pulse will reduce the magnitude of the reflection. For rise times equal to or greater than t_d, no reflection will occur. Analyses should be modified to treat rise times if appropriate.

Structures relatively near the surface may experience surface relief waves which result from the interaction of the wave reflected from the structure with the surface. The effect of such relief waves will be diminished by rarefactions from the structure edges and material inelasticity. Relief waves, as well as subsequent structure and [illegible] reflections, will not greatly affect peak stress, acceleration or velocity. However, the reflections will introduce oscillations of period $2Z_s/C_u$ into the velocity time history. At depths of burial greater than W, where W is the least dimension of the structure roof, the effects of multiple reflection between the structure and the surface can be assumed small. However, the magnitude and effect of reflections should be considered if the oscillations induced will affect individual structural element response or the response of equipment within the structure.

The horizontal response of buried rectangular structures will be similar to the horizontal response of surface flush structures and may be analyzed as outlined in paragraph 7.3.3.

The analysis of cylindrical structures oriented parallel to the ground surface (Fig. 7-46(a)) is complicated by the geometry of the structure. Multidimensional effects become important at the instant the incident wave strikes the structure. The process of interaction for a rigid cylindrical

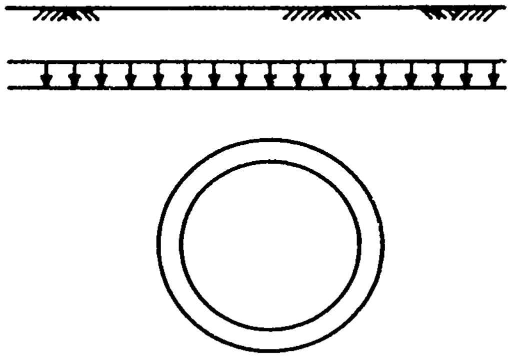

(a) Buried Horizontal Cylinder

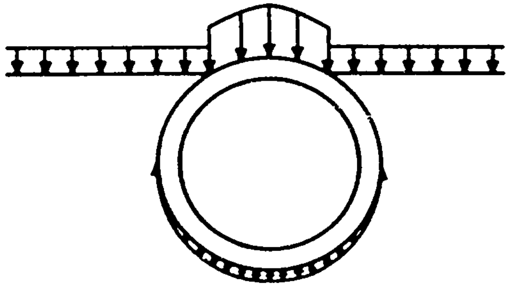

(b) Vertical Stress Components on Horizontal Cylinder Shortly After Arrival of the Incident Wave

Figure 7-46 Buried Horizontal Cylinder Subjected to an Incident Plane Wave structure of infinite length can be described qualitatively as follows.

Upon the incident wave striking the crown of the structure, the stress at the crown doubles and the structure begins to accelerate downward as a rigid body. Within a short period of time the entire bottom half-cylinder experiences stresses due to the motion of the cylinder into the soil while the incident wave may not have progressed far beyond the crown of the cylinder (Fig. 7-46(b)). As the incident wave propagates downward, reflected stresses continue to occur on the upper half cylinder, peak reflected stress being a function of angle between the incident wave and a tangent to the cylinder at the point where the incident wave contacts the cylinder as well as the structure velocity at time the incident wave arrives at the point.

As for rectangular structures, the duration of reflected stresses on the upper half-cylinder is a function of the cylinder motion, the degree of soil inelasticity and the size of the cylinder. The duration of reflections is expected to be relatively small compared to the duration which would occur on the roof of a rectangular structure having a width equal to the cylinder diameter. In addition, the effect of reflected stress is diminished because the shock front impinges at different positions on the cylinder at different times (Ref. 7-27).

An approximate analysis of vertical motions may be made by considering the octagonal cylinder approximation shown in Fig. 7-47(a). The incident loads acting on the flat region (Region Ⓐ) and the inclined regions (Region Ⓑ) are shown in Figs. 7-47(b) and 7-47(c). For an incident shock, the stress in Region Ⓐ is assumed to reflect to twice the incident stress at the instant of impact. The reflection is assumed dissipated after time t_d where t_d is the lesser value given by Eqs. 7-49 or 7-51 where W in Eq. 7-51 is taken as .8R. The stress in Region Ⓐ after time t_d is taken as the

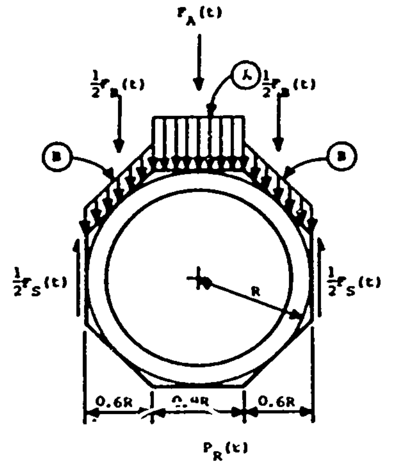

(a) Octagonal Approximation and Acting Loads

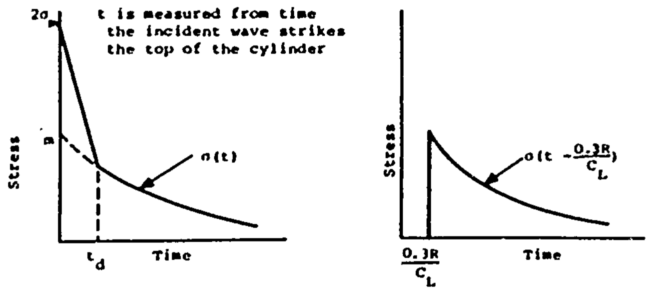

(b) Average Vertical Stress in Region Ⓐ

(c) Average Vertical Stress in Region Ⓑ

Figure 7-47 Approximate Vertical Loads for Estimating Vertical Rigid Body Motions of Horizontal Cylinder free field stress at the depth of the cylinder crown. The total vertical load acting on the cylinder due to vertical stresses in Region Ⓐ is then

$$F_A(t) = 0.8\sigma_A(t)RL \qquad (7\text{-}52)$$

where

$F_A(t)$ = total vertical load on Region Ⓐ

$\sigma_A(t)$ = average vertical stress in Region Ⓐ (Fig. 7-47(b))

R = cylinder outside radius

L = cylinder length

The average vertical component of stress acting on the upper inclined faces of the octagon (Region Ⓑ) is taken as the free field vertical stress at the mid-depth of the inclines (Fig. 7-47(c)). The total vertical load acting on the cylinder due to the vertical components of stress in Region Ⓑ is

$$F_B(t) = \begin{cases} 0 & 0 \leq t < \dfrac{0.3R}{C_L} \\ 1.2\sigma_B(t)RL & t \geq \dfrac{0.3R}{C_L} \end{cases} \qquad (7\text{-}53)$$

where $F_B(t)$ is the total vertical load on Region Ⓑ.

The total load resisting the incident load is taken as

$$F_R(t) = 2\rho C_L v(t)RL \qquad (7\text{-}54)$$

Ignoring shear ($F_S(t)$), the equation of motion is

$$M\dot{v}(t) = F_A(t) + F_B(t) - F_R(t) \qquad (7\text{-}55)$$

which may be solved numerically to estimate the vertical velocity time history up to the time of maximum response. Equations 7-52 through 7-55 may be altered according to the judgement of the analyst to incorporate the effects of a rise time in the incident stress wave, shear on the cylinder or the variation of the vertical stress in Region Ⓑ with depth. Beyond the time of maximum structure velocity, cylinder response is expected to approach the free field velocity in the vicinity of the structure.

Differentials in horizontal load between the front and rear of cylinders will be of short duration. In addition, loading phenomena are two dimensional and involve both compression and shear waves. As a result, simple models are not readily derivable. The horizontal component of stress on both the front and rear face may be taken roughly as the coefficient of lateral earth pressure times the free-field vertical stress in the vicinity of the cylinder. Horizontal cylinder motion can roughly be taken equal to the horizontal free-field motion at the structure location. Two dimensional code analyses will have to be employed to arrive at more accurate response information.

7.3.5 Mounded Structures

Mounded structures (Fig. 7-48) experience loads which are expected to be intermediate between the loads on aboveground and buried structures. The inclined earth boundaries will reduce drag and reflected pressures. However, significant drag and reflection will occur even for slopes as gentle as 1:4 (Ref. 7-18).

The geometric complexity and nonuniform airblast loadings associated with mounded structures are not readily translatable into simple interaction models. However, the bounding loads and motions of mounded structures can be estimated by considering the aboveground and buried or surface flush extremes. In addition, loads on the earth boundaries can be estimated from the reflection and drag coefficient presented in paragraphs 7.2.2 and 7.2.3. With a good deal of judgement, the boundary loads can be transmitted componentwise to the structure surfaces and the structure

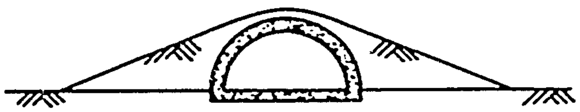

(a) Mounded Arch or Dome

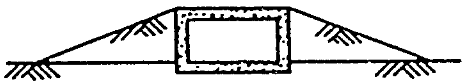

(b) Mounded Rectangular Structure

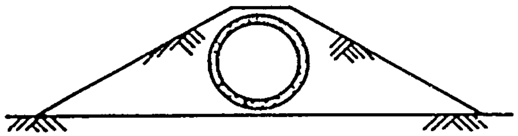

(c) Mounded Cylinder

Figure 7-48 Typical Mounded Structures

response can be estimated by methods similar to those outlined in previous discussions. High confidence analysis will require the use of two dimensional codes.

7.3.6 Effect of Reflections, Outrunning Ground Shock and Crater-Induced Ground Shock

The previous paragraphs have considered structures in unlayered media subjected to superseismic airblast. In general, peak loads, accelerations and velocities of aboveground and near-surface structures will occur as a result of the incident stress wave due to airblast even in layered media and in outrunning regions.

The rise times associated with outrunning ground shock and crater-induced ground shock will generally be sufficiently long so that structures can readily follow the free-field motions. Ground shock which is reflected from underlying layers is also expected to contain substantial rise times due to dispersion which occurs in typical near-surface soils. Accordingly, the loads on structures and the motions of structures are expected to closely coincide with the free field except during interaction with the incident wave due to airblast striking or passing over the structure. The effect of interaction will generally be a lower peak structure acceleration and velocity than occurs in the free field. Loads on incident surfaces will generally exceed the free field for some period during interaction while loads on reactive surfaces will be reduced.

Special cases may occur in which interaction must be considered for ground shock other than the incident wave due to airblast. For example, strong reflections from interfaces of strong impedence mismatch may shock up under certain conditions. The rise times associated with free field ground shock should be reviewed to determine requirements for interaction calculations. The criteria of Eq. 7-27 may be used as a guide to evaluating rise times.

7.4 STRUCTURES IN HARD ROCK

7.4.1 General

Hard rock, typically jointed, presents some unique differences compared to soil or soft rock. Important differences include:

- Unlined inclusions in rock have significant inherent strength
- Structural liners of practical size and strength have deformation and strength properties comparable to hard rock
- Late-time relative displacements along rock joints may seriously affect structure survivability

Structures sited in hard rock may be near-surface or deep underground. Most of the following discussion concentrates on deep underground structures. The concepts and principles, however, are equally applicable to near surface structures. Paragraph 7.4.6 discusses some special considerations for near-surface structures.

A deep underground structure is defined to be a structure buried deep enough so that the direct-induced ground motion effects of a nuclear detonation are the governing phenomena rather than air induced effects. Deep underground installations can be made nearly invulnerable and are generally used for protection of large, one-of-a-kind facilities such as command and control centers which cannot feasibly be hardened by dispersion and redundancy. Such important installations are almost invariably located in hard rock, both to utilize the inherent strength of the rock for protection and because rock is usually found at the depths of burial necessitated by nuclear weapons of the megaton class.

The structures considered herein include unlined tunnels and cavities, cavities with integral lining placed directly against the rock, and liners separated from the rock by a frangible filler or backpacking. Regardless of the configuration, the survivability of the structure is largely governed by the strength of the rock. Structural liners of practical size and strength generally cannot be proportioned to survive conditions associated with large scale closure of rock cavities.

Accordingly, methods of predicting the survivability of deep underground facilities are based mostly upon conditions in the immediately adjacent rock. At large ranges from a detonation, unlined cavities with supporting rock bolts may be sufficient. At lesser ranges, integral tunnel linings may increase survivability through containment of the rock, resulting in some increased rock strength. At ranges nearer the explosion, where local compressive failures or tensile spalls occur, hardening may be accomplished with the use of crushable fillers and integral liners between the rock and facility. The filler serves to absorb spalled and crushed material and to reduce and equalize the pressures transmitted to the liner.

With regard to unlined and integrally lined cavities, loads in the context of pressure distributions are not considered directly. Instead, rock strains are used to predict the survivability of cavities at various ranges from an explosion. Strain can be predicted with reasonable confidence and appears to be an adequate parameter for considering structural integrity (Ref. 7-28). Strain is also used to estimate ranges at which backpacked facilities may be survivable.

The discussions herein are restricted to the environments created by a nuclear detonation. Obviously, the design of a facility in rock requires many other important considerations including site selection, static loads, tectonic forces, construction methods, the effect of multiple openings, etc. References 7-29 and 7-30 provide information on such considerations.

7.4.2 Unlined Cavities

a. Strain Prediction

The free-field direct-induced ground shock parameter which exhibits the least scatter in test data and which can be predicted with most confidence is peak radial particle velocity. Equations 5-56 and 5-65 of Section V relate hard rock peak radial particle velocity to yield and range for contained and near-surface bursts, respectively. For plane waves, a reasonable assumption at distances from an explosion where shock front curvature is not major, peak particle velocity and peak strain are related by the expression

$$\epsilon = \frac{v}{C_L} \qquad (7\text{-}56)$$

where

ϵ = peak strain

v = peak particle velocity

C_L = loading wave velocity of the medium

Various studies (Ref. 7-31, 7-32 and 7-33) have shown that during the passage of a shock wave through a homogeneous elastic medium containing a hole or cavity, the maximum stresses and strains around the boundary of the cavity are essentially the same as those that would exist in the case of a static free-field stress condition equal to the peak dynamic free-field stress, so long as the shock pulse length is equal to or greater than about three times the diameter of the cavity. Therefore, it is assumed that stress concentrations around a cavity comparable to those induced by static loads may be expected for the types of dynamic loads considered herein.

Tests of many materials indicate that the strains retain a distribution approximately consistent with elastic theory even after Hooke's Law no longer applies. This implies that the theoretical stress concentration factor can be interpreted as directly equivalent to a strain concentration factor, even as the material approaches failure (Ref. 7-29). Based on this hypothesis, Ref. 7-29 presents a simple procedure for estimating the probable behavior of the cavity walls in a rock medium exposed to the effects of a nuclear weapon.

The compressive stress (and strain) concentration factor for a cylindrical hole in an elastic medium ranges from 2.00 to 3.00. In terms of the strain corresponding to the unconfined compressive strength of the rock and the maximum compressive strain (stress) concentration factor, the range at which crushing of the rock at the face of the cavity due to compressive failures should cease occurs where the peak intensity of strain in the free-field is given by

$$\epsilon_r = \frac{\epsilon_u}{K} \qquad (7\text{-}57)$$

where

ϵ_r = peak radial free-field strain

ϵ_u = strain at ultimate strength in unconfined compression

K = strain concentration factor (= stress concentration factor)

Stress concentration factors for cylindrical and rectangular cavity configurations and three stress fields are given in Figs. 7-49 and 7-50. Factors for other configurations are presented in Ref. 7-30. In the figures, the parameter M defines the stress field. M = 1 corresponds to a uniform stress field. M = 0 corresponds

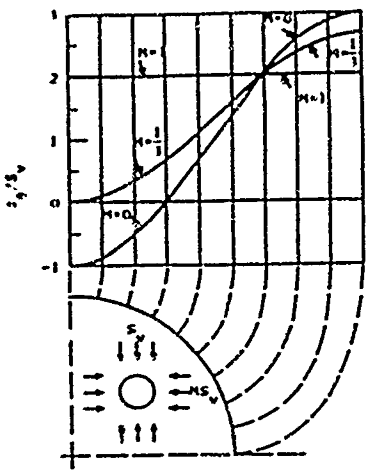

Figure 7-49 Boundary Stress Concentration for Circular Openings (Ref. 7-30)

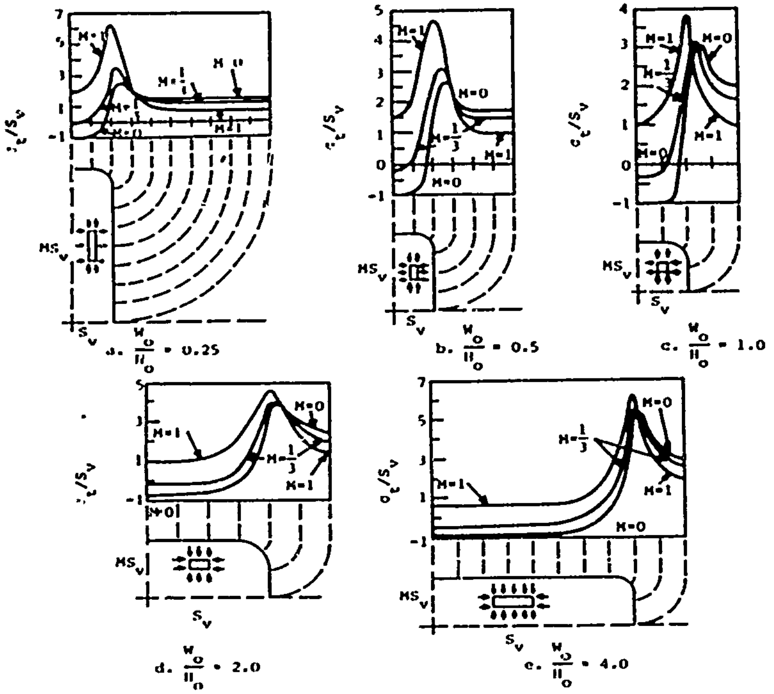

a. $\frac{W_o}{H_o} = 0.25$

b. $\frac{W_o}{H_o} = 0.5$

c. $\frac{W_o}{H_o} = 1.0$

d. $\frac{W_o}{H_o} = 2.0$

e. $\frac{W_o}{H_o} = 4.0$

Figure 7-50 Boundary Stress Concentration for Rectangular Openings With Rounded Corners; Ratio of Fillet Radius to Short Dimension, 1 to 6. (Ref. 7-30) to a uniaxial stress field which might occur at shallow depths, near vertical free surfaces or when large displacements occur. $M = 1/3$ corresponds to uniaxial strain with Poisson's ratio equal to 0.25, a reasonably average value for rock. The ratio W_o/H_o is the width to height ratio for rectangular openings. The concentration factors are derived assuming plane strain conditions in a linearly elastic, isotropic, homogeneous infinite medium. The infinite medium assumption is approximately satisfied if the distance from the opening to the nearest boundary is greater than three times the dimension of the opening in the direction of the boundary.

b. Damage Level Prediction

By appropriate choices of values for ϵ_u and K, Eq. 7-57 can be used to estimate survival ranges, or damage levels at given ranges, for unlined cavities. Interpretation of various test results has led to the following concepts of damage definition and prediction. Damage levels are given as a function of approximate range from a 1 MT (4.184×10^{15} j) surface burst. Other yields may be considered by scaling the 1 MT (4.184×10^{15} j) ranges by the cube root of yield.

1. Crushing and Closure of Cavity (Ref. 7-29)

Close to the point of burst, where the free-field dynamic compressive strain equals or exceeds the strain associated with the compressive strength of the rock in unconfined compression, the walls of the cavity can be expected to crush and even close completely, without taking into consideration strain concentration factors or structure details. This condition would be likely to occur when the ultimate strain approaches 0.5 to 1 percent. For a material such as granite, the range

at which these conditions might be expected to exist is approximately 400 to 500 feet (122 to 152 m) for a 1 MT (4.184×10^{15} j) surface burst.

2. Local Compressive Failure and Rock Drops (Ref. 7-29)

At ranges where the local compressive strain modified by the strain concentration factor is equal to the ultimate failure strain, serious damage in the form of local crushing and rock drops can be expected. Even though the opening may not be filled, large areas of crushing and rock falls around the edge of the cavity are likely to occur. The ranges at which a cavity in a hard rock might be expected to exhibit failures of this type are from 600 to 1000 feet (183 to 304 m) from a 1 MT (4.184×10^{15} j) surface burst.

3. Rock Spalls

Rock spalls may be expected to occur on the incident face of an unlined cavity in rock for distances up to two or three times those corresponding to local compressive failures. The associated peak free-field compressive strains would be on the order of 0.02 to 0.06 percent (Ref. 7-29). Spalling is dependent on the tensile strength of the rock, the amount of damage produced during the mining operation, and the presence of joints, fractures, and fault zones. Spalling is due in part to the formation of a reflected shock wave at the incident surface of the cavity, causing tensile stresses to be induced in the rock, and in part to late time circumferential tension induced around the cavity by the stress field. The circumferential tension causes joints to separate and can free large blocks of rock from the surrounding rock mass. The blocks, in turn, may be expelled into unlined cavities (Ref. 7-34). In the case of lined cavities, individual blocks traveling with a velocity on the order of the late-time free-field velocity, may provide a source of impulse which must be resisted by the cavity liner. Corresponding ranges at which spall can be expected in a hard rock material are 1200 to 2000 feet (365 to 608 m) for a 1 MT (4.184 x 10^{15} j) surface burst.

4. Relative Displacements

At all ranges, for structures near the surface, relative displacements with magnitudes on the order of the peak free-field displacement may occur along major joint sets intersecting the cavity. Such displacements may be the result of late-time joint separation and block slippage or large scale displacement along joint sets which intersect the burst region.

7.4.3 Integrally Lined Cavities

In general, integrally lined cavities are equally as susceptible as unlined cavities to compressive failure and relative rock displacement because liners of practical size and materials have strengths similar to the surrounding rock. However, integral linings may provide adequate strengthening in regions of minor compressive failure, in the spall zone, and in regions of small relative displacement. At the outer limits of the spall zone, rock bolts alone may be sufficient.

The increased cavity strength due to integral linings derives from two sources. In the spall zone, the liner resists spalling and/or prevents rock spalls and loosened blocks from entering the cavity. In the region of minor compressive failure, the lining provides confinement of the rock and thereby increases rock strength (Ref. 7-35). Even though

the rock may be fractured or jointed, a substantial increase in strength is possible. Typical integral liners are composed of a concrete lining in contact with the rock and an inner steel shell. The steel shell provides confinement to the concrete and thereby increases the concrete strength in the same way the concrete increases the rock strength. The thicker the steel lining or the greater its yield strength, the greater the strength of the section. Because both the steel lining and concrete will yield before the rock develops maximum strength, it is necessary to anchor them firmly to the rock so they do not buckle locally and permit local failure of the rock. Anchoring is best achieved by rock bolting (Ref. 7-35).

7.4.4 Structures with Crushable Backpacking

Between the range corresponding to complete cavity closure and that corresponding to local compressive failure, considerable hardening of structures in rock can be accomplished by providing a crushable filler or backpacking between the structural liner and the rock cavity wall. Backpacking materials of proper thickness and characteristics can reduce the magnitude and nonuniformity of the stresses reaching the structure, reduce the accelerations transmitted to the structure, accommodate rock cavity deformations and relative block displacements and absorb spalled projectiles and loosened rock.

The major characteristics of a suitable backpacking material (Ref. 7-29 and 7-35) are as follows:

- The yield point must be low enough so that stresses are attenuated yet high enough to resist static loads
- Large strains at a fairly constant yield stress should be possible so that energy imparted by the deformed, crushed or spalled rock can be absorbed.

- The characteristic impedance should be as low as possible with respect to the surrounding medium so that beneficial reflections from the cavity interface will occur.

Materials exhibiting such characteristics include polyurethane foams and various lightweight cellular or foamed concretes and mortars. Such materials may be produced with a wide variety of yield strengths and densities. A typical stress-strain curve for a foamed concrete is shown in Fig. 7-51. The specimen yields at a relatively constant stress up to strains of about 40%. Beyond 40% strain, the specimen exhibits strain hardening or locking type behavior.

With the use of backpacking, the maximum pressure transmitted to a structural liner can be assumed equal to the pressure causing yield of the packing material so long as the packing is not strained into the locking region. It is important that the dynamic yield stress of the material be used. Reference 7-36 reports laboratory and HEST experiments where the transmitted stress was approximately 60 percent greater than the static yield stress of the backpacking, indicating possible strain rate sensitivity of the packing material.

The events which occur as a shock traverses a backpacked structure are approximately as follow (Ref. 7-36):

- When the shock wave encounters the opening, the impedance mismatch between the backpacking and surrounding medium results in beneficial reflected waves. In a rock medium, considerable spalling and/or crushing would probably occur.
- The transmitted pressure wave travels through the backpacking, crushing it and expending energy.

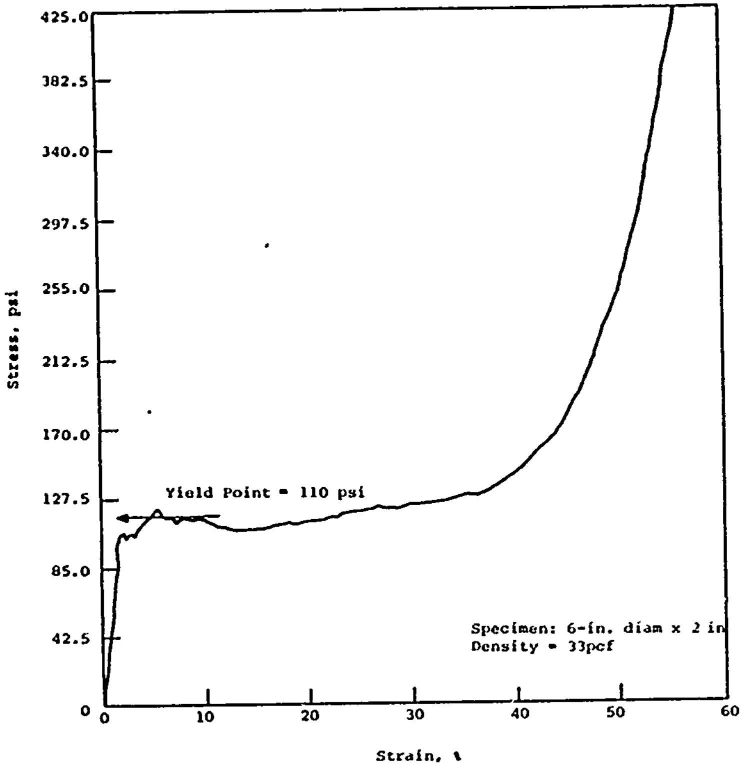

Figure 7-51 Typical Stress-Strain Response for Foamed Concrete (Ref. 7-36)

- The attenuated pressure wave in the backpacking strikes the structure with a peak pressure which is a function of the dynamic yield point of the backpacking and is considerably less than it would be without backpacking.
- Deformation of the cavity wall is accommodated by crushing of the backpacking. In addition, expelled rock projectiles are prevented from impacting the structure if the backpacking is of sufficient thickness.

The design of backpacked structures requires the selection of backpacking thickness and yield stress and estimation of the loads imposed on the structural liner. Procedures for determining such parameters are suggested in Refs. 7-37 and 7-38. For uniform radial movement of a cylindrical cavity wall, the pressure exerted on the packing material and transferred to the structural liner will be uniform. Under such conditions, negligible liner deformation will result. However, with the passage of a shock wave, some nonuniform loading should be expected. The loads on a structural liner are assumed to be a superposition of a uniform radial component and a sinusoidally varying component. Since it is assumed that strain hardening of the backpacking does not occur, the sum of the two components is limited to the yield stress of the backpacking. A method for determining the magnitude of each component is given in Section VIII.

The backpacking thickness must be sufficient to absorb most of the energy imparted by the crushing rock and must keep the cavity walls and expelled rock from contacting the liner. Energy considerations and thickness requirements are also discussed in Section VIII.

7.4.5 Motion of the Walls of Unlined Cavities and Structural Liners

In the case of near-surface structures in soils (paragraph 7.3), preliminary estimates of structure motions were

obtained by assuming the structure to be rigid. Such a procedure, of course, cannot be used for estimates of unlined cavity motions. The rigid body motion of an unlined inclusion is meaningless since equipment and/or facilities will be attached to individual locations on the cavity boundary. Accordingly, it is necessary to estimate motion as a function of location on the cavity boundary.

Consider first the qualitative aspects of interaction in an elastic medium. The diffraction of an incident wave around rectangular and cylindrical cavities is shown in Fig. 7-52. As the incident wave strikes the side-on face of a cavity a tensile reflection occurs and the particle velocities on the side-on face increase at a rate twice that associated with the incident wave. Also immediately, rarefactions from the edges of the side-on face begin to erode the reflection. At some later time, the relief process is complete and the particle velocities of points on the side-on face decay approximately the same as the particle velocity in the adjacent free-field.

After reflecting at the side-on face, the incident wave proceeds to engulf the inclusion. As is illustrated in Fig. 7-52, points on the back or rear face of the structure are not loaded at the same time that points at a corresponding range in the free-field are loaded. Points on the back face first experience a compression wave traveling at the loading wave velocity and at some later time a shear wave.

Motion in the compression wave is largely tangent to the back face and is believed to be relatively weak. Strongest motion is expected to be associated with the shear wave since the shear motion is in a direction most closely aligned with the motion in the free-field. As the shear waves pass through each other and continue to opposite sides of the back face, the motion of locations on the back face

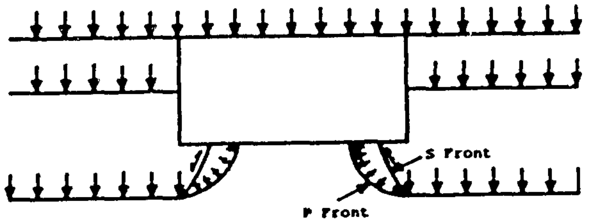

(a) Rectangular Unlined Inclusion

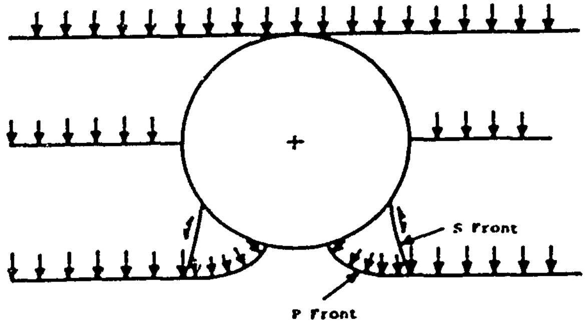

(b) Cylindrical Unlined Inclusion

Figure 7-52 Diffraction of Incident Waves Around Rectangular and Cylindrical Unlined Inclusions

approach the motion in the free field. The concept that shear phenomena govern the early time motion of the rear faces or unlined cavities is in agreement with a recent unpublished code calculation (Ref. 7-34).

The qualitative description of interaction is quantitized in an approximate way in Fig. 7-53 for a rectangular cavity and Fig. 7-54 for a cylindrical cavity. The particle velocity at the mid-point of the roof of a rectangular cavity is assumed to rise to twice the incident free-field particle velocity and decay linearly to the free-field particle velocity in the time required for a rarefaction wave to traverse the entire roof. The mid-point of the floor is assumed not to move until the arrival of the shear waves. Particle velocity is assumed to rise linearly to the peak particle velocity in the free-field in the time required for the shear waves to travel from the mid-point to the edges. The particle velocity time history on the walls parallel to the direction of incident wave propagation may be assumed equal to that of the free-field.

The time histories of particle velocity at the crown and invert of a cylindrical cavity are assumed to vary in a manner similar to the time histories for a rectangular cavity with appropriate changes in characteristic times. The particle velocity-time history at the spring line in the direction of incident wave propagation may be assumed equal to that of the free-field.

Structural liners will generally have an impedance with magnitude on the order of the impedance of hard rock. Accordingly, the motions of points on a structural liner may be estimated by considering the inside surface of the liner to be the boundary of an unlined inclusion. Situations which vary from the near-equal impedance assumption will have to be treated with more sophisticated analysis methods.

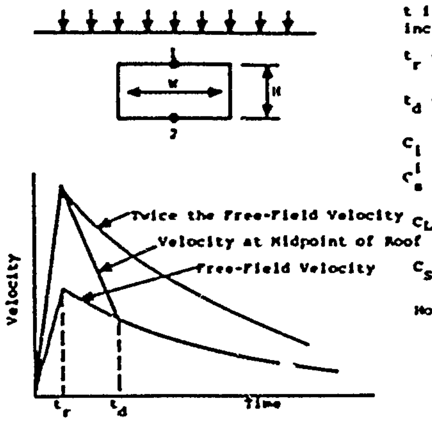

t is measured from arrival of incident wave at roof

t_r = rise time of incident wave

$t_d = \frac{W}{C_L}$

C_l = seismic velocity

C_s^l = shear wave velocity of low stresses

C_L = loading wave velocity associated with peak

C_S = shear wave velocity associated with peak

Note: If $t_d < t_r$ use free-field velocity

(a) Particle Velocity at Midpoint of Roof (Location 1)

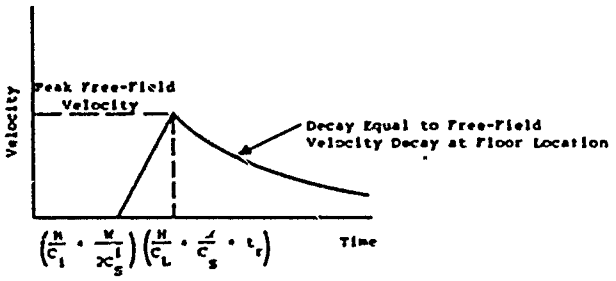

(b) Particle Velocity at Midpoint of Floor (Location 2)

Figure 7-53 Velocity-Time Histories in Direction of Incident Wave on Roof and Floor of Unlined Rectangular Cavity

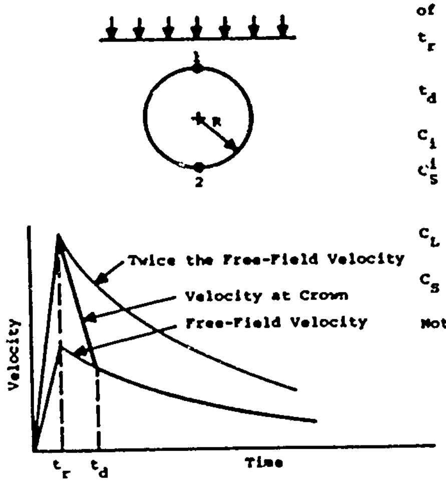

t is measured from arrival of incident wave at roof

t_r = rise time of incident wave

$t_d = \frac{.8R}{C_L}$

C_l = seismic velocity

C_S^l = shear wave velocity associated with low stresses

C_L = loading wave velocity associated with peak

C_S = shear wave velocity associated with peak

Note: If $t_d < t_r$ use free-field velocity

(a) Particle Velocity at Crown (Location 1)

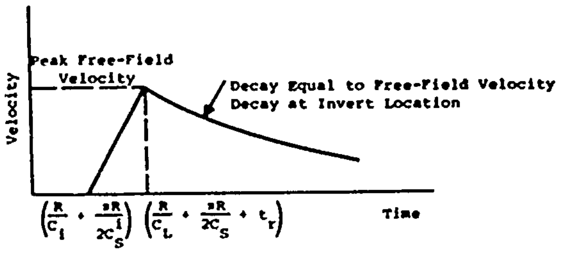

(b) Particle Velocity at Invert (Location 2)

Figure 7-54 Velocity-Time Histories in Direction of Incident Wave at Crown and Invert of Unlined Cylindrical Cavity

The motion of structural liners which are isolated from rock by backpacking is not readily amenable to simple analysis. Gross motion will likely resemble free-field motion at late times. Peak structure accelerations are expected to be less than peak accelerations in the free-field. Detailed analysis will require the application of two dimensional methods.

7.4.6 Near-Surface Structures

The deep underground strain and motion concepts outlined in the preceeding are equally applicable to near surface structures sited in rock. Additional conditions which must be considered are the orientation of the structure with respect to the ground surface and the potential for much larger relative block displacements than occur deep underground.

The critical strain component for a near-surface structure is dependent to some extent on the orientation of the structure. The horizontal strain component due to either direct-induced or airblast-induced ground shock is expected to be the most critical for vertically oriented cylinders. The critical strain component for horizontally oriented cylinders will be either the vertical airblast-induced component or the horizontal direct-induced component. All strain components can be estimated by the methods of Section V. Stress concentration factors and, by assumption, strain concentration factors for horizontally oriented cylinders are the same as for deep underground cylinders. Concentration factors for vertically oriented cylinders, however, should be modified to account for the stress conditions which occur near the surface.

Very large relative block motions along major joint sets are possible in the near-surface region because of the free surface. Such relative displacements may be an order of magnitude or more greater than peak absolute displacements predicted under homogeneous, elastic, isotropic assumptions. References 7-39 and 7-40 describe the relative displacements

which occurred in two large scale simulation tests and the effect of the displacements upon vertical cylindrical cavities and structural liners.

7.5 LOADS DUE TO EJECTA AND RADIATION

7.5.1 Ejecta Loads

Ejecta from cratering results in static load due to ejecta weight and dynamic load due to the impact of earth clods or rock missiles. Only aboveground and surface flush structures are affected. Methods for estimating static weights are given in Section IV. Ejecta impact will result in a local stress wave and in structural element vibration response.

Because of the short duration involved in a missile impact, the vibration response of the structural element may be estimated by assuming the missile delivers an impulse given by

$$I = Mv_o \tag{7-58}$$

where

I = total impulse

M = mass of impacting missile

v_o = impact velocity (see Section IV)

The gross characteristics of the local stress wave induced by an impacting missile can be roughly estimated by assuming that the impacting missile is square in shape (Ref. 7-34). The peak stress can be assumed to occur instantaneously and have a value given by

$$\sigma_{max} = \left[\frac{(\rho_1 C_1)(\rho_2 C_2)}{\rho_1 C_1 + \rho_2 C_2}\right] v_o \tag{7-59}$$

where

σ_{max} = peak stress induced by the impacting missile

ρ_1,ρ_2 = mass density of the missile and element material, respectively

C_1,C_2 = loading wave velocities of the missile and element material, respectively

The peak stress can be assumed to decay to zero in a time given by

$$t_o = \frac{2I}{\sigma_{max}L^2} \qquad (7\text{-}60)$$

where $L = \sqrt[3]{M/\rho_1}$.

Crater debris impacts will generally occur relatively late in time. In analyzing structures subjected to missile impact, consideration should be given to structural degradation which may have occurred due to earlier arriving environments.

7.5.2 Radiation Loads

a. Energy Deposition

When the photons (X rays and gamma rays) and neutrons from a nuclear burst strike an exposed structural element, they penetrate the element and deposit energy in the structural materials. The depth of penetration and rate of deposition of energy are a function of the type and energy spectrum of radiation and the properties of the material subjected to the radiation. If the energy deposition level is sufficiently high, thermomechanical damage can occur in the material. If the materials in the structure and the energy spectrum of the incident radiation are specified, it is possible to compute the energy deposition profile by use of

Monte-Carlo type computer codes. Approximations to transport theory can be used to obtain order-of-magnitude assessments of the radiation intensity required to damage structural materials. Most of the following discussion is from Ref. 7-41 which includes a more extensive treatment of nuclear radiation induced thermomechanical effects on structural materials.

The materials of primary interest in protective construction are portland cement concrete and steel and to a lesser extent the variety of materials used in antenna installations. Concrete backed by a steel plate or concrete in an open steel pan can be adequately treated by considering each material separately. Determining the combined response of a reinforced concrete member or composites of other materials is a complex calculational problem which, according to Ref. 7-41, should be deferred until more experimental data are obtained.

In order to determine the energy deposition in a material, ratios of peak thermal energy deposition to incident radiation fluence (free-field environment) are useful.

The deposition profile Q(x) as a function of distance x into the material may be approximated as a triangle where Q_{max}, the maximum value of Q(x), is the height of the triangle and L is its base. The deposition depth, L, is chosen such that the area of the approximation is equal to the area under the real deposition profile curve. If the radiation fluence is assumed to vary as

$$Q(x) = Q_{max}\exp(-\rho\mu x) \qquad (7\text{-}61)$$

where

μ = mass absorption coefficient for material

ρ = density of the material

x = distance into the material

then the energy deposition in the material at a depth x is $\mu e^{-\rho\mu x}$. The approximate deposition depth is

$$L = \frac{2}{\rho\mu} \tag{7-62}$$

Values of μ for concrete and steel for all energies of photons and neutrons may be found in Ref. 7-41. Table 7-1 lists the concrete constituents and other properties assumed for calculations in Ref. 7-41. Table 7-2 lists the properties and equations describing properties assumed for steel.

Table 7-3, from Ref. 7-41, summarizes the results of calculations of the deposition of radiation energy in concrete and steel. It should be noted that the higher rates of energy deposition result from the lower energy photons, i.e., the photons with energy levels of 1-200 kev deposit more energy per unit mass of material than photons with energy levels above 200 kev or neutrons. One reason for the difference is the greater depths required to absorb the higher energy radiation. X-ray photons fall in the lower energy band and, thus, are more significant in damaging exposed concrete and steel structures at close ranges from a nuclear detonation. For concrete and the exposed lip of a steel pan, the smaller deposition depths given in Table 7-3 correspond to the larger values of Q_{max}. Maximum depositions for 1 cal/cm^2 incident on the surface of a steel pan range from 0.01 cal/gm for neutrons to 700 cal/gm for low-energy photons. In concrete, the range is from

Table 7-1

CONCRETE PROPERTIES USED IN PRELIMINARY CALCULATIONS (REF. 7-41)

COMPOSITION: Element	Weight Percent	Oxide	Weight Percent*
H	1.0	H_2O	9.00
C	0.1		
O	52.9		
Na	1.6	Na_2O	2.15
Al	3.4	Al_2O_3	6.42
Si	33.7	SiO_2	72.94
K	1.3	K_2O	1.60
Ca	4.4	CaO	6.16
Mn	0.2	MnO	0.33
Fe	1.6	FeO	1.40

Average atomic number: 11.25

Density: ρ = 2.3 gm/cm^3

Longitudinal sound speed: c_ℓ = 3500 m/sec

Transverse sound speed: c_t = 0

Bulk modulus: $B_s = \rho(c_\ell^2 - \frac{4}{3} c_t^2)$ = 280 kbar

Head capacity: C_p = 0.156 cal/(gm - °C)

Volumetric coefficient of thermal expansion: $\alpha_v = 3 \times 10^{-5}$/°C

Thermal shock coefficient: τ = 54 bar - gm/cal

Thermal conductivity: k = 0.00413 cal/(sec - cm - °C)

Static tensile strength = 300 psi (207 N/cm^2)**

Static compressive strength = 6000 psi (4140 N/cm^2)**

---

[*] Computed by stoichiometric balance of elemental composition

[**] Measured for standard test cylinders. These numbers serve to identify the concrete rather than provide a measure of actual strength in a one-dimensional situation.

Table 7-2

PROPERTIES OF STEEL USED IN PRELIMINARY CALCULATIONS (REF. 7-41)

On the right side of equations, T is in degrees Kelvin and P is in kilobars.

Density: $\rho = 7.85$ gm/cm^3

Volumetric coefficient of thermal expansion:*

$\alpha_v(°K^{-1}) = 3.51 \times 10^{-5} + 5.1 \times 10^{-8}\ (T - 295) - (6.98 \times 10^{-8}\ P)$

Bulk moduli at constant temperature and entropy:*

$B_t(\text{kbar}) = 1639 - 0.1871\ (T - 295) + 5.06\ P$

$B_s(\text{kbar}) = 1667 - 0.05\ (T - 295) + 5.13P$

Heat capacities at constant pressure:*

$C_p\ (\text{cal/gm-°K}) = 0.0602 + 1.27 \times 10^{-4}\ T + 768T^{-2} - (4.66 \times 10^{-5}\ P)$

$= 0.1064 + 0.97 \times 10^{-4}\ (T - 295) - (4.66 \times 10^{-5}\ P)$

$C_v\ (\text{cal/gm-°K}) = (0.1046)$

Resistivity: 2.8×10^{-5} ohm - cm

Sound speeds for longitudinal and transverse waves:

$c_\ell = 5940$ m/sec $\qquad c_t = 3540$ m/sec

Temperature (°C)	Tensile Strength (kbar)
58	7.0
500	6.3
600	5.3
700	3.8

Thermal shock coefficient:*

$\tau(\text{bar - g/cal}) = 500\ [1 + 4.27 \times 10^{-4}\ (T - 295) + 1.53 \times 10^{-3}\ P]$

$= 500\ [1 + 0.005Q]\ (Q = \text{deposition in cal/gm})$

---

*For pure iron.

Table 7-3

SUMMARY OF DEPOSITION CALCULATIONS (REF. 7-41)

	Type of Radiation		
	Photons		Neutrons
Maximum Energy	1-200 kev	0.2-10 Mev	0.7-14 Mev
Q_{max} deposition (cal/gm)/(cal/cm^2)			
in concrete	0.03-400	∿ 0.02	∿ 0.01
in steel pan	0.1-700	∿ 0.03	∿ 0.01
in reinforcing*	10^{-4}-0.2	∿ 0.02	∿ 0.01
Deposition mass depth for triangular deposition profile (gm/cm^2)			
in concrete	0.005-70	∿ 100	∿ 200
in steel pan	0.003-2	∿ 70	∿ 200
in reinforcing	0.01->20	> 20	> 20
Deposition depth L(cm)			
in concrete	0.002-30	∿ 40	∿ 80
in steel pan	10^{-4}-0.25	9	∿ 25
in reinforcing	0.01- 2.5	> 2.5	> 2.5
Deposition time	10^{-8} sec		10^{-4} sec

---

*Tenth-value thickness or rebar diameter

0.01 to 400 cal/gm. The rebars are shielded by a layer of concrete, in which the lower energy radiation is strongly attenuated, so the lower Q_{max} in the rebar corresponds to the lower deposition depths. For higher energy radiation, the deposition depth in the steel is larger than the rebar diameter and the rebar diameter is listed for this case. The deposition times shown in Table 7-3 are so short that it is obvious that no significant heat transfer can occur until after the energy is deposited in the material.

In order to obtain reasonable estimates of the rate of energy deposition in concrete or steel, it is necessary to have some knowledge of the energy spectrum of the incident radiation. This spectrum will usually exhibit a peak value indicating the energy level of the greatest portion of the neutrons or photons. A mass absorption coefficient corresponding to this energy level is suggested for determining the rate of energy deposition and the total energy deposited in the material. Mass absorption coefficients for concrete are given in Fig. 6-3. The triangular approximation suggested by Eq. 7-62 can be used to determine the deposition depth.

In the absence of information on radiation energy spectra, the information given in Table 7-3 can be used to obtain crude estimates of the probable range in levels of deposition of radiation energy.

b. Equilibrium Temperature Vs. Energy Deposition

At low temperatures, the equilibrium temperature, T_{eq}, that results from a deposition of Q cal/gm is given by

$$T_{eq} - T_o = Q/C_p \qquad (7\text{-}63)$$

where

T_o = ambient temperature (°C)

C_p = heat capacity (cal/(gm-°C))

At higher temperatures, solid-state phase changes, melting, and vaporization complicate the picture. Figures 7-55 and 7-56 show T_{eq} as a function of Q for concrete and iron, respectively. In Fig. 7-55, it is assumed that concrete can be treated as a mixture of its component oxides as given in Table 7-1. The reinforcing bars are treated as steel rods imbedded in concrete and are assumed to have the same properties as iron.

Concrete, with or without reinforcing, is considered to be an infinite slab. Concrete in an open steel pan is considered to be a semi-infinite slab of concrete, surrounded by steel on the bottom and on a lateral edge.

The horizontal plateaus shown in Figs. 7-55 and 7-56 represent a range in energy deposition over which the specified phenomena occur. For example, vaporization of water in concrete begins at about 20 cal/gm and is completed at about 65 cal/gm. Vaporization ranges for the two primary constituents of concrete are also shown.

Temperatures higher than that required for vaporization of the water in concrete could create very high internal pressures in a mass of concrete. It has been suggested that if these pressures exceed the tensile strength of the concrete, extensive internal cracking could occur with a significant loss of strength of the member. Saturated concrete specimens located at ground zero in a nuclear test did not exhibit such behavior; however, it is possible that the incident and

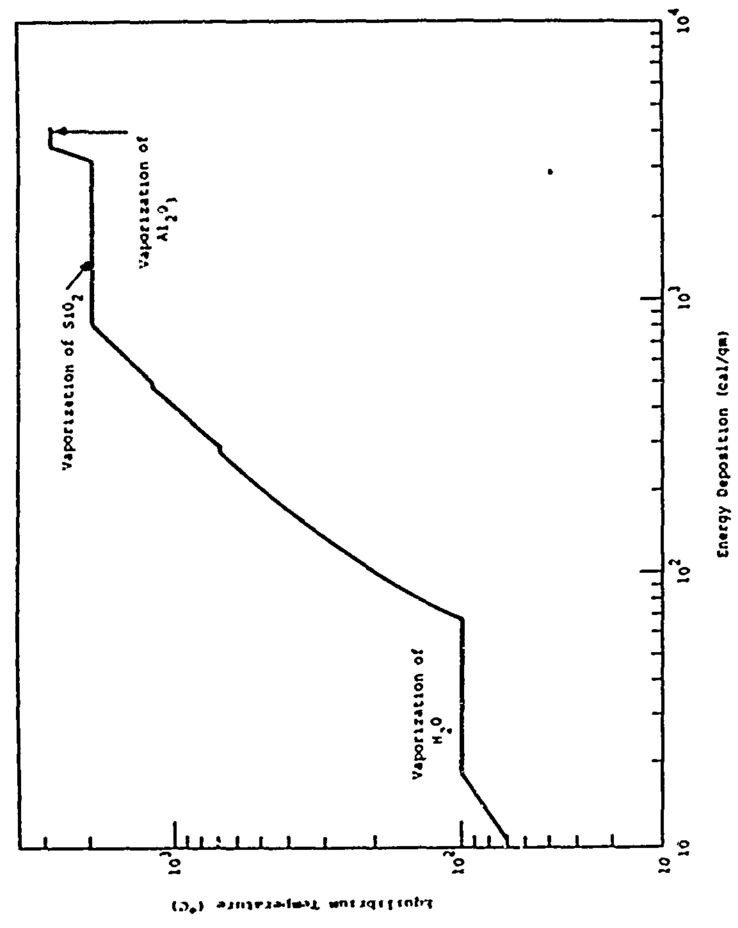

Figure 7-55 Equilibrium Temperature Vs. Energy Deposition for Concrete (Ref. 7-41)

absorbed energy was not sufficiently high to cause extensive vaporization. If the temperature of the concrete exceeds 250-300°C, the concrete may lose some of its strength. The threshold deposition for both water vaporization and strength loss is about 100 cal/gm. The significance of the degradation of strength could depend on what percentage of the total concrete mass was affected.

Similar phenomena could occur in the steel pan or the reinforcing. At an energy deposition of about 260 cal/gm, the steel will begin to melt (Fig. 7-56). Melting might weld two exposed, adjacent steel parts together or cause the loss of reinforcing bar strength. The latter is less likely to occur since some protection is provided by concrete cover.

c. Stress Wave Generation

The deposition of thermal energy generates stress waves in structural materials by two mechanisms--thermal shock and blowoff. Qualitatively, thermal shock occurs as follows: As the material is heated it tends to expand, but the heating is so rapid that there is no time for expansion to take place (i.e., no time for external relief stress waves to arrive). Instead, stresses are set up according to the temperature-dependent stress-strain relation (equation of state) for the solid material. If the temperature exceeds the vaporization temperature for components of the material, the components will vaporize and the expansion of the vapors can blow off a surface layer. The blowoff threshold sets an upper limit to the energy deposition for which thermal shock can occur. Blowoff can occur either before or after local thermal equilibrium is established. The expansion of vapors also imparts a pressure to the unvaporized material. The stress wave so generated can cause further damage to the material by spalling at free surfaces or discontinuities.

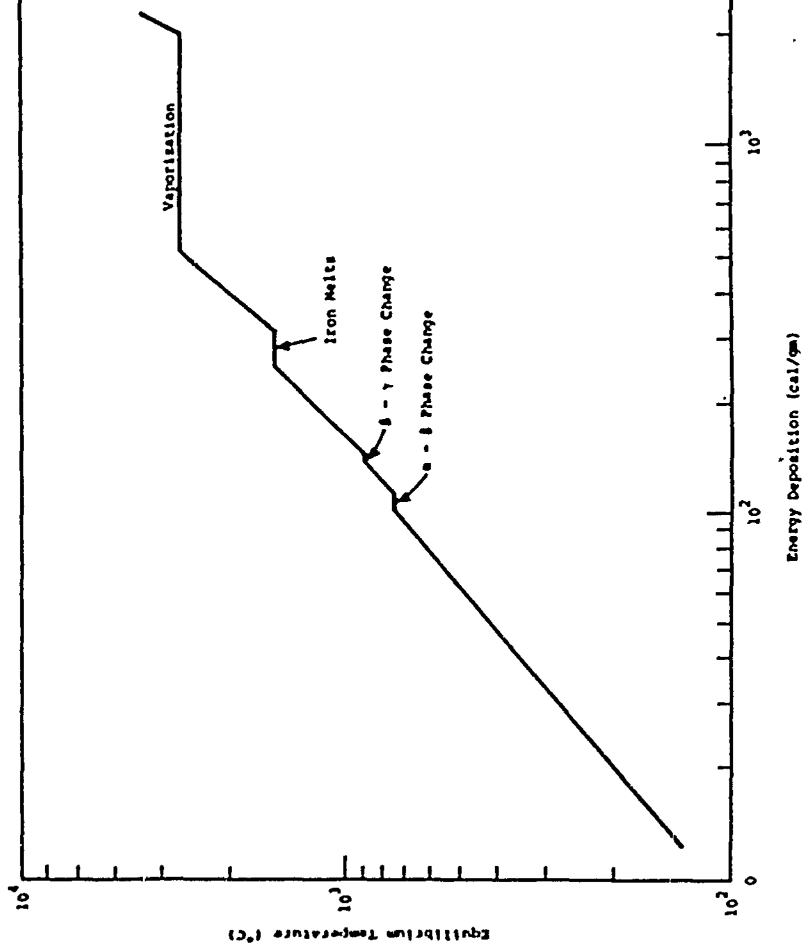

Figure 7-56 Equilibrium Temperature Vs. Energy Deposition for Iron (Ref. 7-41)

If the radiation deposition is spread out in time, there will be time for partial relief of the stress waves as they are being generated. Since this spread tends to reduce the peak stress, calculations based on instantaneous deposition are conservative for design in that they overestimate the peak stresses.

If Q_{max} exceeds 100 cal/gm, it can be assumed that some constituents of the concrete will be vaporized and surface blowoff will occur to a depth where the energy deposition drops to less than 100 cal/gm. This blowoff of material will generate a compression wave in the remaining unvaporized material.

If the peak thermal energy deposition is less than 100 cal/gm it will induce a peak pressure in the concrete given by

$$P_{max} = \tau Q_{max} \tag{7-64}$$

where

P_{max} = peak shock pressure, kbar
Q_{max} = peak energy deposition, cal/gm
τ = thermal shock coefficient, kbar - gm/cal

The thermal shock coefficient depends on several factors, including temperature and material properties. For concrete, a value of 0.054 kbar - gm/cal is given in Table 7-1 and is recommended as an average value for use in preliminary calculations. Reference 7-39 reports values varying from 0.025 to 0.091 kbar - gm/cal.

Using the assumed blowoff threshold of 100 cal/gm and a thermal shock coefficient of 0.054 kbar - gm/cal in Eq. 7-64, 5.4 kbar is obtained as the maximum thermal shock pressure that can be generated by deposition of radiation energy in concrete. Any higher deposition of energy would result in blowoff of concrete. This peak pressure can only be considered an approximation of the actual value because of the considerable uncertainties surrounding the factors affecting peak pressure determination.

The compressive thermal pressure pulse travels toward the free surfaces of the concrete element and is reflected as a tensile wave. If the tensile stress exceeds the spall threshold of the concrete, spalling of the concrete surface will occur. The spall threshold for concrete is reported in Ref. 7-41 to vary from about 0.02 to 2 kbar and depends somewhat on strain rate. The initial compressive wave is followed by a tensile wave (Ref. 7-41) and, if the magnitude of the tension exceeds the tensile strength of the concrete, internal cracking may occur with a degradation of strength. If blowoff of material occurs at the surface, the compression wave generated by blowoff may reduce the effects of the tensile wave. Attenuation of peak stresses will also occur as the thermal stress wave propagates through the concrete. Debonding of reinforcing bars can potentially occur in reinforced concrete if the peak thermal shock pressure in the concrete at reinforcing locations exceeds the spall threshold for concrete.

A similar phenomenon can occur in exposed steel surfaces, except that much higher energy levels are required to cause blowoff or spalling of material. From Fig. 7-56, energy depositions on the order of 500 cal/gm are necessary to vaporize steel. The thermal shock coefficient for steel is given by the expression in Table 7-2. Using Q_{max} equal to 500 cal/gm and a thermal shock coefficient of 0.55 kbar - gm/cal in Eq. 7-64, a peak thermal shock pressure of approximately

300 kbar is obtained. Since steel melts at energy levels on the order of 300 cal/gm, it is questionable whether a peak thermal shock pressure of 300 kbar would ever be reached. As in the case of concrete, reflection of the compression wave at a free surface causes a tensile stress which can cause spallation if the spall threshold of steel is exceeded. Reference 7-41 gives the spall threshold of steel as about 30 kbar.

In summary, the thermomechanical effects of radiation on structural materials are very complex phenomena which are still largely unknown due to lack of pertinent experimental data. Hydrodynamic computer codes have been applied to the problem, but solutions are subject to uncertainties regarding material behavior in an intense radiation environment. Reference 7-41 presents depths of blowoff and impulse and peak pressure imparted to the unvaporized material for a wide range of surface fluences and photon and neutron energies. The information is classified and cannot be included herein.

The thermomechanical effects of radiation might be offset to some extent by use of additional reinforcing steel to increase the resistance of concrete to spalling or the use of internal plates to disperse the thermal shock pulse. Either approach would require extensive study and calculational effort.

d. Ablation

Ablation of structural materials is a function of thermal energy deposition and dynamic pressures in the airblast wave. It is subject to the same degree of uncertainty as thermomechanical effects. Methods outlined in the preceding paragraphs can be used to estimate energy deposition in the materials and a comparison made to that required to melt concrete or steel. Reference 7-42 suggests that the melting point of concrete is approximately 1700°K and the heat of melting is 34 cal/gm. Figure 7-55 indicates that 600-700 cal/gm are required to reach the melting temperature and, thus, 600-700 cal/gm is probably a more realistic range. However, blowoff will occur at energy levels on the order of 100 cal/gm, so it is doubtful whether melting temperatures would ever be reached in concrete.

Steel will melt at energy levels on the order of 250-300 cal/gm and it is expected that airblast dynamic pressures at close-in ranges will ablate the melted material.

7.6 ILLUSTRATIVE EXAMPLES

7.6.1 Loads and Motions for a Shallow Buried Rectangular Structure

a. GIVEN: A buried reinforced concrete structure with dimensions as shown in Fig. 7-57 with 8 feet of cover in a deep alluvial soil and loaded by a 1 MT surface burst at the 100 psi overpressure range.

b. FIND: Estimate the rigid body motion of the structure and the loads acting on the roof and base due to passage of the airblast above the structure.

c. SOLUTION:

1. The first considerations in evaluating response are the characteristics of the airblast and ground shock at the location of the structure. The overpressure-time history at the 100 psi level from a 1 MT surface burst, as determined from Section III, is shown in Fig. 7-58.

The soil is assumed to have a unit weight of 115 pcf, a seismic velocity (C_i) of 1000 ft/sec, a loading wave velocity (C_L) of 500 ft/sec and a strain recovery ratio of 1/3. The peak of the incident ground shock stress wave will arrive at the roof of the structure at a time given by

$$t_p = \frac{z_s}{C_L} = \frac{8\text{ft}}{500\text{ft/sec}} = 0.016 \text{ sec}$$

In order to estimate the degree of ground shock attenuation, a triangular fit to the overpressure-time history which fits the first 0.016 sec closely (Fig. 7-58) is determined to be

$$p = 100 \text{ psi}\left(1 - \frac{t}{0.14\text{sec}}\right)$$

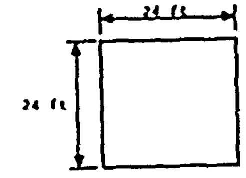

(a) Plan

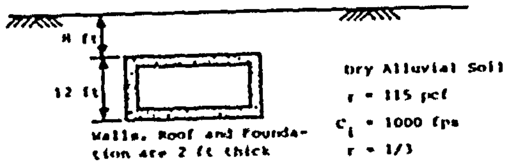

(b) Elevation

Figure 7-57 Dimensions and Configuration of Buried Rectangular Structure for Example 7.6.1

The peak stress at the 8 ft. depth in bilinear-no recovery soil is determined from Fig. 5-17 to be 94 psi. Interpolating linearly between the elastic solution (100 psi) and the bilinear-no recovery solution, the peak stress for r = 1/3 is estimated to be

$$\sigma_m = 94 + (1/3)(100 - 94) = 96 \text{ psi } (66 \text{ N/cm}^2)$$

The effect of stress attenuation is small and for purposes of this example, the overpressure-time history on the *surface is taken as a* reasonable estimate of the free-field stress wave incident on the structure roof, modified if necessary to incorporate the effect of a rise time due to stress wave dispersion in propagation (treated in the following step).

Assume that the response of the structure for 0.15 sec following stress wave arrival is required. A triangular fit to the overpressure-time history (assumed to represent the free-field wave at the structure roof) which contains the same impulse as in the actual overpressure-time history up until 0.15 sec is (Fig. 7-58)

$$\sigma = 100\text{psi}\left(1 - \frac{1}{0.21\text{sec}}\right)$$

The corresponding free-field particle velocity-time history may be determined by the methods of paragraph 5.3.2. Assuming the free-field motion at the surface to be a reasonable representation of the motion at the 8-foot depth, Fig. 5-21 can be used directly to estimate the normalized free-field velocity time history given in Fig. 7-59. The peak free-field velocity is estimated as

$$v = \frac{\sigma_{max}}{\rho c_L} = \frac{(100)(144)}{(115/32.2)(500)}$$

$$v = 8.1 \text{ ft/sec } (2.5 \text{ m/sec})$$

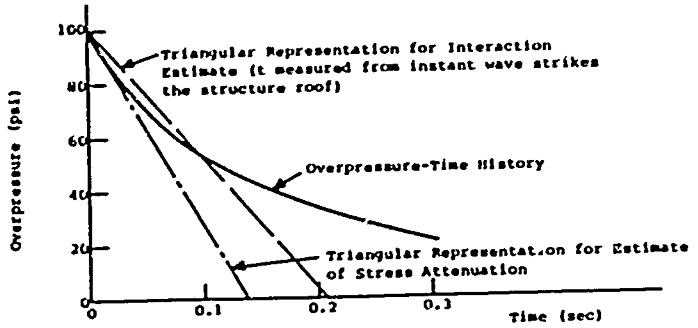

Figure 7-58 1MT-100 psi Overpressure-Time History and Triangular Representations, Example 7.6.1

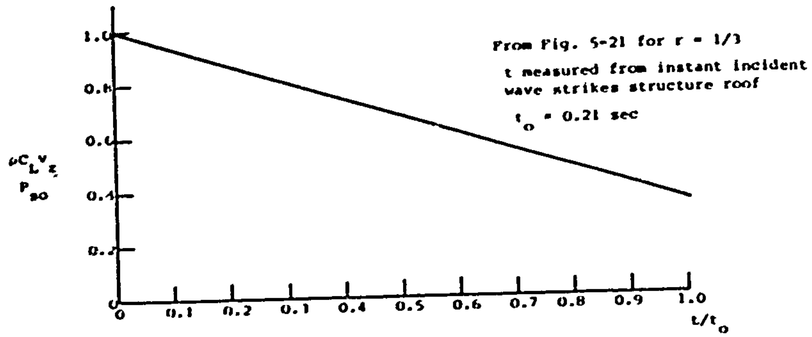

Figure 7-59 Normalized Free-Field Velocity-Time History at Depth of Structure Roof, Example 7.6.1

2. The total weight of the structure is estimated assuming the unit weight of the reinforced concrete to be 150 pcf. The total weight is

$$W = (20\text{x}20\text{x}2)(150)(2) + (24\text{x}12\text{x}2)(150)(2) + (20\text{x}12\text{x}2)(150)(2)$$

$$W = 556{,}800 \text{ lbs}$$

The total mass is therefore

$$M = \frac{556{,}800}{32.2} = 17{,}292 \text{ slugs } (252{,}355 \text{ kg})$$

Given the mass of the structure, the need to include the effect of free-field wave rise time in analysis is estimated by the criteria of Eq. 7-27.

$$\frac{10M}{\rho C_L A} = \frac{10(17292)}{(115/32.2)(500)(24)^2} = 0.168 \text{ sec}$$

The rise time at the 8-foot depth is determined by Eq. 5-44 to be

$$t_r = 0.001 + \frac{Z}{C_L} - \frac{Z}{C_i} = 0.001 + \frac{8}{500} - \frac{8}{1000}$$

$$t_r = 0.009 \text{ sec}$$

which is considerably less than 0.168 sec. Therefore, the assumption of a shock input is reasonable.

3. The detailed treatment of shear, the effect of free surface reflections and loading functions which account for material inelasticity and finite structure area (Fig. 7-45) require the use of numerical procedures which, although relatively simple with the use of a computer, are somewhat tedious for hand calculation. It is assumed initially that shear, reflections and non-ideal loading functions can be ignored. The effect of the assumption is assessed at the end of the example.

Ignoring shear, an upper bound to structure loads and response until the time of maximum structure velocity is defined by Eq. 7-48. The mass ratio is

$$\delta = \frac{\rho C_L A t_o}{M} = \frac{(115/32.2)(500)(24)^2(0.21)}{17292}$$

$$\delta = 12.5$$

The normalized time of maximum velocity is given by Eq. 7-24 using a δ twice that calculated since the structure is buried, i.e.,

$$\tau_m = \frac{1}{25}\ln(25 + 1) = 0.13$$

The actual time of peak velocity is

$$t = 0.13t_o = 0.13(0.21)$$

$$t = 0.027 \text{ secs}$$

The peak normalized structure velocity is given by Eq. 7-25 as

$$\frac{\rho C_L v_{max}}{\sigma_{max}} = [1 - \tau_m] = (1 - 0.13) = 0.87$$

giving a peak velocity of

$$v_{max} = 0.87\frac{\sigma_{max}}{\rho C_L} = 0.87\left[\frac{(100)(144)}{(115/32.2)(500)}\right]$$

$$v_{max} = 7.0 \text{ ft/sec } (2.1 \text{ m/sec})$$

compared with 8.1 ft/sec (2.5 m/sec) in the free field.

The peak structure acceleration occurs at the instant the incident wave strikes the structure and is

$$a_{max} = \frac{2A\sigma_{max}}{M} = \frac{2(24)^2(100)(144)}{17292}$$

$$a_{max} = 959 \text{ ft/sec}^2 = 30\ g$$

compared to a free-field peak acceleration of

$$a_p = 2\frac{v_p}{t_r} = 2\frac{(8.1)}{(0.009)}$$

$$a_p = 1800 \text{ ft/sec}^2 = 56\ g$$

The estimated structure normalized velocity-time history is compared with that of the same structure if surface flush (a lower bound) in Fig. 7-60. The histories to the time of maximum velocity are calculated from Eqs. 7-48 and 7-23 for the buried and surface flush structures, respectively. Beyond the time of maximum structure velocity, the structure motion is assumed to approach the free-field motion.

Normalized stress histories on the buried structure roof and foundation are shown in Fig. 7-61. The stress histories on the roof and foundation until the time of maximum structure velocity are estimated from Eqs. 7-43 and 7-44, respectively. At times beyond the maximum structure velocity, the stress on both the roof and foundation is taken as the free-field stress on the roof. The assumption that the stresses on the roof and base are the same after the time of maximum structure velocity suggests the structure is not accelerating and that the velocity remains constant after the peak velocity is achieved. However, the structure velocity-time history has already been estimated. The loads of Fig. 7-61 should be used only for structural analysis.

4. Paragraph 7.3.4 describes the effect of finite structure area, material inelasticity, shear and free surface reflections. A lower bound load (intermediate between the lower bound given by a surface flush structure and the upper bound treated in previous

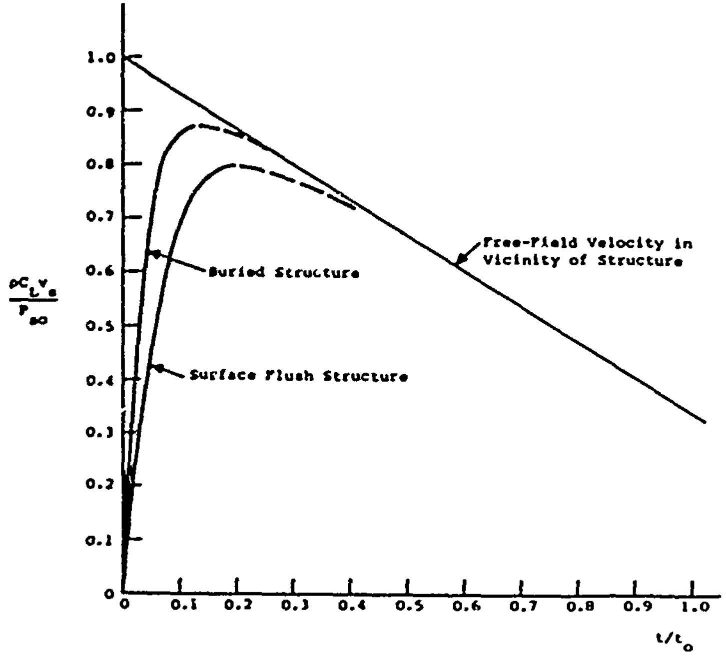

Figure 7-60 Estimated Structure Velocity-Time Histories for Example 7.6.1

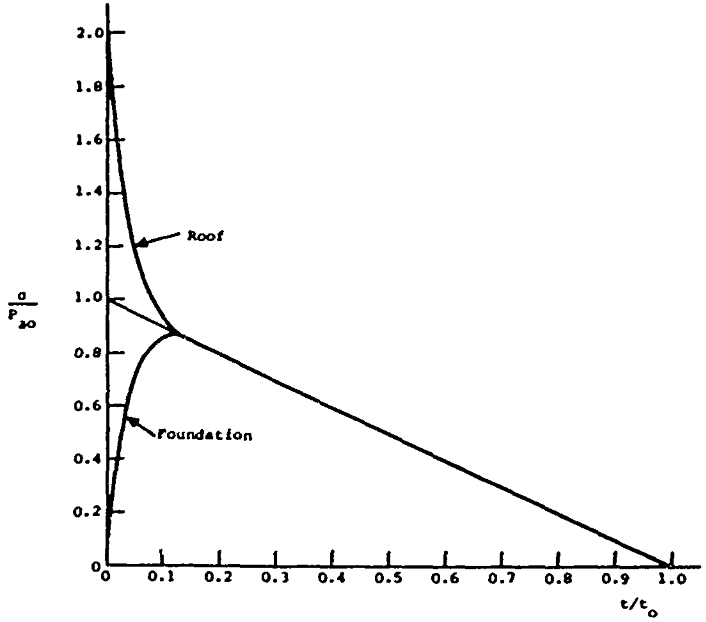

Figure 7-61 Estimated Normalized Stress Histories on Buried Structure Roof and Foundation for Example 7.6.1

steps) is suggested in Fig. 7-45 where the reflection duration is taken as the lesser of the durations given by Eqs. 7-49 or 7-51. For the present structure, the reflection duration is estimated by Eq. 7-49 as

$$t_d = \frac{z_s}{C_L} = \frac{8}{500} = 0.016 \text{ sec}$$

The lower bound roof load of Fig. 7-45 is superimposed upon the load calculated ignoring inelasticity and finite areal extent in Fig. 7-62. The difference is not major considering the overall uncertainties in the airblast and the method of analysis. Accordingly, the calculated load may be taken as a reasonable representation of the load experienced by the roof.

The results of calculations for a long surface flush structure in which the ratio of the area exposed to shear to the area exposed to the incident load was about 27 are given in Fig. 7-38. The effect of shear is to increase structure velocity about 7 to 10%. In the present case, the ratio of area exposed to shear to the area exposed to the incident load is only about 2. In addition, the load acting on the roof at early times is higher than that experienced by a surface flush structure due to reflection. As a result, the effect of shear in the present example is expected to be negligible.

The reflection from the structure roof will subsequently reflect at the ground surface and return to the structure. The reflection front will travel with the unloading wave speed of the soil

$$C_u = \sqrt{\frac{1}{r}}\, C_L = \sqrt{\frac{1}{1/3}}\ (500)$$

$$C_u = 866 \text{ ft/sec } (264 \text{ m/sec})$$

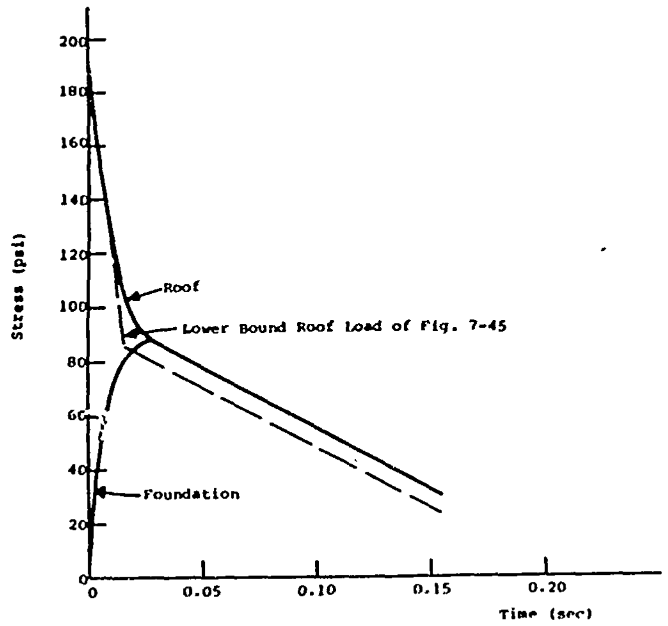

Figure 7-62 Stress-Time Histories on Buried Structure Roof and Foundation for Example 7.6.1

The ground surface reflection front will arrive at the structure at

$$t = \frac{2Z_s}{C_u} = \frac{16}{866} = 0.018 \text{ secs.}$$

and the peak at about

$$t = \frac{Z_s}{C_L} + \frac{Z_s}{C_u} = \frac{8}{500} + \frac{8}{866} = 0.025 \text{ secs.}$$

The strength of the reflection as well as later multiple reflections between the structure and ground surface will be diminished by soil inelasticity and spatial attenuation. The reflections will have no effect upon peak structure acceleration and relatively little effect upon peak structure velocity although the reflections will induce oscillations into the stress history on the roof and the structure motion. The oscillation will have a period of approximately

$$T = \frac{2Z_s}{C_u} = 0.018 \text{ secs.}$$

and will diminish rapidly.

7.6.2 Motion of a Shallow Buried Horizontal Cylinder

a. GIVEN: A reinforced concrete cylinder with dimensions as shown in Fig. 7-63 located at the 200 psi overpressure range from a 1 MT surface burst on deep alluvial soil. There is 9 feet of cover above the cylinder crown.

b. FIND: Estimate the rigid body motion of the cylinder due to passage of the airblast above the cylinder.

c. SOLUTION:

1. Assume the soil to have a unit weight

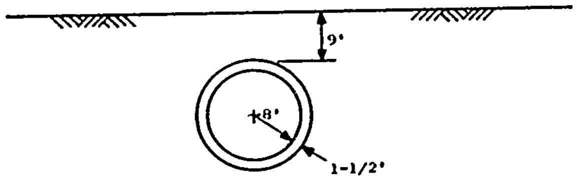

(a) Actual Configuration

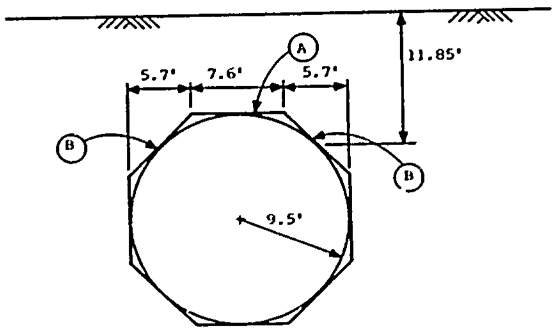

(b) Octagonal Approximation

Figure 7-63 Configurations and Dimensions of Buried Cylinder for Example 7.6.2

(γ) of 115 pcf, a seismic velocity (C_I) of 1000 ft/sec, a loading wave velocity (C_L) of 500 ft/sec and a strain recovery ratio (r) of 1/3. The 1 MT-200 psi overpressure-time history, derived from Fig. 3-7, is shown in Fig. 7-64. The ground shock peak stress arrives at the crown of the cylinder at

$$t = \frac{9}{500} = 0.018 \text{ sec}$$

The triangular representation to the overpressure-time history which fits the first 0.018 sec. closely is

$$p = 200 \text{ psi}\left(1 - \frac{t}{0.08 \text{ sec}}\right)$$

Using Fig. 5-17 and interpolation, the peak vertical soil stress at the cylinder crown is 180 psi. The attenuation of stress is significant and, therefore, the motion analysis should consider the changes in the stress wave which occur between the surface and the cylinder location.

2. It is expected that peak structure response will occur within 0.10 sec. after arrival of the overpressure. A triangular representation to the overpressure-time history which conserves inpulse until 0.10 sec is

$$p = 200 \text{ psi}\left(1 - \frac{t}{0.115 \text{ sec}}\right)$$

A nominal depth at which to estimate the incident stress history is taken as 11.85 feet (Fig. 7-63(b)). The normalized free-field stress and velocity-time histories at 11.85 feet, excluding a rise time, derived using the methods of para. 5.3.2, are shown in Fig. 7-65.

3. Analysis of vertical motions is based upon Fig. 7-47 and Eqs. 7-52 through 7-55. Consider

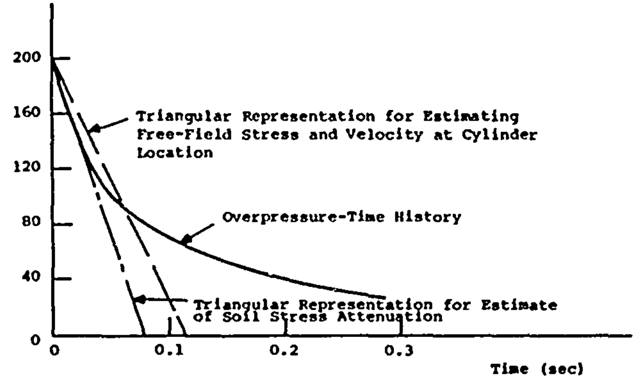

Figure 7-64 1MT-200 psi Overpressure-Time History and Triangular Representations, Example 7.6.2

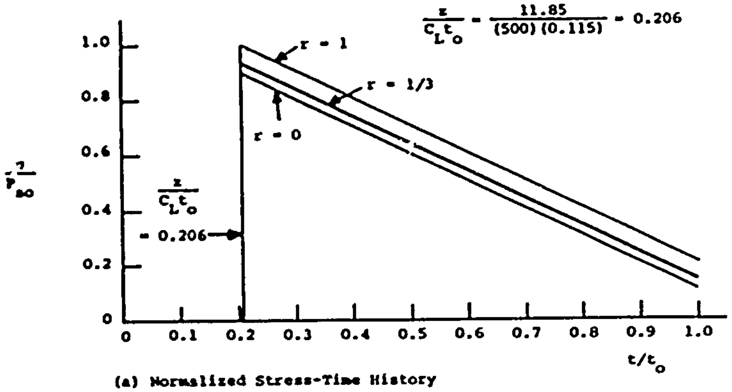

(a) Normalized Stress-Time History

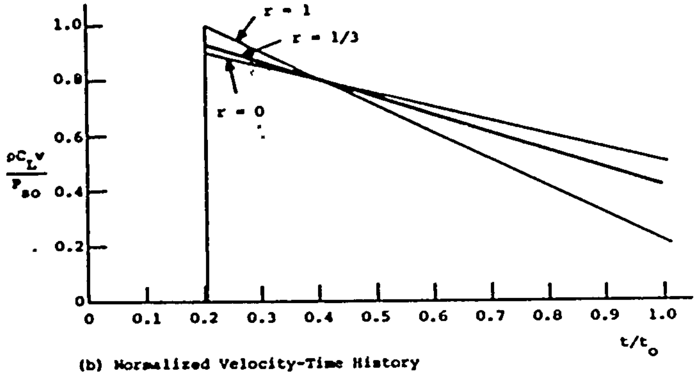

(b) Normalized Velocity-Time History

Figure 7-65 Free-Field Ground Shock Characteristics in Vicinity of Structure, Example 7.6.2

first the effect of rise time on the stress acting in Region A (Figs. 7-47 and 7-63). The rise time of the incident free-field stress wave at the 11.85 ft depth is (Eq. 5-44)

$$t_r = 0.001 + \frac{11.85}{500} - \frac{11.85}{1000} = 0.013 \text{ sec}$$

The duration of the reflection of an incident shock acting on Region A of the octagonal approximation (Fig. 7-47(b)) is the lesser of the times given by Eq. 7-49 or 7-51. Equation 7-49 gives

$$t_d = \frac{z_s}{C_L} = \frac{11.85}{500} = 0.024 \text{ sec}$$

while Eq. 7-51 gives

$$t_d = \frac{0.8R}{C_u} = \frac{0.8(9.5)}{866} = 0.009 \text{ sec}$$

Therefore, Eq. 7-51 governs. Since the rise time of the incident stress wave exceeds the time for a rarefaction to traverse the reflecting surface, the effect of reflection can be considered minor and the incident stress wave applied to Region A without alteration to account for reflection.

The stresses acting in Regions A and B are shown in Fig. 7-66(a) where the estimated incident stress history of Fig. 7-65(a) has been modified to incorporate a rise time. The rise time in Region A is

$$t'_r = 0.001 + \frac{9}{500} - \frac{9}{1000} = 0.10 \text{ sec}$$

The average arrival time of the wave front in Region B lags the arrival in Region A by

$$\Delta t_a = \frac{(11.85 - 9)}{1000} = 0.003 \text{ sec}$$

The average rise time in Region B is

$$t_r = 0.001 + \frac{11.85}{500} - \frac{11.85}{1000} = 0.013 \text{ sec}$$

The decay of the stresses in Regions A and B is taken similar to the stress decay of Fig. 7-65(a)

4. The total incident load acting on the cylinder is shown in Fig. 7-66(b) where a 1-foot slice has been considered. The loads in Regions A and B are

(Eq. 7-52) $F_A(t) = 0.8(9.5\text{ft})(1\text{ft})\sigma_A(t)$

$F_A(t) = 7.6\sigma_A(t)$

(Eq. 7-53) $F_B(t) = 1.2(9.5\text{ft})(1\text{ft})\sigma_B(t)$

$F_B(t) = 11.4\sigma_B(t)$

The total load is simply the summation of F_A and F_B in time.

5. Ignoring shear the equation of motion for the cylinder is given by Eq. 7-55. The mass of a 1 foot slice of the cylinder is

$$M = \frac{W}{g} = \frac{1}{32.2}\left[\pi(9.5^2 - 8^2)\right](150)(1)$$

$$M = 384.2 \text{ slugs}$$

The resisting force is

$$F_R(t) = 2\rho C_L R L v(t)$$

$$F_R(t) = 2(115/32.2)(500)(9.5)(1)v(t)$$

$$F_R(t) = 33928.6v(t)$$

The equation of motion is therefore

$$384.2\dot{v}(t) = F_A(t) + F_B(t) - 33928.6v(t)$$

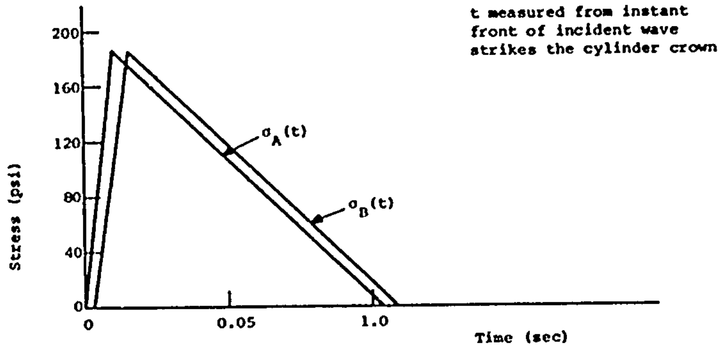

t measured from instant front of incident wave strikes the cylinder crown

(a) Stresses Acting on Incident Surfaces

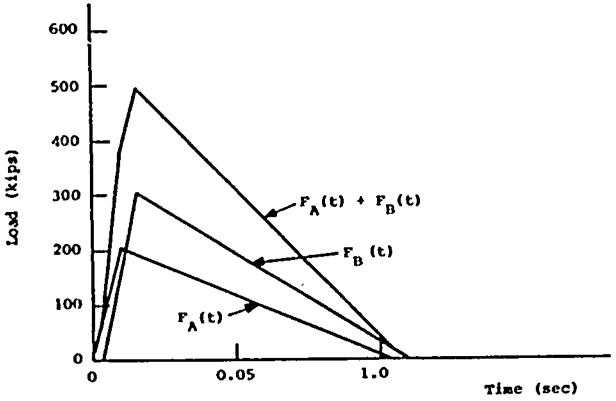

(b) Loads Acting on Incident Surfaces

Figure 7-66 Incident Loads on Cylinder Approximation, Example 7.6.2

where $\dot{v}$ is in ft/sec^2, v is in ft/sec and F is in pounds. A numerical solution to the equation of motion to the time of maximum structure velocity is shown in Fig. 7-67. Beyond the time of maximum velocity the structure velocity is assumed to approach the free-field velocity in the vicinity of the structure, taken in Fig. 7-67 to be the free-field velocity at the 11.85-foot depth. It can be seen that the peak structure velocity is about 11.7 ft/sec compared with a peak free-field velocity of 15 ft/sec.

The numerical procedure used in this case was an explicit time integration approach in which the equation of motion was written

$$Ma^n = F^n - Kv^n$$

where a^n, v^n and F^n are the acceleration, velocity and forcing function at t^n. Defining

$$a^n = \frac{1}{\Delta t}\left|v^{n+\frac{1}{2}} - v^{n-\frac{1}{2}}\right|$$

and $$v^n = \frac{1}{2}\left|v^{n+\frac{1}{2}} + v^{n-\frac{1}{2}}\right|$$

where Δt is the time step and $v^{n \pm \frac{1}{2}}$ is the velocity at $t^n \pm \frac{1}{2}\Delta t$, the recursive equation is

$$v^{n+\frac{1}{2}} = \frac{F^n}{\left[\frac{M}{\Delta t} + \frac{K}{2}\right]} + \frac{\left[\frac{M}{\Delta t} - \frac{K}{2}\right]v^{n-\frac{1}{2}}}{\left[\frac{M}{\Delta t} + \frac{K}{2}\right]}$$

Taking $\Delta t = 0.002$ sec in the present case, the recursive equation is

$$v^{n+\frac{1}{2}} = \frac{\left(F^n + 175{,}115.7v^{n-\frac{1}{2}}\right)}{209{,}044.3}$$

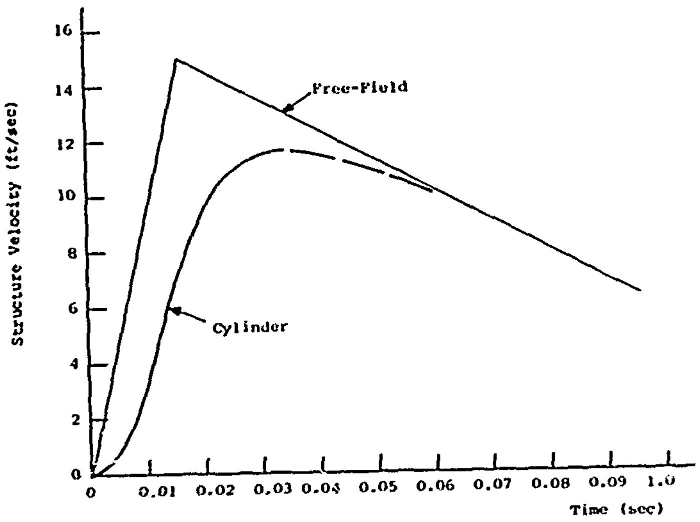

Figure 7-67 Cylinder Velocity-Time History

which provides convergent and sufficiently accurate results for this problem.

6. The peak structure acceleration is given approximately by

$$[\dot{v}(t)]_{max} = \frac{1}{384.2}\,[F(t) - 33928.6v(t)]_{max}$$

which may be determined as

$$[\dot{v}(t)]_{max} = 670\ ft/sec^2 = 21\ g$$

at t = 0.011 sec. The peak free field acceleration is approximately

$$a_p = 2\left(\frac{15ft/sec}{0.016}\right) = 1875\ ft/sec$$

$$a_p = 58\ g$$

7.4.1 Boundary Motions of an Unlined Cylindrical Tunnel

a. GIVEN: A 1 MT surface burst on granite with a seismic velocity 18,000 ft/sec.

b. FIND: The motions of the crown and invert of a 20-foot diameter unlined cylindrical tunnel located 2000 feet from the burst.

c. SOLUTION:

1. Assume that the tunnel is sufficiently deep so that the free-field motions at the location of the tunnel may reasonably be taken as the motion beneath the burst at the same range (i.e., free surface effects are of minor influence). Free field peak velocity, displacement and acceleration are estimated from Eqs. 5-65, 5-66 and 5-67.

$$v = 25ft/sec\left[\frac{1MT}{1MT}\right]^{2/3}\left[\frac{2kft}{1kft}\right]^{-2}$$

$$v = 6.25ft/sec\ (1.9\ m/sec)$$

$$d = 4.5\ in\left[\frac{1MT}{1MT}\right]^{5/6}\left[\frac{2kft}{1kft}\right]^{-3/2}$$

$$d = 1.6\ in\ (0.004\ m)$$

$$a = 140g\left[\frac{1MT}{1MT}\right]\left[\frac{2kft}{1kft}\right]^{-4}$$

$$a = 8.75\ g$$

2. The radial velocity-time history at the 2000 ft range may be estimated using Fig. 5-47, Eqs. 5-76 and 5-77. Taking average values, the rise time to peak velocity is estimated as

$$t_r = \frac{1}{8}\frac{R}{C_i} = \frac{1}{8}\frac{2000}{(18000)}$$

$$t_r = 0.014\ sec$$

and the total positive phase duration of the velocity pulse is

$$t_d = \frac{3}{4}\frac{R}{C_i} = \frac{3}{4}\frac{2000}{18000}$$

$$t_d = 0.083\ sec$$

yielding an estimated positive phase velocity time history as shown in Fig. 7-68, where parabolas have been fit to the velocity rise and decay.

3. Velocity-time histories at the crown (defined as the point at which the incident wave first strikes for tunnels not directly beneath the burst) and the invert are estimated using Fig. 7-54.

At the crown, the peak velocity will rise to about twice the incident peak velocity if the rarefaction clearing time exceeds the rise time of the incident pulse. Assuming C_L to be 3/4 the seismic velocity, the rarefaction clearing time for the structure

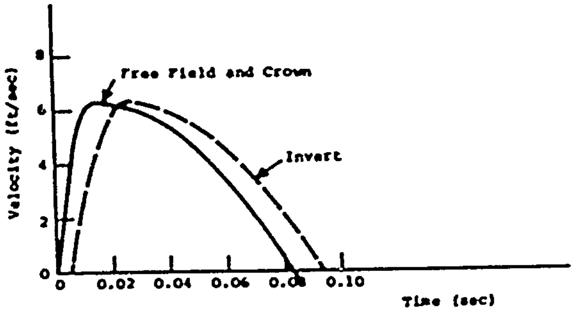

Figure 7-68 Free-Field, Crown and Invert Velocity-Time Histories for Example 7.6.3

is

$$t_d = \frac{0.8R}{C_L} = \frac{0.8(20ft)}{3/4(18000ft/sec)}$$

$$t_d = 0.001 \text{ sec}$$

which is less than the rise time of the incident wave. Accordingly, the reflection at the crown can be ignored and the estimated history is the same as the free-field history.

At the invert, motion begins to occur at a time estimated as

$$t = \frac{R}{C_i} + \frac{\pi R}{2C_s^i} = \frac{20ft}{18000} + \frac{\pi(20ft)}{2(9000)}$$

$$t = 0.005 \text{ sec}$$

where C_s^i is assumed to be $1/2C_i$ and t is measured from the arrival of the incident wave at the crown. The invert point reaches the peak free-field velocity in a time estimated as

$$t = \frac{R}{C_L} + \frac{\pi R}{C_s} + t_r = \frac{20}{3/4(18000)} + \frac{\pi(20)}{3/4(9000)} + 0.014$$

$$t = 0.025 \text{ sec}$$

The estimated history is also shown in Fig. 7-68.

7.7 REFERENCES

7-1 Constantino, D.J., Robinson, R.R., Salmon, M.A., "A Simplified Soil-Structure Interaction Model to Investigate the Response of Buried Silos and Cylinders," Proceedings of the Symposium on Soil-Structure Interaction, University of Arizona, Tucson, Ariz., September 1964. (U)

7-2 BARBS Code User's Guide, Agbabian-Jacobsen Associates Document No. R-6820-968, prepared for U.S. Army Corps. of Engineers, Huntsville, Ala., August 1970. (U)

7-3 Benzley, S.E. and Bertholf, L.D., TOODY II-A, A Computer Program for Two Dimensional Wave Propagation CDC 6600 Version, SC-DR-69-156, Sandia Laboratories, Albuquerque, N.M., November 1969. (U)

7-4 Trulio, J.G., Theory and Structure of the AFTON Code, AFWL-TR-66-19, Air Force Weapons Laboratory, Kirtland AFB, N.M., February 1969. (U)

7-5 Wilson, E.L., A Computer Program for the Dynamic Stress Analysis of Underground Structures, Report No. 68-1, Waterways Experiment Station, Vicksburg, Miss., January 1968. (U)

7-6 Ghosh, S. and Wilson, E.L., Dynamic Analysis of Axisymmetric Structures Under Arbitrary Loading,(U) Report No. EERC 69-10, University of California.

7-7 Belytochko, L., Chiapetta, R.L. and Rouse, J.D., A Computer Code for Dynamic Stress Analysis of Media-Structure Problems with Nonlinearities (SAMSON), 4 Vols., AFWL-TR-72-104, Air Force Weapons Laboratory, Kirtland AFB, N.M., February 1973. (U)

7-8 Leistner, H.L., et al., Structure-Medium Interaction and Design Procedures Study, Volume I - Analysis Method, Theory, Verification, and Applicability, SAMSO TR-69-313, Space and Missile Systems Organization, Norton AFB, Calif., October 1969. (U)

7-9 DEPS Code Modeling Techniques for SAFEGUARD Structures, Agbabian-Jacobsen Associates Document No. R-6820-1178, prepared for U.S. Army Corps of Engineers, Huntsville, Ala., April 1970. (U)

7-10 Design of Structures to Resist Nuclear Weapons Effects, ASCE Manual of Engineering Practice No. 42, American Society of Civil Engineers, New York, N.Y., 1964. (U)

7-11 Glasstone, S., Editor, The Effects of Nuclear Weapons, U.S. Government Printing Office, Washington, D.C., April 1962. (U)

7-12 Newmark, N.M. and Haltiwanger, J.D., Principles and Practices for Design of Hardened Structures, SWC-TDR-62-138, Air Force Special Weapons Center, Kirtland AFB, N.M., December 1962. (U)

7-13 Kaplan, K. and Wiehle, C., Air Blast Loading in the High Shock Strength Region, DASA 1460, Defense Atomic Support Agency, Washington, D.C., February 1965. (Part I - SFRD, Part II - U)

7-14 Brode, H.L., Height of Burst Effects at High Overpressures, RM6301, The Rand Corporation, Santa Monica, Calif., July 1970. (U)

7-15 Structures to Resist the Effects of Accidental Explosions, AFM 88-22, Hq. USAF, June 1969. (U)

7-16 Hoerner, S.F., Fluid Dynamic Drag, Published by author at 148 Busterd Drive, Midland Park, N.J., 1958. (U)

7-17 "Wind Forces on Structures", Trans. ASCE, Vol 126, 1961. (U)

7-18 Osborn, J. and Srinivasa, D., (Private Communication), Air Force Weapons Laboratory, Kirtland AFB, N.M., June 1973. (U)

7-19 Clark, R.O. and McMurtry, W.M., An Analysis of Airblast Loading of Structures, AFWL-TR-68-121, Air Force Weapons Laboratory, Kirtland AFB, N.M., January 1969. (U)

7-20 Glass, I.I., and Hall, J.G., Handbook of Superseismic Aerodynamics, Section 18, NAVORD Report No. 1488, Vol. 6, 1969. (U)

7-21

7-22 Merritt, J.L. and Newmark, N.M., Design of Underground Structures to Resist Nuclear Blast, SRS149, Department of Civil Engineering, University of Illinois, Urbana, Ill., July 1962. (U)

7-23 Heierli, W., Mass Effects in Shelter Design, FMB 66-1, Research Institute for Military Engineering, Switzerland, January 1966. (U)

7-24 Lakhov, G.M. and Polyakova, N.E., Waves in Solid Media and Loads on Structures (1967), Translation FTD-MT-24-1137-71, Foreign Technology Division, Wright-Patterson AFB, Ohio, March 1972. (U)

7-25 Plamondon, M.A., and Doughty, J.S., Investigations Into the Vertical Rigid Body Motions of Surface Flush Structures, Part I - Elementary Theory, Draft Report, Air Force Weapons Laboratory, Kirtland AFB, N.M., May 1973. (U)

7-26 Doughty, J.S., (Private Communication), Air Force Weapons Laboratory, Kirtland AFB, N.M., February 1973. (U)

7-27 Allgood, J.R., Summary of Soil-Structure Interaction, Technical Report R-771, Naval Civil Engineering Laboratory, Port Hueneme, Calif., July 1972. (U)

7-28 Newmark, N.M. and Merritt, J.L., Design of Nearly Invulnerable Structures in Granite (U) (Operation PILEDRIVER), DASA 1399, Defense Atomic Support Agency, Washington, D.C., May 1964. (U)

7-29 Merritt, J.L. and Newmark, N.M., "Part Five - Effects on Underground Structures and Equipment," Nuclear Geoplosics, DASA-1285(V), Defense Atomic Support Agency, Washington, D.C., May 1964. (U)

7-30 Obert, L., Duvall, W.I., and Merrill, R.H., Design of Underground Openings in Competent Rock, Bulletin 587, Bureau of Mines, U.S. Government Printing Office, Washington, D.C., 1960. (U)

7-31 Paul, S.L., Interaction of Plane Elastic Waves with a Cylindrical Cavity, Ph.D. Thesis, University of Illinois, Urbana, Ill., 1963. (U)

7-32 Yoshihara, T., Interaction of Plane Elastic Waves with an Elastic Cylindrical Shell, Ph.D. Thesis, University of Illinois, Urbana, Ill., 1963. (U)

7-33 Newmark, N.M., Design of Structures for Dynamic Loads Including the Effects of Vibration and Ground Shock, Department of Civil Engineering, University of Illinois, Urbana, Ill., July 1973. (U)

7-34 Plamondon, M.A., (Private Communication), Air Force Weapons Laboratory, Kirtland AFB, N.M., March 1974. (U)

7-35 Newmark, N.M., Design Concepts for Composite Integral Tunnel Lining, Contract No. DA-25-066-eng-13,599, U.S. Army Engineer District, Omaha, Nebr., 9 September 1964. (U)

7-36 Linger, D.A., Effect of Backpacking on Structure-Medium Interaction, AFWL-TR-68-40, Air Force Weapons Laboratory, Kirtland AFB, N.M., July 1968. (U)

7-37

7-38

7-39 Higgins, C.J., Post-Test Investigation of HANDEC Silos, AFWL-TR-70-39, Air Force Weapons Laboratory, Kirtland AFB, N.M., 1970. (U)

7-40 Higgins, C.J., Post Test Investigation of ROCKTEST II Silos, AFWL-TR-70-177, Air Force Weapons Laboratory, Kirtland AFB, N.M., 1971. (U)

7-41

7-42

SECTION VIII

BEHAVIOR OF STRUCTURAL ELEMENTS

8.1 INTRODUCTION

A structure under the application of external loads will deform and internal forces will develop in its members. These internal forces resist the deformation of the structure and are defined as the resistance of the structure. For stable structures, the resistance increases as the external loads increase, and the variation of resistance with deformation is defined as the resistance function of the structure.

To satisfy equilibrium, the vector sum of the external and internal forces acting on a free body must equal zero. The resistance of a structure in equilibrium, therefore, must equal the applied loads. The importance of the concept of a structure's resistance to deformation becomes apparent when the structural response (deformation) to dynamically applied loads is discussed in Section IX.

In view of the very large loads associated with nuclear weapon effects, allowance of inelastic, or plastic behavior is generally mandatory to maintain practical structural proportions for any but the almost trivial threat conditions. Accordingly, plastic (and ultimate strength) behavior of the more common structural elements is emphasized in the following paragraphs. Structural deformations are often described in terms of the ductility ratio, which is simply the ratio of maximum deformation to the maximum elastic deformation. The allowable ductility ratio depends on the properties of the material from which the element is fabricated and the function of the element in the structural system. In some cases, large inelastic deformations are permissible. In other cases, elastic behavior is required. The mode of

failure is also important in that brittle catastrophic failures must be avoided, while some inelastic response of a ductile nature is tolerable in most instances. In cases such as these, it is frequently necessary to construct load deformation relationships considering the geometry and proportions of the member as well as the material properties in order to derive a rational ductility ratio. While the concept of ductility ratio is only applicable to those systems where the effective response can be described by one coordinate, it is sometimes applied to more complex structures by simplifying assumptions regarding their mode of response.

The following paragraphs of this section discuss the properties of structural steel and concrete under static and dynamic loading and the effects of nuclear and thermal radiation on these properties. The general behavior of reinforced concrete and steel members under flexural, axial, combined flexural-axial, and shear loads is reviewed and specific structural elements such as one- and two-way slabs, columns, etc. are treated. Where applicable, simplified procedures are presented for obtaining rapid estimates of the behavior of such elements. Although the discussions of the behavior of structural elements are primarily in terms of static behavior, the expressions presented are applicable to dynamic behavior with appropriate adjustment of the material property parameters. Unless specified otherwise, all expressions are presumed to apply to both design and analysis, i.e., for loads greater than the allowable, the member is assumed to fail. In many areas there is insufficient theory or data to provide other guidance. The concepts and relationships are illustrated with examples at the end of the section.

8.2 PROPERTIES OF STRUCTURAL MATERIALS

8.2.1 Steel

a. Uniaxial Properties

Structural metals can be separated into two general groups according to the shape of their stress-strain curves. In one group are those metals which do not exhibit a sharp yield point. This group includes metals such as aluminum and copper with a face-centered-cubic crystalline structure and those steels which have been heat treated or cold worked until they lose their definite yield point. Many of the high strength steels are included in this group. The second group includes those metals which exhibit definite yield points and pronounced yielding zones. This group includes those metals having a body-centered-cubic crystalline structure such as the standard structural carbon and low alloy steels. Typical static stress-strain curves for the two groups of metals under uniaxial loading are shown in Fig. 8-1(a).

The curves for the low carbon steels show upper and lower yield points. The upper yield point is the point from which the initial drop in stress occurs and is of little practical significance in structural analysis. The lower yield point is usually taken as the lowest value of stress after the initial dropoff and before the stress starts to increase again. It is considered to represent the practical yield strength of the steel. Figure 8-1(b) shows simplified versions of stress-strain curves for these types of steels.

For steels which do not exhibit upper and lower yield points, the yield stress is taken to be

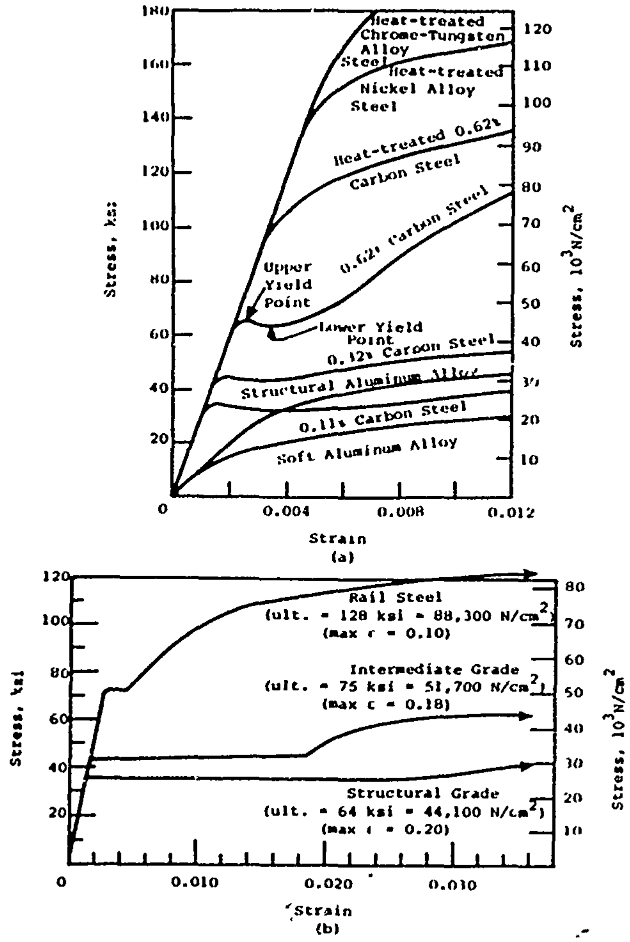

Figure 8-1 Typical Stress-Strain Curves for Various Metals (Ref. 8-1)

that stress where the stress-strain curve becomes horizontal. The high strength steels do not have definite yield points or extended plastic ranges and their yield strength is specified in terms of the stress at some arbitrary strain (normally 0.002 to 0.005).

The low carbon steels are preferred for most structural applications because of their greater ductility under uniaxial loads. Because of this ductility, structural steels are able to undergo large deformations beyond the elastic limit without fracture. This is a desirable feature for all structures, but it is especially advantageous for protective construction applications. Intermediate and structural grade reinforcing steels used in concrete construction have the stress-strain characteristics shown in Fig. 8-1(b).

Most structural steels of interest begin to yield at strains of about 0.002 or less. As shown in Fig. 8-1(b), the more ductile steels can undergo fairly large strains beyond this point before the onset of strain hardening. On the basis of strain alone, ductility ratios of 20 to 30 or higher would appear permissible for the low carbon structural steels. Practically, strains of these magnitudes could severely distort the member and degrade its structural capacity, and ductility ratios on the order of 3 to 5 are normally used for design purposes. The higher ratios are probably appropriate for vulnerability analysis where severe damage is the criterion. While the high strength steels yield at higher strains, their overall ductility may be lower because of limited plasticity beyond yielding. They can, however, be used advantageously in those applications requiring elastic or nearly elastic response.

b. Triaxial Properties

Under many loading conditions, the critical section of a structural element can be subjected to biaxial or triaxial stresses. Depending on the magnitude of the stress components and whether they are compressive or tensile, the element could have a greater or lesser resistance to deformations than that calculated on the basis of uniaxial stresses. If elastic response is specified, the element's capacity can be determined using one of the various theories of failure. Slightly different results are obtained depending on the theory of failure chosen. The maximum shearing stress theory is assumed herein to reasonably predict the strength of ductile materials under the stress conditions normally encountered in most load resisting elements. It is not applicable to the state of stress consisting of nearly equal triaxial tensile stresses where failure occurs by brittle fracture rather than yielding. According to the maximum shearing stress theory, inelastic action begins when

$$(\sigma_{max} - \sigma_{min})/2 = f_y/2 \tag{8-1}$$

where

σ_{max} = maximum value of normal triaxial stress

σ_{min} = minimum value of normal triaxial stress

f_y = yield stress for material as determined in uniaxial tension test

For those applications where inelastic deformations may be acceptable, the response of elements subjected to triaxial states of stress can be investigated by application of the theories of plasticity to the specific conditions of interest. No general guidance can be provided herein.

c. Rapidly Applied Loads

The mechanical properties of some structural materials are affected by the rate at which straining takes place. Those metals having definite yield points and pronounced yielding zones show a marked variation in mechanical properties with changes in loading rate. In general, yield strengths will be higher under rapid strain rates than under slowly applied loads. A large part of the increase in strength with rapid strain rate is attributed to a lesser amount of plastic deformation having time to occur during dynamic loading. Accordingly, a higher stress would be required to produce a failing strain. If this line of reasoning is correct, the modulus of elasticity of the material should not be greatly affected by strain rate, and it should be possible to utilize a static load deformation relationship with a reasonable dynamic yield stress for design and analysis of structures subjected to blast loads. The limited amount of experimental data that are available support this approach. As the strain rate increases, the yield stress increases to some dynamic value while the modulus of elasticity remains constant. Because of the higher yield strength and constant modulus of elasticity, there is also an increase in the yield-point strain. In addition, there is an increase in the strain at which strain hardening begins and some slight increase in ultimate strength.

In an actual structure, the strain rate is determined by the response of the structure to the dynamic loads. A dynamic analysis can provide estimates of maximum strain rates which, in general, will vary with time and location in the structure. Since structural response, strain-rate and yield strength are

interdependent, a trial and error method of analysis is necessary. However, in view of uncertainties in other variables, great precision in evaluation of strain rate effects is not normally justified. Reference 8-2 suggests that strain rate effects can be estimated from the time required to reach yield stress. Figure 8-2 shows the effect of time to yield on the yield strength of A-7 structural and two grades of reinforcing steel. The time to yield can also be obtained from a dynamic analysis, but Ref. 8-2 states that it is generally in the range of 0.2 to 0.5 times the fundamental period of vibration of the element.

A time to yield of about 1 sec is representative of static yield strength. Many classes of structural elements will have time to yield in the range of 0.01 to 0.1 seconds. For these ranges in time, Fig. 8-2 indicates an average increase in yield strength, due to strain rate effects, of about 10 percent. Thus in the absence of structural response data to define strain-rate, it can be assumed that the dynamic yield strength is approximately 10 percent greater than the static lower yield point strength.

Although only two types of steel are included in Fig. 8-2, similar increases are expected for other ductile steels. The higher strength steels, without definite yield points and pronounced yielding ranges, do not exhibit as high an increase. It is suggested that their dynamic yield strength be taken equal to the static values. The strain-rate effect on ultimate strength is usually neglected for all steels. The dynamic shear yield strength is taken equal to 0.6 times the dynamic tension yield strength, and ultimate shear strength is taken equal to 0.75 times the ultimate tensile strength.

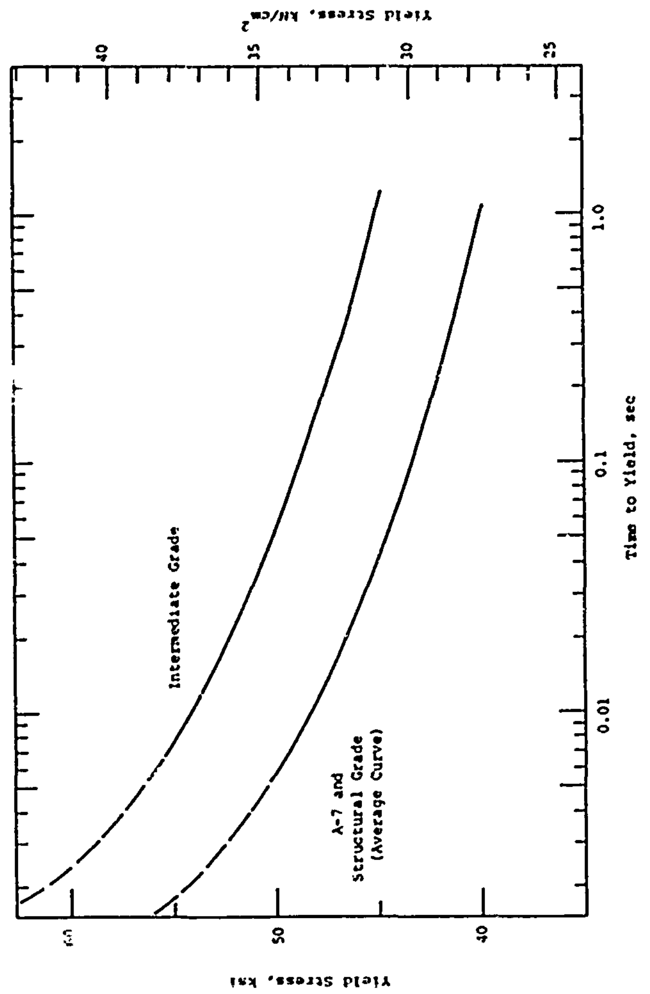

Figure 8-2 Strain Rate Effect on Yield Stress of A-7 and Reinforcing Steel (Ref. 8-2)

Under certain conditions of triaxial loading, steel loses much of its ductility. In the absence of dynamic test data for triaxial states of stress, it is suggested that dynamic properties be assumed equal to those specified for static conditions in triaxial load cases.

Although a protective structure is not required to withstand a large number of nuclear attacks such that fatigue becomes a significant problem, some familiarity with the phenomena can be useful in many aspects of protective construction design and analysis. At low applied stress levels, fatigue will rarely be significant except possibly after a very large number of cycles or in the presence of unusual conditions. In protective construction applications, however, plastic behavior is the rule rather than the exception and the number of load reversals a member can be expected to withstand can be drastically reduced. The overall effect depends upon numerous variables, including number of cycles, temperature, load level, type of material and others.

In the case of steel structures, the number of cycles of load reversal and percent strain expected in protective construction applications should not adversely affect the structures resistance to loads to any significant degree. Depending on the level of straining and number of load reversals, there may be a decrease in stiffness and increased tendency for buckling of flanges. To the contrary, there is some experimental evidence of increased resistance to deformation after the first cycle of loading. Figure 8-3 shows the force-deformation relations for a steel frame subjected to three cycles of loading. A significant stiffening

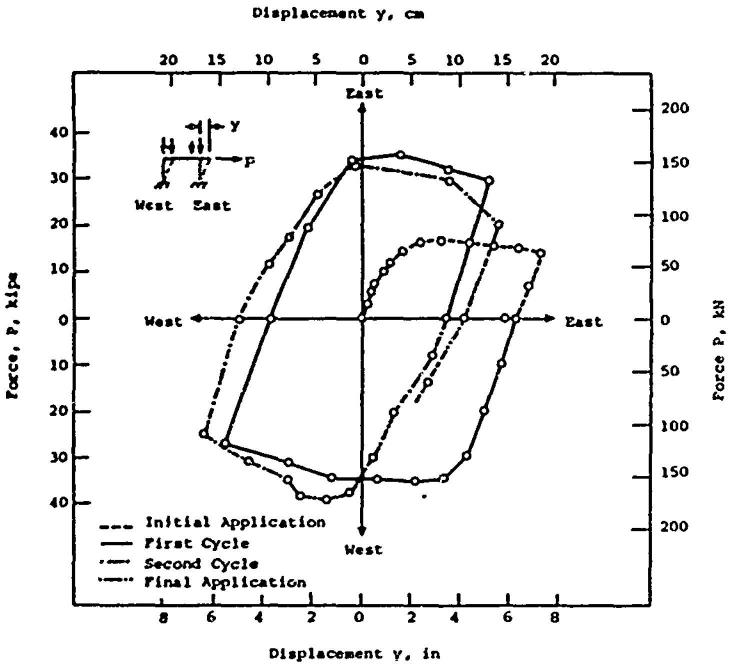

Figure 8-3 Force-Deformation Relations for Steel Frame (Ref. 8-3)

of the system is apparent. The many variables affecting system response preclude general guidance regarding the effect of load reversal. The designer or analyst should be aware, however, that such changes can occur even under very low numbers of load cycles.

d. Radiation Effects

The behavior of structural materials in the intense radiation environments accompanying a nuclear burst is a very complex phenomenon and still requires much additional theoretical and experimental investigation. However, some simplifying assumptions can be made to obtain gross indications of the type and extent of damage to be expected.

The gamma ray, neutron, X ray, and thermal environments produced by a nuclear detonation may cause considerable damage to facilities and structural elements on or above the ground surface at close-in ranges. These radiations can result in changes in properties of the materials and thermomechanical damage to structural elements. Both types of effects are a function of the type of radiation and its energy spectrum. Thermomechanical effects are also influenced by the properties of the material, structural configuration and details of the facility or element, and rate of delivery of the radiation.

Radiation effects on material properties generally result from disruption of the crystalline structure of the material. Because of their greater path lengths in the material, neutrons are the most significant radiation in causing changes in material properties. The most important effect of gamma radiation is the production of electrons which can cause similar changes but to a lesser degree.

Discussions of theoretical and experimental studies of the effects of radiation on structural metals and alloys are included in Refs. 8-4 and 8-5. Most of the experimental data contained in these references were gathered from studies in nuclear reactors or particle accelerators, and some of the data pertaining to total radiation dose were obtained from much longer exposures to the radiation source than would be experienced in nuclear explosions. Although many of the material responses are probably not dose-rate sensitive, the possibility of dose-rate sensitivity should not be overlooked.

One of the most important factors governing radiation effects on metals is the temperature of irradiation. Other important variables are melting point, crystal structure, prior thermal and mechanical history, radiation environment, and neutron flux. In general, metals and alloys become harder, stronger, and less ductile after exposure to neutron radiation. Figures 8-4(a) and (b) show the effects of fast neutron fluence on the yield and ultimate strengths of carbon and low-alloy steels. As shown in these figures, significant increases in yield and ultimate strength can result from exposure to nuclear radiation but only at fairly high neutron fluences. Some of these changes disappear at higher temperatures, so thermal radiation can complicate estimates of the net effect of nuclear radiation.

The composition and initial strength of steels do not necessarily have a great influence on their change in properties after irradiation (Ref. 8-4). The nine steels circled in Fig. 8-4(a) had initial yield strengths varying from 40,000 to 150,000 psi (27,600 to 103,400 N/cm^2), but after irradiation, their increases in yield strengths were approximately the same.

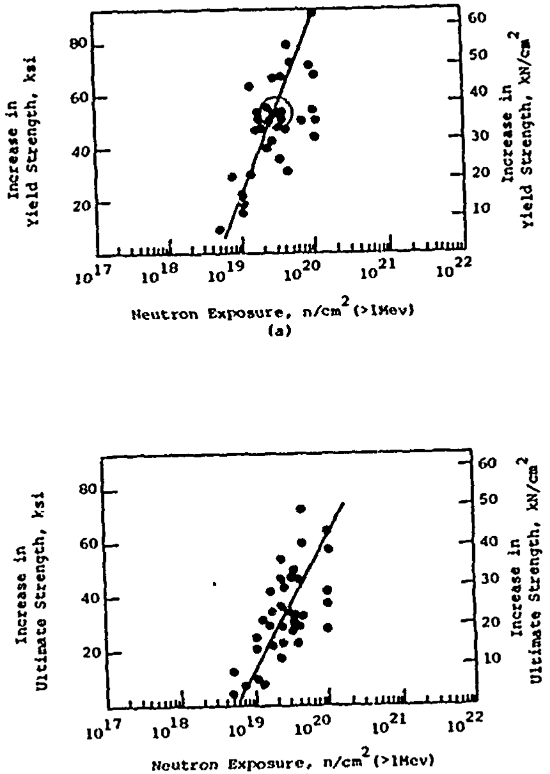

Figure 8-4 Effect of Neutron Radiation on Strength of Carbon and Low-Alloy Steels (Ref. 8-4)

Carbon and low-alloy steels also exhibit a decrease in ductility when subjected to neutron radiation. The decrease in ductility is quite variable and, for the steels reported in *Ref.* 8-4, the percentage of decrease in elongation at failure varied from 6 to 80 percent. The transition temperature for change from brittle to ductile behavior is also affected by irradiation with increases of up to 500°F (278°C) noted. At the transition temperature, there is a marked decrease in the energy absorbing capacity of the material. For some common types of steel, the transition temperature ranges from 0 to -100°F (-18 to -56°C), thus a 500°F (278°C) increase would result in brittle characteristics over most temperature ranges of interest. Figure 8-5 shows the effect of neutron radiation on the energy absorbed at fracture, and it is apparent that large decreases in ductility are possible. Fairly high temperature annealing after radiation can greatly reduce the effects of radiation.

If the structure under consideration is expected to be subjected to a neutron fluence in excess of 10^{18} n/cm^2, it is recommended that a detailed analysis be made of the combined neutron and thermal environment in order to evaluate the effect on properties of steel portions of the structure. Because of the uncertainties regarding the net effect of neutron and thermal radiation, it is recommended that no increase in yield or ultimate strength be assumed for design purposes.

Thermal effects on the properties of structural steels will depend on the amount of radiation energy deposited in the element and the resulting increase in temperature. Reference 8-6 states that the

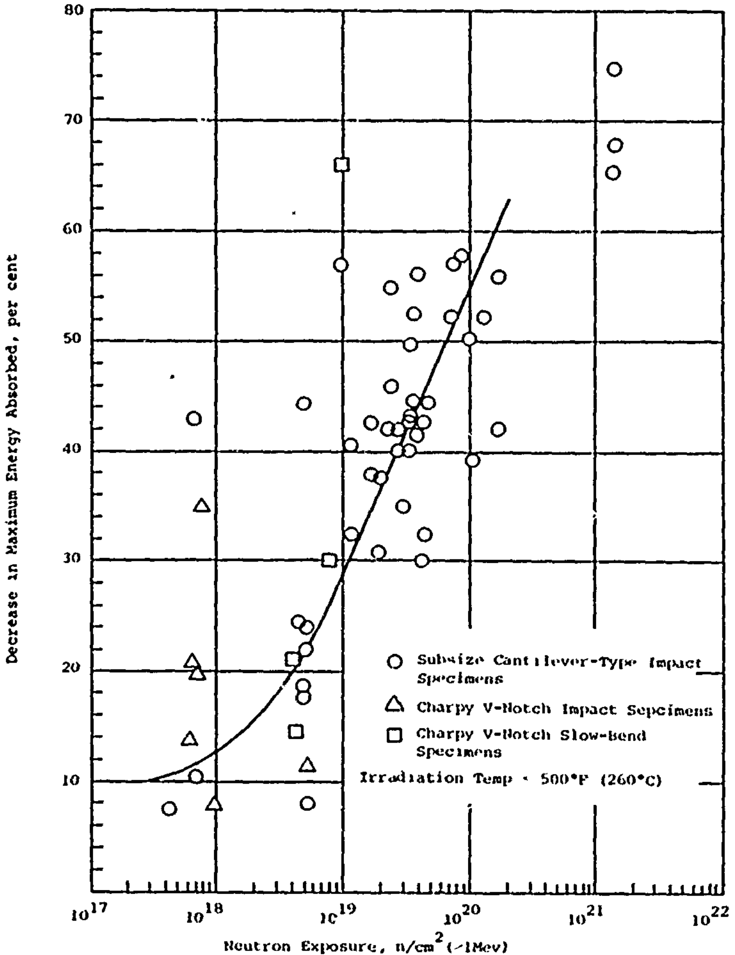

Figure 8-5 Effect of Neutron Radiation on the Notch Toughness of Carbon and Low-Alloy Steels in the Region of Shear Fracture (Ref. 8-4)

carbon steels used in plates and structural shapes exhibit strain aging in the constant temperature range of 300° to 700°F (149° to 371°C), such that at about 500°F (260°C), the tensile strength is about 10 percent higher than it is at room temperature. At constant temperatures above 700°F (371°C), the yield and tensile strengths of all steels decrease with increasing temperature, and at about 1000°F (538°C), the yield strength of the carbon steels is about 70 percent of that at room temperature. The high-strength low-alloy structural steels lose about 40 percent of their strength over the same increase in temperature. The deposition of energy by neutron, gamma and X radiation can also cause significant increases in temperature of exposed steel elements. At higher radiation intensities, the temperature increases may be large enough to melt, spall or vaporize portions of the structure. These problems are treated in Section VII.

8.2.2 Concrete

a. Uniaxial Properties

Since concrete is used mostly in compression, its compressive stress-strain characteristics are of primary importance. Figure 8-6 shows a typical set of stress-strain curves for uniaxial compression cylinder tests at normal, moderate, loading rates on concrete 28 days old. Several important characteristics of concrete can be noted in these curves. First, the stress-strain relationship is obviously nonlinear over most of its range. Second, concrete is a brittle material in comparison with structural steel and reaches its maximum strength at strains near the yield point of some reinforcing steels. Third, the slope of the initial portion of the stress-strain curve increases with

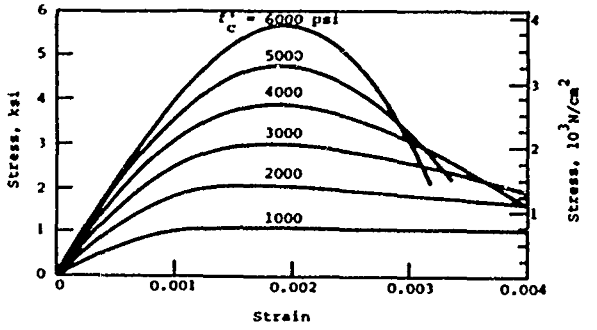

Figure 8-6 Typical Stress-Strain Curves for Concrete (Ref. 8-7)

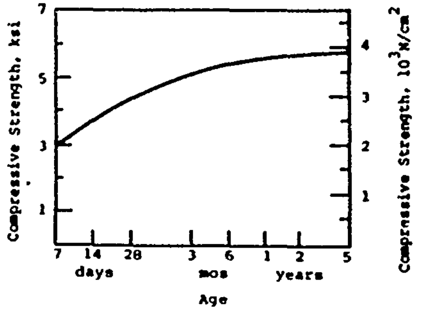

Figure 8-7 Effect of Age on Concrete Compressive Strength f'_c (Ref. 8-7)

increasing compressive strength. A modulus of elasticity corresponding to this initial slope is computed from the empirical relationship.

$$E_c = 33w^{1.5}\sqrt{f'_c}\ \text{psi} \qquad (8\text{-}2)$$

$$= 1.38\times10^{7}w^{1.5}\sqrt{f'_c}\ \text{N/cm}^2$$

where

w = weight of concrete, lb/ft^3 or N/cm^3

f'_c = specified compressive strength of concrete, psi or N/cm^2

Among the many variables affecting the compressive strength of concrete are the types of material constituents, their proportions, method and time of curing and age. Most of these variables are accounted for by specifying a 28-day strength of test cylinders. As shown in Fig. 8-7 the strength of a concrete mix will normally continue to increase beyond its 28-day strength. While it is conservative to neglect this increase for design purposes, the analyst should be aware that the actual strength of a concrete may be 50 percent or more greater than that specified at 28 days.

Although concrete is normally used in compression, its tensile strength may be of significance in some applications. The flexural tension strength (modulus of rupture) of concrete is usually related to its tensile splitting strength. For sand-gravel concretes, Ref. 8-7 states that the tensile splitting strength can be reasonably estimated as 6 to 7 times $\sqrt{f'_c}$, and the modulus of rupture as 1.25 to 1.75 times the tensile splitting strength. The smaller of the above factors applies to higher strength concretes and the larger to lower strength concretes. The allowable shear stress is a function of the total stresses acting on a section and is discussed in later paragraphs.

As shown in Fig. 8-6, the maximum load (stress) capacity of concrete occurs at a strain of about 0.002 and drops off rapidly at higher strains. It is obvious that when strength of the structural element is controlled by crushing of the concrete, only low ductility ratios are allowable unless some provision is made to increase the ductility of the material.

Because of its limited ductility and low tensile strength, concrete structural elements are usually reinforced with steel. This is particularly true in the case of flexural members subjected to bending forces. If the member is underreinforced, yielding of the steel will occur before the concrete crushes. Fairly large strains can occur in the more ductile reinforcing steels before the onset of strain hardening, and the ductility of the concrete member is increased significantly. However, at large strains, cracking of the concrete reduces the compression area, and a concrete compression failure is likely to occur.

As in the case of steel structures, functional requirements must be considered in determining an allowable ductility ratio. Compression and shear failures due to yielding of reinforcing steel are considered ductile behavior. Since some inelastic behavior is usually allowable in all structures, it is suggested that ductility ratios of 1 to 2 be used for reinforced concrete members whose strength is limited by compressive or shear strength of the concrete. Ductility ratios between 3 and 5 are appropriate for all other reinforced concrete members. For target analysis, where severe damage may be the objective, a ductility ratio of 8 is suggested for brittle elements and 20 for ductile underreinforced elements.

b. Triaxial Properties

As in the case of structural steels, concrete may under certain conditions be subjected to biaxial or triaxial states of stress. Its total load (stress) carrying capacity is affected by the relative magnitude of the stress components and whether thay are compressive or tensile.

Reference 8-8 reports on a series of biaxial and triaxial tests of concrete with a nominal unconfined compression strength of 4000 psi (2760 N/cm^2). It concludes that none of the existing theories of failure can be used directly to describe the failure characteristics of concrete under triaxial stresses. Figures 8-8 and 8-9 present some of the experimental results of the study. Although there is some uncertainty in extending the results to the stress conditions in real structures and to other concrete strengths, they can be considered a qualitative measure of the effect of biaxial and triaxial states of stress.

Figure 8-8 shows the relationships between the three principal stresses at failure for the case where all stresses are compressive. The dots represent experimental data points and σ_1, σ_2 and σ_3 are the principal triaxial stresses. The principal stresses are normalized by dividing by σ_r, the unconfined uniaxial compressive strength of the concrete as obtained from cube tests. All tests were conducted on cube specimens.

For the biaxial stress condition ($\sigma_3 = 0$), a confining pressure (σ_2) of $0.3\sigma_1$ increases the compressive strength of the concrete by about 30 percent. A triaxial state of stress can result in more dramatic increases. At a uniform lateral confining pressure of

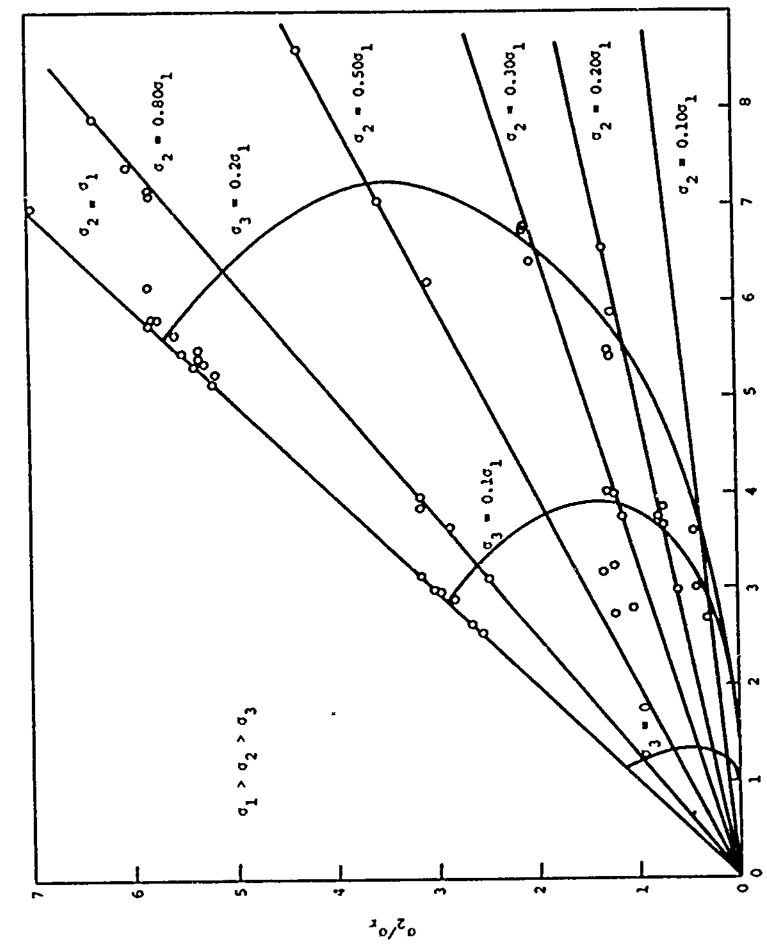

Figure 8-8 Normalized Triaxial Compression Data (Ref. 8-8)

$0.2\sigma_1$, the compressive strength is increased by 450 percent. Reference 8-8 indicates even larger increases for higher confining pressures. The triaxial compressive strength decreases with decreasing minimum principal compressive stress, σ_3, and for any significant magnitude of tensile stress, it drops below the uniaxial compressive strength. The uniaxial tensile strength was found to be about $0.1\sigma_r$ and it was only slightly reduced by equal triaxial tensile stresses.

Figure 8-9 shows the effect of biaxial and triaxial compressive stresses on the stress-strain relationships for concrete cubes. Also plotted in Fig. 8-9 for comparison is an unconfined compressive (uniaxial) stress-strain curve representing averages of data reported in Ref. 8-8. The numbers identified with each curve indicate the ratios of principal stress in the order σ_1, σ_2, and σ_3. Note the much larger stresses and strains associated with the triaxial tests. In the triaxial tests, maximum σ_1 stresses occured at strains in the σ_1 direction ranging from 0.006 to over 0.04. Although the concrete was severely fractured at these strains, it continued to support the applied loads as long as it was confined. The crack pattern depended on the ratios between the principal stresses.

While it is difficult to establish design or analysis criteria from the limited data available, it is obvious that under certain conditions of loading concrete is significantly stronger than indicated by normal unconfined compressive strength tests. Massive concrete structures, or those confined by steel enclosures or reinforcing steel, are sure to derive some increased resistance due to the confining effect of the surrounding material. High airblast or

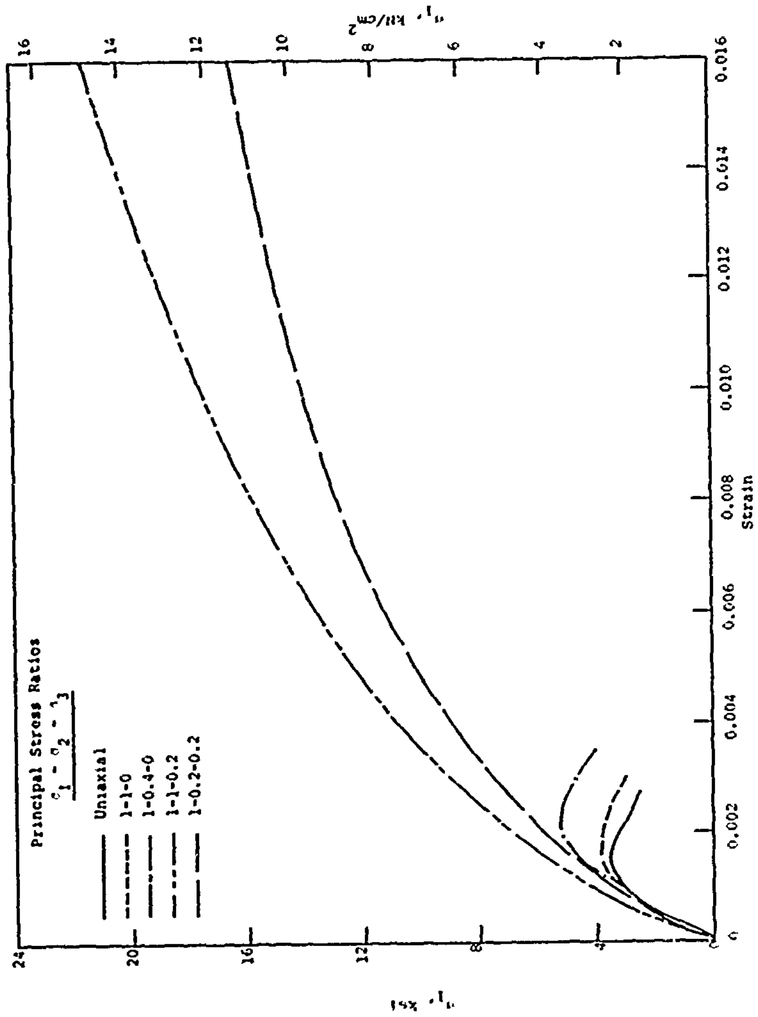

Figure 8-9 Effect of Confining Stresses on Stress-Strain Properties of Concrete (Ref. 8-8)

soil pressures can also provide some degree of confinement. Reference 8-9 suggests that the effect of confining pressures can be estimated from

$$\sigma_a = 0.85f'_c + 4.1\sigma_2 \qquad (8\text{-}3)$$

where

σ_a = axial compressive strength

σ_2 = uniform lateral confining pressure

f'_c = unconfined compressive strength

Equation 8-3 gives lower axial compressive strengths than indicated by data reported in Ref. 8-8 but agrees well with results obtained from cylinders confined laterally by fluid pressures. Equation 8-3 is not directly applicable to the case of nonuniform lateral confining pressures.

If the loading conditions of interest correspond to the concrete strength and stress states treated in Ref. 8-8, the results reported therein can be used to estimate the triaxial compressive strength of the concrete. In the absence of guidance for other conditions, use of Eq. 8-3 is recommended.

Transverse reinforcement, such as normally provided in columns, can result in significant lateral confinement of the concrete under some conditions. Reference 8-9 states that the confining pressure provided by spiral or circular hoops can be estimated from

$$\sigma_2 = \frac{2A''_s f''_s}{a\bar{D}} \qquad (8\text{-}4)$$

where

A''_s = cross-sectional area of transverse reinforcement

f''_s = stress in transverse reinforcement

a = pitch of transverse reinforcement

$\bar{D}$ = diameter of confined concrete

Rectangular hoops are not as efficient in confining the concrete and the lateral confining pressure should not be taken greater than

$$\sigma_2 = \frac{A''_{sh} f''_{sh}}{ah''} \qquad (8\text{-}5)$$

where

A''_{sh} = cross-sectional area of transverse hoop reinforcement

f''_{sh} = stress in transverse hoop reinforcement

h'' = longer dimension of rectangular concrete area enclosed by hoop

a = vertical spacing center to center of hoops

The confining pressures obtained from Eq. 8-4 or 8-5 are used in Eq. 8-3 to obtain the axial compressive strength of the concrete. If the reinforcing steel has a well defined yield point, f_y, the maximum resistance is attained when the stress in the transverse reinforcing is taken equal to f_y. At strains associated with the higher stress capacity of the confined concrete, the concrete shell outside the transverse reinforcing may no longer be capable of resisting loads. Accordingly, the load carrying capacity at these stress levels should be based on the concrete within the transverse reinforcing. Confinement will also increase the allowable stress and ductility of reinforced concrete members subjected to bending or combined bending and axial loads, even though only a portion of the cross-section may be under compressive stresses. In some cases, however, there may be a slight reduction in overall load carrying capacity due to loss of effectiveness of the material outside the transverse reinforcing.

c. Rapidly Applied Loads

Experimental data indicate that the unconfined (uniaxial) compressive strength of concrete also increases with rate of loading. As in the case of steel, the strain rate can be related to the time required to yield the element. The average strain rate is obtained by dividing the yield strain by the time to yield. A dynamic analysis could be used to determine response times, but average values can be used to obtain an estimate of the effect of loading rate upon compressive strength. Using the assumption previously made for steel, that a wide class of structures will have times to yield of 0.01 to 0.1 second strain rates from about 0.02 to 0.20 per second are obtained (for a yield strain of 0.002). For these strain rates, Fig. 8-10 indicates *an average increase in compressive* strength of about 20 percent. Reference 8-2 suggests that increases of 20 to 40 percent are possible for structures and loadings of interest.

For those instances where the actual strain rate is known, the effect on unconfined compressive strength can be obtained from Fig. 8-10. For other cases, an increase of 20% is suggested as representing a median value for most design conditions of interest. *For purposes of target analysis*, a value of 30 percent may be more appropriate. The increase in

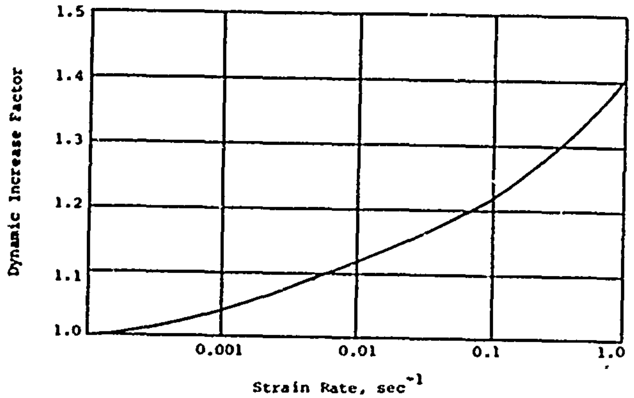

Figure 8-10 Dynamic Increase Factor for 28-Day Concrete (Ref. 8-10)

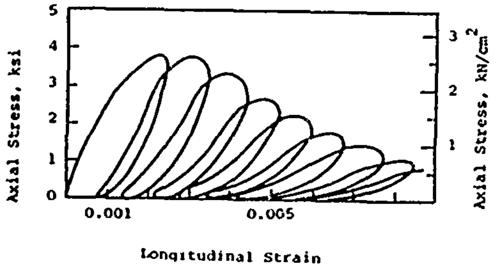

Figure 8-11 Repeated Loading of Plain Concrete in Compression (Ref. 8-3)

ultimate strength due to dynamic loading should be applied to the static unconfined compression strength at the time of loading. As noted previously, the strength of concrete at the time of loading will normally exceed its 28-day strength. If the allowable compressive strength is increased due to confining pressures, it is recommended that no further increase be assumed due to rapidly applied loads.

A small number of load cycles which exceed the elastic limit of the concrete may cause significant changes in its resistance. Figure 8-11 shows the effect of repeated loading of plain concrete in compression. Note that there is some softening of the material within two cycles of loading, and the deformations increase with each cycle. After eight cycles, its resistance is about 25 percent of what it was for the first. Reinforced concrete members may behave similarly, but the overall effects depend on structural details of the member and the magnitude of the load. Figure 8-12 shows the effect of repeated loads on singly-reinforced concrete beams. Note that although deformations increase with the number of cycles for all beams, the underreinforced beams do not show a decrease in resistance. Maximum resistance of the overreinforced ($p = 0.0219$) beam is controlled by concrete strength, and spalling and cracking of the material causes a more rapid degradation of the resistance. Repeated yielding of the longitudinal reinforcing can cause spalling or partial loss of bond and also degrade structural resistance. Although no general guidance is possible as to the magnitude of the effect, the designer should be aware that some degradation of resistance can occur under repeated cycles of loading. It can be conservatively neglected for target analysis.

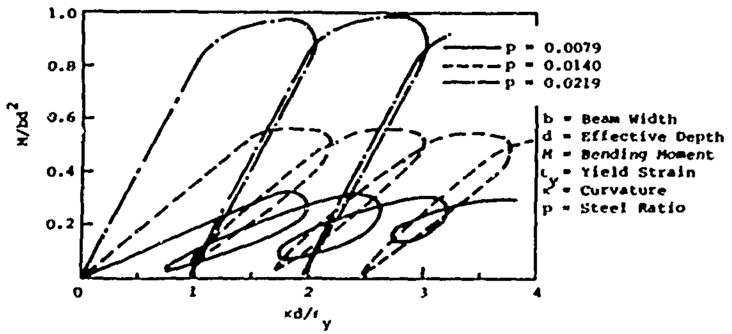

Figure 8-12 Repeated Loading of Singly-Reinforced Beam in Bending (Ref. 8-3)

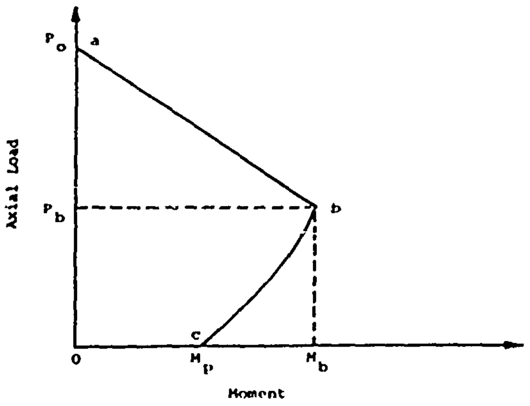

Figure 8-13 Interaction Diagram for Reinforced Concrete Beam-Column

d. Radiation Effects

Reference 8-5 reports that neutron fluences of less than 3×10^{19} n/cm^2 or gamma fluxes of less than 10^6 rads per hour will not change the properties of portland cement concrete. Reference 8-4 reports significant decreases in compressive strength after neutron fluences of 5×10^{19} n/cm^2 but attributes the decrease to temperature effects. If the radiation levels exceed those given above, experiments should be conducted to determine the neutron and gamma effects on concrete properties. An alternative is to provide shielding to reduce radiation levels to the above values.

The deposition of energy due to absorption or capture of thermal, X rays, gamma, or neutron radiation can cause heating, melting, spalling or vaporization of exposed portions of concrete structures. These phenomena are treated in Section VII.

Ordinary concrete will withstand heating to about 600°F (316°C) without losing much of its strength; above 600°F, it rapidly loses strength. Dehydration of concrete is noticeable at 200°F (93°C); however, the process is slow and is retarded by the formation of dehydration products. Above 600°F, dehydration is rapid and exposure to temperatures of 1000°F (538°C) or above, even for short periods of time, will completely dehydrate concrete with a general loss of strength resulting. Concrete with a high aluminum content is heat resistant to much higher temperatures than ordinary concrete. High density concrete does not withstand high temperatures as well as ordinary concrete (Ref. 8-11).

Structural steel softens or melts at energy deposition levels lower than those required to

vaporize concrete, and, in some instances, concrete might be used to provide protection to exposed steel elements. Although concrete's fire-resistant properties have been long recognized in conventional construction, the radiation effects problem is somewhat different. While a concrete cover should provide excellent protection from thermal radiation, its effectiveness for the other forms of radiation will depend on the characteristics of the radiation.

Although Ref. 8-11 does not define short periods of time in regard to temperature effects on material properties, the periods of exposure are probably much longer than that expected from a nuclear detonation. The above criteria can be considered conservative guidance for protective construction design.

8.3 REINFORCED CONCRETE

The load resistance of a ductile structure is normally limited by excessive deformation of one or more of its structural elements. Aside from buckling, a reinforced concrete member may fail in one or more of three possible modes, (1) excessive compressive strain in the concrete, (2) excessive strain in the reinforcing steel, or (3) excessive shear deformation in the member. Of the three modes of failure, only yielding of the reinforcing steel possesses any significant degree of ductility. Since ductile response is of utmost importance in protective construction, most reinforced concrete members are proportioned so that the strength of the member is controlled by the reinforcing steel.

Reinforced concrete members designed to resist the very high pressures resulting from nuclear weapons frequently have span-to-depth ratios much smaller than those commonly used in conventional structures. In some ways, the behavior of these deep members under load deviates from that observed in members of conventional dimensions. There are only limited data available on the strength and behavior of very deep reinforced concrete members, and the procedures presented herein are based on these data as well as on studies of the behavior of members of conventional proportions.

The procedures and equations described in the following paragraphs are generally applicable to cast-in-place and precast reinforced concrete members. Although some of the expressions are also applicable to ultimate strength of prestressed concrete members, there are differences in allowable stresses, reinforcement ratios, etc. These differences are treated in Refs. 8-7 and 8-12. Because of the limited use of prestressed concrete in hardened facilities, this material is not treated specifically in this manual.

8.3.1 Flexural Loads

The moment capacity of reinforced concrete members can be predicted reasonably well by use of conventional ultimate strength expressions. When strains in the reinforcing steel reach the strain hardening region, prediction of the ultimate flexural strength of members is more complex. For example, tests of deep reinforced concrete members indicate that some modifications should be made to the ultimate load equations ordinarily used for conventional beam design to account for strain hardening and higher ultimate concrete strains. The design equations presented herein consider only the yield range of the reinforcing steel prior to strain hardening, and if steel percentages are such as to ensure ductile response of the member, consideration of ultimate concrete strain is not necessary in most instances. Ultimate concrete strain could be a factor in those members containing compression reinforcement. After crushing of the concrete, the compression steel may lose its effectiveness because there is not concrete available for bond transfer or prevention of buckling.

The product of inelastic stress distribution coefficients also appears to be higher for deep members than for members of ordinary proportions. Conservative values are used in the equations presented herein. In most cases of interest, the use of conventional ultimate strength design methods will give reasonable results for design of protective construction.

The flexural mode of response is heavily dependent upon the percentage of tensile steel employed. If insufficient steel is used, the steel may be incapable of resisting the tensile force carried by the concrete before cracking. For such members, the load deflection relationship is characterized by a sudden rapid increase in deflection when the concrete cracks. If, on the other hand, an excessively large percentage of steel is used, the concrete crushes on the compression side before the tensile steel yields. When this happens, the member loses practically all of its load-carrying capacity and a very brittle failure results. To avoid either of these undesirable failure characteristics and to ensure ductile response, Ref. 3-7 recommends that reinforced concrete flexural members with tensile reinforcing only should be proportioned so that

$$p \le \frac{59{,}200}{87{,}000 + f_y}\left[\frac{f'_c}{f_y}\right] \quad \text{(English)}$$

$$\le \frac{40{,}800}{60{,}000 + f_y}\left[\frac{f'_c}{f_y}\right] \quad \text{(SI)} \qquad (8\text{-}6)$$

where

p = tension reinforcing steel ratio = A_s/bd

A_s = cross sectional area of tension steel

b = width of member

d = effective depth of member = distance from extreme compression fiber to center of tensile steel

f'_c = unconfined compressive strength of concrete, psi or N/cm^2

f_y = yield strength of steel, psi or N/cm^2

Equation 8-6 is valid for $f'_c \le 5000$ psi (3450 N/cm^2) and decreases by about 6 percent for each 1000 psi (690 N/cm^2) increase in f'_c. A tension steel ratio less than 0.02 will normally be less than that calculated from Eq. 8-6.

The ductility of a reinforced concrete member in flexure can be estimated from its propert . Reference 8-9 defines ductility in terms of beam curvatures at ultimate and yield loads. It is given by

$$\mu = \frac{\kappa_u}{\kappa_y} = \frac{\epsilon_{cu}}{\epsilon_y}\left[\frac{1 - k}{k_u}\right] \qquad (8\text{-}7)$$

where

κ_u = beam curvature at ultimate moment

κ_y = beam curvature at yield moment

k = $\sqrt{(np)^2 + 2np} - np$

k_u = pf_y/f_{cu} (members with tension reinforcing only)

n = E_s/E_c

E_s = modulus of elasticity of steel

E_c = modulus of elasticity of concrete

f_{cu} = average compressive stress in concrete at ultimate strength

ϵ_{cu} = strain in concrete at ultimate strength

ϵ_y = yield strain for reinforcing steel

In design, ϵ_{cu} is typically taken equal to 0.003 and f_{cu} as $0.7f'_c$ for $f'_c \le 5000$ psi (3450 N/cm^2). For higher concrete strengths

$$f_{cu} = 1500 + 0.4f'_c \text{ psi}$$
$$= 1030 + 0.4f'_c \text{ N/cm}^2 \qquad (8\text{-}8)$$

In any case, μ should not be taken greater than 20 for design, regardless of the value calculated from Eq. 8-7. Design moment capacity of a rectangular member subjected to bending only is given by

$$M_p = pf_y bd^2(1 - 0.59pf_y/f'_c) \qquad (8\text{-}9)$$

The addition of compression steel normally has little effect on the ultimate moment capacity of underreinforced members (those meeting criteria of Eq. 8-6). While compression reinforcement is often provided to increase the ductility or rebound resistance of the member, any increase in flexural resistance therefrom is usually neglected in the design process. When it is considered necessary or desirable to treat compression reinforcement, Ref. 8-13 recommends the following expression for ultimate moment capacity be used.

$$M_p = bd^2 f_y\left|(p - p')\left(1 - \frac{0.59(p - p')f_y}{f'_c}\right) + p'\left(1 - \frac{d'}{d}\right)\right| \qquad (8\text{-}10)$$

where

p' = compression steel ratio = A'_s/bd

A'_s = cross sectional area of compression steel

d' = depth from extreme compression fiber to center of compression steel

Equation 8-10 assumes that both compression and tension reinforcing have reached their yield strength. This criterion is satisfied when (Ref. 8-13)

$$p - p' \geq \frac{62{,}900}{87{,}000 - f_y}\left|\frac{f'_c\, d'}{f_y d}\right| \quad \text{(English)}$$

$$\geq \frac{43{,}300}{60{,}000 - f_y}\left|\frac{f'_c\, d'}{f_y d}\right| \quad \text{(SI)} \qquad (8\text{-}11)$$

Equation 8-11 is valid for $f'_c \leq 5000$ psi (3450 N/cm^2) and decreases by about 6 percent for each 1000 psi (690 N/cm^2) increase in f'_c.

The ultimate ductility ratio for a beam with compression reinforcing can be obtained from Eq. 8-7 by taking (Ref. 8-9)

$$k_u = (p - p')f_y/f_{cu}$$

Compression steel will generally increase the ductility of a beam, but, as in the case of singly reinforced beams, the ductility ratio should not be taken greater than 20.

The preceding expressions are based upon both the tension and compression steel having yielded and $p > p'$. When $p = p'$, the strain in the compression steel can be determined by analysis of the section, i.e.,

$$\epsilon'_s = \frac{\epsilon_{cu}(\bar{x} - d')}{\bar{x}}$$

$$\left(\frac{\bar{x}}{d}\right)^2 + \frac{p}{0.72}\left(\frac{E_s}{f'_c}\right)\left(\epsilon_{cu} - \frac{f_y}{E_s}\right)\left(\frac{\bar{x}}{d}\right) - \frac{p\epsilon_{cu}}{0.72}\left(\frac{E_s}{f'_c}\right)\left(\frac{d'}{d}\right) = 0 \qquad (8\text{-}12)$$

where $\bar{x}$ is the distance from the extreme compression fiber to the neutral axis and ϵ'_s is the strain in the compression steel. The neutral axis is determined by solving the quadratic expression and ϵ'_s then compared with the yield strain. If the compression steel has yielded, Eq. 8-10 is valid. Otherwise, the moment capacity must be calculated from the section and material properties.

When the flange thickness of I or T sections exceeds the depth to the neutral axis of the member, Eq. 8-9 can be used to determine the moment capacity. The member width, b, is taken equal to the overall flange width. If the flange thickness is less than the depth to the neutral axis, Ref. 8-7 gives the moment capacity as

$$M_p = b'd^2f_y\left|p_F\left(1 - \frac{t}{2d}\right) + (p_w - p_F)\left(1 - 0.59(p_w - p_F)\frac{f_y}{f'_c}\right)\right| \qquad (8\text{-}13)$$

where

b = overall flange width

b' = width of web of I or T section

p_F = tensile steel ratio required to balance the compression force in the overhanging portion of the flanges

$$= 0.85\,\frac{f'_c(b - b')t}{f_y b'd}$$

p_w = total tensile steel ratio = $A_s/b'd$

t = flange thickness

The total tensile steel ratio includes that required to balance the compression force in the overhanging flanges, p_F, plus that required to balance the compression force in the rectangular section of the beam, p_b. As for the rectangular beams, it is desirable to limit the total amount of reinforcing to ensure that yielding of the tensile steel occurs before crushing of the concrete. Reference 8-7 recommends that the total tensile steel ratio be limited to

$$p_w \leq 0.75(p_b + p_F) \qquad (8\text{-}14)$$

The steel ratio given by Eq. 8-6 is equal to $0.75p_b$, so Eq. 8-14 can be rewritten as

$$p_w \leq p + 0.75p_F \qquad (8\text{-}15)$$

where p is obtained from Eq. 8-6. Confinement of the concrete in the compression area of flexural members should increase their ductility by allowing greater strains to occur in the concrete before crushing. Because of the possible loss of concrete outside the *reinforcing cage* there may be a small decrease in ultimate moment from that calculated from unconfined sections. However, under some conditions strain hardening in the confined section can partially or completely offset this decrease.

8.3.2 Axial Loads

The following discussion is applicable to short columns subjected to pure axial loads. Combined bending and axial loads and long columns are covered in later sections.

If *slenderness effects* are neglected, the limiting strength of a reinforced concrete member under pure axial load is given by

$$P_o = 0.85f'_c A_c + f_y A_{st} \qquad (8\text{-}16)$$

where

A_c = cross sectional area of the concrete

A_{st} = total cross sectional area of the longitudinal reinforcing steel

The coefficient 0.85 in Eq. 8-16 accounts for observed differences between static tests of compression members and unconfined cylinder compression tests. In view of the rapid loading rates and other uncertainties encountered in protective construction applications, a coefficient of 1.0 can be assumed in many instances without significant decrease in accuracy. Equation 8-16 can also be written in the form

$$P_o = (0.85f'_c + p_t f_y) A_g \qquad (8\text{-}17)$$

where p_t is the total steel ratio based upon the gross cross section area of the member, A_g.

If the member is provided with spiral or hoop reinforcing, the allowable stress determined from Eqs. 8-3 through 8-5 is substituted for 0.85 f'_c in the above equations. At strain levels associated with the higher stress capacity of the confined concrete, the concrete outside the spiral or hoop reinforcing may no longer be capable of *resisting loads*, and *capacity should* be based on the area of the concrete within the spiral or hoop.

The strength of reinforced concrete structural elements under pure axial loads is normally limited by crushing *of the concrete*. Since concrete fails at relatively small compressive strains, compression elements will usually have very low ductilities. The addition of spirals, hoops or other forms of lateral steel reinforcing not only increases the load resistance of the element but can also increase ultimate concrete strains and ductility ratios by a factor of 5 or more.

8.3.3 Combined Flexural and Axial Loads

A member subjected to *combined bending* and axial loads encompasses both beam and column behavior, and the degree to which either behavior predominates depends upon the relative magnitudes of the two *loadings* and the sectional properties of the member. The entire range of limiting combinations of moment and axial load may be summarized in an interaction diagram such *as shown* in Fig. 8-13. In this figure, P_o is the ultimate axial load capacity of the member when carrying no moment (eq. 8-17), and M_p is the ultimate moment capacity when no axial forces are present (Eq. 8-9 or 8-10). M and P, as used in the diagram, are the values of moment and thrust computed for a given loading condition. Any point on the curve abc represents a combination of M and P, which, according to the ultimate strength theory, will just fail the member. Over the range a-b, the member will fail by crushing of the concrete. *Point b represents* the balance point where limiting strain in the concrete occurs simultaneously with yield stress in the tension steel. In the range b-c, failure is initiated by *yielding* of the tension steel. Any load combination which falls within the area bounded by the interaction curve and the coordinate axes is considered a safe load. *Those falling* outside this area are assumed to cause failure of the member. It is evident from Fig. 8-13 that the presence of a small axial load can substantially increase the moment capacity of an underreinforced member.

In constructing a diagram such as shown in Fig. 8-13, values of P_o and M_p can be obtained using Eqs. 8-17 and 8-9 (or 8-10), respectively. For symmetrically reinforced rectangular members, the axial load at the balance point is given by (Ref. 8-7)

$$P_b = f'_c bd \left| \frac{62,900}{87,000 + f_y} \right| \text{lbs}$$
$$= f'_c bd \left| \frac{43,300}{60,000 + f_y} \right| \text{N} \qquad (8\text{-}18)$$

Equation 8-18 is valid for $f'_c \leq 5000$ psi (3450 N/cm^2) and decreases by about 6 percent for each 1000 psi (690 N/cm^2) increase in f'_c. The moment at the balance point is given by (Ref. 8-7)

$$M_b = P_b e_b \qquad (8\text{-}19)$$

where

$e_b = (0.20 + 0.91 p_t f_y / f'_c)t$ (from plastic centroid) (8-20)

t = thickness of member in the direction of bending

p_t = total steel ratio for member, A_{st}/A_g

The variation of P with M can be assumed to be linear over the range a-b without significant error. Over the range b-c, the axial load capacity under combined axial load and bending, P_u, for a rectangular, symmetrically reinforced member is given by (Ref. 8-13)

$$P_u = 0.85 f'_c bd \left| 1 - \frac{e}{d} - p + \sqrt{\left(1 - \frac{e}{d}\right)^2 + 2p \left|(m - 1)\left(1 - \frac{d'}{d}\right) + \frac{e}{d}\right|} \right| \qquad (8\text{-}21)$$

where

e = eccentricity of the axial load with respect to the centroid of the tension reinforcement calculated by conventional methods of frame analysis

$m = f_y / 0.85 f'_c$

The corresponding moment in the range b-c is

$$M = P_u e' \qquad (8\text{-}22)$$

where e' is the eccentricity from the plastic centroid of the section calculated by conventional methods of frame analysis. A linear variation of P with M could be taken as a quick approximation over the range b-c and is conservative for design purposes. Interaction curves for typical reinforced concrete members are presented later (Fig. 8-20).

Reference 8-7 gives the following approximate equations for spiral reinforced circular members. The eccentricity measured from the plastic centroid for the balanced case is given by

$$e_b = (0.24 + 0.46 p_t f_y / f'_c)D \qquad (8\text{-}23)$$

where p_t is the ratio of the total cross section area of longitudinal reinforcing to the gross cross section area of the member and D is the outside diameter of the concrete section. The eccentricity given by Eq. 8-23 is with respect to the plastic centroid of the cross section. When the eccentricity of the load is greater than that given by Eq. 8-23, tensile stresses in the steel govern the strength of the member and the axial load is given by (Ref. 8-13)

$$P_u = 0.85 f'_c D^2 \left[\sqrt{\left(\frac{0.85e'}{D} - 0.38\right)^2 + \frac{p_t m d}{2.5D}} - \left(\frac{0.85e'}{D} - 0.38\right) \right] \qquad (8\text{-}24)$$

where d is the diameter of the circle through centers of longitudinal reinforcing arranged in a circular pattern.

The reader is reminded that the preceding expressions, along with practically all material from Refs. 8-12 and 8-13, are oriented toward <u>design</u>. That is, assumed stress blocks and strains are selected with the objective of providing safe, rational structures. Consequently, use of this material directly will give misleading results in an attempted failure analysis, wherein one must return to basic principles and make assumptions based on failure rather than survival.

The allowable load on a compression member is also a function of its slenderness ratio defined by

$$R_s = \frac{K_s L}{r} \qquad (8\text{-}25)$$

where

L = the unsupported length of the member

K_s = an effective length factor

r = the radius of gyration of the member cross section

The unsupported length of a member is defined as the clear distance between floor slabs, beams, girders or other structural members capable of providing lateral support. Effective length factors are given in Fig. 8-14 for various types of end restraints. Reference 8-12 recommends that the radius of gyration for reinforced concrete compression members with rectangular cross sections be taken equal to 0.30 times the overall dimension in the direction in which the stability is being considered. For circular cross sections, it is taken equal to 0.25 times the diameter. For compression members braced against sidesway, the effect of slenderness may be neglected when (Ref. 8-12)

$$R_s < 34 - 12\, M_1/M_2 \qquad (8\text{-}26)$$

where

M_1 = smaller value of end moment acting on member; sign is positive if member is bent in single curvature.

M_2 = larger value of end moment acting on member; sign is always positive.

For members not braced against sidesway and R_s less than 22, the effects of slenderness can be neglected; for R_s greater than the above values, the applied moment must be modified to account for the reduced strength of the member. The modified moment is given by (Ref. 8-12)

$$M_m = F\, M_2 \qquad (8\text{-}27)$$

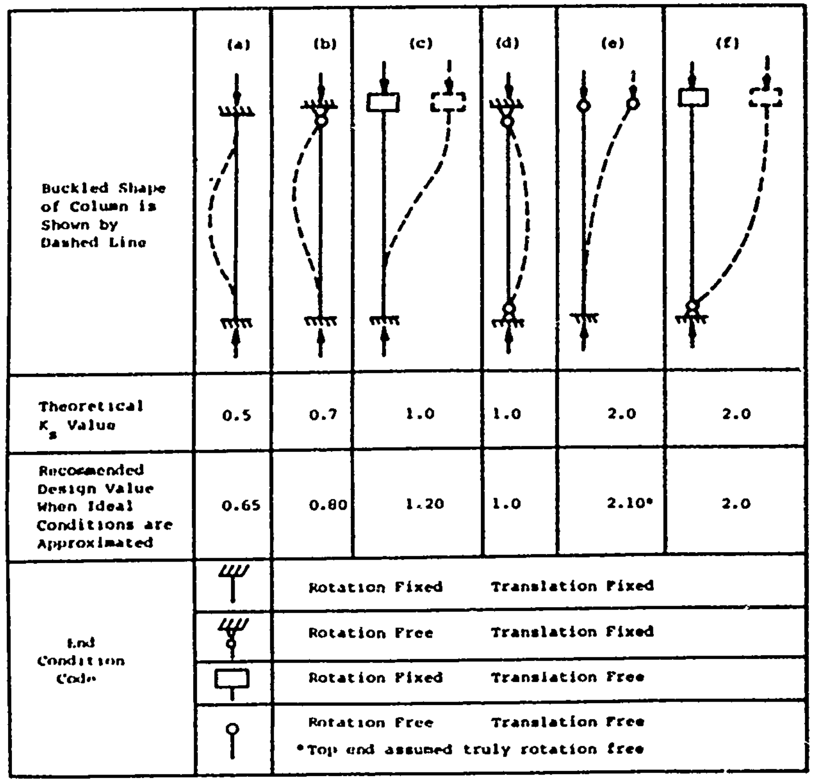

	(a)	(b)	(c)	(d)	(e)	(f)
Buckled Shape of Column is Shown by Dashed Line						
Theoretical K_s Value	0.5	0.7	1.0	1.0	2.0	2.0
Recommended Design Value When Ideal Conditions are Approximated	0.65	0.80	1.20	1.0	2.10*	2.0

End Condition Code

	Rotation Fixed	Translation Fixed
	Rotation Free	Translation Fixed
	Rotation Fixed	Translation Free
	Rotation Free	Translation Free

*Top end assumed truly rotation free

Figure 8-14 Effective Length Factors for Various End Conditions

where

$$F = \frac{C_m}{1 - P_u/P_c} \text{ but not less than } 1.0 \qquad (8\text{-}28)$$

$$P_c = \frac{\pi^2 E_c I_c}{(K_s L)^2} \qquad (8\text{-}29)$$

The modulus of elasticity of the concrete (E_c) is obtained from Eq. 8-2. The moment of inertia of the concrete (I_c) can be taken equal to the average of that for the cracked and uncracked transformed cross sections. For rectangular sections, it is approximated by (Ref. 8-14)

$$I_c = \frac{bd^3}{2}(5.5p + 0.083) \qquad (8\text{-}30)$$

For members braced against sidesway and without lateral loads applied to the member between supports, C_m is given by (Ref. 8-12)

$$C_m = 0.6 + 0.4(M_1/M_2) \text{ but not less than } 0.4 \qquad (8\text{-}31)$$

For all other cases, $C_m = 1.0$.

While the presence of small axial loads can increase the moment capacity of a reinforced concrete member, any axial load decreases its ductility in terms of ultimate curvature. The ductility generally decreases with increasing axial load, and at axial loads corresponding to the balance point for unconfined sections, it may be as low as 1 to 2. Confinement of the concrete by spirals or hoop reinforcement increases the member's ductility, but the same general decrease with axial load is indicated. Since the shell of concrete outside the spiral or hoop reinforcing is considered ineffective in the strain regions at which this lateral reinforcement becomes effective, ultimate moment capacity for a given axial load is reduced in comparison with an unconfined section. The reduction can be significant

at loads near the balance point. Reference 8-9 obtains a generalized relationship between section properties, applied axial load and ductility for rectangular members in which the yield strength of the longitudinal reinforcement is 40,000 psi (27,600 N/cm^2). It assumes that, for a specified axial load, the curvature at a section developed at first yielding of the longitudinal reinforcement can be equated to the curvature developed when the confined concrete reaches a probable limit strain of 0.01. It applies to members with closely spaced hoops and longitudinal reinforcement concentrated principally in two opposite faces. The relationship is summarized in Fig. 8-15. In this figure

P = axial load on the member

$q'' = \frac{A''_{sh} f''_{yh}}{a h'' f'_c}$

a = pitch of transverse reinforcement

A''_{sh} = area of cross section of hoop reinforcement

h'' = longer dimension of rectangular concrete area enclosed by a particular hoop

f''_{yh} = yield strength of hoop reinforcement

All other terms are as previously defined. The ductility ratio in terms of curvature at ultimate and yield loadings is obtained by entering the figure with the appropriate value of q and proceeding horizontally to the p'/p value for the section. From this intersection proceed vertically to the $P/f'_c bd$ value and then horizontally to the appropriate $(1+4.1q'')b''/b$ curve. The κ_u/κ_y value is read as the abscissa of this last intersection. The procedure is demonstrated by the broken line with arrows in Fig. 8-15.

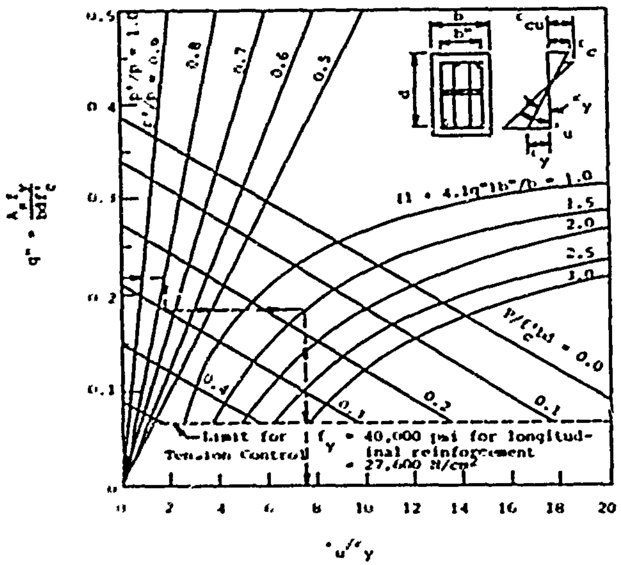

Figure 8-15 Variation of ϵ_u/ϵ_y for Tied Columns of Confined Concrete for Various Combinations of Parameters (Ref. 8-9)

8.3.4 Shear

Shear failures are generally brittle in nature with little advance warning of distress in the member. In order to assure ductile behavior of reinforced concrete members, it is necessary that the ultimate strength of the member in shear be greater than its ultimate flexural strength. There are two modes of shear failure, pure shear and diagonal tension. The pure shear mode of failure is characterized by the rapid propagation of a nearly vertical crack through the depth of the member in the region of the support. A minimal amount of horizontal reinforcement inhibits the formation and propagation of such cracks. A few pure shear failures have been observed in members with low span-to-depth ratios, but only at concrete strengths less than 3000 psi (2070 N/cm^2) and high reinforcing steel ratios ($p > 0.02$). Pure shear failures are improbable in members properly proportioned for protective construction applications.

The diagonal tension failure mode is characterized by diagonal cracks which propagate through the member from a point near the tensile steel toward the compression face. When the crack has penetrated to the point where the remaining compression zone of the concrete is insufficient to sustain the bending stresses, the concrete crushes and the member fails. In order to avoid a diagonal tension failure, the shearing force, V, on a cross section of the member must be less than a limiting value which is a function of the total load system acting on the member and the physical characteristics of the member, i.e., dimensions, concrete strength, reinforcing, etc.

a. Conventional Members

The ultimate shear capacity of reinforced concrete members can be considered to include two components, that contributed by the concrete alone and that contributed by shear reinforcing. The critical section for shear in members of conventional proportions (L/d>5) is assumed to occur at a distance equal to the effective depth of the member, d, from the face of the support. The ultimate shear capacity is defined in terms of the average shear stress on a cross section of the member.

For rectangular members of conventional proportions, Ref. 8-12 gives the ultimate shear capacity contributed by the concrete as

$$V_{uc} = bd[(1.9\sqrt{f'_c} + 2500pdV'/M')] \text{ lb}$$
$$= bd[(1.58\sqrt{f'_c} + 1720pdV'/M')] \text{ N} \qquad (8\text{-}32)$$

where

V' = shear at the critical section in pounds or newtons

M' = moment at the critical section in inch pounds or centimeter newtons

Limits on Eq. 8-32 are as follows:

$\frac{V_{uc}}{bd}$ shall not exceed $3.5\sqrt{f'_c}$ psi $(2.9\sqrt{f'_c}$ N/cm^2,

and

$\frac{V'}{M'}d$ shall not be taken greater than 1.0 in determining V_{uc}

Reference 8-15 reports a comparison between shear capacity predicted by Eq. 8-32 and results of 430 tests of beams without web reinforcing. The ratios of test to calculated strengths varied from 0.65 to 1.91 with an average value of 1.18. Only a very small number of cases fell below 1.0. From these comparisons, it was concluded that Eq. 8-32 represents a reasonable lower bound to the test data and is adequate for design purposes. The maximum allowable shear stress of $3.5\sqrt{f'_c}$ psi $(2.9\sqrt{f'_c}$ N/cm^2) also appears reasonable for design, although it does not represent a lower bound to the data.

If an axial compressive load is applied to the member, the shear capacity of the concrete increases and is still given by Eq. 8-32, except that M" must be substituted for M' and the ratio V'd/M" can have values in excess of 1.0. M" is given by

$$M'' = M' - N(4h-d)/8 \qquad (8\text{-}33)$$

where

N = axial load in pounds or newtons (positive for compression loads, negative for tensile loads)

Equations 8-32 then become

$$V_{uc} = bd\left[1.9\sqrt{f'_c} + \frac{20,000\ pV'd}{8M'-N(4h-d)}\right] \text{ lb}$$
$$= bd\left[1.58\sqrt{f'_c} + \frac{13,760\ pV'd}{8M'-N(4h-d)}\right] \text{ N} \qquad (8\text{-}34)$$

Reference 8-12 states that V_{uc}/bd calculated from Eq. 8-34 cannot exceed

$$3.5\sqrt{f'_c}\ \sqrt{1 + 0.002N/bh} \text{ psi}$$
$$2.9\sqrt{f'_c}\ \sqrt{1 + 0.002N/bh} \text{ N/cm}^2$$

If the member is subjected to a tensile axial load, the reduced shear capacity is given by

$$V_{uc} = 2bd(1 + 0.002N/bh)\sqrt{f'_c} \text{ lb}$$
$$= 1.66bd(1 + 0.002N/bh)\sqrt{f'_c} \text{ N} \qquad (8\text{-}35)$$

where N is negative for tensile loads.

Test data reported in Ref. 8-15 indicate that Eqs. 8-34 and 8-35 represent a reasonable lower bound for design purposes with average ratios of actual to predicted strength of 1.29 for compression and 1.57 for tension loads. The total variations in actual to predicted shear capacities were 0.99 to 1.63 for the compression tests and 1.07 to 2.34 in the tension tests. The ratios for the tension tests represent the ratio of actual to predicted axial load at failure with a constant laterally applied load.

The added shear capacity contributed by shear (web) reinforcing is given by

$$V_{us} = d\,\frac{A_v f_y}{s} \qquad (8\text{-}36)$$

where

s = spacing of vertical web reinforcing

A_v = total cross section area of web reinforcing over distance s

The vertical web reinforcing ratio is defined at the ratio of the area of the vertical web reinforcing to the gross horizontal area, bs. Equation 8-36 assumes the web reinforcing is placed perpendicular to the longitudinal axis of the member. In using Eq. 8-36, Ref. 8-12 suggests that V_{us}/bd should not exceed $8\sqrt{f'_c}$ psi ($6.64\sqrt{f'_c}$ N/cm^2). The total shear capacity is then given by

$$V_u = V_{uc} + V_{us} \qquad (8\text{-}37)$$

Reference 8-15 compared test results to strengths predicted by Eq. 8-37 but applied a limiting value of $8\sqrt{f'_c}$ psi ($6.64\sqrt{f'_c}$ N/cm^2) to Eq. 8-37 rather than Eq. 8-36. Only about 5 percent of the test beams exhibited strengths less than that predicted by Eq. 8-37; therefore, it can be considered a suitable lower bound for design purposes. A

limiting value of the web reinforcing contribution to shear strength is not reported in Ref. 8-15. Only total shear capacity was determined, and there is no apparent comparison between similar beams with and without web reinforcing. The ratios of actual to predicted shear capacity varied from 0.836 to 2.50. The average ratio was 1.445, and less than 10 percent of the beams tested exceeded the predicted strength by more than 100 percent. On the basis of these tests and the guidance provided in Ref. 8-12, it is recommended that the shear stress calculated from Eq. 8-37 not exceed $11.5\sqrt{f'_c}$ psi ($9.55\sqrt{f'_c}$ N/cm^2) for design purposes. This limit corresponds to 1.445 times $8\sqrt{f'_c}$ or the sum of the maximum allowable values of Eqs. 8-32 and 8-36. An additional provision is that the individual limits of Eqs. 8-32 and 8-36 should not be exceeded. Reference 8-12 also places restrictions on the placement and allowable stresses in web reinforcing and should be consulted for detailed design guidance. Only one concrete contribution to total shear capacity is used in Eq. 8-37. It is obtained from Eq. 8-32, 8-34 or 8-35 as appropriate.

The limiting value of shear stress given above is based on tests of beams without axial force. Reference 8-15 presented no data on beams with web reinforcing and subjected to bending, shear and axial loads. In the absence of other guidance it is suggested that the maximum allowable shear stress for members subjected to such loads be taken as the sum of the limits for Eqs. 8-34 or 8-35 and 8-36.

Since most test beams exceeded the ultimate shear capacities predicted by Eqs. 8-32 through 8-37, higher capacities are appropriate for analysis. It should also be noted that the ultimate strength of members designed according to the preceeding shear criteria will normally be limited by flexural strength. On the basis of test results reported in Ref. 8-15, an increase of 50 percent of the shear capacity indicated by Eq. 8-32 or 8-34 represents a reasonable upper bound to the shear capacity of members without web reinforcing. An increase of 100 percent of the capacity indicated by Eq. 8-37 represents a reasonable upper bound to the shear capacity of members with web reinforcing. The test results reported in Ref. 8-15 do not suggest an upper bound to the shear capacity of members subjected to axial tension loads.

b. Deep Members

For deep members ($L/d \le 5$) with loads applied to the top surface of the compression region, the shear capacity contributed by the concrete is greater than that predicted by Eq. 8-32. Reference 8-12 recommends use of

$$\begin{aligned} V_{uc} &= bd(3.5 - 2.5M'/V'd)(1.9\sqrt{f'_c} + 2500pdV'/M') \text{ lb} \\ &= bd(3.5 - 2.5M'/V'd)(1.58\sqrt{f'_c} + 1720pdV'/M') \text{ N} \end{aligned} \qquad (8\text{-}38)$$

with the provisions that

$$1.0 \le (3.5 - 2.5M'/V'd) \le 2.5$$

and

$$V_{uc}/bd \le 6\sqrt{f'_c} \text{ psi } (5\sqrt{f'_c} \text{ N/cm}^2)$$

The critical section for shear in deep members is assumed to occur at a distance of 0.15L from the support for uniformly loaded members, and 0.5 times the distance between a concentrated load and the support for concentrated loads, but not over a distance d for either case. Equation 8-38 represents a conservative lower bound to test results presented in Ref. 8-16 and is suitable for design purposes.

As in the case of conventional members, web reinforcing contributes additional shear capacity. Reference 8-16 recommends an orthogonal system of reinforcing as the most effective in resisting shear failures in deep members. In such a system, longitudinal web reinforcing is distributed uniformly over the depth of the member. The shear capacity contributed by this system is given by

$$V_{us} = f_y d \left| \frac{A_v}{12s}\left(1 + \frac{L}{d}\right) + \frac{A_{vH}}{12s_H}\left(11 - \frac{L}{d}\right) \right| \qquad (8\text{-}39)$$

where

A_{vH} = total cross section area of longitudinal web reinforcing over distance s_H

s_H = vertical spacing of longitudinal web reinforcing

The total shear capacity of the deep member is then given by Eq. 8-37 as for conventional members. Limits on Eq. 8-37 for deep members are given in Ref. 8-12 as

$$\begin{aligned} V_u/bd &\le 8\sqrt{f'_c} \text{ psi} \\ &\le 6.64\sqrt{f'_c} \text{ N/cm}^2 \end{aligned} \qquad \text{for } L/D < 2$$

and

$$\begin{aligned} V_u/bd &\le 0.67(10 + L/d)\sqrt{f'_c} \text{ psi} \\ &\le 0.55(10 + L/d)\sqrt{f'_c} \text{ N/cm}^2 \end{aligned} \qquad \text{for } 2 < L/d \le 5$$

Since there are no experimental data upon which an evaluation of Eq. 8-39 can be based, it is necessary to base its evaluation on total shear capacity. Reference 8-16 compares test results with shear capacity predicted by equations similar to Eq. 8-38, 8-39 and 8-37. Reference

8-16 suggests a coefficient of 1.33 (for uniform loads) for the M'/V'd term in Eq. 8-38 and limits total shear stress to $8\sqrt{f'_c}$ psi ($6.64\sqrt{f'_c}$ N/cm^2) for all members with L/d $\leq$ 5. (Reference,8-12 would permit a maximum total shear stress of $10\sqrt{f'_c}$ psi ($8.3\sqrt{f'_c}$ N/cm^2) for beams with an L/d of 5.) None of the test beams which failed in shear exhibited a shear capacity less than predicted. Even if adjustments are made to account for the difference in limits between Ref. 8-12 and 8-16, Eqs. 8-38, 8-39 and 8-37 appear to give a reasonable lower bound to observed results. Reference 8-12 contains additional guidance on minimum amounts and placement of web reinforcing for deep members.

As in the case of conventional members, observed shear capacities exceeded predicted capacities in most instances, and higher values appear appropriate for target analysis. On the basis of the limited data reported in Ref. 8-16, an increase of 50 percent over the shear capacity predicted by Eq. 8-38 is suggested as an upper bound for members without web reinforcing. An increase of 100 percent over that predicted by Eqs. 8-37, 8-38 and 8-39 is suggested as a reasonable upper bound for members with web reinforcing.

Although the effect of axial loads on the shear capacity of deep members has not been studied as extensively as for those of conventional proportions, it is assumed that similar effects would be observed. For deep members subjected to axial loads, it is recommended that the value of M' in Eq. 8-38 be replaced by M" calculated from Eq. 8-33. The limits imposed on concrete shear capacity still apply.

8.3.5 Bond

All modes of failure previously discussed are closely coupled to and are, in fact, inseparable from a bond mode of failure. *This mode of failure* is generally prevented if the reinforcement is well anchored by bond development length, hooks, or mechanical anchorage. If a bond failure is not prevented, the bars will not serve their function in other modes of behavior considered. The tension or compression forces in the reinforcement at each section must be developed on each side of that section by an adequate embedment length or end anchorage or a combination of the two. If no mechanical end anchorage is provided, the tension or compression forces in the reinforcing must be resisted by shear-type bond stresses distributed over the contact area between the bars and the concrete. If bars without deformations are used, the resistance consists only of adhesion and mechanical friction between the bar and the concrete. With adequate mechanical end anchorage, the full strength of the bars may be developed, even though the shearing stresses over the contact area between the bars and the concrete cause bond failure. With deformed bars, the projecting ribs bear against the surrounding concrete and provide greatly increased bond strength. When a bond failure occurs with deformed bars, it genbrally results in splitting of the concrete along the bars due to a wedging action of the bar deformation. Reference 8-7 states that the ultimate resisting bond force, in force per unit length of bar, is largely independent of bar size or perimeter. Since the force in the bar causing bond failure increases with its area, bond is a more serious problem with the larger bars. The critical sections for development of reinforcement in flexural members are generally at points of maximum moment gradient. Table 8-1 from Ref. 8-12 provides guidance as to the required development lengths, L_d, of deformed bars in tension.

Table 8-1

DEFORMED BAR BOND DEVELOPMENT LENGTH (Ref. 8-12)

BAR SIZE	English (in)	SI (cm)
#11 or Smaller	$0.04Af_y/\sqrt{f'_c}$, but not less than $0.0004Df_y$	$0.019Af_y/\sqrt{f'_c}$, but not less than $0.00058Df_y$
#14	$0.085f_y/\sqrt{f'_c}$	$0.260f_y/\sqrt{f'_c}$
#18	$0.11f_y/\sqrt{f'_c}$	$0.337f_y/\sqrt{f'_c}$

A = cross section area of individual bar

D diameter of bar

If the reinforcement is placed horizontally in the top of a member with more than 12 inches (30 cm) of concrete below it, the values obtained from Table 8-1 are multiplied by 1.4. For reinforcement whose f_y is greater than 60,000 psi (41,370 N/cm^2), the values obtained from Table 8-1 are multiplied by the factor $2-60{,}000/f_y$ (or $2-41{,}370/f_y$). The development length for bars in compression is given by

$$L_D = 0.02f_yD/\sqrt{f'_c} \text{ in} \qquad (8\text{-}40)$$

$$= 0.024f_yD/\sqrt{f'_c} \text{ cm}$$

but not less than $0.0003f_yD$ or 8 inches ($0.00044f_yD$ or 20.3 cm). Additional guidance on development of bond strength is contained in Ref. 8-12.

8.4 STRUCTURAL STEEL

The design or analysis of structural steel members is generally based upon inelastic behavior of the member. For steel, the design procedure is referred to as plastic design. Plastic design not only makes use of the plastic theory of bending (plastic moment condition) but also the redistribution of moment due to the formation of plastic hinges (the mechanism condition).

In designing or analyzing the ability of steel members to resist blast effects, many of the concepts and equations developed for the plastic analysis of steel structures under static loads are used. Therefore, an understanding of the conditions and equations governing static behavior is essential. A number of references (such as Refs. 8-17 and 8-18) contain discussions of plastic analysis and design of steel structures for static loads and should be referred to for detailed guidance. Only general procedures can be treated herein. The expressions presented are suggested for both design and analysis.

8.4.1 Flexural Loads

If a steel member is subjected to pure bending, its ultimate moment capacity is given by

$$M_p = f_yZ \qquad (8\text{-}41)$$

where Z is the plastic section modulus of the member. The plastic section modulus is equal to the static moment of the cross section area of the member about the centroidal axis.

Reference 8-18 includes plastic section modulus tables for common structural steel sections, and Fig. 8-16 gives general expressions for the plastic section modulus of several common structural shapes. Equation 8-41 assumes that the member is properly supported and proportioned so as to allow development of a plastic hinge at the critical section. If the member

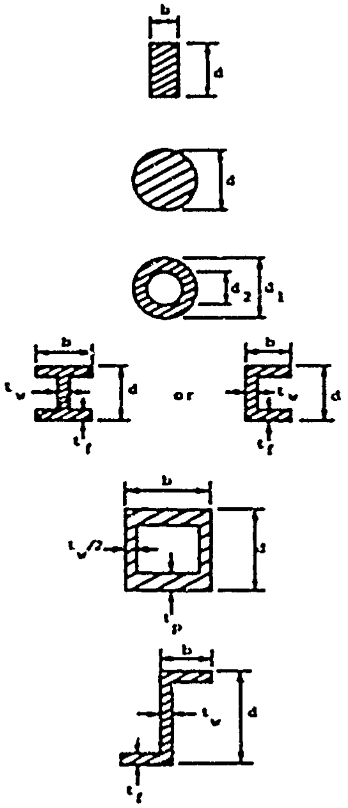

$Z = bd^2/4$

$Z = d^3/6$

$Z = \frac{1}{6}(d_1^3 - d_2^3)$

$Z = dt_w\left(\frac{d}{4} - t_f\right) + bt_f\left(d - t_f\right) + t_w t_f^2$

Z = same as wide flange or channel

Z = same as wide flange or channel

Figure 8-16 Plastic Section Moduli for Common Structural Shapes

is not properly supported or proportioned, buckling may occur before the fully plastic moment can be developed. To ensure the ability of a steel member to sustain fully plastic hinge formation, it is necessary that the member be properly braced to prevent lateral buckling and that the elements of the member meet minimum thickness requirements. All elements of members that may be subjected to compression should have width-to-thickness ratios that meet the requirements of Table 8-2 from Ref. 8-18. Table 8-2 gives maximum width-thickness ratios for flanges of rolled, wide-flange shapes and similar built-up, single-web shapes that are subjected to compression involving hinge rotation under ultimate loading.

Table 8-2

MAXIMUM THICKNESS RATIOS FOR STEEL MEMBERS (Ref. 8-18)

f_y, ksi	f_y, kN/cm^2	$b/2t_f$	d_w/t_w
36	24.8	8.5	43
42	29.0	8.0	40
45	31.0	7.4	38
50	34.5	7.0	36
55	37.9	6.6	35
60	41.4	6.3	33
65	44.8	6.0	32

b = width of flange; t_f = thickness of flange (if thickness of flange varies, use average thickness); d_w = depth of web; t_w = thickness of web.

8.4.2 Axial Loads

Reference 8-18 specifies that the slenderness ratio, $R_s = K_s L/r$, in the plane of bending of compression members which would develop a plastic hinge at ultimate loading should not exceed the value C_c given by

$$C_c = \sqrt{\frac{2\pi^2 E}{f_y}} \tag{8-42}$$

where all terms are as previously defined. Compression members in structures which must resist blast loadings usually will have slenderness ratios smaller than C_c. For those members meeting the criteria of Eq. 8-42, the maximum strength of an axially loaded member is given by

$$P_u = A f_a \tag{8-43}$$

where

A = gross cross section area of the member

f_a = axial stress permitted in absence of bending moment

The allowable stress, f_a, is based on the slenderness ratio in the directions of its strong and weak axes. Reference 8-17 suggests the use of the following for wide flange columns.

$$f_{ax} = f_y - \frac{f_p(f_y - f_p)R_s^2}{\pi^2 E} \tag{8-44}$$

$$f_{ay} = f_y - \frac{(f_y - f_p)R_s}{\pi}\left|\frac{f_p}{E}\right|^{1/2}$$

where

f_{ax} = allowable stress when member is restrained from bending in weak direction

f_{ay} = allowable stress when member is not restrained in the weak direction

$f_p = f_y - f_r$

f_r = residual stresses due to cooling of section

According to Ref. 8-17, wide flange shapes used as columns can be expected to have residual compressive stresses as high as 13,000 psi (8960 N/cm^2). In computing the allowable stress for dynamic loads, it is suggested that residual stresses not be increased in proportion to the dynamic increase in yield strength. Since most compression members are braced in the weak direction to avoid reductions in load capacity, the first of Eqs. 8-44 will normally determine f_a. It is the basis of expressions for axial load capacity in Ref. 8-18.

8.4.3 Combined Flexural and Axial Loads

Reference 8-18 specifies that members subjected to combined axial load and bending moment should be proportioned so as to satisfy Eqs. 8-45 and 8-46.

$$\frac{P}{P_u} + \frac{C_m M}{1 - \frac{P}{E_s A}\left|\frac{R_s}{\pi}\right|^2 M_n} \le 1.0 \tag{8-45}$$

$$\frac{P}{P_y} + \frac{M}{1.18 M_p} \le 1.0 \text{ for } M \le M_p \tag{8-46}$$

where

M = maximum applied moment

P = applied axial load

M_n = maximum moment resistance of the member in absence of axial load; can be taken equal to M_p for members braced in weak direction

$P_y = f_y A$

The slenderness ratio R_s is calculated for the direction of bending. The coefficient C_m is as previously defined in Eq. 8-31. If the member is not braced in the weak direction, M_n is given by (Ref. 8-18)

$$M_n = (1.07 - L\sqrt{f_y}/3160r_y)M_p \text{ in-lbs}$$
$$= (1.07 - L\sqrt{f_y}/2624r_y)M_p \text{ cm-N} \quad (8\text{-}47)$$

where r_y is the lesser radius of gyration and f_y is in ksi or kN/cm^2. Figure 8-17 is an interaction diagram for steel members. Note that any significant amount of axial load reduces the moment capacity of the section. The cross hatched area shows the extent of variation for rolled shapes likely to be used in the plastic design of continuous beams and rigid frames. Reference 8-19 states that differences in the values of M/M_p for any value of P/P_y reflect differences in the proportion of the total cross sectional area located in the web of the member. The thicker the web, other dimensions remaining the same, the less the reduction in plastic bending resistance caused by a given axial load. For members prevented from buckling, the moment capacity is satisfactorily given by (Ref. 8-17)

$$M = M_p \qquad 0 \le P/P_y \le 0.15$$
$$M = 1.18(1 - P/P_y)M_p \qquad 0.15 \le P/P_y \le 1.0 \quad (8\text{-}48)$$

and the required plastic section modulus is approximately given by (Ref. 8-17)

$$Z = Z_t(0.85 + P/P_y) \quad (8\text{-}49)$$

where the load ratio P/P_y and Z_t are based on the initial trial section neglecting the axial load. Equation 8-48 is shown in Fig. 8-17 as dotted straight lines.

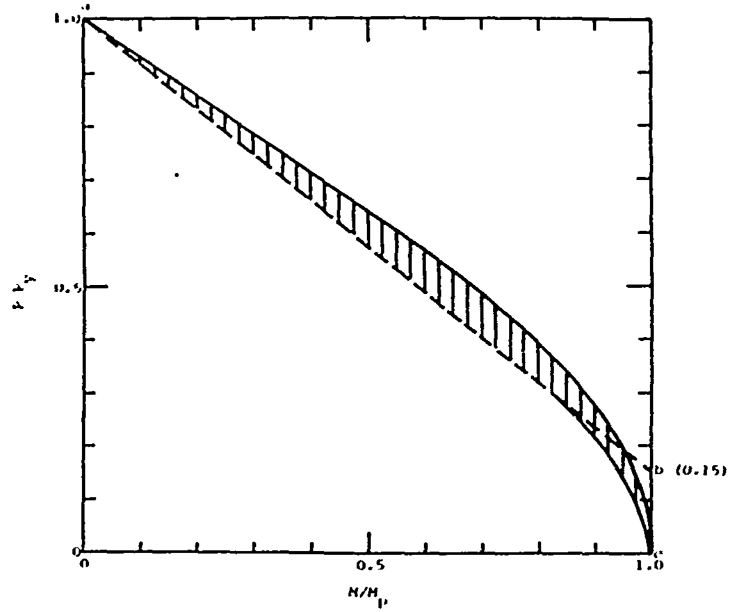

Figure 8-17 Interaction Diagram for Steel Members Subjected to Combined Flexural and Axial Loads (Ref. 8-19)

K_s values given in Fig. 8-14 are also applicable to steel members. Maximum allowable depth-to-thickness ratios are shown in Table 8-2 for members subjected to plastic bending for cases where the axial load applied to the member exceeds $0.27f_yA$ (A is the cross section area of the member). For axial loads less than $0.27f_yA$,

$$\begin{aligned} \max \frac{d_w}{t_w} &= \frac{412}{\sqrt{f_y}} \left|1 - 1.4\left(\frac{P}{P_y}\right)\right| && \text{(English)} \\ &= \frac{342}{\sqrt{f_y}} \left|1 - 1.4\left(\frac{P}{P_y}\right)\right| && \text{(SI)} \end{aligned} \qquad (8\text{-}50)$$

where f_y is given in ksi or kN/cm^2.

8.4.4 Shear

Shear is of interest in steel members primarily because of its possible influence on the plastic moment capacity of the member. At rigid or continuous supports, where combined bending and shear exist, the assumption of an ideal elastic-plastic stress-strain relationship indicates that during the progressive formation of a plastic hinge there is a shrinkage of the web area available for shear. This reduced area might then result in the initiation of shear yielding and thereby reduce the moment capacity. However, since WF sections carry moment predominantly through the flanges and shear through the web, and since combinations of high shear and high moment generally occur at points where the moment gradient is steep, it has been found experimentally that the member will achieve its full plastic moment capacity if the average shear stress over the full web area is less than the yield stress in shear (Ref. 8-20).

From Ref. 8-18, the shear capacity of I-shaped steel sections with unstiffened webs is given by

$$V_u = 0.55\, f_y t_w h \qquad (8\text{-}51)$$

where

V_u = ultimate shear capacity

t_w = web thickness

h = total depth of member

When the web of a built-up section is designed to carry a significant part of the total moment requirement of the section, the shear influence cannot be neglected and the member should be investigated for possible moment capacity loss through shear yield. Reference 8-21 recommends that the moment capacity of such a section be defined by

$$M = bt_f(d_w + t_f)f_y + 0.25t_w d_w^2\sqrt{f_y^2 - 3v^2} \qquad (8\text{-}52)$$

where

b = flange width

t_f = flange thickness

d_w = depth of web = $h - 2t_f$

v = average web shear stress

Reference 8-17 states that in most instances the theoretical reduction in moment capacity of I-shaped structural sections is partially or completely offset by strain hardening effects. It also suggests the use of Eq. 8-51 for design.

8.5 ONE-WAY SLABS AND BEAMS

8.5.1 Reinforced Concrete

The moment capacity of a reinforced concrete beam or one-way slab can be obtained from Eqs. 8-9, 8-10 or 8-13. Over the range of recommended steel percentages and obtainable concrete strengths, Eq. 8-9 can be approximated with little error by

$$M_p = 0.9pf_y bd^2 \qquad (8\text{-}53)$$

Thus the flexural resistance of a simply supported rectangular beam of width b and length L in terms of uniformly distributed load, p_f, is

$$p_f = 7.2pf_y\left(\frac{b}{a}\right)\left(\frac{d}{L}\right)^2 \qquad (8\text{-}54)$$

where a is the width of the area over which the load, p_f, is applied. For a one-way slab, a is equal to b.

The moment capacities of rectangular beams and one-way slabs with compression reinforcement and T-beams are given by Eqs. 8-10 and 8-13.

If compression reinforcing is neglected, the uniform load corresponding to the ultimate flexural capacity of continuous members with equal end moment capacities is given by

$$p_f = \frac{8}{L^2a}\left(M_p^c + M_p^e\right) = 7.2\left(p_c + p_e\right)f_y\left(\frac{b}{a}\right)\left(\frac{d}{L}\right)^2 \qquad (8\text{-}55)$$

where

p_c and p_e = tensile steel ratios at the center and ends

M_p^c and M_p^e = fully plastic moment capacities at the center and ends

(Equation 8-55 is applicable only to underreinforced members.)

Equations applicable to other support and load conditions can be derived by equating the appropriate expression for moment capacity to the expression for maximum moment in the member. Figure 8-18 presents expressions for several of the more common load and support conditions.

The expressions for flexural capacity of indeterminate members assume the formation of plastic hinges at the supports and midspan. For other load and support conditions, a structural analysis should be performed to obtain the significant moments and these moments equated to the flexural capacities given by the appropriate equation in paragraph 8.3.1.

Member	Flexural Capacity	Shear Capacity
	$p_fa = 7.2p_cf_yb\left(\frac{d}{L}\right)^2$	$p_sa = \frac{2V_u}{L}$
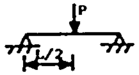	$p_f = 3.6p_c\frac{bd^2}{L}f_y$	$p_s = 2V_u$
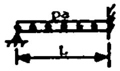	$p_fa = 7.2\left(p_c + \frac{p_e}{2}\right)f_yb\left(\frac{d}{L}\right)^2$	$p_sa = \frac{2V_u}{L} - \frac{2M_p^e}{L^2}$
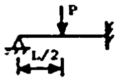	$p_f = 3.6\left(p_c + \frac{p_e}{2}\right)\frac{bd^2}{L}f_y$	$p_s = 2V_u - \frac{2M_p^e}{L}$
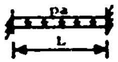	$p_fa = 7.2(p_c + p_e)f_yb\left(\frac{d}{L}\right)^2$	$p_sa = \frac{2V_u}{L}$
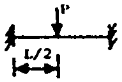	$p_f = 3.6(p_c + p_e)\frac{bd^2}{L}f_y$	$p_s = 2V_u$

p_e = tensile steel ratio at the end
p_c = tensile steel ratio at mid-span
b = beam width
a = width of contributory load area
d = depth to center of steel
M_p^e = plastic moment capacity at fixed end of beam
V_u = ultimate shear capacity of section (Eq. 8-37)
f_y = steel yield stress
p_f = uniform load resistance of member based on flexural capacity
p_s = uniform load resistance of member based on shear capacity
P_f = concentrated load resistance of member based on flexural capacity
P_s = concentrated load resistance of member based on shear capacity

Figure 8-18 Static Flexural and Shear Capacity of Rectangular Reinforced Concrete Beams and One-Way Slabs

Figure 8-18 also includes approximate expressions for the shear capacity of a beam or one-way slab. These expressions are approximate since they are based upon shear at the support rather than at the critical points referred to in paragraph 8.3.4. The ultimate shear resistance, V_u, is determined from Eqs. 8-32 and 8-36 for conventional beams and Eqs. 8-38 and 8-39 for deep members.

If the beam or slab is subjected to an axial load, Eqs. 8-34 or 8-35 can be used to obtain the section shear capacity. The effect of axial load on moment capacity of the beam or slab can be determined in accordance with the procedures of paragraphs 8.3.3 and 8.6.1.

In order to assure ductile response of the member, the tension reinforcing steel ratio should be limited to the range of 0.0025 to 0.02 wherever possible. The ratio should be at least 0.0025 for any flexural member. When compression reinforcing is provided, the difference between the compression and tension steel ratios should not exceed 0.015.

Some vertical web reinforcing should also be provided for all flexural members. A minimum reinforcement ratio of 0.0015 is suggested for all L/d ratios. A minimum horizontal shear reinforcement ratio of 0.0025 should be distributed throughout the depth of beams with L/d ratios less than or equal to 5. In those cases where analysis indicates a requirement for vertical shear reinforcing, a minimum reinforcing ratio of 0.005 should be used.

8.5.2 Steel

Figure 8-19 gives expressions for the flexural capacity of steel beams for several support and load conditions. With the exception of the propped cantilever subjected to a uniform load, the expressions for indeterminate members assume the formation of plastic hinges at the fixed ends and center of the spans. In the case of the propped cantilever subjected to a uniform load, the plastic hinges form at the fixed end and a point 0.414L from the propped end. Also shown in Fig. 8-19 are beam capacities based upon the shear capacity given by Eq. 8-51. Since superposition does not hold in plastic analysis, the expressions of Fig. 8-19 cannot be combined to obtain results for other loading conditions. For other loading and support conditions, the critical moments and shears can be obtained from the applied loads through a structural analysis. These quantities can then be compared to the moment and shear capacities of the member as given by Eqs. 8-41 and 8-51. The plastic section modulus is obtained from the appropriate expression in Fig. 8-16.

8.6 COMPRESSION MEMBERS

8.6.1 Reinforced Concrete

The strength of a column, ring section or any other type of compression member subjected to pure axial load can be obtained from Eqs. 8-16 or 8-17; however, it is questionable practice to design any compression member for zero moment. Construction inaccuracies and/or slight load eccentricities will likely cause unintentional moments. It is recommended, therefore, that all members subject to axial load be designed in accordance with Section 10.3.6, ACI Code 318-71 (Ref. 8-12). This section requires that a minimum load eccentricity of at least 1 in (2.54 cm) or 0.05D be assumed for spiral columns and 0.10t for tied columns in these cases where no moment exists.

Member	Flexural Capacity	Shear Capacity
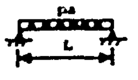	$p_f a = 8.0 \frac{f_y Z}{L^2}$	$p_s a = \frac{2V_u}{L}$
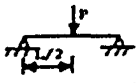	$P_f = 4.0 \frac{f_y Z}{L}$	$P_s = 2V_u$
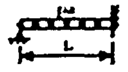	$p_f a = 12.0 \frac{f_y Z}{L^2}$	$p_s a = \frac{2V_u}{L} - \frac{2M_p^e}{L^2}$
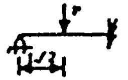	$P_f = 6.0 \frac{f_y Z}{L}$	$P_s = 2V_u - \frac{2M_p^e}{L}$
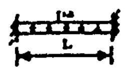	$p_f a = 16 \frac{f_y Z}{L^2}$	$p_s a = \frac{2V_u}{L}$
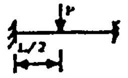	$P_f = 8 \frac{f_y Z}{L}$	$P_s = 2V_u$

a = width of contributory loading area

Z = plastic section modulus

f_y = steel yield stress

V_u = total shear resistance of section (Eq. 8-51)

M_p^e = fully plastic moment at end of span

p_f = uniform load resistance of member based on flexural capacity

p_s = uniform load resistance of member based on shear capacity

P_f concentrated load resistance of member based on flexural capacity

P_s concentrated load resistance of member based on shear capacity

Figure 8-19 Static Flexural and Shear Capacity of Steel Beams

The procedure presented in paragraph 8.3.3 for combined flexural and axial loads can then be used to design or analyze the member. If the member is subjected to shearing forces, they must be provided for in accordance with procedures outlined in paragraph 8.3.4.

As noted in paragraphs 8.2.2b and 8.3.2, the use of spirals or ties in reinforced concrete compression members increases the allowable stresses and ductility of the member. These increases are derived from lateral confinement of the concrete and lateral support of the longitudinal reinforcement provided by spirals or ties. When required, Ref. 8-12 recommends that spiral reinforcement be at least 0.375 in (0.953 cm) in diameter for cast in place construction. The clear spacing between spirals should not be greater than 3.0 in (7.62 cm) nor less than 1.0 in (2.54 cm). The ratio of spiral reinforcing should be not less than

$$p_s = 0.45\left|\frac{A_g}{A_c'} - 1\right| \frac{f_c'}{f_y},$$

where

A_g = gross cross sectional area of member

A_c' = area of core of spirally reinforced concrete member measured to outside diameter of spiral

f_y = yield strength of spiral material, but not more than 60,000 psi (41,370 N/cm^2)

p_s = v_s/v_c

v_s = volume of spiral reinforcement

v_c = total volume of core measured out-to-out of spiral

Where required, hoop reinforcing for tied members should be at least #3 (0.952 cm diameter) bars for #10 (3.23 cm diameter) or smaller longitudinal reinforcing and at least #4 (1.27 cm diameter) bars for larger size longitudinal reinforcing. The spacing of ties should not exceed 16 longitudinal bar diameters, 48 tie bar diameters or the least dimension of the member.

Preplotted interaction diagrams for axial and bending loads are a valuable tool in the analysis of reinforced concrete members and can greatly reduce the amount of computation. Figure 8-20 is a series of such diagrams for commonly encountered reinforced concrete sections. Similar diagrams for other sections can be found in most texts on reinforced concrete.

8.6.2 Steel

The procedures for design and analysis of structural steel columns are similar to those for reinforced concrete. In contrast to reinforced concrete members, any amount of moment applied to a steel member will reduce its capacity as a compression member. Equations in paragraph 8.4.2 define the ultimate compressive load capacity of an axially loaded steel member. Equations of paragraph 8.4.3 must be satisfied for members subjected to combined bending and compressive loads. The provisions of paragraph 8.4.4 must be satisfied for members subjected to shearing forces.

8.7 TWO-WAY SLABS AND PLATES

8.7.1 Reinforced Concrete

a. Flexural Resistance

Tests have verified that the ultimate capacity of reinforced concrete slabs can be predicted with confidence by the Yield Line Theory (Ref. 8-22). Furthermore, according to Ref. 8-22 the results are always on the conservative side for design purposes, i.e., the calculated ultimate load being 80 to 90 percent of the actual ultimate load. It is thought that

$P_t\ m$ not defined

$P_t = \frac{A_s + A_s}{A_c} \quad m \quad \frac{P_s}{0.85 f'_c}$

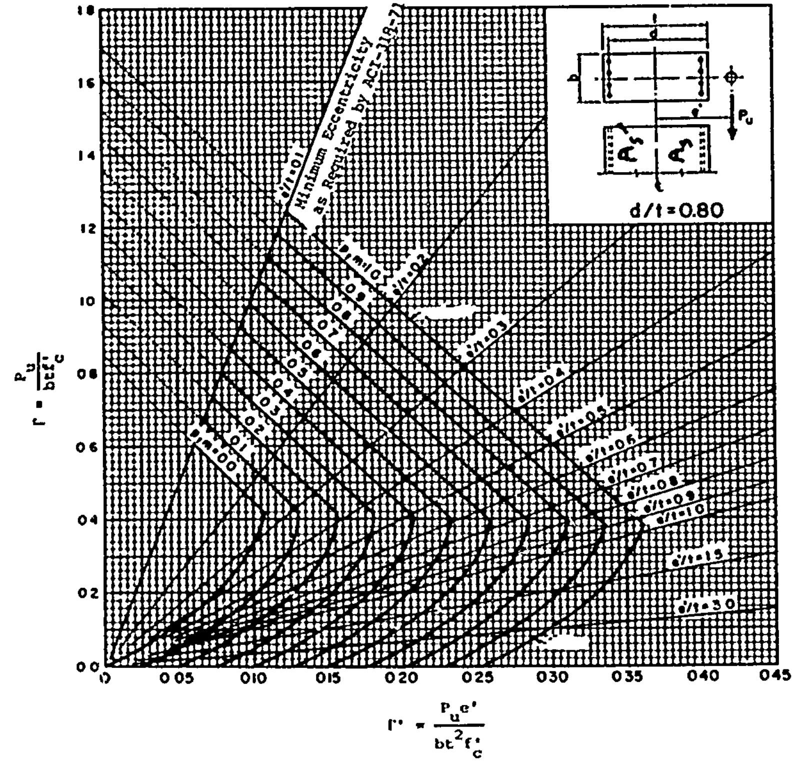

(a) Rectangular Sections with Symmetrical Reinforcement, d/t = 0.80

Figure 8-20 Interaction Curves for Reinforced Concrete Sections

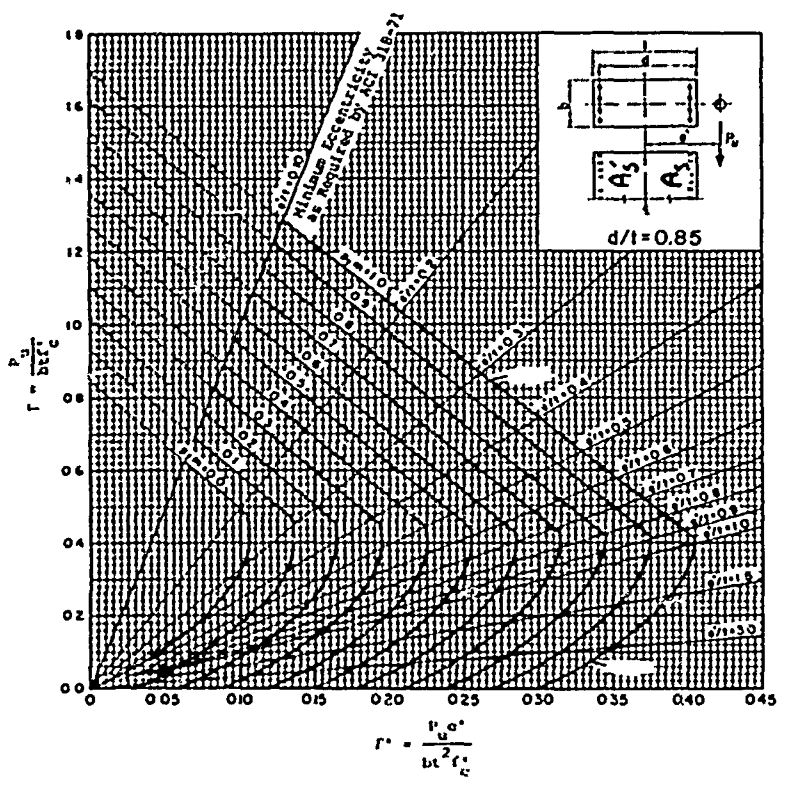

(b) Rectangular Sections with Symmetrical Reinforcement, d/t = 0.85

Figure 8-20 (cont.) Interaction Curves for Reinforced Concrete Sections

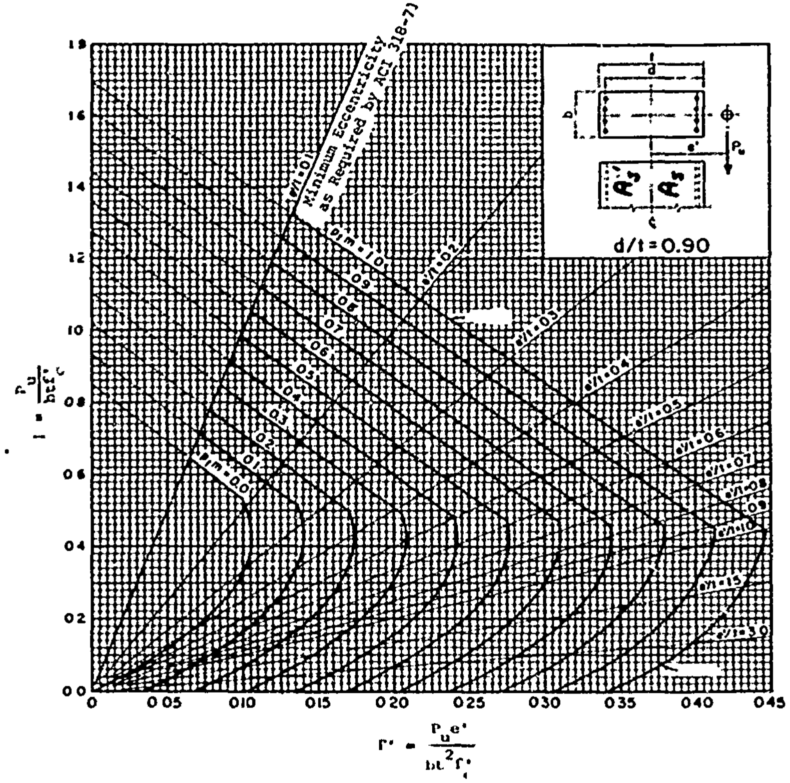

(c) Rectangular Sections with Symmetrical Reinforcement, d/t = 0.90

Figure 8-20 (cont.) Interaction Curves for Reinforced Concrete Sections

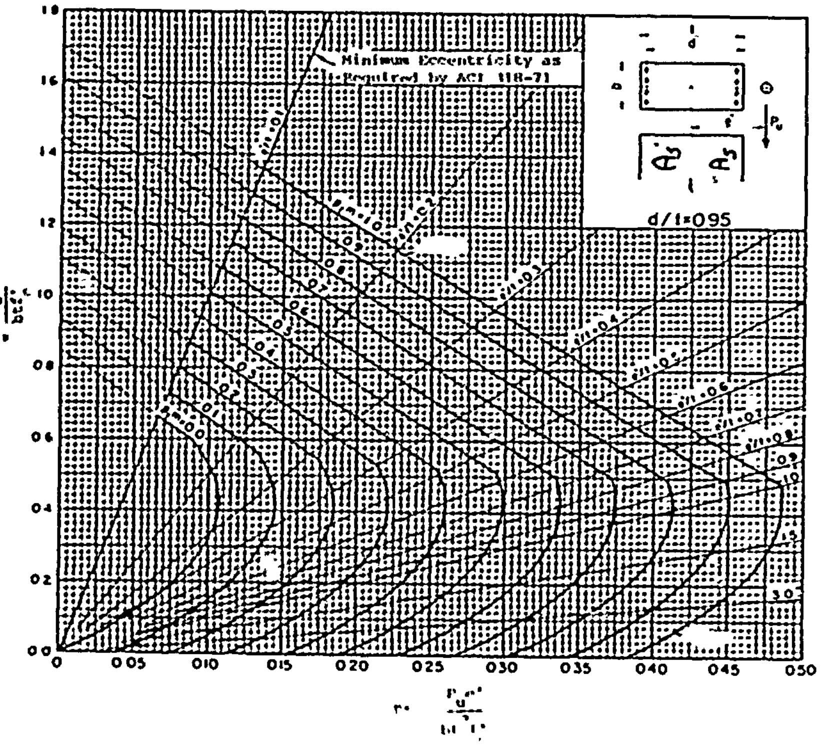

(d) b. [illegible] with symmetrical reinforcement, d/t = 0.95

Figure 8-20 (cont.) Interaction Curves for Reinforced Concrete Sections

this results from strain hardening of the reinforcement together with membrane action of the slab when the slab experiences relatively large deflections near failure.

The Yield Line Theory is well covered in the literature, e.g., Refs. 8-22, 8-23 and 8-24. For the general case of a rectangular two-way slab, continuous over all four supports (Fig. 8-21) and subjected to a uniform load, Ref. 8-23 gives the following expression for the required ultimate moment capacity at the center.

$$M_{sc} = \frac{w\alpha^2 L^2}{6\gamma_{34}^2}\left[\sqrt{3 + \gamma_c\left(\frac{\alpha\gamma_{12}}{\gamma_{34}}\right)^2} - \frac{\alpha\gamma_{12}\sqrt{\gamma_c}}{\gamma_{34}}\right]^2 \qquad (8\text{-}56)$$

where

M_{sc} = ultimate moment capacity per unit width of slab at the center of and in the direction of the short span

α = ratio of the short span to the long span

γ_c = ratio of ultimate moment capacity in long span direction to that in short span direction at center of slab

γ_{12} = $\sqrt{1 + i_1} + \sqrt{1 + i_2}$

γ_{34} = $\sqrt{1 + i_3} + \sqrt{1 + i_4}$

i_1, i_2 = ratios of ultimate moment capacities at supports 1 and 2 to that at center of long span

i_3, i_4 = ratios of ultimate moment capacities at supports 3 and 4 to that at center of short span

w = uniform load applied to slab

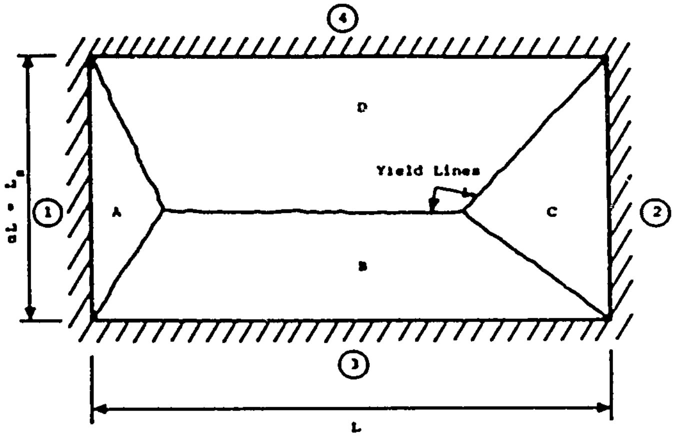

Figure 8-21 Yield Lines for a General Rectangular Slab

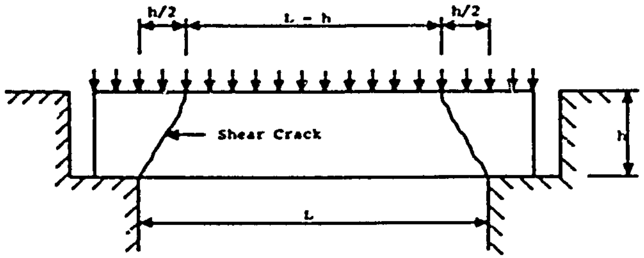

A_{SH} = Shear Area = $\pi h(L - h)$

A_L = Loaded Shear Area = $\frac{\pi}{4}(L - h)^2$

Figure 8-22 Two-Way Slab Shear Mode of Failure

If it is assumed that the moment capacities are equal at both supports of each span, Eq. 8-56 can be rearranged to give ultimate load capacity in terms of the moment capacities at the supports and mid-span. Thus,

$$p_f = \frac{24(M_{sc}+M_{se})}{L_s^2}\left[\sqrt{3+\alpha^2\left(\frac{M_{Lc}+M_{Le}}{M_{sc}+M_{se}}\right)} - \alpha\sqrt{\frac{M_{Lc}+M_{Le}}{M_{sc}+M_{se}}}\right]^{-2} \quad (8\text{-}57)$$

where

M_{se} = ultimate moment capacity per unit width of slab at the supports of and in the direction of the short span

M_{Lc} = ultimate moment capacity per unit width of slab at the center of and in the direction of the long span

M_{Le} = ultimate moment capacity per unit width of slab at the supports of and in the direction of the long span

The ultimate moment capacities at the critical sections can be obtained from Eq. 8-9 or 8-53 using appropriate properties of the slab. Equations 8-56 and 8-57 can also be applied to simply supported slabs by setting moment capacity at the edges equal to zero.

For rectangular slabs of reasonable relative dimensions and steel percentages, the critical yield line pattern can be assumed to be symmetrical, i.e., intersects the corners at 45 degrees, area A equals area C and area B equals area D in Fig. 8-21. The resistance, expressed as a uniformly distributed load, corresponding to this yield line pattern can be obtained by considering the equilibrium of segments A and B. Since the true yield lines depend on slab properties, agreement between the resistances obtained for the two segments would be a fortuitous case. Reference 8-2 suggests using an average value weighted on the basis of the areas of the two segments. The resulting resistance is given by

$$p_f = 10.8(p_{se} + p_{sc})\left|\alpha\left(\frac{p_{le} + p_{lc}}{p_{se} + p_{sc}}\right) + \frac{2 - \alpha}{3 - 2\alpha}\right| f_y\left(\frac{d}{L_s}\right)^2 \qquad (8\text{-}58)$$

where

p_{se} = average tensile steel ratio at the edge spanning in short direction

p_{sc} = average tensile steel ratio at the center spanning in short direction

p_{le} = average tensile steel ratio at the edge spanning in long direction

p_{lc} = average tensile steel ratio at the center spanning in long direction

Results obtained from Eq. 8-58 may, in some instances, overestimate the resistance of the slab, but generally not in amounts sufficient to warrant analysis by a more refined application of the Yield Line Theory in preliminary analyses (Refs. 8-22 and 8-24). Edge panels, however, or other cases where unsymmetrical support conditions exist, should be checked for adequacy.

For the case of a circular slab subjected to a uniform load and continuously supported at its edges, the flexural resistance is given by (Ref. 8-23)

$$p_f = \frac{6\left(M_p^c + M_p^c\right)}{R^2} \qquad (8\text{-}59)$$

where

M_p^c = ultimate moment capacity per unit width of slab at center of slab

M_p^c = ultimate moment capacity per unit width of slab at edge of slab

R = radius of the slab

Equation 8-59 can also be defined in terms of the reinforcing steel ratios at the center and edges of the slab (Ref. 8-2).

$$p_f = 5.4\ f_y\left(\frac{d}{R}\right)^2 (p_c + p_e) \qquad (8\text{-}60)$$

where

p_c = average tension steel ratio at center of slab

p_e = average tension steel ratio at edge of slab

Since the yield line patterns for two-way slabs are similar for simple or continuous supports, Eqs. 8-56 through 8-60 are also applicable to simply supported slabs. For these cases, the moment capacity at the supports is simply set equal to zero. References 8-23 and 8-24 treat other support conditions in some detail.

Under some conditions the reinforced concrete slab may be subjected to both axial and lateral components of load. For example, the walls of a shallow buried structure subjected to ground shock loading will transmit significant axial compressive components of load to its roof slab. These loads can significantly increase the flexural resistance of the roof slab. A similar condition arises in the case of roof loads transmitted to side walls. The effect of such axial loads on slab resistance can be estimated by application of the principles described in paragraphs 8.3.3 and 8.6.1. Careful consideration, however, must be given to whether the possible time-phasing of the axial and flexural load components will be more likely to produce beneficial or harmful results.

b. Shear Resistance

Shear failures in two-way slabs with dimensions encountered in normal construction are unlikely due to the large perimeter area available to resist the shearing forces. Exceptions are those cases where concentrated loads are applied to the slab through columns or other similar structural members. In some instances, it may be necessary to provide additional reinforcement at column-to-slab connections to prevent shear failures. In some protective construction applications, two-way slabs carry loads of very high intensity, and the possibility of shear failure increases.

References 8-25 through 8-29 summarize a series of tests of deep square two-way slabs and conclude that shear is the governing mode of failure. As in the case of beams and one-way slabs, there are differences in the shear behavior of conventional and deep ($L/d \leq 5$) two-way slabs. In either type slab, the shear resistance can be expressed as

$$p_s = C_v \sqrt{f'_c}\, A_{SH}/A_L \qquad (8\text{-}61)$$

where

p_s = shear resistance of slab (expressed as uniform load)

A_{SH} = area resisting shear (Fig. 8-22)

A_L = loaded area producing shear (Fig. 8-22)

C_v = an empirical constant

The shear mode of failure was typically found to be a circular cone-shaped section as indicated in Fig. 8-22 being forced out from the center of the slab.

Reference 8-12 suggests that the critical section for shear occurs at a distance of d/2 from the reaction and $C_v = 4.0$ ($C_v = 3.32$ in SI). It is recommended that these criteria be applied to two-way slabs of conventional ($L/d > 5$) proportions. For square slabs, Eq. 8-61 becomes

$$p_s = 16\sqrt{f'_c}\,\frac{d}{L - d} \quad \text{psi}$$
$$= 13.28\sqrt{f'_c}\,\frac{d}{L - d} \quad \text{N/cm}^2 \qquad (8\text{-}62)$$

where L is the clear span of the slab.

Experimental data indicate that deep slabs can sustain higher shear stresses than allowed by Eq. 8-62. Reference 8-27 recommends

$$p_s = 12\sqrt{f'_c}\, A_{SH}/A_L \quad \text{psi}$$
$$= 9.96\sqrt{f'_c}\, A_{SH}/A_L \quad \text{N/cm}^2 \qquad (8\text{-}63)$$

as a lower bound to deep slab test results. For a deep square slab, Eq. 8-63 becomes

$$p_s = 48\sqrt{f'_c}\,\frac{h}{L - h} \quad \text{psi}$$
$$= 39.85\sqrt{f'_c}\,\frac{h}{L - h} \quad \text{N/cm}^2 \qquad (8\text{-}64)$$

where h is the total depth of the slab and other terms are as previously defined.

Equations 8-63 and 8-64 are based on an earlier experimental study (Ref. 8-30) of deep circular slabs. A lower bound to test data for deep circular slabs is given by

$$p_s = 36\sqrt{f'_c}\,\frac{h}{L - 2h} \qquad \text{psi} \qquad (8\text{-}65)$$

$$= 29.89\sqrt{f'_c}\,\frac{h}{L - 2h} \qquad \text{N/cm}^2$$

The above expressions (Eqs. 8-63 and 8-65) are suggested for design of deep slabs. An upper bound to the experimental data, which is appropriate for analysis, is obtained by changing the coefficient 12 in Eq. 8-63 to 19 (or 15.78 in SI units) and the coefficient 36 in Eq. 8-65 to 54 (or 44.84). For rectangular slabs, it is suggested that Eq. 8-64 be used with L taken as the average of the two spans. If the ratio of short-to-long span is less than 0.5, the shear resistance of the two-way slab should be taken equal to that of a one-way slab spanning in the short direction.

It is noted that Eqs. 8-63 through 8-65 do not consider the effect of tension reinforcing on shear capacity. Test data reported in Ref. 8-27 indicate that, although the shear resistance of deep slabs is slightly higher with tension reinforcing, it is relatively insensitive to the tension reinforcement ratio over the range $0.001 \le p \le 0.015$. In the slab tests bounded by Eq. 8-63, the tension reinforcement ratio varied from 0 to 0.015 in each direction and the compression reinforcement ratio varied from 0 to 0.005. Although the strength of the slabs tested did not vary significantly over the range of tension reinforcing, the presence of reinforcing steel was found to affect the severity of the failure. In most cases, those slabs with no reinforcing broke into small fragments. Those with reinforcing, although severely damaged, did tend to stay together.

Reference 8-30 indicates that moment and axial forces affect the shear strength of deep two-way slabs in a way similar to that observed for beams and one-way slabs. Increasing moment at the critical section will generally decrease the allowable shear stress. Compressive axial loads increase and axial tension loads lower shear capacity of concrete sections. If moment and axial loads can be determined with reasonable confidence, it is suggested that a unit width of the two-way slab be analyzed as a beam column spanning in the short direction using the procedures described in paragraph 8.3.3. The shear capacity of the two-way slab can be estimated as $\frac{2}{3}(1 + \alpha)$, but not less than one, times that of the beam.

In the event shear capacity is required above that provided by the concrete alone, additional strength can be provided in the form of vertical and/or horizontal web reinforcing. The amount of reinforcing required can be determined from Eq. 8-36 or 8-39 as appropriate.

c. Supporting Beams

The beams supporting a slab must be designed for the actual load distribution on the beam, which varies as the edge shear of the supported slab. For a square slab, the flexural resistance of supporting beams with symmetrical support restraints can be determined by assuming a triangular load distribution with the maximum load intensity at the center of the beam. For this case, the support beam resistance, expressed as a uniform load on the slab, is

$$p_f = 10.8(p_e + p_c)\,f_y\left(\frac{b}{a}\right)\left(\frac{d}{L}\right)^2 \qquad (8\text{-}66)$$

where

a = center-to-center distance between adjacent slabs

For the beam under the long side of a two-way slab, the loading may be assumed trapezoidal, which leads to

$$p_f = 7.2(p_e + p_c)f_y\left(\frac{b}{a}\right)\left(\frac{d}{L}\right)^2\left[\frac{1}{1 - \frac{1}{3}(\alpha)^2}\right] \qquad (8\text{-}67)$$

where the terms are as previously defined except that a is the center-to-center distance between adjacent long beams. The flexural resistance of the beam under the short span of a rectangular slab is obtained from Eq. 8-66 with a taken equal to the short span.

The shear resistance of beams supporting a two-way slab can be determined using the equations of paragraph 8.3.4.

8.7.2 Steel

For some structural elements, steel plate is a more practical material than reinforced concrete. Access doors, hatches, and cover plates are examples of the types of structural elements which lend themselves to fabrication from steel plate. The maximum deflections and stresses in these elements will be affected by plate geometry and the type of support provided at the edges of the plates. Unless it is combined with a system of stiffeners, a flat plate provides very low flexural resistance to lateral loads. In most cases, large deflections of the plate will result in the applied loads being carried primarily through membrane action. The flexural load capacity of steel plates can be estimated from Eqs. 8-56 or 8-59 by inserting the appropriate moment capacities at the critical sections. The large deflections of simple flat plates can be reduced by use of grillages of beams or stiffeners. The same basic relationships could be applied with moment capacities

based on the properties of the grillage. Torsional effects should be investigated in all cases.

8.8 REINFORCED CONCRETE SHEAR WALLS

Reinforced concrete shear walls are structural elements which are designed to resist lateral loads in the plane of the wall. When properly designed and integrated into the structural system of a building, they provide considerable resistance to lateral deformations. In many instances, they can be presumed to provide the total resistance to lateral deformations. The interior columns can then be designed to resist only axial loads. Shear walls are effective elements for transmitting shear between successive floors of multistory buildings. They are usually constructed integral with floor slabs, columns, beams and other shear walls oriented at 90 degrees. In these cases, the other elements contribute to the strength, stiffness and stability of the shear walls.

Figure 8-23 is a simplified representation of a typical shear wall and shows its principal elements. The procedures for design and analysis described in the following paragraphs are based largely on static tests of model walls of the type shown in Fig. 8-23. The walls were reinforced with equal percentages of reinforcing steel uniformly distributed throughout the walls in vertical and horizontal directions.

Figure 8-24 shows typical load-deflection curves for the test walls. The deflection increased linearly with load up to the point where first cracking occurs. Beyond this point, the load deflection relationship is a function of the proportions of the wall and the relative percentages of reinforcing steel in the shear panel and adjacent framing elements. Walls with smaller L/H ratios (about 1) will generally exhibit ultimate load capacities greater than the cracking load. The difference in load carrying capacity is largely a function of the amount of reinforcing steel in the wall panel and columns. Walls with larger L/H ratios (greater than 2) will usually sustain ultimate

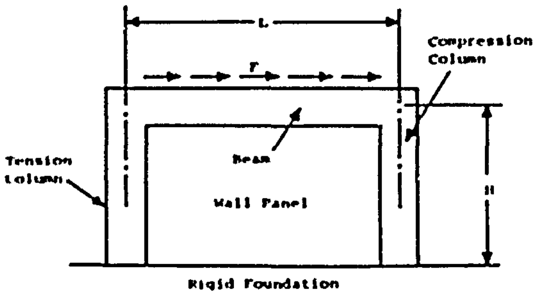

Figure 8-23 Principal Elements of a Shear Wall

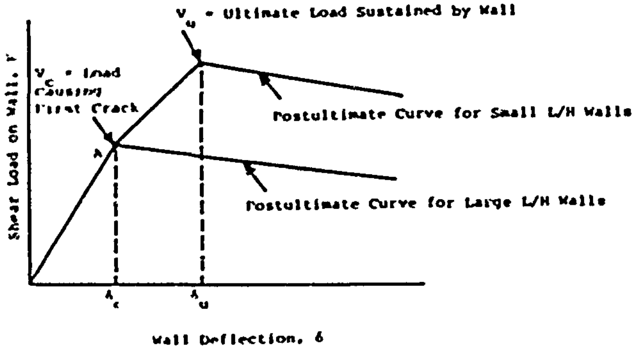

Figure 8-24 Characteristic Load-Deflection Curves for Shear Walls

loads about equal to the cracking load.

The horizontal static load resistance of the wall at first cracking is given by (Ref. 8-1)

$$R_c = 0.1f'_cLt \qquad (8\text{-}68)$$

where

L = wall length center-to-center of columns (see Fig. 8-23)

t = thickness of the shear panel

The ultimate static resistance of the wall is a function of the compression column and panel influence factors. It is given by (Ref. 8-1)

$$R_u = \frac{C}{1 + 10P/C} + \frac{2.1P}{P/C + 0.6} \qquad (8\text{-}69)$$

where

$C = A_s f'_c\left[15 + 1.9(L/H)^2\right]$ = column influence factor

A_s = area of column steel in column on compression edge of panel

$P = f_y pt[H + L]$ = panel influence factor

p = steel ratio in each direction (assumed equal)

H = wall height to center of top beam

The deflection at first cracking is (Ref. 8-1)

$$\delta_c = \frac{R_cH}{E_c}\left(\frac{H^2}{3I} + \frac{2.2}{Lt}\right) \qquad (8\text{-}70)$$

where

I = moment of inertia about centroid of horizontal section through shear wall including frame but neglecting all reinforcement

The shear wall deflection at which the ultimate resistance is reached is given by the relation (Ref. 8-1)

$$\delta_u = 24\delta_c H/L \qquad (\delta_u \geq \delta_c) \qquad (8\text{-}71)$$

where δ_c is the deflection at first cracking as given by Eq. 8-70. When R_u is equal to or less than R_c, Eq. 8-71 has little significance. However, in all cases it can be used as a design criterion to indicate the upper limit of deflection for which the shear wall may be designed.

The series of tests upon which Eqs. 8-68 through 8-71 are based considered a limited range of variations in the properties of the walls and columns. The reinforcing steel ratio was varied from 0.01 to 0.033 in the columns and from 0 to 0.015 in the walls. Concrete strength varied from 2000 to 4000 psi (1380 to 2760 N/cm^2) and the yield strength of the reinforcing steel varied from 42,000 to 52,000 psi (28,950 to 35,850 N/cm^2). The L/H ratios varied from 0.9 to 3.0 and P/C ratios varied from 0 to 3.26. Applicability of these equations to combinations of properties outside these limits is uncertain.

The shear wall tests indicated that the ultimate shear resistance was not affected to any significant degree by the simultaneous application of vertical loads unless these loads exceeded the lateral load. Thus in most cases of interest, the effect of vertical loads on shear wall resistance can be neglected. The simultaneous application of loads normal to the plane of the shear wall will have an effect on its strength. This type of loading can arise in the case of exterior walls subjected to airblast loading. The combined normal and shear load resistance at first cracking is defined by the straight line interaction equation

$$\frac{R'_c}{R_c} + \frac{N'_c}{N_c} \leq 1 \qquad (8\text{-}72)$$

where

R'_c = applied shear load at first cracking under combined loading

N'_c = total normal load at first cracking under combined loading

N_c = total normal load resistance at first cracking with no shear load

$$= \frac{0.1 f'_c L t^2}{6H(0.07 - 0.04H/L)}$$

The ultimate combined normal and shear load resistance is defined by the circular interaction equation

$$\left(\frac{R'_u}{R_u}\right)^2 + \left(\frac{N'_u}{N_u}\right)^2 \leq 1 \qquad (8\text{-}73)$$

where

R'_u = ultimate applied shear load under combined loading

N'_u = normal load applied at yielding of reinforcement under combined loading

N_u = normal load resistance at yield of reinforcement with no shear load

The normal load resistance at yielding with no shear load can be obtained from the appropriate beam and slab equations in paragraphs 8.3 and 8.7. Wall deflections in the direction of the shear load are not significantly affected by vertical loads and Eqs. 8-71 and 8-72 are applicable. Although Eq. 8-69 was developed for single story shear walls, it can be applied to individual stories of multistory buildings. Openings in shear walls reduce their strength and should be avoided if possible. If openings cannot be avoided, the shear strength should be based upon application of the preceding equations to the individual portions of the walls between openings.

8.9 CYLINDERS

8.9.1 Introduction

Cylinders are used primarily in underground protective construction applications and may be oriented either vertically or horizontally depending upon the intended function. The behavior of buried cylinders is significantly affected by the properties of the surrounding soil mass. Most of the experimental data that are available are for cylinders buried in cohesionless soil. Such other data as are available indicate that thrusts and moments developed in cylinders buried in cohesive soil will be considerably larger than for the same cylinder in cohesionless soil.

In addition to the properties of the surrounding soil mass, the behavior of buried cylinders is dependent upon the depth of burial. The full advantage of earth cover in reducing the loads transmitted to a cylinder from the surrounding soil appears to be substantially realized at a depth of burial of one diameter. Except for further attenuation of the peak free-field soil pressure from above, little advantage is gained with depths of burial greater than one diameter. The minimum recommended depth of burial is one-eighth diameter, and significant structural section economy can be realized with depths of burial of at least one-half diameter.

Although always dependent upon the specifics of the particular structure-medium interaction phenomena involved, buried cylinders usually possess sufficient flexibility to allow reduction of load asymmetries. Because of this ability to adjust to load nonuniformities and the absence of stress raisers due to structural discontinuities, cylinders are typically able to resist imposed loads more efficiently than rectangular structures.

8.9.2 General Behavior

Thrust, or normal axial force, is the only internal force generated in a perfectly round cylindrical section subjected to a centrally directed uniform external pressure, i.e., shear and moment are everywhere zero in the section. Accordingly, cylinders are exceedingly efficient in resisting large loads under these conditions. Unfortunately, real structures are rarely, if ever, perfectly constructed, and the pressures imposed on a buried structure as a result of a nuclear detonation are highly nonuniform.

The nonuniform pressure distribution shown in Fig. 8-25 can be used to represent a large majority of actual load cases encountered in the design and analysis of hardened structures. The internal thrust, shear and moment resulting from the pressure distribution shown can be expressed as

$$P_0 = -qR + \frac{\bar{p}R}{3} \cos 2\theta \qquad (8\text{-}74)$$

$$V_0 = -\frac{2}{3}\bar{p}R\sin 2\theta \qquad (8\text{-}75)$$

$$M_0 = \frac{\bar{p}R^2}{3} \cos 2\theta \qquad (8\text{-}76)$$

where q is the magnitude of the uniform component and $\bar{p}$ is the maximum amplitude of the nonuniform component of external pressure. Elastic stresses in the section from these internal forces can be determined with very little error by conventional beam analysis methods provided the curvature parameter, R/c, (see Fig. 8-25) is greater than 10. For values of R/c less than 10, the elastic stress can be found by

$$\sigma = K\left[\frac{Mc}{I} + \frac{P}{A}\right] \qquad (8\text{-}77)$$

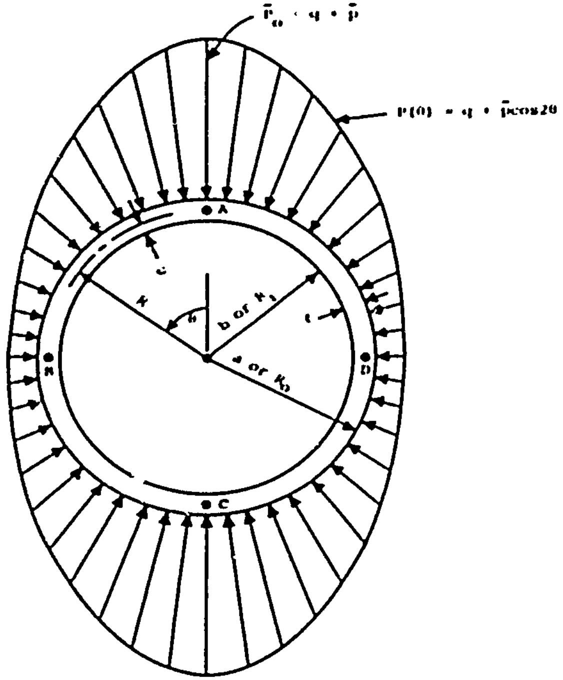

Figure 8-25 Circular Ring Subjected to Nonuniform External Pressure

where

K = Winkler-Bach curvature correction factor

I = moment of inertia of the cross section

A = area of the cross section

Values of K for a rectangular cross section are shown in Table 8-3 from Ref. 8-31. Values of K for other cross section shapes are also contained in Ref. 8-31.

For a perfectly round ring, the deflection due to uniform external pressure will be negligible, and the elastic deflection can be taken as that due to the nonuniform component, $\bar{p}$, i.e.,

$$\delta_{\bar{p}} = \frac{\bar{p}R^4}{9EI}\cos 2\theta \qquad (8\text{-}78)$$

Table 8-3

CURVATURE CORRECTION FACTORS FOR STRAIGHT-BEAM FORMULA (Ref. 8-31)

Section	$\frac{R}{C}$	Factor K		y_o*
		Inside Fiber	Outside Fiber	
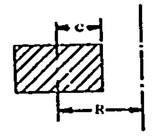 K independent of section dimensions.	1.2	2.89	0.57	0.305R
	1.4	2.13	0.63	0.204R
	1.6	1.79	0.67	0.149R
	1.8	1.63	0.70	0.112R
	2.0	1.52	0.73	0.090R
	3.0	1.30	0.81	0.041R
	4.0	1.20	0.85	0.021R
	6.0	1.12	0.90	0.0093R
	8.0	1.09	0.92	0.0052R
	10.0	1.07	0.94	0.0033R

If the ring has an initial eccentricity δ_o, the deflection due to the uniform pressure component q can be expressed as

$$\delta_q = \delta_o \cos 2\theta \left[\frac{q}{q_{cr} - q}\right] \tag{8-79}$$

where

$$q_{cr} = 3EI/R^3$$

Taking δ_o as the peak deflection due to the nonuniform component, i.e., $\bar{p}R^4/9EI$,

$$\delta_q = \frac{\bar{p}R^4}{9EI} \cos 2\theta \left[\frac{q}{q_{cr} - q}\right] \tag{8-80}$$

A peak probable elastic deflection to be expected, then, can be taken as

$$\delta_{max} = \delta_{\bar{p}} + \delta_q = \frac{\bar{p}R}{3} \cos 2\theta \left[\frac{1}{q_{cr} - q}\right] \tag{8-81}$$

and a maximum probable moment for elastic design as

$$\begin{aligned} M_{max} &= M_{\bar{p}} + M_q = M_0 + qR\delta_{max} \\ &= \frac{\bar{p}R^2}{3} \cos 2\theta \left[\frac{1}{1 - q/q_{cr}}\right] \end{aligned} \tag{8-82}$$

The expressions and assumptions presented thus far are generally applicable for elastic behavior of ring sections of any material. These basic relations can be specialized to some degree to fit the particular ring material properties and design or analysis objective of interest.

8.9.3 Steel Rings

Steel is a reasonably homogeneous and isotropic material and thus lends itself to certain analytical simplifications. Taking maximum values of thrust and moment from Eqs. 8-74 and 8-76, the expression for maximum fiber stress (Eq. 8-77) in a ring for the loadings of Fig. 8-25 can be written

$$\sigma_{max} = K\left[2\bar{p}\left(\frac{R}{t}\right)^2 + \left(q + \frac{\bar{p}}{3}\right)\left(\frac{R}{t}\right)\right] \tag{8-83}$$

Equation 8-83 gives maximum stress in the extreme fiber of the ring based on elastic theory, i.e., setting $\sigma_{max} = \sigma_y$, Eq. 8-83 gives a relation between $\bar{p}$ and q for initial yield in the ring. It is shown in Ref. 8-32 that first yield will occur at Points B and D shown in Fig. 8-25 and that the relationship between $\bar{p}$ and q at collapse (fully plastic hinges at A, B, C and D) can be expressed by

$$\bar{p}^2 + 12\sigma_y\bar{p} + 9q^2 = 9(t\sigma_y/R)^2 \tag{8-84}$$

With the substitutions

$$\frac{\bar{P}_o}{\sigma_y} = \frac{1 + \beta}{\beta}\left(\frac{q}{\sigma_y}\right) \qquad \text{and} \qquad \beta = q/\bar{p}$$

where $\bar{P}_o = q + \bar{p}$, Eqs. 8-83 and 8-84 can be written

$$\left(\frac{\bar{P}_o}{\sigma_y}\right)_{elastic} = \frac{K(1 + \beta)}{2\left(\frac{R}{t}\right)^2 + \left(\beta + \frac{1}{3}\right)\left(\frac{R}{t}\right)} \tag{8-85}$$

$$\left(\frac{\bar{P}_o}{\sigma_y}\right)_{collapse} = \frac{6(\beta + 1)}{1 + 9\beta^2}\left\{-1 + \left[1 + \left(\frac{t}{2R}\right)^2\left(1 + 9\beta^2\right)\right]^{1/2}\right\} \tag{8-86}$$

With the preceding equations, it is possible to select cylinder section properties for either elastic or ultimate strength behavior if the loads are known. Alternatively, combinations of $\bar{p}$ and q to initiate yielding or to collapse the section can be estimated if the section properties are known.

Steel sections selected on the basis of strength, as with the equations above, are more susceptible to failure by buckling than reinforced concrete sections due to the thinner steel wall thickness required. Various buckling possibilities due to nonuniform external loads are investigated in Ref. 8-32. Figure 8-26 from that reference is provided as a guide as to whether stability rather than strength considerations control in the selection of cylinder section properties.

In cases where yielding occurs before the possibility of buckling, it is desirable to know the load-deformation function after yield and before collapse in order to estimate the reserve strength available after yield and the deflections involved. This problem is investigated in Ref. 8-32 where it was found, as expected, that the deflections are strongly dependent upon the pressure ratio, $\beta = q/\bar{p}$, and the ring thickness parameter, R/t. Expressions from Ref. 8-32 for determining deflections after yielding are summarized in Table 8-4. These equations are quite cumbersome for hand solution but are readily solved with the aid of a digital computer. Figure 8-27 illustrates the type results obtained.

It will be recalled that the presence of axial force in steel members subjected to combined bending and axial loads reduces the moment capacity of the member. For steel sections stressed beyond the yield point, larger axial forces result in larger deflections for the same total pressure, $\bar{P}_o = q + \bar{p}$. This axial force effect on deflection is apparent in Fig. 8-27 where it may be seen that an increase in β (which means an increase in q with respect to $\bar{p}$ and, in turn, an increase in thrust) results in an increase in deflection for the same total pressure, $\bar{P}_o$. For thin rings, axial force will be small with respect to the bending force, and the deflections can be taken with little error as due to $\bar{p}$ alone. Thin ring deflections are also shown in Fig. 8-27 for comparative purposes.

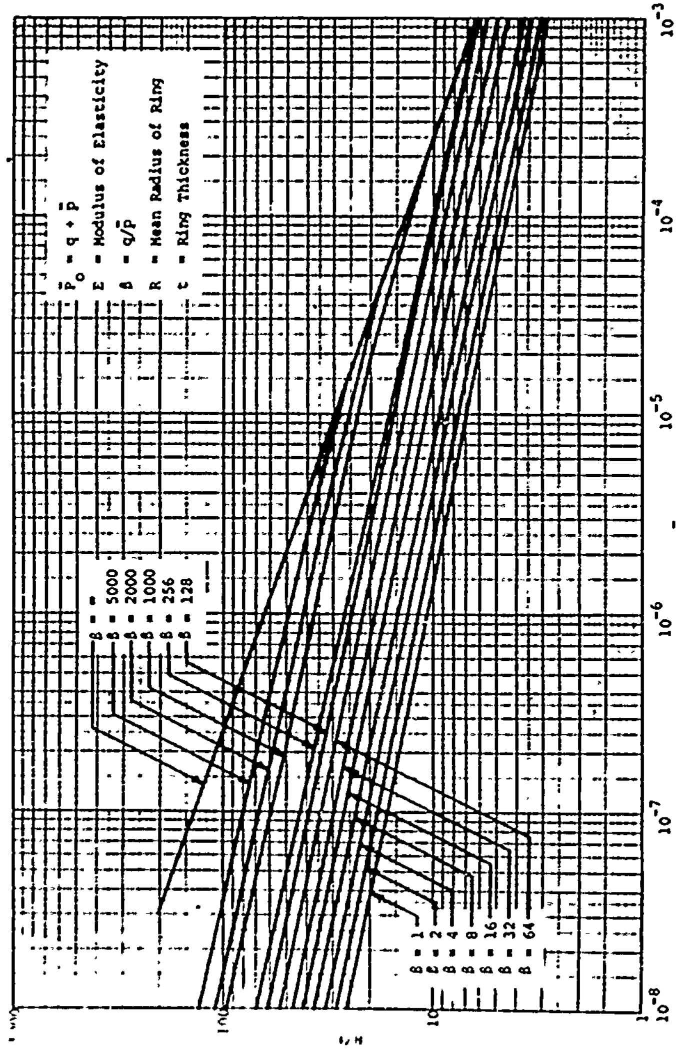

Figure 8-26 Critical Buckling Ratios for Ring Loaded with Nonuniform Pressure (Ref. 8-32)

Table 8-4

EQUATIONS FOR INELASTIC DEFORMATION OF HOMOGENEOUS RING (Ref. 8-32)

$$\frac{\delta_A}{\delta_{Ae}} = \frac{2(\beta + 1)}{(\bar{P}_{oe}/\sigma_y)} \left\{ \frac{(t/R)^2}{6 \cdot 2} \int_0^{\theta_e} \frac{\cos\theta d\theta}{\left[1 - \frac{2}{3}\left(\frac{M_\theta}{M_e}\right) + \left(\frac{\bar{P}_\theta}{\bar{P}_e}\right)^2\right]^{1/2}} + \frac{2}{3}\left(\frac{\bar{P}_o}{\sigma_y}\right) \frac{\frac{2}{3} - \sin\theta_e + \frac{1}{3}\sin^3\theta_e}{\beta + 1} - \frac{1}{6}\left(\frac{R}{t}\right)^2\left(\frac{M_B}{M_e}\right) (1 - \sin\theta_e) \right\}$$

$$\theta_e = \frac{1}{2}\cos^{-1}\left\{ \frac{\dfrac{\left(1 - \frac{M_B}{M_e}\right)(\beta + 1)}{\left(\frac{\bar{P}_o}{\sigma_y}\right)\left(\frac{R}{t}\right)} + \beta + 2\left(\frac{R}{t}\right)}{\left[\frac{1}{3} - 2\left(\frac{R}{t}\right)\right]} \right\}$$

$$\frac{M_B}{M_e} = \frac{M_{BP}}{M_e}\left\{ 1 - \left[\frac{\left(\frac{M_{BP}}{M_e}\right) - \left(\frac{M_{Be}}{M_e}\right)}{\frac{M_{BP}}{M_e}}\right]\left[\frac{\left(\frac{\bar{P}_{oc}}{\sigma_y}\right) - \left(\frac{\bar{P}_o}{\sigma_y}\right)}{\left(\frac{\bar{P}_{oc}}{\sigma_y}\right) - \left(\frac{\bar{P}_{oe}}{\sigma_y}\right)}\right] \right\}$$

$$\frac{\delta_{Ae}}{R} = \frac{4}{3(\beta + 1)}\left(\frac{\bar{P}_{oe}}{E}\right)\left(\frac{R}{t}\right)^3 \qquad \frac{M_\theta}{M_e} = 4\left(\frac{P_o}{\sigma_y}\right)\left(\frac{R}{t}\right)^2 \frac{\cos^2\theta}{\beta + 1} - \frac{M_B}{M_e} \qquad \frac{M_{Be}}{M_e} = \frac{2}{\beta - 1}\left(\frac{\bar{P}_{oe}}{\sigma_y}\right)\left(\frac{R}{t}\right)^2$$

Table 8-4 (cont.)

EQUATIONS FOR INELASTIC DEFORMATION OF HOMOGENEOUS RING (Ref. 8-32)

$$\frac{M_{BP}}{M_e} = \frac{3}{2}\left\{1 - \left(\frac{\bar{P}_{oc}}{\sigma_y}\right)^2\left(\frac{R}{t}\right)^2\left[\frac{1 + 3\beta}{3(1 + \beta)}\right]^2\right\} \qquad \frac{P_\theta}{P_e} = \left(\frac{\bar{P}_o}{\sigma_y}\right)\left(\frac{R}{t}\right)\frac{\cos 2\theta - 3\beta}{3(\beta + 1)}$$

Symbols (refer to Fig. 8-25)

δ_A = deflection at Point A

δ_{Ae} = Point A deflection at elastic limit

β = $q/\bar{p}$

$\bar{P}_o$ = $(q + \bar{p})_{max}$

$\bar{P}_{oe}$ = $\bar{P}_o$ at first yield

$\bar{P}_{oc}$ = $\bar{P}_o$ at collapse

t = ring thickness

R = ring mean radius

σ_y = yield stress

M_θ = moment at angle θ

M_e = moment capacity at first yield

M_B = moment at Point B

P_θ = thrust at angle θ

P_e = thrust capacity

θ_e = angle θ at threshold of plasticity (ring quadrant inelastic from $\theta = 0$ to θ_e and elastic from θ_e to $\pi/2$)

M_{Be} = moment at B at first yield

M_{BP} = fully plastic moment capacity at B

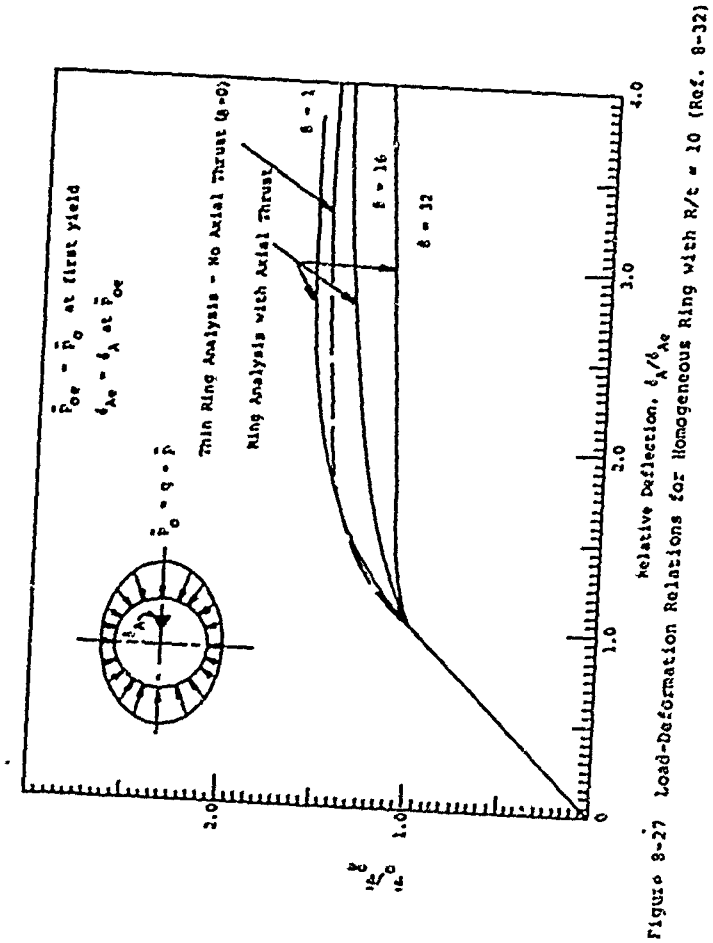

Figure 8-27 Load-Deformation Relations for Homogeneous Ring with R/t = 10 (Ref. 8-32)

8.9.4 Reinforced Concrete Rings

Specialization of the basic ring relations for reinforced concrete sections is a great deal more difficult and cumbersome than for steel due to the nonhomogeneity and nonlinear behavior of reinforced concrete. Consequently, simplified analytical expressions for behavior of reinforced concrete sections are even less precise than those for steel. Although the simplified methods can be used with reasonable confidence to provide a safe design, such methods are more often than not capable of providing only a crude estimate of the behavior of the member. When knowledge of the structural response in some detail is required, it is generally necessary to reformulate the problem from fundamental principles and utilize a computer to solve the resulting expressions.

Since the external loads imposed on a buried cylinder may come from any direction, the properties of reinforced concrete rings are typically made constant with respect to the angular position θ. This results in equal tension and compression steel ratios, i.e., $p = p'$. Accordingly, Eq. 8-10 reduces to

$$M_p = pd^2 f_y (2 - t/d) \tag{8-87}$$

where t is the thickness of the section. Equation 8-87 is valid only when both tension and compression steel have yielded (see Eq. 8-12 for verification of yield in the compression steel) and in the absence of significant axial force. When these conditions are satisfied, the steel ratio for each face in terms of the load function of Fig. 8-25 can be found from

$$p = \frac{\left(\frac{\bar{F}_o}{f_y}\right)\left(\frac{R}{d}\right)^2}{3(\beta + 1)(2 - t/d)} \tag{8-88}$$

The above equations are rarely applicable since significant axial force will almost always be present in reinforced concrete rings.

As discussed previously, a certain amount of axial force increases the moment capacity of reinforced concrete sections up to a point. It is desirable for purposes of design and for ductility of the section to select section properties consistent with the portion b-c of the interaction diagram of Fig. 8-13. To assure this objective, it is necessary that the section be such that the axial force, P, is less than P_b, the axial force at the balance point. The maximum thrust in the ring (Eq. 8-74) can be expressed as

$$P_{max} = \left(\frac{\bar{P}_o R}{3}\right)\left(\frac{3\beta + 1}{\beta + 1}\right) \tag{8-89}$$

Combining Eqs. 8-89 and 8-18 results in

$$\left(\frac{\bar{P}_o}{f'_c}\right) = 2.2\left|\frac{87,000}{87,000 + f_y}\right| \left(\frac{d}{R}\right) \left(\frac{\beta + 1}{3\beta + 1}\right) \qquad \text{English}$$

$$= 2.2\left|\frac{60,000}{60,000 + f_y}\right| \left(\frac{d}{R}\right) \left(\frac{\beta + 1}{3\beta + 1}\right) \qquad \text{SI} \tag{8-90}$$

An effective depth, d to assure $P_u < P_b$ can be found from Eq. 8-90. Then, with the relations

$$P_u = \left(\frac{\bar{P}_o R}{3}\right)\left(\frac{3\beta + 1}{\beta + 1}\right)$$

$$P_u e' = \frac{\bar{P}_o R^2}{3(\beta + 1)}$$

and the interaction diagrams of Fig. 8-20, a ring section can be designed along the principles outlined in paragraph 8.3.3. A similar procedure for design of reinforced concrete rings is described in paragraph 8.11.3.

Reinforced concrete rings are rarely governed by buckling considerations because of the thicker sections involved. A quick estimate of the buckling pressure can be made with Eq. 8-79 with E and I determined from Eqs. 8-2 and 8-30, respectively. Figure 8-26 can also be used to estimate the buckling pressure by entering the figure with the conversions

$$\left(\frac{\bar{P}_o}{E}\right)_{RC} = n\left(\frac{\bar{P}_o}{E}\right)_{steel}$$

$$\left(\frac{R}{d}\right)_{RC} = \left|12 I_c/d^3\right|^{1/3}\left(\frac{R}{t}\right)_{steel}$$

where $n = E_s/E_c$ and I_c/d^3 can be determined from Eq. 8-30. Equation 8-30 is obviously a general approximation of the moment of inertia of a reinforced concrete section in that it contains only two variables, the effective depth, d, and the tension steel ratio, p. A more rational value (although not necessarily worth the additional computational effort in all cases) can be obtained by

$$\frac{I_c}{d^3} = \frac{k^3}{3} + pk^2(2n - 1) - 2pk\left[(n - 1)\left(\frac{d'}{d}\right) + n\right] + p\left[(n - 1)\left(\frac{d'}{d}\right)^2 + n\right] \tag{8-91}$$

where

$$k = -p(2n - 1) + \sqrt{p^2(2n - 1)^2 + 2p\left[(n - 1)\left(\frac{d'}{d}\right) + n\right]}$$

$d' = t - d$, and p is the steel ratio in one face ($p = p'$ for symmetrical cylinder sections).

Elastic deflections of reinforced concrete rings can be estimated in a variety of ways. Equation 8-78 or 8-81 can be used with E and I from Eqs. 8-2 and 8-30, respectively. The following expression from Ref. 8-32 can be used.

$$\left(\frac{\delta_e}{R}\right)_{RC} = \frac{n}{9(I_c/d^3)(\beta + 1)}\left(\frac{\bar{P}_{oe}}{E_s}\right)\left(\frac{R}{d}\right)^3 \tag{8-92}$$

or

$$\frac{(\delta_e)_{RC}}{(\delta_e)_{steel}} = \frac{n}{12I_c/d^3}$$

A quick estimate of the deflection at yield in the steel can be obtained from

$$\delta_y = \frac{R^2}{1215d} \qquad (8\text{-}93)$$

The pressure ratio based on ACI working stress design developed in Ref. 8-32 for determining the limit of applicability of Eq. 8-92 is

$$\frac{\bar{P}_{oe}}{f'_c} = \frac{1.35(\beta + 1)}{\dfrac{(R/t)(3\beta + 1)}{k + 2p(n - 1)} + \dfrac{(R/t)^2}{0.5k(1-k/3) + p(n - 1)(1 - d'/d)(1 - d'/kd)}} \qquad (8\text{-}94)$$

At the collapse pressure ratio (Eq. 8-90), the ultimate deflection can be estimated by (Ref. 8-32)

$$\frac{\delta_u}{R} = \frac{f_y/E_s}{2\left|1 - \dfrac{87,000}{87,000 + f_y}\left(\dfrac{3\beta - 1}{3\beta + 1}\right)\right|} \quad \text{(English)}$$

$$= \frac{f_y/E_s}{2\left|1 - \dfrac{60,000}{60,000 + f_y}\left(\dfrac{3\beta - 1}{3\beta + 1}\right)\right|} \quad \text{(SI)} \qquad (8\text{-}95)$$

and

$$\left(\frac{\delta_u}{\delta_e}\right)_{RC} = \frac{\text{Eq. 8-95}}{\text{Eq. 8-92}}$$

8.9.5 Horizontal Cylinders

In order for the cylindrical section shown in Fig. 8-25 to collapse with a four-hinge mechanism, it is necessary that points A and C move inward and points B and D move outward. Any such outward movement in a buried cylinder will be resisted by the surrounding soil which will result in increased lateral pressure, i.e., an increase in q relative to $\bar{p}$. A net effect is the smoothing out of the nonuniform pressure component as mentioned previously along with a reduction in moment.

This trend is noted in the survey of buried cylinder test data reported in Ref. 8-33. Relatively flexible cylinders tend to mobilize more passive soil resistance at the springline, points B and D, with a corresponding decrease in moment at these points. Evidence of this type of behavior can also be inferred from the caving mode of failure noted many times in buried cylinder tests. The caving mode of failure is a three-hinge mechanism with plastic hinges at A and at θ = 30 to 60 degrees on both sides of A (Fig. 8-25). For a cylinder loaded from above, it appears plausible that mobilization of lateral earth pressures could force the ring toward a $\bar{p} \to 0$ behavior leaving the upper arc of the section to carry the applied pressure by beam action. Very stiff cylinders will not deflect as readily and will tend to develop larger springline moments.

Although it was concluded in Ref. 8-33 that moments at the crown and invert (points A and C in Fig. 8-25) will generally be larger than at the springline, it is still recommended that cylinder sections be designed symmetrically since the load may come from any direction as mentioned previously. As shown in Section VII, it is quite possible that the maximum ground shock loading may be horizontal rather than vertical and the springline in the connotation discussed thus far becomes the crown, and vice versa.

A significant point noted in Ref. 8-33 was the effect of soil discontinuities on the loads transmitted to buried cylinders. For this reason and the uncertainties associated with cylinders buried in cohesive soils, it was recommended that buried cylinders be placed in select backfill of granular soil. Particular attention should be paid to bedding underneath the cylinder as is done with well-constructed buried pipelines. It was also noted that culvert and sewer pipe failures are usually associated with bending stresses or excessive deflection and almost never with direct compressive strengths of the sections, which points out the wisdom of designing for some magnitude of alternating pressure, $\bar{p}$. A minimum steel ratio of 0.005 in each face and in both directions, is also recommended.

A buried horizontal cylinder can be designed or analyzed as outlined in preceding paragraphs after determination of the loads of interest as described in Section VII. A coefficient of lateral soil pressure can be incorporated into the load function of Fig. 8-25 by

$$K_o = p_h/p_v = \frac{\beta - 1}{\beta + 1} \tag{8-96}$$

For relatively thin cylindrical sections, the use of the mean radius, R, is generally applicable for determination of both load and section response. For the larger thicknesses typically encountered with reinforced concrete sections, it is advisable to use the outer radius, R_o, for determination of load and the mean radius for section response.

8.9.6 Vertical Cylinders

Vertical cylinders are generally utilized for missile silos and access shafts to deeper facilities in protective construction. The primary differences between design or analysis of vertical and horizontal cylinders are (1) vertical cylinders will experience significant axial loads from the closure or closure footings, and (2) that portion of a vertical cylinder near the surface can expect to experience larger alternating components of pressure than the lower part of the vertical cylinder.

In the absence of better information, values of $\bar{p}_o = p_{so}$ and $\beta = 1$ can be used for design of vertical cylinders from a depth of $2R_o$ to the surface. Below a depth of $2R_o$, $\bar{p}_o$ can be taken as the horizontal free-field soil pressure and β as 20. Axial loads from the closure are assumed to be carried by the cylinder in column action.

For purposes of target analysis, a judgment must be made as to the most probable loads and the response of the structure estimated as previously described.

8.9.7 Circular Arches

The behavior of circular arches is similar in many respects to that of horizontal cylinders, i.e., a 180-degree circular arch can be treated as one-half the ring shown in Fig. 8-25 with expressions previously furnished and appropriate consideration of the arch footings at points B and D. Arches may be employed aboveground in protective construction applications. In these cases, the previous discussion of the effect of the surrounding soil on the structural behavior is, of course, not applicable. Whether aboveground or buried, however, the loading on the arch can be expected to contain both uniform and nonuniform components. After selection of loads applicable to the case of interest as described in Section VII and a judgment made as to appropriate values for q and $\bar{p}$, the previous expressions are generally applicable for design or analysis taking the maximum thrust and moment as (180-degree arch only)

$$P_{max} = \left(\frac{\bar{p}_o R}{3}\right)\left(\frac{3\beta + 1}{\beta + 1}\right)$$

$$M_{max} = \frac{\bar{p}_o R^2}{3(\beta + 1)}$$

It will almost always be found necessary to consider the interaction of axial force and moment in arches as was found to be the case with cylinders.

It is usually appropriate to treat arches with central ang[illegible] of less than 90 degrees as straight members. For central angles between 90 and 180 degrees, one can begin with Eqs. 8-74 and 8-76 taking θ as one-half the central angle and point A (Fig. 8-25) as the crown of the arch and develop expressions to fit the particular problem and boundary conditions of interest.

Simplified expressions which can be used for preliminary investigation of arches with central angles between 90 and 180 degrees are presented in Ref. 8-2. These expressions assume a uniform load component, p_c, and a non-uniform component of constant magnitude p_f which acts inward on the windward side and outward on the leeward side (see Fig. 7-20). After selection of appropriate values for p_c and p_f based upon consideration of the actual peak applied load and the problem at hand (aboveground, buried, etc.),

$$P_{max} = p_c R \tag{8-97}$$

$$M_{max} = \frac{1}{8} p_f (\phi R)^2 \left|\frac{\gamma^2}{\gamma^2 - 1}\right| \quad \text{(hinged arch)} \tag{8-98}$$

$$M_{max} = \frac{1}{11.7} p_f (\phi R)^2 \left|\frac{\gamma^2}{\gamma^2 - 0.6}\right| \quad \text{(fixed arch)} \tag{8-99}$$

$$(p_c)_{cr} = \frac{EI}{R^3} (\gamma^2 - 1) \quad \text{(hinged arch)} \tag{8-100}$$

$$(p_c)_{cr} = \frac{EI}{R^3} (\gamma^2 - 1)(2 + 1/\gamma) \quad \text{(fixed arch)} \tag{8-101}$$

where

ϕ = one-half the arch central angle (radians)

$\gamma = \pi/\phi$

The above values for $(p_c)_{cr}$ assume the arch to be buried with a depth of cover of at least one-fourth its span. For aboveground arches, two-thirds the above $(p_c)_{cr}$ values are recommended (Ref. 8-2).

8.10 DOMES

8.10.1 Introduction

The response of a dome to blast effects must consider two components of loading and their associated response modes. The importance of either component depends upon the position of the dome relative to the ground surface. For a fully buried dome, the loading tends to be of a more symmetrical nature and, as such, produces predominately compressive stresses within the dome. On the other hand, when the dome is on the ground surface, the reflection and drag phases of the loading pulse generate more of an unsymmetrical loading. This latter case, for convenience of identification, is referred to as the flexural mode, even though the stresses produced by it are primarily membrane stresses. The two components of load are discussed in Section VII and illustrated in Fig. 7-23, which also identifies the notation used in the following discussion.

The membrane analysis presented herein neglects the effect of the discontinuity of a dome shell caused by the foundation or ring beam at the springline. Although this boundary influence is local in nature, it should be considered in final design or analysis. Reference 8-34 treats the problem of edge effects on domes.

Under the uniform radial loading associated with the compression mode, the dome is assumed to deflect into a shape consistent with a membrane stress state, and a state of uniform compression exists everywhere within the dome. These compressive forces per unit width are

$$T_\alpha = T_\theta = \frac{p_c R}{2} \qquad (8\text{-}102)$$

where p_c is a uniform radial pressure.

The drag and reflection phases of the blast wave generate an unsymmetrical loading on the dome. This loading is approximated as a radial force varying sinusoidally, in both meridional and circumferential directions, as shown in Fig. 7-23.

At any point, the intensity of the sinusoidal load is given as $p_f \sin\alpha\cos\theta$; the corresponding membrane forces per unit width are given by

$$T_\alpha = -\frac{p_f R}{3\sin\phi}\left\{\frac{(2+\cos\alpha)(1-\cos\alpha)\cos\alpha}{(1+\cos\alpha)\sin\alpha}\right\}\cos\theta \qquad (8\text{-}103)$$

$$T_\theta = -\frac{p_f R}{3\sin\phi}\left\{\frac{(3+4\cos\alpha+2\cos^2\alpha)(1-\cos\alpha)}{(1+\cos\alpha)\sin\alpha}\right\}\cos\theta \qquad (8\text{-}104)$$

$$T_{\alpha\theta} = -\frac{p_f R}{3\sin\phi}\left\{\frac{(2+\cos\alpha)(1-\cos\alpha)}{(1+\cos\alpha)\sin\alpha}\right\}\sin\theta \qquad (8\text{-}105)$$

The force $T_{\alpha\theta}$ represents a shearing force per unit width in the dome shell at the foundation.

The buckling resistance of the dome should be higher than that in the compression and flexural modes of response. Reference 8-35 defines the buckling resistance of spherical shells, expressed in terms of a uniform radial load, to be

$$p_{cr} = \frac{2Eh^2}{R^2\sqrt{3(1-\nu^2)}} \qquad (8\text{-}106)$$

where ν is Poisson's ratio for the dome material.

Experimentally determined critical pressures for thin shells deviate considerably from the classical elastic value given by Eq. 8-106. The two principal reasons for these differences are thought to be that small deflection theory, although adequate for the computation of buckling loads for plates and bars, breaks down when applied to shells, and that the initial imperfections in shape have a pronounced influence in reducing the critical load. For concrete shells, creep must also be considered. Because of these factors, the present thinking of shell roof designers is that actual buckling loads are about 1/2 to 1/3 those given by Eq. 8-106. However, since the shells used in protective construction are relatively thick and have a low dead load to design load ratio, reductions in the critical pressure are not expected to be as severe.

For a dome that is barely fully buried, the critical buckling pressure may be taken as that given by Eq. 8-106; for an aboveground dome, the buckling pressure is about 2/3 of that value. For intermediate depths, interpolate linearly between these two limits. When the depth of burial is greater than that necessary to constitute the fully buried case, the possibility of buckling need not be investigated.

8.10.2 Reinforced Concrete

It is recommended that a minimum steel ratio of 0.0025 be used in each direction in each face of reinforced concrete domes.

a. Uniform Compression Mode

The resistance of a reinforced concrete dome in this mode is obtained from Eq. 8-17 for axial load capacity of reinforced concrete sections and Eq. 9-102 for thrust.

$$P_c = (1.7f'_c + 2p_t f_y)h/R \qquad (8\text{-}107)$$

b. Flexural Mode

Although it is referred to as the flexural mode, the unsymmetrical loads of Fig. 7-23 are resisted primarily by membrane action. Since the magnitude of thrust caused by the flexural components of load varies with location, it is theoretically possible to vary the percentage of steel. Practically, it is best to provide a thrust capacity equal to the maximum value required. For a hemispherical dome, the maximum thrust is

$$T_\theta = p_f R \qquad (8\text{-}108)$$

and the resistance of a reinforced concrete dome in the flexural mode, expressed in terms of the maximum value of the nonuniform load component, is

$$P_f = (0.85f'_c + p_t f_y)h/R \qquad (8\text{-}109)$$

c. Shear

The shear resistance of the dome cross section can be determined from expressions in paragraph 8.3.4. The maximum value of the horizontal shear occurs at the springline and is given by

$$P_s = 2p_f R/3 \qquad (8\text{-}110)$$

d. Buckling

The buckling strength of a reinforced concrete dome is found from Eq. 8-106 by substituting appropriate values of properties of the section. The critical uniform radial pressure on a spherical dome required to cause buckling is approximated by

$$P_{cr} = 1.2E_c h^2/R^2 \qquad (8\text{-}111)$$

8.10.3 Steel

a. Uniform Compression Mode

The resistance of a steel dome in this mode is given by

$$P_c = 2f_y h/R \qquad (8\text{-}112)$$

b. Flexural Mode

The resistance of a steel dome in the flexural mode is given by

$$P_f = f_y h/R \qquad (8\text{-}113)$$

c. Shear

The shear capacity of the steel dome cross section can be determined from guidance in paragraph 8.4.4 and this capacity compared to the value given by Eq. 8-110.

d. Buckling

The buckling strength of a steel dome is obtained from Eq. 8-106 by substituting appropriate values of the properties of the steel cross section.

8.11 COMPOSITE ELEMENTS

8.11.1 Closures

A commonly used structural concept for large closures at high overpressure levels is the concrete slab confined by a steel shell as shown in Fig. 8-28. In most cases, the steel shell serves multiple functions as reinforcing for the concrete, an electromagnetic radiation shield, and a concrete spall inhibitor.

Although experimental data indicate that deep members of this type will rarely, if ever, fail in flexure,

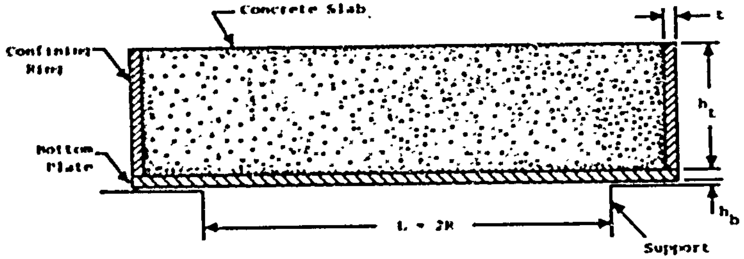

Figure 8-28 Composite Slab Configuration

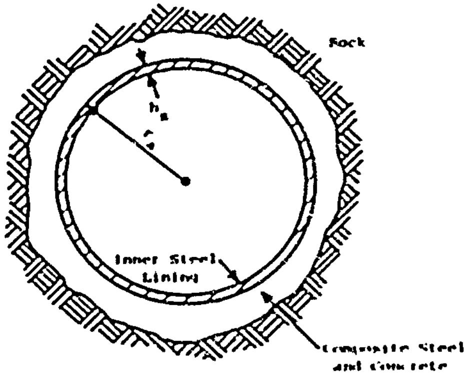

Figure 8-29 Cross Section of Composite Tunnel Liner

their flexural resistance might be a significant factor for some slab geometries. Reference 8-30 suggests a method for estimating the flexural load capacity which includes an allowance for increased moment capacity due to horizontal thrust generated by friction between the bottom of the slab and its supports. If it is assumed that the support bearing area has a width of one-fourth the clear span radius, the flexural capacity of simply supported, circular, composite slabs is given by

$$P_f = \frac{5.4 f_y h_b d}{R^2} + \frac{1.1 P_{so} d}{R} + \frac{0.6 P_{so} h_b}{R} \quad \text{(English)}$$

$$= \frac{3.7 f_y h_b d}{R^2} + \frac{0.8 P_{so} d}{R} + \frac{0.4 P_{so} h_b}{R} \quad \text{(SI)} \qquad (8\text{-}114)$$

where

d = effective depth of slab

P_f = uniformly distributed ultimate load

h_b = thickness of bottom steel plate

R = clear span radius

Theoretical and experimental investigations of deep slabs have indicated that the ultimate strength of these members is strongly dependent on their shear capacity. Reference 8-36 suggests an approach to evaluating the shear capacity of composite members which considers a contribution made by the bottom steel plate and the confining steel ring. If it is assumed that the critical section for shear occurs at 0.2R from the support, the ultimate shear capacity is given by

$$P_s = 2 f_y \left(\frac{h_b}{R}\right) + 30\sqrt{f'_c}\left(\frac{h_t}{R}\right) + 3 f_y \left(\frac{h_t}{R}\right)\left(\frac{t}{R}\right) \quad \text{(English)} \qquad (8\text{-}115)$$

~~= [illegible] (SI)~~

$$P_s < f'_c + 4.1 f_y \left(\frac{t}{R}\right)$$

where

h_t = depth of concrete within the steel shell

t = thickness of the confining steel ring

Although the range of applicability of Eqs. 8-114 and 8-115 has not been established, it is recommended that they be used for R/d ratios of less than, or equal to, 6. For R/d ratios greater than 6, it is suggested that the closure be treated as a two-way slab as outlined in paragraph 8.7.

8.11.2 Rock Cavity Linings

The structural configuration considered is shown in Fig. 8-29, a composite steel and concrete liner. The following procedure for analysis of such liners is taken from Ref. 8-37 where it is discussed in greater detail and applied to a variety of conditions. The analysis method can be applied to horizontal or vertical tunnels in rock.

A stress concentration factor of 2, corresponding to a circular hole subjected to equal compressive stresses in two perpendicular directions, i.e., a uniform stress field, is assumed for the analysis. It is also assumed that the steel lining will behave elastic-plastically, and, for strains beyond yielding, the entire cross section is stressed to the yield point, i.e., buckling does not occur. The radial stresses and circumferential strains are assumed to be equal in the concrete and steel at the interface between the two liners. The same relationship is assumed for the interface between the concrete and rock. A condition of uniform plane strain is also assumed.

The radial pressure exerted by the steel liner against the inner surface of the concrete liner is given by

$$\sigma_{ra} = \frac{h_s f_y}{r_a} \qquad (8\text{-}116)$$

where

h_s = thickness of the steel liner

r_a = radius to inside of concrete lining

In the inelastic range, the circumferential strength of the concrete lining is given by

$$\sigma_0 = f'_c + k_s\sigma_{ra} \qquad (8\text{-}117)$$

where

$k_s = \tan^2(45° + \phi/2)$

ϕ = apparent angle of internal friction of material

The factor k_s relates maximum and minimum principal stresses in the liner material and, for concrete, is generally taken to be equal to 4. For most rocks, the value of k_s ranges from 4 to about 10 or 12 (Ref. 8-37). The insitu values of k_s for rock are probably lowered by the occurrence of joints and other irregularities.

From the preceding equations and assumptions and a given strain value for the steel liner, the radial stress and circumferential strain at the inside surface of the concrete liner are established. Proceeding from this point, using appropriate properties of the medium in which stress and strain are being determined, corresponding quantities can be determined at the interface between succeeding elements and, finally, to a free-field stress.

The analysis requires evaluation of two expressions involving the difference in radial and circumferential stresses at the point of interest. These expressions are related to the elastic and inelastic ranges.

$$S = \frac{E\epsilon_0}{1 - \nu^2} - \left|\frac{1 - 2\nu}{1 - \nu}\right|\sigma_r \qquad \text{(Elastic)} \qquad (8\text{-}118)$$

where

S = elastic stress factor

E = modulus of elasticity for medium of interest
ϵ_θ = circumferential strain at point
ν = Poisson's ratio for medium of interest
σ_r = radial stress at point

$$Y = \sigma_u + (k_s - 1)\sigma_r \qquad \text{(Inelastic)} \qquad (8\text{-}119)$$

where

Y = inelastic stress factor
σ_u = unconfined compressive strength of medium of interest

If the value of S is known at a given radius, r_1, its value at another radius can be found from

$$S_2 = S_1\left(\frac{r_1}{r_2}\right)^2 \qquad (8\text{-}120)$$

where

S_1 = known value of S
r_2 = new radius

Similarly, for the inelastic case

$$Y_2 = Y_1\left(\frac{r_2}{r_1}\right)^{k_1-1} \qquad (8\text{-}121$$

where Y_1 is the known value of Y. If S is greater than Y at a given radius, the conditon of the material is plastic, and if it is less, the condition is elastic. The boundary between the elastic and inelastic regions of the material occurs at a radius, r_e, where S is equal to Y. This radius can be found from

$$\frac{S}{Y} = \left(\frac{r_e}{r}\right)^{k_s+1} \qquad (8\text{-}122)$$

where r is the radius corresponding to the known values of S and Y. At $r = r_e$, the condition is elastic and the radial and circumferential stresses are both equal to the uniform free-field stress. Then

$$\sigma_\theta + \sigma_r = S + 2\sigma_r = 2p_o \qquad (8\text{-}123)$$

where p_o is the free-field stress.

The free-field stress can also be determined from the values of S and Y at $r = r_e$ as follows

$$P_o = K_f Y^{\left(\frac{2}{k_s+1}\right)} S^{\left(\frac{k_s-1}{k_s+1}\right)} - \left(\frac{\sigma_u}{k_s-1}\right) \qquad (8\text{-}124)$$

where

$$K_f = \frac{k_s + 1}{2(k_s - 1)}$$

In the inelastic region, if Y is known σ_r can be determined from Eq. 8-119. In the elastic region, where S is known, σ_r is obtained from Eqs. 8-123 and 8-124. If P_o is known, σ_r can be obtained from Eq. 8-123.

In both the elastic and inelastic regions, the circumferential strain is obtained from

$$\epsilon_\theta = \frac{1-\nu^2}{E}\left[S + \left(\frac{1-2\nu}{1-\nu}\right)\sigma_r\right] \qquad (8\text{-}125)$$

In summary, starting with an initial given thickness of steel and concrete liners and a specified value of strain in the steel liner, the corresponding free-field stress capacity can be determined from the above procedure.

Figure 8-30 from Ref. 8-37 can be used to facilitate analysis of a liner. The data presented are for $k_s = 4$ and a stress concentration factor of 2. The abscissa in Fig. 8-30 is S on a logarithmic scale, the ordinate is Y, also on a logarithmic scale. Lines sloping up to the right are values of r_e/r and lines sloping upward to the left are a parameter, Q, defined to be

$$Q = P_o + \frac{\sigma_u}{k_s - 1} \qquad (8\text{-}126)$$

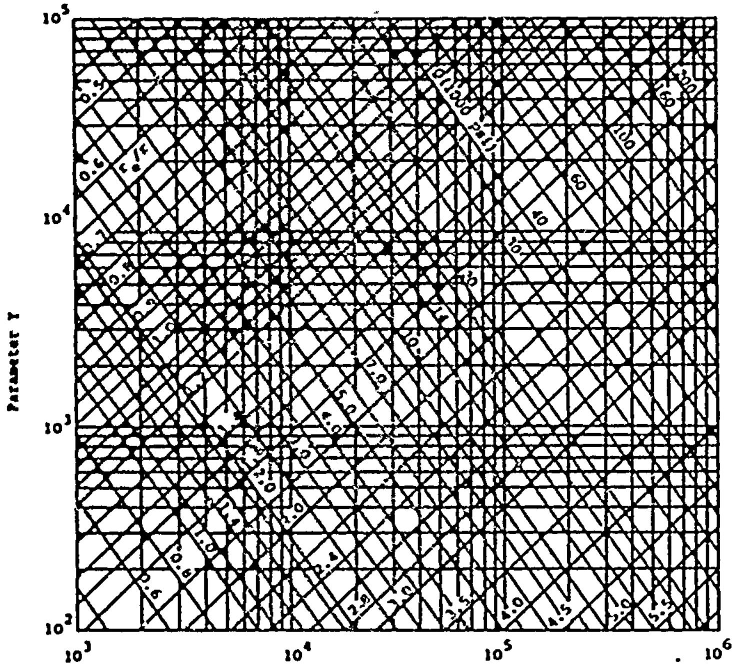

(Stress concentration factor = 2; k_s = 4)

Figure 8-30 Chart for Computation of Stresses in Tunnel Linings (Ref. 8-37)

The scales for Q and r_e/r are also logarithmic. Above the line r_e/r equal to 1 the behavior is elastic; below this line, behavior is inelastic. If σ_r and ε_θ are known for a radius r, then S and Y can be calculated from Eqs. 8-118 and 8-119. A point is thereby established on Fig. 8-30 which gives values of r_e/r and Q. If the point falls below the line r_e/r equal to 1, p_o can be determined from Eq. 8-126 and the radius at which elastic action begins can be determined. If the conditions are desired at a different radius, r_2, a new point is established at the same Q value and the new ratio, r_e/r_2. This point establishes values of Y and S at the new radius. If the point falls in the elastic region of Fig. 8-30, the value of Y is not valid, but the value of S is always valid.

If Y is valid, σ_r can be calculated from Eq. 8-119 since σ_u and k_s are known for a given material. With σ_r known, ε_θ can be determined from Eq. 8-125 using the new value of S.

If the new point falls in the elastic region of Fig. 8-30, σ_r can be determined from Eq. 8-123, since both S and p_o are known. Equation 8-125 can then be used to determine ε_θ.

If the original point falls in the elastic region, p_o can be determined using Eq. 8-125. For this case, the initial value of Y is not valid and p_o is used to establish an initial value of Q using Eq. 8-126. This value of Q, with S, establishes a starting point for determination of parameters at other radii. In going from one radius to another, Q is always a constant.

8.11.3 Liners With Crushable Backpacking

a. Introduction

Another concept for composite liners in high pressure regions is shown in Fig. 8-31. This concept

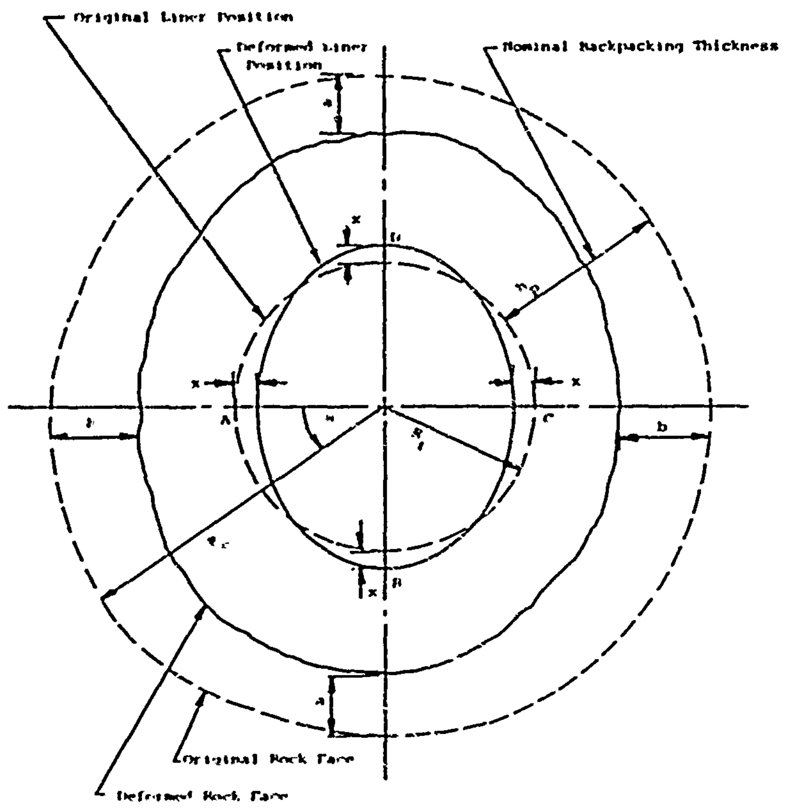

Figure 8-31 Assumed Deformation of Rock Face, Liner and Backpacking

is typically employed in rock media. The crushable backpacking can be one of several materials, e.g., foamed concrete or polyurethane foam, which have essentially elastic-plastic stress-strain curves and can withstand relatively large strains before the onset of strain hardening. The following analytical procedure is taken from Refs. 8-38 and 8-39.

The backpacking thickness must satisfy two criteria: (1) absorb energy transmitted by the stress wave in the rock, and (2) keep the crushed rock from contacting the structural liner. If it is assumed that the strain energy absorbed by the backpacking must be at least equal to the strain energy which would have been absorbed in the rock that was removed to form the cavity, then the minimum thickness of backpacking is given by

$$h_p = R_o \left\{ 1 \pm \sqrt{1 + \frac{\sigma_y(\varepsilon_y - 2\varepsilon_r)}{2\sigma_o\varepsilon_o}} \right\} \qquad (8\text{-}127)$$

where

R_o = radius of the undeformed cavity

σ_y = yield stress of the rock

σ_o = yield stress of backpacking material

ε_y = yield strain of the rock

ε_r = peak direct-induced radial strain (Eq. 5-75 and Eq. 5-56 or 5-65)

ε_o = limit of strain in backpacking before strain hardening occurs

Equation 8-127 neglects the small elastic deformation of the backpacking.

The idealized stress-strain curve for rock can be obtained from an unconfined compression test similar to that used for concrete. One technique for obtaining an idealized elastic-plastic stress-strain curve from such tests consists of adjusting the yield stress for the idealized curve so that the strain energies, represented by the area under the idealized and real stress-strain curves, are approximately equal at the strain level of interest. Similarly, an idealized stress-strain curve is required for the backpacking. Representative idealized curves that might be obtained are illustrated in Figs. 8-32 and 8-33.

The estimated inward displacements of the rock surface shown in Fig. 8-31 are taken as

$$a = \varepsilon_r R_o \qquad (8\text{-}128)$$

$$b = 100\varepsilon_r R_o \qquad (8\text{-}129)$$

If b is found to be greater than $\varepsilon_o h_p$, bulking of the rock controls the required backpacking thickness. In this case, h_p must be made large enough to preclude straining the backpacking into the strain-hardening region by rock bulking.

The inward motion of the rock will impose loads on the liner that can be represented by the load function shown in Fig. 8-25, i.e., $\bar{p}_o = q + \bar{p}\cos 2\theta$. So long as the backpacking is not deformed into the strain-hardening region, the peak pressure that can be imposed on the liner is

$$\bar{p}_o = q + \bar{p} = \sigma_o \qquad (8\text{-}130)$$

where σ_o is the yield stress of the backpacking. For the

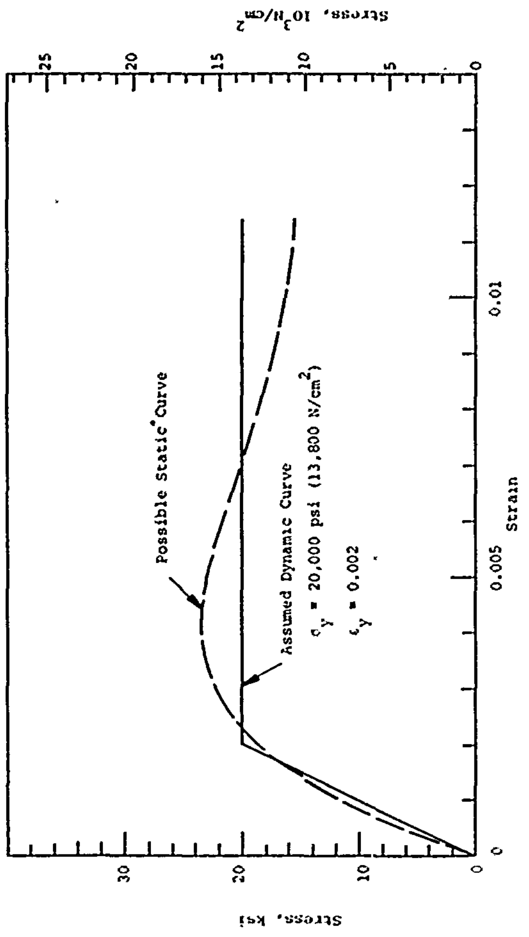

Figure 8-32 Assumed Dynamic Stress-Strain Curve for Rock

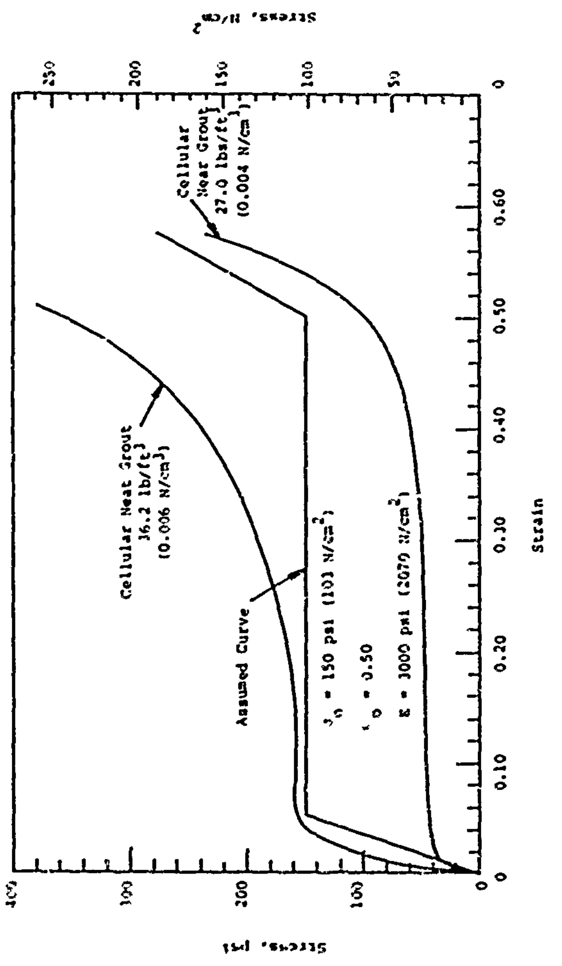

Figure 8-33 Assumed Stress-Strain Curve for Backpacking

liner deflections, x, shown in Fig. 8-31, the net strain in the backpacking will be $(b - x)/h_p$ along the horizontal axis and $(a + x)/h_p$ along the vertical axis. The average of the pressures corresponding to these points is the uniform component of pressure, q, and the difference from the average is the nonuniform component, $\bar{p}$, as illustrated in Fig. 8-34.

The first step in the design process consists of determining the properties of the rock and backpacking material. These properties are preferably determined from experimental data; otherwise they must be assumed (see Figs. 8-32 and 8-33). With these properties and the required functional space envelope defined by R_i, the required rock cavity radius R_o for the threat of interest is established on the basis of Eq. 8-127 or 8-129, depending upon whether or not bulking of the rock controls. A trial liner section is selected and an interaction diagram plotted in terms of q and $\bar{p}$. Net strain in the backpacking due to liner deflection and allowable strain in backpacking due to liner deflection are plotted as functions of $\bar{p}$ beneath the $q - \bar{p}$ interaction diagram. The most economical sect'on has been found when the intersection of the predicted and allowable packpacking strain curves due to liner deflection corresponds to the allowable $\bar{p}$ from the $q - \bar{p}$ interaction diagram. The final ·step is to check the possibility of buckling of the liner.

b. Reinforced Concrete

For preliminary design or analysis, the liner can be approximated as a beam subjected to a bending moment and an axial compressive load. Its length is taken as one-fourth of the ring circumference. Interaction diagrams such as Fig. 8-20 are used to facilitate

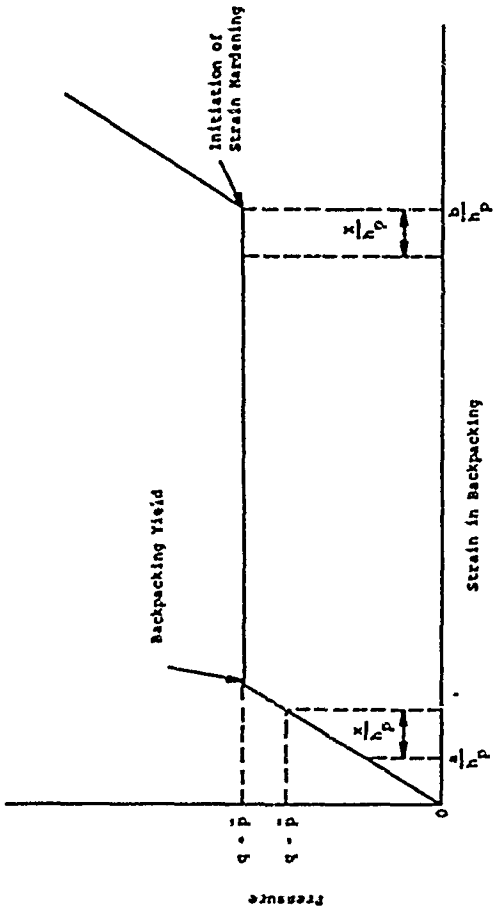

Figure 8-34 Relation Between Pressure in Backpacking and Deformations of Liner and Rock Face

the process. In order to simplify the initial calculations, the thrust due to the *nonuniform component* ($\bar{p}$) of load is neglected.

Using $P_u = qR$ and $M = P_u e' = \bar{p}R^2/3$ along with the expressions for Γ and Γ' from Fig. 8-20, q and $\bar{p}$ can be defined in terms of the properties of the reinforced concrete liner, i.e.,

$$q = \frac{\Gamma t f'_c}{R_i + t/2} \tag{8-130}$$

$$\bar{p} = \frac{3\Gamma' t^2 f'_c}{(R_i + t/2)^2} \tag{8-131}$$

where

t = the thickness of the liner

R_i = inside radius of the liner

A trial thickness can be obtained by solving Eq. 8-130 for t taking q equal to the yield stress of the backpacking and assuming a value of Γ, i.e.,

$$t = \frac{qR_i}{\Gamma f'_c - q/2} \tag{8-132}$$

A Γ *of 0.45 or less is suggested* in order to keep P_u below the balance point and avoid brittle failures. A *steel ratio* is then assumed (between 0.005 and 0.02) and concrete protection for the reinforcing determined in accordance with Ref. 8-12. With this latter step, it is now possible to determine the d/t ratio and select the appropriate interaction diagram from Fig. 8-20. The interaction diagram is then replotted in terms of q and $\bar{p}$ using Eqs. 8-130 and 8-131. The line $q + \bar{p} = \sigma_o$ shown in Fig. 8-35 represents the upper limit to the combination of σ and $\bar{p}$ allowable for the selected backpacking.

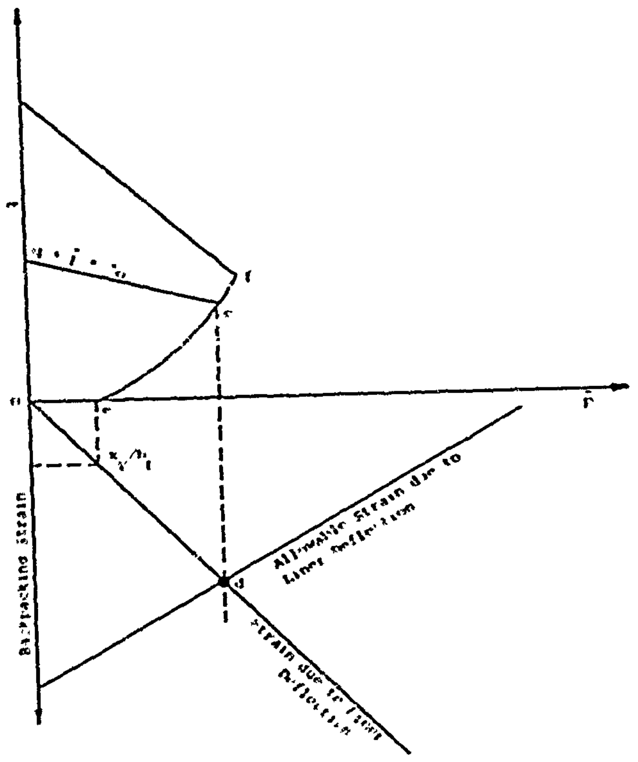

Figure 8-35 Typical Interaction Diagrams for Reinforced Concrete Liner and Backpacking Material

Next, strains in the backpacking due to deflection of the liner are calculated. Equation 8-93 can be written

$$\frac{x_y}{h_p} = \frac{(R_i + t/2)^2}{1215dh_p} \qquad (8\text{-}133)$$

The value obtained from Eq. 8-133 corresponds to $\bar{p}$ when $q = 0$ (see Fig. 8-35) and defines the backpacking strain due to deflection of the liner. Allowable strain in the backpacking as a function of $\bar{p}$ is established by considering total strain in the backpacking and the relation (see Fig. 8-34)

$$q - \bar{p} = \sigma_p$$

where $\sigma_p = E_p\epsilon_p$ is the stress in the backpacking, E_p is the modulus of elasticity and $\epsilon_p = (a + x)/h_p$, the strain in the backpacking. The most economical section has been found when the three lines shown in Fig. 8-35 intersect at point d.

The final step is to check the buckling strength of the section to be sure it is at least equal to σ_o and verify that the section can carry the additional thrust due to the nonuniform component of load and remain in the ductile region of the interaction diagram (curve e-f in Fig. 8-35). The more rational expressions for behavior of the section given in Paragraph 8.9.4 can be used when more precise analyses are required.

c. Steel Liner

Design of steel liners with crushable backpacking can be accomplished with the same basic procedure outlined above for reinforced concrete liners. Buckling of the section, however, will almost always be found to be more critical than for reinforced concrete sections.

Properties of the backpacking and the surrounding medium must be known or assumed. Deformation of the cavity and the required backpacking thickness are determined as previously described. Since buckling of the section typically controls, it is suggested that a trial section be selected on the basis of Eq. 8-79 with $q_{cr} = 1.25\sigma_o$, where σ_o is backpacking yield stress. For purposes of illustration, the following discussion will be in terms of a steel liner of uniform thickness.

The moment of inertia of a rectangular cross section of unit width is $t^3/12$. Accordingly a trial thickness can be found by

$$t = R_i[5\sigma_o/E_B]^{1/3} \qquad (8\text{-}134)$$

After selection of a trial thickness, $R = R_i + t/2$ should be used in subsequent calculations.

Taking maximum axial force and moment from Eqs. 8-74 and 8-76 and the thrust and moment capacity of the section as $P_y = f_y t$ and $M_p = f_y z$, respectively, we can write (for a rectangular cross section)

$$\frac{P}{P_y} = \frac{qR + \bar{p}R/3}{f_y t} \qquad (8\text{-}135)$$

$$\frac{M}{M_p} = \frac{4\bar{p}R^2}{3f_y t^2} \qquad (8\text{-}136)$$

An interaction diagram such as shown in Fig. 8-17 can not be constructed in terms of $\bar{p}$ and q. The value of $\bar{p}$ at points b and c (Fig. 8-17) can be found by setting Eq. 8-136 equal to one, i.e.,

$$\bar{p}_c = \frac{3f_y t^2}{4R^2} \qquad (8\text{-}137)$$

The value of q at point b is found by setting Eq. 8-135 equal to 0.15 and using the value of $\bar{p}$ from Eq. 8-137.

$$q_b = \frac{f_y t}{R}\left(0.15 - \frac{t}{4R}\right) \qquad (8\text{-}138)$$

At point a, $\bar{p}$ is zero and $P/P_y = 1$, which leads to

$$q_a = f_y t/R \qquad (8\text{-}139)$$

The three points thus determined are connected by straight lines to form the design $q - \bar{p}$ interaction diagram shown qualitatively in Fig. 8-36. The allowable backpacking strain versus liner deflection curve as a function of $\bar{p}$ is constructed as described above for the reinforced concrete section. Backpacking strain due to liner deflection as a function of $\bar{p}$ for $q = 0$ can be found from

$$\frac{\delta_L}{h_p} = \frac{4R^4\bar{p}}{3E_s t^3 h_p} \qquad (8\text{-}140)$$

As before, the most economical section has been found when the three lines intersect at point d as illustrated in Fig. 8-36. When more detailed analyses are required, the procedures outlined in paragraph 8.9.3 can be employed.

Suitable steel liners can be designed with appreciable savings of metal by considering stiffeners, wide flange sections, etc., which increase the buckling stability of the section without appreciable loss in strength capability. The procedure outlined above would be applicable, but the expressions become more cumbersome, e.g., the expressions for I and Z are more complicated than the simple functions of t applicable to rectangular sections.

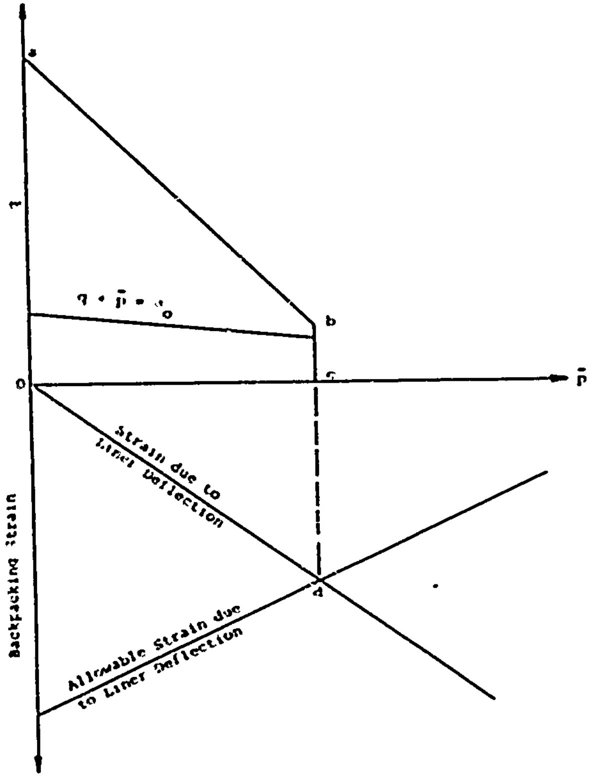

Figure 8-36 Typical Interaction Diagrams for Steel Liner and Backpacking Material

8.12 ILLUSTRATIVE EXAMPLES

8.12.1 <u>Closure Investigation</u>

a. GIVEN: A composite closure such as shown in Fig. 8-28 with the following properties.

h_b = 1.0 in (2.54 cm)	t = 1.0 in (2.54 cm)
d = 48.5 in (1.26 m)	f_y = 40,000 psi (27,600 N/cm^2)
R = 108 in (2.74 m)	
h_t = 48.0 in (1.22 m)	f'_c = 3750 psi (2580 N/cm^2)

b. FIND: The capacity of the closure in terms of a uniformly distributed load and the proportions of a two-way reinforced concrete slab to carry the same load.

c. SOLUTION: Determine the shear capacity of the composite slab as given by Eq. 8-115.

$$p_s = \frac{(2)(40{,}000)(1)}{108} + \frac{(30)(3750)^{1/2}(48)}{108} + \frac{(3)(40{,}000)(48)(1)}{(108)^2}$$

$$= 740 + 816 + 494 = 2050 \text{ psi } (1410 \text{ N/cm}^2)$$

Determine the flexural capacity of the composite slab as given by Eq. 8-114 taking p_{so} = 2050 psi.

$$p_f = \frac{(5.4)(40{,}000)(1)(48.5)}{(108)^2} + \frac{(1.1)(2050)(48.5)}{108} + \frac{(0.6)(2050)(1)}{108}$$

$$= 899 + 1010 + 11 = 1920 \text{ psi } (1320 \text{ N/cm}^2)$$

Composite slabs of these proportions are generally governed by shear rather than flexural behavior, so estimate the capacity of the given slab as 2000 psi (1380 N/cm^2).

To determine the proportions of a replacement two-way reinforced concrete slab, take the closure as simply supported and solve Eq. 8-60 for d with $p_c = 0.01$ $(p_c = 0)$, i.e.,

$$d = \left[\frac{p_f R^2}{5.4 f_y p_c}\right]^{1/2} = \left[\frac{(2,000)(108)^2}{(5.4)(40,000)(0.01)}\right]^{1/2}$$

$$d = 104 \text{ in } (2.64 \text{ m})$$

A slab of these proportions (L/d = 2.1) is obviously a deep slab and exceedingly unlikely to fail in flexure. Therefore, estimate the slab proportions based on shear in deep slabs as outlined in paragraph 8.7.1.b.

Equation 8-61 can be written in terms of h, the total slab depth (see Fig. 8-22) as

$$h = \frac{2Rp_s}{4C_v\sqrt{f'_c} + p_s}$$

Taking $C_v = 19$ leads to

$$h = \frac{(2)(108)(2000)}{(4)(19)(3750)^{1/2} + 2000} = 65.0 \text{ in } (1.65 \text{ m})$$

Calculate estimated reinforcement by solving Eq. 8-60 for p_c taking the slab as simply supported and the effective depth, d, as 62 in (1.57 m).

$$p_c = \frac{p_f R^2}{5.4\ f_y d^2} = \frac{(2000)(108)^2}{(5.4)(40,000)(62)^2} = 0.028$$

The given composite slab with a total depth of 49 in (1.24 m), then has a capacity of about 2000 psi (1380 N/cm^2). A two-way reinforced concrete slab with the same capacity would have a total depth of 65 in (1.65m) and a reinforcement ratio of 0.028. The steel would typically be laid both ways and in both faces in anticipation of rebound.

8.12.2 Buried Cylinder Behavior as a Function of Lateral Earth Pressure

a. GIVEN: A buried cylinder of uniform thickness and homogeneous elastic-plastic material with a radius-to-thickness ratio, R/t, of 10.

b. FIND: The loads to cause collapse of the cylinder for coefficients of lateral earth pressure, K_o, of 0, 1/4, 1/2, 3/4 and 1.

c. SOLUTION: Consider first the loading function shown in the following sketch.

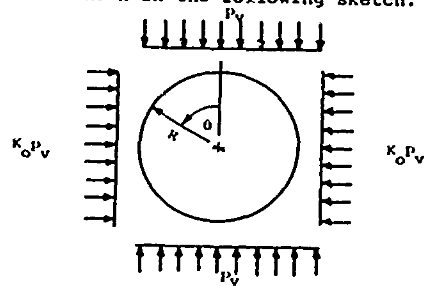

Expressions analogous to Eqs. 8-74 through 8-76 for the above loading can be shown to be

$$P_\theta = p_v R(K_o \cos^2\theta + \sin^2\theta)$$

$$V_\theta = -0.5 p_v R(1 - K_o)\sin 2\theta$$

$$M_\theta = 0.25 p_v R^2(1 - K_o)\cos 2\theta$$

Considering only one quadrant of the ring on the basis of symmetry, the four-hinge mechanism discussed in paragraph 8.9.3 is represented by hinges at $\theta_1 = 0°$ and $\theta_2 = 90°$. The caving mode mentioned in paragraph 8.9.5 would be represented by hinges at $\theta_1 = 0°$ and $0° < \theta_2 < 90°$. Making use of the criterion (Ref. 8-32)

$$\frac{M_\theta}{M_o} + \left(\frac{P_\theta}{P_o}\right)^2 \leq 1$$

where M_o is the moment capacity and P_o the thrust capacity of the section in the absence of other forces, the following expressions for collapse of the ring can be derived.

$$\left(\frac{p_v}{\sigma_y}\right)_{30^\circ} = \frac{12(K_o - 1)}{25K_o^2 + 6K_o + 1} \pm 4\sqrt{\left|\frac{3(1 - K_o)}{25K_o^2 + 6K_o + 1}\right|^2 + \frac{2}{25K_o^2 + 6K_o + 1}\left(\frac{t}{R}\right)^2}$$

$$\left(\frac{p_v}{\sigma_y}\right)_{45^\circ} = \frac{2(K_o - 1)}{5K_o^2 + 2K_o + 1} \pm 2\sqrt{\left|\frac{1 - K_o}{5K_o^2 + 2K_o + 1}\right|^2 + \frac{2}{5K_o^2 + 2K_o + 1}\left(\frac{t}{R}\right)^2}.$$

$$\left(\frac{p_v}{\sigma_y}\right)_{90^\circ} = \frac{K_o - 1}{K_o^2 + 1} \pm \sqrt{\left|\frac{1 - K_o}{K_o^2 + 1}\right|^2 + \frac{2}{K_o^2 + 1}\left(\frac{t}{R}\right)^2}$$

The subscripted angular values denote values of θ_2 and σ_y is the yield stress of the ring material in the preceding equations. Negative values of the above equations indicate p_v to be opposite in direction to that assumed, i.e., tensile rather than compressive external pressures.

It is of interest to attempt a comparison of the collapse loads from the load function above (Load A) with those of the load function shown in Fig. 8-25 (Load B). Interaction equations for the $q + \bar{p}\cos 2\theta$ loading are as follows.

$$\theta_2 = 30^\circ\text{:}\quad 72q^2 - 36q\bar{p} + 72\sigma_y\bar{p} + 5\bar{p}^2 = 72\sigma_y^2(t/R)^2$$

$$\theta_2 = 45^\circ\text{:}\quad 18q^2 - 6q\bar{p} + 12\sigma_y\bar{p} + \bar{p}^2 = 18\sigma_y^2(t/R)^2$$

$$\theta_2 = 90^\circ\text{:}\quad 9q^2 + 12\sigma_y\bar{p} + \bar{p}^2 = 9\sigma_y^2(t/R)^2 \qquad \text{(Eq. 8-84)}$$

The values of $\bar{p}$ and q are related to each other by Eq. 8-96 for the various values of K_o to solve the expressions above.

The preceding equations were solved for the given values of K_o and the results summarized in Table 8-5. Several points are apparent from these results.

- The $K_o = 1$ condition (hydrostatic pressure) requires by far the largest collapse load for both cases.
- Load case A results in lower collapse loads for all values of K_o less than one and for all failure modes.
- The $\theta_2 = 90^\circ$ mechanism has the lowest and the $\theta_2 = 45^\circ$ the highest collapse load for both load cases (investigation of $\theta_2 = 15^\circ$, 60° and 75° gives results greater than for $\theta_2 = 90^\circ$ and less than for $\theta_2 = 45^\circ$).

Based on these results, a caving mode of failure cannot occur, i.e., the ring fails in the 4-hinge mechanism ($\theta_2 = 90^\circ$) before the pressure reaches the value required for a caving mode of failure. A possible explanation of the fact that such failures do occur might be that the surrounding soil increases the moment capacity at the springline ($\theta_2 = 90^\circ$) either by lending the section greater stiffness or forcing the behavior toward $K_o = 1$ behavior in that area. Another general result which should be noted is the effect on the collapse load of any nonuniformity in the applied pressure.

8.12.3 Liners with Crushable Backpacking

a. GIVEN: A rock medium represented by Fig. 8-32 and a backpacking material with properties as shown in Fig. 8-33; a threat characterized by a strain in the rock of $\epsilon_r = 0.0025$; a required inner liner radius, R_i, of 16 feet (4.88m).

Table 8-5

COMPARISON OF BURIED CYLINDER COLLAPSE LOADS

Load / Mechanism	$K_o = 0$ Load A	$K_o = 0$ Load B	$K_o = 1/4$ Load A	$K_o = 1/4$ Load B	$K_o = 1/2$ Load A	$K_o = 1/2$ Load B	$K_o = 3/4$ Load A	$K_o = 3/4$ Load B	$K_o = 1$ Load A	$K_o = 1$ Load B
	$\frac{100p_v}{\sigma_y}$	$\frac{100\bar{p}_o}{\sigma_y}$	$\frac{100p_v}{\sigma_y}$	$\frac{100\bar{p}_o}{\sigma_y}$	$\frac{100p_v}{\sigma_y}$	$\frac{100\bar{p}_o}{\sigma_y}$	$\frac{100p_v}{\sigma_y}$	$\frac{100\bar{p}_o}{\sigma_y}$	$\frac{100p_v}{\sigma_y}$	$\frac{100\bar{p}_o}{\sigma_y}$
θ_2 = 30°(caving)	1.333	1.989	1.770	2.615	2.609	3.736	4.533	5.970	10.000	10.000
θ_2 = 45°(caving)	1.990	2.953	2.625	3.814	3.769	5.187	6.053	7.314	10.000	10.000
θ_2 = 90°(4-hinge)	0.995	1.491	1.321	1.968	1.952	2.860	3.596	4.896	10.000	10.000

Load A: $p_v = p_v$; $p_h = K_o p_v$

Load B: $p(\theta) = q + \bar{p}\cos 2\theta$

K_o = coefficient of lateral earth pressure = $\frac{p_v}{p_h} = \frac{q - \bar{p}}{q + \bar{p}}$

$\bar{p}_o = q + \bar{p}$

b. FIND: Suitable reinforced concrete and steel liners based upon f'_c = 3750 psi (2586 N/cm^2) for the concrete and f_y = 40,000 (27,580 N/cm^2) for the reinforcing steel and the steel section.

c. SOLUTION: First, estimate the thickness of reinforced concrete liner required with Eq. 8-132; set q equal to the backpacking yield stress, σ_o, and take Γ as 0.45.

$$t = \frac{(150)(192)}{(0.45)(3750) - 150/2}$$

$$t = 17.9 \text{ in, } say \text{ 18 in (45.7 cm)}$$

The radius to the outside of the liner thus becomes 192 + 18 = 210 in (5.33 m).

Next, determine the required radius, R_o, of the rock cavity and the thickness of the backpacking, h_p. Rewrite Eq. 8-127 as

$$\frac{h_p}{R_o} = 1 \pm \sqrt{1 + \frac{\sigma_y(\epsilon_y - 2\epsilon_r)}{2\sigma_o\epsilon_o}}$$

$$= 1 \pm \sqrt{1 + \frac{(20,000)[0.002 - (2)(0.0025)]}{(2)(150)(0.50)}}$$

$$\frac{h_p}{R_o} = 0.225$$

Check this value against the rock bulking requirement (Eq. 8-129), i.e.,

$$100\epsilon_r R_o \leq \epsilon_o h_p$$

$$\frac{h_p}{R_o} \geq \frac{100\epsilon_r}{\epsilon_o}$$

$$\geq \frac{(100)(0.0025)}{0.50}$$

$$\frac{h_p}{R_o} \geq 0.500$$

It is seen, therefore, that bulking of the rock controls and the rock cavity radius must be at least twice the thickness of the backpacking. Therefore,

$$R_o = R_i + t + h_p \qquad (\text{and } h_p/R_o = 0.5)$$

$$h_p = 210 \text{ in } (5.33 \text{ m})$$

$$R_o = 420 \text{ in } (10.67 \text{ m})$$

Construct a $q - \bar{p}$ interaction diagram.

For the first trial, set

$$p_t = \frac{A_{st}}{bt} = 0.01 \qquad (p = 0.005 \text{ each face})$$

$$d/t = 0.85 \qquad (d = 0.85 \times 18 = 15.3 \text{ in or } 38.9 \text{ cm})$$

$$m = \frac{f_y}{0.85f'_c} = \frac{40{,}000}{(0.85)(3750)} = 12.5$$

$$p_t m = (0.01)(12.5) = 0.125$$

Substituting various quantities determined above into Eqs. 8-130 and 8-131 leads to

$$q = \frac{\Gamma(18)(3750)}{192 + 9} = 335.8\Gamma$$

$$\bar{p} = \frac{\Gamma'(3)(18)^2(3750)}{(192 + 9)^2} = 90.2\Gamma'$$

These expressions are solved by picking as many values of Γ and Γ' as needed from the $p_t m$ curve = 0.125 of Fig. 8-20(b) to construct a meaningful $q - \bar{p}$ interaction diagram. For example,

Point	Γ	$q = 335.8\Gamma$	Γ'	$\bar{p} = 90.2\Gamma'$
$P_u = 0$	0	0	0.043	3.9
(arbitrary)	0.1	33.6	0.084	7.6
(arbitrary)	0.2	67.2	0.116	10.5
(arbitrary)	0.3	100.8	0.136	12.3
Bal Pt	0.46	154.5	0.143	12.9
$M = 0$	0.95	319.0	0	0

These values are plotted in Fig. 8-37.

Now construct the corresponding backpacking strain interaction diagrams as a function of $\bar{p}$. The allowable curve is independent of the liner, per se, and is constructed as follows. For $\bar{p} = 0$, the liner has no deflection and the strain in the backpacking is taken as that due to the movement of the rock face, a (see Figs. 8-31 and 8-34).

$$\epsilon_a = \frac{a}{h_p} = \frac{(0.0025)(420)}{210} = 0.005$$

The maximum elastic strain for the selected backpacking is 0.05 (see Fig. 8-33). Therefore, the maximum allowable strain due to deflection of the liner is 0.05 - 0.005 = 0.045. Plot $\bar{p} = 0$ and $x/h_p = 0.045$. Take an arbitrary value of x/h_p, say 0.035, and find the corresponding value of $\bar{p}$.

$$\epsilon_p = 0.035 + 0.005 = 0.04$$

$$\sigma_p = E_p\epsilon_p = (3000)(0.04) = 120 \text{ psi } (82.7 \text{ N/cm}^2)$$

$$q - \bar{p} = 120 \text{ psi and } q + \bar{p} = \sigma_o = 150 \text{ psi}$$

$$\bar{p} = 15 \text{ psi } (10.3 \text{ N/cm}^2)$$

Since the allowable strain function is a straight line, the two points thus determined are sufficient to plot the curve.

For the backpacking strain versus liner deflection curve, plot $x/h_p = 0$ for $\bar{p} = 0$. At $q = 0$, $\bar{p} = 3.9$ psi (2.69 N/cm^2). With Eq. 8-133 (a linear function of d),

$$\frac{x_y}{h_p} = \frac{(192 + 9)^2}{(1215)(15.3)(210)} = 0.0103$$

The combined interaction diagrams thus determined are shown in Fig. 8-37.

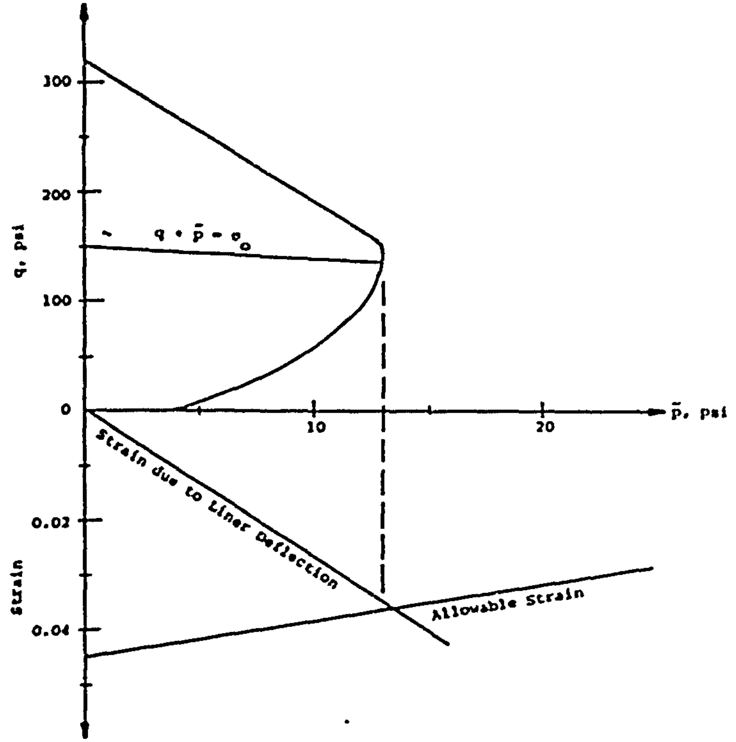

Figure 8-37 Interaction Diagrams for Reinforced Concrete Liner Example

As may be seen in Fig. 8-37, the trial section is reasonably satisfactory. Estimate the buckling strength of the trial section with Eq. 8-79.

$E_c = (33)(145)^{1.5}(3750)^{1/2} = 3.52 \times 10^6$ psi $(2.42 \times 10^6$ N/cm$^2)$

$\frac{1}{2}A_{st} = A_s = \frac{1}{2}(0.01)(18) = 0.09$ in^2 $(0.58$ cm$^2)$

$p = A_s/d = 0.09/15.3 = 0.006$

$I_c = (0.5)(15.3)^3[(5.5)(0.006) + 0.083] = 207.7$ in^3 $(3404$ cm$^3)$

$q_{cr} = (3)(3.52 \times 10^6)(207.7)/(201)^3 = 270$ psi $(186.2$ N/cm$^2)$

$q_{cr} > \sigma_o$ OK

The analyses may be continued utilizing more refined procedures described in the text to the extent necessary for the particulars of the problem of interest.

To select a solid steel liner, begin with Eq. 8-134.

$$t = 192\left[\frac{(5)(150)}{2.9 \times 10^7}\right]^{1/3} = 5.68, \text{ say } 6.0 \text{ in } (15.2 \text{ cm})$$

Leave the rock cavity radius, R_o, equal to 420 in (10.67 m) as previously determined. The backpacking thickness becomes

$$h_p = R_o - R_i - t = 420 - 192 - 6 = 222 \text{ in } (5.64 \text{ m})$$

Construct the $q - \bar{p}$ interaction diagram (Eqs. 8-137 through 8-139).

$$\bar{p}_c = \frac{(3)(40{,}000)(6)^2}{(4)(195)^2} = 28.4 \text{ psi } (19.6 \text{ N/cm}^2)$$

$$q_b = \frac{(40{,}000)(6)}{195}\left[0.15 - \frac{6}{(4)(195)}\right] = 175 \text{ psi } (120.8 \text{ N/cm}^2)$$

$$q_c = \frac{(40{,}000)(6)}{195} = 1231 \text{ psi } (849 \text{ N/cm}^2)$$

The allowable backpacking strain curve due to liner deflection is constructed in the same fashion as for the reinforced concrete liner.

$$\epsilon_a = \frac{\Delta}{h_p} = \frac{(0.0025)(420)}{222} = 0.0047$$

$$\text{Allowable } \epsilon_p = 0.05 - 0.0047 = 0.0453$$

$$\epsilon_p = 0.035 + 0.0047 = 0.0397$$

$$\sigma_p = (3000)(0.0397) = 119.1 \text{ psi } (82.1 \text{ N/cm}^2)$$

$$\bar{p} = 15.45 \text{ psi } (10.65 \text{ N/cm}^2)$$

Use Eq. 8-140 to find the strain in the backpacking due to linear deflection as a function of $\bar{p}$.

$$\frac{\Delta}{h_p} = \frac{(4)(195)^4\bar{p}}{(3)(2.9 \times 10^7)(6)^3(222)} = 0.00139\bar{p}$$

The combined interaction diagrams are shown in Fig. 8-38. The trial section appears somewhat overstrength as might be expected since it was proportioned on the basis of stability rather than strength.

For a second trial, investigate the hollow section shown in the following sketch.

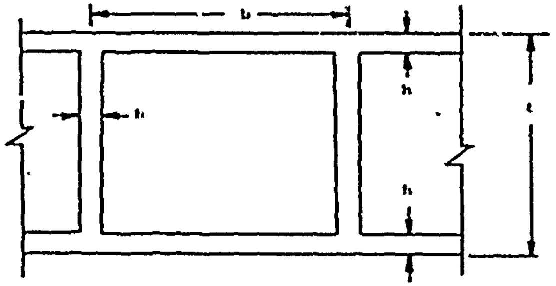

Hollow Steel Liner Section

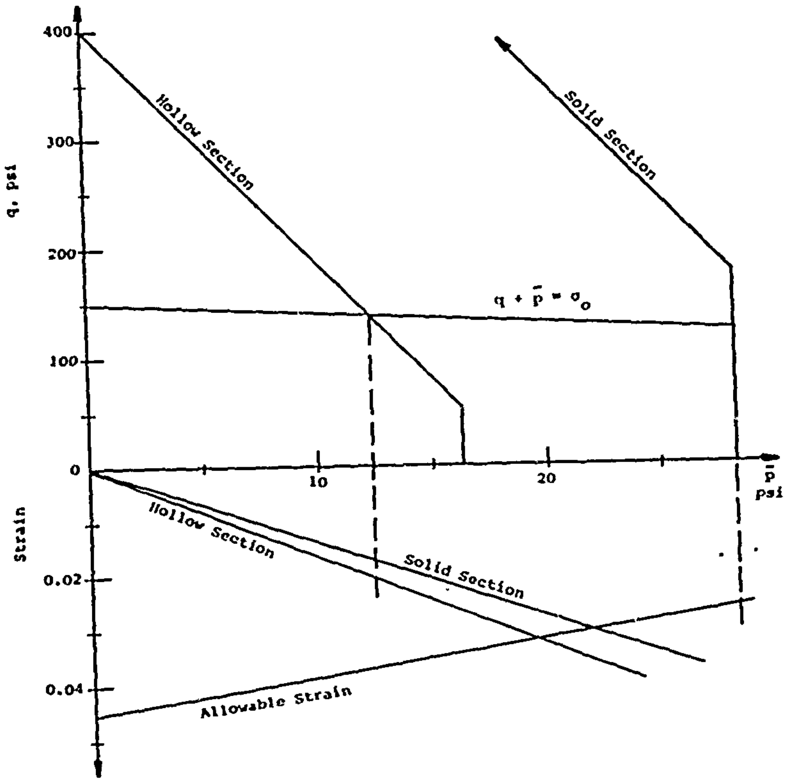

Figure 8-38 Interaction Diagrams for Steel Liner Example

Taking b = t and h = t/10,

$$A/t = 0.28t$$

$$I/t = 0.0447t^3$$

The analogous expression for Eq. 8-134 for these values of area and moment of inertia is

$$t = R_i \left| \frac{9.3\sigma_o}{E_s} \right|^{1/3}$$

$$t = 192 \left| \frac{(9.3)(150)}{2.9 \times 10^7} \right|^{1/3} = 6.98, \text{ say } 7.0 \text{ in } (17.8 \text{ cm})$$

Similarly, with $Z/t = 0.106t^2$ from Fig. 8-16,

$$\bar{p}_c = \frac{f_y t^2}{3.15R^2} = \frac{(40{,}000)(7)^2}{(3.15)(195.5)^2} = 16.3 \text{ psi } (11.2 \text{ N/cm}^2)$$

$$q_b = \frac{f_y t}{3R} \left| 0.126 - \frac{t}{3.15R} \right| = \frac{(40{,}000)(7)}{(3)(195.5)} \left| 0.126 - \frac{7}{(3.15)(195.5)} \right|$$

$$q_b = 54.7 \text{ psi } (37.7 \text{ N/cm}^2)$$

$$q_a = 0.28tf_y/R = (0.28)(7)(40{,}000)/195.5$$

$$q_a = 401 \text{ psi } (277 \text{ N/cm}^2)$$

The allowable backpacking strain remains essentially the same (h_p = 221 in versus 222 in previously). For the backpacking strain due to liner deflection,

$$\frac{\delta}{h_p} = \frac{\bar{p}R^4}{0.402E_s t^3 h_p} = \frac{(195.5)^4 \bar{p}}{(0.402)(2.9 \times 10^7)(7)^3(221)} = 0.00165\bar{p}$$

The combined interaction diagrams for the hollow section are also shown in Fig. 8-38 and indicate the section should be somewhat stronger for most efficient utilization of the selected backpacking.

8.13 REFERENCES

8-1 Norris, C.H., et al., Structural Design for Dynamic Loads, McGraw-Hill Book Co., New York, N.Y., 1959. (U)

8-2 Newmark, N.M. and Haltiwanger, J.D., Principles and Practices for Design of Hardened Structures, AFSWC-TDR-62-138, Air Force Special Weapons Center, Kirtland AFB, N.M., December 1962 (U)

8-3 Newmark, N.M. and Rosenblueth, E., Fundamentals of Earthquake Engineering, Prentice Hall, Inc., Englewood Cliffs, N.J., 1971. (U)

8-4 Effects of Radiation on Materials and Components, Reinhold Publishing Corp., New York, N.Y., 1964. (U)

8-5 Penkovskii, V.V., Effects of Radiation on Metals and Other High-Melting Materials, Elsevier Publishing Co., New York, N.Y., 1964. (U)

8-6 Manual of Steel Construction, Seventh Edition, American Institute of Steel Construction, Inc., New York, N.Y., 1970. (U)

8-7 Winter, G., et al., Design of Concrete Structures, McGraw-Hill Book Co., New York, N.Y., 1964. (U)

8-8 Endebrock, E.G. and Traina, L.A., Static Constitutive Relations Based on Cubical Specimens, AFWL-TR-72-59, Air Force Weapons Laboratory, Kirtland AFB, N.M., December 1972. (U)

8-9 Blume, J.A., Newmark, N.M. and Corning, L.H., Design of Multistory Reinforced Concrete Buildings for Earthquake Motions, Portland Cement Association, Chicago, Ill., 1961. (U)

8-10 Keenan, W.A., Strength and Behavior of Laced Reinforced Concrete Slabs Under Static and Dynamic Load, R-620, Naval Civil Engineering Laboratory, Port Hueneme, Calif., April 1969. (U)

8-11 Tipton, R.C., Jr. (Editor), Reactor Handbook, Volume I, Materials, Second Edition, Interscience Publishers, Inc., New York, N.Y., 1960. (U)

8-12 Building Code Requirements for Reinforced Concrete, ACI 318-71, American Concrete Institute, Detroit, Mich., 1971. (U)

8-13 American Concrete Institute Standard Building Code Requirements for Reinforced Concrete, ACI 318-63, American Concrete Institute, Detroit, Mich., 1963. (U)

8-14 Biggs, J.M., Introduction to Structural Dynamics, McGraw-Hill Book Co., New York, N.Y., 1964 (U)

8-15 American Concrete Institute Manual of Concrete Practice, Part 2, "Shear and Diagonal Tension", Report of ACI-ASCE Committee 326, American Concrete Institute, Detroit, Mich., 1968. (U)

8-16 Crist, R.A., Static and Dynamic Shear Behavior of Uniformly Loaded Reinforced Concrete Deep Beams, AFWL-TR-71-74, Air Force Weapons Laboratory, Kirtland AFB, N.M., November 1971. (U)

8-17 Beedle, L.S., Plastic Design of Steel Frames, John Wiley and Sons, Inc., New York, N.Y., 1958. (U)

8-18 Manual of Steel Construction, Seventh Edition, American Institute of Steel Construction, Inc., New York, N.Y., 1970. (U)

8-19 Plastic Design in Steel, American Institute of Steel Construction, Inc., New York, N.Y., 1959. (U)

8-20 "Commentary on Plastic Design in Steel: Additional Design Considerations-I, Chapter 6," Journal of the Engineering Mechanics Division, American Society of Civil Engineers, October 1959. (U)

8-21 Baker, J.F., Horne, M.R. and Heyman, J., The Steel Skeleton, Vol. 2, Cambridge University Press, 1956. (U)

8-22 Hognestad, E., "Yield Line Theory for the Ultimate Flexural Strength of Reinforced Concrete Slabs," ACI Journal, March 1953. (U)

8-23 Jones, L.L., Ultimate Load Analysis of Reinforced and Prestressed Concrete Structures, Interscience Publishers, New York, N.Y., 1962. (U)

8-24 Ferguson, P.M., Reinforced Concrete Fundamentals, With Emphasis on Ultimate Strength, John Wiley and Sons, Inc., New York, N.Y., 1958. (U)

8-25 Albritton, G.E., et al., Response of Deep Two-Way Reinforced and Unreinforced Concrete Slabs to Static and Dynamic Loading, Technical Report N-69-2, Report No. 1, U. S. Army Engineer Waterways Experiment Station, Vicksburg, Miss., March 1969. (U)

8-26 Albritton, G.E., et al., Response of Deep Two-Way Reinforced and Unreinforced Concrete Slabs to Static and Dynamic Loading, Technical Report N-69-2, Report No. 2, U. S. Army Engineer Waterways Experiment Station, Vicksburg, Miss., October 1969. (U)

8-27 Albritton, G.E., et al., Response of Deep Two-Way Reinforced and Unreinforced Concrete Slabs to Static and Dynamic Loading, Technical Report N-69-2, Report No. 3, U. S. Army Engineer Waterways Experiment Station, Vicksburg, Miss., November 1969. (U)

8-28 Albritton, G.E., et al., Response of Deep Two-Way Reinforced and Unreinforced Concrete Slabs to Static and Dynamic Loading, Technical Report N-69-2, Report No. 4, U. S. Army Engineer Waterways Experiment Station, Vicksburg, Miss., November 1969. (U)

8-29 Rhomberg, E.J., Shear Strength of Deep Reinforced Concrete Slabs, AFWL-TR-68-126, Air Force Weapons Laboratory, Kirtland AFB, N.M., May 1969. (U)

8-30 Gamble, W.L., et al, A Study of Launch Facility Closures, SAMSO-TR-67-15, Space and Missile Systems Organization, Norton AFB, Calif., November 1967. (U)

8-31 Seely, F.B. and Smith, J.O., Advanced Mechanics of Materials, Second Edition, John Wiley and Sons, Inc., New York, N.Y., August 1961. (U)

8-32 Anderson, R.H., et al, Structural Behavior of Ring Sections under Nonuniform External Pressure, AFWL-TR-65-145, Air Force Weapons Laboratory, Kirtland AFB, N.M., March 1966 (U)

8-33 Hendron, A.J., et al, Design of Cylindrical Reinforced Concrete Tunnel Liners to Resist Air Overpressures, CR 68.010, Naval Civil Engineering Laboratory, Port Hueneme, Calif., June 1968. (U)

8-34 Effect of Edge Loads on Domes, Portland Cement Association, Chicago, Ill., March 1960. (U)

8-35 Timoshenko, S. and Woinowsky-Krieger, S., Theory of Plates and Shells, McGraw-Hill Book Co., New York N.Y., 1959. (U)

8-36 Crist, R.A. and Vaughan, R.G., Dynamically Loaded Circular Composite Slabs, Phase I: Project Goliath, AFWL-TR-68-9, Air Force Weapons Laboratory, Kirtland AFB, N.M., October 1968. (U)

8-37 Newmark, N.M., Design of Rock Silo and Rock Cavity Linings, Report for Space and Missile Systems Organization, Norton AFB, Calif., August 1969. (U)

8-38

8-39

SECTION IX

DYNAMIC RESPONSE OF STRUCTURAL SYSTEMS

9.1 INTRODUCTION

Most real structures are very complex in their behavior even under static loads and their response to dynamic loads can include additional complications due to various combinations of elastic and inelastic vibrational modes.

The usual approach to determining the dynamic response of a structure or structural element to some specific loading is to first model or represent the structure as a system of finite structural elements and masses connected together at a discrete number of nodal points. If the force-displacement relationships are known for the individual elements, various methods of structural analysis can be used to study the behavior of the assembled structure. Most structures are made up of beams, girders, columns, slabs, plates and shells, with each of these elements having distributed mass and stiffness. If certain assumptions are made regarding stiffness of connections, lumping of masses, stiffnesses and applied loads, it is possible to replace these structures and structural elements with equivalent systems. The accuracy of the structural analysis depends largely upon the accuracy of the assumptions made in obtaining the replacement system. In general, the more complex the structure, the greater the number of individual elements required to accurately describe its response.

Figure 9-1 shows three simple structures and three possible representations as idealized spring-mass systems. Other representations are possible and the one chosen should satisfy the data and accuracy required of the analysis. In these figures F(t) is the externally applied load, M is the mass of the

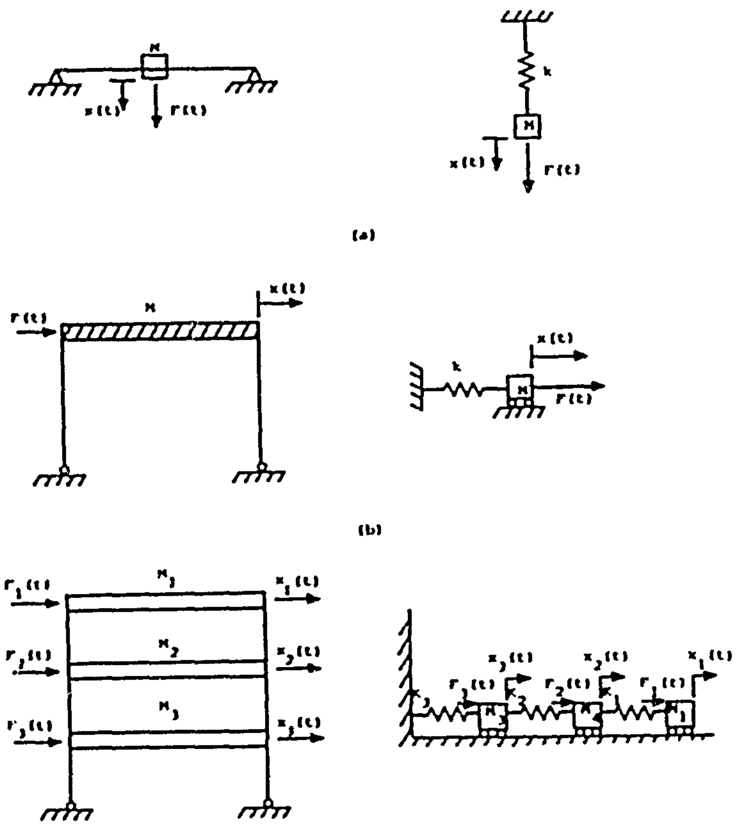

(a)

(b)

(c)

Figure 9-1 Idealized Spring Mass Systems

structure, x is the displacement of the mass and k is a spring constant which is determined from the properties of the structure. The response of the spring-mass system to the loading function F(t) is determined using well-established numerical analysis techniques or rigorous solutions of the differential equation of motion for the system. Rigorous solutions are possible only for those cases where the loading and resistance functions can be expressed in relatively simple mathematical terms.

The difficulty in obtaining a solution to the dynamic response of a spring-mass system will also depend on the number of degrees of freedom of the system. The degree of freedom of a system is defined to be the minimum number of independent displacement variables necessary to completely describe the configuration of the system. Figures 9-1(a) and (b) show single degree of freedom systems and Fig. 9-1(c) a three degree of freedom system. Even the idealization of the simple structures shown in Fig. 9-1 requires certain simplifying assumptions regarding the mode of response of the real structure. For example, that shown in Fig. 9-1(b) assumes the mass to be rigid and the absence of vertical or rotational motions.

The following paragraphs of this section present methods for obtaining the response of both single degree of freedom and multiple degree of freedom systems to various types of loading functions. Approximate methods of analysis which reduce multiple degree of freedom systems to equivalent single degree of freedom systems are also presented.

9.2 SINGLE DEGREE OF FREEDOM SYSTEMS

9.2.1 General

A discussion of the response of single degree of freedom systems is an important introduction to the principles of structural dynamics. In addition, many structures and structural elements can be represented with acceptable accuracy by single degree of freedom systems and later paragraphs of this section describe techniques for obtaining properties of the equivalent systems and the response of these systems to dynamic loads. In the following discussions it is assumed that the points of support for the structural element do not move and therefore do not affect the response of the element. The influence of support motions is considered in paragraph 9.5.

9.2.2 Undamped Elastic Systems

a. Classical Solution

The first step in obtaining a solution to the response of a single degree of freedom system is to isolate the mass, M, and apply the external forces acting on the mass as shown in Fig. 9-2. The more general case would also include a damping force. However, for purposes of this discussion, it is assumed that damping can be neglected and the resistance function is linear-elastic as in Fig. 9-3(a). Starting with the elementary equation

$$P = \frac{d}{dt}(Mv) \qquad (9\text{-}1)$$

where

P = algebraic sum of the forces acting on the mass, M

v = velocity of the mass

If it is assumed that the mass is a constant, the above equation becomes

$$P = M\frac{dv}{dt} = M\ddot{x} \qquad (9\text{-}2)$$

where

$\ddot{x}$ = acceleration of the mass

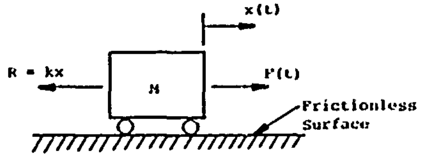

Figure 9-2 Single Degree of Freedom System

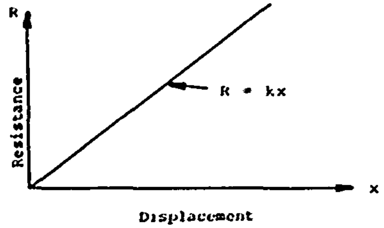

(a) Linear Elastic

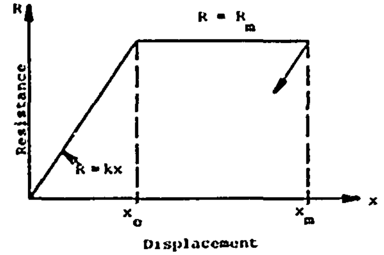

(b) Elastic-Plastic

Figure 9-3 Idealized Resistance Functions

Summing the forces acting in the x direction on the mass in Fig. 9-2, we obtain the following equation of motion

$$M\ddot{x} + kx = F(t) \qquad (9\text{-}3)$$

Rearranging terms and letting $\omega_N = \sqrt{k/M}$ we obtain

$$x + \omega_N^2 x = \frac{F(t)}{M} \qquad (9\text{-}4)$$

ω_N is the natural circular frequency of the single degree of freedom system in radians per second. The natural period of the system, T_N, is given by

$$T_N = 2\pi\sqrt{\frac{M}{k}} \qquad (9\text{-}5)$$

The natural period of the system is the time required to complete one cycle of free vibration.

The solution of Eq. 9-3 depends on the forcing function F(t) and the initial velocity and displacement of the mass. The four idealized forcing functions shown in Fig. 9-4 can be used to approximate many loadings of interest for protective construction design and analysis. It is usually assumed that the system is initially at rest in an equilibrium position at the time the load is first applied. With these assumptions regarding initial conditions for the system and for the four idealized loading functions shown in Fig. 9-4, the following solutions to Eq. 9-4 can be obtained.

<u>Triangular Pulse with Zero Rise Time</u>

$$x = \frac{F_o}{k}\left|1 - \cos\omega_N t + \frac{\sin\omega_N t}{\omega_N t_o} - \frac{t}{t_o}\right| \text{ for } t \le t_o$$

$$= \frac{F_o}{k}\left|\frac{1}{\omega_N t_o}\left(\sin\omega_N t - \sin\omega_N(t-t_o)\right) - \cos\omega_N t\right| \text{ for } t \ge t_o \qquad (9\text{-}6)$$

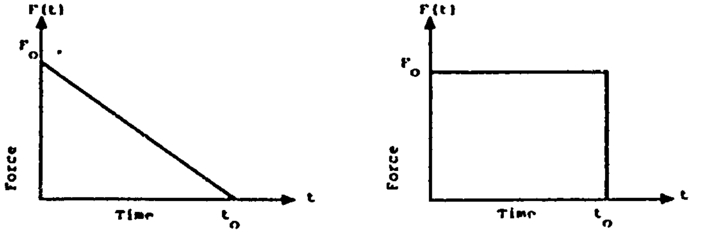

(a) Triangular Pulse with Zero Rise Time

$$F(t) = \begin{cases} F_o(1-t/t_o) & \text{for } 0 \le t \le t_o \\ 0 & \text{for } t \ge t_o \end{cases}$$

(b) Rectangular or Step Pulse

$$F(t) = \begin{cases} F_o & \text{for } 0 \le t \le t_o \\ 0 & \text{for } t \ge t_o \end{cases}$$

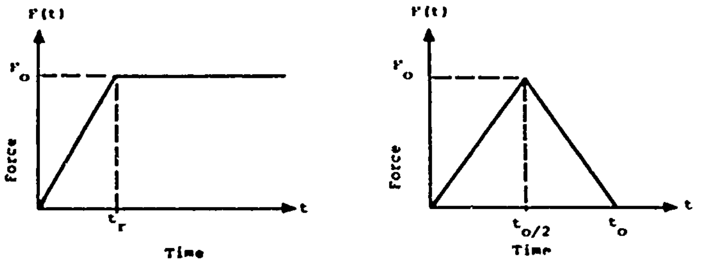

(c) Step Pulse with Finite Rise Time

$$F(t) = \begin{cases} F_o(t/t_r) & \text{for } 0 \le t \le t_r \\ F_o & \text{for } t \ge t_r \end{cases}$$

(d) Symmetrical Triangular Pulse

$$F(t) = \begin{cases} F_o\left(\frac{2t}{t_o}\right) & \text{for } 0 \le t \le t_{o/2} \\ F_o\left[1 - \frac{2t-t_o}{t_o}\right]; & t_{o/2} < t < t_o \\ 0 & \text{for } t \ge t_o \end{cases}$$

Figure 9-4 Idealized Forcing Function

Rectangular or Step Pulse

$$x = \frac{F_o}{k}\left|1 - \cos \omega_N t\right| \quad \text{for } t \leq t_o$$

$$x = \frac{F_o}{k}\left|\cos \omega_N (t-t_o) - \cos \omega_N t\right| \quad \text{for } t \geq t_o \tag{9-7}$$

Step Pulse with Finite Rise Time

$$x = \frac{F_o}{k}\left[\frac{1}{t_r}\left(t - \frac{\sin \omega_N t}{\omega_N}\right)\right] \quad \text{for } t \leq t_r$$

$$x = \frac{F_o}{k}\left[1 + \frac{1}{\omega_N t_r}\left(\sin \omega_N (t-t_r) - \sin \omega_N t\right)\right] \quad \text{for } t \geq t_r \tag{9-8}$$

Symmetrical Triangular Pulse

$$x = \frac{F_o}{k}\left[\frac{2}{t_o}\left(t - \frac{\sin \omega_N t}{\omega_N}\right)\right] \quad \text{for } 0 \leq t \leq \frac{t_o}{2}$$

$$x = \frac{F_o}{k}\left[\frac{2}{t_o}\left(t_o - t + \frac{1}{\omega_N}\left\{2 \sin \omega_N \left(t - \frac{t_o}{2}\right) - \sin \omega_N t\right\}\right)\right]$$

$$\text{for } t_o/2 \leq t \leq t_o \tag{9-9}$$

$$x = \frac{F_o}{k}\left[\frac{2}{\omega_N t_o}\left(2 \sin \omega_N \left\{t - \frac{t_o}{2}\right\} - \sin \omega_N t - \sin \omega_N \left\{t - t_o\right\}\right)\right] \quad \text{for } t \geq t_o$$

Expressions for velocity and acceleration can be found by differentiation of the above equations. The time of maximum displacement can be found by solving the velocity expressions for those times when the velocity is equal to zero. These times can then be substituted into the displacement equations to obtain the maximum response x_m. Similarly peak velocities

can be obtained from the expressions for acceleration.

It is convenient to describe the dynamic response of single degree of freedom systems in terms of nondimensional variables whenever appropriate. In this manner the solutions can be applied to many specific problems. One such nondimensional variable is the dynamic load factor (DLF). This factor is defined as the ratio of the dynamic deflection at any time to the deflection which would have resulted from static application of the peak force, F_o, from the force-time history. Thus,

$$DLF = \frac{x}{x_{st}} = \hat{\chi} \tag{9-10}$$

where

$$x_{st} = \frac{F_o}{k} \tag{9-11}$$

Deflections, spring forces and stresses are all proportional in elastic systems so that the dynamic load factor can be applied to any of these variables in order to obtain the ratio of dynamic to static effects. Thus, the maximum spring force is the product of the maximum values of the applied force and the dynamic load factor.

$$F_s = \hat{\chi}\, F_o \tag{9-12}$$

Figure 9-5 is a typical plot of the response of two single degree of freedom elastic systems to the triangular pulse shown in Fig. 9-4(a). Figure 9-5 can also be interpreted as the response of a single degree of freedom system to triangular pulses of two different durations. Several points should be noted in Fig. 9-5. The two curves show a significant difference in system response for systems with different periods. Clearly, when the load duration is long compared to the natural period of the system, the response is greater than that where the load duration is only a fraction of the natural period of the system. In

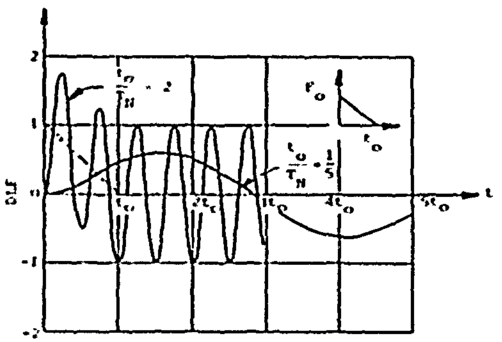

Figure 9-5 Typical Response of Two Single Degree of Freedom, Undamped Systems to a Triangular Pulse with Zero Rise Time

the former case, maximum response occurs while the load is still applied to the system. In the latter case, maximum response occurs after the load has been removed. For smooth forcing functions the predominant motions are at the frequency of the system. After the load has been removed, the system will continue to vibrate in pure harmonic motion if there is no damping present in the system. If damping is present, the amplitude of vibrations will gradually decrease to zero. For most cases of interest, it is convenient to neglect damping since maximum response normally occurs in the first cycle of vibration where damping is of lesser importance. Equations 9-6 through 9-9 apply only to undamped elastic systems. The effects of damping are discussed in greater detail in paragraph 9.4.

Only the maximum response of the system is required in many problems. If the forcing function varies with time, the dynamic load factor is usually based upon the maximum value of the load, F_o, that occurs during the period of interest.

Figures 9-6 through 9-8 are charts of maximum dynamic load factors for various types of loading functions. Charts of time to reach maximum displacement are also presented.

b. Numerical Integration

Numerical integration is another technique for solution of the differential equation of motion. It is the most general and versatile method of analysis for problems of interest. It can be applied to any system with a finite number of degrees of freedom and can treat any force-displacement-time relationship, ranging from linear elastic to nonlinear, viscoelastic-plastic relations. The method of numerical integration has found wide application on electronic computing devices for compiling

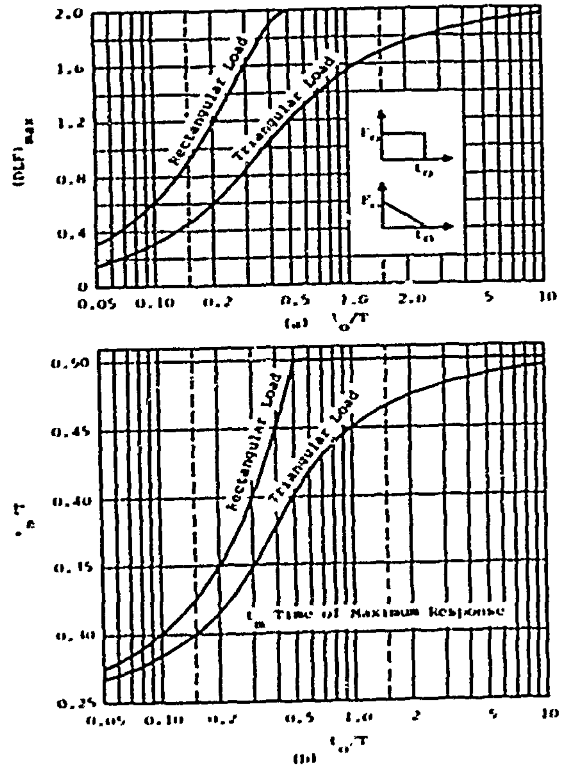

Figure 9-6 Maximum Response of Undamped Single Degree of Freedom Elastic System to Triangular and Step Pulses with Zero Rise Time (Ref. 9-1)

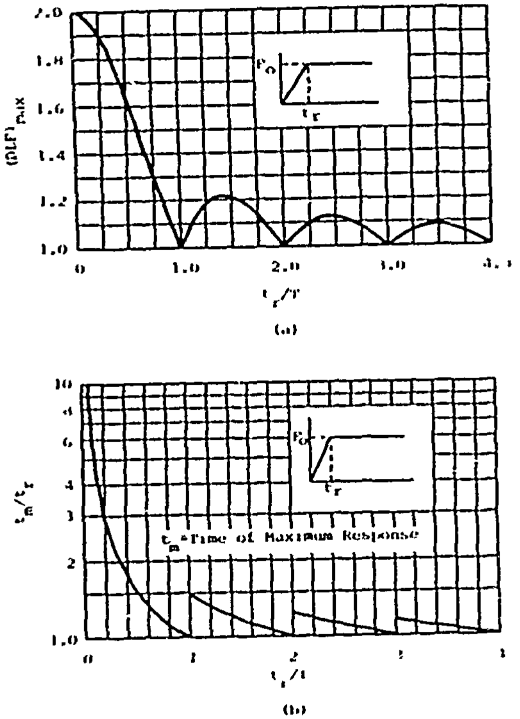

Figure 9-7 Maximum Response of Undamped Single Degree of Freedom Elastic System to Step Pulse with Finite Rise Time (Ref. 9-1)

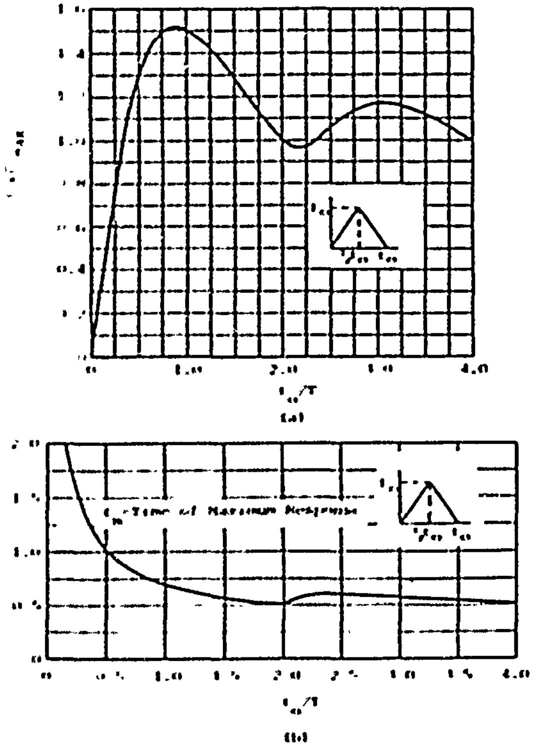

Figure 9-8 Maximum Response of Undamped Single Degree of Freedom Elastic System to Symmetrical Triangular Pulse (Ref. 9-1)

the solutions to simple problems, and for the rapid solution of problems in the dynamics of complicated systems. For hand computation, the method is best suited to systems of a few degrees of freedom with simple force-resistance relations, such as the bilinear elastic or elastic-plastic resistances.

Rewriting Eq. 9-3 in the form

$$\ddot{x} = \frac{F(t) - kx}{M} \qquad (9\text{-}13)$$

it is seen that if F(t) and x are known at any particular instant of time, the acceleration of the mass, M, can be calculated. The basis of the method of numerical integration is the subdivision of time into intervals, Δt, and an assumption of the nature of the variation of the acceleration during the time interval. The procedure recommended herein is presented in Refs. 9-2 and 9-3. It is convenient to adopt the notation developed in Ref. 9-2. If we let $\ddot{x}_n$, $\dot{x}_n$, x_n, be the acceleration, velocity and displacement respectively at time $t = t_n$, then the velocity and displacement of the mass at time $t = t_n + \Delta t$ are given by

$$\dot{x}_{n+\Delta t} = \dot{x}_n + \frac{1}{2}\,\Delta t \quad (\ddot{x}_n + \ddot{x}_{n+\Delta t}) \qquad (9\text{-}14)$$

$$x_{n+\Delta t} = x_n + \Delta t\,\dot{x}_n + \frac{(\Delta t)^2}{2}\,\ddot{x}_n + \beta(\ddot{x}_{n+\Delta t} - \ddot{x}_n)(\Delta t)^2 \qquad (9\text{-}15)$$

If the variation of the acceleration over the time interval Δt is linear, β is taken equal to 1/6. If a constant acceleration equal to the average of $\ddot{x}_n$ and $\ddot{x}_{n+\Delta t}$ is assumed over the time interval, β is taken equal to 1/4. Values of β of 0, 1/12, and 1/ 8 can also be given simple geometric interpretations.

The method proceeds as follows. The acceleration, velocity, and displacement are computed at t = 0 from the given initial conditions. Then for t = Δt, the acceleration $\ddot{x}_{n+\Delta t}$ is assumed. Using Eqs. 9-14 and 9-15, the velocity and displacement, ~~$x_{n+\Delta t}$~~ at time $t_n + \Delta t$ are computed. Knowing the displacement $x_{n+\Delta t}$, the resistance kx can be evaluated. This value is then substituted into Eq. 9-13 and the assumed acceleration checked. If the assumed and resultant acceleration are not in agreement, the computed acceleration can be used for the next trial until the procedure converges.

The important questions which arise in the application of numerical integration are convergence, rate of convergence, stability, length of time interval, and choice of β. All of the questions are interrelated and have been studied fairly extensively. Some of the results of these studies are presented in Table 9-1 and 9-2. In Table 9-1, the rate of convergence for an undamped single degree of freedom system is presented for various values of β and $\Delta t/T_N$ (the time interval scaled by the natural period of vibration). The smaller the value of the rate of convergence, the more rapid the convergence. In Table 9-2, the stability and convergence limits for an undamped single degree of freedom system are given for common values of β. The scaled time interval $\Delta t/T_N$ must be less than both these limits to insure both stability and convergence. For systems with several degrees of freedom, the stability and convergence limits must be applied in terms of the natural period of the highest mode of vibration, i.e., the minimum natural period. The choice of a time interval also determines the number of cycles of iterations required to properly describe structural response and therefore affects the cost of the analysis in terms of computer time. Another consideration is that the time interval should be small enough to adequately describe the time variation of the forcing function.

Table 9-1

RATE OF CONVERGENCE

$\Delta t/T_N$	$\beta = 0$	$\beta = 1/12$	$\beta = 1/8$	$\beta = 1/6$	$\beta = 1/4$
0.05	0	0.008	0.012	0.016	0.025
0.10	0	0.033	0.049	0.066	0.099
0.20	0	0.132	0.197	0.263	0.395
0.25	0	0.206	0.308	0.411	0.617
0.318	0	0.333	0.500	0.667	1.000
0.389	*	0.500	0.750	1.000	1.500
0.450	*	*	1.000	1.333	2.000

* $\Delta t/T_N$ exceeds the limits for convergence or stability

Table 9-2

STABILITY AND CONVERGENCE LIMITS

	$\beta=0$	$\beta=1/12$	$\beta=1/8$	$\beta=1/6$	$\beta=1/4$
Stability Limit, $\Delta t/T_N$	0.318	0.389	0.450	0.551	∞
Convergence Limit, $\Delta t/T_N$	∞	0.551	0.450	0.389	0.318

The choice of β governs the accuracy and ease of application of the method. Extensive work in the application of this method has resulted in the following conclusions. A $\beta = 1/6$ is best suited for forced vibrations of systems with damping and with initial velocity and displacement. The best results in amplitude of response for an undamped system are obtained using $\beta = 1/4$. A $\gamma = 1/12$ gives the most rapid and accurate results for an undamped system without initial velocity. For very rapid results, where accuracy is not of primary importance, $\beta = 0$ often proves useful.

9.2.3 Elastic-Plastic Systems

Up until now it has been assumed that the resistance of the single degree of freedom system is linear and elastic. A system with an elastic-plastic resistance function is shown in Fig. 9-3(b). For this system, the response is elastic up to the elastic limit x_e. The resistance then remains constant over the displacement range, $x_e \leq x \leq x_m$, where x_m is the maximum displacement. As the displacement starts to decrease, the unloading response is again assumed to be elastic. Figures 9-9 through 9-12 are charts of the maximum response of an undamped, elastic-plastic single degree of freedom system for various loading functions. Charts of time to reach maximum displacement are also given. In the plastic region, spring resistance is no longer proportional to displacement so separate plots are required to different ratios of peak load to maximum spring resistance. Maximum response is expressed as a ratio of the maximum displacement, x_m, to the yield displacement, x_e. This ratio

$$\mu = \frac{x_m}{x_e} \qquad (9\text{-}16)$$

is often referred to as the ductility ratio and is often specified as a design parameter. For values of $\mu \leq 1.0$ the system

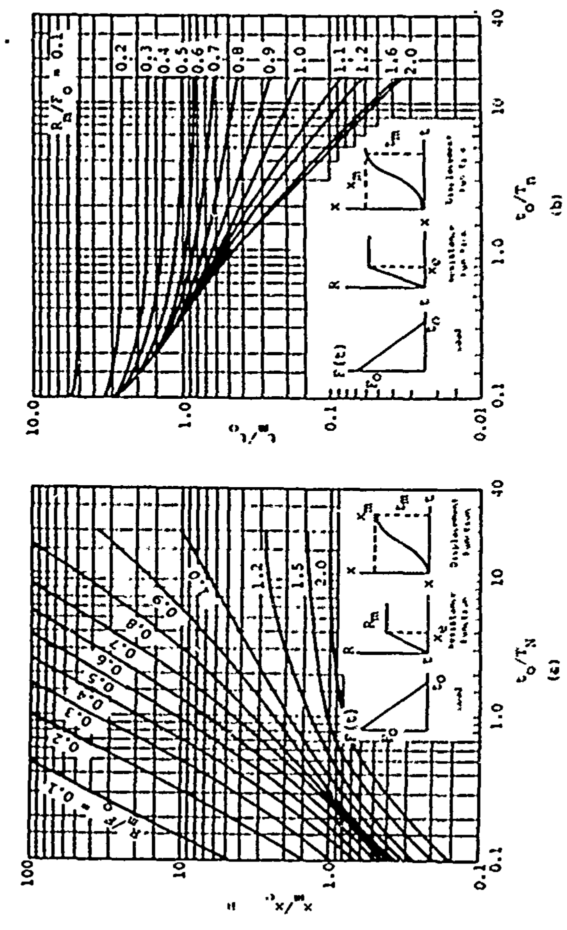

Figure 9-9 Maximum Response of Undamped Single Degree of Freedom Elastic-Plastic System to Triangular Pulse with Zero Rise Time (Ref. 9-1)

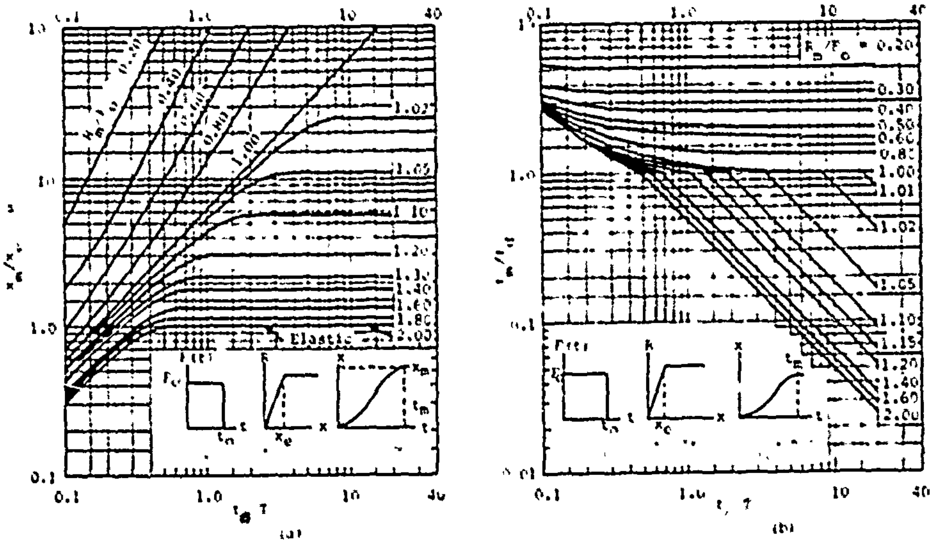

Figure 9-10 Maximum Response of Undamped Single Degree of Freedom Elastic-Plastic System to Rectangular Pulse with Zero Rise Time (Ref. 9-1)

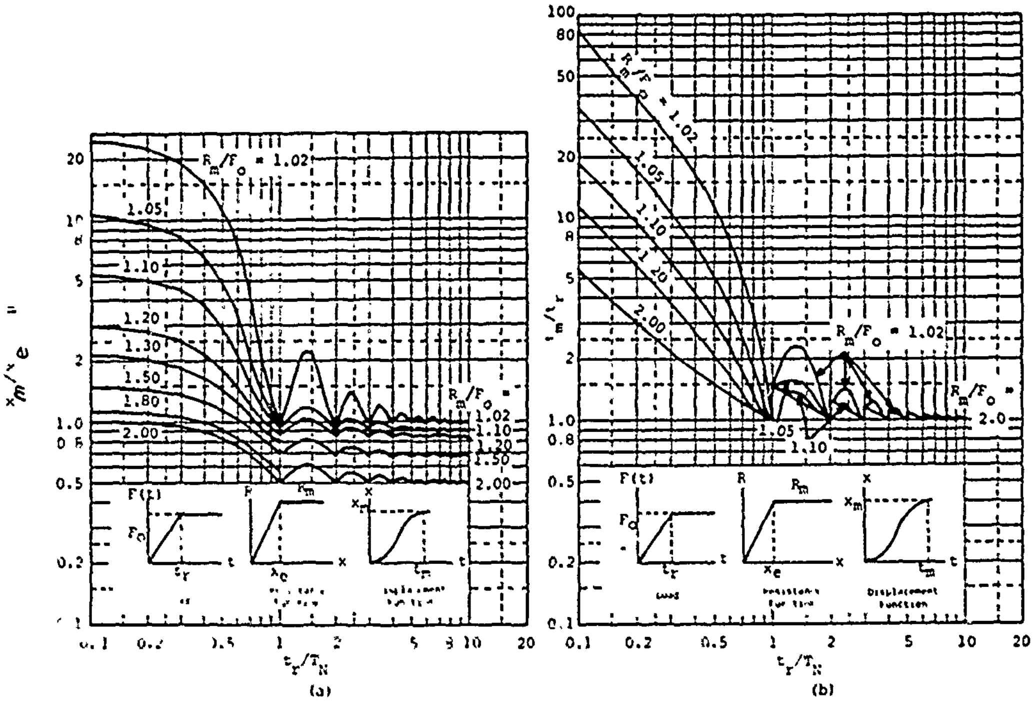

(a) (b)

Figure 9-11 Maximum Response of Undamped Single Degree of Freedom Elastic-Plastic System to Step Pulse with Finite Rise Time (Ref. 9-1)

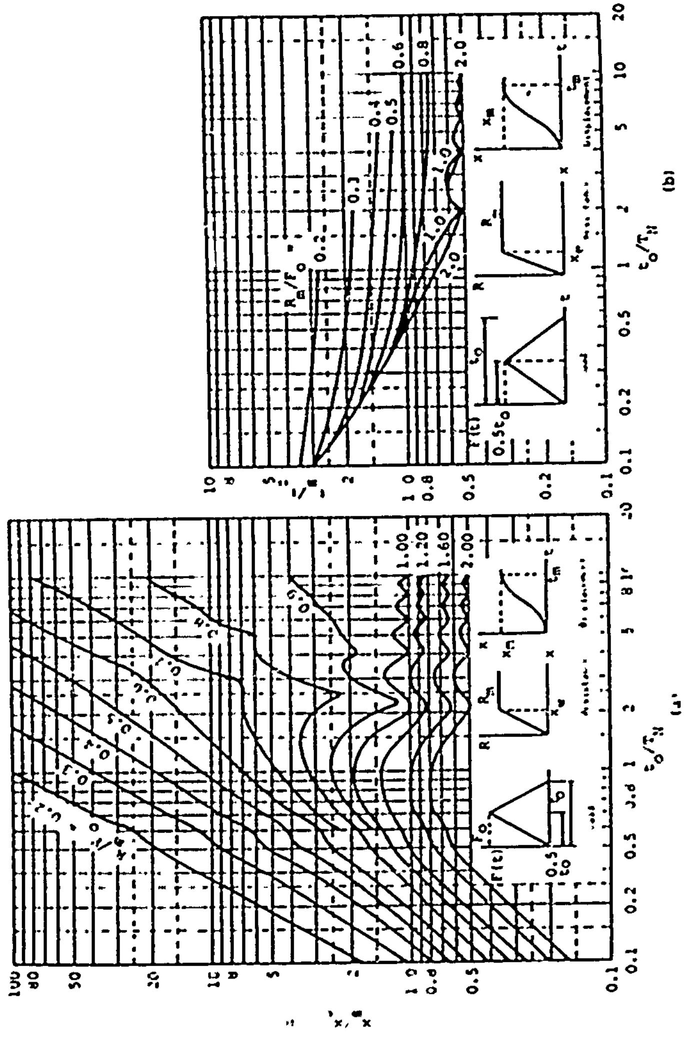

Figure 9-12 Maximum Response of Undamped Single Degree of Freedom Elastic-Plastic System to Symmetrical Triangular Pulse (Ref. 9-1)

remains elastic. In protective construction, if the larger displacements and inelastic response can be tolerated, it is advantageous to design for ductility ratios greater than one. Ductility ratios up to 10 or 20 can be used under certain conditions.

For R_m/F_o ratios greater than 2.0, system response is elastic for the loadings considered and the curves of Figs. 9-6 through 9-8 should be used. In cases where only the maximum response is required, the response charts offer a significant computational advantage over rigorous solutions or numerical integration techniques. In some instances, such as design of shock isolation systems, a detailed time-displacement history may be required and the latter approaches are necessary.

Another form of response chart for elastic-plastic systems is shown in Fig. 9-13. The forcing function for Fig. 9-13 is an initially peaked triangular pulse as shown in Fig. 9-4(a), and the displacement-resistance function is as shown in Fig. 9-3(b). If any two of the three parameters on this chart are known, the third can be obtained. For example, if the ductility, μ, and the duration of the force, t_o, are known, then the ratio of the peak force to yield resistance, F_o/R_m, can be found. The time of maximum response, t_m, is also given in Fig. 9-13.

Equation 9-17 can be used to determine the pressure necessary to cause a specified response of an elastic-plastic system subjected to an initially-peaked, triangular force with an initial impulse, I_o, also applied at t = 0 (Ref. 9-4)

$$\frac{F_o}{R_m} = \frac{F'_o}{R_m} + \frac{F''_o/R_m}{1+0.7\ T_N/t_o} \qquad (9\text{-}17)$$

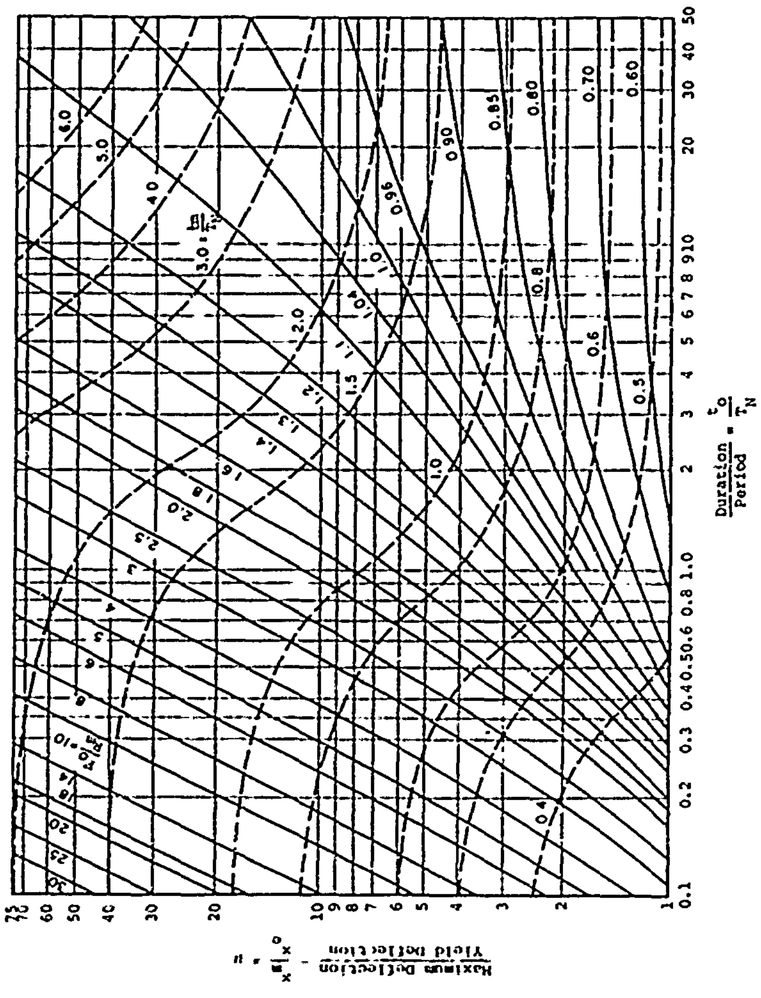

Figure 9-13 Response of Undamped Single Degree of Freedom Elastic-Plastic System to Triangular Pulse with Zero Rise Time (Ref. 9-5)

where

$$\frac{F'_o}{R_m} = \frac{T_N}{\pi t_o}\left\{(2\mu-1)^{1/2} - \frac{\pi I_o}{R_m T_N}\right\}$$

and

$$\frac{F''_o}{R_m} = 1 - \frac{1}{2\mu} - \frac{1}{2\mu}\left[\frac{\pi I_o}{R_m T_N}\right]^2 \qquad (9\text{-}18)$$

9.2.4 Rebound

In the design of members subjected to dynamic loading, it is often necessary to consider the negative displacement or rebound, which can occur after the member has reached its maximum positive displacement.

Figure 9-14 gives approximate values of the rebound resistance required for a fixed-base, undamped, single degree of freedom system subjected to an initially peaked triangular force pulse. Entering the chart with the value of the ductility factor, μ, and the ratio of the duration of the load pulse to the natural period of the system, t_o/T_N, it is possible to read directly the required rebound resistance, r, in terms of the yield resistance, R_m.

The values obtained from Fig. 9-14 will almost always indicate larger rebound resistances than actually required for nuclear blast loads. This is because Fig. 9-14 is most accurate for peak response which occurs after the load is no longer acting on the system. For long duration loads such as nuclear blast loads, the structure reaches its maximum deflection while the positive forces are still large, and the rebound is reduced. The following semiempirical relation can be used to estimate the required rebound resistance after the first half-cycle of response while relatively large positive forces are still acting on the system.

$$\frac{r}{R_m} = -\frac{1}{3.71}\left\{\ln\left[\frac{7\mu}{(t_o/T_N)^{2.82}}\right]\right\} \qquad \left(-1 \le \frac{r}{R_m} \le 0\right) \qquad (9\text{-}19)$$

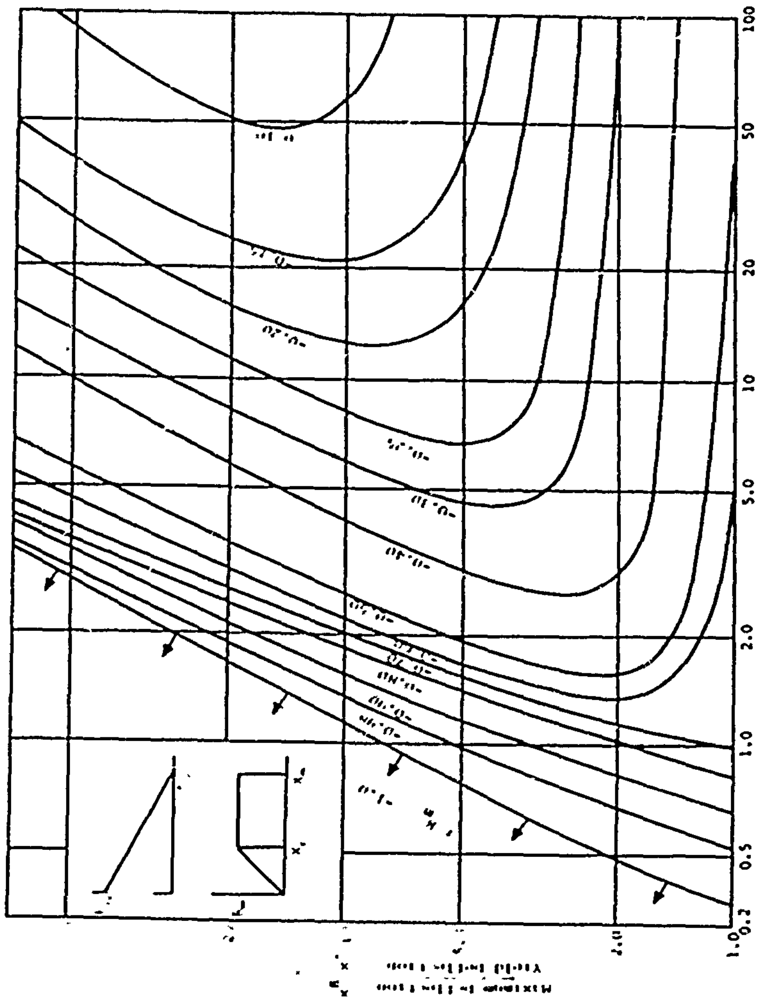

Figure 9-14 Required Rebound Resistance for Fixed-Base, Undamped, Single Degree of Freedom Systems (Ref. 9-5)

When Fig. 9-14 indicates large rebound resistance required and Eq. 9-19 shows little or none, a more detailed analysis of the system considering the load and response time-histories will be necessary to estimate the actual rebound resistance required.

9.3 EQUIVALENT SINGLE DEGREE OF FREEDOM SYSTEMS

9.3.1 General

As stated previously, a rigorous dynamic analysis is feasible only where the structural loading and resistance functions can be expressed in relatively simple mathematical terms. Although numerical analysis techniques are much more flexible, they also become tedious for more than a few degrees of freedom. As the number of degrees of freedom increase, hand calculations become impractical, and electronic computers must be used to solve complex multiple degree of freedom systems. Fortunately, it is possible to reduce many common structural elements to an equivalent single degree of freedom system which can then be analyzed with accuracy sufficient for most engineering purposes. In view of the uncertainties in loads and material properties encountered in protective construction design, more complex analytical techniques are often not justified.

A propped cantilever is shown in Fig. 9-15 with two possible equivalent single degree of freedom systems. Ideally, the displacement, velocity and acceleration of the models should at all times be equal to those of the actual structure. There should also be an equivalence of kinetic energy, strain energy and work done by external forces between the real and equivalent systems. In practice it is not always possible to obtain an exact equivalence and the degree of error will depend on the complexity of the actual structure. The usual approach is to define the system as one in

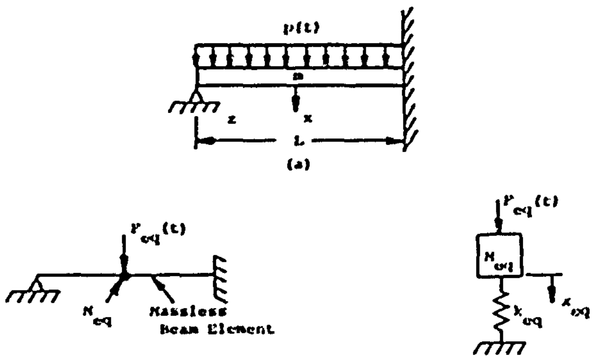

Figure 9-15 Equivalent Single Degree of Freedom System

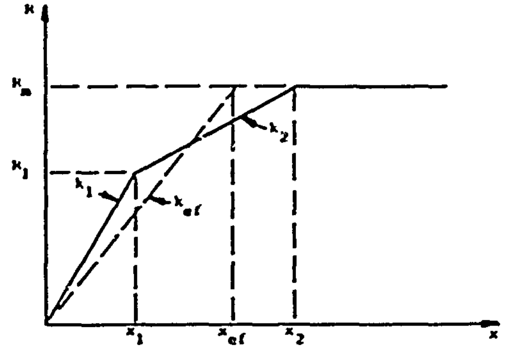

Figure 9-16 Effective Resistance Function

which the equivalent displacement, velocity and acceleration are equal to that at some significant point in the actual system. Knowing these parameters for the equivalent system, a good approximation can be obtained for the complete response of the actual system. It is also necessary to define an equivalent forcing function which has the same time dependence as the real load.

The constants of the equivalent system are evaluated on the basis of an assumed deformed shape of the actual structure. This shape is usually taken as that resulting from the static application of the dynamic loads. This approach is not quite the same as that of using the first mode shape, but it yields more accurate results for many systems, especially for stress computations.

9.3.2 Transformation Factors for Beams and Slabs

It is convenient to develop transformation factors which convert the real system into the equivalent system. When the load, mass, resistance and stiffness of the real structure are multiplied by the corresponding transformation factors, these parameters are obtained for the equivalent single degree of freedom system.

Reference 9-6 states that if the static deflected shape of the structure under the specified loads is denoted by $\phi(z)$, the equivalent mass and force are defined by (kinetic energy considerations)

$$M_{eq} = \int_0^\ell m(z)\phi^2(z)dz \qquad (9\text{-}20)$$

and (external work considerations)

$$F_{eq} = \int_0^\ell p(z)\phi(z)dz \qquad (9\text{-}21)$$

respectively, where $m(z)$ and $p(z)$ are functions describing the mass and applied load distributions on the real structure. For lumped mass systems or concentrated loads the corresponding equations are

$$M_{eq} = \sum_{n=1}^{j} M_n \phi_n^2 \tag{9-22}$$

and

$$F_{eq} = \sum_{n=1}^{j} F_n \phi_n \tag{9-23}$$

where ϕ_n is again an assumed shape function. The mass and load transformation factors are given by

$$K_M = \frac{M_{eq}}{M_t} \tag{9-24}$$

and

$$K_L = \frac{F_{eq}}{F_t} \tag{9-25}$$

where

M_t = total mass of the real structure

F_t = total force on the real structure

For the example shown in Fig. 9-15(a), where both mass and force are uniformly distributed

$$M_t = \int_0^L m\,dz = mL \tag{9-26}$$

and

$$F_t = \int_0^L p(t)\,dz = p(t)L \tag{9-27}$$

Since the maximum resistance is the total load having the given distribution which the structure can support statically and the stiffness is equal to the total load of the same distribution required to cause a unit displacement at the

significant point, it follows that the resistance factor, K_R, must always equal the load factor K_L. Then

$$K_R = \frac{R_{meq}}{R_m} = K_L \tag{9-28}$$

and

$$K_R = \frac{k_{eq}}{k} = K_L \tag{9-29}$$

where R_m and k are the actual and R_{meq} and k_{eq} are the equivalent resistances and spring constants, respectively.

The single degree of freedom systems analyzed in paragraph 9.2 had either linear or bilinear resistance displacement functions, but not all structures exhibit such behavior even if ideal hinge behavior is assumed. The propped cantilever shown in Fig. 9-15, for example, would have a displacement-resistance function similar to that shown in Fig. 9-16. The initial stiffness, k_1, represents beam response up to the displacement x_1 where a hinge forms at the fixed end. Stiffness k_2 applies over the range $x_1 \leq x \leq x_2$ and the maximum resistance is reached at x_2 where a hinge forms at midspan. The bilinear representation of the resistance displacement function over the range $0 \leq x \leq x_1$ is an idealization of the actual function since hinge formation is not instantaneous. If the simplified analysis presented in paragraph 9.2 is to be applied, a further idealization is necessary. The recommended approach is to select an effective stiffness, k_{ef}, so that the area under the two curves, which represent absorbed energy, is equal for the real and equivalent systems. When the effective stiffness and shape functions have been selected, Eqs. 9-20 through 9-23 can be used to obtain transformation factors which transform the mass, load and stiffness of the real structure into equivalent characteristics of a single degree of freedom replacement system.

Transformation factors have been worked out for a number of common types of structural elements and support conditions. Tables 9-3 through 9-5 give factors for beams and one-way slabs, and Tables 9-6 and 9-7 give factors for two-way slabs. Table 9-8 presents factors for circular slabs. The tables also include a load-mass factor which is defined to be the ratio

$$K_{LM} = \frac{K_M}{K_L} \qquad (9\text{-}30)$$

This ratio can be used to define the equations of motion for the equivalent system

$$K_{LM}M_t\ddot{x} + kx = F_t(t) \qquad \text{(elastic region)} \qquad (9\text{-}31)$$

$$K_{LM}M_t\ddot{x} + R_m = F_t(t) \qquad \text{(plastic region)} \qquad (9\text{-}32)$$

In the elastic region the natural frequency of the system is

$$\omega_N = \left|\frac{k}{K_{LM}M_t}\right|^{1/2} \qquad (9\text{-}33)$$

and the natural period is

$$T_N = 2\pi\left|\frac{K_{LM}M_t}{k}\right|^{1/2} \qquad (9\text{-}34)$$

The maximum resistances and spring stiffnesses given in Table 9-3 are those corresponding to the real system and are the conventional expressions for these quantities and should be multiplied by the load factor to obtain the resistance for the equivalent system. M_p is the ultimate or plastic flexural strength of the member. It is assumed that the member is designed so that shear strength is not critical.

The maximum resistances given in Tables 9-4 and 9-5 are those which occur at the upper limit of each range. Spring stiffnesses are given for each range as well as an

R_m in TERMS OF TOTAL LOAD ON ELEMENT

Table 9-3

TRANSFORMATION FACTORS FOR BEAMS AND ONE-WAY SLABS (Ref. 9-6)

Loading Diagram	Strain Range	Load Factor	Mass Factor K_M		Load-Mass Factor K_{LM}		Maximum Resistance R_m	Spring Constant k	Dynamic Reaction V
			Concentrated Mass*	Uniform Mass	Concentrated Mass*	Uniform Mass			
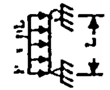	Elastic	0.64	...	0.50	...	0.78	$\frac{8M_p}{L}$	$\frac{384EI}{5L^3}$	$0.39R + 0.11F$
	Plastic	0.50	...	0.33	...	0.66	$\frac{8M_p}{L}$	0	$0.38R_m + 0.12F$
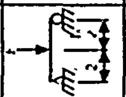	Elastic	1.0	1.0	0.49	1.0	0.49	$\frac{4M_p}{L}$	$\frac{48EI}{L^3}$	$0.78R - 0.28F$
	Plastic	1.0	1.0	0.33	1.0	0.33	$\frac{4M_p}{L}$	0	$0.75R_m - 0.25F$
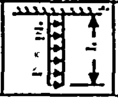	Elastic	0.4	...	0.26	...	0.65	$\frac{2M_{ps}}{L}$	$\frac{8EI}{L^3}$	$0.69R + 0.31F$
	Plastic	0.5	...	0.33	...	0.66	$\frac{2M_{ps}}{L}$	0	$0.75R_m + 0.25F$
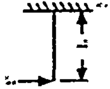	Elastic	1.0	1.0	0.24	1.0	0.24	$\frac{M_{ps}}{L}$	$\frac{3EI}{L^3}$	$1.36R - 0.36F$
	Plastic	1.0	1.0	0.33	1.0	0.33	$\frac{M_{ps}}{L}$	0	$1.5R_m - 0.5F$

*The concentrated mass is lumped at the concentrated load

Dynamic Reactions should be multiplied b 1.75 for concentrated load, elastic cases

Table 9-4

TRANSFORMATION FACTORS FOR BEAMS AND ONE-WAY SLABS (Ref. 9-6)

M_{ps} = ultimate moment capacity at support
M_{pm} = ultimate moment capacity at midspan

Loading Diagram	Strain Range	Load Factor K_L	Mass Factor K_M		Load-Mass Factor K_{LM}		Maximum Resistance R_m	Spring Constant k	Effective Spring Constant k_E	Dynamic Reaction V
			Concentrated Mass*	Uniform Mass	Concentrated Mass*	Uniform Mass				
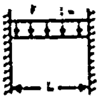	Elastic	0.53	...	0.41	...	0.77	$\frac{12M_{ps}}{L}$	$\frac{384EI}{L^3}$	......	0.36R + 0.14F
	Elastic-Plastic	0.64	...	0.50	...	0.78	$\frac{8}{L}(M_{ps} + M_{pm})$	$\frac{384EI}{5L^3}$	$\frac{307EI}{L^3}$	0.39R + 0.11F
	Plastic	0.50	...	0.33	...	0.66	$\frac{8}{L}(M_{ps} + M_{pm})$	0	......	$0.38R_m + 0.12F$
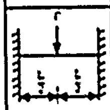	Elastic	1.0	1.0	0.37	1.0	0.37	$\frac{4}{L}(M_{ps} + M_{pm})$	$\frac{192EI}{L^3}$	......	0.71R - 0.21F
	Plastic	1.0	1.0	0.33	1.0	0.33	$\frac{4}{L}(M_{ps} + M_{pm})$	0	......	$0.75R_m - 0.25F$

*Concentrated mass is lumped at the concentrated load.

Use load factor of 1.75 for concentrated load,
Elastic case reactions

Table 9-5

TRANSFORMATION FACTORS FOR BEAMS AND ONE-WAY SLABS (Ref. 9-6)

Loading Diagram	Strain Range	Load Factor K_L	Mass factor K_M		Load-Mass factor K_{LM}		Maximum Resistance R_m	Spring Constant k	Effective Spring Constant kE	Dynamic Reaction V
			Concentrated Mass*	Uniform Mass	Concentrated Mass*	Uniform Mass				
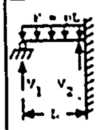	Elastic	0.58	....	0.45	....	0.78	$\frac{8M_{ps}}{L}$	$\frac{185EI}{L^3}$	$\frac{MO}{L^3}$	$V_1 = 0.26R + 0.12F$ $V_2 = 0.43R + 0.19F$
	Elastic-Plastic	0.64	....	0.50	....	0.78	$\frac{4}{L}(M_{ps} + 2M_{pm})$	$\frac{384EI}{5L^3}$		$V = 0.39R + 0.11F \pm M_{ps}/L$
	Plastic	0.50	....	0.33	....	0.66	$\frac{4}{L}(M_{ps} \pm 2M_{pm})$	0		$V = 0.38R_m + 0.12F \pm M_{ps}/L$
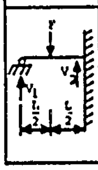	Elastic	1.0	1.0	0.43	1.0	0.43	$\frac{16M_{ps}}{3L}$	$\frac{107EI}{L^3}$	$\frac{106EI}{L^3}$	$V_1 = 0.25R + 0.07F$ $V_2 = 0.54R + 0.14F$
	Elastic-Plastic	1.0	1.0	0.49	1.0	0.49	$\frac{2}{L}(M_{ps} + 2M_{pm})$	$\frac{48EI}{L^3}$		$V = 0.78R - 0.28F \pm M_{ps}/L$
	Plastic	1.0	1.0	0.33	1.0	0.33	$\frac{2}{L}(M_{ps} + 2M_{pm})$	0		$V = 0.75R_m - 0.25F \pm M_{ps}/L$

*Concentrated mass is lumped at the concentrated load.

Table 9-6

TRANSFORMATION FACTORS FOR TWO-WAY SLABS: SIMPLE SUPPORTS, UNIFORM LOAD (Ref. 9-6)
For Poissons Ratio = 0.3

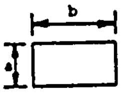

V_A = total dynamic reaction along short edge; V_B = total dynamic reaction along long edge.

Strain range	a/b	Load factor K_L	Mass factor K_M	Load-mass factor K_{LM}	Maximum resistance	Spring constant k	Dynamic reactions V_A	V_B
Elastic	1.0	0.46	0.31	0.67	$\frac{12}{a}(M_{pfa} + M_{pfb})$	$\frac{252EI}{a^2}$	0.07F + 0.18R	0.07F + 0.18R
	0.9	0.47	0.33	0.70	$\frac{1}{a}(12M_{pfa} + 11M_{pfb})$	$\frac{230EI}{a^2}$	0.06F + 0.16R	0.08F + 0.20R
	0.8	0.49	0.35	0.71	$\frac{1}{a}(12M_{pfa} + 10.3M_{pfb})$	$\frac{212EI}{a^2}$	0.06F + 0.14R	0.08F + 0.22R
	0.7	0.51	0.37	0.73	$\frac{1}{a}(12M_{pfa} + 9.8M_{pfb})$	$\frac{201EI}{a^2}$	0.05F + 0.13R	0.08F + 0.24R
	0.6	0.53	0.39	0.74	$\frac{1}{a}(12M_{pfa} + 9.3M_{pfb})$	$\frac{197EI}{a^2}$	0.04F + 0.11R	0.09F + 0.26R
	0.5	0.55	0.41	0.75	$\frac{1}{a}(12M_{pfa} + 9.0M_{pfb})$	$\frac{201EI}{a^2}$	0.04F + 0.09R	0.09F + 0.28R
Plastic	1.0	0.33	0.17	0.51	$\frac{12}{a}(M_{pfa} + M_{pfb})$	0	0.09F + 0.16R_m	0.09F + 0.16R_m
	0.9	0.35	0.18	0.51	$\frac{1}{a}(12M_{pfa} + 11M_{pfb})$	0	0.08F + 0.15R_m	0.09F + 0.18R_m
	0.8	0.37	0.20	0.54	$\frac{1}{a}(12M_{pfa} + 10.3M_{pfb})$	0	0.07F + 0.13R_m	0.10F + 0.20R_m
	0.7	0.38	0.22	0.58	$\frac{1}{a}(12M_{pfa} + 9.8M_{pfb})$	0	0.06F + 0.12R_m	0.10F + 0.22R_m
	0.6	0.40	0.23	0.58	$\frac{1}{a}(12M_{pfa} + 9.3M_{pfb})$	0	0.05F + 0.10R_m	0.10F + 0.25R_m
	0.5	0.42	0.25	0.59	$\frac{1}{a}(12M_{pfa} + 9.0M_{pfb})$	0	0.04F + 0.08R_m	0.11F + 0.27R_m

For Slabs $V_A + V_B$ represent the total reaction along the a or b dimension

Table 9-7

TRANSFORMATION FACTORS FOR TWO-WAY SLABS: FIXED SUPPORTS, UNIFORM LOAD (Ref. 9-6)
For Poissons Ratio = 0.2

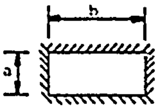

V_A = total dynamic reaction along short edge; V_B = total dynamic reaction along long edge.

Strain range	a/b	Load factor K_L	Mass factor K_M	Load-mass factor K_{LM}	Maximum resistance	Spring constant k	Dynamic reactions V_A	V_B
Elastic	1.0	0.33	0.21	0.63	$29.2M^0_{psb}$	$810EI/a^2$	0.10F + 0.15R	0.10F + 0.15R
	0.9	0.34	0.23	0.68	$27.4M^0_{psb}$	$742EI/a^2$	0.09F + 0.14R	0.10F + 0.17R
	0.8	0.36	0.25	0.69	$26.4M^0_{psb}$	$705EI/a^2$	0.08F + 0.12R	0.11F + 0.19R
	0.7	0.38	0.27	0.71	$26.2M^0_{psb}$	$692EI/a^2$	0.07F + 0.11R	0.11F + 0.21R
	0.6	0.41	0.29	0.71	$27.3M^0_{psb}$	$724EI/a^2$	0.06F + 0.09R	0.12F + 0.23R
	0.5	0.42	0.31	0.72	$30.2M^0_{psb}$	$806EI/a^2$	0.05F + 0.08R	0.12F + 0.25R
Elastic-Plastic	1.0	0.46	0.31	0.67	$(1/a)\ 12(M_{pfa} + M_{psa}) + 12(M_{pfb} + M_{psb})$	$252EI/a^2$	0.07F + 0.18R	0.07F + 0.18R
	0.9	0.47	0.33	0.70	$(1/a)\ 12(M_{pfa} + M_{psa}) + 11(M_{pfb} + M_{psb})$	$230EI/a^2$	0.06F + 0.16R	0.08F + 0.20R
	0.8	0.49	0.35	0.71	$(1/a)\ 12(M_{pfa} + M_{psa}) + 10.3(M_{pfb} + M_{psb})$	$212EI/a^2$	0.06F + 0.14R	0.08F + 0.22R
	0.7	0.51	0.37	0.73	$(1/a)\ 12(M_{pfa} + M_{psa}) + 9.8(M_{pfb} + M_{psb})$	$201EI/a^2$	0.05F + 0.13R	0.08F + 0.24R
	0.6	0.53	0.39	0.74	$(1/a)\ 12(M_{pfa} + M_{psa}) + 9.3(M_{pfb} + M_{psb})$	$197EI/a^2$	0.04F + 0.11R	0.09F + 0.26R
	0.5	0.55	0.41	0.75	$(1/a)\ 12(M_{pfa} + M_{psa}) + 9.0(M_{pfb} + M_{psb})$	$201EI/a^2$	0.04F + 0.09R	0.09F + 0.28R
Plastic	1.0	0.33	0.17	0.51	$(1/a)\ 12(M_{pfa} + M_{psa}) + 12(M_{pfb} + M_{psb})$	0	0.09F + 0.16R_m	0.09F + 0.16R_m
	0.9	0.35	0.18	0.51	$(1/a)\ 12(M_{pfa} + M_{psa}) + 11(M_{pfb} + M_{psb})$	0	0.08F + 0.15R_m	0.09F + 0.18R_m
	0.8	0.37	0.20	0.54	$(1/a)\ 12(M_{pfa} + M_{psa}) + 10.3(M_{pfb} + M_{psb})$	0	0.07F + 0.13R_m	0.10F + 0.20R_m
	0.7	0.38	0.22	0.58	$(1/a)\ 12(M_{pfa} + M_{psa}) + 9.8(M_{pfb} + M_{psb})$	0	0.06F + 0.12R_m	0.10F + 0.22R_m
	0.6	0.40	0.23	0.58	$(1/a)\ 12(M_{pfa} + M_{psa}) + 9.3(M_{pfb} + M_{psb})$	0	0.05F + 0.10R_m	0.10F + 0.25R_m
	0.5	0.42	0.25	0.59	$(1/a)\ 12(M_{pfa} + M_{psa}) + 9.0(M_{pfb} + M_{psb})$	0	0.04F + 0.08R_m	0.11F + 0.27R_m

Table 9-8

TRANSFORMATION FACTORS FOR CIRCULAR SLABS

FOR POISSON'S RATIO = 0.3

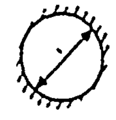

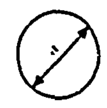

Fixed Edges a = Diameter of slab Simple Supports

Edge Condition	Strain Range	K_L	K_M	K_{LM}	Maximum Resistance	Spring Constant	Dynamic Reaction
Simple Supports	Elastic	0.46	0.30	0.65	$18.8\ M_{pc}$	$\frac{216EI}{a^2}$	$0.28F + 0.72R$
	Plastic	0.33	0.17	0.52	$18.8\ M_{pc}$	0	$0.36F + 0.64R_m$
Fixed Supports	Elastic	0.33	0.20	0.61	$25.1\ M_{ps}$	$\frac{880EI}{a^2}$	$0.40F + 0.60R$
	Elastic-Plastic	0.46	0.30	0.65	$18.8\ (M_{pc} + M_{ps})$	$\frac{216EI}{a^2}$	$0.28F +$ [illegible]
	Plastic	0.33	0.17	0.52	$18.8\ (M_{pc} + M_{ps})$	0	$0.36F + 0.64R_m$

effective value appropriate for all ranges. This value would correspond to the value k_{ef} shown in Fig. 9-16.

The transformation factors given in Tables 9-6 through 9-8 are based upon approximations to classical plate theory in the elastic range and yield line theory in the plastic range. In the latter range, the rectangular plates are assumed to be planar between yield lines. In the simply supported case, there is obviously an elastic-plastic, or transition, range, but the behavior is exceedingly complex. In order to simplify the procedure, this range has been ignored. In the case of fixed supports, the elastic range has been terminated when the moment along most of the edge has reached ultimate. This transition point cannot be determined precisely, and the limiting resistances given are estimates. For the elastic-plastic range, it has been assumed that the shape (but not the resistance) and hence the factors, are the same as those for simply supported slabs. For two-way slabs, the maximum resistances and spring constants are given in terms of the total load on the slab. The notation is as follows:

M_p = ultimate bending moment capacity

M_{pfa} = total ultimate positive bending moment capacity along midspan section parallel to short edge, a

M_{pfb} = total ultimate positive bending moment capacity along midspan section parallel to long edge, b

M_{psa} = total ultimate negative moment capacity along short edge, a

M_{psb} = total ultimate negative moment capacity along short edge, b

I = moment of inertia of cross section per unit width

M'_{psa} = ultimate negative bending moment capacity per unit width at center of edge a in direction of long span, b

M^*_{psb} = ultimate negative bending moment capacity per unit width at center of edge b in direction of short span, a

M_{pc} = ultimate positive bending moment capacity per unit width at center of circular slab

M_{ps} = ultimate negative bending moment capacity per unit width at edge of circular slab

V_A = total dynamic reaction along one short edge

V_B = total dynamic reaction along one long edge

9.3.3 Frames

Following the general principles and procedures outlined above, we can also obtain transformation factors for frames such as the one shown in Fig. 9-17(a). The masses m_1 and m_2 are uniformly distributed along the roof and sides and the dynamic load includes a concentrated force at roof level plus a uniformly distributed load on one wall surface. The frame is assumed to deflect horizontally as shown in Fig. 9-17(b) with the side walls remaining straight. The displacement of the replacement system is taken to be equal to that at the top of the frame, and the mass of the equivalent system is given by

$$M_{eq} = m_1 L + 2/3\, m_2 h \qquad (9\text{-}35)$$

The equivalent force is equal to

$$F_{eq} = F(t) + p(t)\,\frac{h}{2} \qquad (9\text{-}36)$$

The equivalent stiffness, k_{eq}, is equal to the actual stiffness of the frame referred to a horizontal load applied at the top of the frame, and is the concentrated force required to produce a unit horizontal displacement of the roof.

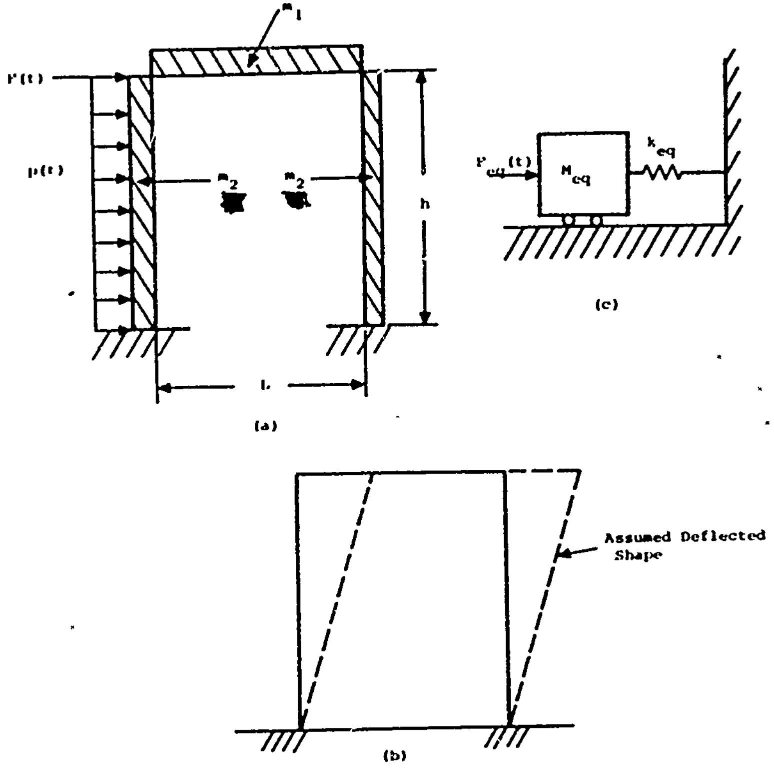

Figure 9-17 Equivalent Single Degree of Freedom System

The maximum resistance of both the actual and equivalent system is simply the maximum horizontal force which can be carried by the frame. If the girders are rigid compared to the columns (the more common case) then

$$R_m = R_{meq} = \frac{4M_{uc}}{h} \tag{9-37}$$

where

M_{uc} = ultimate bending moment capacity of each column.

With the properties of equivalent system shown in Fig. 9-17(c) established, the next step is a single degree of freedom analysis to obtain frame deflections and, from these deflections, stresses within the frame. For multistory frames, it is generally sufficiently accurate to lump the load and mass at the floor levels on the basis of tributary wall area.

9.3.4 Other Structural Elements

Although transformation factors can be obtained for a variety of structural elements or systems, the technique is practical only for relatively simple systems. The primary requirements are assumed deflected shapes in the different strain ranges of interest and the maximum resistance in each range. Shear distortion may be important in some cases and should be considered in determining the deflected shape, spring constant and maximum resistance.

9.3.5 Dynamic Reactions

It is important to recognize that the dynamic reactions of the real structural element have no direct counterpart in the equivalent single degree of freedom system (Ref. 9-7). The reaction of the equivalent system, i.e., the spring force, is not the same as the real reaction. This is

true because the simplified system was deliberately selected so as to have the same dynamic deflection as the real system, rather than the same force or stress characteristics. Structure-foundation interaction will also have a significant effect on the magnitude of the reactions. In spite of these difficulties and uncertainties, it is of interest to obtain some estimate of reactions since they are always related to the maximum shear in the element and also because they are necessary for the design of the supporting structures.

Expressions for the reactions may be obtained by considering the dynamic equilibrium of the complete element. The dynamic equilibrium of the element includes consideration of inertia forces, which are assumed to be proportional to the ordinate of the deflected shape. Tables 9-3 through 9-8 include factors for calculating the dynamic reactions of the various structural elements. The general form of the expression is

$$V = C_1F + C_2R \tag{9-38}$$

where

V = the dynamic reaction at one end or edge of the element, except in the case of circular slabs where V represents the total reaction at the supports

C_1, C_2 = coefficients obtained from the tables

F = total force applied to the element

R = resistance of the element

Both F and R are functions of time, and V will normally reach a maximum when the deflection of the element reaches its ~~maximum~~ yield displacement i.e. $R = R_m$. The dynamic reactions can be calculated as follows.

a. Calculate natural period and obtain resistance-displacement function for structural element from given properties.

b. With the period of the element, its resistance-displacement function, and characteristics of the forcing function known, obtain maximum response from appropriate chart in Figs. 9-6 through 9-13.

c. Determine F and R at the time of maximum displacement

d. Obtain appropriate C_1 and C_2 from Tables 9-3 through 9-8 for given structural element and strain range.

NOT TRUE EXCEPT FOR Elastic case For plastic region must determine F at time of yielding. Then use this F and Rm to obtain V

e. Calculate total reaction as

$$V = C_1P + C_2R + \text{Dead Load Contribution} \qquad (9\text{-}39)$$

It should be noted that Eq. 9-38 also holds for static conditions where R = F and, therefore, in the case of beam elements the sum of C_1 and C_2 must equal 1/2. In the case of two-way slabs, two sets of coefficients are given, one each for the long and short span supports. In this case, the sum of the coefficients for V_A and V_B must equal 1/2. For circular slabs the sum of the coefficients must equal one. As stated before, F and R represent the total loads or the total resistance of the structural element. Therefore, Eq. 9-39 yields the total reaction at the support.

9.4 DAMPED SYSTEMS

All structural systems contain damping to some degree. It can occur in several forms including internal friction in structural materials, friction losses associated with slippage between structural components and resistance to motion provided by air or other fluids surrounding the structure.

The importance of damping in dynamic analyses depends largely on the characteristics of the applied load and the time span of interest for structural response. It is generally of greater significance in problems of continuing vibration than those of maximum response under short duration loads. The general effects of damping are to oppose motions, reduce amplitudes of vibration and reduce system frequencies of vibration.

It is generally assumed, for purposes of analysis, that structural damping is of the viscous type. This type of damping produces a force which is proportional to the velocity of the mass and it is represented by the dashpot in Fig. 9-18(a). The differential equation of motion becomes

$$M\ddot{x} + c\dot{x} + kx = F(t) \qquad (9\text{-}40)$$

where c is the damping coefficient.

For the case of Coulomb, or constant friction, damping shown in Fig. 9-18(b), the equation of motion is

$$M\ddot{x} + kx \pm F_f = F(t) \qquad (9\text{-}41)$$

where F_f is the frictional force which always acts to oppose the motion of the mass.

As for the undamped case, the solutions to Eq. 9-40 and 9-41 depend on the nature of the forcing function and the initial conditions of the system. In order to demonstrate the effects of damping on a vibrating system, consider the case of free vibration of the system shown in Fig. 9-18(a). For F(t) = 0, the general solution to Eq. 9-40 is given by

$$x = e^{-\beta\omega_n t}\left|\frac{\dot{x}_o + \beta\omega_n x_o}{\omega_d}\sin\omega_d t + x_o\cos\omega_d t\right| \qquad (9\text{-}42)$$

where

$\dot{x}_o$ = velocity at t = 0

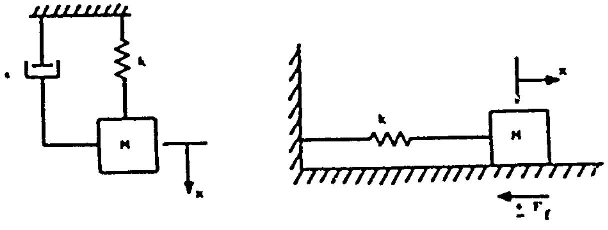

(a) (b)

Figure 9-18 Damped Single Degree of Freedom Systems

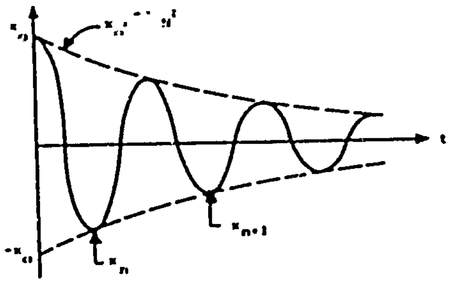

Figure 9-19 Free Vibration of Damped Single Degree of Freedom System

x_o = displacement at $t = 0$

ω_N = $\sqrt{K/M}$

β = c/c_{cr} = damping ratio or fraction of critical damping

c_{cr} = $2\sqrt{KM}$ = critical damping coefficient

ω_d = $\omega_N\sqrt{1 - \beta^2}$ = damped natural frequency of system

Equation 9-42 is applicable only for $\beta < 1$.

Figure 9-19 is a plot of the free vibration of a viscously damped single degree of freedom system with an initial displacement. (The response of the system with Coulomb damping is similar to that shown in Fig. 9-19 except that the decay of peak amplitude is linear.) The amplitude of vibration of the system decreases in each cycle and the ratio of successive displacement amplitudes is given by

$$\frac{x_{n+1}}{x_n} = e^{-2\pi\beta\omega_N/\sqrt{\omega_N^2 - \beta^2\omega_N^2}} = e^{-2\pi\beta/\sqrt{1 - \beta^2}} \tag{9-43}$$

The natural logarithm of Eq. 9-43 is referred to as the logarithmic decrement and is often used as a measure of damping. As β approaches 1, the frequency of vibration approaches zero and when $\beta = 1$, the motion is no longer periodic. The amount of damping at this point is known as critical damping ($\beta = 1$). Systems with damping greater than critical are said to be overdamped and are of limited interest in protective construction applications.

The amount of damping found in most structures is much less than critical. Typical values fall between 5 and 10 percent (Ref. 9-7) and this amount of damping only slightly affects the natural frequency of vibration, i.e., $\omega_d = 0.995\ \omega_N$.

However, there is a greater effect on the amplitude of free vibrations with each peak approximately half that of the preceding peak.

The effect of damping on forced vibrations depends on the nature of the forcing function. For the case of a system with 10 percent of critical damping, initially at rest, subjected to a suddenly applied constant force, F_o, the maximum response is 1.75 F_o/k. From Eq. 9-7 for an undamped system subjected to the same load function, the maximum response is 2 F_o/k. Similar differences are encountered between the damped and undamped cases for other loading functions of interest in protective construction.

If a system is subjected to periodic forces of long duration, with periods near that of the system, damping can be of much greater importance. For example, rotating machinery placed on a shock-mounted floor could subject the system to a force of the form

$$F(t) = F_o \sin \omega t \qquad (9\text{-}44)$$

where

ω = frequency of rotation of the machinery

F_o = maximum amplitude of force

The maximum amplitude of the force is proportional to the unbalanced mass and rotational frequency of the machinery. For the general case of an elastic system with damping, the maximum dynamic load factor is given by

$$\hat{X}_{max} = \frac{1}{\sqrt{\left|1 - \left(\frac{\omega}{\omega_N}\right)^2\right|^2 + 4\,\frac{\beta^2\omega^2}{\omega_N^2}}} \qquad (9\text{-}45)$$

Examination of Eq. 9-45 indicates that as ω approaches

ω_N, the response of an undamped system ($\beta = 0$) becomes infinitely large. This condition, $\omega = \omega_N$, is known as resonance.

It is obvious that at a point near resonance even a small amount of damping can have a significant effect on system response. Although resonance is very unlikely for most structural loadings of interest in protective construction, the designer or analyst should be alert to the possibility of objectionable motions from other causes.

9.5 RESPONSE TO SUPPORT MOTIONS

9.5.1 , General

Another very important class of problems often encountered in protective construction design and analysis is the response of a system to motion of its base. Two examples of this type problem are the response of a structure to ground shock and the response of a shock isolated platform to support motions.

Motion of the supports of structural elements can significantly affect the loading and response of the element as well as the load it transmits to its supports. Such motions might cause a reduction in the moments and shears in a closure system or beam or the loads on a buried structure. Conversely, they can also cause greater absolute and relative displacements and accelerations of the supported element. In some instances, it is possible to incorporate motions of the supports into a dynamic analysis by using a modified spring resistance; in others, it is necessary to analyze the system as a multiple degree of freedom system.

Figure 9-20 represents a single degree of freedom system subjected to a base motion which is a function of time. The general equation of motion for this system is

$$\ddot{x} + \frac{c}{M}(\dot{x} - \dot{y}) + \frac{k}{M}(x - y) = 0 \qquad (9\text{-}46)$$

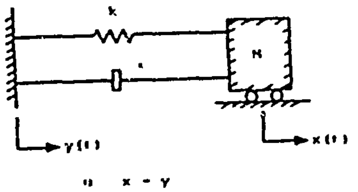

Figure 9-20 Single Degree of Freedom System Subjected to Base Motion

or

$$\ddot{x} + 2\beta\omega_N\dot{u} + \omega_N^2 u = 0 \tag{9-47}$$

where

$\dot{u} = \dot{x} - \dot{y}$ = relative velocity between mass M and support

$u = x - y$ = relative displacement between M and support

Another form of Eq. 9-47 is

$$\ddot{u} + 2\beta\omega_N\dot{u} + \omega_N^2 u = -\ddot{y} \tag{9-48}$$

where

$\ddot{x} = \ddot{u} + \ddot{y}$

Equation 9-48 is more convenient if the disturbing function is described in terms of a support acceleration, $\ddot{y}$.

For undamped systems, Eq. 9-46 can be written

$$M\ddot{x} + kx = ky \tag{9-49}$$

and Eq. 9-48 (noting that $\omega_N^2 = k/M$) in the form

$$M\ddot{u} + ku = -M\ddot{y} \tag{9-50}$$

Noting the similarity between Eqs. 9-3, 9-49 and 9-50, it is seen that if the variation of support motion with time corresponds to one of the forcing functions shown in Fig. 9-4, and if the substitutions $F_o = ky_o$ or $F_o = -M\ddot{y}_o$ are made, Eqs. 9-6 through 9-9 are also solutions to Eqs. 9-49 and 9-50. In these substitutions y_o and $\ddot{y}_o$ are taken equal to the peak values of support displacement and acceleration, respectively. Similarly, the appropriate dynamic load factors from Figs. 9-6 through 9-8 can be used to estimate the peak response of a system. For absolute displacements of the mass described by Eq. 9-49

$$x_{max} = y_o \hat{X} \tag{9-51}$$

and for relative displacements described by Eq. 9-50

$$u_{max} = \frac{\ddot{y}_o}{\omega_N^2} \hat{x} \qquad (9\text{-}52)$$

Use of Eqs. 9-51 and 9-52 is subject to the same assumptions as Eqs. 9-6 through 9-9, i.e., they are applicable only to elastic, undamped single degree of freedom systems initially at rest.

9.5.2 Shock Response Spectra

In general, a shock response spectrum is a plot of the peak response of an elastic, undamped single degree of freedom system to a given transient input as a function of the system natural frequency. Shock spectra have a wide variety of applications in structural dynamics and protective construction, including modal analysis of multidegree of freedom systems. Some of the basic shock response spectra concepts are introduced in the following paragraphs.

Consider the system shown in Fig. 9-20 but without the damping element. The force in the spring at any instant in time will be the spring constant k times the relative displacement, u, between the support and the mass. In the elastic range, the energy stored in the spring at any point in time will be

$$U = \frac{1}{2} ku^2 \qquad (9\text{-}53)$$

If this stored energy were instantaneously converted to kinetic energy, that energy could be expressed as

$$U = \frac{1}{2} Mv^2 \qquad (9\text{-}54)$$

where v is the velocity of the mass. Equating the above two expressions for energy leads to

$$v = \sqrt{\frac{K}{M}}\, u = \omega_N u \qquad (9\text{-}55)$$

The velocity defined by Eq. 9-55 is not a real velocity and is only equal to or approximately equal to the true relative velocity for certain support motions and frequency ranges. Accordingly, the quantity v as found above is often called the pseudo-velocity.

Note that for an undamped system. Eq. 9-47 can be written

$$\ddot{x} = -\omega_N^2 u \qquad \text{or} \qquad -\frac{\ddot{x}}{\omega_N} = \omega_N u \qquad (9\text{-}56)$$

From Eqs. 9-55 and 9-56 it is seen that

$$\omega_N u = v = -\frac{\ddot{x}}{\omega_N} \qquad (9\text{-}57)$$

The quantities u, v and $\ddot{x}$ in Eq. 9-57 are instantaneous values of relative displacement, pseudo-velocity and absolute acceleration of the mass, and it logically follows that their peak values are similarly related. Setting

$$\begin{aligned} D &= |u|\ \text{max} \\ V &= |v|\ \text{max} \\ A &= |\ddot{x}|\ \text{max} \end{aligned} \qquad (9\text{-}58)$$

then the quantities D, V and A in systems without damping must also satisfy Eq. 9-57 and

$$\omega_N D = V = \frac{A}{\omega_N} \qquad (9\text{-}59)$$

Equation 9-59 also applies approximately for systems with small amounts of damping.

A convenient way of presenting Eq. 9-59, which relates peak values of relative displacement, pseudo-velocity, acceleration of the mass, and the system natural frequency, is with a 4-way logarithmic plot. Taking the logarithm of Eq. 9-59 leads to

$$\log \omega_N + \log D = \log V = \log A - \log\omega_n \quad (9\text{-}60)$$

These relationships are shown qualitatively in Fig. 9-21 where any horizontal line in the figure has the equation

$$\log V = \text{constant} \quad (9\text{-}61)$$

and represents a line of constant peak pseudo-velocity. Similarly, any vertical line is a line of constant natural frequency.

$$\log \omega_N = \text{constant} \quad (9\text{-}62)$$

Then from Eq. 9-60

$$\log D = \log V - \log \omega_N = \text{constant} \quad (9\text{-}63)$$

and

$$\log A = \log V + \log \omega_N = \text{constant} \quad (9\text{-}64)$$

Equations 9-63 and 9-64 represent lines of peak relative displacement and peak acceleration of the mass, respectively. Equation 9-63 will be a straight line with a slope of plus 1 and Eq. 9-64 a straight line with a slope of minus 1.

Figure 9-21 is merely one of many ways in which shock response spectra can be portrayed. Any response parameter plotted as a function of a spectrum of frequencies can be called a shock response spectrum. It is often found convenient to express the various response parameters in dimensionless form by normalizing them with respect to the maximum value of the input function. The resulting response spectra can then be applied to a wide range of input functions having similar variations with time. Peak values of these normalized quantities can be considered peak amplification factors for the

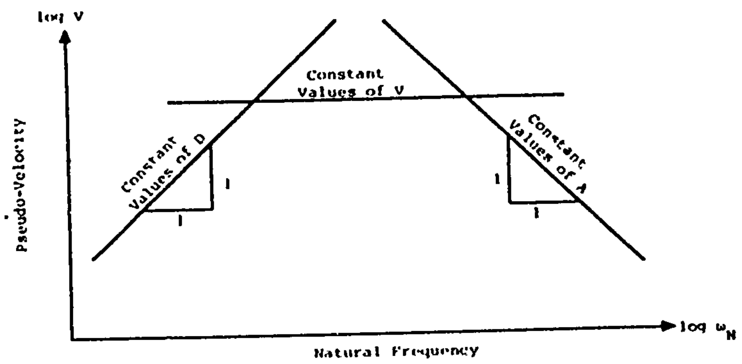

Figure 9-21 Four-Way Logarithmic Shock Spectrum Plot for Undamped Single Degree of Freedom System

parameters of interest. Shock response spectra for single degree of freedom systems are discussed further below.

9.5.3 Elastic Single Degree of Freedom Shock Response Spectra

The response of a single degree of freedom system to support motions is, of course, strongly dependent upon both the physical characteristics of the system and the nature of the support motions. As noted previously, the response of elastic undamped single degree of freedom systems to four types of support motion can be determined using Eqs. 9-6 through 9-9; provided appropriate terms are used for the forcing function. References 9-8 and 9-9 present rather extensive treatments of the effects of various input motions on shock response spectra and the determination of peak response values.

In order to demonstrate the use of a shock response spectrum, consider a rectangular acceleration input to the support of an undamped single degree of freedom system. The maximum relative displacement between the mass and the support, which is also the maximum deformation of the spring, is given by Eq. 9-52. If an acceleration pulse duration t_o of 0.5 second and a peak amplitude $\ddot{y}_o$ of 1g are assumed, a shock response spectrum such as shown in Fig. 9-22 can be constructed by using maximum dynamic load factors from Fig. 9-6 in Eq. 9-52. Figure 9-22 shows the maximum relative displacement due to the rectangular acceleration pulse as a function of the system circular natural frequency. If it were desired to choose a systems whose maximum spring deformation would not exceed 10 inches (25.4 cm), *Fig.* 9-22 shows that the system's natural frequency would have to be greater than about 9 rad/sec. Alternatively, if it were known that the system of interest had a natural frequency of 5 rad/sec, the maximum spring deformation to be expected would be in the neighborhood of 29 inches (73.16 cm). With the specific scales used for its coordinate axes,

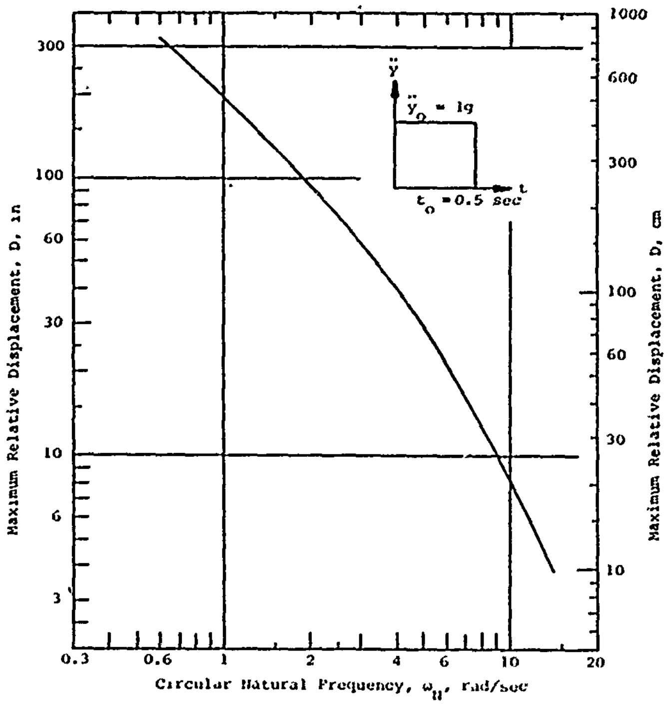

Figure 9-22 Maximum Relative Displacement Spectrum for Undamped Elastic System Subjected to a Rectangular Acceleration Pulse of Finite Duration

Fig. 9-22 is applicable only to systems subjected to the assumed support motion. This particular waveform is of little practical significance in protective construction, since the support velocity associated with the rectangular acceleration pulse never returns to zero.

A four-way logarithmic response spectrum for a triangular velocity pulse input is shown in Fig. 9-23. Although Fig. 9-23 is for a particular input waveform (symmetrical triangular velocity pulse), it is considerably more general than Fig. 9-22 because its coordinate scales are in dimensionless form. Note that the frequency parameter is expressed in terms of the product of pulse duration and system frequency. Peak relative displacement, psuedo-velocity and mass acceleration are all expressed as ratios to the corresponding support motion parameter. The three support motion parameters are related by simple geometrical considerations so that whichever peak value is specified the other two can be readily calculated. The notation $t_m \geq t_o$ at the top of Fig. 9-23 indicates that for values of $t_o f$ less than 1.0 the maximum response occurs during free vibration after the disturbing function has returned to zero. Figure 9-23 is used in a manner similar to that described for Fig. 9-22 except that the given parameters must be transformed into dimensionless form and the data obtained from the spectrum must be transformed into absolute values of the parameter of interest.

Note that only peak values of the response parameters are obtained from the response spectra and that these values are strictly applicable only for the given waveforms. Reference 9-8 presents a large number of spectra plots for various types and shapes of input waveforms, e.g., triangular, sine and parabolic support velocity and displacement functions, etc. In addition, procedures are given for constructing approximate spectra plots when the input velocity or displacement waveform is not known precisely.

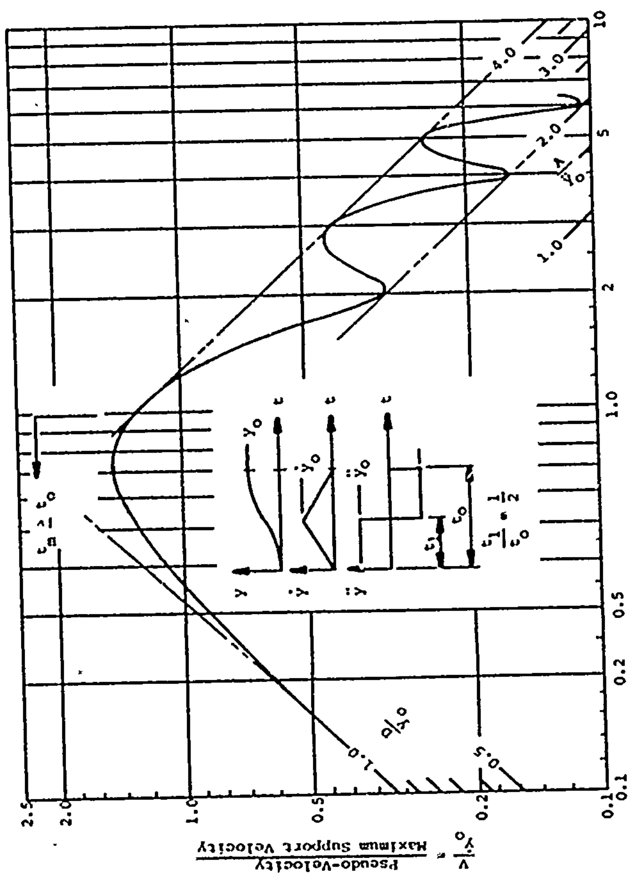

Figure 9-23 Deformation Spectrum for Undamped Elastic System Subjected to a Symmetrical Triangular Velocity Pulse (Ref. 9-8)

The effect of damping on the response of an elastic single degree of freedom system is indicated in Fig. 9-24. As might be expected, the effect of damping on the response of a single degree of freedom system subjected to base support motions is to reduce the peak values and to smooth out irregularities in the response curves.

The undamped curve ($\beta = 0$) in Fig. 9-24, although for a half-cycle parabolic velocity pulse, is seen to be not too different in general shape from the curve of Fig. 9-23 for a symmetrical triangular half-cycle velocity pulse input. It may be concluded, then, that the response of an undamped system is not greatly affected by the waveform differences between the symmetrical triangular and parabolic pulses.

9.5.4 Elastic-Plastic Single Degree of Freedom Shock Response Spectra

As discussed in earlier paragraphs, it is sometimes advantageous to allow a system to yield when subjected to dynamic loads or base motions. One important application of this concept is the design of supports for acceleration sensitive items of equipment. By allowing such supports to yield, it is often possible to limit forces or accelerations to levels lower than those which would cause equipment failure. The inelastic response of the supports causes significant changes in the shock response spectra for the system. If the spring in Fig. 9-20 has an elastic-plastic resistance function as shown in Fig. 9-25, it is necessary to consider the effect of spring yielding on the response of the mass if the spring yields before reaching its maximum displacement. It is convenient to relate the maximum response of the elastic-plastic system to that of an elastic system having the same stiffness as the initial stiffness of the elastic plastic system. Referring to Fig. 9-25, we can define a reduction factor to be

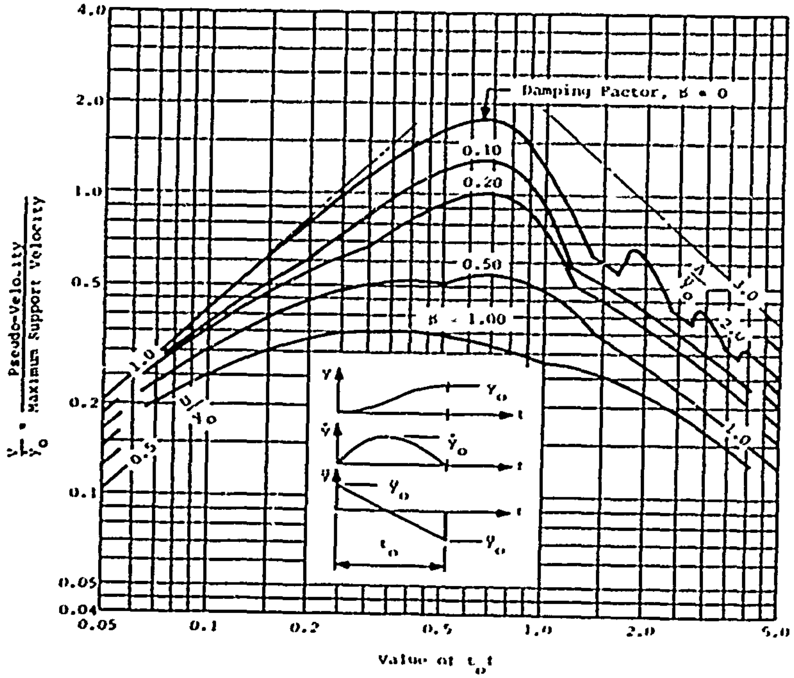

Figure 9-24 Deformation Spectra for Damped Elastic System Subjected to a Half-Cycle Parabolic Velocity Pulse (Ref. 9-8)

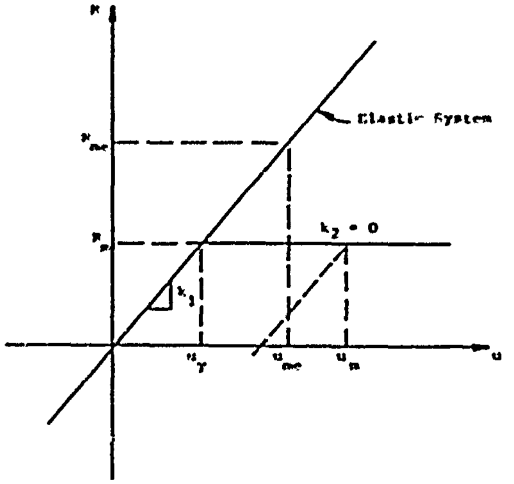

Figure 9-25 Resistance Function for Single Degree of Freedom Elastic-Plastic System

$$C = \frac{R_m}{R_{me}} = \frac{u_y}{u_{me}} \qquad (9\text{-}65)$$

where

u_{me} = maximum relative displacement of related elastic system

u_y = yield relative displacement of elastic-plastic system

R_m = maximum resistance of elastic-plastic system

and

$$R_{me} = k_1 u_{me} \qquad (9\text{-}66)$$

For an elastic system, R_m and u_y are equal to R_{me} and u_{me}, respectively, and the reduction factor is equal to unity.

The ductility factor (Eq. 9-16) can also be defined in terms of relative displacements as

$$\mu = \frac{u_m}{u_y} \qquad (9\text{-}67)$$

where u_m is the maximum relative displacement of an elastic-plastic system. Equation 9-65 can then be written in the form

$$C = \frac{u_m}{\mu u_{me}} \text{ or } \frac{u_m}{u_{me}} = \mu C \qquad (9\text{-}68)$$

For a system without damping, the spring force is proportional to the acceleration of the mass. Therefore,

$$\frac{R_m}{R_{me}} = \frac{\ddot{x}_m}{\ddot{x}_{me}} = C \qquad (9\text{-}69)$$

where $\ddot{x}_m$ and $\ddot{x}_{me}$ denote maximum absolute accelerations of the masses in the elastic-plastic and elastic systems, respectively.

The relationship between elastic and elastic-plastic single degree of freedom systems for three limiting forms of support motion are described below. In each case the system is undamped and initially at rest.

Instantaneous Displacement Change. For an instantaneous displacement change, the initial value of the relative displacement will be equal to y_o for both elastic and elastic-plastic systems. Since there is no additional energy input to the system, this will also be the absolute maximum deformation, and the reduction factor from Eq. 9-68 with $u_m = u_{me} = y_o$ will be

$$C = \frac{1}{\mu} \tag{9-70}$$

This relationship is also applicable to systems subjected to input displacements where the rise time is small compared to the natural period of the system.

Instantaneous Velocity Change. When a system is subjected to an instantaneous velocity change, $\dot{y}_o$, the energy imparted to the system is $\frac{1}{2} m\dot{y}_o^2$ regardless of whether the system is elastic or elastic-plastic. By equating energies in the equivalent elastic and the elastic-plastic systems (See Fig. 9-25) at the point of maximum deformation, the reduction factor is found to be

$$C = \frac{1}{\sqrt{2\mu - 1}} \tag{9-71}$$

This relationship also holds for an arbitrary input waveform, provided both elastic and elastic-plastic systems reach their absolute maximum displacements during free vibration and the elastic-plastic system does not yield during forced vibration. This requires that the yield displacement of the elastic-plastic system be equal to or greater than the maximum deformation of the elastic system during forced vibration. It should also be applicable to systems subjected to quarter-cycle velocity pulses where the rise time is small compared to the system natural period (i.e., half-cycle acceleration pulses of short duration).

Instantaneous Acceleration Change. The reduction factor for this case can be shown to be (Ref. 9-8)

$$C = \frac{\mu}{2\mu - 1} \tag{9-72}$$

This relationship would also be applicable for acceleration pulses with a short rise time and long duration compared to the natural period of the system.

Table 9-9 summarizes values of the reduction factor and the ratio u_m/u_{me} (= μC) corresponding to different values of μ for the above three input functions. An examination of the data in Table 9-9 indicates that a relatively small amount of inelastic action can produce a significant reduction in the required yield resistance, R_m. It is also obvious that for μ values of 1.5 or less, the reduction factor and ratio u_m/u_{me} are relatively insensitive to the form of input. This is not true, however, for larger values of μ.

Response spectra for elastic-plastic systems can be plotted for specific values of μ in a format similar to that for elastic systems. The pseudo-velocity, V, for an elastic-plastic system is defined on the basis of the initial elastic range of the load deformation relation for the system.

$$V = \omega_N u_y \tag{9-73}$$

Note that ω_N is the undamped natural frequency corresponding to k_1 in Fig. 9-25 and that u_y is the yield deformation and not the maximum relative displacement.

The pseudo-acceleration, A, for an elastic-plastic system is defined as

$$A = \omega_N^2 u_y \tag{9-74}$$

For an elastic-plastic system without damping, Eq. 9-74 is also equal to the peak acceleration of the mass.

Table 9-9

COMPARISON OF REDUCTION FACTORS

μ	Reduction Factor, $C = R_m/R_{me}$			$u_m/u_{me} = \mu C$		
	Displ. Step	Velocity Step	Accel. Step	Displ. Step	Velocity Step	Accel. Step
1	1.00	1.00	1.00	1.00	1.00	1.00
1.25	0.80	0.82	0.83	1.00	1.02	1.04
1.5	0.67	0.71	0.75	1.00	1.06	1.12
2	0.50	0.58	0.67	1.00	1.16	1.33
3	0.33	0.45	0.60	1.00	1.34	1.80
5	0.20	0.33	0.56	1.00	1.67	2.78
10	0.10	0.23	0.52	1.00	2.29	5.26

General rules for construction of elastic-plastic response spectra when the nature of the input waveform is not known precisely can be found in Ref. 9-8. On the four-way logarithmic undamped response plot shown in Fig. 9-26a, the set of diagonal lines with positive slopes represent constant values of yield displacement, u_y, and the diagonal lines with negative slopes represent constant values of pseudo-acceleration, A. Horizontal lines are constant values of pseudo-velocity V. Values of u_y, V and A can be determined directly for a given value of μ. The maximum deformation, u_m, can be determined from Eq. 9-67. The apparent multi-valued character of portions of Fig. 9-26a is due to the fact that more than one value of u_y can produce the same ductility factor, μ. The effect of damping for the same input waveform is indicated in Fig. 9-26b.

The effects of plastic action and damping on the response of a single degree of freedom system subjected to a half-cycle parabolic velocity pulse are illustrated in Table 9-10. The values shown in the table are from Figs. 9-26a and 9-26b. These values are not necessarily indicative of any general response trends, but rather they illustrate the complex relationship between input, system frequency, inelastic action and damping on the dynamic response of a single degree of freedom system.

9.5.5 Optimum Shock Isolator Response Spectra

In any design process, a measure of merit is required for differentiation between alternative designs. For shock isolation systems, the shock response spectrum is a tool frequently used for this purpose. The response spectrum presents peak acceleration of the isolated object as a function of peak relative displacement between the object and its supporting base. For the shock response spectrum, the isolation element between the object and the base is a linear spring with either no or with small amounts of viscous damping.

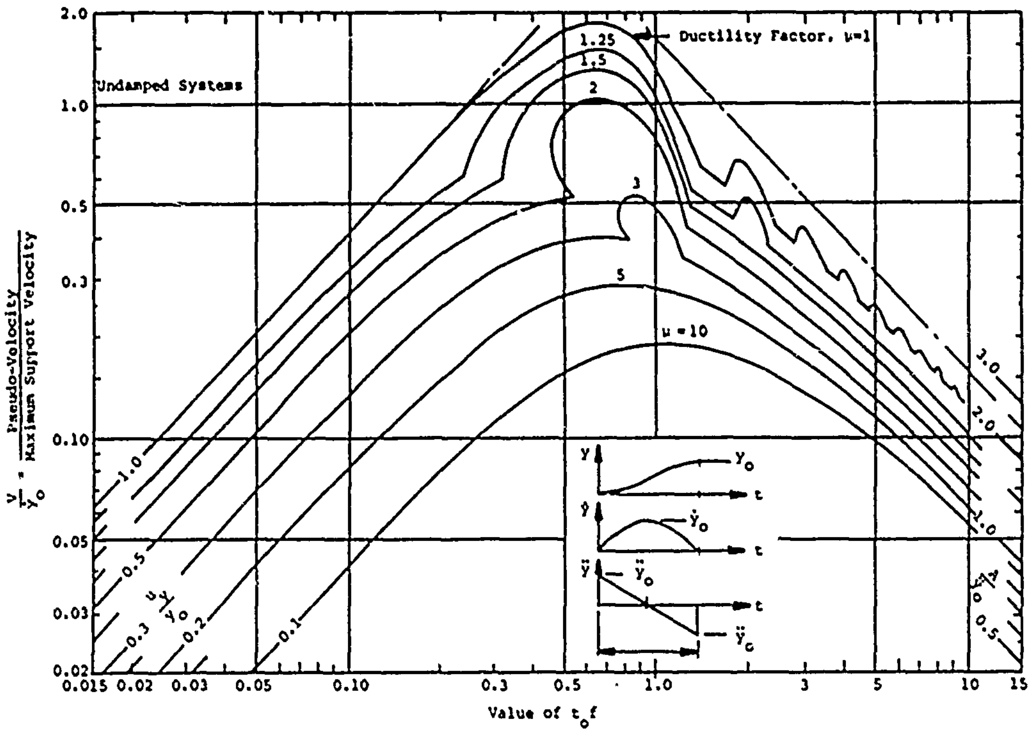

Figure 9-26a Deformation Spectra for Undamped Elastic-Plastic Systems Subjected to a Half-Cycle Parabolic Velocity Pulse (Ref. 9-8)

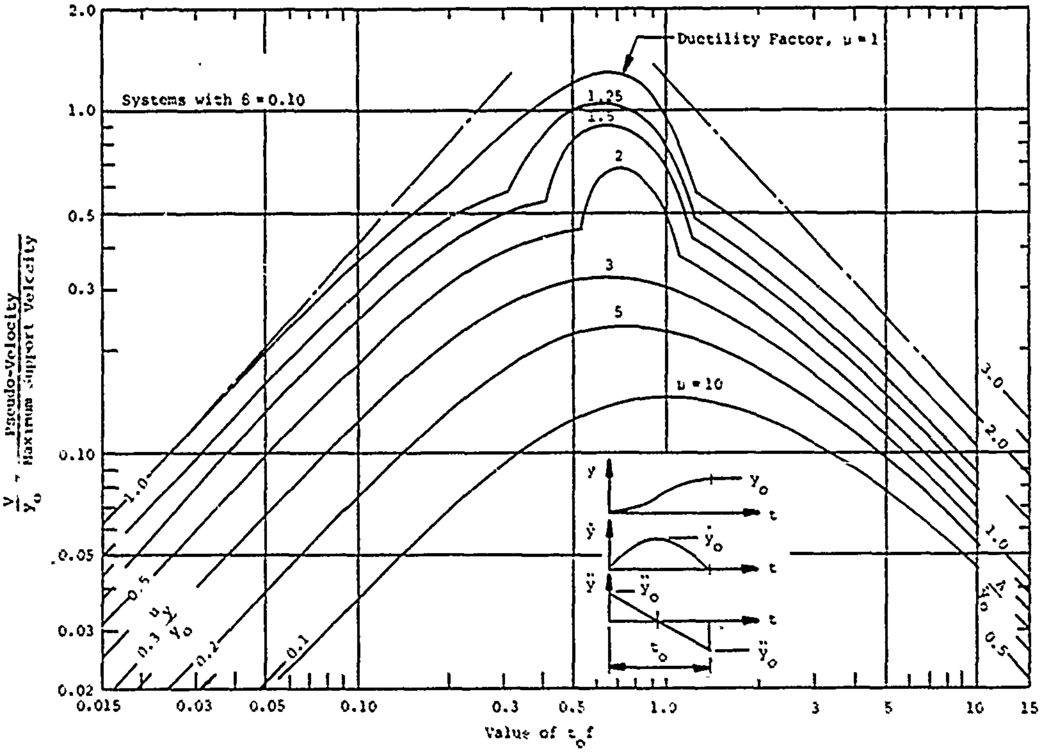

Figure 9-26b Deformation Spectra for Elastic-Plastic Systems With Ten Percent Critical Damping Subjected to a Half-Cycle Parabolic Velocity Pulse (Ref. 9-8)

Table 9-10

COMPARISON OF RESPONSE VALUES OF HALF-CYCLE PARABOLIC VELOCITY PULSE

Ductility μ	Damping ζ	$\omega_N \approx 5$ rad/sec			$\omega_N = 9$ rad/sec		
		u_{max} (in)	u_{max} (cm)	A (g)	u_{max} (in)	u_{max} (cm)	A (g)
1	0	13.4	34.0	0.9	9.3	23.6	2.0
1	0.1	10.1	25.7	0.7	6.8	17.3	1.5
2	0	10.0	25.4	0.3	11.0	27.9	1.2
2	0.1	8.4	21.3	0.3	7.4	18.8	0.8
3	0	11.1	28.2	0.2	6.8	17.3	0.5
3	0.1	8.7	22.1	0.1	5.3	13.5	0.4

The natural frequency of the isolation element is the parametric variable that distinguishes one shock isolation system design from another.

The trade-off limit diagram (Ref. 9-16) presents peak acceleration of the isolated object as a function of rattlespace required. In the case of the trade-off limit diagram, the isolation element is an ideal, passive constant force device. A device of this sort instantaneously exerts a constant force which resists relative displacement between the isolated object and its base. Figure 9-27a shows a schematic and the velocity-time history of the constant force isolation system. At point 1, the velocity of the isolated object has reached the velocity of the base. Area RS 1 represents the peak relative displacement between the object and the base up to the time at which the velocities matched. From point 1 to point 2, the relative velocity between object and base is reversed. Rattlespace RS 1 is recovered such that at point 2 the object is in its original position relative to the base. Between points 2 and 3, rattlespace RS 2 is accumulated. The greater of RS 1 and RS 2 is the peak relative displacement required. It can be shown (Ref. 9-17) that for a given peak acceleration on the isolated object, the minimum possible rattlespace required is achieved with use of just such a constant force device. The trade-off limit diagram presents this optimally minimum rattlespace as a function of peak acceleration on the isolated object with the isolator force level as the parametric variable that distinguishes one design from another.

It has been found beneficial to present the response of constant force isolators to a specific waveform in a manner that will allow direct comparison to the more conventional single degree of freedom response spectrum. Although the concept of frequency has no meaning in the case of constant force isolators, a pseudo frequency can be defined based upon the performance of the system.

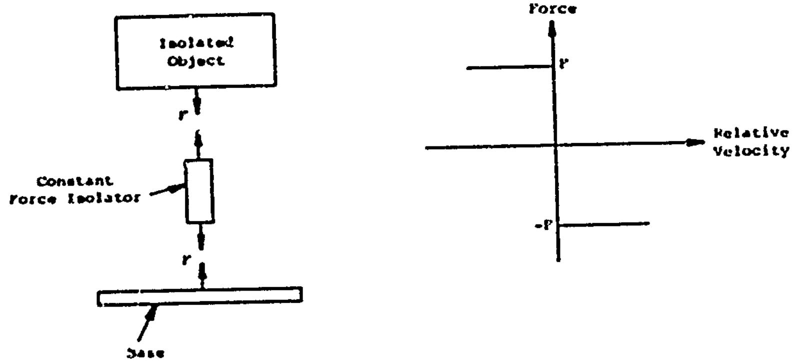

Constant Force Isolator Schematic

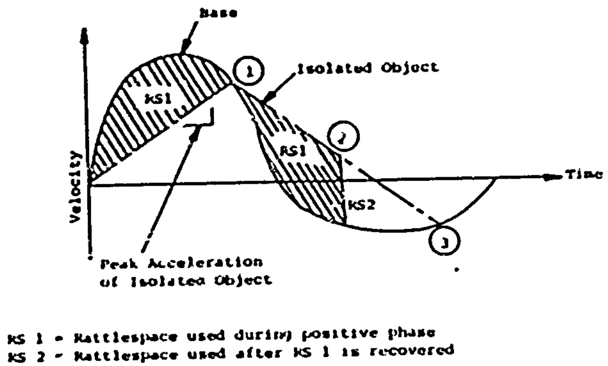

Velocity-Time History of Base and Isolated Object

Figure 9-27a Schematic and Velocity-Time History of Constant Force Isolation System (Ref. 9-17)

Using the relationships described previously, the rattlespace or maximum relative displacement, D, can be determined for a given maximum allowable acceleration level, A. These values, coupled with the basic shock spectra approach can be used to define a pseudo frequency

$$\omega_p^2 = \frac{A}{D}$$

and the corresponding pseudo velocity

$$V = \frac{A}{\omega_p} = \omega_p D$$

These parameters can then be plotted on the typical shock spectra 4-way logarithmic plot to indicate the best possible isolation performance. This plot, along with the more conventional shock spectra curves, can better inform the designer of the importance of the ground shock environments and serve to provide a basis for comparison of the performance of a selected isolation scheme.

As an example of this comparison, see Fig. 9-27b which compares the response of both linear undamped single degree of freedom isolators with the optimum isolator when subjected to a particular input waveform (symmetrical triangular velocity pulse).

9.6 MULTIDEGREE OF FREEDOM SYSTEMS

9.6.1 General

In most instances, it is not possible to represent a real structure by a single degree of freedom system with sufficient accuracy. This is particularly true if it is necessary to describe the motion environment or determine stresses at various points in the structure. In these instances the structure must be analyzed as a multidegree of freedom system and the complexity of the problem increases

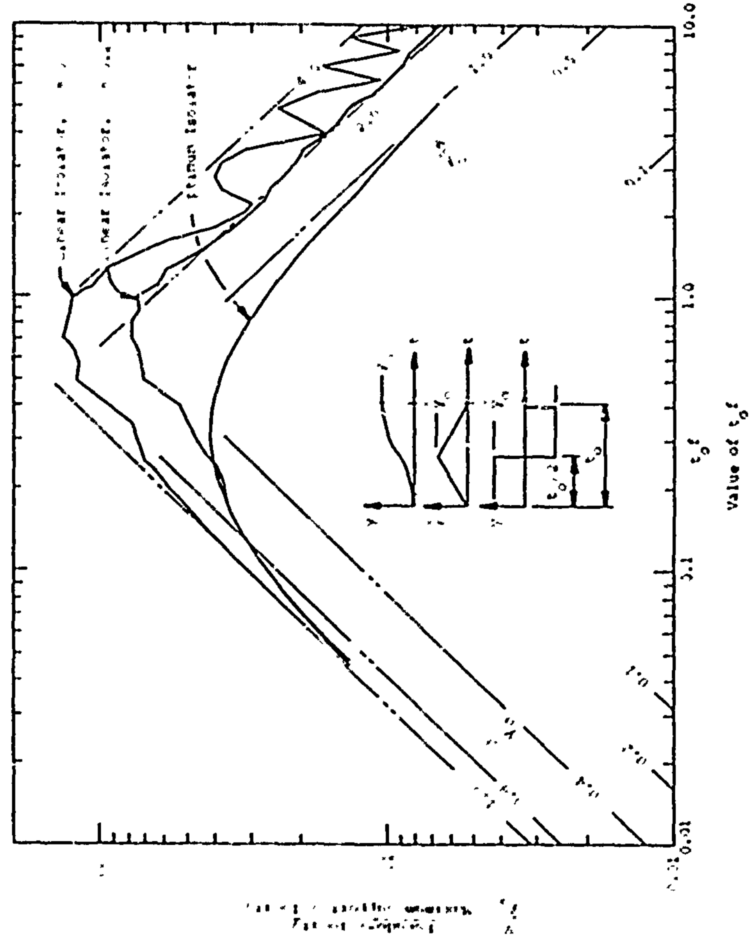

Figure 9-27b Deformation Spectra for Linear and Optimum Isolators Subjected to a Symmetrical Triangular Velocity Pulse

since there are as many modes of vibration as there are degrees of freedom. The number of degrees of freedom is equal to the number of independent coordinates required to completely define the configuration of the structure at all times. In the most general case, six coordinates are required to describe the position of each mass. Since real structures are distributed mass systems with infinite degrees of freedom, simplifications are normally necessary to permit analysis. The real structure is usually approximated by an assemblage of finite, idealized substructures or elements which are connected at a finite number of node points. The types of elements most commonly used include beam-columns, tension-compression bars, triangular plates, quadrilateral plates, tetrahedrons, hexahedrons and simple springs. Distributed masses are normally lumped at node points. Figure 9-28 shows some simple examples of finite element representations of real structures. Even these simple structures can be approximated in other ways, e.g., the arch could be modeled using rectangular or triangular plate elements, the rectangular structure could be modeled using plate elements or a combination of plate and beam elements, etc.

The location of node points is determined by the analyst and is based on considerations of load distribution, real structure characteristics and information required from the analysis. Efficient finite element representation of complex structures requires considerable experience and insight on the part of the analyst and very little general guidance can be provided. Increasing the number of node points allows greater detail in the analysis but does not necessarily assure a proportionate increase in the accuracy of the results.

In some forms of dynamic analysis, e.g., the modal method of analysis, it is necessary to determine the normal modes of vibration of the structure. The number of node points and the freedom of motion allowed each node point

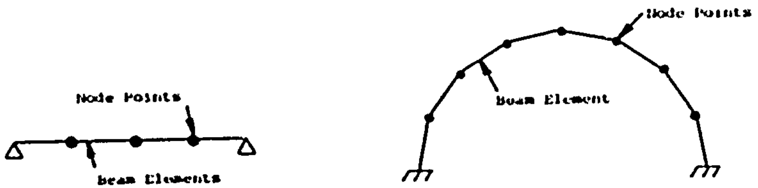

(a) Simple Beam (b) Arch

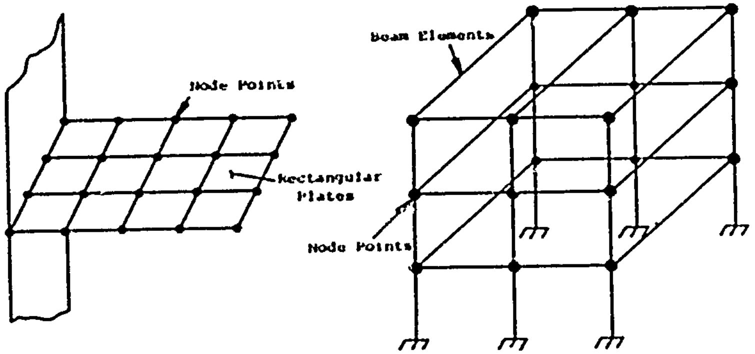

(c) Cantilever Plate (d) Rectangular Structure

Figure 9-28 Finite Element Representation of Simple Structures

determines the number of modes of vibration possible in the finite element representation. In three dimensional problems, a single node point may have as many as six degrees of freedom (3 translational and 3 rotational). In practice, some of these degrees of freedom are often restrained to reduce the computational effort. A finite element model has the same number of normal modes as degrees of freedom. Associated with each mode of vibration is a frequency and characteristic shape. The distinguishing feature of a normal mode is that the system could, under certain circumstances, vibrate freely in that mode alone, and during such vibrations the ratio of the displacements of any two masses is constant with respect to time. The number of mode shapes which should be included in a dynamic analysis depends on several factors including the geometry of the real structure, the frequency spectrum of the loading function and the purpose of the analysis. If the objective is to determine shock inputs to an item of equipment, an item sensitive to a broad spectrum of frequencies would require the inclusion of a greater number of modes than one sensitive to a narrow band of frequencies. A complex input motion also justifies the inclusion of a greater number of mode shapes than a simple sinusoidal input. In the absence of other controlling factors the finite element representation should allow extraction of mode shapes corresponding to frequencies at least twice that of the upper limit of the frequency range of interest. Most computer programs used for dynamic analysis allow the establishment of an upper cut-off frequency for the analysis. In some instances the number of node points will be limited by the capabilities of a computer or computer program. Although some programs such as NASTRAN are limited only by computer storage capability, computation costs rapidly increase with the degrees of freedom allowed the mathematical model.

An additional consideration in the spacing of node points arises in the computation of stresses in an element.

A closer spacing is required in regions where high stress gradients are expected. Since the finite element approach assumes stresses to be constant over some types of elements, a coarse spacing of elements could overlook significant stress concentrations.

The computational effort connected with the analysis of multidegree of freedom systems rapidly increases with the number of degrees of freedom. Although up to three or four degrees of freedom might be handled by hand calculations, most problems require the use of electronic computers. Programs such as NASTRAN, STARDYNE, SAMSON, DYNATIER, SOILTIER, INELASTIER, and SAP IV include both static and dynamic analysis capability. Except for the SAMSON and INELASTIER codes the above programs are limited to linear-elastic materials. These and other similar programs normally are designed to accept [illegible] descriptions of member properties, structure geometry and load characteristics and offer various options as to calculated parameters. Optional loading functions include static or time varying loads or displacements at specified node points. Output options include normal mode shapes and frequencies, response histories and stresses in members. Most programs also include some form of check for errors in input data.

Certain simple multidegree of freedom systems do lend themselves to hand computations. In some cases the mathematical techniques used for analysis are identical to those used in the computer programs; in others, different methods of analysis are more convenient. The following paragraphs of this section introduce some of these methods as well as other aspects of multidegree of freedom systems.

9.6.2 Free Vibration of Multidegree of Freedom Systems

An important first step in most dynamic analyses is the determination of normal modes of vibration including characteristic shapes and frequencies. Experienced analysts can often draw important conclusions regarding the dynamic response of a system to specified loads from its normal modes alone.

The natural frequencies and characteristic shapes of an undamped system having N masses and N degrees of freedom can be obtained directly by solution of a system of N equations of motion. With no external forces applied to the system the equations of motion can be obtained by considering the equilibrium of each mass in the system. The equations would have the form

$$\begin{aligned} &M_1\ddot{y}_1 + k_{11}y_1 + k_{12}y_2 + \dots k_{1N}y_N = 0 \\ &M_2\ddot{y}_2 + k_{21}y_1 + k_{22}y_2 + \dots k_{2N}y_N = 0 \\ &\dots\dots\dots\dots\dots\dots\dots\dots \\ &M_N\ddot{y}_N + k_{N1}y_1 + k_{N2}y_2 \dots\dots k_{NN}y_N = 0 \end{aligned} \qquad (9\text{-}75)$$

where the k's are stiffness coefficients, which are spring constants or combinations thereof. For example, the coefficient k_{12} represents a force applied to M_1 due to a unit displacement of M_2 in the direction y_2 with all other y's equal to zero. The various y's might represent displacements in different directions and/or rotations about different axes, and the determination of these stiffness coefficients alone represents a large computational effort for complex structures. The system of equations can be solved in various ways. For example, it can be shown that vibration in a normal mode is always harmonic and, if solutions of the form

$$y_1 = A_1 \sin \omega t_1;\; y_2 = A_2 \sin \omega t;\; \dots\; y_N = A_N \sin \omega t$$

are assumed and substituted in Eqs. 9-75 and terms are rearranged, the system of equations becomes

$$
\begin{aligned}
(k_{11}-M_1\omega^2)A_1 + k_{12}A_2 + \ldots\ldots + k_{1N}A_N &= 0 \\
k_{21}A_1 + (k_{22}-M_2\omega^2)A_2 + \ldots\ldots + k_{2N}A_N &= 0 \\
\cdots\cdots\cdots\cdots\cdots\cdots\cdots\cdots\cdots\cdots\cdots\cdots \\
k_{N1}A_1 + k_{N2}A_2 + \ldots\ldots + (k_{NN}-M_N\omega^2)A_N &= 0
\end{aligned}
\qquad (9\text{-}76)
$$

A nontrivial solution of the above system of equations exists only if the determinant of the coefficients of the A's is equal to zero. Expansion of the detriminant of these coefficients yields a frequency equation which can then be solved for ω. There will be N real roots to the frequency equation; some may be equal and some may be zero. Each value of ω is substituted back into Eqs. 9-76 to obtain a set of amplitude coefficients, A_N, for each frequency. These coefficients define the characteristic shapes for each frequency. They define the relative, not absolute, amplitude of motion at each node point. This type of problem is called a characteristic or eigenvalue problem and the quantities ω^2 are called characteristic values or eigenvalues. The characteristic shapes are often called eigenvectors. The direct solution of the frequency equation becomes extremely cumbersome as the number of modes increases and iterative or approximate methods of solution are often used.

Figure 9-29 shows three different types of undamped two degree of freedom systems. The system shown in Fig. 9-29(a) is described as a far coupled system since a reaction is generated at the support by a displacement x_2 even if x_1 is equal to zero. In the close coupled system of Fig. 9-29(b) only adjacent masses or node points are affected by a displacement of any one mass. For the system shown in Fig. 9-29(b), Eqs. 9-75 become

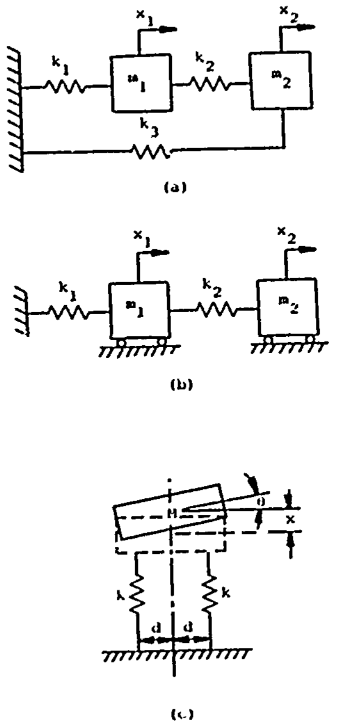

(a)

(b)

(c)

Figure 9-29 Two Degree of Freedom Systems

$$m_1\ddot{x}_1 + (k_1 + k_2)\,x_1 - k_2x_2 = 0$$
$$m_2\ddot{x}_2 - k_2x_1 + k_2x_2 = 0 \qquad (9\text{-}77)$$

The corresponding equations for the two degree of freedom system shown in Fig. 9-29(c) are

$$m\ddot{x} + 2kx = 0$$
$$I\ddot{\theta} + 2kd^2\theta = 0 \qquad (9\text{-}78)$$

where I = mass moment of inertia. It is seen that the coordinates x_1 and x_2 appear in both Eqs. 9-77 while x and θ each appear in only one of Eqs. 9-78. Equations 9-77 are thus coupled, and determination of the response of the system requires simultaneous solution of two differential equations. Equations 9-78, on the other hand, are uncoupled, and the system response can be found by solving each separately as an independent single degree of freedom system. It should also be noted that the number of degrees of freedom does not necessarily correspond to the number of masses. The system shown in Fig. 9-29(b) will be used to demonstrate the method of solution of the equations of motion.

Since the free vibrations are harmonic motions, general solutions can be assumed of the form

$$x_1 = a_1 \sin \omega t + b_1 \cos \omega t$$
$$x_2 = a_2 \sin \omega t + b_2 \cos \omega t \qquad (9\text{-}79)$$

Since sine and cosine functions differ only by a phase angle, the above expressions can also be written

$$x_1 = \Lambda_1 \sin (\omega t + \phi)$$
$$x_2 = \Lambda_2 \sin (\omega t + \phi) \qquad (9\text{-}80)$$

where Λ_1 and Λ_2 are peak amplitudes of the motion. Substituting Eqs. 9-80 into Eqs. 9-77 leads to

$$[(k_1 + k_2) - m_1\omega^2]\,\Lambda_1 - k_2\Lambda_2 = 0$$
$$-k_2\Lambda_1 + (k_2 - m_2\omega^2)\,\Lambda_2 = 0 \qquad (9\text{-}81)$$

The determinant of the coefficients must be equal to zero for a nontrivial solution so

$$\begin{vmatrix} [(k_1 + k_2) - m_1\omega^2] & -k_2 \\ -k_2 & (k_2 - m_2\omega^2) \end{vmatrix} = 0 \qquad (9\text{-}82)$$

Expanding the determinant and solving for ω^2 results in

$$\omega^2 = \frac{1}{2}\left\{\frac{k_1+k_2}{m_1} + \frac{k_2}{m_2} \pm \sqrt{\left(\frac{k_1+k_2}{m_1} + \frac{k_2}{m_2}\right)^2 - \frac{4k_1k_2}{m_1m_2}}\right\} \qquad (9\text{-}83)$$

Equation 9-83 is the frequency equation for the two degree of freedom system, and it defines two values of ω (disregarding negative values) which satisfy Eqs. 9-80. These are the natural frequencies corresponding to the two modes of free vibration of the system. Depending upon the conditions which initiate the motion, vibrations may occur at either or both of the natural frequencies and at any amplitude. If $m_1 = m_2 = m$ and $k_1 = k_2 = k$, Eq. 9-83 becomes

$$\omega^2 = \frac{k}{2m}\,(3 \pm \sqrt{5})$$

or

$$\omega_1 = \sqrt{0.382\ k/m} \quad \text{and} \quad \omega_2 = \sqrt{2.618\ k/m} \qquad (9\text{-}84)$$

The lowest natural frequency, ω_1 in the case above, is called the fundamental frequency.

The characteristic shape associated with each natural frequency is found by substituting the values of ω from Eq. 9-84 into Eq. 9-81. Taking $m_1 = m_2 = m$, $k_1 = k_2 = k$, and $\omega = \omega_1$, Eq. 9-81 becomes

$$(2k - 0.382k)A_{11} = kA_{21}$$

and the amplitude ratio is

$$\frac{A_{21}}{A_{11}} = 1.618$$

For the second mode Eq. 9-81 becomes

$$(k - 2.618k)A_{22} = kA_{12} \text{ and } \frac{A_{22}}{A_{12}} = -0.618$$

The first subscript on A designates the mass (or node), and the second subscript designates the vibration mode.

Although it is not possible to determine unique values for the amplitudes, the amplitude ratios do allow description of mode shapes since they hold true for all displacements. By assigning an arbitrary value on one amplitude, all other amplitudes are fixed in relative magnitude. If the two degree of freedom system of Fig. 9-29(b) is assumed to represent the two story frame shown in Fig. 9-30(a) and an arbitrary value of 1.0 is assigned to A_1 for both modes, the mode shapes are shown in Figs. 9-30(b) and (c).

If the system is vibrating freely, i.e., no applied loads, a complete solution is obtained by summing the possible contributions from the two modes, e.g.,

$$x_1 = C_1A_{11} \sin \omega_1 t + C_2A_{11} \cos \omega_1 t$$
$$+ C_3A_{12} \sin \omega_2 t + C_4A_{12} \cos \omega_2 t$$
$$x_2 = C_1A_{21} \sin \omega_1 t + C_2A_{21} \cos \omega_1 t$$
$$+ C_2A_{22} \sin \omega_2 t + C_4A_{22} \cos \omega_2 t$$

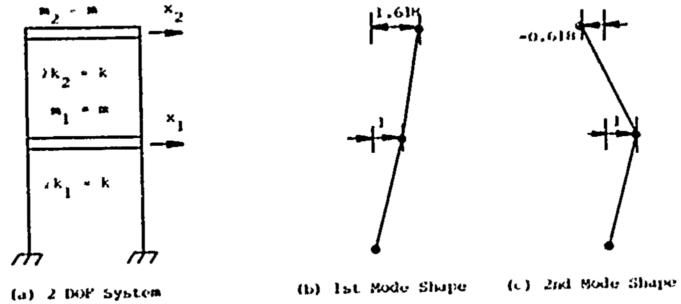

(a) 2 DOF System

(b) 1st Mode Shape

$A_{21}/A_{11} = 1.618$

$\omega_1 = \sqrt{0.382k/m}$

(c) 2nd Mode Shape

$A_{22}/A_{12} = -0.618$

$\omega_2 = \sqrt{2.618k/m}$

Figure 9-30 Natural Mode Shapes for Example Two Degree of Freedom System

The constants C are determined from the initial conditions of the problem.

If the initial conditions $x_1 = x_o$ and $x_2 = \dot{x}_1 = \dot{x}_2 = 0$ at $t = 0$ are applied to the above equations for the system under consideration, it is found that

$$C_1 = C_3 = 0$$
$$C_2 = 0.276x_o$$
$$C_4 = 0.724x_o$$

and the complete solution is

$$x_1/x_o = 0.276 \cos \omega_1 t + 0.724 \cos \omega_2 t$$

$$x_2/x_o = 0.447 \cos \omega_1 t - 0.447 \cos \omega_2 t$$

These equations are plotted as a function of t/T_1 in Fig. 9-31 to illustrate the early portion of the system response. (The contribution of the second mode is incorporated into Fig. 9-31 by noting that $T_2 = T_1\omega_1/\omega_2 = 0.382\ T_1$.)

A very important feature of normal modes of multidegree of freedom systems is the orthogonality of any two modes. The orthogonality condition may be expressed by

$$m_1\Lambda_{11}\Lambda_{12} + m_2\Lambda_{21}\Lambda_{22} + m_3\Lambda_{31}\Lambda_{32} + \dots \tag{9-85}$$
$$= \sum_{i=1}^{N} m_i\Lambda_{ir}\Lambda_{is} = 0 \qquad (r \neq s)$$

where N is the degrees of freedom of the system; Λ_{ir} is the amplitude of the i'th mass (or node) when vibrating only in the r'th mode; Λ_{is} is the amplitude of the i'th mass when vibrating only in the s'th mode; and r and s designate any two normal modes of the system. For a two degree of freedom

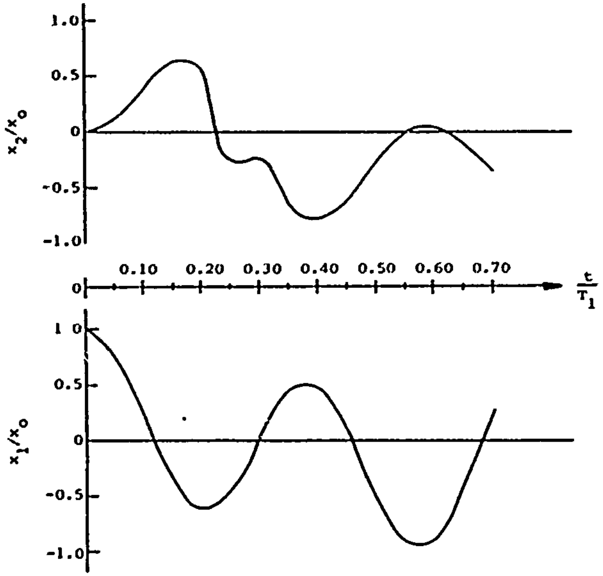

Figure 9-31 Response of Example Two Degree of Freedom System to an Initial Displacement

system, $N = 2$ and Eq. 9-85 becomes

$$m_1\Lambda_{11}\Lambda_{12} + m_2\Lambda_{21}\Lambda_{22} = 0 \qquad (9\text{-}86)$$

In the example system treated above, $m_1 = m_2 = m$; $\Lambda_{11} = \Lambda_{12} = 1.0$; $\Lambda_{21} = 1.618$, $\Lambda_{22} = -0.618$, and Eq. 9-86 shows that

$$(m)(1.0)(1.0) + (m)(1.618)(-0.618) = 0$$

as required by the orthogonality condition.

A second orthogonality condition results from the inertia and spring forces being in equilibrium when a system is vibrating in a *normal mode*. This condition may be expressed by

$$\sum_{g=1}^{m} k_g\Delta_{gr}\Delta_{gs} = 0 \qquad (r \neq s) \qquad (9\text{-}87)$$

where k_g is the stiffness of the g'th spring of m springs in the system; Δ_{gr} is the distortion of the g'th spring in the r'th natural mode; and Δ_{gs} is the distortion of the g'th spring in the s'th natural mode. For a two degree of freedom system,

$$k_1\Delta_{11}\Delta_{12} + k_2\Delta_{21}\Delta_{22} = 0 \qquad (9\text{-}88)$$

For the previous example,

$$k_1 = k_2 = k$$

$$\Delta_{11} = \Delta_{12} = 1.0$$

$$\Delta_{21} = \Lambda_{21} - \Lambda_{11} = 1.618 - 1.0 = 0.618$$

$$\Delta_{22} = \Lambda_{22} - \Lambda_{12} = 0.618 - 1.0 = -1.618$$

resulting in

$$(k)(1.0)(1.0) + (k)(0.618)(-1.618) = 0$$

and the second orthogonality condition is satisfied. Proof

of the above orthogonality conditions is presented in Ref. 9-7. As shown in later paragraphs these orthogonality conditions are extremely useful in some types of dynamic analysis.

The Stodola-Vianello procedure is a numerical iterative procedure for solution of the equations of motion of a multidegree of freedom system. It could be applied to a system of equations such as Eqs. 9-76. Although the basic procedure is simple, its application to other than simple systems is again difficult, if not impossible, for hand calculations. The process is started by assuming a characteristic shape for the system, i.e., a set of values for Λ_N. These values of Λ_N are substituted in one of the Eqs. 9-76 and a value of ω^2 corresponding to this mode shape is computed. This ω^2 value and the assumed set of Λ_N is then used in the remaining equations of Eq. 9-76 to calculate a new set of Λ_N values. The calculated set of Λ_N is then used as a new initial set and the process repeated until acceptable agreement is obtained between the initial and calculated values of Λ_N. The ω^2 term corresponding to this set defines the frequency of that mode. The procedure will converge on either the *highest* or *lowest* mode depending on whether stiffness or flexibility coefficients are used to develop the equations of motion. Other mode shapes are obtained by application of one of the orthogonality conditions. The procedure is too lengthy to demonstrate in this manual, however, it is described in greater detail and demonstrated by example in Ref. 9-7.

Another method of analysis is better suited to obtaining the fundamental mode of vibration of some types of systems and avoids the need to calculate stiffness or flexibility coefficients for the system. It is variously referred to as the modified Rayleigh or Stodola method but the basic operations are the same. Since the Rayleigh-Stodola method requires the calculation of deflections due to vertical loads, its usefulness for hand calculations is also limited to simple systems. It is an iterative procedure based on energy principles and also requires the assumption of a trial mode shape. It can be combined with finite difference methods to analyze a wide variety of structural elements. An initial mode shape is assumed and corresponding inertia forces are calculated. These inertia forces are applied to the system and displacements are calculated. The process is repeated until the desired agreement is obtained between trial and calculated mode shapes. For a lumped mass system the frequency is obtained from

$$\omega^2 = \frac{\sum_{i=1}^{N} M_i \, \phi'_i \, \phi''_i}{\lambda'' \sum_{i=1}^{N} M_i (\phi''_i)^2} \tag{9-89}$$

where

ϕ'_i = assumed mode shape

ϕ''_i = computed mode shape

λ'' = arbitrary constant such that $\lambda''\phi''_i$ is the computed deflection of the i'th mass.

The dead load deflection of the system is normally a good first trial value of the fundamental mode shape. The method can be made to converge to higher mode shapes by eliminating lower mode shape contributions using a sweeping process based on orthogonality conditions. The Rayleigh-Stodola method is demonstrated in paragraph 9.8.1.

9.6.3 Modal Method of Analysis of Multidegree of Freedom Systems

In the modal method of analysis, system responses in the normal modes are determined separately and then superimposed to obtain the total response of the system. As shown in

following paragraphs, it is generally possible to select a coordinate system so that the equations of motion for the system are uncoupled and each normal mode can be treated as a single degree of freedom system. Because the method utilizes the superposition technique it is only applicable to linearly elastic systems. It is widely used in computer programs for the analysis of multidegree of freedom systems.

The modal method of analysis is presented in the following paragraphs utilizing matrix notation. Some familiarity with matrix notation is assumed and Ref. 9-10 is suggested as a comprehensive treatment of this subject. The two degree of freedom system shown in Fig. 9-29(b) is used to more clearly demonstrate some aspects of the method. Equations 9-77, which are applicable to this system, can be considered a special case of the general equations

$$\begin{aligned} m_{11}\ddot{x}_1 + m_{12}\ddot{x}_2 + k_{11}x_1 + k_{12}x_2 &= 0 \\ m_{21}\ddot{x}_1 + m_{22}\ddot{x}_2 + k_{21}x_1 + k_{22}x_2 &= 0 \end{aligned} \tag{9-90}$$

which are written in matrix notation as

$$[m]\,\{\ddot{x}\} + [k]\,\{x\} = 0 \tag{9-91}$$

where [m] is the mass matrix, (a square matrix)

$$[m] = \begin{bmatrix} m_{11} & m_{12} \\ m_{21} & m_{22} \end{bmatrix} \tag{9-92}$$

The acceleration vector, $\{\ddot{x}\}$, is the column matrix

$$\{\ddot{x}\} = \begin{bmatrix} \ddot{x}_1 \\ \ddot{x}_2 \end{bmatrix} \tag{9-93}$$

The stiffness matrix, $[k]$, is also a square matrix

$$[k] = \begin{bmatrix} k_{11} & k_{12} \\ k_{21} & k_{22} \end{bmatrix} \qquad (9\text{-}94)$$

The displacement vector, $\{x\}$, is the column matrix

$$\{x\} = \begin{bmatrix} x_1 \\ x_2 \end{bmatrix} \qquad (9\text{-}95)$$

and the force vector (zero in this case) is the column matrix

$$\{0\} = \begin{bmatrix} 0 \\ 0 \end{bmatrix} \qquad (9\text{-}96)$$

The conventional rules for multiplying square and column matrices should be apparent from comparison of Eq. 9-90 with Eqs. 9-91 through 9-96.

All undamped two degree of freedom system equations of motion can be expressed in the form of Eqs. 9-90 and 9-91. The equations of motion for an N-degree of freedom system can also be expressed in the form of Eq. 9-91, however, the order of the matrices would change. The mass and stiffness matrices would have N columns and rows, and the acceleration, displacement and force matrices would have N rows.

The matrix form of Eq. 9-81 is

$$\left[[k] - \omega^2 [m]\right] \quad \{A\} = \{0\} \qquad (9\text{-}97)$$

It is called the characteristic equation of the system. As in the case of Eq. 9-81, it has a nontrivial solution only if the determinant of the coefficients of $\{A\}$ vanishes, i.e.,

$$\left| [k] - \omega^2 [m] \right| = 0 \qquad (9\text{-}98)$$

Expansion of Eq. 9-98 results in the frequency equation of the system (e.g., Eq. 9-83 for the two degree of freedom system of Fig. 9-29(b)). For a general two degree of freedom system, Eq. 9-98 becomes

$$\left| \begin{bmatrix} k_{11} & k_{12} \\ k_{21} & k_{22} \end{bmatrix} - \omega^2 \begin{bmatrix} m_{11} & m_{12} \\ m_{21} & m_{22} \end{bmatrix} \right| = 0 \qquad (9\text{-}99)$$

Subtracting the mass matrix from the stiffness matrix results in

$$\begin{vmatrix} k_{11} - \omega^2 m_{11} & k_{12} - \omega^2 m_{12} \\ k_{21} - \omega^2 m_{21} & k_{22} - \omega^2 m_{22} \end{vmatrix} = 0 \qquad (9\text{-}100)$$

Expansion of the determinant of Eq. 9-100 yields a quadratic equation in ω^2

$$\omega^4 (m_{11} m_{22} - m_{12} m_{21}) + \omega^2 (k_{12} m_{21} + k_{21} m_{12} - k_{11} m_{22} - k_{22} m_{11})$$

$$+ (k_{11} k_{22} - k_{21} k_{12}) = 0 \qquad (9\text{-}101)$$

Solution of Eq. 9-101 leads to four values of ω, $\pm\omega_1$ and $\pm\omega_2$, but again the negative values of ω are of no physical significance. For the system shown in Fig. 9-29(b)

$$\begin{aligned} k_{11} &= k_1 + k_2 & m_{11} &= m_1 \\ k_{12} &= -k_2 & m_{12} &= 0 \\ k_{21} &= -k_2 & m_{21} &= 0 \\ k_{22} &= -k_2 & m_{22} &= m_2 \end{aligned}$$

Substitution of these values into Eq. 9-101 leads to the solution given by Eq. 9-83.

The general two degree of freedom expansion of Eq. 9-97 is

$$\begin{bmatrix} k_{11} & k_{12} \\ k_{21} & k_{22} \end{bmatrix} - \omega^2 \begin{bmatrix} m_{11} & m_{12} \\ m_{21} & m_{22} \end{bmatrix} \begin{bmatrix} A_1 \\ A_2 \end{bmatrix} = \begin{bmatrix} 0 \\ 0 \end{bmatrix} \qquad (9\text{-}102)$$

or

$$\begin{bmatrix} k_{11} - \omega^2 m_{11} & k_{12} - \omega^2 m_{12} \\ k_{21} - \omega^2 m_{21} & k_{22} - \omega^2 m_{22} \end{bmatrix} \begin{bmatrix} A_1 \\ A_2 \end{bmatrix} = \begin{bmatrix} 0 \\ 0 \end{bmatrix} \qquad (9\text{-}103)$$

Performing the matrix multiplication indicated in Eq. 9-103 leads to

$$(k_{11} - \omega^2 m_{11})\lambda_1 + (k_{12} - \omega^2 m_{12})\lambda_2 = 0$$
$$(k_{21} - \omega^2 m_{21})\lambda_1 + (k_{22} - \omega^2 m_{22})\lambda_2 = 0 \qquad (9\text{-}104)$$

An amplitude ratio can be obtained from either of the above equations

$$\frac{\lambda_2}{\lambda_1} = -\left(\frac{k_{11} - \omega^2 m_{11}}{k_{12} - \omega^2 m_{12}}\right) \text{ or } -\left(\frac{k_{21} - \omega^2 m_{21}}{k_{22} - \omega^2 m_{22}}\right) \qquad (9\text{-}105)$$

Using values previously assumed for the example of Fig. 9-29(b)

$k_{11} = k_1 + k_2 = 2k$ $\qquad m_{11} = m_1 = m$

$k_{12} = -k_2 = -k$ $\qquad m_{12} = 0$

$k_{21} = -k_2 = -k$ $\qquad m_{21} = 0$

$k_{22} = k_2 = k$ $\qquad m_{22} = m_2 = 0$

$\omega_1^2 = 0.382\ k/m$ $\qquad \omega_2^2 = 2.618\ k/m$

If these values are substituted in either of Eqs. 9-105 the results are identical to those obtained previously, i.e.,

$$\frac{\lambda_{21}}{\lambda_{11}} = 1.618 \qquad \frac{\lambda_{22}}{\lambda_{12}} = -0.618$$

In general, the set of differential equations for an N-degree of freedom system will be coupled. If the off-diagonal terms of the mass matrix (e.g., m_{12} and m_{21} in Eq. 9-92) are not zero, the equations of motion are said to be coupled inertially (or dynamically). If the off-diagonal terms of the stiffness matrix (e.g., k_{12} and k_{21} in Eq. 9-94) are not zero, the equations are said to be coupled elastically

(or statically). For the two degree of freedom system represented by Eq. 9-77

$$[m] = \begin{bmatrix} m_1 & 0 \\ 0 & m_2 \end{bmatrix}$$

$$[k] = \begin{bmatrix} (k_1 + k_2) & -k_2 \\ -k_2 & k_2 \end{bmatrix}$$

and it is seen that the equations are coupled elastically, but not inertially. The two matrices immediately above are also symmetric, i.e., $m_{12} = m_{21}$ and $k_{12} = k_{21}$.

The coordinates chosen for systems up to this point have corresponded to the displacements of the masses. There is no compelling requirement that this be the case, except that it is generally easier to relate the equations to the physical problem under consideration. For example, the coordinates

$$y_1 = x_1$$

$$y_2 = x_2 - x_1$$

could also have been chosen to represent the system shown in Fig. 9-29(b). The equations of motion in terms of these new variables would be

$$m_1\ddot{y}_1 + k_1y_1 - k_2y_2 = 0$$
$$m_2\ddot{y}_1 + m_2\ddot{y}_2 + k_2y_2 = 0 \qquad (9\text{-}106)$$

or in matrix form

$$\begin{bmatrix} m_1 & 0 \\ m_2 & m_2 \end{bmatrix} \begin{bmatrix} \ddot{y}_1 \\ \ddot{y}_2 \end{bmatrix} + \begin{bmatrix} k_1 & -k_2 \\ 0 & k_2 \end{bmatrix} \begin{bmatrix} y_1 \\ y_2 \end{bmatrix} = \begin{bmatrix} 0 \\ 0 \end{bmatrix} \qquad (9\text{-}107)$$

Even though the two systems of Eqs. 9-77 and 9-106 appear different, they are equivalent since they describe the same physical system. There are many sets of independent coordinates which may be chosen to represent a multidegree of freedom dynamic system. Any set of such coordinates may be referred to as generalized coordinates. The only restrictions are that the number of coordinates must equal the degrees freedom of the system and the coordinates must be capable of describing the configuration for all time. In the above example, the coordinates y_1 and y_2 are not too convenient, since they result in equations which are coupled both inertially and elastically and neither the mass matrix nor stiffness matrix is symmetric. In general, it will always be possible to select a set of coordinates so that [m] and [k] are diagonal matrices and the equations of motion are uncoupled. The advantage of uncoupled equations is significant since it makes possible the treatment of an N-degree of freedom system as N single degree of freedom systems.

A set of coordinates x_i can be related to a different set of coordinates q_i by a general transformation

$$x_i = \sum_{r=1}^{n} B_{ir}\, q_r \tag{9-108}$$

where the coefficients B_{ir} are constants. In matrix notation Eq. 9-108 becomes

$$\{x\} = [B]\{q\} \tag{9-109}$$

Equation 9-91 may be rewritten in terms of $\{q\}$ as follows.

$$[m][B]\{\ddot{q}\} + [k][B]\{q\} = \{0\} \tag{9-110}$$

Premultiplying Eq. 9-110 by the transpose of the transformation matrix, $[B]^T$, results in an equation analagous to Eq. 9-91.

$$[M]\{\ddot{q}\} + [K]\{q\} = \{0\} \tag{9-111}$$

where

$$[M] = [B]^T[m][B]$$

$$[K] = [B]^T[k][B]$$

In Eq. 9-111, [M] and [K] are symmetric because [m] and [k] are symmetric.

It is possible to find a transformation matrix, $[\beta]$, which will cause [M] and [K] to be diagonal matrices (all off-diagonal terms are zero) and render Eq. 9-111 both inertially and elastically uncoupled. Under such a transformation, Eq. 9-111 becomes

$$\lceil M \rfloor\{\ddot{q}\} + \lceil K \rfloor\{q\} = \{0\} \tag{9-112}$$

where

$$\lceil M \rfloor = [\beta]^T[m][\beta]$$

$$\lceil K \rfloor = [\beta]^T[k][\beta]$$

Equation 9-112 represents a set of N uncoupled differential equations of the type

$$M_{rr}\, \ddot{q}_r(t) + K_{rr}\, q_r(t) = 0 \tag{9-113}$$

which are similar to that of a single degree of freedom system.

The orthogonality of the natural modes of vibration forms the basis for determining the appropriate transformation matrix $[\beta]$. The orthogonality condition (Eq. 9-85) can be expressed in matrix form as

$$\{A^{(r)}\}^T[m]\{A^{(s)}\} = 0 \qquad (r \neq s) \tag{9-114}$$

where $\{A^{(r)}\}$ is the column matrix of amplitudes for the r^{th} mode of vibration. This column matrix is called the r^{th} modal vector. The amplitude of the i^{th} mass (or coordinate) vibrating in the r^{th} mode is written A_{ir}.

Rewriting Eq. 9-97 as

$$[k]\{\Lambda^{(s)}\} = \omega_s^2[m]\{\Lambda^{(s)}\}$$

and premultiplying by $\{\Lambda^{(r)}\}^T$ shows that the orthogonality condition can also be written as

$$\{\Lambda^{(r)}\}^T[k]\{\Lambda^{(s)}\} = 0 \qquad (r \neq s) \tag{9-115}$$

For r = s, Eqs. 9-114 and 9-115 are not equal to zero but yield values

$$M_{rr} = \{\Lambda^{(r)}\}^T[m]\{\Lambda^{(r)}\} \tag{9-116}$$

$$K_{rr} = \{\Lambda^{(r)}\}^T[k]\{\Lambda^{(r)}\} = \omega_r^2 M_{rr} \tag{9-117}$$

where M_{rr} is an arbitrary constant which depends upon the way in which the modal vectors are normalized.

The modal vectors $\{\Lambda^{(r)}\}$ can be arranged in a square matrix of order N called the modal matrix,

$$[\Lambda] = [\{\Lambda^{(1)}\}\{\Lambda^{(2)}\}\ldots\{\Lambda^{(r)}\}\ldots\{\Lambda^{(N)}\}] \tag{9-118}$$

$$\begin{bmatrix} \Lambda_{11} & \Lambda_{12} \cdots \Lambda_{1r} \cdots \Lambda_{1N} \\ \Lambda_{21} \cdots\cdots\cdots\cdots & \vdots \\ \vdots & \\ \Lambda_{r1} \cdots\cdots \Lambda_{rr} \cdots & \Lambda_{rN} \\ \vdots & \\ \Lambda_{N1} & \Lambda_{N2} \cdots\cdots\cdots \Lambda_{NN} \end{bmatrix}$$

Each column of the square matrix of Eq. 9-118 is a modal vector corresponding to one of the N mode shapes of the system. Thus, the orthogonality condition can be written

$$[\Lambda]^T[m][\Lambda] = \lceil M \rfloor \qquad (9\text{-}11$$

$$[\Lambda]^T[k][\Lambda] = \lceil K \rfloor = \lceil \omega^2 M \rfloor \tag{9-120}$$

where $\lceil M \rfloor$ and $\lceil K \rfloor$ are diagonal matrices of terms corresponding to Eqs. 9-116 and 9-117. Comparison of Eqs. 9-119 and 9-120 with Eq. 9-112 indicates that an uncoupled system of equations may be obtained by transforming coordinates using the modal matrix, i.e.,

$$\{x\} = [\Lambda]\{q\} \tag{9-121}$$

In addition, if the modal vectors are normalized such that

$$\{\Lambda^{(r)}\}^T[m]\{\Lambda^{(r)}\} = M_{rr} = 1 \tag{9-122}$$

then Eqs. 9-119 and 9-120 become

$$[\Lambda]^T[m][\Lambda] = [I] \tag{9-123}$$

$$[\Lambda]^T[k][\Lambda] = \lceil \omega^2 \rfloor \tag{9-124}$$

where [I] is the identity matrix (all diagonal terms are one, and all off-diagonal terms are zero). When normalized in this way, the modal vectors are called an orthonormal set and the equations of motion (Eq. 9-112) become

$$\{\ddot{q}\} + \lceil \omega^2 \rfloor\{q\} = \{0\} \tag{9-125}$$

which represents a set of N uncoupled differential equations of the type

$$\ddot{q}_r(t) + \omega_r^2\, q_r(t) = 0 \tag{9-126}$$

Equation 9-126 has solutions of the form

$$q_r(t) = E_r \sin\omega_r t + F_r \cos \omega_r t \tag{9-127}$$

where E_r and F_r are constants determined by the initial conditions. Equation 9-127 can also be written

$$q_r(t) = C_r \cos(\omega_r t - \phi_r) \tag{9-128}$$

where the constants C_r and ϕ_r are amplitudes and phase angles determined by the initial conditions.

Employing Eq. 9-121, the complete free vibration solution in terms of the physical coordinates x becomes

$$\{x\} = [\Lambda]\{q(t)\} = \sum_{r=1}^{N} \{\Lambda^{(r)}\} q_r(t) \qquad (9\text{-}129)$$

where $q_r(t)$ is given by either Eq. 9-127 or Eq. 9-128.

For the two degree of freedom system of Fig. 9-29(b), the modal vectors have been determined previously to be

$$\{\Lambda^{(1)}\} = \begin{Bmatrix} \Lambda_{11} \\ \Lambda_{21} \end{Bmatrix} = \begin{Bmatrix} \Lambda_{11} \\ 1.618\Lambda_{11} \end{Bmatrix} \qquad (9\text{-}130)$$

$$\{\Lambda^{(2)}\} = \begin{Bmatrix} \Lambda_{12} \\ \Lambda_{22} \end{Bmatrix} = \begin{Bmatrix} \Lambda_{12} \\ -0.618\Lambda_{12} \end{Bmatrix} \qquad (9\text{-}131)$$

The modal matrix is then (Eq. 9-118)

$$[\Lambda] = \begin{bmatrix} \Lambda_{11} & \Lambda_{12} \\ 1.618\Lambda_{11} & -0.618\Lambda_{12} \end{bmatrix} \qquad (9\text{-}132)$$

Normalizing according to Eq. 9-123,

$$\begin{bmatrix} \Lambda_{11} & 1.618\Lambda_{11} \\ \Lambda_{12} & -0.618\Lambda_{12} \end{bmatrix} \begin{bmatrix} m & 0 \\ 0 & m \end{bmatrix} \begin{bmatrix} \Lambda_{11} & \Lambda_{12} \\ 1.618\Lambda_{11} & -0.618\Lambda_{12} \end{bmatrix} = \begin{bmatrix} 1 & 0 \\ 0 & 1 \end{bmatrix}$$

performing the indicated matrix multiplications yields

$$\begin{vmatrix} m\Lambda_{11}^2 + 2.618m\Lambda_{11}^2 & m\Lambda_{11}\Lambda_{12} - m\Lambda_{11}\Lambda_{12} \\ m\Lambda_{11}\Lambda_{12} - m\Lambda_{11}\Lambda_{12} & m\Lambda_{12}^2 + 0.382m\Lambda_{12}^2 \end{vmatrix} = \begin{vmatrix} 1 & 0 \\ 0 & 1 \end{vmatrix} \qquad (9\text{-}133)$$

Solving for Λ_{11} and Λ_{12} results in

$$\begin{aligned} \Lambda_{11} &= 0.5257m^{-1/2} \\ \Lambda_{12} &= 0.8506m^{-1/2} \end{aligned} \qquad (9\text{-}134)$$

Substituting Eq. 9-134 into Eq. 9-132, the modal matrix is then

$$[\Lambda] = m^{-1/2} \begin{bmatrix} 0.5257 & 0.8506 \\ 0.8506 & -0.5257 \end{bmatrix}$$

From Eq. 9-129, the solution becomes

$$\begin{aligned} x_1 &= m^{-1/2}[0.5257q_1(t) + 0.8506q_2(t)] \\ x_2 &= m^{-1/2}[0.8506q_1(t) - 0.5257q_2(t)] \end{aligned} \qquad (9\text{-}135)$$

Taking $q_r(t)$ in the form given by Eq. 9-127 and substituting in Eqs. 9-135

$$\begin{aligned} x_1 = m^{-1/2}[&0.5257\ E_1 \sin \omega_1 t + 0.5257\ F_1 \cos \omega_1 t \\ &+ 0.8506\ E_2 \sin \omega_2 t + 0.8506\ F_2 \cos \omega_2 t] \\ x_2 = m^{-1/2}[&0.8506\ E_1 \sin \omega_1 t + 0.8506\ F_1 \cos \omega_1 t \\ &- 0.5257\ E_2 \sin \omega_2 t - 0.5257\ F_2 \cos \omega_2 t] \end{aligned} \qquad (9\text{-}136)$$

If the same initial conditions are assumed for the system of Fig. 9-29(b), i.e.,

$$\left.\begin{aligned} x_1 &= x_o \\ \dot{x}_1 &= x_2 = \dot{x}_2 = 0 \end{aligned}\right\} \text{ at } t = 0$$

the coefficients in Eq. 9-136 are found to be

$$\begin{aligned} E_1 &= E_2 = 0 \\ F_1 &= 0.5257m^{1/2}x_o \\ F_2 &= 0.8506m^{1/2}x_o \end{aligned}$$

The equations of motion for the system thus become

$$x_1/x_o = 0.276 \cos \omega_1 t + 0.724 \cos \omega_2 t$$

$$x_2/x_o = 0.447 \cos \omega_1 t - 0.447 \cos \omega_2 t$$

as determined previously and plotted in Fig. 9-31.

9.6.4 Forced Vibration of Multidegree of Freedom Systems

The modal method of analysis is readily extended to problems of forced vibration or base motion. The general matrix equation for the forced vibration of a multidegree of freedom system is

$$[m]\{\ddot{x}\} + [k]\{x\} = \{F\} \qquad (9\text{-}137)$$

where {F} is the column matrix of applied forces. As in the free vibration problem, the physical coordinates, {x}, may be related to a set of generalized coordinates, {q}, by a general transformation. It has already been shown that taking the transformation matrix, $[\beta]$, to be the modal matrix, $[\Lambda]$, results in a set of uncoupled equations. Thus, Eq. 9-137 can be written as

$$[m][\Lambda]\{\ddot{q}\} + [k][\Lambda]\{q\} = \{F\} \qquad (9\text{-}138)$$

Premultiplying by $[\Lambda]^T$ results in

$$[\Lambda]^T[m][\Lambda]\{\ddot{q}\} + [\Lambda]^T[k][\Lambda]\{q\} = [\Lambda]^T\{F\} \qquad (9\text{-}139)$$

or

$$\{\ddot{q}\} + [\lceil \omega^2 \rfloor]\{q\} = \{P\} \qquad (9\text{-}140)$$

where

$$[\Lambda]^T[m][\Lambda] = [I]$$

$$[I]\{\ddot{q}\} = \{\ddot{q}\}$$

$$[\Lambda]^T[k][\Lambda] = [\lceil \omega^2 \rfloor]$$

$$\{P\} = [\Lambda]^T\{F\}$$

{P} can be interpreted as a set of generalized forces, $P_r(t)$, associated with the set of generalized coordinates, $q_r(t)$.

Equation 9-140 represents a set of N uncoupled differential equations of the form

$$\ddot{q}_r(t) + \omega_r^2 q_r(t) = P_r(t), \quad r=1,2,\ldots,N \qquad (9\text{-}141)$$

which may be solved by the same methods used to analyze single degree of freedom systems. As in free vibration problems, the solution in terms of generalized coordinates may be related to physical coordinates by Eq. 9-121.

9.6.5 Multidegree of Freedom Systems Subjected to Support Motion

The general equation for an undamped multidegree of freedom system subjected to base motion is

$$[m]\{\ddot{u}\} + [k]\{u\} = -\ddot{y}[m]\{1\} = -\ddot{y}\{M\} \qquad (9\text{-}142)$$

where

$\ddot{y}$ = base acceleration

{u} = column matrix of relative displacements between each mass and the base, i.e., $u_i = x_i - y$

{1} = column matrix with all components equal to one

{M} = [m]{1} = column mass matrix

As in free and forced vibration, a set of generalized coordinates, {q}, can be related to the physical coordinates, {u}, using the modal matrix, i.e.,

$$\{u\} = [\Lambda]\{q\} \qquad (9\text{-}143)$$

Equation 9-142 then becomes

$$[m][\Lambda]\{\ddot{q}\} + [k][\Lambda]\{q\} = -\ddot{y}\{M\} \qquad (9\text{-}144)$$

Premultiplying Eq. 9-144 by $[\Lambda]^T$ results in

$$[\Lambda]^T[m][\Lambda]\{\ddot{q}\} + [\Lambda]^T[k][\Lambda]\{q\} = -\ddot{y}[\Lambda]^T\{M\} \qquad (9\text{-}145)$$

or

$$\{\ddot{q}\} + \lceil \omega^2 \rfloor \{q\} = -\ddot{y}[\Lambda]^T\{M\} \qquad (9\text{-}146)$$

where

$$[\Lambda]^T[m][\Lambda] = [I]$$
$$[\Lambda]^T[k][\Lambda] = \lceil \omega^2 \rfloor$$

according to Eqs. 9-123 and 9-124, respectively.

Equation 9-146 may be rewritten

$$\{\ddot{q}\} + \lceil \omega^2 \rfloor \{q\} = -\ddot{y}\{\gamma\} \qquad (9\text{-}147)$$

where $\{\gamma\} = [\Lambda]^T\{M\}$ (9-148)

Equation 9-147 represents a set of N uncoupled differential equations of the form

$$\ddot{q}_r(t) + \omega_r^2 q_r(t) = -\gamma_r \ddot{y}(t), \qquad r=1,2,\ldots,N \qquad (9\text{-}149)$$

where $$\gamma_r = \sum_{i=1}^{N} \Lambda_{ir} M_i \qquad (9\text{-}150)$$

The equation of motion for a single degree of freedom system subjected to base motion is

$$\ddot{W}(t) + \omega^2 W(t) = -\ddot{y}(t) \qquad (9\text{-}151)$$

where W is the relative displacement between the mass and the base. Comparison of Eq. 9-149 with Eq. 9-151 indicates that they are equivalent in form except that the base acceleration in Eq. 9-149 is multiplied by the factor γ_r. This factor is called the modal participation factor. Solutions to Eq. 9-151 for the various modes $(\omega_1, \omega_2, \ldots, \omega_N)$ are multiplied by the appropriate modal participation factor, γ_r, to obtain the contribution of each mode to the complete solution.

The solution in terms of physical coordinates is

$$\{u\} = [\Lambda]\{q\} = [\Lambda]\lceil \gamma \rfloor \{W\} \qquad (9\text{-}152)$$

where

$\lceil \gamma \rfloor$ = diagonal matrix having the modal participation factors on the diagonal

$\{W\}$ = column matrix of solutions to Eq. 9-151 for the various modes

Equation 9-152 represents N equations for the response of the N masses, i.e.,

$$u_i = \sum_{r=1}^{N} \Lambda_{ir} q_r(t) = \sum_{r=1}^{N} \Lambda_{ir}\gamma_r W_r(t), \qquad i=1,2,\ldots,N \qquad (9\text{-}153)$$

where $W_r(t)$ is the solution to Eq. 9-151 for the r^{th} mode.

The solution to Eq. 9-151 assuming zero initial conditions is

$$W(t) = \frac{1}{\omega} \int_0^t \ddot{y}(\tau) \sin \omega(t-\tau)\, d\tau \qquad (9\text{-}154)$$

where τ is a dummy variable of integration. In cases where $\ddot{y}$ is not of simple analytical form, numerical solution methods must be employed.

The absolute accelerations of the masses may be determined from the definition of the relative displacements given in Eq. 9-142. In matrix form, the relative displacements are given by

$$\{u\} = \{x\} - y\{1\} = \{x\} - \{y\} \qquad (9\text{-}155)$$

The absolute acceleration matrix then is

$$\{\ddot{x}\} = \{\ddot{u}\} + \ddot{y}\{1\} = \{\ddot{u}\} + \{\ddot{y}\} \qquad (9\text{-}156)$$

Differentiating Eq. 9-143 twice with respect to time yields

$$\{\ddot{u}\} = [\Lambda]\{\ddot{q}\} \qquad (9\text{-}157)$$

Substituting Eq. 9-157 in Eq. 9-156 results in

$$\{\ddot{x}\} = [\Lambda]\{\ddot{q}\} + \{\ddot{y}\} \qquad (9\text{-}158)$$

Employing Eq. 9-146 and making the substitution $\{m\} = [m]\{1\}$, Eq. 9-158 can be written

$$\{\ddot{x}\} = -\ddot{y}[\Lambda][\Lambda]^T[m]\{1\} - [\Lambda]\lceil -\omega^2 \rfloor\{q\} + \{\ddot{y}\} \qquad (9\text{-}159)$$

Because of the orthogonality of the normal modes of vibration

$$[\Lambda][\Lambda]^T[m] = [\Lambda]^T[m][\Lambda] = [I] \qquad (9\text{-}160)$$

Since

$$\ddot{y}[I]\{1\} = \{\ddot{y}\} \qquad (9\text{-}161)$$

the terms in Eq. 9-159 involving $\ddot{y}$ cancel and Eq. 9-159 becomes

$$\{\ddot{x}\} = -[\Lambda]\lceil -\omega^2 \rfloor\{q\} \qquad (9\text{-}162)$$

or

$$\ddot{x}_i = \sum_{r=1}^{N}\Lambda_{ir}\omega_r^2 q_r(t) \qquad (9\text{-}163)$$

or

$$\ddot{x}_i = -\sum_{r=1}^{N}\Lambda_{ir}\omega_r^2\gamma_r W_r(t) \qquad (9\text{-}164)$$

When it is impossible to prescribe a precise base motion time history, shock disturbances are often specified by a shock spectrum. As described previously, a shock spectrum envelopes the peak response of a single degree of freedom system to the shock as a function of the natural frequency of the system. Single degree of freedom shock spectra may also be employed to obtain upper bounds on the response of multidegree of freedom systems.

For a single degree of freedom system defined by Eq. 9-151, the peak spectral relative displacement, D, is given by

$$D = |W(t)|_{max} \qquad (9\text{-}165)$$

The peak spectral absolute acceleration, a, is defined by

$$a = \omega^2 D = |\omega^2 W(t)|_{max} \qquad (9\text{-}166)$$

An upper case A was used previously in Eq. 9-59. A lower case a is used here to avoid confusion with the modal matrix [Λ].

An upper bound on the response of a multi-degree of freedom system may be obtained by substituting D_r for $W_r(t)$ in Eq. 9-153 and a_r for $\omega_r^2 W_r(t)$ in Eq. 9-164 where the subscript r refers to the various modes of the multidegree of freedom system, i.e.,

$$|u_i|_{max} \le \sum_{r=1}^{N}\Lambda_{ir}\gamma_r D_r \qquad (9\text{-}167)$$

$$|\ddot{x}_i|_{max} \le \sum_{r=1}^{N}\Lambda_{ir}\gamma_r a_r \qquad (9\text{-}168)$$

where the subscript i refers to the various physical coordinates. In matrix form, Eqs. 9-167 and 9-168 are

$$\{|u|_{max}\} \le [\Lambda]\lceil \gamma \rfloor\{D\} \qquad (9\text{-}169)$$

$$\{|\ddot{x}|_{max}\} \le [\Lambda]\lceil \gamma \rfloor\{a\} \qquad (9\text{-}170)$$

The use of shock spectra for analysis of multidegree of freedom systems is illustrated in paragraph 9.8.2.

9.6.6 Damped Multidegree of Freedom Systems

Although damping is readily included in the analysis of single degree of freedom systems, its introduction into multidegree of freedom systems can greatly complicate the analysis. The degree of complication depends on the type of damping and the method of analysis. Only one class of problems is treated herein. References 9-7, 9-11 and 9-12 consider other forms of damping and methods of solution.

Except in special cases, if the standard modal analysis technique is applied to damped multidegree of freedom systems, it will not yield an uncoupled system of equations. However, those special cases can be applied to many practical problems.

The general equation for the forced vibration of a multidegree of freedom system with linear viscous damping is in matrix form

$$[m]\{\ddot{x}\} + [c]\{\dot{x}\} + [k]\{x\} = \{F\} \tag{9-171}$$

where [c] is the matrix of damping coefficients.

The normal modal matrix can be used to transform Eq. 9-171 to

$$\{\ddot{q}\} + [C]\{\dot{q}\} + \lceil \omega^2 \rfloor \{q\} = \{P\} \tag{9-172}$$

where $[C] = [\lambda]^T [c] [\lambda]$ and the other terms are as defined previously. Although [c] is a symmetric matrix, in general it is not diagonal. Thus, Eq. 9-172 does not necessarily represent an uncoupled system of equations. In the special case where the matrix of damping coefficients is proportional to the mass and stiffness matrices, i.e.,

$$[c] = \alpha[m] + \beta[k] \tag{9-173}$$

where α and β are constants, the damping coefficient matrix is also diagonalized by the transformation and Eq. 9-172 is uncoupled and of the form

$$\{\ddot{q}\} + \lceil C \rfloor \{\dot{q}\} + \lceil \omega^2 \rfloor \{q\} = \{N\} \tag{9-174}$$

which represents a system of N equations of the type

$$\ddot{q}_r + C_r \dot{q}_t + \omega_r^2 q_r = N_r \tag{9-175}$$

Letting

$$\lceil C \rfloor = \lceil 2\beta\omega \rfloor \tag{9-176}$$

Eq. 9-175 becomes

$$\ddot{q}_r + 2\beta_r \omega_r \dot{q}_r + \omega_r^2 q_r = N_r \tag{9-177}$$

where β_r is the damping ratio specified for the r^th mode.

It can be seen that Eq. 9-177 has the same form as the equation describing the motion of a damped single degree of freedom system. For zero initial conditions, Eq. 9-177 has a solution

$$q_r(t) = \frac{1}{\omega_{rd}} \int_0^t N_r(\tau)\, e^{-\beta_r \omega_r (t-\tau)} \sin \omega_{rd}(t-\tau)\, d\tau \tag{9-178}$$

where $\omega_{rd} = \omega_r\sqrt{1-\beta_r^2}$ = damped natural frequency of the r^th mode. Thus, as in the case of undamped systems, single degree of freedom solutions can be used to obtain the response of multidegree of freedom systems. The solution in generalized coordinates is transformed into physical coordinates by Eq. 9-121.

The matrix of damping coefficients in Eq. 9-171 is normally difficult to obtain or assume. The modal analysis approach, although limited to special cases, is simpler since it allows the use of damping ratios for modes. If damping coefficients are specified, and are small, a reasonable approximation can be obtained by ignoring the off-diagonal terms of the [C] matrix in Eq. 9-172. With this approach a system of uncoupled equations is obtained and the analysis proceeds as described above. Neglect of the off-diagonal terms implies that damping is sufficiently small that coupling is a second order effect.

9.6.7 Nonlinear Multidegree of Freedom Systems

A rigorous analysis of nonlinear multidegree of freedom systems is impractical in most cases, and some type of numerical analysis is normally used. The numerical integration technique described previously is one procedure that is applicable to both linear and nonlinear systems. The analysis of multidegree of freedom systems utilizes the same basic procedures as described for single degree of freedom systems. Obviously the analysis of multidegree of freedom systems is much more difficult because of the larger number of variables involved. Simplifying assumptions regarding structural properties, e.g., neglect of girder flexibility relative to that of columns and neglect of damping, are often necessary to reduce the complexity of the analysis. The choice of a time step for the numerical integration process also becomes more difficult because of the constantly changing properties of nonlinear systems. In the absence of other guidance, it is recommended that the time step be selected on the basis of the load characteristics and initial elastic properties of the system.

9.7 NATURAL FREQUENCIES OF COMMON SYSTEMS

9.7.1 Beam Elements and Spring Mass Systems

Calculating natural frequencies is one of the important aspects of the analysis of most systems. Table 9-11 includes expressions for calculating the natural frequencies of miscellaneous systems. Table 9-12(a) gives expressions for the lowest natural frequencies of several systems with distributed and concentrated masses. Also given

Table 9-11

NATURAL FREQUENCIES OF MISCELLANEOUS SYSTEMS (Ref. 9-13)

(ω_n = Angular Natural Frequency, rad/sec)

SIMPLE PENDULUM	COMPOUND PENDULUM	SPHERE IN CYLINDRICAL TRACK	PNEUMATIC SYSTEM
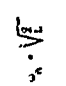	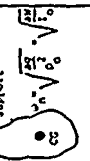		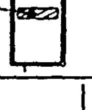
$\omega_n = \sqrt{\frac{g}{L}}$	$\omega_n = \sqrt{\frac{gh}{\rho_o^2}} = \sqrt{\frac{Wh}{I_o}}$	$\omega_n = \sqrt{\frac{5g}{7(R_t - R_s)}}$	$\omega_n = \sqrt{\frac{2pS^2}{mV_o}}$
g = Acceleration of Gravity (g and L in Consistent Units)	ρ_o = Radius of Gyration About Axis of Support g = Acceleration of Gravity W = Weight of Pendulum I_o = Moment of Inertia About Axis of Support	g = Acceleration of Gravity R_t = Radius of Track R_s = Radius of Sphere	p = Pressure at each end Cylinder, lb/in^2 S = Area of Piston, in^2 m = Mass of Piston, lb-sec^2/in. V_o = Volume of each end of Cylinder, in^3
U-TUBE WITH LIQUID	PLANK ON ROTATING DRUMS	TANKS WITH CONNECTING CONDUIT	CYLINDER IN CYLINDRICAL TRACK
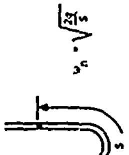	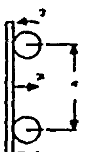	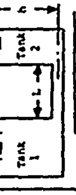	
$\omega_n = \sqrt{\frac{2g}{S}}$	$\omega_n = \sqrt{\frac{2\mu g}{a}}$	$\omega_n = \sqrt{\frac{g(1+S_1/S_2)}{h(1+S_1/S_2)+L(S_1/S_o)}}$	$\omega_n = \sqrt{\frac{2g}{3(R_t - R_c)}}$
g = Acceleration of Gravity	g = Acceleration of Gravity μ = Coefficient of Friction Between Plank and Drum	g = Acceleration of Gravity S_1 = Area of Tank 1 S_2 = Area of Tank 2 S_o = Area of Conduit	g = Acceleration of Gravity R_t = Radius of Track R_c = Radius of Cylinder

Table 9-12(a)

NATURAL FREQUENCIES OF COMMONLY USED SYSTEMS (Ref. 9-13)

MASSIVE SPRINGS (BEAMS) WITH CONCENTRATED MASS LOADS

m = Mass of Load, lb/sec^2/in
$m_s(m_b)$ = Mass of Spring (Beam), lb-sec^2/in
k = Stiffness of Spring, lb/in.
L = Length of Beam, in
I = Area Moment of Inertia of Beam Cross Section, in^4
E = Young's Modulus, lb/in^2
ω_n = Angular Natural Frequency, rad/sec

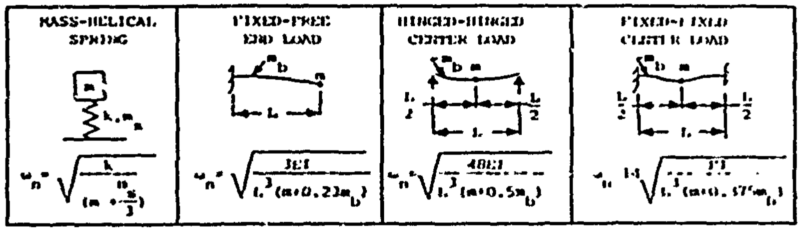

AREA MOMENT OF INERTIA OF BEAM SECTIONS
(With Respect to Axis a-a)

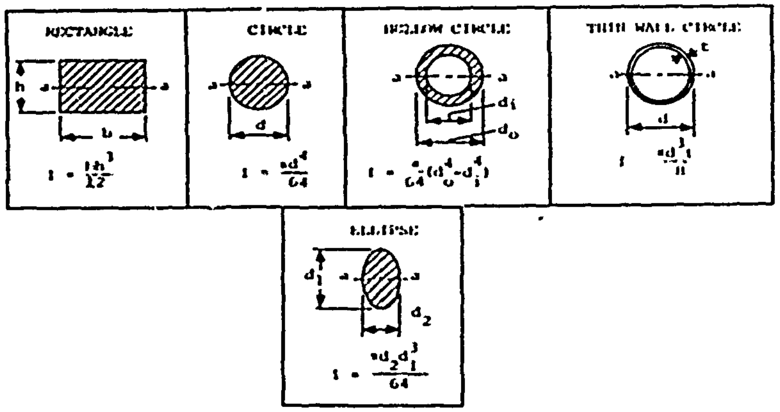

are expressions for calculating the moments of inertia of several types of beam cross sections. Table 9-12(b) presents frequency expressions for several simple spring-mass systems. Note that two frequencies are obtained for the two mass system. Expressions at the bottom of Table 9-12(b) show how parallel and series arrangements of springs are combined to obtain equivalent stiffnesses for use in the frequency equation. Table 9-12(c) presents frequency expressions and characteristic shapes for the five lowest modes of vibration of beams with distributed mass.

The expressions for natural frequencies of beams in Tables 9-12(a) and (c) neglect the effects of shear deflection and rotation of sections. The effects of rotary inertia are small except when the curvature of the beam is large relative to its depth. This condition occurs in stubby beams, i.e., short span relative to depth, or in longer beams vibrating in higher mode shapes. Shear deformations are also small except in the case of stubby beams or those with very thin webs. The combined effects of these two phenomena increase with increasing mode number and the ratio of radius of gyration of the cross section to span. For the first mode of vibration of simply supported and cantilever beams, the decrease in frequency is less than 10 percent for radius of gyration to span ratios less than 0.1 (Ref. 9-13). For the second mode shape, the decrease is approaching 40 percent. References 9-9 and 9-13 describe procedures for including rotary inertia and shear deformation effects in vibration analyses.

Axial loads applied to the beam can increase or decrease its natural frequency depending on whether the load is compressive or tensile. If the axial load is constant the natural frequency of the member with hinged ends

Table 9-12(b)

NATURAL FREQUENCIES OF COMMONLY USED SYSTEMS (Ref. 9-13)

MASS-SPRING SYSTEMS IN TRANSLATION
(Rigid Mass and Massless Spring)

k = Spring Stiffness, lb/in.
m = Mass, lb-sec^2/in.
ω_n = Angular Natural Frequency, rad/sec.

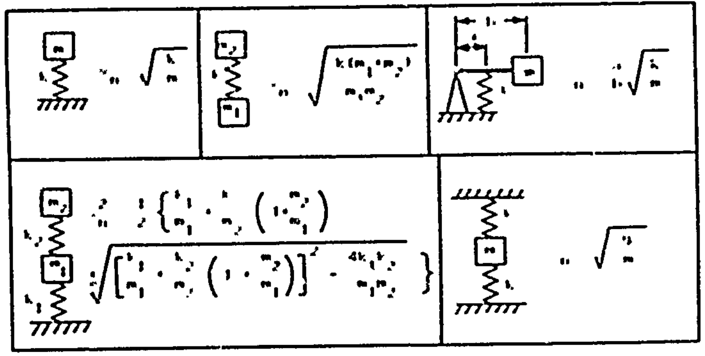

$\omega_n = \sqrt{\frac{k}{m}}$

$\omega_n = \sqrt{\frac{k(m_1+m_2)}{m_1 m_2}}$

$$\omega_n^2 = \frac{1}{2}\left\{\frac{k_1}{m_1} + \frac{k_2}{m_2}\left(1+\frac{m_2}{m_1}\right) \pm \sqrt{\left[\frac{k_1}{m_1} + \frac{k_2}{m_2}\left(1+\frac{m_2}{m_1}\right)\right]^2 - \frac{4k_1k_2}{m_1m_2}}\right\}$$

SPRINGS IN COMBINATION

k_r = Resultant Stiffness of Combination

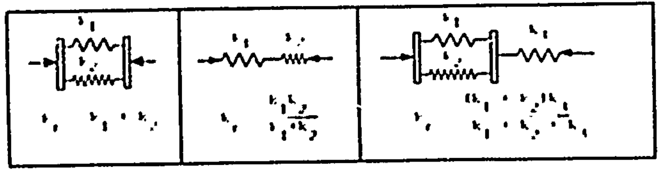

$k_r = k_1 + k_2$

$k_r = \frac{k_1k_2}{k_1+k_2}$

$k_r = \frac{(k_1+k_2)k_3}{k_1+k_2+k_3}$

Table 9-12(c)

NATURAL FREQUENCIES OF COMMONLY USED SYSTEMS (Ref. 9-13)

BEAMS OF UNIFORM SECTION AND UNIFORMLY DISTRIBUTED LOAD

Angular Natural Frequency $\omega_n = A\sqrt{\frac{EI}{\mu L^4}}$ rad/sec

where
E = Young's Modulus, lb/in^2
I = Area Moment of Inertia of Beam Cross Section, in^4
L = Length of Beam, in
μ = Mass Per Unit Length of Beam, lb-sec^2/in^2
A = Coefficient from Table Below

NODES ARE INDICATED IN TABLE BELOW AS A PROPORTION OF LENGTH L MEASURED FROM LEFT END

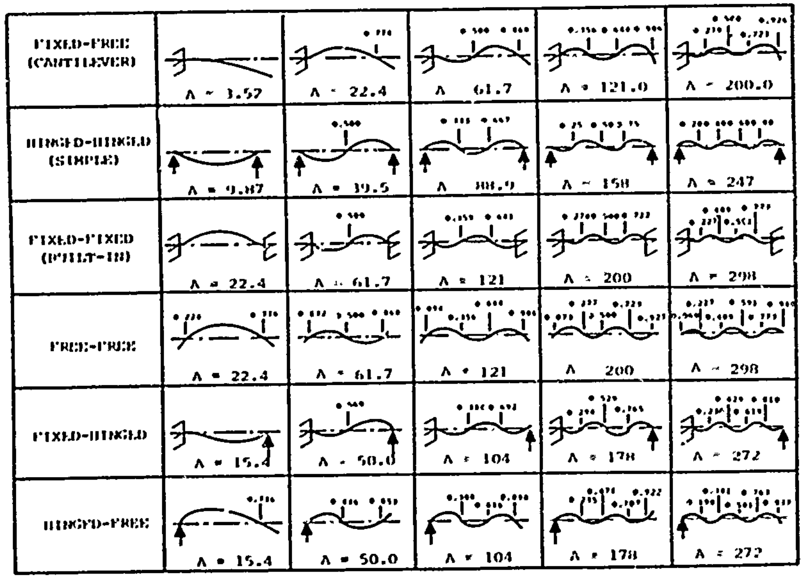

FIXED-FREE (CANTILEVER)	A = 3.52	A = 22.4	A = 61.7	A = 121.0	A = 200.0
HINGED-HINGED (SIMPLE)	A = 9.87	A = 39.5	A = 88.9	A = 158	A = 247
FIXED-FIXED (BUILT-IN)	A = 22.4	A = 61.7	A = 121	A = 200	A = 298
FREE-FREE	A = 22.4	A = 61.7	A = 121	A = 200	A = 298
FIXED-HINGED	A = 15.4	A = 50.0	A = 104	A = 178	A = 272
HINGED-FREE	A = 15.4	A = 50.0	A = 104	A = 178	A = 272

is given by

$$\omega_{NP} = \omega_N \sqrt{1 \pm \frac{\alpha^2}{N^2}} \text{ rad/sec} \qquad (9\text{-}179)$$

where

ω_{NP} = natural frequency with axial load

ω_N = natural frequency without axial load

N = mode number

α^2 = $0.101\ PL^2/EI$

L = length of member

The plus sign is used for tensile loads and the negative sign for compression loads.

9.7.2 Plates

Table 9-12(d) presents expressions for natural frequencies of square and circular plates with various edge conditions. Reference 9-13 contains similar expressions for other plate geometries. The constants given in Table 9-12(d) are applicable to small amplitudes of vibrations, i.e., less than 0.1 or 0.2 times the plate thickness. The effect of larger amplitude motions on natural frequencies depends on support conditions and aspect ratios for the plates. In general, frequency will increase with amplitudes with the increase being lowest for an aspect ratio of one. As in the case of beams, shear deformations and rotary inertia effects on frequencies become significant when the plate thickness becomes large relative to its lateral dimensions. These effects have been neglected in Table 9-12(d).

9.7.3 Rings

Table 9-12(e) presents expressions for the

Table 9-12(d)

NATURAL FREQUENCIES OF COMMONLY USED SYSTEMS (Ref. 9-13)

NATURAL FREQUENCIES OF THIN FLAT PLATES OF UNIFORM THICKNESS

$$\omega_n = B\sqrt{\frac{Et^3}{\rho a^4(1-\nu^2)}} \text{ RAD/SEC}$$

E = Youngs' Modulus, lb/in²
t = Thickness of Plate, in.
ρ = Mass Density, lb/sec²/in⁴
a = Diameter of Circular Plate or Side of Square Plate, in.
ν = Poisson's Ratio

Shape of Plate	Diagram	Edge Conditions	Value of B for Modes							
			1	2	3	4	5	6	7	8
Circular		Clamped At Edge	11.84	24.61	40.41	46.14	103.12			
Circular		Free	6.09	10.53	14.19	23.80	40.88	44.68	61.38	69.44
Circular		Clamped At Center	4.35	24.26	70.39	138.85				
Circular		Simply Supported At Edge	5.90							
Square		One Edge Clamped Three Edges Free	1.01	2.47	6.20	7.94	9.01			
Square		All Edges Clamped	10.40	21.21	31.29	38.04	38.22	47.73		
Square		Two Edges Clamped Two Edges Free	2.01	6.96	7.74	13.89	18.25			
Square		All Edges Free	4.07	5.94	6.91	10.39	17.80	18.85		
Square		One Edge Clamped Three Edges Simply Supported	6.83	14.94	16.95	24.89	28.99	32.71		
Square		Two Edges Clamped Two Edges Simply Supported	8.37	15.82	20.03	27.34	29.54	37.31		
Square		All Edges Simply Supported	5.70	14.26	22.82	28.52	37.08	48.49		

MASSLESS CIRCULAR PLATE WITH CONCENTRATED CENTER MASS

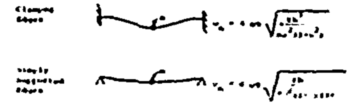

Table 9-12(e)

NATURAL FREQUENCIES OF COMPLETE CIRCULAR RINGS WHOSE THICKNESS IN RADIAL DIRECTION IS SMALL COMPARED TO RADIUS (Ref. 9-13)

TYPE OF VIBRATION	SHAPE OF LOWEST MODE	RECTANGULAR CROSS SECTION	CIRCULAR CROSS SECTION
		ω_n	ω_n
Flexural in Plane of Ring with n complete wave-length in circumference		$\sqrt{\frac{EIg}{\gamma AR^4}\left(\frac{n^2(n^2-1)^2}{n^2+1}\right)}$ n ANY INTEGER > 1	$\sqrt{\frac{E\pi r^4}{4mR^4}\left(\frac{n^2(n^2-1)^2}{n^2+1}\right)}$ n ANY INTEGER > 1
Flexural Normal to Plane of Ring	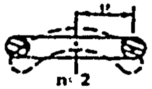		$\sqrt{\frac{E\pi r^4}{4mR^4}\left(\frac{n^2(n^2-1)^2}{n^2+1+\mu}\right)}$ n ANY INTEGER > 1
Torsional	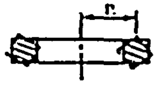	First Mode $\sqrt{\frac{Eg\,I_x}{\gamma R^2\,I_p}}$	$\sqrt{\frac{E\pi r^2}{2mR^2}(n^2+1)}$ n 0, OR ANY INTEGER
Extensional		$\sqrt{\frac{Eg}{\gamma R^2}}$	$\sqrt{\frac{E\pi r^2}{2mR^2}(n^2+1)}$ n=0, OR ANY INTEGER

E Modulus of Elasticity

m = Mass Per Unit of Length

γ = Weight Density

n = Defined for Each Type of Vibration

R Radius of Ring

μ Poisson's Ratio

I = Moment of Inertia with Respect to Axis of Section

I_x = Moment of Inertia with Respect to Radial Line

I_p = Polar Moment of Inertia

A Area

r Radius of Cross Section

natural frequencies of circular rings whose thicknesses in the radial direction are small compared to their radii.

9.7.4 Arches

The vibrational modes of circular arches may be flexural as in lateral vibrations of a beam, extensional as in the case of uniform in and out motions of a ring or axial vibrations of a bar, or a combination of the extensional and flexural modes. The relative importance of these two types of vibrations depends largely on the slenderness ratio defined by

$$\text{Slenderness Ratio} = \frac{S}{r} \qquad (9\text{-}180)$$

where

S = length of the arch axis = $R\theta_o$

R = radius of arch

θ_o = central angle of the arch

r = radius of gyration of arch cross section

At lower slenderness ratios arch vibrations in a given mode shape may alternate between flexural and extensional behavior but at larger slenderness ratios flexural behavior predominates. Reference 9-14 classifies circular arch modes of vibration as either predominantly flexural or predominantly extensional. The flexural modes are further classified as symmetrical or antisymmetrical. The symmetrical modes are characterized by radial displacements which are symmetrical about the crown of the arch while the antisymmetrical modes do not exhibit this symmetry. Figure 9-32 shows examples of the various deflection modes. The first extensional mode might also be considered a symmetrical mode and it is often

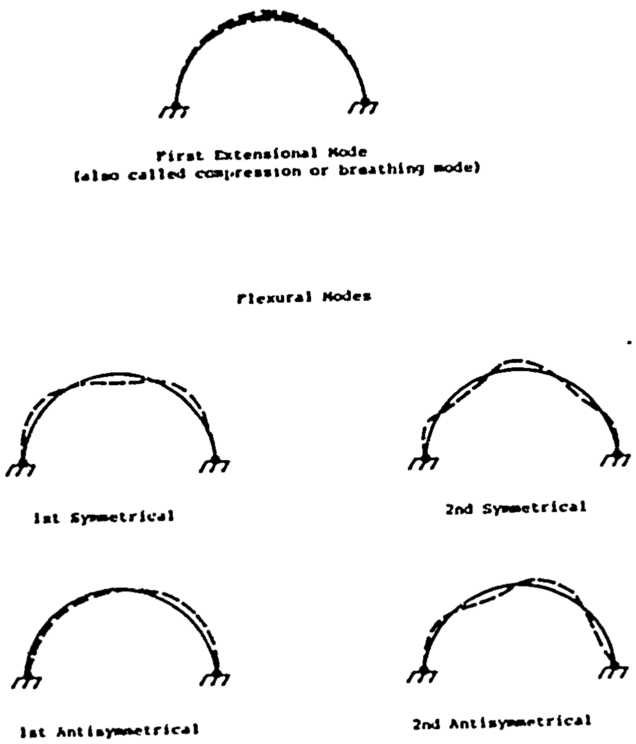

Figure 9-32 Deflection Modes of Circular Arches

referred to as the breathing mode for arch vibrations. For the breathing mode, Ref. 9-14 recommends the frequency of vibration be obtained from

$$\omega_N = \frac{0.97}{R}\sqrt{\frac{EA}{m}} \text{ rad/sec} \qquad (9\text{-}181)$$

where

A = cross sectional area of the arch

m = mass per unit length of arch

References 9-14 and 9-15 suggest that natural frequencies of circular arches in the predominantly flexural modes can be obtained from equations of the form

$$\omega_N = \frac{C_N}{S^2}\sqrt{\frac{EI}{m}} \text{ rad/sec} \qquad (9\text{-}182)$$

where

C_N = dimensionless coefficient depending on arch geometry and mode of vibration

I = moment of inertia of arch cross section

m = mass per unit length of arch

For the N^{th} antisymmetric mode in the predominantly flexural group, Ref. 9-14 recommends for hinged support arches

$$C_N^2 = \frac{\bar{m}^4\pi^4\left|1 - \left(\frac{\theta_o}{\bar{m}\pi}\right)^2\right|^2}{1 + 3\left(\frac{\theta_o}{\bar{m}\pi}\right)^2} \qquad (9\text{-}183)$$

and for fixed support arches

$$C_N^2 = \lambda_{\bar{m}}^4\left[\frac{1 - 2\alpha_{\bar{m}}^2\left(1 - \frac{2}{\alpha_{\bar{m}}\lambda_{\bar{m}}}\right)\left(\frac{\theta_o}{\lambda_{\bar{m}}}\right)^2 + \left(\frac{\theta_o}{\lambda_{\bar{m}}}\right)^4}{1 + 5\,\alpha_{\bar{m}}^2\left(1 - \frac{2}{\alpha_{\bar{m}}\lambda_{\bar{m}}}\right)\left(\frac{\theta_o}{\lambda_{\bar{m}}}\right)^2}\right] \qquad (9\text{-}184)$$

The parameter $\bar{m}$ is a function of mode shape and is given by

$\bar{m} = 2N$ for antisymmetric modes

$\bar{m} = 2N+1$ for symmetric modes

$N = 1,2,3 \ldots N$, corresponding to the N^{th} symmetric or antisymmetric mode of vibration

The parameters $\lambda_{\bar{m}}$ and $\alpha_{\bar{m}}$ are obtained from Table 9-13 for the appropriate value of $\bar{m}$.

Table 9-13

Quantity	$\bar{m} = 1$	$\bar{m} = 2$	$\bar{m} = 3$	$\bar{m} = 4$	$\bar{m} = 5$
$\lambda_{\bar{m}}$	4.730	7.853	10.996	14.137	17.279
$\alpha_{\bar{m}}$	0.983	1.001	1.000	1.000	1.000

For the N^{th} symmetric mode in the predominantly flexural group, Ref. 9-14 recommends for hinged support arches

$$C_N^2 = \bar{m}^4 \pi^4 \frac{\left[1 - \left(\frac{\theta_o}{\bar{m}\pi}\right)^2\right]^2}{1 + \frac{1}{\bar{m}^2} + 2\left(\frac{\theta_o}{\bar{m}\pi}\right)^2} \qquad (9\text{-}185)$$

and for fixed support arches

$$C_N^2 = \lambda_{\bar{m}}^4 \left[\frac{1 - 1.82\left(\frac{\theta_o}{\lambda_{\bar{m}}}\right)^2}{1 + \left(\frac{\lambda_1}{\lambda_{\bar{m}}}\right)^2 + 2\left(1.63 - \frac{5}{\lambda_{\bar{m}}}\right)\left(\frac{\theta_o}{\lambda_{\bar{m}}}\right)^2}\right] \qquad (9\text{-}186)$$

$(\lambda_1 = \lambda_{\bar{m}}$ for $\bar{m} = 1)$

Note that in all cases, the appropriate value of m for antisymmetric or symmetric modes is as defined in Eq. 9-183.

Equations 9-181 through 9-186 are reasonable approximations to computational results reported in Ref. 9-14. Reference 9-15 reports data obtained using a different mathematical approach and covers a wider range of arch parameters. Although the choice of parameters for these two studies does not permit an exact comparison, there is reasonable agreement between values of C_N obtained for similar arch geometries.

9.7.5 Frames and Shear Walls

If the stiffness of the girders is large relative to that of the columns, the natural frequency of a one-story building frame in a lateral vibration mode is given by

$$\omega_N = \sqrt{\frac{\Sigma K g}{W}} \text{ rad/sec} \qquad (9\text{-}187)$$

where

W = total weight of deck, frame, etc. at roof level plus 1/3 weight of walls

ΣK = total lateral stiffness of columns

For columns fixed at both ends, the lateral stiffness is

$$K = \sum \frac{12EI}{h^3} \text{ for all columns} \qquad (9\text{-}188)$$

and for olumns fixed at one end, hinged at the other

$$K = \sum \frac{3EI}{h^3} \text{ for all columns} \qquad (9\text{-}189)$$

where h is the story height. The stiffnesses defined by Eqs. 9-188 and 9-189 are for loads applied at roof level. If the structure includes reinforced concrete shear walls, their stiffnesses must be included in ΣK for Eq. 9-187. The stiffness of shear walls is also defined in terms of the shear force applied at the top of the wall. Prior to cracking the stiffness is given by

$$k_c = \frac{E_c}{H\left[\frac{H^2}{3I} + \frac{2.2}{Lt}\right]} \tag{9-190}$$

where

H = height of the wall to the center of the top beam

L = length of the wall from center to center of columns

t = thickness of the wall panel

I = moment of inertia of horizontal section through the wall and columns neglecting presence of reinforcing steel

At ultimate load the stiffness is given by

$$k_u = k_c\left[\frac{R_u L}{R_c 2H}\right] \tag{9-191}$$

where

R_u = ultimate shear resistance of the shear wall (Eq. 8-69)

R_c = shear resistance of wall at cracking (Eq. 8-68)

One-third the mass of the shear walls must also be added to W in Eq. 9-187.

9.7.6 Domes

As in the cases of arches a spherical dome has many possible modes of vibration. Since most loads are resisted by membrane action in the dome shell, the mode of vibration of primary interest is that associated with uniform

radial motion. The frequency of vibration in this mode is given by

$$\omega_N = \sqrt{\frac{2E}{\rho(1-\nu)R^2}} \text{ rad/sec} \tag{9-192}$$

where

R = radius of the dome

ρ = mass per unit volume of dome material

ν = Poisson's ratio

9.8 ILLUSTRATIVE EXAMPLES

9.8.1 Modified Rayleigh Procedure for Obtaining Natural Frequencies and Mode Shapes

a. GIVEN: A three shelf equipment rack as shown in Fig. 9-33(a). The weight of the equipment and rack is such that

M_1 = 8 lb-sec^2/in (1400 kg)

M_2 = 4 lb-sec^2/in (700 kg)

M_3 = 4 lb-sec^2/in (700 kg)

The total lateral stiffness of vertical members in each level is

k_1 = 6000 lb/in (1050.8 kN/m)

k_2 = 2000 lb/in (350.3 kN/m)

k_3 = 2000 lb/in (350.3 kN/m)

b. FIND: The fundamental (lowest) lateral mode shape and frequency of vibration of the system. Neglect damping.

c. SOLUTION: If the horizontal shelves are assumed to be much stiffer than the vertical members, the real structure can be represented by the model system shown in Fig. 9-33(b).

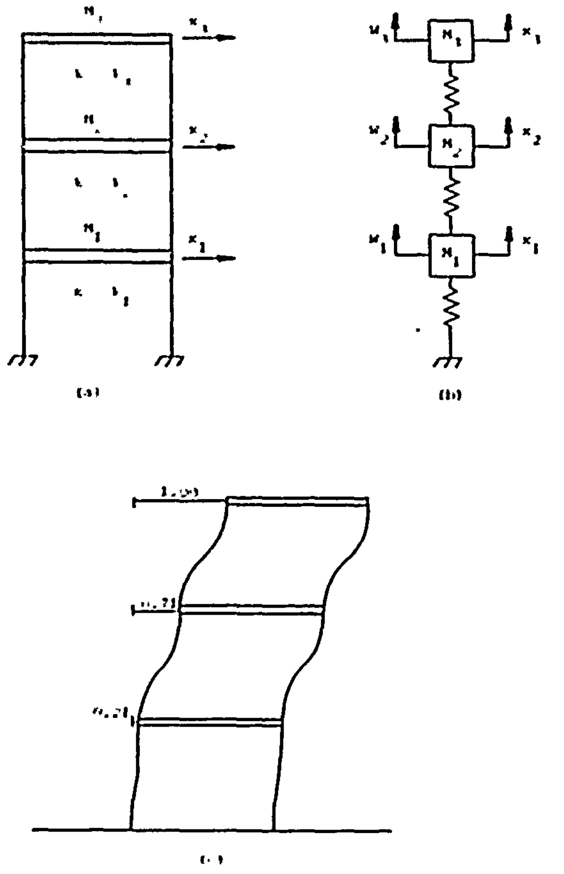

Figure 9-33 Three Shelf Equipment Rack

In accordance with the procedures described in paragraph 9.6.1 the first step is to assume a deflected shape for the fundamental mode. Converting the masses to forces (weight) by multiplying by the acceleration of gravity

W_1 = 3088 lbs (13,736 N)

W_2 = 1544 lbs (6,868 N)

W_3 = 1544 lbs (6,868 N)

Applying these loads as shown in Fig. 9-33(b) the following static deflections are obtained

x_1 = 1.029 in. (2.614 cm)

x_2 = 2.573 in. (6.535 cm)

x_3 = 3.345 in. (8.496 cm)

since only scaled displacements are important, these are normalized with respect to the largest value and entered in Table 9-14 as the first trial assumed mode shape. The product $M_i\phi_i'$ is next computed for each mass and entered in Table 9-14 as shown.

The next step is to compute deflections due to the inertial forces $M_i\phi_i'$. The deflection increment in each spring is equal to the force in that spring divided by its stiffness. These deflections are entered in Table 9-14 and then normalized with respect to the largest value for comparison with the assumed mode shape. Note that the computed deflections do not represent real deflections but only relative values since the product $M_i\phi_i'$ only represents relative values of the inertia forces. Also note that the computed shape agrees fairly well with the assumed mode shape. A second trial should give better agreement.

If the results of the first trial are used in Eq. 9-89 it is found that

Table 9-14

MODIFIED RAYLEIGH PROCEDURE CALCULATION SUMMARY

Trial Number	Mass No.	Assumed Shape ϕ_i'	$M_i\phi_i'$	Computed Deflection $\Lambda''\phi_i''$	Computed Shape ϕ_i''	$M_i\phi_i'\phi_i''$	$M_i(\phi_i'')^2$
1	1	0.308	2.464	0.00159	0.223	0.549	0.398
	2	0.769	3.076	0.00513	0.719	2.212	2.068
	3	1.0	4.0	0.00713	1.0	4.000	4.000
					Sums =	6.761	6.466
2	1	0.223	1.784	0.00144	0.209	0.373	0.349
	2	0.719	2.876	0.00488	0.709	2.039	2.011
	3	1.0	4.0	0.00688	1.0	4.000	4.000
					Sums =	6.412	6.360
3	1	0.209	1.672 (292.6)	0.00142	0.208	0.348 (60.86)	0.346 (60.20)
	2	0.709	2.836 (496.3)	0.00484	0.708	2.008 (351.38)	2.005 (350.70)
	3	1.00	4.0 (700.0)	0.00684	1.00	4.000 (700.00	4.000 (700.00)
					Sums =	6.356 (1112.24)	6.351 (1110.90

$$\omega_1^2 = \frac{\sum_{i=1}^{3} M_i\phi_i'\phi_i''}{\Lambda''\sum_{i=1}^{3} M_i(\phi_i'')^2} + \frac{6.761}{0.00713(6.466)} = 146.6$$

and $\omega_1 = 12.1$ rad/sec

Since the computed mode shape is closer to the true one for the first mode, it is used as the initial shape for a second trial. The operations are the same as for the first trial and the results are presented in Table 9-14. Using values obtained in the second trial

$$\omega_1^2 = \frac{6.412}{0.00688(6.360)} = 146.54$$

and $\omega_1 = 12.1$ rad/sec

Although the second trial has provided a closer approximation to the first mode shape there was no significant change in the calculated natural frequency. This is not true in all cases and results depend on how closely the initial trial mode shape approximates the correct one. A third trial using the calculated shape from the second cycle is also shown in Table 9-14 and indicates closer agreement between assumed and calculated values. The process can be repeated until desired agreement is obtained. The first mode shape is shown in Fig. 9-33(c).

The third cycle of calculations in Table 9-14 presents numerical values in both the English and SI system of units (in parentheses) where the values differ.

9.8.2 Use of Shock Spectra for Analysis of Systems Subjected to Base Motions

a. GIVEN: It is assumed that the two degree of freedom systems shown in Fig. 9-30 represents an equipment rack attached to the floor of a structure. The floor is subjected to horizontal motions in the x-direction only. Figure 9-34 is a shock spectrum representing an envelope of the response of single degree of freedom systems to the floor motions. The masses and stiffnesses of the rack system are such that its lowest natural frequency is 3 Hz.

b. FIND: Using the shock spectrum of Fig. 9-34 determine an upper bound to the peak acceleration of an item of equipment attached to m_2. Neglect the effect of equipment mass on system response.

c. SOLUTION: It has previously been determined (Eq. 9-84) that the natural frequencies of the system shown in Fig. 9-30 are

$$\omega_1 = 0.6181\sqrt{k/m} \qquad \omega_2 = 1.6180\sqrt{k/m}$$

If $\omega_1 = 3$ Hz $\quad \omega_2 = \frac{1.6180}{0.6181}(3) = 7.853$ Hz.

The normal modal matrix previously obtained from Eqs. 9-132 and 9-134 is

$$[A] = m^{-1/2}\begin{bmatrix} 0.5257 & 0.8506 \\ 0.8506 & -0.5257 \end{bmatrix}$$

The modal participation factors are obtained from Eq. 9-148

$$\{\gamma\} = [A]^T\{m\}$$

$$\{\gamma\} = \begin{Bmatrix} \gamma_1 \\ \gamma_2 \end{Bmatrix} = m^{-1/2}\begin{bmatrix} 0.5257 & 0.8506 \\ 0.8506 & -0.5257 \end{bmatrix}\begin{bmatrix} m \\ m \end{bmatrix} = m^{1/2}\begin{Bmatrix} 1.3763 \\ 0.3249 \end{Bmatrix}$$

and $$\lceil \gamma \rfloor = m^{1/2}\begin{bmatrix} 1.3763 & 0 \\ 0 & 0.3249 \end{bmatrix}$$

From Fig. 9-34 the peak absolute accelerations at the two

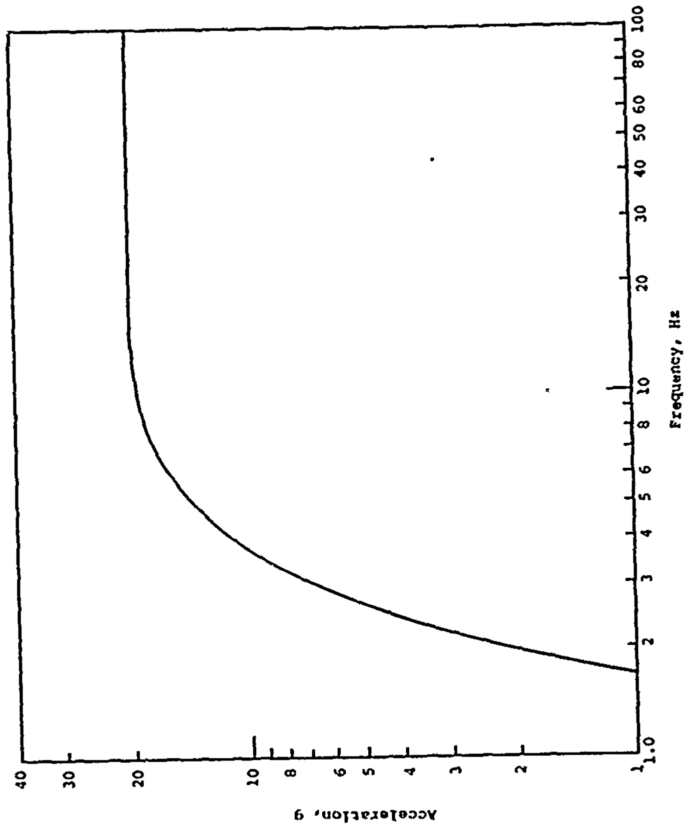

Figure 9-34 Undamped Horizontal Shock Spectrum

natural frequencies are

at 3 Hz $a_1 = 7g$

7.85 Hz $a_2 = 18g$

In matrix notation

$$\{a\} = \begin{Bmatrix} a_1 \\ a_2 \end{Bmatrix} = \begin{Bmatrix} 7g \\ 18g \end{Bmatrix}$$

Equation 9-170 is used to sum the modal contributions.

$$\left|\{\ddot{x}\}_{max}\right| \leq [A]\lceil\gamma\rfloor\{a\}$$

$$\begin{Bmatrix} |\ddot{x}_1|_{max} \\ |\ddot{x}_2|_{max} \end{Bmatrix} \leq m^{-1/2}\begin{bmatrix} 0.5257 & 0.8506 \\ 0.8506 & -0.5257 \end{bmatrix} m^{1/2}\begin{bmatrix} 1.3763 & 0 \\ 0 & -0.3249 \end{bmatrix}\begin{Bmatrix} 7g \\ 18g \end{Bmatrix}$$

$$\begin{Bmatrix} |\ddot{x}_1|_{max} \\ |\ddot{x}_2|_{max} \end{Bmatrix} \leq \begin{Bmatrix} 10.04\ g \\ 5.12\ g \end{Bmatrix}$$

The maximum absolute acceleration of m_1 is 10.04 g and that of m_2 and the attached equipment is 5.12 g.

9.8.3 Dynamic Response to Airblast and Base Motions

a. GIVEN: The one story frame structure shown in Fig. 9-35(a) has a force-displacement relationship represented by Fig. 9-35(b). The structure is subjected to airblast loads and base displacements represented by Figs. 9-36(a) and 9-36(b), respectively.

b. FIND: Response of structure to airblast and base motions. Neglect damping.

c. SOLUTION: The steps in transforming the frame structure into an equivalent single degree of freedom system have been skipped for the sake of brevity.

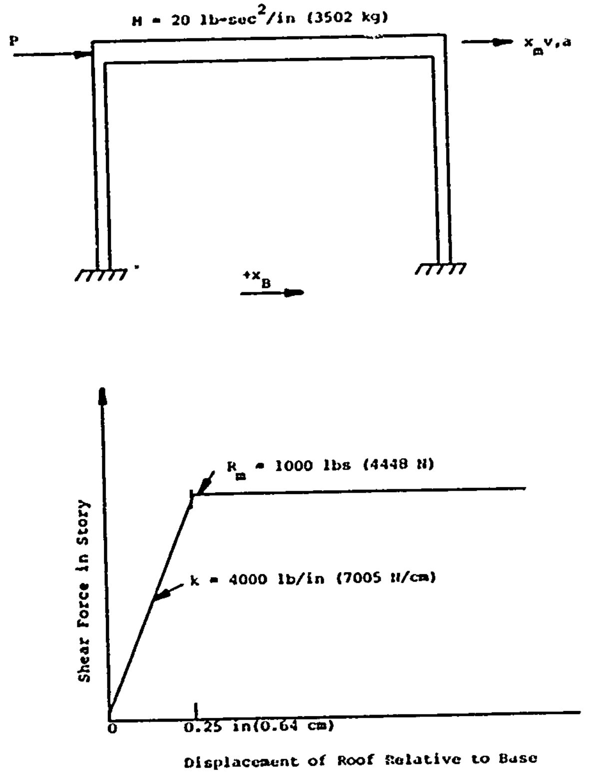

(b)

Figure 9-35 Structural Characteristics of Building

The mass and airblast loads are assumed to be concentrated at the level of the roof. The equivalent mass, load, stiffness and maximum resistance would normally be obtained using the procedures described in paragraph 9.3. The response of the frame is obtained by numerical integration using Eqs. 9-14 and 9-15 with $\beta = 1/4$.

$$\dot{x}_{n+1} = \dot{x}_n + \frac{\Delta t}{2} (\ddot{x}_n + \ddot{x}_{n+1})$$

$$x_{n+1} = x_n + \Delta t \dot{x}_n + \frac{(\Delta t)^2}{2} \ddot{x}_n + \frac{1}{4}(\ddot{x}_{n+1} - \ddot{x}_n)(\Delta t)^2$$

where the subscripts $n + 1$ indicate values of x, $\dot{x}$ and $\ddot{x}$ at the time $t + \Delta t$.

The period of the system is obtained from Eq. 9-5

$$T = 2\pi \sqrt{\frac{M}{K}}$$

$$= 6.28 \sqrt{\frac{20}{4000}} = 0.444 \text{ sec}$$

A Δt of 0.05 sec is selected, so

$$\frac{\Delta t}{T} = \frac{0.05}{0.444} = 0.11$$

and from Table 9-1, reasonably rapid convergence is expected.

The positive direction for acceleration, velocity and displacement of the roof mass and displacement of the base are as indicated in Fig. 9-35(a). Each step of the numerical integration is summarized in Table 9-15.

At $t = 0$ it is assumed that the structure has zero velocity and displacement. At $t = 0$ the applied force is 2000 pounds (8896 N) and the base displacement is zero. Since the relative displacement between the roof and base is zero, no resistance has been developed (see Fig.

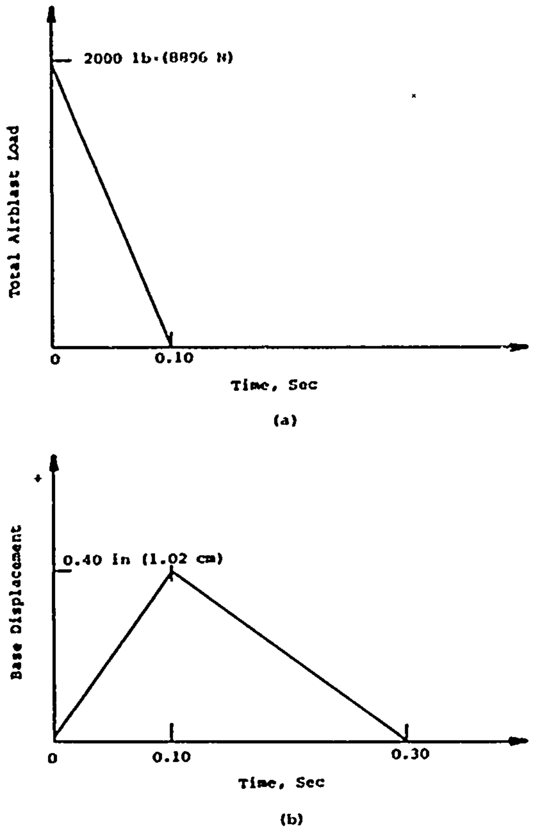

Figure 9-36 Disturbing Functions

9-36(b). The acceleration of the mass is given by

$$a = \frac{P - R}{M} = \frac{2000 - 0}{20} = 100 \text{ in/sec}^2 (2.54 \text{ m/sec}^2)$$

This first step is summarized in Table 9-15. For the next step, the acceleration is assumed to be equal to that calculated from the initial step. Then from Eq. 9-14 with $x_n = \dot{x}_n = 0$, $\Delta t = 0.05$(sec.) and $\ddot{x}_n = \ddot{x}_{n+1} = 100$ in/sec^2

$$\dot{x}_{n+1} = 0 + \frac{0.05}{2}(100 + 100)$$

$$= 5 \text{ in/sec } (12.70 \text{ cm/sec})$$

and from Eq. 9-15

$$x_{n+1} = 0 + 0.05(0) + \frac{(0.05)^2}{2}(100) + \frac{1}{4}(100 - 100)(0.05)^2$$

$$= 0.125 \text{ in } (0.318 \text{ cm})$$

From Fig. 9-36(b) the base displacement at t = 0.05 sec is 0.20 in (0.508 cm). Then

$$x_M - x_B = 0.125 - 0.20 = -0.075 \text{ in } (0.191 \text{ cm})$$

The resistance is

$$(x_M - x_B)k = -0.075(4000) = -300 \text{ lbs } (-1334 \text{ N})$$

and the calculated acceleration is

$$\frac{P-R}{M} = \frac{1000 - (-300)}{20} = 65 \text{ in/sec}^2 \ (165 \text{ cm/sec}^2)$$

Obviously the initial assumption for the acceleration at t = 0.05 sec was in error. The calculated value is used as the new assumed acceleration and the calculations are repeated until the calculated value agrees with the assumed value within the desired degree of accuracy. These calculations are summarized in Table 9-15. A similar process is repeated for the next time increment with the acceleration initially assumed not to change. This step is also shown in Table 9-15.

Another Δt is added and the calculations repeated. It is seen that the displacement in this cycle

Table 9-15

RESULTS OF NUMERICAL INTEGRATION

Time (sec)	Assumed $\ddot{x}_{n+1}$ (in/sec^2)	$\dot{x}$ (in/sec)	x_M (in)	x_B (in)	$x_M - x_B$ (in)	R (lbs)	P (lbs)	$\frac{P-R}{M}$ in/sec^2
0	N.A.	0	0	0	0	0	2000	100
0.05	100.0 65.0 69.4 68.9	5.00 4.13 4.24 4.22	0.125 0.103 0.106 0.106	0.20 0.20 0.20 0.20	-0.075 -0.097 -0.094 -0.094	-300 -388 -377 -377	1000 1000 1000 1000	65.0 69.4 68.9 68.9
0.10	68.9 1.0 8.1 7.0 7.2	7.67 5.97 6.15 6.12 6.13	0.402 0.360 0.365 0.364 0.364	0.40 0.40 0.40 0.40 0.40	0.002 -0.040 -0.035 -0.036 -0.036	8 -163 -140 -144 -144	0 0 0 0 0	-0.4 8.1 7.0 7.2 7.2
0.15	7.2	6.49	0.679	0.30	0.379	1000	0	-50.0
0.14	-50.0	5.27	0.592	0.320	0.272	---	---	---
0.137	-50.0	5.33	0.576	0.326	0.250	1000	0	-50.0
0.30	-50.0	-2.82	---	---	---	---	---	---
0.284	-50.0	-2.00	0.816	0.033	0.783	1000	0	-50.0
0.30	-50.0 -48.6	-2.82 -2.81	0.776 0.776	0 0	0.243 0.243	972 972	0 0	-48.6 -48.6
0.35	-12.8	-4.34	0.597	0	0.064	256	0	-12.8
0.40	28.7	-3.95	0.390	0	-0.144	-574	0	28.7
0.45	28.7	-2.51	0.299	0	-0.304	---	---	---
0.432	49.9	2.69	0.284	0	-0.249	-996	0	50.0
0.486	50.0	0	0.211	0	-0.322	-1000	0	50.0
0.50	49.0	0.70	0.216	0	-0.245	-980	0	49.0
0.55	32.0	2.73	0.301	0	-0.160	-640	0	32.0
0.60	0.5	3.54	0.458	0	-0.003	-11	0	0.5
0.65	-31.1	2.78	0.616	0	0.155	621	0	-31.1
0.70	-48.8	0.78	0.705	0	0.244	977	0	-48.8
0.7158	-50.0	0	0.711	0	0.25	1000	0	-50.0

would exceed the point at which the system goes fully plastic. The resistance cannot exceed 1000 pounds (4448 N) and this maximum resistance is the basis of the calculated acceleration. The displacement is not valid since the system has yielded during this time interval. It is necessary to find the time at which yielding occurs. It can be found by selecting smaller Δt's until the calculated relative displacement is equal to 0.25 inches (0.635 cm). $\Delta t = 0.04$ sec is tried and the calculations are repeated. It is also obvious that the system will be decelerating during this Δt so it is assumed that $\ddot{x}_{n+1} = -50$ in/sec^2 (127 cm/sec^2) for the first trial. This trial still exceeds the elastic displacement, so $\Delta t = 0.037$ sec is tried and works. A larger Δt can now be used since the acceleration is constant for the yielded system. A Δt is chosen so that $t + \Delta t = 0.30$ sec (time when base motion ceases),

$$\Delta t = 0.30 - 0.137 = 0.163 \text{ sec}$$

The calculations are repeated as before, and it is seen that the velocity of the mass is -2.820 in/sec (7.16 cm/sec). The velocity of the base over the period from 0.1 to 0.3 seconds is

$$v = -\frac{0.4}{0.2} = -2.0 \text{ in/sec } (-5.08 \text{ cm/sec})$$

Yielding of the vertical members ceases when the velocity of the mass is equal to that of the base, so the trial is not valid, and the time at which the velocity of the mass is equal to -2.0 in/sec (-5.08 cm/sec) must be determined. Since the acceleration is constant up to the time yielding stops, the time when the velocities are equal can be obtained from Eq. 9-[illegible]:

$$-2.0 = 5.333 - 50\,\Delta t$$

$$\Delta t = 0.1466 \text{ sec}$$

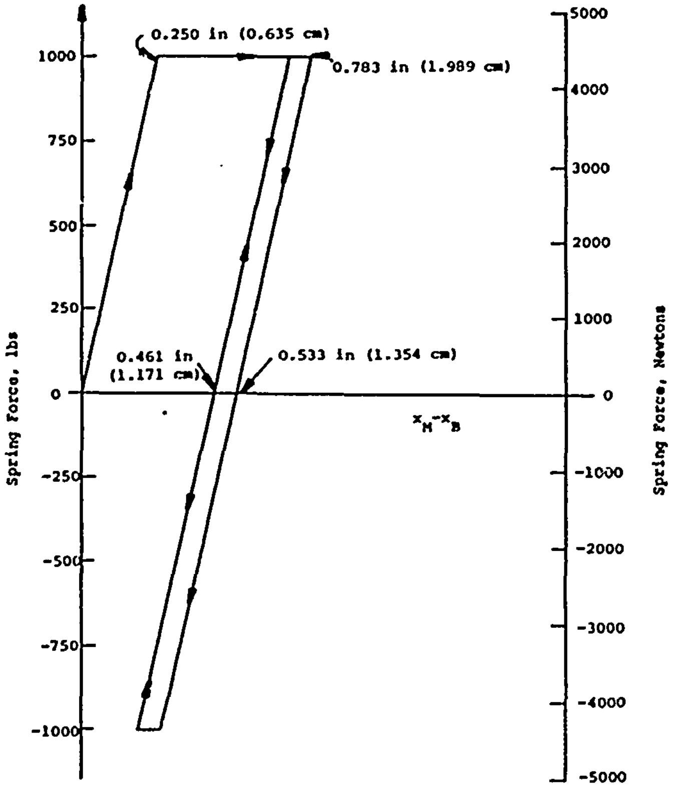

Figure 9-37 Load-Deformation History

After t = 0.284 sec, the system is again elastic, and the next Δt should be selected to coincide with the time when the base motion ceases. Note that since the system is unloading, it is now moving down a load displacement curve which is parallel to the initial curve (see Fig. 9-37). The permanent set in the columns is equal to the maximum displacement minus the elastic recovery

$$x_p = x_m - x_e = 0.783 - 0.25$$
$$= 0.533 \text{ in } (0.135 \text{ cm})$$

This permanent set must be subtracted from the computed displacement of the mass to find the relative displacement and resistance for subsequent steps in the integration. It is the new reference point for vibration. At t = 0.45 sec, it is seen that the displacement has again exceeded the elastic limit and the time of actual yielding must again be found. After a couple of trials, the time is found to be t = 0.432 sec. The next time step to be located is the time at which the velocity is equal to 0, since this means a reversal of the direction of motion and a time of maximum displacement. The acceleration is a constant 50 in/sec^2 (127 cm/sec^2) since R_m = 1000 lb (4448 N) and

$$t = \frac{2.691}{50} = 0.0538 \text{ sec}$$

The system now starts returning along an elastic force displacement portion of the curve. The new permanent displacement and reference point is

$$0.211 + 0.25 = 0.461 \text{ in } (1.17 \text{ cm})$$

After t = 0.486 sec the system is vibrating elastically between absolute displacements of 0.711 in and 0.211 in (0.180 cm and 0.535 cm). This is a relative displacement of 0.25 in (0.635 cm) on each side of the permanent set of 0.461 in (1.17 cm), so the system reaches the yield

point displacement twice in each cycle. The period of vibration is 0.459 sec as compared to the 0.444 sec computed from Eq. 9-5.

The spring force-deformation history starts with the motion of the mass due to the force P being less than that of the base. The spring of the equivalent single degree of freedom system is being compressed and is helping the force, P, accelerate the mass. Shortly after P has decreased to 0, and the base motion has reached its peak, the absolute displacement of the mass exceeds that of the base and the equivalent spring goes into tension. The spring force now starts decelerating the mass. The load-relative displacement relationship is linear until the relative displacement reaches 0.25 inches (0.635 cm) and the spring yields in tension. The relative displacement continues to increase until the velocity of the mass and the base is equal. By this time the relative displacement is 0.783 in (1.99 cm) and the permanent set is 0.533 in (1.35 cm). The velocity of the mass then falls below that of the base and the spring is being compressed elastically. The base motion stops, but the inertia of the mass causes the spring to yield in compression and it reduces the permanent set to 0.461 in (1.17 cm). The spring mass system then oscillates about this neutral position and eventually, with some small amount of damping, will come to rest at a permanent relative displacement of 0.461 in (1.17 cm).

The numerical calculations can be performed with whatever degree of accuracy is desired by the analyst. Greater numbers of significant figures and cycles of iteration yield greater accuracy of calculations but cannot overcome the approximations made in establishing the analytical model. Although, in this example, the calculated acceleration is used for the next trial, experienced personnel can sometimes speed convergency by different processes. Although only one trial is shown in Table 9-15 for each step after t = 0.30 sec, the values are the result of iterations. A plot of the motion of the structure is shown in Fig. 9-38. It is interesting to note that if the base motion had not been included, the maximum response from Fig. 9-13, with T = 0.446 sec would have been 0.375 in (0.951 cm) and from Eq. 9-14 the rebound would have been -0.25 in (0.635 cm).

9.8.4 Natural Frequencies of Circular Arches

a. GIVEN: A reinforced concrete arch is hinged at its supports and has a radius of 15 feet (4.57 m). The overall thickness of the arch cross section is 18 inches (0.457 m) and the effective depth to the tension reinforcing is 15 inches (0.381 m). One percent (p = 0.01) reinforcing steel is placed circumferentially in each face of the arch. Assume f'_c = 5000 psi (3447 N/cm^2) and E_s = 29,000 ksi (19,995 kN/cm^2). The central angle of the arch is 180°. The unit weight of concrete is assumed to be 144 pcf (2308 kg/m^3).

b. FIND: The natural frequencies of the arch in

(a) The first symmetric extensional mode
(b) The first antisymmetric flexural mode
(c) The first symmetric flexural mode

c. SOLUTION: The first step is to calculate several parameters related to properties of the arch.

The modulus of elasticity of the concrete is obtained from Eq. 8-2.

$$E_c = w^{1.5}\, 33\sqrt{f'_c}$$

$$= (144)^{1.5}(33)(5000)^{1/2}$$

$$= 4{,}013{,}000 \text{ psi } (27{,}668{,}700 \text{ kN/m}^2)$$

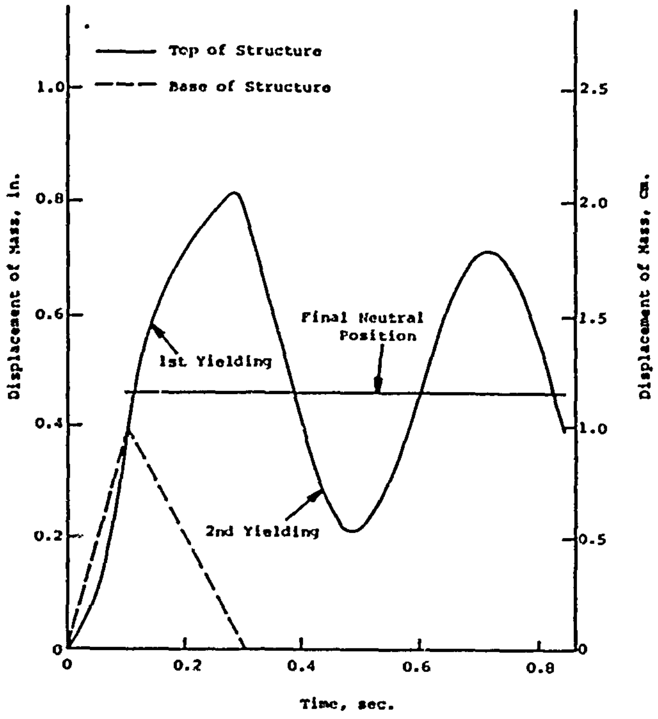

Figure 9-38 Absolute Displacement - Time History for Mass

From Eq. 8-30

$$I_c = \frac{bd^3}{2}\,(5.5p + 0.083)$$

$$= \frac{12(15)^3}{2}\,[5.5\,(0.01) + 0.083]$$

$$= 2794.5 \text{ in}^4\text{/ft of width } (0.0038 \text{ m}^4\text{/m})$$

The mass per unit length of the arch is

$$m = \frac{144(1.5)(1.0)(1.0)}{12(386)}$$

$$= 0.0466\ \frac{\text{lb-sec}^2}{\text{in}^2}\ (1054.45 \text{ kg/m})$$

The length of the arch axis is

$$S = \theta_o R$$

$$= 3.14\ (15 \times 12)$$

$$= 565.5 \text{ in } (14.36 \text{ m})$$

The radius of gyration of the rectangular cross section is given by

$$r = 0.288\ d = 0.289\ (15)$$

$$= 4.33 \text{ in } (0.11 \text{ m})$$

The gross cross sectional area of the arch is

$$A = 18(12) = 216 \text{ in}^2 \text{ for 1-foot wide rib}$$

$$= 0.457 \text{ m}^2 \text{ for 1 m wide rib}$$

From Eq. 9-181 the frequency of vibration in the breathing mode is

$$\omega_N = \frac{0.97}{R}\sqrt{\frac{EA}{m}} = \frac{0.97}{130}\sqrt{\frac{4{,}013{,}000(216)}{0.0466}}$$

$$= 735 \text{ rad/sec} = 117 \text{ Hz}$$

The coefficinet for the first antisymmetric flexural mode is obtained from Eq. 9-183

$$C_N^2 = \frac{\bar{m}^4\pi^4\left|1 - \left(\frac{\theta_o}{\bar{m}\pi}\right)^2\right|^2}{1 + 3\left(\frac{\theta_o}{\bar{m}\pi}\right)^2}$$

where $\bar{m} = 2N = 2(1) = 2$ for first mode

$$C_N^2 = \frac{(2)^4(3.14)^4\left|1 - \left(\frac{3.14}{2(3.14)}\right)^2\right|^2}{1 + 3\left(\frac{3.14}{2(3.14)}\right)^2}$$

$$= 501$$

and $C_N = 22.38$.

From Eq. 9-182 the frequency of the first antisymmetric flexural mode is

$$\omega_N = \frac{C_N}{S^2}\sqrt{\frac{EI}{m}} = \frac{22.38}{(565.5)^2}\sqrt{\frac{4{,}013{,}000(2794.5)}{0.0466}}$$

$$= 34.3 \text{ rad/sec} = 5.46 \text{ Hz}$$

The coefficient for the first symmetric flexural mode is obtained from Eq. 9-185

$$C_N^2 = \frac{\bar{m}^4\pi^4\left|1 - \left(\frac{\theta_o}{\bar{m}\pi}\right)^2\right|}{1 + \frac{1}{\bar{m}^2} + 2\left(\frac{\theta_o}{\bar{m}\pi}\right)^2}$$

where $\bar{n} = 2N+1 = 2(1)+1 = 3$ for first mode

$$C_N^2 = \frac{(3)^4(3.14)^4\left|1 - \left(\frac{3.14}{3(3.14)}\right)^2\right|^2}{1 + \frac{1}{(3)^2} + 2\left(\frac{3.14}{3(3.14)}\right)}$$

$$= 4687$$

and $C_N = 68.46$

From Eq. 9-182 the frequency of the first symmetric flexural mode is

$$\omega_N = \frac{68.46}{S^2}\sqrt{\frac{EI}{m}}$$

$$= 105 \text{ rad/sec} = 16.7 \text{ Hz}$$

9.9 REFERENCES

9-1 Design of Structures to Resist the Effects of Atomic Weapons, Principles of Dynamic Analysis and Design, U. S. Army Corps of Engineers Manual EM 1110-345-415, March 1957. (U)

9-2 Newmark, N.M., "Computation of Dynamic Structural Response in the Range Approaching Failure," Proceedings of the Symposium on Earthquake and Blast Effects on Structures, Los Angeles, Calif., 1952. (U)

9-3 Melin, J.W., Numerical Integration by Beta Method, ASCE Conference on Electronic Computation, Kansas City, Mo., 1968. (U)

9-4 Melin, J.W. and Sutcliffe, S., Development of Procedures for Rapid Computation of Dynamic Structural Response, Structural Research Series No. 171, University of Illinois, Urbana, Ill., 1958. (U)

9-5 Protective Construction Review Guide (Hardening), Office of the Assistant Secretary of Defense, Installations and Logistics, Washington, D.C., June 1961. (U)

9-6 Design of Structures to Resist the Effects of Atomic Weapons, Structural Elements Subjected to Dynamic Loads, U. S. Army Corps of Engineers Manual EM 1110-345-416, March 1957. (U)

9-7 Biggs, J.M., Introduction to Structural Dynamics, McGraw-Hill Book Co., New York, N.Y., 1964 (U)

9-8 Veletsos, A.S., et al., Design Procedures for Shock Isolation Systems of Underground Protective Structures, Vol. 3, Response Spectra of Single Degree of Freedom Elastic and Inelastic Systems, RTD TDR 63-3096 Vol. III, Air Force Weapons Laboratory, Kirtland AFB, N.M., June 1964. (U)

9-9 Jacobsen, L.S. and Ayre, R.S., Engineering Vibrations with Applications to Structures and Machinery, McGraw-Hill Book Co., New York, N.Y., 1958. (U)

9-10 Gere, J.M., and Weaver, W., Matrix Algebra for Engineers, D. Van Nostrand Company, Inc., Princeton, N.J., 1967. (U)

9-11 Meirovitch, L., Analytical Methods in Vibrations, The Macmillan Co., Toronto, Ontario, Can., 1967. (U)

9-12 Chen Yu, Vibrations: Theoretical Methods, Addison-Wesley Publishing Co., Inc., Reading, Mass., 1966. (U)

9-13 Harris, C.M., and Crede, C.E., Shock and Vibration Handbook, McGraw-Hill Book Co., New York, N.Y., 1961. (U)

-14 Veletsos, A.S., et al., "Free In-Plane Vibrations of Circular Arches", Proceedings of the American Society of Civil Engineers, Engineering Mechanics Division, April 1972. (U)

9-15 Wolf, J.A., "Natural Frequencies of Circular Arches", Proceedings of the American Society of Civil Engineers, Structural Division, September 1971. (U)

9-16 Liber, T., Optimal Shock Isolation Synthesis, AFWL TR 65-82, Air Force Weapons Laboratory, Kirtland AFB, N.M., July 1966. (U)

9-17 Klein, G.H., et al., Optimum Shock Isolation for Underground Protective Structures, AFWL TR 69-178, Air Force Weapons Laboratory, Kirtland AFB, N.M., December 1969. (U)

SECTION X

PROTECTION OF STRUCTURE CONTENTS

10.1 INTRODUCTION

10.1.1 General Requirements

Previous sections have presented methods for prediction of nuclear weapon effects and the design or analysis of structures subjected to these effects. It has been shown that it is feasible, within limits, to design structures which will survive very severe ground shock and radiation environments. Another important facet of the problem is to ensure survival of personnel and equipment within these structures. It is possible, for example, that the structure could withstand the airblast, ground shock and radiation effects but the contents be so severely damaged by radiation or structure motions that the facility could not accomplish its intended function. Radiation shielding techniques have been discussed in Section VI. This section deals with the protection of vulnerable components from structural motions due to airblast and ground shock. A recent study (Ref. 10-1) has collected and condensed shock isolation research results pertinent to protective construction. Much of the material in this section has been taken directly from that study.

The objective of shock isolation in protective construction applications is to reduce the magnitude of motions transmitted by a vibrating structure to shock sensitive equipment or personnel. A second consideration in some cases is to reduce the magnitude of motions transmitted by vibrating equipment to its supports. These latter motions can be significant if the equipment is mounted on shock isolated platforms or if large inertia forces are generated by the equipment.

The most common shock isolation problem is that of reducing structural motion inputs to equipment or personnel.

These input motions can be determined or specified in various ways and the choice of the method of analysis is often related to the importance of the item and its position within the structure. For example, a critical piece of equipment, located so that its allowable motions are restricted, would require as detailed a prediction of input motions as is possible. In other cases, crude approximations may be satisfactory.

If a detailed analysis is required, one approach is to model the supporting structure using combinations of finite elements. The properties of the elements are determined using procedures presented in Section VIII and the loads acting at individual node points can be obtained using procedures presented in Section VII. The motions of the structure at the points of attachment of items of equipment are then obtained from a dynamic analysis of the model structure using procedures discussed in Section IX. In the case of massive items of equipment, the weight of the item may affect the motions of the supporting structure. For these cases, the item and its suspension system should also be included in the structural model for final analysis. Results satisfactory for preliminary analyses can often be obtained by a single element, e.g., beam or slab, representation of the supporting structure. The resistance of these elements and their response to static and dynamic loads can also be obtained from procedures outlined in Sections VII, VIII and IX.

In the case of buried structures, it is sometimes assumed that structural motions are equal to free-field motions of the surrounding soil. This approach neglects the response of elements of the structure, as well as relative motions between the structure and soil.

The two most common methods of describing input motions are shock response spectra and time-motion histories. Shock response spectra and time-motion histories are

described in Section IX. Input motions are normally specified as accelerations, velocities and/or displacements of the points of attachment of the item of equipment. Time-motion histories are necessary if a detailed analysis of the shock isolation system is to be made.

Assuming that a shock isolation system is required, the first step in the design process is to define as explicitly as possible the performance objectives of the system. The more detail with which the performance objectives can be specified, the greater will be the assurance that the system will accomplish its objectives.

The general functional objectives of a shock isolation system are to

- Reduce input motions to acceptable levels
- Minimize rattlespace requirements consistent with system effectiveness and cost
- Minimize coupling of horizontal and vertical motions
- Accommodate a spectrum of inputs of uncertain waveforms
- Limit the number of cycles of motion of the isolated body
- Support the system under normal operating conditions without objectionable motions
- Maintain constant attitude under normal operating conditions
- Accommodate changes in load and load distribution
- Maintain system vibration characteristics over long periods of time
- Interface properly with other components or parts of the facility
- Require minimum maintenance

10.1.2 Shock Tolerance of Equipment and Personnel

The requirement for shock isolation is based upon the shock tolerance of critical items of equipment and/or personnel housed within the protective structure. If the predicted shock input exceeds the shock tolerance of personnel, a shock isolation system is required. If the shock input exceeds the shock tolerance of equipment, the equipment can either be ruggedized to increase its shock tolerance or it can be shock isolated. There are practical limits to ruggedization, however, and the costs may exceed those of an isolation system. If the input does not exceed the shock tolerance of the equipment, the equipment can be hard-mounted to the structure.

a. Equipment

Except for extremely simple elements, the most practical means of determining the shock tolerance of an item of equipment is by testing. Even experimental data can be of questionable value if the test input motion characteristics differ greatly from those to be actually experienced. In some cases, a decision regarding the need for shock isolation must be made before detailed characteristics of system components are established. In these cases, the choice lies between specifying minimum acceptable shock tolerances for the new equipment or using whatever data are available for similar types of equipment.

The shock tolerance of equipment can be specified in various ways. Two forms of specification are the shock tolerance spectrum and maximum peak acceleration. A shock tolerance spectrum is simply the spectrum of motions the item is expected to survive or has survived. These spectra are similar to the input spectra previously discussed and are assumed to represent an upper bound of all tolerable motions. They

are normally expressed in terms of allowable accelerations, velocities and/or displacements as a function of frequency and direction of the motion. Extensive experimental effort is necessary to define equipment shock tolerance spectra, and they still do not provide complete assurance as to survival or failure of the equipment. However, it is normally assumed that if the input spectrum does not exceed the tolerance spectrum, shock isolation or ruggedization is not required.

Although the shock tolerance spectrum is a preferred method of presenting the shock tolerance of an item of equipment, the tolerance is often specified in terms of a peak allowable acceleration. Specification of only a peak response acceleration usually leads to an unnecessarily low frequency isolations system with associated large rattlespace requirements. Also, nothing is given on the natural frequencies of the equipment which are important in selecting a shock isolation platform and/or system for the equipment. In spite of the shortcomings, a peak allowable acceleration is frequently all that is given particularly in the early stages of a program.

While the preferred approach is to determine the shock tolerance of a specified item by appropriate tests, such tests are not always practical. In these cases it is necessary to rely on data obtained from shock tests of similar items. References 10-2, 10-3 and 10-4 present some data on the shock tolerance of various types of equipment. Table 10-1 presents data from Ref. 10-4 and can be used in the absence of better guidance. The vulnerability levels given in Table 10-1 represent lower limits of ranges of values given in Ref. 10-4 and were specified for input frequencies near the fundamental frequencies of the various

Table 10-1

ESTIMATES OF FREQUENCY AND VULNERABILITY OF TYPICAL EQUIPMENT ITEMS

Item	Lowest Natural Frequency	Estimated Vulnerability Level, g	
	Hz	No Damage	Severe Damage
Heavy Machinery--Motors, Generators, Transformers, etc. (>4000 lb)	5	10	80
Medium Wt. Machinery--Pumps, Condensers, Air Conditioners, etc. (1000 to 4000 lb)	10	15	120
Light Machinery--Fans, Small Motors, etc. (<1000 lb)	15	30	200
Racks of Communication Equipment, Relays, Rotating Magnetic Drum Units, Large Electronic Equipment with Vacuum Tubes	10	2	20
Small Electronic Equipment, Radios, Incandescent Lamps and Light Bulbs	20	20	200
Cathode Ray Display Tubes	5	1.5	12
Transistorized Computers, Fluorescent Lamps and Fixtures, Nuclear Reactors	10	5	60
Storage Batteries (All Types), Piping, and Duct Work	5	20	280

types of equipment. Estimates of these fundamental frequencies are also given in Table 10-1 and again represent the lower limits of ranges in values given in Ref. 10-4. In general, it can be assumed that the shock tolerance of an item of equipment will be greater at higher natural frequencies. Accordingly, the vulnerability levels in Table 10-1 can be taken as conservative estimates in the absence of better information. An exception would be when the duration and frequency content of the disturbing force were such that resonance could build up in one or more of the higher modes of vibration. This is not the usual case in nuclear blast induced motions, however.

The fundamental frequencies given in Table 10-1 are also useful in determining whether response of the equipment can be neglected in calculating the response of an isolation system. If the fundamental frequency of the equipment is much higher than that of the isolation system, the equipment can be assumed to be a rigid body in most cases. Otherwise, the higher modes should be included in the analysis.

b. Personnel

Estimates of the reaction of the human body to structural motions resulting from a nuclear detonation are based almost entirely on tests related to airborne and motor vehicle environments. The effects on man depend on the magnitude, duration, frequency and direction of the motion, as well as his position at the time of the disturbance. Figure 10-1 presents data on human shock tolerance for various positions and degrees of restraint. In protective structure applications, the initial structural motions can be either up or down and they are normally accompanied by a simultaneous outward motion. Injuries

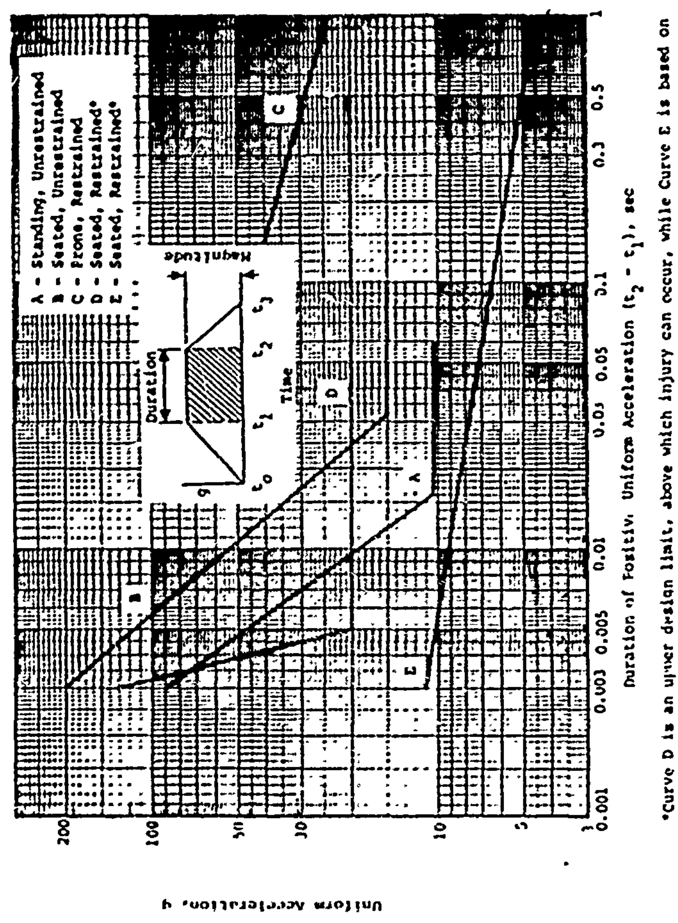

*Curve D is an upper design limit, above which injury can occur, while Curve E is based on subjective comfort responses to centrifuge tests.

Figure 10-1 Human Shock Tolerance to Prevent Internal Injury (Impact Injury Not Considered) (Ref. 10-3)

can result from excessive acceleration of the body or impact with the floor or other objects. Reference 10-5 concludes that a standing man will receive compressive injuries in the body-supporting bones if the upward floor acceleration exceeds 20 g during a long duration loading. The injury threshold is higher for short duration loads. If the floor moves downward rapidly, the man will free-fall a maximum distance equal to the floor displacement. A drop of only 20 inches (50.8 cm) could fracture both legs. Impact with an upward moving floor would increase the probability of fracture. The unrestrained man could also lose his footing and receive injuries due to impact with other objects or the floor.

Because of the possibility of impact injuries to personnel, design criteria will often limit acceleration inputs to much lower values than those indicated in Fig. 10-1. Reference 10-6 suggests limiting upward floor accelerations to 0.75 g and downward accelerations to 0.5 g to avoid injuries to an unrestrained man in the standing position and 0.75 g upward and 1.0 g downward for an unrestrained man in the sitting position. Horizontal acceleration limits of 1.0 g are also recommended for an unrestrained man in the sitting position to avoid whiplash injuries or being thrown out of his chair. These criteria are summarized in Table 10-2. Curves A & B of Fig. 10-1 are applicable to the standing and sitting unrestrained positions, respectively, and represent upper design limits. These curves are appropriate for design only under conditions where impact injuries can be avoided. Values from curve A represent one-half of the shock tolerance limit to allow for the possibility that all of the subject's weight might be on one leg.

Table 10-2

RECOMMENDED DESIGN VALUES FOR HUMAN TOLERANCE TO SHOCK MOTIONS

POSTURE	SHOCK DIRECTION		
	UPWARD	DOWNWARD	HORIZONTAL
Standing Unrestrained	A. 10 g B. 0.75 g	A. 5" (13cm) at > 1 g B. 0.5 g	A. * B. 0.5 g
Sitting Unrestrained	A. 15 g B. 0.75 g	A. 19" (48cm) at > 1 g B. 1.0 g	A. * B. 1.0 g
Prone Unrestrained	A. 40 g B. 0.75 g	A. * B. 1.0 g	A. * B. 0.75 g
Sitting Restrained	A. Curve E, Fig. 10-1 or 15 g	A. Curve E, Fig. 10-1 or 15 g	A. Curve E, Fig. 10-1 or 15 g
Prone Restrained	A. Curve C, Fig. 10-1 or 40 g	A. Curve C, Fig. 10-1 or 40 g	A. Curve E, Fig. 10-1 or 15 g

A. Limiting value of acceleration force to prevent internal injury.

B. Limiting value of acceleration force to avoid possible impact injury.

* Displacement limited, i.e., shock displacement must be attenuated to less than the distance between operator and nearest solid object.

An unrestrained man in the prone position (applicable to sleeping quarters) would be expected to withstand higher accelerations, except that he may be thrown from the bed and sustain injuries upon impact with the floor. For this reason, design criteria are again lower than human shock tolerance; acceleration limits of 0.75 g upward, 1.0 g downward and 0.75 g horizontal are suggested. If the man is in the unrestrained prone position, but inside a completely padded enclosure, he would be partially protected from impact injuries and curve C of Fig. 10-1 is applicable. If the subject is in a sitting position and restrained to prevent leaving the seat and relative motion between head and limbs and body is prevented, curve E of Fig. 10-1 is applicable for upward, downward and horizontal motions. Curve D is used for design of upward ejection seats and does not include the effect of rapid deceleration. Curve C is applicable to upward or downward acceleration for the prone restrained position and curve E for horizontal motions.

In designs where the horizontal and vertical motion inputs are combined, Ref. 10-3 recommends that the vector sum be limited to the lower of the horizontal or vertical limits.

Human shock tolerance to steady state vibrations may be of interest in those instances where there is little damping of shock isolated platforms. As in the case of transient shock, tolerance of steady state vibrations is affected by position and restraint of the individual. Vibration frequencies in the region of 5 to 10 cycles per second are of greater significance since they approximate natural frequencies of the human body. At these frequencies, tolerance of steady state vibrations may be as low as 1.5 - 2.0 g, even in the restrained seated position. Additional data on shock tolerance of the human body are included in Refs. 10-6, 10-7 and 10-8.

10.2 SHOCK ISOLATION PRINCIPLES

10.2.1 General Concepts

A full treatment of the problem of shock isolation is not possible in this manual. The following paragraphs provide an introduction to the subject, discuss some of the important characteristics of shock isolation systems, and reference other sources of more detailed information on particular areas of interest.

In general, the analytical treatment of shock isolation systems is based upon the principles of dynamic analysis presented in Section IX. Since many isolated masses are a complex combination of numerous smaller components, each with its own static and dynamic characteristics, the first step in the analysis is an idealization of the system. In most cases, this means representation of the real system by a simplified mathematical model consisting of a rigid mass, or masses, connected by springs and dash pots as shown in Fig. 10-2. Figure 10-2 represents the simplest case, that of a single degree of freedom system restrained to move in only one direction. In the more general case, the system would have at least six degrees of freedom, i.e., three displacements and three rotations. Under certain conditions, these six modes can be uncoupled and the system analyzed as six single degree of freedom systems. These conditions are discussed in earlier paragraphs.

The single degree of freedom system can also be used to illustrate the importance of some of the parameters affecting the effectiveness of shock isolation systems in general. Consider the single degree of freedom system shown in Figure 10-2. The isolator is represented by the linear spring and

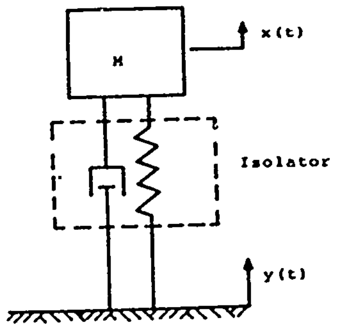

Figure 10-2 Idealized Model of Shock Isolated Mass

viscous damping device enclosed within the dotted square. The suspended mass is assumed to be a rigid body. It is assumed that the base of the system is subjected to a periodic sinusoidal motion whose frequency is ω. The undamped natural frequency of the system is ω_N. The ratio of the maximum absolute displacement of the mass to the maximum displacement of the base is plotted in Fig. 10-3 as a function of the ratio of the frequency of the base motion to the natural frequency of the single degree of freedom system. The ratio of displacements is called the absolute transmissibility of the system. Several curves are presented for various damping ratios (ratio of actual viscous damping coefficient to critical damping coefficient; see Section IX). When the frequency of the disturbing motion is small compared to that of the single degree of freedom system, the displacement of the mass is approximately equal to the displacement of the base. When the frequency of the base motion is several times that of the system, the motion of the mass is a small fraction of the base motion. When the ratio of frequencies becomes large (e.g., 20 to 30), the system can not respond to the base motions to any significant degree. At frequency ratios near one, large motions of the mass are possible and the magnitude is strongly affected by the amount of damping in the system.

One obvious shock isolation approach apparent from Fig. 10-3 is to use a low frequency suspension system so that the ratio of frequencies is always large. However, low frequency (sometimes referred to as soft) systems possess the undesirable characteristics of larger static and dynamic displacements and greater probability of coupling between modes of vibration. Although soft systems may be acceptable under some conditions, other constraints will often preclude their use. One obvious constraint is a limit on the relative motion between the suspended mass and its supports or adjacent parts of the facility. This relative motion determines the amount

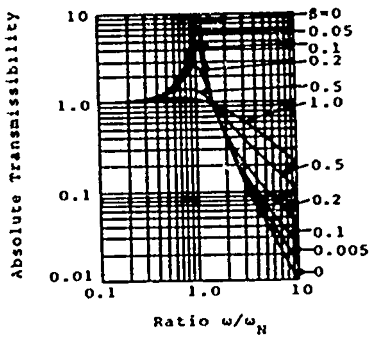

Figure 10-3 Effect of Frequency Ratio and Damping Ratio on Absolute Transmissibility (Ref. 10-8)

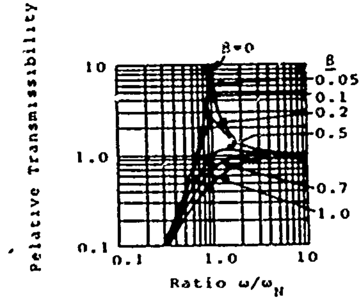

Figure 10-4 Effect of Frequency Ratio and Damping Ratio on Relative Transmissibility (Ref. 10-8)

of rattlespace that must be provided to avoid impact between the mass and other fixed or moving parts of the facility.

Figure 10-4 shows the variation of relative transmissibility with frequency ratio for several percentages of critical damping. Relative transmissibility is defined as the ratio of the maximum relative motion between the mass and base to the maximum displacement of the base. At low frequency ratios (high frequency, or hard, system), there is very little relative motion between mass and base. At high frequency ratios (soft system), the relative displacement can be approximately equal to the base displacement. The damping ratio again strongly affects the response at frequency ratios near one.

The acceleration of the mass will be a function of the force applied to the mass by the spring and damping devices. In the case of linear undamped springs, the force is a function of the relative displacement between the mass and its support. In viscous damping devices, the damping force is a function of the percent damping and the relative velocity between the mass and its supports. Thus, acceleration limits for the critical items will also impose restraints on spring stiffness and the amount of damping in the isolation system. In practice, the characteristics of the shock isolation system are usually some compromise combination of spring stiffness and damping ratio to minimize input motions to the mass for a specified allowable rattlespace or to minimize rattlespace for specified allowable motions of the mass.

Figures 10-3 and 10-4 also demonstrate the need to avoid resonance (frequency ratio of one) between the system and disturbing function. Although the structural motions resulting from nuclear detonations are not steady-state sinusoidal in nature, they frequently are of an oscillatory type and the displacement-frequency ratio relationships discussed above are approximately applicable. References 10-3 and 10-9 contain a

more detailed discussion of the effects of load duration, nonlinear springs, damping, and system frequency on response. The basic objective in shock isolation is to select a combination of isolation system properties which will reduce the input motions to the desired level. In design, it is a cut and try process. System properties are assumed and an analysis is made of system response to input motions. If the shock tolerance and rattlespace criteria are not satisfied, the system must be altered and the analysis repeated until the criteria are satisfied.

10.2.2 Single-Mass Dynamic Systems

In the general case, a single-mass system can have six degrees of freedom; translation in three orthogonal directions and rotations about three orthogonal axes. These systems can also be classified as coupled or uncoupled.

A coupled system is one in which forces or displacements in one mode will affect or cause response in another mode, e.g., a vertical displacement of a single rigid mass might cause rotation of the mass about some axis. An uncoupled system, on the other hand, is one where forces or displacements in one mode do not generate a response in another mode. If the system is completely uncoupled, base translations in any one of three orthogonal directions will excite translations of the mass only in that direction. Similarly, a pure rotation of the base about any one of three orthogonal principal inertia axes through the mass center will excite only pure rotations of the body about that axis. The principal inertia axes are those about which the products of inertia vanish. The principal elastic axes of a resilient element (isolator) are those axes for which an unconstrained element will experience a displacement colinear with the direction of the applied force. The point of intersection of the principal elastic axes of a resilient element is called the elastic center of the resilient element. If the principal elastic axes and the principal inertia axes of the shock isolated system coincide, the modes of vibration are uncoupled. The origin or point of intersection of both sets of axes must lie at the center of gravity of the mass. Such a system is also referred to as a balanced system.

In Figure 10-5, if all the springs have the same stiffness, the elastic center will be located at point A. If the suspended block is of uniform density, its center of gravity is also located at A, and the system is uncoupled for motions input through the springs. Some systems may be uncoupled only for motions in a particular direction. If point B in Fig. 10-5 is the center of gravity of the mass, a pure horizontal displacement of the structure would excite only a horizontal displacement of the mass. A pure vertical displacement of the structure would excite both vertical and rotational displacements of the mass. Thus, vertical and rotational modes are coupled. If the center of gravity were located at point C, then horizontal, vertical and rotational modes are coupled. If the characteristics of the mass and shock isolation system are such that the modes of vibration can be uncoupled, the system can be analyzed as a series of independent single degree of freedom systems. The response of each of these systems can be determined on the basis of input motions and isolator properties in a direction parallel to or about one of the principal inertia axes. The response in each one of these modes can be summed in various ways to obtain the total response of the system. The sum of the maximum responses would neglect differences in phasing and should represent an upper limit of the actual motions. Since it is unlikely that maximum response will occur simultaneously in all modes, the square root of the sum of the squares of the maximums (root mean square values) may represent a more realistic maximum. Superposition of modal responses is appropriate, of course, only for elastic systems.

Although it is not always possible to achieve a dynamically balanced shock isolation system, it offers advantages

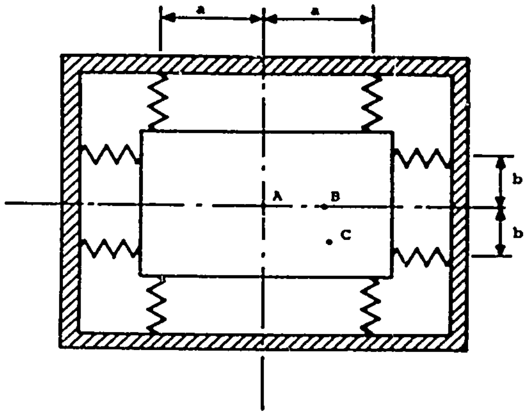

Figure 10-5 Shock Isolation System

other than a simplification of the computation effort. Reference 10-10 suggests that a dynamically balanced system will also result in reduced motions during oscillation. As a result of the absence of coupling of modes in a balanced system and the usual small magnitude of rotational inputs to the system in protective construction applications, rotational motions of the suspended mass will be minimized. This is particularly important in the case of large masses, where small angles of rotation can result in large translations at extreme locations far from the center of gravity.

Because of the advantages of a dynamically balanced system, various approaches are sometimes taken to minimize coupling of modes. One criterion is that frequencies in the six modes should be separated sufficiently to avoid resonance between the modes. This separation should be maintained over some reasonable range of loads which the system might be expected to sustain during its life time. Because of the importance of minimizing rotational modes of response, Ref. 10-10 also suggests avoiding extremely low stiffnesses in these modes. Although increased stiffnesses in the rotational modes will add higher frequency components to system response, there is little rotational energy introduced directly into them, if the system is properly balanced. Higher rotational stiffnesses will also minimize residual inclination of the isolated platform under changing static loads or due to friction forces in the isolators. Most isolation systems will incorporate some features which will allow for changes in the total load and/or distribution of load on the isolation platform. The adjustments can be made by changing properties of the isolators themselves or adjustment of ballast weights on the platform.

If the dynamic system is also a multiple mass system, the system can be analyzed by the modal method of analysis or one of the numerical integration techniques (e.g.,

Refs. 9-3, 9-5 or 9-7). The modal method of analysis requires solution of simultaneous equations of motion to determine characteristic shapes and frequencies of each mode and is limited to the elastic case. The numerical techniques do not require prediction of mode shapes and frequencies and will handle both elastic and inelastic response. The modal method of analysis or numerical integration techniques can also be used for the analysis of multiple degree of freedom, single-mass systems where the various modes of response are coupled.

10.2.3 <u>System Configurations</u>

a. Individual Versus Group Mounting

The two basic approaches to shock isolation in protective construction are to provide individually tailored systems for each component or to group together two or more items on a common platform. In the latter case, a system is selected to satisfy the most stringent criteria. In some cases, where the shock tolerance of the various items differs greatly, a combination of the two approaches may be the most effective solution. Although the relative location or size of some items may make individual mounts the more practical approach in certain cases, group mounting will generally be as reliable and the least costly solution.

There are several advantages of group mounted systems. A group mounted system will be less sensitive to variations in weights of individual items of equipment because of the larger combined weight of all items and the platform. With a number of items, there is also a greater flexibility in controlling the center of gravity of the total mass. A group mounted system can also require less rattlespace than several independently mounted systems, and interconnections between components is greatly simplified if they are all mounted on a single platform.

An important advantage of group systems is cost. Individual mounts will require a large number of isolator units with adjustment systems to accommodate changes in weights or performance requirements. If adjustment capability is not provided, the isolators may have to be redesigned or replaced if weight and performance characteristics change significantly. Although larger, more costly, units are required for the group mounting system, fewer numbers are required, and the cost per pound of supported load can be much lower. The maintenance and spares cost should also be less for the fewer number and types of units required in the group mounted system.

b. Platform Characteristics

It is desirable that the platform for group mounted systems be sufficiently stiff so that the platform and associated mounted equipment can be treated as a rigid body. This criterion is usually satisfied if the lowest natural frequency of the platform is several times larger than the natural frequency of the spring-mass system. When large heavy items of equipment are involved, platforms meeting this stiffness criterion may not be practical. In such cases, it will be necessary to treat the platform-equipment configuration as a multi-mass system.

c. Isolator Arrangements

There are many ways to support a shock isolated item; some desirable features have been mentioned previously in connection with dynamically balanced systems. Some of the more important factors

affecting the selection of an isolator arrangement are

- The size, weight, shape and location of the center of gravity of the suspended mass
- The direction and magnitude of the input motions
- Rotation of the lines of action of the devices should be small over the full range of displacements of the system to avoid system nonlinearities
- Coupling of modes should be minimized
- Static and dynamic instability must be prevented
- It is desirable in most cases, and necessary in some, that the system return to its nominal position
- Space available for isolation system
- Type of isolation devices to be used

Some of the more common general arrangements of isolators are shown in Figs. 10-6, 10-7, 10-8 and 10-9. All systems shown are assumed to have the same arrangement of isolators in a plane through the center of gravity (CG) and perpendicular to the surface of the page.

A symmetrical system would be one similar to that shown in Fig. 10-5 with the intersection of elastic axes and principal inertia axes located at point A. Since the elastic axes of the suspension system and the principal inertia axes of the mass coincide, the system is dynamically balanced and all modes are uncoupled. It is probably the least common of all suspension systems.

In Fig. 10-6(a) the mass is supported by 4 vertical isolators. These isolators must provide horizontal, vertical and rotational stiffnesses in order for the system to be stable under all possible motions. There will be coupling between horizontal displacements

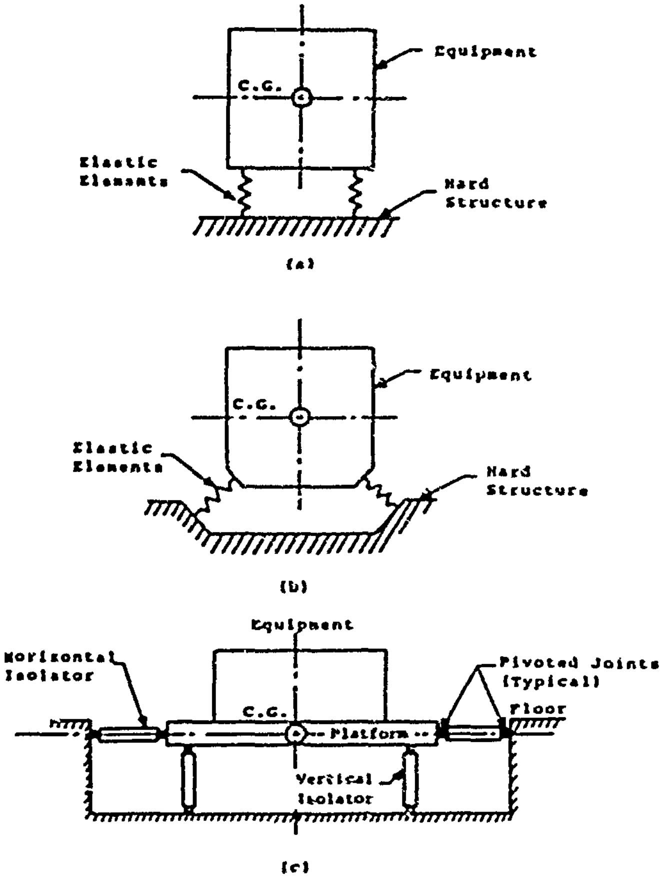

Figure 10-6 Base-Mounted Isolation System Configurations (Ref. 10-10)

and rotations about horizontal axes. This arrangement and that shown in Fig. 10-6(b) are appropriate for those applications where there are no convenient supports for horizontal isolators. Figure 10-6(b) is a preferred arrangement, since the line of action of the isolators can be directed towards the CG of the mass to allow *decoupling of some modes.* As in the case of Fig. 10-6(a), the isolator elements must possess adequate stiffness in axial and lateral directions to insure stability under static and dynamic conditions. In Fig. 10-6(c) the isolator elements are oriented parallel to the three orthogonal system axes. This arrangement provides system stability even when the isolator elements *possess only* axial stiffness. If the CG of the suspended mass is located as shown, decoupling of modes is possible. While it is possible to select isolator properties and geometries so that the lines of action of the isolators pass through the CG of the system under static conditions, response of the system to base motions will obviously alter its geometry. When the line of action of the isolators is changed due to displacement of the mass relative to its supports, coupling of modes of vibration will be introduced. The degree of coupling will be affected by the magnitude of the displacements and the length of the isolators. Although a system which would provide complete decoupling of modes of vibration and under all conditions of response is probably impractical, isolator properties and arrangements should be selected so as to minimize the effect of displacements.

Figure 10-7 shows two arrangements of overhead pendulum shock isolation devices using platforms to support the sensitive components. In both cases the CG of the suspended mass is relatively low.

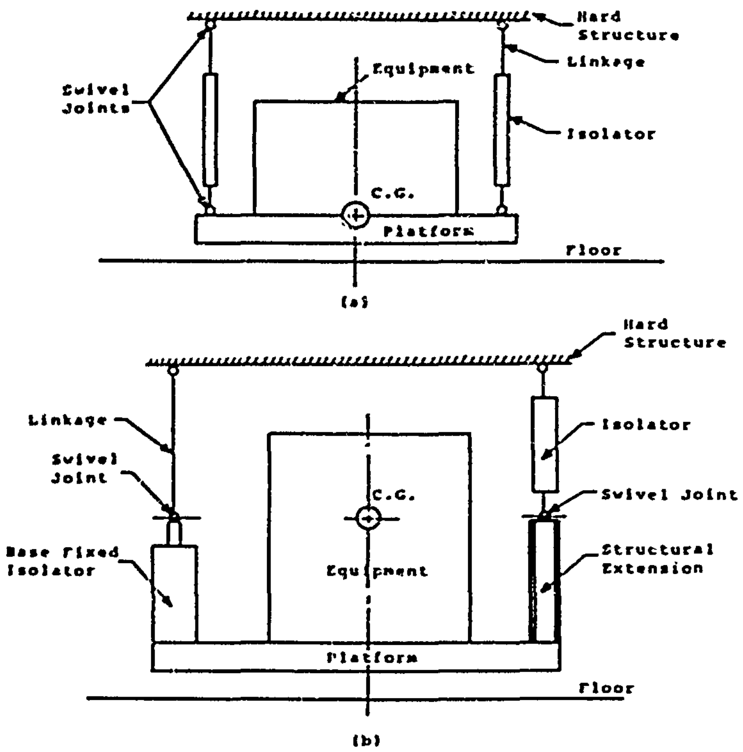

Figure 10-7 Overhead Pendulum Shock Isolation Systems Using Platforms (Ref. 10-10)

These types of suspension systems have been used extensively for supporting large loads in protective structures. The overhead pendulum system normally uses swivel joints at the points of attachment of the isolator elements, so gravity provides the horizontal restoring force (or stiffness). This force and the frequency of the system in the horizontal mode are a function of the total weight of the suspended mass and the length of the pendulum. Each pendulum arm also includes an isolator element which determines system stiffness in the vertical direction. The system is linear for small angular displacements, i.e., $\theta \approx \sin\theta$. Insertion of the vertical isolator elements can introduce additional nonlinearities and coupling between the pendulum and vertical spring modes. Reference 10-7 suggests that if the uncoupled pendulum frequency is near one-half the uncoupled vertical spring frequency, interchange of energy between the modes can lead to pendulum motions greatly exceeding those predicted by linear assumptions. A detailed discussion of this problem is presented in Ref. 10-7.

Since most pendulum systems have low natural frequencies, they are displacement sensitive and will normally require greater rattlespace than other systems. They exhibit very little damping in horizontal modes and it is frequently necessary to add some type of sway dampers as shown in Fig. 10-8(a). These dampers can be one of several types including gas, liquid or friction systems. Since one of the main advantages of overhead pendulum systems is that they require no horizontal stiffness elements, their attractiveness is greatly diminished in those cases requiring horizontal damping.

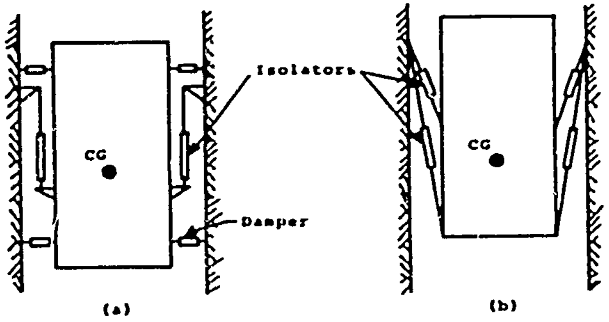

Figure 10-8 Variations of Simple Pendulum Systems

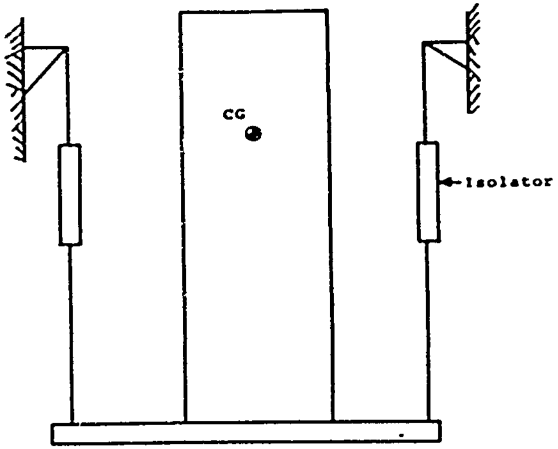

Figure 10-9 High Center of Gravity Pendulum System

The point of attachment of the isolator swivel joint to the platform determines the location of the horizontal elastic axis of the system. Figure 10-7(b) shows two ways of varying the point of attachment so that the horizontal elastic axis can be made to coincide with the CG of the suspended mass at the equilibrium position and help minimize coupling between the modes of response.

Another solution to the low horizontal stiffness and damping characteristics of the overhead pendulum system is to incline the pendulum arms as shown in Fig. 10-8(b). Reference 10-11 presents a detailed analysis of both configurations and the factors affecting their vibration characteristics. It concludes that the inclined pendulum system is less sensitive to changes in CG, provides static and dynamic stability over a wider range of displacements and loading conditions, minimizes coupling between modes, and provides rapid restoration of the system to an equilibrium position.

Another type of overhead pendulum system is shown in Fig. 10-9. This type has been used for missile suspension systems in silos. The pendulum arms can be vertical or inclined. In this system the base dimension may be less than one-half the vertical distance from the platform to the CG of the mass. Since the stiffness of the isolators is limited by vertical isolation requirements, static and dynamic stability problems can arise, even with small rotations of the platform.

Table 10-3 from Ref. 10-3 summarizes pertinent characteristics of the general types of isolation systems. The frequency ranges and relative displacements

Table 10-3

CHARACTERISTICS OF ISOLATION SYSTEMS

	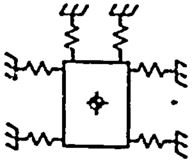 (1)	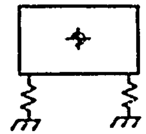 (2)	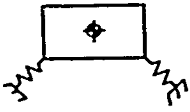 (3)
Feasibility Range	For equipment isolation at low frequency and large relative displacements	For equipment and total structure isolation at low and mid-range frequency and small to moderate relative displacements	For equipment isolation at mid-range frequency and small relative displacements
Dynamic Coupling	Negligible	Very significant for acceleration and displacement response	Negligible
Rattlespace Requirements	Shock spectra values(large horizontal space required for hardware)	Shock spectra values are amplified due to pitch response (minimum space required for hardware)	Shock spectra values
Dynamic Stability	Not critical	Not critical	Not critical
Static Stability	Not critical	May be critical (spring stability must be considered)	Not critical (but spring stability must be considered)
Non-linear Effect	Very significant for acceleration response and rattlespace	Not critical	Not critical

Table 10-3 (cont.)

CHARACTERISTICS OF ISOLATION SYSTEMS

	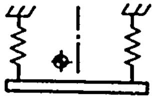 (4)	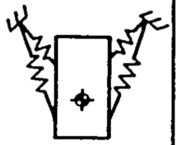 (5)	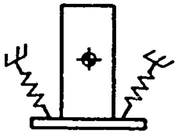 (6)
Feasibility Range	For equipment and personnel platforms at low frequency and large relative displacements	For total structure isolation at low frequency and large relative displacements	For missile mounts at low frequency and moderate relative displacements
Dynamic Coupling	Significant pitch response induced	System characteristics can be selected to minimize coupling	Very significant
Rattlespace Requirements	Shock spectra are amplified due to pitch response	Shock spectra values are acceptable when the geometry optimized for minimum coupling	Shock spectra values are amplified due to pitch response
Dynamic Stability	May be critical	Not critical when optimized	Very critical
Static Stability	May be critical	Not critical when optimized	Very critical
Non-linear Effect	May affect acceleration response and rattlespace	Some effect on acceleration response	Significant effect on acceleration response and rattlespace

referred to in Table 10-3 are defined as follows:

Low frequency range	less than 1 Hz
Mid-frequency range	1 to 10 Hz
Large relative displacements	less than 40 inches (102 cm) vertical and 14 inches (35.6 cm) horizontal (combined)
Moderate relative displacements	less than 15 inches (38.1 cm) vertical and 5 inches (12.7 cm) horizontal (combined)
Small relative displacements	less than 6 inches (15.2 cm) vertical and 2 inches (5.08 cm) horizontal (combined)

The comment in Table 10-3 regarding nonlinearity refers to the error in assuming linear behavior when actual response is nonlinear. The systems shown in Figs. 10-5 and 10-6(c) can be considered equivalent to column (1) of Table 10-3 and those of Fig. 10-7 to column (4).

10.3 SHOCK ISOLATION DEVICES

10.3.1 Introduction

Principles of shock isolation have been discussed in preceding paragraphs. It will have been noted that a fundamental element of every shock isolation system is some sort of energy storage or energy dissipative device. These devices must be capable of supporting the mass to be isolated under static and dynamic conditions and, at the same time, prevent transmission of any harmful shock environment to the mass. In most cases it is required that the isolation device have elastic force-displacement characteristics, so that the system will return to a nominal equilibrium position after termination of the support motions. Reference 10-10 summarizes the desirable features of these devices.

- The dynamic force-displacement relationship of the isolator should be predictable for all directions in which it is required to provide stiffness.
- The isolator should have low mass in order to minimize transmission of high frequency motions to the supported mass.
- The frequency of the isolator should remain constant with changes in load, i.e., its stiffness should vary in direct proportion to the load it supports. This allows the system to remain dynamically balanced throughout changes in supported mass and its position.
- The static position of the isolator element should be adjustable, so that the system can be returned to its nominal position when the suspended load changes.
- The isolator element should have high reliability, long life and low cost.

The various types of isolation devices used in most protective construction applications possess these characteristics in varying degrees. Any real isolator has some mass, and in some applications, the mass can be quite large. Although this mass is often neglected in preliminary calculations, it must be considered in the final analysis. Nonlinear force-displacement characteristics are often accepted to gain some other advantage, and Ref. 10-12 concludes that constant system behavior. In energy dissipative systems, however, it may be necessary to provide other means for restoring the system to its original position. In general, most devices are some compromise combination of the desirable features which best suit the particular application.

Reference 10-10 suggests that the inclusion of energy dissipative (damping) devices in the isolation system offers several significant advantages, e.g., damping can

- Reduce the severity of output motion response
- Reduce the effect of coupling between modes, thus reducing rattlespace requirements
- Restore the system to an equilibrium position more quickly
- Decrease the sensitivity of the system to variations in input motions

Damping can be provided internally in some isolation devices, such as liquid springs, but must be added externally in others, such as helical coil springs. The different types of damping offer advantages and disadvantages which must be considered in the design process. Damping which is proportional to some power of the velocity greater than unity may be effective in attenuating low frequency components but can increase the severity of high frequency components. Reference 10-10 states this characteristic is typical of viscous, hydraulic and quadratic dampers. Coulomb damping, where the force near the equilibrium position is large, could prevent the system from returning to its nominal equilibrium position. Thus, care must be exercised in either adding damping devices to a system or in design of those isolator elements possessing inherent damping characteristics, if degradation of overall isolation system performance is to be avoided. References 10-7, 10-9, and 10-10 include detailed discussions of the effects of damping on system response.

There are numerous types of devices which can be

used to accomplish the shock mitigation function. For example, several idealized mechanical-type springs are shown in Fig. 10-10 along with associated spring constants. In addition to the springs shown in Fig. 10-10, which are all linear and undamped, there are liquid and pneumatic devices which can accomplish the shock mitigation function and may or may not have linear response, may or may not have inherent internal damping properties, and so on. Following paragraphs will introduce some of the more common types of shock isolation devices along with advantages and disadvantages for various applications.

10.3.2 Helical Coil Springs

A helical coil spring is fabricated from bar stock or wire which is coiled into a helical form. A diametral cross section and various end treatments of a typical helical coil spring are illustrated in Fig. 10-11.

The helical coil spring has numerous advantages. It is not strain rate sensitive, is self-restoring after an applied load has been removed, resists both axial and lateral loads, has a linear spring rate and requires little or no maintenance.

For most applications, the coil spring does require a large amount of space in comparison to other available shock isolation systems, and the spring cannot be adjusted to compensate for changes in loading conditions. If the weight of a supported object is changed, it is necessary to either change the spring or add additional springs. For most purposes, the helical coil spring can be considered to have zero damping. If damping is required, it must be provided by external means.

Helical coil springs may be used in either compression or extension. Extension springs are not subject to buckling and may offer a more convenient attachment arrangement. Extension spring attachments, however, are usually more costly

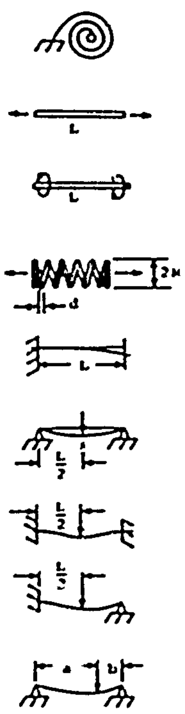

$k = \frac{EI}{L}$ I = Moment of inertia of cross-sectional area
L = Total length

$k = \frac{EA}{L}$ A = Cross-sectional area

$k = \frac{GJ}{L}$ J Torsion constant of cross section

$k = \frac{Gd^4}{64nR^3}$ n = Number of turns

$k = \frac{3EI}{L^3}$

$k = \frac{48EI}{L^3}$

$k = \frac{192EI}{L^3}$

$k = \frac{768EI}{7L^3}$

$k = \frac{3EIL}{a^2b^2}$

Figure 10-10 Idealized Mechanical-Type Springs and Associated Spring Constants

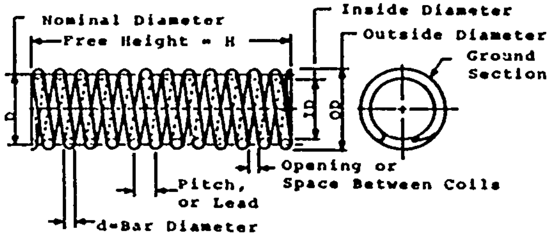

(a) Coil Spring Parameters

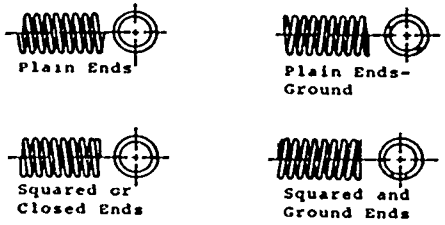

(b) Types of End Treatment

Figure 10-11 Typical Helical Coil Spring (Ref. 10-13) and can cause large stress concentrations at the point of attachment. Coil springs are most generally used in compression for shock isolation applications. Buckling, which can be a problem with compression springs, can be precluded by proper design or through use of guides, which are added either externally or internally to the coils. The following discussion, unless stated otherwise, will be concerned primarily with compression springs.

Helical coil springs may be mounted in two ways, the ends either clamped or hinged. In most shock isolation applications, the spring ends are clamped since this method greatly increases the force required to buckle the spring. If space is at a premium, the energy storage capacity may be increased by nesting the springs (placing one or more springs inside the outermost spring). When nesting springs, it is advisable to alternate the direction of coils to prevent the springs from becoming entangled.

A great variety of materials are available for the fabrication of coil springs. Some of the more commonly used steels are listed in Table 10-4 with their ultimate strength and elastic moduli. Also, the spring can be manufactured from wire as a cold-wound spring or from bars as a hot-wound spring. Hot-wound springs are suggested for wire diameters greater than 0.5 inches (1.27 cm).

The specifications for a helical spring may include some or all of the following: maximum load, maximum static deflection, maximum dynamic deflection, spring rate (stiffness), maximum height, maximum diameter, and factors of safety regarding allowable stresses and bottoming of the spring. As the number of specified parameters increases, the options in selection of spring characteristics which are available to the designer decrease.

Table 10-4

TYPICAL HELICAL COIL SPRING MATERIALS (Ref. 10-8)

Name	Tensile Properties*				Torsional Properties*			
and	Ultimate Strength		Elastic Limit		Ultimate Strength		Elastic Limit	
Composition	10^3lb/in^2	10^3N/cm^2	10^3lb/in^2	10^3N/cm^2	10^3lb/in^2	10^3N/cm^2	10^3lb/in^2	10^3N/cm^2
Carbon Steel SAE 1085	175-230	121-159	130-175	90-121	115-150	79-103	80-105	55-72
Carbon Steel SAE 1095	170-220	117-152	125-170	86-117	110-145	76-100	75-100	52-69
Alloy Steel SAE 4068	200-270	138-186	175-240	121-165	145-200	100-138	105-145	72-100
Chrome-Vanadium Alloy Steel SAE 6150	200-250	138-172	180-230	124-159	140-175	97-121	100-130	69-90
Chrome-Silicon Alloy Steel SAE 9254	250-325	172-224	220-300	152-207	160-200	100-138	130-160	90-110
Silicon-Manganese Alloy Steel SAE 9260	200-250	138-172	180-230	124-159	140-175	97-121	100-130	69-90

* Modulus of elasticity E=30x10^6 psi (20.7x10^{6}N/cm^2); shear modulus G=11.5x10^6 psi (7.93x10^{6}N/cm^2). Use slightly lower values of E and G for hot-wound springs.

The usual specifications for a spring will include at least the maximum load and either the spring rate or an allowable deflection under this load. When used as isolators in protective construction, a dynamic deflection may also be specified. With this guidance, it is possible to determine the required spring characteristics. For a given maximum static axial load and allowable deflection under this load, the axial spring rate is given by

$$k = \frac{W}{\Delta_{st}} \qquad (10\text{-}1)$$

where

W = axial load
Δ_{st} = static deflection

The axial spring rate of a helical coil spring is

$$k = \frac{d^4 G}{8D^3 N} \qquad (10\text{-}2)$$

where

d = spring bar diameter
D = nominal spring diameter
G = shear modulus for spring material
N = number of active coils

A helical coil spring is made up of two classes of coils, depending on their function in the spring. The active coils are those coils which are responsible for the spring's response to loads or displacements. The inactive coils are those coils at the ends of the spring which help provide means of attachment. The number of active coils depends on the required spring characteristics. The number of inactive coils depends on the treatment of the spring ends. In most shock isolation applications, the end will typically be squared and ground (see Fig. 10-11b). The number of inactive coils for this condition is two, one at each end.

From Eq. 10-2 it is seen that a large number of combinations of bar diameter, spring diameter and number of active spring coils will satisfy a given value of spring rate. There are other criteria, however, which must be satisfied and these criteria help narrow the number of workable combinations.

As indicated in an earlier paragraph, the spring will normally be required to deflect some specified amount without bottoming out.' The bottoming out condition occurs when the spring is fully compressed with no space remaining between coils. The total deflection which must be accomodated is given by

$$\Delta_t = C_f \, (\Delta_{st} + \Delta_{dyn}) \qquad (10\text{-}3)$$

where

C_f = factor of safety against bottoming
Δ_{st} = static deflection of spring
Δ_{dyn} = dynamic deflection of spring

Although permanent set may be acceptable in some instances, it is normally required that the system return to its original position. This can be accomplished in various ways, but the most common approach in the case of helical coil springs is to prevent inelastic action. In order to prevent inelastic deformation of the spring in the event of overload, coil springs are usually designed so that the elastic shear strength of the spring is not exceeded when the spring is fully compressed. The load corresponding to full compression is given by

$$P^* = k \, \Delta_t \qquad (10\text{-}4)$$

and the maximum shear stress at full compression is given by

$$\tau_{max} = \kappa \, \frac{8P^* D}{\pi d^3} \qquad (10\text{-}5)$$

where κ is the Wahl correction factor which accounts for the effect of spring coil curvature on maximum stress (Fig. 10-12).

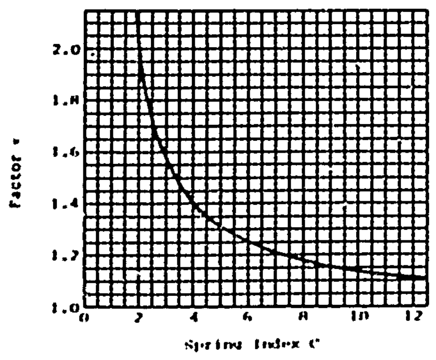

Figure 10-12 Values of Wahl Stress Correction Factor for Round Helical Extension or Compression Springs (Ref. 10-13)

The spring index shown in Fig. 10-12 is the ratio of the mean coil diameter to the bar diameter, i.e.,

$$C = D/d \tag{10-6}$$

Equation 10-5 can be rearranged to give the load required to fully compress the spring in terms of the maximum allowable shear stress, i.e.,

$$P^* = \frac{\pi d^3}{8\kappa D} \tau_{allow} = \frac{\pi d^2}{8\kappa C} \tau_{allow} \tag{10-7}$$

Figure 10-13 gives τ_{allow} for two common spring steels as a function of bar and spring diameter.

The effective solid height of the spring is defined as the overall height of the active coils when fully compressed. The allowable deflection per unit length of effective solid height is

$$\delta = \frac{\Delta_t}{h} = \frac{\pi \tau_{allow}}{\kappa G} \left[\frac{D}{d}\right]^2 = \frac{\pi C^2}{\kappa G} \tau_{allow} \tag{10-8}$$

where h is the effective solid height. The number of active coils is

$$N = \frac{h}{d} \tag{10-9}$$

The total free height of the spring is the overall height under no-load conditions. It is given by

$$H = h + \Delta_t + nd \tag{10-10}$$

where n is the number of inactive coils

In order to prevent lateral buckling of the spring when compressed, limits are placed on the ratio of free height to the mean coil diameter. Figure 10-14 shows the critical buckling ratio for two spring end conditions as a function of the ratio of total axial deflection to free height. Points below and to the left of the curves represent stable ratios. Points above and to the right of the curves represent ratios where lateral buckling is likely to occur unless spring guides

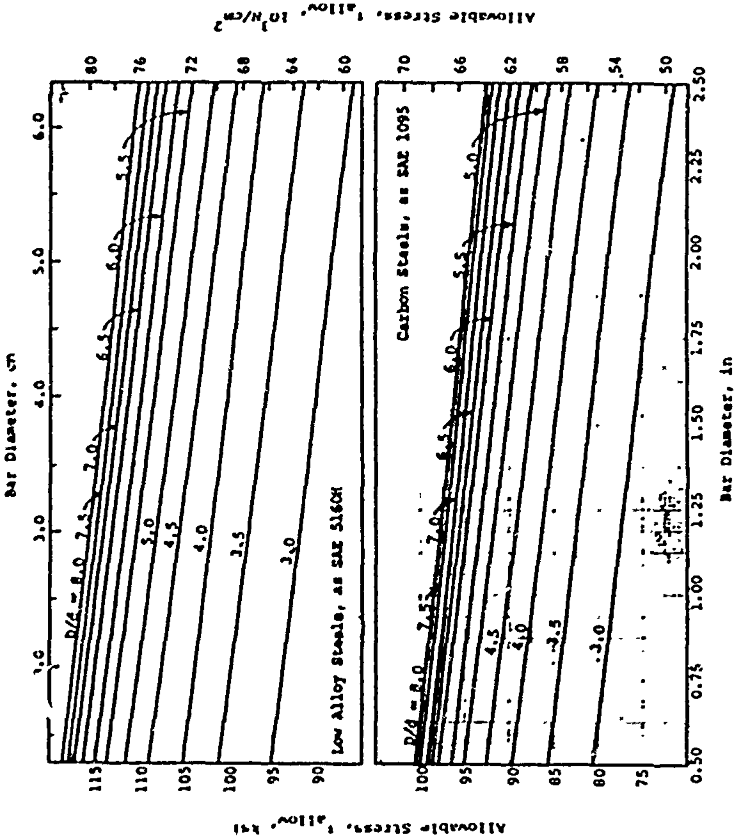

Figure 10-13 Recommended Maximum Stresses for Helical Springs Normally Subject to Dynamic Loading (Ref. 10-3)

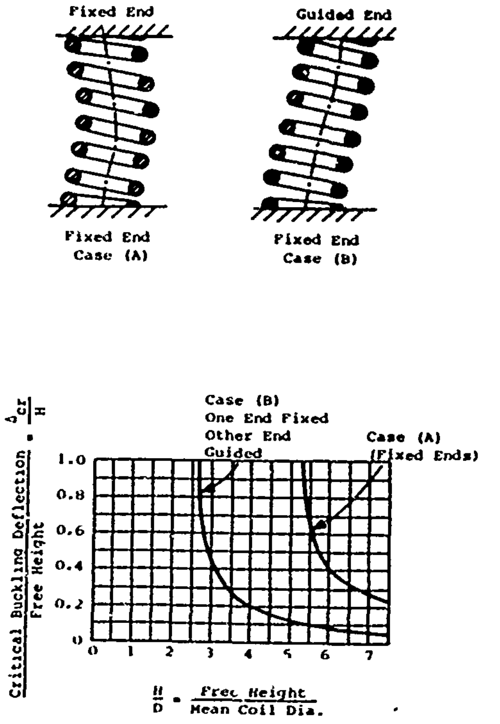

Figure 10-14 Critical Buckling Ratios (Ref. 10-8)

are provided. Case A shown in Fig. 10-14 is not often encountered in practical applications and should be assumed only with careful judgment. Case B, which is generally applicable, can also be used with reasonable accuracy for springs with hinged ends which are constrained to remain aligned axially (Ref. 19-8).

The design process is a trial and error procedure which involves selecting a combination of spring properties which will provide the desired response without causing permanent deformation of the spring. Knowing the weight of the item to be shock isolated and the desired frequency of the isolation system, the required spring rate can be found from

$$k = \frac{4\pi^2}{g} W f^2 \qquad (10\text{-}11)$$

where

W = weight of the item
f = isolation system frequency in Hz
g = gravitational constant

The static deflection is readily found from the relationship of Eq. 10-1. Unless specified otherwise, the dynamic deflection is generally taken equal to the static deflection. The total deflection to be accommodated can now be found by Eq. 10-3 after choosing a suitable value for C_f and the axial load, P^*, to fully compress the spring from Eq. 10-4.

At this point, one can choose a spring index, C, and find the corresponding Wahl correction factor, κ, from Fig. 10-12. Then, with a suitable value for the allowable shear stress, the bar diameter can be found by solving Eq. 10-7 for d. The effective solid height, h, can be found from Eq. 10-8 and the number of active coils from Eq. 10-9. The total free height, H, from Eq. 10-10 should be checked for stability by means of Fig. 10-14. One would now have the required design parameters for a coil spring. The spring rate of the design spring should be calculated with Eq. 10-2 and compared with the desired system

spring rate. If the comparison were not satisfactory, the process described above would be repeated until satisfactory agreement was obtained.

Helical coil springs are also required to resist lateral loads in some applications. In all cases, it is desirable to know how much resistance the spring offers to lateral displacement. For the case of a compression spring under vertical and lateral loads, with E = 30,000,000 psi (20,700,000 N/cm^2) and G = 11,500,000 psi (7,930,000 N/cm^2), Ref. 10-8 gives the lateral spring rate as

$$k_h = \frac{F_h}{\Delta_h} = \frac{d^4 \times 10^6}{C_h ND(0.204H_s^2+0.265D^2)} \quad \text{lb/in}$$
$$= \frac{6.89 \times 10^5\, d^4}{C_h ND(0.204H_s^2+0.265D^2)} \quad \text{N/cm} \qquad (10\text{-}12)$$

where

F_h = lateral force
Δ_h = lateral deflection due to F_h
C_h = factor depending on Δ_{st}/H and H/D
H_s = compressed height of spring $(H - \Delta_{st})$

Values of C_h are given in Fig. 10-15. The ratio of axial to lateral spring rates for springs manufactured from materials where E/G = 2.6 (as above) is given by (Ref. 10-8)

$$\frac{k}{k_h} = 1.44C_h\left[0.204\left(\frac{H_s}{D}\right)^2 + 0.265\right] \qquad (10\text{-}13)$$

It has been found that lateral spring rates calculated from Eq. 10-12 may differ by as much as 25 percent from available test results. The differences are apparently due to deviations of the actual case from the idealized conditions assumed in the theory.

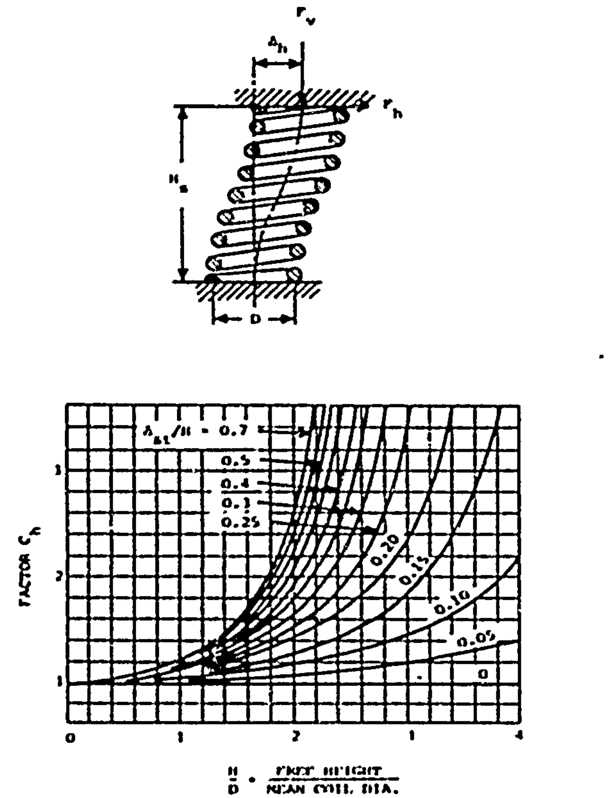

Figure 10-15 Lateral Stiffness of Helical Coil Spring (Ref. 10-8)

10.3.3 Torsion Springs

Torsion springs provide resistance to torque applied to the spring. In shock isolation applications, the torque is usually the result of a load applied to a torsion lever which is part of the torsion spring system. A typical torsion spring shock isolation system is illustrated in Fig. 10-16.

Since the axis of a torsion spring is normal to the direction of displacement, it can be used advantageously when the space in the direction of displacement is limited. Torsion springs have linear spring rates, are non strain rate sensitive, self-restoring, and require little or no maintenance.

Torsion springs cannot be adjusted to compensate for changes in weight of shock isolated equipment, and damping must be provided by external means. The axial length of some types may preclude their use when space is limited.

There are three basic types of torsion springs, (1) torsion bars, (2) helical torsion springs, and (3) flat torsion springs. The type to be used will depend upon the space available and the load capacity required. The torsion bar is normally used for light to heavy loads, the helical torsion spring for light to moderate loads, and the flat torsion spring for light loads. The torsion bar is the type most commonly found in protective structure applications and is the only type discussed in following paragraphs. Reference 10-1 describes procedures for design of the other two types.

The torsion bar is most commonly used where large loads must be supported. A typical bar is illustrated in Fig. 10-17. On the basis of the ratio of energy storage to device weight or volume, the torsion bar is one of the most efficient spring systems. Its diameter and length can be varied to suit the applied load and available space. For most practical

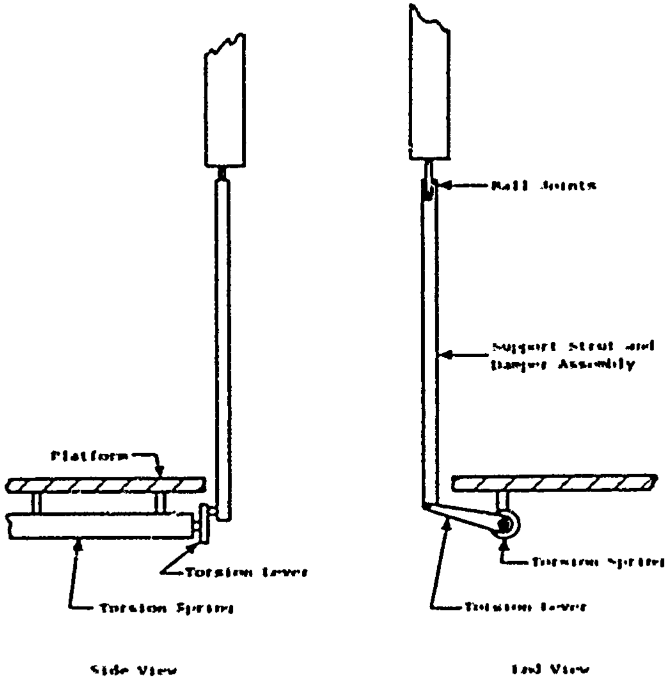

Figure 10-16 Typical Torsion Spring Shock Isolation System

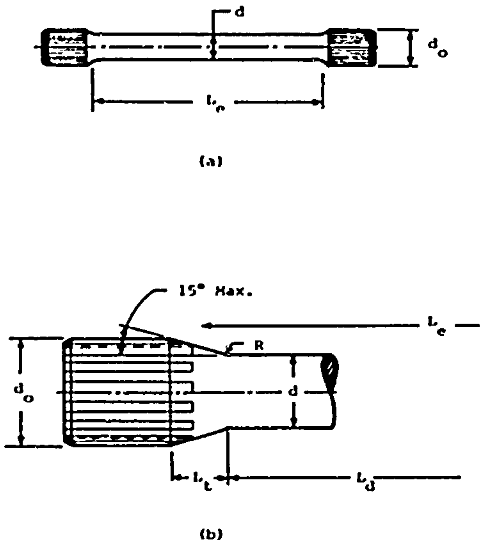

Figure 10-17 Standard Single Torsion Bar with Splined Ends (Ref. 10-3)

purposes, it may be considered to have zero damping, although damping may be added to the shock isolation system through the support strut assembly.

To minimize bending stresses and increase service life, torsion bars should be supported at both ends and fitted with bearings at the end where rotation takes place. This necessitates the additional expense of bearing support and bar anchoring systems. The ends of torsion bars are usually splined to facilitate connections; large stress concentrations can occur in the vicinity of these splines.

The maximum applied load and allowable deflection must be specified or assumed before a torsion bar can be designed. The maximum allowable stress in the bar will depend upon the material used for the bar, the fabrication process, and the anticipated loading conditions.

Steels suggested for use in torsion bars include SAE 8660, SAE 9260, and SAE 9263. Table 10-5 shows the suggested maximum allowable shear stresses for these steels for various fabrication processes. The SAE (Society of Automotive Engineers) recommends a presetting strain of approximately 0.22 radians when loading is in one direction only. In applications where the loading can cause equal or nearly equal rotations in either direction of twist, presetting will not be beneficial.

TABLE 10-5

MAXIMUM ALLOWABLE SHEAR STRESS FOR TORSION BARS (Ref. 10-3)

Allowable Stress		Fabrication Process
(ksi)	kN/cm^2	
140	96.5	Shot Peened and Preset
120	82.7	Preset
105	72.4	Shot Peened
59 to 75	40.7 to 51.7	Unprocessed

The design criteria for a torsion bar isolator will normally include the weight to be supported, the frequency of the system (or spring rate for the bar) and an allowable deflection. If the weight and system frequency are given, the required spring rate in units of force per unit deflection can be determined from Eq. 10-11. The spring rate can be determined from Eq. 10-1 if the supported weight and allowable static deflection are specified. For small deflection angles, the spring rate of a torsion bar isolation system is given by

$$k = \frac{Gd^4}{10.2R^2L_e} \qquad (10\text{-}14)$$

where

G = shear modulus for torsion bar material
d = torsion bar diameter
R = effective length of torsion lever
L_e = effective length of torsion bar

The effective length of the torsion lever is the distance from the torsion bar center to the support strut center. The effective length of the torsion bar is that portion of the bar which is responsible for the bar's action.

It is usual practice to design a torsion bar system so that the lever arm is perpendicular to the support strut at the static position. Then the torque applied to the torsion bar can be reasonably approximated by

$$T \approx RF \qquad (10\text{-}15)$$

where F is the force at the end of the torsion lever. The length of the torsion lever must be determined either from specifications concerning a particular application or by a trial and error process. In the absence of other guidance, a lever arm length equal to twice the maximum deflection is suggested to give a nearly constant spring rate through the total deflection.

The force at the end of the torsion bar is equal to the product of the system spring rate and displacement. At total deflection, the maximum torque is given by

$$T^* = Rk\Delta_t \qquad (10\text{-}16)$$

and the torsion bar diameter required to resist the maximum torque can be found from

$$d = \left[\frac{16T^*}{\pi\tau_{allow}}\right]^{1/3} \qquad (10\text{-}17)$$

The effective torsion bar length required to accommodate the maximum torque and total deflection is given by

$$L_e = \frac{\theta_t d^4 G}{584T^*} \qquad (10\text{-}18)$$

where θ_t is the angular deflection in degrees associated with the total deflection obtained from Eq. 10-3, or

$$\theta_t = \sin^{-1}(C_f \frac{\Delta_{st}}{R}) + \sin^{-1}(C_f \frac{\Delta_{dyn}}{R}) \qquad (10\text{-}19)$$

The portion of the bar with uniform diameter is a function of the effective length and the tapered length (see Fig. 10-17). It is (Ref. 10-3)

$$L_d = L_e - \frac{2}{3} L_t\left[\left(\frac{d}{d_o}\right) + \left(\frac{d}{d_o}\right)^2 + \left(\frac{d}{d_o}\right)^3\right] \qquad (10\text{-}20)$$

where

d_o = diameter of splined end

L_t = length of bar taper

The length of bar taper depends upon the taper angle and the splined end diameter. The minimum splined end diameter recommended by the SAE is 1.2d. The splined ends are faired into the basic bar with a 15° maximum taper angle and a fillet radius of 1.3d (Ref. 10-3). For a maximum taper angle and a minimum splined end diameter, the taper length is

$$L_t = 0.373d \qquad (10\text{-}21)$$

The following procedure is suggested for selecting torsion bar isolator parameters. If the system frequency and supported mass are specified, use Eq. 10-11 to find the required spring rate. If the system weight and allowable static deflection are specified, the required spring rate can be determined from Eq. 10-1. Determine total deflection based upon the static deflection, required dynamic deflection, and factor of safety using Eq. 10-3. Determine the maximum torque at total deflection from Eq. 10-16 using a specified or assumed torsion lever length. The required torsion bar diameter can then be obtained using Eq. 10-17 and an allowable shear stress. The allowable shear stress will depend on the fabrication process selected. The required effective bar length can be obtained from Eq. 10-18 after the total angular deflection has been determined from Eq. 10-19. The bar taper length can be computed after the splined end diameter is selected. If the minimal splined end diameter and maximum taper angle recommended by the SAE are used, the tapered length can be determined from Eq. 10-21. Finally, the required uniform diameter bar length can be obtained from Eq. 10-20. The final design should be checked by computing the design spring rate using Eq. 10-14 and comparing it to the required spring rate.

10.3.4 Pneumatic springs

Pneumatic springs are springs whose action is due to the resiliency of compressed air. They are used in a manner similar to coil springs. The two basic types are the pneumatic cylinder with single or compound air chambers and the pneumatic bellows.

Pneumatic springs have the advantage of being adjustable to compensate for load changes. The spring rate can be made approximately linear over one range of deflection and highly non-linear over another. They are quite versatile due to the variety of system characteristics which can be obtained by regulation of air flow between the cylinder chamber and the reservoir tank. Some of the variations which are possible are:

- Velocity sensitive damping by a variable orifice between chamber and reservoir.
- Displacement sensitive damping by a variable orifice controlled by differential pressure between chamber and reservoir.
- A nearly constant height maintained under slowly changing static load by increasing or decreasing system air content using an external air supply and a displacement sensitive servo-system controlling inlet and exhaust valves.
- A constant height under widely varying temperature achieved by the same system described above.

The disadvantages of pneumatic springs include higher cost and more fragile construction. They have a limited life in comparison to mechanical springs and provide resistance only to axial loads.

a. Pneumatic Cylinders

Pneumatic cylinders are fabricated in the two basic configurations illustrated in Fig. 10-18. The spring rate of the single action cylinder is nonlinear, with an increasing spring rate for positive deflection of the piston and a decreasing spring rate for negative displacements. The double action cylinder also exhibits a nonlinear spring rate with an increasing rate for both positive and negative displacements. These characteristics are illustrated graphically in Fig. 10-19, which is a plot of the stiffness ratio versus the displacement

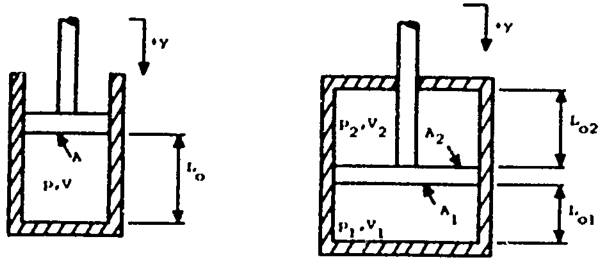

(a) Single Action

(b) Double Action

Figure 10-18 Schematic of Pneumatic Piston Springs

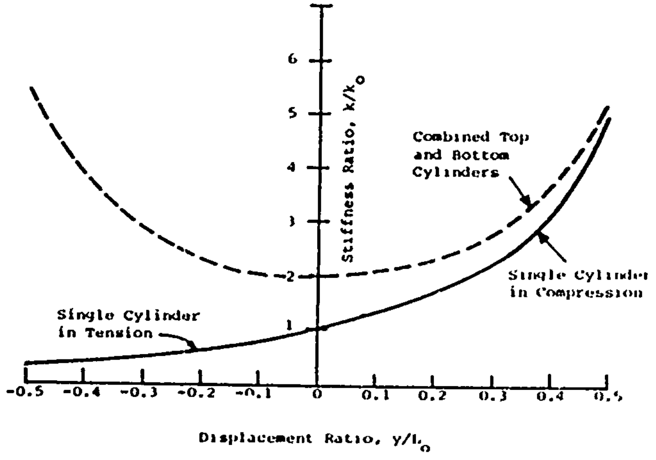

Figure 10-19 Stiffness Variation With Displacement (Ref. 10-3)

ratio. The displacement ratio is defined by

$$\eta = y/L_o \qquad (10\text{-}22)$$

where

y = deflection

L_o = cylinder chamber length (see Fig. 10-20;

$L_{o1} \approx L_{o2} = L_o$ for a double action cylinder at the neutral position)

Note that the spring rates are approximately linear for single action cylinders and almost constant for double action cylinders at displacement ratios less than 0.3.

The spring rate of pneumatic cylinders is a function of displacement. At the neutral position, the spring rate of a single action cylinder is given by

$$k_o = \frac{n\, A\, p_o}{L_o} \qquad (10\text{-}23)$$

where

A = piston area

n = gas constant for air

p_o = cylinder chamber air pressure at static position

The gas constant for air to be used in pneumatic spring computations is a function of temperature; however, for temperatures less than 500°F (260°C), it can be taken equal to 1.4 with only slight error. At positions other than the neutral position, the spring rate can be determined from

$$k(y) = \frac{n\, A\, p'}{(L_o - y)} \qquad (10\text{-}24)$$

where p' is the cylinder pressure at the displaced position. Note that p' must be determined at each position of interest. The piston action is usually considered to be a quasistatic-adiabatic process (zero heat exchange)

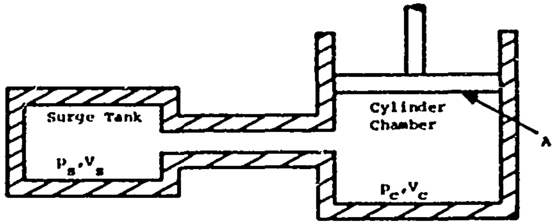

Figure 10-20 Damped Single Action Pneumatic Cylinder

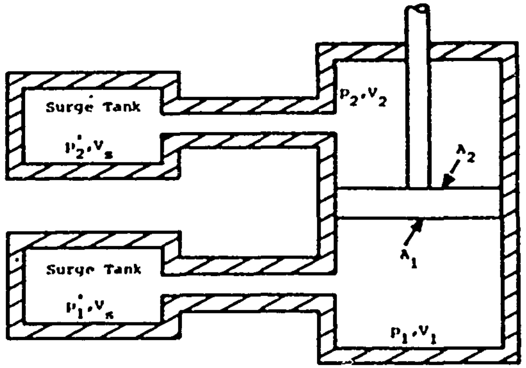

Figure 10-21 Damped Double Action Pneumatic Cylinder

in which case the pressure can be determined from

$$p' = p_o \left[\frac{L_o}{L_o - y} \right]^n \tag{10-25}$$

For double action cylinders the neutral position spring rate is given by

$$k_o = n \left[\frac{p_{o1} A_1}{L_{o1}} + \frac{p_{o2} A_2}{L_{o2}} \right] \tag{10-26}$$

Note that A_1 will differ from A_2 by the area of the piston shaft, although in most cases the differences is negligible. At positions other than the neutral position, the spring rate is given by

$$k(y) = n \left[\frac{p_1' A_1}{(L_{o1} - y)} + \frac{p_2' A_2}{(L_{o2} - y)} \right] \tag{10-27}$$

As in the case of single action pneumatic cylinders, the pressures at displaced positions will determine the spring rate. For a quasistatic-adiabatic process, the pressures are given by

$$p_1' = p_1 \left[\frac{L_{o1}}{L_{o1} - y} \right]^n \tag{10-28}$$

$$p_2' = p_2 \left[\frac{L_{o2}}{L_{o2} + y} \right]^n \tag{10-29}$$

The addition of surge tanks, as illustrated in Figs. 10-20 and 10-21, will provide damping in a pneumatic system. The effect of the surge tanks on the neutral spring rate depends on the displacement frequency (frequency of the dynamic displacements). The neutral position spring rate for low frequency displacement is obtained from the cylinder and surge chamber volumes and pressures at the neutral position. For a single action cylinder with a low displacement frequency, the spring rate for an arbitrary

position of the piston is given by

$$k = \frac{n p' A^2}{V_c + V_s} \tag{10-30}$$

where

V_c' = cylinder chamber volume at arbitrary position

V_s = surge tank volume

At high frequency, the air flow between the cylinder and the surge tank is limited and the spring rates given by Eqs. 10-23 and 10-24 can be used.

For double action cylinders with equal surge tank and cylinder volumes and system pressures on both sides of the piston, the neutral position spring rate for low frequency displacements is given b

$$k = \frac{2 n p_o A^2}{V_c + V_s} \tag{10-31}$$

Equations 10-26 and 10-27 can be used to determine the neutral and displaced spring rates of a damped double action pneumatic cylinder under high frequency displacements. Reference 10-8 contains additional guidance on the effect of surge tanks on pneumatic spring characteristics.

The area of the pneumatic cylinder piston is based upon the allowable pressures in the cylinder and the loads that must be carried under static and dynamic conditions. For single action pneumatic cylinders, the required area is given by

$$A = \frac{k_o \Delta_t}{p_{allow}} \tag{10-32}$$

where p_{allow} is the maximum allowable system pressure.

The pressure which must be maintained at the static neutral position is

$$p_o = \frac{k_o \Delta_{st}}{A} \qquad (10\text{-}33)$$

The final dimension necessary to describe a single action cylinder is the piston chamber length at the static position. If a dynamic displacement has not been specified, the chamber length can be found from

$$L_o = \frac{n A p_o}{k_o} \qquad (10\text{-}34)$$

If a dynamic displacement is specified, the chamber length is based upon an assumed linear response range, i.e., displacement ratio less than 0.3 which leads to

$$L_o = 3.33\, \Delta_{dyn} \qquad (10\text{-}35)$$

The dimensioning of a double action cylinder is more difficult because of the additional pressurized air chamber. The piston area can be estimated from Eq. 10-32, if an allowable pressure has been specified. In the case of double action cylinders, p_{allow} is taken to be the allowable pressure differential between the two sides of the piston. In most cases, the area of the piston shaft can be neglected and the areas A_1 and A_2 considered equal for preliminary design. The length of the chambers can also be taken equal to that given by Eq. 10-35 for a trial design.

The pressures required at the neutral position in the two chambers can then be determined from

$$p_{o2} = \frac{k_o}{2A}\left[\frac{L_o}{n} - \Delta_{st}\right] \qquad (10\text{-}36)$$

$$p_{o1} = \frac{k_o \Delta_{st}}{A} + p_{o2} \qquad (10\text{-}37)$$

The above sizing of the double action cylinder provides a preliminary design configuration which may have to be revised to obtain the desired combination of spring properties.

The following general procedure is suggested for sizing of pneumatic cylinders. If the system frequency and supported weight are specified, Eq. 10-11 can be used to find the required spring rate. The spring rate obtained is the neutral position spring rate. If the system weight and allowable static deflection are specified, the required neutral position spring rate can be approximated by Eq. 10-1. The total deflection to be accommodated is obtained using the specified dynamic deflection and a factor of safety. The maximum allowable air pressure is selected considering pneumatic cylinder size restrictions and load requirements. At this point, the designer must decide whether a double action or single action cylinder is required. If a single action cylinder is to be used, the required piston area is determined from Eq. 10-32 and the required neutral position pressure from Eq. 10-33. The cylinder chamber length is obtained from Eq. 10-34 or 10-35. Note that this is the length at the neutral position and must be greater than the total deflection to be accommodated.

If a double action cylinder is required, the piston area is determined from Eq. 10-32 with p_{allow} taken as the allowable pressure differential between the two sides of the piston. The piston shaft area can be assumed to be negligible (i.e. $A = A_1 = A_2$). The piston chamber length obtained from Eq. 10-35 is assumed equal for both chambers. The neutral position pressures required in the two chambers are determined from Eqs. 10-36 and 10-37.

The neutral and displaced spring rates for a single action, undamped, pneumatic cylinder are determined from Eqs. 10-23 and 10-24, respectively. The neutral spring rate for a double action cylinder is obtained from Eq. 10-26. At other positions, the double action spring rate is obtained from Eq. 10-27.

Damping can be incorporated in the design by the addition of surge tanks. If surge tanks are used, the neutral and displaced spring rates may be altered depending upon the displacement frequency. The low frequency spring rate of a damped single action pneumatic cylinder is given by Eq. 10-30 and the high frequency neutral position spring rate by Eq. 10-23. The low frequency neutral position spring rate of a damped double action cylinder with surge tank and chamber volumes and pressures equal on both sides is given by Eq. 10-31. The high frequency spring rates are given by Eq. 10-26 for the neutral position and Eq. 10-27 for displaced positions.

b. Pneumatic Bellows

The air bag and air bellows are two common configurations for pneumatic bellows and both function in the same general manner. As shown in Fig. 10-22, the air bag consists of a single section subject to shape and volume changes, while the air bellows has two or more sections. Both types are usually constructed of fabric reinforced rubber sections assembled between steel end plates. The bellows type of construction uses one or more annular steel reinforcing rings to divide the axial length of the bag into several sections and increase the practical ratios of length and deflection to diameter. The rolling bellows is actually a positive sealing device sometimes used to replace the usual ring type piston

(a) Air Bag Spring (b) Air Bellows Spring

Figure 10-22 Typical Pneumatic Bellows Configurations (Ref. 10-3)

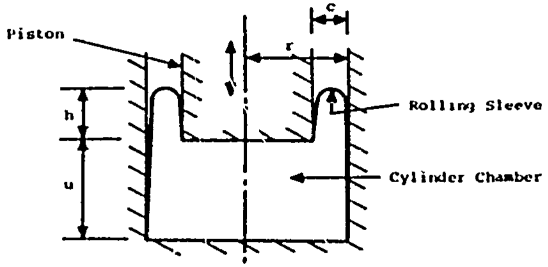

Figure 10-23 Rolling Bellows (Sleeve) Configuration (Ref. 10-3)

seal in air cylinders. The device is shown schematically in Fig. 10-23. The fold in the sleeve moves in the annular space between the piston wall and cylinder wall during relative motion between these parts.

Pneumatic bellows have very nonlinear spring characterisitcs; however, the spring rate tends to become more linear as the amount of compression increases. They are self-restoring and not strain rate sensitive. Although they do not exhibit any significant amount of damping, damping can be provided by the addition of reservoirs to the system. The recommended maximum static operating pressure is usually 100 psi (68.9 N/cm^2). These springs must be inspected regularly to ensure that the proper static height is being maintained. In the case of closed systems, the spring cannot be adjusted to compensate for changes in static loading.

The design of pneumatic bellows is not as simple as other springs, since much of the design data are empirical and determined experimentally for each spring by the manufacturer. Prior to designing a pneumatic bellows spring, a data sheet, which is a plot of the volume, effective area, and load versus deflection, must be obtained from the manufacturer of the spring to be used. A data sheet for one type of bellows spring is shown in Fig. 10-24 as a typical example.

The usual design criteria for a pneumatic bellows spring will include the static load, the maximum spring rate and the maximum dynamic displacement. With these criteria and the manufacturer's data-sheets, the required characteristics of the spring system can be determined. For any specific spring and set of initial conditions, i.e., spring height, internal volume and pressure and load, the dynamic load versus deflection

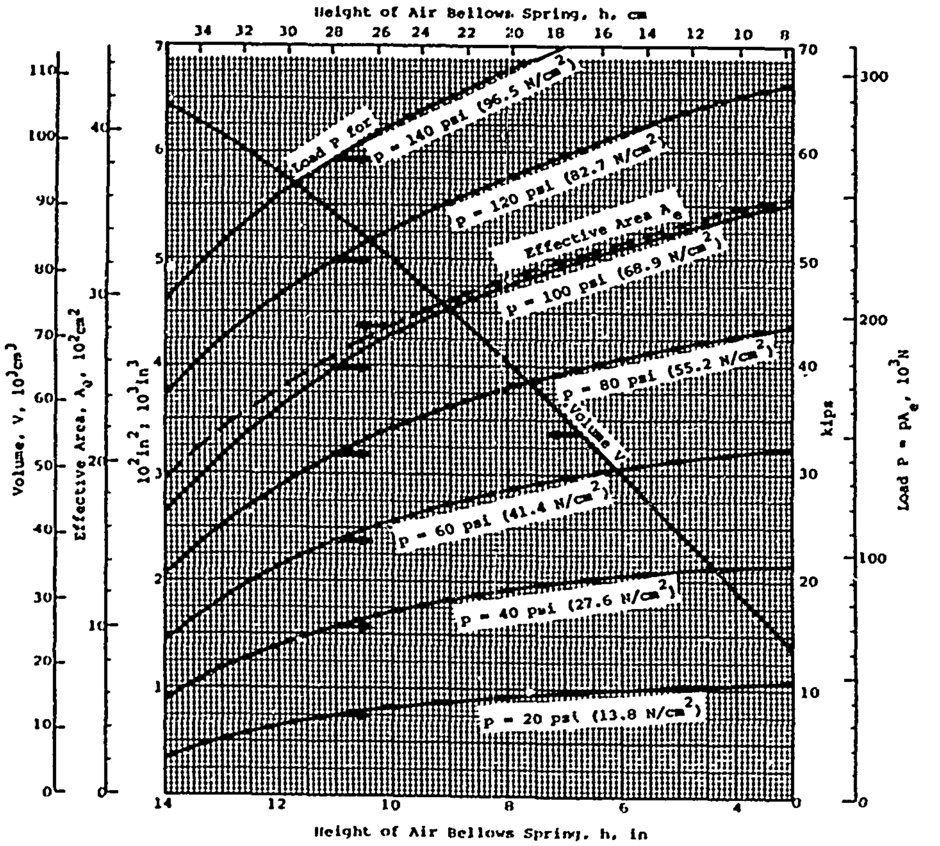

Figure 10-24 Firestone 211A Airmount Spring (Ref. 10-3)

relationships can be determined from the characteristic curves and elementary gas laws. The total available displacement should be twice the specified dynamic displacement plus a safety margin of about 20 percent. Thus

$$y_a = 2.2\, y_d \qquad (10\text{-}38)$$

The displacement will exceed the capacity of a single bellows in some cases, and it will be necessary to have several bellows in series. For N bellows, the maximum compression per bellows is

$$\Delta h = \frac{y_a}{N} \qquad (10\text{-}39)$$

For equal bellows in series, the maximum spring rate of each bellows will be (for N>1)

$$k_i = \left[N k_m\right]^{\frac{1}{N-1}} \qquad (10\text{-}40)$$

where k_m is the maximum spring rate for the system.

A static bellows height must be selected such that Δh will remain within the operating range of the bellows. Once this static height is selected, the associated effective area and volume may be read from the data sheet (e.g., Fig. 10-24). The required static gage pressure, which must be maintained, is

$$p_{gs} = \frac{P_s}{A_{es}} \qquad (10\text{-}41)$$

where

P_s = the static load on the spring

A_{es} = effective area of the bellows at static deflection.

It is customary to use the secant rate for the last 20 percent of the design displacement as a measure of the maximum spring rate of the system. The bellows height at peak dynamic displacement will be

$$h_d = h_{st} - \frac{y_d}{N} \qquad (10\text{-}42)$$

Similarly,

$$h_{0.8d} = h_{st} - 0.8\,\frac{y_d}{N} \qquad (10\text{-}43)$$

The effective areas and volumes for the bellows at these heights can be determined from charts such as Fig. 10-24. The associated pressures can then be found by

$$p_{2a} = p_{1a}\left[\frac{v_1}{v_2}\right]^n \qquad (10\text{-}44)$$

where

p_{2a} = absolute pressure in bellows at volume v_2

p_{1a} = absolute pressure in bellows at volume v_1

n = gas constant, ≈ 1.4 in this case

In terms of gage pressure,

$$\begin{aligned} p_{2g} &= (p_{1g} + 14.7)\left[\frac{v_1}{v_2}\right]^{1.4} - 14.7 \text{ psi} \\ &= (p_{1g} + 10.1\left[\frac{v_1}{v_2}\right]^{1.4} - 10.1 \text{ N/cm}^2 \end{aligned} \qquad (10\text{-}45)$$

Beginning with the static gage pressure (Eq. 10-41) and volume, the gage pressures can be determined for the h_d and $h_{0.8d}$ conditions on the basis of volume change from the static position with Eq. 10-45 and the associated volumes from charts such as Fig. 10-24. Then, with the effective areas from the chart, the maximum spring rate for the bellows can be found from

$$k_i = \frac{p_{dg}\,A_{ed} - p_{0.8dg}\,A_{e0.8d}}{0.2y_d/N} \qquad (10\text{-}46)$$

where

p_{dg} = bellows gage pressure at h_d

A_{ed} = effective area at h_d

$p_{0.8dg}$ = bellows gage pressure at $h_{0.8d}$

$A_{e0.8d}$ = effective area at $h_{0.8d}$

For bellows in series (N>1), the system spring rate can be found by solving Eq. 10-40 for k_m. The spring rate at any displacement can be approximated by

$$k = \frac{\Delta P}{\Delta y} \qquad (10\text{-}47)$$

where ΔP is the change in load corresponding to a Δy change in height.

Reference 10-3 states that if r >> c (see Fig. 10-23) and the displacements are small, the spring rate in the equilibrium position for the rolling sleeve bellows is approximated by

$$k_o = \frac{4.4\,p_s\,r(r-c)^2}{(ru+2ch)} \qquad (10\text{-}48)$$

where r, c, h, and u are defined in Fig. 10-23 and p_s is the pressure on the piston. As for the bellows spring, the spring rate at other positions can be approximated using Eq. 10-47 and the manufacturer's data sheet.

The effective area of the rolling bellows is

$$A_e = \pi r(r-c) \qquad (10\text{-}49)$$

and the volume of air contained in the cylinder at any position is approximately equal to

$$V = \pi r(ru+2ch) \qquad (10\text{-}50)$$

Equations 10-50, 10-45 and 10-49 are used to determine the variation of ΔP with Δy.

If the spring rate for a bellows system is found to be too high, it can be softened by adding a reservoir to increase the total volume of the system. The effect of reservoir volume can be determined from Eqs. 10-45 and 10-46 by letting the volumes be equal to

$$V_t = V_s + V_R \qquad (10\text{-}51)$$

where

V_s = volume of the spring

V_r = volume of the reservoir

Equation 10-51 assumes that there is negligible resistance to air flow between the spring and reservoir. A suitable reservoir volume is easily found by trial and error, but the process can be speeded up somewhat by evaluating two system constants for various volumes. The total volumes must be adjusted until the factor C_s is greater than B_t where these factors are given by (Ref. 10-3)

$$C_s = \frac{k_m y_d + 14.7(A_{ed} - A_{e0.8d})}{5(p_{gs} + 14.7)}\ \text{in}^2$$
$$= \frac{k_m y_d + 10.1(A_{ed} - A_{e0.8d})}{5(p_{gs} + 10.1)}\ \text{cm}^2 \qquad (10\text{-}52)$$

$$B_t = A_{ed}\left[\frac{V_{ts}}{V_{td}}\right]^{1.4} - A'_{e0.8d}\left[\frac{V_{ts}}{V'_{t0.8d}}\right]^{1.4} \qquad (10\text{-}53)$$

where

V_{ts} = total volume of spring and reservoir at equilibrium position

V_{td} = total volume of spring and reservoir at maximum dynamic displacement

$V'_{t0.8d}$ = total volume of spring and reservoir at 0.8 maximum dynamic displacement

Thus, the design process for pneumatic bellows is a process of selecting a unit, or units, which will provide the desired characteristics. These characteristics can be varied somewhat by the choice of cylinder equilibrium pressure and reservoir chamber volume so as to more closely fit the requirements of the specific application.

10.3.5 Liquid Springs

A liquid spring consists of a cylinder, piston rod and a high pressure seal around the piston rod. The cylinder is completely filled with a liquid, and as the piston is pushed into the cylinder, it compresses the liquid to very high pressures.

The configurations of liquid springs are divided into three major classes according to method of loading. The classes are simple compression, simple tension and compound compression-tension. Although they are loaded in different ways, all three types function as a result of compression of the liquid in the cylinders. Schematics of the tension and compression types are shown in Fig. 10-25. The compound spring is merely a more complex mechanical combination of the two basic types. Since the tension type is more common in protective construction applications, it is emphasized in following paragraphs. The

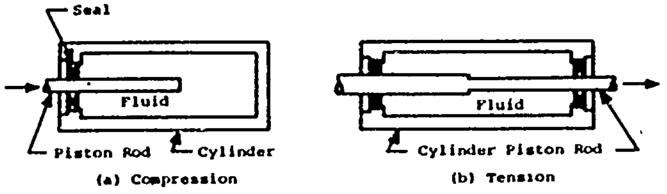

Figure 10-25 Liquid Spring Schematic

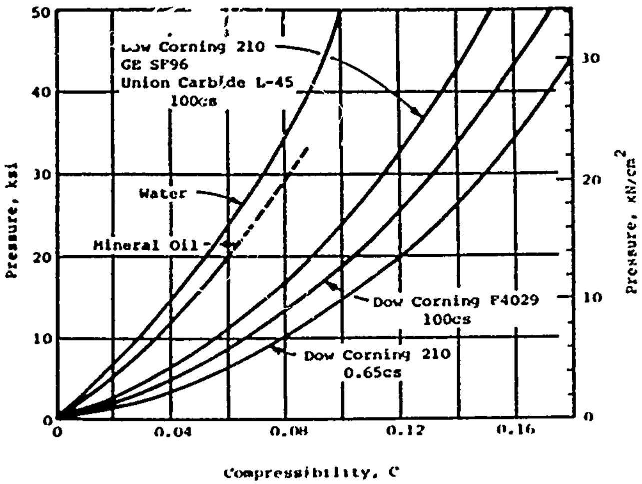

Figure 10-26 Compressibility of Fluids (Ref. 10-3)

cylinders are often fitted with ported heads to guide the pistons and provide damping. Damping can also be provided through the addition of drag plates to the piston rods.

Liquid springs are very compact devices with high, nearly linear, spring rates. They can be adjusted to compensate for load changes, are self-restoring and can absorb large amounts of energy. They are highly sensitive to changes in temperature and fluid volume changes. The latter usually results from fluid chamber leakage or expansion under pressure. Because liquid springs normally operate at high pressures, high quality, close tolerance seals are required around the piston. Friction between the seal and piston provides appreciable damping and increases the spring rate from 2 to 5 percent. Liquid springs are high pressure vessels requiring high quality materials and precision machine work, and as a result, they are normally expensive. However, they are difficult to equal as compact energy absorption devices.

As noted above, the high operating pressures in liquid springs require close tolerance seals around the piston rod. Effective sealing is accomplished by pressure between the seal and the piston rod. These pressures in turn produce a friction deadband which opposes isolator motion. The friction deadband is equal to twice the friction force acting on the rod and must be overcome to initiate isolator rod motion. Input forces less than this friction force will be transmitted without significant attenuation to the isolated mass. The friction deadband can also affect the final position of an isolated item subsequent to its response to input motions. In multiple isolator systems, the stopping of isolators at different positions could result in undesirable tilt or displacement of the system. In general, the effect of a given friction deadband on final system position decreases with increasing isolator spring rate.

An increase in isolator internal pressure will normally increase the width of the friction deadband.

Since the liquid spring is strongly dependent on the characteristics of the fluid in the cylinder, it is important that the fluid selected have the best combination of desirable properties. The desired properties include

- Suitable viscosity
- Temperature and chemical stability
- High compressibility

The viscosity of the fluid is important for two reasons: First, if the viscosity is too low, it may be difficult to maintain a good pressure seal around the piston rod; and second, the damping characteristics of the spring are directly related to the fluid viscosity.

If the spring is to be subjected to temperature changes, the coefficient of thermal expansion for the fluid is important since fluid volume changes will result in pressure changes. The coefficients of thermal expansion for most fluids are decreased by the operating pressures normally encountered in liquid springs. Temperature changes will not be a problem in most shock isolation applications, and, if necessary, steps can be taken to control the fluid temperature.

The compressibility of the spring fluid directly affects the volume of fluid required for a specific application. The higher the compressibility, the less fluid required. The compressibilities of several typical liquid spring fluids are shown in Fig. 10-26. The silicone oils, which include the three lower curves, provide the best combination of desirable properties and are the usual selections for liquid springs. Although Dow Corning's 210 with a viscosity of 0.65 centistoke has the highest compressibility, its low viscosity could cause sealing problems.

The design criteria for liquid springs will normally include the maximum spring rate, static displacement, and the peak dynamic displacement. For a preliminary design, the frictional forces, temperature effects, and volume changes in the chamber due to fluid pressure are generally neglected. A maximum pressure and preload pressure should be selected based upon the spring rate and peak dynamic displacement. For example, a low spring rate and a large peak deflection indicate that high maximum cylinder pressures are not required.

The effective piston area is taken equal to the net cross-section area of the piston rod. The required effective area is obtained from

$$A_e = \frac{k(y_s + y_d)}{P_{max}} \qquad (10\text{-}54)$$

where

y_s = static displacement (equilibrium position)

y_d = maximum dynamic displacement

P_{max} = maximum cylinder pressure

k = spring rate

The static pressure required to maintain the spring at a specified static deflection is obtained from

$$P_s = \frac{k\,y_s}{A_e} + P_{pl} \qquad (10\text{-}55)$$

where P_{pl} is the preload pressure (fluid pressure prior to any load being applied). Defining the cylinder volume under no applied load as V_o, the cylinder volumes at maximum static and dynamic deflections are (neglecting cylinder breathing)

$$V_s = V_o - A_e y_s$$

$$V_d = V_o - A_e(y_s + y_d)$$

The associated compressibilities (Fig. 10-26) are defined as

$$C_s = \frac{V_o - V_s}{V_o} = \frac{A_e y_s}{V_o}$$

$$C_d = \frac{V_o - V_d}{V_o} = \frac{A_e(y_s + y_d)}{V_o}$$

Combining the above equations leads to the following expressions for required cylinder volume under no-load conditions.

$$V_o = \frac{A_e\,y_d}{C_d - C_s} \qquad (10\text{-}56)$$

It is suggested that a factor of safety of five be used in determining the spring cylinder dimensions, because failure of a liquid spring under high pressures could result in fragmentation of the cylinder walls. Failure should be avoided if a working stress equal to 20 percent of the material yield stress is used in all computations.

The required piston rod diameter (see Fig. 10-27) is given by

$$D_r = 2\left[\frac{k(y_s + y_d)}{\pi\sigma_w}\right]^{1/2} \qquad (10\text{-}57)$$

where σ_w is the allowable working stress for the piston rod material. The piston diameter which will provide the required effective area is obtained from

$$D_p = \left[\frac{4A_e}{\pi} + D_r^2\right]^{1/2} \qquad (10\text{-}58)$$

The inside diameter of the cylinder is based upon the required cylinder volume and an assumed cylinder length. Since the piston must be able to deflect in both directions, the cylinder length is usually taken to be slightly greater than twice the peak deflection. When a cylinder length has been

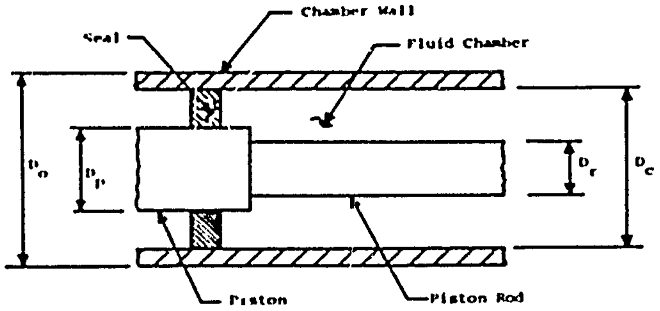

Figure 10-27 Tension Liquid Spring Schematic

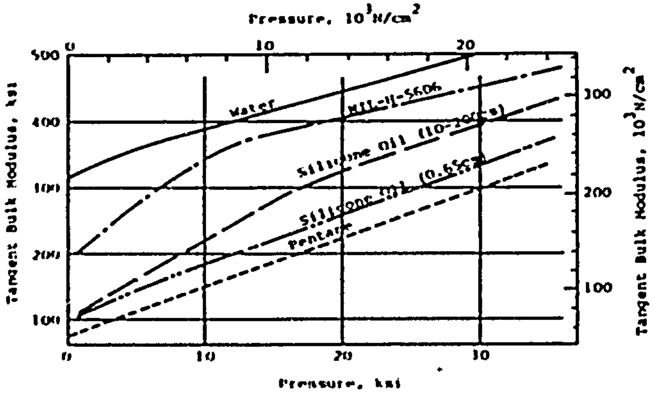

Figure 10-28 Bulk Modulus for Various Fluids

assumed, the cylinder diameter is given by

$$D_c = \left[\frac{4}{\pi}\frac{V_o}{L_c} + D_r^2\right]^{1/2} \qquad (10\text{-}59)$$

where L_c is the length of the cylinder. If the cylinder diameter proves to be excessively large, it may be reduced by selecting a longer cylinder length. The thickness of the cylinder wall can be obtained based on the maximum cylinder pressure and the allowable stress for the selected cylinder wall material. It will frequently be found that thin shell assumptions will not be appropriate in sizing the cylinder wall.

When the dimensions of the liquid spring have been determined, its actual spring rate can be estimated by

$$k = \frac{BA_e^2}{V} \qquad (10\text{-}60)$$

where B is the bulk modulus of the fluid and V is the volume of the cylinder. The stiffness of a liquid spring varies proportionately with the load, which in turn is related to the displacement and cylinder volume.

Figure 10-28 shows typical bulk moduli for various fluids as a function of pressure. The bulk modulus can also be estimated by

$$B = \frac{V_o \Delta p}{\Delta V} \qquad (10\text{-}61)$$

where V_o is the initial volume and ΔV is the change in volume caused by a pressure increment Δp.

The preliminary design procedure for a liquid spring is usually a series of trial and analysis steps until an acceptable configuration is obtained. The effects of temperature and change in cylinder volume due to interval pressures are usually neglected in preliminary design. Normally, static load, peak dynamic displacement, static displacement and maximum spring rate will be specified. When the cylinder fluid has been selected, preload and maximum cylinder pressures must be assumed. These pressures will be functions of the specified spring rates and deflections. The effective area of the piston is obtained from Eq. 1-54, using the assumed maximum cylinder pressure and specified values of the maximum spring rate and displacements. The pressure required to maintain the specified static deflection is given by Eq. 10-55. This is the equilibrium position under static loading. The compressibility of the cylinder fluid at static and maximum cylinder pressures is obtained from curves similar to Fig. 10-26 and the cylinder volume from Eq. 10-56. The physical dimensions of the piston rod, piston and cylinder are obtained from Eqs. 10-57, 10-58 and 10-59, respectively. As indicated previously, these latter steps require assuming a length of cylinder and several trials may be necessary to obtain the desired ratio of diameter to length. The spring rate at various deflections of interest can be obtained from Eq. 10-60.

10.3.6 Other Devices

a. Introduction

The helical, torsion, pneumatic and liquid springs are the more common types of isolators for large masses. There are many other devices especially suited for particular applications and smaller loads. The following paragraphs briefly describe some of these isolators with reference to additional sources of information.

b. Belleville Springs

Belleville springs, also called Belleville washers or coned-disc springs, are esentially spring steel washers which have been formed into a slightly conical

shape. A diametral cross-section of a typical Belleville spring is illustrated in Fig. 10-29. Their main advantage over other types of springs is the ability to support large loads at small deflections with minimum space requirements in the direction of loading. They are useful in protective construction applications requiring limited shock attenuation and as back up systems to reduce shock in the event of bottoming of coil springs. They are relatively inexpensive and readily available in capacities up to about 60,000 pounds (266,850N). Changes in loading conditions are accommodated by the addition or removal of units. Variations in thickness and elastic limit of commercial grade springs may cause the spring rate to vary by as much as ± 20 percent, although special grade springs may be fabricated to maintain the spring rate to within about ± 3 percent.

The steels normally used for the smaller size springs include SAE 1074, 1085, and 1095. Low alloy steels such as silico-manganese steel SAE 9260 or SAE 6150 are preferred for the larger springs. When the loadings are primarily static, the maximum allowable working stresses may be taken equal to the compressive elastic limit of the material. Under these conditions, local yielding may occur around the top inner edge of the spring, resulting in a redistribution of the stresses and a more even distribution of load throughout the spring. The springs may be stacked in either parallel, series, or series-parallel, as shown in Fig. 10-30 to obtain a wide variety of responses. A higher load for a given deflection is obtained from the parallel arrangement. This arrangement is less predictable than the series or individual arrangements because of friction damping and breakaway friction. The series arrangement provides greater deflection for the same load but increases the probability of instability.

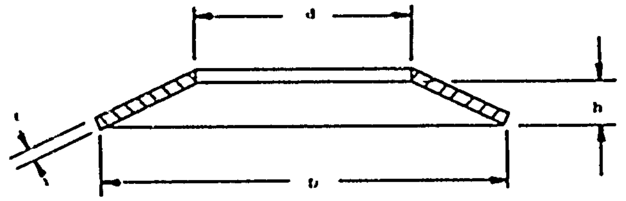

Figure 10-29 Typical Belleville Spring Cross Section

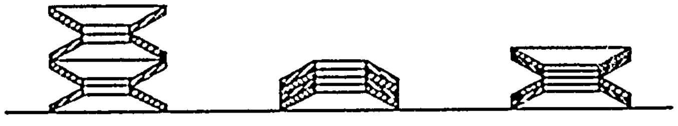
(a) Series (b) Parallel (c) Parallel-Series

Figure 10-30 Typical Belleville Spring Configurations

References 10-1, 10-13, and 10-14 contain guidance for the design of Belleville spring systems.

c. Flat Spring:

A flat spring is simply a steel beam or plate whose physical dimensions and support conditions are varied to provide the desired force displacement relationship. The two basic configurations are the simple spring with one element and leaf springs with multiple elements. They can also be categorized according to the manner in which they are supported. Figure 10-31 shows the more common cantilever and semi-elliptic configurations. They can also be tapered for more efficient use of material. Flat springs normally require only a limited amount of space in the direction of displacement and provide a linear, non strain rate sensitive and self restoring spring. They require little or no maintenance.

The recommended steels for flat springs include SAE 1085, 1095, 4068, 5150 and 9260. These materials are normally shot peened and cold set to extend the life of the springs subjected to many load cycles. Single element flat springs can be considered to have no damping. Leaf springs will exhibit some damping due to the friction between individual elements.

References 10-1, 10-8, 10-13 and 10-14 contain guidance for the design of flat springs.

d. Solid Elastomer Springs

Elastomeric and rubberlike are terms which are often used to describe rubber or similar materials. The term polymer is used to designate rubber in the raw or uncompounded state. Springs made from these materials are often called shock mounts because of their wide use in shock

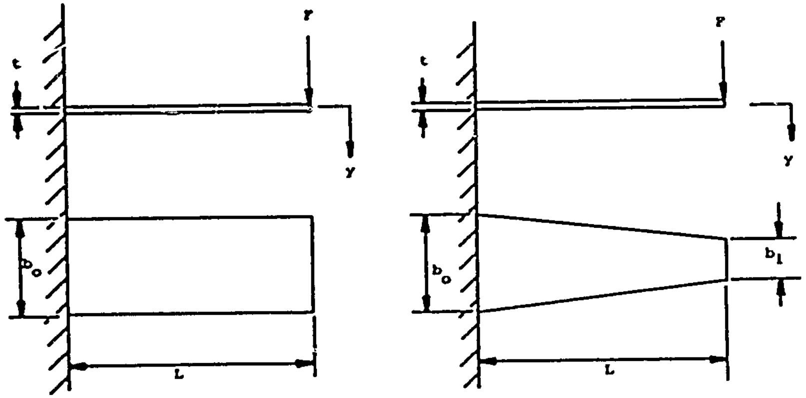

(a) Simple Cantilever Spring

(b) Trapezoidal Cantilever Spring

(c) Cantilever Leaf Spring

(d) Symmetric Semi-Elliptic Leaf Spring

Figure 10-31 Typical Flat Springs

isolation applications. They are normally used in medium to light duty applications and represent an economical solution to the isolation of small items of equipment. These springs are fabricated from a wide variety of natural and synthetic rubbers and compounds and in numerous sizes and shapes to satisfy a wide range of applications. Because of the range in capacity and characteristics of commercially available units, only in unusual cases is it necessary to design a unit. The larger units are usually custom designed for specific applications.

In most applications, the solid elastomer spring will require little space and exhibits good weight to energy storage ratios. In addition to the usual considerations of load and deflection, the selection of an elastomer for a specific application requires consideration of the operating environment. The desirable properties of some elastomers can be significantly degraded when exposed to low or high temperatures, sunlight, ozone, water or petroleum products. Table 10-6 summarizes some of the significant properties of several common polymers and their resistance to various aspects of the environment in which they might be used.

The response of elastomeric springs is nonlinear in most applications because of the nonlinear stress-strain properties of elastomers. The springs are self-damping because of the viscoelastic properties of the elastomers. They are almost always in compression because of bonding limitations. References 10-1 and 10-8 contain guidance for the design of elastomeric springs.

c. Plastic Foams

Although not shock isolation devices, per se, plastic foams have been extensively used in the packaging of shock sensitive items and have also been considered

Table 10-6

PROPERTIES OF SELECTED POLYMERS (Ref. 10-8)

Common Name	Shore A Hardness Range	Max. Tensile Strength		Com-pression set	Tear resist-ance	Resilience		Heat Resistance	Outdoor Aging Resistance
		lb/in^2	N/cm^2			Room temp.	High temp.		
Natural	30-100	4,000	2,760	Good	Good	High	High	Fair	Fair
GR-S	40-100	3,000	2,070	Good	Fair	Fairly high	Fairly high	Fair	Fair
Neoprene	40-95	3,000	2,070	Poor	Good	Fairly high	Fairly high	Good	Excellent
Butyl	40-75	2,000	1,380	Fair	Good	Low	Fairly high	Good	Good
Buna N	20-100	2,500	1,720	Good	Fair	Medium	Medium	Good to excellent	Poor
Thiokol	20-80	1,300	900	Poor	Good	Medium	Fairly high	Fair	Excellent
Silicone	20-90	1,000	690	Excellent	Poor	Fairly high	Medium	Excellent	Excellent
Teflon, kel-F	55-80	3,500	2,400	Fair to good	Fair to good	Low	Medium	Excellent	Excellent
Hypalon	45-95	2,800	1,930	Fair	Fair to good	Fairly high	High	Excellent	Excellent
Polyacry-late	40-90	1,800	1,240	Good	Fair to poor	Low	High	Excellent	Excellent
Viton A	60-90	3,000	2,070	Excellent	Fair to poor	Medium	Medium	Excellent	Excellent

Table 10-6 (cont.)

PROPERTIES OF SELECTED POLYMERS (Ref. 10-8)

Common Name	Low Temperature Flexi-bility	Specific Gravity	Abra-sion Resis-tance	Adhesion Strength	Flex Life	Solvent Resis-tance		Mois-ture Resis-tance	Flame Resis-tance
						Hydro-Carbons	Oxygen-ated		
Natural	Excel-lent	0.93	Excel-lent	Excellent	Excel-lent	Poor	Good	Fair to Good	Poor
GR-S	Good	0.94	Excel-lent	Excellent	Good	Poor	Good	Good to Excel-lent	Poor
Neoprene	Fair	1.23	Good	Good	Good	Good	Poor	Fair to Good	Excel-lent
Butyl	Fair	0.92	Fair - Good	Fair	Fair to Good	Poor	Good	Excel-lent	Poor
Buna N	Fair	1.00	Good	Good	Fair	Excel-lent	Poor	Excel-lent	Poor
Thiokol	Good	1.34	Fair	Poor		Excel-lent	Good	Fair	Poor
Silicone	Excel-	0.95	Poor	Poor	Good	Fair	Good	Excel-lent	Fair
Teflon Kel-F	Fair	1.85	Good	...	...	Excel-lent	Poor to Good	Fair to Excel-lent	Excel-lent
Hypalon	Fair	1.10	Excel-lent	Poor	Good	Good	Fair	Excel-lent	Good
Polyacry-late	Poor	1.09	Good	Poor	Good	Excel-lent	Poor	Fair	Poor
Viton A	Fair	1.85	Good	Fair	Good	Excel-lent	Fair	Excel-lent	Good

for use in some protective construction applications. They are classified as flexible or rigid foams and open or closed cell. The flexible foams exhibit much smaller permanent deformations under transient loads than *rigid foams* of the same strength. Both types show an increase in strength with *increasing denstiy*. Their stress-strain characteristics are highly nonlinear and both types can undergo large (40-60%) strains before the onset of strain hardening. Figure 10-32 shows the load-strain relationships for a typical polyurethane foam. The foam of Fig. 10-32 indicates both energy storage and energy dissipative behavior. The stress-strain properties of some plastic foams are also sensitive to rate of loading and temperature.

The energy-storage and energy-dissipative behavior in open cell plastic foams comes from the viscoelastic properties of the material and the presence of entrapped air. The air has a marked effect on the mechanical behavior because of the airflow resistance and pressure buildup under *dynamic conditions*. As the foam is compressed, the cell pores are reduced in size causing a change in flow resistance. The restricted flow causes hardening of the foam due to air pressure buildup, especially at high strain rates.

Foam isolators offer considerable design flexibility. They can be formed into almost any geometric shape and, hence, configured to avoid local hard points and attendant design problems. Tests on isolator elements subjected to typical nuclear weapon-induced facility shock pulses showed no discernible anomalous behavior nor surging, and high frequencies were effectively attenuated (Ref. 10-15). Flexible foams can be used for multiple-shot applications, although there is some degradation with cyclic

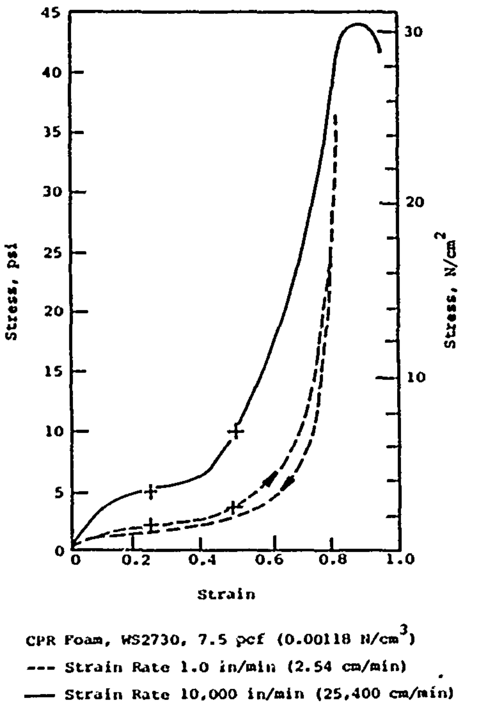

Figure 10-32 Stress-Strain Curve for CPR, WS2730, 7.5 pcf Polyurethane Foam (Ref. 10-15)

loading. Reference 10-15 and 10-16 report on investigations of the use of flexible open cell polyurethane foams for shock isolation of hardened underground facilities.

The distributed nature of foam isolators is attractive in meeting the requirements for omnidirectional force-displacement behavior with minimum translational-rotational coupling for the case of uniform symmetric geometries and mass properties. However, in the case of nonsymmetric geometries and mass properties, a design problem arises in maintaining the force resultant close to the article CG in order to minimize coupling. For this case, it may be necessary to use a set of properly configured discrete foam isolators, or some other technique to tailor the distribution of isolator forces.

For the case of an isolation system consisting entirely of foam, another potential problem that needs investigation is the long term creep due to the steady gravity load. If creep is a problem, foams may still be attractive for lateral isolation in conjunction with other isolators to handle vertical loads.

f. Constant Force Isolators

Cyclic plastic straining of a ductile metal in a fixed strain range produces a hysteresis loop which stabilizes during the first few cycles. Repeated cycling results in almost constant energy absorption per cycle until eventual fatigue failure. Metals such as aluminum can tolerate roughly 1000 such cycles before failure while stainless steel or titanium will approach 10,000 cycles before a fatigue failure (Ref. 10-12).

The narrower the hysteresis loop, the greater the cycles to failure and the greater the total energy absorption at failure. Cyclic plastic straining to failure results in considerably greater energy absorption than unidirectional straining to failure. Specific Energy Absorption (SEA) for N cycles to failure is approximately $\sqrt{N}$ times the SEA for unidirectional straining to failure. These principles are illustrated qualitatively in Fig. 10-33.

One type of constant force isolator is shown schematically in Fig. 10-34. In this type of device, the ring or tube elements are compressed slightly out-of-round into the plastic range. Stroking of the device causes the elements to roll and produces cyclic plastic bending deformation as the points of maximum strain are translated around a ring or tube. To ensure that the elements roll rather than slide, the ratio of squeeze force to roll force is selected so that the sliding friction force is always greater than the roll force, i.e., coefficient of friction x squeeze force > roll force. It is desirable, however, to maintain the squeeze force only as high as necessary to minimize the tube wall thickness and the device weight.

g. Miscellaneous

Preceding paragraphs have discussed various devices and materials commonly encountered in shock isolation or mitigation roles. In addition to these more or less specific shock protection items, structural elements such as beams and plates often enter into consideration of a particular shock isolation application. A great deal of useful information on the dynamic properties of miscellaneous systems is summarized in Table 9-12.

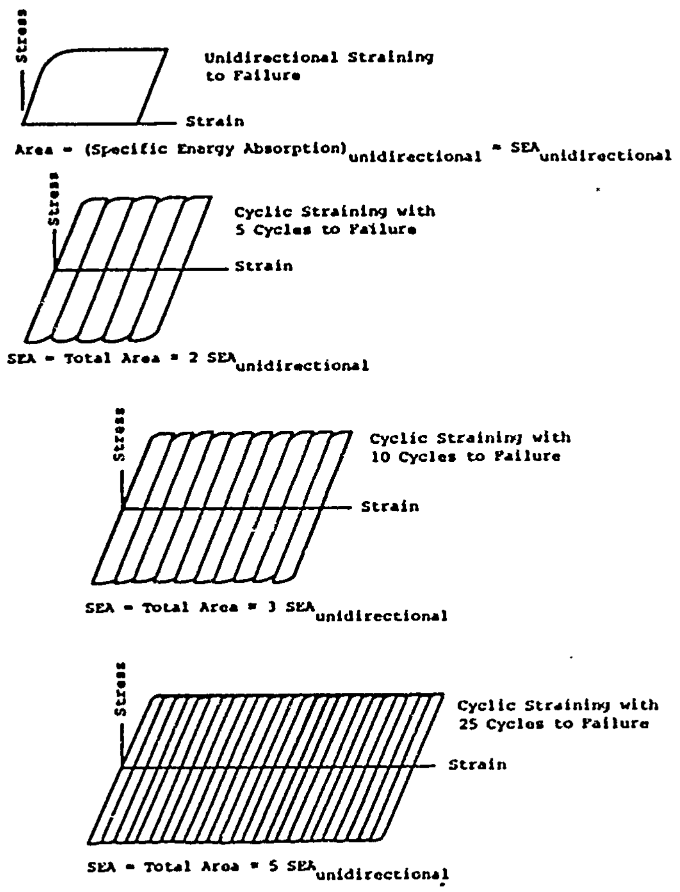

Figure 10-33 Relation Between Hysteresis Loop and Specific Energy Absorption (Ref. 10-12)

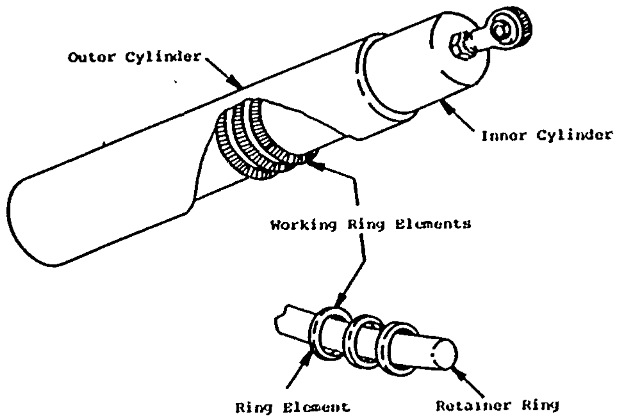

Figure 10-34 Rolling Ring Energy Absorber (Ref. 10-12)

10.4 SUPPORTS FOR HARDMOUNTED EQUIPMENT

10.4.1 General

As noted in earlier paragraphs, some items of equipment do not require shock isolation because the predicted motions at their point of attachment to the supporting structure do not exceed their shock tolerance. These items can normally be hardmounted to the supporting structure. As used herein, a hardmount is defined to be a method of attachment which has not been specifically designed to provide a significant reduction in input motions to the equipment. Since all methods of attachment exhibit some flexibility, there is no precise division between shock isolators and hardmounts and both types of devices will modify input motions to some degree. However, in the case of hardmounts, the modification will generally be of lesser significance.

In contrast to shock isolation systems, hardmounted systems will normally exhibit natural frequencies much higher than those corresponding to the lower modes of vibration of the supporting structure. Although this characteristic offers the advantage of reduced rattlespace, it also implies more efficient transmission of higher frequency components of the support structure motion to the attached item. Thus, it would appear that a more exact structural analysis is required for hardmounted systems in order to include higher modes of vibration. In practice, the need for more exact analyses is often at least partially offset by higher factors of safety in mount design and equipment shock tolerance. However, in the absence of good engineering judgement, higher factors of safety can often lead to unrealistic attachment designs. An alternate approach is to carefully choose, or design, attachments such that the fundamental frequency of the hardmounted system falls below the upper limit or cut-off frequency covered by the dynamic analysis of the supporting structure. Normally, the approach chosen for hardmount design will be a combination of these two and will be based upon considerations of cost, importance of the item, the size and weight of the item and consequences of failure of the attachment system.

The choice of hardmount properties so as to provide reasonable natural frequencies results in other significant benefits. Among these is a greater confidence in the results of the dynamic analyses because they are limited to the lower frequencies. A lower frequency system also provides some attenuation of higher frequency input motions and it is in this region where the greater uncertainties occur as to equipment shock tolerance. Lower frequency systems also reduce the possibility of resonance with high frequency motions resulting from stress wave reflections within structural elements. Although the choice of a reasonable natural frequency will depend on the properties of the supporting structure and the hardmounted equipment, fundamental frequencies in the range of 10 to 1000 hertz appear readily attainable in most applications.

10.4.2 Design Considerations

The first step in the design or analysis of hardmounted systems is a dynamic analysis of the supporting structure to determine input motions at the points of attachment of the systems. In general, the response analysis should include frequency components at least as high as the fundamental frequency of the hardmounted system. Obviously this requirement must be tempered by engineering judgement but, if this frequency range is not adequately covered, some of the most important contributions to equipment motions may not be included. Unless the equipment mass is large relative to that of the structural element to which it is attached, i.e., greater than 10 percent, it is not necessary that the equipment mass be included in the dynamic analysis. Studies reported in Ref. 10-17 indicate that small equipment masses do not significantly affect the motion of the supporting structure. If more than one design loading is specified for the supporting structure, time and motion histories and shock response spectra at the point of attachment of the hardmounted system should be obtained for each of the loadings. An upper bound, or envelope, of these spectra is then used for design or analysis of the hardmount system. Significant errors can result from the use of free-field ground shock spectra alone for design or analysis of hardmounted systems, since only a fortuitous combination of factors would cause free field motions to be equal to those at some point within a structure. Although elastic-plastic shock spectra are preferred for yielding mounts, the elastic shock spectra will provide conservative estimates of peak acceleration for these cases. A similar statement can be made for those mounts which exhibit different moduli in compression and tension, as long as the natural frequency of the system is based on the larger of these moduli.

The shock spectra approach is considered adequate for final design of all simple hardmount systems of a non-critical nature. It is also considered adequate for preliminary design of critical systems and those whose representation as single degree of freedom systems is questionable. It is recommended that preliminary design of the latter groups be verified by a more exact dynamic analysis wherever practical.

Once the peak equipment acceleration is established, the required resistance of the attachment is determined as the product of the equipment mass and its acceleration. In most instances it is necessary to add at least a portion of the mass of the mount to that of the equipment in calculating the

total reaction. If the equipment is subjected to simultaneous accelerations in more than one direction, a corresponding system of forces must be applied to the mount. All forces must be applied through the center of gravity of the mass and its mount. This will normally result in an eccentric load being applied to the mount.

When the system of loads applied to the mount has been defined and a mount configuration selected, the mount can be designed or analyzed using conventional methods of analysis. The design process is an iterative one and several designs may be necessary before an acceptable system is obtained. The designer should be cautioned that a stronger, stiffer, system may not always be the correct solution to a deficient mount, since the stronger mount might subject the equipment to even higher accelerations. Wherever possible, the mount should possess some flexibility in the direction of the applied loads or support motions. Figure 10-33 shows some simple concepts for hardmounts which provide various degrees of flexibility. If relative displacement between the equipment and its supports are acceptable, yielding mounts offer the advantages of reduced equipment accelerations and forces applied to the mount. Care must be taken in these cases to ensure that the mount can undergo the expected deformations without failing or impacting upon some other element. Wherever practical, intimate contact between the hardmounted equipment and exterior wall surfaces should also be avoided to minimize transmission of stress wave generated motions to the equipment. A second and more important advantage of stand-off type attachments, such as those shown in Figs. 10-33(d) and (f), is that tensile and compressive moduli in a direction perpendicular to the wall surface can be made equal.

(a) Flexibility in x and y Directions

(b) Flexibility in y and z Directions

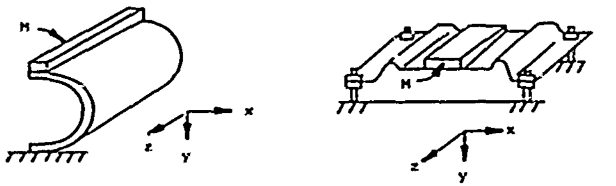

(c) Flexibility in x and y Directions

(d) Flexibility in x and y Directions

(e) Flexibility in x, y and z Directions

(f) Flexibility in x, y and z Directions

Figure 10-35 Simple Hardmount Concepts

10.4.3 Steps in Design or Analysis

Following is a brief summary of the important steps in the design of hardmounts. The analysis procedure is similar except that some steps can be omitted since the system is already specified.

Some of the steps given below might be performed in conjunction with the analysis of the supporting structure and would normally not have to be performed by a designer or analyst concerned only with internal equipment. These steps are included to provide a sense of completeness to the procedure.

Step 1. Define equipment attachment points in and on the structure.

Step 2. Define the dynamic loading that might be applied to the structure.

Step 3. Develop a computer model that will provide realistic structural response data at the points of interest. The degree of sophistication of the model will be measured by an upper cut-off frequency. Some frequency components higher than the cut-off frequency must be included if meaningful data are to be obtained at this frequency. Equipment motions with components beyond this frequency will not be accurately predicted and will, therefore, be of questionable value for design or analysis. It also follows that the model need not be refined to provide data with a cut-off frequency above that for which the shock tolerance of the equipment is known

Step 4. Develop elastic shock spectra for each support point. Spectra should be prepared for each load and component of load and should cover the frequency range up to the cut-off frequency. If elastic-plastic response in equipment supports is contemplated, these spectra should also be computed using the actual structural response for the base motion.

Step 5. For each attachment point, direction, and support type, construct the envelopes of the shock spectra obtained in Step 4.

Step 6. For a particular piece of equipment and location, select a type of attachment device, i.e., elastic or elastic-plastic, cantilever, C-mount, etc. Proportion the attachment to resist the forces caused by acceleration of the equipment mass. For a first trial, it is suggested that a peak acceleration be taken from the shock spectra at the cut-off frequency.

Step 7. Determine the natural frequency of the support and equipment in each direction with the support considered attached to a rigid base.

Step 8. Find the maximum acceleration components at these frequencies from the shock spectra. Determine the magnitude and direction of the resultant acceleration vector.

Step 9. If the resultant peak acceleration from Step 8 is less than the peak acceleration tolerated by the equipment, the equipment support design is acceptable insofar as shock transmission is concerned. If the tolerance level is exceeded, a new design to modify the natural frequencies, nature of support, or support location must be developed.

Step 10. Verify the structural adequacy of the attachment to resist the combined loads corresponding to the accelerations found in Step 8. Modify as necessary

to meet structural strength requirements and restrictions on relative motions.

Step 11. If the initial design is modified, return to Step 7.

The preceeding general steps are a simple statement of a sometimes complex effort. If strictly followed for all hardmount applications, the computation effort would prove exorbitant for complex structures. Short cuts are possible, and the computational effort devoted to a particular item must be determined by its importance.

10.5 ILLUSTRATIVE EXAMPLES

10.5.1 Helical Coil Spring

a. GIVEN: An object weighing 40,000 lbs (177,900N) which requires a 3 Hz shock isolation system in the vertical mode.

b. FIND: Helical coil spring parameters for a base-mounted shock isolation system with a vertical system frequency of 3 Hz. Estimate the horizontal stiffness of the vertical spring design.

c. SOLUTION: Choose eight springs positioned so that the system is dynamically balanced in the vertical mode. The weight carried by each spring will be 40,000/8 = 5000 lbs (22,240N). The desired spring rate from Eq. 10-11 is

$$k = \frac{4\pi^2 (5000)(3)^2}{386} = 4600 \text{ lb/in} = 8060 \text{ N/cm}$$

From Eq. 10-1, the static deflection is

$$\Delta_{st} = \frac{5000}{4600} = 1.09 \text{ in} = 2.76 \text{ cm}$$

Choose $\Delta_{dyn} = \Delta_{st}$ to avoid lift-off or tension in the spring and $C_f = 1.2$. Then from Eq. 10-3,

$$\Delta_t = 1.2(1.09 + 1.09) = 2.62, \text{ say } 2.75 \text{ in} = 6.98 \text{ cm}$$

From Eq. 10-4,

$$P' = (4600)(2.75) = 12{,}650 \text{ lbs} = 56{,}300\text{N}$$

Try a spring index, C, of 4 and an allowable shear stress, τ, 100,000 psi (68,940 N/cm^2). The Wahl correction factor, κ, from Fig. 10-12 is 1.4 for C = 4. Solving Eq. 10-7 for d, we find

$$d = \left[\frac{8\kappa CP'}{\pi\tau_{allow}}\right]^{1/2}$$

$$= \left[\frac{(8)(1.4)(4)(12{,}650)}{\pi(100{,}000)}\right]^{1/2} = 1.34 \text{ in, say } 1.375 \text{ in} = 3.49 \text{ cm}$$

A hot-wound spring is indicated since d > 0.5 in (1.27 cm). From Eq. 10-8 with $G = 10.5 \times 10^6$ psi (7.24×10^6 N/cm^2) for a hot wound spring,

$$\delta = \frac{\pi(4)^2(100{,}000)}{(1.4)(10.5 \times 10^6)} = 0.342 \text{ in/in or cm/cm}$$

Also from Eq. 10-8,

$$h = \Delta_t/\delta = 2.75/0.342 = 8.05 \text{ in} = 20.4 \text{ cm}$$

Choose squared and ground ends for which the number of inactive coils, n, is two. The total free height, Eq. 10-10, thus becomes

$$H = 8.05 + 2.75 + (2)(1.375) = 13.55 \text{ in} = 34.4 \text{ cm}$$

The mean coil diameter for C = 4 = D/d is

$$D = (4)(1.375) = 5.5 \text{ in} = 14 \text{ cm}$$

The buckling ratio

$$H/D = 13.55/5.5 = 2.46$$

which falls in the safe region (left of Curve B) of Fig. 10-14. Buckling of the spring, therefore, should not be a problem.

The number of active coils is needed to check the spring rate of the design parameters chosen thus far. From Eq. 10-9

$$N = 8.05/1.375 = 5.85$$

Then, with Eq. 10-2

$$k = \frac{(1.375)^4(10.5 \times 10^6)}{(8)(5.5)^3(5.85)} = 4830 \text{ lb/in} = 8450 \text{ N/cm}$$

which is slightly greater than the desired spring rate of 4600 lbs/in (8060 N/cm).

Increase N, the number of active coils, to 6. The effective solid height now becomes (Eq. 10-9)

$$h = (6)(1.375) = 8.24 \text{ in} = 21 \text{ cm}$$

and the total free height (Eq. 10-10)

$$H = 8.25 + 2.75 + (2)(1.375) = 13.75 \text{ in} = 34.9 \text{ cm}$$

The resulting buckling ratio is

$$H/D = 13.75/5.5 = 2.5$$

which according to Fig. 10-14 indicates the increased height has not introduced buckling problems. Resolving Eq. 10-2 as above with N = 6, we find k = 4700 lb/in (8230 N/cm), which is within 2.2 percent of the desired spring rate.

Although the above process can be repeated until as close agreement with the target spring rate as desired is obtained, consider the preceding satisfactory. The resulting spring parameters are

$$C = D/d = 4$$

$$d = 1.375 \text{ in} = 3.49 \text{ cm}$$

$D = 5.5$ in $= 14$ cm

$N = 6$

$n = 2$

$k = 4700$ lb/in $= 8230$ N/cm

$\Delta_{st} = \Delta_{dyn} = 5000/4700 = 1.06$ in $= 2.69$ cm

$\Delta_t = 1.2(1.06 + 1.06) = 2.57$, say 2.60 in (6.60 cm)

$h = (6)(1.375) = 8.25$ in $= 21$ cm

$H = 8.25 + 2.60 + (2)(1.375) = 13.6$ in $= 34.5$ cm

Estimate the lateral stiffness of the design spring with Eq. 10-13. The values needed for determination of C_h from Fig. 10-15 are

$\Delta_{st}/H = 1.06/13.6 = 0.078$

$H/D = 13.6/5.5 = 2.74$

The factor C_h for these values is estimated to be about 1.28 from Fig. 10-15, and

$H_s = H - \Delta_{st} = 13.6 - 1.06 = 12.54$ in $= 31.8$ cm

Then, from Eq. 10-13,

$$k/k_h = (1.44)(1.28)\left|0.204\left(\frac{12.54}{5.5}\right)^2 + 0.265\right| = 2.44$$

$k_h = 4700/2.44 = 1925$ lb/in $= 3370$ N/cm

10.5.2 Torsion Bar Spring

a. GIVEN: A 40,000-lb (177,900N) object which required a 1 Hz shock isolation system in the vertical mode.

b. FIND: Torsion bar spring parameters for a vertical system frequency of 1 Hz.

c. SOLUTION: Choose four springs positioned so that the system is dynamically balanced in the vertical mode. The weight carried by each spring will be 40,000/4 = 10,000 lbs (44,475N). The desired spring rate is (Eq. 10-11)

$$k = \frac{4\pi^2(10,000)(1)^2}{386} = 1020 \text{ lb/in} = 1790 \text{ N/cm}$$

The static deflection is (Eq. 10-1)

$\Delta_{st} = 10,000/1020 = 9.8$ in $= 24.9$ cm

Take $\Delta_{dyn} = \Delta_{st} = C_f = 1.2$. The total deflection (Eq. 10-3) becomes

$\Delta_t = 1.2(9.8 + 9.8) = 23.5$ in $= 59.7$ cm

Estimate the lever arm length as 2 x 23.5 = 47.0, say 48.0 in (122 cm). Then from Eq. 10-16,

$T^* = (48.0)(1020)(23.5) = 1.15 \times 10^6$ lb-in $= 1.30 \times 10^7$ N-cm

Choose $\tau_{allow} = 105,000$ psi (72,400 N/cm^2) (Table 10-5) and find the required bar diameter from Eq. 10-17.

$$d = \left[\frac{(16)(1.15 \times 10^6)}{(3.14)(105,000)}\right]^{1/3} = 3.82, \text{ say } 3.85 \text{ in} = 9.78 \text{ cm}$$

Determine the twist angle from Eq. 10-19.

$$\theta_t = \sin^{-1}\left|\frac{(1.2)(9.8)}{48}\right| + \sin^{-1}\left|\frac{(1.2)(9.8)}{48}\right| = 28.3°$$

Solve Eq. 10-18 for the required bar length.

$$L_e = \frac{(28.3)(3.85)^4(11.5 \times 10^6)}{(584)(1.15 \times 10^6)} = 106 \text{ in} = 269 \text{ cm}$$

Check the spring rate with Eq. 10-14.

$$k = \frac{(11.5 \times 10^6)(3.85)^4}{(10.2)(48.0)^2(106)} = 1010 \text{ lb/in} = 1770 \text{ N/cm}$$

The parameters as determined, then, should provide the desired spring rate. The required bar length, about 9 feet (2.69m), may cause difficulty in some applications, however. The other torsion bar properties, L_d, d_o, and L_t, are readily determined as described in paragraph 10.3.3 once L_e and d have been established.

10.5.3 Pneumatic Spring

a. GIVEN: An object weighing 25,000 lbs (111,200N) which can withstand an acceleration of 25g in any direction. The object is to be located in a buried protective structure where the peak free-field vertical ground motion parameters have been estimated to be

Displacement: 15 in = 38.1 cm

Velocity: 250 in/sec = 635 cm/sec

Acceleration: 485 g

b. FIND: A preliminary double action pneumatic spring design which will protect the object from shock damage in the vertical mode.

c. SOLUTION: The fragility level of the object is given as 25 g in any direction. Estimate the fragility in the vertical direction as 0.707 x 25 g = 17.7 g.

The only information given on the shock input the object might be subjected to is in terms of peak free-field ground motion. With no more information than this and for a preliminary design, it will be assumed that the protective structure will move as a rigid body with the free field ground motion and that an adequate shock response spectrum can be constructed with the following simple relations.

$$D = d = 15 \text{ in} = 38.1 \text{ cm}$$

$$V = 1.5v = (1.5)(250) = 375 \text{ in/sec} = 953 \text{ cm/sec}$$

$$A = 2.0a = (2.0)(485) = 970 \text{ g}$$

where D is the maximum relative displacement expected between the support and the object; V is the peak spectrum velocity; and A is the peak acceleration the object will feel (for an undamped system).

The above values are plotted in Fig. 10-34. The assumed fragility level in the vertical direction, 17.7 g, is shown as the dash line in the figure. As may be seen, the dash line intersects the peak response envelope at a frequency of about 3.5 Hz. Consequently, an isolation system with a frequency of 3.5 Hz or less should prevent the object from experiencing an acceleration greater than 17.7 g. As may also be noted from Fig. 10-34, any system with a frequency of less than about 4 Hz may be subjected to a relative displacement (spring distortion) of as much as 15 in (38.1 cm).

Choose four springs located so as to provide a dynamically balanced system. The weight to be supported by each spring is 25,000/4 = 6250 lbs (27,800N). Select a system frequency of 3 Hz. The desired spring rate is (Eq. 10-11)

$$k = \frac{4\pi^2(6250)(3)^2}{386} = 5760 \text{ lb/in} = 10{,}080 \text{ N/cm}$$

Since the stiffness of an air spring increases under dynamic loading, arbitrarily reduce the static spring rate in this case about 10 percent, say 5200 lb/in (9100 N/cm). The static deflection thus becomes (Eq. 10-1)

$$\Delta_{st} = 6250/5200 = 1.20 \text{ in} = 3.05 \text{ cm}$$

Take $\Delta_{dyn} = 15.0$ in (38.1 cm) and $C_f = 1.2$. Then, the total deflection (Eq. 10-3) is

$$\Delta_t = 1.2(1.20 + 15.0) = 19.4, \text{ say } 20 \text{ in} = 50.8 \text{ cm}$$

Estimate the chamber length with Eq. 10-35 with Δ_{dyn} = 1.2 x 15 = 18 in = 45.6 cm.

$$L_o = L_{o1} = L_{o2} = (3.33)(18.0)$$
$$= 60.0 \text{ in} = 152 \text{ cm}$$

Use Eq. 10-32 with an allowable differential pressure of 200 psi to estimate the piston area.

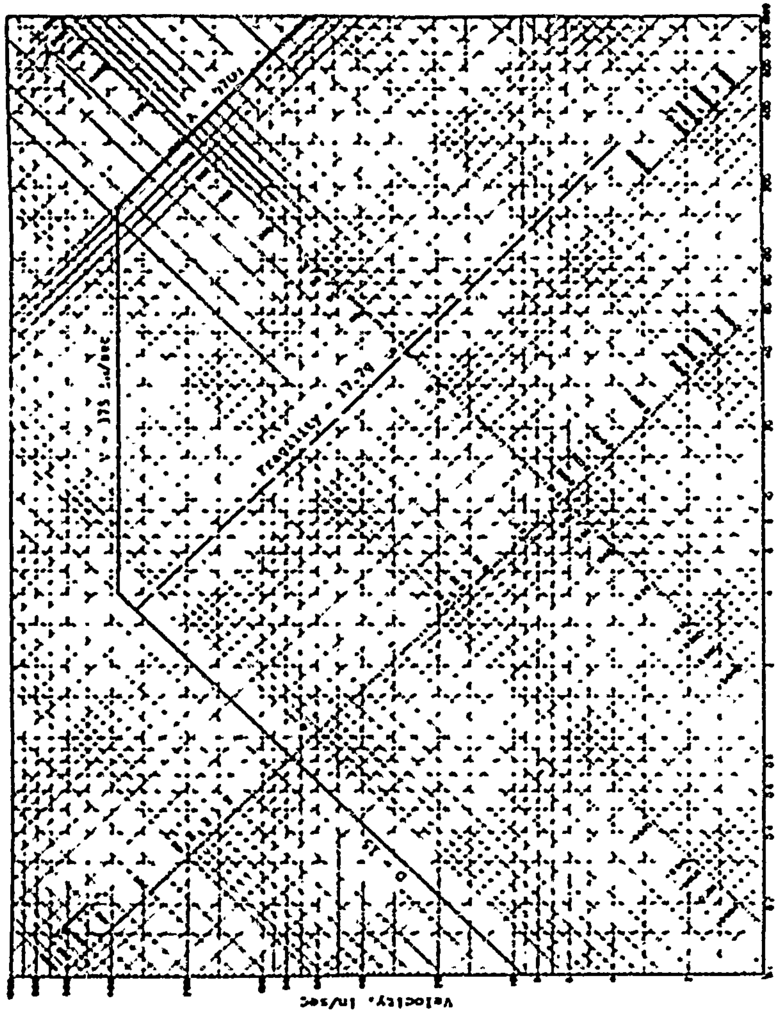

Figure 10-36 Example Vertical Shock Response Spectrum

$$A = \frac{(5200)(20.0)}{200} = 520 \text{ in}^2 = 3355 \text{ cm}^2$$

The associated piston diameter would be about 25.8 in (65.5 cm). If the piston rod had a diameter of 2 in (5.08 cm), the area of the rod would be 3.14 in^2 (20.26 cm^2), or about a 0.6 percent reduction in A_2. Call this negligible and take $A = A_1 = A_2$.

The chamber pressures at the neutral position with n = 1.4 (Eqs. 10-36 and 10-37) are

$$P_{o2} = \frac{5200}{(2)(520)} \left|\frac{60}{1.4} - 1.20\right| = 208 \text{ psi} = 143 \text{ N/cm}^2$$

$$P_{o1} = \frac{(5200)(1.20)}{520} + 208 = 220 \text{ psi} = 152 \text{ N/cm}^2$$

The spring rate at the neutral position can be found with Eq. 10-26.

$$k_o = 1.4\left|\frac{(220)(520)}{60.0} + \frac{(208)(520)}{60.0}\right|$$

$$= 5200 \text{ lb/in} = 9100 \text{ N/cm}$$

The associated frequency is

$$f_o = \frac{1}{6.28} \left|\frac{(5200)(386)}{6250}\right|^{1/2} = 2.85 \text{ Hz}$$

The peak dynamic excursion expected is 15 in (38.1 cm). The chamber pressure for this condition (Eqs. 10-28 and 10-29) would be

$$P_1' = 220\left|\frac{60.0}{60.0 - 15.0}\right|^{1.4} = 328 \text{ psi} = 226 \text{ N/cm}^2$$

$$P_1' = 208\left|\frac{60.0}{60.0 + 15.0}\right|^{1.4} = 152 \text{ psi} = 105 \text{ N/cm}^2$$

The spring rate at the extended position (Eq. 10-27) is

$$K(y) = 1.4\left|\frac{(328)(520)}{60.0 - 15.0} + \frac{(152)(520)}{60.0 + 15.0}\right| = 6770 \text{ lb/in} = 11{,}850 \text{ N/cm}$$

and the associated frequency is

$$f(y) = \frac{1}{6.28}\left|\frac{(6770)(386)}{6250}\right|^{1/2} = 3.26 \text{ Hz}$$

The pneumatic spring parameters determined above, then, give a frequency which is slightly low at the neutral position and slightly high at the anticipated peak dynamic displacement and should be adequate for a preliminary design.

10.5.4 Liquid Spring

a. GIVEN: The same conditions as in Example 10.5.3 above.

b. FIND: A preliminary tension liquid spring design to satisfy the same requirements as the air spring above.

c. SOLUTION: Choose $p_{max} = 25{,}000$ psi (17.230 N/cm^2) and $y_s = y_d = 15$ in (38.1 cm). Liquid spring stiffnesses increase under dynamic loading as do air springs. Consequently, estimate the spring rate somewhat less than the desired average stiffness as was done for the air spring, e.g., 5200 lb/in (9100 N/cm). The required effective area (Eq. 10-54) thus becomes

$$A_e = \frac{(5200)(15.0 + 15.0)}{25{,}000} = 6.24 \text{ in}^2 = 40.3 \text{ cm}^3$$

Take the preload pressure as zero. The static pressure (Eq. 10-55) is

$$p_s = \frac{(5200)(15.0)}{6.24} = 12{,}500 \text{ psi} = 8620 \text{ N/cm}^2$$

Choose Dow Corning F-4029 as the spring fluid. The factor C_d (based on p_{max}) from Fig. 10-26 is 0.12, and the static compressibility C_s (based on p_s) is about 0.075. The required cylinder volume under no-load conditions (Eq. 10-56) is

$$V_o = \frac{(6.24)(15.0)}{0.12 - 0.075} = 2080 \text{ in}^3 = 34{,}100 \text{ cm}^3$$

The maximum load expected on the piston rod would be about

$$P = k(y_s + t_d) = 5200(15.0 + 15.0) = 156{,}000 \text{ lbs} = 694{,}000 \text{ N}$$

Choosing a steel with a tensile yield stress of 75,000 psi (51,700 N/cm^2) and a margin for safety of 5, the allowable working stress in the rod is about 15,000 psi (10.340 N/cm^2). The required area of the rod thus becomes

$$A_{rod} = P/\sigma_w = 156{,}000/15{,}000 = 10.4 \text{ in}^2 = 67.1 \text{ cm}^2$$

and the associated diameter is $D_r = 3.64$ in (9.25 cm). The piston area required is the sum of the rod and effective areas.

$$A_p = 10.4 + 6.24 = 16.64 \text{ in}^2 = 107.4 \text{ cm}^2$$

The piston diameter $D_p = 4.61$ in (11.7 cm). Select a cylinder length based on Eq. 10-3 with $C_f = 1.2$.

$$L_c = 1.2(15.0 + 15.0) = 36.0 \text{ in} = 91.4 \text{ cm}$$

The required net cylinder area is

$$A_{c\ net} = V_o/L_c = 2080/36 = 57.8 \text{ in}^2 = 146.8 \text{ cm}$$

The gross cylinder area is the sum of the rod and net cylinder areas.

$$A_{c\ gross} = 10.4 + 57.8 = 68.2 \text{ in}^2 = 440 \text{ cm}^2$$

The inside cylinder diameter $D_c = 9.31$ in (23.6 cm). (The above diameters could have been found directly from Eqs. 10-57, 10-58 and 10-59, if desired.)

The cylinder volume at the static position is

$$V_s = V_o - A_e y_s = 2080 - (6.24)(15.0) = 1986 \text{ in}^3 = 32{,}500 \text{ cm}^3$$

The volume at peak dynamic displacement is

$$V_d = V_o - A_a(y_s + y_d) = 2080 - (6.24)(15.0 + 15.0)$$

$$= 1893 \text{ in}^3 = 31,000 \text{ cm}^3$$

The estimated bulk modulus of the spring fluid in this range (Eq. 10-61) is

$$B = \frac{(2080)(12,500)}{93.0} = 280,000 \text{ psi} = 193,000 \text{ N/cm}^2$$

The static and dynamic spring rates (Eq. 10-60) become

$$k_s = \frac{(280,000)(6.24)^2}{1986} = 5490 \text{ lb/in} = 9600 \text{ N/cm}$$

$$k_d = \frac{(280,000)(6.24)^2}{1893} = 5760 \text{ lb/in} = 10,080 \text{ N/cm}$$

and the associated natural frequencies are

$$f_s = 2.94 \text{ Hz}$$

$$f_d = 3.01 \text{ Hz}$$

The requirements in this situation, then, could be satisfied with liquid springs with internal dimensions of about 9.31 inches (23.6 cm) diameter and 36 inches (91.4 cm) length with a maximum internal pressure of 25,000 psi (17,230 N/cm^2). As may be seen, these devices are considerably more compact than air springs for the same requirements.

10.6 REFERENCES

10-1 Crawford, R.E., Higgins, C.J., and Bultmann, E.H., A Guide for the Design of Shock Isolation Systems for Ballistic Missile Defense Facilities, TR S-23, U.S. Army Construction Engineering Research Laboratory, Champaign, Ill., August 1973. (U)

10-2 Eubanks, R.A. and Juskie, B.R., "Shock Hardening of Equipment", Shock and Vibration Bulletin No. 32, Part 3, The Shock and Vibration Information Center, Washington, D.C., April 1963. (U)

10-3 Study of Shock Isolation for Hardened Structures, Department of the Army, Office of the Chief of Engineers, Washington, D.C., June 1966, AD 639303. (U)

10-4

10-5 Hirsch, A.E., Man's Response to Shock Motions, David Taylor Model Basin Report 1797, Washington, D.C., January 1964, AD 436809. (U)

10-6 Goldman, D.E.and Von Gierke, H.E., The Effects of Shock and Vibration on Man, NMRI Report 60-3, Naval Medical Research Institude, Bethesda, Md., January 1960, AD 241621. (U)

10-7 A Guide for the Design of Shock Isolation Systems for Underground Protective Structures, AFSWC TDR 62-64, Air Force Special Weapons Center, Kirtland AFB, N.M., December 1962. (U)

10-8 Harris, C.M. and Crede, C.E., Shock and Vibration Handbook, McGraw-Hill Book Company, New York, N.Y., 1961. (U)

10-9 Veletsos, A.S., Design Procedures for Shock Isolation Systems for Underground Protective Structures, RTD-TDR-63-3096, Vol III, Air Force Weapons Laboratory, Kirtland Air Force Base, N.M., June 1964. (U)

10-10 Saffell, H.R., Development of Standard Design Specifications and Techniques for Shock Isolation Systems, Document No. SAF-37, Vol. I, U.S. Army Engineer Division, Huntsville, Ala., August 1971. (U)

10-11 A Study of the Feasibility of Shock Isolating Very Large Manned Underground Structures, AFWL TDR-64-53, Air Force Weapons Laboratory, Kirtland Air Force Base, N.M., June 1964. (U)

10-12 Platus, David L., et al., Investigation of Optimum Passive Shock Isolation Systems, AFWL-TR-72-148, Air Force Weapons Laboratory, Kirtland Air Force Base, N.M., November 1972. (U)

10-13 Handbook of Mechanical Spring Design, Associated Spring Corporation, Bristol, Conn., 1964. (U)

10-14 Shigley, J.E., Mechanical Engineering Design, McGraw-Hill Book Company, New York, N.Y., 1963. (U)

10-15 Liber, T., et at., Shock Isolation Elements Testing for High Input Loadings - Volume II, Foam Shock Isolation Elements, SAMSO-TR-69-118, Space and Missile Systems Organization, Norton Air Proce Base, Calif., June 1969. (U)

10-16 Voltz, W.A., "Application of Polyurethane Foam to Shcok Isolation of Large Silo-Based Missiles," Shock and Vibration Bulletin No. 36, Part 2, The Shock and Vibration Information Center, Washington, D.C., January 1967. (U)

10-17 Schreyer, H.L., and Romesberg, L.E., Numerical and Theoretical Study of the Response of Hardmounted Equipment, AFWL TR 73-253, Air Force Weapons Laboratory, Kirtland Air Force Base, N.M. January 1974. (U)

SECTION XI

DESIGN AND ANALYSIS OF STRUCTURAL SYSTEMS

11.1 INTRODUCTION

11.1.1 General

This section utilizes the information presented in preceeding sections to describe methods of design and analysis of structures subjected to a nuclear environment. The relationship between design and analysis has already been discussed to some extent in Section II. The primary difference in the two processes is in the degree and direction of conservatism regarding structure loads and resistance. In structural design, maximum loads and minimum resistance are normally assumed. In analysis, the combination will probably be affected by the objective of the analysis. In assessing the vulnerability of one's own facility, the assumptions regarding load and resistance may not differ greatly from those used in design. Different assumptions will be appropriate for other analysis objectives.

In both design and analysis, a decision must be made as to what constitutes failure or unsatisfactory performance of the structure. This decision is largely based upon the function of the structure, and evaluation of the performance of a facility will normally require consideration of all the nuclear weapon effects and their interaction with the facility. Although structural deformations and the performance of internal equipment are of primary importance in most cases, nuclear radiation, EMP and thermal effects can be of equal importance.

The following paragraphs discuss procedures for the design or analysis of various general types of structures. These discussions deal primarily with nuclear weapon effects. It is assumed that a conventional structural design or analysis is also accomplished to assure proper performance under normal dead and live loads.

11.1.2 Design

The design process is an iterative procedure of trial and analysis. An initial trial section is selected and then analyzed to determine if its response to the imposed loads is within specified bounds. One of the first steps in the process is to describe the environment for which the facility is to be designed. As indicated in Section II, the phenomena of interest will depend upon the type of facility, i.e., aboveground, shallow buried, deep underground, and the threat, i.e., weapon yield, height of burst, etc. Once the structure type has been selected, the loads can be determined and trial sections selected for the structural components. It is suggested that the structural components be designed first to resist the dynamic loads imposed by airblast and/or ground shock. After adequate resistance to these loads is provided, the degree of protection afforded from the other nuclear weapon effects can be determined. In some instances, it may be necessary to adjust the initial design to provide the required protection from other effects.

In order to start the design process, it is necessary to obtain an initial trial section. If it is assumed that some inelastic response is allowable and the positive phase duration of the dynamic load is long relative to the fundamental period of the element ($t_o > \sim 3T_N$), the required maximum static resistance of the element can be estimated by

$$R_m = F_o\left[\frac{1}{1 - \frac{1}{2\mu}}\right] \qquad (11\text{-}1)$$

where

F_o = peak value of the load

μ = ductility ratio

Thus, for a specified ductility ratio, the required static resistance of the element can be obtained from Eq. 11-1 in terms of the peak applied load. This required resistance can then be translated into structural dimensions using expressions from Section VIII for properties of the structural element. It is suggested that the dynamic yield strength of steel and dynamic compressive strength of concrete be used in expressions of Section VIII irregardless of whether the objective is design or analysis. A dynamic analysis of this trial section is then made and dimensions adjusted as necessary to obtain the desired response. Although Eq. 11-1 was derived for long duration loads with instantaneous rise times, it can be used in obtaining a trial section for other long duration load functions.

In those cases where the load duration is short compared to the period of the element ($t_o < \sim 3T_N$), the load can be treated as an impulse whose magnitude is equal to the area under the force versus time curve. For this case, the required resistance can be estimated by

$$R_m = \frac{i\omega_N}{\sqrt{2\mu - 1}} \qquad (11\text{-}2)$$

where

i = impulse

ω_N = natural frequency of system (rad/sec)

The advantage of allowing inelastic action to occur is obvious from Eqs. 11-1 and 11-2. For large ductility ratios, the required maximum resistance is equal to the peak load for long duration loads and approaches zero for impulsive loads. For a ductility ratio of one (elastic response), the required maximum resistance is twice the peak load for long duration loads and equal to $i\omega_N$ for impulsive loads.

The ductility of a structural element will depend upon its configuration, proportions and the materials from which it is constructed. The two materials most commonly used in protective construction are reinforced concrete and steel. Ductilities of 20-50 are possible in underreinforced concrete and steel members in flexure as discussed in Sections II and VIII. The ductility ratio will be much less for brittle modes of failure, possibly 2-10. The selection of a ductility ratio for use in design should be based upon consideration of the functional requirements of the structure as well as its ductility limit at failure. Since every effort is made in design to avoid brittle modes of failure, ductility ratios of 1.0 to 1.3 are generally selected for columns, shear response modes, etc. Ductilities of 3 to 10 may be chosen for the flexural mode depending upon the function of the structure or member.

Equations 11-1 and 11-2 along with most of the discussion to this point have been concerned with the initial phase of the design process, i.e., selection of a trial section. The simplification of the load function, idealization of the structural behavior and approximation of the structure's dynamic response in terms of a single degree of freedom system are generally adequate (and recommended) for this purpose and for quick feasibility studies. As the design process continues, the designer must begin to take account of the probable actual load function and the interaction of the structure deformations and motions with the load or surrounding medium in arriving at a final design.

11.1.3 Analysis

While the basic analytical techniques used for design and analysis are identical in many instances, the criteria used for determining structural response or motion environment might differ greatly. The fact that the analyst is provided the materials, configuration and proportions of a structure or structural element does not necessarily simplify the process in comparison with design. The objective of the analysis will to some extent determine its difficulty and required accuracy. The most difficult type of analysis is that required to determine the ultimate strength of a structure. While conservative design procedures have been developed through extensive research and experience, relatively little is known regarding failure or collapse of a structure. In general, the analyst should use the best available information on material properties and the more sophisticated methods of analysis in order to minimize uncertainties in results. Depending on the degree of conservatism desired, it may be appropriate to assume minimum loading conditions and maximum strength of materials.

In many cases of target analysis, only sparse information is available regarding properties of the structure. A reasonable approach in such cases is to assume that design procedures, material properties and construction techniques are similar to those used in the nearest comparable geographical region for which such information is available. Admittedly, this approach may only provide crude estimates but, in some instances, it may be the only one open to the analyst.

11.2 ABOVEGROUND STRUCTURES

Aboveground structures are discussed in general terms in *Section II* with respect to primary nuclear weapon effects, types of burst, advantages and disadvantages. Nuclear effects phenomenology is addressed in Section III through VI; Section VII presents guidance for translating the phenomenology into loads needed for structural design and analysis. This paragraph will illustrate in summary fashion application of the of the data in preceding sections to aboveground structures.

The proportions of aboveground structures, almost without fail, will be controlled by reflected pressure, dynamic pressure or radiation. Ground shock and crater missiles must always be considered, but it will usually be found that the structure must necessarily be so far from the burst to avoid collapse due to airblast that these effects rarely control. As a class, aboveground structures will not be found practical for the more severe threats.

11.2.1 Rectangular Structures

By definition, rectangular structures will consist of planar structural elements with straight-line intersections. As such, they may be easier to treat analytically, but they will not demonstrate the load-carrying efficiency of other shapes.

Assume that it has been determined that a certain essential function will be afforded the required survivability through combined dispersion and hardening provided it can be located at a point where the incident peak overpressure from nuclear weapons of 2kT to 10MT ($8.4 \times 10^{12} - 4.2 \times 10^{16}$ j) is 10 psi ($6.9 \ N/cm^2$). Also, let it have been determined that the envelope to house the function is adaptable to 20 x 20 x 8-foot (6.1 x 6.1 x 2.4-meter) modules. A preliminary investigation of the feasibility of providing the necessary protection by an aboveground rectangular building is desired.

a. Exterior Walls

To get started, estimate a trial section on the basis of Eq. 11-1 knowing that the time of duration of the 10MT load will be long relative to the period of structural elements commonly encountered in protective construction. Ignore the reflected pressure spike for the time being and take $P_o = P_{so} = 10$ psi.

Let it have been determined that inelastic action to the extent of $\mu = 3$ will be acceptable. From Eq. 11-1,

$$R_m = 10\left[\frac{1}{1 - 1/(2)(3)}\right] = 12 \text{ psi } (8.27 \text{ N/cm}^2)$$

Choose reinforced concrete as the structural material with $f'_{dc} = 3750$ psi (2590 N/cm^2) and $f_{dy} = 40{,}000$ psi (27,600 N/cm^2) where f'_{dc} and f_{dy} are dynamic strength parameters for the concrete and reinforcing steel, respectively. Take the wall section as a one-way slab, 1 inch (2.54 cm) wide, an 8-foot (2.4 m) span, and fixed at both ends. From Eq. 8-55 with $a = b = 1$ inch, $p_f = R_m$, $p_c = p_c = 0.01$,

$$d = L\left[\frac{R_m}{7.2(p_c + p_c)f_{dy}}\right]^{1/2} = 96\left[\frac{12}{7.2(0.01 + 0.01)40{,}000}\right]^{1/2}$$

$d = 4.38$, say 4.5 in (11.4 cm)

Select the thickness of the section, t, as 6.0 inches (15.2 cm) to provide steel cover. The resistance provided by the trial section is (Eq. 8-55)

$$R_m = (7.2)(0.01 + 0.01)(40{,}000)\left(\frac{1}{1}\right)\left(\frac{4.5}{96}\right)^2 = 12.7 \text{ psi } (8.73 \text{ N/cm}^2)$$

Determine the natural period of the element as described in paragraph 9.3.2. The resistance R, corresponding to the deflection x, (Fig. 9-16) is found from Table 9-4 to be $R_1 = 12M_{ps}/L$. Similarly, since $M_{ps} = M_{pm}$, $R_m = 16M_{ps}/L$. Also, $k_1 = 384EI/L^3$ and $k_2 = 384EI/5L^3$. Refer to Fig. 9-16.

$$x_1 = \frac{R_1}{k_1} = \frac{12M_{ps}L^2}{384EI}$$

$$x_2 = x_1 + \frac{R_m - R_1}{k_2} = \frac{32M_{ps}L^2}{384EI}$$

$$x_{ef} = x_2 + x_1 - \frac{R_1}{R_m}x_2 = 0.0521\ M_{ps}L^2/EI$$

$$k_{ef} = \frac{R_m}{x_{ef}} = 307EI/L^3$$

(This value of k_{ef} could, have been read directly from Table 9-4 in this particular case.) Let the density of the reinforced concrete be 145 lb/ft^3 (0.023 N/cm^3). With Eqs. 8-2 and 8-30,

$$E = (33)(145)^{1.5}(3750)^{1/2} = 3.54 \times 10^6 \text{ psi } (2.44 \times 10^6 \text{ N/cm}^2)$$

$$I = (0.5)(1)(4.5)^3[(5.5)(0.01) + 0.083]$$

$$I = 6.29 \text{ in}^4 \ (262 \text{ cm}^4)$$

The total mass of the section is

$$M_t = \frac{(6)(1)(96)(145)}{(1728)(386)} = 0.125 \text{ lb-sec}^2\text{/in } (0.219\text{N-sec}^2\text{/cm})$$

With $K_{LM} = 0.78$ from Table 9-4 and Eq. 9-34,

$$T_N = 2\pi\left[\frac{(0.78)(0.125)(96)^3}{(307)(3.54 \times 10^6)(6.29)}\right]^{1/2} = 0.022 \text{ sec}$$

The exposed exterior wall height will be about 8.5, say 9 feet (2.74 m) high. For a wall panel 20 feet (6.1 m) long, the distance S for use in Eq. 7-7 is thus 9 feet. The shock front velocity for both yields is 1400 fps (427 mps) from Fig. 3-11.

$$t_s = \frac{(3)(9)}{1400} = 0.019 \text{ sec} \qquad \text{(Eq. 7-7)}$$

For $t_s/T_N = 0.019/0.022 \approx 0.86$ and $\mu = 3$, $R_m/F_o \approx 0.79$ from Fig. 9-9(a). On this basis, the trial section should be able to withstand something like $F_o = 12.7/0.79 = 16.1$ psi (11.1 N/cm^2) during the reflected pressure spike. From Fig. 9-9(b), the time of peak response of the section will be $t_m \approx (0.76)(0.019) = 0.014$ second, or during the time the reflected pressure spike is acting on the wall. The peak reflected pressure (vertical wall) from Fig. 7-3 is 25.8 psi (17.8 N/cm^2) for both yields. While this does not necessarily mean that the trial section will collapse, it does indicate that the design conditions have been exceeded.

Estimate that the required static resistance needed will be on the order of $0.8P_{ro} = (0.8)(25.8) = 20.6$, say 20 psi (13.8 N/cm^2). The required effective depth is

$$d = 96\left[\frac{20}{(7.2)(0.01 + 0.01)(40,000)}\right]^{1/2} = 5.66\text{, say } 5.75 \text{ in } (14.6 \text{ cm})$$

Select t = 7.25 inches (18.4 cm). The resistance provided is

$$R_m = (7.2)(0.01 + 0.01)(40,000)\left(\frac{1}{1}\right)\left(\frac{5.75}{96}\right)^2 = 20.7 \text{ psi } (14.2 \text{ N/cm}^2)$$

The approximate moment of inertia of the new section is

$$I = (0.5)(1)(5.75)^3[(5.5)(0.01) + 0.083]$$

$$I = 13.12 \text{ in}^4 \quad (546 \text{ cm}^4)$$

and the new total mass is

$$M_t = \frac{(7.25)(1)(96)(145)}{(1728)(386)} = 0.151 \text{ lb-sec}^2\text{/in } (0.265 \text{ N-sec}^2\text{/cm})$$

The natural period of the revised section is

$$T_N = 2\pi\left[\frac{(0.78)(0.151)(96)^3}{(307)(3.54 \times 10^6)(13.12)}\right]^{1/2} = 0.017 \text{ sec}$$

For $\mu = 3$ and $t_s/T_N = 0.019/0.017 = 1.12$, F_o allowable is about $20.7/0.85 = 24.4$ psi (16.8 N/cm^2) versus the applied 25.8 psi (17.8 N/cm^2). Call this satisfactory for the present and look at the effect of the total pressure pulse on the section.

One can be reasonably certain that peak response of the section will occur early in the pressure-time history, so the values for t_{oo} as described in paragraph 3.2.4 will be of interest. It appears unreasonable to use P_{ro} as the peak value of the approximate function. One should, however, consider both overpressure and dynamic pressure.

The peak free-field dynamic pressure for both yields is 2 psi (1.38 N/cm^2). The front face drag coefficient $C_{df} = 1.0$ from Fig. 7-8, assuming an ideal blast wave. Neglect the decay of the free-field overpressure and dynamic pressure during the time t_s and approximate a load function with zero rise time and a peak value of 10 + 2 = 12 psi (8.3 N/cm^2) from Fig. 3-10. For a 1 MT surface burst and $P_{so} = 12$ psi, t_{oo} 0.6 second.

$$2\text{kT}: t_o = 0.6\left[\frac{0.002}{1}\right]^{1/3} = 0.076 \text{ sec} \qquad \text{(Eq. 3-1)}$$

$$10\text{MT}: t_o = 0.6\left[\frac{10}{1}\right]^{1/3} = 1.291 \text{ sec} \qquad \text{(Eq. 3-1)}$$

For $\mu = 3$ and $t_o/T_N = 0.076/0.017 = 4.5$, R_m/F_o 1.16 from Fig. 9-9(a). This would indicate that the trial section could withstand about $20.7/1.16 = 17.8$ psi (12.3 N/cm^2) from the 2kT weapon. Similarly, for $t_o/T_N = 1.291/0.017 = 75.9$, $R_m/F_o \sim 1.20$, and F_o allowable for the 10MT weapon is about $20.7/1.20 = 17.3$ psi (11.9 N/cm^2).

It appears that the revised wall section will be reasonably satisfactory, at least at this point in the design process. Before making further refinements in the section with the approximate methods utilized thus far, it is recommended that one proceed onward and select preliminary trial sections for the remainder of the structure.

b. Roof

Investigate the roof as a two-way slab similar in proportions to the wall, i.e., t = 7.25 inches (18.4 cm), d = 5.75 inches (14.6 cm) and steel ratio of 0.01 both ways, both faces. Allow for girders 12 inches (30.5 cm) wide, which results in clear spans of 19 feet (5.8 m). Take the slab as fixed on all four edges. Find the elastic-plastic resistance provided by the slab from Table 9-7.

$$a/b = 1 = \text{aspect ratio}$$

$$M_{pfa} = M_{psa} = M_{pfb} = M_{psb} = aM^{o}_{psb} \; (= aM_p)$$

$$R_m = \frac{1}{a}[12(aM_p + aM_p) + 12(aM_p + aM_p)]$$

$$R_m = 48M_p \text{ lb-in/in (or N-cm/cm)}$$

Evaluate M_p with Eq. 8-53.

$$M_p = (0.9)(0.01)(40,000)(1)(5.75)^2 = 11,900 \text{ lb } (52,900 \text{ N})$$

$$R_m = \frac{(48)(11,900)}{(19 \times 12)^2} = 11.0 \text{ psi } (7.58 \text{ N/cm}^2)$$

(This value for the resistance could have been found directly with Eq. 8-54, which is also based upon the value of M_p from Eq. 8-53.)

Determine the natural frequency of the slab as was done above for the wall section.

$$x_1 = \frac{R_1}{K_1} = \frac{29.2M_pa^2}{810EI} = 0.036M_pa^2/EI$$

$$x_2 = x_1 + \frac{R_m - R_1}{k_2} = 0.111M_pa^2/EI$$

$$x_{ef} = x_2 + x_1 - \frac{R_1}{R_m}x_2 = 0.079M_pa^2/EI$$

$$k_{ef} = \frac{R_m}{x_{ef}} = 608EI/a^2$$

$$M_t = \frac{(19 \times 12)^2(7.25)(145)}{(1728)(386)} = 81.9 \text{ lb-sec}^2\text{/in } (143 \text{ N-sec}^2\text{/cm})$$

$$E = 3.54 \times 10^6 \text{ psi } (2.44 \times 10^6 \text{ N/cm}^2)$$

$$I = 13.12 \text{ in}^4\text{/in } (546 \text{ cm}^4\text{/cm})$$

$$K_{LM} = 0.67$$

$$T_N = 2\pi\left[\frac{(0.67)(81.9)(19 \times 12)^2}{(608)(3.54 \times 10^6)(13.12)}\right]^{1/2} = 0.063 \text{ sec}$$

No reflected pressure would be expected on the roof from a surface burst. Further, the dynamic pressure would cause a reduction in pressure on the roof due to lift (C_{dr} = -0.4 from Fig. 7-8) for a surface burst. For a quick look at the allowable peak dynamic load on the roof due to a surface burst, assume a zero rise time for the overpressure pulse and neglect the lift due to the dynamic pressure. The rise time of the roof loading (Fig. 7-12(c)) becomes

$$t_r = L/U = 20/1400 = 0.014 \text{ sec}$$

R_m/F_o from Fig. 9-11(a) for $t_r/T_N = 0.014/0.063 = 0.22$ and

$\mu = 3$ is roughly 1.18. The peak allowable dynamic load on the roof is thus $F_o = 11.0/1.18 = 9.3$ psi (6.43 N/cm^2). The time of maximum response from Fig. 9-11(b) is $t_m \approx (5.5)(0.014) = 0.077$ second, which is some time after the roof load has reached its peak and begun to decay. Considering that the lift due to the dynamic pressure ($\approx 0.4 \times 2 = 0.8$ psi $= 0.55$ N/cm^2) has been neglected, the trial roof section appears satisfactory for a peak incident overpressure of 10 psi (6.9 N/cm^2) from a surface burst.

c. Girders

Select a trial section in accordance with paragraph 8.7.1(c). With Eq. 8-66, take $p_f = 11.0$ psi $=$ 7.58 N/cm^2 (the resistance provided by the roof slab), $p_e = p_c = 0.01$, f_y as before, $a = 20$ feet (6.1 m), $L = 19$ feet $= 5.8$ m (allowing for columns), and find

$$bd^2 = \frac{(11.0)(20 \times 12)(19 \times 12)^2}{(10.8)(0.01 + 0.01)(40{,}000)} = 15{,}900 \text{ in}^3 \quad (260{,}300 \text{ cm}^3)$$

For $b \approx 0.7d$, $d = 28.4$, say 28.5 inches (72.4 cm); $b = 20$ inches (50.8 cm); and take $t = 31.0$ inches (78.7 cm). The resistance provided by the trial section in terms of uniform loading is (Table 9-4)

$$M_{ps} = M_{pm} = (0.9)(0.01)(40{,}000)(20)(28.5)^2 \quad \text{(Eq. 8-53)}$$

$$= 5.85 \times 10^6 \text{ lb-in}$$

$$R_m = \frac{(8)(1.17 \times 10^7)}{(19)(12)} = 410{,}000 \text{ lb} \quad (1.82 \times 10^6 \text{ N})$$

The tributary load area is one-fourth that of the two adjacent slabs plus the girder.

$$A = (2)\left(\tfrac{1}{4}\right)(19 \times 12)^2 + (19 \times 12)(20) = 30{,}560 \text{ in}^2 \quad (197{,}000 \text{ cm}^2)$$

The resistance provided in terms of a uniform pressure is

$$R_m = 410{,}000/30{,}560 = 13.4 \text{ psi} \quad (9.25 \text{ N/cm}^2)$$

Determine the natural period of the girder.

$$I = (0.5)(20)(28.5)^3[(5.5)(0.01) + 0.083] \quad \text{(Eq. 8-30)}$$

$$= 31{,}900 \text{ in}^4 \quad (1.33 \times 10^6 \text{cm}^4)$$

$$E = 3.54 \times 10^6 \text{ psi} \quad (2.44 \times 10^6 \text{ N/cm}^2)$$

$$k_{ef} = 307EI/L^3 \quad \text{(Table 9-4)}$$

$$M_t = \frac{(20)(31)(19 \times 12)(145)}{(1728)(386)} = 30.8 \text{ lb-sec}^2\text{/in} \quad (53.9 \text{ N-sec}^2\text{/cm})$$

$$K_{LM} = 0.78 \quad \text{(Table 9-4)}$$

$$T_N = 2\pi\left[\frac{(0.78)(30.8)(19 \times 12)^3}{(307)(3.54 \times 10^6)(31{,}900)}\right]^{1/2} = 0.018 \text{ sec} \quad \text{(Eq. 9-34)}$$

Adjust the period to make allowance for the mass of slab moving with the girder by the factor $(M_t'/M_t + 1)^{1/2}$ where M_t' is one-fourth the mass of the two adjacent slabs.

$$T_N = 0.018\left[\frac{30.8 + 41.0}{30.8}\right]^{1/2} = 0.0275 \text{ sec}$$

The rise time for the load coming on the girder is 0.014 second as determined for the roof. For $t_r/T_N = 0.014/0.0275 = 0.051$ and $\mu = 3$, R_m/F_o from Fig. 9-11(a) is roughly 1.10. The allowable F_o for the girder (in terms of a uniformly distributed load) thus becomes $13.4/1.10 = 12.2$ psi (8.40 N/cm^2). The allowable F_o on a girder supporting adjacent slabs should be on the order of four-thirds the expected uniformly distributed load to account for the assumed actual triangular distribution (paragraph 8.7.1(c)). On this basis, F_o allowable $\approx$ (0.75) (12.2) = 9.1 psi (6.3 N/cm^2), which is reasonably close to the peak expected pressure expected on the roof as discussed above. Call the girder satisfactory.

d. Columns

The discussion thus far has been in terms of typical panels associated with nominal 20-foot (6.1 m) square modules. For a multiple bay structure, interior columns will generally be utilized. These members are usually designed elastically ($\mu = 1$) and may or may not be expected to resist horizontal loads.

To obtain a trial section, consider the load tributary area to be one panel. The column will carry a nominal roof panel, two girders framing in, and the exterior pressure on a roof panel. The natural period of a typical column in the vertical mode will be so short that almost any rise time will cause the dynamic load to appear to be applied statically (see Fig. 9-11(a) for larger t_r/T_N). Accordingly, take

$$P_u = W_{roof} + 2W_{girder} + (P_{so} - 0.4q_o) \times A_{roof}$$

$$W_{roof} = \frac{(20 \times 12)^2 (7.25)(145)}{1728} = 35{,}100$$

$$W_{girders} = \frac{(2)(20 \times 12)(20)(31 - 7.25)(145)}{1728} = 19{,}200$$

$$P_{roof} = [10 - (0.4)(2)](20 \times 12)^2 = \underline{530{,}000}$$

$$P_u = 584{,}200 \text{ lbs } (2.6 \times 10^6 \text{ N})$$

Take $p_t = 0.02$, $d/t = 0.85$, $e'/t = 0.10$ and go to Fig. 8-20(b).

$$p_t m = \frac{(0.02)(40{,}000)}{(0.85)(3750)} = 0.251$$

With the given values, read

$$P' = 0.8 = P_u / btf'_c$$

Set $b = t$ (square column) and solve for t.

$$t = \left[\frac{584{,}200}{(0.8)(3750)}\right]^{1/2} = 14 \text{ in } (35.6 \text{ cm})$$

(The same result can be achieved by solving the expression for $P' = 0.08$.) A 14-inch square column, then, would be satisfactory for the given conditions. It may be found desirable or convenient to choose the column dimensions the same as the width of the girders framing in (20 inches (50.8 cm) in this case). If so, the section could be recalculated with some savings in steel.

e. Other Considerations

Preceding paragraphs have summarized preliminary investigation of principal elements comprising typical aboveground rectangular structures. It will have been noted that the elements have all been proportioned on the basis of flexural strength. This is generally adequate up to this point since protective construction design methods and procedures (and those in conventional practice, as well) are strongly oriented toward assuring ductile behavior. Bending-axial force interaction has been introduced somewhat indirectly only in selection of a trial column section.

If the study objective was only to get a feel for the structural requirements for quick comparative purposes, the designer or analyst would be about ready at this point to move on to the next concept, threat spectrum, etc., except for consideration of radiation. Investigation of the incident radiation environment as per paragraph 6.8.1 for the given threat would reveal negligible radiation effects on structural strength.

(Similar results would be found for ground shock, crater ejecta and missiles.) Depending upon what was to be housed in the facility, however, radiation shielding requirements can cast the problem in an entirely different light. For example, if it were required that the facility protect personnel from residual radiation, investigation of the shielding requirements as per paragraph 6.8.3 would indicate required concrete thicknesses of about 20 inches (50 cm) rather than the nominal 7 inches (18 cm) required for structural strength.

If the study objective was to produce an actual facility design, the process has only barely begun. The trial sections selected have been on the basis of single modules and interior sections at that. A framing plan has to be chosen integrating the modules into a structural entity. As the individual elements are assembled, the assumed trial dimensions change somewhat, requiring reanalysis. During this iteration, one would begin to consider foundation requirements (assumption of a mat foundation equal to the roof is usually sufficient during the initial trial); dynamic reactions and shear capacity of the elements would be investigated; areas of probable large axial force would be investigated for possible effect on the moment capacity of the member; and the part played by the exterior walls in carrying horizontal loads by shear wall action would be considered. The structure would be reasonably completely defined at the end of this phase.

The next iteration would begin to consider the effects of structure motions and would employ more refined analytical techniques as warranted (the process has become one almost completely of analysis at this stage). The structure is sufficiently well defined by now so that rational assumptions can be made as to the

probable dominant modes of response. If equipment or personnel within the structure require protection from the motion environment, estimates of the probable response of the isolation system support points can begin to be made and suitable isolation system parameters selected. The effects of foundation motions combined with the airblast loading would be considered (see, e.g., paragraph 9.8.3). The direction of the process from this point forward will ordinarily be governed by the results of preceding steps and the primary objectives of the effort. Typically, following stages consist of revision and reanalysis until the designer or analyst has satisfied himself that all pertinent weapon effects and realistic possibilities have been considered and suitable provisions made therefor.

f. Summary

Typical situations encountered in the design and analysis of aboveground rectangular structures have been summarized and briefly illustrated above. In a broad sense, the primary considerations addressed above are applicable in general to all types of protective facilities.

It will have been observed that aboveground structure requirements in the threat range considered are overwhelmingly dictated by radiation shielding requirements if personnel or sensitive equipment are involved, i.e., a factor of 3 in thickness required. In addition, the severe loads imparted by reflected and dynamic pressures on objects which project up into the airblast wave should have been noticed (e.g., peak loads on the exterior wall as opposed to the roof). Finally, the interplay between free-field effects, structure geometry and interaction with the free-field environment and the resulting effect on structural response (which is common to all types of protective facilities) should have begun to become apparent.

11.2.2 Arches

Arches are somewhat more efficient in load-carrying capability than rectangular structures as has been mentioned previously. This can be attributed to geometry, both for more efficient response and for presenting less resistance to air flow than rectangular structures. The preceding statement applies to airblast loading perpendicular to the longitudinal axis of the arch; vertical endwalls, if provided, will be subjected to the same type loading as exterior walls of rectangular structures.

To illustrate some of the principles involved in arch response, let it be desired to make a quick estimate of the capability of a given aboveground arch structure to withstand the environment associated with the 35 psi (24.1 N/cm^2) incident peak overpressure contour from a 2kT (8.4 x 10^{12}J) surface burst. The pertinent parameters for the arch shell are (refer to Fig. 7-20):

R = 50 ft (15.2 m)	f'_c = 5375 psi (3710 N/cm^2)
t = 20 in (50.8 cm)	f_{dy} = 50,000 psi (34,500 N/cm^2)
d = 18 in (45.7 cm)	$\phi = \pi/3$
p = 0.01 (both faces)	w_c = 150 lb/ft^3 (0.024 N/cm^3)
p_t = 0.018	I = 402 in^4/in (16,730 cm^4/cm)

B = 86.6 ft (26.4 m)

$E_c = 3.99 \times 10^6$ psi (2.75×10^6 N/cm^2)

Hinged ends

a. Airblast Loading Parameters

Determine required free-field parameters from Section III. From Fig. 3-5,

1MT: i = 11.0 psi-sec (7.58 N-sec/cm^2)

t_o = 1.1 sec

With Eq. 3-2,

$$2kT:\ i = 11.0\left[\frac{0.002}{1}\right]^{1/3} = 1.39 \text{ psi-sec } (0.96 \text{ N-sec/cm}^2)$$

$$t_o = 1.1\left[\frac{0.002}{1}\right]^{1/3} = 0.139 \text{ sec}$$

The shock front velocity, U, from Fig. 3-11 is 1950 fps (594 mps), and the peak dynamic pressure, q_o, is 20 psi (13.8 N/cm^2) from Fig. 3-18.

Refer now to Fig. 7-21.

$\tau = B/U = 86.6/1950 = 0.044$ sec

$t_r = (1 - \phi/\pi)\tau = 0.030$ sec (compression)

$t_r = \tau/2 = 0.022$ sec (flexural)

$p_c = P_{so}$ = 35 psi (24.1 N/cm^2)

b. Arch Compression Mode

The compression mode natural frequency can be found with Eq. 9-181.

$$m = \frac{(20)(1)(1)(150)}{(1728)(386)} = 0.0045 \text{ lb-sec}^2/\text{in}^3 \ (0.0012\text{N-sec}^2/\text{cm}^3)$$

$$\omega_c = \frac{0.97}{600}\left[\frac{(3.99 \times 10^6)(20)(1)}{0.0045}\right]^{1/2} \approx 215 \text{ rad/sec}$$

$$T_c = 2\pi/\omega \approx 0.029 \text{ sec}$$

The resistance required in the compression mode for $t_r/T_c = 0.030/0.029 \approx 1.0$ from Fig. 9-11(a) with $\mu = 1$ is $R_m \approx 1.10P_o$, or about 38.5 psi (26.5 N/cm^2). The resistance provided in the compression mode can be estimated with Eq. 8-97 taking P_{max} from Eq. 8-17.

$$p_c\text{provided} = \frac{[(0.85)(5375) + (0.018)(50,000)](20)}{600}$$

$$= 182 \text{ psi } (125 \text{ N/cm}^2)$$

The arch section thus appears quite adequate in the compression mode on the basis of strength. Even for a zero rise time, the required resistance for elastic response would be only twice the applied peak pressure, or 70 psi (48.3 N/cm^2).

Check the section for buckling with Eq. 8-100 (hinged ends). For an aboveground arch,

$$(p_c)_{cr} = \frac{2}{3}\left[\frac{(3.99 \times 10^6)(402)}{(600)^3}\right]\left[(3)^2 - 1\right] = 39.6 \text{ psi } (27.3 \text{ N/cm}^2)$$

The performance of the section in the compression mode, then, is controlled more by stability than by strength.

c. Arch Flexural Mode

Estimate the natural frequency of the arch in the first antisymmetrical flexural mode with Eq. 9-182.

$\theta_o = 2\phi$

$S = 2\phi R = (2)(\pi/3)(600) = 1256$ in (3190 cm)

$N = 1$

parameter $\bar{n} = 2$

$$C_N^2 = \frac{(2)^4\pi^4\left[1 - \left(\frac{2\pi/3}{2\pi}\right)^2\right]^2}{1 + 3\left(\frac{2\pi/3}{2\pi}\right)^2} = 922 \qquad (9\text{-}183)$$

$C_N = 30.4$

mass $m = 0.0045$ lb-sec^2/in^3 (0.0012 N-sec^2/cm^3)

$$\omega_f = \frac{30.4}{(1256)^2}\left[\frac{(3.99 \times 10^6)(402)}{0.0045}\right]^{1/2} = 11.5 \text{ rad/sec}$$

$T_f = 2\pi/\omega = 0.546$ sec

The resistance required in the flexural mode for $t_r/T_f = 0.022/0.546 \sim 0.004$ is off the response chart of Fig. 9-11(a). Estimate the required resistance with Eq. 11-2 with $\mu = 3$ and the weapon overpressure impulse.

$$R_m \text{ required} = \frac{(1.39)(11.5)}{\sqrt{(2)(3) - 1}} = 7.1 \text{ psi } (4.9 \text{ N/cm}^2)$$

The resistance provided can be estimated with Eq. 8-98 with M_{max} from Eq. 8-53 ($\gamma = 3$)

$$p_f \text{ provided} = \frac{(8)(0.9)(0.01)(50{,}000)(18)^2}{[(\pi/3)(600)]^2}\left[\frac{(3)^2 - 1}{(3)^2}\right]$$

$$= 2.64 \text{ psi } (1.82 \text{ N/cm}^2)$$

On the basis of the preceding, then, the section is likely to suffer distress in the flexural mode (resistance required = 7.1 psi vs. 2.64 psi resistance provided). Resolving Eq. 11-2 with $R_m = 2.64$ psi indicates inelastic action would occur to the extent of μ equal to 18 or 19.

d. Radiation Effects

The first step in evaluating radiation effects on the arch and its contents is to define the free-field environment. From Fig. 3-14, 35 psi (24.1 N/cm^2) peak overpressure will occur at 550 ft (168 m) ground range from a 1kT (4.184 x 10^{12}j) surface burst. Using Eq. 3-1, the corresponding range for a 2kT (8.4 x 10^{12}j) surface burst is

$$R = \left(\frac{2}{1}\right)^{1/3}(550) = 692 \text{ ft } (211 \text{ m})$$

The initial gamma dose if found from Eq. 6-1.

$$\alpha = \left[1 + 6\left(\frac{0.002}{1}\right)^2\right] \Big/ \left[1 + 0.03\left(\frac{0.002}{1}\right)^2 + 0.005\left(\frac{0.002}{1}\right)^3\right]$$

$$= 1$$

$$\lambda = 1070 + 1.5\left[\frac{0.002}{1}\right]^2$$

$$= 1070 \text{ ft } (326 \text{ m})$$

It is seen from the above that small yield weapons have little influence on the parameters α and λ. The initial gamma dose is (for a fission yield of 2kT, i.e., $f = 1.0$)

$$D_\gamma = \frac{2}{3}\left\{7 \times 10^{13}(1.0)(1)\left[\left(\frac{0.002}{1}\right)\left(\frac{1}{692}\right)^2\right]\exp\left\{-\left(\frac{1.1}{1}\right)\left(\frac{692}{1}\right)\left(\frac{1}{1070}\right)\right\}\right\}$$

$$= 18.67 \times 10^4\ e^{-0.711}$$

$$= 9.16 \times 10^4 \text{ roentgens}$$

Note that the initial gamma dose has been reduced by a factor of 2/3 to account for the effect of a small yield surface burst and the density of air taken equal to 1.1gm per liter.

The integrated neutron flux is obtained from Eq. 6-2.

$$D_n = 2 \times 10^{22}\left[\frac{0.002}{1}\right]\left[\frac{1}{692}\right]^2 \exp\left[-\left(\frac{692}{1}\right)\left(\frac{1.1}{1}\right)\Big/780\right]$$

$$= 8.35 \times 10^{13}\ e^{-0.976}$$

$$= 3.15 \times 10^{13} \text{ n/cm}^2 = 7.87 \times 10^4 \text{ rad}$$

The X ray photon energy spectrum of the weapon must be known in order to estimate the X radiation environment at the arch. Since the energy spectrum is unspecified, a peak value of 1Mev is assumed for calculational purposes. At this photon energy level, Fig. 6-3 shows the mass absorption coefficient for both concrete and air to be equal to 0.063 cm^2/gm.

$$Y_r = 0.6(0.002) = 0.0012\text{MT}$$

and the X radiation intensity at the arch is obtained from Eq. 6-5.

$$P = 8 \times 10^3\left[\frac{0.0012}{1}\right]\left[\frac{1}{0.211}\right]^2\exp\left[-\left(\frac{0.063}{1}\right)\left(\frac{0.211}{1}\right)\left(\frac{1.1}{1}\right) \times 10^5\right]$$

$$\doteq 216.6\ e^{-1462} \sim 0$$

$$\sim 0$$

As may be seen, the X radiation is insignificant at the location of the arch.

Prediction of EMP field strength requires reference to classified sources. For calculational purposes herein, a peak intensity of 50,000 volts/meter is assumed.

The integrated thermal flux is obtained from Eq. 6-10 using a transmission factor of 1.

$$Q = 1.8 \times 10^4(1)\left[\frac{0.002}{1}\right]\left[\frac{1000}{692}\right]^2$$

$$= 75 \text{ cal/cm}^2 \ (315\text{j/cm}^2)$$

Residual gamma radiation at the range of the arch might be very high because of its close proximity to ground zero. Fallout will begin very early, so the decay of fission products will be much less than that at greater ground ranges. Wind direction will be a significant factor and could drastically alter the total dose. Since the 692 ft (211 m) range scaled to 1 MT is only

$$R = 692\left(\frac{1}{0.002}\right)^{1/3} = 5480 \text{ ft } (1670 \text{ m})$$

Figure 6-11 cannot be used to estimate the unit-time reference dose rate. A maximum value of 10,000 r/hr is selected as the unit-time reference dose rate. From Fig. 6-13, the dose rate 10 hours later is still

$$\text{Dose Rate} = 0.064(10{,}000) = 640 \text{ r/hr}$$

and the total dose of radiation accumulated over a 24 hr period is obtained from Fig. 6-14 as

$$\text{Dose} = 8.7 \times \text{1-hr ref dose} = 87{,}000 \text{ r}$$

This is the total dose accumulated by an exposed, unprotected item or person.

Except for X radiation, all of the above radiation environments represent significant threats to unprotected personnel or equipment. A rough approximation of the shielding effectiveness of the concrete arch can be obtained by neglecting the effect of the radiation source and arch geometry.

From Fig. 6-15, the dose transmission factor for 20 in (50.8 cm) of concrete is 0.075 for initial gamma. This would reduce the initial gamma dose inside the arch to

$$\text{Dose} = 0.075(9.16 \times 10^4) = 6{,}870 \text{ r (still a lethal dose)}$$

The 20 inches (50.8 cm) of concrete is a more effective shield for the lower energy residual gamma. From Fig. 6-16, the dose transmission factor is 0.0028. This would reduce the 24 hr accumulated dose within the arch to

$$\text{Dose} = 0.0028(87{,}000) = 244 \text{ r}$$

The tenth-value thickness of concrete for neutron shielding is approximately 10 in (25.4 cm). Thus, 20 in (50.8 cm) of concrete will attenuate the incident dose by a factor of 100. The neutron dose inside the arch would be

$$\text{Dose} = 0.01(7.87 \times 10^4) = 787 \text{ rad}$$

The 20 in (50.8 cm) of concrete will provide complete shielding from 75 cal/cm^2 of thermal radiation.

In order to evaluate the arch as an EMP shield, some assumptions must be made. It is assumed that the reinforcing steel is welded at all joints and intersections and that all openings are designed to avoid degradation of the effectiveness of the arch as an EMP shield. Let the length of the arch be 125 ft (38.1 m).

The aspect ratio of the arch is

$$\frac{H}{B} = \frac{25.0}{86.6} = 0.29$$

Its cross section area is approximately

$$A = \frac{120(3.14)(50)^2}{360} - \frac{86.6(25)}{2} = 1535 \text{ ft}^2 \ (142.6 \text{ m}^2)$$

An equivalent rectangular structure would be

72.8 ft (22.18 m) wide
21.1 ft (6.43 m) high

The length of 125 ft (38.1 m) would be the same for both the actual and the equivalent rectangular structure.

The total circumferential steel ratio p_t = 0.018 translates into 2.16 in^2/ft (0.457 cm^2/cm) of reinforcing in each face of the arch shell. It is assumed that a minimum steel ratio of 0.0025 is provided in the longitudinal direction. This translates into 0.6 in^2/ft (0.127 cm^2/cm) in the longitudinal direction. The longitudinal steel requirement could be satisfied by #7 bars at 12 in (30.48 cm) spacing. The circumferential requirement could be satisfied by #9 bars at 5.5 in (13.97 cm) spacing in each face. The different spacing and bar sizes in the two directions prohibits direct application of Fig. 6-17 and 6-19 for evaluating shield effectiveness. A conservative estimate of the attenuation will be obtained by assuming a 12 in x 12 in (30.48 cm x 30.48 cm) mesh of #7 bars. From Fig. 6-17 using the J = 60 ft (18.3 m) curve, the attenuation for a 14 in (35.56 cm) spacing of #14S bars is about 25.5dB. From Fig. 6-19, a 12 in x 12 in (30.48 cm x 30.48 cm) spacing of #7 bars results in an attenuation decrease of about 1.2dB. The net attenuation is

$$\text{Attenuation} = 25.5 - 1.2 = 24.3\text{dB}$$

A 5.5 in x 5.5 in (13.97 cm x 13.97 cm) spacing of #7 bars would increase the attenuation by 11dB, and the total would be

$$\text{Attenuation} = 25.5 + 11 = 36.5\text{dB}$$

The EMP shielding provided by the given structure, then, probably lies somewhere between 24 and 36dB. According to Fig. 6-25, additional shielding would be necessary if EMP-sensitive equipment were to be housed in the arch.

11.2.3 Domes

Domes can be one of the most efficient structural shapes in terms of load-carrying capability. For comparative purposes, a preliminary section for a reinforced concrete dome to resist the airblast loading given in the preceding paragraph for the arch will be investigated (i.e., 35 psi (24.1 N/cm^2) from a 2kT (8.4 x 10^{12}j) surface burst). Assume the following values for the dome.

R = 50 ft (15.2 m)

E_c = 3.99 x 10^6 psi (2.75 x 10^6 N/cm^2)

f'_{dc} = 5375 psi (3710 N/cm^2)

f_{dy} = 50,000 psi (34,500 N/cm^2)

ϕ = $\pi/3$

w_c = 150 lb/ft^3 (0.024 N/cm^3)

B = 86.6 ft (26.4 m)

The airblast loading parameters are essentially the same as those determined in the preceding paragraph for the arch, i.e., (refer to Fig. 7-21)

U = 1950 fps (594 mps)

τ = D/U = 86.6/1950 = 0.044 sec

t_r = 0.030 sec (compression)

t_r = 0.022 sec (flexural)

p_c = 35 psi (24.1 N/cm^2)

Based on the slope of the tangent to the dome at the springline, the reflection factor from Fig. 7-4 is about 3 for α = 30° and P_{so} = 35 psi. P_{im} for the 120° dome, then, would be about 105/sin60° = 121 psi (83.6 N/cm^2). The peak value of the drag component, P_{dm}, is only about 0.8 psi (0.6 N/cm^2) and is so small with respect to P_{im} that this loading component can be neglected.

From Eq. 8-162, the thrust per unit width due to the uniform compression load component is

$$T_\alpha = T_0 = \frac{p_c R}{2} = \frac{35(600)}{2}$$

$$= 10{,}500 \text{ lb/in } (18{,}375 \text{ N/cm}^2)$$

The maximum thrust due to the flexural component is given by Eqs. 8-103 and 8-104.

$$\text{Max } T_\alpha = \frac{121(600)}{3}\left[\frac{(2 + 0.5)(1 - 0.5)(0.5)}{(1 + 0.5)(0.866)}\right]$$

$$= 11{,}640 \text{ lb/in } (20{,}370 \text{ N/cm})$$

$$\text{Max } T_0 = \frac{121(600)}{3}\left\{\frac{[3 + (4)(0.5) + (2)(0.5)^2](1 - 0.5)}{(1 + 0.5)(0.866)}\right\}$$

$$= 51{,}230 \text{ lb/in } (89{,}650 \text{ N/cm})$$

Taking p = 0.0025 in each direction in each face of the dome shell, Eq. 8-17 can be written

$$h = \frac{T_{max}}{(0.85f'_c + p_t f_y)}$$

$$h = \frac{10{,}500}{(0.85)(5375) + 0.005(50{,}000)}$$

$$= 2.2 \text{ in } (5.6 \text{ cm}) \text{ (compression)}$$

$$h = \frac{51{,}230}{0.85(5375) + 0.005(50{,}000)}$$

$$= 10.6 \text{ in } (26.9 \text{ cm}) \text{ (flexure)}$$

The total thickness required for both components is

$$2.2 + 10.6 = 12.8 \text{ say } 13.0 \text{ in } (33.0 \text{ cm})$$

The buckling strength is given by Eq. 8-111 using a reduction factor of 2/3.

$$P_{cr} = \frac{2}{3}\left[\frac{1.2E_c h^2}{R^2}\right] = \frac{2}{3}\left[\frac{1.2(3.99 \times 10^6)(13)^2}{(600)^2}\right]$$

$$= 1498 \text{ psi } (1032 \text{ N/cm}^2)$$

The natural frequency of the dome is given by Eq. 9-192.

$$\omega_N = \sqrt{\frac{2E}{\rho(1 - \nu)R^2}}$$

where

$$\rho = \frac{150}{1728(386)} = 0.00022 \frac{\text{lb-sec}^2}{\text{in}} \; (0.00039 \text{ N-sec}^2\text{/cm})$$

Taking $\nu = 0.1$,

$$\omega_N = \sqrt{\frac{2(3.99 \times 10^6)}{0.00022(1 - 0.1)(600)^2}} = 335 \text{ rad/sec}$$

$$T_N = \frac{2\pi}{\omega_N} = \frac{6.28}{335} = 0.019 \text{ sec}$$

Assume $t_o = 2t_r$ and use Fig. 9-12.

$$\frac{t_o}{T_N} = 3.2 \text{ for uniform compression load}$$

$$\frac{t_o}{T_N} = 2.3 \text{ for flexural component}$$

From Fig. 9-12 assuming a ductility ratio of 1.5,

$$\frac{R_m}{F_o} = 0.97 \text{ for compression}$$

$$\frac{R_m}{F_o} = 0.89 \text{ for flexure}$$

Since $R_m/F_o = 1$ was assumed for the initial sizing of the shell thickness, it is slightly overdesigned. However, in view of the increase in R_m/F_o with increasing t_o/T_N shown in Fig. 9-12 and the approximation of the actual load function as a symmetric triangular pulse, the trial thickness will not be reduced.

Check the shear strength of the shell at the springline. The shear capacity is given by Eq. 8-32.

$$V_{uc} = bd[1.9f'_c + 2500\rho dV'/M']$$

Since it is assumed that bending moments in the shell are small, take

$$\frac{V'}{M'} d = 1.0$$

Also assume $d = 0.85h = 0.85(13.0) = 11.1$ in (28.2 cm). Then, the shear resistance provided is

$$V_{uc_1} = 11.1(1)[1.9\sqrt{5375} + 2500(0.0025)(1)]$$

$$= 11.1[139 + 6.25]$$

$$= 1612 \text{ lb/in } (2821 \text{ N/cm})$$

The maximum shear force is given by Eq. 8-105.

$$\text{Max } T_{\alpha 0} = \frac{121(600)}{3}\left[\frac{(2 + 0.5)(1 - 0.5)}{(1 + 0.5)(0.866)}\right]$$

$$= 23{,}280 \text{ lbs/in } (40{,}740 \text{ N/cm})$$

Since the shearing force exceeds the shear capacity, shear reinforcing must be added to the section. The excess shear is

$$V_{us} = 23,280 - 1612 = 21,668 \text{ lbs } (96,300 \text{ N})$$

From Eq. 8-36, the required area of shear reinforcing is

$$A_v = \frac{V_{us}}{f_y} = \frac{21,668}{(50,000)}$$

$$= 0.039 \text{ in}^2/\text{in } (0.099 \text{ cm}^2/\text{cm})$$

$$= 0.468 \text{ in}^2/\text{ft } (\#6 \text{ @ } 12 \text{ in would give } 0.44 \text{ in}^2/\text{ft})$$

As may be seen, then, a dome with about a 13-inch (33 cm) shell will provide about the same blast resistance as a 20-inch (50.8 cm) arch shell for the threat condition investigated. As is frequently found to be the case with aboveground structures, radiation shielding requirements rather than blast resistance could control the required shell thickness in this particular instance.

11.3 SHALLOW BURIED STRUCTURES

Shallow buried structures as a class can be designed to withstand much more severe incident nuclear weapon effect environments than can aboveground structures. This is due largely to being located out of the direct airblast wave and the avoidance of the reflected and dynamic pressure loads. Consequently, it will be found that the design threat places the shallow buried structure considerably closer to the point of detonation. This results in higher incident overpressures, more severe ground shock and crater effects, and greater radiation intensities than were found for aboveground structures. Another difference that will be found is that the surrounding soil can lend some additional strength to the buried structure under certain conditions. The primary differences between

aboveground and buried structures are that the nature of the loads will be different and that the response of the buried structure will be different due to its interaction with the surrounding soil medium.

11.3.1 Rectangular Structures

Assume that a certain facility must be located so that it will be subjected to 100 psi (68.9 N/cm^2) peak overpressure from a 1 MT (4.2 x 10^{15} j) surface burst. It has been decided to place the facility underground so that the minimum depth of cover over any portion of the structure is 8 feet (2.44 m). Functional requirements of the facility require that the structure be approximately 20 feet by 20 feet (6.1m x 6.1m) in plan dimensions. The facility will be constructed at a site where the soil is a dry alluvium whose unit weight is 115 pcf (18,075 N/m^3) and the coefficient of lateral earth pressure is 0.5.

For purposes of design, assume the following material properties

f'_{dc} = 5375 psi (3706 N/cm^2)

f_{dy} = 50,000 psi (34,474 N/cm^2)

E_c = 3.99 x 10^6 psi (2.75 x 10^6 N/cm^2)

Only the roof of the structure will be considered for this example. In order to obtain a trial section, it is assumed that there is no attenuation or modification of the pressure wave acting on the ground surface as it is transmitted through the soil to the roof of the structure. From Fig. 3-10, the durations of the effective triangular representations of the 100 psi (68.9 N/cm^2) overpressure-time curves are

t_{oo} = 0.12 sec $\quad$ t_{50} = 0.22 sec $\quad$ t_i = 0.37 sec

The roof slab can be treated as a square two-way slab fixed at all four edges. It is also assumed that the ultimate moment capacity at the center of the slab and its supports is equal in both directions. From Eq. 8-56, the required ultimate moment capacity is

$$M_{sc} = \frac{w\alpha^2 L^2}{6\gamma_{34}^2}\left[\sqrt{3 + \gamma_c\left(\frac{\alpha\gamma_{12}}{\gamma_{34}}\right)^2} - \frac{\alpha\gamma_{12}\sqrt{\gamma_c}}{\gamma_{34}}\right]^2$$

For the assumed slab geometry and ratios of moment capacities,

$$\alpha = 1 = \gamma_c$$

$$\gamma_{12} = \gamma_{34} = 2\sqrt{2}$$

If a dynamic load factor (DLF) of 1 is assumed for the first trial,

$$w = P_{so} = 100 \text{ psi } (68.9 \text{ N/cm}^2)$$

Substituting in Eq. 8-56,

$$M_{sc} = \frac{100(1)^2(20 \times 12)^2}{6(2\sqrt{2})}\left[\sqrt{3 + 1\left(\frac{(1)(2\sqrt{2})}{(2\sqrt{2})}\right)^2} - \frac{1(2\sqrt{2})\sqrt{1}}{2\sqrt{2}}\right]^2$$

$$= 339{,}462 \text{ in-lb/in } (1{,}509{,}900 \text{ cm-N/cm})$$

With a tensile steel ratio, $p = 0.02$ and $f_{dy} = 50{,}000$ psi (34,474 N/cm^2), the required effective depth of the slab can be obtained from Eq. 8-53.

$$d = \sqrt{\frac{M_{sc}}{0.9pf_y}} = \sqrt{\frac{339{,}462}{(0.9)(0.02)(50{,}000)}}$$

$$= 19.42 \text{ say } 19.5 \text{ in. } (49.5 \text{ cm})$$

The natural period of the slab in its fundamental mode of vibration can be obtained from Eq. 9-34 using transformation factors and spring constant from Table 9-7. From this table, $K_{LM} = 0.67$ and $k = 252\ EI/L^2$. The moment of inertia of the slab cross section is obtained from Eq. 8-30.

$$I = \frac{bd^3}{2}(5.5p + 0.083) = \frac{1(19.5)^3}{2}(5.5 \times 0.02 + 0.083)$$

$$= 715.6 \text{ in}^4\text{/in } (11{,}727 \text{ cm}^4\text{/cm})$$

The total mass of the roof slab is based on a total thickness of 22 in (55.9 cm).

$$M_t = \frac{150(20)(20)(22)}{386(12)} = 285\frac{\text{lb-sec}^2}{\text{in}} \qquad (49{,}895\text{kg})$$

and the natural period is

$$T_N = 6.28\sqrt{\frac{0.67(285)(240)^2}{252(3.99 \times 10^6)(715.6)}}$$

$$= 0.0246 \text{ sec}$$

The period of the slab will be increased by the mass of soil cover. Since the depth of cover is less than one-half the span, it is possible that all of it may vibrate with the roof slab. The total mass of soil is

$$M_t' = \frac{8(20)(20)(115)}{386} = 953.4\frac{\text{lb-sec}^2}{\text{in}} \qquad (166{,}900\text{kg})$$

The modified period of the slab is given by

$$T_N' = \sqrt{\frac{M_t + M_t'}{M_t}}\,T_N = \left[\frac{285 + 953.4}{285}\right]^{1/2}(0.0246) = 0.040 \text{ sec}$$

Allow inelastic action to the extent indicated by $\mu = 3$. With a natural period of 0.04 second, peak response of the section is likely to occur early in the loading history. Choose t_{oo} as the duration of the equivalent triangular pressure pulse (ref. paragraph 3.2.4). For $t_o/T_N = 0.12/0.04 = 3$ and $\mu = 3$, the DLF (R_m/P_o) from Fig. 9-9(a) is about 1.05. From Fig. 9-9(b), $t_m \approx 0.32t_o = 0.038$ second, indicating that t_{oo} is adequate as an effective duration. The required maximum resistance is

$$R_m \text{ required} = 1.05(100) = 105 \text{ psi} \quad (72.4 \text{ N/cm}^2)$$

The required moment capacity becomes

$$M_u = 1.05(339,462) = 356,435 \text{ in-lb/in } (1,585,500 \text{ cm-N/cm})$$

and for p = 0.02, the required effective depth is

$$d = \sqrt{\frac{356,435}{(0.9)(0.02)(50,000)}} = 19.9 \text{ say } 20.0 \text{ in } (50.8 \text{ cm})$$

Repeating the previous calculations for the new depth of 20.0 in (50.8 cm), the new period of vibration is found to be 0.050 sec. A recheck of the DLF in Fig. 9-9 shows that the design is adequate for preliminary considerations. The total thickness of the slab would be on the order of 23 inches (58.4 cm) to provide steel cover.

A more detailed analysis of the loads acting on the roof would be made using the procedures outlined in Section VII for a final design. See paragraph 7.6.1 for more detailed load and structure motion determination for this example structure.

11.3.2 Arches

For purposes of comparing structural efficiency, assume that a 180-degree arch with the same cross section has been selected for the facility considered above. With all material properties remaining the same, the arch should offer a much larger resistance to the airblast induced ground shock.

The arch analysis can proceed in several ways and be based on different assumptions. The following analysis presents two possible approaches. One assumes that the 180° arch can be treated as a half cylinder subjected to the load shown in Fig. 8-25.

It is assumed that $\bar{P}_o$ in Fig. 8-25 is equal to the peak vertical stress in the soil. For $K_o = 0.5$ it is determined that $\beta = 3$ (Eq. 8-96). For $\beta = 3$,

$$q = 3\bar{p}$$

and $\bar{P}_o = p_v = q + \bar{p} = 4\bar{p}$

Using Eqs. 8-74 and 8-76, the maximum combination of moment and thrust will occur at the springline of the arch ($\theta = 90°$).

$$P_0 = -qR - \frac{\bar{p}R}{3} = -3\bar{p}(120) - \bar{p}\,\frac{(120)}{3}$$

$$= -400\bar{p} \text{ (compression)}$$

$$M_0 = \frac{\bar{p}R^2}{3} = \bar{p}\,\frac{(120)^2}{3}$$

$$= 4800\bar{p}$$

The eccentricity of the load is

$$e' = \frac{M_0}{P_0} = \frac{4800\bar{p}}{400\bar{p}} = 12 \text{ in } (30.5 \text{ cm})$$

and $\frac{e'}{t} = \frac{12}{23} = 0.52.$

For the given section,

$$p_t = \frac{A_s}{bt} = \frac{0.04(1)(20)}{1(23)} = 0.0348$$

$$m = \frac{f_{dy}}{0.85f'_{dc}} = \frac{50,000}{0.85(5375)} = 10.94$$

and $p_t m = 0.0348(10.94) = 0.381$ say 0.4

$$bt^2 f'_{dc} = 1(23)^2(5375) = 2,840,000 \text{ in-lb/in } (1.96 \times 10^6 \text{ cm-N/cm})$$

Entering Fig. 8-20(b), the intersection of the line $e'/t = 0.52$ and the curve $p_t m = 0.4$ gives $\Gamma' = 0.225$. Thus,

$$M_{max} = 4800\bar{p} = 0.225(bt^2 f'_c) = 0.225\ (2,840,000)$$

$$= 639,000 \text{ in-lb/in.} (2,842,000 \text{ cm-N/cm})$$

or

$$\bar{p} = 133 \text{ psi } (91.8 \text{ N/cm}^2)$$

Then

$$p_v = 4\bar{p} = 4(133) = 532 \text{ psi } (367 \text{ N/cm}^2)$$

A second approach is to use the equations of paragraph 8.12.2 to calculate thrust and moment at the springline ($\theta = 90°$).

$$P_\theta = p_v R(K_o \cos^2\theta + \sin^2\theta) = p_v(120)(1) = 120p_v$$

$$M_\theta = 0.25p_v R^2(1 - K_o)\cos 2\theta = 0.25p_v(120)^2(0.5)(-1) = 1800p_v$$

The eccentricity is

$$e' = \frac{M_\theta}{P_\theta} = \frac{1800p_v}{120p_v} = 15 \text{ in } (38.1 \text{ cm})$$

and $\frac{e'}{t} = \frac{15}{23} = 0.65$.

Entering Fig. 8-20(b), the intersection of the line $e'/t = 0.65$ and the curve $p_t m = 0.4$ occurs at $\Gamma' = 0.225$. Thus,

$$M_\theta = 1800p_v = 0.225bt^2f'_c = 0.225\ (2{,}840{,}000)$$

$$= 639{,}000 \text{ in-lb/in } (2{,}842{,}000 \text{ cm-N/cm})$$

or

$$p_v = 355 \text{ psi } (245 \text{ N/cm}^2)$$

It is obvious from the preceding arch calculations that the load resistance of arch elements is very sensitive to the assumed distribution of load acting on the element. Such results are expected and the objective of the analysis, e.g., design or target analysis will normally determine the approach chosen. Both of the above solutions assume that the arch foundations are allowed some lateral motion so that some adjustment in the imposed loads is possible.

The dynamic loading effect on arch resistance will now be checked as in the case of the flat slab. In the high overpressure region, the airblast wave is moving at very high velocities and the airblast induced ground shock wave is nearly horizontal. For this direction of loading, the most probable mode of deformation of the arch is that of the first symmetrical flexural mode (see Fig. 9-32). The frequency of vibration of the arch in this mode is given by Eqs. 9-182 and 9-185. From Eq. 9-185,

$$C_n = \sqrt{\frac{\bar{m}^4\pi^4\left[1 - \left(\frac{\theta_o}{\bar{m}\pi}\right)^2\right]^2}{1 + \frac{1}{\bar{m}^2} + 2\left(\frac{\theta_o}{\bar{m}\pi}\right)^2}}$$

$$= \sqrt{\frac{(3 \times 3.14)^4\left[1 - \left(\frac{1}{3}\right)^2\right]^2}{1 + \frac{1}{9} + 2\left(\frac{1}{3}\right)^2}} = \sqrt{4677}$$

$$= 68.4$$

From Eq. 9-182,

$$\omega_N = \frac{C_N}{S^2}\sqrt{\frac{EI}{m}}$$

where

$$S = \pi R = 3.14(120) = 376.8 \text{ in } (9.57 \text{ m})$$

$$I = \frac{bd^3}{2}(5.5p + 0.083) = \frac{1(20.0)^3}{2}[5.5(0.02) + 0.083)]$$

$$= 772 \text{ in}^4\text{/in } (12{,}650 \text{ cm}^4\text{/cm})$$

$$m = \frac{150(1)(23)(1)}{386(1728)} = 0.0052 \text{ lb-sec}^2/\text{in}^2 \text{ (0.910 kg/cm)}$$

$$\omega_N = \frac{68.4}{(376.8)^2}\sqrt{\frac{3.99 \times 10^6(772)}{0.0052}}$$

$$= 371 \text{ rad/sec} = 59.0 \text{ Hz}$$

The natural period in this mode is

$$T_N = \frac{1}{f} = \frac{1}{59.0} = 0.017 \text{ sec}$$

The period of vibration of the arch will be increased somewhat by the added mass of soil cover. The amount of soil which vibrates with the arch is uncertain but should not exceed 0.5 to 1.0 times the span of the structure. Reference 8-2 suggests that the effect of soil mass be neglected since in some instances the surrounding soil also acts to stiffen the arch structure. In order to demonstrate the procedure, the soil will be included here. For a minimum depth of cover of 8 feet (2.44 m), the average depth of cover can be calculated as

$$H_{avg} = \frac{(8 + R)2R - \pi R^2/2}{2R}$$

$$= \frac{(8 + 10)(2)(10) - 3.14(10)^2/2}{20}$$

$$= 10.15 \text{ ft (3.09 m)}$$

Distributing this mass of soil along the circumference of the arch, it is found that

$$m' = \frac{10.15(115)(20)}{144(386)} = 0.42 \text{ lb-sec}^2/\text{in}^2 \text{ (29 kg/cm)}$$

and the modified period is

$$T'_N = \sqrt{\frac{m' + m}{m}}\; T_N = \left[\frac{0.42 + 0.0052}{0.0052}\right]^{1/2}(0.017)$$

$$= 0.154 \text{ sec}$$

Using $t_{oo} = 0.12$ sec as the load duration, $t_o/T_N = 0.78$. For $\mu = 3$, a DLF of 0.75 is obtained from Fig. 9-9(a) and $t_m \approx 0.102$ from Fig. 9-9(b). On this basis, the dynamic resistance provided could be estimated as

$$R_m = \frac{532}{0.75} = 709 \text{ psi (489 N/cm}^2\text{) for sinusoidal load distribution}$$

$$R_m = \frac{355}{0.75} = 473 \text{ psi (326 N/cm}^2\text{) for } p_h = 0.5p_v$$

The time of peak response is indicated to occur fairly late with respect to the t_{oo} equivalent duration (0.102 vs 0.12 sec). Repeating the above calculations with an effective duration of $t_{50} = 0.22$ sec results in

$$t_o/T_N = 0.22/0.154 = 1.4$$

$$DLF = R_m/F_o = 0.9 \text{ (Fig. 9-9(a) with } \mu = 3)$$

$$t_m = (0.56)(0.22) = 0.123 \text{ (Fig. 9-9(b))}$$

$$R_m = 532/0.90 = 591 \text{ psi (408 N/cm}^2\text{) for sinusoidal load}$$

$$R_m = 355/0.90 = 394 \text{ psi (272 N/cm}^2\text{) for } K_o \text{ load}$$

Based on the preceding simplified procedures, then, it is seen that an arch section of the proportions of the nominal 100 psi (68.9 N/cm^2) slab could be expected to resist 350 to 700 psi (241 to 483 N/cm^2) for the conditions investigated.

11.3.3 Domes

A shallow buried reinforced concrete dome of the same cross section as the preceding slab and arch should prove stronger than either. Although the dome would require a diameter greater than 20 ft (6.1 m) to provide the same floor area of a 20 ft x 20 ft (6.1 m x 6.1 m) rectangular structure, a 20-foot diameter is used for comparative purposes. It is assumed that the dome is hemispherical, i.e., $\phi = 90$ degrees.

Experimental or theoretical information which might form a basis for specifying load distribution on buried domes is practically nonexistent. For purposes of analysis herein, it is assumed that the buried dome will be subjected to both flexural and uniform components of airblast induced ground shock. The relative magnitude of these two components will be determined from the relationship

$$p_h = K_o p_v$$

It is assumed that the dome is subjected to a uniform compressive load equal to p_v plus a flexural component equal to the difference between the vertical and horizontal stresses, i.e.,

$$p_c = p_v$$

$$p_f = K_o p_v = 0.5 p_v$$

Two approaches are possible in analyzing the given dome's resistance to these components of load. One uses Eqs. 8-103 through 8-105 and the interaction curves of Fig. 8-20, the other uses Eqs. 8-107 and 8-109. The latter approach is used in these calculations. Equations 8-107 and 8-109 can be written in the form

$$h_c = \frac{p_c R}{(1.7f'_{dc} + 2p_t f_{dy})} = \frac{p_v R}{(1.7f'_{dc} + 2p_t f_{dy})}$$

$$h_f = \frac{p_f R}{(0.85f'_{dc} + p_t f_{dy})} = \frac{0.5 p_v R}{(0.85f'_{dc} + p_t f_{dy})}$$

The sum of these two thicknesses gives the total thickness required to resist both components of load.

$$h_t = h_c + h_f = \frac{p_v R}{(0.85f'_{dc} + p_t f_{dy})} \qquad (\text{for } K_o = 0.5)$$

Rearranging terms and substituting specified values of the dome cross section, it is found that

$$p_v = \frac{h_t(0.85f'_{dc} + p_t f_{dy})}{R} = 23\left[\frac{0.85(5375) + 0.0348(50{,}000)}{120}\right]$$

$$= \frac{23(6309)}{120} = 1209 \text{ psi } (834 \text{ N/cm}^2)$$

The frequency of vibration of the dome in the uniform radial mode is given by Eq. 9-192.

$$\omega_N = \sqrt{\frac{2E}{\rho(1-\nu)R^2}} = \sqrt{\frac{2(3.99 \times 10^6)}{0.00021(1-0.1)(120)^2}}$$

$$= 1712 \text{ rad/sec} = 273 \text{ Hz}$$

The period of vibration is

$$T_N = \frac{1}{f} = \frac{1}{273} = 0.004 \text{ sec}$$

The mass contribution of the soil cover is

$$m' = \frac{\left[(3.14)(10)^2(8+10) - \frac{4}{6}(3.14)(10)^3\right]115}{386(2)(3.14)(120)^2}$$

$$= 0.0117 \frac{\text{lb sec}^2}{\text{in}^3} \ (0.318 \text{ kg/cm}^2)$$

and for the concrete shell

$$m = \frac{23(1)(1)(150)}{1728(386)} = 0.0052 \frac{\text{lb-sec}^2}{\text{in}^3} \ (0.142 \text{ kg/cm}^2)$$

The modified period of vibration of the dome is

$$T'_N = \sqrt{\frac{m+m'}{m}}\, T_N = \left[\frac{0.0052 + 0.0117}{0.0052}\right]^{1/2}(0.004)$$

$$= 0.007 \text{ sec}$$

Taking t_{oo} as the effective duration and $\mu = 1.5$ leads to

$$t_o/T_N = 0.12/0.007 = 17.1$$

$$R_m/F_o = 1.5 \qquad \text{(Fig. 9-9(a))}$$

$$t_m \approx (0.04)(0.12) = 0.005 \text{ sec} \qquad \text{(Fig. 9-9(b))}$$

Using t_{oo} as the effective duration appears appropriate and the dynamic resistance provided would be estimated at

$$R_m = \frac{1209}{1.5} = 806 \text{ psi } (556 \text{ N/cm}^2)$$

As expected, then, the dome has considerably more load-carrying capability than either the flat slab or arch sections.

11.3.4 Horizontal Cylinders

Consider a 16-foot (4.88 m) inside diameter reinforced concrete tunnel located so that it may be subjected to 200 psi (138 N/cm^2) peak overpressure from a 1 MT (4.2 x 10^{15} j) surface burst. A radiation shielding analysis has indicated that a depth of cover of 9 feet (2.74 m) over the crown is required to reduce the initial nuclear radiation to an acceptable level. The tunnel will be located in a soil with a seismic velocity of 1000 fps (305 mps) and a coefficient of lateral earth pressure, $K_o = 0.25$.

The tunnel is buried less than one diameter, so neglect any beneficial arching effects. Also, neglect any attenuation in peak pressure with depth for purposes of this investigation (see paragraph 5.7.3 for a procedure for estimating peak pressure attenuation with depth). Assume a loading such as shown in Fig. 8-25 for design. For $K_o = 0.25$, $\beta = 5/3$ from Eq. 8-96; allow inelastic action to the extent indicated by $\mu = 3$ and anticipate that the load duration will be long with respect to the natural period of the section. To get started, provide a static resistance based on Eq. 11-1, i.e.,

$$R_m = 200\left[\frac{1}{1 - 1/(2)(3)}\right] = 240 \text{ psi } (165.5 \text{ N/cm}^2)$$

Take

$$f'_{dc} = 5375 \text{ psi } (3710 \text{ N/cm}^2)$$

$$f_{dy} = 50{,}000 \text{ psi } (34{,}500 \text{ N/cm}^2)$$

Solve Eq. 8-90 for d with $\bar{P}_o = 240$ psi and $R = 96$ in (2.44 m).

$$d = \frac{\bar{P}_o(87{,}000 + f_{dy})(R)(3\beta + 1)}{2.2f'_{dc}(87{,}000)(\beta + 1)}$$

$$d = \frac{(240)(87{,}000 + 50{,}000)(96)[(3)(5/3) + 1]}{(2.2)(5375)(87{,}000)[(5/3) + 1]}$$

$$d = 6.9 \text{ say } 7 \text{ in } (17.8 \text{ cm})$$

Select $t = 9$ in (22.9 cm) which makes $R = 100.5$ in (2.55 m).

The applied thrust and moment with $\bar{P}_o = 240$ psi (165.5 N/cm^2) are

$$P_{max} = \left(\frac{\bar{P}_oR}{3}\right)\left(\frac{3\beta + 1}{\beta + 1}\right) = \left[\frac{(240)(100.5)}{3}\right]\left[\frac{3(5/3) + 1}{(5/3) + 1}\right]$$

$$= 18{,}090 \text{ lb/in } (31{,}680 \text{ N/cm})$$

$$M_{max} = \frac{\bar{P}_oR^2}{3(\beta + 1)} = \frac{(240)(100.5)^2}{3[5/3) + 1]}$$

$$= 303{,}000 \text{ in-lb/in } (1.35 \times 10^6 \text{ cm-N/cm})$$

A corresponding eccentricity is

$$e' = \frac{M_{max}}{P_{max}} = \frac{303{,}000}{18{,}090} = 16.75 \text{ in } (42.5 \text{ cm})$$

For the trial section, $d/t = 7/9 = 0.78 \approx 0.80$, and $e'/t = 16.75/9 = 1.86$. Take $p_t = 0.035$; then,

$$p_t m = \frac{p_t f_{dy}}{0.85 f'_{dc}} = \frac{(0.035)(50{,}000)}{(0.85)(5375)} = 0.383$$

At the intersection of the lines $e'/t = 1.86$ and $p_t m = 0.38$ in Fig. 8-20(a),

$$\Gamma = 0.08 \text{ and } \Gamma' = 0.14$$

The resistance provided by the trial section is

$$P = \Gamma b t f'_{dc} = (0.08)(1)(9)(5375)$$

$$= 3870 \text{ lb/in } (6780 \text{ N/cm}) \quad < 18{,}090 \text{ lb/in req'd}$$

$$M = \Gamma' b t^2 f'_{dc} = (0.14)(1)(9)^2(5375)$$

$$= 60{,}950 \text{ in-lb/in } (271{,}000 \text{ cm-N/cm})$$

$$< 303{,}000 \text{ in-lb/in req'd}$$

The initial trial section thus appears quite deficient. Estimate a new thickness based on the applied moment calculated above. Keep $p_t m = 0.38$ and choose $\Gamma' = 0.20$ in Fig. 8-20(a).

$$t = \sqrt{\frac{M_{max}}{\Gamma' b f'_{dc}}} = \sqrt{\frac{303{,}000}{(0.20)(1)(5375)}}$$

$$= 16.8 \text{ say } 17 \text{ in } (43.2 \text{ cm})$$

Set the effective depth at 13.5 in (34.3 cm) which results in $d/t = 0.80$. The radius R becomes 96 + 8.5 = 104.5 in (265 cm). Recalculate the applied thrust and moment.

$$P_{max} = \left[\frac{(240)(104.5)}{3}\right]\left[\frac{3(5/3) + 1}{(5/3) + 1}\right]$$

$$= 18{,}810 \text{ lb/in } (32{,}940 \text{ N/cm})$$

$$M_{max} = \frac{(240)(104.5)^2}{3[(5/3) + 1]}$$

$$= 327{,}600 \text{ in-lb/in } (1.46 \times 10^6 \text{ cm-N/cm})$$

The corresponding eccentricity is

$$e' = \frac{327{,}600}{18{,}810} = 17.4 \text{ in } (44.2 \text{ cm})$$

and $e'/t = 17.4/17 = 1.02$. At the intersection of the e'/t and $p_t m$ lines in Fig. 8-20(a),

$$\Gamma = 0.16 \quad \text{and} \quad \Gamma' = 0.165$$

The resistances provided by the new trial section are

$$P = (0.16)(1)(17)(5375) = 14{,}620 \text{ lb/in } (25{,}600 \text{ N/cm})$$

$$M = (0.165)(1)(17)^2(5375) = 256{,}300 \text{ in-lb/in}$$

$$(1.14 \times 10^6 \text{ cm-N/cm})$$

The new trial section still appears deficient. Take t = 18 in (45.7 cm) and d = 15.25 in (38.7 cm) resulting in $d/t = 0.85$. Repeating the preceding calculations,

$$\text{Required } P_{max} = 18{,}900 \text{ lb/in } (33{,}100 \text{ N/cm})$$

$$\text{Required } M_{max} = 330{,}740 \text{ in-lb/in } (1.47 \times 10^6 \text{ cm-N/cm})$$

$$e' = 330{,}740/18{,}900 = 17.5 \text{ in } (44.4 \text{ cm})$$

$$e'/t = 17.5/18 \approx 0.97$$

$$\Gamma = 0.19 \text{ (Fig. 8-20(b) for } p_t m = 0.038)$$

$$\Gamma' = 0.193 \text{ (Fig. 8-20(b) for } p_t m = 0.038)$$

$$P \text{ provided} = (0.19)(1)(18)(5375) = 18{,}380 \text{ lb/in } (32{,}200 \text{ N/cm})$$

$$M \text{ provided} = (0.193)(1)(18)^2(5375) = 336{,}100 \text{ in-lb/in}$$

$$(1.5 \times 10^6 \text{ cm-N/cm})$$

This trial section appears reasonably adequate. Check the dynamic resistance provided.

As mentioned in a previous paragraph on the buried arch, there is reason to believe that the effect of the surrounding soil on the natural period may essentially cancel itself out due to increasing the stiffness of the section as well as adding to its mass. The phenomenon appears even more complex for a buried cylinder than for an arch in that gravity should tend to work against any mass of soil on the lower half responding with the cylinder. Accordingly, neglect the effect of the surrounding soil and estimate the natural frequency of the tunnel section with Table 9-12(e) in the flexural mode with n = 2.

$$\omega_n = \sqrt{\frac{EgI}{\gamma AR^4}\left[\frac{n^2(n^2-1)^2}{n^2+1}\right]}$$

$E = 3.99 \times 10^6$ psi $(2.75 \times 10^6\ N/cm^2)$

$g = 386\ in/sec^2\ (9.80\ m/sec^2)$

$\gamma = 0.0868\ lb/in^3\ (0.0236\ N/cm^3)$

$A = 18\ in^2\ (116\ cm^2)$

$R = 105$ in (2.67 m)

$A_{st} = p_t bt = (0.0345)(1)(18) = 0.621\ in^2\ (4.01\ cm^2)$

$p = 0.5A_{st}/bd = (0.5)(0.621)/(1)(15.25) = 0.02$

$I = 0.5bd^3(5.5p + 0.083) = (0.5)(1)(15.25)^3[(5.5)(0.02) + 0.083] = 342\ in^4/in\ (5,600\ cm^4/cm)$

$\omega_n = 141$ rad/sec = 22.5 Hz

$T_N = 1/f = 1/22.5 = 0.044$ sec

The equivalent zero rise time triangles for a 1 MT $(4.2 \times 10^{15}$ j) surface burst at the 200 psi $(138\ N/cm^2)$ peak overpressure contour from Fig. 3-10 are

$t_{oo} = 0.045$ sec $t_{50} = 0.11$ sec $t_i = 0.27$ sec

As indicated earlier, peak pressure attenuation with depth has been neglected for a tunnel buried this shallow.

The rise time of the pressure pulse may have some effect, however. As indicated in paragraph 7.3.4, it appears reasonable to estimate the rise time on the basis of the 9-foot (2.74 m) depth of cover. For soil, $C_L \approx 0.5C$ and for the given soil,

$$t_r = \frac{9}{C_L} - \frac{9}{C} = \frac{9}{500} - \frac{9}{1000} = 0.009 \text{ sec}$$

If the pressure pulse of Fig. 9-11 were assumed,

$t_r/T_N = 0.009/0.044 = 0.20$

$R_m/F_o = 1.18$ (for $\mu = 3$)

$t_m = (3.3)(0.009) = 0.030$ sec

Assuming a zero rise time and $t_o = t_{oo}$ in Fig. 9-9,

$t_o/T_N = 0.045/0.044 = 1.02$

$R_m/F_o = 0.83$ (for $\mu = 3$)

$t_m = (0.7)(0.045) = 0.032$ sec

Assuming a zero rise time and $t_o = t_{50}$ in Fig. 9-9,

$t_o/T_N = 0.11/0.044 = 2.5$

$R_m/F_o = 1.02$ (for $\mu = 3$)

$t_m = (0.37)(0.11) = 0.041$ sec

Assuming the zero rise time and $t_o = t_{oo}$ does not appear too reasonable since the estimated rise time is about 0.009/0.045 = 20 percent of the assumed duration. Similarly, the finite rise time and non-decaying peak pressure (Fig. 9-11) is not too realistic. The overpressure pulse duration for a 1 MT surface burst and 200 psi from Fig. 3-5 is $t_o = 0.92$ second. As may be seen in Fig. 3-7, the incident overpressure has begun to decay quite rapidly at $t = 0.01t_o = 0.009$ sec (which happens to coincide with the rise time in this example). Accordingly, it appears safe to assume that the required dynamic resistance lies somewhere between $1.02P_o = 204$ psi ($141\ N/cm^2$) and $1.18P_o = 236$ psi ($163\ N/cm^2$). As will be recalled, the resistance provided is about 240 psi. The last trial section, then, could be considered satisfactory for the intended purpose. See paragraph 7.6.2 for estimated vertical motions of this example structure.

11.3.5 Vertical Cylinders

Consider a requirement for a missile launch tube to be located to withstand the environment associated with a peak incident overpressure of 70 psi ($48.3\ N/cm^2$) from a 1 MT (4.2×10^{15} j) surface burst. The required inside diameter for the tube is 6 feet (1.83 m). Further, the tube cannot be allowed to deflect more than 1/1000 of the inside diameter or the missile might be damaged. It has been determined that the soil at the intended site has a coefficient of lateral earth pressure $K_o = 0.75$. An estimate of the feasibility of the requirement is desired.

The maximum deflection requirement of $0.001 \times 72 = 0.072$ in (1.83 mm) will very likely preclude the allowance of any inelastic action. Equation 11-1 with $\mu = 1$ indicates a dynamic resistance of $2P_o = 140$ psi ($96.5\ N/cm^2$) might be required. Assume the load function shown in Fig. 8-25. For $K_o = 0.75$, $\beta = 7$ from Eq. 8-96. Try a steel material with a Young's modulus of 2.9×10^7 psi ($2.0 \times 10^7\ N/cm^2$) and a dynamic yield stress of 50,000 psi ($34{,}500\ N/cm^2$). For $\bar{P}_o = 140$ psi and $\beta = 7$, $q = 122.5$ psi ($84.5\ N/cm^2$) and $\bar{p} = 17.5$ psi ($12.1\ N/cm^2$).

As discussed in paragraph 8.9.3, buckling of steel rings, particularly under nonuniform loads, is more likely to control the section proportions than strength considerations. For the given conditions, the parameter $\bar{P}_o/E = 140/2.9 \times 10^7 = 4.8 \times 10^{-6}$. Enter Fig. 8-26 with this value of $\bar{P}_o/E$ and find $R/t = 11$ for $\beta = 8$ (≈ 7).

$$R = R_i + t/2 = (36 + t/2) \text{ in}$$

$$\frac{R}{t} = \frac{36 + t/2}{t} = 11$$

$$t = 3.42 \text{ say } 3.50 \text{ in } (8.89 \text{ cm})$$

$$R = 36 + 1.75 = 37.75 \text{ in } (95.9 \text{ cm})$$

$$R/c = 37.75/1.75 = 21.6 > 10 \text{ and } K \approx 1 \text{ (Table 8-3)}$$

Estimate the probable peak deflection with Eq. 8-81.

$$\delta_{max} = \frac{\bar{p}R}{3}\left[\frac{1}{q_{cr} - q}\right]$$

$$q_{cr} = 3EI/R^3$$

$$I = bt^3/12 = (1)(3.5)^3/12 = 3.57 \text{ in}^4/\text{in } (58.5 \text{ cm}^4/\text{cm})$$

$$q_{cr} = (3)(2.9 \times 10^7)(3.57)/(37.75)^3 = 5770 \text{ psi } (3980\ N/cm^2)$$

$$\delta_{max} = \frac{(17.5)(37.75)}{3}\left[\frac{1}{5770 - 122.5}\right] = 0.039 \text{ in } (0.99 \text{ mm})$$

The trial section selected on the basis of stability thus appears quite adequate in terms of the maximum deflection requirement. The peak stress to be expected can be estimated with Eq. 8-83.

$$\sigma_{max} = K\left[2\bar{p}\left(\frac{R}{t}\right)^2 + \left(q + \frac{\bar{p}}{3}\right)\left(\frac{R}{t}\right)\right]$$

$$= 1\left[(2)(17.5)\left(\frac{37.75}{3.5}\right)^2 + \left(122.5 + \frac{17.5}{3}\right)\left(\frac{37.75}{3.5}\right)\right]$$

$$= 5460 \text{ psi } (3760\ N/cm^2)$$

The required dynamic resistance can be checked as was done for the horizontal cylinder in the preceding paragraph. It will be found that the DLF (R_m/F_o) is indeed 2.0 for elastic response for any of the simplified pulse shapes one chooses to assume, i.e., setting $\bar{P} = 140$ psi ($96.5\ N/cm^2$)

is valid. The feasibility of satisfying the stipulated requirement at this point, therefore, would appear to hinge primarily on the practicality of fabricating the proposed tube out of 3.5-inch (8.89-cm) steel plate.

The section could obviously be much lighter except for the possibility of buckling. Three possibilities to reduce the buckling problem which come readily to mind are: (1) A deeper hollow or composite steel section. (2) A reinforced concrete tube. (3) Limiting the magnitude of $\bar{P}_o$ applied to the section by surrounding the tube with a crushable backpacking. If the investigation were to be continued from this point, it would be appropriate to begin to define the expected loads more precisely as described in Sections V and VII and to employ more sophisticated analytical procedures than the simplified methods illustrated above.

11.4 DEEP UNDERGROUND STRUCTURES

The nuclear weapon effects of primary importance in considering deep underground structures will be cratering, ground shock and EMP. In designing a deep facility to survive a nuclear burst directly above it, the installation must be well outside the crater rupture zone and also be at a range where the ground shock environment can be resisted with practicable structural systems. At such depths, ample shielding for all radiation effects except EMP is provided by the earth medium. Airblast effects are somewhat meaningless with the burst point essentially directly overhead. The possibility of occurrence of block motions (large relative displacements along joint or fracture planes) is far less likely for deep underground facilities than would be the case when considering facilities located near the surface in a rock medium.

One must keep in mind, however, that the preceding remarks are applicable primarily only to the core of the deeply buried installation. To be useable, the core must have means of entrance and exit, communications links, life support system, and so on. A deep underground facility as a total system, therefore, will necessarily involve shallow buried, and possibly aboveground, structural systems as well as those deeply buried.

11.4.1 Unlined Tunnels

As has been mentioned previously, deep underground facilities are almost invariably located in rock. Rock in itself can be a very competent structural material provided it is reasonably free of major shear or fault zones and joint patterns. The range at which an unlined tunnel or cavity can be expected to survive a given threat by virtue of the inherent strength of the rock medium itself is always of interest when considering a deep underground installation. For example, it is obvious that multiple entrances and exits will be necessary to provide balanced survivability of the total system by redundancy and dispersion against large yield weapon threats. Making maximum possible use of unlined tunnels in such cases can result in considerable savings in the total system cost.

Let it be desired to estimate the range at which an unlined cylindrical tunnel would survive large yield contact surface bursts. Combining Eqs. 5-65 and 7-56, one may write

$$c = \frac{25\text{fps}}{C_L}\left[\frac{W}{1\text{MT}}\right]^{2/3}\left[\frac{1000\text{ft}}{R}\right]^2 \qquad \text{(English)}$$

$$= \frac{27.3\text{mps}}{C_L}\left[\frac{W}{10^{15}\text{j}}\right]^{2/3}\left[\frac{100\text{m}}{R}\right]^2 \qquad \text{(SI)}$$

Consider a granite medium characterized by a seismic velocity, C, of 18,000 fps (549 mps); a specific gravity of 2.65; a Young's modulus of 10 x 10^6 psi (6.9 x 10^6 N/cm^2); an unconfined compressive strength of 25,000 psi (17,200 N/cm^2); and a modulus of rupture of 2500 psi (1720 N/cm^2).

It can be assumed that a cylindrical unlined cavity will survive in the free-field strain environment associated with the modulus of rupture tensile strength of the rock (i.e., the maximum tensile stress concentration factor is one for $M = 0$ in Fig. 7-49 for a circular inclusion). A reasonable value for the allowable tensile strain for the rock described above would be $\varepsilon = 0.0005$. With this strain and $C_L = 0.75C = 13{,}500$ fps (4110 mps) for hard rock, the preceding equation can be solved for the survival range, R.

$$R = 1920\ \text{ft}\left[\frac{W}{1\text{MT}}\right]^{1/3} \qquad \text{(English)}$$

$$= 365\ \text{m}\left[\frac{W}{10^{15}\text{J}}\right]^{1/3} \qquad \text{(SI)}$$

To get an idea of the effect of the rock medium on the survival range for unlined tunnels, consider a limestone with a seismic velocity of 12,000 fps (3660 mps); specific gravity of 2.35; Young's modulus of 6×10^6 psi (4.1×10^6 N/cm^2); unconfined compressive strength of 15,000 psi (10,300 N/cm^2); and a modulus of rupture of 1500 psi (1030 N/cm^2). A reasonable value for the modulus of rupture tensile strain for this rock would be 0.0003. As before, with $C_L = (0.75)(12{,}000) = 9000$ fps (2740 mps) and $\varepsilon = 0.0003$,

$$R = 3040\ \text{ft}\left[\frac{W}{1\text{MT}}\right]^{1/3} \qquad \text{(English)}$$

$$= 579\ \text{m}\left[\frac{W}{1\text{MT}}\right]^{1/3} \qquad \text{(SI)}$$

The expressions above illustrate a method by which survival ranges for a cylindrical unlined tunnel can be estimated as a function of contact surface burst yield. Other burst conditions and inclusion shapes can be treated in basically the same fashion incorporating the appropriate yield equivalance and stress concentration factors as described in Sections V and VII. See paragraph 7.6.3 for illustration of a procedure for estimating motions of a deep underground unlined tunnel section.

11.4.2 Integral Liners

Let it be desired to estimate the environment in terms of free-field stress that a given integral liner can be expected to survive. The liner is constructed in rock and is a composite of steel plate and concrete. The inner radius of the concrete liner is 7.0 feet (2.13 m) and it has a thickness of 24 inches (60.96 cm). The inner steel plate liner has a thickness of 1 inch. The concrete, rock and steel properties are as follows:

$E_c = 5 \times 10^6$ psi (3.45×10^6 N/cm^2)

$E_r = 10 \times 10^6$ psi (6.9×10^6 N/cm^2)

$f'_c = 5000$ psi (3447 N/cm^2)

$\sigma_{ur} = 25{,}000$ psi (17,200 N/cm^2)

$f_y = 40{,}000$ psi (27,580 N/cm^2)

Poissons Ratio for concrete $= \nu_c = 0.1$

Poissons Ratio for rock $= \nu_r = 0.15$

$k_{sc} = 4$

$k_{sr} = 8$

The uniform pressure exerted by the steel liner against the inner surface of the concrete is calculated from Eq. 8-116.

$$\sigma_{ra} = \frac{h_s f_y}{r_a} = \frac{1.0(40{,}000)}{(84)}$$

$$= 476.2\ \text{psi}\ (328.3\ \text{N/cm}^2)$$

The elastic stress factor is calculated from Eq. 8-118.

$$S = \frac{E_c \varepsilon_0}{1 - \nu_c^2} - \left[\frac{1 - 2\nu_c}{1 - \nu_c}\right]\sigma_r$$

The circumferential strain and radial stress are assumed to be equal in the steel and concrete liners at their interface. A circumferential strain of 0.01 is assumed to be reasonable for the steel liner. Substituting in the preceding equation,

$$S = \left[\frac{5 \times 10^6(0.01)}{1 - (0.1)^2}\right] - \left[\frac{1 - 2(0.1)}{1 - 0.1}\right]476.2$$

$$= 50{,}081 \text{ psi } (34{,}530 \text{ N/cm}^2)$$

The inelastic stress factor is obtained from Eq. 8-119.

$$Y = \sigma_u + (k_s - 1)\sigma_r$$

For the concrete liner, σ_u is taken equal to f'_c and

$$Y = 5000 + (4-1)(476.2)$$

$$= 6429 \text{ psi } (4432 \text{ N/cm}^2)$$

Since S is greater than Y, the concrete is in a plastic condition at its inner radius. The radius to the point at which the concrete is elastic is obtained from Eq. 8-122.

$$\frac{r_c}{r} = \left[\frac{S}{Y}\right]^{\frac{1}{k_s + 1}} = \left[\frac{50{,}081}{6429}\right]^{\frac{1}{5}}$$

or r_c $1.51r = 1.51(84) = 126.7$ in (3.22 m)

Since the outer radius of the concrete is 108 in (2.74 m), the entire thickness of concrete is in a plastic condition.

The inelastic stress factor at the outer radius of the concrete is found from Eq. 8-121.

$$Y = Y_1\left(\frac{r}{r_1}\right)^{k_s - 1} = 6429\left(\frac{108}{84}\right)^3$$

$$= 13{,}664 \text{ psi } (9420 \text{ N/cm}^2)$$

The radial stress at the concrete-rock interface is obtained from Eq. 8-119.

$$\sigma_r = \frac{Y - \sigma_u}{k_s - 1} = \frac{13{,}664 - 5000}{3}$$

$$= 2888 \text{ psi } (1991 \text{ N/cm}^2)$$

The elastic stress factor at the concrete-rock interface is calculated from Eq. 8-120.

$$S = S_1\left(\frac{r_1}{r}\right)^2 = 50{,}081\left(\frac{84}{108}\right)^2$$

$$= 30{,}296 \text{ psi } (20{,}388 \text{ N/cm}^2)$$

The circumferential strain is calculated from Eq. 8-125.

$$\epsilon_\theta = \frac{1 - \nu_c^2}{E_c}\left[S + \left(\frac{1 - 2\nu_c}{1 - \nu_c}\right)\sigma_r\right] = \frac{1 - (0.1)^2}{5 \times 10^6}\left[30{,}296 + \left(\frac{1 - 0.2}{1 - 0.1}\right)2888\right]$$

$$= 0.0065$$

The circumferential strain and radial stress in the rock and concrete are assumed to be equal at their interface. Relate these stresses and strains to free field rock stresses away from the tunnel. The initial steps of the stress analysis in the rock are similar to those for concrete. The elastic stress factor is calculated from Eq. 8-118.

$$S = \frac{E_r\epsilon_\theta}{1 - \nu_r^2} - \left[\frac{1 - 2\nu_r}{1 - \nu_r}\right]\sigma_r$$

$$= \frac{10 \times 10^6(0.0065)}{1 - (0.15)^2} - \left[\frac{1 - 0.30}{1 - 0.15}\right]2888$$

$$= 64{,}117 \text{ psi } (44{,}208 \text{ N/cm}^2)$$

The inelastic stress factor is obtained from Eq. 8-119.

$$Y = \sigma_{ur} + (k_{sr} - 1)\sigma_r = 25{,}000 + 7(2888)$$

$$= 45{,}216 \text{ psi } (31{,}176 \text{ N/cm}^2)$$

As in the case of the concrete, the elastic stress factor is greater than the inelastic factor so the rock at the concrete-rock interface is in a plastic condition. The boundary between the elastic and inelastic regions is computed from Eq. 8-122.

$$\frac{r_e}{r} = \left[\frac{S}{Y}\right]^{\frac{1}{k_{sr}+1}} = \left[\frac{64,117}{45,216}\right]^{\frac{1}{9}}$$

or $r_e = 1.04r = 1.04(108) = 112.3$ in $= 9.36$ ft (2.85 m)

At this range, the elastic stress factor is given by Eq. 8-120.

$$S = S_1\left(\frac{r_1}{r_e}\right)^2 = 64,117\left(\frac{108}{112.3}\right)^2$$

$$= 59,300 \text{ psi } (40,886 \text{ N/cm}^2)$$

At the boundary between the elastic and plastic regions $S = Y$, and the free field stress corresponding to the assumed liner conditions is obtained from Eq. 8-124.

$$p_o = K_{fr}Y^{\left(\frac{2}{k_{sr}+1}\right)}S^{\left(\frac{k_{sr}-1}{k_{sr}+1}\right)} - \left(\frac{\sigma_{ur}}{k_{sr}-1}\right)$$

$$= 0.643(59,300)^{0.222}(59,300)^{0.777} - \frac{25,000}{7}$$

$$= 34,140 \text{ psi } (23,540 \text{ N/cm}^2)$$

Thus for the specified liner and rock properties, the liner is capable of withstanding free field rock stresses of approximately 34,140 psi (23,540 N/cm^2).

11.4.3 Backpacked Structures

Preliminary trial sections for reinforced concrete and steel liners surrounded by crushable backpacking were selected in paragraph 8.12.3 for the rock medium depicted in Fig. 8-32. Estimate the ranges from large yield surface bursts at which these structural systems will (1) be expected to survive and (2) probably be collapsed.

Equation 5-56 can be written in the form

$$v = A \text{ fps}\left[\frac{W}{1MT}\right]^{2/3}\left[\frac{1000\text{ft}}{R}\right]^2$$

where A is a coefficient depending on the type of burst. Combining with Eq. 7-56 and solving for R,

$$R = 1000\left[\frac{A}{\iota C_L}\right]^{1/2}\left[\frac{W}{1MT}\right]^{1/3} \text{ft}$$

$$= 189\left[\frac{A}{\iota C_L}\right]^{1/2}\left[\frac{W}{10^{15}j}\right]^{1/3} \text{m}$$

The desired ranges can be estimated with the preceding equation, provided appropriate values for A, ι and C_L are selected.

A reasonable value for the seismic velocity of the rock in this example would be 18,000 fps (5490 mps). For hard rock,

$$C_L = 0.75C = (0.75)(18,000) = 13,500 \text{ fps } (4115 \text{ mps})$$

Properly designed backpacked liners can be expected to survive a free-field strain environment of about one-half the ultimate strain of the rock associated with an unconfined compressive test, provided allowance is made for stress (strain) concentration at the inclusion. Choose a compressive stress concentration factor of 3 for a circular inclusion (Fig. 7-49) and estimate the ultimate strain of the given rock at 0.01. On this basis, a value for the free-field strain associated with survival of the backpacked liners becomes

$$\epsilon_s = \frac{1}{2} \times \frac{1}{3} \times 0.01 = 0.00167$$

The value of Λ for a contact surface burst is 25 fps (7.62 mps) as indicated in Eq. 5-65. For a slightly buried burst and a yield equivalence of 0.16 from Table 5-8, an appropriate value for Λ is 60 fps (18.3 mps). The estimated survival ranges thus become

$$R_s = 1000\left[\frac{25}{(0.00167)(13,500)}\right]^{1/2}\left[\frac{W}{1MT}\right]^{1/3}$$

$$= 1053\left[\frac{W}{1MT}\right]^{1/3} ft = 199\left[\frac{W}{10^{15} j}\right]^{1/3} m \qquad \text{(contact)}$$

$$R_s = 1000\left[\frac{60}{(0.00167)(13,500)}\right]^{1/2}\left[\frac{W}{1MT}\right]^{1/3}$$

$$= 1630\left[\frac{W}{1MT}\right]^{1/3} ft = 308\left[\frac{W}{10^{15} j}\right]^{1/3} m \qquad \text{(slightly buried)}$$

It can be assumed that no structural system yet devised will survive an environment where the free-field rock strain is on the order of the ultimate compressive strain capacity of the rock, i.e., $\epsilon_c = 0.01$ for this example. The ranges at which the liners will very probably be collapsed, then, are

$$R_c = 1000\left[\frac{25}{(0.01)(13,500)}\right]^{1/2}\left[\frac{W}{1MT}\right]^{1/3}$$

$$= 430\left[\frac{W}{1MT}\right]^{1/3} ft = 81.3\left[\frac{W}{10^{15} j}\right]^{1/3}_{.} m \qquad \text{(contact)}$$

$$R_c = 1000\left[\frac{60}{(0.001)(13,500)}\right]^{1/2}\left[\frac{W}{1MT}\right]^{1/3}$$

$$= 667\left[\frac{W}{1MT}\right]^{1/3} ft = 176\left[\frac{W}{10^{15} j}\right]^{1/3} m \qquad \text{(slightly buried)}$$

The simplified expressions above illustrate to some extent the effect of type of burst on potential damage

levels for deep underground structures. The contact burst expressions in conjunction with the first unlined cavity example of paragraph 11.4.1 (which assumed a similar rock formation) can also be useful in furnishing insight as to where lined and unlined cavities begin to become appropriate when considering a total deep underground facility system. As was pointed out in paragraph 11.4.1, the basic expressions of this paragraph can also be used for other rock media and/or burst conditions with appropriate adjustment of the parameters involved.

11.5 AUXILIARY SYSTEMS

This paragraph deals with auxiliary systems which are an important part of all types of protective structures and which can sometimes become a weak link in an otherwise satisfactory system. Structural design or analysis of auxiliary systems is accomplished using the appropriate techniques described in preceding sections. Only special requirements or unusual features are discussed below.

11.5.1 Air Entrainment Systems

A supply of clean air in adequate quantities is usually an essential part of a protective structure. There are two general approaches to providing this supply, self-contained systems or fresh air ventilation systems. The self-contained systems are similar to those provided for submarines. Provision of outside air requires special treatment to assure that airblast and other harmful nuclear weapon effects are kept out of the protected area. The problems related to designing air entrainment systems are largely a function of the peak overpressures incident on openings at the ground surface. The intake and exhaust openings must be designed to remain intact under all predicted conditions of airblast and ground shock and prevent entry of pressure or debris into the structure. It may be necessary in some instances to design a special structure to prevent crater ejecta from blocking the openings.

Harmful overpressures must be prevented from entering those parts of the structure wich contain personnel or sensitive equipment. This can be accomplished by an appropriately designed air entrainment system or blast valves or both. Blast valves are normally in an open position and can be closed by remote sensing devices or by direct action of the blast wave in the duct. Regardless of the method of actuation, each valve requires a finite period of time to close the duct. This delay time is a characteristic of the valve design. The importance of this delay will depend on how large an increase in pressure it will allow inside the facility. One solution to the delay problem is to actuate the valve with a sensor installed in the duct at some distance upstream from the valve. This distance should be larger than the distance the blast wave will travel in the duct in the time required to close the valve. If the valve is installed at the end of a duct, it must be designed to withstand a peak reflected pressure which is a function of the overpressure at that point. If the blast wave passes a blast valve installed in the sidewall of the duct and subsequently reflects from some other surface within the duct, it may still subject the valve to a higher pressure at later times.

Various treatments of duct walls have been suggested to increase attenuation of blast waves entering the entrainment system, and some have proven effective. Such treatments also increase friction losses in the system, however. Many ventilation systems include filters to prevent entry of dust or other contaminants. In these installations, the filters must be protected or the airblast

resistance of these filters may determine the allowable peak pressure in the air entrainment system. Elementary principles for treatment of air entrainment systems will be summarized in following paragraphs.

When an airblast wave impinges on a duct or tunnel entrance, a new wave front forms inside the entrance and propagates down the passage. The relationship between peak pressures in the incident blast wave and the new wave inside the duct depends on the orientation of the duct axis with respect to the incident wave and on the form and extent of the area surrounding the entrance. Figure 11-1 shows the effect of angle of incidence on peak pressures inside a tunnel or duct for a wide range of peak overpressures and is based upon experimental data from several sources.

a. Side-on Orientation

The side-on orientation shown in case 1 of Fig. 11-1 corresponds to a 90-degree angle of incidence with the duct axis. As the blast wave traverses the entrance, it expands or diffracts into the opening causing some turbulence and multiple reflections near the entrance. A single shock will normally reform within a distance of 5-10 tunnel diameters from the entrance. Curve 1 in Fig. 11-1 shows the variation of maximum peak overpressure inside the tunnel or duct as a function of incident peak overpressure and is based upon data reported in Ref. 11-1. As might be expected for the side-on case, the interior peak pressures are lower than those incident on the tunnel entrance.

Most of the data used in the referenced study are for a shock wave of constant pressure, and the relationship shown in Fig. 11-1 is applicable only if the positive phase duration, t_o, of the incident wave satisfies the condition

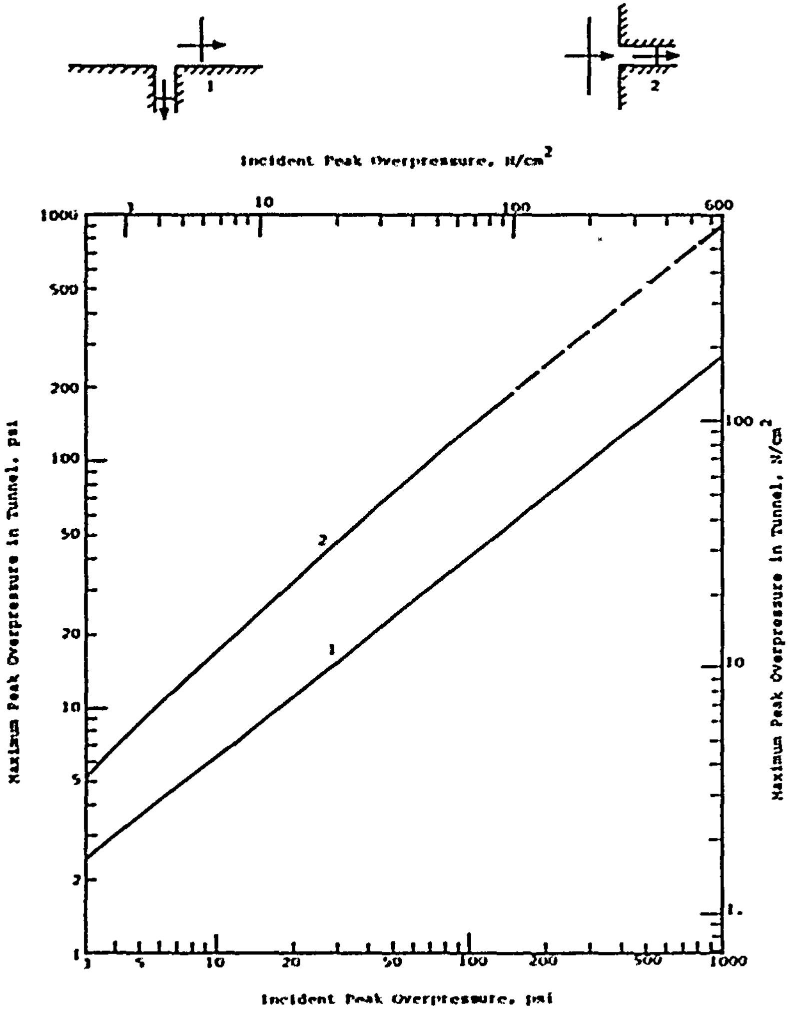

Figure 11-1 Maximum Peak Overpressure in a Tunnel or Duct vs. Incident Peak Overpressure for Two Angles of Incidence (Ref. 11-1)

$$t_o \geq \frac{25\,D}{c_o} \qquad (11\text{-}3)$$

where

D = tunnel diameter

c_o = ambient sound velocity

If the duration is less than that given by Eq. 11-3, the peak pressures inside the tunnel will be less than those given in Fig. 11-1.

b. Face-on Orientation

The face-on orientation shown in case 2 of Fig. 11-1 corresponds to a 0-degree angle of incidence with the duct axis. In this case, the surface geometry at the entrance exerts an important influence on blast pressures in the passage. Figure 11-2 shows the effect of the radius of the surface at the entrance to the radius of the opening on peak pressures inside the tunnel. For the case where the radius of the surface is equal to the radius of the tunnel, the peak pressure inside the tunnel is equal to the incident peak pressure. This might correspond to a duct protruding from the face of a cliff. At the other extreme, if the surface area at the entrance is sufficiently large, the peak overpressure inside the passage will be higher than that in the incident wave due to the reflection process at this surface. Curve 2 in Fig. 11-1 shows the variation of peak overpressure inside the duct with incident peak overpressure and assumes the entrance is surrounded by a large, smooth reflecting surface normal to the axis of the duct. This relationship is applicable only if the distance from the edge of the entrance to the edge of the reflecting surface is at least two duct diameters. Any rigid surface

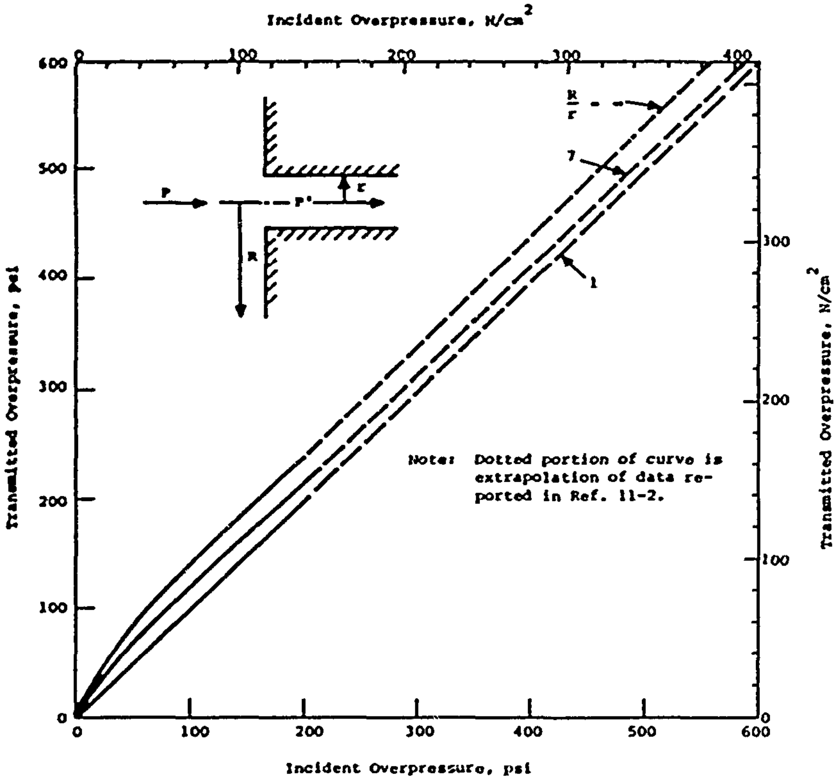

Figure 11-2 Incident Blast Overpressure vs. Transmitted Blast Overpressure for a Face-on Tunnel with Various Baffle-Tunnel Radii Ratios (Ref. 11-2)

capable of withstanding the reflected pressure can be considered an adequate reflecting surface, and unless it has a roughness with perturbations comparable in size to the duct diameter, it can be considered smooth. The duration condition given by Eq. 11-3 also applies. If the minimum reflecting surface size and duration criteria are not met, pressures inside the passage will be less than those given by Fig. 11-1. The dashed portion of curve number 2 represents an extrapolation of experimental data. For angles of incidence between zero and 90 degrees, values of peak overpressure can be obtained by interpolation between curves 1 and 2 of Fig. 11-1.

c. Overpressure Attenuation in Straight Tunnels or Ducts

Within a distance of 5 to 10 diameters from the entrance, a new shock front forms, and the maximum peak overpressure will occur at or near this point. As the blast wave moves through a straight passage, the peak overpressure decreases due to friction and viscosity effects and one-dimensional expansion of the wave. From Ref. 11-3, the rate of decrease is given by

$$\Delta P_{21} = \Delta x (P_{21} - 1)\left[\frac{RS}{777A}\left(\frac{P_{21}}{6 + P_{21}}\right)^{1/2} + \frac{K}{\bar{t}_i}\right] \qquad (11\text{-}4)$$

where

Δx = increment of length of tunnel or duct

P_{21} = ratio of shock pressure to ambient pressure

$$= \frac{P_{so} + P_o}{P_o}$$

R = roughness factor for tunnel = $(1 + 2\iota C)^2$

c = mean height of protuberances per unit length

C = mean number of protuberances per unit length

S = perimeter of tunnel or duct cross section

A = area of tunnel or duct cross section

$K = \frac{1}{U} - \frac{1}{u_o + c_1}$

c_1 = sound velocity behind the shock front

$$= c_o\left[P_{21}\left(\frac{6 + P_{21}}{1 + 6P_{21}}\right)\right]^{1/2}$$

U = shock front velocity (Fig. 3-11)

u_o = particle velocity behind the shock front (Eq. 3-7)

$\bar{t}_1$ = average time intercept

$$= t_{io} + \frac{\Delta x}{4}\left(\frac{1}{c_o} - \frac{1}{U}\right)$$

t_{io} = time intercept at beginning of increment Δx

For concrete surfaces, a roughness factor, R, of 2 is suggested. For smooth ducts, R = 1. The initial time intercept, t_{io}, can be taken equal to t_{oo} from Fig. 3-10.

The attenuation of peak overpressure in a tunnel or duct is obtained from Eq. 11-4 by a series of successive calculations using a value of Δx that results in a value of ΔP_{21} less than 5 percent of P_{21}. Shorter intervals are time consuming, unless the equation is programmed for computer solution, and longer intervals result in inaccuracies. Each ΔP_{21} is subtracted from the preceding P_{21} in order to obtain a new P_{21} for the next interval. After each interval, a time increment of

$$\Delta t = \frac{\Delta x}{4}\left(\frac{1}{c_o} - \frac{1}{U}\right) \qquad (11\text{-}5)$$

is added to the average time intercept, $\bar{t}_1$, for that interval to obtain a new time intercept, t_{io}, for the following interval. If the overpressure attenuation is to be calculated in a straight section following a bend or junction, the peak overpressure is first reduced in accordance with procedures described below. It is assumed that the bends or junctions do not change the time intercept of the wave entering these sections. Each bend or junction will decrease the peak overpressure in the blast wave. Experimental studies have provided some data as to the magnitude of these decreases.

d. 90-Degree Bends

If the radius of curvature of the bend is greater than 5 times the duct diameter, it can be assumed that the decrease in peak overpressure due to the bend is negligible (Ref. 11-2). Reference 11-4 indicates that each sharp 90-degree bend in a duct will reduce the peak overpressure by about 6 percent. Since the effect of radius of curvature has not been determined, it will be assumed that this reduction applies to all bends whose radius of curvature is less than 5 times the duct diameter. The effect of n bends, then, is

$$P_n = P_{so}(0.94)^n \qquad (11\text{-}6)$$

where

P_n = peak overpressure in the tunnel after n 90-degree bends

P_{so} = peak overpressure in the tunnel just ahead of the first bend

n = number of 90-degree bends

Equation 11-6 neglects losses due to friction or pressure attenuation between bends. The minimum duration condition of Eq. 11-3 also applies, and it is assumed that there is no change in tunnel cross section in the bend.

e. T-Shaped Junctions

There are two cases for this type of intersection, and peak overpressures will depend upon the direction in which the blast wave enters the intersection. Figure 11-3 shows the variation of peak overpressures in the remaining two branches of the intersection as a function of peak overpressure entering the intersection. The minimum duration condition of Eq. 11-3 applies, and it is assumed that the three branches have equal cross sectional areas. If a side tunnel is much smaller than the tunnel through which the blast wave is moving, case 1 of Fig. 11-1 can be used to obtain an estimate of the peak overpressure in the side tunnel. The dashed portions of the curves shown in Fig. 11-3 represent extrapolations of the experimental data, which is shown by the solid portions of the curves.

f. Other Junctions

Figures 11-4 and 11-5 show incident versus transmitted peak overpressures for Y and X cross sections. It is assumed that all tunnel branches have the same cross section area and that the duration condition of Eq. 11-3 is satisfied.

g. Area Increases in Tunnels or Ducts

A blast wave passing through an area increase in a tunnel undergoes a decrease in overpressure. For a long duration or step incident wave, the transmitted wave is always peaked close to the area change,

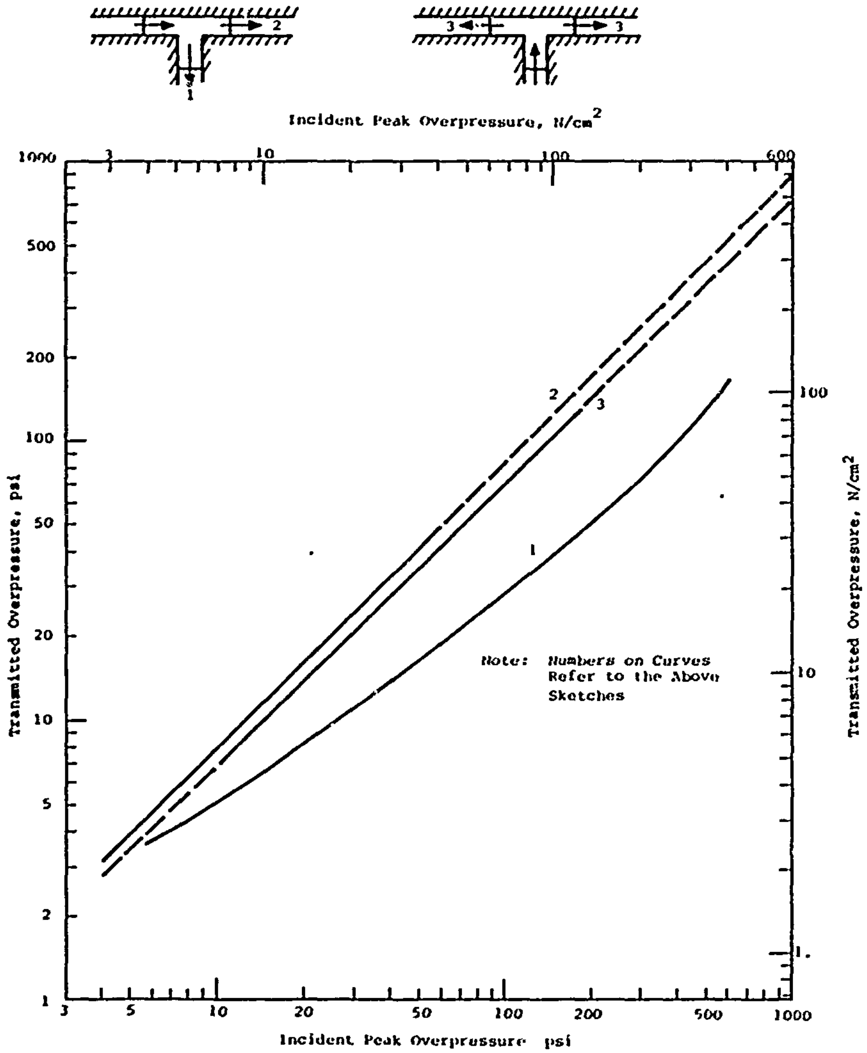

Figure 11-3 Transmitted vs. Incident Peak Overpressure for Equal Area T-Shaped Sections

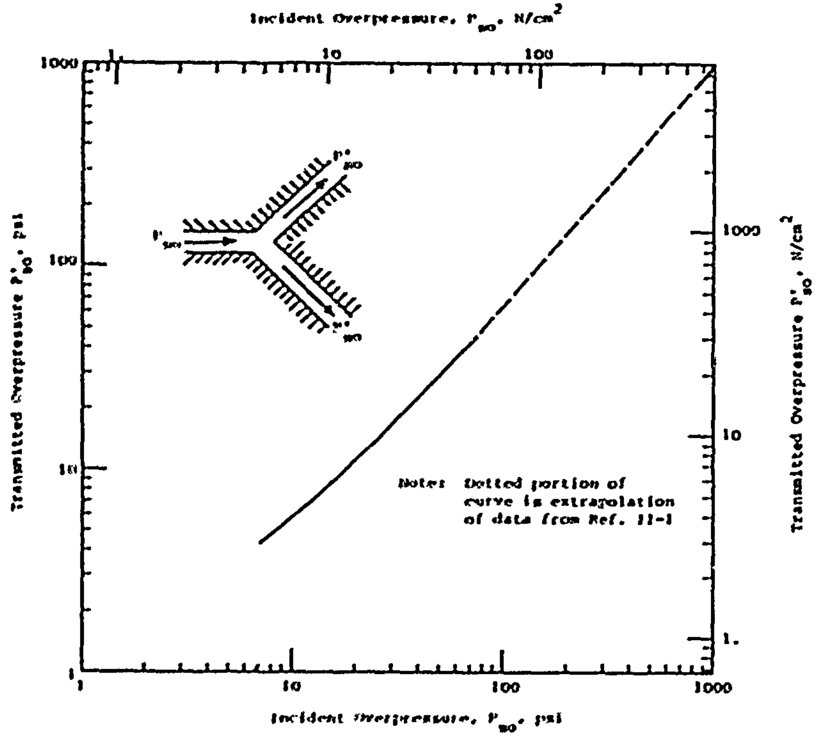

Note: Dotted portion of curve is extrapolation of data from Ref. 11-1

Figure 11-4 Incident vs. Transmitted Overpressure for Y Configuration (Ref. 11-1)

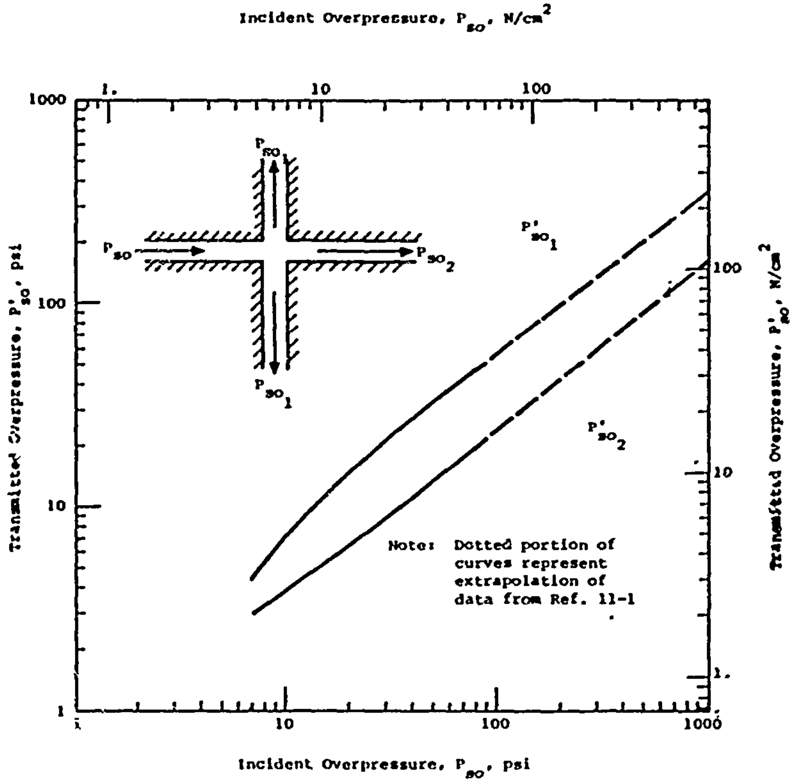

Note: Dotted portion of curves represent extrapolation of data from Ref. 11-1

Figure 11-5 Incident vs. Transmitted Overpressure for a Cross Configuration (Ref. 11-1) but after several diameters of the new increased area, the wave tends to flatten out. In all cases, the strength of the wave decreases after passing into a larger tunnel area.

If the flow behind the incident wave is initially supersonic--that is, greater than about 56 psi (38.6 N/cm^2)--a shock is transmitted and an upstream-facing shock forms in the transition section or is swept downstream into the larger area, depending on the area ratio and the strength of the incident wave. The upstream-facing shock formed by the expansion affects the pressure-time history close to the transition section. The transmitted overpressure shown in Fig. 11-6 occurs several diameters downstream of the transition where the peak has disappeared and the wave again flattens out.

Shock tube experiments show that the ratio of incident pressure to transmitted pressure is dependent only on the incident pressure ratio and the area ratio. The diameter of the small and large tunnels does not affect the results, provided that the area ratio is kept constant.

h. Shock Wave Filling of Chambers

A shock wave impinging on a chamber entrance produces two distinct processes in the chamber. First, a shock emerges from the entrance and expands as a hemispherical front. The peak overpressure of this front will depend on many factors including the size and shape of the entrance, shape and size of the chamber, and peak overpressure of the incident wave. Reflections inside the chamber might cause the chamber overpressure to exceed that incident on the entrance.

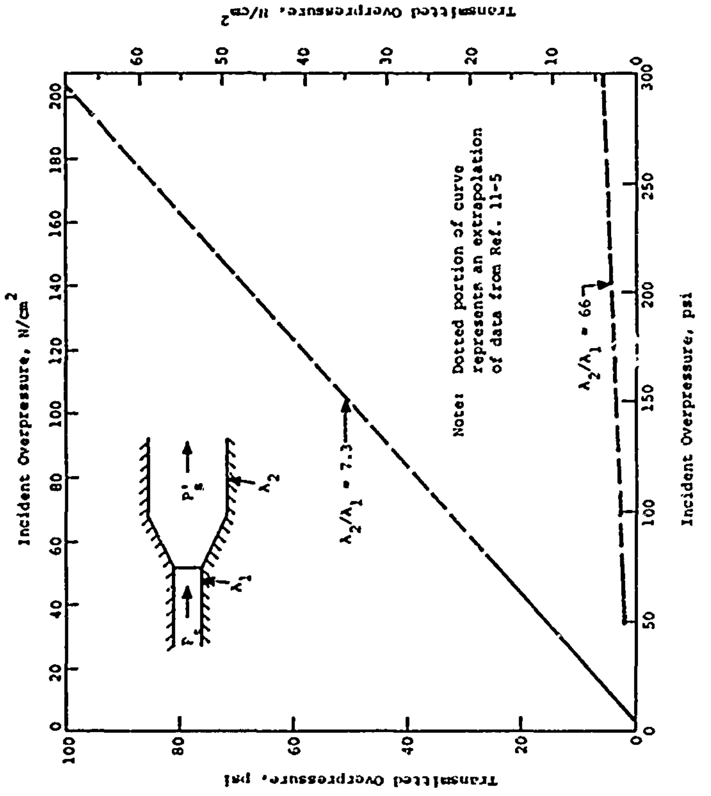

Figure 11-6 Incident Overpressure vs. Transmitted Overpressure for a Tunnel with an Area Increase (Ref. 11-5)

The second process is the quasi-steady flow which continues to increase the static pressure in the chamber until it equals the incident pressure at some later time.

Reference 11-5 describes a simple technique for determining the fill rate in a chamber for incident overpressures up to 150 psi (103 N/cm^2) using the equation

$$\Delta P_c = C_p \Delta t (A/V) \qquad (11\text{-}7)$$

where

ΔP_c = the change in chamber pressure over time interval Δt

C_p = an experimentally determined coefficient

A = area of the entrance to the chamber

V = volume of the chamber

The procedure consists of incremental calculation of the increase in chamber pressure using Eq. 11-7 with the coefficient C_p selected from Fig. 11-7 on the basis of the pressure differential inside and outside the chamber. The first step is to plot the pressure-time history of the wave incident on the chamber entrance. This pressure-time history is then divided into equal time increments, Δt. At time $t = 0$, the pressure differential will be equal to P_{so}, the peak overpressure incident on the entrance. A value of C_p is selected from Fig. 11-7 based on this pressure differential and a ΔP_c is computed using Eq. 11-7. This ΔP_c is added to the overpressure in the chamber at $t = 0$ and a new pressure differential calculated. In calculating the new pressure differential, account must be taken of the decay in incident overpressure, P_{so}, during the interval Δt. With a new C_p based on the new

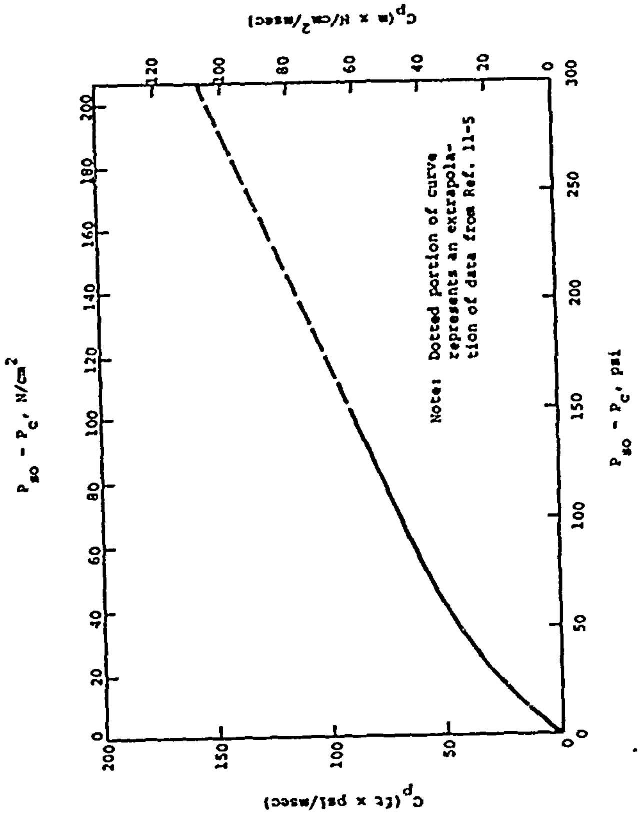

Figure 11-7 C_p vs. Pressure Differential Between Incident Wave and Chamber (Ref. 11-5) pressure differential, a second value of ΔP_c is calculated from Eq. 11-7. This new ΔP_c is added to the previous chamber overpressure, and the process is repeated for all the time intervals. The results of the above computations can be plotted to obtain a curve showing the pressure-time history inside the chamber. When the pressure differential $(P_{so} - P_c)$ becomes negative, the value of C_p should also be taken negative, so that ΔP_c is negative, resulting in a decrease in chamber pressure.

The results of an example chamber-filling problem from Ref. 11-5 are shown in Fig. 11-8 for an incident pressure wave with $P_{so} = 20$ psi (13.8 N/cm^2) and $t_o = 1.0$ sec. The example entrance area to chamber volume ratio (A/V) used for 0.01 and the time increment, Δt, was 0.025 sec.

For situations not adequately covered by the simplified procedure outlined above, the method reported in Ref. 11-6 may be used. The procedure in Ref. 11-6 considers entrance ducts of finite length, multiple entrances and exits, and includes a more rigorous treatment of the gas dynamics phenomena than the simplified method outlined above.

i. Example

To illustrate some of the procedures outlined above, consider the system shown in Fig. 11-9 subjected to a peak overpressure of 1000 psi (690 N/cm^2) from a 1 MT (4.2 x 10^{15}j) surface burst. As shown, the airblast wave is oriented side-on to the entrance to the system. Find the peak overpressures at pertinent points in the system and the time of arrival at the entrance to the capsule.

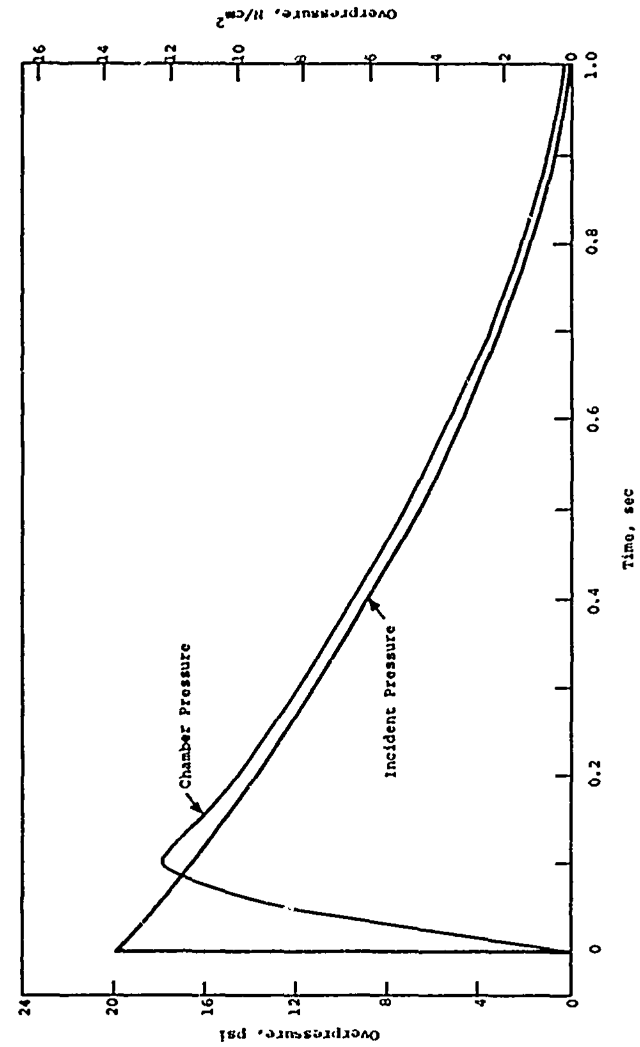

Figure 11-8 Typical Incident and Chamber Pressure-Time Histories (Ref. 11-5)

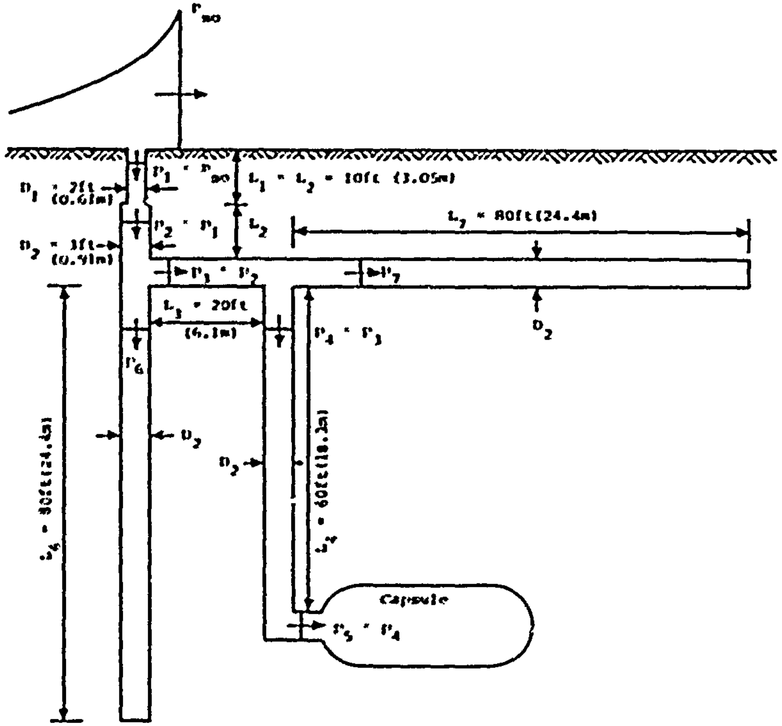

Figure 11-9 Example Air Entrainment System

The first step is to determine if the incident blast wave satisfies the criterion of Eq. 11-3. From Fig. 3-5 the positive phase duration for 1000 psi from a 1 MT surface burst is $t_o = 1.2$ sec; take c_o = 1100 fps (335 mps). For the curves previously given to be valid,

$$t_o \text{ must be } \gtrsim \frac{25D_1}{c_o}$$

or

$$t_o \gtrsim \frac{25(2.0)}{1100} = 0.045 \text{ sec}$$

so the criterion is satisfied.

For 1000 psi incident side-on at the entrance, Fig. 11-1 indicates a peak pressure of about 260 psi inside the system entrance. Thus

$$P_1 = 260 \text{ psi } (179 \text{ N/cm}^2)$$

$$U_1 = 4400 \text{ fps } (1340 \text{ mps}) \text{(Fig. 3-11)}$$

A calculation with Eq. 11-4 will show that attenuation in the straight sections of the system will be negligible for the lengths involved in this example.

A reduction in peak pressure will occur at the change in system diameter. The ratio of the areas is proportional to

$$\left(\frac{D_2}{D_1}\right)^2 = \left(\frac{3}{2}\right)^2 = 2.25$$

Figure 11-6 shows pressure ratios for an area ratio of 7.3. For an area ratio of 1 (no change in area), the peak pressure would not change. For these two limits, the pressures past the transition section would be

$p_2 = 88$ psi (60.7 N/cm^2) (for $A_2/A_1 = 7.3$)

$p_2 = 260$ psi (179 N/cm^2) (for $A_2/A_1 = 1.0$)

Interpolate between these two values to obtain a rough estimate for $A_2/A_1 = 2.25$

$$p_2 \approx 260 - \left(\frac{2.25 - 1.0}{7.3 - 1.0}\right)(260 - 88) = 226 \text{ psi } (156 \text{ N/cm}^2)$$

$U_2 = 4200$ fps (1280 mps)

At the first intersection, the pressures in each branch are obtained from Fig. 11-3.

$p_3 \doteq 58$ psi (40.0 N/cm^2)

$U_3 = 2300$ fps (701 mps)

$p_6 \doteq 200$ psi (138 N/cm^2)

$U_6 = 3900$ fps (1190 mps)

At the second intersection, Fig. 11-3 is again applicable and

$p_4 \doteq 18$ psi (12.4 N/cm^2)

$U_4 = 1600$ fps (488 mps)

$p_7 \doteq 48$ psi (33.1 N/cm^2)

$U_7 = 2200$ fps (670 mps)

At the turn near the capsule, Eq. 11-6 is applicable.

$p_5 = 18(0.94)^1 = 16.9$ psi (11.7 N/cm^2)

Thus for 1000 psi (690 N/cm^2) incident on the entrance, only about 16.9 psi (11.7 N/cm^2) is indicated at the capsule. Since losses in the straight sections were neglected, the actual pressure might be even less. The pressure loss at the expansion section is also probably greater than that estimated by the simple interpolation.

The time of arrival of the first shock $p_5 \sim 16.9$ psi (11.7 N/cm^2) at the capsule can be estimated as

$$t_a \doteq \frac{L_1}{U_1} + \frac{L_2}{U_2} + \frac{L_3}{U_3} + \frac{L_4}{U_4}$$

$$= \frac{10}{4400} + \frac{10}{4200} + \frac{20}{2300} + \frac{60}{1600} \approx 0.051 \text{ sec } (51 \text{ ms})$$

Consider now the pressure p_6. This shock should reach the bottom of duct L_6 at about

$$t_a \doteq \frac{L_1}{U_1} + \frac{L_2}{U_2} + \frac{L_6}{U_6} = \frac{10}{4400} + \frac{10}{4200} + \frac{80}{3900}$$

$$= 0.025 \text{ sec } (25 \text{ ms})$$

If it were assumed that p_6 shocked up to $p_{6r} \approx 1200$ psi $= 826$ N/cm^2 (see Fig. 7-3) and that p_{6r} propagated at $U_{6r} = 1500$ fps (457 mps) as indicated in Fig. 7-16, this shock would reach duct L_3 at about

$$t = 0.025 + \frac{L_6}{U_{6r}} = 0.025 + \frac{80}{1500} = 0.078 \text{ sec } (78 \text{ ms})$$

Since $p_{6r} > p_{so}$, it would not appear unreasonable to expect p_{6r} to begin to vent to the atmosphere.

Extrapolating Curve 1 in Fig. 11-3 for $p_{6r} = 1200$ psi

$p_3' \doteq 500$ psi (345 N/cm^2)

$U_3' = 5800$ fps (1770 mps) (Fig. 3-11)

Similarly,

$p_4' \sim 100$ psi (69 N/cm^2)

$U_4' = 2900$ fps (885 mps)

and $p_5' \doteq 100(0.94)^1 = 94$ psi (64.9 N/cm^2). The arrival time of this second shock could be estimated at

$$t_a \approx 0.078 + \frac{L_3}{U_3'} + \frac{L_4}{U_4'} = 0.078 + \frac{20}{5800} + \frac{60}{2900}$$

$$= 0.099 \text{ sec (99 ms)}$$

Based on the greatly oversimplified investigation above, then, it would appear that a second shock 5 times stronger than the first might reach the capsule about 50 ms after the first shock arrival. The behavior of the shock p_7 in duct L_7 has not been looked at since it would appear to be less severe than the p_{6r} considerations. The pressure p_{7r} could conceivably work against p_3' and force an increase in beneficial venting to the atmosphere. In any event, it appears rather certain that a blast valve with considerable strength will be required at the capsule.

11.5.2 Utility Systems

The utility systems for protective structures are similar in most respects to those of any other type of facility. One important difference is the need for EMP protection for electrical systems in the majority of cases. Inadequate attention to details of utility connections can seriously degrade and perhaps negate an otherwise effective EMP shielding system. References 11-7 and 11-8 contain many suggestions for decreasing the vulnerability of a facility to EMP.

Although utility systems for protective structures are similar to those for conventional facilities, there are some aspects which require special treatment. Included are the following.

- Obviously all vital utility connections to protective structures should be underground because of the low airblast resistance of aboveground systems.
- Exterior underground connections to a structure should be made at a point of least relative motion between the soil and the structure. In most cases, this will be a point near the bottom of the structure. Special connectors are provided in some installations to increase the strength of electrical and communication cables at these points.
- Electrical and communications cables should be laid with sufficient slack to accomodate ground motions without failure.
- Supports for utility systems should be spaced close enough to prevent failure of cables and conduits when subjected to acceleration forces.
- Brackets and trays supporting cables and conduits on the interior of structures should be designed to resist the acceleration forces generated by structure motions.
- Utility connections to shock mounted items must possess sufficient slack or flexibility to accomodate relative displacements without failing.
- Utilities must not infringe upon rattlespace around shock mounted items.
- All components may be subjected to large accelerations and if not able to withstand these accelerations they must be ruggedized or shock isolated.

11.5.3 Structural Details

The structural elements in protective structures are assumed to be capable of developing their fully plastic resistance and exhibiting ductile rather than brittle behavior. In order to assure that these elements behave as expected, it is sometimes necessary to examine structural details which under normal circumstances might be of minor importance.

The need for ductility in protective structures has been discussed in several sections of this manual. The limits recommended in *Section VIII* on percent tension reinforcing in reinforced concrete members should assure ductile response of such members. It is suggested that at least 0.5 percent reinforcing be provided in each face of all flexural members. Continuity of reinforcement is assured by adequate lapping, welding or other acceptable splicing technique. Welding should not be considered for steels with carbon contents in excess of 0.35 percent without proof that the welding techniques do not adversely affect the properties of the steel. The location of splices in tension reinforcing should be staggered to avoid creation of planes of weakness in the member. Web reinforcing should be placed perpendicular to the axis of the member so that planes of weakness are not formed in the event of a reversal of load. Hoop ties (those which encircle both tension and compression steel) are effective restraints of bars in compression and should not be spaced greater than 0.5 times the effective depth of the section. Columns reinforced with continuous spirals will normally exhibit greater ductility than those using conventional ties. When heavy concentrations of longitudinal reinforcing are required, particularly in the vicinity of lap splices, adequate transverse reinforcement (ties, stirrups, or transverse bars) should be provided to prevent bond failure by splitting of the concrete. For this reason, lapped splices should be avoided in regions of high tensile stresses in the steel. When mounting plates for items of equipment are embedded in concrete sections, they should be tied to the main reinforcement by welding or hooks.

Steel structures will normally exhibit considerable ductility simply because of the stress-strain properties of structural steel. Failure of connections and buckling of members can, however, cause failures before fully plastic strengths are realized. Weldable steel should be specified and welded joints should be designed to provide proper continuity and minimize stress concentrations. Wherever possible, compression members should be restrained against end rotations about both axes. Web and flange stiffeners can significantly reduce the possibility of local failures at junctures between members. Width-to-thickness ratios for flanges of compression members which should not be exceeded if local buckling is to be avoided are presented in Section VIII.

11.6 REFERENCES

11-1 Information Summary of Blast Patterns in Tunnels and Chambers (Second Edition), Memorandum Report No. 1390, Aberdeen Proving Ground, Md., March 1962. (U)

11-2 Swatosh, J.J., and Birukoff, R., Blast Effects on Tunnel Configurations, AFSWC TR 59-48, Air Force Special Weapons Center, Kirtland AFB, N.M., October 1959. (U)

11-3 Clark, R.O., Theory for Viscous Attenuation in Ducts Based on the Kinetic Theory of Gases Experimentally Verified to a Shock Strength of 68, AFWL TR 65-204, Air Force Weapons Laboratory, Kirtland AFB, N.M., July 1966. (U)

11-4 Clark, R.O., and Coulter, G.A., Attenuation of Air Shock Waves in Tunnels, BRL 1278, Ballistic Research Laboratories, Aberdeen Proving Ground, Md., June 1960. (U)

11-5 Hallanger, L.W., Blast Attenuation Systems for Ventilation Openings (U), R 475, U.S. Naval Civil Engineering Laboratory, Port Hueneme, Calif., September 1966. (OUO)

11-6 Clark, R.O., and McMurtry, W.M., Shock Wave Filling of Chambers, AFWL-TR-70-73, Air Force Weapons Laboratory, Kirtland AFB, N.M., September 1970. (U)

11-7 EMP Threat and Protective Measures, TR-61, Department of Defense, Office of Civil Defense, Washington, D.C., August 1970. (U)

11-8 EMP Protective Systems, TR-61B, Department of Defense, Office of Civil Defense, Washington, D.C., November 1971. (U)

DISTRIBUTION

OF ORIGINAL PRINTING

No. Cys	
	Hq USAF, Wash, DC 20330 [Headquarters United States Air Force]
1	(SAMI) [Study Information Service]
1	(PRE) [Director, Civil Engineering]
1	(PREE) [Engineering Division]
1	(PREV) [Environmental Protection Group]
1	(PREPB) [Military Construction Branch]
1	(RDPQ, 1C370) [Test Support Division]
1	(RDQPN, 1D425) [Nuclear Programs Division; 1 cy only]
1	(RDQS) [Deputy Director, Strategic Forces]
1	(XOOWD) [Deputy Director, Operational Test and Evaluation, Test Analysis and Evaluation Division]
1	Hq USAF, AFTAC, Patrick AFB, FL 32925 [Air Force Technical Applications Center]
1	AFCEC (PREC), Tyndall AFB, FL 32401 [Air Force Civil Engineering Center]
	*AFISC, Norton AFB, CA 92409 [Air Force Inspection and Safety Center]
1	(PQAL) [Technical Library]
1	*Dir Nuc Safety (SN), Kirtland AFB, NM 87117 [Director of Nuclear Safety]

MAJOR AIR COMMANDS

No. Cys	
	AFSC, Andrews AFB, Wash, DC 20334 [Air Force Systems Command]
1	(DO) [DCS/Operations]
1	(DOB) [Civil Engineering]
1	(DLSP) [Physical and Sciences Division]
1	(XRP) [Programs]

DISTRIBUTION (cont'd)

No. Cys	
	TAC, Langley AFB, VA 23365 [Tactical Air Command]
1	(DEE) [Directorate, Engineering and Construction]
1	(LGMD) [Weapon Systems Development Division]
	CINCSAC, Offutt AFB, NE 68113 [Strategic Air Command]
1	(DEE) [Directorate, Engineering and Construction]
1	(DOXS) [Simulation and Analysis Division; 1 cy only]
1	(XPFC) [Director, Future Systems]
	ADC, Ent AFB, CO 80912 [Aerospace Defense Command]
2	(DOA) [Office of Operations Analysis]
1	(XPQDQ) [Advanced Planning Division] ATTN: Maj G. Kuck
1	(XPXY) [Systems Simulation; nuclear effects and laser reports]
1	AUL (LDE), Maxwell AFB, AL 36112
1	AU (ED, Dir, Civ Eng), Maxwell AFB, AL 36112 [Air University; DCS/Education, Director, Civil Engineering]
	AAC, APO Seattle 98742 [Alaskan Air Command]
1	(DEE) [Directorate, Plant Engineering] ATTN: LtCol R. Hirth
	AFIT, Wright-Patterson AFB, OH 45433 [Air Force Institute of Technology]
1	(Tech Lib, Bldg 640, Area B) [Technical Library]
1	(CES) [Civil Engineering School]
	CINCUSAFE, APO New York 09012 [United States Air Forces in Europe]
1	(DOA) [Operations Analysis]
	CINCPACAF, APO San Francisco 96553 [Pacific Air Forces]
1	(DOA) [Director, Operations Analysis]

DISTRIBUTION (cont'd)

No. Cys	
	USAFA, CO 80840 [United States Air Force Academy]
1	(DFSLB) [Director of Library; <u>NO</u> classified reports]
3	(DFCE) [Department of Civil Engineering]
	NUMBERED AIR FORCES
	5 AF, APO San Francisco 96525
1	(DEE) [Director, Civil Engineering]
	7 AF, APO San Francisco 96310
1	(DEE) [Director, Civil Engineering]
	13 AF, APO San Francisco 96274
1	(DEE) [Director, Civil Engineering]
	AFSC ORGANIZATIONS
	ARL, Wright-Patterson AFB, OH 45433 [Aerospace Research Laboratory; <u>NO</u> classified reports]
1	(STINFO Ofc)
	AFML, Wright-Patterson AFB, OH 45433 [Air Force Materials Laboratory]
1	(Tech Lib) [Technical Library]
	AFFDL, Wright-Patterson AFB, OH 45433 [Air Force Flight Dynamics Laboratory]
1	(Lib) [Library]
1	(STINFO Ofc)
1	(FB/ATTN: Lt Col G. Leigh)

DISTRIBUTION (cont'd)

No. Cys	
	SAMSO, P. O. Box 92960, WWPC, Los Angeles, CA 90009 [Space and Missile Systems Organization; Worldway Postal Center]
1	(Tech Lib) [Technical Library]
1	(DEN) [Civil Engineering, Plant Engineering]
	ESD, L.G. Hanscom Fld, Bedford, MA 01730 [Electronic Systems Division]
1	(DEE) [Civil Engineering]
	ADTC, Eglin AFB, FL 32542 [Armament Development and Test Center]
1	(Tech Lib) [Technical Library]
	RADC, Griffiss AFB, NY 13441 [Rome Air Development Center]
1	(Doc Lib) [Document Library]
	KIRTLAND AFB ORGANIZATIONS
	AFSWC, Kirtland AFB, NM 87115
1	(HO) [Historian; 1 cy ALL reports]
	AFWL, Kirtland AFB, NM 87117 [Air Force Weapons Laboratory]
5	(SUL) [Technical Library]
5	(DE) [Civil Engineering Research Division]
}50	(DEV) [Facility Survivability Branch]
5	(DEX) [Experimental Branch]
5	(DEZ) [Aerospace Facilities Branch]
1	(DYT) [Theoretical Physics Branch]
5	(SA) [Analysis Division]
1	(IN) [Foreign Technology Office]
1	Commander, Field Command, DNA, ATTN: Capt T. Edwards, Kirtland AFB, NM 87115
	OTHER AIR FORCE AGENCIES
1	AFOSR, 1400 Wilson Blvd, Arlington, VA 22209 ATTN: W. Walker

---

DISTRIBUTION (cont'd)

No. Cys	
1	USAF Reg Civ Eng, 526 Title Bldg, Atlanta, GA 30303 [USAF Regional Civil Engineer--Eastern Region]
1	USAF Reg Civ Eng, 630 Sansome St, San Francisco, CA 94111 [USAF *Regional Civil Engineer--Western Region*]
1	USAF Reg Civ Eng, 1114 Commerce St, Dallas, TX 75202 [USAF Regional Civil Engineer--Central Region]
	ARMY ACTIVITIES
1	Comdg Off, Diamond Lab (Lib), Wash, DC 20438 [Harry Diamond *Laboratory, Library; 1 cy only*]
1	Comdg Off, USACDC, Inst Nuc Stud, Ft Bliss, TX 79916 [US Army Combat Developments Command, Institute for Nuclear Studies]
1	Dept Army NIKE-X Fld Ofc (AMCPM-NXE-FB), Bell Tel Lab, Whippany, NJ 07981 [US Army NIKE-X Field Office, Bell Telephone Laboratory]
	Comdg Off, BRL, Aberdeen Pvg Gnd, MD 21005 [Ballistic Research Laboratory]
1	(AMXBR-TB, J. Meszaros) [Library; 1 cy only]
1	Chief of Eng (ENGMC-EM), Dept Army, Wash, DC 20315 [Chief of Engineers, Department of the Army]
	Dir, USA Eng WW Exp Sta, P. O. Box 631, Vicksburg, MS 39181 [US Army Engineers Waterways Experiment Station]
3	(WESRL)
1	Teledyne Brown Engineering, 300 Research Park, Huntsville, AL 35810 ATTN: Dr. M. C. Patel
1	Dir, NSA (C513), Ft Meade, MD 20755 [National Security Agency; ALL TREES, EMP, WEBS reports]

DISTRIBUTION (cont'd)

No. Cys	
	NAVY ACTIVITIES
1	ONR, Dept Navy (Code 418), Wash, DC 20360 [Office of Naval Research, Field Projects Branch, Department of the Navy]
1	Dir, NRL (Code 2027), Wash, DC 20390 [Naval Research Laboratory, Technical Library]
1	*Comdr, NOL (Code 730), White Oak, Silver Spring, MD 20910 [Naval Ordnance Laboratory, Technical Library]
3	NCEL, Port Hueneme, CA 93041 [Navy Civil Engineering Laboratory]
1	*Comdg Off, NWEF (Code ADS), Kirtland AFB, NM 87117 [Naval Weapons Evaluation Facility]
	OTHER DOD ACTIVITIES
	Dir, DNA, Wash, DC 20305 [Defense Nuclear Agency; ALL DNA-funded reports]
2	(APTL) [Technical Library]
5	(SPSS)
2	(STAP)
	DDR&E, Wash, DC 20301
1	(Asst Dir, Strat Wpns) [Assistant Director, Strategic Weapons]
	Dir, DIA, Wash, DC 20305 [Defense Intelligence Agency; ALL DNA-funded reports].
1	(DIAAP-8B)
1	(DIAST-3)

DISTRIBUTION (cont'd)

No. Cys	
1	Dir, OSD, ARPA (NMR), 1400 Wilson Blvd, Arlington, VA 22209 [Director, Advanced Research Projects Agency, Nuclear Monitoring Research Office; ALL DNA-funded reports]
1	Comdr, FC DNA (FCSD-A4), Kirtland AFB, NM 87115 [Field Command, Defense Nuclear Agency; ALL DNA-funded reports; classified reports to FCSD-A2, Classified Control Branch]
1	Chief, LVLO (FCTD-N-DNA), P. O. Box 2702, Las Vegas, NV 98104 [Las Vegas Liaison Office; ALL DNA-funded reports]
1	JSTPS (JLTW), Offutt AFB, NE 68113 [Joint Strategic Target Planning Staff; ALL DNA-funded reports]
2	DDC (TCA), Cameron Sta, Alexandria, VA 22314 [Defense Documentation Center; ALL reports]
	AEC ACTIVITIES
1	Sandia Lab, Kirtland AFB, NM 87115 [Sandia Laboratories]
1	Dr. M. Merritt
	Dir Ofc, LLL, P. O. Box 808, Livermore, CA 94550 [Lawrence Livermore Laboratory; name of recipient must be noted on all classified reports]
1	(Tech Info Dept) [Technical Information Department]

DISTRIBUTION (cont'd)

No. Cys	
1	LLL (Lib), Bldg 50, Rm 134, Berkeley, CA 94720 [UNCLASSIFIED reports only]
1	Dir, LASL, P. O. Box 1663, Los Alamos, NM 87554 [Los Alamos Scientific Laboratory]
	OTHER
1	Bechtel Corporation, ATTN: P. L. Williams, P. O. Box 3965, San Francisco, CA 94119
1	6987 Security Sq (USAFSS), ATTN: Maj T. Jackson, APO San Francisco 96360
1	Director, ARPA, The Pentagon, ATTN: Dr. Stan Ruby (NMRO-RM, 3O170), Wash, DC 20315
	Physics International Company, 2700 Merced St, San Leandro, CA 94557
1	ATTN: Mr. Fred Sauer
1	ATTN: Dr. C. Godfrey
	TRW Systems, Inc., One Space Park, Redondo Beach, CA 90278
3	ATTN: Dr. P. Dai
	Holmes & Narver, Inc., 400 East Orangethorpe, Anaheim, CA 92801
1	ATTN: R. Kennedy
	The Boeing Company, P. O. Box 3707, Seattle, WA 98124
2	ATTN: Mr. Ron Carlson
	IIT Research Institute, 10 West 35th St, Chicago, IL 60616
1	ATTN: Library
	Aerospace Corporation, P. O. Box 95085, Los Angeles, CA 90045
1	ATTN: Library

DISTRIBUTION (cont'd)

No. Cys	
	TRW Systems Group, 600 E. Hill St, Bldg 527, Rm 710, San Bernardino, CA 92402
3	ATTN: Mr. Greg Hulcher
	Agbabian Associates, 250 N. Nash St., El Segundo, CA 90245
1	ATTN: M. Agbabian
	Applied Theory, Inc., 1010 Westwood Blvd, Los Angeles, CA 90024
1	ATTN: Dr. J. G. Trulio
1	Consulting and Special Engineering Services, Inc., P. O. Box 1206, Redlands, CA 92373
	The Rand Corporation, 1700 Main St, Santa Monica, CA 90406
1	ATTN: Library
	R&D Associates, P. O. Box 3580, Santa Monica, CA 90403
2	ATTN: Dr. H. Cooper
	Systems, Science and Software, P. O. Box 1620, La Jolla, CA 92037
1	ATTN: Library
	Weidlinger Associates, 110 East 59th St, New York, NY 10022
1	ATTN: Dr. M. Baron
	Director, U.S. Army Construction Engineering Research Lab, P. O. Box 4005, Champaign, IL 61820
1	ATTN: Library
1	ATTN: Dr. J. Prendergast
	Institute of Geophysics & Planetary Physics, University of California, Los Angeles, CA 90024
1	ATTN: Dr. Robert Post

DISTRIBUTION (cont'd)

No. Cys	
	US Army Cold Regions Research Lab, Hanover, NH 03755
1	ATTN: Mr. Scott Blouin
	McDonald Douglas Astro. Company, 5301 Bolsa Ave, Huntington Beach, CA 92647
1	ATTN: K. McClymonds
1	ATTN: K. Narasimhan
	University of Illinois, Urbana Campus, Dept of Civil Engineering, Urbana, IL 61801
1	ATTN: Dr. N. M. Newmark
1	ATTN: Dr. W. Hall
1	ATTN: Dr. J. Haltiwanger
	4756th CES, Tyndall AFB, FL 32401
1	ATTN: DEP/Maj J. Eddings
	Science Applications, Inc., 335 Jefferson S.E., Albuquerque, NM 87108
1	ATTN: Dr. Key Shunk
	7551 Combt Spt Group, Box 79, APO New York 09150
1	ATTN: Maj John C. Galloway
5	Civil Engineering Research Facility, Box 188, University Station, Albuquerque, NM 87103
3	Mechanics Research, Inc., 9841 Airport Blvd, Los Angeles, CA 90045
10	Civil Nuclear Systems Corp., 1200 University Blvd N.E., Albuquerque, NM 87102
	R. M. Parsons Company, 617 West Seventh Street, Los Angeles, CA 90017
1	ATTN: Mr. Herb Saffell

DISTRIBUTION (cont'd)

No. Cys	
	Army Engineer District, Huntsville, P. O. Box 1600 West Station, Huntsville, AL 35807
1	ATTN: HNDSE-R/Mr. Michael Dembo
1	Mr. Paul Smith, P. O. Box 3080, Charlottesville, VA 22903
	Braddock, Dunn and McDonald, Inc., 5301 Central Avenue N. E., Albuquerque, NM 87108
1	ATTN: Mr. George Pringle
1	Shock & Vibration Information Center, Naval Research Laboratory Code 8404, Washington, DC 20390
	Test Construction Division, P. O. Box 208, Mercury, NV 89023
1	ATTN: Lt Col Roy Goodwin
	IBM, 1701 North Ft. Myer Drive, Rosslyn, VA 22203
1	ATTN: Mr. Constantine T. Tsitsen
1	Jack Cahoon & Associates, 2400 Bob Wallace Ave., Huntsville, AL 35805
1	Official Record Copy (Dr. M. A. Plamondon, AFWL/DEV)

AFSC—Andrews AFB Md 1975